APPLICATIONS OF CO_2 IN HOMOGENEOUS CATALYSIS

Philip G. Jessop

Department of Chemistry, Queen's University, Kingston, ON, Canada

Introduction

Carbon dioxide can serve as a solvent for homogeneous catalysis but it is capable of much more. Over the past 4 years, we and others have shown that it can be used as an extractant for the removal of products from ionic or polymeric liquid solvents after homogeneous catalysis, as a modifier of liquid phase solvent properties, as an agent for accelerating solventless reactions of some solids, and as a trigger for partitioning and miscibility changes. All of these capabilities of CO_2 can be used to modify the selectivity, increase the turnover frequency, or achieve the recycling of homogeneous catalysts. In addition, of course, CO_2 can serve as a reagent. Our recent results in these areas will be presented.

Homogeneous Catalysis in Supercritical CO_2

Homogeneous catalysis has been performed in supercritical CO_2 ($scCO_2$)[1] since Kramer and Leder's isomerization experiments in the 1970's,[2] although most work in this area has been done since the mid 1990's.[3] Examples of increased rates[4,5] or selectivities[6] compared to those in liquid solvents have been observed. In many cases, catalyst solubility in $scCO_2$ was found to be insufficient, especially when triarylphosphine ligands were employed. This problem has been addressed by switching to trialkylphosphines[4] or by putting fluorinated groups on the meta or para positions of the triarylphosphines.[7] New data, obtained in collaboration with Beckman's group, will be presented showing that incorporation of ether or ester groups into the phosphines increases the solubility of the ligand in $scCO_2$. Solubility data comparing PPh_3 with electronically similar ligands containing heteroaromatic rings (e.g. structure **1**) or ester-containing substituents (e.g. structure **2**) will be presented.[8] On a weight fraction basis, both are significantly more soluble than PPh_3, while on a mole fraction basis ligand **1** has by far the greater solubility.

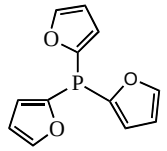

1

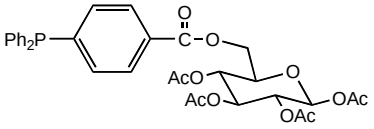

2

Biphasic Catalysis

Homogeneous catalysts are too expensive and often too toxic to be allowed to be lost in the product stream. Traditional methods for recovering the catalyst usually involve destroying the catalyst, but newer techniques including biphasic catalysis make it possible to recover the catalyst without damage. Biphasic catalysis involves two mutually immiscible fluids and relies on the catalyst partitioning exclusively into one phase (the catalyst-bearing phase) while the product partitions primarily into the other phase. Many systems of this type suffer from nonexclusive partitioning of the catalyst, leading to catalyst losses, and partial miscibility of the two fluid phases, leading to loss of one solvent in the other.

CO_2/Ionic Liquid Mixtures. Blanchard et al.[9] showed that a common ionic liquid, N,N-butylmethylimidazolium hexafluorophosphate ([bmim]PF_6]) is completely insoluble in $scCO_2$. The Jessop group showed that this fact, combined with the observation that heavy aromatic compounds (in analogy to asymmetric ligands of the BINAP type) partition essentially exclusively into the ionic liquid (IL) phase rather than the $scCO_2$ phase. This was the basis for a catalyst successful recycling scheme,[10] in which homogeneous catalysis was performed in an IL following which product was extracted by $scCO_2$, leaving behind a reusable catalyst solution in IL. The product could thus be obtained free of solvent or catalyst.

CO_2/Liquid Polymer Mixtures. The excellent performance of the CO_2/IL biphasic catalysis method encouraged further research in this area in the Jessop group, but it became obvious that the method could be improved by finding a cheaper replacement for the IL. The ideal replacement would be cheaper, halide-free and entirely nontoxic. PEG (poly(ethylene glycol)) was chosen, even though at room temperature it is a solid. PEG is nontoxic, very inexpensive, and able to dissolve catalyst precursors and organic substrates. The solubility of PEG in $scCO_2$ is very low, especially at molecular weights over 1000 g/mol. The fact that it is a solid at room temperature is less problematic than it sounds because a) the melting point is only 20-40˚C above room temperature, and b) the melting point of PEG is significantly lower in the presence of $scCO_2$. Early tests with a simple homogeneous hydrogenation showed that biphasic catalysis could be performed in the PEG/$scCO_2$ mixture, that the product could be easily extracted by the $scCO_2$, and that the catalyst solution could then be recycled multiple times.[11]

Continued work in this area involves the evaluation of several possible liquid polymers and other nonvolatile solvents. Some, such as glycerol and polyols, have been rejected because they are incapable of dissolving catalyst precursors and substrates. Others such as poly(dimethylsiloxane) and eicosane have been rejected because they are too soluble in $scCO_2$. Liquids that are currently being considered are shown in Figure 1. Their polarities are illustrated in Figure 2.

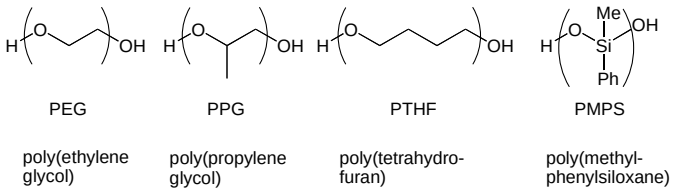

Figure 1. The structures of liquid polymers being considered as potential solvents for biphasic homogeneous catalysis.

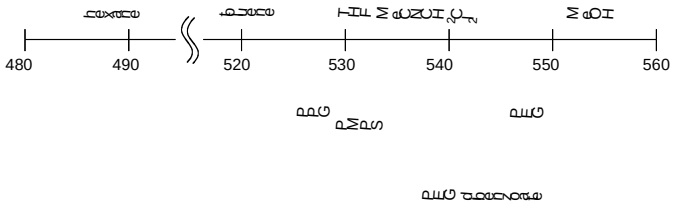

Figure 2. The polarity of liquid polymers compared to traditional liquid solvents, shown on a scale of Nile Red absorption maxima.

Obedient Catalysts and Solvents

Bergbreiter[12] introduced the idea of "smart" ligands or catalysts, meaning ligands or catalysts that change their nature or solubility when circumstances require it, without need for a signal from the human operator. In his work, the ligands formed complexes that had lower solubility at higher temperatures, so that if an exothermic reaction got carried away and the temperature rose as a result, the catalyst would automatically precipitate and thereby slow down the reaction.

In a collaboration between the Jessop group and the Eckert and Liotta groups at Georgia Tech., we have been exploring the possibility of designing "obedient" ligands and solvents, which reversibly change their nature upon receiving a signal or input from the human operator. For example, cyclohexane is fluorophobic (meaning that it can not dissolve highly fluorinated compounds) but cyclohexane with CO_2 dissolved therein (at >30 bar CO_2) is fluorophilic and therefore capable of dissolving fluorinated compounds[13] or being miscible with fluorinated liquids.[14] Thus cyclohexane is a very simple example of an obedient solvent with CO_2 dissolution as the trigger for the change. This fact was used as the basis for a method that causes an "obedient" catalyst to switch back and forth between being homogeneous and being heterogeneous. Powdered fluorous silica with a highly fluorinated catalyst precursor complex adsorbed on its surface is placed in a solution of substrate in cyclohexane. Dissolution of CO_2 into the cyclohexane triggers the extraction into solution of the catalyst from the silica, thereby allowing homogeneous catalysis to take place. After the reaction, the CO_2 pressure is released, triggering the redeposition of the catalyst back onto the silica, so that the catalyst becomes heterogeneous for the purposes of catalyst/product separation.

CO_2 as a Reagent or Substrate

Research by many groups has been directed at increasing the rate of reactions of CO_2 and increasing the range of reactions in which CO_2 acts as a reagent or substrate. Recent results in the Jessop group include the development of a facile method for combinatorial catalyst discovery for CO_2 fixation at high pressure,[15] and new or improved syntheses of formic acid,[15-18] formanilide,[19] carbanilide,[19] tetraalkylureas,[20] and carboxylic acids (in progress).

CO_2 in Other Roles

Carbon dioxide can assist homogeneous catalysis in many other ways. CO_2 dissolved in organic solvents lowers the melting point, viscosity, and polarity of the liquid phase and increases mass transfer rates and the solubility of reagent gases. These changes can directly affect rates and selectivities of catalysis.[16,21-26]

Carbon dioxide can also be used to accelerate solventless reactions of some solids,[27] by taking advantage of the melting-point lowering that occurs in the presence of CO_2. In a similar manner, the final yields of some reactions can be increased.

Carbon dioxide can also serve as an in-situ temporary protecting group, as reported by Leitner.[28]

Concluding Remarks

Although it is considered a waste material, CO_2 can be useful for the promotion of homogeneous catalysis in a wide variety of ways, not all of which have been presented here. In similar ways, CO_2 can promote other kinds of reactions; research in other groups continues along those lines. While it is not claimed that use of CO_2 in this manner will have any significant effect on the global warming problem, it is precisely the fact that CO_2 is a waste product that makes it inexpensive enough to be considered for some of these roles.

Acknowledgement. The author acknowledges the great assistance of his students, postdoctoral fellows, and collaborators (whose names appear in the references) and support from the Division of Chemical Sciences, Office of Basic Energy Sciences, U. S. Department of Energy (grant number DE-FG02-99ER14986) and from the Natural Sciences and Engineering Research Council, Canada. The author, Canada Research Chair in Green Chemistry, also acknowledges the support of the Canada Research Chairs program.

References

(1) Jessop, P. G.; Leitner, W., Eds. *Chemical Synthesis using Supercritical Fluids*; VCH/Wiley: Weinheim, 1999.
(2) Kramer, G. M.; Leder, F.; Exxon Research and Engineering Co.: U. S., 1975, p 5.
(3) Jessop, P. G.; Ikariya, T.; Noyori, R. *Chem. Rev.* **1999**, *99*, 475-493.
(4) Jessop, P. G.; Ikariya, T.; Noyori, R. *Nature* **1994**, *368*, 231-233.
(5) Kainz, S.; Brinkmann, A.; Leitner, W.; Pfaltz, A. *J. Am. Chem. Soc.* **1999**, *121*, 6421-6429.
(6) Burk, M. J.; Feng, S.; Gross, M. F.; Tumas, W. *J. Am. Chem. Soc.* **1995**, *117*, 8277-8278.
(7) Kainz, S.; Koch, D.; Baumann, W.; Leitner, W. *Angew. Chem., Int. Ed. Engl.* **1997**, *36*, 1628-1630.
(8) Ablan, C. D.; Jessop, P. G.; Beckman, E. *in preparation* **2003**.
(9) Blanchard, L. A.; Hancu, D.; Beckman, E. J.; Brennecke, J. F. *Nature* **1999**, *399*, 28-29.
(10) Brown, R. A.; Pollet, P.; McKoon, E.; Eckert, C. A.; Liotta, C. L.; Jessop, P. G. *J. Am. Chem. Soc.* **2001**, *123*, 1254-1255.
(11) Heldebrant, D. J.; Jessop, P. G. *J. Am. Chem. Soc.* **2003**, *125*, 5600-5601.
(12) Bergbreiter, D. E.; Zhang, L.; Mariagnanam, W. M. *J. Am. Chem. Soc.* **1993**, *115*, 9295-9296.
(13) Jessop, P. G.; Olmstead, M. M.; Ablan, C. D.; Grabenauer, M.; Sheppard, D.; Eckert, C. A.; Liotta, C. L. *Inorg. Chem.* **2002**, *41*, 3463-3468.
(14) West, K. N.; Bush, D.; Hallett, J. P.; Brown, J. S.; Liotta, C. L.; Eckert, C. A. In *Proceedings of the 2nd International Meeting on High Pressure Chemical Engineering*; Brunner, G., Ed.: Hamburg, Germany, 2001.
(15) Tai, C. C.; Chang, T.; Roller, B.; Jessop, P. G. *Inorg. Chem.* **2003**, *42*, 7340-7341.
(16) Thomas, C. A.; Bonilla, R. J.; Huang, Y.; Jessop, P. G. *Can. J. Chem.* **2001**, *79*, 719-724.
(17) Munshi, P.; Main, A. D.; Linehan, J.; Tai, C. C.; Jessop, P. G. *J. Am. Chem. Soc.* **2002**, *124*, 7963-7971.
(18) Tai, C. C.; Pitts, J.; Main, A. D.; Linehan, J.; Munshi, P.; Jessop, P. G. *Inorg. Chem.* **2002**, *41*, 1606-1614.
(19) Munshi, P.; Heldebrant, D.; McKoon, E.; Kelly, P. A.; Tai, C.-C.; Jessop, P. G. *Tetrahedron Lett.* **2003**, *44*, 2725-2727.
(20) Tai, C. C.; Huck, M. J.; McKoon, E. P.; Woo, T.; Jessop, P. G. *J. Org. Chem.* **2002**, *67*, 9070-9072.
(21) Combes, G. B.; Dehghani, F.; Lucien, F. P.; Dillow, A. K.; Foster, N. R. In *Reaction Engineering for Pollution Prevention*; Abraham, M. A., Hesketh, R. P., Eds.; Elsevier: Amsterdam, 2000, pp 173-181.
(22) Musie, G.; Wei, M.; Subramaniam, B.; Busch, D. H. *Coord. Chem. Rev.* **2001**, *219*, 789-820.
(23) Subramaniam, B.; Busch, D. H. In *Carbon Dioxide Conversion and Utilization*; Song, C., Gaffney, A. F., Fujimoto, K., Eds.; ACS: Washington, 2002, pp 364-386.
(24) Wei, M.; Musie, G. T.; Busch, D. H.; Subramaniam, B. *J. Am. Chem. Soc.* **2002**, *124*, 2513-2517.
(25) Sellin, M. F.; Webb, P. B.; Cole-Hamilton, D. J. *Chem. Commun.* **2001**, 781-782.
(26) Jessop, P. G.; Stanley, R.; Brown, R. A.; Eckert, C. A.; Liotta, C. L.; Ngo, T. T.; Pollet, P. *Green Chem.* **2003**, *5*, 123-128.
(27) Jessop, P. G.; DeHaai, S.; Wynne, D. C.; Nakawatase, D. *Chem. Commun.* **2000**, 693-694.
(28) Wittmann, K.; Wisniewski, W.; Mynott, R.; Leitner, W.; Kranemann, C. L.; Rische, T.; Eilbracht, P.; Kluwer, S.; Ernsting, J. M.; Elsevier, C. L. *Chem. Eur. J.* **2001**, *7*, 4584-4589.

Carbon dioxide as a solvent for synthesis and processing

Andrew B Holmes, Wilhelm T. S. Huck, Klaus Kahle, Connie K. Y. Lee, and Christine K. Luscombe

Melville Laboratory, Department of Chemistry, University of Cambridge, Lensfield Road, Cambridge CB2 1EW, United Kingdom

Abstract

Supercritical carbon dioxide is emerging as a potentially interesting solvent for synthesis and processing under environmentally benign conditions. In this paper we address three features of the use of carbon dioxide where the particular benefits of the solvent realise different consequences from those observed in conventional organic solvents.
We first examined the dipolar cycloaddition of nitrile oxides to alkenes and alkynes and show that the regiocontrol obtained can be tuned according to the solvent density. We then address the applications of the Suzuki cross-coupling reaction using a solid phase supported palladium catalyst to make conjugated aromatic materials. Extension to the use of conventional solvents allows the synthesis of CO_2-philic oligomeric fluorene derivatives. Finally, we demonstrate the patterned deposition of a fluorinated polymer onto a patterned silicon wafer substrate.

Nitrile Oxide Cycloadditions in Supercritical Carbon Dioxide

Apart from the Diels-Alder reaction,[1, 2] there has been little reported on cycloaddition chemistry in $scCO_2$. 1,3-Dipolar cycloadditions are an important class of cycloadditions, typically giving rise to 5-membered heterocycles, many of which are of pharmaceutical interest. In the present study, eactions of nitrile oxides and olefins were examined in $scCO_2$. The scope of nitrile oxide cycloadditions in $scCO_2$ was exemplified in high yielding reactions of mesitonitrile oxide with numerous alkenes and alkynes bearing various functional groups.

Synthesis of fluorine-containing polyfluorenes

Many factors determine whether or not a polymer shows solubility in liquid or supercritical CO_2. Amongst them are the polymer backbone architecture, the amount and the nature of CO_2-philic groups and the distribution of such groups within the polymer. In order to find the optimal structure of a CO_2 soluble polyfluorene and its content of CO_2-philic fluorine, the first aim was to synthesise a range of homo- and copolymers with various degrees of fluorination and then carry out solubility tests in supercritical carbon dioxide. While one possibility of varying the fluorine content is altering the length of the fluorinated side chain, another approach is the synthesis of copolymers containing fluorinated as well as non-fluorinated units (Fig. 2).

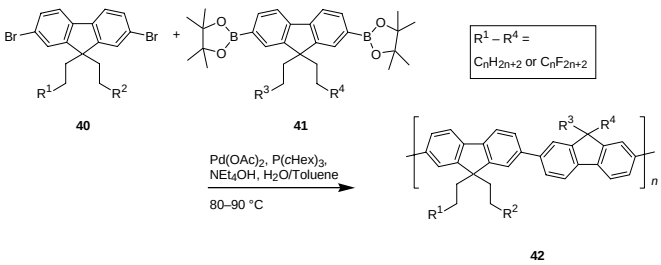

Fig. 1: Synthesis of partially fluorinated polyfluorenes **42** by Suzuki polymerization.

The polymerization reactions were carried out under the conditions optimized for the synthesis of alkyl substituted polyfluorenes. The polymers produced in this way were quite soluble under the reaction conditions if they contained at least 25% of non-fluorinated alkyl substituents. Any higher degree of fluorination led to the precipitation of polymer that then proved insoluble in all common solvent. A possible reason for the lack of solubility of the polymers is a high degree of crystallinity caused by interactions of the fluorinated side chains as well as the stiffness of the polymer. In order to make the polymers more flexible, a series of linkers was introduced into the backbone. Since these linkers break down the conjugation of the resulting polymers, it is important that a minimum conjugation length is maintained to allow efficient electroluminescence. This work shows sufficient promies to justify further research.

Patterned Deposition in sc Carbon Dioxide

Considerable progress has been made in recent years in using compressed CO_2 for deposition of fluorinated coatings on surfaces . One particularly attractive application is in advanced photolithography where there has been much interest in submicron feature sizes using fluoropolymers which are transparent at 157 nm. A preliminary study into the potential use of compressed CO_2 as an alternative solvent for inkjet printing is presented. This technique should have many applications in the deposition of organic and polymeric materials for optoelectronic devices. Preliminary results were carried out using a 10 cm^3 stainless steel high pressure reaction vessel equipped with a sapphire window.

Typical procedure for deposition of a polymer in CO_2 onto a patterned Si wafer

A solution of fluorolink® in compressed CO_2 was prepared in a 500 cm^3 reaction vessel as follows. Fluorolink® (0.5 g) was charged into the vessel and then sealed. Liquid carbon dioxide was withdrawn from a supply cylinder (BOC, CP grade; 99.995%), passed through the chiller (2) and compressed by the air driven liquid piston pump (Haskell MCPV-71). The chiller was required to avoid cavitation of the pump. The CO_2 stream was then heated to the desired conditions by the use of heat exchanger and directed to the reaction vessel.

The pressure was raised by the pump to 100 bar and maintained at this condition by the back pressure regulator (Go Products, Model PR-57). The vessel was located within an insulated air bath, which was maintained at a constant temperature of 35°C (±0.1 ºC) during the process. The temperature was recorded using type K thermocouples (RS Electronics) encased in 316 stainless steel and displayed on a temperature indicator (T200, RS Electronics). The pressure was measured by a pre-calibrated pressure transducer and a dedicated indicator (Druck PTX 52100 and DPI 262, respectively), which had an accuracy of ±0.3 %. After a short equilibration time (10 mins) in which the polymer became solubilized in the CO_2, the cell was vented via a heated nozzle (length 10 cm; diameter 127 m) and the contents were delivered onto a patterned Si wafer which was held at a distance (*d*) 3 cm away from the nozzle outlet for a period of 30 s. Pressure drop within the vessel during spraying was minimized by increasing the stroke rate of the piston pump to maintain the pressure within the system. The patterned Si wafer was prepared using UV mask lithography on alkyltrichlorosilane self-assembled monolayers (SAMs) at the Base Technology Centre, Seiko-Epson, Suwa, Japan.

The following parameters were altered in order to obtain the best results for deposition: the polymer {poly(1*H*,1*H*,2*H*,2*H*-perfluorooctyl acrylate), poly(1*H*,1*H*,2*H*,2*H*-perfluorooctyl methacrylate) and Fluorolink®}, the solution concentration (0.02 - 0.1 wt%), temperature within the reaction vessel (25 – 35 °C), time for deposition (5 – 30 s), the nozzle temperature during deposition (25 – 35 °C), nozzle dimensions (length 5 – 10 cm; diameter 127 m) and finally the distance (*d*) from nozzle outlet to wafer (3 – 10 cm).

Our results suggest that better patterns are observed after deposition by using more concentrated solutions at 35 °C, lowest possible nozzle diameter and nozzle lengths of 10 cm. Under these conditions we were able to obtain good resolution with 5 m dot sizes. Improved deposition also occurred when the distance between the Si wafer and the nozzle was reduced. At lower temperatures precipitation of the polymer occurred at the tip of the nozzle. Increasing the nozzle temperature reduced the amount of precipitation. When nozzles with a larger capillary diameter were used, the polymer was deposited unevenly leading to poor pattern replication. Similarly when the distance between the wafer and nozzle was increased, poor pattern replication was observed. Improved deposition was achieved when the duration of the experiment was extended to 30 s. This is presumably due to the improved mass transfer from the solution onto the wafer allowing a more even distribution of the polymer solution.

References

(1) Renslo, A. R.; Weinstein, R. D.; Tester J. W.; Danheiser, R. L. *J. Org. Chem.*, **1997**, *62*, 4530. *(b)* Weinstein, R. D.; Renslo, A. R.; Danheiser, R. L.; Harris, J. G.; Tester, J. W. *J. Phys. Chem.*, **1996**, *100*, 12337. *(c)* Weinstein, R. D.; Renslo, A. R.; Danheiser, R. L.; Tester, J. W. *J. Phys. Chem. B*, **1999**, *103*, 2878.

(2) Clifford, A. A.; Pople, K.; Gaskill, W. J.; Bartle, K. D.; Rayner, C. M. *J. Chem. Soc., Chem. Commun*., **1997**, 595. (*b*) Clifford, A. A.; Pople, K.; Gaskill, W. J.; Bartle, K. D.; Rayner, C. M. *J. Chem. Soc., Faraday Trans*., 1998, **94**, 1451.

THE COUPLING OF EPOXIDES AND CARBON DIOXIDE IN THE PRESENCE OF HOMOGENEOUS TRANSITION-METAL CATALYSTS. PRODUCTION OF POLYCARBONATES *VS* CYCLIC CARBONATES

Donald J. Darensbourg, Ryan M. Mackiewicz, Andrea L. Phelps, and Jody L. Rodgers

Texas A&M University, Department of Chemistry,
College Station, TX 77843

Introduction

Over the past decade a variety of efficient homogeneous catalysts or catalyst precursors have been developed to couple the thermodynamically stable carbon dioxide molecule with highly reactive substrates. One of the most promising processes involves the coupling of carbon dioxide and epoxides to afford cyclic carbonates or polycarbonates (eq. 1).[1] The production of polycarbonates from carbon dioxide and epoxides represents an environmentally benign synthetic route to these biodegradable thermoplastics which are mostly prepared by the interfacial polycondensation of diols and phosgene.[2]

Although we and others have made significant advances in the synthesis of these useful thermoplastics from carbon dioxide and epoxides much of the fundamental knowledge concerning the reaction kinetics of these processes is lacking, due in part to the practical challenges associated with sampling and analyzing systems at elevated temperatures and pressures. This information is needed for making this process applicable to the synthesis of a variety of copolymers possessing a range of properties and uses. Here, studies examining in detail the mechanistic aspects of metal catalyzed carbon dioxide/epoxide coupling reactions employing *in situ* infrared spectroscopic methods will be presented.[3] In addition, we have attempted to establish a clear mechanistic view of carbon-oxygen bond forming processes resulting from carbon dioxide insertion into M–O bonds using model organometallic derivatives.[4]

Experimental

Methods and Materials. All syntheses and manipulations were carried out on a double manifold Schlenk vacuum line under an argon atmosphere or in an argon filled glovebox. Glassware was flame dried before use. All solvents were freshly distilled prior to being used. Epoxides were purchased from Lancaster Synthesis and were distilled from calcium hydride. Catalysts were prepared by literature methods. Infrared spectra and kinetic measurements were monitored on ASI's ReactIR 1000 system equipped with a MCT detector and a 30 bounce SiCOMP in situ probe. ^{1}H and ^{13}C NMR spectra were recorded on Unity + 300 MHz or VXR 300 MHz superconducting high resolution spectrometers.

Copolymerization of Cyclohexene Oxide/Propylene Oxide and Carbon Dioxide. A weighed sample of the catalyst complex was dissolved in 20 ml of the appropriate epoxide. The solution was rapidly loaded *via* an injection port into a 300 mL stainless steel Parr autoclave that had been previously dried overnight at 80ºC under vacuum. The reactor was pressurized to 700 psi with CO_2, heated to the desired temperature and stirred for the required time period. After that time, the autoclave was cooled and the CO_2 vented into a fume hood. The reactor was opened and the polymer was isolated from the viscous/solid mixture by dissolution in small amounts of methylene chloride followed by precipitation from methanol.

High Pressure *in situ* Kinetic Measurements. High pressure reaction kinetics were carried out using a stainless steel Parr autoclave modified with a silicon probe to connect to the ASI ReactIR 1000 system (see Figure 1). The formation rates of the polycarbonate and the cyclic carbonate were monitored by following the ν(C=O) of the polycarbonate at ~1750 cm^{-1} and of the cyclic carbonate at ~1825 cm^{-1} (see Figure 2).

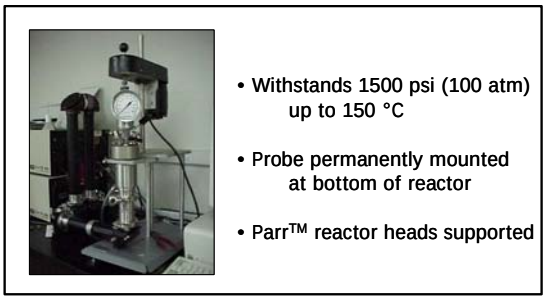

Figure 1. ASI ReactIR™ 1000 with high pressure probe.

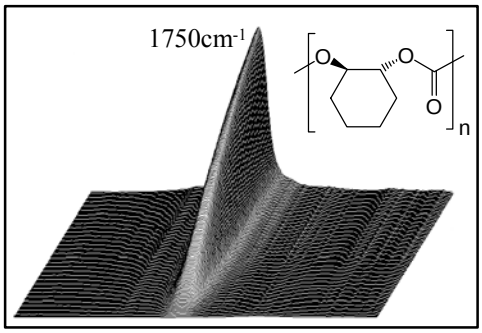

Figure 2. *In situ* infrared monitoring in the ν(CO_2) region for polymer formation from CO_2/cyclohexene oxide.

Polymer Characterization. Polymer samples were first characterized by ^{1}H NMR and IR spectroscopy. The amount of ether linkages were determined *via* ^{1}H NMR by integrating the peaks corresponding to the methine protons of the polyether at ~3.45 ppm and the polycarbonate at ~4.6 ppm. The presence or absence of the corresponding cyclic carbonate was investigated by monitoring the presence or absence of the ν(C=O) of the cyclic carbonate at ~1825cm^{-1}. Finally, M_w and M_n measurements were carried out using GPC.

Results and Discussion

We have examined a wide variety of zinc and chromium based derivatives as catalysts for the coupling of carbon dioxide and propylene oxide or cyclohexene oxide. In these studies, as well as those reported by other researchers, the reaction of carbon dioxide and propylene oxide favors production of cyclic carbonate, whereas, the analogous process involving cyclohexene oxide affords mostly polycarbonates. We have ascribed this difference in product selectivity to the ring strain placed on the five-membered carbonate ring in order to accommodate the conformational requirements of the alicyclic cyclohexyl ring. This is evident from a comparison of the crystal structures of cyclic propylene carbonate and cyclic cyclohexylene carbonate (see Figure 3).[5]

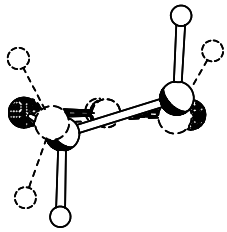

Figure 3. Overlay of the carbonate groups from propylene carbonate (dotted) and cyclohexene carbonate (solid).

Indeed, we have quantified the product selectivity for cyclic carbonate *vs* polycarbonate production in processes catalyzed by (salen)$Cr^{III}Cl$ derivatives. Comparative kinetic measurements were performed as a function of reaction temperature to assess the activation barrier for production of cyclic carbonates and polycarbonates for the two different classes of epoxides, i.e., alicyclic(cyclohexene oxide) and aliphatic(propylene oxide).[6] As anticipated in both instances the unimolecular pathway for cyclic carbonate formation has a larger energy of activation than the bimolecular enchainment pathway. That is, the energies of activation determined for cyclic propylene carbonate and polypropylene carbonate formation were 100.5 kJ-mol^{-1} and 67.6 kJ-mol^{-1} respectively, as compared with the corresponding values for cyclic cyclohexyl carbonate and polycyclohexylene carbonate production of 133 kJ-mol^{-1} and 46.9 kJ-mol^{-1}. The small energy difference in the two concurrent reactions for the propylene oxide/CO_2 process (33 kJ-mol^{-1}) accounts for the large quantity of cyclic carbonate produced at elevated temperatures in this instance.

We have examined a wide variety of (salen)CrNu, where Nu = nucleophile, derivatives as catalysts for the copolymerization of epoxides and carbon dioxide, however at this time we will focus on one of the more active derivatives thus far investigated, complex **1** (see Figure 4). The presence of a cocatalyst which can bind to the axial vacant site at the chromium center has been shown to improve the activity of complex **1** (see Table 1).

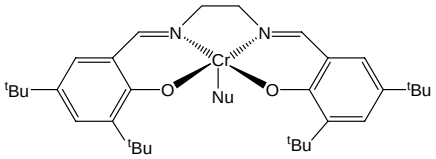

Figure 4. Typical (salen)Cr^{III}Nu (**1**), Nu = Cl(**1a**) , N_3(**1b**), catalyst for the copolymerization of epoxides and carbon dioxide.

Table 1. Copolymerization Data Using Different Cocatalysts.[a]

Complex	Cocatalyst (eq)	TON[b]	TOF[c]	% carbonate
1a	N-methylimidazole (5)	95	24	69%
	PPh_3 (3)[d]	157	39	96%
	PCy_3 (3)	578	145	99%
	PPNCl (1)[e]	1004	251	>99%
1b	N-methylimidazole (5)	189	47	90%
	PPh_3 (3)	284	71	96%
	PCy_3 (3)[f]	391	98	97%
	PPNCl (1)	1022	255	>99%

[a] 50 mg of catalyst dissolved in 20 mL of cyclohexene oxide and injected into a 300 mL Parr autoclave. The reactor was charged to 55 bar CO_2 pressure and heated to 80ºC for 4 hours. [b] moles of epoxide consumed / mol. of Cr. [c] moles of epoxide consumed / mol. of Cr / hour. [d] For a 24 hr run, M_n = 22,700 and PDI = 1.55. [e] For a 4 hr run, M_n = 5980 and PDI = 2.05, whereas for a 12 hr run, M_n = 16,800 and PDI = 1.92. [f] For a 10 hr run, M_n = 10,800 and PDI = 1.54.

Scheme 1 summarizes the reaction operative during the CO_2/epoxide coupling process. The relative importance of end pathway is closely linked to the nature of the salen ligand, the cocatalyst, and the epoxide. For example, while a more electron donating salen increases the rate of polymerization with cyclohexene oxide, this seems to have the opposite effect for propylene oxide and tends to decrease the rate of conversion for both cyclic and polymer. A similar situation was observed when changing the cocatalyst, where triphenylphosphine has been shown to produce polymer with no cyclic carbonate, while tricyclohexylphosphine produced mostly polyether and a small amount of polymer. This is to be contrasted with the data in Table 1 for cyclohexene oxide and carbon dioxide copolymerization. Furthermore, as previously demonstrated, copolymerization using cyclohexene oxide is further enhanced through the use of anionic cocatalysts. However, when using a PPN^+Cl^- cocatalyst, this was not the case for propylene oxide as cyclic carbonate was the major product.

Scheme I

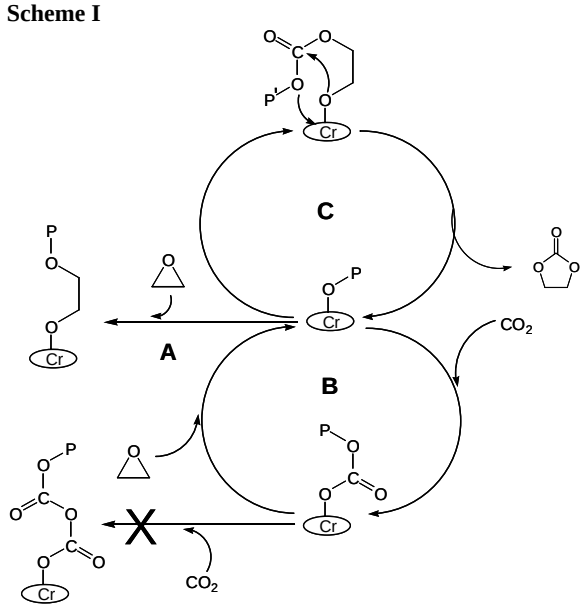

Finally, the use of other epoxide substrates based on the cyclohexyl backbone in the copolymerization with carbon dioxide, such as [2-(3,4-epoxycyclohexyl)ethyl]trimethoxysilane, offers the opportunity of affording industrially useful thermoplastics *via* crosslinking of the silane units.[7]

References

(1) Darensbourg, D. J.; Holtcamp, M. W.; Struck, G. E.; Zimmer, M. S.; Niezgoda, S. A.; Rainey, P.; Robertson, J. B.; Draper, J. D.; Reibenspies, J. H. *J. Amer. Chem. Soc.*, **1999**, *121*, 107.

(2) Koning, C.; Wildeson, J.; Parton, R.; Plum, B.; Steeman, P.; Darensbourg, D. J. *Polymer* **2001**, *42*, 3995.

(3) Darensbourg, D. J.; Yarbrough, J. C. *J. Am. Chem. Soc.* **2002**, *124*, 6335.

(4) Darensbourg, D. J.; Lee, W-Z.; Phelps, A. L, Guidry, E. *Organometallics* **2003**, *ACS ASAP*

(5) Darensbourg, D. J.; Lewis, S. J.; Rodgers, J. L.; Yarbrough, J. C. *Inorg. Chem.* **2003**, *42*, 581.

(6) Darensbourg, D. J.; Yarbrough, J. C., Ortiz, C. G.; Fang, C. *J. Am. Chem. Soc.* **2003**, *125*, 7586.

(7) Darensbourg, D. J.; Rodgers, J. L.; Fang, C. C. *Inorg. Chem.* **2003**, *42*, 4498.

SYNTHESIS OF CARBONATE BY REACTION OF CARBON DIOXIDE WITH PGE

Sang-Wook Park[a], Dae-Won Park, Tae-Young Kim, Mi-Young Park, and Kwang-Joung Oh

[a]Division of Chemical Engineering, Pusan National University, Pusan 609-735, Korea

Introduction

Recently, the chemistry of carbon dioxide has received much attention[1], and its reaction with oxiranes leading to five-membered cyclic carbonate (oxirane-CO_2 reaction) is well-known among many examples[2,3]. These carbonates can be used as aprotic polar solvent and sources for polymer synthesis[4]. In the oxirane-CO_2 reaction, high pressure (5-50 atm) of CO_2 has been thought to be necessary[2]. The oxirane-CO_2 reactions under atmospheric pressure have been reported[4] only recently. Many organic and inorganic compounds including ammines, phosphines, quaternary ammonium salts, and alkali metal salts are known to catalyze the oxirane-CO_2 reaction[3]. Most purpose of these papers have been to show the reaction mechanism, the pseudo-first-order reaction rate constant with respect to the concentration of oxirane, and the catalyst dependence of its conversion.

In the mass transfer accompanied by a chemical reaction, the diffusion may have an effect on the reaction kinetics. It is considered worthwhile to investigate the reaction kinetics of the gas-liquid heterogeneous reaction such as the oxirane-CO_2 reaction.

In this study, a chemical absorption mechanism of carbon dioxide into the toluene solution of phenyl glycidyl ether(PGE) and Aliquat 336(QX), and the experimental value of the equilibrium reaction constant between PGE and Aliquat 336 were presented, from which the reaction rate constant of reaction of CO_2 was obtained using the measured molar flux and liquid-side mass transfer coefficient of CO_2 at 85°C and 1 atm.

Theory

The overall reaction between PGE and CO_2 at atmospheric pressure of CO_2 is presented as follows[5].

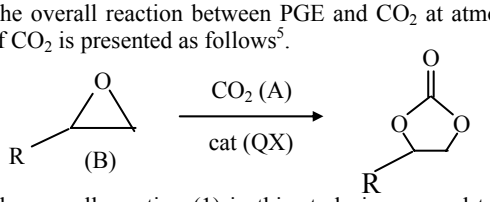

(1)

The overall reaction (1) in this study is assumed to consist of three steps as follows[5];

The three steps are (i) a reversible reaction of PGE and QX to form complex, C_1, (ii) reaction of C_1 and carbon dioxide to form complex,C_2, and (iii) dissociation reversible reaction of C_2 to form QX and five-membered cyclic carbonate.

$$B + QX \rightleftharpoons C_1 \quad \text{(i)}$$

$$A + C_1 \longrightarrow C_2 \quad \text{(ii)}$$

$$C_2 \rightleftharpoons QX + C \quad \text{(iii)}$$

The mass balances accompanied by the overall reaction $(A + B \xrightarrow{k_c} P)$, which consists of reaction(i)-(iii), and initial and boundary conditions are presented as follows,

$$D_A \frac{\partial^2[A]}{\partial z^2} = \frac{\partial[A]}{\partial t} + k_c[A][B] \quad (2)$$

$$D_{C1} \frac{\partial^2[B]}{\partial z^2} = \frac{\partial[B]}{\partial t} + \nu k_c[A][B] \quad (3)$$

$$t = 0, z > 0; [A] = 0, [B] = [B]_o \quad (4)$$

$$t > 0, z = 0; [A] = [A]_i, \frac{\partial[B]}{\partial z} = 0 \quad (5)$$

$$t > 0, z = \infty; [A] = 0, [B] = [B]_o \quad (6)$$

The mass balances, (2) and (3), and the conditions, (4)-(6) are rearranged the dimensionless forms as follows;

$$\frac{\partial^2 a}{\partial x^2} = \frac{\pi}{4}\frac{\partial a}{\partial \theta} + m\,a\,b \quad (7)$$

$$\frac{\partial^2 b}{\partial x^2} = \frac{\pi}{4} r \frac{\partial b}{\partial \theta} + \nu\, r\, q\, m\, a\, b \quad (8)$$

$$\theta = 0, x > 0; a = 0, b = 1 \quad (9)$$

$$\theta > 0, x = 0; a = 1, \frac{\partial b}{\partial x} = 0 \quad (10)$$

$$\theta > 0, x = \infty; a = 0, b = 1 \quad (11)$$

where,

$$a = \frac{[A]}{[A]_i},\ b = \frac{[B]}{[B]_o},\ x = \frac{z}{\delta},\ \theta = \frac{t}{t_o},\ \delta = \frac{D_A}{k_L},\ q = \frac{[A]_i}{[B]_o}$$

$$t_o = \frac{4D_A}{\pi k_L^2},\ m = \frac{k_c[B]_o D_A}{k_L^2},\ r = \frac{D_A}{D_{BI}},$$

The enhancement factor(β), which is defined as ratio of absorption rate of CO_2 with chemical reaction to that without the chemical reaction, is presented as follow;

$$\beta = -\left.\frac{\partial a}{\partial x}\right|_{x=0} \quad (12)$$

The measured enhancement factor, which is obtained under the given experimental condition such as concentration of PGE, Aliquat336, and the agitation speed of the impeller, is used to get the reaction rate constant by the comparison of its value with the value estimated from Eq.(12).

Experimental

Absorption experiments were carried out in a semi-batch flat-stirred agitated vessel constructed of pyrex glass of 0.075 m inside diameter and of 0.13 m in height. Four equally spaced vertical baffles, each one-tenth of the vessel diameter in width, were attached to the internal wall of the vessel. A straight impeller with 0.034 m in length, 0.017 m in width and 0.005 m in thickness was used as the liquid phase agitator and located at the middle position of the liquid phase of 0.3 dm^3. The absorption rates of CO_2 were obtained from the difference of the flow rate of CO_2 between inlet and outlet of the vessel at 85°C. The molar flux of CO_2 absorbed into the liquid was obtained from the measured rate of absorption.

Results and Discussion

The concentration profiles of components A and B can be obtained by the numerical analysis (FEMLAB) of the equations (7) and (8). The estimated values concentration of component A and B are shown in **Fig.1** under the typical reaction condition such as [PGE]= 0.1 kmol/m^3, [QX]= 0.05 kmol/m^3, T= 85°C. As shown in **Fig.1**, the concentration of CO_2 decreases and that of B increases as the depth of the liquid increases. Using the measured molar flux of CO_2 according to the change of fed concentrations of component, PGE and QX, the reaction rate constant of the reaction (1), which can be obtained under the boundary condition such as [A]=0 at z=0, is 0.53 m^3/kmol·s at 85°C.

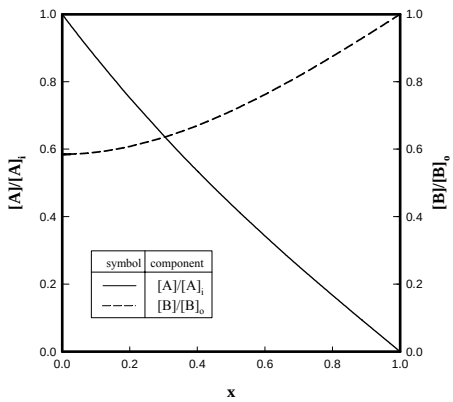

Figure.1. Concentration profile of A and C1. ($[B]_o$=0.1 kmol/m^3, $[QX]_o$=0.05 kmol/m^3, T=85°C)

The measured value of absorption rate of CO_2 at the concentration of PGE in the range of 0.1~2.0 kmol/m^3, that of Aliquat336 of 0.05 kmol/m^3, and the agitation speed of impeller of 50 rev/min are plotted against the concentration of PGE in **Fig. 2**. As shown in **Fig.2**, the absorption rate of CO_2 increased as increasing of PGE concentrations. The reaction rate constant(k_2) was estimated by comparison of enhancement factor obtained from the measured absorption rate of CO_2 in **Fig.2** with the value in Eq.(12).

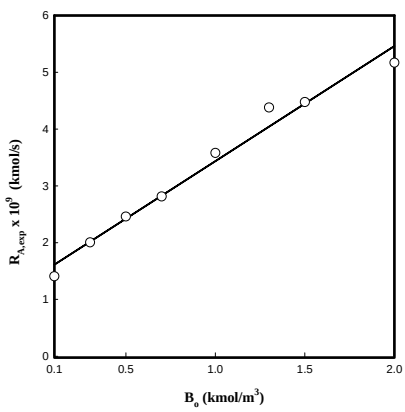

Figure. 2. Effect of PGE concentration on flux of CO_2.

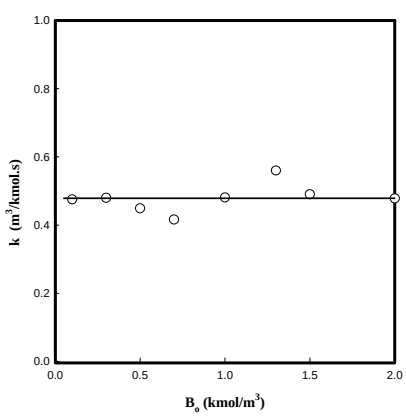

Figure. 3. Effect of PGE concentration on reaction rate constant.

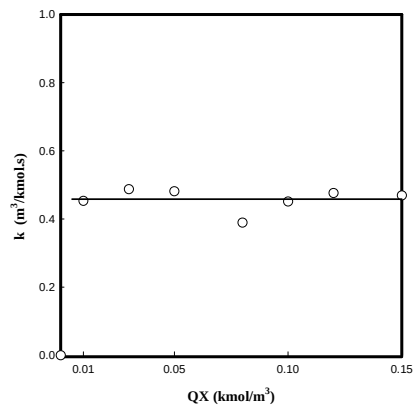

Figure. 4. Effect of QCl concentration on reaction rate constant.

The values of k_2 are plotted against the concentration of PGE in **Fig.3**. As shown in **Fig.3**, the reaction rate constants are constant as 0.434-0.592 m^3/kmol.s at the PGE concentration in the range of 0.5-2.0 kmol/m^3. Also the values of k_2, which are estimated by using the experiments at the concentration of PGE of 1.0 kmol/m^3 and those of Aliquat336 in the range of 0.01-0.15 kmol/m^3, are plotted against the concentration of Aliquat336 in **Fig.4**. As shown in **Fig.4**, the reaction rate constants were constant in the range of Aliquat 336 concentrations.

Conclusion

Carbon dioxide was absorbed into the toluene solution of phenyl glycidyl ether(PGE) as a oxirane and tricaprylylmethylammonium chloride (Aliquat 336, QX) as a catalyst using a semi-batch flat-stirred absorber at 85°C and 1atm to obtain a five-membered cyclic carbonate, phenoxy methyl ethylene carbonate. The reaction mechanism of oxirane – CO_2 reaction divided into three steps was used to obtain the reaction kinetics using the mass balance equations. The reaction rate constant in the overall reaction between CO_2 and PGE was obtained by the numerical solution of the mass balance equation using the measured molar flux of CO_2 and the liquid-side mass transfer coefficient of CO_2 at given concentration of PGE and QX.

Acknowledgement

This work was supported by KOSEF (Grant No : R01-2003-000-100200-0), the Brain Korea 21 project in 2003, and Brain Busan 21 program.

References

1. Inoue, S., In organic and bioorganic chemistry of carbon dioxide ; Inoue, S., N. Yamazaki, Eds., Kodansha Ltd., Tokyo, 1982.
2. Peppel, W.J., *Ind. Eng. Chem.*, 50(5), 767-770 (1958).
3. Kihara, N., Hara, N., and Endo, T., *J. Org. Chem.*, 58, 6198-6202 (1993).
4. Rokicki, G., *Makromol. Chem.* 186, 331-337 (1985).
5. Aida, T. and S. Inoue, *J. Am. Chem. Soc.*, 105, 1304-1309 (1983).

SELECTIVE FORMATION OF ETHYLENE FROM CO_2 BY CATALYTIC ELECTROLYSIS AT A THREE-PHASE INTERFACE

Kotaro Ogura, Hiroshi Yano, and Takayasu Tanaka

Department of Applied Chemistry, Yamaguchi University, Tokiwadai, Ube 755-8611, Japan

Introduction

Chemical conversion of CO_2 to fuels or chemicals is a challenging subject for chemists in connection with the mitigation of greenhouse effect and the carbon resource after the exhaustion of petroleum. Several methods for chemically converting CO_2 have been proposed: e.g., hydrogenation over heterogeneous catalyst at high temperature or in supercritical conditions, electrochemical and photochemical reduction. CO_2 conversion should be achieved with the aid of low input energy and products be highly valuable so that the conversion process may be feasible without accompanying the secondary generation of CO_2. Hence, the most desirable process is an artificial photosynthesis in which CO_2 is convertible to valuable substances with a solar cell as the energy source at room temperature. To attain such a process, we have developed the catalytic electrolysis process in which CO_2 is converted selectively to ethylene at room temperature.[1-4] The conversion reaction takes place at the three-phase (gas/liquid/solid) interface on a Cu(I) halide-confined Cu-mesh electrode.

Experimental

The electrolysis cell used is described elsewhere.[1] The three-phase interface was constructed on a pure copper-mesh (purity 99.99%, 50 mesh, Nilaco Co.) which was fixed along with a glass filter (average pore size, 20 μm) at the bottom of a cathode compartment. The electrolytic solution was prevented from dropping by the glass filter. The solution surface was forced up by the pressure of CO_2 blown up from the lower part, and the electrolyte meniscus was extended on the copper mesh. Thus, the three-phase zone consisting of gas, liquid and solid was built, and electrochemical reactions took place predominantly in this zone. The copper-mesh put on the glass filter was bound to a Teflon cylinder tightened with a Teflon cap. The cylinder with the copper-mesh was attached to the cathode compartment via an O-ring, which was separated from an anode compartment by a cation-exchange membrane (Selemion CMV 10, Asahi Glass Co.). The purified CO_2 gas was circulated via the cathode compartment with a circulating pump. The three-phase provided on the Cu-mesh electrode was sustained during the electrolysis by adjusting the rate of CO_2. The net surface area of the Cu-mesh was 10.2 cm^2.

Copper-mesh electrode was modified by CuCl, CuBr and CuI. Before this work, the Cu-mesh electrode was immersed in a concentrated HCl solution to remove Cu oxide, and washed with doubly distilled water. The modification of copper(I) halides was done by the application of electric charge of 220C at a constant potential of +0.4V vs Ag/AgCl in a 0.1M HCl and a 0.5M KBr solution (pH 3) or by passing the electric charge of 20C at +0.2V in a 0.5M KI solution of pH 3. The thickness of CuCl, CuBr and CuI films thus obtained were 7.8, 9.5 and 7.5μm, respectively. The film thickness was measured with a field emission scanning electron microscope (FE-SEM, Horiba EMAX-7000). The electrolysis of CO_2 was performed by the galvanostatic method. Various amounts of electric charge were applied with a constant current (usually 250mA) by changing the electrolysis time. Platinum or copper gauze with a large surface area and an Ag/AgCl/saturated KCl electrode were used as the anode and reference electrodes, respectively. The electrolytes mainly used were 3M or 4M KCl, KBr and KI solutions of pH 3. The change in pH of catholyte during the electrolysis was monitored with a pH controller (NPH-660NDE, Nissin Co.). The electrolyte in the anode compartment was a 0.5M $KHSO_4$ solution of pH 0. In some experiments, a concentrated solution of sulfuric acid was added to the anode compartment between times during the electrolysis in order to indirectly lower the pH of the catholyte.

A Shimadzu GC-8AIT and a GC-8AIF gas chromatograph with a Porapak N column and an active carbon or alumina column were used for the determination of gaseous samples. Aqueous samples were analyzed with a Shimadzu organic analyzer (LS-10AD type) and a Shimadzu GC-MS spectrometer. The electrochemically deposited copper halides were characterized with an X-ray diffractometer (Shimadzu XD-D1), and the XRD patterns were recorded with X-ray line of Cu-Kα (30kV, 30mA).

Results and Discussion

The electrolysis of CO_2 was performed at the three-phase interface on a copper(I) halides-confined Cu-mesh electrode in a potassium halide solution. In **Figure 1**, the conversion percentage of CO_2 obtained with a CuBr-confined Cu-mesh electrode in a KBr solution of pH 3 is shown versus the applied amount of electric charge. The CO_2 conversion increases with increasing the amount of electric charge until about 4500C, but beyond this amount the conversion percentage approximates a constant value of 68%. As seen from this figure, however, the conversion continues to increase when the pH of the catholyte was lowered by adding a concentrated solution of sulfuric acid to the anolyte between times during the electrolysis, and the conversion percentage reached 88% at the electric charge of 8928C. Hence, it is suggested that the approach of the conversion percentage to the constant value in the electrolysis charged with more than 4500C is attributed to the deficiency of proton concentration for the CO_2 reduction, which is discussed below.

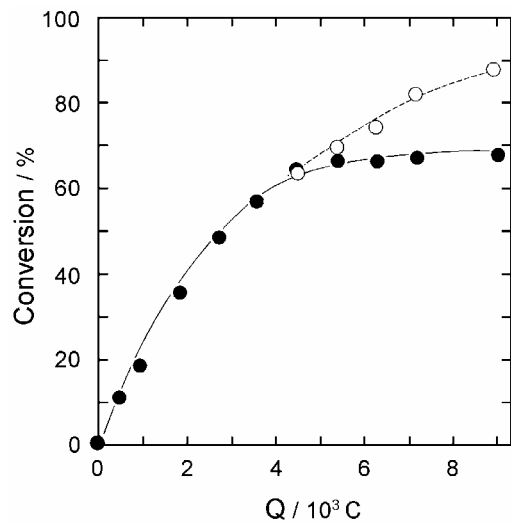

Figure 1. Plot of the conversion percentage of CO_2 versus the applied amount of electric charge in a 4 M KBr solution. The reduction of CO_2 was performed with a CuBr-confined Cu-mesh electrode at a constant current of 250 mA. The pH of the catholyte was lowered by adding a H_2SO_4 solution between times to the anolyte: ---○---, and such a pH-controlling was not given: —●—. The area of a copper-mesh substrate, 10.2 cm^2; initial volume of CO_2, 577 cm^3.

Table 1 Current efficiencies for the products obtained with a CuBr-confined Cu-mesh electrode in the galvanostatic reduction of CO_2[a)]

Run	Q [b)]	Potential [c)]	pH [d)]	Current efficiency / %									Conv. [e)]	Selec. [f)]	η [g)]
	C	V	−	Ethylene	Methane	CO	Ethane	Ethanol	Formic [h)]	Acetic [i)]	Lactic [j)]	H_2	%	%	%
1	453	−2.08 ~ −1.98	2.93	72.4	6.2	5.9	0.6	2.1	1.8	1.7	0.3	15.9	11.5	68.6	107
2	903	−2.10 ~ −1.93	2.69	62.5	5.9	4.6	0.6	1.1	1.3	1.2	0.1	21.0	19.0	71.0	98
3	2699	−2.10 ~ −1.92	2.75	48.2	2.2	5.2	0.5	1.0	2.0	1.1	0.2	13.4	48.9	64.3	74
4	4483	−2.08 ~ −1.89	3.78	39.2	1.0	4.0	0.4	0.6	2.9	0.3	0.0	10.6	66.3	63.2	59
4 [k)]	4500	−2.12 ~ −1.87	2.09	40.7	1.2	2.7	0.3	0.3	2.8	0.3	0.0	10.6	63.3	68.8	59
5	7157	−2.18 ~ −1.89	5.01	25.9	0.8	1.9	0.2	0.3	2.3	0.3	0.0	7.3	67.9	64.1	39
5 [k)]	7160	−2.13 ~ −1.89	2.32	33.3	0.9	2.8	0.2	0.3	2.1	0.4	0.0	7.1	81.9	69.1	47
6	8981	−2.15 ~ −1.88	6.14	21.0	0.4	1.5	0.6	0.2	1.7	0.2	0.0	9.9	68.6	65.6	36
6 [k)]	8928	−2.12 ~ −1.91	2.17	30.4	0.7	1.5	0.3	0.3	1.5	0.5	0.0	6.1	87.7	74.0	41

a) Electrolyte, 4M KBr, initial pH, 3.0; the apparent area of a copper-mesh surface, 10.2 cm^2; the thickness of confined CuBr film, 7.9 μm; applied current, 250 mA; initial volume of CO_2, 577 cm^3; catholyte, 232 cm^3; Anode, copper net; anolyte, a 0.5M $KHSO_4$ solution of pH 0. Cathode and anode compartments were separated by a cation-exchange membrane.
b) Amount of the electric charge applied in the electrolysis. This value was varied by changing the electrolysis time under the galvanostatic condition. C: coulomb (=ampere×sec)
c) Change in electrode potential (vs. Ag/AgCl) during the galvanostatic reduction.
d) Final pH of the catholyte. e) Conversion percentage of CO_2.
f) Selectivity for the formation of ethylene on the basis of carbon content.
g) Total current efficiency in the reduction. h) formic acid. i) acetic acid. j) lactic acid.
k) A concentrated solution of sulfuric acid was added to the $KHSO_4$ solution in the anode compartment between times during the electrolysis in order to indirectly lower the pH of the catholyte.

The major gases generated in the electroreduction of CO_2 were C_2H_4, CO and H_2, and their current efficiencies are plotted versus the applied amount of electric charge in **Figure 2**. The current efficiency for C_2H_4 decreases with an increase of amount of electric charge, but it still maintains more than 20% even at the electric care of 8900C. This current efficiency was risen to be 30% at the same electric charge when the pH of the catholyte was lowered by controlling the pH of the anolyte.

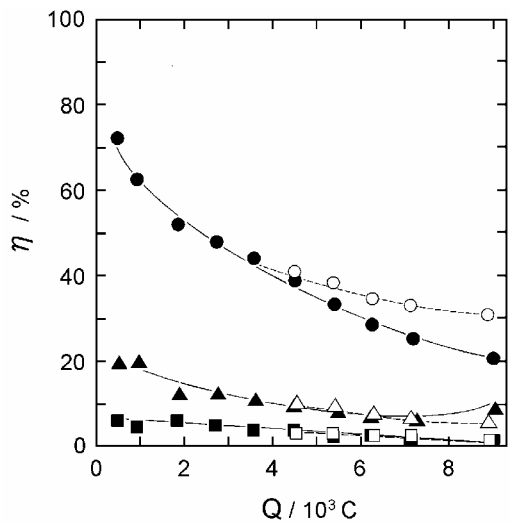

Figure 2. Plot of the current efficiencies for C_2H_4 (○, ●), CO (□, ■), and H_2 (△, ▲) versus the applied amount of electric charge. A H_2SO_4 solution was added to the anolyte: ---○---, ---△---, ---□---, and not: —●—, —▲—, —■—. The experimental conditions were the same as those given in Figure 1.

The detailed distribution of the products is exhibited in **Table 1**. The electrolysis was performed for a given period of time by applying a constant current of 250mA, and the electrode potential was −2.1V~−1.9V vs Ag/AgCl. The major gaseous products were C_2H_4 and CO, the formation of CH_4 was negligible, and the current efficiencies of liquid products were very low except that of formic acid in the prolonged electrolysis. In the electrolysis of Run 1~6 without adjusting the pH of the catholyte, the pH rose as the amount of electric charge was increased, and it became 6.14 after the electrolysis charged with 8981C (Run 6). On the other hand, in Run 4^k~6^k, the pH of the catholyte was adjusted to around 2.2 by adding a H_2SO_4 solution to the anolyte. As compared with the former results, the conversion percentage of CO_2 and the current efficiency for C_2H_4 were always enhanced, i.e., compare between the results of Run 4 and 4^k, 5 and 5^k, and 6 and 6^k. This means obviously that the concentration of protons in the catholyte is insufficient for the efficient reduction of CO_2 in the former case. It is noted that such a high current efficiency and a conversion percentage were brought about by adjusting the pH of the catholyte not directly but through the proton transport from the anode compartment. The current efficiency and conversion percentage were both considerably decreased when the pH of the catholyte was directly controlled by adding strong acid. This is probably caused by the transformation of an interfacial structure of the three-phase zone including adsorbed intermediates. Interestingly, the current efficiency for hydrogen evolution was smaller in the catholyte of which pH was suppressed low compared to that in the catholyte without pH-controlling. The selectivity for the formation of C_2H_4 estimated on the basis of carbon content was 74% at the applied electric charge of 8928C. The selective conversion of CO_2 to C_2H_4 is attributed to the immobilized CuX which operates as a heterogeneous catalyst by offering adsorption sites for reduction intermediates such as CO and methylene radicals.[3] A part of CuX is reduced to Cu ($CuX + e^- \rightarrow Cu + X^-$) simultaneously with the reduction of CO_2, but new copper(I) halide is always formed on the Cu-mesh electrode by the reduction ($Cu^{2+} + X^- + e^- \rightarrow CuX$) of Cu^{2+} ions which are afforded through the cation-exchange membrane from the anode compartment. Therefore, the electrochemical conversion of CO_2 continue to proceed via the catalysis reactions involving CuX.

References

1) H. Yano, F. Shirai, M. Nakayama, and K. Ogura, J. Electroanal. Chem., 519, 93 (2002).
2) K. Ogura, Electrochemistry, 71. 676 (2003).
3) K. Ogura, H. Yano, and F. Shirai, J. Electrochem. Soc., 150, D163 (2003).
4) H. Yano, T. Tanaka, M. Nakayama, and K. Ogura, J. Electroanal. Chem., in press.

SYNTHESIS AND ALTERNATING COPOLYMERIZATIONS OF CARBON DIOXIDE WITH CYCLOHEXENE OXIDE OVER (6-Me-pyCAr$_2$O)Zn(OAc) COMPLEXES CONTAINING BIDENTATE PYRIDINE-ALKOXIDE LIGANDS

Il Kim, Sang Mook Kim, Jae Sung Kim, Gi Wan Son, Dae Won Park, Chang-Sik Ha*

Division of Chemical Engineering, Pusan National University, Jangjeon-dong, Geumjeong-gu, Busan, 609-735, Korea; e-mail:ilkim@pnu.edu

Abstract

The reaction of 2-lithio-6-methylpyridine or 2-lithiopyridine and the appropriated diarylketone followed by hydrolysis yields 6-Me-pyCAr$_2$OH pyridine alcohols (**1a**, Ar = -C$_6$H$_5$; **1b** = 4-Me-C$_6$H$_4$; **1c** = 4-Cl-C$_6$H$_4$; **1d** = 4-Me$_2$N-C$_6$H$_4$) or pyCAr$_2$OH pyridine alcohols (**2a**, Ar = -C$_6$H$_5$; **2b** = 4-Me-C$_6$H$_4$; **2c** = 4-Cl-C$_6$H$_4$; **2d** = 4-Me$_2$N-C$_6$H$_4$). The reactions of zinc acetate with 1 equiv of lithiated products of **1a-d** and **2a-d** proceed rapidly to afford LiOAc salt and mono(ligand) complexes (6-Me-pyCAr$_2$O)Zn(OAc) (**3a-d**) and (pyCAr$_2$O)Zn(OAc) (**4a-d**), respectively, in high yield. The copolymerizations of carbon dioxide with cyclohexene oxide using 3**a-d** complexes were investigated. The (6-Me-pyCAr$_2$O)Zn(OAc) showed comparable yield and CO$_2$ incorporation with the β-diiminate zinc complexes. **3c** complex gave high polymers with high carbonate linkage (> 60%) and narrow polydispersity (< 2.0), indicating single active sites.

Introduction

Jordan and coworkers[1] described the synthesis of new group 4 metal alkyl complexes of the general form (Ox)$_2$MR$_2$ and (pyCR$_2$O)$_2$MR$_2$ which contain quinolato or pyridine-alkoxide ancillary ligands. The reaction of 2-lithiopyridine and the appropriated diarylketone followed by hydrolysis yields pyCAr$_2$OH pyridine alcohols. The reaction of M(NMe$_2$)$_4$ (M = Ti, Zr, Hf) with 2 equiv of pyCAr$_2$OH yielded (pyCAr$_2$O)$_2$M(NMe$_2$)$_2$ complexes (**Chart 1**) which adopt distorted octahedral structure with *trans*-O, *cis*-py, *cis*-amide arrangement of ligands and are active for the ethylene polymerizations.[1]

Chart 1

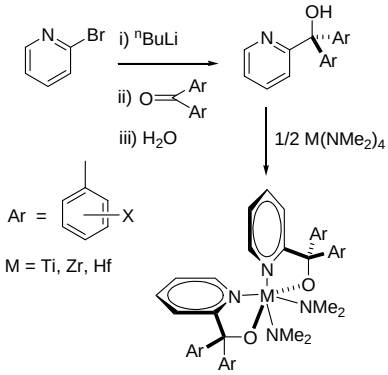

Coates developed β-diiminate zinc complexes for preparation of aliphatic polycarbonate (PC).[2] The β-diiminate zinc complex showed significantly higher activity than previous catalysts and produced aliphatic PC with very narrow polydispersity. These homogeneous single-site zinc complexes can give different activity and structure of the resulting copolymer according to β-diimine ligand structure. The specific objectives of this study were to develop efficient synthetic routes to (pyCAr$_2$O)Zn(OAc) complexes for the preparation aliphatic polycarbonate. Initial efforts to activate these complexes for the alternating copolymerization of carbon dioxide with cyclohexene oxide (CHO) are also described.

Experimental

General procedure. All reactions with air and/or moisture sensitive compounds were carried out under dry nitrogen using standard Schlenk line techniques. ^{1}H NMR spectra were measured on a Varian Gemini 2000 & HP5P with CDCl$_3$ as a solvent. Gel permeation chromatography (GPC) analyses were carried out using a Waters-400 spectrometer using polystyrene as a standard and dimethyl formamide as a solvent. All materials such as zinc(II) acetate [Zn(OCOCH$_3$)$_2$] and n-butyl lithium were purchased from Aldrich and used without further purification. Cyclohexene oxide (CHO, Aldrich) was distilled for 6 hours over sodium metal and stored over Linde type 4Å molecular sieves. Tetrahydrofuran (THF) and methylene chloride were refluxed over sodium and stored over 4Å molecular sieves under dry nitrogen.

Preparation of ligands and catalysts. Pyridine alcohol ligands were prepared according to literature procedures.[1] To a solution of ligand (1.28 mmol) in THF (10 mL), n-BuLi (1.6M in hexane, 0.88 mL, 1.41 mmol) was added dropwise at 0 ℃. Reacting the mixture for 5 min at 0 ℃, the solution was cannulated to a solution of zinc acetate (0.24 g, 1.41 mmol) dissolved in THF (10 mL). After stirring overnight at room temperature, the suspension was filtered and the clear solution was dried in vacuum. The resulting metal complexes were recrystallized in toluene and hexane and then characterized by ^{1}H NMR spectra.

(6-Me-pyCAr$_2$O)Zn(OAc) (**3a**, Ar = -C$_6$H$_5$); light yellow solid (57 % yield). ^{1}H NMR (CDCl$_3$, 300 MHz) δ 7.58 – 6.62 (13H, m, ArH), 2.50 (3H, s, Py-Me), 1.49 (3H, s, OAc).

(6-Me-pyCAr$_2$O)Zn(OAc) (**3b**, Ar = 4-Me-C$_6$H$_4$); pale yellow solid (63 % yield). ^{1}H NMR (CDCl$_3$, 300 MHz) δ 7.54 – 6.60 (11H, m, ArH), 2.59 (3H, s, Py-Me), 2.33 (3H, s, Ph-Me), 2.23 (3H, s, OAc).

(6-Me-pyCAr$_2$O)Zn(OAc) (**3c**, Ar = 4-Cl-C$_6$H$_4$); light yellow oil (21 % yield). ^{1}H NMR (CDCl$_3$, 300 MHz) δ 7.52 – 6.79 (11H, m, ArH), 2.50 (3H, s, Py-Me), 1.19 (3H, s, OAc).

(6-Me-pyCAr$_2$O)Zn(OAc) (**3d**, Ar = 4-Me$_2$N-C$_6$H$_4$); yellow solid (49 % yield). ^{1}H NMR (CDCl$_3$, 300 MHz) δ 7.43 – 6.57 (11H, m, ArH), 2.85 (12H, s, NMe), 2.48 (3H, s, Py-Me), 1.51 (3H, s, OAc).

(pyCAr$_2$O)Zn(OAc) (**4b**, Ar = 4-Me-C$_6$H$_4$); pale yellow solid (52 % yield). ^{1}H NMR (CDCl$_3$, 300 MHz) δ 7.57 – 6.77 (11H, m, ArH), 2.17 (3H, s, Ph-Me), 2.09 (3H, s, OAc).

Copolymerization of CO$_2$ with cyclohexene oxide. The copolymerizations were performed in a 10 mL high-pressure reactor equipped with a thermometer and a magnetic stirrer. The reactor was charged with catalyst (3.7×10^{-5} mol) and CHO (3.7×10^{-2} mol) in a dry box, and then transferred to a bath controlled at a desired temperature. The vessel was pressurized to 6.8 bar with CO$_2$ and allowed to stir. After 2 h of polymerization, the copolymer was dissolve in minimum amount of methylene chloride and precipitate from excess methanol. The product was then dried in vacuum.

Results and Discussion

Ligand Synthesis. Pyridine-alcohols **1a-c** were prepared by addition of 2-lithio-6-methylpyridine to the appropriate ketone,

followed by aqueous workup (eq 1), using the approach developed originally by Holm.[3] These compounds are isolated as sharp-melting white to tan crystalline solids following recrystallization. The use of symmetric ketones yields symmetric 6-Me-pyCR$_2$OH alcohols, which in turn simplifies the stereochemical possibilities for metal complexes.[4]

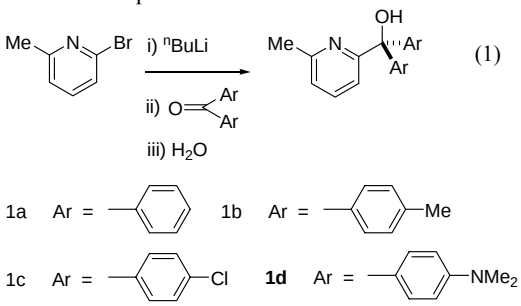

Similar ligands pyCAr$_2$OH pyridine alcohols (**2a**, Ar = -C$_6$H$_5$; **2b** = 4-Me-C$_6$H$_4$; **2c** = 4-Cl-C$_6$H$_4$; **2d** = 4-Me$_2$N-C$_6$H$_4$) without methyl substituent in 6-position of the pyridine ring were also successfully synthesized according to the similar procedures.

Synthesis of (6-Me-pyCAr$_2$O)M(OAc) (M = Zn, Mn) complexes. The reactions of zinc acetate or manganese acetate with 1 equiv of lithiated products of **1a-c** proceed rapidly to afford LiOAc salt and mono(ligand) complexes (6-Me-pyCAr$_2$O)M(OAc) [M = Zn (**2a-c**), Mn (**3a-c**)] in high yield (eq 2).

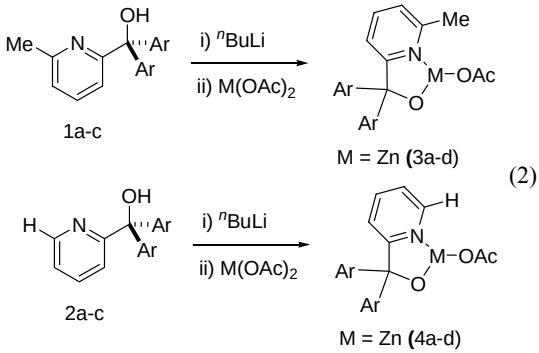

Alternating copolymerization of CO$_2$ with cyclohexene oxide. Semi-batch copolymerizations of CHO and CO$_2$ using Zn complexes have been carried out at the temperature range between 30 and 70 ℃ at a constant pressure of CO$_2$ (6.8 bar). Copolymerization of CHO and CO$_2$ leads to the copolymers of the following general structure:

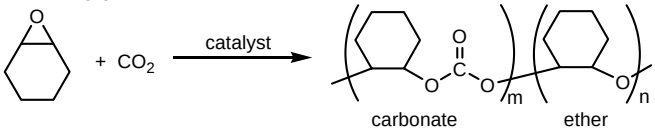

If the alternating copolymerization is perfect, only carbonate groups should be generated. However, homopolymerization of CHO results in ether linkage. The typical IR spectrum of the resultant copolymers obtained from 3b catalyst system is shown in **Figure 1**. It was found that the IR spectrum showed the strong absorption band at 1745 and 1238 cm^{-1} characteristic of stretching vibration of C=O bond and C-O-C bond of the carbonate group, respectively. The content of carbonate and ether linkages can be estimated exactly by assigning ^{1}H NMR spectrum of methine hydride (3.3 – 4.0 ppm) in cyclohexane backbone. Zinc complexes bearing ligands (**1a-c**) with 6-methyl substituted pyridyl produced aliphatic PCs which have high carbonate contents (≥ 60 %) as shown in Table 1. It is interesting to note that the **3d** catalyst bearing ligand with electron donating NMe$_2$ group on the aryl ring showed only negligible activity, while **3c** catalyst with electron withdrawing Cl group showed highest activities. Copolymers obtained by **3c** catalyst recorded highest molecular weight, demonstrating the electron withdraw group retards chain termination reaction. In addition the methyl group on the pyridyl ring influences both catalytic activity and CO$_2$ reactivity (compare **3b** and **4b** in Table 1). The Mn acetate complexes bearing **1b** and **2b** ligands were also prepared and utilized for the copolymerization of CO$_2$ and CHO, resulting in negligible activities. All Zn complexes bearing pyridine alcohol ligand can produce aliphatic PC with high molecular weight and narrow PDI at mild conditions.

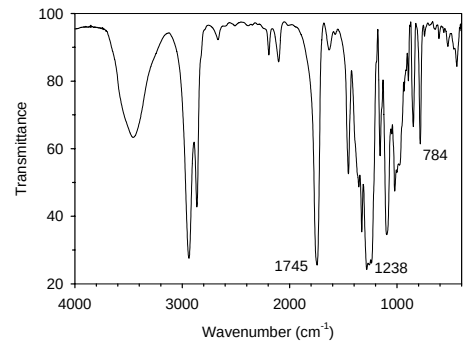

Figure 1. The typical IR spectra of CO$_2$/CHO copolymer obtained by 3b at 30 ^{o}C.

Table 1. Results of CO$_2$/CHO copolymerizations

No.	Cat.	Temp.	Yield (%)	M$_n$	MWD	Carbonate (%)
1	**3a**	30	22.8	4660	1.38	74.5
2		50	19.6	3830	1.10	72.2
3		70	19.2	3610	1.14	69.9
4	**3b**	30	15.4	4250	1.06	72.9
5		50	10.4	3890	1.04	56.4
6		70	11.6	3620	1.05	50.6
7	**3c**	30	26.8	6820	2.05	61.5
8		50	30.6	9540	2.55	62.6
9		70	26.0	5590	1.96	51.5
10	**3d**	30	nil	-	-	-
11		50	0.8	-	-	0.2
12		70	1.4	-	-	0.2
13	**4b**	30	13.6	3500	1.04	43.6
14		50	12.2	3560	1.03	47.3
15		70	11.2	3370	1.03	35.5

Acknowledgment

This work was supported by grant No. R01-2003-000-10020-0 from the Basic Research Program of the Korea Science & Engineering Foundation. IK is also grateful to the Brain Korea 21 Project in 2003.

References

1. Kim, I., Nishihara, Y., Jordan, R.F., Rogers, R.D., Rheingold, A.L., Yap, G.P.A., *Organometallics*, **1997**, *16*, 3314.
2. Chen, M., Lobkovsky, E.B., Coates, G.W., *J. Am. Chem. Soc.*, **1998**, *120*, 11018.
3. Schultz, B.E., Gheller, S.F., Muetterties, M.C., Scott, M..J., Holm, R.H., *J. Am. Chem. Soc.* **1993**, *115*, 2714.
4. Tsukahara,T. Swenson,D.C.,Jordan.R.F.*Organometallics,* **1997**, *16*, 3303.

HYDROGENATION OF NITROBENZENE WITH SUPPORTED TRANSITION METAL CATALYSTS IN SUPERCRITICAL CARBON DIOXIDE

Fengyu. Zhao[a,b,c], Rong Zhang[b], Maya Chatterjee[b], Yutaka Ikushima[b,c], and Masahiko Arai[c,d]

a, Japan Society for the Promotion of Science, Domestic Research Fellow. b, Supercritical Fluid Research Center, National Institute of Advanced Industrial Science and Technology, Sendai 983-8551, Japan. c, CREST, Japan Science and Technology Corporation (JST), Japan. d, Division of Materials Science and Engineering, Graduate School of Engineering, Hokkaido University, Sapporo 060-8628, Japan.

Introduction

The selective hydrogenation of nitro-compounds is commonly used to manufacture amines, which are important intermediates for dyes, urethanes, agro-chemicals and pharmaceuticals. Hydrogenation of nitrobenzene is used to produce aniline, which can be carried out in gas or liquid phase by using supported metal catalysts and organic solvents such as alcohols, acetone, benzene, ethyl acetate, or aqueous acidic solutions.[1,2] The use of these solvents has some drawbacks owing to their toxicity, flammability, or environmental hazards. In addition, the solvent may play a crucial role in the stabilization of reactive intermediates and have a decisive influence on chemical reactions. Therefore, the choice of solvent is important and a green solvent should be considered for contemporary chemical processes. Supercritical carbon dioxide ($scCO_2$) is an environmentally acceptable replacement for conventional organic solvents, due to its environmentally benign, non-toxic, and non-flammable nature, low cost, and wide tuning ability of solvent properties.[3,4] Moreover, the rate of catalytic hydrogenation in a gas-liquid system is not so high because of a low solubility of gaseous hydrogen in common solvents. In contrast, hydrogen is completely miscible with $scCO_2$, and this is beneficial for enhancement of hydrogenation reactions. [5]

The present work has been undertaken to study the catalytic hydrogenation of nitrobenzene in $scCO_2$ and in ethanol at a low temperature of 35 ℃ using several supported transition metal catalysts. The influence of metals (Pt, Pd, Ru, and Rh), supports (C, SiO_2, and Al_2O_3), and solvents ($scCO_2$ and ethanol) on the catalytic activity and selectivity has been investigated.

Experimental

Materials. All the chemicals were purchased from Wako Pure Chemicals Industries and used without further purification. Carbon- and alumina-supported Pd, Rh, Pt and Ru catalysts were also purchased from Wako. Silica-supported Pd and Pt catalysts were prepared using ion-exchange method. All the catalysts were reduced by hydrogen at 300℃ for 2 h before activity measurements.

Activity measurement. The activity of those catalysts was tested for the hydrogenation of nitrobenzene, which was carried out in a 50 mL high-pressure autoclave. Nitrobenzene (2.0 g (16.2 mmol)) and catalyst (0.01 g) were charged into the reactor and the reactor was flushed with 2.0 MPa CO_2 for three times. The reactor was then heated up to the desired temperature of 35℃ and then H_2 and compressed liquid CO_2 were introduced up to the desired pressure with a high-pressure liquid pump. The hydrogenation reaction was conducted while stirring with a magnetic stirrer. After the reaction, the reactor was cooled to room temperature and the reaction mixture was analyzed with a gas chromatograph (HP 5890, HP5 capillary column with 0.53 mm in diameter, 0.25 μm in film, and 15 m in length) using a flame ionization detector.

Catalyst characterization. X-ray diffraction (XRD) patterns of catalysts were measured on Rigaku RINT 220VK/PC powder diffractometer operated at 40 kV and 20 mA, using CuKα monochromatized radiation (λ = 0.154178 nm). The crystallite size of supported metals was calculated using the Scherrer equation, $D = K\lambda/(\beta\cos\theta)$, where K is a constant taken as 0.9, λ is the wavelength of the X-ray radiation, β is the peak width at half maximum.

Results and Discussion

Hydrogenation of nitrobenzene in organic solvents was reported to produce aniline along with several intermediate products such as nitrosobenzene (NSB), phenylhydroxylamine (PHA), azoxybenzene (AOB), azobenzene (AB) and hydrazobenzene (HOB), which are formed in several parallel and consecutive reactions. It has been observed in the present work that all the catalysts show 100% selectivity towards aniline in $scCO_2$ at 50℃. In order to compare the influence of metal and support on both activity and selectivity, the reaction has been carried out at a lower temperature of 35℃. At this temperature as well, PHA and HOB were not detected to form.

The influence of metals has been examined using C-supported catalysts (Table 1). In $scCO_2$, the highest conversion of 71% was obtained with Pt/C catalyst; however, the selectivity to aniline was lower compared to these obtained with the other catalysts. The Pd/C, Ru/C, and Rh/C catalysts exhibit 100% selectivity to aniline in $scCO_2$. In a conventional organic solvent of ethanol, Pt/C also shows a higher conversion compared with the other catalysts. With Ph/C and Ru/C catalysts, no products were detected in ethanol. For all the catalysts used, both the conversion and selectivity to aniline obtained in $scCO_2$ are higher than these obtained in ethanol. The order of activity is Pt > Pd > Rh, Ru in $scCO_2$ as well as in ethanol. The solubility of H_2 in ethanol and CO_2 calculated according to Henry's law and equation state for ideal gases, indicated that the concentration of H_2 in CO_2 is 15 times higher than that in ethanol.

Table 1 Results of hydrogenation of nitrobenzene in $scCO_2$ and in ethanol with different carbon supported metal catalysts at 35℃

Solvent	Catalyst	Time (min)	Conversion (%)	Selectivity (%)			
				AN	NSB	AB	AOB
CO_2 14.0 MPa	5% Pd/C	10	52	100	--	--	--
	5% Pd/C	50	100	100	--	--	--
	5% Pt/C	10	71	79	4	12	5
	5% Pt/C	50	100	100	--	--	--
	5% Ru/C	10	4	100	--	--	--
	5% Rh/C	10	12	100	--	--	--
Ethanol	5% Pd/C	10	21	68	16	--	16
	5% Pt/C	10	63	58	4	26	12
	5% Ru/C	10	0	--	--	--	--
	5% Rh/C	10	0	--	--	--	--

Next, the total conversion and the selectivity to aniline obtained with various supported metal catalysts in $scCO_2$ and ethanol were shown in figure 1. In $scCO_2$, all the Pd catalysts indicate 100%

selectivity to aniline, while the Pt catalysts have lower selectivity to aniline. With the Pt catalysts, some amounts of NSB, AOB, and AB were produced. In ethanol, the same byproducts were also detected with all the Pt and Pd catalysts. Higher aniline selectivity values were obtained in $scCO_2$ than these obtained in ethanol for all the catalysts used. The order of the total conversion with respect to the supports is C > Al_2O_3, SiO_2 in $scCO_2$ for both Pt and Pd. It is interesting to see that the total conversion in ethanol is higher than that obtained in $scCO_2$ for Al_2O_3 and SiO_2 supported Pt and Pd catalysts; on the contrary, the conversion in $scCO_2$ is higher than that in ethanol for Pd/C and Pt/C catalysts.

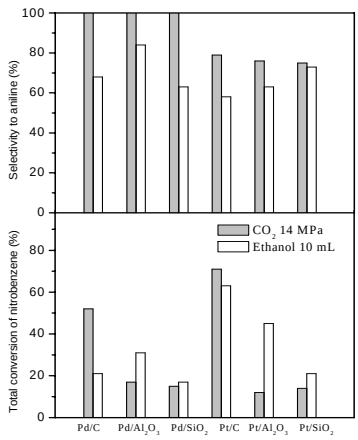

Figure 1. Nitrobenzene hydrogenation in $scCO_2$ and in ethanol at 35℃. Reaction conditions: nitrobenzene 2.0 g (16.2 mmol), catalyst 0.01g, H_2 4.0 MPa, temperature 35℃, reaction time 10 min.

These results can be explained with metal particle size and the interaction between reaction medium and metal particle. The metal particle size on the supports were quite different and a larger metal particle presented on the C-supported Pd and Pt catalysts as calculated by Scherrer equation. The nitrobenzene hydrogenation proceeded on the surface of metal particles, the higher activity presented in $scCO_2$ for Pd/C and Pt/C catalysts indicates a significant interaction existed between $scCO_2$ molecular and the larger Pt and Pd metal particle, which benefits the formation of aniline, thus, the higher selectivities to aniline have been obtained in $scCO_2$ than these obtained in ethanol for all the catalysts used.

The CO_2 pressure presents a significant effect on the reaction conversion and product selectivity in Figure 2. The conversion increases with increasing CO_2 pressure up to 12 MPa , which can be explained by the phase behavior and the concentration of nitrobenzene distributed in liquid and CO_2 phases. The concentration of nitrobenzene in CO_2 increases with increasing CO_2 pressure; when CO_2 pressure was raised to 12 MPa, a completely miscible mixture (NB, H_2 and CO_2) was formed. In this case the mass transfer resistance between gas (H_2) and liquid (NB) was decreased with increasing CO_2 pressure and then it disappeared at 12 MPa as a result of the phase changes to a homogeneous phase. This is a reason for that the conversion increases with increasing CO_2 pressure. The selectivity to aniline increases and has a maximum at 8.0 MPa, and then it decreases with increasing CO_2 pressure for both Pd/C and Pt/C catalysts. It was supposed that density variation around the critical point would cause a change in chemical or physical properties and affects the activity and selectivity of a reaction. The density of $scCO_2$ is highly pressure dependent, for instance, to change CO_2 pressure from 6.0 MPa to 8.0 MPa, the density changes from 160.0 to 520.8 kg/m^3 [6].

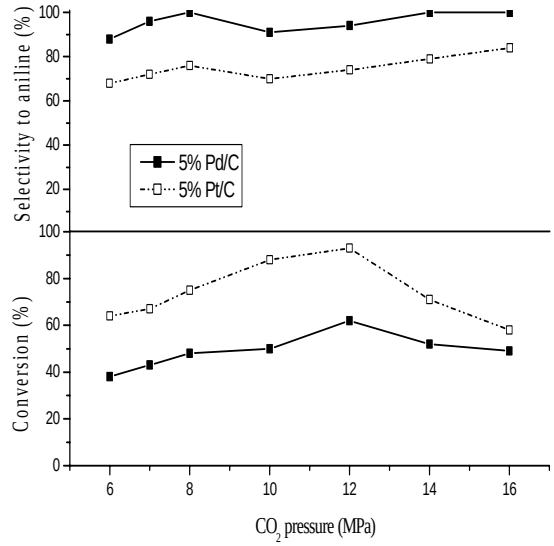

Figure 2 Influence of CO_2 pressure on the total conversion and selectivity to aniline. Reaction conditions: nitrobenzene 2.0 g (16.2 mmol, 0.324 mmol/ml in the reactor), catalyst 0.01g, H_2 4.0 MPa, temperature 35℃, reaction time 10 min.

The transition metal catalysts of Pd, Pt, Ru, and Rh supported on carbon presented a similar active order of Pt > Pd > Ru, Rh in $scCO_2$ as well as in ethanol. An active order of supports is C >Al_2O_3, SiO_2 in $scCO_2$ for both Pd and Pt catalysts. Higher selectivity to aniline has been obtained in $scCO_2$ compared with that in ethanol. the hydrogenation of nitrobenzene catalyzed with Pd/C and Pt/C catalysts was successfully conducted in $scCO_2$ with a 100% yield to aniline at a lower temperature of 35℃ for 50 min. Clearly, $scCO_2$ is a suitable replacement for organic solvent in the hydrogenation of nitrobenzene and the present hydrogenation is an environmentally benign and "green" process as it is free of harmful organic solvents. In addition, it is easy to separate the organic phase (the desired product, aniline), aqueous phase (the only byproduct, water), gas phase (CO_2, H_2).

Acknowledgements

The authors would like to thank Dr. M. Shirai for fruitful discussions, and thanks also to Dr. Y. Hakuta for measurement of TEM images.

References

1. Figueras, F.; Coq, B., *J. Mol. Catal. A Chem.* **2001,** 173, 223.
2. Torres, C. C.; Jablonski, E. L.; baronetti, G. T.; Castro, A. A.; de Miguel, S. R.; Scelza, O. A.; Blanco, M. D.; Pena Jimenez, M. A.; Fierro, L. G., *J. Appl. Catal. Gen.* **1997**, 161, 213.
3. Leitner, W., *Acc. Chem. Res*. **2002**, 35, 746.
4. Baiker, A., *Chem. Rev*. **1999**, 99, 453.
5. Zhao, FY.; Ikushima, Y.; Chatterjee, M.; Sato, O.; Arai, M., *J. Supercrit. Fluids*, **2003**, 27, 65.
6. Arai, M.; Nishiyama,Y.; Ikushima, Y., *J. Supercrit. Fluids*, **1998**, 13, 149.

Effects of Molecular Composition and Carbonization Reactivity of FCC Decant Oil and its Derivatives on Mesophase Development

Semih Eser and Guohua Wang

Department of Energy and Geo-Environmental Engineering
and
Energy Institute
The Pennsylvania State University, 101 Hosler Building University Park, PA 16802

Introduction

FCC decant oil is the primary feedstock to delayed coker to produce needle coke, a premium carbon precursor to synthetic graphite electrodes. Mesophase development during coking, determines the graphitizability of the needle coke product. Mesophase development, in turn, depends on the molecular composition of the feedstocks [1,2].

In a commercial delayed coking unit, liquid-phase carbonization (coking) takes place in insulated coke drums as the feed, heated in a tubular furnace, flows upward in the drums [3]. Liquid products from delayed coking are separated into light and heavy oils by distillation in a fractionator. Fresh feed (typically decant oil) is also fed to the fractionator. The furnace charge (coker feed) comes from the bottom of the fractionator that includes the heavy ends of both fresh feed and liquid products from coking.

Most studies on delayed coking have used FCC decant oil as the feedstock material, although the actual coker feed may have a very different composition from that of the parent decant oil. The objective of this study is to analyze the molecular composition of the coker feeds as compared to the parent decant oils. Laboratory carbonization experiments were carried out on the decant oil and coker feed samples as well as on the bottom and top fraction (gas oil) of the decant oils separated by vacuum distillation. Samples of hydrotreated gas oil were also carbonized under comparable conditions. Semi-coke and asphaltene yields from the carbonization experiments were determined to compare the carbonization reactivity of different samples. Mesophase development was monitored by polarized-light microscopy of semi-coke samples.

Experimental

The samples used for both analysis and carbonization experiments include two sets of decant oils (DO3-1 and DO3-3), coker feed (CF3-1 and CF3-3), and gas oil (GO3-1 and GO3-3). Samples of hydrotreated gas oil (HYD3-1 and HYD3-3) and vacuum tower bottoms (VTB3-1 and VTB 3-3) were used only in the carbonization experiments.

Gas Chromatography/Mass Spectrometry (GC/MS), was used to determine the concentrations of GC-amenable aromatic compounds, using a method reported elsewhere [4].

Carbonization experiments were carried out in 15 mL tubing bomb reactors under autogenous pressure at two different temperatures using a sample size of 4 g. A lower temperature (450°C) was used to determine the product yield from the carbonization of individual samples for 15 min to 180 min. Carbonization at higher temperature (500°C) for 4 – 6 h was carried out to examine the optical texture of semi-coke products to monitor mesophase development.

Semi-coke samples were prepared in epoxy resin pellets, and the polished pellets were examined using a polarized light microscope. We used a 1.1 mm X 1.1 mm mask and 10X object lens to acquire surface images. At least 150 images were examined for each sample. The extent of mesophase development that produced the semi-coke texture was expressed in terms of an Optical Texture Index (OTI) [1] as a measure of structural anisotropy. Higher OTI, higher is the degree of anisotropy in terms of the shape and size of optical units observed under a polarized-light microscope. The desired needle coke anisotropy will consist mostly of the flow domain texture that represents elongated regions of liquid crystalline (mesophase) structures. Domains, and small domains represent a decreasing extent of anisotropy in this order.

Products from low temperature (450°C) carbonization were separated into semi-coke (dichloromethane insoluble), asphaltenes (dichloromethane soluble and pentane insoluble), and maltenes (pentane solubles) to determine the semi-coke and asphaltene yields.

Results and Discussion

Table 1 shows the OTI of semi-cokes obtained from carbonization of different samples. The two decant oil samples produced semi-cokes with very different OTI under the same experimental conditions: 83 for DO03-1 and 66 for DO03-3. A similar trend was observed when comparing the semi-coke textures for the respective derivatives (except HYD), although the differences were not as significant as that obtained with the DO samples, In contrast, HYD03-1 gave a lower value of OTI than that of HYD03-3. Within each sample set, CF produced more developed textures than the parent DO. This difference was particularly pronounced for sample Set 03-3 where CF OTI (82) is much higher than DO OTI (66), indicating a substantially improved mesophase development from CF03-3 compared to DO03-3. GO produced the worst optical texture within each sample set. GO3-1 produced a better texture than GO3-3, whereas HYD03-1 produced a worse texture than HYD03-3. This reversal in the trend of texture development suggests that hydrotreatment can very significantly change the resulting optical texture obtained from the carbonization of the hydrotreated products compared to the starting GO. VTB produced better textures than DO and CF in both sample sets. While VTB produced the most developed texture in Set 03-1 (OTI:95), HYD gave the most developed texture in Set 03-3 (OTI: 94).

Table 1. Optical Texture Indices for semi-cokes produced by carbonization at 500°C, for 4 h and 6 h (GO and HYD).

	Set 03-1	Set 03-3
DO	83	66
CF	88	82
GO	61	54
HYD	87	94
VTB	95	86

Figures 1-4 present the concentrations of polyaromatic hydrocarbons in DO, CF, and GO and n-alkanes in DO in both sample sets. It is shown in Figure 1 that DO3-1 has a higher overall pyrenes/phenathrenes (py/ph) ratio compared to DO3-3.

Figure 2 compares the n-alkanes distributions in DO samples. The DO3-3 has higher concentrations of large n-alkanes (>20 carbon atoms) than DO3-1. These differences in the composition of the aromatic compounds and n-alkanes in the two DO samples can be related to the difference observed in the semi-coke textures between DO3-1 and DO3-3 semi-cokes. It has been reported that higher py/ph ratios and lower concentrations of large alkanes in decant oils lead to higher degrees of mesophase development upon carbonization [1].

A comparison of Figure 1 and Figure 3 shows that CF samples have much higher py/ph ratios than the corresponding DO samples. Again, this difference can explain the more developed textures

obtained from CF compared to the corresponding DO. It is noted, however, that CF3-3 has a higher py/ph ratio than CF3-1, although the semi-coke texture from CF3-1 is slightly worse tan CF3-3. This discrepancy may be attributed to the difference in the composition of the heavy ends that cannot be resolved by GC/MS. The fact that VTB3-1 produced a much better texture than VTB3-3 (Table 1) suggests a significant difference in the molecular composition of the heavy ends of the two samples. It should be noted that VTB constitutes a significant fraction of CF. Laser Desorption/Mass Spectrometry and High-Pressure Liquid Chromatography results indicated that five-ring aromatics (benzopyrene and benzopyrenes) are more abundant in CF and VTB [5].

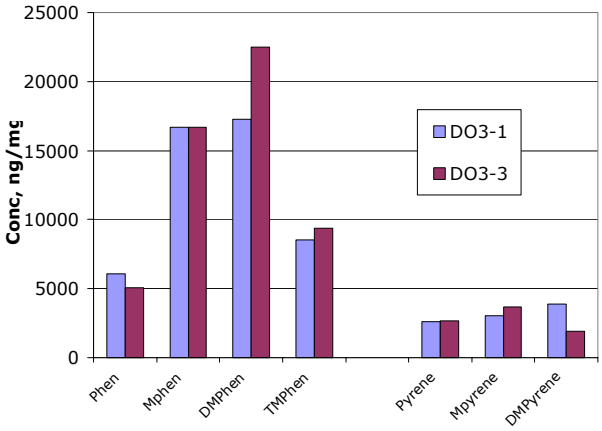

Figure 1. PAHs in decant oils (DO)

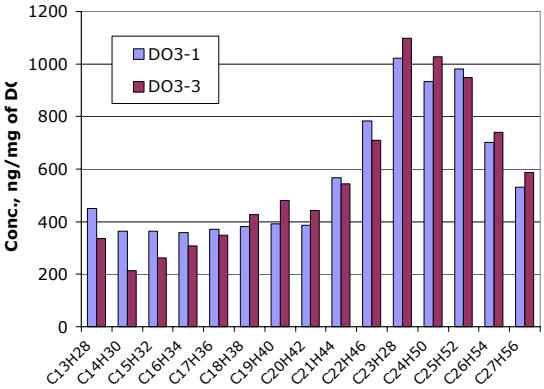

Figure 2. n-alkanes in decant oils (DO)

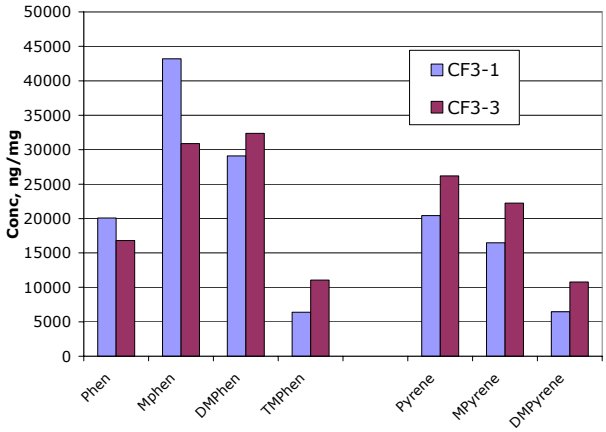

Figure 3. PAHs in Coker Feed (CF)

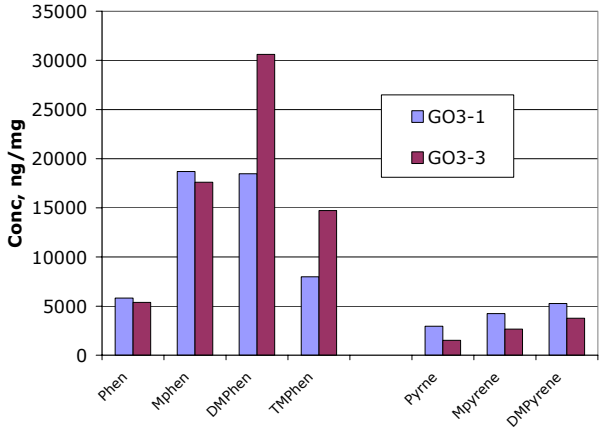

Figure 4. PAHs in Gas Oil

Figures 5-7 present the semi-coke and asphaltene yields from carbonization at 450˚C. Figure 5 shows that DO03-3 has the highest semi-coke yield among the samples after relatively long reaction times(>120 min). In contrast. HYD03-3 gave the lowest semi-coke yields, as expected. A sharp increase was observed in the semi-coke yield from GO during the very early stages of carbonization between 15 and 30 minutes, CF03-3, on the other hand, showed a slow and steady increase in the semi-coke yield throughout the reaction time period. Figure 6 shows the asphaltene yields. Among the samples, CF03-3 stands out with much higher asphaltene yields than the other samples throughout the whole reaction time period. HYD03-3, on the other hand, gave the lowest asphaltene yields among the samples (with the exception of GO after 3 h). GO shows comparable asphaltenes yield to those of HYD and DO during the early stages.

A comparison of coke and asphaltene yields shows that the conversion of asphaltenes to semi-coke proceeds most slowly during the carbonization of CF03-3. A very rapid initial increase in asphaltene yields from CF03-3 does not translate into a rapid build-up of semi-coke yield, indicating a prolonged presence of a fluid phase that would promote mesophase development. In direct contrast, GO03-3 shows a very fast conversion of asphaltenes to semi-coke during the early (<60 min) and, particularly later stages (>120 min) of carbonization. DO also shows a relatively fast formation of semi-coke from the asphaltenes. GO03-3 and DO03-3

gave the least developed textures in the sample set, as shown in Table1.

The asphaltene and semi-coke yields from VTB03-3 show a different trend from that of the other samples. A very rapid initial increase in asphaltene yield is followed by a rapid conversion of asphaltenes to semi-coke, as shown in Figure 7. Relatively well-developed mesophase from VTB03-3 despite a fast conversion of asphaltenes into semi-coke may be attributed to a favorable interaction between the evolution of volatiles and the carbonizing viscous phase (with high asphaltene contents) to form elongated anisotropic domains.

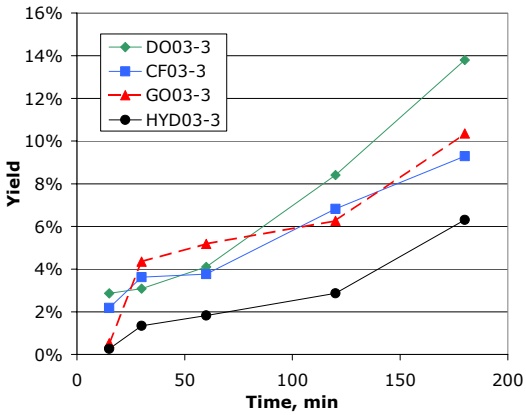

Figure 5. Coke yield at 450˚C for Set 03-3.

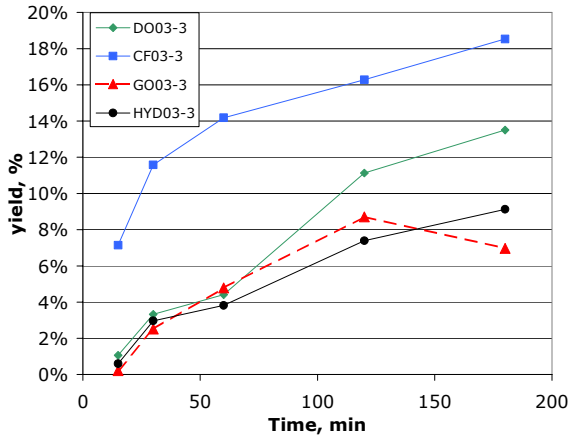

Figure 6. Asphaltene yield s at 450˚C for Set 03-3

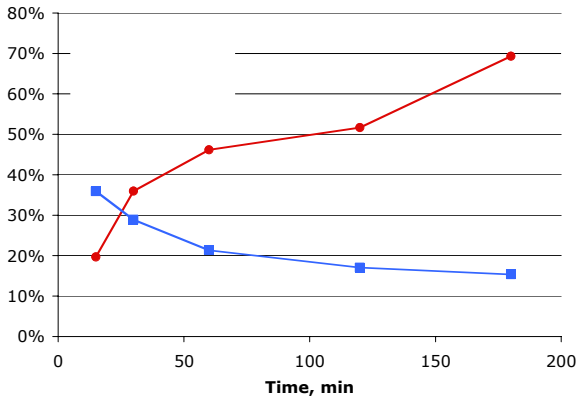

Figure 7. Coke and asphaltene yields from VTB03-3 at 450˚C

Conclusions

Significant differences were observed between the molecular composition of FCC decant oil and its derivatives in two different sample sets. Coker feeds have higher concentrations of aromatic compounds and possess higher pyrenes/phenanthrenes ratios compared to the parent decant oils. Differences in the extent of mesophase development from decant oil, coker feed, gas oil, hydrotreated gas oil, and vacuum tower bottoms can be explained by differences in their molecular composition that is closely related to their carbonization reactivity. In general, slower conversion of asphaltenes into semi-coke favors a high degree of mesophase development. Conversely, at high asphaltene levels during carbonization, effective deformation of viscous anisotropic domains during conversion to semi-coke also promotes mesophase development.

Acknowledgements. We thank Carbon Research Center at Penn State and Chicago Carbon Company for their financial support. Many helpful discussions with Robert Miller of CCC are gratefully acknowledged.

References

1. Eser, S. in Supercarbon: Synthesis, Properties and Applications, ed. By Yoshimura, S. and Chang, R.P.H., Springer-Verlag, Berlin, 1998, p. 147.
2. Mochida, I., Fujimoto, K. and Oyama, T. in Chemistry and Physics of Carbon, Vol 24, ed. By Thrower, P. A., Marcel Dekker Inc., New York, 1994, p111.
3. Gary, J. H. and Handwerk, G. E., Petroleum Refining, Marcel Dekker, New York, 2001, pp. 71,72.
4. Filley, R.M. and Eser, S., Energy Fuels, 1997,11, p. 623.
5. Eser, S., Dutta, R. Wang, G. and Clemons, J., Proceedings(in CD) of International Conference on Carbon, Beijing, 2002, Keynote Presentation, Session 32.

SIMULATED DISTILLATION OF HEAVY FRACTION BY CAPILLARY SUPERCRITICAL FLUID CHROMATOGRAPHY. EVALUATION AND COMPARISON WITH GC

Laure Dahan$., Didier Thiebaut$, Fabrice Bertoncini, Didier Espinat* and Alain Quignard**

$: Ecole Supérieure de Physique et de Chimie Industrielles de Paris
10, rue Vauquelin, 75231 Paris cedex 05, France.
*: Institut français du Pétrole
IFP-Lyon -BP3-69390 Vernaison-France

Introduction

Simulated distillation (Simdis) based on gas chromatography (GC) is widely used in the petroleum industry for evaluation of fossil fuels as well as petroleum feeds and cuts treated in refining and conversion processes. Through a calibration curve relating the boiling point of normal paraffins to their elution temperature or retention time, simdis gives the hydrocarbon distribution of the sample (in weight percent) versus the boiling range of the fraction (expressed in Atmospheric Equivalent Boiling Point, AEBP). The conditions used for simdis[1] are tuned to provide results in agreement with preparative distillation that gives the True Boiling Point (TBP) curve (described in ASTM D2892). Several methods have been standardized (ASTM D2887, D5307) for samples with a final boiling point (FBP) up to 538 °C (1000 °F). Much effort has gone into extending the range of eluted compounds and the standardization of a method up to an FBP of 700 °C is in progress (ASTM proposed test method, 1994). However, at oven temperatures up to 430 °C in high-temperature GC, the resistance of high molecular-weight hydrocarbons (HMHs) to cracking reactions is questionable[2,3,4]. This is not the case in supercritical-fluid chromatography (SFC) as high temperatures are not needed and the mechanism for extending the upper limit depends on sample solubility not volatility. Indeed, the main advantage of SFC over GC techniques comes from the solvent strength of the mobile phase. The polarity of the most commonly used supercritical mobile-phase, CO_2, depending on the operating conditions, varies between that of pentane and toluene, making SFC a potentially powerful technique for the elution of HMH at much lower temperatures than GC. This communication presents recent advances in Simdis of heavy fractions using SFC. Compared to GC, SFC calibration range is extended up to C_{120} hydrocarbons and can be extrapolated to nC_{162}, As in GC, using element selective detectors SFC could be the tool of choice for better quantitation of conversion in heavy petroleum-fraction processing.

Experimental

Samples. The samples of feed and effluents of hydrotreatment units were obtained from IFP pilot plants. The so-called feed A is a vacuum residue having the following properties: viscosity (100°C) = 1000 cst; density15/4 = 1.028; % weigh eluted at FBP (D 2887) = 48 %w/w. The effluents were obtained after demetallization (HDM) and after HDM and desulfurization (HDS) unit. Polyethylene standard like Polywax 650 and 1000 were also used to generate retention time versus boiling point calibration.

Characterization Method. An ISCO 100D supercritical fluid syringe pump equipped with specific cooling device was used. The chromatographic column was placed into a HP 6890 gas chromatograph equipped with a flame ionization detector and coupled to G 2350 A atomic emission (Agilent technologies). Splitless injections were done using a Valco Valve CI4WE1 using 1200 nl loop at 120°C after dilution into xylene for dissolving samples[3]. A (5 m x 0.05 mm x 0.2 µm) capillary column DB-5 from JW was used as stationary phase. GC simdis was performed upon the ASTM standard method (ASTM D2887, D5307 and ASTM proposed test method for HT-GC, 1994)[4] for samples with a FBP up to 538 °C and 700 °C, respectively. The SFC system is described in **Figure 1**.

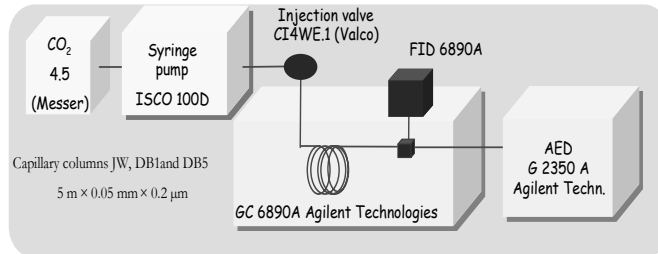

Figure 1. SFC-AED-FID hyphenation

Results and discussion

SFC simdis. Operating conditions (type stationary phase, oven temperature and pressure gradient, injection) were optimized to obtain true relation ship between retention and boiling point and to avoid discrimination of sample during the injection step. Besides, it has been necessary to obtain the lowest difference between the retention of different compounds having the same boiling point (e.g. alkanes and aromatics) for better accuracy of distillation curves. Polydimethylsiloxane bounded phases were carried out to provide no selectivity versus structure[3,5]. Thanks to optimisation of phase ratio, the heaviest compound eluted was n-C_{118}, what was quite higher than previously reported (C_{108})[5]. An example of chromatogram of standard mixture is given on **Figure 2**.

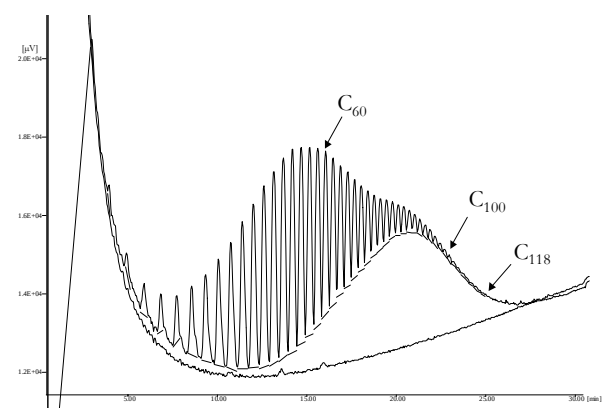

Figure 2. Chromatogram of polywax 655/1000 mixture (50/50 w/w/). Conditions: Column DB5 (5 m × 0,05 mm × 0,2 µm); 6.6 g/L; Flow-rate (CO_2) = 3 ml / min; T_{oven} = 160°C; Pressure (CO_2) 100 bars to 500 bars (30 min) at 13.3 bars/min.

Routine detection of n-C_{120} (750 °C) was observed, what means a benefit of 20 carbons benefit with regard to HT- GC (e.g. end point benefit of 50 °C). Repeatability was daily checked as critical for simdis: 20 injections of a test mixture over 35 days lead to retention time RSD less than 0.3%.

Model of retention vs. number of carbon atoms in SFC. Owing to the lack of resolution, it was not possible to identify elution peaks at the end of the chromatogram of Polywax 1000. In order to calibrate this part of the chromatogram, a model calculating n-paraffins retention times between C_{50} and C_{100} as a function of their

number of carbon atoms has been implemented. This model has been performed to check for retention time of n- paraffins in the range of C_{100} to C_{120}, for whom retention times were known from the chromatogram, and to predict retention times in the range of C_{120} to C_{162}. The comparison between calculated and measured retention times for the identified alkanes over C_{100} lead to a bias lower than 0.07 minute. The extrapolated retention times have been used to generate simulated distillation curves from C_{26} (412 °C) to C_{162} (817 °C). The **Figure 3** shows measured retention times (from C_{26} to C_{118}) and extrapolated retention times (from C_{100} to C_{162})

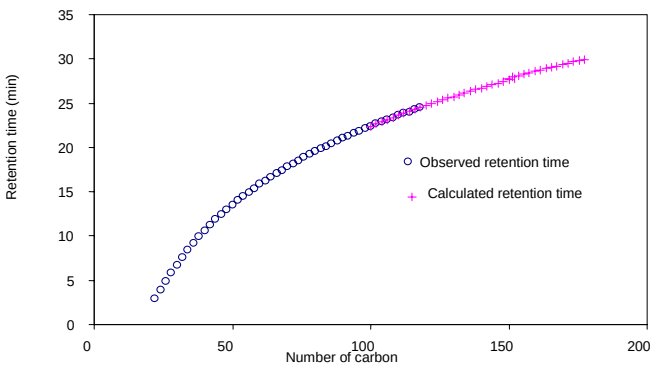

Figure 3. Comparison of extrapolated and measured retention times.

This model was carried out to characterize heavy ends using *extended SFC simdis*.

Application to feed and cuts of hydroconversion units. Our system was carried out to characterize feed A (vacuum residue) for hydroconversion unit. **Figure 4** shows the chromatogram and the upper boiling point limit typically obtained using HT-GC (nC_{106}, 731°C) and extended SFC (nC_{162}, 817°C) are indicated on the chromatogram.

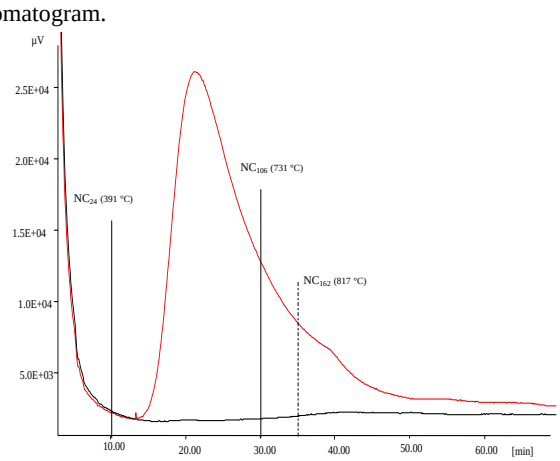

Figure 4. Chromatogram of A feed (vacuum residue)
Conditions: Column DB5 (5 m × 0,05 mm × 0,2 µm); 100 g/L; Flow-rate (CO_2) = 2 ml/min; T_{oven} = 160°C; Pressure (CO_2) 100 bars (5 min) to 550 bars (30 min) at 13.3 bars/min.

Clearly, the ability of SFC to provide the elution of HMW enables a better representation of the feed: the FBP according to HT-GC simdis corresponds to 74 % w/w of eluted fraction using SFC, what is quite less than 85 % w/w of the eluted fraction at FBP using extended SFC simdis. **Figure 5** shows simulated distillation curves obtained for HT-GC, SFC and extended SFC.

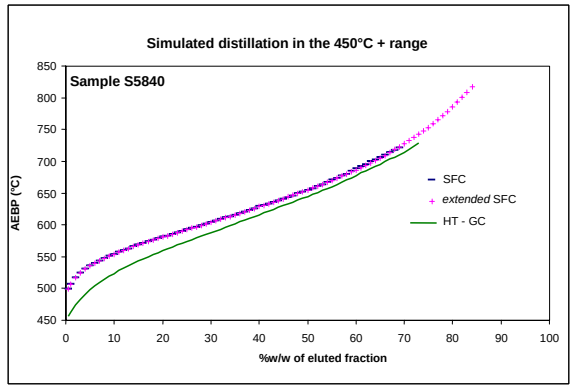

Figure 5. Comparison of simdis curves using HT-GC, SFC and extended SFC.

It is obvious that good agreement is observed between the GC and SFC data in the range of 450 °C to 731°C, as previously reported[3,5]. Using extended SFC, the upper limit can be raised above 810 °C, enabling approximately 90% of this heavy residue to be characterized. **Table 1** reports the weight percent of eluted faction corresponding at several boiling points and different samples.

Table 1 : weight percent of eluted fraction for feed and effluents obtained using extended SFC.

Boiling point (°C)	Feed A (vacuum residue) % w/w	Effluent HDM % w/w	Effluent HDM - HDS % w/w
500	0.58	0.57	4.98
600	28.3	39.72	11.07
700	63.66	70.54	51.39
750	74.39	78.89	78.53
800	81.91	84.52	88.5

As opposite to the GC simdis, SFC simdis extends the range of this application up to nC_{162}, providing better quantitation of conversion in heavy petroleum-fraction processing.

Conclusions

SFC is well adapted to the characterization of heavy hydrocarbons because of the solvating properties of supercritical fluids and could be applied in routine simulated distillation for extending the range of the technique. Besides, work is on progress to take benefit from detection facilities of SFC to perform specific Simdis curves.

References

1) Peaden, P. A. *J. High Resol. Chromatogr.* **1994,** *17*, 203.
2) Schwartz, M. M.; Brownlee, H. E.; Boduszynski, R. G.; Su, F. *Anal Chem.* **1987,** *59*, 1393.
3) Roberts, I. Supercritical-fluid chromatography, in Adlard, E. R., Ed., *Chromatography in the Petroleum Industry*, Elsevier, NL, 1995, Chap.11,.
4) Durand, J. P.; Bré, A.; Béboulène, J. J., Ducrozet, A., Carbonneaux, S. *19th Int. Symp. on Capillary Chromatography and Electrophoresis*, Wintergreen, May **1997.**
5) Robert, E.; in Caude, M.; Thiebaut, D.; Ed "*Supercritical fluid chromatography and extraction*", Harwood Academic Publishers, amsterdam,1999, chap.9..

MOLECULAR RECONSTRUCTION OF VACUUM GASOILS

Jan J. Verstraete, Nadège Revellin, Hugues Dulot, and Damien Hudebine

Institut Français du Pétrole - Development Division
PO Box 3, 69390 Vernaison, France

Introduction

In petroleum refining, both the accurate design and the optimization of conversion processes require the development of reliable kinetic models. In order to account for the differences in reactivity of the various species, more rigorous models containing molecule-based reaction pathways are needed. Such models expect a molecular description of the feed, however. Unfortunately, for petroleum cuts boiling above the naphtha range (gasoil, VGO, residue,), a molecular description can no longer be obtained directly from analyses.

To circumvent this lack of molecular information, a detailed description needs to be obtained from more global analyses. This process of approximating the composition in individual components of a feedstock from overall characterization data of the mixture has lately been referred to as "molecular reconstruction". The idea of these molecular reconstruction algorithms is to generate a discrete set of molecules whose properties mimic the properties of the petroleum cut to be represented.

Liguras and Allen[1] proposed to use a predefined set of key components and to numerically adjust their molar fractions in order to obtain a mixture that closely resembles the input analytical data. Unfortunately, this approach is based on an *a priori* definition of the components, while the adjustment of the mixture composition requires a large amount of analytical data, which are not necessarily available to refiners. To overcome these limitations, Neurock et al.[2] developed a method that was termed "stochastic reconstruction". To arrive at a description on a molecular level, a set of distributions of molecular structural attributes was first defined and then sampled by a Monte Carlo method so as to obtain an equimolar mixture of molecules. When coupled to an optimization loop, the method has been proved able to yield mixtures that closely reproduce the properties of heavy asphalthene fractions[3].

During previous work[4], two different algorithms were developed to generate a complex mixture of molecules from standard petroleum analyses: a stochastic reconstruction technique and a reconstruction method based on information entropy maximization. These algorithms were validated on FCC gasolines and on Light Cycle Oils (LCO)[5]. In the present work, a combination of both approaches will be applied to the molecular reconstruction of vacuum gasoils.

General description of the algorithm

The proposed algorithm consists in two distinct steps. After defining a molecule construction scheme tailored to the specific petroleum cut, a large set of molecules is generated via a stochastic reconstruction method. This generation is iteratively improved until it results in an equimolar mixture whose properties are close to this reference petroleum fraction. This mixture is subsequently used as a starting point and its representativeness is improved by modifying the molar fractions of the various molecules via an information entropy maximization method.

Generation of an initial set of molecules. In the first step, a set of molecules that are typical of the petroleum cut to be represented needs to be created. In this work, a stochastic reconstruction algorithm is used to create a large set of molecules that are assembled from a number of structural attributes (polycyclic cores, rings, chains, substituents,). In order to create a molecule, the type and number of these attributes are selected by randomly sampling a set of parametric distributions of the building blocks via a Monte Carlo method. During the assembly of the selected structural attributes into a molecule, a "construction scheme" and "building rules" are used to avoid the creation of unfeasible or unlikely molecules. The construction scheme is a decision tree that controls the sequence in which the various attributes are sampled. The building rules are constraints that are used to correctly assemble the various building blocks and to discard unlikely molecules based on thermodynamic or likelihood grounds. The molecule construction procedure is repeated N times in order to obtain an equimolar mixture of N molecules. For each molecule, pure compound properties are calculated from their structure, either directly by inspection (e.g. chemical formula, molecular weight, NMR, mass spectra) or numerically by group contribution methods (e.g. density, boiling point). The average properties of the mixture of N molecules are then obtained through mixing rules and compared to the available analytical data of the petroleum cut (elemental analysis, density, molecular weight, mass spectrometry,). The deviation between the experimental and simulated data is then quantified via an objective function. An elitist genetic algorithm finally modifies the parameters of the distributions for the structural attributes to minimize this objective function (Figure 1). By this procedure, the generated set of molecules is successively modified until a mixture is obtained that mimics the properties of the petroleum fraction to be represented.

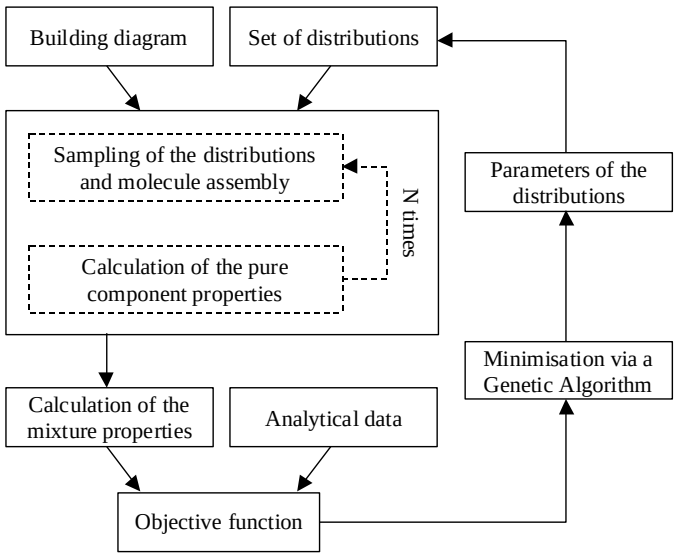

Figure 1. Stochastic reconstruction algorithm.

Enhancement of the molecule-based representation. The initial set of molecules that has been generated by the above described stochastic reconstruction method only yields an average representation of the vacuum gasoil. In order to improve the representativeness of the set of molecules, it is possible to further adjust the molar fractions of these molecules based on the available analytical data. In this work, the adjustment is carried out by maximizing the information entropy. This criterion ensures that, in absence of sufficient information, the distribution of the set of molecules will remain uniform. The introduction of constraints (i.e. analytical data for the petroleum cut to be represented) distorts the uniform distribution of the set in order to match this information. In the current implementation of the algorithm, the only restriction of the method is that the various constraints need to be linear. As

opposed to the stochastic reconstruction technique, the entropy maximization method uses a classical optimization technique. For a more detailed description of the algorithm, the reader is referred to Hudebine et al.[5].

Application to vacuum gasoils

In order to apply the above-described method to the molecular reconstruction of vacuum gasoils, an adapted molecule construction scheme needs to be defined. This requires detailing, on the one hand, the type and distribution of each structural attribute, and the construction scheme and building rules on the other hand.

The choice of the structural attributes and their distributions has been guided by knowledge of the chemical nature of these cuts, although care has been taken to minimize the number of attributes. For vacuum gasoils, the number of polycyclic cores per molecule was limited to one. The corresponding distribution for this attribute must therefore be a histogram with 2 bins: 0 or 1. Analogously, the number of rings in the polycyclic cores was limited to 7. To reduce the number of parameters, the corresponding distribution is considered to be a gamma distribution. Table 1 lists the distributions used to build a vacuum gasoil.

Table 1. Description of the Structural Attributes Used

Structural attribute	Distribution	Values	Param.
1. Number of polycyclic cores	Histogram	0 or 1	1
2. Number of rings	Gamma	0 .. 7	2
3. Presence of aromatic rings	Histogram	0 or 1	1
4. Number of benzenes	Exponential	0 .. 7	1
5. Number of hetero-atomic rings	Histogram	0, 1 or 2	2
6. Number of thiophenes	Histogram	0 or 1	1
7. Number of pyridines	Histogram	0 or 1	1
8. Number of pyrroles	Histogram	0 or 1	1
9. Alkyl chain probability	Histogram	0 or 1	1
10. Sulfide substituent probability	Histogram	0 or 1	1
11. Amine substituent probability	Histogram	0 or 1	1
12. Length of a paraffin chain	Exponential	> 0	1

The construction scheme allows to define the sequence in which the distributions are sampled. For a given molecule, the number of polycyclic cores is first selected. If this number is equal to 0, the molecule is a paraffin. Distribution 12 is then used to determine its length and each carbon atom is tested to define whether a sulfide or amine substituent should be added (distributions 10 and 11). If the number of cores is equal to 1, distribution 2 gives the total number of rings in the core, while distribution 3 indicates whether aromatic rings are present. In the latter case, the number of benzene rings and the number of hetero-atomic rings are given by distributions 4 and 5 respectively, while the number of naphthenic rings is calculated by difference. The type of the hetero-atomic rings is defined by distributions 6, 7 and 8. Once the various elements are assembled into a polycyclic core, each peripheral carbon atom is tested to check whether an alkyl chain should be inserted or not (distribution 9). The length of the alkyl chains is determined by distribution 12. Finally, distributions 10 and 11 are used to add sulfide and amine substituents.

With this molecular construction scheme, the stochastic reconstruction was used to generate an initial set of 5000 molecules that was obtained after minimization of the objective function. The latter contains the differences between the experimental and calculated values for the elemental analysis, the density, the basic nitrogen content, the liquid chromatography S.A.R. distribution and the detailed Fisher[6] mass spectrometry analysis. As can be seen in Table 2, the properties of the initial equimolar mixture of molecules obtained at the end of the stochastic reconstruction step are already close to the corresponding experimental values. Some differences still exist, especially in the simulated distillation curve, which was not included in the objective function, and in the Fisher analysis.

The second step of the algorithm adjusts the molar fractions of the various molecules via an entropy maximization method that minimizes the differences between experimental and calculated values for the simulated distillation curve, the elemental analysis, the basic nitrogen content, the liquid chromatography S.A.R. distribution and the detailed Fisher mass spectrometry analysis. The properties of the resulting final mixture are very close to the corresponding experimental values, indicating that this mixture is a good representation of the actual vacuum gasoil.

Table 2. Comparison of the Properties of the Vacuum Gasoil and of the Corresponding Molecular Set

	Exp.	Initial	Final
Simulated Distillation			
0% (°C)	388	*363*	363
5% (°C)	426	*374*	424
10% (°C)	434	*388*	434
30% (°C)	454	*434*	455
50% (°C)	476	*469*	475
70% (°C)	501	*511*	501
90% (°C)	529	*592*	528
95% (°C)	536	*626*	537
100% (°C)	543	-	568
Elemental analysis			
Carbon (wt%)	87.09	87.04	87.10
Hydrogen (wt%)	12.27	12.33	12.28
Sulfur (wt%)	0.47	0.43	0.49
Nitrogen (wt%)	0.17	0.20	0.13
Density at 15°C (g/ml)	0.9247	0.9294	*0.9246*
Basic nitrogen (wt%)	0.06	0.12	0.04
Liquid chromatography class			
Saturates (wt%)	58.6	59.1	58.6
Aromatics (wt%)	31.6	32.1	31.6
Resins (wt%)	9.8	8.8	9.8
Partial Fisher mass spectrometry			
C_nH_{2n+2} (wt%)	18.0	18.8	18.0
C_nH_{2n} (wt%)	15.2	5.4	15.2
C_nH_{2n-2} (wt%)	29.3	8.6	29.3
C_nH_{2n-4} (wt%)	0.0	7.1	0.0
C_nH_{2n-6} (wt%)	4.6	7.5	4.6

Conclusions

A molecular reconstruction algorithm was developed for vacuum gasoils. The proposed two-step algorithm first generates an initial equimolar set containing a large number of molecules via a stochastic reconstruction method. The representativeness of this mixture is subsequently refined by modifying the molar fractions of the various molecules via an information entropy maximization method. The properties of the resulting set of molecules are very close to vacuum gasoil to be represented, indicating that this mixture can now be used as input to a detailed reaction scheme for hydrocarbon conversion processes.

Acknowledgements. The authors wish to acknowledge G. Bailleux for his contribution to this work.

References

(1) Liguras, D.K.; and Allen, D.T.; *Ind. Eng. Chem. Res.*, **1989**, *28* (6), 674-683
(2) Neurock, M.; Nigam, A.; Trauth, D.; and Klein, M.T.; *Chem. Eng Sci.*, **1994**, *49* (24A), 4153-4177
(3) Trauth, D.M.; Stark, S.M.; Petti, T.F.; Neurock, M.; and Klein, M.T.; *Energy & Fuels*, **1994**, 8 (3), 576-580
(4) Hudebine, D.; Ph.D. thesis, Ecole Normale Supérieure - Lyon, **2003**
(5) Hudebine, D.; Vera, C.; Wahl, F.; and Verstraete, J.J.; 2002 AIChE Spring Meeting, New Orleans, LA, March, 10 - 14
(6) Fisher, I.P.; and Fischer, P.; *Talanta*, **1974**, *21*, 867-874

CHARACTERIZATION OF ASPHALTENES FROM MARLIM VACUUM RESIDUE USING HEPTANE TOLUENE MIXTURE

B.Avid, S. Sato, T. Takanohashi, I.Saito

Institute of Energy Utilization, National Institute of Advanced Industrial Science, 16-1 Onogawa, Tsukuba 305-8569, Japan

Introduction

Thermal cracking processes are commonly used today to convert petroleum vacuum residue (VR) into distillable liquid products. Petroleum asphaltenes (AS), the heaviest, most aromatic component of crude oil, tend to precipitate to cause coking during thermal and catalytic processing of petroleum residues. Except of the temperatures and residence times of the cracking, a number of factors are important during coking such as, the asphaltene concentrations in the feed, molecular weight, structure, aromaticity, metal and heteroatom content of the asphaltenes and nature of solvent [1-4]. The objective of this process is to maximize the yield of cracked products, on the other hand, to avoid the formation of coke deposits. These goals are only achievable through a better understanding of mechanism of the process and asphaltene structure. It is well recognized that asphaltenes from different crude oil sources can have vastly different properties. For example, two types of asphaltenes exist in the Athabasca bitumen- one type tending to lower molecular weight and having a few condensed aromatic rings per unit and the other type having a higher molecular weight and considerably more (up to c.30) condensed aromatic rings per unit [5]. Rahimi pointed out that only a portion of the asphaltenes converted to coke while the remaining portion converted to maltenes and gases [1]. Most of these studies have been concerned with simplified systems, in which asphaltenes had been extracted from their natural medium by precipitation in an excess of n-heptane (or n-pentane) and then redissolved in different solvents or re-mixing with VR to characterize the asphaltenes structure, molecular size, coke formation, aggregation and so on. Despite of these efforts, there are currently not clear picture of the asphaltene structure, conversion and mechanism of thermolysis.

The objective of this work was to separate the Marlim VR by using n-heptane-toluene mixtures and examine the behavior of the separated fractions in the coking test. The elemental analysis, NMR and GPC were applied to characterize the separated asphaltenes.

Table 1. Properties of Marlim Vacuum Residue

Elelental analysis	
C, wt %	87.2
H, wt %	10.6
N, wt %	0.69
S, wt %	0.98
O, wt %, by diff.	0.53
H/C ratio	1.45
V, ppm	73
Ni, ppm	59
fa	0.29
Molecular weight	935
Asphaltene, wt %	13.3

Experimental

The VR from Marlim crude oil (Brazil) has been used in this experiment (Table 1). The asphaltenes were precipitated from VR using n-heptane-toluene mixture (heptol), and soluble part, i.e. maltene (MA) was recovered from heptol. The content of toluene in the mixture was ranged from 0 % to 60% (by volume) and separated products were named as AS0%-AS60% and MA0%-MA60%, respectively. All samples were analysed by NMR, GPC and elemental analyses.

NMR analysis was carried out by a JEOL Lambda 500 spectrometer by applying inverse gated decoupling and DEPT pulse sequence of 45° and 135°. The distribution of aliphatic CH_3, CH_2 and CH and quaternary aromatic carbon were determined by ^{13}C-NMR and DEPT techniques [6-8].

Average molecular weight was measured by GPC system (JASCO) using KF403HQ Shodex column (exclusive limit 70,000) and Evaporative Laser Scattering Detector (ELSD) with chloroform as an eluent and polyethylene as calibration standard for molecular weight. Experiments for coke formation were carried out batchwise in an 18 ml quartz tube. The tube was loaded with 3 g of reactant and placed in a 50 ml metal reactor and pressurized with nitrogen at 1 MPa. The reactor was heated in an agitated oven at 430 °C for 1 hour and cooled to room temperature. Then reactor was vented and gas was analysed by GC, liquid product was washed by toluene and kept overnight.

The toluene insoluble product (coke) was separated by centrifuge and cake was washed again by toluene. Toluene was removed from the filtrate by rotary evaporation followed by vacuum drying at 60 °C overnight to give the coke yield.

Results and discussion

The Marlim VR was separated into the asphaltene (AS) and maltene (MA) fractions by heptol. In the case of 60% heptol, the VR was completely dissolved (no precipitation), meanwhile yield of AS 40 % was negligible, and therefore the separated products from 0 to 30 % heptol were used in further investigations. The Marlim VR and different maltene fractions (MA0%-MA30%) were examined by coking test and results of these shown in Fig.1.

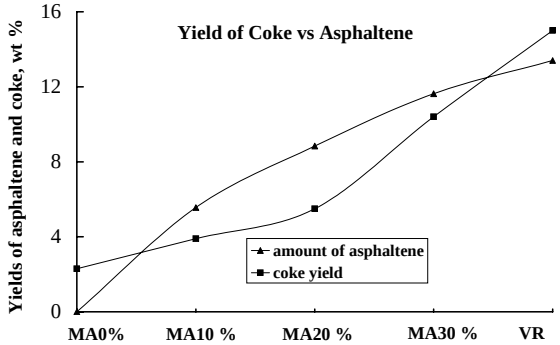

Fig.1. The correlation between coke and asphaltenes

The purpose of the experiment was just to examine the conversion of different asphaltene fractions into coke under normal processing condition. Coke is defined is insoluble in an aromatic solvent such as benzene or toluene. As mentioned before, the high content of asphaltene in vacuum residues tends to give high yield of coke. As

shown in Fig. 1, the yield of the coke was increased by 2.2 wt% with increasing of asphaltene by 9.3 wt% in the MA0% to MA 20%. The influence of asphaltene for the coke formation was negligible. But from the MA20% to MA30 %, yield of the coke was increased obviously, i.e. coke yield was raised from 5.5 to 10.5 wt%, even the content of asphaltene increased just by 3.1 wt% in this range. In this case, the increment of coke was two times higher than asphaltene increment. As can be seen from the results obtained in this work, the asphaltene exerts differently for the coke formation due to asphaltene properties. i.e. asphaltenes in the MA0%-MA30% fractions were not same, or according to Rahimi [1], the portions of asphaltenes, which are converted into the coke or maltene were significantly different in the fractions. By the other hand, portion of asphaltenes converts into maltene or gas was higher in the AS of the MA10% and MA20 % than in the MA 30%, or portion of asphaltene converts into coke was higher in the MA30%. In order to clarify the properties of different asphaltene fractions, Marlim VR asphaltene was separated into AS 0-10%, AS10-20%, AS 20-30% and AS 30 % and these fractions were analysed by elemental analysis, NMR (Fig.2) and GPC (Table 2).

The elemental analyses of the separated AS were similar, except hydrogen content. The hydrogen content of fractions is decreasing from AS0-10 % to AS30 %, and as well AS0-10% and AS10-20 % have a higher H/C ratio than AS20-30% and AS30 %. Average molecular weights (Mn) of the AS are in the range of 690 to 810 daltons. Also there is a little increase of Mn from AS0-10 % to AS20-30%. But the difference is not so high. The ^{1}H NMR analysis shows a similar distribution of the different asphaltene fractions. The aromatic proton content (Ha) is around 11%. The aromaticity (*fa)* is increasing from fraction AS0-10% to AS30 %, i.e. AS20-30% and AS30 % have a higher *fa* (0.53) than first 2 fractions and total AS (0.48). The AS20-30 % and AS30% had the highest percentage of quaternary aromatic carbon (*QAC)*, which are equal to around 40 wt% and AS 0-10% and AS10- 20% had a lower *QAC* (35-37 wt%). The distribution of non aromatic carbons shows that fraction of CH is decreasing from AS0-10% to AS30 %, the distribution of CH_2 was opposite, i.e. increasing in this range. It is likely that the AS, which have a higher aromaticity and quaternary aromatic carbon, produces more coke than AS with lower *fa* and *QAC*. Therefore, AS 0-10% and AS10-20 % were named as GOOD AS and AS20-30% and AS30 % are BAD AS.

Conclusions

The Marlim VR was separated into asphaltene (AS) and maltene (MA) fractions using n-heptane-toluene mixtures and separated MA fractions examined for coking test and results show that the AS is consisted of BAD AS and GOOD AS. So the asphaltene were fractioned into AS 0-10%, AS10-20%, AS 20-30% and AS 30 %. The AS 20-30% and AS30% have a higher aromaticity and quaternary carbons and produce more coke than the AS 0-10% and AS10-20%.

Acknowledgements

B.A. would like to thank for the JSPS fellowship. Also we are grateful to Dr. Y.Sugimoto, M. Kouzu and Mr. H. Ozawa (AIST) for help on using apparatus for coke experiments.

References

1. Rahimi P., Gentzis T., Taylor E., Carson D., Nowlan V., Cotte E., *Fuel*, **2001**, 80, 1147-54
2. Rahmani S., Mccaffrey W., Gray M.R., *Energy & Fuel*, **2002**, 16, 148-154
3. Groenzin H., Mullins O.C., *Journal of Phys. Chem. A.* **1999**, 103, 11237-45
4. Rahmani S., Mccaffrey W., Dettman H., Gray M.R., *Energy & Fuel*, **2003,** 17, 1048-56
5. Mitchell, D.L. and Speight, J.G. *Fuel*, **1973**, 52, 149-152
6. Netzel, D., *Anal. Chem*., **1987**, 59, 1775- 1779
7. Kotlyar, L.S., Morat, C. and Ripmeester, J.A., *Fuel*, **1991**, 70, 90-94
8. Masuda K., Okuma O., Nishizawa T., Kanaji M. and Matsumura T., *Fuel*, **1996**, 75 (3), 295-299

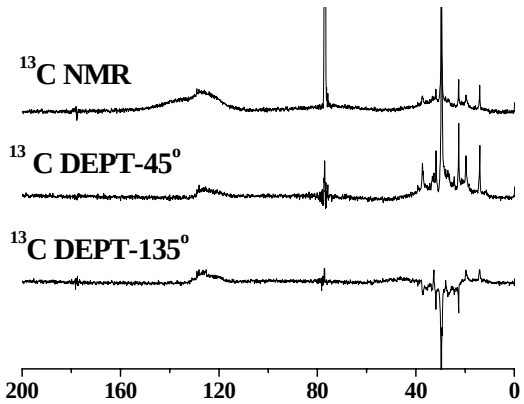

Fig.2. Typical NMR spectra of the asphaltene fractions

Table 2. Properties of the Marlim VR Asphaltenes

Sample name	Total AS	AS0-10%	AS10-20%	AS 20-30%	AS 30%
Recovery, wt%	14.2	4.1	4.7	3.6	1.8
Elemental analysis, wt%					
C	86.2	85.9	86.5	87.3	85.8
H	8.01	8.40	8.27	8.11	8.01
N	1.28	1.25	1.29	1.32	1.19
S	1.27	1.27	1.21	1.21	1.24
O	3.24	3.22	2.73	2.06	3.76
H/C	1.11	1.17	1.14	1.11	1.11
Mn (GPC)	691	743	748	806	758
NMR analysis, %					
^{1}H-NMR					
Ha	10.5	11.1	11.4	12.4	11.1
Hα	16.7	15.7	16.7	16.5	16.3
Hβ	51.6	56.8	56.2	53.0	52.7
Hγ	21.2	16.3	15.6	18.1	19.9
^{13}C-NMR					
fa	0.48	0.49	0.50	0.53	0.53
QAC	34.9	36.2	37.4	39.1	40.5
Distribution of non-aromatic carbons					
CH	20.53	15.90	15.89	13.57	10.09
CH2	61.24	64.39	64.85	67.43	70.56
CH3	18.23	19.71	19.26	19.00	19.35

QAC- Quaternary aromatic carbon

Heavy product from co-processing of FCC slurry and coal as bitumen modifier

Yongbing Xue, Jianli Yang, Zhenyu Liu, Zhiyu Wang, Zenghou Liu, Yunmei Li and Yuzhen Zhang***

State Key Laboratory of Coal Conversion
Institute of Coal Chemistry, Chinese Academy of Sciences
Taiyuan 030001, P.R.China

** Institute of Heavy Oil Research, Petroleum University (Dongying)
Dongying 257061, P.R.China

Introduction

Co-processing of coal and petroleum resid has been developed to produce liquid fuels, and has gained significant advancements during past several decades. In this work the co-processing process is adopted to produce a bitumen modifier under mild conditions. The modifier is the heavy portion of the co-processing products including un-reacted materials and ash in the coal. Oil is a byproduct. Market price of similar natural occurring modifier is about $500-$750/t in China, which is much higher than the prices of oil and road paving asphalt.

Bitumen on road experiences a wide range of static and dynamic stress at varying temperature under different environmental conditions. The lifetime of the road surface is limited due to aging of bitumen in asphalt concrete mix. Addition of non-vulcanized nature and synthetic polymers to improve the properties of paving asphalt are well known and widely used (1, 2). Reclaimed rubber, pulverized waste tire and special naturally occurring asphalt (such as Trinidad lake asphalt) are also used as additives (3, 4). Addition of these materials improves durability of asphalt surface, adhesion of bitumen to aggregate, deformation resistant at great load and freeze resistance.

Due to super road performance (4), compared to other additives, Trinidad lake asphalt (TLA) has been used in bitumen modification worldwide.

In this study slurry, from fluidized catalytic cracking (FCC) unit, and coal is co-processed. The heavy product, named MCSC (modifier from co-processing slurry and coal), is tested for possible usage on bitumen modification. Modification ability and physical and chemical properties of MCSC are presented and compared with TLA.

Experimental

The FCC slurry (FCCS), from Shijiazhuang Petroleum Refinery of China, and a Chinese bituminous coal (YZ), were used to make the modifier, MCSC. The properties of FCCS and the coal are listed in Tables 1 and 2. The base bitumen used to test the modification ability of the modifier was Binzhou 90# (AH 90 in Chinese standard specification) with a penetration value of 95. The base asphalt was mixed mechanically with the modifier.

The co-processing was carried out in a 50-liter autoclave with a magnetic stirrer under hydrogen or nitrogen pressures of 8-14 MPa at temperatures of 400-450°C for 1-3 hours. The coal was pulverized to <100 mesh and impregnated with a Fe (1 wt%) or a Mo (0.04-0.4 wt%) catalyst precursor (5). The ratios of FCCS to coal were 1:1 and 2:1. The autoclave was directly connected to a 40-liter vacuum distillation unit. After the co-processing, the mixture was discharged into the distillation unit and the oils were distilled out at 330°C and 0.01MPa. The residual materials were MCSC and collected from the bottom of the distillation column. Typically the MCSC yield ranged from 65-80% and oil yield 10-25% (boiling point ranged from 100-450°C).

The Technical Specifications of JTJ 036-98 for Construction of Highway Modified asphalt Pavement, and standard test methods JTJ 052-2000 for Bitumen and Bituminous Mixtures of Highway Engineering by Ministry of Communications of The People's Republic of China, were used.

Table 1. The Properties of the FCCS Used, wt% as[1]

Elemental composition				
C	H	N	S	H/C, atomic
88.97	8.12	0.48	1.35	1.1
Group composition				
Saturates	Aromatics	Resins	Asphaltenes	
6.7	65.7	18.7	8.9	

1: "as" denotes "as received"

Table 2. The Properties of the Coal, wt% as[1]

Proximate analysis				
Moisture	Ash	Volatile Matter		
1.50	4.17	42.86		
Ultimate analysis				
C	H	N	S	H/C, atomic
75.92	5.01	1.32	2.02	0.79

1: "as" denotes "as received"

Results and Discussion

The properties of a typical MCSC and TLA are compared in Table 3. There is no significant difference in physical properties listed in the first five lines. The main differences are in the last two lines, which reveal the higher aromaticity of MCSC than TLA, the lower hydrogen content and the higher aromatic hydrogen distribution in MCSC. The high contents of organic residue and pre-asphaltene are significant factors, which differentiate MCSC from TLA.

Comparisons of modification abilities of MCSC and TLA are given in Tables 4 and 5. The mixing ratio of the modifier to the base bitumen is 20:80. The notation 90#/MCSC refers to a modified Binzhou 90# by MCSC, 90#/TLA refers to a modified Binzhou 90# by TLA. From Table 4 it can be seen that both MCSC and TLA alter the properties of the base bitumen, increasing the softening point by about 4-8°C and decreasing the penetration value by about 51-54 points. This indicates that the modified bitumen becomes harder than the base bitumen. Usually, this change may result in loss of viscous-elasticity to some extent. But the data show that the viscous-elasticity of the modified bitumen samples is still very good as demonstrated by the high ductility values at 15°C and 25°C. The Retained penetration (the ratio of penetration value after and before TFOT, thin-film oven test, which represents the ability on resisting the fast aging) of both modified samples are also higher, suggesting higher high-temperature stability. The ductility of 101 mm for 90#/MCSC at 15°C suggests higher low-temperature stability of the sample. All these data suggest that the properties of 90#/MCSC are significantly better than that of 90#/TLA.

Table 5 compares dynamic stabilities between 90#/MCSC and 90#/TLA samples determined in the rutting test. Rutting is generated at a wheel path of carriageway in the cases of warmer climate

* Corresponding author. Tel/Fax: +86-351-404-8571
E-mail address: jyang@sxicc.ac.cn

conditions, heavily trafficked roads, approaches to intersections and climbing lanes. Dynamic stability of hot mix asphalt (HMA) against rutting is an important property of asphalt mixture in wearing course. It represents the ability to resist shoving rutting under traffic and elevated temperature. For hot mix modified bitumen mixture this value should be greater than 800-3000 wheel passes/mm depending on the climate encountered. It is clear that the dynamic stabilities of both samples are similar and meet the highest required value.

Table 3. The Properties of Typical MCSC and TLA

Items	MCSC	TLA
Specific gravity	1.15	1.39-1.44
Softening point (R&B), ^{o}C	102	93-99
Penetration at 25°C, 100g, 5s	8	0-4
Weight loss after thin-film oven test, %	<1	<2
Solubility in trichloroethylene, %	53	52-55
Inorganic residue, %	3	35-39
Organic residue, %	20	8
Preasphaltene, %	33	0.73
THF solubles, %	75	56
H/C, atomic	0.8	1.4
Aromatic/aliphatic hydrogen ratio by FTIR	7.4	0

Table 4. The Properties of Binzhou 90# and Two Modified Bitumen

Items	90#	90# /MCSC	90# /TLA
Softening Point (B&R), ℃	44.2	48.0	51.7
Penetration at 25℃, 100g, 5s	95	44	41
Ductility at 25 ℃, 5cm/min, cm	>150	>150	>150
Ductility at 15 ℃, 5cm/min, cm	>150	101	52
Flash point, ℃	>240	>240	>240
TFOT			
Softening Point (B&R), ℃	48.7	53.6	56.1
Penetration at 25℃, 100g, 5s	57	36	26
Retained penetration after thin-film oven test, %	60	82	63
Ductility at 25℃, 5cm/min, cm after thin-film oven test	150	144	100
Weight lost, ％	0.100	0.255	0.418

Table 5. The Results of the Rutting Test

Sample	90#/MCSC	90#/TLA
Dynamic stability, wheel passes/mm (60°C, 0.7 MPa)	2000-3500	3100

Further comparison on the properties of 90#/MCSC and 90#/TLA samples with ASTM standard specification, D5710-95, designated to Trinidad lake modified asphalt, showed that both modified samples meet the specifications.

It was also found that the properties of the modifier are related on the co-processing conditions used, such as temperature, atmosphere, pressure, type of catalyst, catalyst loading, FCCS to coal ratio and reaction time. Two or more modifiers can also be blended to obtain the desired properties. The properties of the modifier can be manipulated by controlling the co-processing conditions.

.

Conclusions

A heavy product (MCSC) produced from co-processing of a fluidized catalytic cracking slurry with a coal was used as bitumen modifier in asphalt concrete mix. The modification capability of MCSC is similar to that of a commercial bitumen modifier, Trinidad lake asphalt (TLA), and meets ASTM standard specification of D5710-95. Comparing to TLA, MCSC contains more aromatic, condensed, small molecular weight component.

Acknowledgement.

The Natural Sciences Foundation of China (20076050, 20076049) and Chinese Academy of Sciences are acknowledged for the financial supports. Chief Engineer Yanti Wang of Shijiazhuang Petroleum Refinery, Director Zhe Wang of Shanxi Provincial Communications Planning Survey and Design Institute, Chief Manager Zhigang Ye of Shandong SHTAR Science and Technology, Professor Bijiang Zhang of Institute of Coal Chemistry, and Manager Wen Zhou of department of bitumen of Sino Fame LTD. are also acknowledged for their valuable suggestions and providing FCCS and asphalt samples. The project is also partially supported by the Special Funds for Major State Basic Research Project (G19990221).

References

(1) Yang, Z.; Cheng, G. *Petroleum Asphalt*, **2001**, *15*, 1
(2) Xue Y.; Yang, J.; Liu, Z. *Highway* 2001, *11*, 120
(3) Ye, Z.; Kong, X., Yu J.; Wei Q;. Jiang, Z *Journal of Wuhan University of Technology*, **2003**, *25*, 11
(4) Shen, J.; *Journal of Foreign highway*, **2000,** *20*, 28
(5) Yang, J.; Zhu, J.; Xu, L.; Liu, Z.; Li, Y.; Li, B. *Fuel*, **2002**, *81*:, 1485

CHARACTERIZATION AND CRACKING PERFORMANCE OF THE MODIFIED USY ZEOLITES WITH MIXED ORGANIC ACID

Chunmin Song and Zifeng Yan

Chemistry Division
State Kay Laboratory for Heavy Oil Processing
University of Petroleum
No. 271, Bei'er Road
Dongying, China, 257061

Introduction

Fluid catalytic cracking (FCC) is one of the most important refining processes, and plays a key role in whole petroleum refining industry. 70-80% gasoline, 30-40% diesel oil and 50% propylene is come from catalytic cracking units, especially in China. Industrially, cracking reaction of hydrocarbons is catalyzed by the acid-form zeolite, especially by Ultrastable Y zeolites, which were prepared by steam dealumination of Y zeolite at high temperatures.[1] The distribution of the cracking products depends on the performance of zeolites and the reaction conditions. Hence the nature of acid sites of zeolites may strongly influence the performance of the catalytic cracking of hydrocarbon. Therefore many researchers have attempted to modify or post-synthesize zeolites to obtain optimum number and strength of acid sites and suitable pore structure with high activity and given selectivity. In addition, with the feedstocks of FCC being heavier and poorer and the tendency of increasing lighter olefins and diesel, the features of the mesopores and acid sites of USY zeolites will not meet the variation of materials in the future. Thus the modification of USY zeolite have been further paid much attention.[2]

There are different ways to modify the Y zeolite, such as hydrothermal treatment, vapor phase substitute dealumination of the high temperature, post-synthesis using $(NH_4)_2SiF_6$ and extraction by acid complexation.[3] Here the USY zeolites were treated with tartaric acid and citric acid in unbuffered system. In this process, the skeletal aluminum atom might be coordinately extruded by complex form from the skeleton of zeolite. Furthermore, the crystal structure, physical adsorption property, stability, catalytic cracking property of the modified zeolites were investigated by XRD, N_2 adsorption, FT-IR and micro-activity test(MAT). The nanopore volume, distribution and cracking Performance of the modified USY zeolites were extensively investigated in this paper.

Experimental

Preparation of modified USY zeolites. The USY parent zeolite supplied by Lanzhou Work of catalyst, whereas USY is already in its hydronium form, in which Si/Al ratio is 11.8 and the unit cell constant is 2.4432 nm. The process as follows: 6 gram of USY zeolite was placed into a three-necked flask with a certain amount dilute nitric acid as the solvent and this mixture was stirred and heated to 90℃. Then the mixed tartaric acid and citric acid solution was added. The solution was stirred for 4 h at 90℃. After reaction, the gel was filtered, washed, and dried overnight at 120℃.

Characterization Methods. The crystal structure parameter of samples was measured by X-ray diffraction (XRD) technique with a Rigaku D/max-IIIA X-ray diffractometer using Cu Kα radiation. N_2 adsorptions for the samples were carried out on a Micromeritics ASAP-2010 instrument using nitrogen as adsorbate at 77K. Before adsorption measurements the samples were degassed for 4 h at 673K. The mesopore size data were analyzed by the BJH method. The micropore size distribution was obtained by H-K method.

Micro-activity test (MAT). The modified sample was powdered, and mixed with kaolin clay matrix in the proportion of 30:70 wt% to prepare modified zeolite catalyst, while the diameter of catalyst particle is about 100-150 mesh. The catalyst was treated at 800°C with 100% steam for 4 hours prior to catalytic reaction. The catalytic cracking activity of the catalyst was assessed with an MRCS-8006 type microreactor, which is designed according to ASTM D-3907-80. The feedstock is Shenghua VGO, supplied by Shenghua Oil Refinery Factory, University of Petroleum. The density of feedstock is 0.8857 g/cm^3(20°C). Reaction temperature was 550°C and the ratio of catalyst to oil was 3. The liquid products were analyzed by HP5880A chromatography of simulating distillation. The vapor products were analyzed by HP5890Ⅱ GC equipped with a FID and a 50m fused silicon capillary column. The reacted catalyst were analyzed by self-made carbon mensuration, and worked out coke content of catalyst. The amount of gasoline and of diesel was calculated by simulating distillation. The distillates <204°C was distributed to gasoline part, and between 205 and 350°C was assigned as diesel part, and >350°C referred to heavy oil part, which might be assigned as the not converted feed part.

Results and Discussion

USY zeolite is typical active component for hydrocarbon cracking catalysts, which has special nanopore and acid sites. The special nanopores insure the product selectivity and acid sites hold out the high conversion of heavy hydrocarbons. It means that optimization of nanopore and acid sites of zeolites might be the key to design the effective catalyst of hydrocarbons cracking. The current USY zeolites that has been employed industrially is obtained by hydrothermal dealumination under high temperature. Its dealumination degree is rather limited, and that the non-framework aluminum formed during the steam treatment may affect the catalytic performance of zeolites catalysts. Here USY zeolites were modified with tartaric and citric acid in unbuffered system. The modification results indicate that modified zeolite samples with higher Si/Al ratio can be prepared by this method, which shows higher yields of lighter olefin and diesel oil in traditional FCC process. The investigation indicates that the PH value and the amount of the tartaric and citric acid have greatly influence, and that the treatment time and the drop velocity of the acids has little influence on the modification.

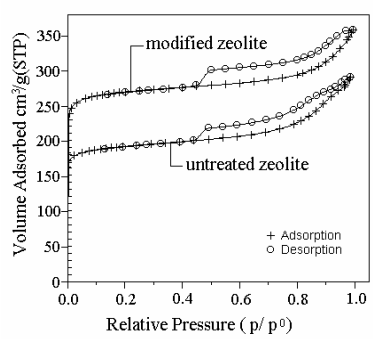

Figure 1. Nitrogen adsorption isotherms of untreated zeolite and modified zeolite.

The results of XRD patterns show that the Si/Al ratio of modified samples increases as compare to that the parent zeolite. This indicates that chemical dealumination of USY zeolite result in framework reconstruction of USY zeolite skeleton. Aluminum is subsequently removed from the zeolite crystal as a soluble tartaric and citric aluminum complex. Simultaneously, some extraframework silica fills the skeleton vacancies left by dealumination. Thus, the

structure differences exist between USY and midified samples due to framework dealumination and formation of mesopores.

The isotherms of nitrogen adsorption shown in **Figure 1** indicate that this is in good agreement with the reported in the literature[4], which attribute to type Ⅳ with a distinct hysterasis loop. Furthermore, the nitrogen adsorption amount of the modified samples is increased, but the shape of the isotherm is not change. The micropore distribution of modified samples shown in **Figure 2** indicates that the number of micropore is increased. It means that the pore volume of modified samples is rather more developed than that of the untreated zeolite and the pore distribution gradient is not obviously changed.The increase of micropore may be beneficial not only to the rebuilding of the framework, which leads to the transformation of larger mesopores into several micropores, but also to the enlarging tendency of the existing micropores. Micropore is the major nanopore in modified zeolite. However, it might be favor the deep cracking reactions to produce much more LPG or lighter olefins due to micropore volume increasing.

The mesopore distribution of modified zeolite and untreated zeolite is shown in **Figure 3**. It indicate that secondary mesopore volume is positively improved, and the secondary mesopore diameters of modified samples were concentrated at ca. 3.8 nm, which might be desirable for FCC processes of residual oil or heavy feedstocks. Furthermore, it is also advantage for production of diesel fraction in FCC process.

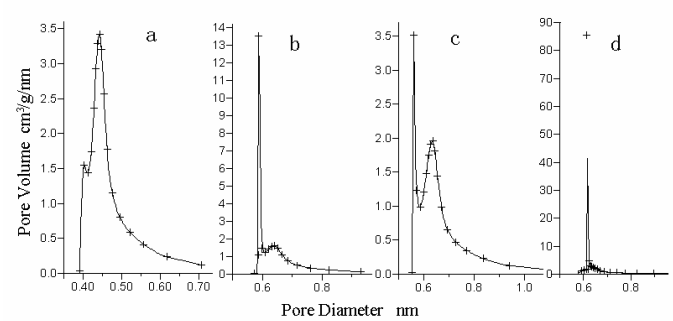

Figure 2. The micropore distribution of modified zeolites(where a is untreated zeolite; b, c and d are modified zeolites).

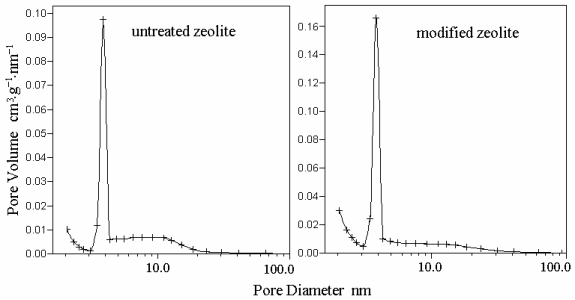

Figure 3. The mesopore distribution of modified zeolite and untreated zeolite

The IR spectra show that the hydroxyls with IR bands of 3610 and 3575 cm^{-1} in the micropors or small cages bears the stronger acidity and much more sites than those in mesopore or larger cavities. The special acid distribution is rather preferable to produce more diesel oil and lighter olefins in FCC process. The catalytic performance of the modified zeolite catalyst is shown in **Figure 4** and **Figure 5**. The result indicates that the diesel yields of the modified samples are effectively improved, and the activity of the modified catalyst have slightly decreased. Simultaneously, the coke formation of the modified samples ware obviously inhibited, and the yield of lighter olefins have partially increased. This is due to the acid sites of the modified samples decrease in number, but enhance in strength. Generally, the lighter olefins should be preferably produced on stronger acid sites in micropores or small cavity, while the diesel distillate is mainly formed on the medium and weaker of acid sites in mesopores or supercages. The modified zeolites have the gradient distribution of acid sites and nanopores. The gradient distribution of acid sites in mesoporres or large cavity might effectively inhibits the occurrence of the hydrogen transfer reaction and deep cracking and coke formation, which result in the increase of the yield of lighter olefin and diesel, decrease of the coke yield. Furthermore, the result of the fixed bed evaluation using amplificatory modified samples is in good agreement with that of laboratory test (MAT). Thus optimization of nanopores and acid sites of USY modified with tartaric acid and citric acid in unbuffered system might result in an industrial process to design novel FCC catalysts.

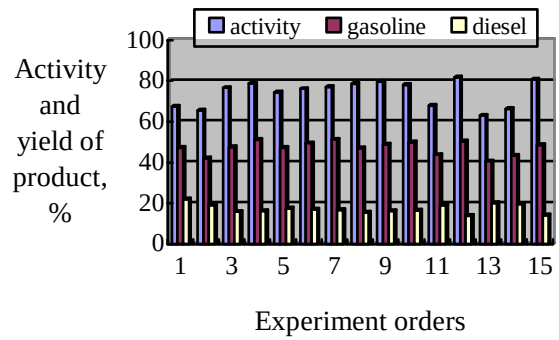

Figure 4. The activity and the yield of gasoline and diesel (where 15 is untreated sample).

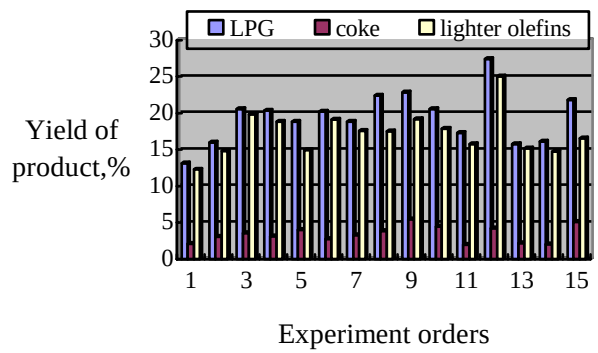

Figure 5. Profile of the product yield (where 15 is untreated sample).

Acknowledgments

We gratefully acknowledge financial support by PetroChina Company Limited (Grant No. 010301-04).

References

1. Fleisch, T.H., Meyers, B.L., Ray, G. J., Hall, J. B., Marshall, C. L., *J. Catal.*, **1986**, 99, 11.
2. Zhou, P., *Petrol. Proc. Petrochem. (China)*. **1997**, 28, 52.
3. Liu, X. M.; Qian, L.; Yan, Z. F., *J. Petrochem. Univ. (China)*, **1997**, *10*, 4-26.
4. Nguyen, C., Sonwane, C.G., *Langmuir*, **1998**, 14, 4950

HYDROISOMERIZATION OF N-TETRADECANE OVER P MODIFIED Pt/SAPO-11 CATALYST

Cheng-Hui Geng, Fei Zhang, Zhi-Xian Gao, Jing-Lai Zhou*

Institute of Coal Chemistry,Chinese Academy of Sciences
Taiyuan 030001, P. R. China

Introduction

As is well known, the hydroisomerization process uses a metal/acid zeolite catalyst that has been described as bifunctional[1]. Noble metal such as Pt, Pd, and bimetal supported on ZSM-12, mordenite, USY, L-zeolite and β-zeolite have been employed as the bifunctional catalysts for hydrocarbon hydroisomerization process[2]. With these classical catalysts, high isomerization selectivity has been obtained only at relatively low conversion levels, but the selectivity decreases drastically at higher conversion levels and thus the formation of cracking products predominates.

Recently, great improvements have been achieved by using SAPO-11 supported Pd or Pt catalysts[3,4,5,6,7]. Generally SAPO-11 has a lower acidity than zeolites[8], and has been proved to more suitable for constituting catalysts that manifest better performance for long-chain hydrocarbon isomerization. The aim of this work is to investigate the effect of the phosphor modification of SAPO-11 on the catalytic activity, product selectivities and time-on-stream stability. The effects of reaction conditions on the catalytic performance were tested by varying reaction parameters such as temperature, pressure and WHSV, as well as the H_2/CH (H_2 to hydrocarbon) ratio. The obtained data were compared with our previous findings and used to interpret the formation of feed isomers as well as their distributions.

Experimental

Catalyst. The calcined SAPO-11 sample was mixed with a certain amount of alumina, and extruded into cylindrical shape. After drying at 120℃, the extrudate was crushed and sieved to obtain particles with a diameter of about 0.5mm. For P modification, the particle was impregnated with a dilute orthophosphoric acid, followed by drying and calcination at 120℃ and 500℃, respectively. The amount of P in the sample was designed to be 1% by weight.

SAPO-11 supported Pt catalysts were prepared by incipient wetness method. The obtained samples containing 0.4% platinum are denoted as 0.4Pt/SAPO-11 for non-modified and 0.4Pt/SAPO-11(P) for P-modified samples, respectively. The acidity of support was measured by NH_3-TPD, and the dispersion of Pt was estimated by H_2 chemisorption measurement at room temperature on a self-equipped apparatus system. Details on these characterizations can be found elsewhere[9].

Catalytic activity measurements. Hydroconversions of *n*-tetradecane were carried out in a 10ml fixed bed reactor system. Previous to activity measurements, the catalyst was pretreated in-situ first with air, then with H_2 up to 400℃ for 2h. Reaction products were analyzed in a GC with a flame-ionization detector. Product identification was achieved by GC-MS and by comparing the retention time of some pure compounds with separate GC injections. The carbon numbers of all the peaks were settled, but only some of the structures could be identified.

Results and Discussion

The hydroconversion of n-tetradecane on the two Pt/SAPO-11 catalysts gave both isomerization and cracking products, but with a higher selectivity to feed isomers at low temperatures. The cracking products consisted of spectra of C_1-C_{13} hydrocarbons with pretty high percentage of C_3-C_7. Minor amount of C_1 and C_2 were obtained, which suggests that the hydrogenolysis on the Pt/SAPO-11 catalysts of 0.4 metal loading is negligible.

As was expected, the conversion of *n*-tetradecane increased with reaction temperature, while the selectivity to tetradecane isomers decreased gradually. At higher temperatures, with conversion level reaching more than 90%, the cracking reactions became pronounced, giving an isomerization selectivity of less than 10%. As shown in **Fig1**, both the activity and isomerization selectivity are improved by P modification, especially at low temperature range. This may be attributed to the increase of weak acidity by P modification as indicated by NH_3-TPD data.

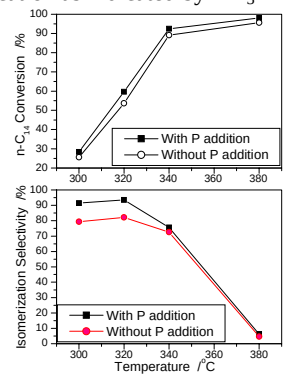

Fig1. Effect of reaction temperature on the hydroconversion of n-C_{14} over 0.4Pt/SAPO-11(P) and 0.4Pt/SAPO-11 catalysts
Condition: P=30atm, WHSV=2.0h^{-1}, H_2/C_{14}=8.7(mol/mol).

Comparing these results with our previous findings[10], which shown more than 80% isomerization selectivity of even at 90% conversion over a SAPO-11 catalyst of the same metal loading, we come to the conclusion that the catalytic behavior is largely influenced by the nature of SAPO-11 molecular sieve.

The effect of total reaction pressure on n-C_{14} hydroconversion was investigated, and the results are presented in **Table1**. As shown in the table, both the conversion of n-C_{14} and the yield of feed isomers decrease with increasing pressure. The results indicate a negative reaction order with respect to hydrogen, which is consistent with the known data[11,12].

Table1. Effect of Pressure on N-C_{14} Hydroconversion over 0.4Pt/SAPO-11(P) Catalyst

P atm	Conv %	Y_{iso} %	S_{iso} %	Monomers /%	Distribution of monomers		
					3	2, 4	5, 6, 7
10	84.8	77.4	91.3	61	0.21	0.28	0.51
20	68.7	61.8	90.0	76	0.21	0.27	0.52
30	59.6	55.8	93.5	78	0.22	0.30	0.49

Reaction conditions: temperature 320℃; Whsv2.0 h^{-1}; H_2/CH 8.7

As shown in **Table2**, the conversion of n-C_{14} and the yield of liquid as well as the yield of isomers increased with decreasing whsv. The retention time of feed on the catalyst increases with the decreasing of whsv, and thus the increase of conversion is expectable.

The influence of H_2/CH ratio on n-C_{14} hydroconversion is shown in **Table3**, the conversion of n-C_{14} decreases with increasing the partial pressure of hydrogen (the H_2/n-C_{14}(mole) from 4.3 to 8.7), while the isomerization selectivity increases. The changes are relatively small with a higher WHSV of 4.1h^{-1}. It should be point out that at pretty low H_2/CH ratio, catalyst deactivation became predominant. All these reflect the importance of H_2 in the

* Corresponding author, E-mail: gaozx@sxicc.ac.cn

isomerization process. And the role of H_2 during isomerization might be the same as we have discussed in a previous paper[1 3].

Table2 Effect of WHSV on N-C_{14} Hydroconversion over 0.4Pt/SAPO-11(P) Catalyst

WHSV h^{-1}	Y_l %	Conv %	Y_{iso} %	S_{iso} %	Monomers /%	Dis. of monomers 3	2, 4	5, 6,7
4.1	98.4	34.3	32.7	95.3	87	0.20	0.32	0.48
3.0	99.1	44.6	42.6	95.5	85	0.19	0.29	0.52
2.0	98.8	59.6	55.8	93.5	78	0.22	0.30	0.49
1.0	97.6	83.8	74.8	89.2	64	0.22	0.30	0.48

Temperature320℃ Pressure 30atm; H_2/CH 8.7mol/mol

Table3. Effect of H_2/CH Ratio on the Hydroisomerization of N-C_{14} over 0.4Pt/SAPO-11(P) Catalyst at 30atm

Temp ℃	H_2/CH mol/mol	Whsv h^{-1}	Conv %	Y_{iso} %	S_{iso} %	Monomers %	Dis.of monomers 3	2, 4	5, 6,7
300	4.3	2.0	39.8	33.6	84.6	85	0.21	0.31	0.48
300	8.7	2.0	28.4	25.9	91.5	86	0.23	0.29	0.48
320	4.3	4.1	37.0	33.3	90.2	84	0.21	0.30	0.49
320	8.7	4.1	34.3	32.7	95.3	87	0.20	0.31	0.49

It was found that the catalytic behavior of 0.4Pt/SAPO-11(P) catalyst with time on stream was largely influenced by operating parameters. A larger H_2 partial pressure inhibited the *n*-tetradecane conversion, while a slower deactivation was observed. Noticeable catalyst deactivation was observed at a lower reaction pressure, especially at atmospheric pressure, while at pressures higher than 10atm, the isomerization process was stabilized in 30 minutes (**Fig2**).

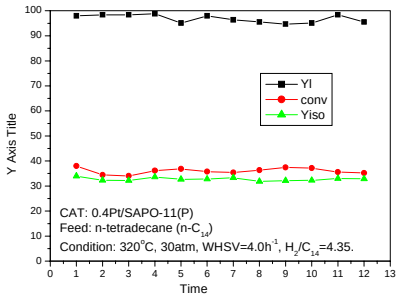

Figure 2 Catalytic performance of 0.4Pt/SAPO-11(P) catalyst in n-C_{14} hydroconversion. (Yl=Yield of Liquid)

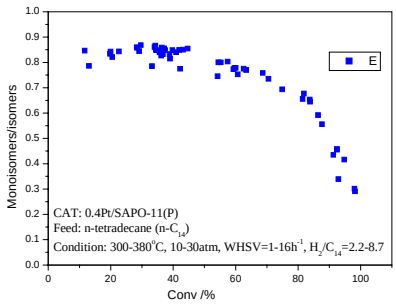

Figure 3. Change of Monoisomers/isomers ratio as a function of the n-tetradecane conversion over 0.4Pt/SAPO-11(P) catalyst

Though the change of reaction variables, such as pressure, whsv and H_2/CH ratio, did affect the distribution of the isomerization products (Table 1-3). It has been found that the distribution can only be correlated with conversion level of n-C_{14} as shown in **Fig.3**. The content of mono-isomers in the isomerization products decreases with increasing conversion level, indicating secondary transformation of mono-branched isomers to multi-branched isomers. However, the distribution of mono-branched isomers was found to be independent of conversion level. In the conversion range up to 90%, the distribution of positional mono–branched isomers changes little (**Fig4**). Of the mono-branched isomers, most are central positional methyl branched isomers, namely, 4-, 5-, 6-, 7-methyltridecane, which is highly desired components for diesel and lube base oil.

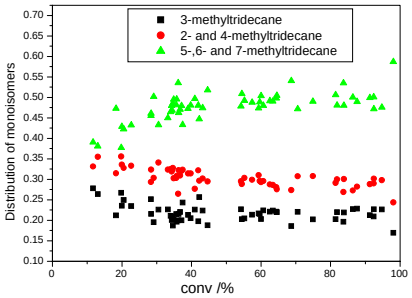

Figure 4. The distribution of mono-branched isomers as a function of n-tetradecane conversion over 0.4Pt/SAPO-11(P) catalyst

Conclusions

An increase of activity was observed with the P modified catalyst, and isomerization selectivity was also improved especially at low temperature with a conversion up to 85%. The content of mono-isomers decreased with increasing conversion levels of n-tetradecane, while the distribution of the mono-isomers changed little. The high Pt dispersion and relatively large amount of weak acidity of P modified Pt/SAPO-11 catalyst account for the improved hydroisomerization performance. Comparing these results with our previous findings, we come to the conclusion that the catalytic behavior is largely influenced by the nature of SAPO-11 molecular sieve.

Acknowledgement. Financial aid from Fushun Petrochemical Company is gratefully acknowledged. The authors thank the State key laboratory of Coal Conversion for basic sample characterizations and collecting the GC-MS data. The authors are indebt to Dr. Zhao Liangfu, Ms. Li Yuan, Ms. Wang Hairong and Mr. Dong Lingyao who participated in this work.

References

1 Weitkamp, J., *Ind. Eng. Chem. Prod. Res. Dev.* 1982; 21, 550.
2 Zhang W. and Smirniotis P.G. *J. Catal.*, 1999, 182, 400–416.
3 Thomson, R.T., Noh, M.M., Wolf, E.E. *Am. Chem. Soc. Symp. Ser*. 1990, 437, 75.
4 Choung, S.J., Butt, J.B. *Appl. Catal*. 1990, 64, 173.
5 Halik, C., Chaudri, S.N., Lercher, J.A., *J. Chem. Soc. Faraday Trans.* 1989, I 85, 3879.
6 Martens, J.A., Grobet, P.J., Jacobs, P.A. *J. Catal*. 1990, 126, 299.
7 Thomson, R.T., Wolf, E.E., Montes, C., Davis, M.E. *J. Catal*. 1990, 124, 401.
8 Hasha, D., Saddalrriaga, L., Hataway, P.E., Cox, D.F. and Davis, M.E., *J. Am. Chem. Soc.* 1988, 110, 2127.
9 Geng C.-H., *Ph. D. Thesis*, Institute of Coal Chemistry, Chinese Academy of Sciences, 2003.11.
1 0 Geng, C.-H., Zhang F. Gao, Z.-X., .Zhao, L.-F., and Zhou. J.-L., *Proc.3rd Asia-Pacific Congress on Catalysis*, Dalian, China Oct.12-15, 2003; pp804-805.
1 1 Hollo, A., Hancsok, J., Kallo. D. *Appl. Catal. A: General*, 2002, 229, 93-102.
1 2 Chao, K.-J., Lin, C.-C., Lin, C.-H., Wu, H.-C., Tseng C.-W., Chen; S.-H., *Appl. Catal. A: General*, 2000, 203, 211-220.
1 3 Gao, Z.-X., Geng, C.-H., .Zhao, L.-F., Zhang F. and Zhou. J.-L., *Proc.4th Korea-China Joint Workshop on Clean Energy Technology*, Jeju Island, Korea. Oct. 2002; pp267-273.

DEPOSIT FORMATION CAUSED BY THERMAL STRESSING OF PETROLEUM AND COAL-DERIVED JET FUELS ON INCONEL 718 AND FUEL PRE-TREATMENT EFFECT

Orhan Altin and Leslie R. Rudnick

The Energy Institute
The Pennsylvania State University
University Park, PA 16802, USA
Phone: 814-865-2490

Introduction

Jet fuel is presently used as a coolant in military aircraft, in addition to its primary use as a propellant. It is used to cool the lubrication system, avionics, electrical systems, and environmental control systems, and is also used as a hydraulic fluid (1). The trend of advanced aircraft toward increasing performance results in the formation of carbon deposits on the metal cooling line surfaces. The buildup of deposits in aircraft fuel systems is a major concern because of resulting possibility of fuel system failure. To achieve optimal performance capabilities for the next generation of jet engines, significant improvement in jet fuel thermal stability is necessary. This objective has led Penn State University and U. S. Air Force to initiate a program to develop a jet fuel that would be thermally stable up to 480˚C (900˚F). Napthene-rich coal derived jet fuels have been shown to be more thermally stable than their petroleum-derived counterparts. The thermal stability requirements of these advanced fuels indicate the types of hydrocarbons and potential additives that may be present in advanced fuels (2,3). Exposure of metallic surfaces to jet fuels at temperatures higher than 400˚C lead to carbonaceous deposits (4-6). Various metallic alloy candidates were examined at Penn State to observe their catalytic activity in carbon deposit formation from jet fuel decomposition and found that Inconel X and Inconel 718 collected significantly less amount of deposit at 500 and 600 ˚C during jet fuel stressing experiments (7-8). The sulfur level and type of sulfur compounds present in the jet fuel are also crucial parameters from the surface catalytic effect point of view. It was found that sulfur compounds decomposed to form elemental sulfur which has high tendency to react with the alloying elements of metal surface resulting severe surface corrosion (9-10).

Hydroperoxides and peroxides are early precursors in the oxidative degradation of hydrocarbons. Activated alumina is effective in destroying organic peroxides and hydroperoxides present in organic samples. In earlier preliminary work (11), it was found that a small amount of alumina added to a sample, and then rempved by filtration just prior to thermal treatment of jet fuel, resulted in less color change and essentially no carbonaceous deposit formation under conditions that produced significant quantities of deposit in darkly colored products. These earlier studies prompted the experiments described herein.

This study examines the thermal stability behavior of 1:1 and 3:1 blends of hydrotreated refined chemical oil (HDT-RCO with hydroterated light cycle oil (HDT-LCO), and JP-8 on Inconel 718 surface at 500˚C of fuel temperature in terms of carbon deposit amount and microscopic deposit morphology.

Experimental

The fuels tested in the thermal stressing experiments on Inconel 718 are coal-based blends (1:1 vol) HDT-RCO/HDT-LCO), (3:1 vol) HDT-RCO/HDT-LCO), and petroleum-based JP-8. None of the jet fuel range materials contained additives. The nominal composition of Inconel 718 alloy is (wt%) Ni: 52.5, Fe:18.5, Cr:19, Mo:3.05, Al:0.5, Ti:0.9, Nb+Ta:5.13, Cu:0.15, Mn:0.18, Si:0.18, C:0.04, S:0.0008. The alloy foils, 15 cm x 3 mm x 0.6 mm, were cut and rinsed in acetone. Thermal stressing of fuels was carried out at 470˚C fuel temperature (525˚C wall temperature) and 250 psig (17 atm), 500 psig (34 atm) and 900 psig (61 atm) in the presence of Inconel 718 alloy foil. The fuel was subjected to stressing for 5 hr at a 4 ml/min flow rate. The alloy foil was placed in the 20 cm and 1/4 in OD glass lined stainless steel tube reactor. Chemical composition of jet fuels was determined by using GC/MS analysis. Sulfur content of the jet fuels was measured by using GC/PFPD. The total amount of carbon deposition on metal coupons was determined using a LECO Multiphase Carbon Analyzer. The deposits formed on Inconel 718 surface were characterized by temperature-programmed oxidation (TPO), Field Emission SEM, and energy-dispersive spectroscopy (EDS).

Results and Discussion

Carbon Deposit Analysis - Thermal stressing of petroleum-derived, and coal/petroleum blended fuels in the presence of Inconel 718 has been shown to produce a wide range of carbon deposit amounts (12). Carbon deposit amounts are given in terms of µg C per cm^2 of Inconel 718 alloy.

In this study, as a result of reaction at 500˚C and 250 psig, jet fuel consisting of a hydrotreated mixture of 3:1 RCO/LCO (as received) produced higher levels of carbon deposit (33.7µgC/cm^2) than a hydrotreated mixture of 1:1 RCO/LCO (as received) (9.8µgC/cm^2) (Table 1). In this report, as received is meant to be hydrotreated product, stored in the presence of air. At 500 psig under similar conditions, the 3:1and 1:1 fuels gave 3.9 and 3.6µg/cm2, respectively, and at 900 psig, the results were 5.7 and 2.9 µgC/cm^2, respectively. These results suggest that consistently lower deposits can be obtained with the hydrotreated 1:1 RCO/LCO fuel. The sulfur content of the hydrotreated mixture of 3:1 RCO/LCO (as received) is 68.1 ppm, which is about four times the sulfur content of the hydrotreated mixture of 1:1

RCO/LCO (as received). In fact the 1:1 fuel has a sulfur content of only 16 ppm.

One strategy in this work was to evaluate the effect of removing peroxides and hydroperoxides that are expected to be present in the fuels due to the practice of storing fuels in the presence of air. It is believed, although not quantified in this study, that the reduction of peroxides and hydroperoxides present in a fuel would result in a reduced rate of formation of carbonaceous deposits when the fuels were thermally stressed. These peroxy compounds serve to initiate the process of fuel degradation and result in deposit formation. By removing these peroxides, the process of degradation should be retarded.

A common way to remove polar impurities from an organic compound or mixture of compounds is to treat the sample with activated alumina or similar material. In this study, Brockmann, Activity Grade I alumina was used. In general, about 100 grams of alumina was used to treat 1.5 liters of jet fuel.

The results of thermally stressing these alumina-treated samples shows that at 500˚C and 250 psig, the hydrotreated mixture of 3:1 RCO/LCO (alumina treated) produced much lower levels of carbon deposit (3.8µgC/cm^2) than hydrotreated mixture of 3:1 RCO/LCO (as received) (33.7µg/cm^2). This benefit was also achieved at 500 C and 500 psig where ~0 ug/cm2) deposit was observed for the alumina treated sample versus 3.9 µgC/cm^2 for the as received sample.

The sulfur content of the filtered sample of hydrotreated mixture of 3:1 RCO/LCO was measured to be 64 ppm, very slightly lower than the as received sample. This implies, but does not prove, that sulfur removal is not causing the very large decrease in the quantity of deposit formation. It is possible that a specific sulfur-containing component that initiates deposit formation is being removed, but it is more likely that the removal of peroxides and hydroperoxides is contributing to the improved thermal stability performance of alumina-treated fuels

In a similar set of experiments in which the fuels were recycled through the reactor for 5 passes, it was found that at 500˚C and 500 psig, the values for 3:1 and 1:1 blends only changed from 3.9 to 5.9 µgC/cm^2 and from 3.6 to 3.1µgC/cm^2, respectively (Table 2). Mechanistically, this implies that components that affect carbon deposit react rapidly to produce deposit in the first pass and are not stable enough to survive and produce additional deposit in subsequent passes. Thus, if they can be removed the fuel should remain more stable.

It is interesting to compare these results to those from the thermal stressing of JP-8, a completely petroleum-derived fuel. Untreated JP-8 produced 5.3-7.0 µgC/cm^2 of deposit when thermally stressed at 500˚C and 250 psig for 5 hours (Table 3). The result for as-received hydrotreated mixture of 1:1 RCO/LCO is almost as good as JP-8 under these conditions and the coal-derived blended fuel only contains 16 ppm sulfur as opposed to the 714 ppm found in the JP-8.

TPO and FESEM/EDS analysis - Using TPO in conjunction with SEM/EDS analysis, an attempt was made to understand the carbon deposit structural and morphological properties resulting from these experiments. Figures 1a and 1b illustrate oxidation profiles of carbon deposits from petroleum and coal/petroleum blended fuels. For most of the examined fuels, mainly three carbon deposit burn-off temperature ranges exist; the TPO peaks before 300˚C, between 300 and 450˚C, and after 450˚C. The carbon deposits burnt away before 300˚C can be attributed to highly amorphous and homogeneously formed, the deposits between 300 and 450˚C are filamentous-more ordered structures containing metal particles which decrease the burn-off temperature, the deposits giving peaks higher than 450˚C are presumably formed due to strong catalytic effect of Ni and Fe alloying elements of Inconel 718 alloy (7).

Figures 1a and 1b show the TPO profiles of carbon deposits from thermal stressing of RCO/LCO (1/1) and RCO/LCO(3/1), respectively at 500˚C and pressures of 250, 500, and 900 psig for 5h. The different pressure experiments indicate that as pressure increases amount of carbon deposit accumulation reduces significantly for both fuels. The dominant TPO peak appeared at 400˚C for 500 and 900 psig pressure experiments indicating that the pressure effect above 500 psig is mostly on the amount of deposit not on the carbon deposit morphology. At 250 psig, however, TPO peaks at 500 and 600˚C were observed and this result strongly indicates the generation of very reactive radical formation resulting in catalytic carbon deposit formation.

SEM images in Figure 2 clearly show the difference between the RCO/LCO fuels blending ratio effect on carbon deposit formation in the presence of Inconel 718 alloy at 500˚C and 500 psig for 5h. The 3:1 RCO/LCO fuel thermal decomposition produced large amount of carbon deposits almost totally covered the alloy surface. However, RCO/LCO 1:1 fuel thermal stressing resulted in significantly less amount of carbon deposition which is in the particulate form on the alloy surface. Therefore, one can conclude that increase in the RCO ratio facilitates the carbon deposit formation, which might be due to higher sulfur content and RCO hydrocarbon composition.

Conclusions

Carbon deposition from aircraft fuels begins at fuel temperatures on the order of 500˚C, depending upon fuel and metal surface properties. In this work it was found that filtering coal-based jet fuels improves performance in thermal stressing studies by lowering the amount of carbonaceous

deposits. Furthermore, the morphology of the deposit is changed. Although measured sulfur contents of the filtered jet fuels were numerically slightly lower than the unfiltered samples, the sulfur contents were not significantly changed by the filtering process. Sulfur contents of coal-based jet fuels are significantly lower than JP-8 and 1:1 HDT RCO:LCO at 16 ppm sulfur is a good fuel. It is believed, although not quantified in this study, that the reduction in deposits is due to a reduction in peroxides and hydroperoxides present in unfiltered, air exposed jet fuel samples. These peroxy compounds serve to initiate the process of fuel degradation and result in deposit formation. By removing these peroxides, the process of degradation is retarded. We are continuing to investigate the chemistry of these observations.

Acknowledgments: This work was funded by the Air Force Research Laboratory/Aero Propulsion and Power Directorate, Wright Patterson AFB. We thank Prof. H. H. Schobert of PSU for his support. We also want to thank Lu Sun for total sulfur analysis of fuels.

References

(1) Zabarnick, S.; *Ind. Eng. Chem. Res*. **1994**, *33*, 1348.
(2) Edwards, T.; Harrison, W. E.; Schobert, H. H.; AIAA 97-2848.
(3) Edwards, T.; Atria, J. V.; ASME, 97-GT-143.
(4) Stickles, R. W.; Dodds, W. J.; Koblish, T. R.; Sager, J.; Clouser, S.; *Agard Conf. Proceed. 536, Fuels and Comb. Techn. for Adv. Aircraft Engines*, Italy, **1993**, *20*.
(5) Linne, D. L.; Meyer, M. L.; Edwards, T.; Eitman, D. A.; AIAA-97-3041.
(6) Altin, O.; Eser, S.; *Ind. Eng. Chem. Res*., **1999**, *39(3)*, 642.
(7) Altin, O.; Eser, S.; *Ind. Eng. Chem. Res.* , **2001**, *40*, 589.
(8) Elliot, P.; Hampton, A. F.; *Oxid. Met*., **1980**, *14*, 449.
(9) Taylor, W. F.; *Ind. Eng. Chem. Prod. Res. Dev*., **1976**, 15, 64.
(10) Zhang, F.; Altin, O.; Eser, S.; *Prepr. Am. Chem. Soc., Fuel Div. Pet.*, **2000**, 220.
(11) Rudnick, L. R., unpublished results.
(12) Altin, O. Bock G., Eser, S.; *Prepr. Am. Chem. Soc., Div. Pet. Chem.*, **2000**, 47(3), 208.

Table 1. Total Carbon Deposit Amounts from As Received Coal Derived-Blended Jet Fuels Thermal Decomposition on Inconel 718 at 470˚C (Twall=525˚C) and 34 atm (500 psig) for 5 h with a 4 mL/min Flow Rate.

Fuel Type	P, psig	C Deposit, (µg C/cm^2)
HDT 3:1 RCO/LCO	250	33.7
HDT 3:1 RCO/LCO	500	3.9
HDT 3:1 RCO/LCO	900	5.7
HDT 3:1 RCO/LCO	500	5.9 (5 passes)
HDT 1:1 RCO/LCO	250	9.8
HDT 1:1 RCO/LCO	500	3.6
HDT 1:1 RCO/LCO	900	2.9
HDT 1:1 RCO/LCO	500	3.1 (5 passes)

Table 2. Total Carbon Deposit Amounts from Coal Derived-Blended Jet Fuels After Alumina Treatment Thermal Decomposition on Inconel 718 at 470˚C (Twall=525˚C) and for 5 h with a 4 mL/min Flow Rate.

Fuel Type	P, psig	C Deposit, (µg C/cm^2)
HDT 3:1 RCO/LCO	250	3.8
HDT 3:1 RCO/LCO	500	~ 0

Table 3. Total Carbon Deposit Amounts from Petroleum Derived Jet Fuels After Alumina Treatment Thermal Decomposition on Inconel 718 at 470˚C (Twall=525˚C) and for 5 h with a 4 mL/min Flow Rate.

Fuel Type	P, psig	C Deposit, (µg C/cm^2)
JP-8	250	5.3 – 7.0
JP-8	500	1.0
JP-8	900	0.2

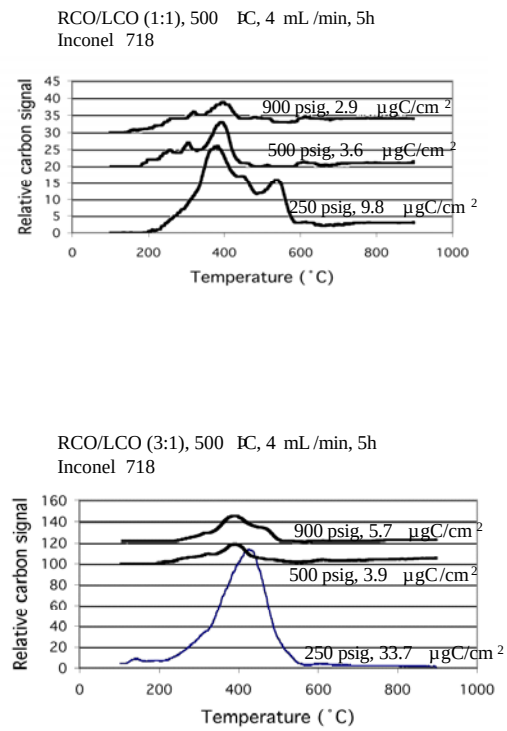

Figure 1. TPO profiles of carbon deposits from thermal stressing of coal-derived-1:1 and 3:1 blended fuels at different pressures on Inconel 718 at 470˚C fuel temperature (Twall=525˚C) for 5h with 4 mL/min flow rate.

RCO/LCO:3/1

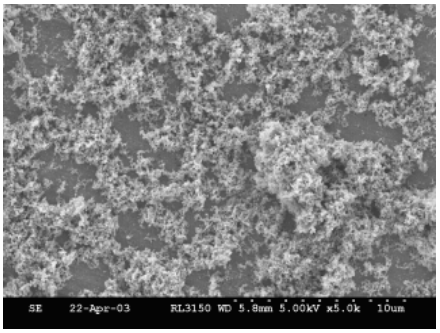

5x

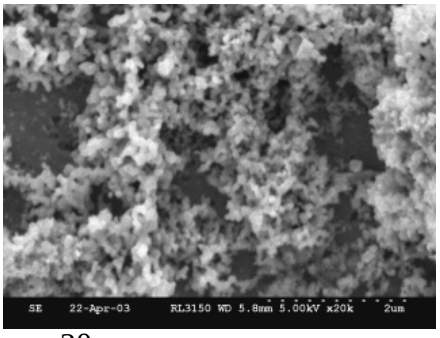

20x

RCO/LCO:1/1

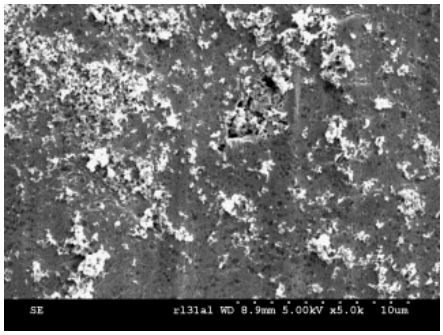

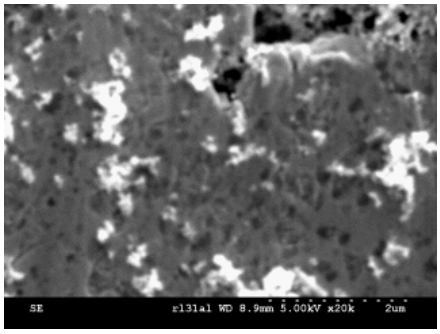

Figure 2. SEM images of carbon deposits from thermal stressing of coal-derived blended fuels on Inconel 718 at 470˚C (Twall=525˚C) and 500 psig for 5h with a 4 mL/min flow rate.

Significant Reduction of Carbon Deposit by Hydrogen Donor Addition to JP-8 Jet Fuel at High Temperatures

J. J. Strohm, O. Altin, C. Song, S. Eser

The Energy Institute and Department of Energy and Geo-Environmental Engineering, The Pennsylvania State University
209 Academic Projects Building, University Park, PA 16802
*Email: csong@psu.edu; sxe2@psu.edu

Introduction

Advanced high-Mach aircraft will require the fuel to perform a dual role as a coolant for mechanical and electrical systems in addition to serving as the propellant, thus increasing the thermal stability requirements of the fuel[1]. The conventional paraffin-based fuels have poor thermal stability due to the high susceptibility of the paraffinic components to free radical reactions[2]. Uncontrolled radical reactions will lead to fuel decomposition which ultimately leads to carbonaceous deposit formation in both the bulk of the fuel and on the surfaces of various fuel system components.

Previous work conducted at Penn State has shown hydrogen donors such as tetralin can help control such radical reactions reducing carbon formation from the pyrolytic degradation of paraffinic fuels[3]. In the presence of dissolved oxygen, traditional hydrogen donors can undergo autoxidative reactions, resulting in retardation of the donor's effectiveness in the pyrolytic regime. Recently, a binary donor consisting of a 1:1 blend of tetralin and α-tetralone has shown excellent oxidative resistance while reducing the formation of polyaromatics and subsequent carbon formation[4,5].

The effect of the trace amount of some sulfur compounds appears to be significant on the rate of deposit formation and metal surface degradation. Taylor[6] examined the role of sulfur compounds in deposit formation for a JP-5. Selected compounds were added in amounts to give a sulfur concentration in the fuel of 3000 ppm. Diphenyl sulfide (DPS) and phenyl benzyl sulfide (PBS) were added to JP-5 fuel and it was observed that both sulfur compounds enhanced the deposition throughout the temperature range with maxima occurring in the 427 to 482˚C range, but phenyl benzyl sulphide exerted much more significant effect. Polysulfides, disulfides, thiol, and other sulfides increased deposition dramatically. On the other hand, benzothiophene and diphenzothiophene did not contribute to the formation of deposits. Increasing the level from 300 to 3000 ppm approximately doubled the amount of deposits with both DPS and PBS compounds.

This study aims at further understanding the role of hydrogen donors on the formation of solid carbons d during thermal stressing of jet fuel through examination of the morphology and reactivity of the deposits from JP-8 stressed with the addition of various concentrations of tetralin and a binary donor of tetralin and α-tetralone

Experimental

Thermal stressing of JP-8 fuels was performed in the presence of Inconel 600 foils, the elemental composition of which is listed in Table 1. For each experiment a foil having approximate dimensions of 100 x 3 x 0.1 mm was placed at the bottom of a 1/4" o.d. isothermal flow reactor lined with a glass coating developed by Alltech Corporation. Prior to inducing the fuel into the system, the reactor was heated to 500°C wall temperature under argon flow at 500 psig.

Table 1. Elemental Composition of Inconel 600

Ni, %	Fe, %	Cr, %	Mn, %	Cu, ppm	C, ppm	Si, ppm	S, ppm
72	8	15.5	1.0	5000	1500	5000	150

The hydrogen donors used in this study was tetralin and a binary donor of 1:1 mixture of tetralin and α-tetralone, which was added to JP-8 in varying concentrations. The fuel was pre-heated to 200°C before entering the reactor, which was held at a constant 475°C bulk fuel outlet temperature. Pressure was maintained at 500 psig throughout each experiment. Each experiment was conducted for 5 hours with 4mL/min flow of fresh fuel.

Carbon deposits on the metal foils were analyzed by temperature programmed oxidation (TPO) using a LECO R412 Multiphase Carbon Analyzer to determine the total amount of carbon on the surface in μg of carbon per square centimeter (μgC/cm^2). Morphology of the deposits was characterized by a Hitachi S-3500N scanning electron microscope (SEM).

Results and Discussion

Tetralin addition. Figure 1 shows the TPO profiles of carbon deposits detected from thermal stressing of JP-8 with and without tetralin additions of 1, 2, 5 and 10 vol.%. Without any tetralin addition, JP-8 produced 25.7 μgC/cm^2 on the Inconel 600 foil. With only 1% addition of tetralin the total amount of carbon is reduced by nearly 46% to 14.2 μgC/cm^2. Further increasing the tetralin content to 2 and 5% further reduced the amount of carbon by 81.3%. Above 5% tetralin addition, the total amount of carbon produced on the foils began to increase slightly from 4.8 to 5.7 μgC/cm^2 with 5 and 10% tetralin addition, respectively.

The SEM images of the foils without tetralin addition are presented in Figure 3. The surface shows near complete coverage by metal sulfides (NiS, FeS) and filamentous carbon with regions of amorphous carbon. With the addition of 2 and 5% tetralin the carbon formed on the surface is significantly reduced, as shown in the SEM images in Figure 4. The addition of tetralin also shows nearly no filament formation on the surface whereas some needle-like metal sulfide formations are apparent. By combining the TPO and SEM analysis, we see that peak III of the TPO analysis is significantly reduced with the addition of tetralin, thus indicating that peak III can be attributed to catalytically initiated filamentous carbon on the surface. Although filamentous carbon is nearly eliminated with tetralin addition greater than 2%, there still are regions of amorphous deposits, which correspond to peak II of the TPO profiles.

It appears shows that the formation of sulfides on the surface is also significantly reduced upon tetralin addition, as implied by SEM analysis. Previous studies have shown that

certain sulfur compounds, such as biphenylsulfide (BPS) will increase carbon deposition while other sulfur compounds such as thiophene and benzothiophene can reduce carbon formation[7,8]. Altin and coworkers concluded that some organo-sulfur compounds such as BPS will facilitate the formation of Ni and Fe sulfides, which in turn will increase carbon deposition due to the formation of high surface area which increases the retention time of reactive hydrocarbon molecules on metal substrate to decompose further. The upward growth of metal sulfide crystals produces nano metal particles which accelerate the filamentous carbon deposits. From the decrease in the formation of sulfides when tetralin is added to the JP-8, it is concluded that tetralin is aiding in stabilizing the reactive sulfur species which lead to the formation of sulfides and subsequent carbide formation, thus reducing the formation of filamentous carbon on the surface.

Binary donor addition. TPO analysis of the Inconel 600 foils after thermal stressing of JP-8 with 1, 2 and 5 vol.% addition of a 1:1 mixture of tetralin and tetralone is presented in Figure 2. Similar to tetralin addition, there is a reduction in carbon deposits by nearly 50% with only 1% addition of the binary donor. Further addition of the binary donor further reduced the total amount of carbon formed on the surface of the foil. However the degree of carbon reduction of the binary donor is not as high as that of only tetralin addition.

SEM examination shows that even with 5 vol.% addition of the binary donor to the JP-8, there is significant filamentous carbon formation with a larger reduction in amorphous deposits. With the addition of the binary donor, there is still significant formation of sulfides on the surface.

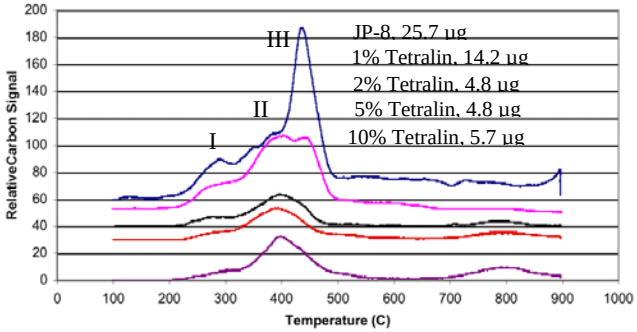

Figure 1. Effect of tetralin addition to JP-8 deposit formation from thermal decomposition at 475°C for 5 hours as analyzed by TPO.

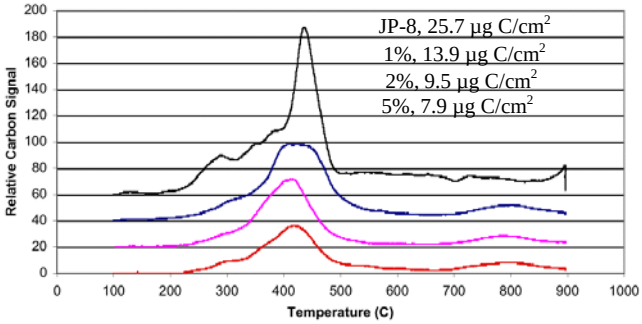

Figure 2. Effect of a binary donor comprised of a 1:1 mixture of tetralin and tetralone to JP-8 deposit formation from thermal decomposition at 475°C for 5 hours as analyzed by TPO.

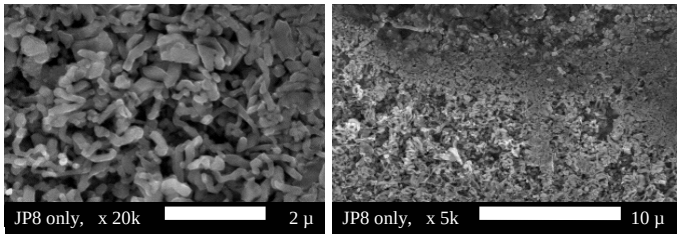

Figure 3. SEM imaging of the Inconel 600 surface after 5 hours of thermal stressing of JP-8 only at 475°C (magnification at 20k and 5k).

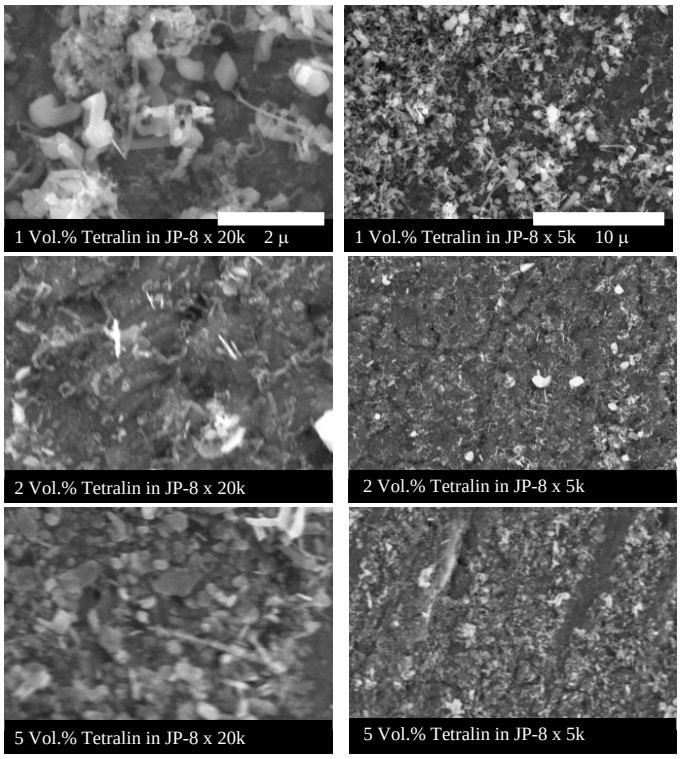

Figure 4. SEM imaging of the Inconel 600 surface after 5 hours of thermal stressing of JP-8 with 1, 2 and 5 vol.% tetralin addition at 475°C (magnification at 20k and 5k).

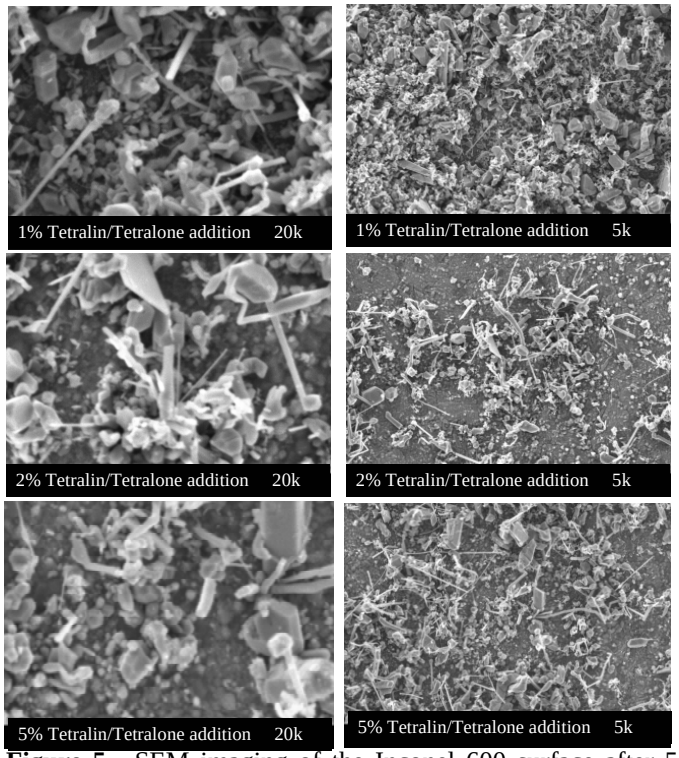

Figure 5. SEM imaging of the Inconel 600 surface after 5 hours of thermal stressing at 475°C of JP-8 with 1, 2 and 5 vol.% of a binary donor of tetralin and tetralone (magnification at 20k and 5k).

Conclusions

Addition of only 2 vol.% tetralin to JP-8 jet fuel showed a significant reduction in carbon deposit accumulation on the surface by over 81% when compared to JP-8 without any additives. The carbon deposition that resulted from pyrolytic stressing of JP-8 with tetralin addition is mainly amorphous carbon with little presence of filamentous carbon and sulfide formation. Tetralin has the ability not only to help prevent bulk deposits, but is able to stabilize the organic sulfur compounds present in JP-8. By the reduction of sulfide formation, amorphous and filamentous carbon formations are significantly reduced.

The addition of up to 5 vol.% of a binary donor, which is comprised of a 1:1 mixture of tetralin and tetralone, lower degree of reduction in amorphous carbon is observed. This implies that although previous work as shown that the binary donor is more effective in reducing the bulk deposits associated with the formation of polyaromatics, the binary donor is not able to reduce the filamentous carbon. Sulfide formation was also significant from the decomposition of organic sulfur compounds in the JP-8 even with binary donor additions. The decomposition of the sulfur compounds present in the JP-8 fuel leads to the formation of amorphous and filamentous carbon growth. The filaments present on the surface with the addition of the binary donor are longer and thinner than the filaments observed with JP-8 only. This implies that the binary donor is reducing the levels of polyaromatics and bulk deposits, thus the metal sites that are active for the growth of such filaments remain active since they are not being encapsulated by carbon, as is the case when no additive is added to JP-8.

Acknowledgement. We are grateful for financial support from the U.S. Air Force Office of Scientific Research. We thank Mr. Jean-Philippe Alphonse Kouassi for his help with the experiments.

References

(1) Edwards, T. and Zabarnick, S. *Ind. Eng. Chem. Res.* **1993**, 32, 3117.
(2) Song, C.; Eser, S.; Schobert, H.H.; Hatcher, P.G. *Energy & Fuels* **1993**, *7*, 234-243.
(3) Song, C.; Lai, W.-C.; Schobert, H.H. *Ind. Eng. Chem. Res.* **1994,** *33*, 548.
(4) Strohm, J.J.; Andresen, J.M.; Song, C. *Prepr. Pap. – Am. Chem. Soc., Div. Fuel Chem.*, **2002**, *47*(3), 189.
(5) Strohm, J.J.; Brandt, A.J.; Eser, S.; Song, C. *Prepr. Pap. – Am. Chem. Soc., Div. Fuel Chem.* **2003**, *48*(2), 857.
(6) Taylor, W. F., *Ind. Eng. Chem. Prod. Res. Dev.* **1976**, 15, 64.
(7) Altin, O., Raymundo-Pinero, E., Eser, S., *Proceedings, Carbon 2002, International Carbon Conference*, Paper # E038, CD, **2002**..
(8) Raymundo, E.; Altin, O.; Eser, S. *Prepr. Pap. – Am. Chem. Soc., Div. Pet. Chem.* **2002**, 47(3), 216.

STACKING STRUCTURE OF AROMATIC LAYERS IN DTF COAL CHARS AND ITS RELATION TO GASIFICATION PROPERTY

Noriko Yoshizawa, and Katsuhisa Maruyama

National Institute of Advanced Industrial Science and Technology

16-1 Onogawa, Tsukuba, 305-8569 Japan

Yoshio Yamada

Fukui University
3-9-1 Bunkyo, Fukui, 910-8507 Japan

Introduction

Gasification property or reactivity of coal char has often been discussed with the microstructure of a sample. Pore structure of a sample is important for the accessibility of reaction gas, which is often considered in simulation studies for the prediction of gasification reactions. Also, study of crystallographic structure in a solid part could lead to a lot of microscopic information of a char sample. Generally, solid part of coal char consists of aromatic carbon layers existing separately, or in parallel with each other to form graphitic stacking structure. There are also a considerable amount of carbon atoms out of aromatic layers depending upon heat-treatment conditions of a sample. X-ray diffraction (XRD) measurement is a powerful technique to study the structure of carbon materials with such characteristics. So far, many authors[1,2] used the results of XRD measurements in their studies, mainly for comparing the reaction rate to the crystallite sizes. A stacking height, on the other hand, has been almost not related to gasification properties of a char sample. But carbon crystallites composed of single or stacked aromatic layers are often considered to act as walls of "slit-shaped micropores". This slit-shaped model is now widely regarded as a reasonable model of micropores in carbon materials. Therefore, the stacking structure of aromatic layers estimated by an appropriate method can be related to the gasification reactivity of a char.

One of the difficulties, however, in using the structural parameters by a XRD measurement for a numerical characterization of coal char is a degree of accuracy. Size of graphitic crystallite is often estimated with Scherrer's equation in many cases. But this method is based on the assumption that the sample is composed of crystallites in the same size, which is far from the fact confirmed by the observations with transmission electron microscope (TEM). Instead, some of us have standardized the characterization method named STAC-XRD analysis, based on the earlier studies by Hirsch[3] and Shiraishi[4].

In this paper, we numerically characterized the stacking structure of aromatic layers in 10 types of coal chars by STAC-XRD method, and investigated the relationship of the structural parameters to a gasification property of the sample.

Experimental

XRD measurement. STAC-XRD method aims especially at characterizing the stacking structure of aromatic layers in carbonaceous substances or carbon materials with less crystallinity. The process is described in detail elsewhere[5,6]. Briefly, the parameters below are evaluated by this method: interlayer spacing (d_{002}), stacking index (*SI*; related to crystallinity), distribution of the number of stacking aromatic layers per stack (*N*), and the average number of layers per stack (N_{ave}). Among all these parameters, *N* distribution and N_{ave} are calculated by the statistic method assuming the distribution of crystallite size. XRD patterns were measured at 2 =10-41˚ by the step-scanning method (=0.2˚, 25 second at each angle) using a Rigaku RU-300 goniometer with CuK radiation under 40kV-80mA operating conditions. A peak corresponding to the carbon 002 reflection is included in this range.

Gasification property. The parameter T_{cr} was used to indicate the reaction property. This was originally established by Advanced Fuel Research Inc.[7] as a reactivity index at an early stage of gasification. The determination of T_{cr} relies on a thermogravimetric analysis technique, in which the weight loss is measured while the sample is heated at a constant rate in the presence of a reactive gas. For further details of the determination process of T_{cr}, see ref.7.

Samples. Original coals (60 mesh size under) listed in Table 1 were stirred in HCl (18 %) at 50 ˚C for 8 hours, followed by a drying process at 105 ˚C. According to the analysis of ash content, Ca and Fe were removed below 0.1 wt% by the deashing of all the samples. The deashed coals were then heat-treated in a N_2 flow in a drop tube furnace (DTF; 1150 mm in height, 42 mm in diameter) in which the temperature was controlled at 1723 K. The residence time was approximately 1.5 seconds. Original coals without the acid-treatment were also heat-treated for comparison. BET specific surface areas of the deashed chars also shown in Table 1 were determined by the measurement of CO_2 adsorption isotherms at 303 K.

Results and Discussion

STAC-XRD analysis clarified that, concerning *N* distributions of deashed chars, aromatic layers included in the stacks with *N*=2 and 3 accounted for 65-80 % of all stacking layers in all the char samples. Most of them indicated the gradual declines of fractions with the increase of *N*, while some chars made from coals with higher C contents, such as SS037 and SS035, obviously showed the development of stacking structure with larger *N*: fraction of *N*=3 had a higher proportion than *N*=2, and a ratio of *N*>4 occupied over 20 %.

Figure 1 and 2 indicate the N_{ave} and *SI* of every sample plotted against their T_{cr} values. It is very clear that these structural parameters of demineralized chars have stronger correlations with T_{cr} than non-demineralized ones. In other words, characteristics of the stacking structure described with the parameters N_{ave} and *SI* can be fundamentally linked with the concentration of active site for the gasification reaction. We cannot found good correlation like this between %C and T_{cr} for the same series of chars. Concerning the difference of chars originated from the same coal, the deashed chars moderately tend to have smaller N_{ave} and larger *SI* with smaller T_{cr} than the non-deashed chars. The trend is, however, not proportional to the amount of specific elements in ash. At least, the chars from coals including relatively more amount of Ca (wt% of total ash, as CaO; 7.4 % in SS037; 8.54 % in SS027; 9.55 % in SS005) have a large difference in their *SI* values between deashed and non-deashed status. The element Ca in ash has been considered as catalyst for coal gasification. By the TEM observation, we could not see any distinctive features even around the metal particles, but found some regions in which aromatic layers of 1-1.5 nm are oriented along the surface of the particles.

Table 1. List of original coals used in this study.

sample	Elemental analysis (wt%, daf)					Ash /wt%	Surface area of deashed char /m^2g^{-1}
	C	H	N	S	O		
SS037	90.64	4.23	1.30	0.40	3.44	16.54	20.6
SS035	88.31	5.14	1.58	0.48	4.49	14.54	26.6
SS021	84.38	4.67	1.95	0.46	8.54	14.43	29.2
SS008	82.37	5.40	1.78	0.44	9.64	11.90	24.0
SS002	81.20	6.06	1.57	0.58	10.59	14.52	28.5
SS027	80.61	4.93	1.01	0.68	12.77	10.24	29.7
SS005	78.72	6.22	1.17	0.11	13.78	12.08	29.4
SS034	78.30	6.75	1.32	0.74	12.89	8.69	37.8
SS026	76.82	5.78	1.39	0.34	15.67	12.48	28.7
SS039	74.72	5.58	1.59	0.27	17.85	12.00	68.1

More specifically for every structural parameter, T_{cr} increased with the increase of N_{ave}. Development of stacking structure in the direction of stacking height can cause a closure of slit-shaped micropores, considering that the micropores of this type is basically formed by a mis-configuration among layers or stacks. This view is also supported by the result of specific surface areas (Table 1). It is necessary, at this point, to explain the concentration of active sites for gasification reaction of coal char in connection with the total surface area (TSA). The concept of active sites is often expressed with active surface area (ASA)[1] determined by an oxygen chemisorption measurement. From the structural point of view, it is also related to the size of aromatic layers, as mentioned in the first section of this paper. We have not estimated ASA values for every deashed char sample in this study. But the TEM observation found out that there are very few differences in layer sizes (ca. 1nm) among these char samples. It means that we do not have to take too much into account the difference of reactivity due to the size of aromatic layers. ASA values of every deashed char can be therefore influenced by the accessibility of reactive gas, i.e., open pore structure as well as stacking structure of aromatic layers constituting the pore walls. Also in a simplified image, porous texture including stacks with fewer aromatic layers is more reactive because of these layers having more occasions of exposure to the reactive gas. The relationship between T_{cr} and N_{ave} is consistent for the reason above. The similar results were provided by the observation with TEM[2].

As for *SI*, it also increased with the increase of T_{cr}. Definition of *SI* represents the ratio of carbon atoms contributing to the stacking structure, and accordingly the subtraction 1-*SI* gives the relative amount of carbons present in single aromatic layers or on the periphery of aromatic layers. It is likely that around single layers the structure is ordered relatively locally, which would produce more microporous region than around the stacking structure. It is also well known that carbon atoms out of the crystalline component are preferentially oxidized in themselves due to their higher reactivity than those in the crystalline component. Interlayer spacings (d_{002}), on the other hand, did not show any clear correlations with the reaction parameters. It is presumably because that the carbon 002 peaks in all the samples were too broad to indicate the strict positions of maximum intensity.

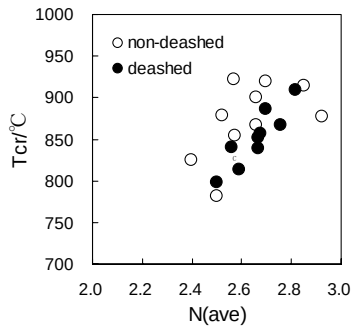

Figure 1. Reaction parameter T_{cr} plotted against the average number of aromatic layers in a stack (N_{ave}).

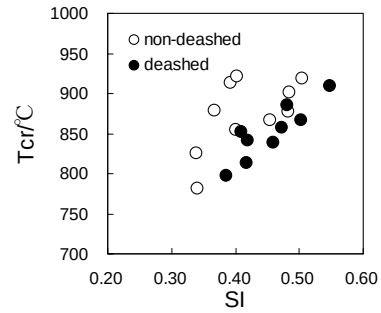

Figure 2. Reaction parameter T_{cr} plotted against the stacking index (SI).

Conclusions

We found that the structural parameters obtained by STAC-XRD were proportionally related to the gasification properties at an early stage of gasification process, which is consistently explained by the slit-shaped micropore model.

Acknowledgement. This work was financially supported by NEDO for collaborative study with CCUJ in BRAIN-C project. We also thank Mr. Tsuyoshi Teramae in Idemitsu Kosan Co. Ltd. for helpful suggestions.

References

(1) Radovic, L.R.; Walker, P.L., Jr.; Jenkins, R.G. *Fuel* **1983**, *62*, 849-856.
(2) Davis, K.A.; Hurt, R.H.; Yang, N.Y.C.; Headley, T.J. *Combust. Flame* **1995**, *100*, 31-40.
(3) Hirsch, P.B. *Proc.Roy.Soc.* **1954**, *A226*, 143-169.
(4) Shiraishi, M.; Kobayashi K. *Bull. Chem. Soc. Jap.* **1973**, 46, 2575-2578.
(5) Yoshizawa, N.; Maruyama, K.; Yamada, Y.; Zielinska-Blajet, M. *Fuel* **2000** *79* , 1461-1466.
(6) Yoshizawa, N.; Maruyama, K.; Yamada, Y.; Ishikawa, E.; Kobayashi, M.; Toda, Y.; Shiraishi, M. *Fuel* **2002**, *81*, 1717-1722.
(7) Wojtowicz, M.A.; Bassilakis, R.; Serio, M.A. *The Evaluation of Char Reactivities for the BRAIN-C Project, FY2000 Final Report*, Advanced Fuel Research, Inc.: East Hartford, CT, **2001**.

Dissolution, Swelling Properties, and Complex Formation of Clays in NMP/CS_2 Mixed Solvents

Pakorn Opaprakasit, Paul C. Painter, and Michael M. Coleman

The Energy Institute
Penn State University
University Park, PA 16802

Introduction

Solvent swollen coals and the extract solutions that can be obtained from them are complex systems, displaying a rich range of behavior that can vary from coal to coal and with the nature of the solvent. Certain coals, notably Upper Freeport have a significantly enhanced solubility in this mixed solvent system and suspensions of the extracted parent coal and certain solutions of the extracts form gels and display viscoelastic behavior[1]. The nature of the interactions in this mixed solvent system and the mechanism by which small amounts of certain additional additives further enhance coal solubility remains largely unknown, although some progress has been made as a result of recent studies[2,3].

Dyrkacz[3] reported the results on a systematic study of this solvent pair, using both spectroscopic and physical property measurements, and concluded that the presence of some type of NMP chain oligomer at particular concentrations may indeed be an important factor. However, even though the results suggested that there was weak complex formation between the mixed solvent components, there was no evidence that these complexes were long-lived.

In recent work we have proposed that π-cation complexes can form in coal and act as cross-links or junction zones similar to those found in ionomers[4,5]. Accordingly, we decided to determine if NMP/CS_2 could also form complexes with this solvent system and present some preliminary results here.

Experimental

Montmorillonite clay was obtained from Nanoclay co. under the brand name Cloisite Na^+. Infrared spectroscopic measurements were recorded on a Digilab model FTS 45 FTIR spectrometer at a resolution of 2 cm^{-1}. UV-Vis spectroscopic measurements were performed on a Perkin Elmer spectrometer model Lambda 2S.

Results and Discussion

Clay Swelling and Cation Extractability of Solvents in Contact with Clay. Information concerning clay/solvent interaction could be important, because most coals have a significant amount of mineral matter that could act as a source of the cations that can form ionomer-like junction zones or cross-links in the organic component of coal through π–cation interactions[4]. For example, montmorillonite clays contain alkali and alkali earth cations in the interlayer spaces of their aluminosilicate sheets. These cations bind to the sheet layers by an ionic interaction. It therefore seemed intriguing to examine what fraction of these cations could be extracted by NMP and CS_2, and whether the amount of extracted cation is enhanced by the 1:1 mixed solvent.

We will start by examining the swelling properties of the montmorillonite, Cloisite Na^+. This clay was placed in various solvents and its volume change was recorded after 2 days of contact. The results show that the non-polar solvents used in this study are more effective swelling agents than their polar-solvent counterparts. The swelling ratios observed in toluene and CS_2 are almost identical at 2.1, while those in more polar solvents, pyridine and NMP, are 1.9 and 1.3, respectively. Interestingly, the swelling ratio observed in the NMP/CS_2 mixed solvent is similar to that observed in neat NMP (1.3), which is much lower than that in neat CS_2. These results show that CS_2 alone is an effective swelling agent. However, when mixed with NMP, this ability is diminished.

We next examined the ability of solvents to extract cations from the montmorillonite clay by measuring the amount of Na^+ extracted from Cloisite Na^+ after 2 days of clay/solvent contact. The Na^+ cation was chosen to represent the clay cations, because of its abundance in this type of clay and its extractability was calculated using a calibration curve generated from standard solutions. The results are summarized in **table 1**. The extraction yield from CS_2 and toluene is, as expected, below the detection limit of the instrument, indicating that although these non-polar solvents swell the clay considerably, they are not capable of extracting this cation from the clay galleries or interlayers. The yield obtained from pyridine and NMP is 1 and 6%, respectively. This result indicates that NMP and pyridine can disrupt the clay/cation interactions and extract Na^+ species. NMP is roughly an order of magnitude more effective than pyridine. The corresponding result for an NMP/CS_2 mixed solvent is somewhat greater than pure NMP, 8% (2 days extraction). However, when the clay was placed in the solvent for 30 days, the amount of extracted Na^+ increases by a factor of almost 10, to 41%. It is apparent that NMP is the most effective single solvent in extracting Na^+ cations, but the addition of CS_2 enhances the extraction yield considerably. The mechanism of this enhancement, however, remains unknown.

Table 1. The amount of extracted Na^+ cation from Cloisite Na^+ montmorillonite clay after 2 days of clay/solvent contact

Sample	Extraction Yield	
	g of Na^+ / 1 g of clay (x 10^5)	Wt. %*
Toluene	0	0
CS_2	0	0
Pyridine	0.8	1
NMP	5.9	6
NMP/CS_2 (2 days)	7.2	8
NMP/CS_2 (30 days)	38.1	41

* Calculated on a basis of cation exchange capacity, $93 \times 10^{-5} gNa^+/1g$ of clay

Interactions between Cations and NMP/CS_2 Solvent. Given the results we previously obtained concerning π-cation interactions in coal[4,5], together with the results we obtained from swelling clays and cation extractability of solvents, it was decided to consider the changes that occur to CS_2, NMP and the 1:1 mixtures of these solvents in acid and base environments. Color change was used as a simple initial indicator of interactions. The results indicate that neat CS_2 is transparent and its color remains unchanged upon mixing with acid solutions. However, a color change is observed when this solvent is mixed with strong base solutions. The degree of color change seems to increase with the basicity of the added species. For example, the color of a CS_2/NaOH solution is more intense than that of a CS_2/triethylamine mixture. Although CS_2 is a non-polar solvent, this is not surprising, because CS_2 is a very polarizable molecule and charge/induced dipole interactions are known to occur in these systems. The resulting perturbation of the CS_2 π orbitals results in a shifting of absorption bands to the visible region. When pyridine and NMP alone are added to CS_2, however, the mixture remains transparent. Clearly, any interaction in these systems is not as strong, but could still occur.

A more precise measure of interactions than color change is provided by UV-Visible absorption spectroscopy. The spectra of the single and mixed solvents are shown in **figure 1.** The spectrum of CS_2 shows strong absorbancies in the UV region near 304 and 321 nm, while NMP also has a strong UV absorption near 252 nm, together with a shoulder at 275 nm. The bands can be assigned to $n \rightarrow \pi^*$ and $\pi \rightarrow \pi^*$ transitions, respectively[6]. When these two compounds are mixed, the absorption maximum red-shifts to 359 nm. This absorption is most likely associated with the $n \rightarrow \pi^*$ transition of CS_2, whose energy gap is reduced as a result of an interaction. The mixture also absorb strongly throughout the region lower than 360 nm. These results are most likely due to a dipole/induced dipole interaction between the strong dipole of NMP and the highly polarizable S=C=S bonds. Additionally, when a small amount of NaOH is added, the absorption maximum further red-shifts to 374 nm, with a shoulder appearing in the visible region at 467 nm. This is consistent with the results obtained from the color change experiments, where a reddish-yellow solution was observed.

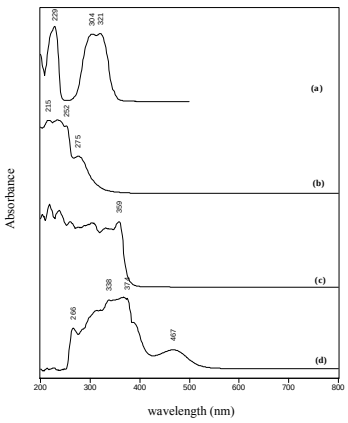

Figure 1. UV-Vis spectra of CS_2 (a), NMP (b), NMP/CS_2 1:1 v/v binary solvent (c), and NMP/CS_2/NaOH 20:20:1 v/v (d)

We now turn to discuss the effect of additives on the FTIR spectra of the solvents. The results are shown in **figure 2**. The spectra of neat CS_2 and CS_2/HCl mixtures are very similar, with ν_3 and $\nu_3 + \nu_1$ bands at 1527 cm^{-1} and 2170 cm^{-1}, respectively. However, the main $\nu_3 + \nu_1$ band of CS_2 appears at a lower wavenumber, 2155 cm^{-1}, when mixed with strong bases, but still has a shoulder near 2170 cm^{-1}. The corresponding ν_3 mode at 1527 cm^{-1} also decreases in intensity and lower frequency shoulders appear, near 1500 cm^{-1} in the spectrum of CS_2/NaOH mixtures. This indicates that the CS_2 π bonds are strongly perturbed by cations.

The spectra of CS_2 and CS_2 in cyclohexane are also examined, as shown in **figure 3**. Because CS_2 and cyclohexane should interact through weak dispersion forces only, this latter spectrum should reflect any changes due to the dilution of CS_2/CS_2 interactions and provide the appropriate basis for comparison of spectroscopic changes observed in more polar solutions. In this solvent, CS_2 has a ν_3 band at 1524 with a shoulder at 1517 cm^{-1} and a $\nu_3 + \nu_1$ combination mode at 2172 cm^{-1}. This band also has a shoulder, near 2159 cm^{-1}. The spectrum of neat CS_2 shows a broader band pattern that is probably due to some sort of self-association effect (presumably due to strong dispersion interactions). The corresponding bands of CS_2 in pyridine, however, shift to 2165 and 1519 cm^{-1}, and there is further shift to 2161 and 1520 cm^{-1} in the presence of NMP. This shift indicates an interaction that again perturbs the CS_2 π-bonding system. However, the band shift observed in these two mixtures is different from that found in CS_2/strong base solutions, where the main band apparently does not shift but decrease in intensity, with a new absorption mode appearing as a shoulder at lower wavenumber. This suggests an interaction or transient complex formation with some CS_2 molecules, but not others.

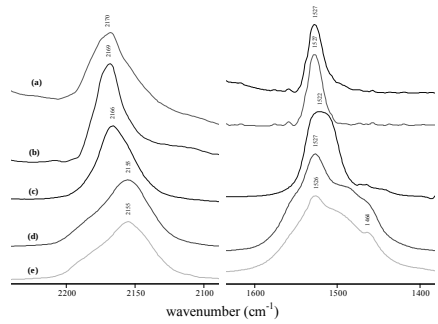

Figure 2. FTIR spectra of CS_2 + HCl (a), neat CS_2 (b), CS_2 + Triethylamine (c), CS_2 + NaOH (d), and CS_2 + NH_4OH (e)

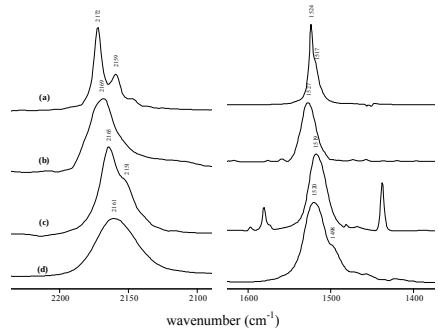

Figure 3. FTIR spectra of CS_2 in cyclohexane (a), neat CS_2 (b), CS_2 + pyridine (c), and CS_2 + NMP (d)

Conclusions

The interaction between the "magic" binary solvent of NMP and CS_2, and its role in promoting extractability of Upper Freeport coal has been studied. It is likely that a complex formation of these mixed solvents and cations plays a key role. The results indicate that NMP/CS_2 is capable of extracting significant amount of and forming a complex to cations from montmorillonite clay. Given that Upper Freeport coal contains significant amounts of mineral matter, principally clays, the information obtained from these clay experiments may be important in reaching an understanding of the coal dissolution process. Nevertheless, the nature of the cations present in Upper Freeport coal remains uncertain and needs further investigation.

Acknowledgement. The authors gratefully acknowledge the support of the Office of Chemical Sciences, U.S. Department of Energy, under grant No. DE-FG02-86ER13537. P.O. is a recipient of and partially supported by the Development and Promotion of Science and Technology Talent Project (DPST), Thailand.

References

(1) Iino, M.; Takanohashi, T.; Ohsuga, H.; Toda, K. *Fuel,* **1988,** *67,* 1639-1647.
(2) Chen, C.; Iino, M. *Prepr. Pap.- Amer. Chem. Soc., Div Fuel Chem,* **2000,** *45,* 89.
(3) Dyrkacz, G. R. *Energy & Fuels*, **2001**, 15, 918-929.
(4) Opaprakasit, P.; Scaroni, A. W.; Painter, P. C. *Energy & Fuels*, **2002**, 16, 543-551.
(5) Opaprakasit, P.: Ph.D. Thesis, the Pennsylvania State University, **2003**.
(6) Rao, C. N. R. *Ultra-Violet and Visible Spectroscopy Chemical Applications;* Butterworths: London, **1975**.

GASIFICATON CHARACTERISTICS OF CARBONS PRODUCED UNDER AN ENTRAINED BED GASIFIER CONDITION

*Kouichi Miura, Shinichi Nakai,Hiroyuki Nakagawa,Shiro Kajitani**

° Department of Chemical Engineering, Kyoto University,
Kyoto-Daigaku Katsura, Nishikyo, Kyoto 615-8510, JAPAN
*Central Research Institute of Electric Power Industry (CRIEPI)
Kanagawa 240-0196, JAPAN

Introduction

Coal gasification to produce gaseous fuel such as CO and H_2 is well known as one of key technologies for utilization of coal. Coal gasification mainly involves two steps: the initial rapid devolatilization of coal to produce char, tar and gases and the subsequent gasification of the char produced. Char gasification, being the slower step, is believed to control the overall conversion process. Therefore, numerous studies have been performed to examine the gasification rate of char. It is, however, known that solid carbon called coke (soot) is formed from the volatiles produced during the initial devolatilization at high temperature above 1000°C. Since the gasification reactivity of the coke is expected to be rather low, it is important to examine if the coke is really formed and to estimate the gasification reactivity of the coke if it is formed.

In this study it was examined if the coke is actually formed at high temperature and high pressure from the equilibrium calculation and experiments using a pressurized drop tube furnace (PDTF). Next, the reactivity of the solid carbons prepared was examined using temperature-programmed reaction (TPR) technique.

Experimental

Coal Sample. The coal used was Bontang coal from Indonesia (C: 78.3, H: 5.4, N: 1.9, O: 14.5 %d.a.f., VM: 42.4, FC: 51.8, Ash: 5.8 W d. b.). It was received as pulverized form, and dried at 108 °C for more than 8 h before use.

Preparation of solid carbons at high temperature and high pressure using a PDTF. Solid carbons were prepared at by using a pressurized drop tube furnace(PDTF) in a nitrogen stream[1]. The coal was rapidly heated to a desired temperature under pressurized condition and the solid carbons and gaseous products produced were collected by a movable water-cooled probe. By changing the axial position of the probe the residence time (τ) of the coal was changed. The gaseous products were analyzed for H_2, CH_4, CO, CO_2 by use of GCs. The carbon yield was estimated from the ash balance. The pyrolysis conditions employed are listed in Table 1. The experimental runs were abbreviated to R-pressure in MPa-temperature in °C/100-residence time in s. The experimental conditions employed for the runs of R-2.1-12-4.3 and R-2.1-14-4.3 are rather close to those in entrained bed gasifier.

A char was also prepared at 1200 °C in a 0.1 MPa of nitrogen atmosphere (τ = 1 min) using a thermobalance under a heating rate of 1500 °C /min for comparison purpose (TG-0.1-12-600).

Table 1 Pyrolysis conditions employed by a PDTF

Run	*P* [MPa]	*T* [℃]	τ [s]	Ultimate analysis[wt%, daf] C	H	N	O(dif.)
TG-0.1-12-600	0.1	1200	60	91.0	0.6	1.1	7.4
R-0.15-12-5.2	0.15	1200	5.2	95.6	0.5	1.4	2.5
R-0.15-14-5.2	0.15	1400	5.2	97.4	0.4	0.8	1.4
R-0.6-12-3.5	0.6	1200	3.5	94.9	0.6	1.6	2.9
R-0.6-14-3.5	0.6	1400	3.5	96.5	0.5	1.4	1.6
R-0.6-14-0.85	0.6	1400	0.85	92.8	0.3	0.7	6.2
R-2.1-12-4.3	2.1	1200	4.3	96.8	0.5	1.2	1.5
R-2.1-14-4.3	2.1	1400	4.3	98.3	0.3	0.6	0.8

Gasification of solid carbon and char. Gasification of solid carbon or char was performed by use of a thermobalance (Shimadzu, TGA-50) under atmospheric pressure using the so-called temperature-programmed reaction (TPR) technique. A very small amount of sample (<0.3 mg) was dispersed in high-grade quartz wool and the sample with the quartz wool was placed on a platinum mesh basket. It was then heated at 10 °C/min from 110 to 1300 ° C in a pure CO_2 flow. The conversion (*X*) vs. temperature (*T*) relation-ships obtained were analyzed to estimate the rate parameters of the samples.

Equilibrium calculation. Equilibrium calculation was made using CHEMKIN Collection III. The products were assumed to be H_2, CH_4, H_2O, CO, CO_2, and C (solid carbon) because the pyrolysis temperatures were very high.

Results and Discussion

Pyrolysis of coal at high temperature and high pressure using a PDTF. Figure 1 compares the experimentally obtained pyrolysis yields with the equilibrium yields at 2.1 MPa for three temperatures. The yields of products are represented by mole fraction. The product yields coincided with the equilibrium calculations above 1200 °C at 2.1 MPa. These results clearly indicate that the equilibrium state is attained immediately at high pressure and the products solely consist of CO, H_2 and solid carbon under the conditions.

Figure 2 compares the experimentally obtained solid carbon yields and calculated ones at 2.1 MPa for different temperatures. The char yield for TG-0.1-12-600 is also shown for comparison. At 1200°C the solid carbon yield obtained at 2.1 MPa was much larger than the char yield at 0.1 MPa. At 0.1 MPa the pyrolysis products contained tar and

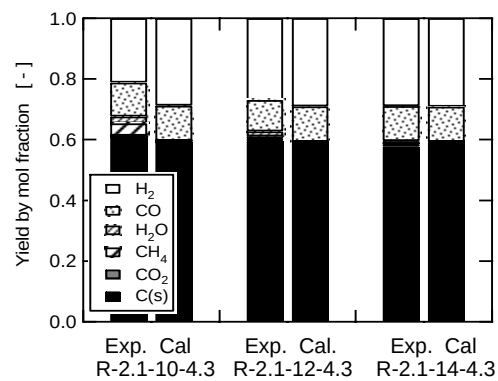

Figure 1. Comparison of experimentally obtained pyrolysis yields and calculated ones.

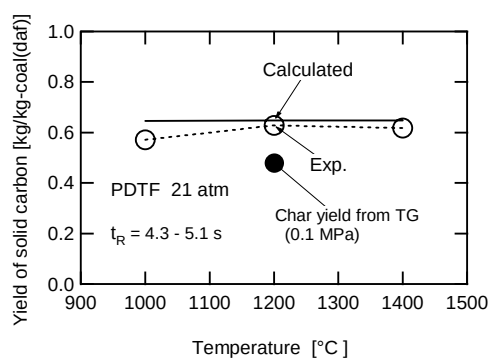

Figure 2. Comparison of experimentally obtained solid carbon yields and calculated ones.

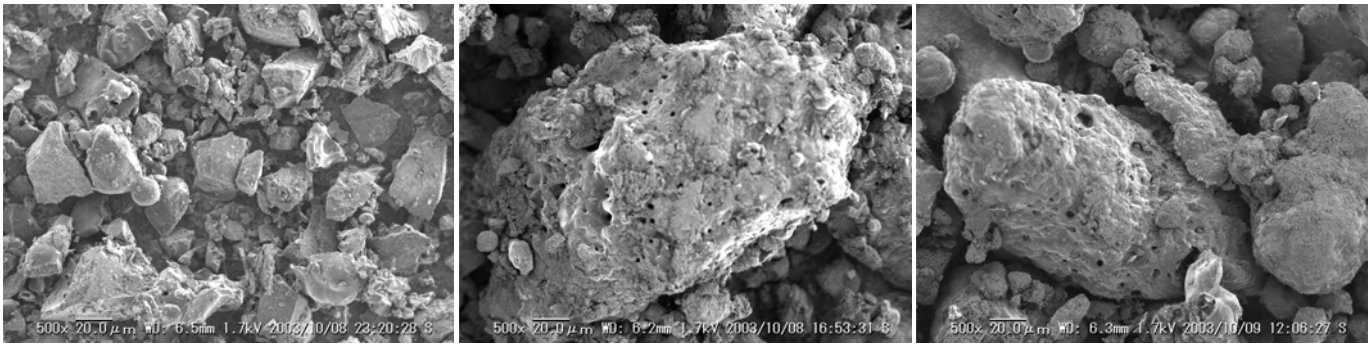

TG-0.1-12-600 (Prepared by TG) R-0.15-12-5.2 (1200 ° C, 0.15MPa) R-2.1-12-4.3 (1200 ° C, 2.1MPa)

Figure 3. SEM images of the char and the solid carbons prepared at 1200 ° C under different pressures.

hydrocarbon gases in addition to the char, CO, and H_2. These results indicate that the solid carbon obtained at 2.1 MPa surely contains char and coke produced from tar components. The ultimate analyses of the char and the solid carbons obtained are also given in Table 1. It is clear that the carbon content increases with the severity of the pyrolysis conditions. The solid carbon prepared under the severest pyrolysis conditions (R-2.1-14-4.3) consisted of 98.3%of carbon.

Figure 3 shows SEM images of the char and the solid carbons prepared at 1200 °C at 0.1, 0.15, and 2.1 MPa. The char obtained at 0.1 MPa using the TG (TG-0.1-12-600) retains the shape and morphology of the raw coal, but the shape and morphology of the solid carbon obtained at 0. 15MPa using the PDTF (R-0.15-12-5.2) are completely different from those of the raw coal. Agglomeration of the solid particles and the deposition of small particles on larger particles are clearly observed, indicating that coal particles were fused and tar components deposited as coke on the fused particles during the pyrolysis. On the other hand, the solid carbon obtained at 2.1 MPa (R-2.1-12-4.3) is judged to consist solely of particles fused during the pyrolysis.

Summarizing the results given above, we can depict the pyrolysis behavior at two extreme conditions as follows. At low pressure and slow heating rate tar and hydrocarbon gases in addition to char and inorganic gases are produced during the early stage of pyrolysis. Those components are finally converted to coke, CO, and H_2 if they are exposed to high temperature. At high pressure and large heating rate, on the other hand, little tar and hydrocarbon gases are produced during the early stage of pyrolysis due to either the suppression of the volatilization of the components or rapid transformation of the components to coke, CO, and H_2 within coal particles. The net difference of the two extreme pyrolysis conditions at equilibrium conditions is that the coke and the char are separated at low pressure and slow heating rate and that the coke are char are both retained in the particles at high pressure and large heating rate. This means that the solid carbons obtained at high pressure using the PDTF consists of char and coke.

Estimation of gasification reactivity of the solid carbon through the TPR experiment. Figure 4 shows the 1-*X vs. T* relationships obtained by the TPR experiments for the solid carbons. Several solid carbons were clearly gasified in two stages, which means that the solid carbons consist of two parts. The more reactive part and the less reactive part were, respectively, judged to be char and coke. The proportion of the coke in the solid carbon (*Y*) and the gasification rate parameters for the two parts were estimated by applying the Bhatia model[2] to the 1st and and 2nd stages by using the technique proposed by Mura et al.[3,4]:

Next, the rate constants at 1200 °C of the 1st and the 2nd stages were estimated using the estimated parameters, and they are shown in Figure 5. The rate constants for the 2nd stage (coke) were smaller than those of the 1st stage by the order of 1. The Y values ranged from 0.4 to 0.6. suggesting that the fraction of coke in the solid carbon is considerably large. Thus the reactivity of the solid carbon produced under an entrained bed condition was characterized.

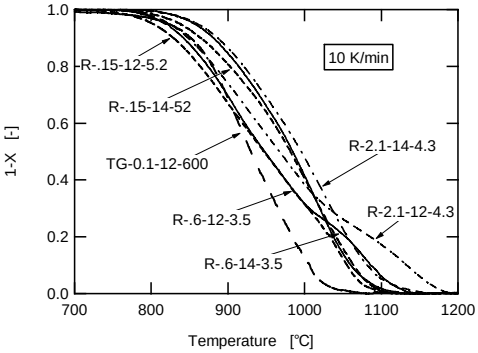

Figure 4. 1-*X* vs. *T* relationships obtained by TPR in an atmospheric CO_2..

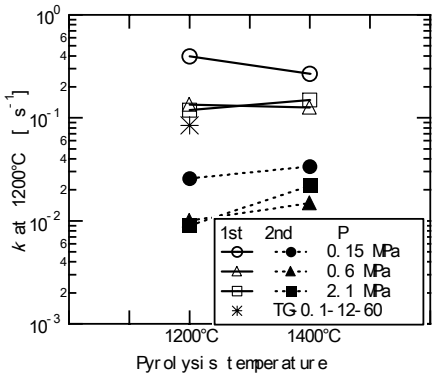

Figure 5. Gasification rate constants at 1200 ° C estimated from the gasification parameters for the 1st and the 2nd stage gasifica-tions.

References

(1) Kajitani S, Hara S, Matsuda H. *Fuel*, **81**, 539(2002).
(2) Bhatia, S.K., and Perlmutter, D.D., *AIChE J*., **26**, 379(1980).
(3) Miura, K. and Silveston, P.L., *Energy Fuels*, **3**, 243 (1989).
(4) Miura K., Nakamura H., Hashimoto K., *Energy Fuels*, **5**, 47 (1991).

HYDROTHERMAL UPGRADING OF BROWN COAL WITHOUT WATER ADDITION

K. Laursen, M. Sakaguchi, H. Nakagawa, K. Miura

Department of Chemical Engineering
Kyoto University, Kyoto-Daigaku Katsura
Nishikyo, Kyoto 615-8510, JAPAN

Introduction

Low rank coals (brown coal and lignite) are very abundant in several regions throughout the world and they constitute a significant resource for both energy and fossil fuel derived products. However, in spite of their quantity and relatively low market price, these low-rank coals have not been utilized to nearly the same extent as higher rank coals. The lack of interest in low-rank coal is mainly due to the high water content (40-70 wt%)[1-2], which makes it economically unfeasible to transport the coal without some form of upgrading. Due to the problematic high water content most upgrading methods include removal of the moisture before any further treatment. The drying process is energy consuming, requiring up to 20% of the chemically bonded energy[1] and this significantly reduces the net energy output for low-rank coal. Methods used for water removal include: thermal evaporative, hydrothermal (i.e., non-evaporative) and mechanical dewatering processes as well as combinations of mechanical and thermal dewatering[3].

The work presented here focused on hydrothermal dewatering of a brown coal with very high moisture content. Hydrothermal treatment is commonly conducted by adding extra water to the coal prior to treatment and creating slurries with specific dry coal to water ratios ranging from 1:2 up to as high as 1:5[1-2, 3-6]. Because some brown coals should contain sufficient moisture to produce hydrothermal conditions without water addition, we wanted to explore this option for upgrading brown coal. The aim of this study was to evaluate the effects of the hydrothermal conditions on the chemistry and structure of the upgraded coal, with the objective of utilizing the upgraded coal for production of coke and coal-water-mixtures.

Experimental

Samples and experimental conditions. Hydrothermal treatment was conducted on Loy Yang coal from Latrobe Valley, Victoria, Australia. To reduce the particle size and homogenize the coal, a.r. Loy Yang was blended for 5 min and stored in airtight containers. For some experiments the blended coal was subjected directly to hydrothermal treatment (referred to as raw), whereas in other cases extra water was added to the blended coal to create a slurry with a coal:water ratio of 1:3. (referred to as slurry). The sample size for both raw coal samples and slurries was maintained at 5 g. Hydrothermal treatment was conducted in a 20 cm^3 stainless steel autoclave equipped with an in-situ thermocouple and connected to a pressure meter. The sealed autoclave was flushed with N_2 and inserted into a preheated fluidized sand bath and heated to the treatment temperature. In selected experiments the autoclave was pressurized with N_2 to 7 and 15 atm prior to heating. Hydrothermal treatment was conducted at 200, 250, 300 and 350°C for 30 and 180 min. Upon completion, the hot autoclave was cooled in water, and the sample was removed from the autoclave. The autoclave was carefully rinsed with distilled water and the total coal sample was filtrated on 0.45 μm filter.

Analytical methods. Proximate and ultimate compositions of a.r., blended and treated samples were determined using a CHN-corder (Yanaco, MT-6) and thermo gravimetry (Perkin Elmer, Pyris1). Moisture content was determined by drying to constant weight at 110°C in a vacuum oven. Organic carbon released to the waste water was analyzed by TOC (Shimadzu TOC 5000A). Changes in the coal structure were traced by use of in-situ FTIR (JEOL, Winspec 50) and XRD measurements (Shimadzu, XD-610).

Results and Discussion

Table 1 shows the results of proximate and ultimate analyses of "as-received" Loy Yang and a batch of blended coal. The a.r. coal has a moisture content of 58%, and mechanical blending of the coal led to a one percent decrease to 57%. The carbon content is in the upper range for lignite's[7], while the ash content is very low (1.6%) making the coal very suitable for upgrading. The change in proximate composition due to mechanical blending was insignificant, and probably mainly related to sample in-homogeneity. The high moisture content of a.r. Loy Yang leads to a coal:water ratio of approximately 1:1.2. Measured temperature vs. pressure relationship during the treatment of a.r. coal closely followed the vapor pressure cures (Figure 1) revealing that hydrothermal conditions are maintained throughout the experiments.

Table 1. Ultimate and proximate analyses of Loy Yang coal.

Sample	Ultimate comp. (wt%) (d.a.f.)				Proximate comp. (wt%) (d.b.)			Moisture
	C	H	N	O	Fixed C	Volatiles	Ash	(a.r.)(wt%)
as-rec.	67.3	4.9	0.9	26.9	47.0	51.5	1.6	58
blend	67.3	4.3	0.4	28.2	47.2	51.3	1.5	57

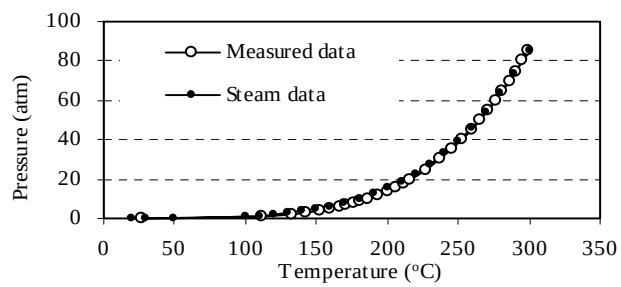

Figure 1. Temperature and pressure relationship measured during treatment of a.r. Loy Yang coal and vapor pressure curve.

The moisture content of raw coal samples treated for 30 min decreased with increasing temperature from 60% in a blank sample (i.e. sample rinsed with water and filtrated) to 26% in samples treated at 350°C (Table 2). Increasing the treatment time to 180 min led to no further moisture content reductions at any of the tested temperatures.

Table 2. Effects of treatment temperature and time.

Temperature (°C)	time (min)	Moisture (wt%)	Carbon d.a.f (wt%)	Ash (wt%)	Yield (% d.b)	TOC (mg/ g coal)
20*		62	65.2	1.26	95	0.0736
200	30	56	67.3	0.92	94	0.2640
250	30	40	67.8	1.12	96	0.6930
300	30	22	71.7	1.09	94	1.1910
350	30	26	79.0	1.00	84	1.6890
200	180	54	69.8	1.05	97	0.3610
250	180	40	70.0	1.09	87	0.9980
300	180	23	73.4	0.98	79	2.2840
350	180	26	83.0	1.18	69	2.8980

* washed and filtrated under the same conditions as used for treated samples

As expected, the carbon content increased with treatment temperature, and at higher temperatures (i.e., 300 and 350°C) the carbon content of the solid also increased with treatment time (Table 2). Dissolved C increased with temperature, and also with time; a significant increase was seen for the 300 and 350°C samples treated

for 180 min. High solid yield was achieved at 200 to 300°C for 30 min treatment, but a decrease was seen when the temperature was increase to 350°C. For long-term treatment the yield decreased significantly with increasing temperature. The hydrothermal treatment led to a slight decrease in ash content (10-15%), but there was no systematic changes with temperature. Because the composition of the ash in many cases is more important than the actual amount, especially for low ash content coals, work is currently being undertaken to identify the changes in the ash composition.

As shown above, a combination of increasing temperature and pressure leads to a chemical upgrading of the coal. To determine the relative effect of the two independently, the reactor was pressurized prior to heating with 7 and 15 atm N_2 (Table 3). Increasing the pressure "artificially" above the steam pressure with N_2 did not lead to any significant or systematic changes in the composition of the treated coal. This would indicate that the temperature is the more controlling factor during hydrothermal treatment.

Table 3. Effects of treatment pressure.

Temperature (°C)	Preheating N_2 pressure (atm)	Treatment pressure (atm)	Moisture (wt%)	Carbon d.a.f (wt%)	TOC mg/ g coal
200	0	16	56	67.3	0.2640
250	0	41	40	67.8	0.6930
300	0	98	22	71.7	1.1910
200	7	28	50	66.3	0.2066
250	7	47	47	67.3	0.4780
300	7	102	23	70.1	1.8917
200	15	32	53	63.0	0.1690
250	15	61	40	68.8	0.3186
300	15	113	33	72.4	1.6150

A series of experiments were conducted to evaluate the differences in the products from raw coal treated samples and slurries (Table 2 and Table 4). The slurries were prepared by pouring the coal and the water into the autoclave. The sample were either heated with no further blending or blended for 1 min in the autoclave with an ultrasonic irradiation prior to heating. Comparisons between the raw hydrothermally treated samples (Table 2) with a coal:water ratio of 1:1.2 and the slurries reveal that a lower final moisture content can be reached if no extra water is added to the coal prior to treatment. The C content of the treated coal seems to be unaffected by the coal:water ratio.

Table 4. Effects of coal water ratio.

Temperature (°C)	Coal : water	Mixing	Moisture (wt%)	Carbon d.a.f (wt%)	TOC (mg/ g coal)
200	1:3	no	62	65.4	0.2002
250	1:3	no	57	67.1	1.7574
300	1:3	no	45	72.0	2.1450
200	1:3	yes	63	66.7	0.9519
250	1:3	yes	62	67.7	0.9510
300	1:3	yes	53	71.8	1.7886

The low ash content of Loy Yang makes it very suitable for both XRD and FTIR analysis of the organic structure because no interfering and dominating inorganic peaks are seen. Two broad diffraction peaks around 20° and 26° 2-theta representing alkyl and aromatic structures, respectively, are present in coal, and the relative intensity of the two peaks reflects the rank of the coal[8]. Preliminary XRD results of dried raw coal and 3 samples treated for 180 min at 200, 250 and 300°C, respectively, are shown in Figure 2. These preliminary XRD analyses show that treatment at 200 and 250°C does not chance the structure, but treatment at 300°C leads to an upgrading of the coal towards a higher rank coal structure. Work is currently being undertaken to quantify these observed changes.

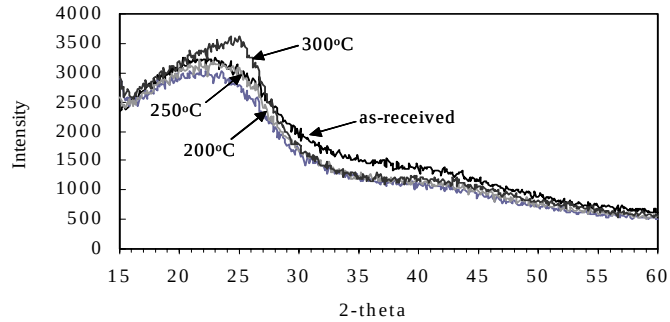

Figure 2. X-ray diffractograms of as-received and hydrothermal treated Loy Yang coal.

In-situ FTIR is powerful tool for tracking coal structure changes during heatup[9-10]. FTIR spectra of a.r. and a sample treated at 300°C for 30 min shows a significant decrease in the peak representing carboxyl groups around 1700 cm^{-1} in the treated sample (Figure 3). Significant peak reduction is also seen for the peaks in the region 2800-3800 cm^{-1} representing OH-groups[9-10]. Further work is currently being done to quantify these changes in carboxyl and OH-groups.

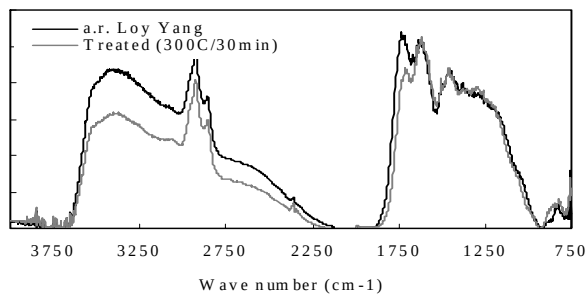

Figure 3. FTIR spectra of a.r. Loy Yang and treated coal.

Conclusions

Hydrothermal experiments conducted in an autoclave on a high-moisture-content coal (Loy Yang) revealed that hydrothermal conditions can be maintained in the autoclave with out addition of water. The drying process is more efficient when no further water is added and high-yield carbon-rich solids can be produced. FTIR and XRD analyses confirm that the upgrading process involves loss of carboxyl and OH groups.

Acknowledgement. Karin Laursen acknowledges financial support from the Japan Society for Promotion of Science (JSPS).

References

(1) Bergins, C. *Fuel*, **2003**, 82, 355-364.
(2) Allardice, D.J.; Clemow, L.M.; Favas, G.; Jackson, W.R.; Marshall, M. and Sakurovs, R. *Fuel*, **2003**, 82, 661.
(3) Couch, G.R. Lignite upgrading. IEA Coal Research, 1990.
(4) Favas, G. and Jackson, W.R. *Fuel*, **2003a**, 82, 53.
(5) Favas, G. and Jackson, W.R. *Fuel*, **2003b**, 82, 59.
(6) Favas, G., Jackson, W.R. and Marshall, M. *Fuel*, **2003**, 82, 71.
(7) Taylor, G.H., Teichmüller, M., Davis, A.; Diessel, C.F.K., Littke, R. and Robert, P. Organic petrology. Gebrüder Borntraeger. 1998.
(8) Mochida, I. and Sakanishi, K. *Fuel*, **2000**, 79, 221.
(9) Miura, K.; Mae, K.; Li, W.; Kusakawa, T.; Morozumi, F.; and Kumano, A. *Energy Fuel*, **2000**, 15, 599.
(10) Worasuwannarak, N.; Nakagawa, H. and Miura, K. *Fuel*, **2002**, 81, 1477.

IN SEARCH OF A HIGH-VALUE CARBON PRODUCT FROM CO-COKING

María M. Escallón, Gareth D. Mitchell, Harold H. Schobert and Leslie Rudnick

The Energy Institute, The Pennsylvania State University, University Park, PA 16802

KEYWORDS: Co-coking, graphite

Introduction

As applied here, co-coking involves the simultaneous thermal treatment of a bituminous coal and a petroleum product such as decant oil [1]. Investigation of co-coking at The Energy Institute (The Pennsylvania State University) has centered around two main objectives, 1) to obtain a coal-based liquid [1-5] that will improve the thermal stability of jet fuel in the pyrolytic regime and 2) to obtain a high-value carbonaceous material [6,7].

As this is a complementary paper to previous preprints, product assessment of the co-coking distillate has been reported elsewhere [8]. However, the focus of the current paper will be on the solid product. In particular, our approach has been to determine if the THF-insoluble residue from co-coking experiments could be use to generate synthetic graphite. Credit for selling such a product to the graphite industry could offset processing cost for the jet fuel. In addition, it is possible that the blend of the petroleum stream and coal could reduce the cost of graphite since coal is a less expensive feedstock.

Experimental

Samples:

The decant oil was obtained from Seadrift Coke in Texas and was selected because it is a material used to make premium coke.

A number of compatible coals with regard to thermoplastic properties, ash and sulfur values were evaluated in past investigations [1]; that work led in the selection of Powellton seam coal. This coal was mined in Boone County, West Virginia and as received by us, was mechanically cleaned at the nearby Marfork coal cleaning plant. Hereafter this coal will be called "whole clean Powellton".

Procedure:

Approximately 20 g of the mixture decant oil / coal (2:1) was added to the type of reactor bomb described previously [5,8,9]. Briefly, the reactor has three sections (bomb, transfer pipe and catchpot) and is vented to avoid excessive pressure and secondary reactions among volatile components. The reactor was assembled, purged with N_2, and then heated in a sand bath held at a constant temperature of 465°C. Experiments were conducted by varying the reaction time from 2 to 12 hours in 2 hour increments.

When the reaction was completed at each specific time interval, bombs were cooled to room temperature, the apparatus was disconnected and the solid product was Soxhlet extracted with THF and dried for 1 hour at 100°C in an oven. The THF-insoluble fraction is hereafter called "semi-coke". Each test was run in duplicate to provided sufficient material for necessary analytical procedures.

Characterization of the semi-coke was carried out by using a Zeiss Universal microscopy, proximate analyzer -LECO MAC-400, -LECO 600 CHN elemental analyzer, total sulfur in a LECO SC-132, and TGA in a Perkin Elmer TGA-7. Semi-coke was thermally graphitized under nitrogen in a Centorr Vacuum Industries series 45 furnace at 2280°C; the graphitization at 2900°C was carried out by OENL in He. Samples were evaluated by XRD analysis using SCINTAG 2-normal powder diffraction apparatus.

For microscopic analysis, about a quarter of the solid residue was split out as removed from the Soxhlet, embedded in a cold setting epoxy resin, placed under vacuum and then in a centrifuge to force a density/particle size gradient. After hardening, samples were cut in half longitudinally to expose the gradient and mounted in 25 mm diameter molds. The hardened samples were polished for reflected light microscopy using a series of grit papers (400 and 600 grit) and alumina polishing slurries (0.3 mm and 0.05 mm). The carbon material was evaluated in white light using an oil immersion objective at a total magnification of 625 X in polarized or cross-polarized light. Point count analysis was performed by traversing the sample based upon a 0.4 x 0.4 mm grid and identifying the textural elements under a crosshair held in the microscope eyepiece. A total of 1000 counts was accumulated, 500 from each of two polished mounts. The textural elements identified and shown in Table 2 have been described previously [7].

The remainders of each THF-insoluble fraction from duplicate runs were combined and crushed to pass a 60 mesh sieve (0.25mm) and then distributed for standard analyses, i.e., proximate, ultimate and sulfur. Samples to be analyzed in the Perkin Elmer TGA were first dried at 110°C for 1h prior to the run. About 10 mg of sample was placed in the pan; the run started from room temperature to 800°C in nitrogen at 10°C/min.

For the XRD, the samples were ground with a mortar to get -60 mesh; samples were pestle and then sprinkled over the surface of a quartz zero background sample holder coated with a thin layer of petroleum jelly. X-ray diffraction data were acquired using SCINTAG 2-normal powder diffraction. The scan conditions were 2-70 degrees 2-theta, continuous scan, 2 deg. per minute and power settings 30 mA, 35 kV. The standard used was graphite ICDD 41-1487.

Results and Discussion

Volatile Matter and TGA. Table 1 compares the elemental analysis and volatile matter (VM) of the semi-coke from the blend (co-coking) at different reaction times and from the decant oil (at 6 hours) to establish a comparison. Volatile matter of the 6h semi-coke from the decant oil is higher than the one from the blend at the same reaction time. In addition, volatile matter decreases in the blend as the reaction time increases. Furthermore, it is likely that those semi-cokes with higher nitrogen or oxygen (by difference) values and lower carbon content may have a slightly higher concentration of the chemical remnants of coal. Although this could reflect differential reaction between components of the blends, it could also suggest a sampling

Table 1: Elemental analysis and volatile matter, dry basis

Reaction time (h)	C	H	N	S	O (diff)	VM
Blend						
2	90.57	3.30	0.93	0.63	0.00	13.23
4	89.45	3.14	1.10	0.66	1.44	11.09
6	90.18	3.34	1.12	0.68	0.73	10.19
8	89.15	3.02	1.06	0.70	1.43	10.00
10	90.27	2.78	1.18	0.70	1.04	9.26
12	90.72	3.01	1.25	0.71	0.51	9.59
Decant oil						
6	94.77	3.68	0.39	0.71	0.00	15.00
Coal Raw	85.78	5.06	1.49	0.80	5.14	29.22

problem. As coal remnants are not uniformly mixed with remnants of the decant oil in these semi-cokes.

Figure 1 shows the thermogram obtained by heating three semi-coke samples in N_2 atmosphere to 800°C at 10°C/min. These results are comparable with those found in Table 1 for volatile matter (VM) in that, as reaction time increases, the volatile matter decreases. In the TGA, as reaction time increases, the weight loss in lower for the semi-coke at 12h than that for the semi-coke at 2h. The reason for this is thought to be that as reaction time increases in the reactor, more condensation reactions occur, leading to larger compounds that do not evolve at 800°C (for TGA) or 950°C (for proximate analysis).

Figure 1: Thermograms of semi-cokes (blend) at different reaction time. Weight %

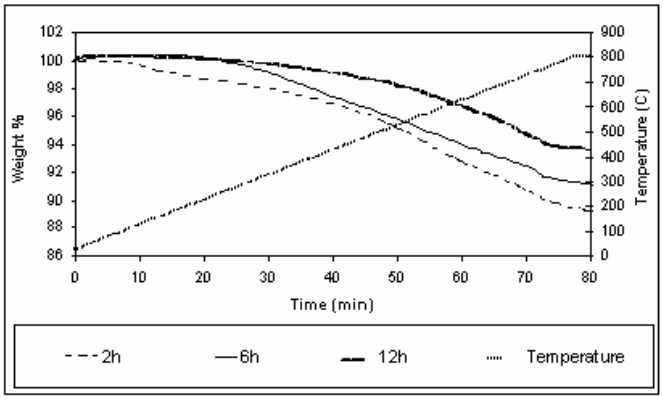

Optical microscopy provides some insight into the interactions between coal particles and the decant oil.

As seen in Figure 2, a typical region of semi-coke derived from coking the whole Powellton coal alone in the reactor bomb stands in contrast to the left half of Figure 3, which shows the type of optical texture derived from decant oil. If there were no interactions between the components of the blend, it would be relatively easy to determine the concentration of each. However, the right half of Figure 3 shows how the texture derived from the vitrinite of this coal can become enlarged or enhanced during co-coking. The fact that these types of textures were not seen in the semi-coke from either coal or decant oil and that small, angular regions of coal-derived inertinite (i) reside in the right half of Figure 3, demonstrates that these regions are remnants of coal particles that have been greatly influenced by co-coking. Nearly 98% of the vitrinite-derived carbon forms observed in the co-coking blends have isochromatic areas enlarged from 1-2 microns to 3-6 microns in diameter.

Based on the volumetric distribution of carbon textures shown in Table 2, a number of important observations can be made regarding the influence of reaction time. As time increases, the carbon textures derived from the vitrinite portion of coal becomes more fully enhanced by interaction with the decant oil; the amount of isotropic carbon derived from the decant oil decreases; and there is a steady decrease in the overall size of the isochromatic areas derived from the decant oil, i.e. mosaic and small domain concentration increases at the expense of domain and flow domain textures.

It is curious to note that after 6h of reaction, the decant oil-derived semi-coke had a significant amount of the isotropic carbon remaining, whereas no isotropic carbon derived from the decant oil was observed in the 6h co-coking run. Also, it is interesting to note that the carbon derived from the decant oil was devoid of flow domain texture. However, this could have been a function of friability as a fairly high concentration of small particles (<20μm) was observed in the sample and could represent broken fragments of the flow domain.

Figure 2: Semi-coke from the coking of coal at 6h

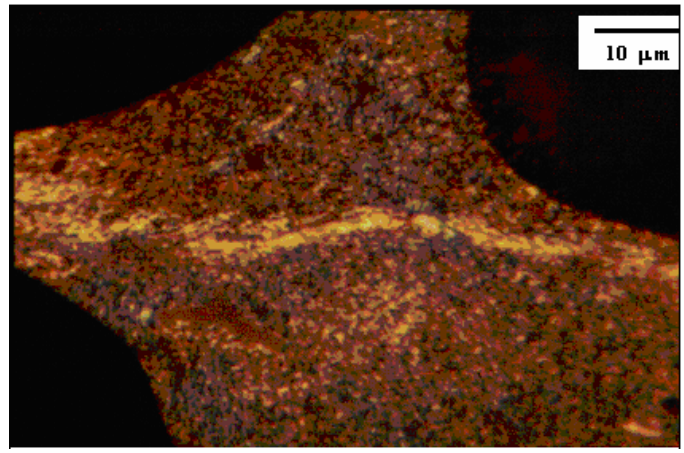

Figure 3: Semi-coke from the co-coking at 6h. Indistinct interface between enhanced coal-derived (right) and mosaic texture derived from the decant oil (left).

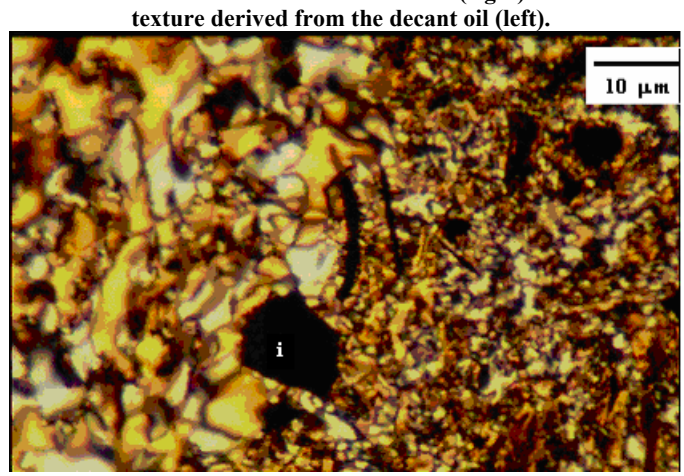

The mosaic texture from the blend which is decant oil-derived also is different. As shown in Table 2, the isochromatic units decrease: *small domain* (10-60 μm) is greater in the blend than in decant oil whereas *domain* (>60μm) and *flow domain* is less in the blend than in the decant oil. There is no doubt about the decant oil and coal interaction. However, the question remains what this apparent change in optical order will have on the graphitizability of the carbon product.

The three blend samples (THF-insoluble fractions from the blend at 6, 10 and 12h), in addition to one from the decant oil at 6h and one from coal at 6h were graphitized and examined by X-ray diffraction. Hereafter, these samples are going to be named as THF-I-G-B-6h, THF-I-G-B-10h and THF-I-G-B-12h for the blend samples, THF-I-G-DO-6h for the decant oil and THF-I-G-C-6h for the coal. All three samples appear to contain graphite matching the graphite standard ICDD 41-1487. There is also evidence of an amorphous phase in each sample.

Table 2: Proportion of textures derived from coal and decant oil compared with the normalized concentration of decant oil textures, Vol. %

	Origin of textures		Normalized concentration of decant oil-derived textures				
Ident. (h)	% Coal-Derived	% Petroleum-Derived	% Isotropic	% Mosaic	% Small Domain	% Domain	% Flow Domain
Decant oil							
6	1.6	98.4	16.0	15.4	36.3	32.3	0.0
12	0.0	100	3.8	7.2	42.2	45.7	1.1
Blend							
2	39.4	60.6	6.3	13.7	60.9	16.0	3.1
4	37.8	62.2	1.0	20.1	60.8	16.2	1.9
6	35.9	64.1	0.0	24.3	64.1	10.6	1.0
8	41.9	58.1	0.0	20.0	64.0	12.0	4.0
10	35.3	64.7	0.0	19.8	66.3	13.3	0.6
12	31.4	68.6	0.0	20.4	66.5	12.2	0.9

Tables 3 to 5 show the results of the XRD analysis. The interlayer spacing d_{002}, the degree of graphitization, **g,** from the equation of Seehra and Pavlovic and the probability of random disorientation between any two neighboring layers, **p,** was calculated [10]

EQ 1: $\mathbf{g} = (3.440-d_{002}) / (3.440-3.354)$
Where 3.354 Å is the interlayer spacing in graphite and 3.440, the value for a carbon with no graphitic order. The probability of random disorientation between any two neighboring layers, **p**, is given by
EQ 2: $d_{002} = 3.354 + 0.086\mathbf{p}$

The crystalline height, **Lc** was calculated by following by following the Scherrer formula
EQ 3: $t= 0.9\lambda / B\cos \eta_B$, where t corresponds to Lc
These calculations are explained in detail elsewhere [11,12].

As shown in Table 3, even at intermediate reaction time (6h) and low graphitization temperature (2280ºC), XRD results suggest a similar structural change in the THF-insoluble fraction of the decant oil (THF-I-G-DO-6h) and blend (THF-I-G-B-6h) far exceeding that of the coal-derived semi-coke (THF-I-G-C-6h). The observations made during optical microscopy of the THF-insoluble fraction of the blend in Figure 3 hinted that some improvement may be realized.

Table 3: Effect of graphitization on three different materials at 2280°C

	Interlayer spacing, $\mathbf{d_{002}}$, **Å**	Stacking height, $\mathbf{L_c}$, **Å**	Random dis-orientation, **p**	Degree of graphitization **g**
THF-I-G-B-6h				
2280°C	3.365	313	0.128	0.872
THF-I-G-DO-6h				
2280°C	3.363	338	0.105	0.895
THF-I-G-C-6h				
2280°C	3.392	136	0.442	0.558

Comparing the degree of graphitization, THF-insoluble from the blend is equivalent to that of the decant oil; the difference between them is only 2.5%; however, the blend is very far from the coal's THF-insoluble whose degree of graphitization is very low (0.558). The random disorientation of the blend is higher than that from the decant oil. This can be explained by the presence of inertinite and mineral matter which has not evolved at 2280°C. It is expected that at higher graphitization temperature (2900°C), the random disorientation will be lower for the blend compared to that at 2280°C.

Table 4 shows the difference in the random disorientation and degree of graphitization with the graphitization temperature at 2280 and 2900°C for the blend and for the decant oil. It is seen that the random disorientation decreases nearly twice as much for the blend at 6h with increasing graphitization temperature. The degree of graphitization is about 5% higher for the graphitized decant compared to the blend. This difference could stem from the presence of inertinite in the coal which may not graphitize.

Table 4: Comparison of the principal XRD characteristics of the graphitized THF-insoluble fraction for the blend and decant oil at two different graphitization temperatures

	Interlayer spacing, $\mathbf{d_{002}}$, **Å**	Stacking height, $\mathbf{L_c}$, **Å**	Random dis-orientation, **p**	Degree of graphitization **g**
THF-I-G-B-6h				
2280°C	3.365	313	0.128	0.872
2900°C	3.359	246	0.058	0.942
THF-I-G-DO-6h				
2280°C	3.363	338	0.105	0.895
2900°C	3.355	310	0.012	0.988

Since the degree of graphitization increases and random disorientation decreases as graphitization temperature increases, the influence of reaction time on the graphitized semi-coke can be assessed. Table 5 comparisons of the principal XRD characteristics for the blend at 2900°C varying the reaction time. As seen that the graphitized semi-coke at 12h has the higher degree of graphitization compared to those at 6 and 10h. Therefore, the higher reaction time generates a higher the degree of graphitization that is comparable to the value derived from graphitized decant oil at 6h.

Table 5: Comparison of the principal XRD characteristics of the graphitized THF-insoluble fraction for the blend at 2900°C graphitization temperature varying semi-coke reaction time

	Interlayer spacing, $\mathbf{d_{002}}$, **Å**	Stacking height, $\mathbf{L_c}$, **Å**	Random dis-orientation, **p**	Degree of graphitization **g**
THF-I-G-B-6h				
2900°C	3.359	246	0.058	0.942
THF-I-G-B-10h				
2900°C	3.360	310	0.070	0.930
THF-I-G-B-12h				
2900°C	3.355	271	0.012	0.988

Conclusions

Optical microscopy shows that the interaction between decant oil and coal is gives rise to a new structure which does not correspond to the structure of the decant oil and coal coked alone. In addition, the anisotropy is higher in the blend than in the decant oil.

Graphite is formed by the further heating of the semi-coke. The carbon materials obtained in the co-coking process show a potential use in the graphite manufacture since the deviation between the data

of the blend and decant oil is below 5% at 2900°C and 2.5% at 2280°C.

The higher reaction time in the blend leads in a higher value of degree of graphitization. The blend at 12h has identical values compared to the decant oil at 6h at 2900°C.

Acknowledgements

The authors want to thank Nichole Wonderling for her assistance with X-ray diffraction. Thanks to Andrzej Piotrowsky for help with the graphitizability furnace at The Energy Institute and Peter Pappano for the graphitization of the samples at 2900°C.

The authors are pleased to acknowledge the financial support for this work provided by the Air Force Office of Scientific Research. We thank Seadrift Coke for the sample of decant oil used in this work.

References

(1) Fickinger, A. E. Master Thesis, The Pennsylvania State University, **2000**.

(2) Fickinger, A. E.; Badger, M. W.; Mitchell, G. D.; Schobert, H. H. *Fuel Chemistry Division Preprints* **1999**, *44*, 106-109.

(3) Fickinger, A. E.; Badger, M. W.; Mitchell, G. D.; Schobert, H. H. *Fuel Chemistry Division Preprints* **2000**, *45*, 299-303.

(4) Fickinger, A. E.; Badger, M. W.; Mitchell, G. D.; Schobert, H. H. *Fuel Chemistry Division Preprints* **1999**, *44*, 684-687.

(5) Escallón, M. M.; Mitchell, G. D.; Schobert, H. H.; Badger, M. W. *Fuel Chemistry Division Preprints* **2003**, *48*, 197-198.

(6) Badger, M. W.; Mitchell, G. D.; Karacan, C. O.; Herman, N.; Senger, B.; Adams, A.; Schobert, H. H. "Coal-based products from the co-coking process for use in anodes for aluminum electrolysis," The Energy Institute, Alcoa Inc. & Preptech Inc., 2002.

(7) Badger, M. W.; Mitchell, G. D.; Karacan, C. O.; Wincek, R. T. *Fuel Chemistry Division Preprints* **2001**, *46*, 564-566.

(8) Escallón, M. M.;Venkataraman, R.; Clifford, D.J.; Schobert, H. H. *Petroleum Chemistry Division Preprints* **2003**, *48*, 147-149.

(9) Escallón, M. M. Master thesis, Pennsylvania State University, 2004. In press.

(10) Atria, J. V.; Rusinko, F. J.; Schobert, H. H. *Energy & Fuels* **2002**, *16*, 1343-1347.

(11) Pappano, P. J. Doctorate Thesis, The Pennsylvania State University, **2003**.

(12) West, A. R. *Solid-state chemistry and its applications*; Second ed.; John Wiley & Sons, **1989**.

Challenges and Progress in the Conversion of Natural Gas to Fuels and Chemicals

Enrique Iglesia

Department of Chemical Engineering, University of California at Berkeley and Chemical Sciences Division, E.O. Lawrence Berkeley National Laboratory, Berkeley, CA 94720
iglesia@cchem.berkeley.edu

Low heteroatom and high hydrogen contents make natural gas an attractive feedstock for the synthesis of fuels and chemicals currently derived from petroleum. This keynote lecture describes recent progress in concept demonstrations and technological applications as well as in the fundamental understanding of the kinetic and thermodynamic constraints prevalent in direct and indirect methane conversion routes to fuels and chemicals. These recent advances combine catalyst improvements with the design and implementation of novel chemical reactors and separation schemes. These topics are discussed also in the context of their thermal efficiency and of their impact on potential strategies to minimize CO_2 formation and the economic viability of CO_2 sequestration.

Gas conversion processes will produce predominately liquid fuels in remote locations, because the prevalent economies of scale and the required field depletion rates will require large process throughputs. These throughputs are too large for chemical markets, with the possible exception of the ethylene and methanol markets. Depletion strategies based on methane conversion to liquid fuels will ultimately be replaced by the direct use of natural gas as a fuel, as pipelines and liquefied natural gas facilities develop together with the local economies and the required distribution infrastructures. Concurrent production of commodity and intermediate chemicals in large natural gas conversion complexes will increase economic incentives for first-of-a-kind technologies and possibly lead to their earlier deployment. The significant market penetration of wax, lubricants, and linear α-olefins from initial coal and gas conversion deployments by Sasol attests to the potential for co-production of chemicals, but also to their significant impact on relatively small chemical markets. The use of natural gas for chemicals syntheses will continue, using both remote and local fields, well beyond the remote gas-to-liquids commercialization time window, because natural gas provides clean and economical routes to methanol and ammonia, as well as to other chemicals currently derived from crude oil.

The conversion of natural gas to useful products is discussed here in the context of a methane refinery, possibly located far from markets, and designed to produce fuels, chemicals, and intermediates currently derived from crude oil. Process simplicity, minimal cycling of process and reaction conditions, and high conversions per pass lead to higher practical thermal efficiencies and lower capital costs for both direct and indirect processes for converting natural gas to fuels and chemicals. Direct conversion routes, however, provide paths to only a few desired products, and the high reactivity of these products typically requires their kinetic protection or selective extraction, both of which increase process complexity and costs. Indirect routes via synthesis gas provide broader options for final products or intermediates. They require less toxic and expensive oxidants than indirect functionalization routes involving bisulfate or halogenated methane derivatives. Direct paths involve C-H bond activation and the conversion of the resulting CH_x or CH_yO species to desired products within a single vessel. Pyrolysis, oxidative coupling, selective oxidation (to methanol or formaldehyde), partial oxidation (to synthesis gas; H_2/CO) and reforming with either steam or carbon dioxide are direct (one-step) methane conversion routes. Direct processes can produce only a few products (H_2/CO, acetylene, ethylene, benzene, methanol, formaldehyde). In many cases, these reaction products are much more reactive than the CH_4 reactant, either because of their weaker C-H bonds or their unsaturated character. Thus, they progress along reaction paths that ultimately lead to thermodynamically more stable carbon or CO_2 products. Only H_2/CO mixtures, useful only as intermediates to more useful products, reach equilibrium yields without significant formation of carbon or CO_2, and only as a result of the thermodynamic preference for H_2 and CO at conditions used for partial oxidation and reforming reactions.

High product yields in most direct routes therefore require continuous removal of desired products from the reaction zone or the thermodynamic or kinetic protection of these products against subsequent reactions. These approaches increase process complexity and second-law inefficiencies. In general, maximum attainable yields depend on the thermodynamic tendency of a given product to oxidize to CO_2 or to dehydrogenate to solid carbon. Weaker C-H bonds in products tend to favor their activation at lower reaction temperatures in the absence of thermodynamic or kinetic protection. Thus, low temperatures actually disfavor desired products in such cases, because subsequent reactions of such desired products have much lower activation energies that CH_4 activation steps leading to the desired initial products.

Direct paths become indirect when desired products are made via the initial formation of chemically-protected intermediates, which must be subsequently converted to the desired products. In such cases, the first step forms a protected form of methane, which resists further conversion to CO_2 or carbon because of its low reactivity, while a second step in a downstream vessel "de-protects" this intermediate and forms the desired products in higher yields than by the corresponding direct routes. For example, synthesis gas (H_2/CO) is in effect a thermodynamically protected, but quite reactive, form of “activated” methane, useful to form a broad range of hydrocarbons and oxygenates. High-temperature CH_4 reactions with H_2O, CO_2, or even O_2 form minor amounts of CO_2 because of thermodynamic constraints imposed by high reaction temperatures at typical reactant stoichiometries.

Synthesis gas conversion processes are significantly more advanced in development than direct processes and than other two-step conversion schemes using methane bisulfate or halogen derivatives. Indirect gas conversion processes via synthesis gas are currently practiced for methanol synthesis and for hydrocarbon formation via the Fischer-Tropsch synthesis. Diesel-range hydrocarbons (via Fischer-Tropsch synthesis) and gasoline (via methanol to gasoline) can be produced with thermal efficiencies as high as 80% of their respective theoretical values (78% and 75%). These indirect processes have continuously evolved with advances in synthesis gas generation, in the design and deployment of three-phase bubble columns for synthesis gas conversion, and in the development of improved catalytic materials for the selective synthesis of paraffins, intermediate size α-olefins, and higher alcohols. Small modular gas conversion plants using catalytic partial oxidation in monolith reactors and CO hydrogenation in bubble columns may also create future opportunities for combining H_2 and power generation and the synthesis of commodity petrochemicals, and even of liquid fuels, in smaller scales than for remote fuels-based gas to liquid plants.

Clean diesel products and intermediate range α-olefins can be efficiently produced via Fischer-Tropsch synthesis pathways, but lighter olefins, such as ethene and propene, and gasoline-type hydrocarbons require an additional process step, in which methanol derived from synthesis gas reacts on shape-selective catalysts.

Attractive routes for the synthesis of oxygenates with C-C bonds will require new approaches involving bifunctional dehydrogenation-condensation pathways. Multifunctional reactors combining membrane separations with chemical reactions and cyclic reactors for temporal separation of reactants and products hold significant promise for increasing the efficiency of synthesis gas generation and direct conversion steps, but their ultimate impact on capital costs and thermal efficiencies remain unclear.

Acknowledgement.
The author acknowledges the financial support from BP through the Methane Conversion Cooperative for the contributions of his own group mentioned in this manuscript. The specific technical contributions of many members of his research group are also acknowledged with thanks, specifically those of Drs. Junmei Wei, Haichao Liu, and Jeffrey Zalc, and of Ms. Patricia Cheung and Mr. Howard Lacheen. The guidance and technical input of Drs. Theo Fleisch and Graham Butler and of other BP technical staff are also gratefully acknowledged.

NOVEL ZERO-CO_2 EMISSION TECHNOLOGY OF CATALYTIC PRODUCTION OF HYDROGEN AND AROMATICS FROM METHANE AND BIOGAS FOR FUEL CELL SOCIETY

Masaru Ichikawa

Catalysis Research Center, Hokkaido University
Sapporo 001-0021 Japan

Introduction

Since a decade ago, we have developed a novel zero-CO_2 emission technology with Mo/Re based zeolite catalysts for catalytic dehydrocondensation of methane to produce hydrogen and benzene/naphthalene as aromatic products. We have constructed a fixed bed demonstration plant of this direct methane reforming process at Muroran, Hokkaido, and succeeded to operate in 2001-2003 a stable and feasible performance with kg-scale Mo/HZSM-5 catalysts. This sustainable technology is available to produce hydrogen and aromatics such as benzene and naphthalene from biogas(60%CH_4+40%CO_2) derived from cows excrements, sewage and biomass. Benzene (cyclohexane) and naphthalene(decalin) as liquid organic hydrides are good for efficient and safe storage, transportation and supply of hydrogen to fuel cell systems. We have developed the organic hydride technology using a cyclic conversion of cyclohexane-benzene (or decalin-naphthalene) which is conducted by pulse-spray technique with a heated Pt-based catalysts at 250-300°C for an efficient, safety and feasible storage and supply to PEM fuel cell car, home electric generator and non-wiring (cable) transportation of electricity generated by solar cells, windmills and other renewable sources. A "Cyclohexane/decalin Hi-way" concept is discussed for 21st century sustainable hydrogen energy from methane and biogas for fuel cell society.

Novel Catalytic Technology of Direct Methane(Biogas) Reforming towards Hydrogen and organic hydrides for Chemical Industry and Fuel Cell Society

We have developed in 1996-2000 the novel Mo carbide and Re based zeolite (HZSM-5, MCM-22) catalysts which exhibit the practically efficient performances (20% conv, over 90%selectivity) for dehydrocondensation of methane(natural gas and biogas) to simultaneously produce benzene and naphthalene with a bulky hydrogen, and the feasible catalyst stability by addition of a few percents CO/CO_2 or hydrogen to methane feed has been demonstrated due to an effective removal of coke formed on the catalysts. We have constructed the 1 Kg catalyst-scale demonstration plant of this direct reforming process at Muroran, Hokkaido, and proceeded the operation with kg-scale catalysts of Mo supported zeolites to produce benzene/naphthalene and hydrogen with a low coke formation at 700-750 ^{o}C and 3-5 bar. This catalytic technology of methane direct reforming is evaluated as non-CO_2 emission and eco-feasible process to produce hydrogen and benzene (cyclohexane) and naphthalene(decalin)as efficient storage and supply of hydrogen for fuel cells.

New Technology of Hydrogen Storage and Supply to Fuel Cell Systems Using Organic Hydrides for Fuel Cell Society

The novel technology of hydrogen supply infra-structures using liquid organic hydrides such as cyclohexane and decalin recently emerge for 21st century hydrogen eco energy society connected with reliable PEM fuel cell. A novel catalytic converter of cyclohexane(or decalin) are developed with carbon-based Pt catalysts to efficiently supply pure hydrogen at moderate temperatures of 250-350 ^{o}C. A cyclic conversion of cyclohexane-benzene (or decalin-naphthalene) system is available for efficient, safety and feasible storage and supply (50-500 l/min) by hydrogen station for hydrogen fuel car, home electric generator and non-wiring (cable) transportation of electricity generated by solar cells, windmills and other renewable sources.

This is promising sustainable technology of zero-CO2 emission hydrogen supply from methane and biogas using organic hydrides connected with reliable PEM fuel-cell systems, as follows.

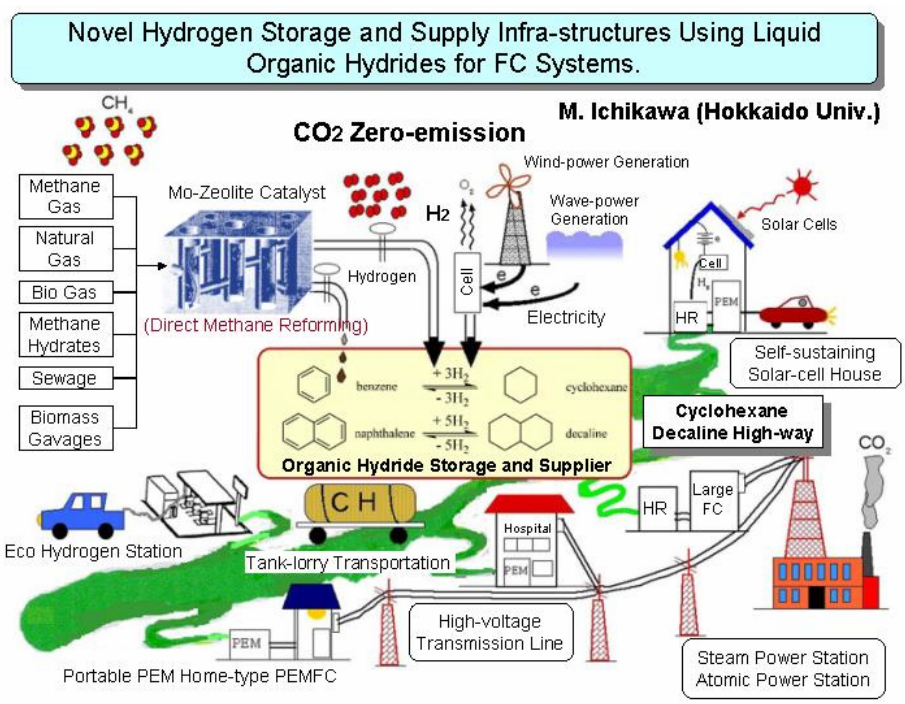

Towards an efficient process for small-scale, decentralized conversion of methane to synthesis gas or hydrogen

Dirk Neumann, Mark Kirchhoff, and Götz Veser[*]

Department of Chemical Engineering
1249 Benedum Hall, University of Pittsburgh
Pittsburgh, PA 15261, USA

Introduction

Methane is one of the major contributing gases to global warming. According to a recent study by the IPCC [1], about 70% of all atmospheric methane is of anthropogenic origin, and this value has shown a particularly strong growth rate through the 1990s with an average increase of about 7 ppt/yr. However, since methane has a very short atmospheric lifetime of about 8 – 12 years, it also appears to be one of the most promising greenhouse gases for short-term measures to counter global warming trends with (almost) immediate impact [2].

In the US, more than a third of all methane emissions result from landfills [3]. These emissions not only represent a significant environmental problem, but at the same time also are a waste of a valuable and renewable natural resource. However, these sources are too small and often too remote to be exploited with existing industrial technology for methane utilization (other than combustion). With current trends towards a more sustainable economic growth and a clean, hydrogen-based economy, however, it seems necessary to develop technologies for efficient, small-scale and decentralized utilization of these and similar methane resources.

Direct 'valorization' of methane, i.e. the direct conversion of methane to higher value products via process routes such as methane coupling, is currently neither efficient nor economical. The only available route for methane valorization is therefore the indirect route via the production of synthesis gas, a mixture of CO and hydrogen, followed by secondary processes such as methanol or Fischer-Tropsch syntheses. In these indirect processes, the syngas production step is currently the limiting factor particularly for small-scale processes, with about 60% of overall investment costs.

Catalytic partial oxidation (CPO) of methane to synthesis gas has recently found much attention as alternative to the industrially dominant, highly endothermic steam reforming route ($CH_4 + H_2O$ B $CO + 3\ H_2$, $\Delta H_R = 206$ kJ/mol). CPO is a mildly exothermic reaction and has thus the potential to be run autothermally ($CH_4 + 0.5\ O_2$ B $CO + 2\ H_2$, $\Delta H_R = -36$ kJ/mol). This independence on external heat sources is quintessential for an efficient small-scale, decentralized process. Furthermore, the reaction is characterized by the extremely high reaction rates typical for catalytic oxidation processes at high temperatures ($T > 800^oC$). This allows for catalytic contact times in the order of about 10 ms and thus for extremely compact reactors with large through-puts.

However, for all its advantages over the conventional steam-reforming route, adiabatic CPO of methane is far from optimal. Simple thermodynamic calculations demonstrate that adiabatic temperatures are too low to achieve optimal methane conversions and syngas selectivities, and even these adiabatic temperatures are only achieved via internal combustion of some of the methane feed, hence intrinsically capping the maximum attainable yields at autothermal process conditions [4].

However, combining the CPO reaction route with an efficient heat-integrated reactor concept, a very efficient overall process can be attained. In this report, we briefly present some of our recent results on CPO of methane in a catalytic reactor with integrated regenerative heat-exchange via reverse-flow operation.

Experimental Set-up

The experimental set-up has been described in more detail in a previous publication [4]. The reactor consists of a stainless steel – quartz glass double tube, in which the catalyst is positioned between two extruded cordierite monoliths which serve as heat reservoirs. Four valves are positioned pair-wise on either end of the reactor to allow switching of the flow direction at reverse-flow operation. If the flow direction is reversed periodically at an appropriate frequency, the heat of the exothermic oxidation reaction is "integrated" and reactor temperatures are increased well beyond the adiabatic limit.

Moveable thermocouples allow measurement of temperature profiles, while reactant and product concentrations are measured via mass spectrometry and gas chromatography.

The catalysts used are platinum precipitated from a salt solution on an alumina foam monolith, and a novel nanocomposite catalyst, in which platinum nanoparticles are anchored in a high-temperature stabilized ceramic matrix [5].

Results and Discussion

Pt-Alumina Catalyst. Figure 1 shows results from CPO of methane with air over a platinum-coated alumina foam monolith at stationary reactor operation ('SS') and at reverse-flow operation ('RFR') versus methane/oxygen ratio. One can see that the regenerative heat-integration in the RFR leads to a significant improvement in methane conversion of about 20% over the whole range of conditions (left graph), as well as drastic improvements in hydrogen selectivity of up to 40% (right graph).

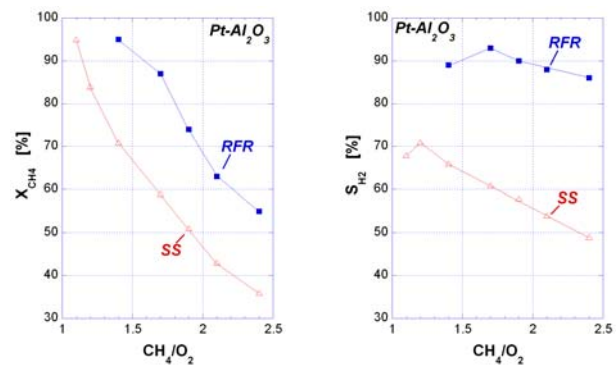

Figure 1. Experimental results for CPO of methane over an alumina supported Pt catalyst in a comparison between steady-state (SS) and reverse-flow operation (RFR). Methane conversions (left graph) and hydrogen selectivities (right graph) are shown versus methane/ oxygen-ratio at a reactor feed of 4 slm methane/air. The duration of one half-period at RFR operation was 15 s.

While methane conversion increases continuously with decreasing methane/oxygen ratio due to the increasing amount of oxygen available for methane oxidation, hydrogen selectivity shows a maximum near $CH_4/O_2 = 1.2$ at SS which shifts to about $CH_4/O_2 = 1.7$ at reverse-flow operation. This maximum can be explained by the superposition of two effects: The overstoichiometric supply of oxygen for $CH_4/O_2<2.0$ leads to some total oxidation, hence reducing selectivities. At the same time, the exothermicity of the total oxidation reaction also increases temperatures and hence thermo-dynamically attainable selectivities, thus helping process selectivities. The observed shift in the maximum therefore indicates that less total oxidation is needed to achieve high reaction temperatures, as reactor temperatures are already increased due to the heat-integration. Heat-integration thus leads to an effective conversion of thermal energy (heat) into chemical energy (process yields).

Reactor Simulations. The experimental investigations were complemented by a detailed simulation study of the reaction behavior at reverse-flow operation of the reactor in order to obtain a better understanding for the reaction kinetics at high-temperature unsteady-state conditions. A heterogeneous one-dimensional reaction-diffusion reactor model was coupled with detailed reaction kinetics for the catalytic surface reaction which had previously been validated against experimental results at stationary reactor operation [6]. Figure 2 shows results from one simulation: catalyst temperatures (left graph) and water concentrations (mass fractions, right graph) in the catalyst zone are shown for one half period immediately after flow reversal.

The reactor model confirms the (qualitative) experimental observation that maximum catalyst temperatures are kept below 1500°C and thus maintain within a range. Furthermore, one can see that a strong (spatial) temperature maximum develops near the catalyst entrance which matches with the maximum in water concentration in this location. This indicates that some total combustion of methane is occurring near the catalyst entrance, the exothermicity of which results in strong temperature maxima.

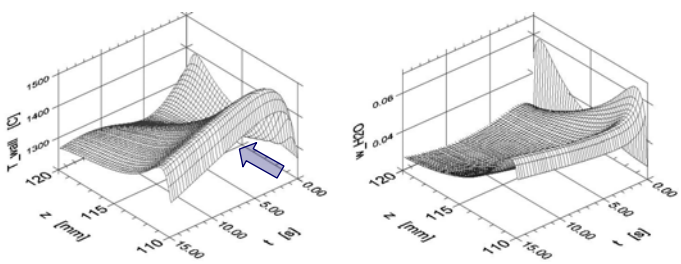

Figure 2. Simulation results for CPO of methane over a Pt catalyst at reverse-flow reactor operation. Temperature profiles in the catalyst bed (top graph) and water concentrations (mass fractions, bottom graph) are shown versus catalyst length (z) and time after flow reversal (t). Flow direction is from right to left as indicated by the arrow in the top graph. Reactor feed is methane/air at room temperature with CH_4/O_2 = 2.0 and RFR periodicity is 15 s.

At the same time, one can also see that the *temporal* temperature maximum in the catalyst zone corresponds to a *minimum* in water concentration. This is due to the (transient) increase in reaction temperature due to heat-integration which leads to an improvement in selectivity and hence to a decrease in the amount of water formed in the reaction.

This results again highlights the above mentioned complex interplay between reactor temperatures and reaction selectivity: while low selectivity results in high reactor temperatures, these high temperatures in turn improve reaction selectivity and hence counter the increasing temperatures.

Pt-BHA Nanocomposite Catalyst. As seen above, heat-integrated reactor concepts alone are not sufficient to achieve optimal reaction temperatures. Development of an efficient process should always involve reactor engineeering in combination with the design of adapted catalyst systems. We recently developed novel nano-composite catalyst systems, in which well-defined noble metal nanoparticles are embedded in a ceramic matrix, yielding highly active, selective and high-temperature stable catalyst systems [5].

Figure 3 shows experimental results in CPO of methane over a Pt-barium hexa-aluminate (Pt-BHA) nanocatalyst at stationary reactor operation ('SS') and reverse-flow operation ('RFR') with varying methane/oxygen ratio. One can see that the results both at SS and RFR are significantly improved in comparison to the conventional supported platinum catalyst (see fig. 1). Furthermore, heat-integration again leads to a strong improvement in conversions and selectivities for this catalyst, raising methane conversion at stoichiometric conditions to about 80% with hydrogen selectivities of about 95%. While this is still far from the thermodynamically allowed complete conversion at perfect selectivity, it is a drastic improvement in comparison to the values of less than 50% conversion and about 55% H_2 selectivity at conventional stationary reactor operation with a conventional catalyst.

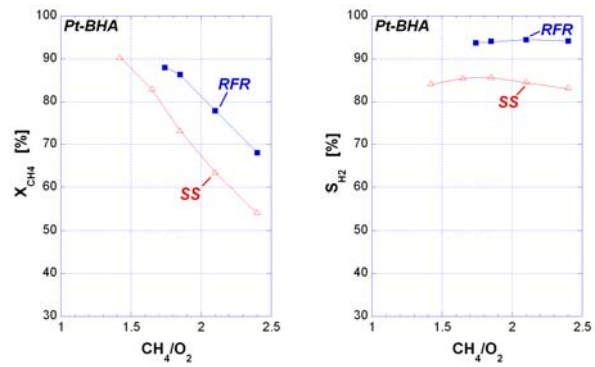

Figure 3. Experimental results for CPO of methane over a novel nanocomposite Pt-BHA catalyst in a comparison between steady-state (SS) and reverse-flow operation (RFR). Methane conversions (right graph) and hydrogen selectivities (left graph) are shown versus methane/oxygen-ratio at a reactor feed of 4 slm methane/air. The duration of one half-period at RFR operation was 15 s.

Conclusions

We presented some recent results from our ongoing studies towards the development of a flexible and efficient process for methane valorization via direct catalytic partial oxidation to synthesis gas or hydrogen.

The combination of reactor engineering with catalyst development, and of experimental investigations with numerical simulation is essential for the development of such processes which we see as critical enabling technologies for a more efficient and sustainable utilization in particular of small-scale, decentralized and remote methane resources.

Acknowledgement. Financial support by the German Science Foundation (DFG), the Funds of the Chemical Industry (VCI), and the Max-Planck-Society (MPG) are gratefully acknowledged.

References

(1) Climate Change 2001: The Scientific Basis, IPCC, **2001**, http://www.grida.no/climate/ipcc_tar/wg1/index.htm.
(2) EPA Report on US Methane Emissions, **1999**, http://www.epa.gov/ghginfo/pdfs/07-complete.pdf
(3) Hansen, J.; Sato, M.; Ruedy, R.; Lacis, A; Oinas, V; *Proc. Natl Acad. Sci.* **2000**, *97*, 9875.
(4) Neumann, D.; Veser, G. *AIChE Journal*, **2003**, accepted.
(5) Schicks, J.; Neumann, D.; Specht, U.; Veser, G., *Catal. Today* **2003**, *81*, 287
(6) Frauhammer, J.; Veser, G., *Chem. Eng. Sci*. **2000**, *55*, 2271

STRUCTURAL REQUIREMENTS AND ACTIVATION PATHWAYS IN REACTIONS OF METHANE CATALYZED BY SUPPORTED METALS

Junmei Wei and Enrique Iglesia

Department of Chemical Engineering, University of California at Berkeley,
Berkeley, CA, 94720, USA

CH_4 reactions with CO_2 or H_2O lead to synthesis gas mixtures, which are used to produce valuable fuels and chemicals. Rigorous assessments of the relevant elementary steps and of the effects of metal dispersion and support on reaction rates and selectivities have remained elusive. Here, we report isotopic tracer and kinetic studies that provide a simple mechanistic picture and a unifying kinetic treatment of CH_4/CO_2, CH_4/H_2O, and CH_4 decomposition reactions on supported Rh, Ni, Pt, Ru, and Ir catalysts. The required kinetic processes are exclusively limited by the first activation of a C-H bond in CH_4 and the relevant rate constant is unaffected by the presence or the concentration of co-reactants (H_2O, CO_2) or by the identity of the support. The elementary steps proposed and confirmed by kinetic and isotopic evidence provide a rigorous basis for treating the dynamics of carbon formation during CH_4 reforming. On all metals, turnover rates increased with increasing metal dispersion. This reflects the higher reactivity of coordinatively unsaturated surface atoms for C-H bond activation reactions.

The kinetic effects of CH_4, H_2O, and CO_2 pressures on CH_4 reaction rates were measured at 850-1000 K and 0.1-1.5 MPa total pressure over a wide range of reactant ratios. Transport artifacts were excluded using dilution strategies. Measured reaction rates were corrected for the distance of the overall reaction from thermodynamic equilibrium in order to obtain rigorous values of the forward kinetic rates. On all catalysts, CH_4 reactions rates were proportional to CH_4 pressure, independent of co-reactant pressure, and identical for CH_4/CO_2, CH_4/H_2O, and CH_4 decomposition reactions, indicating that these reactions are mechanistic equivalent and that C-H bond activation is the sole kinetically-relevant step in all three reactions. These conclusions were confirmed by identical CH_4/CD_4 kinetic isotope effects for reforming and decomposition reactions and by undetectable H_2O/D_2O isotopic effects. The kinetic relevance of C-H bond activation is consistent with the relative rates of chemical conversion and isotopic mixing in $CH_4/CD_4/CO_2$ mixture and with the isotopic evidence for the quasi-equilibrated nature of co-reactant activation and H_2 and H_2O desorption obtained from reactions of $CH_4/CO_2/D_2$ and $^{12}CH_4/^{12}CO_2/^{13}CO$ mixtures. Taken together, these quasi-equilibrated steps involved in H_2O, H_2, and CO formation lead to equilibrated water-gas shift reactions. These elementary steps provide also a rigorous basis for a kinetic treatment of carbon formation processes during CH_4 reactions at high temperatures on metal surfaces and for the assembly of carbon filaments as specific side products of these reactions [1].

Turnover rates were obtained from forward reaction rates and metal dispersions. Turnover rates and metal dispersions are based on strongly chemisorbed H_2 or on H_2-O_2 titration measurements. Turnover rates for CH_4-H_2O reaction increase with increasing dispersion and decreasing size of Rh, Ir, Pt, Ru and Ni clusters supported on various oxides (Figure 1). Identical turnover rates and dispersion effects rates were observed CH_4-CO_2 reactions, as expected from the rigorous kinetic equivalence of CH_4-CO_2 and CH_4-H_2O reactions. On all metals, turnover rates increased monotonically with increasing metal dispersion, suggesting that the coordinatively unsaturated surface atoms prevalent in small crystallites are significantly more active than those in the low-index planes predominately exposed on larger metal crystallites. Similar effects have been measured and predicted theoretically for model metal surfaces [2,3]. These low-coordination surface atoms appear to provide more stable binding sites for CH_x and H products and for the relevant activated complexes. Similar CO oxidation rates were measured before and after CH_4 reactions on all of the noble metals, indicating that metal dispersion is not affected by unreactive deposits or sintering during catalysis. The identity of the support does not influence turnover rates, and previous literature claims for support effects, attributed to co-reactant activation on the supports, are inconsistent with these data and with the kinetic irrelevance of co-reactant activation steps. Supports, however, influence metal dispersion, and in this manner, they can affect turnover rates.

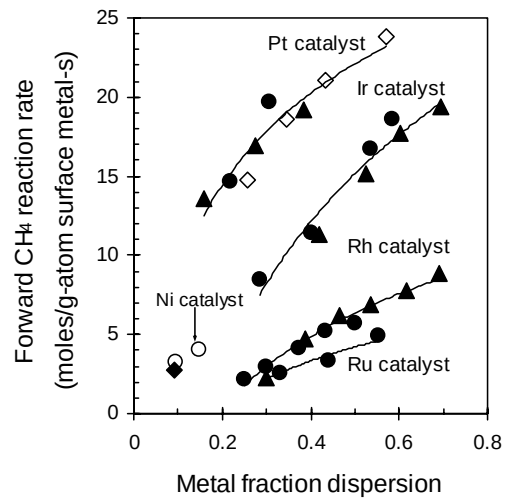

Figure 1. Forward CH_4 turnover rates for H_2O reforming of CH_4 on different metal clusters as a function of metal dispersion on various supports (873 K, 20 kPa CH_4, (▲) ZrO_2, (●) γ-Al_2O_3, (◇) ZrO_2-CeO_2 as support, (○) MgO-A (♦) MgO-B).

This study was supported by BP as part of the Methane Conversion Cooperative Research Program at the University of California at Berkeley.

References

(1) Wei, J.; and Iglesia, E. submitted to J. Catal.
(2) Beebe, T.P.; Goodman, D.W.; and Kay, B.D. *J. Chem. Phys.*, **1987**, 87, 2305.
(3) Watwe, R.M.; Bengaard, H.S.; Rostrup-Nielsen, J.R.; Dumesic, J.A.; and Norskov, J.K. J. Catal., 2000, 189, 16.

C_1 Coupling via Bromine Activation and Tandem Catalytic Condensation and Neutralization over CaO/Zeolite Composites.

Ivan M. Lorkovic,[a] Maria L. Noy,[a] Walter A. Schenck,[a] Mike Weiss,[b] Jeffrey H. Sherman,[b] Eric W. McFarland,[b,c] Galen D. Stucky,[a] and Peter C. Ford[a]*

[a.]Department of Chemistry and Biochemistry, University of California, Santa Barbara, CA 93106.
[b]Gas Reaction Technogies, Inc., 301B S. Wimbrow Dr. Sebastian, FL 32958
[c]Department of Chemical Engineering, University of California, Santa Barbara, CA 93106

Introduction

Although much of the world's methane is stranded, utilization of available methane as a chemical feedstock begins in practice with its conversion to methanol by partial oxidation to syn gas followed by recondensation. Subsequent conversion of CH_3OH to olefins was made possible by discoveries in the early seventies by Mobil scientists,[1-4], and later generalized by other workers to CH_3X (X = halide, SH, NH_2, OCH_3) condensation.[5-14] The proposed mechanism[15, 16] is an initial dehydrative coupling to form the actual catalyst, a relatively ill-defined adsorbed cyclic hydrocarbocation (carbon pool). The technology has been widely developed for multiple product outputs, and may be considered an alternative to the reliable but extreme steam cracking method of olefin production from low and middle petroleum distillates. For CH_3Cl, formed from CH_4 oxychlorination, the product in most cases is an aromatic-rich liquid together with HCl and water,[8-9] with some variation depending on the promoters used.[10-14] While this chloromethane chemistry has been well characterized and the kinetics are favorable, the process has not been commercialized.

Above, we demonstrated a two step technique for partial oxidation of alkanes by oxygen in which a two electron oxidation of a C-H bond is effected by bromine, giving HBr and bromoalkane (Equation 1).[17-20]

$$RH + Br_2 \rightarrow RBr + HBr \qquad (1)$$

These intermediates were further converted either to unsaturated hydrocarbons (for C_2+) or to oxygenates by reaction with a metal oxide solid reactant. The metal oxide served to remove HBr actively, and to direct the output to specific partial oxidation products dependent upon the metal oxide composition and reaction conditions. Complete recovery of bromine and regeneration of the metal oxide was accomplished by reaction of the spent solid with O_2.

During the course of development of active and regenerable metathesis materials, oxides of calcium were investigated because of their lack of facile redox activity (leading to deep oxidation), stoichiometric HBr neutralization capacity, and the nearly thermoneutral regeneration of $CaBr_2$ with O_2 to give CaO and Br_2 (ΔG^o = 14.9 kcal/mol). We observed that while activated HZSM-5 (Si:Al = 80) rapidly lost catalytic CH_3Br coupling activity over the course of 10 minutes, calcium oxide zeolite composites[#] quantitatively neutralized HBr and effected the presumably superacidic condensation of methyl bromide to higher olefins (Eq. 2).

$$HBr + CH_3Br + CaO/ZSM\text{-}5 \rightarrow 1/n\,(C_nH_{2n}) + H_2O + CaBr_2/ZSM\text{-}5 \qquad (2)$$

Figure 1 shows the time dependent product output from two serial continuous flow reactors for methane bromination (1) at 525° C. followed by reaction over a bed of CaO-ZSM-5 at 400° C. (2). Retention of bromine within the second packed bed under these conditions is better than 99.9%, while the product ouput is very similar to that observed for CH_3OH coupling over Ca/ZSM-5.[21]

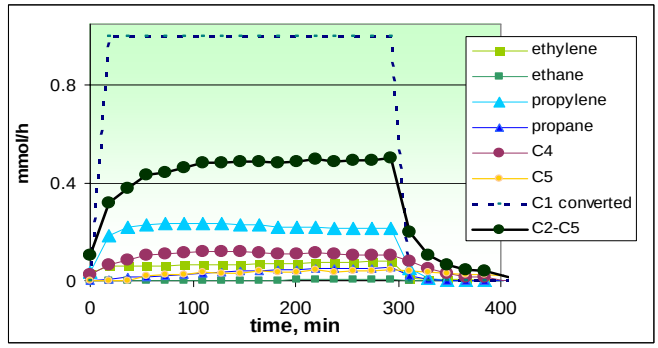

Fig. 1. Output of dual stage reactor with a feed of CH_4:Br_2 (5:0.5 cc/min). First Stage: Plug flow reactor (1 x 100 mm glass tube, 500° C. space time = 0.3 s. Br_2 conversion = 100%, CH_4 conversion = 8.2%). Second Stage: Fixed bed: (10 x 100 mm plug of 5 g. Ca-ZSM-5, 400 C, space time = 20 s, WHSV = 0.04 h^{-1}).

The reaction in Figure 1 represents HBr sequestration to 50-75% of neutralization capacity (5 hours, 5cc/min CH_4, 0.5 cc/min Br_2(g)) of the solid. After more than 10 runs and regenerations (525 C, 5 hours, 5 cc/min O_2, quantitative Br_2 recovery), the coupling/neutralization reactivity and product distribution of the regenerated solid (50% selectivity to C_2-C_5) remained unchanged within experimental error. Furthermore, these materials are also catalytic (Eq. 3) in that even after HBr breakthrough due to metal

$$CH_3Br \xrightarrow[CaBr_2/ZSM\text{-}5]{\rightarrow\rightarrow\rightarrow} 1/n(CH_2)_n + HBr \qquad (3)$$

oxide depletion, the conversion of bromomethanes under the conditions shown in Figure 1 continues (Figure 2). This catalytic reactivity allows use of more specialized auxiliary metal oxides for HBr sequestration and Br_2 recovery.

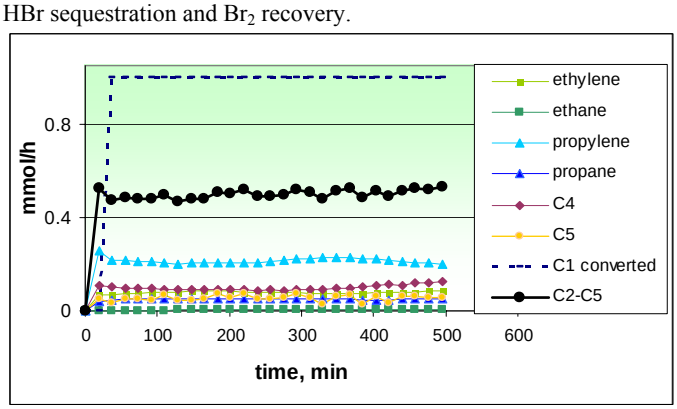

Figure 2. Continued methane bromination and condensation over the same Ca/ZSM-5 bed (5.0 g) used in Figure 1 past the HBr saturation limit (reached at ~100 min) of the bed. Feed: CH_4:Br_2 (5:0.5 cc/min). First Stage: Plug flow reactor (1 x 100 mm glass tube, 500° C. space time = 0.3 s. Br_2 conversion = 100%, CH_4 conversion = 8.2%). Second Stage: Fixed bed: (10 x 100 mm plug of 5 g. Ca-ZSM-5, 400 C, space time = 20 s, WHSV = 0.04 h^{-1}).

Methane partial oxidation by free radical bromination leads to significant buildup of CH_2Br_2 as well as some $CHBr_3$ at appreciable methane conversion. Over CaO/ZSM-5, CH_2Br_2 condenses predominantly to adsorbed carbon in the absence of CH_3Br while cross coupling between CH_2Br_2 and CH_3Br is manifest in the higher output of aromatics (best represented as mesitylene C_9H_{12}), when both species are present (Figure 3).

Notably, with pure CH_3Br feed, the yield of C_2-C_5 is significantly higher, and that of adsorbed carbon and aromatics significantly lower than observed for a mixed bromomethane feed, Figure 3.

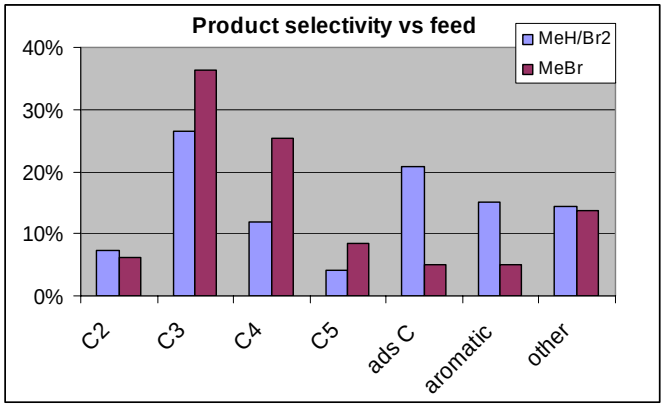

Fig. 3 Comparison of product selectivity for methane/bromine reaction product feed vs pure CH_3Br feed (conditions as in Fig. 1).

The advantage of Br_2 over other halogens in this partial oxidation scheme may be understood in terms of the reduction potential of Br_2 to Br^- (1.07 V vs NHE), which in comparison with Cl_2 (1.36 V) and I_2 (0.54 V), makes alkane bromination significantly less exothermic, yet spontaneous enough to go to completion. Bromine also allows for utilization of a wider range of metal oxides as bromide metathesis reagents because the reoxidation of metal bromides by O_2 (1.23 V) can be accomplished under relatively mild conditions. Despite the slightly lower selectivity for monobromination versus monochlorination for comparable methane conversion, a higher degree of reversibility is expected for the weaker C-Br bonds[22] than exists for C-Cl bonds for corresponding C_1 species. In addition, CH_3Br and CH_2Br_2 are expected to be significantly easier to separate from each other than are CH_3Cl and CH_2Cl_2. Hence polybrominated methanes are not necessarily lost from a methane conversion process and may be induced to comproportionate with CH_4 feed, raising overall CH_3Br, and ultimately olefin, yield.[23]

We direct further work towards establishing the generality of the condensation reactivity of CH_3Br over microporous solids to give olefins or other products and draw on analogies to CH_3OH coupling.[21] Ultimately our goal is to utilize the three step low temperature route -- bromination, coupling, regeneration -- to streamline the production of higher hydrocarbons from methane, technology which is presently dominated by processes involving CH_3OH or synthesis gas as intermediates. Selective bromination and reactor configurations favoring comproportionation of methane and CH_2Br_2 or $CHBr_3$ to CH_3Br are potential routes to improved carbon utilization.

Acknowledgements: This research was funded by Gas Reaction Technologies, Inc., through a sponsored research agreement with the University of California.

Notes

CaO/ZSM-5 composites were prepared by wet impregnation of 1 part $Ca(NO_3)_2$ to 4 parts H-ZSM-5, (Si:Al = 80:1, obtained from Zeolyst Corp.), drying at 125° C. overnight, followed by calcination at 500° C. overnight. Catalytic coupling reactivity was not evident until after the first CH_3Br/HBr metathesis/regeneration cycle.

References

1. C. D. Chang and A. J. Silvestri, *J. Catal.* 1977, **47**, 249.
2. C. D. Chang, W. H. Lang, and A. J. Silvestri, *US Pat*. 3 998 898, 1976.
3. C. D. Chang and W. H. Lang, in *US Pat*. 3 899 544, 1975
4. S. A. Butter, A. T. Jurewicz, and W. W. Kaeding, *US Pat*. 3 894 107, 1975.
5. J. F. Haw, W. Song, D. M. Marcus, and J. B. Nicholas, *Acc. Chem Res*. 2003, **36**, 317.
6. S. Svelle, S. Kolboe, U. Olsbye, and O. Swang, *J. Phys. Chem. B*, 2003, **107**, 5251.
7. V. N. Romannikov and K. G. Ione, *Kinet. Katal.*, 1984, **25**, 75.
8. R. P. Noceti and C. E. Taylor, *US Pat*. 4 769 504, 1988.
9. C. E. Taylor, R. P. Noceti, and R. R. Schehl, in 'Direct Conversion of Methane to Liquid Hydrocarbons through Chlorocarbon Intermediates', ed. D. M. Bibby, C. D. Chang, R. F. Howe, and S. Yurchak, Amsterdam, 1988.
10. G. A. Olah, H. Doggweiler, J. D. Felberg, S. Frohlich, M. J. Grdina, R. Karpeles, T. Keumi, S.-I. Inaba, W. M. Ip, K. Lammertsma, G. Salem, and D. C. Tabor, *J. Am. Chem. Soc.* 1984, **106**, 2143.
11. C. M. White, L. J. Douglas, J. P. Hackett, and R. R. Anderson, *Energy and Fuels*, 1992, **6**, 76.
12. Y. Sun, S. M. Campbell, J. H. Lunsford, G. E. Lewis, D. Palke, and L.-M. Tau, *J. Catal.* 1993, **143**, 32.
13. D. K. Murray, T. Howard, P. W. Goguen, T. R. Krawietz, and J. F. Haw, *J. Am. Chem. Soc.* 1994, **116**, 6354.
14. K.-J. Jens, in 'Methane Conversion via Methyl Chloride: Condensation of Methyl Chloride to Light Hydrocarbons', ed. D. M. Bibby, C. D. Chang, R. F. Howe, and S. Yurchak, Amsterdam, 1988.
15. J. R. Anderson, *Appl. Catal.*, 1989, **47**, 177.
16. F. Banderman and P. Lersch, *Appl. Catal.* 1991, **75**, 133.
17. X.-P. Zhou, A. Yilmaz, G. A. Yilmaz, I. M. Lorkovic, L. E. Laverman, M. J. Weiss, J. H. Sherman, E. W. Mcfarland, G. D. Stucky, and P. C. Ford, *Chem. Commun.* 2003, 2294.
18. X.-P. Zhou, I. M. Lorkovic, G. D. Stucky, P. C. Ford, J. H. Sherman, and P. Grosso, *US Pat*. 6 462 243, 2002.
19. X.-P. Zhou, I. M. Lorkovic, G. D. Stucky, P. C. Ford, J. H. Sherman, and P. Grosso, *US Pat*. 6 472 572, 2002.
20. X.-P. Zhou, I. M. Lorkovic, and J. H. Sherman, *US Pat*. 6 486 368, 2002.
21. M. Stoecker, *Microporous Mesoporous Mat.*. 1999, **29**, 3.
22. D. R. Lide, 'CRC Handbook of Chemistry and Physics 1999-2000: A Ready-Reference Book of Chemical and Physical Data', CRC Press, 2000.
23. I. M. Lorkovic, P. Grosso, J. H. Sherman, E. M. Mcfarland, P. C. Ford, and G. D. Stucky. *Manuscript in Preparation*.

DIRECT SYNTHESIS OF ACETIC ACID FROM METHANE AND CARBON DIOXIDE OVER SiO_2 AND TiO_2 SUPPORTED Pd AND Rh CATALYSTS

Yihui Ding, Wei Huang, Ping Jin, and Kechang Xie

Key laboratory of Coal Science and Technology, Ministry of Education and Shanxi Province; Institute of Coal Chemistry and Engineering, Taiyuan University of Technology, Taiyuan 030024, Shanxi, China

Introduction

Based on the beneficial experience in synthesis of acetic acid from CO_2 and H_2, the pioneer noticed of two pieces of information in support of this research. One was the level 435.43 kJ/mol of bond energy of H–H bond in H_2, which is equivalent to that of C–H in CH_4; the other was the same intermediate CH_x involved in both CH_4 activation and CO_2 hydrogenation. And this led to a novel and interesting route to conversion of greenhouse gases, CH_4 and CO_2, directly to acetic acid by a two-step sequence employing heterogeneous catalysts like Cu-Co oxides[1]. In this work, we have investigated the supported transition metal catalysts and found that Pd and Rh catalysts exhibited a better performance.

Experimental

The catalysts were prepared by incipient wetness impregnation of silica from an aqueous solution of their chlorides. The slurry was dried at 110 °C for 16 h and then calcined at 500 °C for another 5 h. The reaction was implemented in a micro-reactor at atmospheric pressure with 400 mg catalyst (sized 40-60 mesh). A flowing argon (at a flow rate of 100 cm^3/min) was first used for 10 min to purge out the impurity gases in the reactor. The catalyst was then reduced from the room temperature to 400 °C. The reactor was maintained at this temperature for 2.5 h. The catalyst was then cooled in argon (or nitrogen) stream to the desired temperature. After that, a two-step sequence began with exposing the catalyst to a flow of CH_4 (85 cm^3/min) for 5 min and CO_2 (85 cm^3/min) for 10 min in turn. More CO_2 was fed to increase the yields on the basis of the consumed CH_4. The products were collected at ice-water mixture temperature by a bubbling absorber filled with caustic soda solution (50 ml). After reaction for 20 turns around 5 h, the products were analyzed by IC20 gas chromatography.

Results and Discussion

Figure 1 shows the yield of acetic acid synthesized directly from CH_4 and CO_2 over Pd/SiO_2 catalysts, while Figure 2 presents the results obtained from Rh/SiO_2 catalysts.

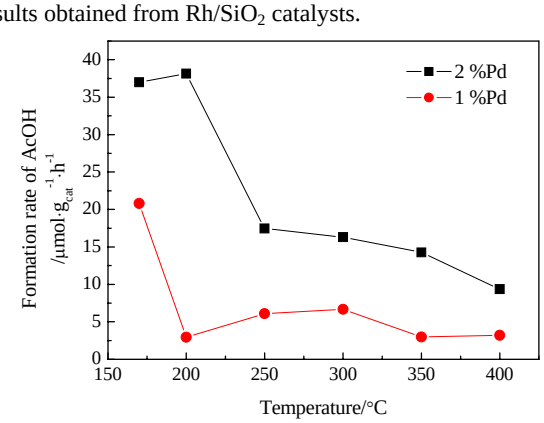

Figure 1. The formation rate of AcOH over Pd/SiO_2 at different temperatures

One can observe an apparent decline and a slight decline vibrated in acetic acid yield along with the temperature rises from 170 to 400 °C in the presence of catalyst 2%Pd/SiO_2 and 1%Pd/SiO_2.The maximum yield of acetic acid is 37.0 and 38.2 μmol/g_{cat}·h at 170 °C and 200 °C of the former, and the latter is 20.8 μmol/g_{cat}·h. An interesting point we noticed is that some formic acid was also formed for reaction carried out at 300 °C over both 2%Pd/SiO_2 and 1%Pd/SiO_2.

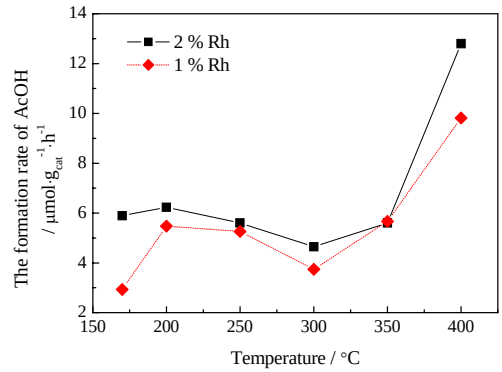

Figure 2. The formation rate of HCOOH over Rh/SiO_2 at different temperatures

The catalysts Rh/SiO_2 can also give to acetic acid. However, its catalytic activity was not as good as we expected. As represented in Figure 2, the yield of acetic acid does not exhibit a marked decline, but ascend as the temperature rises. The best results we obtained in our experiments are 12.8 μmol/g_{cat}·h for 2%Rh/SiO_2 and 9.8 μmol/g_{cat}·h for 1%Rh/SiO_2 at 400 °C. And no formic acid was observed. Unsurprisingly, a higher yield can be achieved by using more supported amount of metal.

TiO_2-supported Rh, Pd catalysts give results similar to SiO_2. The yield of acetic acid over Pd catalyst is higher than Rh catalyst, as shown in Figure 3. And, only Pd catalyst can lead to a formation of formic acid too. The yield of formic acid is shown in Figure 4.

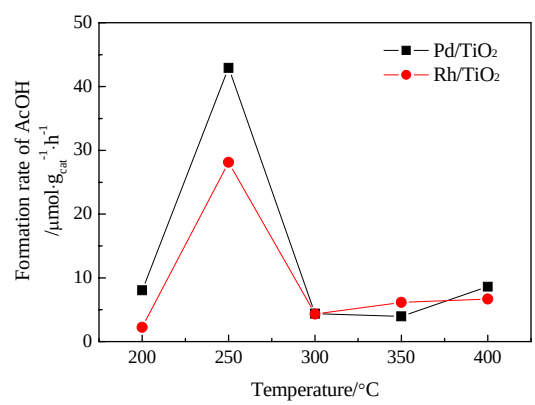

Figure 3. The formation rate of AcOH over Pd, Rh/TiO_2 at different temperatures

The present investigation has confirmed the effectiveness of the direct synthesis of acetic acid directly from methane and carbon dioxide. This route provides a potentially valuable means to convert directly greenhouse gases, CH_4 and CO_2, to acetic acid, a useful target molecule for methane conversion[2]. Further study is being conducted.

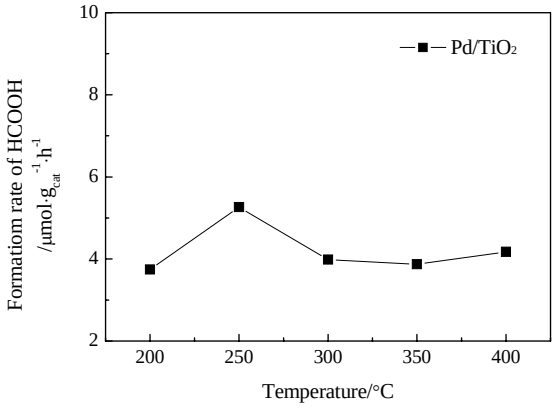

Figure 4. The formation rate of HCOOH over Pd /TiO_2 at different temperatures

Acknowledgement
The authors are grateful to the support from both the National Natural Science Foundation and the Research Foundation to Returned Scholars of Shanxi Province, China.

References

(1) Huang, W.; Xie, K.C.; Wang, J.P. *J. Catal*., **2001**, *201*,100.
(2) Lin, M.; Sen, A. *Nature*, **1994**, *368*, 613.

PARTIAL OXIDATION OF METHANE TO SYNGAS OVER $BATI_{1-X}NI_XO_3$ CATALYSTS

Cuili Guo, Jinli Zhang, Wei Li, Pingfan Zhang and Yiping Wang

School of Chemical Engineering, Tianjin University, Tianjin 300072, China

Introduction

Catalytic partial oxidation of methane to syngas is a slightly exothermic, highly selective, and energy efficient process. It gives syngas with H_2 to CO ratio of 2:1 that is suitable for F-T and methanol syntheses. Hence, much effort has been devoted to partial oxidation of methane to syngas in the presence of catalysts. Perovskite catalysts have attracted much attention for more than two decades due to their potential commercial applications as catalysts [1-3]. Lago et al[4] observed that a series of cobalt-containing perovskites $LnCoO_3$(Ln=La, Pr, Nd, Sm, and Gd) have high activity and selectivity for the partial oxidation of methane to syngas. Slagtern and Olsbye[5]and Provendier[6] concluded that the addition of a third metal into the perovskite structure is necessary to stabilize the catalytic system. Supported Ni catalysts on $CaTiO_3$,$SrTiO_3$ and $BaTiO_3$ oxides have been investigated[7]. Ni/$SrTiO_3$ and Ni/$BaTiO_3$ showed that high activity for POM.

In this study, partial oxidation of methane was investigated over $BaTi_{1-X}Ni_XO_3$ catalysts. We evaluated the catalysts prepared with different Ni loading amount and with different calcination temperatures. The reaction mechanism and activity are discussed.

Experimental

A series of $BaTi_{1-X}Ni_XO_3$ catalysts were prepared by the sel-gel method with x values ranged from 0 to 0.3. The calculated amounts of tetrabutyl titanate, citric acid and glycol were mixed and stirred to solution under reflux. The calculated amounts of $Ba(NO_3)_2$ and $Ni(NO_3)_2.6H_2O$ were added to the hot solution with stirring and to make nitrate decomposition. A gel was obtained by adding triethanelamine. The nanometer powders of $BaTi_{1-X}Ni_XO_3$ were made by calcining the dried gel for 2h at different temperature (600,700 and 800 °C).

X-ray diffraction（XRD）patterns were obtained with a Rigaku 2038 diffractometer using CuKα radiation at a rate of 4°/min. The XRD patterns of $BaTi_{1-X}Ni_XO_3$ shows that the pure perovskite structure is formed. The particle textures of the samples were investigated using a JEOL TEM-100X Ⅱ transmission electron microscope. The TEM images of $BaTi_{1-X}Ni_XO_3$ indicate that the mean sizes of the particles are 13 to 21 nm and particles distributions are uniform. Specific surface areas were derived from N_2 adsorption isotherms that were determined with a Chem BET-3000 instrument. The values of the BET specific surface area of $BaTi_{1-X}Ni_XO_3$ are in the 10-16 m^2/g.

The methane oxidation reaction was carried out in a fixed bed quartz reactor(8 mm in i.d.) filled with 300 mg catalyst at atmospheric pressure. The feed gas mixture were composed of CH_4,O_2 and N_2 with a space velocity of $3\times10^5\ h^{-1}g^{-1}$.The products were analyzed on-line by a SP3420 gas chromatograph equipped with TCD.

Results and Discussion

Table 1 lists the results of activity and selectivity of $BaTi_{1-X}Ni_XO_3$ with different x values(Ni content) in POM reaction at 950 ℃, which indicate that the activity of $BaTiO_3$ is very low and the activity of $BaTi_{1-X}Ni_XO_3$ increase significantly with the addition of Ni into the perovskite. The activity of $BaTi_{0.8}Ni_{0.2}O_3$ is the highest with CH_4 conversion of 95% and CO selectivity of 98%.

Table 1. Effect of x Value in $BaTi_{1-x}Ni_xO_3$ on the Activity at 950 ℃

X value	CH_4 conversion (%)	CO selectivity (%)
0($BaTiO_3$)	40	75
0.1($BaTi_{0.9}Ni_{0.1}O_3$)	89	97
0.2($BaTi_{0.8}Ni_{0.2}O_3$)	95	98
0.3($BaTi_{0.7}Ni_{0.3}O_3$)	86	96

Figure 1 shows the catalytic activity for partial oxidation of CH_4 at CH_4/O_2 mole ratio of 2:1 with a space velocity of $4.4\times10^5\ h^{-1}g^{-1}$ over $BaTi_{0.8}Ni_{0.2}O_3$ calcined at different temperatures. From Figure 1, we can see that with the increase of calcination temperature, the activation temperature of $BaTi_{0.8}Ni_{0.2}O_3$ decrease and the optimum reaction temperature scarcely change. It is suggested that the perovskite catalysts should be calcined at low temperatures, since the activity of $BaTi_{0.8}Ni_{0.2}O_3$ was significantly reduced with an increase of calcination temperature from 600 to 800 ℃.

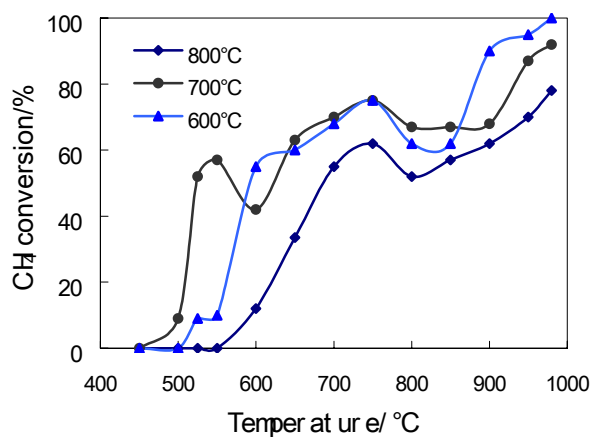

Figure 1. CH_4 conversion versus temperature

The results reveal that the calcination temperature of the $BaTi_{1-X}Ni_XO_3$ has a close relation with activity. The increase of calcination temperature can lead to a decrease in surface area and an increase in crystal size, which make concentration of active oxygen decrease. Thereby the catalytic activity of $BaTi_{1-X}Ni_XO_3$ decreases.

Figure 1 shows CH_4 conversion increase with the increase of reaction temperature. It is found from experiments that the temperature difference between reaction temperature and control temperature changed from 24℃ to -4℃ with the increase of reaction temperature, which indicate the heat of reaction gradually decrease. These results suggest that the combustion of a part of CH_4 to H_2O and CO_2 (exothermic reaction) first took place in the lower temperature and reforming reaction of CH_4 with H_2O and CO_2 (endothermic reaction) was followed in the higher temperature for POM over $BaTi_{1-X}Ni_XO_3$. This result is agreement with the results in literature [7].

Figure 2 shows the catalytic activity for partial oxidation of methane at CH_4/O_2 mole ratio of 2:1 with a space velocity of $4.4\times 10^5 h^{-1}g^{-1}$ over $BaTi_{0.8}Ni_{0.2}O_3$ at different reaction time. The results show that the catalytic activity of $BaTi_{0.8}Ni_{0.2}O_3$ increases with the increase of the reaction time. When the reaction time is over 3h, the catalytic activity of $BaTi_{0.8}Ni_{0.2}O_3$ remained unchanged after 40h of operation at 950 ℃. This indicates that the activation stage of the catalyst is needed at the initiation stage of reaction and that catalyst is stable under the POM reaction at 950℃ for 40h.

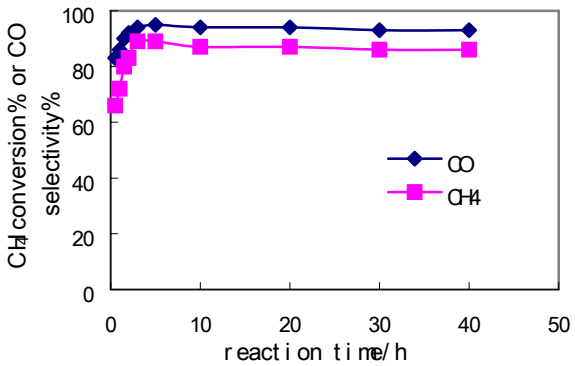

Figure 2. CH_4 conversion and CO selectivity versus reaction time

Conclusions

From the results above, we can conclude that perovskite $BaTi_{1-X}Ni_XO_3$ are highly efficient catalysts for POM. The calcination temperature of the $BaTi_{1-}Ni_XO_3$ can affect the activation temperature. The addition of Ni into the perovskite structure makes activity increase significantly. The most active system $BaTi_{0.8}Ni_{0.2}O_3$ presents a stable activity, with no deactivation at 950℃ during 40h test.

References

(1) Ferri, D.; Forni, L. *Appl. Catal. B.* **1998**, *16*, 119.

(2) Cimino, S.; Lisi, L.; Pirone, R.; Russo, G.; Turco, M. *Catal. Today* **2000**, *59*, 19.

(3) Shu, J.; Kaliaguine, S. *Appl. Catal. B.* **1998**, *16*, L303.

(4) Lago, R.; Bini, G.; Pena, M.A.; Fierro, J.L.G. *J. Catal*. **1997**, *167*, 198.

(5) Slagtern, A.; Olsbye, U. *Appl. Catal. A.* **1994**, *110*, 99.

(6) Provendier, H.; Petit,C.; Estournes, C.; Libs, S.; Kiennemann, A. *Appl. Catal. A.* **1999**, *180*, 163.

(7) Takehira, K.; Shishido, T.; Kondo, M. *J. Catal.*, **2002**, *207*, 307.

ESTIMATING REACTIVITY OF ASPHALTENES BY A COMBINATION OF QUANTUM CHEMICAL CALCULATION AND STATISTIC ANALYSIS

Xiaoliang Ma, and Chunshan Song*

The Energy Institute, The Pennsylvania State University
409 Academic Activities Building, University Park, PA 16802
*E-mail: mxx2@psu.edu

1. Introduction

Asphaltenes are the most polar and heavy substances existing in petroleum, which cause serious problems in oil recovery, pipelines, and especially in thermal and catalytic processing of petroleum residues due to coking. Many approaches have been examined in molecular presentation of asphaltenes for several decades. Recently, some average molecular structures of asphaltenes have been constructed on the basis of elemental composition, detailed structural parameters from NMR data, pyrolysis gas chromatography/mass spectrometry and others [1-6], which allows one to estimate quantitatively the reactivity of asphaltenes at molecular level on the basis of chemical structural models of asphaltenes.

Some approaches to estimating reactivity of aromatic compounds on the basis of computational chemistry have been reported [7-11]. These approaches incorporated some quantum chemical parameters including ionization potential, bond order, π-electron density or frontier orbitals to estimate the hydrogenation reactivity and electrophilic reactivity, which allows one to compare the reactivity of a family of compounds. However, for estimating the reactivity of asphaltenes, these methods are not directly applicable because 1) asphaltenes are composed of mixtures of hundreds of organic molecules rather than a single macromolecule, 2) there are many reactive sites even in a single macromolecule in asphaltene, and 3) not only HOMO and LUMO but also HOMO-1, HOMO-2, … and LUMO +1, LUMO +2, … contribute to the reactivity of the macromolecule since the energy levels of these orbitals are close to the frontier orbitals in the macromolecule of polycyclic aromatics. Consequently, it is necessary to develop a quantitative method to estimate the reactivity of asphaltene on the basis of its chemical structural model. In the present study, we have developed an approach as a new estimation method by using a distribution function of superdelocalizability to estimate the reactivity of asphaltenes. This method combines the quantum chemical calculations and statistic analysis.

2. Structural Models of Asphaltenes

The chemical structural models for three asphaltenes, Khafji ($C_{142}H_{157}N_2O_2S_4$), Maya ($C_{125}H_{134}N_2O_3S_3$) and Iranian ($C_{109}H_{108}N_2O_3S_3$), are shown in Figure 1. The model for each asphaltene contains three macromolecules, representing an average chemical structure of the asphaltene. These models were constructed by researchers at National Institute of Advanced Industrial Science and Central Research Laboratories, Idemitsu Kosan Company, on the basis of the analytical data (including ultimate analysis, ^{1}H-NMR, ^{13}C-NMR and laser desorption mass spectrometry) of the asphaltenes obtained respectively from fractionation of Khafji, Maya, and Iranian vacuum residues using n-heptane as a solvent [2,12].

3. Computational Methods

All quantum chemistry calculations in this study were performed by using a semi-empirical molecular orbital method, the PM3 parameters, in CAChe version 5.0. Geometries of the asphaltene macromolecules and some aromatics were optimized. Bond order, net atomic charges, ionization potential, electrophilic frontier density and electrophilic superdelocalizability were calculated. The electrophilic superdelocalizability was defined as:

$$S^E(x) = 2 \sum_{i=1}^{N} [\phi_i(x)^2]/(\alpha - E_i)$$

Here, N is the total number of the occupied orbitals, $\phi_i(x)$ is the value of the filled orbital i at point x, E_i is the energy of that orbital in electron volts (eV), α is the reagent energy[13, 14]. The statistic analysis was performed by using a frequency function in Microsoft Excel.

4. Results and Discussion

Correlation of Hydrogenation Reactivity of Aromatics with the Calculated Parameters There are not many comparable quantitative data in the literature for hydrogenation reactivity of aromatic hydrocarbons. A set of pseudo–first-order rate constants for hydrogenation of benzene, biphenyl, naphthalene and 2-phenylnaphthalene catalyzed by Co-Mo/Al_2O_3 were determined by Spare and Gates [15]. In order to determine which calculated parameter is more sensitive to hydrogenation reactivity, bond order, ionization potential, electrophilic frontier density and electrophilic superdelocalizability (ESD) for the four aromatic hydrocarbons were calculated and correlated with their hydrogenation rate constants. The results revealed that ESD values of the aromatic hydrocarbons show a better correlation with their hydrogenation reactivities, indicating that we can use ESD values as an index for hydrogenation reactivity. This is probably because the π-complex intermediates formed in hydro-genation process transfer electrons from the higher occupied molecular orbitals of the hydrocarbons to an unoccupied d-orbital on the metal. The higher ESD values result in a more facile electron transfer from the hydrocarbons to the metal, and thus, a stronger adsorption of the hydrocarbons on the active sites on the catalyst surface.

Estimating Hydrogenation Reactivity of Asphaltenes by a ESD Distribution Function The EDS values for all atoms in three asphaltene models were calculated. As well known, it is unsuitable to compare the hydrogenation reactivity of asphaltenes by only comparing the reactivity of one or a couple of sites in each asphaltene model or by only comparing the reactivity of a macromolecule in each asphaltene. In order to solve this problem, we built a distribution function of ESD values for the three asphaltenes on the basis of the structural models. The higher percentage of the atoms in a range of high ESD value indicates the higher hydrogenation reactivity of the asphaltene. Percentage of the atoms in each asphaltene structural model as a function of ESD value is shown in Figure 2. The percentage of the atoms with ESD value higher than 1 increases in the order of Maya < Khafji < Iranian, indicating that the hydrogenation reactivity of the asphaltenes increases in the same order. A distribution function of the bond order for three asphaltenes were also calculated and the results imply a similar trend for hydrogenation reactivity. The distribution function of the bond order also shows that there are higher percentages of weaker C-C bonds in Khafji asphaltenes than in the others, indicating its higher thermal

creaking reactivity. The estimated hydrogenation reactivity and thermal cracking reactivity in the present study are in agreement with the experimental results obtained by Central Research Laboratories, Idemitsu Kosan Company [16]. It has been shown in previous studies that asphaltenes from different Company sources show different reactivities in catalytic and thermal hydroprocessing [17,18].

5. Acknowledgment

We gratefully acknowledge the financial support by Idemitsu Kosan Company and New Energy and Industrial Technology Development Organization (NEDO). We thank Mr. R. Tanaka, Dr. T. Takanohashi and Dr. S. Sato for providing the structural models of the three asphaltenes and for helpful discussions.

6. Reference

1. Shen, Y.; Mullins, O. C. Eds. Asphaltenes, Fundamentals and Applications, Plenum Press, New York, London, 1995.
2. Sato, S., Sekiyu Gakkaishi, 1997, 40, 46.
3. Artok, L.; Su, Y. Hirose, Y.; Hosokawa, M.; Murata, S.; Nomura, M. Energy & Fuels 1999, 13 287.
4. Groenzin, H.; Mullins, O. C. Pet. Sci. Technol. 2001, 19, 219.
5. Sheremata, J. M.; McCaffrey, W. C.; Gray, M. R. *Prepr., Div. Fuel Chem., Am. Chem. Soc*. 2001, 46, 351.
6. Sato, S.; Takanohashi, T. Tanaka, R. *Prepr., Div. Fuel Chem., Am. Chem. Soc*. 2001, 46, 353.
7. Geneste, P.; Amblard, P.; Bonnet, M.; Graffin, P. J. Catal. 1980, 61, 115.
8. Nag, N. K. Appl. Catal. 1984, 10, 53.
9. Ma, X.; Sakanishi, K.; Isoda, T.; Mochida, I. *Energy & Fuels* 1995, 9, 33-37.
10. García-Cruz, I.; Martínez-Magadá, J. M. Guadarrama, P.; Salcedo, R.; Illas, F. J. Phys. Chem. A 2003, 107, 1597-1603.
11. Marston, G.; Monks, P.; Wayne, R. P. Correlations between Rate Parameters and Molecular Properties, in *General Aspects of the Chemistry of Radicals*, Alfassi, Z. B. Ed.; John Wiley and Sons: New York, 1999, p.429.
12. Takanohashi, T. Sato, S.; Tanaka, R., Fuel Chem. Div. Preprints 2001, 46(2), 357.
13. Fukui, K.; Yonezawa, T.; Nagata, C. Bull Chem. Soc. Japan, 1954, 27, 423.
14. Fukui, K.; Yonezawa, T.; Nagata, C. J. Chem. Phys., 1957, 26, 831.
15. Sapre, A. V. Gates, B. C. Ind. Eng. Chem. Process Des. Dev. 1981, 20, 68-73.
16. Tanaka, R., personal communication, 2003.
17. Song, C.; Nihonmatsu, T.; Nomura, M. Ind. Eng. Chem. Res., 1991, 30 (8), 1726-1734.
18. Song, C.; Hanaoka, K.; Nomura, M. Energy & Fuels, 1992, 6 (5), 619-628

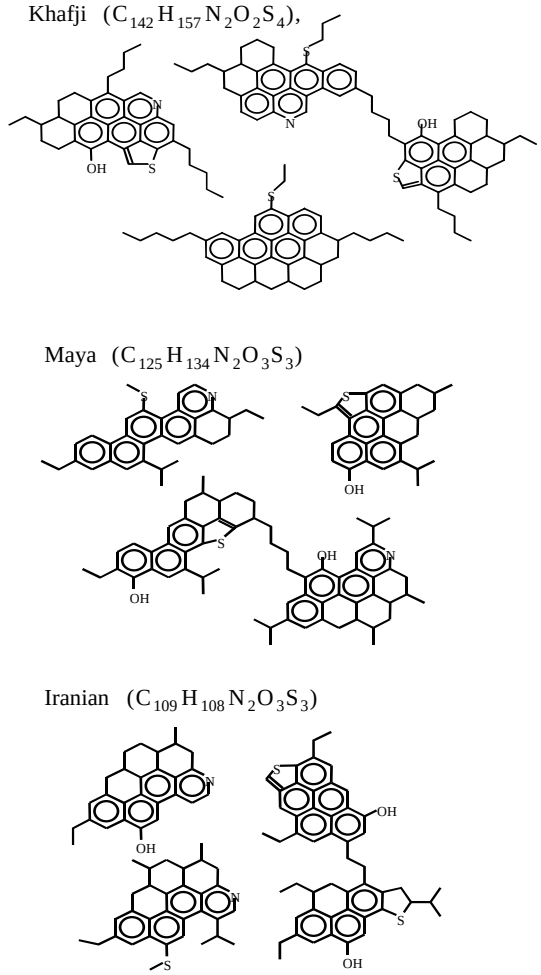

Figure 1. Chemical structural models of three asphaltenes

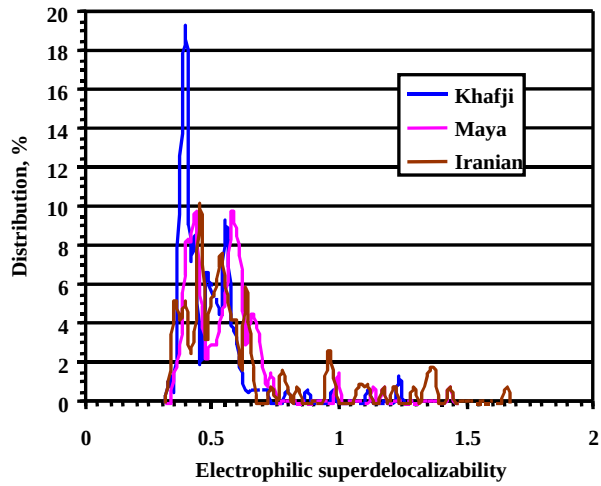

Figure 2. Distribution of electrophilic superdelocalization values on three asphaltenes

Hydrogenation of naphthalene on HY/MCM-41 supported sulfided-NiMo catalysts

LIU Yunqi LI Wangliang, LIU Chunying Cui Min, LIU Chenguang

College of Chemistry & Chemical Engineering,
University of Petroleum, China, Dongying,
Shandong257061
E-mail liuyq@mail.hdpu.edu.cn

Abstract:

A series of mesoporous molecular sieves MCM-41 with different Si/Al molar ratios were synthesized by hydro-thermal method. The influence of aluminum contents on the properties and pore structure of MCM-41 molecular sieves were investigated. The supported Ni-Mo catalysts with MCM-41 and γ-Al_2O_3 as supports were synthesized by impregnating with Ni-Mo-P solution. The activity of the catalysts was characterized by hydrogenation of naphthalene. The influence of Si/Al ratio of MCM-41 on hydrogenation activity of the catalysts was investigated. The results indicated that the relative crystalinity of MCM-41 decreases with the increase of aluminum content in the molecular sieves; however, the hydrogenation activity of the catalysts, especially the ring-opening activity, increases with the increase of aluminum content. The synergistic effect for hydrogenation of naphthalene was found by mixing MCM-41 and HY molecular sieves. At 360°C，the catalysts with HY and MCM-41 mixture as supports has higher activity. The reaction network for hydrogenation of naphthalene includes two parallel pathways; naphthalene was hydrogenated to tetralin, then the isomerization and ring-opening of tetralin occurred, or tetralin was further hydrogenated to decalin, followed by the isomerization and ring-opening of decalin.

Key words: MCM-41 molecular sieve, naphthalene, hydrogenation, activity, reaction mechanis

1. Introduction:

There is an increasing demand for environmentally friendly hydrocarbons and clean-burning high performance fuels, such as distillate fuels like diesel and jet fuels. Distillate fuels typically contain paraffins, naphthenes, and aromatics. For fuels quality parameters such as cetane, gravity and emissions, paraffins are the most desirable components, followed by naphthenes, followed by aromatics. The least desirable are multi-ring aromatic compounds. Owing to more and more strict environmental and clean-fuel legislation, deep hydrodearomaticisation of diesel has been the focus of many recent studies. Many approaches has been applied in the synthesis of catalysts such as using different types of zeolite as supports [1], adding promoters [2], etc.

MCM-41 mesoporous molecular sieve has become one of the world-wide known materials since 1992 for its high surface area and meso-size porosity [3]. MCM-41has shown its advantages in the fields of catalysis, material and organic compounds synthesis [4,5]. Corma et al[6] reported that the activity on one stage mild hydrotreatment of vacuum gasiol on NiMo catalysts supported on MCM-41 molecular sieves, is superior in HDS, HDN and HC reaction, compared to that of catalysts woth the same Ni, Mo content supported on amorphous-alumina or on USY zeolite. T. Halachev[7] reported the catalytic activity of (P)NiMo/Ti-HMS and (P)NiW/Ti-HMS catalysts in the hydrogenation of naphthalene. Condam et al[8] found that cis- and trans-declins easily produced on Pt/MCM-41 compared to Pt/Al_2O_3 and Pt/TiO_2.In this paper, we have synthesized a serial of Al-MCM-41 with difference Si/Al ratios and investigated the performance of hydrogenation of naphthalene on MCM-41 supported sulfided-NiMo catalysts. Based on the relative weak acidity on Al-MCM-41, we also investigated the catalytic performance of modified sulfided-NiMo catalysts supported in mixed Al-MCM-41 with the HY zeolite. For the modified catalysts, the activity and ring-opening products concentration increase with the addition of HY zeolite. These result are benefit from the synergistic effect of combination microporous with mesoporous zeolites.

2. Experimental

2.1 The preparation of MCM-41 with difference Si/Al ratios

Al-MCM-41 with Si/Al ratios of ∞，60，50，40，25 were synthesized following the procedure given in Ref[1] using hexadecyltrimethylammonium bromide(purity ⩾ 99%) as template, sodium silicate solution (SiO_2⩾wt%24.19%) as silica source and pseudobohemite as aluminum source. The sol-gel was crystallized under 120℃ in 24h.The as-synthesized material was calcinated in a N_2 atmosphere at 550℃during 1h followed by a 6h calcinations in the air at the same temperature.

2.2 The preparation and characterization of catalysts

The supports were prepared in the following procedure: molding, desiccantion, ion-exchanging with 1 mol.l^{-1} NH_4NO_3 solution for 3 times and calcinations. The catalysts Al-MCM-41 and catalysts modified by adding HY zeolite (15%) were compared to the reference catalysts (Mo-Ni-P/HY(15%)-Al_2O_3. Mo-Ni-P catalysts were prepared by the incipient wetness impregnation technique with the required amount of an aqueous solution of ammonium heptamolybdate, base nickel cabnate and phosphoric acid to obtain catalysts. By these strategies, we prepared three different kinds of catalysts: (1) sulfided-NiMo supported on different MCM-41(Si/Al= ∞) content(0, 20%, 40%, 60%); (2) Al-MCM-41 supported sulfided-NiMo catalysts with different metal oxides content (20%, 26%, 32%, 40%);(3) sulfided-NiMo supported on mixed support of combination Al-MCM-41 with HY zeolite

X-ray powder diffraction (XRD) were carried on D/Max-III type spectrometer with Cu Kα radiation, Voltage is 400KV and electrical current 40mA. Surface area,pore volume and average pore diameter were calculated from the adsorption-desorption isotherms of N_2 at 77.35K on a ASPA-2010 adsorption apparatus. The acidity of molecular sieves and catalysts were measured by adsorption-desorption of pyridine. The alumina content in the MCM-41 molecular sieves was measured by chemical-titration method [9].

Reaction system and procedure

2.3 The evaluation of catalytic performance and products identification

The experiments of evaluation of catalytic performance were performed in a fixed bed stainless tubular reactor (10mm internal

diameter and 0.8mlength) in a micro-reactor. The catalysts were pre-sulfided before hydrodearomatization reaction by using CS_2 at 4 MPa under 340℃ for 3h. The reaction condition for hydrodearomatic were 340-370℃, H_2 pressure is 4.0MPa, H_2/Oil ratio is 500,WHSV=$1h^{-1}$. The products were analyzed by a Varian-3400 gas chromatography equipped with a 0.25mm×30m HP CP-1 capillary column and a flame ionization detector and the product identification was carried out by gas chromatography-mass spectrum (GC-MS).

3. Result and discussion:

3.1 The effect of sol-gel Si/Al molar ratio on MCM-41 structure

Fig.1 shows the XRD pattern of pure silica MCM-41 and Table1 depicts the influence of the feed Si/Al ratio on the XRD peak intensity of 100 plane and other properties of MCM-41. A decrease in Si/Al ratio decrease the intensity of the main XRD peak, indicting that increasing Al content of the feed hindered the crystallization process. In Fig.2, the pore diameter distribution of a typical as-synthesized MCM-41 has figured out and the open pore size focus on 2.8-3.0nm.

From table 1 it can be seen with the aluminum added in MCM-41, relative crystalline of molecular sieves decrease, that is because aluminum inserting into Si-O tetrahedron can cause lattice disfigurement and have bad effect to hexagon structure. With the increase of aluminum in MCM-41 the acidity of molecular sieves increase.

3.2 The product identification of hydrodearomatication of naphthalene

The product identification was made by GC and GC-MS analysis. Figure3 shows a typical GC chromatogram of the product. Some products were identified by comparison of GC retention time with those of the standard samples, Other products were identified by GC-MS, which data system searches automatically the associated database spectra of molecules and gives a best fit match.

3.3 The effect of total H_2 pressure on naphthalene conversion and products distribution

To investigate the effect of total H_2 pressure on naphthalene conversion and products distribution. We selected a Catalyst with the formula of MoNi(P)/MCM-41 (20%,Si/Al=∞)-Al_2O_3 and test temperature condition is 370□, the ratio of H_2 and oil is 500,WHSV is $1.0h^{-1}$. From Fig.3 it can be seen that the naphthalene conversion increase with the increase of total H_2 pressure. This is because naphthalene hydrogenation and deep-hydrogenation reaction consume hydrogen which causes the molar of gas decrease. From the equilibrium of the reactions the conclusion can be drawn that increasing H_2 pressure is benefit for naphthalene conversion. Fig 4 shows that the effect of H_2 pressure on the products distribution of naphthalene hydrogenation products

The products can be divided into three parts, which are the tetralin and its isomers, decline and its isomers and ring-opening products. The former two parts is from the hydrogenation pathway and ring-opening products is from the hydrocracking pathway. From Fig.4 it can be seen that naphthalene conversion and the activity of deep-hydrogenation and ring-opening increase with the increase of total H_2 pressure. Increasing total H_2 pressure is good for naphthalene conversion, ring-opening reaction and cetane number improvement.

3.3 The effect of metal content on the naphthalene conversion and products distribution

The MCM-41 is a kind of mesoporous zeolite with high surface area and large pore diameter. This is easy for high concentration active components to disperse on its surface. From Table3 it can be seen that the catalysts activity increase with the increase of metal content. As a result naphthalene conversion increases and deep-hydrogenation products such as decalins and ring-opening increase. But the metal content in the catalysts increases to 40%, the activity of catalyst decrease. The possible reason is that excessive metal may form big particles which deposit on the catalysts. This can block the aperture of catalysts and confine the diffusion of reactant.

3.4 The acidic component of supports on the naphthalene conversion and products distribution

From the above results it can be seen that the acidity on the MCM-41 is too weak which causes the number of acidity sites are too small and the acidity strength of catalysts are too weak. This does no good to naphthalene deep-hydrogenation and ring-opening. As a result the main products on NiMo/MCM-Al_2O_3 are tetralins while declins and ring-openings are not as many, which just cause a little increase of centane number. In order to improve the performance in catalytic ring-opening reaction, it is necessary to add the acidic component. HY is a microporous zeolite and its acidy is stronger than MCM-41. So we selected HY molecular sieve as acidic component and added it in the supports. From the Table it can be seen that naphthalene conversion increased with the HY content added to the catalysts increase. The catalysts1 with HY/MCM-41/Al_2O_3 in the support have the high conversion. Catalysts 2 with only HY/MCM-41 have the highest ring-opening content This can be attributed to the interaction of HY acidic component and the synergistic effect for hydrogenation of naphthalene was found by mixing MCM-41 and HY molecular sieves.

Conclusions

1. A series of MCM-41 moliecular sieves with different Si/Al molar ratio were synthesized by hydrothermal method .With the decrease of Si/Al, alumina oxide content and acid sites increased while the relative crystalinity decreased.
2. Total H_2 pressure plays an important role in naphthalene hydrogenation. With pressure increased the activity of deep-hydrogenation and ring-opening increase sharply.
3. The conversion of naphthalene increase with metal oxides active components content on the catalysts with the supports MCM-41 mesoporous zeolites increased
4. Catalysts added HY zeolites naphthalene deep-hydrogenation, especially the ring-opening properties increase.

References

[1] Corma A.,.Martinez A, et al, Catalytic performance of new dealuminated ITQ-2 zeolite for mild hydrocracking and aromatic hydrogenation processes, Journal of Catalysis, 2001, 200, 295~269

[2] Brunn, et al, January 24, 1984,United States Patent,4427534

[3] Beck J S, Vartuali J C, et al., A mow family of mesoporous molecular sieves prepared with liquid-crystal template, J. Am. Chem. Soc.,1992, 114:10834~10843

[4] Schmidt R, Stocker M, et al, MCM-41:a model system for adsorption studies on mesoporous materials, Microporous Mater.,1995,3:443~448

[5] Xu X Z, Su J M , Da J W , Test on FCC catalyst containing MCM-41 zeolite in a semi-commercial unit, Petroleum Processing and Petrochemical (Chinese) , 2001, 32 (8) : 46~50

[6] A.Corma,A.martinez,et al., Hydrocracking of vacuum gasoil on the novel mesoporous MCM-41 aluminosilicate catalyst, Journal of Catalysis,1995,153,25~31.

[7] Halachev T, Nava R, Dimitrov L, Catalytic activity of (P)NiMo/Ti-HMS and (P)NiW/Ti-HMS catalysts in the hydrogenation of naphthalene, Applied catalysis A:General 1998,169,111~117

[8] Reddy C M, Song C S , Synthesis of mesoporous molecular sieves and their application for catalytic conversion of polycyclic aromatic hydrocarbons, Preprints,Am.Chem.Soc.Div.,1996,41(3):906~909

[9] Feng Chengwu et al, Analytical Chemistry Experiment, Publishing House of University of Petroleum (East China) , 1995, 229~231

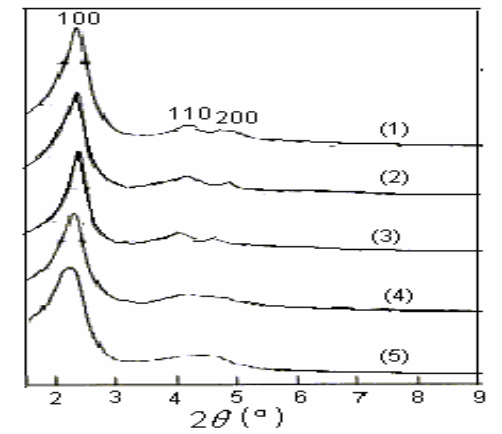

Fig.1 XRD pattern of as-synthesized MCM-41molecular sieves

(1)Si/Al=∞;(2)Si=60;(3) Si=50;(4) Si=40;(50) Si=25

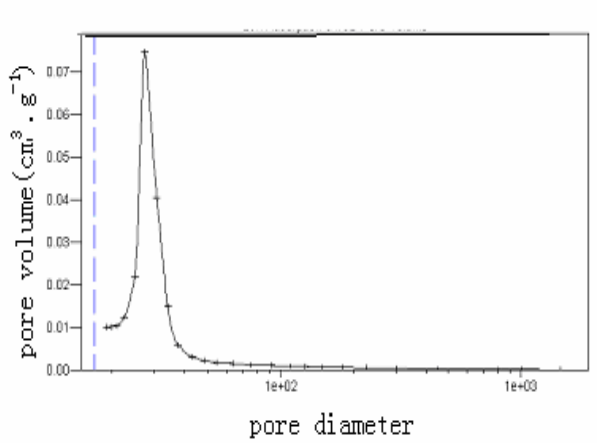

Fig.2 Pore diameter distribution of typical as-synthesized MCM-41

Table1 Effect of Si/Al molar ratio on structure of MCM-41

Si/Al，molar ratio		∞	25	40	50	60
XRD	2θ, °	2.104	2.078	2.231	2.191	2.143
	Relative crystallinity*, %	100	89.8	85.4	82.4	80.7
	d_{100}, nm	4.193	4.245	3.956	4.028	4.114
	Half brand width, nm	0.320	0.320	0.320	0.340	0.340
BET	Surface area, $m^2.g^{-1}$	791	1294	860	794	770
	Pore volumn, $cm^3.g^{-1}$	0.57	1.05	0.68	0.64	0.66
	Pore diameter, nm	2.8	3.2	3.1	2.7	2.9
Acidity, m%		18.4	29.5	26.3	24.7	21.3
$W(Al_2O_3)$, m%		—	3.76	1.62	1.50	1.37

Relative crystallinity: the crystallinity of MCM-41(Si/Al=∞) is 100 while others are realtive to this value

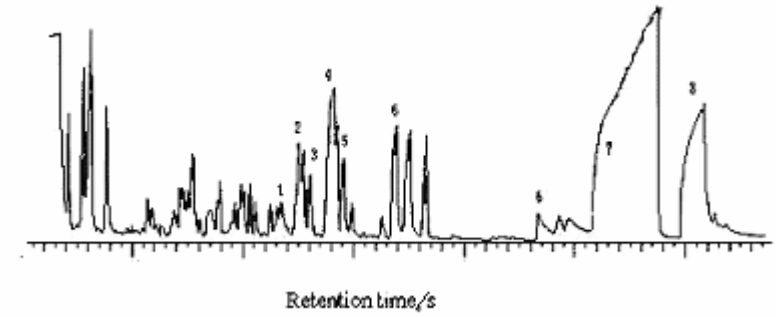

Fig. 3 GS-MS of the products for hydrogenation of naphthalene1-butylcyclohexane; 2-cis-decaline; 3-methylindane and its isomers; 4-trans-decaline; 5-butylbenzene; 6-methylindene and its isomers; 7-tetralin; 8-naphthalene

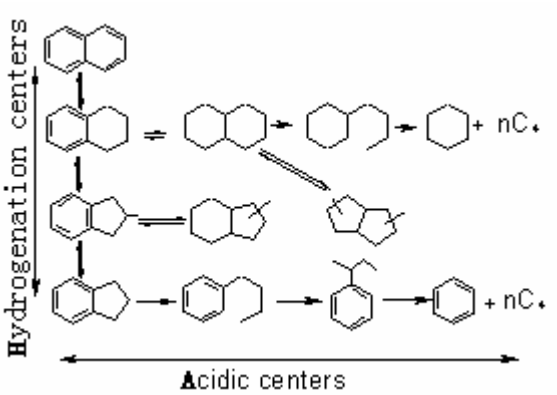

Fig.4 Reaction pathways for hydrogenation of naphthalene sulfurized CoMo catalysts

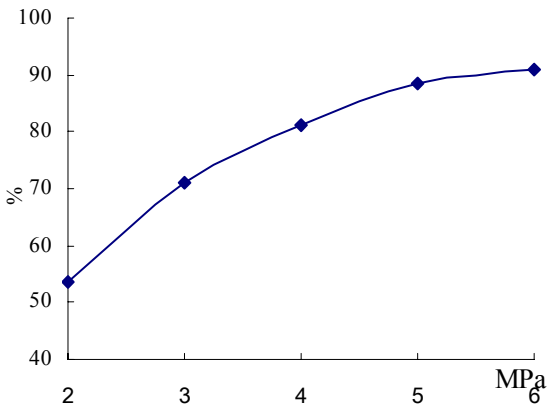

Fig.3 The effect of pressure on the conversion of naphthalene

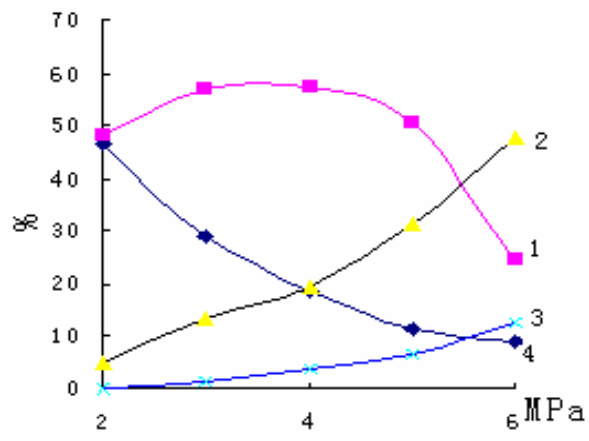

Fig.4 The effect of H_2 pressure on the distribution of products
1—tetralin and its isomers；2—declins and its isomers；3—ring-opening products；4—naphthalene

Table 3 : the effect of metal content on the naphthalene hydrogenation

Metal content，($NiO+MoO_3$)，m%	W(production)，m%				Conversion，%
	Naphthalene	Tetralins	Decalins	Openings	
20	16.96	66.97	9.69	5.34	83.04
26	14.63	63.69	12.23	9.45	85.37
32	9.69	62.06	17.89	9.79	90.31
40	11.84	55.14	23.68	8.45	88.16

Table 4 The properties of catalysts added HY zeolite

Catalysts	T,°C	W(products),%				Conversion, %
		Naphthalene	Tetralins	Declins	Other products	
	340	13.88	24.29	27.00	32.66	86.12
Reference	350	16.81	27.14	30.73	23.37	83.19
	360	18.62	20.13	34.78	22.18	81.38
	340	6.91	60.23	16.05	17.35	93.09
Catalyst 1	350	7.23	49.87	21.21	19.27	92.77
	360	10.24	40.24	19.58	25.32	89.76
	340	9.45	39.52	18.83	29.60	91.55
Catalysts 2	350	11.25	32.10	18.23	35.46	88.75
	360	13.77	24.71	13.97	40.72	86.23

Reference catalyst: Mo-Ni-P/HY(15wt%)-Al_2O_3
Catalyst 1: Mo-Ni-P/MCM-41(45wt%)-HY(15wt%)-Al_2O_3
Catalyst 2: Mo-Ni-P/ HY(20 wt%)- MCM-41

DOWNHOLE UPGRADING OF WOLF LAKE OIL USING THAI/CAPRI PROCESSES - TRACER TESTS

Malcolm Greaves and TianXiang Xia

Improved Oil Recovery Group, Department of Chemical Engineering,
University of Bath, Bath BA2 7AY, England
Tel: 44 1225 826624 Email: M.Greaves@bath.ac.uk

Keywords: In situ combustion, air injection, heavy oil, in situ upgrading, THAI, *CAPRI*

Introduction

With worldwide conventional oil production expected to peak during the present decade, the need to reevaluate heavy oil resources is becoming more imperative. The vast heavy oil and tar sands resources in Canada, Venezuela, the United States and other parts of the world will play an important role in sustaining our future energy supply [1].

THAI –'Toe-to-Heel Air Injection' is an integrated reservoir-horizontal wells process, which uses air injection to propagate a combustion front from the toe-position to the heel of the horizontal producer (HP). Fig 1 is a schematic representation of the basic features of the process [2].

THAI is a stable and robust in-situ combustion process, as defined by the absence of oxygen breakthrough at the production well, as well as no tendency for severe gas overriding [3]. The stability of the THAI process depends on two key factors: (1) a high temperature burning zone, which is more advanced in the top part of the oil layer, exhibiting controlled (stable) gas override behaviour, and (2) deposition of coke, or heavy residue, inside the HP. The coke which is deposited inside the HP acts as a gas seal.

THAI is a new, more advanced variant of the conventional in-situ combustion (ISC) process, which operates as a short-distance, as opposed to long-distance displacement process [4]. Due to the well arrangement used in THAI, the mobilised oil ahead of the combustion front only travels a short distance (down) to the exposed section of the HP. Since THAI operates at much higher temperatures than SAGD, it can achieve significant in-situ upgrading, andn thereby maximize oil recovery. THAI is currently the subject of a pilot development at Christina Lake, Canada (2005).

CAPRI is the catalytic extension of the THAI process, incorporating an annular layer of catalyst, emplaced on the outside of the perforated horizontal producer well, along its whole length [5, 6]. The reaction conditions created ahead of the combustion front, prior to reactants passing down through the mobile oil zone to contact the catalyst, are established by the THAI process. Further upgrading of the produced oil is achieved by catalytic conversion, as the mobilised oil passes through the catalyst layer.

Although, extensive tests on the performance of THAI and CAPRI have been made, only basic upgrading data have been reported so far. The present study aims to quantify the extent and nature of the oil upgrading during an experiment dry and wet phases of THAI and CAPRI. Gas, oil, water and solid residue analyses are used to infer mechanisms of upgrading and to begin to gauge the economic (sweep and recovery) and environmental (gas emissions and produced water quality) impact associated with the eventual field operation of the process.

Experiments

Two three-dimensional in situ combustion tests were carried out in a rectangular, low pressure stainless steel cell, measuring 0.6 m x 0.4 m x 0.1 m, equipped with ports for air injection and production. Heavy Wolf Lake crude oil (10.5 ^{o}API) was mixed with wet sand prior to packing into the cell, representing a homogeneous oil reservoir. A NiMo hydrodesulfurization (HDS) catalyst was packed around the downstream half of the horizontal producer, as shown in Fig. 2. The tests were designed in such a way as to incorporateboth THAI and CAPRI modes in a single test..

Details of the construction of the 3-D combustion cell and operation have been reported previously [2, 6]. The test conditions are listed in Table 1. Synthetic brine was used in the first THAI/CAPRI test (Run 2000-07), in order to simulate the connate water in the reservoir formation. In the second test (Run 2001-01), a tracer was added to the oil, consisting of a mixture of hydrocarbons (see Table 2). The purpose of the organic tracer was to investigate the mechanisms for oil upgrading achieved during the THAI and CAPRI processes.

It should be noted that the sandpack used in these tests did not contain kaolinite. While 3% kaolinite was added into the sandpacks used in all previous 3-D cell tests, more closely simulating an oil reservoir. The Canadian heavy oil reservoirs typically contain 5% ~ 10% of clays, such as kaolinite, illinite, montmorillionite, and chlorite[7]. It is well-known that kaolinite is a thermal cracking catalyst. Therefore, the present series of experiments represents the a worst case scenario for thermal upgrading of heavy oil by THAI-CAPRI.

Results and Discussion

The main results from the two THAI/CAPRI tests are summarised in Table 3.

Run 2000-07. This was a combined dry and wet THAI/CAPRI test, in which deuterated water was injected together with the injected air (CAPRI), as tracer during the second wet combustion period. The performance of the combustion process obtained in this test was similar that observed from standard 3-D combustion cell test on Wolf Lake heavy oil (sandpack containing 3% kaolinite) [2]. A stable, high temperature combustion front (500~600°C) was propagated along the HP, during the dry and wet combustion periods. The excellent sweep of the combustion front, in a 'Toe-to-Heel' manner, achieved a high oil recovery, at 87% OOIP.

Figure 3 shows the variation of the API gravity and viscosity for samples of the produced oil collected during the experiment. Before the combustion front reached the catalyst layer, the degree of thermal upgrading of the produced oil was only about 2 API points. This is very low, compared to a normal THAI test on Wolf Lake heavy oil. This is because no clay was added into the sandpack for Run 2000-07.

The effect of catalyst on the produced oil is clearly evident in Figure 3. The API gravity of the produced oil jumped from an API value of 14 , up to 24, during the period of 240 to 400 minutes. As the combustion front approached the catalyst section along the HP, mobilized oil, already partially upgraded in the THAI process , underwent further catalytic conversion reactions. During the second wet combustion mode, with deuturated water injection, the upgrading trend was reduced slightly from 22 ^{o}API to 20 ^{o}API. The viscosity of the produced oil achieved by CAPRI was 10 ~ 40 mPas, down from the original 24,400 mPas for Wolf Lake Crude Oil.

Run2001-01. The Wolf Lake oil was 'spiked' with the hydrocarbon mixture, before it was mixed with the previously wetted sand for the THAI/CAPRI test. The performance of this test was similar to Run 2000-07. The cumulative oil recovery achieved was also very high, at 82% OOIP, again because of the high effective 'toe-to-heel' sweep of the combustion front (500~600°C) through the

sandpack. The produced oil was also upgraded to 23 API point, mainly during the CAPRI test.

In addition to post-mortem insoection of the collected liquid and solid samples, a number of further analyses on the bulk materials were conducted. Metals analysis and molecular analysis were performed on the selected samples of gas, oil, water and solid residues from Run 2001-01 (see Table 4). The results are discussed below.

SARA/PIN. Improvement in the produced oil quality during THAI/CAPRI is quantified using SARA(Saturates, Aromatics, Resins, Asphaltenes) and PIN (Paraffins, iso-Paraffins, Naphthenes). This HPLC procedure shows some variability, but no substantial change through the THAI stage. However, there is a substantial increase in the more desirable oil component (saturates) during the CAPRI stage. It is noticeable that Resins + Asphaltenes fractions decrease substantially (Figure 5), indicating the conversion of these groups to saturates, is one possible mechanism for oil upgrading.

Elemental analysis. This can be used a measure of carbon rejection, or hydrogen addition, associated with oil upgrading (see Table 4). Elemental sulfur decreases once the THAI wet stage commences, but is maintained at lower levels through the CAPRI stage. The maximum sulfur reduction of 39% was achieved in the CAPRI stage. The onset of lower sulfur numbers with start of water injection suggests a mechanism of hydrogen donation from the water , or water-gas-shift reactions in the presence of exposed sulfur (after cleavage of S-C bonds) and evolution as H_2S (hydrodesulfurization). This appears to be effective prior to the combustion front encountering with the HDS catalyst. A similar mechanism might be relevant for nitrogen, which is reduced to nearly one fifth of its original level.

Distribution of organic tracer compounds. The distribution of tracer compounds in the produced oil from Run 2001-01 was measured by GCMS. The ratio of tracer concentration, to that in the original 'spiked' oil, is shown in Figure 6. The increase in n-paraffins just before the start of water injection in THAI is considered a significant indicator of hydrous pyrolysis as an upgrading mechanism. Because normal alkanes have been reduced in-reservoir from the Wolf Lake oil (via biodegradation), these compounds must have been generated de novo. Hydrous pyrolysis of asphaltenes is the proposed mechanism as normal alkenes are virtually absent and the abundance of normal alkanes increases during the wet stages. Changes in the relative abundance of the introduced compounds are variously attributed to continuous (nC_{11}, alkylphenyls) or episodic (and nC_{20}) distillation, cracking and converting to derivative products (squalane, perhydrofluorene), cracking with polymerization downstream with subsequent cracking later in the run (decylthiophene, dimethyldibenzothiophene).

The coincidence of increased normal alkane generation during the THAI and CAPRI wet phases supports a hydrous pyrolysis (kerogen or oil + $H_2O \rightarrow CO_2 + H_2$) or the water-gas shift reaction ($CO + H_2O \rightarrow CO_2 + H_2$). Coke gasification coupled with the water-gas-shift reaction could accompany this mechanism or become dominant in the near vicinity of the combustion front, particularly in the CAPRI stage.

Conclusion

In situ upgrading of heavy oil using THAI (thermal) and CA*PRI* (thermal–catalytic) processes achieves substantial upgrading of produced oil and as well as high oil recovery, up to 87%OOIP. The results of two tracer THAI/CAPRI tests indicate that hydrous pyrolysis of asphaltenes and the water-gas shift reaction are the main mechanisms, or routes of hydrogenation of the thermally or catalytically cracked oil, producing alkenes in the upgraded oil. The distillation effect of the light fraction also contributes to some (small amount) of upgrading of the produced oil.

The catalytically upgraded oil contains substantially higher levels of saturates and reduced heavy ends. There are also significant environmental benefits because of the large reduction in heavy metals and sulphur, with potential reductions in refinery loadings. Thus, THAI and CAPRI processes are likely to make an important contribution towards sustainable energy supply in the near future.

Acknowledgement. The authors are grateful to the Engineering and Physical Sciences Research Council (EPSRC), United Kingdom, for supporting the THAI and CAPRI research at the University of Bath, via Research Grants: GL/L71773 and GR/M93017. We would like to thank S.W. Imbus and V.P. Nero (ChevronTexaco Energy Research Technology Co., Houston, TX USA) for providing the tracer compounds for the THAI/CAPRI tests and carrying out the analyses, as well as valuable discussion.

References

(1) Lanier, D.:"Heavy oil – A major energy source for the 21st century", Paper No. 039, *Proc.*, 7th. UNITAR International Conference on Heavy Oil and Tar Sands, Beijing, China, 27-30 October (1998)

(2) Xia T X, Greaves M., Turta A T, and Ayasse C.: "THAI – A 'Short-Distance Displacement' In Situ Combustion Process for the Recovery and Upgrading of Heavy Oil", *Trans. IChemE,* (2003) *March*, 81(A) pp295-304

(3) Xia T X, Greaves M and Turta A.: "Main Mechanism for Stability of THAI –'Toe-to- Heel Air Injection', Paper 2003-30, Canadian International Petroleum Conference, Calgary, Canada, 10-12 June (2003).

(4) Xia T X and Greaves, M.: "Upgrading Athabasca Tar Sand Using Toe-to-Heel Air Injection", *J. Can. Pet. Tech.*, (2002) **41**, No. 8, 51-57.

(5) Greaves, M, Abdul El-Saghr and Xia, T. X.: "CAPRI Horizontal Well Reactor for Catalytic Upgrading of Heavy oil", ACS Symposium, Division of Petroleum Chemistry, on Advances in Oil Field Chemistry: Downhole Upgrading, 20-25, Washington, DC, August, (2000). [ACS PREPRINTS, Vol. 45, No. 4, pp595-598]

(6) Xia T X and Greaves M.: "3D Physical Model Studies of Downhole Catalytic Upgrading of Wolf Lake Heavy Oil Using THAI", *J. Can. Pet. Tech.*, (2002) **4**, No. 8, pp58-64.

(7) 'Chemical and Physical Properties of Oil and Sand Solid', Chapter 2, in *Some Physical Properties of Bitumen and Oil Sand,* ed. by D. R. Prowse, Revision #2, Alberta Research Council Oil and Sands Research Department, Alberta, Canada (1983).

Table 1 Experimental Conditions of 3-D cell THAI/CAPRI Tests

Run	2000-07	2001-01
3-D Cell	0.6m × 0.4m × 0.1m	
Internal insulation	6 mm ceramic fiber layer	
Silicon Sand, W50, (kg)	34.1	29.09
Porosity (%)	39.05	
Gas permeability (mD)	1503	
Wolf Lake oil (kg)	6.90	
'Spiked' oil (kg)		5.63
Water (kg)		1.48
Synthetic Brine (kg)	1.74	
Na (ppm)	7,474	
Ca (ppm)	140	
Mg (ppm)	73.5	
Cl (ppm)	11,506	
SO_4 (ppm)	560	
HCO_3 (ppm)	254	
Total Salt (ppm)	20,007	
Catalyst (CoMo HDS)	Regenerated, 1/16" extrudate	
Catalyst loading (g)	191.1	172.5
Catalyst length (m)	0.3	
Well configuration	2VIHP	
Ignition	Hot Nitrogen	
Air flux (Sm3/m2h)	15	
Initial sandpack temp. (^oC)	20	
Back pressure (psig)	20 - 25	

Table 2 Tracers used in Run 2001-01

		ρ	Amount		
Standards		g/ml	g	moles	ppm
undecane	n-C_{11}	0.74	2.1	0.013	282
1-phenylhexane	$C_{12}H_{18}$	0.86	4.2	0.026	570
perhydrofluorene	*tricyc*-C_{13}	0.92	2.1	0.012	282
9,10-dimethyl anthracene	$C_{16}H_{14}$	1.10	1.9	0.009	265
4,6-dimethyld ibenzothiophene	$C_{14}H_{12}S$	1.20	2.1	0.010	282
1-phenyldecane	$C_{16}H_{26}$	0.86	2.3	0.011	315
3-decylthiophene	$C_{14}H_{24}S$	0.91	2.0	0.009	277
eicosane	n-C_{20}	0.78	2.1	0.007	282
cholestane	*tetracyc*-C_{48}	1.49	2.1	0.006	282
squalane	*i*-C_{30}	0.86	4.2	0.010	565
Synthetic Crude Standard		0.88	25		3401
DILUANTS			29	ml	
hexadecane	n-C_{12}		5	ml	
dodecane	n-C_{16}		65	ml	
1-phenyltridecane	$C_{19}H_{32}$		40	ml	
Total Mixture (liq at 50^oC)			139	ml	

ρ -Density

Table 3 Results of THAI/CAPRI Tests (Wolf Lake Heavy Oil, 10.5 ^{o}API)

Run	2000-07	2001-01
Recovery method	Primary	
Combustion mode	Dry and Wet	
Overall period (hr)	12.25	12
Pre-ignition period (hr)	2.25	2.25
Air injection period (hr)	10.0	9.75
Dry phase (hr)	7.0	6.75
Wet phase (hr)	3.0	3.0
Normal water injection (hr)	1.5	3.0
WOR (m^3/1000Sm^3)	0.3	0.3
Air injection rate (l/min)	10	
Peak temperature (^oC)	500~600	
Produced gas composition (% average)		
CO_2	14.56	15.38
CO	4.88	5.49
O_2	3.25	3.88
CO/(CO+CO_2)	0.251	0.263
H/C ratio	0.05	0.0
O_2 utilisation (%)	84.5	81.5
Furn consumption (%OOIP)	7.7	9.6
Oil Recovery (%OOIP)	87.1	82.0
Residual oil (%OOIP)	2.9	5.39
AOR (Sm^3/m^3)	1130	1070
Combustion front velocity (m/hr)	0.05	0.05

Table 4 Elemental Analysis of Produced Oil (Run 2001-01)

Sampling time (min)		%C	%H	%O	%N	%S
0		83.89	10.74	1.07	0.41	4.86
20		76.28	11.38	7.84	0.37	4.50
65		76.38	10.47	7.54	0.36	4.39
123	Wet	71.41	10.95	12.75	0.30	3.73
180	THAI	60.04	11.06	21.37	0.22	2.99
209	CAPRI	75.56	12.45	6.73	0.22	3.18
356		85.27	11.23	0.83	0.08	2.97
389		84.73	12.60	1.08	0.07	3.05
453	Wet	84.56	10.59	0.76	0.13	3.41
512		84.57	10.59	0.74	0.13	3.46
>512		84.17	11.56	0.68	0.15	3.47

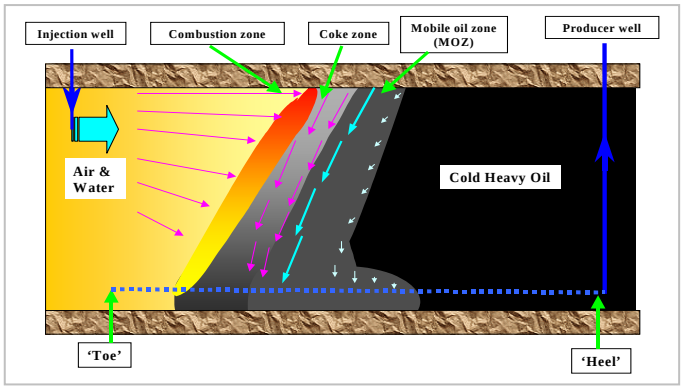

Figure 1. THAI – 'Toe-to-Heel Air Injection' Process

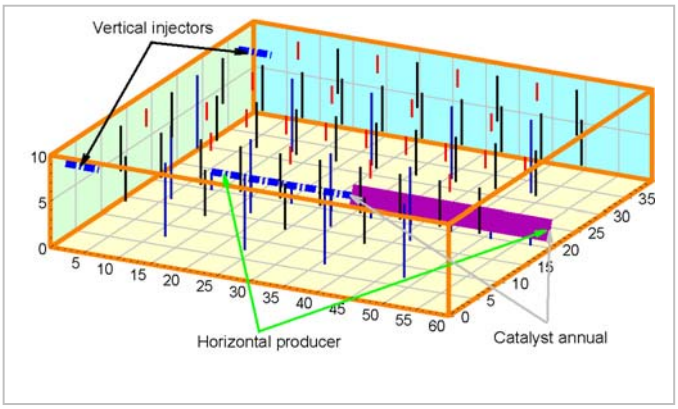

Figure 2. 3-D Combustion cell for the THAI/CAPRI tests

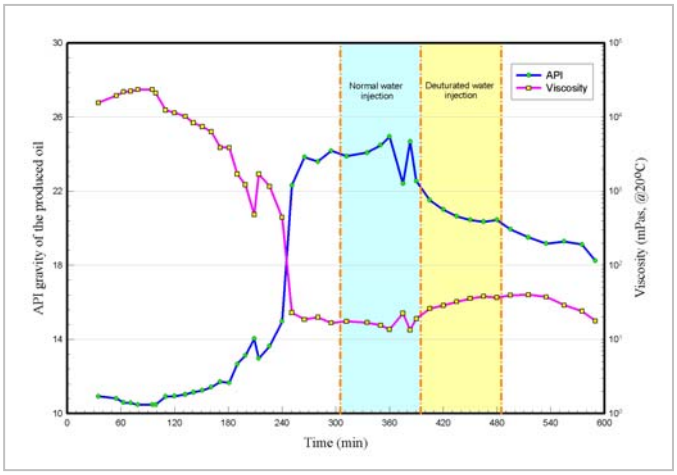

Figure 3. In situ upgrading of produced oil (Run 2000-07)

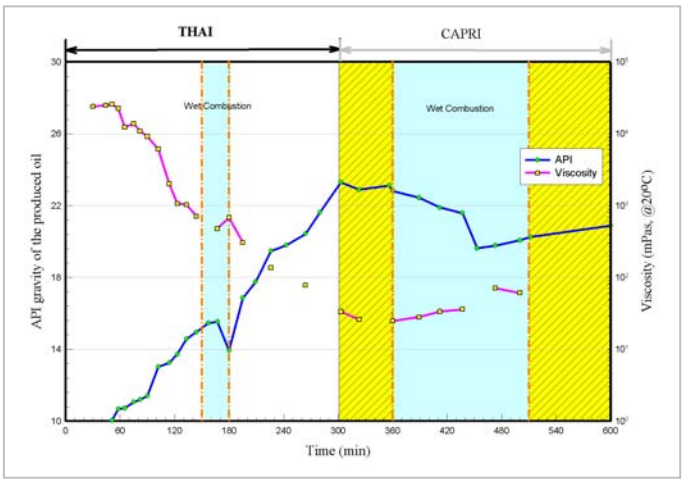

Figure 4. In situ upgrading of produced oil (Run 2001-01)

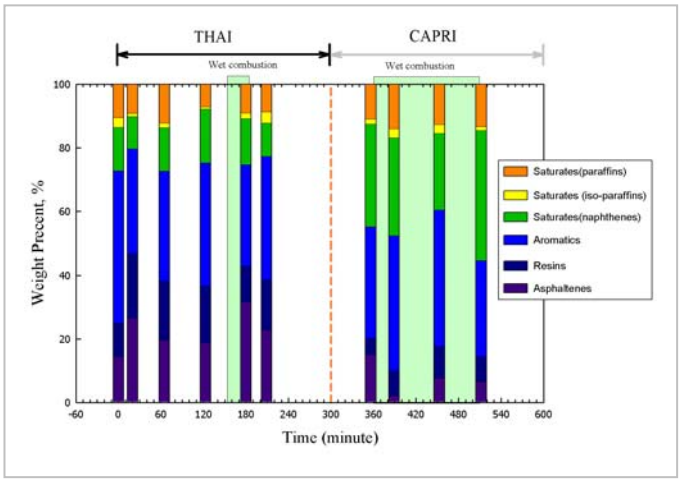

Figure 5. SARA/PIN analysis of produced oil (Run 2001-01)

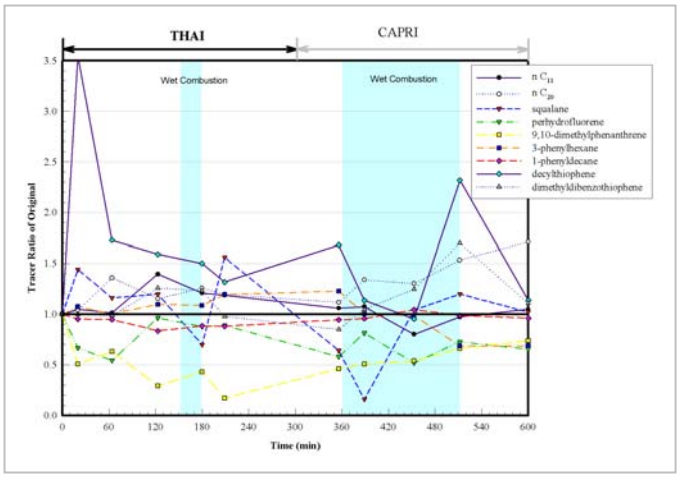

Figure 6. Tracer compounds in produced oil (Run 2001-01)

THE WRITE PROCESS FOR PRODUCING PIPELINEABLE HEAVY OIL

PART I: OPTIMIZATION OF THE DISTILLATE RECOVERY UNIT

Lee E. Brecher

Western Research Institute (WRI), 3474 North Third Street, Laramie, Wyoming 82070

Abstract

The WRI Thermal Enhancement (WRITE) process is a field deployed bitumen upgrader capable of converting non-upgraded bitumen (as produced by in-situ production processes) into a residuum free heavy oil whose density and viscosity exceed the specifications for Canadian pipelines without the need for costly diluent additions. The WRITE process proceeds in two stages. The first is a low temperature thermal separation designed to remove distillate from the incoming stream and recover it as usable product suitable for blending with virgin oil or with overhead from the second stage. The heavy material not recovered from the distillate recovery unit flows to the continuous coker from which there is produced gas, a lighter cracked oil that is recovered as an overhead product and coke.

Process optimization begins with the distillate recovery unit (DRU) where the yield and quality of the oil recovered depend upon temperature, residence time, sweep gas composition and volume, and the nature of the incoming oil. The DRU optimization program seeks to understand each of these effects and to use that understanding in order to optimize the yield and quality of oil produced in the DRU.

Introduction

In addition to converting bitumen into a residuum free heavy oil whose density and viscosity exceed the specifications for Canadian pipelines, the process also produces sufficient quantities of coke to meet both its own thermal energy needs and also those of the production process as well. The bottomless heavy oil produced by the process may be transported to any refinery accessible to Canadian crude oils for further upgrading into finished products. The producer using the WRITE process is thus freed from the constraints imposed by diluent addition, has a reduced need for natural gas, and produces a product acceptable to any refinery or upgrader accessible to Canadian crude oils. This leads to four significant advantages for the producer:

(1) Each pound of non-upgraded bitumen fed to the process produces 0.6 to 0.8 pounds of residuum-free heavy oil that meets the Canadian pipeline specifications for density and viscosity and thus may be transported without diluent. Total flow per barrel of product is reduced by 50% or more from the production area and no diluent return lines are needed.

(2) The product crude is residuum-free and may be processed further in conventional upgraders to produce 30 to 40EAPI syncrude or it may be processed in refineries to finished products. The fact that the product contains no residuum removes the restriction that it be processed at a facility with a coker.

(3) After startup, approximately 75 pounds of coke are produced per barrel of process feed. This material has a heating value of around 15,000 Btu per pound and is sufficient not only for process needs but can also be used for the generation of production steam and offsite needs. The small quantities of gas produced can be recovered and reformed to provide process hydrogen if needed.

(4) The flash and distillate recovery units are designed to accommodate feeds with up to 10% BS&W. As a result, minimal feed pretreating and conditioning is required. Similarly, the system is capable of continuously coking the bottoms from the distillate recovery unit. The large, semi-batch equipment characteristic of that used in delayed coking is unnecessary. System modularity with regard to the distillate recovery unit and the coker allow maximum flexibility for integration of the upgrading equipment with the production facility.

Experimental

Cold Lake crude received from Alberta Energy Company (now EnCana) was used as the starting feed in all of the optimization studies. This oil was processed in the one-barrel-per-day DRU located at WRI's Advanced Technology Center (1) at stage temperatures of up to 700°F. The bottoms from each of these runs were processed further in the 6-inch rotary screw coker to produce light, cracked overhead product for blending with the corresponding DRU overheads. DRU yields as a function of stage temperature are shown in Figure 1 and selected DRU overhead properties are shown in Figure 2. Storage stability of the liquid products was performed according to ASTM D4625 and the compatibility tests were carried out according to a test developed by Wiehe (2). Products from processing Athabasca bitumen in the WRITE process have been shown to be relatively stable during 4 weeks storage at 43°C, in spite of having high olefinic content. Furthermore, the distillate products are compatible with most Alberta crude oils (3).

Results and Discussion

Four levels of processing severity are being investigated in the DRU optimization study and the results of these tests are summarized in Figure 1. The first level of processing severity involves normal distillation (the NBP curve used in the NCUT economic evaluation) and produces DRU overhead yields approaching 25% as the stage temperature approaches 750°F. Increasing the processing severity slightly, as was done in the stability and compatibility study (2), enables yields of >30% to be achieved at temperatures below 700°F, while moderate increases in severity enable these results to be extended to yields exceeding 40% at temperatures below 675°F. A new series of experiments is presently being planned with the objective of achieving DRU yields in excess of 45% while maintaining temperature below 650°F.

An examination of Figure 2 shows no perceptible changes occurring in overhead product quality, at least not as measured by API gravity, as processing severity is increased. Quite the contrary situation exists with the DRU bottoms, however, as the density of this oil shows marked increases with increasing processing severity.

Conclusions

These activities have confirmed that as-produced, non-upgraded bitumen from Canadian oil sands can be converted continuously into residuum-free, synthetic heavy oil, along with associated quantities of gas and coke. The naphtha fraction of the produced oil comprises about 6% by weight of the total oil and contains olefins and di-olefins that will have to be hydrotreated before its addition to the pipeline. The remainder of the oil, comprising about 67% by weight of the total oil fed, has a density and a viscosity compatible with

specifications governing Canadian pipelines and can be admitted without the need for diluent. Stability and compatibility testing on this oil has shown it to be stable and compatible with other common Albertan crude oils. Energy for the process is available in the coke produced as a process by-product and the gases produced contain sufficient hydrogen to stabilize the naphtha fraction. Processing conditions are mild, do not involve the use of excessive temperatures or pressures and allow the presence of BS&W in the feed oil.

Acknowledgements. This project was funded by the US Department Energy (USDOE) under Cooperative Agreement No. DE-FC26-98FT40322. This support is gratefully acknowledged.)

Disclaimer

This report was prepared as an account of work sponsored in part by an agency of the United States Government. Neither the United States Government nor any agency thereof, nor any of their employees, makes any warranty, expressed or implied, or assumes any legal liability or responsibility for the accuracy, completeness, or usefulness of any information, apparatus, product, or process disclosed, or represents that its use would not infringe privately owned rights. Reference herein to any specific commercial product, process, or service by trade name, trademark, manufacturer, or otherwise, does not necessarily constitute or imply its endorsement, recommendation, or favoring by the United States Government or any agency thereof. The views and opinions of authors expressed herein do not necessarily state or reflect those of the United States Government or any agency thereof.

References

1- Brecher, Lee. E., "The Use of TaBoRR as a Heavy Oil Upgrader", Presented at the 20th Annual Pacific Coast Oil Show & Conference, Kern County Fairgrounds, Bakersfield, November **2001**

2- Parviz Rahimi, Lee E. Brecher and Theo deBruijn, "Stability and compatibility of liquid products obtained from cold lake bitumen using the WRITE process", Presented at the 8 th International conference on stability and handling of liquid fuels, Steamboat Springs, Colorado September 14-19, **2003**

3- Brecher, Lee E., Rahimi, P, deBruijn, T and Flaherty, G., "Preliminary assessment of the TABORR process and the stability and compatibility of its products", Presented at the Petroleum Chemistry Division, 225th ACS National Meeting, New Orleans, LA, March 23-27, **2003**

4- Parviz M. Rahimi, Jinwen Chen, Lee Brecher and Theo deBruijn, "Hydrotreating of liquid products from cold lake bitumen obtained in the WRITE process", Presented at the Division of Fuel Chemistry, 227th ACS National Meeting, Anaheim, CA, March 28-April 1, **2004**

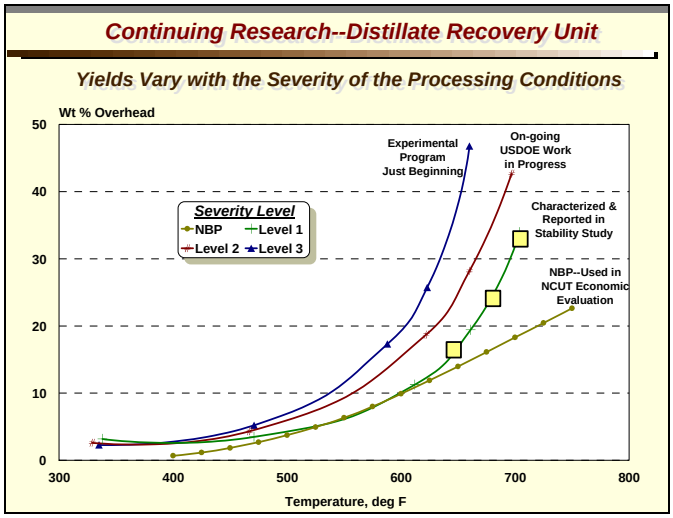

Figure 1. DRU yields as a function of stage temperature

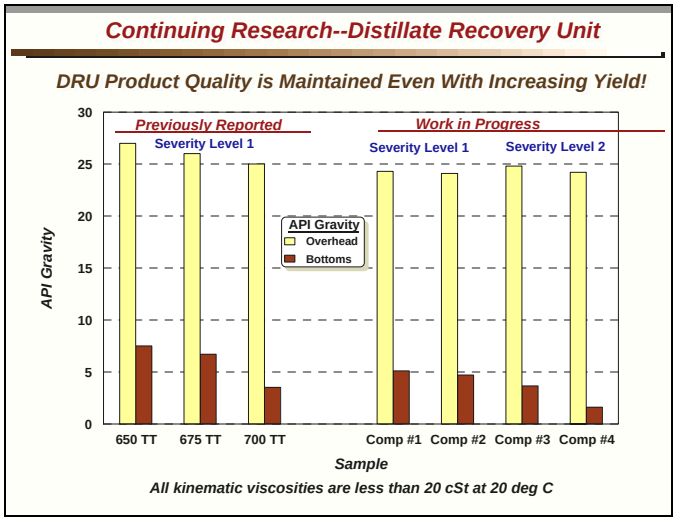

Figure 2. Selected DRU overhead properties

HYDROTREATING OF LIQUID PRODUCTS FROM COLD LAKE BITUMEN OBTAINED IN THE WRITE PROCESS

Parviz M. Rahimi[1], Jinwen Chen[1], Lee Brecher[2] and Theo deBruijn[1]

[1]National Centre for Upgrading Technology (NCUT), 1 Oil Patch Drive, Suite A202, Devon, Alberta T9G 1A8 Canada
[2]Western Research Institute 3474 North Third Street, Laramie, Wyoming 82070

Abstract

The WRITE process is a new emerging thermal cracking technology for the conversion of heavy oils and bitumen to synthetic crudes. The distillate products of any thermal bitumen processing, including the WRITE process, contain unsaturated compounds such as olefins and di-olefins. It is desirable to remove or convert these materials to saturated compounds before they reach refineries for processing. Hydrotreating of WRITE distillate products (-250°C) containing a significant amount of olefins and di-olefins was performed in a batch autoclave using spent commercial $NiMo/Al_2O_3$ hydrotreating catalyst. It was shown that at relatively mild conditions all di-olefins were converted to olefins or saturated compounds, but conversion of olefins required higher severity. Hydrotreating reactivity of WRITE products was compared with that of coker naphtha.

Introduction

When heavy hydrocarbons such as bitumen are subjected to thermal treatment for the production of synthetic crude, in the absence of hydrogen (to cap the intermediate free radicals) a significant amount of olefins and di-olefins are formed through free radical disproportionation reactions. The analytical procedures such as FIA and bromine number, developed for the determination of the olefin content for refinery products, are not suitable for crudes. In both of these methods components such as aromatics interfere with analyses, resulting in erroneous results.

Most existing and emerging upgrading technologies for conversion of heavy oils and bitumen to transportation fuels are based on thermal processes like visbreaking, coking and pyrolysis. These processes are performed in the absence of catalysts and hydrogen where a significant amount of unsaturated products are produced. Among those unsaturated compounds there are products such as conjugated di-olefins that are very reactive and can polymerize and form coke in different parts of a refinery. Although compounds with isolated olefinic bonds form in higher concentration than di-olefins during thermal reaction, they are less reactive. In the presence of oxygen, olefins can form hydroperoxide and initiate a free radical chain reaction. Due to their high reactivity, these materials can form sediment and sludge during fuel storage and the refining processes.

The WRITE process (Western Research Institute Thermal Enhancement) is a new thermal process for heavy oil conversion that is currently under review by a number of producers in Alberta. It is expected that the liquid products from this process will contain some olefins and di-olefins. The presence of these unsaturated materials in synthetic crudes has raised some concerns related to their stability during storage, pipelining and subsequent processing in refineries. The pipeline specification for the olefin content in crude is set by CAPP (Canadian Association for Petroleum Producers) at <1% by volume. Another pipeline specification, which is indirectly related to the olefin content of crude, is based on the bromine number of the –250°C cut and is set at <10 $gBr_2/100g$.

The objectives of this preliminary research are: 1) to investigate hydroprocessing conditions at which the –250°C distillate fraction products obtained from Cold Lake bitumen in the WRITE process meet pipeline specifications for bromine number (<10 gBr2/100g); 2) to compare hydrotreating reactivity of the –250°C distillate fraction from the WRITE process with fluid coker naphtha at the same reaction severity.

Experimental. Hydrotreating experiments were carried out in a 300 mL stirred tank autoclave equipped with a catalyst basket. In a typical experiment, about 104 g of feed (coker naphtha or WRITE –250°C distillate fraction) was placed in the reactor. A spent commercial $NiMo/Al_2O_3$ hydrotreating catalyst (18.6 g) was used in all experiments. The reaction temperature and hydrogen partial pressure used in these experiments are shown in Table 1. When the internal temperature of the autoclave was 5°C below the set point, the yield period time was begun. The autoclave furnace was turned off 60 minutes from this time. After the reactor cooled down to room temperature, the gas contents of the autoclave transferred to a gasbag; the gas volume in the bag was measured and the content was analysed by gas chromatography. The reactor was opened and the liquid contents were removed and analyzed for bromine number and diene content (UOP-326-82).

Results and Discussions

The WRITE process is a new thermal processing technology that is currently being considered for the conversion of bitumen from oil sands to liquid fuels (1). Products from processing Athabasca bitumen, in the WRITE process, were shown to be relatively stable during 4 weeks storage at 43°C, in spite of having high olefinic content. Furthermore, the distillate products were compatible with most Alberta crudes (2). The refiners wish to receive feedstocks with no olefins or di-olefins content and discount streams that are high in such components. There are two options for removing unsaturated compounds from petroleum feedstocks. Olefinic compounds can be either extracted and used as petrochemical feedstock (3) or hydrotreated to form stable hydrocarbons.

In the present work it was decided to investigate the feasibility of hydrotreating the WRITE distillates (-250°C fraction) to produce products that were acceptable by refineries in terms of the olefin and di-olefin contents. Since a limited quantity of WRITE product was available, only a series of batch autoclave hydrotreating runs were performed to investigate the optimum conditions for the removal of olefins and di-olefins. We plan to carry out an extensive hydrotreating study using bench-scale continuous operation when larger quantities of distillates are available. For the purposes of comparison with the hydrotreating reactivity of the WRITE liquid products, we also selected a fluid coker naphtha and performed hydrotreating with the same catalyst and under similar reaction conditions.

Analysis of feedstocks and hydrotreated products from the coker naphtha and the WRITE feedstock (-250°C fraction) are shown in Table 1. Two analytical tests, namely diene number (UOP-326-82) and bromine number (ASTM D-874), were used to determine the degree of saturation of the unsaturated compounds after hydrotreatment. In the absence of more accurate analytical methods for quantitative determination of unsaturated compounds (olefins and di-olefins), we used the existing analytical methods to follow the directional changes in the properties of the distillate as a function of hydrotreating severity.

The analysis shown in Table 1 indicates that the coker naphtha had higher diene as well as higher bromine numbers compared to the WRITE feed.

The higher reactivity of dienes compared to olefins is clear for both feedstocks as these materials are converted to olefinic or saturated compounds at the lowest hydrotreating severity employed. The diene concentration in coker naphtha changed from 13.9 $gI_2/100g$ in the feed to 0.5 $gI_2/100g$ in the product at a reaction temperature of 200°C. Similar results were obtained in hydrotreating the WRITE feed. The diene concentration changed from 4.2 $gI_2/100g$ in the feed to 0.0 $gI_2/100g$ in the hydrotreated products at the same reaction temperature. The conversion of isolated olefinic double bonds to saturated compounds required higher temperature and hydrogen pressure compared to the dienes conversion. The data in Table 1 also show that at lower reaction severity the saturation of olefinic compounds in the coker naphtha, as determined by bromine numbers, is faster than that in the WRITE feed. However, at higher reaction severity olefins in the WRITE feed are hydrogenated faster than those in coker naphtha.

Table 1. Properties of Feedstocks and Hydrotreating Products

Feed	Temp. and H_2 Partial *P*	Diene $gI_2/100g$	Bromine # $gBr_2/100g$
Coker Naphtha feed		13.9	84.2
WRITE feed		4.2	53.3
Coker Naphtha	*200°C/500psi*	0.5	76.7
WRITE feed	*200°C/500psi*	0.0	50.0
Coker Naphtha	*300°C/700psi*	0.07	50.8
WRITE feed	*300°C700psi*	0.0	27.4
Coker Naphtha	*350°C/1000psi*	0.3	19.7
WRITE feed	*350°C/1000psi*	0.0	9.0

Conclusions

This study demonstrated that it is possible to convert olefins and di-olefins, produced during the thermal reaction of Athabasca bitumen in the WRITE process, by mild hydrotreating. It was shown that the hydrotreating reactivity of WRITE distillates (-250°C) was comparable to that of fluid coker naphtha.

Acknowledgement. This project was funded by WRI through the US Department Energy (USDOE). Partial funding for NCUT has been provided by the Canadian Program for Energy Research and Development (PERD), the Alberta Research Council (ARC) and the Alberta Energy Research Institute (AERI).

References

1- Brecher, Lee E., Rahimi, P, deBruijn, T and Flaherty, G., "Preliminary assessment of the TABORR process and the stability and compatibility of its products", Presented at the Petroleum Chemistry Division, 225th ACS National Meeting, New Orleans, LA, March 23-27, **2003**

2- Parviz Rahimi , Lee E. Brecher and Theo deBruijn, "Stability and compatibility of liquid products obtained from cold lake bitumen using the write process", Presented at the 8 th International conference on stability and handling of liquid fuels, Steamboat Springs, Colorado September 14-19, **2003**

3- Sharma, Y.K., Reimert, R, and Singh, I.D. "Stabilization studies of middle distillate fuels: Structural composition of insoluble by FTIR spectroscopy", Petroleum Science and Technology, 21, 7-8, 1055-1063, **2003**

IMPROVED MOLIBDENUM SULPHIDE NANODISPERSED CATALYST FOR HYDRO PROCESSING, PREPARED VIA MICROEMULSIONS

Emir Escalona[2], Rebecca Wang[1], Carlos Scott[2], Josephine Hill[1], Pedro R. Pereira-Almao[1]

[1]Department of Chemical and petroleum Engineering, University of Calgary. 2500 University Drive, NW. Calgary. Alberta. Canada
[2]Centro de Catalisis, Petroleo y Petroquimica, Escuela de Quimica, facultad de Ciencias. Universidad Central de Venezuela. Los Chaguaramos. Caracas. Venezuela

Introduction

Due to environmental restrictions as well as to limitations of performance of traditional fixed bed catalysts for hydro processing extra heavy feedstocks, the generation of micro-nano size catalyst particles within the feed at conditions close to the ones available in the reaction zone is an important alternative. It has allowed the proposition of a set of many different new processes that could be considered the third generation hydro processing of residues and bitumen.

Oil soluble compounds of those transition metals catalytically active for hydro processing yield very good results [1] but their preparation is expensive. Most of the inorganic forms of these transition metals are much less expensive, for instance, ammonium heptamolibdate is perhaps the least expensive form of Mo with the highest metal proportion within the salt. Nevertheless its insolubility in the reaction media prevents from obtaining a good dispersion of the metal, which makes necessary to incorporate significant amounts of the compound to get sufficient catalysis.

Traditionally more considered for heavy crude oils transporting [2] the use of emulsions and micro emulsions are an alternative way of incorporating well dispersed catalysts for heavy feedstocks hydro processing. In this paper the preparation of micro/nano dispersed Mo particles by thermal decomposition of ammonium heptamolibdate emulsions was studied. The effects of nature and quantity of pre-sulphuring agents dissolved in the emulsion as well as the effect of surfactant were some of the variables determined by using a Design of Experiment method.

Experimental

Emulsions preparation

1-metilnaphtalene (1-MN), an oil lubricant base and a Light Vacuum Gas oil were all used as different oil basis for the preparation of the emulsions. The aqueous phase was prepared containing ammonium heptamolibdate (7.5% Mo) with or without ammonium sulphide at two different concentrations (3 and 10%). Also different percentages of surfactant were used from 1 to 10%.

Thermal decomposition of the emulsions

The emulsions were decomposed in two different reactor set-ups, an autoclave reactor and a continuous reactor, in a temperature range between 200 and 300C at either atmospheric pressure or at 1000 psig., In the case of using autoclave a mechanical stirring was set at 300 rpm. In the autoclave the emulsion was entered into the reactor once the temperature and pressure conditions were reached. After 5 minutes, the thermally decomposed solid is recovered by centrifuging, washing several times with toluene and dried at 125C during 4 hours.

Solids Characterization

X Ray Photoelectron spectroscopy (XPS)

A Leybold-Heraeus equipment model LH-11 was used. The radiation was provided with an Al anode (1486.6 eV) and a power of 350 watts. Pass energy at 50 eV. The C_{1s} line (284.6 eV) was used as reference for calibration of Binding Energies (BE) for the different elements as well as for charge effects correction.

X Ray Diffraction (XRD)

A diffractometer DRX Philips model PW3710 at powder was used, employing a graphite monochromator. An APD program from Phillips was used for detection and recording. A scintillate detector was used. Continuous scan of the diffraction angles was performed from 5.00 until 75.69° (2θ). A Cu anode Kα1 emission line was used.

Surface area

The samples were pretreated in a degasifier VacPrep 061 from Micromeritics at 120°C, desorbed under vacuum (1×10^{-4} torr) for 2 hours. Specific surface area is determined by adsorption-desorption of nitrógeno following the standard BET method. The microporous volume was determined with the t method, the pore radii distribution by the method of Roberts with the cylinder pores model. Additionally a pore distribution was performed on some solids using the BJH method (Barret, Joyner, Hallenda).

Results and Discussion

In figure 1 are shown the XRD analysis of some solids prepared by thermal decomposition of the emulsions prepared using 1-Methyl Naphthalene as the oil phase. It can be observed that these solids are poorly crystallized showing a pattern of amorphous Molybdenum Disulfide. The main reflections observed are the ones corresponding to the faces 002, 100, 103 and 110. Nevertheless, differences are perceived regarding the intensities of the reflections in particular that of the face 002.

Based on the intensities of the face 002, the solids obtained from the decomposition of emulsions containing 3% ammonium sulphide were the ones showing higher piling. It seems that the use of a higher proportion of ammonium sulphide decreases the piling. In addition, the use of higher proportions of surfactant also resulted in reduced ray intensities particularly in the phase 002. Apparently a lower drop size in the emulsion conduces to a lower extent of crystals growing and to a higher disorder of lamellas when the progression is done from macro emulsions (1% surfactant) toward micro emulsions(10%).

In figure 2, are shown the XPS spectra obtained for the solids prepared via flashing and decomposition of the emulsions. The signal centred at 226.3 eV is assigned to the binding energy of the sulphur 2s orbital. As observed each spectrum is the result of the overlapping of signals corresponding to the principal oxidation states of Mo, which are centred at 229.1 and 232.3 eV, representing the doublets 3d, $3d_{5/2}$ and $3d_{3/2}$. These results suggest that Mo is mostly present under the oxidation state +4, even though the intensities do not correspond with the existence of a unique oxidation state.

In table 1 the BET areas of some of the solids obtained and their corresponding catalytic activity for the hydrodesulphurisation of Thiophene are presented. The solids prepared with the higher proportion of surfactant, which implies lower drop size (micro emulsions) present higher surface area as well as much higher catalytic activity for the desulphurisation of Thiophene.

The results presented were very similar to the ones obtained by preparation of the ultra dispersed solids in a continuous decomposition set-up, in which the conditions were implemented to produce nano particles of both Mo oxide as well as Mo Sulphide.

This second solid was also obtained by incorporating to the aqueous Mo solution different proportions of ammonium sulphide. Thus the pre-sulphuring at an early emulsion preparation stage eliminates the need for addition of pre-sulphuring agents as required when Mo oxide is first obtained.

Reduced nano particle size, increased disordered lamellar nano particles and consequently enhanced catalytic activity were obtained by this continuous method which simulates at lab scale a real on line incorporation of the catalyst occurring in a slurry type hydro conversion processing of hydrocarbon residues.

Conclusions

Nano particles of Mo oxide and Mo sulphide were produced via thermal decomposition of emulsions and micro emulsions containing Mo Heptamolibdate in the aqueous phase by using both a batch and a continuous reaction set-up. The solids obtained presented differences in the pre-sulphuring level due to the proportions of ammonium sulphide incorporated to the aqueous solutions. The solid produced from micro emulsions, prepared with increased amounts of surfactants were found the more dispersed and active toward the Thiophene HDS reaction test. No significant differences were found for the two different preparation set-ups employed.

References

[1] *Bearden R., Aldridge C. L.*, Energie Progress, **1** (1981) 44.
[2] *Ng F.T.T. Rintjema R.T.* Stud. Surf. Sci. Catal., **73** (1992) 51.

Acknowledgment

Emir Escalona, first author of this work, was partly supported by PDVSA-INTEVEP and the batch experiments were done at that site in Los Teques. Venezuela.

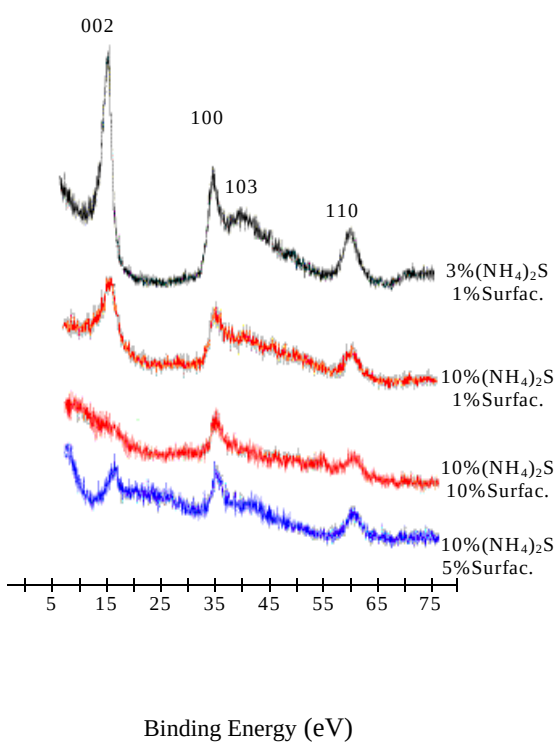

Figure 1. Diffractograms of different solids prepared

Table 1. BET Area and Catalytic Activity

Sample	Area (m^2/g.)	Rel.Activity
3%$(NH_4)_2S$/1%Surf.	3	1
10%$(NH_4)_2S$/1%Surf.	5	4
10%$(NH_4)_2S$/5%Surf.	10	49
10%$(NH_4)_2S$/10%Surf.	38	54

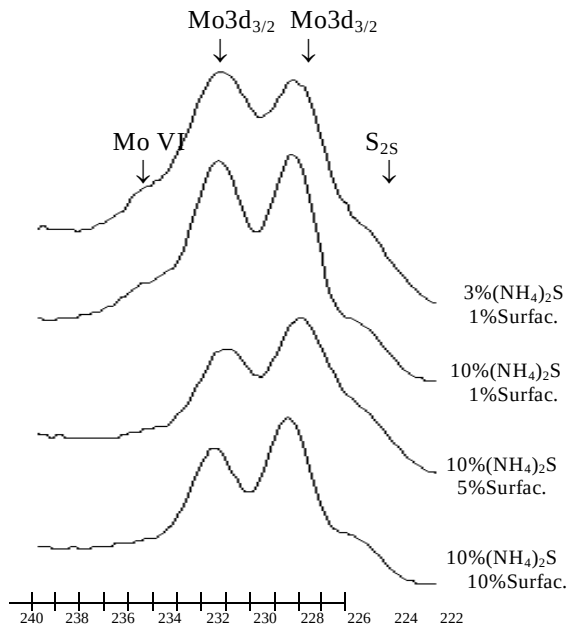

Figure 2. XPS spectra of the different solids.

REMOVAL OF NICKEL AND VANADIUM FROM HEAVY CRUDE OILS BY EXCHANGE REACTIONS

John G. Reynolds

Forensic Science Center
University of California
Lawrence Livermore National Laboratory
P. O. Box 808, L-178
Livermore, CA 94551

Introduction

Current Methods of Heavy Crude Oil Processing. The upgrading of heavy crude oil occurs generally by either hydrogen addition- or carbon rejection-type processes[1]. Hydrotreating is attractive because US refineries have moderately high capacity, but it is costly because it requires added hydrogen, requires appropriate metallurgy to handle the severity of conditions (high temperature and pressure), and, because of poor catalysts lifetimes (because of high metals in heavy crude oils), has high catalysts costs and non-productive downtime. In addition, with heavy crude oils, boiling point reduction is necessary for conversion to transportation fuels, so an additional cracking step is required.

Hydroconversion circumvents this cracking problem. However, similar problems to hydrotreating are encountered, such as hydrogen and metallurgy costs, with the additional problems of technology development (just beginning to become commercially available), and capital equipment investment.

Fluidized cat cracking (FCC) is also attractive because US refineries have very high capacity. Process wise, it is ideal because of the cracking step necessary to produce light components. However, FCC catalysts are notoriously metals intolerant (although new generations of RFCC catalysts show some promise), and with high S and N contents of heavy feeds, high SO_x and NO_x emissions during catalyst regeneration can be costly to abate.

Coking is also an attractive upgrading method for heavy crude oils. The US has very high capacity and more units are relatively cheap to build because severe-service metallurgy is not required. The drawbacks include poor quality products such as coke and coker gas oils, and fairly large yield losses due to the carbon rejection through coke.

Pretreatment of Heavy Crude Oils to Remove Metals. The high metals levels of heavy crude oils currently necessitate the processing to be costly, either through the high costs of hydrogen addition or high yield loss due to carbon rejection. If metals could be removed in a pretreatment step before the heavy crude oil enters processing streams, then heavy crude oils could be more cost effectively processed by traditional methods. Hydrotreating could be utilized to a greater extent to remove the high S and N levels (for which the catalysts are specifically designed) without the quick deactivation by metals poisoning. Very-active zeolites could be used in FCC for the extensive cracking needed for boiling point reduction, and coking could be used less because the other processes could be used more, therefore avoiding such high carbon yield losses to coking. Hydroconversion units may not have to be built avoiding high capital expenditure.

The approach to the pretreatment step for metals removal can be by various methods. In this report, surrogate metal solutions containing the metal bound as petroporphyrin, or petroporphyrin fractions isolated from heavy crude oils are treated with a variety of chemical agents, and then washed with aqueous solutions to remove the metals.

Experimental

Reagents. Ethylenediamine tetraacetic acid (EDTA) $\bullet 2H_2O$ was purchased from Sigma; disodium salt of EDTA (Na_2EDTA), nitrilotriacetic acid (NTA), disodium NTA (Na_2NTA), diethylenetriamine pentaacetic acid (DEPTA), N-(2-hydroxyethyl)ethylene diamine triaacetic acid (N-HEEDTA), trisodium N-HEEDATA (Na_3N-HEEDTA), benzoic acid, malic acid, malonic acid, maleic acid, maleic anhydride, fumeric acid, oxalic acid, triethylcitrate, hexamethylenetetraamine (HMTA), phthalocyanine, tetraphenyl porphyrin, catechol, di-*t*-butyl catechol, coumarin, formic acid, diethyldithiocarbamate sodium salt ($(Et_2dtcNa)(H_2O)_3$, Et_2dtc diethylammonium salt ($Et_2dtcEt_2NH_2$), *t*-butyl hydroperoxide, cumene hydroperoxide, peroxyacetic acid, sodium sulfide nonahydrate ($Na_2S\bullet 9H_2O$), Fuller's Earth, bentonite, montmorillonite, pyridine-N-oxide, 3-pyridylcarbinol-N-oxide, acetone oxime, titanium tetrakis-*i*-propoxide ($Ti(OCH(CH_3)_2)_4$), titanium oxide acetyl acetonate ($TiO(acac)_2$), fluorosulfonic acid (FSO_3H), trifluoro sulfonic acid (CF_3SO_3H), DMF, and 1-MN were purchased from Aldrich Chemical Co; tartaric acid was purchased from Baker Chemical Co.; CH_2Cl_2, toluene, and methanol were purchased from Baxter Scientific; DMF was purchased from EM Scientific; carbon dioxide, carbon monoxide, oxygen were purchased from Matheson; titanium dioxide (TiO_2), was purchased from Allied Chemical Co; VO(etio) and Ni(etio), were purchased from Midcentury Chemical Co., Posen, IL. 1,4,8,11-tetraazacyclotetradecane (Cyclam) was prepared by the method of Richman and Atkins[2].

Reactions. The following is a typical reaction mixture (weights and volumes were chosen to give 10 to 200 ppm by weight porphyrin solutions which were easy to monitor by UV-vis spectroscopy): 0.0024 g VO(etio) were dissolved in 20 ml of 1-MN, toluene, DMF, or CH_2Cl_2 and heated to the appropriate reaction temperature with a constant control heating mantle (J-KEM Scientific Model 210). The starting concentration was then determined by UV-vis spectroscopy. Approximately 0.04 ml (~ 100 mole equiv.) of the ligand or reagent were added. Aliquots of the reaction mixture were taken at various times to primarily monitor the disappearance-appearance of the porphyrin species.

Analyses. The fractions were examined for porphyrin content by UV-vis and second derivative UV-vis spectroscopy utilizing an HP 8452A diode array system. The spectra were collected as zero order using maximum integration time. Second derivative spectra were calculated after averaging. The entire fraction was dissolved in either CH_2Cl_2 or toluene. The amount of solvent was determined by diluting the sample so the spectral region less than 380 nm was on scale. This ranged from 25 to 100 ml in most cases.

Results and Discusssion

Screening Studies. Most reagents were tested using vanadyl etio porphyrin (VO(etio)) and watching the characteristic UV-vis spectrum change. The most effective reagents were found to be maleic acid in dimethylformamide (DMF), montmorillonite in 1-methyl naphthalene (1-MN), CF_3SO_3H in 1-MN, and FSO_3H in 1-MN, with the fastest (maleic acid at 100 mole equivalents) completely reacting with VO(etio) in 10 min. or less.

These agents were found through the testing of many different types of chemical agents, having functional groups, chelating ability, and oxidation-reduction properties. Table 1 shows an example of test data using carboxylic acids and mixtures as the

reactants. The results for all materials used in the screening studies are summarized:

- Amino-carboxylate compounds: nitrilotriacetic acid works well in DMF
- Polyamino compounds: none
- Dithiocarbamates: none
- Carboxylic acid compounds: malic, benzoic, maleic, and malonic work well in DMF
- Clays: montmorillonite works well in 1-MN
- Catechol compounds: none
- Coumarin works well in DMF
- Amino-N-oxides: none
- S^{2-} does not work
- Hydroperoxides: *t*-butyl and cumene work well in DMF
- Peroxyacetic acid works very well in methylene chloride
- Oxo-titanium compounds: none
- Superacids: fluoro- and trifluoromethane sulfonic acids work well in 1-MN

Solvent effects were found for most agents tested also. Most exhibited some activity in DMF, while little or no activity in 1-MN. The agents tested in methylene chloride also generally showed excellent activity.

Table 1. Screening Studies on the Reactivity of Carboxylic Acids with VO(etio)

Reactant	Solvent System	Time Reacted	Temperature ° C	% P Removed
Tartaric	DMF	1.5 h	153	NR
Triethyl citrate	DMF	2 h	120	50
Triethyl citrate	*o*-xylene	3 h	142	NR
	o-xylene	18 h	142	NR
+ diethanol amine	1-MN	24 h	NA	NR
Succinic	1-MN	1 h	160	NR
	1-MN	2.5 h	222	NR
Malic	DMF	21 h	NA	99
+ quinoline	1-MN	24 h	189	18
Oxalic	DMF	24 h	153	NR
2-Ethylhexanoic	DMF	30 m	146	NR
+ air	DMF	1 h	130	NR
Fumaric	DMF	30 m	145	23
Benzoic	DMF	3.5 h	153	100
Benzoic	*o*-xylene	3 h	126	NR
	o-xylene	18 h	142	NR
+ HMTA	1-MN	8 h	184	28
+ diethanolamine	1-MN	24 h	NA	NR
Maleic	DMF	10 m	153	100
Maleic Anhydride	DMF	1 h	132	58
Malonic	DMF	24 h	153	100

HMTA = hexamethylenetetraamine

Superacid Reactions. A more detailed examination of the effectiveness of low concentrations of the superacids, fluorosulfonic acid (FSA) and trifluoromethane sulfonic acid (TFMSA), as demetallation agents for nickel and vanadium porphyrin compounds was conducted. Superacids were found to be extremely effective in demetallating vanadyl etio (VO(etio)) and nickel (Ni(etio)) etio porphyrin screening compounds as shown above. For examples, almost complete reaction was observed for VO(etio) in toluene at 72°C and 100 mole equivalents of TFMSA at 3 min. reaction time, while only 30% reaction was observed with CF_3COOH (another recognized strong acid) under similar conditions at 60 min. reaction time. Figure 1 shows the test results for TFMSA at 200 mole equivalent.

The porphyrin fractions isolated from Hondo 650°F$^+$ and Kern River 650°F$^+$ residua took 600 mole equivalents and 45 min. at 79°C for essentially complete reaction. Only 60% reaction of the petroporphyrins could be attained using 600 mole equivalents at room temperature.

The mechanism of reaction appears to be dependent on the porphyrin species. The behavior of VO(etio) with TFMSA suggests an adduct-type compound is formed first which then goes on to form demetallated and other products. The adduct-type compound appears to regenerate VO(etio) upon reaction with acidic water. Ni(etio) and H_2etio were found to immediately produce the non-metallated porphyrin dication, H_4etio^{+2}, with no evidence of unreacted porphyrin. The reaction of VO(TPP) with TFMSA exhibited evidence of the H_4TPP^{2+}.

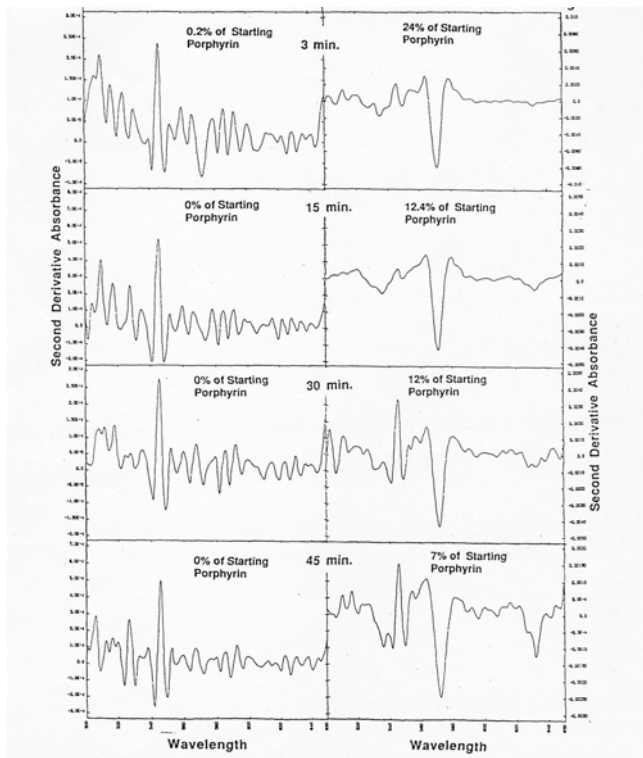

Figure 1. Second derivative UV-vis spectra of the reaction of VO(etio) porphyrin with 200 mole equivalents of TFMSA in toluene at 72°C. The y-axis is the second derivative relative absorbance. The Figures on the left side are the spectra after reaction and the figures on the right side are the corresponding spectra after water wash.

Acknowledgement. This work was funded through a CRADA between Phillips Petroleum Company and LLNL. This work was performed under the auspices of the U. S. Department of Energy by the University of California Lawrence Livermore National Laboratory under Contract No. W-7405-ENG-48.

References

1. Schuetze, B. and Hofmann, H., *Hydrocarbon Processing*, 1984, **63**(2), 75-82.
2. Richman, J. E., and Atkins, T. J., *J. Am. Chem. Soc*., 1974, **96**(7), 2268-2270.

PREDICTION OF DENSITY AND CETANE NUMBER OF DIESEL FUEL FROM GC-FIMS AND PIONA HYDROCARBON COMPOSITION BY NEURAL NETWORK

Hong Yang, Yevgenia Briker, Renata Szynkarczuk and Zbigniew Ring

The National Centre for Upgrading Technology, Devon, AB, Canada, T9G 1A8

Introduction

Modeling and optimization of bitumen upgrading processes require reliable correlations to predict the key properties of the product stream based on its computer-generated composition. In the approach taken by the National Centre for Upgrading Technology (NCUT), these models are designed so that this computer-generated composition is equivalent to the various available chromatographic tests. This effectively decouples the development of the main parts of any process model: the reactor and product quality models. As part of its process modeling program, NCUT has assembled a large database of diesel fuels. The chemical compositions of the diesel fuels were characterized by several chromatographic methods. A neural network approach was then taken to correlate fuel properties such as density, aniline point, cloud point, viscosity, refractive index, molecular weight and cetane number with chemical compositions. This work presents the preliminary results on the correlation of density and cetane number with the hydrocarbon compositions of diesel fuels given by the sum of GC-FIMS (Gas Chromatograph-Field Ionization Mass Spectrometry) and PIONA results (normal paraffins, isoparaffins, olefins, naphthenes and aromatics).

Method

One hundred fourteen diesel samples were prepared by blending 15 original diesel components obtained from Canadian refineries and derived from both conventional crude oil and oil-sands bitumen. Cetane number and density (g/cm^3, 15.6^{o}C) of the diesel fuels were measured using the ASTM D613 and ASTM D4052 methods, respectively. Hydrocarbon type compositions of the fuels were determined by GC-FIMS and PIONA. In each sample, the material boiling in the 200 – 343°C range was analyzed by GC-FIMS while PIONA was used to analyze the material boiling at temperatures lower than 177°C. The sum of GC-FIMS and PIONA results, weighted with the corresponding mass fractions, gave the total hydrocarbon composition of the blend. For the GC-FIMS determinations, a 30 m x 250μm x 0.25μm HP1-MS non-bonded column was used. The injection (0.2μL; 19:1 split) was made with the oven at 45°C. The AC PIONA analyzer based on HP GC 5890 instrument was used to perform the analysis. It was operated under the 'mode 20'conditions (normal paraffins, isoparaffins, naphthenes, and aromatics). Further details are reported elsewhere[1].

A three-layer Ward backpropagation network with three hidden slabs (WSGN – NeuroShell® software, Ward System Group Inc. MD, USA) was used in neural network correlations[2]. Including the original diesel fuels and the diesel blends, a total of 129 samples were used to construct the neural network correlations. The 129 samples were divided into three data sets: training set, test set and production set. Two steps were required to create the three-layer backpropagation neural network model: a training step and a validation step. In the training step, the neural network was supplied with the training data set, including the input and corresponding output values. The network learned the trends contained in the data set and correlated the inputs and outputs by finding the optimum set of weights that minimized the differences between the predicted outputs and the actual outputs. The test set was used with calibration during the training process to prevent over-training of networks, such that they would generalize well on new data. During the validation step, the neural network was provided with the production data set, not seen during the training step, to compute an average error for the test set of this model. The training terminated when 20,000 epochs had passed since reaching of the minimum average error for the test data set.

Twelve hydrocarbon types were used as neutral network inputs, and density or centane number was the network output. Table 1 lists the maximum and minimum values of the inputs and outputs for all the diesel samples used in this study. As shown in the table, the diesel samples used in this work cover a wide range of chemical composition and physical properties.

Table 1. Maximum and minimum values of the neural network inputs and outputs

	Max	Min
Inputs (mass%)		
Isoparaffins	33.09	0.70
n-Paraffins	20.95	0.37
Monocycloparaffins	29.42	1.60
Dicycloparaffins	28.38	0.27
Polycycloparaffins	31.80	1.29
Alkylbenzenes	18.31	5.81
Benzocycloalkanes	31.36	3.08
Benzodicycloalkanes	10.37	0.09
Diaromatics	62.51	0.74
Triaromatics	3.92	0.00
Tetraaromatics	0.63	0.00
Aromatic sulfurs	5.07	0.01
Outputs		
Density (g/ml @15.6°C)	0.9569	0.7985
Centane (CN)	58.4	18.7

Results and Discussion

The consistency of the blending process was checked by comparing the density of the diesel blends measured by ASTM D4052 with the calculated weight averaged density derived from original diesel fuels by the following equation:

$$d = \sum_{1}^{n} diWi$$

where n is the number of original diesel blending components that contributed to the blend, d_i is the density of the ith blending component, Wi is the weight fraction of the ith component in the blend. Figure 1 plots the calculated densities of the blends versus those measured by ASTM D4052. Good agreement between the two sets of data is demonstrated there.

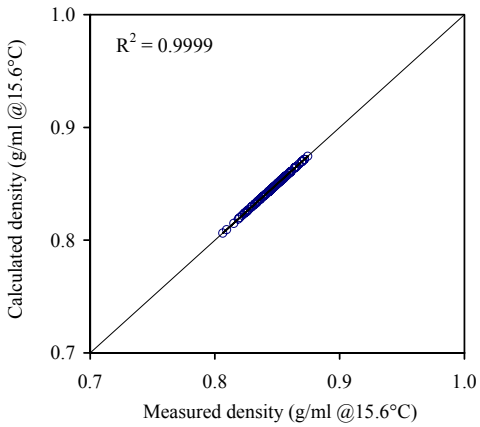

Figure 1.
Comparison of weighted average density with measured density

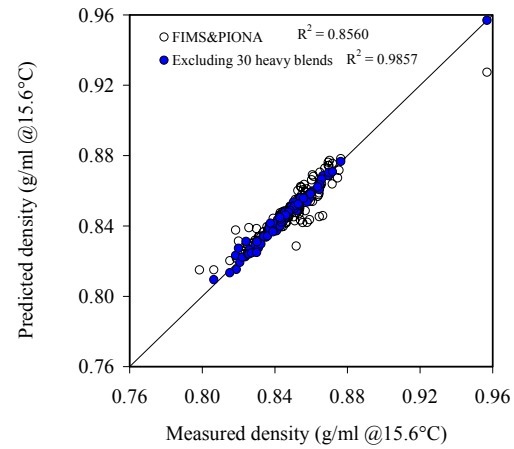

Figure 2.
Comparison of calculated density with measured density with (○) and without (●) 30 heavy diesel blends

Density correlation

The twelve hydrocarbon types listed in Table 1 were used as inputs, and density as the output for the three-layer Ward backpropagation network. Seventy-five diesel blends were chosen as the neural network training data set. To cover the whole range of the diesel fuels in this study, the training data set included the 15 original diesel blending components that contained the maximum and minimum values of inputs and outputs. Twenty diesel blends were included in the test set and 34 diesel blends were in the production set.

The densities of all the diesel blends were calculated with the obtained neural network models. The results are plotted in Figure 2 (open circle) showing parity between the calculated and measured densities. Unfortunately, the correlation coefficient obtained was only 0.8560.

In order to improve the predictions, we carefully examined the boiling range (Simdist ASTM D2887) of the diesel blends, and found that 30 diesel blends contained substantial amount of material boiling higher than 343°C. Since the GC-FIMS method we employed could only give reliable hydrocarbon compositions in the range between 200 to 343°C, the hydrocarbon compositions of these 30 heavier diesel blends were found erroneous. A new neural network model was completed after we removed the 30 blends from the data set. The new model was used to calculate the densities of the remaining 99 diesel blends. The results were compared with the previous ones in Figure 2 (close circle). A significant improvement was achieved. A correlation coefficient of 0.9875 was obtained in this case.

Cetane number correlation

Neural network correlations for predicting cetane numbers from the diesel fuels' chemical compositions were established using both full diesel blends (129 sample data) and diesel blends without the 30 heavy samples (99 sample data). Figure 3 shows the neural network predicted versus measured cetane numbers in both cases. The results indicate that the removal of the 30 heavy diesel blends benefits the cetane number correlation.

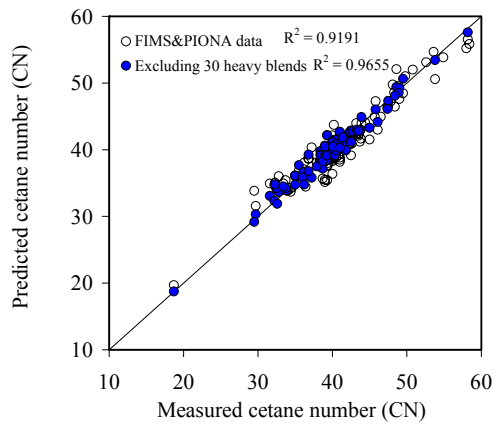

Figure 3.
Comparison of calculated cetane number with measured cetane number with (○) and without (●) 30 heavy diesel blends

NCUT had previously developed neural network correlations for densities and cetane numbers of diesel fuels from chemical compositions using the same three-layer Ward backpropagation network [3]. A smaller database with 69 diesel blends was used in that case. LC/GC-MS (liquid chromatography (LC)/gas chromatography-mass spectrometry) was used to determine the chemical compositions of diesel fuels. Good correlation results were obtained in our previous study. In the present work, the chemical composition was determined by the sum of PIONA and GC-FIMS. GC-FIMS has several advantages over GC-MS. In GC-FIMS the sample can be analyzed entirely without separating into saturate and aromatic fractions, which reduces the error caused by lost of lighter and heavy ends during the separation procedure. GC-FIMS can also distinguish n-paraffins from iso-paraffins, which increases the prediction accuracy of the correlations since n-paraffins and iso-paraffins have different effects on cetane number and density. The statistical results

of density and cetane number obtained in the present work and previous work are compared in Table 2.

Table 2. Comparison of the statistical results for density and cetane number predictions using neural network models devrived from GC-MS and GC-FIMS +PIONA results

	Density		Cetane number	
	GC-MS	GC-FIMS PIONA	GC-MS	GC-FIMS PIONA
R-square	0.96	0.99	0.91	0.97
Mean absolute error	0.004	0.002	1.32	0.72
Max absolute error	0.009	0.007	6.9	2.85
Percentage with 5%	100	100	81.2	94.9

Two conclusions can be drawn from Table 2. First, the mean absolute error for cetane number prediction from both neural network models were below the reproducibility limits of the ASTM D613 engine test method, which was between 2.8 to 4.8 depending on the cetane number of diesel fuel. However, the mean error for the density prediction was not as good as the reproducibility of the ASTM D4052 test (0.0005). Second, the neural network correlations developed using more detailed hydrocarbon composition (sum of GC-FIMS and PIONA) as well as a larger database (the current work) resulted in substantial improvements of density and cetane number predictions over the neural network correlations developed using GC-MS and the smaller database. The mean absolute error for density decreased from 0.004 to 0.002 when the current model replaced the previous neural network model. The mean absolute error for cetane number reduced from 1.32 to 0.72 when the new model was used. These correlations could probably be further improved by introducing more inputs or slightly different inputs to the correlations. The former requires a greater experimental database but the latter could be done using the same database.

Conclusions

A neural network method was used to establish correlations for density and cetane number for a diesel fuel from its chemical composition determined by GC-FIMS and PIONA. The results show that reliability of the hydrocarbon compositions is very important to create accurate neural network correlations. Significant improvement was obtained for both density and cetane number correlation after the removal from the database of 30 heavy diesel blends that could not be characterized correctly by the GC-FIMS method. The neural network correlation could predict the cetane number with mean absolute error well below the reproducibility limit of the ASTM engine test method. However, further effort is needed to develop a better correlation for density prediction. Our results also showed that significantly better neural network correlations were obtained using hydrocarbon compositions derived from GC-FIMS + PIONA and a large database.

Acknowledgement. Partial funding for this work has been provided by the Canadian Program for Energy Research and Development (PERD), the Alberta Research Council and The Alberta Energy Research Institute. The authors wish to thank NCUT's analytical staff for all the analyses.

References

(1) Briker, Y.; Ring, Z.; Iacchelli, A.; McLean, N.; Fairbridge, C., Malhotra, R.; Coggiola, M.; Young, S.; *Energy & Fuels*, **2001**, *15*, 996.
(2) NeuroShell® 2 Manual. Ward Systems Groups, Inc. MD. 1996.
(3) Yang, H.; Ring, Z.; Briker, Y.; Mclean, N.; Friesen, W.; Fairbridge, C.; *Fuel*, **2002**, *81*, 65.

UTILIZING BIOMASS AND WASTE FOR POWER PRODUCTION - A DECADE OF CONTRIBUTING TO THE UNDERSTANDING, INTERPRETATION AND ANALYSIS OF DEPOSITS AND CORROSION PRODUCTS

Flemming Jappe Frandsen

Associate Professor
Combustion and Harmful Emission Control Research Centre
Department of Chemical Engineering, Technical University of Denmark
Building 229, DK-2800 Lyngby, Denmark
Phone: +45 45 25 28 83, Fax: +45 45 88 22 58,
E-mail: ff@kt.dtu.dk

Through the years, Danish utilities have gained significant knowledge on how to minimize or even avoid ash deposition problems in utility boilers, firing worldwide high-volatile bituminous coals. In the early 90ties, the Danish Government decided on a 20 % reduction in the CO_2-emission before the year 2005, based on the 1988-level. Biomass is considered CO_2-neutral due to its short time of regeneration compared to fossil fuels. Thus, the Danish power producers are enjoined to burn 1.0 Mtons of straw, 0.2 Mtons of wood chips and 0.2 Mtons of straw/wood chips (free choice) every year beyond year 2005. As a consequence of this, the CHEC Research Centre, Department of Chemical Engineering, Technical University of Denmark, being partly funded by the Danish power utilities, has during the last decade, investigated ash and deposit formation, and corrosion, in utility boilers fired with coal, petcoke, orimulsion, and different types of biomass (straw (barley, rape and wheat), wood (beech, spruce, fibreboard, bark and waste wood), shea nuts, olive stones etc.).

This paper summarizes our findings, including recent activities on: 1) deposit formation during coal-wheat straw co-firing in a suspension-fired boiler, 2) a pilot-scale study of ash and deposit formation in the Sandia Multi-Fuel Combustor (MFC), 3) a full-scale measuring campaign dealing with the effect of co-firing of biomass on the ash and deposit formation, 4) a second full-scale measuring campaign addressing low-temperature corrosion of tubes in the air pre-heater of a straw-fired utility boiler, 5) a lab-scale study of the corrosion of superheater materials in straw-fired utility boilers, and, finally, 6) a fundamental study on ash and deposit formation in municipal solid waste incinerators. The paper provides insight into the experience gained on ash, deposit and corrosion formation in thermal fuel conversion systems fired with solid non-fossil fuels, and focuses attention on how these results fit into our current understanding of this subject. A complete and updated list of references covering our research activities within this area during the last decade is provided.

INVESTIGATION OF FORMATION PATHWAYS OF AEROSOL PARTICLES FORMED DURING FIXED BED COMBUSTION OF WOODY BIOMASS FUELS

Markus Jöller[1], Thomas Brunner[1], Ingwald Obernberger[1], Ilse Letofsky-Pabst[2]

[1] Institute for Resource Efficient and Sustainable Systems
Graz University of Technology, Inffeldgasse 25C, Graz, Austria
[2] Research Institute for Electron Microscopy
and Fine Structure Research
Graz University of Technology, Steyrergasse 17, Graz, Austria

Introduction

The use of biomass combustion for the production of heat and electric power has already become an important factor for energy supply. A big share of this kind of energy supply is covered by fixed bed combustion of woody biomass fuels in combustion plants with a size range from a few kW of thermal output to large plants in the MW range. But all of these plants suffer more or less from ash related problems, which are deposition of fly ashes and subsequent slagging and fouling and additionally, particle emissions have to be prevented.

In order to decrease the ash related problems inside the combustion plants as well as harmful emissions, detailed knowledge about fly ash formation and deposition mechanisms is required. The results from these investigations are expected to be helpful for the implementation of measures, which can influence the formation and deposition of ashes.

Fly ash formation during combustion of woody biomass. In order to get more information about fly ash formation and behavior and to determine possible influencing parameters, investigations of fly ashes were performed by many researchers in the past for coal combustion as well as for biomass combustion (e.g. 1-4).

At the Institute for Resource Efficient and Sustainable Systems (RNS) investigations concerning biomass combustion were performed for three woody biomass fuels, which are frequently used in fixed bed furnaces for energy production, namely chemically untreated wood, bark and waste wood (5). The results have shown a bimodal particle size distribution (PSD). One mode, the coarse fly ash particles, consists of particles with a diameter larger than 1 µm, the particles of the second mode, the aerosols, are submicron. Chemical analyses of coarse fly ashes showed mainly compounds, which have under the given conditions in biomass furnaces a low volatility. The coarse fly ashes investigated consisted mainly of oxides and sulphates of Ca, Mg, Si and K.

The average chemical composition of aerosol particles could be obtained by wet chemical analyses of particles sampled on Berner-type low-pressure impactor (BLPI) stages. It could be derived that low volatile elements were enriched in coarse fly ash particles in opposite to volatile elements, which were enriched in aerosol particles. At least the distribution of Zn followed the PSD, which suggested an even distribution in the particles. These results could also be gained from scanning electron microscopy (SEM)/ electron diffraction X-ray spectrometry (EDX) analyses of single particles, which provided average compositions.

Regarding the aerosols, three particle formation theories could be derived (6). The different chemical compositions of biomass fuels lead to different release behaviours of aerosol forming elements and in the following to different particle formation pathways.

During the combustion of chemically untreated wood chips mainly ash forming compounds of the elements K, S, and Cl are released to the gas phase. These compounds may react further and undergo gas to particle conversion processes during flue gas cooling. The supersaturated ash vapours may nucleate or condense on the surface of particles, which are entrained directly from the fuel bed (primary particles). Due to chemical analyses of aerosol particles, which showed K, S and Cl as the main components, the presence of considerable amounts of primary particles, which could suppress nucleation of new particles, could be ruled out. Therefore, nucleation and afterwards condensation should be the dominating particle formation mechanisms.

Compared to pure wood fuels bark contains considerably more low volatile compounds of the elements Ca and Mg, but also more K, Cl, S and Zn. During the combustion process a certain amount of the low volatile compounds is directly released as primary particles in the submicron as well as in the supermicron size range. Especially the submicron primary particles, which contain mainly CaO according to chemical analyses, may provide surface for further condensation of ash forming vapours. Additionally, Zn plays an important role for aerosol formation during bark combustion. According to thermodynamic equilibrium calculations Zn is expected to evaporate during combustion on the grate and as soon as oxidising conditions prevail in the flue gas ZnO should form. ZnO has a very low vapour pressure and therefore it should immediately form particles, which subsequently act as seeds for further condensation of aerosol forming matter. Therefore, during the combustion of bark nucleation of new particles may be suppressed partially by primary particles (CaO) and ZnO particles.

A third main pathway for aerosol formation could be derived for the combustion of waste wood, which contains considerably higher amounts of Zn than pure wood and bark. This surplus of Zn compared to other fuels mainly originates from paintings. Due to the great amount of ZnO particles, which form in the way as described for bark combustion, a further nucleation of ash forming vapours may be suppressed completely.

The condensation of ash forming vapours on aerosols containing Ca and Zn has not been proved yet. For that reason the analyses of aerosol particles regarding their composition in the core as well as in the outer layer were aspired. The only way to achieve a sufficiently high resolution for such particle analyses was the use of transmission electron microscopy (TEM) in combination with EDX analyses. Therefore, aerosol samples were taken on copper grids from combustion plants and subsequently analysed by TEM.

Experimental

Aerosol sampling. The particle sampling was performed during the combustion of chemically untreated wood (spruce) and bark at the boiler outlet of a combustion plant with a 440 kW_{th} flame tube boiler. The samples were taken in the way that copper grids, which were precoated with a carbon layer, were fixed on polycarbonate filters. After that, flue gas from the boiler outlet was sucked over the polycarbonate filters for some seconds. Then the copper grids were removed from the filter and forwarded to the Research Institute for Electron Microscopy and Fine Structure Research in order to perform the TEM/EDX analyses.

TEM/EDX Analyses. For the visual characterisation of the aerosol particles, pictures were taken with a CCD camera and evaluated. Furthermore, in order to detect the compositions of the aerosol particles EDX spectra were taken. Firstly, to detect the composition of the particles' cores the analysis point was set in the centre of the particle image. Secondly, for the outer layer analysis the electron beam was placed in a way that it touched the particle shells.

The instrument used for these investigations was a Philips CM20/STEM with an acceleration voltage of 200 kV and a LaB_6 cathode. The EDX spectra were recorded using a light element detector (HPGe).

Results and Discussion

The particles found on the TEM-grids had various sizes between several nanometres and about 0.2 µm. It seemed that bigger particles,

which were found during previous fly ash characterisation investigations could not be caught with the copper grids. Nevertheless, the particles captured were in the right size range for TEM analyses (< 0.3µm). The visual evaluation of the particles showed mostly small agglomerate-like particles as it can be seen in Figure 1.

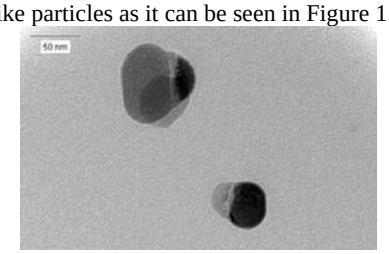

Figure 1. Picture of aerosol particles taken with a CCD camera

EDX analyses of aerosol particles from the combustion of wood chips (spruce) and bark showed that for chemically untreated wood the dominating species were K-compounds (mostly K_2SO_4) as it had been expected from former investigations. Also for aerosol particles from bark combustion K_2SO_4 and KCl were dominating the composition. Interestingly, no particles containing Ca could be found, which leads to the conclusion that Ca, although it had been detected in that particle size range by wet chemical analyses of impactor samples, originates from bigger particles, which could not be fixed on the TEM grids. The Ca in particles smaller than 200 nm in impactor samples was found most probably due to non-ideal particle precipitation efficiency of the impactor stages and particle bounce off to stages with smaller cut diameter.

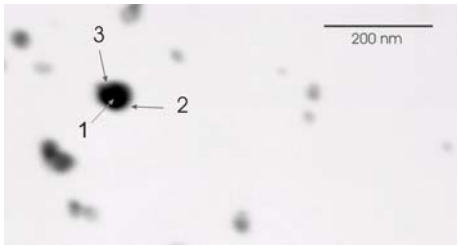

Figure 2. Locations of TEM analyses on aerosol particles

In order to determine if ZnO particles had been present before the formation of condensed K_2SO_4 and KCl, particles were investigated in more detail. During TEM analyses Zn was found in some aerosols from bark combustion. The particles were analysed at different points such as shown in Figure 2. The analyses of point 1 in Figure 2, which covered shell and core of the particle, showed a Zn/K mass ratio of 0.27 (± 20%). In contrast, the analysis of point 2, which just hit the particle shell, did not show any Zn. Point 3 showed a similar result as point 2. The analyses spectra of the points 1 and 2 are plotted in Figure 3. Generally, the Zn containing particles investigated showed this build-up. From that it could be concluded that Zn most probably had formed ZnO particles, which further acted as condensation seeds for other ash forming species. Regarding aerosol formation during waste wood combustion, chemical analyses of aerosol particles and simulation calculations suggest a higher suppression of nucleation of ash forming compounds by ZnO particles, but TEM/EDX analyses have still to be performed.

The formation pathways described could also be confirmed by aerosol formation simulations (7), which were performed in order to find the most influencing variables on formation mechanisms. Calculations of aerosol formation and behaviour in a biomass furnace with fixed grate and flame tube boiler were performed and the results were compared with measurements. In fact, modelling results similar to the measured results could be obtained when Ca and Zn were considered in the simulation as primary particles. Zn was inserted as peak of ZnO particles with a diameter < 0.1 µm and Ca was implemented as a broad peak of particles containing mainly CaO ranging from 0.3 to several hundred µm. Simulation results of PSDs and chemical compositions of the aerosols were similar to the measured values.

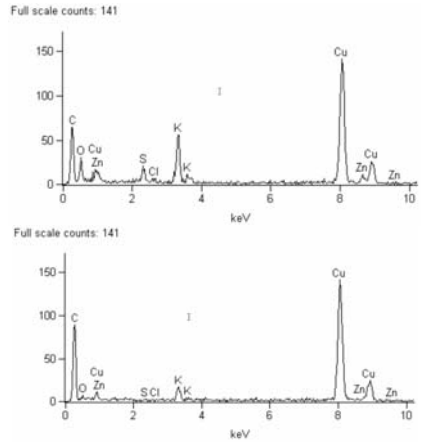

Figure 3. Spectra of point analyses no. 1 and 2 displayed in Figure 2

Conclusions

Investigations of aerosol formation during fixed bed combustion of chemically untreated wood, bark and waste wood were performed in order to derive influencing measures on particle formation and deposition. Three main aerosol formation pathways could be derived:

During the combustion of chemically untreated wood ash forming compounds of K, S and Cl are released into the gas phase and subsequently may react and further form particles by nucleation and condensation. During the combustion of bark submicron and supermicron Ca-containing particles are entrained from the fuel bed in considerable amounts. Especially the submicron particles provide condensation surface for further ash forming compounds and may suppress nucleation partly. For particle formation from bark combustion and especially from waste wood combustion Zn becomes important. As confirmed by thermodynamic data, the amounts of Zn released to the gas phase form mainly ZnO, which undergoes nucleation and condensation and forms particles with a diameter below 100 nm. These particles act as seeds for further condensation of alkali chlorides and sulphates as well as for gaseous heavy metal compounds and can therefore suppress nucleation to a certain extent depending on their concentration in the flue gas.

TEM analyses of aerosols in a size range below 200 nm from combustion of wood chips (spruce) and bark were performed in order to proof these theories. The results confirmed the expected particle formation pathways. Furthermore, these aerosol formation processes could be reproduced quite accurately by simulation calculations, which show results similar to measured PSDs and wet chemical analyses of aerosol particles.

References

(1) Wilemski, G., Srinivasachar, S., Sarofim, A.F. In *Inorganic transformations and ash deposition during combustion*; ASME, New York, 1992; pp. 545-564.
(2) Kauppinen, E.I., Pakkanen, T.A. *Environ. Sci. Technol.* **1990**, 24, 1811.
(3) Valmari, T., Kauppinen, E.I., Kurkela, J., Jokiniemi, J., Sfiris, G., Revitzer, H. *J. Aerosol Sci.* **1998**, 29, 445.
(4) Obernberger, I., Dahl, J., Brunner, T. In *Biomass: A growth opportunity in green energy and value added products, Vol. 2*; Overend, R.P., Chornet, E., Ed.; Pergamon-Elsevier Science Ltd., Oxford, 1999; pp. 1377-1383.
(5) Brunner, T.; Obernberger, I.; Jöller, M.; Arich, A.; Pölt, P. In *Aerosols from Biomass Combustion*; Nussbaumer, T., Ed.;Verenum, Zürich, 2001; pp. 75-80.
(6) Obernberger, I.; Brunner, T.; Jöller, M. In *Aerosols from Biomass Combustion*; Nussbaumer, T., Ed.; Verenum, Zürich, 2001; pp. 69-74.
(7) Jöller, M., Brunner, T., Obernberger, I.; Submitted for publication to *J. Aerosol Sci.* **2003**.

RELEASE OF INORGANIC ELEMENTS DURING WOOD COMBUSTION

Simone C. van Lith, Peter Arendt Jensen, Flemming J. Frandsen, and Peter Glarborg

CHEC Research Center
Department of Chemical Engineering
DTU-building 229
DK-2800 Lyngby, Denmark
E-mail: chec@kt.dtu.dk

Abstract

The objective of this work is to quantify the release of inorganic metal species, S and Cl from wood at combustion conditions that resemble grate combustion. This was done by performing lab-scale experiments at well-controlled conditions. The obtained quantitative release data are essential for the development of models for aerosol and fly-ash formation and behavior, aiming to understand the ash-related problems occurring during combustion of wood in power plants. Experimental release data obtained in the temperature range of 500-850°C are presented for spruce and fiberboard. The results show that the release is strongly dependent on the temperature and on the inorganic composition of the fuel.

Introduction

Biomass fuels contain a certain amount of inorganic elements, of which a part may be released during combustion on the grate to form inorganic gases and particular matter (aerosols and fly-ashes), while the remaining part forms a bottom ash fraction. This formation of inorganic gases and particulate matter may lead to problems. First of all, the gases that are formed and emitted to the atmosphere include environmentally harmful gases (e.g. SO_2 and HCl). Inside combustion units, the formation of particular matter causes deposit formation on superheater tubes, which in turn leads to a reduction of the heat transfer efficiency to the water/steam system and may cause corrosion of the superheater tubes.

Although woody biomass fuels are often thought to be 'less problematic fuels' due to their relatively low ash content, ash-related problems are also observed in wood-fired boilers. Woody biomass generally has a low concentration of K, S and Cl compared to other solid fuels such as straw and coal, but the amount of Ca and heavy metals (such as Zn, Cu and Pb) is relatively high in most woody biomass fuels; especially bark contains a relatively high amount of Ca, and waste wood contains a relatively high amount of heavy metals. Combustion of wood may therefore lead to serious problems due to aerosol formation. Not only the quantity of ash, but also the composition of the ash and the volatility of the ash-forming matter are important when studying the release of inorganic elements during wood combustion.

Objectives

To be able to tackle problems involving aerosol and fly-ash formation and emissions of gaseous pollutants during the combustion of woody biomass, it is essential to understand the quantity and the mechanism of the release of the ash-forming matter from the fuel during combustion. The objective of this work is to quantify the release of inorganic metal species, S and Cl during combustion of woody biomass at well-controlled conditions.

Experimental

Equipment and Method. Combustion experiments were conducted in a lab-scale reactor, resembling the conditions in a grate-fired boiler. The experimental set-up was especially designed to study the release of inorganic elements during wood combustion, and consists of an electrically heated oven with an alumina tube inside, in which a fuel sample can be inserted and a gas can be introduced in order to provide a pyrolysis or combustion atmosphere around the fuel sample. Batch experiments with small sample sizes (30-45 g) were done at different temperatures in the range of 500-1150°C. The release of various inorganic elements during combustion was quantified by performing accurate weight measurements and chemical analysis of the biomass feedstock and the residual ash samples, and performing mass balance calculations. Focus was on the alkali metals K and Na, the alkaline earth metals Ca and Mg, and the heavy metals Cu, Zn, Pb and Cd, since they were known to form aerosols during wood combustion. Furthermore, the non-metals S and Cl were studied, since they were expected to influence the volatility of the metal elements. The influence of fuel type and chemical composition of the fuel was investigated by using various types of woody biomass fuels.

Fuel samples. The fuels used in this experimental study are spruce (wood chips), beech (wood chips), bark and fiberboard. These wood biomass fuels are samples from the same batch as the fuels that were used in the EU-project 'Bio-Aerosols'[1], in the formation and behavior of aerosols from wood combustion on a grate were investigated. In the present paper results are given for spruce and fiberboard. The fuels were dried in open air at room temperature and milled using a 4 mm-screen before they were used in the experiments, in order to obtain physically and chemically homogenous samples. The chemical characteristics of the fuels are shown in Table 1.

Table 1. Chemical Characteristics of the Fuels Investigated

Fuel type	Spruce	Beech	Bark	Fiberboard
Moisture (wt%)	6.6	4.5	10.7	6.8
Ash (wt% d.b.)	0.95	0.52	4.41	1.24
Volatiles (wt% d.b.)	82.7	84.8	72.9	80.3
Cl (wt% d.b.)	<0.01	<0.01	0.01	0.05
S (mg/g d.b.)	0.1	0.12	0.42	0.3
K (mg/g d.b.)	0.85	0.92	2.4	0.64
Na (mg/g d.b.)	0.02	0.01	0.07	0.18
Ca (mg/g d.b.)	1.9	1	16	1.5
Mg (mg/g d.b.)	0.2	0.21	0.76	0.21
Si (mg/g d.b.)	0.43	0.03	2.2	0.55
Al (mg/g d.b.)	0.08	0.01	0.45	0.35
Fe (mg/g d.b.)	0.08	0.05	0.33	0.26
Ti (mg/g d.b.)				4.5
Cu (mg/kg d.b.)	2	1.6	5	3.9
Zn (mg/kg d.b.)	14	3.7	67	27
Cd (mg/kg d.b.)	0.14	0.032	0.25	0.18
Pb (mg/kg d.b.)	0.44	0.4	1.6	16

(d.b. = dry basis)

It can be observed that the main ash forming elements are Ca, K and Si in the case of all fuels. Furthermore, all fuels contain relatively low amounts of Cl and S. Heavy metals like Cu, Zn, Pb and Cd are also present in small amounts in the fuels, of which Zn is the most dominant element. Spruce and beech both have very low ash contents (< 1 wt% d.b.), fiberboard has a slightly higher ash content (around 1

wt% d.b.) and bark has the highest ash content (around 4 wt% d.b.). Bark contains a high amount of Si and Al, probably due to the presence of sand and clay minerals attached to the fuel. Fiberboard contains a high amount of Ti, originating from the pigments in the coating.

Results and Discussion

Quantitative release data were obtained for spruce and fiberboard in the temperature range of 500-1150°C. The experimental results show that the release of the studied elements is strongly dependent on the temperature and the inorganic composition of the fuel. In general, a high release of Cl, S, Zn, Pb, and Cd was observed, up to 100% at high temperature (above 850°C). The elements K, Na, and Mg were found to be released at lower levels, whereas no release was observed for the elements Ca, Si, Al and Fe.

Figure 1 shows the release of Cl, S and K during combustion of spruce and fiberboard as a function of temperature in the range of 500-850°C. In this temperature range, a very high release of Cl (~100%) and S (~75%) and a low release of K (up to ~30%) were observed for spruce. Cl was found to be (almost) completely released already at 500°C. Preliminary thermodynamic equilibrium studies of spruce indicated that Cl may start to be released around 500°C, in the form of $HCl_{(g)}$ or $KCl_{(g)}$. Since the concentration of Cl in the fuel is very low, a complete release of Cl around 500°C seems likely. The equilibrium calculations also showed that the release of K starts around 850-900°C, by the formation of $K_2SO_{4(g)}$. This may explain the steeper increase in the release observed between 800 and 850°C. The high release of S is not well understood yet. S is expected to be released mainly in the form of $SO_{2(g)}$ and $K_2SO_{4(g)}$, but the release of $SO_{2(g)}$ is also not expected to occur at temperatures below 900°C in the case of spruce.

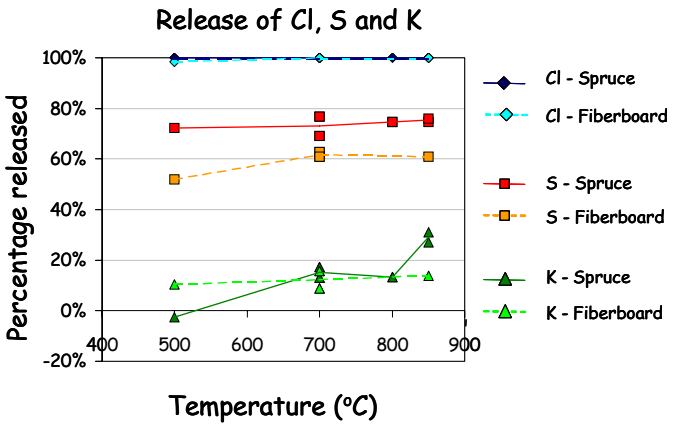

Figure 1. Release of Cl, S and K during combustion of spruce and fiberboard as a function of temperature in the range of 500-850°C.

Similar release trends were observed for fiberboard, although the release of S and K was lower in this case (see Figure 1). This may be due to a difference in speciation of these elements in the ash. The presence of certain inorganic elements may have an influence on the volatility of other elements. For example, in the case of fiberboard, the high content of Ti in the ash may play a role in decreasing the volatility of certain elements.

Figure 2 shows the release of Zn, Pb and Cd during combustion of spruce and fiberboard as a function of temperature in the range of 500-850°C. For spruce, it was found that the release of Zn and Pb increased form ~0 at 500°C to ~100% at 850°C, whereas Cd was released almost completely at 500°C. Completely different release trends were found for fiberboard, where the lower amounts of Zn, Pb and Cd released may again be due to the presence of other inorganic elements in the ash.

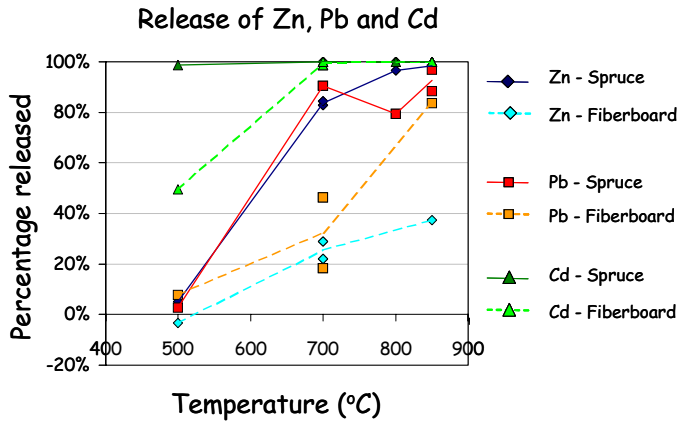

Figure 2. Release of Zn, Pb and Cd during combustion of spruce and fiberboard as a function of temperature in the range of 500-850°C.

Detailed thermodynamic equilibrium studies, as well as investigations of the structures and chemistry of the fuels and ashes will be performed in order to obtain a better understanding of the release data and the possible release mechanisms.

Conclusions

The release of inorganic elements during wood combustion was investigated by performing lab-scale experiments at well-controlled conditions and was found to be strongly dependent on the temperature and the inorganic composition of the fuel. In general, a high release of Cl, S, Zn, Pb, and Cd was observed, up to 100% at high temperature (above 850°C). The elements K, Na, and Mg were released at lower levels. This paper shows the results of the experimental release data for spruce and fiberboard in the temperature range of 500-850°C.

The obtained quantitative experimental data on the release of inorganic elements during wood combustion can be used as input data for aerosol and fly-ash formation and behavior models aiming to find solutions for ash-related problems during wood combustion.

Acknowledgements. The Danish Technical Research Council (STVF) is acknowledged for funding the project. Violeta Alonso Ramírez and Laura Lambea are acknowledged for their contributions to the experimental work.

References

(1) Aerosols in fixed-bed biomass combustion - formation, growth, chemical composition, deposition, precipitation and separation from flue gas', Final Report, EU Contract no. ERK6-CT-1999-00003, Project no. NNE5-1999-00114, 2003.

SLAG FORMATION AND POTASSIUM VOLATILIZATION FROM RICE STRAW BLENDED WOOD FUEL

P. Thy,[1] B.M. Jenkins,[2] R.B. Williams[2], and C.E. Lesher[1]

[1]Department of Geology
[2]Department of Biological and Agricultural Engineering University of California
One Shields Avenue
Davis, CA 95616

Introduction

There is experimental evidence that the addition of straw to conventional biomass boiler fuels in some instances may reduce potassium fouling. The results of an evaluation of urban wood fuel ash[1] show that potassium is strongly partitioned into the vapor phase. It is also known[2] that fundamental differences exist at superliquidus conditions between wood and rice straw ash melts. Contrary to expectations, potassium is retained in rice straw slag, but strongly volatilized from wood slag. The potential of these preliminary findings is that the addition of rice straw to conventional wood based fuels may be beneficial and may reduce potassium losses and thereby fouling.

We present the results of a systematic experimental study of the high temperature melting relations of ashes produced by mixing rice straw and wood. We use a high temperature vertical quench furnace that let us determine the phase relations at various temperatures by allowing run products to be rapidly quenched and recovered from the high-temperature environment. The predictions of the subscale ash experiments are tested using an atmospheric fluidized bed combustor (AFBC). The laboratory scale combustor allows us to better simulate the complexities of full-scale application than is possible with the atmospheric rapid quench furnace.[3,4]

Ash Melting Experiments

Experimental and Analytical Procedures

Starting materials for the melting experiments consist of two biomass fuels. The first is mixed whole tree chips of white fir and ponderosa pine, typical of clean fuel types received at commercial plants (ash content 1.1%, dry basis). The other is a M202 rice straw variety from California (ash content 20%). The two fuels were ashed at 525 ^{o}C using standard procedures. A total of six ash blends with from 10 to 50 % rice straw ash were prepared from the wood and rice straw ashes (Figure 1; Table 1). The compositions of the ashes and the ash blends are summarized in the Table 1, normalized to 100 % volatile free.

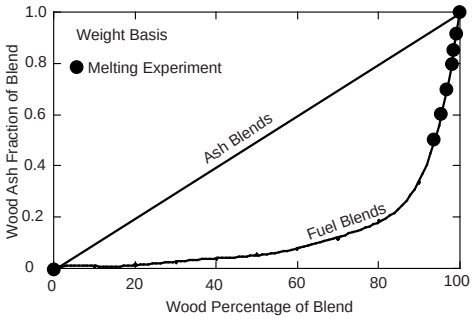

Figure 1. Wood ash fraction as a function of wood percentage in blend (ash or fuel) on a weight basis. Dots are the investigated fuel ash blends.

About 50-mg powder for each experiment were pressed in a pellet and mounted onto a 0.004" diameter Pt-wire. These mounted pellets were suspended into the furnace at the desired temperature. Temperature was monitored by a Pt/^{90}Pt^{10}Rh thermocouple that was positioned near the ash pellet. Duration of the experiments varied to about 24 hours and temperature from the near solidus to the liquidus conditions. The experiments were terminated in air by pulling the sample out of the furnace.

Table 1. Summary of Ash Blends Used in the Experiments

	Rice Straw	R 50% W 50%	R 40% W 60%	R 30% W 70%	R 20% W 80%	R 15% W 85%	R 10% W 90%	Wood
SiO2	82.28	53.91	47.07	39.74	31.87	27.72	23.40	14.26
TiO2	0.01	0.09	0.11	0.13	0.15	0.16	0.17	0.20
Al2O3	0.10	2.04	2.51	3.01	3.55	3.84	4.13	4.76
Fe2O3	0.11	0.79	0.95	1.13	1.32	1.42	1.52	1.74
MnO	0.10	0.43	0.51	0.60	0.69	0.74	0.79	0.90
MgO	1.79	4.18	4.76	5.37	6.04	6.39	6.75	7.52
CaO	1.75	21.42	26.16	31.24	36.69	39.57	42.56	48.90
Na2O	0.15	0.34	0.38	0.43	0.48	0.51	0.54	0.59
K2O	13.04	14.42	14.76	15.11	15.50	15.70	15.91	16.35
P2O5	0.67	2.38	2.79	3.24	3.71	3.96	4.22	4.77
Total	100.00	100.00	100.00	100.00	100.00	100.00	100.00	100.00

R, rice straw ash; W, wood ash. Each blended composition is calculated to 100 %.

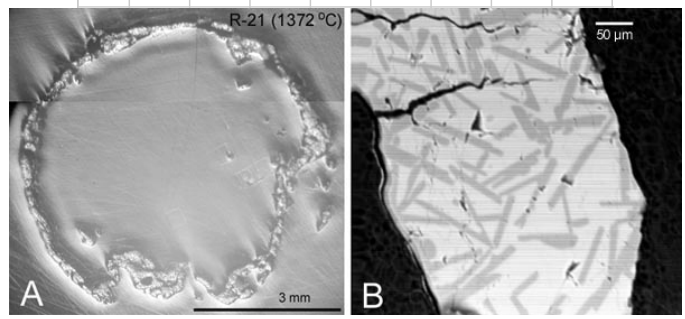

Figure 2. Rice straw ash products. (A) Reflected microscope image of experimental product at 1372°C. The product is composed of a large bubble with a thin outer wall. Scale bar is 3 mm. (B) Back-scattered electron image of the silicate wall in Figure 2A. The dark tabular grains are a quartz polymorph. Light gray is glass. Scale bar is 50 µm.

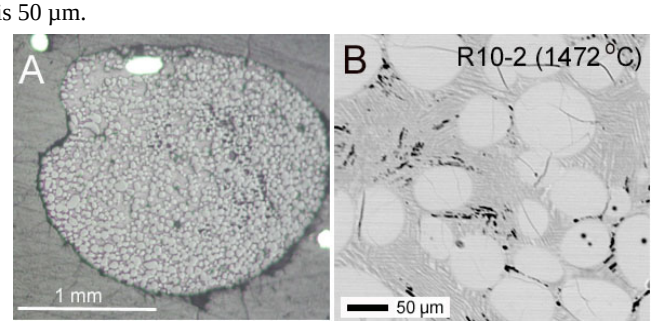

Figure 3. 10% rice straw ash blend products. (A) Reflected microscope image of the product heated at 1472°C. The experimental product is a compacted droplet of rounded larnitic grains and an interstitial quenched melt. Scale bar is 1 mm. (B) Back-scattered electron image of the center of the same experimental product as in Figure 3A. The lighter rounded grains are larnite. The quenched interstitial melt is composed of two unidentified phases. Scale bar is 50 µm.

Melting Results

The initial tests involve the characterization of the melting relations of the two pure ashes (rice straw and wood) as a function of temperature between their respective liquidus and solidus conditions.

These initial experiments form the basis for testing the effects on melting blends of the two ashes. Here we only show two examples of the experimental products. Figure 2A shows a reflected light microscope image of pure rice ash heated to 1372°C. This experimental product is composed of a large bubble with a thin outer wall, likely caused by the release of CO_2 during heating. The back-scattered electron image of the silicate wall indicates dark, needle-shaped quartz polymorphs and light gray glass.

The experimental products on an ash blend with 10 % rice straw ash are illustrated in Figure 3. Figure 3A shows a reflected microscope image of the product from 1472°C. This product is highly compacted and composed of droplets of rounded larnitic grains and an interstitial quenched melt. The back-scattered electron image of Figure 3B shows the textural relationships between rounded larnite grains and quenched interstitial melt composed of two unidentified phases.

Elemental Losses and Phase Appearances

The proportions of the solid phases and the coexisting liquid in the experimental products are estimated by least-squares, linear approximations of the compositions of the phases in the experimental products to the composition of the starting ash mixtures. In addition to the phase proportions in weight percentages, this type of calculation also allows estimates of the elemental losses, either directly from the deviations from the actual composition of ash mixtures or alternatively by including the element in question as an oxide in the calculations. This was done for K_2O and Na_2O for which the largest losses were detected.

The calculated losses of K_2O are illustrated in Figure 4. K_2O is strongly volatilized from the pure wood ash as well as from the wood ash blended with small amounts of rice straw ash (10 and 15 %). On the other hand, K_2O is partly retained in the blends with higher rice straw ash as well as in the pure rice straw ash. The loss correlates positively with the experimental temperature.

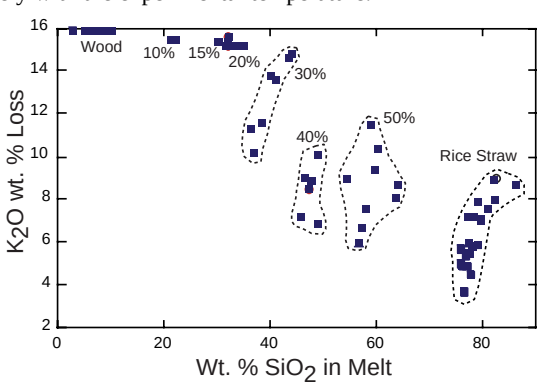

Figure 4. Losses of K_2O (wt. %, ash basis) from the experimental products as a function of SiO_2 content of melt.

The liquid-mineral relations for wood ash were only determined in a narrow interval between 1400 and 1550°C. Within this temperature interval, the melt proportion increases and the larnite proportion decreases with increasing temperature. The proportion of periclase is relatively constant except for a slight drop at the highest melting temperatures. We can extrapolate to a rather uncertain liquidus temperature of 1950-2050°C.

The addition of rice straw ash to the wood ash causes a strong drop in liquidus temperature. With 10 % added rice straw ash, the liquidus temperature is still too high to be directly determined. The mineral phases detected well below the liquidus are, as for the pure wood ash, larnite and periclase. With 15 % added rice straw ash, the liquidus has dropped sufficiently to allow an indication of the liquidus phase as larnite. Periclase is no longer detected at any melting temperature. With 20 % added rice straw ash, the liquidus mineral is larnite at 1403±11°C. Åkermanite appears at 1299±10°C. With 30 % added rice straw ash, wollastonite and åkermanite appear nearly simultaneously on the liquidus at 1264±11°C and are followed by leucite at 1217±11°C. With 40 % added rice straw ash, the liquidus phase is wollastonite at 1282±14°C and with leucite and diopside appearing nearly simultaneously at a temperature of 1212±11°C. With 50 % added rice straw ash, the liquidus phase is wollastonite at 1307±11°C and diopside appears at a temperature of 1263±11°C.

Because temperature dependent losses of K_2O are seen for some blends, it is possible that the estimated liquidus temperatures in part reflect the changing bulk composition of the slag. This mean that estimates of melting relations and liquidus temperature cannot be based on bulk ash compositions, as often done, but must take into consideration temperature dependent changes in bulk composition.

An important observation is that the retention in the slag of K_2O can be correlated with the appearance of leucite. Leucite is a K_2O and Al_2O_3 rich phase that is stabilized at relatively low temperature and low melt fraction in coexisting melts relatively enriched in Al_2O_3 and K_2O. The appearance of leucite, thus, strongly controls retention of K in the slag. This is seen for the 30 to 50 % rice straw blends. The observed variation in the behavior of potassium for the range of slag compositions investigated in this study can be explained by a marked decrease in potassium loss with increasing rice straw in the slag.

The liquidus temperature (or complete melting point) was bracketed in four series of experiments (50, 40, 30, and 20 %). The liquidus temperature for pure rice was extrapolated to approximately 1575°C. The true liquidus for a starting composition with 12 wt. % K_2O may very well be below 1100°C; however, for practical purposes the 'elevated' liquidus temperature shown on Figure 5 may be more relevant.

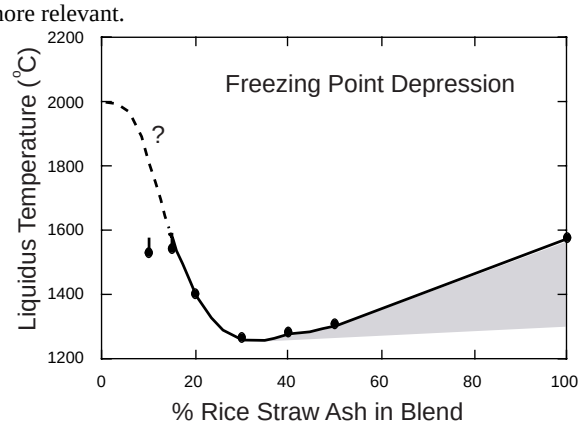

Figure 5. Experimentally determined liquidus temperatures as a function of weight % rice straw ash in the ash blend.

The resulting freezing point depression as a function of the percentage of rice straw ash in the blends is shown in Figure 5. It is seen that the addition of small amounts of rice straw ash to the blend will strongly affect the melting points until an amount of about 20 % rice straw ash (~25°C/wt.% rice ash). From about 20 % rice straw, the liquidus levels out and reaches a minimum at about 30 % rice (1264°C). With increasing rice straw ash, the liquidus temperature rises steadily to 50 % straw ash, and probably also beyond, to an apparent 1536°C for pure rice straw ash (4°C/wt.% rice ash).

Fluidized Bed Combustion

Combustion tests were conducted in an atmospheric laboratory scale fluidized bed combustor.[5,6] The first three experiments used the

2.4 % rice straw blend with either an 800-900°C or a 1000°C reactor wall temperature. The fourth experiment used the 9.6 % rice straw blend and a reactor wall temperature of 1000°C. Two control experiments were conducted using either a pure wood fuel or a leached rice straw fuel, both with a reactor wall temperature of 1000°C.

The fuel blends for the fluidized bed testing were selected based on the results of the bench top melting experiments on fuel ash blends. In these experiments, a minimum liquidus temperature was observed for a 30 % rice straw ash blend. We selected two fuel blends bracketing this ash composition: (1) 2.6 % rice straw and 97.4 % wood fuel and (2) 9.6 % rice straw and 90.4 % wood fuel. As control fuels, we selected two additional fuels; (3) 100 % wood fuel and (4) a 10.7 % leached rice straw and 89.3 % wood fuel blend. Pure rice straw fuel and higher straw blends were not tested since these fuels are well know readily to cause bed agglomeration.[6,7]

The main findings discussed here relate to observation of bed agglomeration. The experiment using the 9.6 % rice straw fuel blend was terminated by strong bed agglomeration that plugged the reactor and defluidized the bed. This was seen as a marked drop in differential bed pressure and rise in bed temperature. The agglomeration was estimated to have affected 25 % of the total bed material, but was concentrated in the central part of the reactor (Figure 6). This agglomeration estimate is based on the extracted bed after the experiment and is calculated on a weight basis relative to the original bed material. Figure 6 shows how silicate material forms as a film along the grain boundary and cements the bed particles together. The result is a highly porous bed cemented along a few grain boundaries. Minor agglomeration was observed in two other experiments, in both cases insufficient to have affected combustion. These were an experiment using the 2.4 % rice straw blend that indicate about 1 % agglomeration of the bed and an experiment using the leached rice straw blend likewise showed minor bed agglomeration (~0.1 %).

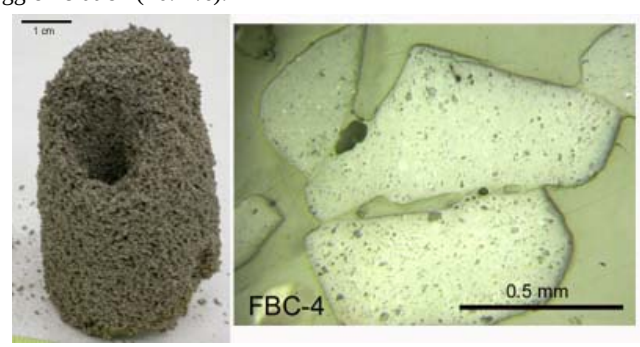

Figure 6. Agglomerated bed extracted from the fluidized bed reactor after termination of an experiment using a 9.6 % rice straw blend and a reactor temperature of 1030°C. The vertical channel is after a thermocouple rod. Right is shown bed agglomeration of bed particles (mullite) by silicate cement (Ca-K-Mg-P-Si).

The bed agglomeration percentages are summarized in Figure 7 as a function of percent rice straw content in the fuel blend. Bed agglomeration is expected to depend on fuel composition, combustion temperature, and duration. All experiments showing bed agglomeration were done with a 1000°C furnace wall temperature and maximum reactor temperature between 1030 and 1090°C. The highest reactor temperature was achieved for the experiment using the pure wood fuel (1090°C) without agglomeration. Minor agglomeration was found for the experiment using the leached straw fuel blend (1040-70°C). The highest agglomeration was found for the experiment using the 9.6 % rice straw blend (1030°C). Of the experiments based on the 2.6 % rice straw blend, only the experiment with the highest reactor temperature (1050°C) showed modest bed agglomeration. Two experiments using the same 2.6 % rice straw blend revealed no bed agglomeration (825 and 920°C, respectively). These results indicated that the fuel composition and combustion temperature control the extent of bed agglomeration. Figure 7 illustrates the effects on adding rice straw to a wood based fuel. The bed agglomeration measured as fraction of total bed on a weight basis increases exponentially with increasing rice straw in the fuel blend. The duration of the individual combustion experiments was not significantly different (2-6 hours) to allow the effect of continuous combustion and duration on agglomeration to be evaluated.

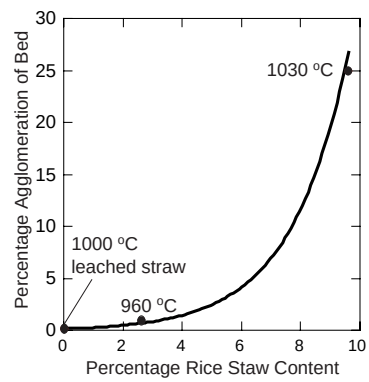

Figure 7. Estimated bed agglomeration as a function of rice straw in the fuel.

The combustion temperature also has a significant effect. For the 2.6 % rice straw blend, only the experiment with the highest combustion temperature showed minor agglomeration, while the lowest temperature experiments on the same fuel blend did not reveal agglomeration. The effect of duration was not investigated in the present study. The results for the short duration tests conducted reveal no clear correlation between duration and extent of bed agglomeration.

Analyses of the agglomerates revealed no significant mineralogical changes in the bed material with extent of agglomeration. Bed agglomeration is, therefore, attributed to either sintering of bed particles aided by potassium released during combustion or to the deposition of partially molten ash fragments or particles. Studies of the cause of agglomeration are currently in progress using the scanning electron microscope.

Conclusions

The blending of rice straw with wood based biomass fuels is shown to result in marked change in the behavior of potassium and its partitioning between the solid inorganic slag and the flue gas. Potassium is increasingly retained in the slag with increasing rice straw ash component. Strong retention is in addition controlled by low melting temperature approaching the solidus temperature for the slag and the saturation of potassium-aluminum-silicate minerals in the slag. The liquidus temperature shows a marked freezing point depression from above 2000°C to about 1260 °C for blends with a content of about 30 % rice straw ash. This content is equivalent to about 3 % rice straw content in the fuel. The complete melting intervals from liquidus to solidus conditions of ash blends are about 100-150°C.

These results suggest the addition of a small amount of straw to a predominantly wood fuel will have the effect of lowering melting temperature and the relative potassium loss to the flue gas. If combustion temperature can be controlled to within, or below, the

melting interval of the resultant ash/slag (<1260°C), the loss of potassium can be minimized. An obvious drawback of adding straw materials is that the total volume of ash and slag will dramatically increase by a factor of 10-20 compared to clean wood. A pure wood fuel will loses most of its K_2O content, around 2 g K_2O/kg fuel. On the other hand, rice straw fuel will lose a lower fraction (0.3) of its original K_2O content, around 8 g K_2O/kg fuel. The determined (and interpolated) K_2O losses on a fuel intake basis are illustrated in Figure 8 showing a rapid increase in K_2O loss until a rice straw fraction of 20% after which the loss levels and remains fairly constant at 7-8 g/kg fuel.

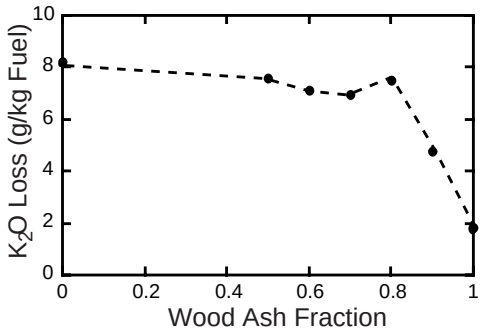

Figure 8. Experimental determined, near-solidus K_2O losses (g) on basis of fuel intake (kg) plotted as a function of wood ash fraction of blend. (wt. basis).

Fuel blend and bed medium composition, reactor temperature, and duration are the principal controls on bed agglomeration in fluidized bed combustors. The extent of bed agglomeration in our laboratory scale experimental combustor shows an exponential increase with rice straw component suggesting that a maximum of 7-8 % rice straw blends may be permissible for this type of biomass boiler. It is also shown that boiler operation below the minimum solidus temperature (~ 1050°C) dramatically reduces potassium losses and therefore bed agglomeration.

Addition of rice straw to wood fuel decreases the fractional volatilization of potassium. However, because of the large difference in the ash fractions of the two fuel components, will not decrease the total fuel potassium volatilized that will rapidly increase until a straw fuel component of 20%. The principal problem in fluidized bed combustion thus appears not to be the fractional potassium loss to the flue gas, but rather the large increase in inorganic material that can severely affect the bed operation, may be deposited on firesides, and will be transported as ash particles to the heat exchange surfaces.

Acknowledgement. This work was supported by California Energy Commission's Energy innovation Small Grant (EISG) Program.

References

1 Thy, P., Jenkins, B.M., and Lesher, C.E., 1999. High temperature melting behavior of urban wood fuel ash. Energy and Fuels 13, 839-850.
2. Thy, P., Lesher, C.E., and Jenkins, B.M., 2000. Experimental determination of high temperature elemental losses from biomass fuel ashes. Fuel 79, 693-700.
3. Salour, D., Jenkins, B.M., Vafael, M., and Kayhanian, M., 1993. Control of in-bed agglomeration by fuel blending in a pilot scale straw and wood fueled AFBC. Biomass and Bioenergy 4, 117-133.
4. Jenkins, B.M., Baxter, L.L., Miles, T.R., Miles, T.R, Jr., Oden, L.L., Bryers, R.W., and Winther, E., 1994. Composition of ash deposits in biomass fueled boilers: results of full-scale experiments and laboratory simulations. ASAE International Summer Meeting, Kansas City, Kansas.
5. Bakker, R.R., Jenkins, B.M., and Williams, R.B., 2002. Fluidized bed combustion of leached rice straw. Energy and Fuels 16, 356-365.
6. Jenkins, B.M., Bakker, R.R., and Wei, J.B., 1996. On the properties of washed straw. Biomass and Bioenergy 10, 177-200.

QUANTIFICATION OF THE RELEASE OF Cl, K AND S TO THE GAS PHASE FROM COMBUSTION OF ANNUAL BIOMASS

Jacob N. Knudsen, Peter A. Jensen, and Kim Dam-Johansen

Department of Chemical Engineering
Building 229, Technical University of Denmark
2800 Kgs. Lyngby
Denmark

Introduction

The use of annual biomass such as straw, stalks and shells in heat and power generation is an interesting option in order to provide renewable energy and to reduce the net CO_2 emissions. In Europe and North America, straw is the most available biomass resource with a yearly production around 800 million tons[1]. In Denmark, straw is a particular interesting bio-fuel since it is an agricultural waste-product being available in surplus. However, the use of straw as a fuel in combined heat and power plants has proven to be a technical challenge. This is among other things, due to the relatively high concentrations of the elements: potassium, chlorine and sulfur. Formation of acidic pollutants and high mass loadings of aerosols together with deposition on heat transfer surfaces of potentially corrosive components are among the encountered problems[2-4].

During the conversion of annual biomass in grate-fired furnaces, Cl, K and S are partly released to the gas phase, but may also be partially retained in the bottom ash. Clearly, the extent of Cl, K and S release to the gas phase is directly related to the problems mentioned above. In order to predict the impacts of a given fuel in a combustion system, the release behavior of Cl, K and S needs to be investigated. In this work, the influence of combustion temperature and fuel composition on the gas phase release of Cl, K and S have been determined.

Experimental

Biomass fuels. Four biomass fuels with distinctive different ash composition were selected for the release investigation. As seen in Table 1, the concentration range of Cl, K, S and Si is particularly broad. Prior to use, the fuels were thoroughly homogenized in a hammer-mill and the fines were removed. The resulting particle-size fraction was 0.5-10 mm.

Table 1. Characteristics of the Biomass Fuels Applied in the Experimental Investigation.

Fuel	Wheat	Oat	Barley	Carinata
Moisture (%)	8.4	7.8	8.5	7.3
Ash (%, dry)	4.8	3.8	6.9	4.9
Ca (%, dry)	0.35	0.72	0.34	0.60
Cl %, dry)	0.27	0.05	0.79	0.05
K (%, dry)	1.2	0.55	2.3	1.4
P (%, dry)	0.05	0.11	0.06	0.14
S (%, dry)	0.17	0.14	0.20	0.26
Si (%, dry)	0.79	0.27	0.81	0.05
K/Si (mol/mol)	1.1	1.5	2.0	20
Cl/K (mol/mol)	0.25	0.10	0.38	0.04

Release quantification. An electrically heated laboratory flow-reactor was applied to combust small samples of biomass at well-controlled conditions. To simulate the heating rate of an industrial grate-fired boiler, an experimental procedure was utilized where the biomass sample was inserted into a preheated reactor. The release of Cl, K and S from the sample was subsequently quantified by a chemical analysis of the residual ash and a mass balance on the system. A series of experiments at different temperatures were conducted, in order to quantify the release as a function of combustion temperature. The influence of ash composition on the Cl, K and S release was investigated by conducting experiments with biomass fuels with different mineral content and composition.

Analytical. The residual ash samples were dissolved by pressurized digestion in a $HF/HNO_3/H_2O_2$ mixture, subsequently neutralized with boric acid and analyzed by ICP-OES.

Results and Discussion

Potassium. It is seen in **Figure 1** that potassium is released to the gas phase above 700°C and that the release increases with the applied combustion temperature for all biomass fuels regardless of the ash composition. Between 20 and 50% of the total potassium has been released at 900ºC. At temperatures above 900ºC the relative potassium release increases almost linearly with temperature until 60 to 90% is released at 1150ºC. The local temperature on the grate in grate-fired furnaces is fluctuating, but frequently above 900-1000ºC[5]. This implies that significant amounts of the fuel-potassium are released to the gas phase during grate combustion of annual biomass.

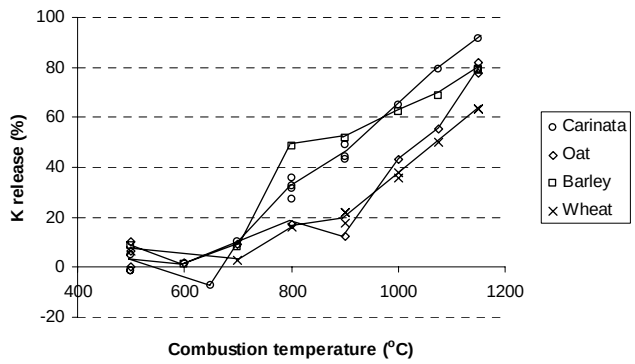

Figure 1. Release of potassium as a function of temperature.

It is furthermore seen in **Figure 1** that the release of potassium is greatly affected by the ash composition. The biomass fuels with the higher Si and lower Cl content relative to K (oat and wheat straw) display the lower potassium release. Potassium can be incorporated into silicate structures[6]. The vapor pressure of potassium fixed in silicate structures is relatively low, which implies that less potassium is released from biomass fuels having a low K/Si ratio. According to Table 1, the K/Si molar ratio of the wheat, oat and barley straw is low compared to the one of carinata and a lower potassium release is expected. However, a high concentration of chlorine relative to potassium may increase the volatility of potassium, due to the relatively high vapor pressure of KCl at combustion relevant temperatures. This indicates that chlorine promotes the release of potassium to the gas phase. A significant fraction of the potassium in the chlorine-rich barley straw is released between 700 and 800°C, the interval where KCl is found to evaporate[6]. This implies that chlorine may facilitate the release of potassium, although the biomass contains substantial amounts of silicon relative to potassium.

Thus, at grate combustion conditions it is expected that the release of potassium to the gas phase will be considerable for biomass fuels containing high amounts of chlorine and/or potassium relative to silicon. On the contrary, the potassium release is expected to be low for high-silicate fuels with low chlorine content.

Chlorine. It appears in **Figure 2** that chlorine is released in two steps for the samples which contain substantial Cl (barley and wheat). Between 30 and 60% is released in the first step below 500ºC. The remaining Cl is released in the second step between 650 and 800ºC. The observed two-step chlorine release is in agreement with observations in the literature[6]. It has been demonstrated that chlorine is released as HCl during the fuel devolatilization at 200-400ºC. The second release-step of chlorine is linked to the evaporation of KCl[6], which mainly occurs between 700 and 800ºC as seen in **Figure 2**. This is consistent with the observed step-like increase in the potassium release between 700 and 800ºC for the chlorine-rich fuels as shown in **Figure 1**.

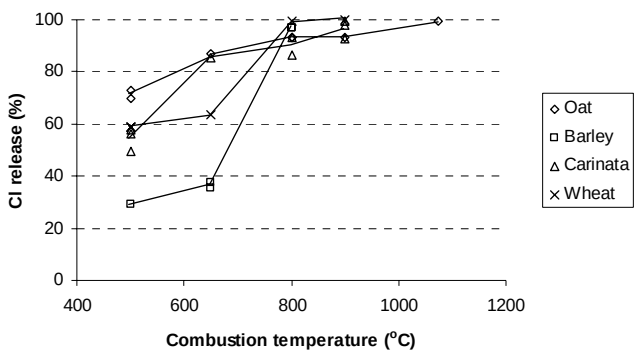

Figure 2. Release of chlorine as a function of temperature.

For the samples which have a relatively low Cl content (oat and carinata), the chlorine release is gradually increasing as a function of combustion temperature. In general a higher fraction of the fuel-chlorine appears to be released at lower temperatures for the low-chlorine fuels. This is most likely an effect of concentration rather than a true mechanistic difference. Significantly less KCl must be evaporated from the low-chlorine fuels, thus the evaporation rate becomes important at lower temperatures.

Nevertheless, the investigation indicates that combustion of annual biomass above 800ºC results in nearly complete release of Cl to the gas phase. The ash composition or the absolute Cl content of the fuel does not affect this fact. The temperature on the grate in grate-fired furnaces is typically significantly above 800ºC[5], which implies that most fuel-chlorine will be released to the gas phase during grate-combustion of annual biomass.

Sulfur. Unlike the observed release behavior of Cl and K, **Figure 3** reveals that the sulfur release appears to be more sensitive to the ash composition than the combustion temperature.

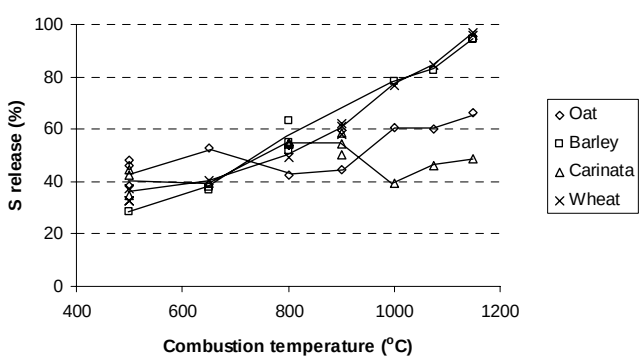

Figure 3. Release of sulfur as a function of temperature.

In case the biomass fuel contains relatively high amounts of Ca and K compared to Si, (oat and carinata), approximately 50% of the sulfur is released almost independently of the applied combustion temperature. On the other hand, if the Si concentration is high, the sulfur release increases with combustion temperature. Calcium and potassium are the elements facilitating sulfur capture in the residual ash. It appears in Table 1, that the content of Ca and K in the fuels is sufficient to retain all fuel-sulfur. However, in the high-silicate fuels, calcium and potassium are to a large extent incorporated into glassy silicate structures. The retention of sulfur in Ca-K-silicates is low, hence, the sulfur release to the gas phase is observed to be higher for high-silicate fuels.

It appears in **Figure 3** that the sulfur release is greater than 40% at all temperatures and for all of the investigated biomass fuels. This is related to the occurrence of substantial amounts of volatile organic sulfur in annual biomass. Earlier work[7] has indicated that annual biomass fuels contain both organic sulfur and inorganic sulfate. The organic sulfur is released to the gas phase during devolatilization at 200-400ºC, whereas the inorganic sulfate is retained in the char.

Altogether, the experimental work indicates that the sulfur release in grate-fired boilers is controlled by the organic-to-inorganic sulfur ratio in the fuels and the accessibility of potassium and calcium. The accessibility of potassium and calcium is largely determined by the relative concentration of silicate in the fuel.

Conclusions

The experimental investigation revealed that both the combustion temperature and the ash composition greatly affected the extent of Cl, K and S release to the gas phase at grate combustion conditions. The release of potassium was largely determined by the fuels content of chlorine and silicon along with the combustion temperature. The fuel-chlorine was found to be completely released to the gas phase at combustion temperatures above 800°C, regardless of the ash composition. The sulfur release was predominantly controlled by the association of sulfur in the fuel together with the accessibility of Ca and K.

Acknowledgement. This work is part of the CHEC (Combustion and Harmful Emission Control) research centre funded by Elsam, Elkraft, the Danish and Nordic Energy Research programs, the Technical Research Council of Denmark and the Technical University of Denmark.

References

(1) Hall, D. O.; Overend, R. P. Biomass. *Regenerable energy*, John Wiley & sons, Chichester, 1987, Chapter 4.

(2) Michelsen, H. P.; Frandsen, F. J.; Dam-Johansen, K.; Larsen, O. H. *Fuel Processing Technology*. **1998**, *54*, 95-08.

(3) Sander, B.; Henriksen, N.; Larsen, O. H.; Skriver, A.; Ramsgaard-Nielsen, C.; Jensen, J. N.; Stærkind, K.; Livbjerg, H.; Thellefsen, M.; Dam-Johansen, K.; Frandsen, F. J.; van der Lans, R.; Hansen, J. *Emissions, Corrosion and Alkali Chemistry in Straw-Fired Combined Heat and Power Plants*, 1st World Conference on Biomass for Energy and Industry. June 2000, Sevilla, Spain.

(4) Christensen, K. A.; Stenholm, M.; Livbjerg, H. *J. Aerosol Sci*. **1998**, *29*, 421-444.

(5) Van der Lans, R.; Pedersen, L.T.; Jensen, A.; Glarborg, P.; Dam-Johansen, K. *Biomass and Bioenergy*. **2000**, *19*, 199-208.

(6) Jensen, P.A.; Frandsen F.J.; Dam-Johansen, K.; Sander, B. *Energy & Fuels*, **2000**, *14*, 1280-1285.

(7) Knudsen, J.N.; Lin, W.; Frandsen, F.J.; Dam-Johansen, K. *Sulfur Transformations during Thermal Conversion of Biomass, Power Production in the 21st Century*, Engineering Foundation Conference, Snowbird, Utah, USA, 28 Oct. - 2 Nov. **2001**.

SLAGGING BEHAVIOUR OF WOOD ASH UPON ENTRAINED-FLOW GASIFICATION CONDITIONS: PRELIMINARY STUDIES

B. Coda, M.K. Cieplik, J.H.A. Kiel

Energy Research Centre of the Netherlands, ECN
P.O. Box 1, 1755 ZG Petten, The Netherlands

Introduction

Entrained flow gasification is one of the most promising technologies to convert biomass streams for large-scale applications aimed at (integrated) production of power, hydrogen and chemicals (e.g. Fischer-Tropsch diesel fuels). Application of biomass streams in entrained-flow gasifiers similar to those employed in coal gasification (e.g. slagging gasifiers) requires R&D concerning fuel feeding and ash behavior, especially with regard to ash slagging tendencies.

This paper present results related to characterization of slag behaviour of selected wood streams - beech, willow, wood mixture - under simulated (pressurized, oxygen blown) entrained-flow gasification conditions. Wood ash in the fuel is very low (about 1% fuel weight), and characterized by high alkaline-earth and alkali metals content. Therefore its application upon conditions typical of slagging gasifiers requires careful adaptation, since the latter are designed for higher fuel ash content (typically > 6% fuel weight) and operate at a temperature where coal ash can form a molten slag (typically 1300-1500 °C).

Methods

The approach is based on experimental and modeling work. Experiments were performed in an atmospheric-pressure entrained-flow reactor, equipped with an integrated, premixed and multi-stage flat flame gas burner[1]. A scheme of the reactor is shown in **Figure 1**.

The ring-shaped, concentric, staged gas burner is used to simulate the (high) initial heating rates, and serves as a source for the reaction atmosphere. The alumina reactor, placed in a two-stage electrically-heated furnace, is designed to mimic the temperature-time history that coal/biomass/char particles experience in entrained-flow gasifiers. The flamefront temperature can be set as high as 2600 °C, while the reactor/furnace can withstand 1750 °C. The residence times possible to achieve in the system are a couple of hundreds milliseconds scale, allowing for high degrees of conversion of biomass fuels. The slagging behavior of the ash has been characterized by means of a deposition probe, on which top an alumina plate was placed, kept uncooled. The probe was set axially at different positions along the reactor, thus simulating different particle residence times. For this experimental campaign, the reactor furnace temperature was set at 1450 °C, while flame temperature has reached approx. 2050 °C (see **Figure 2**).

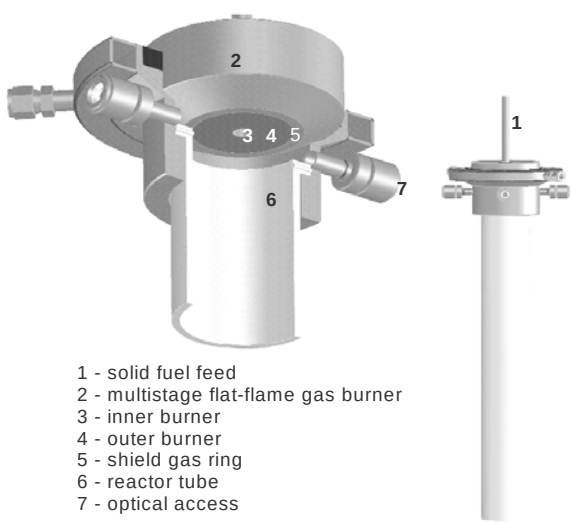

Figure 1. Schematic of the LCS test rig

SEM/EDX techniques have been applied to characterize the slag sample obtained. In addition, knowledge on slagging/melting tendencies of the selected fuels has been studied using an equilibrium model (FACTSAGE computer model) minimizing Gibbs free energy of an hypothetical (pressurized) entrained-flow gasification system, as well as simulating operation conditions close to the experimental ones.

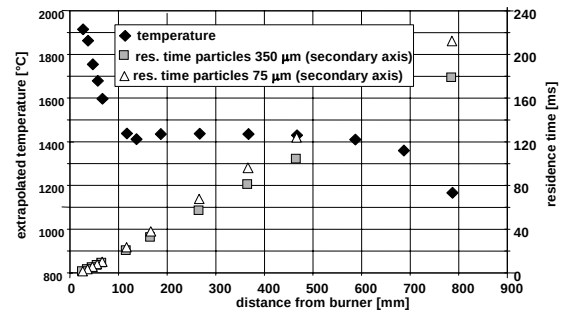

Figure 2. Experimental Temperature/Residence Time Profiles

Fuels. Experiments have been performed with three different woods: beech, willow, and a mixed wood that is commonly utilized in a Dutch power station. Fuel ash composition is shown in **Table 1**.

	beech	willow	wood mixture
Ash content (wt%)	1.01	1.9	1.51
Cl (wt% daf)	0.0037	0.02	0.19
S (wt% daf)	0.017	0.057	0.4
Si (mg/kg fuel)	171	618	417
Al (mg/kg fuel)	48	60	94
P (mg/kg fuel)	89	708	192
Mg(mg/kg fuel)	366	524	252
K(mg/kg fuel)	1151	2894	974
Ca(mg/kg fuel)	3096	5720	2417
Fe (mg/kg fuel)	47	68	116
Na(mg/kg fuel)	8	210	53

Table 1. Fuel Ash Content and Fuel Ash Composition

Results and Discussion

The results of the experimental campaign have shown that wood ash is not prone to form a fluid slag at typical operating temperatures of slagging gasifiers (e.g. 1300-1500 °C). **Figure 3** shows a SEM picture of a particle of beech ash slag after an experiment of 2 hrs. duration time. On the top of the deposit probe no uniform melt/ash layer was found, but rather single (clusters of) ash particles in which the original wood particle structure is still recognizable. Shifting the deposit probe position from 300 to 760 mm (corresponding to changing the residence time from 80 to 220 ms) does not improve the melting behavior of the ash. Only a small share of particles undergoes an enhanced melt formation due to formation of a Ca-silicate structure.

The results of the experimental campaign were well correlating with the predictions of the FACT-SAGE thermodynamic equilibrium program in terms of molten slag composition, which predict that overall at 1400 °C only 17% of the total ash-forming constituents in

the wood will form a molten slag. Condensation of CaO is predicted to begin in the temperature window 1800-1700 °C. At 1000 °C, 74% of the total Ca in the fuel will form condensed CaO. Alkalis will exclusively form gaseous species overall the temperature range 2000-1000 °C, over a wide pressure range 5-30 bars. The experimental results were similar for the three types of wood ash investigated. For willow, it has been experimentally found out that the higher fuel phosphor content might partly enhance the melting behavior of the slag. **Figure 4** shows a typical (cluster of) particles upon gasification of willow: a molten slag structure, phosphor-enriched, is recognizable, whereas the non-molten structure is composed predominantly by CaO.

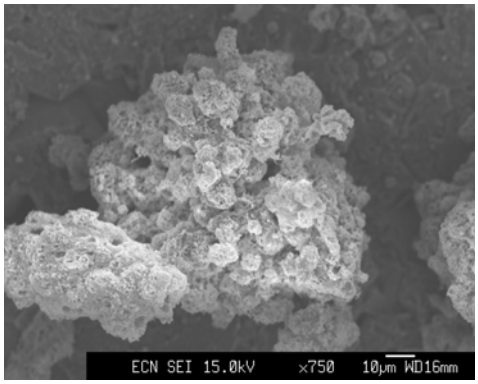

Figure 3: Micrograph of a beech gasification slag deposit

Changing the material substrate of the deposit probe plate was seen not to influence the melting behavior of the ash; on the contrary, wood ash particles have been homogeneously encapsulated in the melt when a pre-existing melt on the deposit probe-plate was present.

Since the wood ashes are not prone to melt under typical operating process temperatures of entrained flow slagging gasifiers, additives will be required which will lower the melting point of the ash.

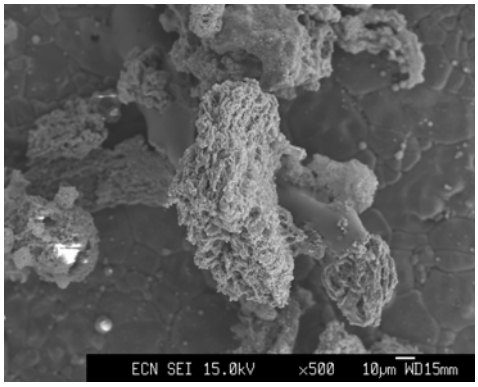

Figure 4: Micrograph of a willow gasification slag deposit

In this respect, additives rich in quartz or clay may enhance the overall fluidity of the slag. Experiments performed with beech wood mixed with SiO_2, (~99% purity), in agreement with thermodynamic calculations and with standard ash fusion test (DIN 51730), have shown that adding quartz on a molar ratio Si: Ca_{fuel} = 1:1; 2:1 (correspondent to 600 g – 1200 g quartz/kg fuel ash) may be sufficient to decrease the melting point of the ash system down to typical process operating temperatures.

Under experimental conditions, a layer of molten slag, (Ca-Silicate) was found on the deposit probe plate. When adding quartz, alkaline earth (and, to a less extent, alkali) metals will tend to be encapsulated in the silicon-based melt. Clay compounds have been predicted by thermodynamic calculations to perform in a similar way as SiO_2 in terms of increasing the total molten slag amount in the system.

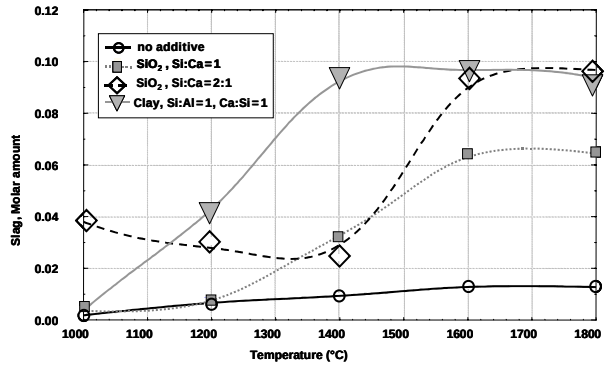

Figure 5: Influence of different additives on slag amount

Figure 5 shows the results of the thermodynamic equilibrium predictions plotting the molten slag amount versus temperature.

When adding a clay with a share of Al: Si=1:1 and Si: Ca_{fuel}=1:1 molar ratio), 90% of the total ash forming constituents will constitute a liquid melt at 1400 °C, according to thermodynamic predictions. This is due to the fact that Ca will be effectively encapsulated in the Al/Si based matrix.

Application of empirical viscosity models, such as Urbain-Kalmanovitch[2], to the investigated optimal wood/flux mixtures, show that viscosity may reach values in the range 8-15 Pa*s, thus achieving both sufficient fluidity to allow free flow and easy slag tapping is possible over typical temperature conditions. However, availability of data on slag flow properties in the composition range of wood ash with flux streams is limited[3], and more work is needed to assess quantitatively the characteristics of the slag flow in terms of viscosity versus slag composition and temperature.

Conclusions

Wood ash is not prone to form a fluid molten slag at typical operating conditions of (pressurized, oxygen-blown) entrained-flow gasifiers due to the formation of high-temperature melting compounds (e.g. CaO). Flux addition with quartz-based or clay-based compounds is a promising option to improve slag behavior by reducing the melting point of the slag. Further work is required to assess quantitatively the characteristics of the slag flow, especially in terms of viscosity versus slag composition and temperature.

Acknowledgement. The financial contribution of SDE (Agency for research in Sustainable Energy) is gratefully acknowledged. The authors express their thanks to B. van der Drift and H. Boerrigter, ECN Biomass, for fruitful discussions.

References

(1) Kiel, J.H.A.; Eenkhoorn, S.; and Heere, P.G.T., Ash behaviour in entrained flow gasification: preliminary studies, EC*N. Brandstoffen, Conversie en Milieu [BCM]* ECN-C--99-037, 1999.

(2) Browning, G.J.;Bryant, G.w.;Hurst, H.J; Lucas, J.A.; and Wall, T.F., *Energy &Fuels*, **2003**,*17*, 731-737.

(3) Vargas, S.; Frandsen, F.J.; and Dam-Johansen, K., *Progress in Energy and Combustion Science*, **2001**, *27*, 237-429.

EXTENDING THE CAPABILITY OF CFD CODES TO ASSESS ASH RELATED PROBLEMS IN BIOMASS FIRED BOILERS

Søren K. Kær[1], Lasse A. Rosendahl[1], and Larry L. Baxter[2]

[1] Aalborg University
Institute of Energy Technology
DK-9220 Aalborg Ø.
Denmark

[2] Brigham Young University
Dep. Chemical Engineering
350 Clyde Building
Provo, UT 84602

Abstract

This paper discusses the application of FLUENT™ in the analysis of grate-fired biomass boilers. A short description of the concept used to model fuel conversion on the grate and the coupling to the CFD code is offered. The development and implementation of a CFD-based deposition model is presented in the reminder of the paper. The growth of deposits on furnace walls and super heater tubes is treated including the impact on heat transfer rates determined by the CFD code. Based on the commercial CFD code FLUENT™, the overall model is fully implemented through the User Defined Functions. The model is configured entirely through a graphical user interface integrated in the standard FLUENT™ interface. The model considers fine and coarse mode ash deposition and sticking mechanisms for the complete deposit growth, as well as an influence on the local boundary conditions for heat transfer due to thermal resistance changes. The model is applied to the straw-fired Masnedø boiler. Results are in good qualitative agreement with both measurements and observations at the plants.

Nomenclature

A	Area [m]
C_c	Cunningham slip correction [-]
C_f	Friction factor [-]
C_v	Constant volume specific heat [J/(kg K)]
d	Diameter [m]
d_m	Molecular diameter [m]
dt	Incremental time [s]
f	Fraction [-]
F	Force [N]
k	Thermal conductivity [W/(m K)]
k_B	Boltzmann's constant [J/K]
k^+	Dimensionless roughness height [-]
Kn	Knudsen number [-]
L_1	Lift force on particle [N]
m	Mass [kg]
$\dot{m}$	Mass flow rate [kg/s]
Nu	Nusselt number [-]
p	Probability [-]
Pr	Prandtl number [-]
r	Reflectance [-]
R	Conduction resistance coefficient [m^2K/W]
R_g	Gas constant [J/(kg K)]
Re	Reynolds number [-]
s_n	Norm. momentum accommodation coef. [-]
s_t	Tang. momentum accommodation coef. [-]
S	Particle to gas density ratio [-]
Stk	Stokes number [-]
t	Time [s]
T	Temperature [K]
u	Velocity [m/s]
u^*	Friction velocity [m/s]
U	Gas velocity [m/s]
V	Volume [m^3]

Greek letters:

ε_s	Surface roughness height [m]
$\varepsilon_{deposit}$	Deposit porosity [-]
ϕ_p	Particle concentration [kg/m^3]
γ	Specific heat ratio [-]
η	Efficiency [-]
ν	Kinematic viscosity [m^2/s]
ρ	Density [kg/m^3]
τ_p	Particle relaxation time [s]
τ_w	Wall shear stress [Pa]

Subscripts:

cell	Computational cell property
d	Deposition, deposit
g	Gas property
imp.	Impaction
in	Inlet property
liq.	Liquid
out	Outlet property
p	Particle property
s	Surface property
stick	Sticking
Tu	Turbulent
Th	Thermophoresis
vol	Volume
+	Boundary layer property

Introduction

In Denmark, as well as internationally, boiler manufacturers are set increasing demands for fuel-flexible and efficient boilers. To meet these demands still more advanced design tools are needed and the use of Computational Fluid Dynamics (CFD) is increasing. To improve the design tools used by Danish boiler manufacturers and operators in design, operation optimisation and trouble-shooting of biomass fired boilers a Computational Fluid Dynamics (CFD) based tool is under development. Mechanistic models are developed and integrated into the commercial CFD code FLUENT™ to tailor the predictive capabilities of the code to the specific needs of the boiler industry and power utility companies.

This paper discusses an overall modelling concept for grate-fired boilers and outlines a model that relates ash deposition behaviour during biomass combustion in grate-fired furnaces to fuel properties, boiler operating conditions, and boiler design. In this paper focus is on straw combustion, however, the long-term objective is for the model to embrace a wide range of fuel types and mixes.

The accumulation of deposits on heating surfaces reduces heat transfer rates from the flue gas to the steam circuit causing a decrease in plant efficiency if they cannot be removed according to the design assumptions of the boiler. In case of severe slagging and fouling unscheduled plant shutdown may result due to the formation of unmanageable amounts or forms of deposits. A typical example of super heater deposits from Masnedø CHP plant, Denmark is illustrated in **Figure 1**.

Figure 1 Super heater deposits formed during straw combustion at Masnedø CHP plant (picture taken from the grate looking upwards). Courtesy of Lars Fenger, ENERGI E2.

In recent years, attention has been given to mechanistic descriptions of deposit formation [1,2,3,4,5,6] however, with only limited attention directed towards biomass firing in grate-based boilers. The fluid mechanics and thermodynamics of the flow and combustion processes influence the deposition processes through particle residence times, particle motion, mixing processes, temperature patterns and heat transfer rates. Comprehensive investigation and modelling of the interaction of these mechanisms can only be obtained by incorporating deposit formation models into Computational Fluid Dynamics (CFD) codes.

Model setup

The commercial CFD code FLUENT™ is used as the framework to solve the turbulent fluid flow, gas and particle combustion, heat transfer and particle transport. The deposition model was implemented through the User Defined Functions (UDF) and a Graphical User Interface (GUI) was included in the standard FLUENT™ interface to ensure ease of use. This allows the user to choose any of the standard FLUENT™ models to solve the fluid dynamics and combustion processes while at the same time being able to include the deposition model. **Figures 2** and **3** illustrate two of the deposition model menu items integrated into FLUENT™.

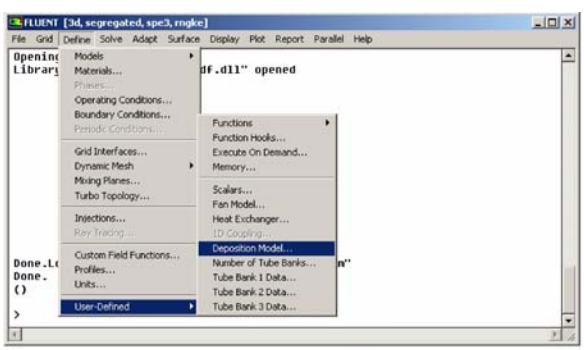

Figure 2 The Graphical User Interface integrated into FLUENT™ for easy configuration of the deposition model.

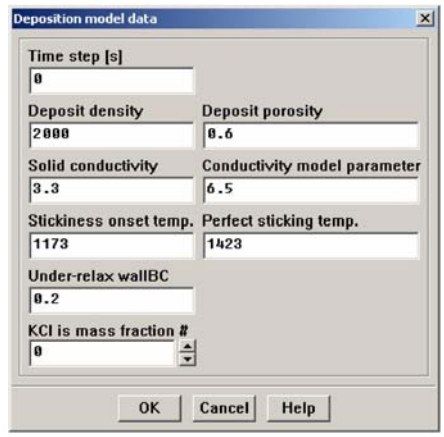

Figure 3 The deposition model configuration panel in FLUENT™.

In the predictions presented in this paper, the steady-state governing equations were solved using the SIMPLE algorithm and the effect of turbulence on the mean flow field was accounted for using the RNG k-ε model. Radiative heat transfer was modelled using the Discrete Ordinates model available in FLUENT™. A two-step reaction mechanism was used for the gas combustion with CO as the intermediate species. The reaction rates were modelled using a combination of chemical kinetics and turbulent mixing (Eddy-Break-Up).

In terms of the geometrical model, the secondary and tertiary platen super heaters in the first and second passes were approximated as slabs and the primary super heater and economizer tube banks in the third pass were accounted for using source terms in the momentum and energy equations. **Figure 4** illustrates the approach used.

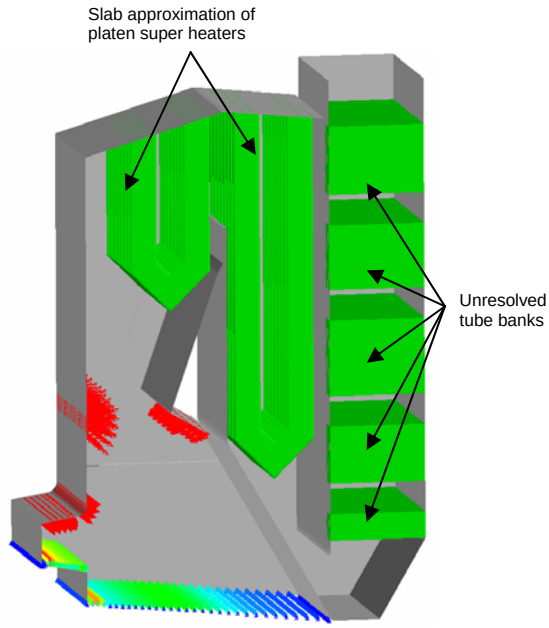

Figure 4 Illustration of the slab approximation used for platen super heaters and the source term approach used for tube banks.

Fuel conversion in bed

Fuel conversion on the grate plays a key-role as boundary conditions in the analysis of the boiler free-board processes. A stand-

alone model[7] was used to predict fuel conversion on the grate. The bed model uses a moving column approach where a three dimensional package of fuel is tracked along the grate while the conversion processes are taking place. In the horizontal direction gas and fuel properties are represented at discrete node points. The principle is illustrated in **Figure 5**.

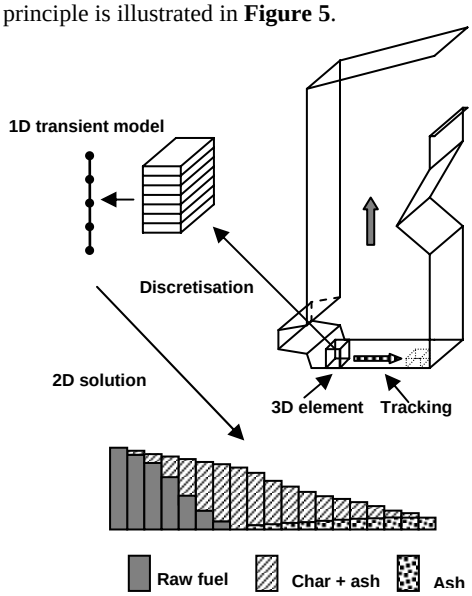

Figure 5 Schematic of the bed combustion modelling concept applied.

This approach results in a two dimensional picture of the bed composition and temperature patterns as indicated at the bottom of **Figure 5**. Profiles of gas velocity, temperature and composition at the bed surface are transferred to the CFD model as boundary conditions. This is discussed in more details in a later section.

Ash formation and transport

In biomass combustion the release of volatile ash fractions (mainly alkali) and entrainment of non-volatile mineral matter lead to a characteristic bimodal fly ash size distribution. **Figure 6** illustrates the ash formations paths.

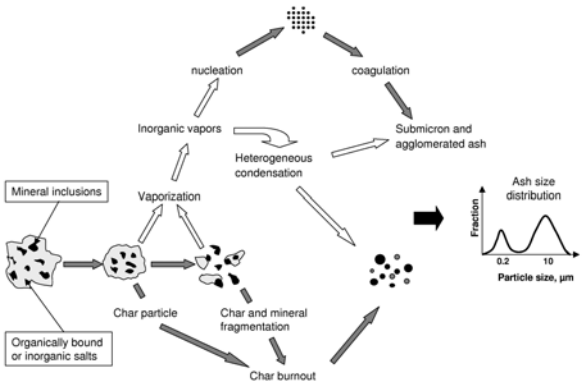

Figure 6 Schematic of the ash formation routes leading to a bimodal fly ash size distribution.

Information about the local flux of ash leaving the grate in the form of vapours and entrained particles is required by the deposition model. This is illustrated in **Figure 7**.

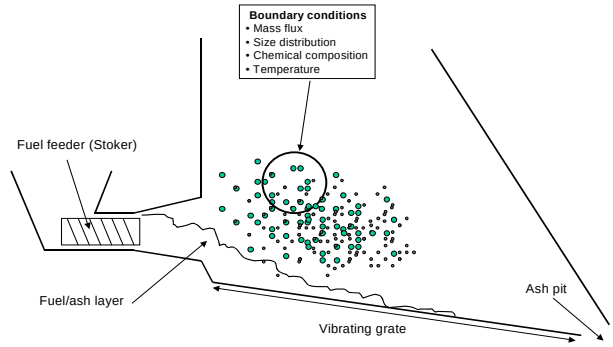

Figure 7 Schematic illustration of boundary conditions required at the grate.

For the entrained particles, the chemical composition as well as the particle size distribution are also required.

Vapour release. During straw combustion alkali salts are the main vapour forming species. Potassium chloride is the predominant stable alkali-bearing species released from the fuel bed at the prevailing combustion temperatures[8]. Chlorine and potassium is released from the fuel matrix early in the combustion process at temperatures around 200-400°C[9]. Potassium re-deposits at the particle surface as discrete KCl particles or intercalates into the char[10]. The amount of potassium that subsequently vaporizes is often determined by the amount of chlorine available to form stable vapours rather than the amount of potassium in the fuel[8]. The mechanisms controlling potassium release rates are not sufficiently well understood to model the conversion and release processes in detail. As a first-order approximation in this paper, the evaporation rate was predicted using mass transfer correlations subject to the constraint that 70 wt% of the total chlorine is released to the gas phase.

Entrainment of coarse non-volatile ash. The chemical composition as well as the particle size distribution of the entrained ash fraction originating from non-volatile species is difficult to determine at a location just above the grate. The chemical composition of fly ash samples collected at locations where the flue gas temperature is below the dew point of alkali vapours cannot be used due to enrichment in these species. The ash composition at high temperatures was approximated from bottom ash chemical analyses[11]. A density of 2000 kg/m^3 was used for these particles. Table 1 presents the major species found in the bottom- and fly ashes from Slagelse CHP plant, Denmark.

Table 1, Major Species in Bottom and Fly Ash Samples Collected from a Straw-Fired Boiler[11].

Species [wt%]	SiO_2	Fe_2O_3	CaO	MgO	Na_2O	K_2O
Bottom ash	68	0.56	10	2	0.4	11
Fly ash	27	0.66	4.7	0.82	0.7	32

A size distribution obtained from CCSEM analysis of the bottom ash is used for the entrained particles. This is a fairly rough approximation however, pending more detailed measurements; it seems to be the best option available. **Figure 8** shows the size distribution used for the entrained non-volatile ash fraction.

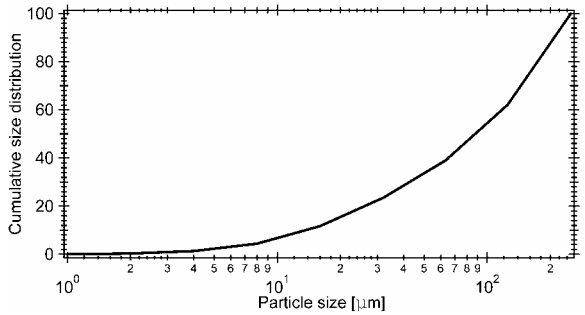

Figure 8 Measured cumulative size distribution from the bottom ash of a straw fired boiler[11].

Based on field measurements, 20 wt% of the total fuel ash is assumed to be entrained in the flue gas. The local flux of ash particles entrained from the grate is approximated from a linear dependence on the local velocity of air through the fuel layer i.e. proportional to the Stokes drag force. The temperature is assumed to equal the temperature of the fuel bed predicted by the bed model.

Ash transport modelling. An Eulerian mass fraction equation is used to represent KCl vapour and sub-micron particles formed by condensation of these vapours. The entrained, relatively coarse, particles dominated by silicates are represented in a Lagrangian frame by the Stochastic Separated Flow model[12] by numerical integration of the particle equation of motion:

$$\frac{d\left(m_p \vec{u}_p\right)}{dt} = \sum_i \vec{F}_i \qquad (1)$$

Ash deposition model

Special attention was given to the deposition mechanisms governed by boundary layer phenomena. Due to limited computational resources these mechanisms cannot be accounted for in full-scale simulations of utility boilers by traditional Lagrangian particle tracking. The computational grid insufficiently resolves the details of the boundary layer and modelling of the complex turbulence patterns requires closures that are not feasible or even non-existent. To resolve these problems, this work adapts the approach based on deposition velocity correlations suggested by[3]. **Figure 9** illustrates the modelling concept.

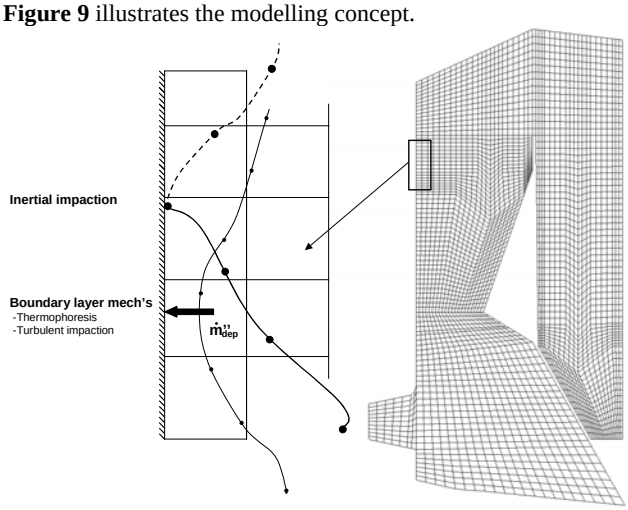

Figure 9 Schematic of the CFD-based ash deposition modelling concept.

The modelling concept used to represent deposition by boundary layer phenomena relies on dimensionless deposition velocities as defined in Equation 2.

$$u_d^+ = \frac{u_d}{u^*} \qquad u^* = \sqrt{\frac{\tau_w}{\rho_g}} \qquad (2)$$

As such this approach follows the same basic idea as in turbulence modelling where wall functions have been used with great success for decades to predict shear stresses, heat and mass transfer. The deposition mass flux is found from multiplication of the deposition velocity with the near-wall particle concentration:

$$\dot{m}''_d = u_d \, \phi_p \qquad (3)$$

The total deposition velocity is calculated by adding the deposition velocities due to turbulent impaction and thermophoresis:

$$u^+_{d,total} = u^+_{d,Tu} + u^+_{d,Th} \qquad (4)$$

The near-wall particle concentration is predicted from the Eulerian transport equation for the sub-micron particles and the Lagrangian trajectories for the particles in the micron-range. Specifically, for the Lagrangian model, the contribution from one trajectory to the particle concentration in a next-to-wall cell is given by:

$$\phi_p = \int_{t_{cell,in}}^{t_{cell,out}} \frac{\dot{m}_{trajectory}}{V_{cell}} \, dt \qquad (5)$$

Boundary layer deposition in tube banks. For water walls and platen super heaters the shear velocity (required in Equation 2) is calculated directly using wall functions in the CFD model. This information is not available for the unresolved tube banks. Instead, an estimate is made from Reynolds analogy using a Nusselt number correlation for circular tubes in cross-flow:

$$\tau_w = \frac{C_f}{2} \rho U_g^{\,2} \qquad (6)$$

and

$$\frac{C_f}{2} = \frac{Nu}{\mathrm{Re}\,\mathrm{Pr}} \qquad (7)$$

Boundary layer deposition takes place on all tubes in the tube bank. The tube surface area available for deposition in each cell inside the tube bank is taken to be the ratio of the total surface area of all tubes in the bank to the tube bank volume (this ratio is termed A_{vol}) multiplied by the cell volume. At each time step in the trajectory calculation (Δt) the deposited mass is removed from the trajectory:

$$\dot{m}_{out} = \dot{m}_{in} - u_{d,total} \, \phi_p \, A_{vol} \, V_{cell} \, \eta_{stick} \qquad (8)$$

with

$$\phi_p = \frac{\dot{m}_{trajectory} \, \Delta t}{V_{cell}} \qquad (9)$$

For the sub-micron particles forming from vapour condensation, the concentration is calculated from the Eulerian transport equation as mentioned above.

Turbulent deposition. Detailed numerical predictions[13,14] and experimental studies[15] of particle transport in boundary layers support the original idea[16] that deposition of particles with dimensionless relaxation times between 0.25 and 20 occurs due to the interaction with coherent structures (turbulent bursts). The dimensionless particle relaxation time is defined as:

$$\tau_p^+ = \frac{1}{18} C_c \, S \, d_p^+ \quad with \quad d_p^+ = \frac{d_p u^*}{\nu} \qquad (10)$$

Using numerical methods to establish a limiting trajectory

leading to deposition in a viscous plane stagnation point flow representing the coherent eddies in the boundary layer a model that considers the surface roughness introduced by deposited particles was derived[17]:

$$u^+_{d,Tu} = \left[\frac{\left(0.64k^+ + \frac{d^+}{2}\right)^2}{3.42} \right]^{\frac{1}{(1+\tau_p^{+2}L_1^+)}} \times \frac{1+8\exp\left(-\frac{(\tau_p^+-10)^2}{32}\right)}{27.03\ \ (1-\tau_p^{+2}L_1^+)} \tag{11}$$

with the following definitions of the non-dimensional lift force and roughness height:

$$L_1^+ = \frac{3.08}{S\,d_p^+} \qquad k^+ = \frac{\varepsilon_s u^*}{\nu} \tag{12}$$

Figure 10 presents the dimensionless deposition velocity as a function of dimensionless relaxation time based on Equation 11:

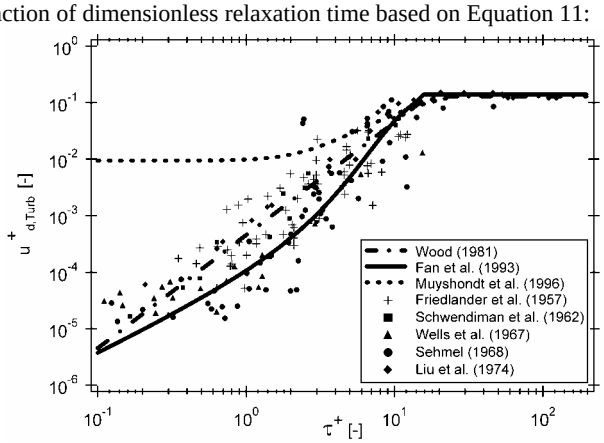

Figure 10 Comparison of dimensionless turbulent deposition velocity correlations with measurements.

It is worthwhile noting that turbulent eddy impaction should not be confused with the deposition caused by vortex shedding at the downstream side of a tube. Turbulent eddy impaction is the result of coherent structures associated with spontaneous turbulent bursts in the boundary layer whereas vortex shedding behind a tube is a bulk flow feature.

Thermophoretic deposition. In most combustion applications a significant temperature gradient exists across the viscous boundary sub-layer causing an enhanced deposition rate of particles with dimensionless relaxation times less than ≈1 (at typical combustion conditions) due to a significant thermophoretic force[18].

A number of correlations giving the thermophoretic force as a function of the Knudsen number have been suggested and that given in Equation 12 is adopted in this work[19].

$$F_{Th} = \frac{1.15\,Kn\left(1-\exp\left(-\frac{\alpha}{Kn}\right)\right)\sqrt{\frac{4}{3\pi}\phi\pi_1 Kn}\,\frac{k_B}{d_m^2}\nabla T d_p^2}{4\sqrt{2}\,\alpha\left(1+\frac{\pi_1}{2}Kn\right)} \tag{13}$$

where

$$\phi = 0.25(9\gamma-5)\frac{c_v}{R_g}$$

$$\alpha = 0.22\left(\frac{\frac{\pi}{6}\phi}{1+\frac{\pi_1}{2}Kn}\right)^{\frac{1}{2}} \tag{14}$$

$$\pi_1 = 0.18\frac{\frac{36}{\pi}}{(2-S_n+S_t)\frac{4}{\pi}+S_n}$$

The thermophoretic force calculated from Equation 13 was non-dimensionalised as given by Equation 15 and is shown as a function of the Knudsen number in **Figure 11**. Correlations suggested by other investigators as well as measurements are also included.

$$F^*_{Th} = \frac{F_{Th}}{\left(d_p/2\right)^2\left|\nabla T\right|}10^5 \tag{15}$$

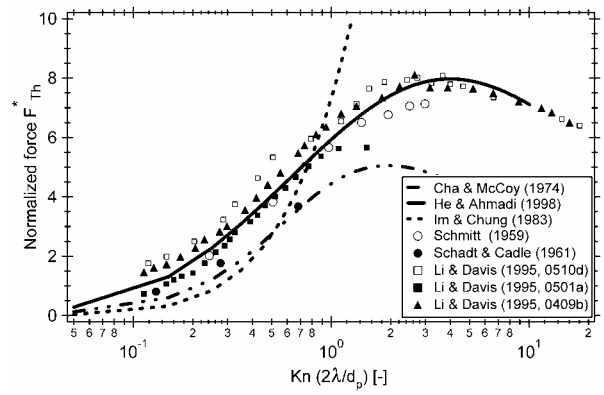

Figure 11 Comparison of predicted dimensionless thermophoretic forces with measurements.

The dimensionless deposition velocity due to thermophoresis relates to the thermophoretic force as given by Equation 16[19].

$$u^+_{Th} = \frac{F_{Th}\,\tau_p}{m_p u^*} \tag{16}$$

Inertial impaction. The inertia of particles larger than about 10 μm is sufficient for their trajectories to deviate from the gas streamlines in regions of strong streamline curvature (e.g. around super heater tubes). Inertial impaction is often the major transport mechanism contributing to deposit build-up. The characteristic time scales of the particle motion and the flow field, expressed through the Stokes number, govern the rate of inertial impaction. The rate of inertial impaction onto a tube in cross flow becomes significant at Stokes numbers larger than unity[20]. For water walls and pendant super heaters, the inertial impaction rate is calculated by monitoring when a particle trajectory meets the surface.

For the tube banks represented by three-dimensional volumes, the approach outlined above is not applicable. Instead, an empirical correlation is used that relates the Stokes number to the impaction efficiency, η_{imp}. The Stokes number is given as:

$$Stk = \frac{\rho_p\,d_p^2\,U_g}{9\,\mu_g\,d_{tube}} \tag{17}$$

The impaction efficiency is defined as the ratio of the number of particles that strike the surface to the number directed towards the surface in the free stream. For a circular tube, the impaction efficiency can be related to the Stokes number as:

$$\eta_{imp} \approx \frac{1}{1 + b(\Phi)^{-1} - c(\Phi)^{-2} + d(\Phi)^{-3}} \quad (18)$$

where

$$\Phi = Stk - a \quad (19)$$

with the following values of the constants: a=0.125, b=1.25, c=-0.014 and d=0.00508. This approach is only used for the first row of tubes in a tube bank. For an in-line tube arrangement, subsequent rows are subject to much slower inertial impaction rates. The ratio of the surface area of tubes in the flow direction to the total flow area gives the probability that a particle is directed towards a tube. Taking the sticking propensity into account, the overall deposition efficiency is:

$$\eta_{bank} = \frac{N_{tubes,per}\, d_{tube}}{L}\, \eta_{imp}\, \eta_{stick} \quad (20)$$

where $N_{tubes,\ per}$ (the number of tubes perpendicular to the flow direction) and L (tube bank dim. 1) are defined as shown in **Figure 12**. After passing the first row of tubes in the bank, the mass flow of particles represented by the trajectory is:

$$\dot{m}_{out} = \dot{m}_{in}(1 - \eta_{bank}) \quad (21)$$

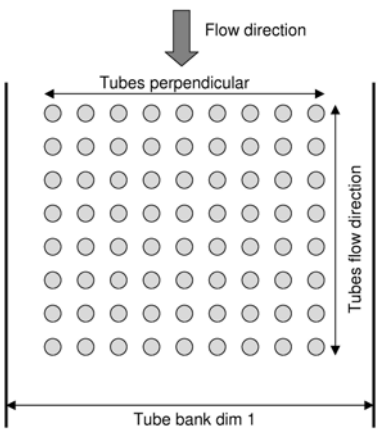

Figure 12 Geometric data required for tube banks.

Ash sticking propensity

The subject of ash sticking propensity has been given considerable attention in the literature, however, so far no generally accepted modelling methodology has been developed, especially not focusing on conditions typical for biomass combustion. In mechanistic modelling approaches to ash deposition in coal combustion, the most frequently used approach is that of[21]. Neglecting resuspension and other deposit removing mechanisms, the net fraction of particles contributing to deposit growth is given by:

$$\eta_{stick} = \underbrace{p(T_p)}_{\text{particles}} + \underbrace{\left[1 - p(T_p)\right] p(T_s)}_{\text{deposit surface}} \quad (22)$$

The influence from condensed alkali vapours on the sticking propensity cannot be disregarded in straw-fired boilers[22]. Deposit growth in the presence of condensed material has been discussed by for example[23,24,25] and [26]. It has been found that molten alkali salts (predominantly KCl in straw combustion) at the deposit and particle surfaces efficiently capture the silica-rich particles[27,28]. Based on this observation it was suggested that the sticking propensity is proportional to the fraction of melt at the surface[27]. In this work the melt fraction based sticking concept is developed further towards a form applicable in the context of a CFD analysis.

It was found by[27] that biomass ashes collected from the super heaters, the furnace walls and the bottom ash exhibit a characteristic melting behaviour. Roughly, melting occurs in two temperature regimes; one corresponding to melting of alkali salts; and one to melting of silicates. This was approximated as given in **Figure 13**:

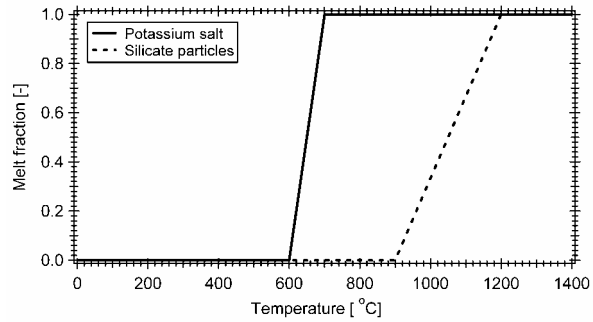

Figure 13 Approximated melting curves of potassium salt and silica-rich particles.

From these assumptions, the local temperature and composition (indicated by T and X in Equation 23) dependent melt fraction can be estimated and used in the prediction of sticking propensity for the particle as well as the deposit surfaces.

$$f_{melt}(T,X) = f_{melt,KCl}(T)\frac{m_{KCl}}{m_{total}} + f_{melt,silicate}(T)\frac{m_{silicate}}{m_{total}} \quad (23)$$

As an alternative to this approach the particle viscosity can be used for silica-rich particles. This approach was applied in the original paper[21] where a reference viscosity is defined and the sticking propensity modelled as:

$$p(T,X) = \begin{cases} \dfrac{\eta_{ref}}{\eta} & \eta > \eta_{ref} \\ 1 & \eta \le \eta_{ref} \end{cases} \quad (24)$$

Particles that are predicted to stick to the heating surface are removed from the prediction such that, statistically, particles cannot deposit twice.

Deposit physical properties

The deposit porosity varies depending on temperature and chemical composition. Experimental findings suggest the porosity of the inner layer of potassium salt may be as high as 0.9[29]. A deposit consisting of coarse weakly sintered silicate particles typically has a porosity of around 0.6[1]. The fractions of liquid and solid phases influence the local porosity. A simple correlation based on the ratio of liquid to solid volumes was proposed by[1] and adopted by[4,5]:

$$\varepsilon_{deposit} = 1 - \left[(1-\varepsilon_0) + \frac{V_{liq}}{V_{solid}}(1-\varepsilon_0)\right] \quad (26)$$

The thermal conductivity of deposits is a complex function of many parameters including the deposit microstructure and the degree of connectedness between individual particles in the deposit. In the literature, a large number of correlations have been proposed giving the thermal conductivity of ash[30]. In the present work, the simple correlation proposed by[1] in a study of deposit heat transfer is used:

$$k = (1-F)\,k_{solid} + F\,k_{gas} \quad (27)$$

where the weighting factor, F, is defined as:

$$F = \frac{2^n}{2^n - 1}\left(1 - \frac{1}{(1+\varepsilon_{deposit})^n}\right) \quad (28)$$

Based on the heat flux predicted by the CFD code, the deposit layer thickness, the thermal conductivity, and the clean tube temperature (T_{tube}) the deposit surface temperature can be determined from:

$$T_d = \dot{q}'' R + T_{tube} \quad (29)$$

where the conduction resistance coefficient (R) is determined as:

$$R = \sum_{i=1}^{N} \frac{dx_{i,deposit}}{k_{i,deposit}} \quad (30)$$

The summation is over the deposit layers generated in each time step.

A model is currently being implemented in FLUENT™ that allows the radiative properties of the deposit to be determined from the optical properties of the deposited material. In the meantime a constant emissivity was estimated in the simulations presented in this paper. In the new model, the emittance of the initial particulate layers is determined using the theory of imbedded invariance[31]. The single particle properties required by this approach are determined from Mie theory. The spherical reflectance of the particulate deposit is given as[31]:

$$r_s = 1 - 2\gamma H_1 \quad (31)$$

with

$$\gamma = \sqrt{(1-w)} \quad (32)$$

Where w is the single-scattering albedo. H_1 is the first moment of the H-function. The H-function is defined as[31]:

$$H(x) = 1 + \frac{w}{2} x H(x) \int_0^1 \frac{H(x')}{x + x'} dx' \quad (33)$$

The H function is complicated to evaluate, however good approximations exist for practical applications. **Figure 14** presents a comparison of predicted and measured emittance of a particulate deposit.

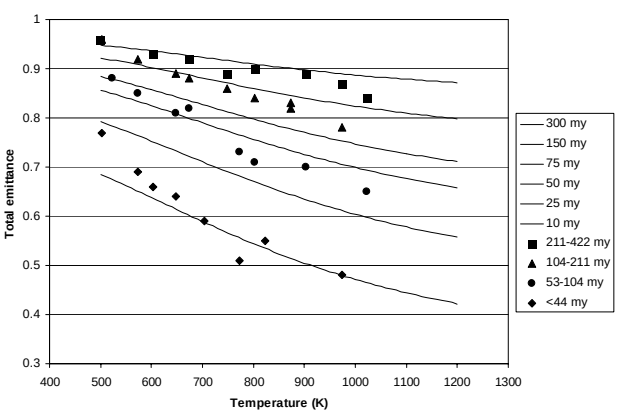

Figure 14 Comparison of predicted and measured emittance of a particulate deposit.

The properties of a completely fused slag with a smooth surface may be approximated as an optically smooth surface. The normal reflectance of a smooth surface is given by[32].

$$r_n = \frac{(n_\lambda - 1)^2 + k_\lambda^2}{(n_\lambda + 1)^2 + k_\lambda^2} \quad (34)$$

where n and k are the real and complex parts of the refractive index, respectively. The spherical reflectance can be found from a similar expression although with a somewhat more complicated functional dependence on n and k[32].

Full-scale model demonstration

The applicability of the deposition models described is demonstrated using the straw-fired boiler at Masnedø CHP plant as a test case. In this context some of the most significant results will be presented. For further discussions of the results please refer to[7].

Gas and fuel inlet conditions. The combustion air inlet conditions and locations are indicated in **Figure 15** showing the lower part of the furnace.

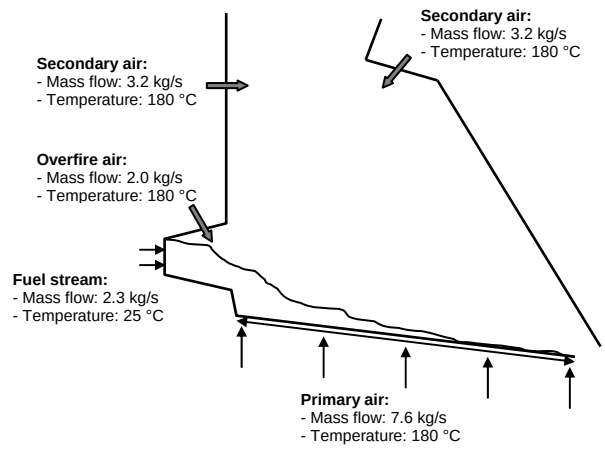

Figure 15 Boundary conditions used for the Masnedø simulations.

Approximately 50% of the total air is primary air supplied from under the grate. In this particular case, the grate air includes ignition air injected close to the fuel feeder. The remaining 50% is split between over fire air and secondary air with the major fraction being secondary air.

Inlet condition for the CFD model. Predicted profiles of gas velocity, temperature and composition at the top of the fuel bed is used as boundary condition for the CFD analysis of the free-board. **Figure 16** illustrates velocity and temperature profiles.

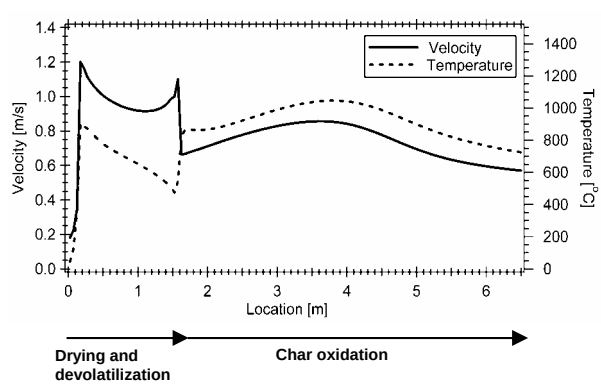

Figure 16 Predicted velocity and temperature profiles at the bed surface.

The drying and devolatilisation phases are characterised by high velocities due to rapid mass release from the fuel, and relatively low temperatures. At the onset of char oxidation, the temperature increases whereas the velocity decreases. **Figure 17** shows the composition of the evolving gases.

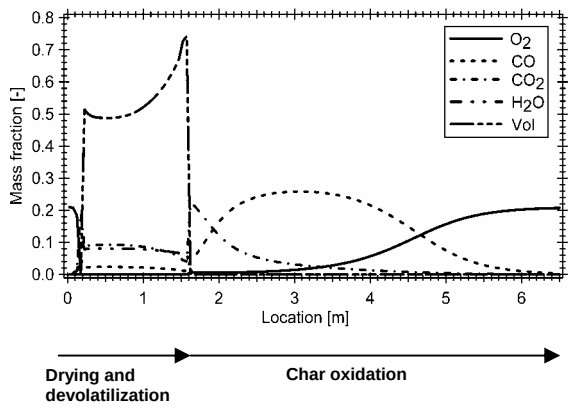

Figure 17 Predicted gas composition at the fuel bed surface.

The devolatilisation zone is dominated by volatiles (approximated as a pseudo-gas with a given C, H and O content), water vapour and carbon dioxide evolution. In the char oxidation region carbon monoxide and dioxide are the primary products. Towards the end of the grate, an increasing amount of oxygen leaves the bed as char conversion is nearly completed.

Measured and predicted gas properties. Sampling of gas phase species and temperature measurements were undertaken at Masnedø CHP plant in November 1998 during straw firing[33]. Approximate locations of the measurement ports are illustrated in **Figure 18**. The exact locations were difficult to establish except for the insertion length of the probe, which was reported to be 1.3m. To illustrate the implications of not knowing the exact probe locations, the variation in predicted values within a distance of ±0.5m (worst-case) from the estimated probe location is indicated by error bars.

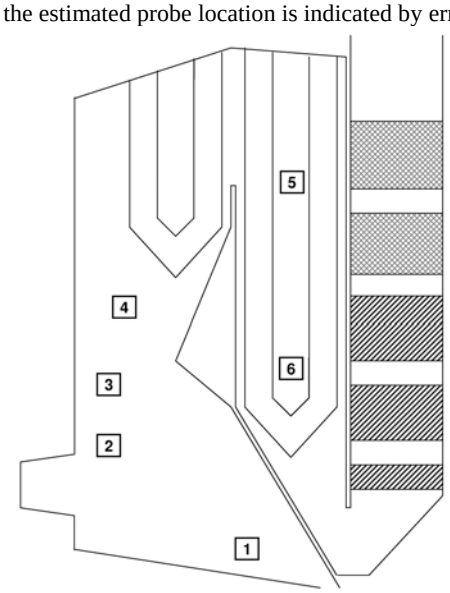

Figure 18 Estimated measurement locations for the full-scale data.

Figure 19 compares measured temperatures with calculated values. An error bar is given for each of the calculated temperatures illustrating the variation within a distance of ±0.5m of the estimated port location. In regions of strong gradients, the uncertainty is considerable.

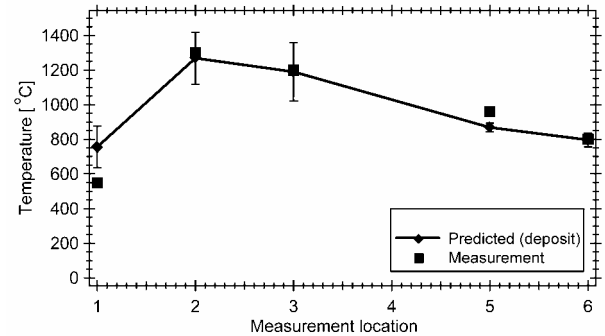

Figure 19 Comparison of predicted and measured temperatures.

The predicted temperatures are in very good correspondence with the measurements except at location 1, which is just above the grate. The calculated value is about 200 °C too high mainly due to the inlet value predicted by the bed model being too high. The measurement port is located approximately at the location where char burnout is completed on the grate. Most likely the difference can be ascribed to an inaccurate prediction of this location. This is supported by the observation that, during the measurements, the temperature at this measurement location varied several hundreds of degrees depending on the fuel load on the grate[33]. The standard deviations of the measurements have not been reported for the case of 100% straw firing, however, from standard deviations reported from measurements during co-firing with other biofuels it was estimated to be within ±50 °C.

Figure 20 shows calculated and measured oxygen and carbon dioxide concentrations at the same locations. Error bars in Figure 16 indicate the standard deviations of the concentration measurements. The uncertainty of the calculated value (related to the port location) is not included but from the variation of temperature it was estimated to be within ±15% of the local value.

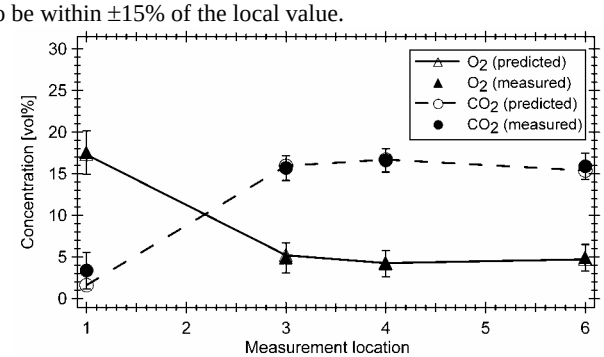

Figure 20 Comparison of measured and predicted oxygen and carbon dioxide concentrations.

As for the temperatures, the agreement with measurements is favourable and in this case also at the first measurement port. The concentrations at location 6 and to a lesser extent location 4 are given almost exclusively by the overall stoichiometry of the combustion process and consequently they are fairly easy to capture by the model. At locations 1 and 3, the concentrations are influenced by local mixing rates and finite reaction rates and as such they are considerably more difficult to predict accurately. The influence from

finite reaction rates can be identified from the co-existence of oxygen, carbon monoxide and volatiles at ports 1 and 3. Carbon monoxide and volatiles concentrations are compared to measured values in **Figure 21**.

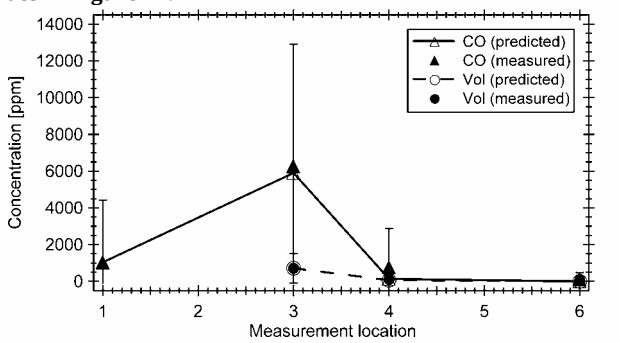

Figure 21 Comparison of measured and predicted carbon monoxide and volatiles concentrations.

When compared to the oxygen and carbon dioxide concentrations, the carbon monoxide and volatiles concentrations exhibit much larger standard deviations in the measurements. This is mainly due to combustion fluctuations introduced by grate vibrations[33]. Obviously, the steady state model used in this work cannot capture such time dependent phenomena. Still, the time-averaged solution obtained by the CFD model is in good correspondence with the time-averaged measurements.

Deposit formation predictions. The predictions presented here assume the contribution to the sticking propensity from the deposit surface is zero and shedding mechanisms were not accounted for. **Figure 22** illustrates the deposition mass flux. The unit of the legend is $gm^{-2}h^{-1}$.

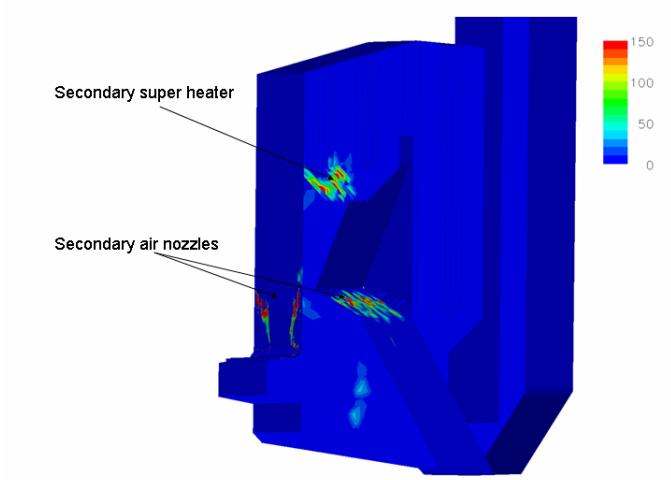

Figure 22 Predicted deposition mass flux in $gm^{-2}h^{-1}$.

It is difficult to undertake a quantitative validation of the predicted deposition rates as sufficiently detailed experimental data are not available. As such, the predictions should mostly be used to get an idea about areas of potential deposit formation problems.

Overall, the fastest deposition rates are found around the secondary air nozzles, located at the front and back walls just below the level of the nose, and on the windward part of the secondary super heater. These locations are characterized by strong streamline curvature that leads to inertial impaction of particles larger than about 10-20 μm. These locations of rapid deposit growth are consistent with observations from the plant.

The contributions to the deposition flux from inertial impaction and boundary layer controlled mechanisms (mainly turbulent eddy impaction and thermophoresis) are illustrated in **Figures 23** and **24** focusing on the secondary super heater.

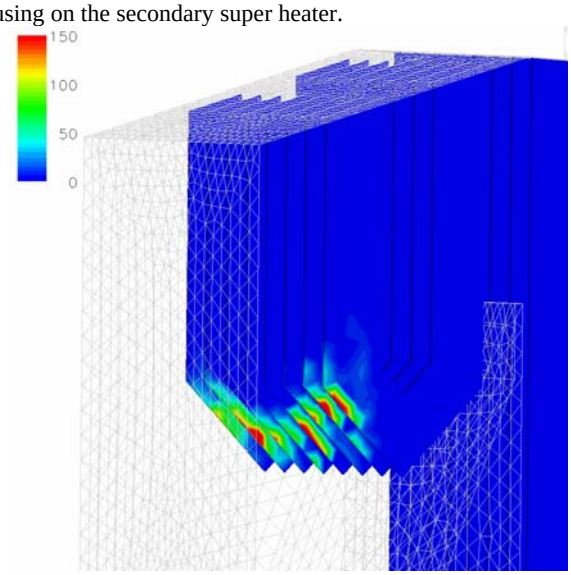

Figure 23 Close-up of the secondary super heater showing inertial impaction flux in $gm^{-2}h^{-1}$.

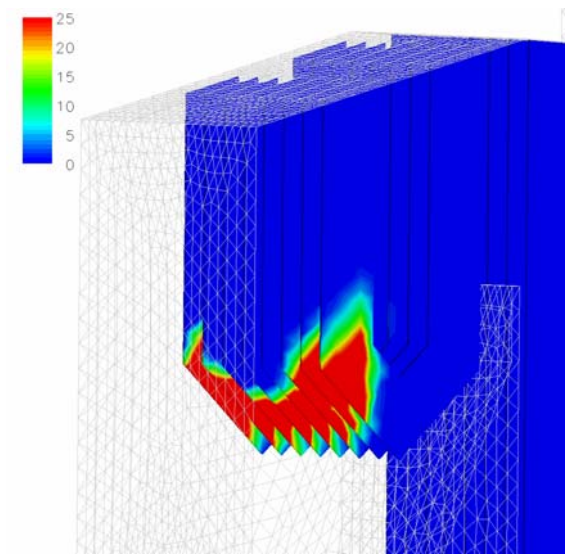

Figure 24 Close-up of the secondary super heater showing boundary layer controlled deposition flux in $gm^{-2}h^{-1}$.

It is seen that the inertial impaction is highly localized at the forward part of the super heater whereas deposition by boundary layer controlled mechanisms is more evenly distributed around the perimeter of the super heater panel. The inertial impaction flux is almost an order of magnitude higher than the boundary layer rate. Deposition probes were used to determine deposition fluxes in a Danish straw-fired boiler located in Slagelse[22]. This boiler uses the same firing technology as the one for which predictions are reported in this paper. Depending on exposure time rates in the range 60-100 $gm^{-2}h^{-1}$ were reported[22]. This is in good overall agreement with the results shown in **Figures 23** and **24**.

The model also considers deposition of vapours (assumed to

form aerosols before deposition). Although this mechanisms is not significant in terms of the total mass deposited it does provide a "glue" that influences the sticking of larger particles. The rates of this mechanism are shown in **Figure 25**.

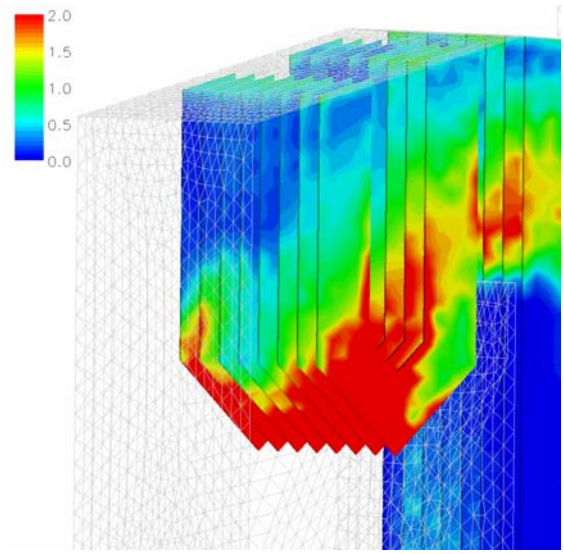

Figure 25 Close-up of the secondary super heater showing vapour deposition flux in $gm^{-2}h^{-1}$.

Compared to the two previous plots, the vapour deposition fluxes are significantly lower but most of the super heater is influenced. This mechanism is important as an initiator for subsequent capture of larger particles. The increase in heat transfer surface temperature (at the deposit surface) after 24 hours of operation is shown in **Figure 26**.

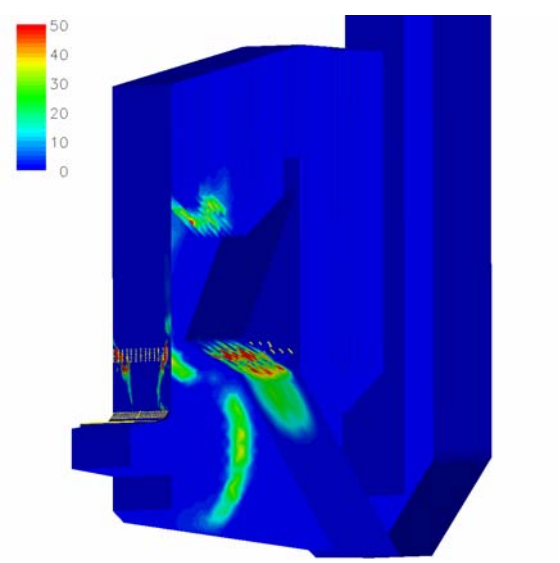

Figure 26 Heat transfer surface temperature increase after 24 hours of exposure to ash deposition.

It is seen that a 50 degrees increase in surface temperature results from the first 24 hours of exposure to ash deposition. The resulting influence on heat transfer rates in the furnace is still only minor; however, a beginning change in surface stickiness will occur as the temperature is approaching the melting temperature of the alkali dominated deposits.

To validate predicted deposit compositions qualitatively, comparison is made with deposits collected from the secondary super heater (mature deposits) and from deposition probes at Masnedø CHP plant[28]. The mature deposits all had the characteristic structure with; an inner part rich in potassium and chlorine; a middle layer dominated by potassium and chlorine but with increasing amounts of silicon and calcium; and an outer part predominantly formed from potassium, silicon and calcium. The major elements found in the layers are given in Table 2.

Table 2, Major Elements found in the Mature Deposits from the Secondary Super Heater in wt%[28].

Location/species [%wt]	Cl	S	K	Ca	Si
Full	5.6	3.8	20.9	8.1	17.1
Inner layer	34.4	2.9	47.0	1.1	1.7
Middle layer	29.4	1.6	39.5	4.9	5.5
Outer layer	0.1	1.1	16.0	11.2	26.2

There is no information about the exact location on the super heater from where the deposits were collected and the predictions show a significant variation between locations. Therefore, detailed comparison with the model predictions is not meaningful; however, some overall qualitative conclusions can still be drawn.

For the inner layer, the model predictions indicate that, in a relatively small region, Ca and Si-rich particles deposit in significant amounts. This region is characterized by a high loading of Ca and Si-rich particles (entrained from the grate) and at the same time the temperature level is sufficient for these particles to be sticky. Elsewhere on the super heater, KCl dominates the deposit. On a mass basis, about 60% of the inner layer has been predicted to consist of KCl. However, on an area basis this ratio is significantly higher.

For the outer layer, the model predictions show a reduction of the fraction of KCl to about 4-5% on a mass basis. In terms of the deposit surface, a sticking propensity of 0.5 has been assumed for these predictions. The presence of K in the outer deposit layer in the measurements reflects the reaction of K with Si and Ca in the deposit. This reaction has not been accounted for by the model.

Overall for the second case, the deposit accumulation rates have increased by a factor of 10-15 compared to those found during the formation of the inner layer. This trend, which is consistent with experimental observations, has been indicated by the time evolution of the deposited mass shown in **Figure 26**.

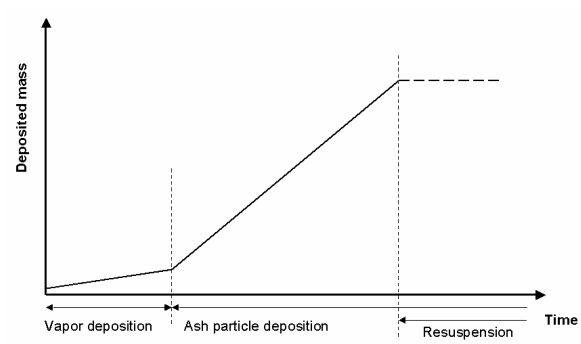

Figure 26 Illustrative trends in the deposited mass as a function of time.

Mixing pattern and operational implications. As mentioned above, the overall oxygen concentration in the stack is approximately 5 vol% (see **Figure 16**) suggesting relatively high overall excess oxygen. Based on the predictions reported here, and a number of similar boilers modelled by the authors, there are significant indications that poor mixing between the bulk flue gas flow and the air being injected through the secondary air ports result in locally reducing conditions. **Figure 27** shows predicted oxygen concentrations in a cross-section of the furnace. Dark areas represent low oxygen concentrations. Please note that the colouring was chosen to provide good resolution of low concentration regions by decreasing the maximum value to a mass fraction of 0.06.

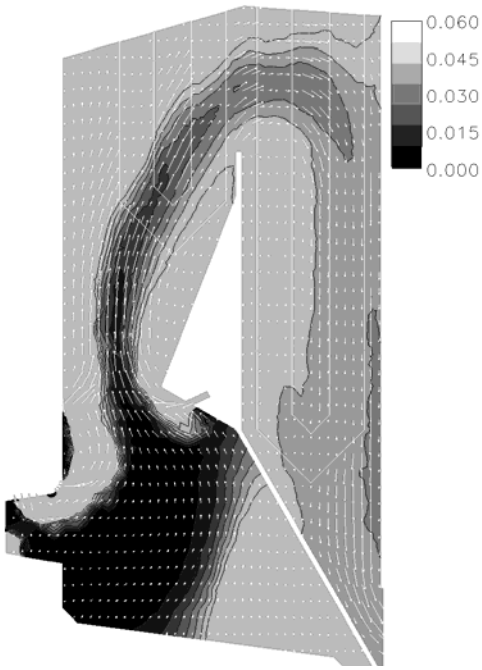

Figure 24 Contour plot illustrating the existence of a striated flow pattern with a near-zero oxygen concentration in the main flow path.

There is a clear striation of the flow with very low oxygen concentrations in the centre part of the boiler and relatively high concentrations near the walls. The low oxygen region in the centre has, at the same time, high velocities and high temperatures.

The low oxygen, high velocity and high temperature alley potentially increases problems related to ash deposition and associated corrosion of the platen super heaters. Under reducing conditions chemical equilibrium predictions show that a larger fraction of the potassium reacts with silica[27] increasing the stickiness of fly ash particles. The high gas temperature adds further to increase the particle stickiness. Due to the high gas velocity, particles deposit efficiently by inertial impaction.

In terms of corrosion risk, the reducing conditions change the most stable form of potassium from sulphates to chlorides at typical heat transfer surface temperatures. Chlorides are much more aggressive towards the boiler tubing compared to the sulphates. These concerns become more important as still more exotic fuel blends are burned to follow developments in fuel prices.

Conclusions

A numerical modelling approach to predict ash deposition and the influence on heat transfer rates in straw-fired boilers has been developed and demonstrated. The model was implemented in the commercial CFD programme FLUENT™. Using a Danish straw-fired boiler as test case, the model was found to correctly predict operational trends observed at the facility. In the future, a significant effort will be put into further improvements and validation of the modelling concept. Planned extensions include the ability to handle co-firing conditions, and inclusion of the model to predict radiative properties.

Acknowledgement. This work was funded by the Danish Energy Research Programme, the Danish Public Service Obligations programme, ELSAM A/S and Babcock & Wilcox Vølund Aps.

References

(1) Richards, G., Slater, P. and Harb, J. (1993) “Simulation of ash deposit growth in a pulverized coal-fired pilot scale reactor”, Energy & Fuels, 7, 774-781.
(2) Baxter, L. (1993) “Ash deposition during biomass and coal combustion: A mechanistic approach”, Biomass and Bioenergy, 4 (2), 85-102.
(3) Pyykönen, J. and Jokiniemi, J. (1997) “Development of a prediction scheme for pulverized coal-fired boiler slagging”, The Engineering Foundation Conference on: Impact of mineral impurities in solid fuel combustion, November 2-7, Kona, Hawaii.
(4) Wang, H., Harb, J. (1997) “Modeling of ash deposition in large-scale combustion facilities burning pulverized coal”, Progress in Energy and Combustion Science, 23, 267-282.
(5) Hecken, M., Reichelt, L. and Renz, U. (1999) “Numerical simulation of slagging films in the pressurized coal combustion facility Aachen”, Proceedings of the 4th International Symposium on Coal Combustion, Peking.
(6) Lee, F., Lockwood, F. (1999) “Modelling ash deposition in pulverized coal-fired applications”, Progress in Energy and Combustion Science, 25, 117, 132.
(7) Kær, S. K. (2001) “Numerical investigation of deposit formation in straw-fired boilers”, Ph.D. Thesis, Institute of Energy Technology, Aalborg University, Denmark.
(8) Baxter, L. et al. (1998) ”The behavior of inorganic material in biomass-fired power boilers: field and laboratory experiences”, Fuel Processing Technology, 54, 47-78.
(9) Jensen, P., Sander, B., Dam-Johansen, K. (1999) ”Release of potassium and chlorine during straw pyrolysis”, In Overend, R. and Chornet, E. (Eds.), Proceedings of the Fourth biomass conference of the Americas, Pergamon, 1169-1175.
(10) Wornat, M. et al. (1995) ”Structural and compositional transformations of biomass during combustion”, Combustion and Flame, 100, 131-143.
(11) Frandsen, F., Hansen, L., Sørensen, L., Hjuler, K. (1998) “Characterisation of ashes from biofuels”,Final report EFP-95, The Danish Energy Research Programme, ISBN 87-7782-000-2.
(12) Shuen, J.-S., Chen, L.-D., Faeth, G. (1983) “Evaluation of stochastical model of particle dispersion in turbulent round jet”, AIChE Journal, 29 (1), 167-170.
(13) McLaughlin, J. (1989) “Aerosol particle deposition in numerically simulated channel flow”, Physics of Fluids A, 1 (7), 1211-1224.
(14) Brooke, J.W., Kontomaris, K., Hanratty, T.J. and McLaughlin, J.B. (1989) “Turbulent deposition and trapping of aerosols at a wall”, Physics of Fluids A, 4 (4), 825-834.
(15) Kaftori, D., Hetsroni, G. and Banerjee, S. (1995) “Particle behavior in the turbulent boundary layer. I. Motion, deposition, and entrainment”, Physics of Fluids, 7 (5), 1095-1106.

(16) Owen, P. (1969) “Pneumatic Transport”, Journal of Fluid Mechanics, 39, 407-432.
(17) Fan, F.G. and Ahmadi, G. (1993) “A sublayer model for turbulent deposition of particles in vertical ducts with smooth and rough surfaces”, Journal of Aerosol Science, 24, 45-64.
(18) Cameron, J.H., Goerg-Wood, K. (1999) “Role of thermophoresis in the deposition of fume particles resulting from the combustion of high inorganic containing fuels with reference to kraft black liquor”, Fuel Proc. Tech., 60, 49-68.
(19) He, C. and Ahmadi, G. (1998) “Particle deposition with thermophoresis in laminar and turbulent duct flows”, Aerosol Science and Technology, 29 (6), 525-546.
(20) Rosner, D. and Tandon, P. (1995) “Rational prediction of inertially induced particle deposition rates for a cylindrical target in a dust-laden stream”, Chem. Eng. Science, 50 (21), 3409-3431.
(21) Walsh, P. et al. (1990) “Deposition of bituminous coal ash on an isolated heat exchanger tube: Effect of coal properties on deposit growth”, Progress in Energy and Combustion Science, 16, 327-346.
(22) Jensen, P., Stenholm, M. and Hald, P. (1997) “Deposition investigation in straw-fired boilers”, Energy & Fuels, 11, 1048-1055.
(23) Rosner, D., Nagarajan, R. (1987) “Towards a mechanistic theory of net deposit growth from ash-laden flowing combustion gases: self-regulated sticking of impacting particles and deposit erosion in the presence of vapor deposited - or submicron mist - 'glue'”, AIChE Symposium Series, 289-296, Heat Transfer - Pittsburg 1987.
(24) Ross, J., Anderson, R., Nagarajan, R. (1988) “Effect of sodium on deposition in a simulated combustion gas turbine environment”, Energy & Fuels, 2 (3), 282-289.
(25) Nagarajan, R., Anderson, R. (1988) “Effect of coal constituents on the liquid-assisted capture of impacting ash particles in direct coal-fired gas turbines”, The Gas Turbine and Aeroengine Congress, Volume 88-GT-192, Amsterdam, The Netherlands, ASME.
(26) Hansen, L. (1998, March) “Melting and sintering of ashes”, Ph.D. Thesis, Department of Chemical Engineering, DTU, Denmark.
(27) Nielsen, H. P. (1998, November) “Deposition and high-temperature corrosion in biomass-fired boilers”, Ph.D. Thesis, Department of Chemical Engineering, DTU, Denmark.
(28) Hansen, L. et al. (2000) “Influence of deposit formation on corrosion at a straw-fired boiler”, Fuel Processing Technology, 64, 189-200.
(29) Robinson, A., Buckley, S., Yang, N., Baxter, L. (2000) “Experimental measurements of the thermal conductivity of ash deposits: Part 2. Effects of sintering and deposit microstructure”, Technical Report SAND2000-8600, Sandia National Laboratories.
(30) Rezaei, H. et al. (2000) “Thermal conductivity of coal ash and slags and models used”, Fuel, 79, 1697-1710.
(31) Hapke, B. (1993). “Theory of reflectance and emittance spectroscopy”, Cambridge University Press
(32) Siegel, R. and Howell, J. R., (2001), Thermal Radiation Heat Transfer, 4th ed., Taylor and Francis-Hemisphere, Washington.
(33) van der Lans, R. (1999) “Gas concentrations and temperature measurements during straw and biomass co-firing in the grate furnace of Masnedø combined heat and power plant”, CHEC report 9914, Department of Chemical Engineering, Danish Technical University, Denmark.

A Novel Biomimetic Catalyst for Electrochemical Hydrogen Production

Licheng Sun,[1*] Sascha Ott,[1] Mikael Kritikos,[2] Björn Åkermark,[1] Reiner Lomoth[3]

[1] *Department of Organic Chemistry, Arrhenius Laboratory, Stockholm University, S-10691 Stockholm, Sweden, licheng.sun@organ.su.se*

[2] *Department of Structural Chemistry, Arrhenius Laboratory, Stockholm University, S-10691 Stockholm, Sweden*

[3] *Department of Physical Chemistry, BMC, Uppsala University, BOX 579, S-75123, Uppsala, Sweden*

Introduction

To totally solve the problems of pollution and green house effects, the ultimate mean is to use renewable energy source such as solar energy which has been used by nature through photosynthesis for billion years. Hydrogenases are a class of natural enzymes which catalyse the metabolism of hydrogen in cyanobacteria and other microorganisms. They can thereby function either as sinks for energy-rich electrons or provide the organisms with reducing power from hydrogen oxidation.[1-3] Hydrogenases are generally divided into two families, the nickel-iron (Ni-Fe) hydrogenases and the iron only(Fe-Fe) hydrogenases, reflecting the different base metals present in the active site. Biologically, the two families differ from each other. The Ni-Fe hydrogenases seem to be more involved in hydrogen oxidation, whereas the iron only hydrogenases tend to catalyse preferentially the production of hydrogen.[4-5] It is this remarkable ability of the iron only hydrogenases which has inspired chemists of the bioinorganic community to synthesize close mimics to the active site of the natural system in the search for active hydrogen production catalysts.[6-8] From crystallographic as well as theoretical studies of the enzyme, the active site is known to consist of two iron nuclei, which are in bonding distance.[9,10] They are linked by a dithiolate bridge, recently suggested to possess the structure S-CH_2-NH-CH_2-S (azadithiolate = ADT).[11,12] Apart from a cysteine-linked [Fe_4S_4] cluster which is part of the electron transfer chain to and from the active site, diatomic ligands carbonyl and cyanide occupy the remaining coordination sites around the iron nuclei.

As biomimetic models for the active sites of Fe-only Hydrogenases, numerous reports have emerged in the bioinorganic literature.[13-22] We have recently described the concept of light-driven proton reduction, using a ruthenium polypyridine complex as the light-harvesting component and a biomimetic model of the iron hydrogenase as proton activation catalyst.[23-24] This projected process commences with the absorption of a photon by the ruthenium photosensitizer. The photo-excited ruthenium complex is oxidatively quenched by the dinuclear iron site, giving rise to a reduced iron species. After regeneration of the photosensitizer (by an external electron donor), this process is repeated to afford a doubly reduced diiron species which could then drive the reduction of protons.

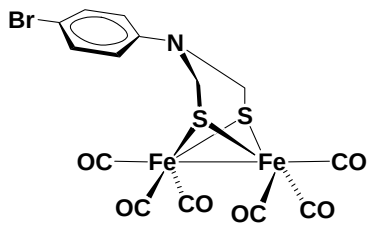

1

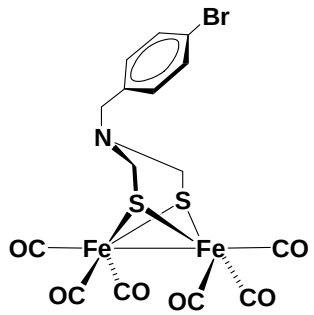

2

In this paper two biomimetic systems **1** and **2** where a 2-aza-1,3-dithiol bridged Fe-dimer complexes have been synthesized and characterized. The catalytic electrochemical hydrogen evolution of these two complexes have been investigated.

Results and discussion

The bromo-substituted iron complexes **1** and **2** were synthesized by applying a recently published procedure for the preparation of some related complexes.[25] Thus, the lithium salt of diironhexacarbonyldisulfide was reacted with the respective *N,N*-di(chloromethyl)-4-bromoaniline and *N,N*-di(chloromethyl)-4-bromobenzylamine, which in

turn were synthesized from the *p*-bromoaniline and *p*-bromobenzylamine in two steps.

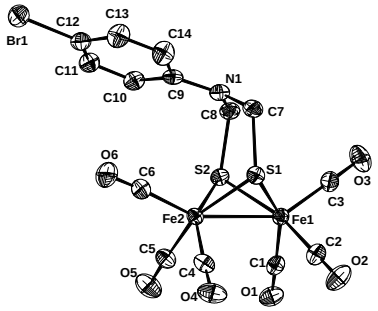

From the X-ray crystal structure it is shown that the $[(\mu\text{-S})_2Fe_2(CO)_6]$ unit of **1** is very similar to those found in other $[(\mu\text{-S})_2Fe_2(CO)_6]$ structures reported.[26] In the central $[(\mu\text{-SR})_2Fe_2(CO)_6]$ unit the two Fe atoms and the two S atoms form a butterfly conformation in which the metal

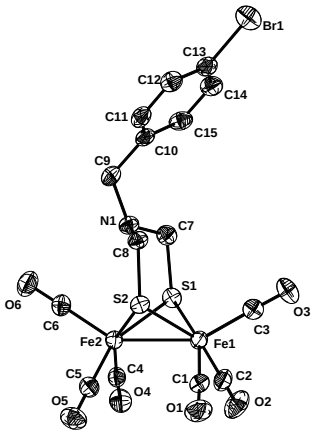

atoms are connected to each other through a Fe-Fe single bond (2.494 Å). In contrast to the Fe-Fe distances the S···S contacts vary slightly more, 3.075 Å. The Fe-C and C-O distances and Fe-C-O angles are all normal with one exception. The Fe-C-O angles for the carbonyls closest to the amine functionality (i e trans to the Fe-Fe bond) in **1** deviate significantly from the expected 180° linear arrangements with value of 175.6(7)°. The non-bonding C···N distance between the amine and the closest carbonyl carbon atom in **1** is 3.578 Å. Moreover, the nitrogen atom deviates from the plane defined by C7, C8 and C9 by 0.174(5) Å. This non-planarity ruptures the potential π -conjugation between the phenyl ring and the nitrogen p-orbital.

In contrast to the structure features of **1**, the benzyl moiety in complex **2** resides in a pseudo-equatorial position of the mettaloheterocycle with the nitrogen lone-pair pointing towards an iron nucleus. In the crystal structure, the non-bonding C···N distance between the amine nitrogen and the nearest carbonyl carbon atom in **2** is significantly shorter than that in 1 (3.0 Å vs. 3.5 Å). After protonation of **2**, a close proximity of the proton to the diiron active site can therefore be anticipated. In acetonitrile solution of **2** in the presence of $HClO_4$, an acidic form $\mathbf{2}H^+$ has been observed by ^{1}HNMR. The UV-Vis absorption maximum is shifted from 328 nm to 332 nm. Two isobestic points at 325 and 362 nm are preserved during the titration, indicating the formation of a single protonation product. Electrochemical hydrogen evolution has been observed in case of **2** at the reduction potential of -1.5 V vs. Fc^0/Fc^+. The turnover numbers of this catalysis have been determined as 25. No hydrogen production was found without the complex **2** at the same condition. The catalytic mechanism for this process is proposed as shown in

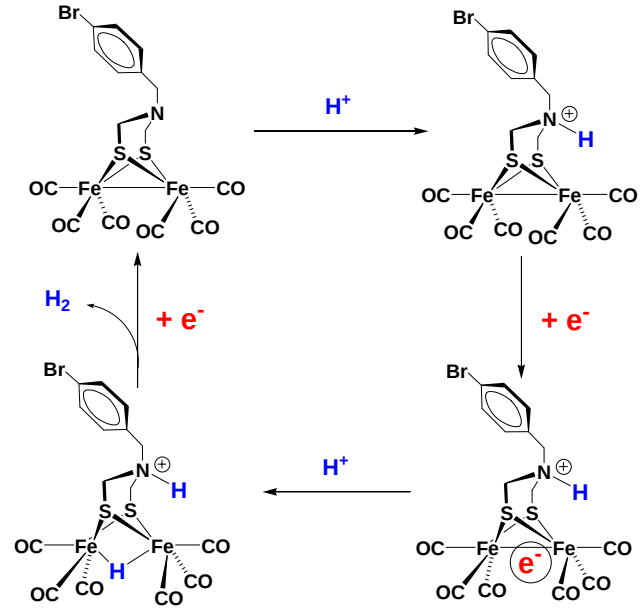

Scheme-1. This is the first example of electrochemical hydrogen production catalysed by a novel biomimetic model of hydrogenase active site, where a 2-aza-1,3-dithiol bridged Fe-dimer complex has been used.

Acknowledgements

Financial support for this work was provided by the Swedish Energy Agency, the Knut and Alice Wallenberg Foundation and the Swedish Research Council (VR).

References

(1) Nicolet, Y.; Lemon, B. J.; Fontecilla-Camps, J. C.; Peters, J. W. *Trends Biochem. Sci.* **2000**, *25*, 138-143.

(2) Peters, J. W. *Curr. Opin. Struct. Biol.*, **1999**, *9*, 670-676.

(3) Frey, M. *ChemBioChem* **2002**, *3*, 152-160.

(4) Adams, M. W. W. *Biochim Biophys Acta* **1990**, *1020*, 115-145.

(5) Cammack, R. *Nature* **1999**, *397*, 214-215.

(6) Alper, J. *Science* **2003**, *299*, 1686-1687.

(7) Darensbourg, M. Y.; Lyon, E. J.; Smee, J. J. *Coord. Chem. Rev.* **2000**, *206-207*, 533-561.

(8) Evans, D. J.; Pickett, C. J. *Chem. Soc. Rev.* **2003**, *32*, 268-275.

(9) Peters, J. W.; Lanzilotta, W. N.; Lemon, B. J.; Seefeldt, L. C. *Science* **1998**, *282*, 1853-1858.

(10) Nicolet, Y.; Piras, C.; Legrand, P.; Hatchikian, E. C.; Fontecilla-Camps, J. C.*Structure* **1999**, *7*, 13-23.

(11) Nicolet, Y.; de Lacey, A. L.; Vernede, X.; Fernandez, V. M.; Hatchikian, E. C.; Fontecilla-Camps, J. C. *J. Am. Chem. Soc.* **2001**, *123*, 1596-1602.

(12) Fan, H.-J.; Hall, M. B. *J. Am. Chem. Soc.* **2001**, *123*, 3828-3829.

(13) Winter, A.; Zsolnai, L.; Huttner, G. *Z. Naturforsch.* **1982**, *37b*, 1430-1436.

(14) Lawrence, J. D.; Rauchfuss, T. B.; Wilson, S. R. *Inorg. Chem.* **2002**, *41*, 6193-6195.

(15) Lyon, E. J.; Georgakaki, I. P.; Reibenspies, J. H.; Darensbourg, M. Y. *Angew. Chem. Int. Ed.* **1999**, *38*, 3178-3180.

(16) Lyon, E. J.; Georgakaki, I. P.; Reibenspies, J. H.; Darensbourg, M. Y. *J. Am. Chem. Soc.* **2001**, *123*, 3268-3278.

(17) Razavet, M.; Davies, S. C.; Hughes, D. L.; Pickett, C. J. *Chem. Commun.* **2001**, 847-848.

(18) Razavet, M.; Borg, S. J.; George, S. J.; Best, S. P.; Fairhurst, S. A.; Pickett, C. J. *Chem. Commun.* **2002**, 700-701.

(19) George, S. J.; Cui, Z.; Razavet, M.; Pickett, C. J. *Chem. Eur. J.* **2002**, *8*, 4037-4046.

(20) Zhao, X.; Georgakaki, I. P.; Miller, M. L.; Mejia-Rodriguez, R.; Chiang, C.-Y.; Darensbourg, M. Y. *Inorg. Chem.* **2002**, *41*, 3917-3928.

(21) Gloaguen, F.; Lawrence, J. D.; Rauchfuss, T. B.; *J. Am. Chem. Soc.* **2001**, 9476-9477.

(22) Gloaguen, F.; Lawrence, J. D.; Rauchfuss, T. B.; Benard, M.; Rohmer, M.-M. *Inorg. Chem.* **2002**, *41*, 6573-6582.

(23) S. Salyi, M. Kritikos, B. Åkermark, L. Sun, *Chem. Eur. J.* **2003**, 9, 557-560.

(24) Ott, S.; Kritikos, M.; Åkermark, B.; Sun, L. *Angew. Chem. Int. Ed.* **2003**, 3285-3288.

(25) Lawrence, J. D.; Li, H.; Rauchfuss, T. B. *Chem. Commun.* **2001**, 1482-1483.

(26) Lawrence, J. D.; Li, H.; Rauchfuss, T. B.; Benard, M.; Rohmer, M.-M. *Angew. Chem. Int. Ed.* **2001**, *40*, 1768-1771.

Effective Fixation of Carbon Dioxide and Its Application to Polymer Synthesis

Takeshi Endo

Department of Polymer Science and Engineering, Faculty of Engineering, Yamagata University, 4-3-16 Jonan, Yonezawa, Yamagata 992-8510, Japan

Introduction

Recently, the chemistry of carbon dioxide has much attention, since carbon dioxide is the most inexpensive and infinite carbon resources. Furthermore, greenhouse effect due to carbon dioxide has gained much attention and decreasing atmospheric carbon dioxide is a critical problem.[1] From these viewpoints, many chemists have studied on development of efficient methods for CO_2 recovery. Among them, chemical CO_2 fixation by primary or secondary amines have been most intensively studied and have become one of the most promising methods for CO_2 recovery.[2] However, detailed study concerning CO_2 fixation by tertiary amines. Reaction of epoxide with CO_2 is also attractive candidate for efficient CO_2 fixation; however, high pressure of CO_2 has been generally necessary.[3] In the course of our works on chemical CO_2 fixation, we present the reversible CO_2 fixation by amidine derivatives and the reaction of epoxides with CO_2 under atmospheric pressure leading to the cyclic carbonate.

Experimental

Materials. *N*-Methyltetrahydropyrimidine (**MTHP**) was synthesized according to the reported procedure.[4] Epoxides were distilled from CaH_2 and stored under nitrogen. *N,N*-dimethylformamide (DMF) and *N*-methylpyrrolidone (NMP) were dried and distilled from CaH_2.

Instruments. ^{1}H-NMR and ^{13}C-NMR spectra were recorded with JEOL JNM-270EX or JEOL JNM-GX500 spectrometer with tetramethylsilane (TMS) as an internal standard. IR spectra were recorded with a Jasco FT/IR-5300 spectrometer. Size exclusion chromatography (SEC) was used to determine number average molecular weight (*M*n) and molecular weight distribution (*M*w/*M*n) of polymer samples with respect to polystyrene standards (Tosoh).

Reversible CO_2 fixation by MTHP. CO_2 was bubbled into anhydrous DMF solution (10 mL) of **MTHP** (982 mg, 10 mmol) at 25 °C for 3 h to afford **MTHP-CO_2** in quantitative fixing efficiency (weight increase in the reaction mixture was 440 mg). Subsequently, a DMF solution of **MTHP-CO_2** was heated to 65 °C for 2 h to regenerate **MTHP** quantitatively. The cycle was repeated two times. The structure of **MTHP-CO_2** was confirmed by ^{1}H NMR, ^{13}C NMR, and IR spectra.

Reaction of epoxide with CO_2. A mixture of epoxide (10 mmol), catalyst (5.0 mmol), and naphthalene (0.128 g) was introduced in a two-necked flask equipped with a rubber septum. After the atmosphere was replaced with CO_2, 10.0 mL of NMP was introduced using a syringe through a rubber septum to dissolve the mixture. The solution was allowed to stand at 100 °C with continuous stirring. Periodically, a small portion of the reaction mixture was removed out through rubber septum, diluted with dichloromethane, and washed with water. The organic extract was analyzed by HPLC to estimate the conversion of epoxide and yield of carbonate using naphthalene as an internal standard.

Results and Discussion

1. Reversible CO_2 Fixation by Amidines

The CO_2 fixation by primary or secondary amines to afford the corresponding ammonium carbamates have been already reported,[2] however, detailed study concerning CO_2 fixation by tertiary amines have not been carried out. Recently, we have found that *N,N,N'*-trialkylamidines, such as *N*-methyltetrahydropyrimidine (**MTHP**) can construct reversible CO_2 fixation, where CO_2 was fixed at 25 °C and was released at 65 °C quantitatively (Figure 1).[5]

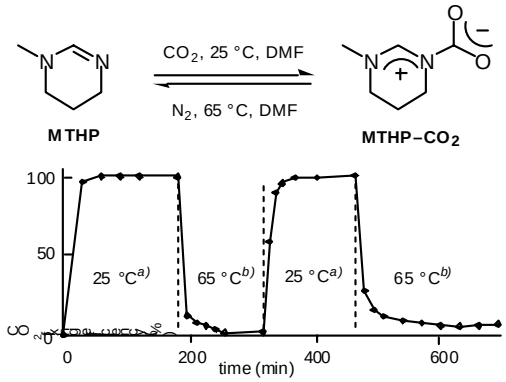

Figure1. Reversible CO_2 fixation and release by **MTHP** in DMF. Conditions: *a)* under CO_2 flow (200 mL/min). *b)* under N_2 flow (200 mL/min).

2. Reversible CO_2 Fixation by Polymer Bearing Amidine Moiety

The polymer bearing amidine moiety (poly(**THPSt**)) was prepared by the synthesis of 4-(1,4,5,6-tetrahydropyrimidine-1-yl)methylstyrene (**THPSt**) and its radical polymerization. Poly(**THPSt**) could fix CO_2 in *N,N*-dimethylformamide (DMF) at 25 °C in 73 % fixing efficiency (Scheme 1).

Scheme 1

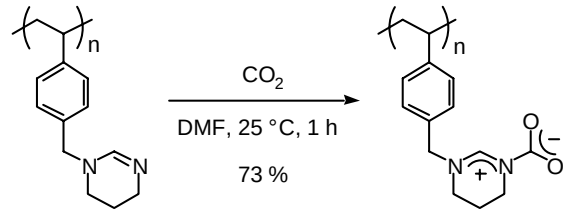

poly(**THPSt**)

The CO_2 fixation in the solid state using polymer bearing amidine moiety may be one of the most simple, economical, and effective methods for CO_2 recovery. Poly(**THPSt**) was found to fix CO_2 in the solid state (30 %). The copolymer of **THPSt** with *N*-vinylacetamide (**NVA**), poly(**THPSt**$_{50}$-*co*-**NVA**$_{50}$) exhibited the higher fixing ability (48 %) than poly(**THPSt**), presumably due to the decrease in steric hindrance between the adjacent pendant groups. Poly(**THPSt**$_{50}$-*co*-**NVA**$_{50}$) was cast from its MeOH solution to form a film that could fix CO_2 at 45 °C in 34 % fixing efficiency. As shown in Scheme 2, the film could conduct the reversible CO_2 fixation, where CO_2 was fixed at 45 °C and was released at 95 °C.

Scheme 2

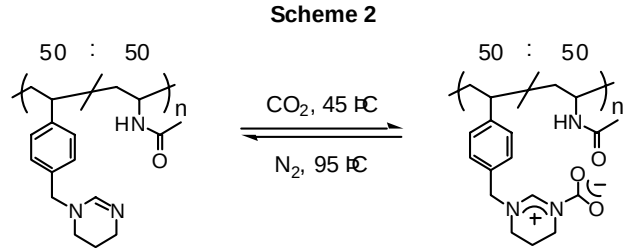

poly(**THPSt**$_{50}$-*co*-**NVA**$_{50}$)
film (ca. 0.014 μm)

3. Reaction of Epoxide with CO_2

Scheme 3

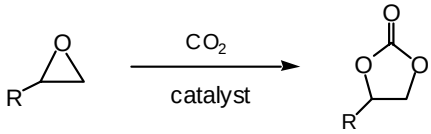

The reaction of epoxides with CO_2 have been already reported. However, high pressure of CO_2 is generally necessary.[3] We have found that alkali metal halides such as lithium bromide show high catalytic activity for this reaction to afford the five-membered cyclic carbonates under atmospheric pressure in excellent yield.[6] The order of intrinsic activity is following order: chloride > bromide > iodide, which is the order of nucleophilicity of the anion, and lithium salt > sodium salt > benzylammonium salt, which is in accord with the order of Lewis acidity of the cation. The reaction may proceed via nucleophilic attack of halide to epoxide to form β-haloalkoxide which reacts with CO_2 followed by cyclization (Scheme 4).

Scheme 4

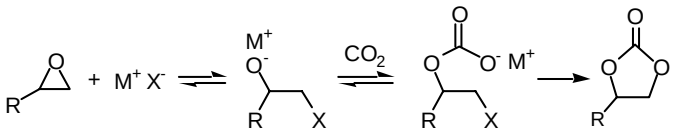

4. Polymer Reaction of Polymer Bearing Epoxide Moiety with CO_2

The incorporation of CO_2 into the polymers bearing epoxide moiety under atmospheric pressure is useful from the viewpoint of CO_2 fixation and the functionality of produced cyclic carbonate. Quantitative incorporation of CO_2 into poly(glycidyl methacrylate) was accomplished in the presence of NaI and Ph_3P as catalyst under atmospheric pressure of CO_2 (Scheme 5).[7] The polymer could react with primary amines selectively at room temperature to afford the corresponding polymer containing 2-hydroxyethylurethane moiety quantitatively.

Scheme 5

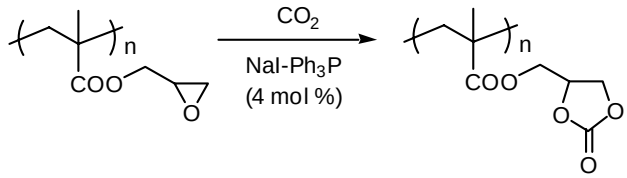

5. Syntheis of Bis(cyclic carbonate)s and Their Polyaddition with Diamines

Bis(cyclic carbonate)s were prepared by the reaction of the corresponding bis(epoxide)s with CO_2. Polyaddition of bis (cyclic carbonate)s and diamines afforded the corresponding poly(hydroxyurethane)s with *M*n 20,000–30,000 in excellent yields (Scheme 6). The presence of water, methanol, or ethyl acetate in the solvent had little effect on *M*n of the resulting polymer, indicating the high chemoselectivity of the polyaddition reaction.[8]

Scheme 6

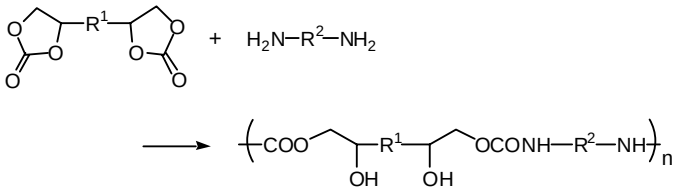

Conclusion

In this paper, we described several examples for the CO_2 fixation by amidines and epoxides. The reversible fixation–release system of CO_2 by amidine and the polystyrene derivatives having amidine moiety were accomplished. The reaction of epoxide with CO_2 in the presence of alkali metal halides proceeded under atmospheric pressure to afford the corresponding five-membered cyclic carbonate in excellent yield. Further, this reaction was applied to polymer system, i.e., quantitative incorporation of CO_2 into poly(glycidyl methacrylate) and polyaddition of bis(cyclic carbonate)s and diamines to afford the poly(hydroxyurethane)s.

References

[1] For example, Braustein, P.; Matt, D.; Nobel, D., *Chem. Rev.* **1988**, *88*, 747.

[2] For example, Sartori, G.; Savage, D. W., *Ind. Eng. Chem. Fundan* **1983**, *22*, 239.

[3] Peppel, W. J., *Ind. Eng. Chem*. **1958**, *50*, 767.

[4] For the synthesis of **MTHP**, see: Seckin, T.; Alici, B.; Cetinkaya, E.; Ozdemir, I. *J. Polym. Sci., Part A: Polym. Chem.* **1997**, *35*, 2411.

[5] Endo, T.; Nagai, D.; Tomohiro, M.; Hiroshi, Y.; Bungo, O. *Macromolecules* **2003**, submitted.

[6] Kihara, N.; Hara, N.; Endo, T., *J. Org. Chem*. **1993**, *58*, 6198.

[7] (a) Kihara, N.; Endo, T., *Makromol. Chem*. **1992**, *193*, 1481. (b) Kihara, N.; Endo, T., *Macromolecules* **1992**, *25*, 4824. (c) Kihara, N.; Endo, T., *J. Chem. Soc. Chem. Commun*. **1994**, 937. (d) Kihara, N.; Endo, T. *Macromolecules* **1994**, *27*, 6239.

[8] Kihara, N., Endo, T., *J. Polym. Sci. Part A: Polym. Chem*. **1993**, *31*, 2765.

NOVEL PROCESS FOR STYRENE FROM ETHYLBENZENE WITH CARBON DIOXIDE

Sang-Eon Park[a] and Jong-San Chang[b]

[a]Department of Chemistry, Inha University, Incheon 402-751, Korea
[b]Catalysis Center for Molecular Engineering, Korea Research Institute of Chemical Technology (KRICT), Taejon 305-600, Korea

Introduction

The utilization of carbon dioxide, which is known as a main contributor to the greenhouse effect, has been of global interest from both fundamental and practical viewpoints in green chemistry.[1] The application of supercritical CO_2 is one of the most exciting ideas to replace volatile organic solvents in green chemistry approach.[2] As another way of the utilization, it is worthwhile to note that carbon dioxide can be used as an oxygen source or oxidant. It has been proposed that carbon dioxide plays a role as the soft oxidant to abstract hydrogen from simple or functionalized hydrocarbons through the catalytic activation of carbon dioxide to form CO and oxygen species.[3-7]

Vapor-phase dehydrogenation of ethylbenzene (EBDH) is a representative process to produce styrene (SM), an important monomer for synthetic polymers. This is one of the ten most important industrial processes. However, it is thermodynamically limited and, moreover, very energy - consuming process. As an alternative way, the oxidative dehydrogenation of ethylbenzene (EB) has been proposed to be free from thermodynamic limitation regarding conversion, operating at lower temperatures with an exothermic reaction.[8] However, this process with use of strong oxidant, oxygen, suffers from loss of selectivity for styrene due to the production of carbon oxides and oxygenates. Recently, the utilization of carbon dioxide as an oxidant for the EBDH has been attempted to explore new technology for producing styrene selectively. We have recently developed a novel process for dehydrogenation of ethylbenzene to produce styrene using carbon dioxide as soft oxidant, so-called $SODECO_2$ (Styrene Production via Oxidative Dehydrogenation of Ethylbenzene with Carbon Dioxide as Soft Oxidant) process. This work deals with characteristics of this novel process.

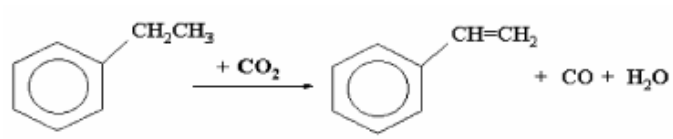

Results and Discussion

The EBDH reaction is generally carried out in vapor phase at 600 - 650°C under steam. The important roles of steam in the industrial dehydrogenation of EB are classified as follows: providing heat to the endothermic dehydrogenation, diluting EB in order to increase equilibrium conversion, and preventing coke deposition on the catalyst.[11] Although steam is widely used in the EB dehydrogentaion due to these beneficial roles, the use of steam has a drawback of losing latent heat of condensation during subsequent separation particularly in a mass process.[11,12] Characteristics of steam and carbon dioxide are summarized in Table 1. It is easily presumable that carbon dioxide can play the same beneficial roles of steam mentioned above.

Table 1. Comparison of Carrier Gases for Dehydrogenation of Hydrocarbons

Characteristics	Steam	Carbon Dioxide
Function	Not oxidant Diluent	Soft oxidant Diluent
Heat capacity	Medium (37.0 J/mol·K at 673K)	High (49.1 J/mol·K at 673K)
Advantage	High selectivity Catalyst stability Coke resistance Keeping oxidation state	High selectivity Activity enhancement Equilibrium shift Cheap carrier gas
Disadvantage	Expensive diluent Highly endothermic High latent heat High operation cost	Not commercialized Endothermic Catalyst deactivation

In the case of steam as diluent, it has been pointed out that the present commercial processes require an excess of superheated steam (steam/EB = 7 - 12 mol/mol), so that they consume a large amount of latent heat of steam upon condensation at a liquid-gas separator following a reactor.[9] Moreover, in conventional dehydrogenation units, selectivity and conversion are linked so that high conversion and high selectivity cannot be achieved simultaneously. To achieve high selectivity, conventional plants are limited to less than 70 % conversion. For overcoming these drawbacks, the ABB/UOP SMART™ (Styrene Monomer Advanced Reheat Technology) process has been recently proposed (*See* http://www.uop.com/petrochemicals/processes_products/smart_sm_intro.htm). The major reactions in the process are the EBDH to styrene and the subsequent oxidation of the hydrogen produced in the first reaction. This hydrogen is reacted with oxygen over a highly selective catalyst. In the process, the removal of hydrogen from the process substantially increases single-pass EB conversions while maintaining high SM selectivity.

We propose here another process using carbon dioxide in order to solve the problems due to use of steam such as high-energy consumption and thermodynamic limitation. The main concept of this new technology is started from the utilization of carbon dioxide as the soft oxidant in oxidative catalysis. We pay attention to the possibility to utilize oxygen atoms of a carbon dioxide molecule as the oxidant to abstract hydrogen atom in dehydrogenation of hydrocarbons because the C-H bond dissociation through the hydrogen abstraction with oxygen species is generally accepted to be the rate-determining step in dehydrogenation of hydrocarbons. Thus, the main role of CO_2 in the process is illustrated to play the function of hydrogen abstraction from ethyl group of ethylbenzene, leading to the enhanced activity as well as selectivity over the catalysts that are capable of activating CO_2 to generate atomic surface oxygen.

Besides the role of CO_2, another important thing to consider for the CO_2 utilization is how to and where to bring a large amount of CO_2 with high concentration. Fortunately, there are many processes to produce CO_2 by-product with relatively high concentration in petrochemical industry, for example, gas-phase partial oxidation, reforming, etc. Based on these ideas, we propose the new process for producing styrene, so-called the $SODECO_2$. In addition to the above advantages, it is advantageous in the $SODECO_2$ process that very cheap carbon dioxide thus obtained from by-product of petrochemical oxidation or reforming process is utilized without further purification instead of using expensive steam diluent. Subsequent advantages of the process are: (1) energy saving by the replacement of steam which

requires high loss of latent heat of water, (2) easy retrofit of current steam processes, and (3) lower reaction temperature due to the ability of equilibrium alleviation, etc. Figure 1 shows the schematic diagram of the $SODECO_2$ process that was constructed based on the above concepts.

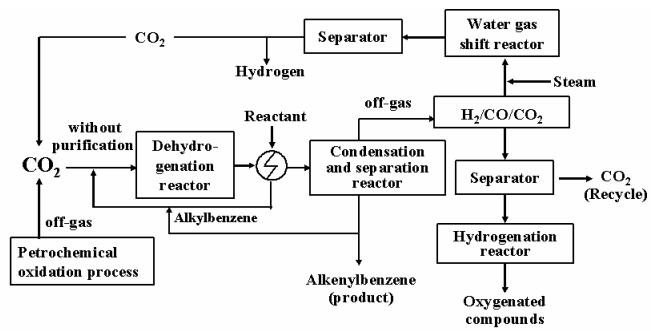

Figure 1. Schematic diagram of the $SODECO_2$ process.

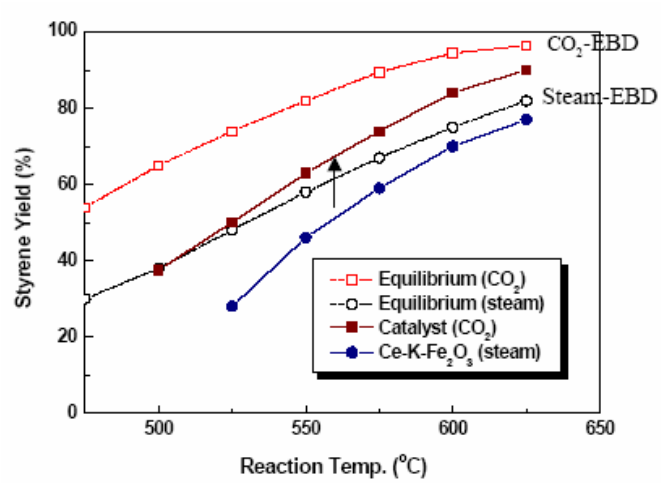

Figure 2. Catalytic activities of CO_2-EBD and commercial steam-EBD catalysts. Reaction conditions: Temp. = 600°C, LHSV = 1.0 h^{-1}, CO_2/EB = 1/1. Reaction condition: P = 0.75 atm, LHSV = 1.0 h^{-1}, CO_2/EB = 5/1 (CO2 Cat.) H_2O/EB = 10/1 (Steam Cat.) Catalyst volume = 100 ml. For CO_2-EBD reaction, CO_2 conversion = 42% at 560°C.

The dehydrogenation catalyst employed comprises oxygen-deficient iron oxide or vanadium oxide and promoters with transition metal oxides. In the case of iron oxide-based catalyst, oxygen-deficient iron sites can produce CO efficiently from the CO_2 dissociation, and the adsorbed oxygen on the catalyst surface can also play a role on hydrogen abstraction from EB. Dispersion of the oxygen-deficient sites or oxygen defects in the catalyst appears to be more efficient for the CO_2 dissociation and thereby the oxidative dehydrogenation of EB. In the case of vanadium oxide- based catalyst, redox behavior of vanadium oxide is found to play a key role in accordance with Mars-van-Krevelen mechanism. Carbon dioxide for this reaction is used as the soft oxidant to provide oxygen species on reduced catalyst surface and, consequently, reoxidize the reduced vanadium species. Figure 2 illustrates characteristic behavior of the dehydrogenation catalyst employed in CO_2-EBDH according to reaction temperature, clearly indicating that the designed catalyst for CO_2-EBDH can experimentally alleviate the chemical equilibrium of EBDH with steam.

The present process in this work is demonstrated under the mini-pilot plant operation equipped with the multi-tubular heat exchanger-type fixed-bed isothermal reactors. Table 2 compares the operation conditions and results of the commercial steam and $SODECO_2$ processes. Through the scale-up work for the process, using CO_2 as the oxidant high selectivity for styrene (>97%), activity enhancement (> 30%) and a drop in reaction temperature (40-50°C) through equilibrium alleviation have been accomplished and compared with conventional dehydrogenation process. Moreover, the energy consumption required for the EB dehydrogenation using carbon dioxide is estimated to be much lower (> 30%) than that for the currently operating process using steam.

Table 2. Comparison of catalyst performance between commercial and $SODECO_2$ processes.

Conditions	Commercial Process	$SODECO_2$ Process
Temp. (°C)	575-675	525-575
Pressure (atm)	75	75
LHSV (h^{-1})	0.75-1	1.0
Carrier/EB (mol)	8-12	2-10
Styrene yield (%)	60-66	55-65
SM Selectivity (%)	94.0-96.5	97.0-98.0
Catalyst lifetime	2 years	In research
By-products	H_2, BTX	BTX, CO/H_2 = 1.0-1.5

Conclusions

This work demonstrates that the utilization of carbon dioxide as soft oxidant in dehydrogenation of ethylbenzene to styrene can produce the novel process, $SODECO_2$. This process has several beneficial advantages: (1) energy saving by the replacement of steam which requires high loss of latent heat of water, (2) lower reaction temperature due to the ability of equilibrium alleviation, and (3) use of very cheap CO_2 thus obtained from by-product of petrochemical process without further purification.

Acknowledgment

This work was supported by the Korean Ministry of Science and Technology (Institutional Research Program).

References

1. Inui, T., Anpo, M., Izui, K., Yanagida, S., Yamaguchi, T. (eds.), Advances in Chemical Conversions for Mitigating Carbon Dioxide, Stud. Surf. Sci. Catal., Vol. 114, Elsevier: Amsterdam, 1998.
2. DeSimone, J.M., *Science*, 2002, **297**, 799.
3. Krylov, O.V., Mamedov, A.Kh., *Ind. Eng. Chem. Res.*, 1995, **34**, 474.
4. Chang, J.-S., Park, S.-E., Park, M.S., *Chem. Lett.*, 1997, 1123.
5. Park, S.-E., Yoo, J.S., Chang, J.-S., Environmental Challenges and Greenhouse Gas Control for Fossil Fuel Utilization in the 21st Century (eds. M.M. Maroto-Valer, Y. Song, C. Song), Chapter 33, Kluwer Academic/Plenum: New York, 2002.
6. Vislovskiy, V.P., Chang, J.-S., Park, M.-S., Park, S.-E., *Catal. Commun.*, 2002, **3**, 227.
7. Chang, J.-S., Vislovskiy, V.P., Park, M.-S., Hong, D.Y., Yoo, J.S., Park, S.-E., *Green Chemistry*, 2003, **5**, 587.
8. Cavani, F., Trifiro, F., *Appl. Catal. A*, 1995, **133**, 219.
9. Mimura, N., Takahara, I., Saito, M., Hattori, T., Ohkuma, K., Ando, M., *Catal. Today*, 1998, 45, 61.

SIMULTANEOUS CARBON DIOXIDE FIXATION IN THE PROCESS OF NATURAL ASTAXANTHIN PRODUCTION BY A MIXED CULTURE OF *HAEMATOCOCCUS PLUVIALIS* AND *PHAFFIA RHODOZYMA*

*Qing-lin Dong; Xue-ming Zhao**

Department of Biochemical Engineering, School of Chemical Engineering & Technology, Tianjin University, Tianjin 300072, People's Republic of China. Email: xmzhao@tju.edu.cn,

Introduction

Carbon dioxide is considered as a major greenhouse gas causing the global warming problem. To find a solution, many attempts have been made through out the world, among which, biological CO_2 fixation (BCF) is thought to be an environment friendly way to remove CO_2 using microalgal photosynthesis. Up to now, microalgae biotechnologies have been practiced to convert CO_2 emitted from power plant [1] and lime production plant [2] into algal biomass. However, there still exist some problems remaining unsolved, such as lower CO_2 conversion rate, high concentration O_2 evolved in photosynthesis, which cause inhibitory effects on cell growth.

Astaxanthin is a kind of high value carotenoid (US$2500/kg) possessing strong biological antioxidation. *Haematococcus pluvialis* and *Phaffia rhodozyma* are the two main different species of microorganisms used in the production of astaxanthin through biotechnology. *H. pluvialis* is a green alga that absorbs CO_2 and evolves O_2 in photosynthesis; While, *P. rhodozyma* is a sort of red yeast which can use a variety of organic materials as fermenting substrates, generating CO_2 and carboxylic acids[3-4], which restrain both cell growth and astaxanthin formation of the red yeast. On the contrary, O_2 is required for astaxanthin synthesis in *P. rhodozyma* fermentation [5]. However, at present, both of the two species are all cultured purely, and under this culture regime, astaxanthin production declines due to the changes of pH, CO_2 and O_2 concentrations in the media through out the culture process. In this study, the mixed culture method for *H.pluvialis* with *P. rhodozyma* was used trying to fix CO_2 released in red yeast fermentation simultaneously and also to stimulate astaxanthin production.

Materials and Methods

Microorganisms. *H. pluvialis* and *P. rhodozyma(AS2-1557)* were obtained from Institute of Hydrobiology and Institute of Microbiology , Chinese Academy of Science respectively. *H. pluvialis* was maintained at 4℃ in a liquid BBM medium; *P. rhodozyma* was maintained on a slant of yeast malt agar (YM agar, Difco) at 4℃.

Culture Media and Conditions. The seed culture of *H. pluvialis* was prepared by transferring 5ml of the alga liquid culture into a 500ml-flask containing 100ml BBM medium (supplemented with 0.25g/l acetate). The seed culture of *P. rhodozyma* was prepared by inoculating the yeast from the fresh slant into a 500ml flask containing 100ml YM medium. Both cultures were shaken at 110 rpm in an orbital shaker (with top cool white fluorescent lamps) at 23.8℃ under light intensity 15μmol photons/m^2.s for 48h. Pure cultures of *H. pluvialis* and *P. rhodozyma* were conducted by transferring 3ml seed cultures into 250ml-flasks containing 30ml culture media respectively. Mixed cultures were conducted in the same way except that the inoculum contained 1.5ml of each seed culture. The flasks were incubated under12μmol photons/m^2.s constant light intensity (adjusted to 30μmol photons/m^2.s after 48h) provided by top cool white fluorescent lamps at 23.8℃, 110rpm in a rotary shaker for 120h.Culture media were prepared from BBM by supplementing it with glucose, the glucose concentrations (g/l) were as follows: 3, 5, 10, 15, 20, 25 respectively.

Biomass Measurement (dry cell weight). 5ml samples of each culture were centrifuged at 5000rpm for 10 min, the supernatants were transferred into 50ml tubes for residual sugar and nitrogen analysis, the cell pellets were rinsed with distilled water twice, then dried in a electrical oven at 105℃ for 2h to constant weight.

Determination of Residual Sugar. Residual sugar in the culture media was quantified by DNS method.

Astaxanthin Extraction and Quantification. *H. pluvialis* pure culture and mixed culture: cells were harvested by centrifuging 5ml samples at 5000 rpm for 10 min. The supernatant was discarded, the cell pellets were re-suspended in 3ml 30%(v/v) methanol containing 5% KOH (w/v) and heated at 70℃ in a water bath for 5 min to destroy the chlorophyll. The mixture was centrifuged and the supernatant discarded, the remaining cell pellets were extracted with 2ml dimethyl sulphoxide and 5 ml acetone. All the steps were carried out in the dark. For *P. rhodozyma* pure culture, the extraction process was conducted in the same way with an exception of chlorophyll destroying step. Astaxanthin was quantified by HPLC using a 250×4.6 mm Ultrasphere C_{18} column, the eluting solvent was ethyl acetate: methanol: water=5:18:2 (v/v/v) with a flow rate of 1 ml/min, peaks were measured at 480 mm.

Results and Discussion

Mixed cultures were compared with pure cultures of *H. pluvialis* and *P. rhodozyma* on four aspects: biomass, glucose utilization efficiency, glucose conversion rate, and astaxanthin production, just trying to find out the feasibility of combining CO_2 fixation with astaxanthin production.

Table 1. shows that the biomass concentrations of mixed cultures of *H. pluvialis* and *P. rhodozyma* were much higher than those of the two pure cultures, which were nearly the sum of the two pure cultures when glucose concentration was in the range of 3-5g/l, and increased as the glucose concentration rose. On contrast, biomass concentrations of pure cultures of *H. pluvialis* and *P. rhodozyma* decreased when glucose concentrations were higher than 10g/l and 15g/l respectively.

The reason for higher biomass production of mixed cultures may be as follow: CO_2 released through *P. rhodozyma* fermentation could be absorbed by *H. pluvialis* for photosynthesis, since the dissolved CO_2 in the culture medium is very low and could not meet the need of *H. pluvialis*, so supplementing CO_2 or sodium acetate are required. To deal with this problem, usually air or pure CO_2 were pumped into the high-cell-density microalgal cultures. In this way, however, CO_2 conversion rate is not high. While, in the mixed cultures of *H. pluvialis* and *P. rhodozyma*, CO_2 releasing and uptaking, both processes took place in the same medium, gas exchanged much easily and more efficiently. This conclusion is also confirmed by the results of glucose utilization efficiencies, as shown in Figure 1. For mixed culture and *P. rhodozyma* pure culture, glucose could be utilized totally when its concentration was below 20 g/l, but for *H. pluvialis*, glucose could not be used efficiently when the concentration was higher than 5g/l. Taking biomass concentrations and glucose conversion rates of the three cultures into account, the glucose conversion rates of mixed cultures were higher than both of the pure cultures of the two species, and lower glucose concentrations resulted in higher utilization efficiencies and conversion rates, especially when glucose concentration was between 3-5g/l (Figure 2), this is

because higher glucose concentration inhibits both *H. pluvialis* and *P. rhodozyma* growth. Therefore we can conclude that CO_2 evolved from the red yeast *P. rhodoxyma* fermentation was absorbed or fixed rapidly by the green alga *H. pluvialis* in the process of photosynthesis, the highest glucose conversion rate (52.0%) was obtained by mixed culture when glucose concentration was 3g/l, which indicates, for CO_2 fixation purpose, lower glucose concentration is more favorable and fed-batch culture techniques should be employed

.

Table 1. Biomass production of Different Cultures.

	Biomass production (DCW g/l)		
Glucose (g/l)	Mixed culture	H. pluvialis	P. rhodozyma
3	1.56±0.01	0.54±0.04	1.12±0.13
5	2.45±0.02	0.61±0.12	1.42±0.08
10	3.32±0.35	0.69±0.47	3.22±0.07
15	4.82±0.19	0.68±0.22	5.11±0.11
20	5.32±0.31	0.65±0.11	5.08±0.02
25	5.70±0.28	0.62±0.13	5.02±0.01

. Data are expressed as mean ± standard deviation of three replicates

Table 2. Astaxanthin Production of Different Cultures.

	Volumetric astaxanthin content (mg/l)		
Glucose (g/l)	Mixed culture	H. pluvialis	P. rhodozyma
3	12.95±0.11	3.68±0.16	1.09±0.03
5	8.86±0.09	2.99±0.12	1.61±0.13
10	6.50±0.15	2.34±0.17	1.95±0.11
15	5.62±0.12	2.02±0.13	2.05±0.07
20	2.15±0.08	1.96±0.04	1.51±0.02
25	2.10±0.10	1.71±0.03	1.36±0.04

. Data are expressed as mean ± standard deviation of three replicates

Table 2. summarizes the astaxanthin production of different cultures. Mixed culture could remarkably promote astaxanthin production comparing with the two pure cultures, which are more than the sum of the two single cultures when glucose concentration was in the range of 3-15g/l. Maximum volumetric astaxanthin production 12.95 mg/l was obtained by mixed culture when glucose concentration was 3mg/l, which was 3.5 and 11 times that of *H. pluvialis* and *P. rhodozyma* pure cultures respectively.

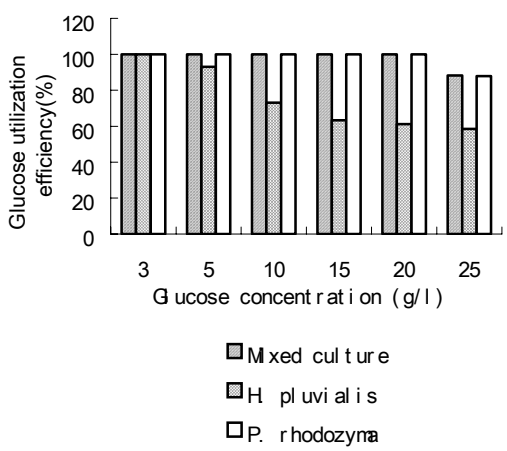

Figure 1. Glucose utilization efficiency of cultures at different glucose concentrations

The reasons for this may come from three aspects: (1) O_2 released by *H. pluvialis* in photosynthesis enhances the astaxanthin production of *P. rhodozyma*, because the conversion of carotene to astaxanthin catalyzed by ß-carotene hydroxylase and ß-carotene ketolase is oxygen-required, if O_2 supplying rate is under 30mmol/h, cell growth and astaxanthin production decline evidently, and astaxanthin production increases as O_2 concentration in the medium rises. (2) Considering biomass, nitrogen and glucose utilization efficiencies, under mixed culture regime, glucose and nitrogen were utilized efficiently, and higher biomass concentration was obtained so as to increase astaxanthin production. Furthermore, higher nitrogen utilization efficiency resulted in lower nitrogen concentration in the media, which is beneficial to astaxanthin formation both for *H.pluvialis* and *P.rhodozyma*. (3) pH in mixed culture keeps constant at 7.0 due to the interaction between *H. pluvialis* and *P. rhodozyma* which is more favorable for astaxanthin synthesis than pHs are 6.0, 8.0, and 9.0 for *H. pluvialis*.

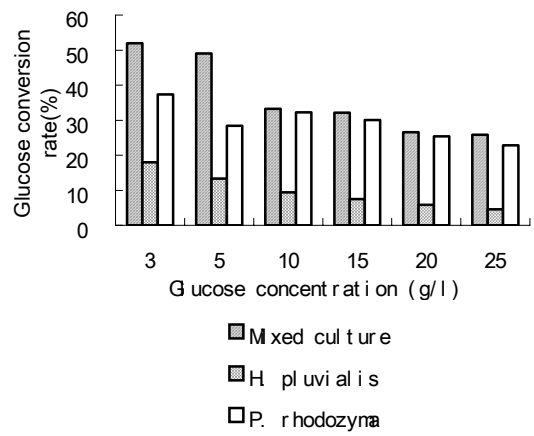

Figure 2. Glucose conversion rate of cultures at different glucose concentrations

Conclusions

Mixed culture of *H. pluvialis* and *P. rhodozyma* presents a new way for combining CO_2 fixation with high value co-product (astaxanthin) formation, promoting glucose utilization efficiency and conversion rate, keeping pH constant as well as increasing astaxanthin production. This culture regime lays a foundation for developing a new technique to put yeast or bacterium fermentation together with algae cultivation.

Acknowledgement. This project was supported by the National Natural Science Foundation of China (Grant No. 20036010).

References

(1) Benemann, J. R. Microalgae for greenhouse gas abatement: An international R&D opportunity. *Ambiente (Tpoint)*, **2003**, 1, 24-28
(2) Pulz, O. Photobioreactors: production systems for phototrophic microorganisms. *Appl. Microbiol. Biotechnol*., **2001**, 57(3), 287-293
(3) Johnson, E. A.; An, G. Astaxanthin from microbial. Sources. *Crit. Rev. Biotechnol*., **1991**, 11, 297-326
(4) Endang, K.; Philippe, G. Growth kinetics and astaxanthin production of *Phaffia rhodozyma* on glycerol as carbon source during batch fermentation. *Biotechnol. Lett*., **1998**, 20(10), 929-934
(5) Johnson, E. A.; Lewis, M. J. Astaxanthin formation by the yeast *Phaffia rhodozyma*. *J. Gen. Microbiol.*, **1979**, 115, 173-183

COMPARATIVE STUDIES ON THE PERFORMANCE OF IMMOBILIZED QUATERNARY AMMONIUM SALT CATALYSTS FOR THE ADDITION OF CARBON DIOXIDE TO GLYCIDYL METHACRYLATE

Dae-Won Park, Eun-Seon Jeong, Byung-Soo Yu, Il Kim, Kwang-Joong Oh, Sang-Wook Park

Division of Chemical Engineering, Pusan National University, Pusan 609-735, Korea

Introduction

Quaternary onium salts are widely used as phase transfer catalysts in the field of organic synthesis [1]. The quaternary onium salts bounded to polymer resins have been reported by several authors [2]. Most published works on resin-bound quaternary onium salts use styrene-divinylbenzene related resins because large amount of technology is available on these resins due to their use as ion-exchange resin support. The polymer-supported catalysts can be easily separated from reaction mixtures and can be reused, or they can be used in flow systems such as fixed-bed and fluidized-bed reactors. However, the polymer-supported catalysts have yet some drawbacks such as diffusion limitations, high cost, tendancy to swell, mechanical and thermal instability. Several inorganic supports, involving metal oxides, zeolites and clays have been substituted for polymers. Clay material has high physical strength and chemical resistance towards acid and alkali treatment [3]. Montmorillonite is one of the most widely used support for immobilized and anchored catalysts [4]. It is naturally abundant material and available as inexpensive material. Since the discovery of ordered mesoporous silica [5], there have been continuous efforts to improve their stability and catalytic performance. Recently, the incorporation of 3-choloro propyl methyl substituents on MCM-41 was reported [6].

In our previous work [7], we reported the synthesis of 4-(phenoxymethyl)-1,3-dioxane-2-one (PMEC) from CO_2 and phenyl glycidyl ether (PGE) using immobilized quaternary salt catalysts. In the present study, we studied the addition of carbon dioxide to glycidyl methacrylate (GMA). We prepared five differently supported quaternary ammonium salt catalysts to facilitate their separation after reaction. The different supports are (1) soluble poly(ST-*co*-VBC), C1 (2) insoluble poly(ST-DVB-VBC), C2 (3) macroporous poly(ST-DVB-VBC), C3 (4) poly(ST-*co*-VBC)-MMT, C4 (5) MCM-41, C5. A kinetic study on the reaction with the supported catalysts was also carried out in a semi-batch reactor with a continuous supply of carbon dioxide into the reactor.

Experimentals

The soluble polymer-supported quaternary ammonium catalysts were prepared as shown in Scheme 1. The synthesis of poly(ST-*co*-VBC) was carried out by the radical copolymerization of vinylbenzyl chloride(VBC) with styrene(ST) using 2,2'-azobis(isobutyronitrile) [AIBN]as an initiator in toluene at 60 ℃ for 5 h and then at 80 ℃ for 2 h under nitrogen, followed by precipitation into methanol and two reprecipitations from tetrahydrofuran(THF) solution into methanol. The addition of the obtained polymer(10mmol) with 15mmol of trialkylamine was performed in 15 mL of dimethylformamide(DMF) at 80 ℃ for 48 h. The resulting polymer was purified by reprecipitating twice from methanol solution into ethyl ether, and dried at 50 ℃ under vaccum.

Insoluble poly(ST-DVB-VBC) catalyst were prepared as shown in Scheme 2. A solution of gelatin(1.0 g) and 0.6 mL of 0.1% methylene blue in 100 g of water was added to a 500 mL four-neck flask fitted with a reflux condenser. A mixture of 14.6 g of ST, 0.4 g of DVB, and 0.1 g of AIBN was added dropwise to the aqueous solution. The solution was partially polymerized at 70 ^{o}C for 4 h. Then 5.0 g of VBC was added slowly with vigorous stirring (600rpm). The mixture charged with VBC was polymerized again for 17 h at 70 ^{o}C. The obtained polymer support was washed 3 times by stirring in refluxing methanol. After vacuum drying, the polymer support was placed in toluene, and trialkylamine was added to the solution.

The macroporous polystyrene beads were prepared using the same method of synthesis poly(ST-DVB-VBC). Isooctylalcohol was just added to the mixture of ST and DVB solution. The obtained polymer support was extracted by methanol to remove isooctylalcohol. After vacuum drying, trialkylamine was attached to the polymer support.

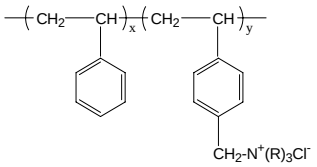

R : trialkylamine

Scheme 1

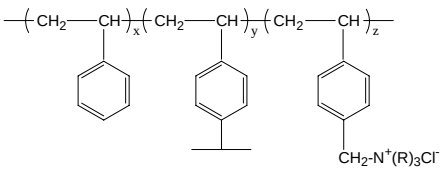

R : trialkylamine

Scheme 2

Insoluble poly(ST-co-VBC)-MMT supported catalysts are prepared as shown in Scheme 3. Poly(ST-co-VBC) was dissolved in acetone and treated with 2% trialkylamine by stirring overnight at room temperature to obtain a polymeric ammonium salt. A suspension of MMT in water was stirred overnight, and then a solution of the polymeric ammonium salt in acetone was added dropwise and stirring was continued for 24 h at room temperature. The white precipitate product was filtered, washed with acetone several times and dried at 100 ℃ under vacuum to give the ST-VBC-MMT intercalate. The quaternization was carried out with tributylamine to produce the final poly(ST-*co*-VBC)-MMT supported catalyst.

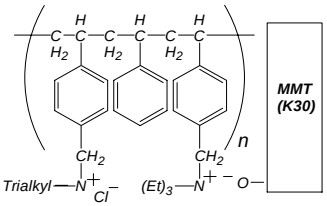

Scheme 3

Organically modified MCM-41 materials were synthesized according to a previous report[6] using a mixture of 3-chloropropyl-dimethoxymethyl silane (ClPDMMS, Shin-etsu Chemicals) and tetraethyl orthosilicate (TEOS, TCI) as Si sources.

Cetyltrimethylammonium bromide (CTMABr, TCI) was used as a template and tetra-methylammonium hydroxide (25% aqueous TMAOH, Aldrich) was used to provide alkalinity of the medium. A typical molar ratio of the various constituents in the synthesis mixture was: 4.0 TEOS : 1.5 ClPDMMS : 1.25 C_{16}TMABr : 2.5 TMA-OH : 300 H_2O. The quaternization of the 3-chloropropyl methyl modified MCM-41 was performed by the same procedure used for the other supported catalysts.

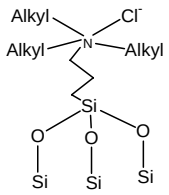

Scheme 4

Results and Discussion

The amount of quaternary ammonium salt bound to the different supports was analyzed by an elemental analyzer (Vario EL), and the results are shown in Table 1.

Table 1. The attached amount of benzyltributylammonium chloride to the supports.

Support	C1(1)	C2(2)	C3(3)	C4(4)	C5(5)
Attached amount (mmol/g)	0.894	1.087	1.326	2.200	1.720

(1) mole ratio of ST/VBC = 90/10
(2) weight ratio of ST/DVB/VBC = 73/2/25
(3) isooctylalcohol 30wt%
(4) mole ratio of ST/VBC = 30/70
(5) mole ratio of TEOS/ClPDMMS = 4/1.5

In order to study the catalytic activity of the different types of supported catalysts, the addition reaction of GMA and CO_2 was performed with the catalysts of equal amount of attached quaternary ammonium salts. Therefore, 0.2 mmol of pendant benzyltributylammonium bromide residues was used with 20 mmol of GMA. We can consider time variant conversion of GMA with different types of catalysts. The soluble poly(ST-*co*-VBC) supported catalyst, showed the highest conversion of GMA. However, this catalyst has a drawback of separation after reaction, since it needs another precipitation step for the reuse of the catalyst. Macroporous poly(ST-DVB-VBC) catalyst showed higher GMA conversion than poly(ST-DVB-VBC). Macroporous structure seems to favor the diffusion of GMA to the active site. And poly(ST-*co*-VBC)-MMT supported catalyst showed higher GMA conversion than Cl-propylmethyl-MCM-41 catalyst

For the addition reaction of CO_2 with GMA using immobilized catalysts, the following elementary reaction steps can be proposed, where we set R=GMA, P=DOMA, and QX=supported quaternary ammonium salt catalyst.

$$R + QX \underset{k_2}{\overset{k_1}{\rightleftharpoons}} RQX^* \quad (1)$$

$$RQX^* + CO_2 \xrightarrow{k_3} P + QX \quad (2)$$

k_1, k_2 and k_3 are reaction rate constants. The rate of formation of P can be written as

$$dP/dt = k_3[CO_2][RQX^*] \quad (3)$$

The active intermediate RQX* has a very short lifetime because of its high reactivity, therefore, pseudo steady state approximation can be applied. Since the addition reaction of CO_2 with GMA is carried out in a semi-batch reactor with a constant flow of CO_2, the concentration of GMA varies only because the concentration of dissolved CO_2 in solvent can be assumed constant.

$$dP/dt = k'[R][QX] \quad (4)$$

where k' is $k_1k_3[CO_2]$ / (k_2 + $k_3[CO_2]$). Since the catalyst concentration does not change during the reaction, the pseudo first-order rate equation can be applied.

$$\ln([GMA]_0/[GMA]) = kt \quad (5)$$

From the slope of the linear plot between ln ($[GMA]_0/[GMA]$) vs. time, one can estimate the pseudo first-order rate constant k. The results are summarized in Table 2. Soluble poly(ST-*co*-VBC) supported quaternary ammonium salt showed the highest reaction rate constants and the lowest activation energy.

The stability of the catalysts was tested by reusing them four successive times after separation from the reaction mixture at each experimental run. Insoluble catalysts were easily separated. However, the soluble poly(ST-*co*-VBC) was separated by precipitation in diethylether. All the catalysts maintained their catalytic activities showing less than 12 % loss of initial activity after 4th runs. Surface analysis of the used catalysts by energy dispersive spectroscopy (EDS, Jeol JXA-8600) confirmed the maintenance of chloride group bound to the polymer support after 4th run.

Table 2. First-order reaction rate constant(k) and activation energy(E) for different catalysts

Temp. (℃)	Rate constant k (h^{-1})				
	C1	C2	C3	C4	C5
80	0.383	0.111	0.137	0.067	0.051
90	0.410	0.150	0.179	0.113	0.094
100	0.485	0.210	0.208	0.169	0.144
110	0.504	0.235	0.245	0.218	0.196
E (kJ/mol)	10.31	28.14	20.79	44.09	50.56

Acknowledgement

This work was supported by the Korea Science and Engineering Foundation (R01-2003-000-10020-0), and by the Brain Korea 21 and Brain Busan 21 project.

References

1. Starks, C. M., Liotta, C. L. and Halpern, M. "Phase Transfer Catalysis", Chapman & Hall, New York (1994).
2. Akelah, A. and Moet, A. "Functionalized Polymers and Their Applications", Chapmann & Hall, London (1990).
3. Akelah, A., Rehab, A., Selim, A. and Agag, T. *J. Mol. Catal.* 94 (1994) 311.
4. Moronta, A., Ferrer, V., Quero, J., Arteaga, G. and Choren, E. *Appl. Catal. A: Gen.* 230 (2002) 127.
5. Kresge, C. T., Leonowicz, M. E., Roth, W. J., Vartuli, J. C. and Beck, J. S. *Nature* 359 (1992) 710.
6. Bhaumik, A. and Tatsumi, T. Catal. Lett. 66 (2000) 181.
7. Yu, B. S., Shin, D. H., Lee, H. S., Park, S. W. and Park, D. W. ACS Symp. 226, Preprint of Div. Environ. Chem. 43(2) (2003) 159.

ENZYMATIC CONVERSION OF CO_2 TO METHANOL: EFFECTS OF MODIFICATION OF SILICA GEL AND ADH ON ENZYME ACTIVITY

Hong Wu, Shufang Huang, and Zhongyi Jiang

School of Chemical Engineering and Technology
Tianjin University
Tianjin 300072
P.R.China

Introduction

CO_2 can be converted to methanol through an enzymatic approach in the following three steps:

$$CO_2 \xrightarrow[\text{NADH}]{F_{ate}DH} HCOOH \xrightarrow[\text{NADH}]{F_{ald}DH} HCHO \xrightarrow[\text{NADH}]{ADH} CH_3OH$$

$F_{ate}DH$, $F_{ald}DH$ and ADH are formate dehydrogenase, formaldehyde dehydrogenase and alcohol dehydrogenase respectively and are co-encapsulated in a silica gel formed by sol-gel process. Reduced nicotinamide adenine dinucleotide (NADH) is used as a terminal electron donor for each reduction step.[1,2] To understand the whole process more clearly and get the optimized results, the above three reactions are studied separately. In this paper, we concentrate on the third one.

Immobilized enzyme has advantages over free enzyme such as easy separation and reusability. However, most immobilized enzymes show lower activities than that of the free enzymes. Lower productions were also found in our study where the enzymes were immobilized in silica matrix by sol-gel process.[1] This may be due to the diffusion hindrance of the substrate from bulk solution to the gel, the accessibility hindrance of the immobilized enzyme in the three-dimensional silicate network and the microenvironment for the enzymes.

Herein, an improved sol-gel method using polyethylene glycol (PEG) as a multifunctional agent and an enzyme modification method using methoxypolyethylene glycol (mPEG) as a modifier are reported. Larger pore size and more flexible structure of the gel are expected by using the first method while more suitable microenvironment for enzyme is expected by using the second method. Mainly due to their hydrophilicity, linear structure and bio-compatability, PEG and mPEG are selected as modifiers. Modified gel properties were characterized by BET and IR and were compared with unmodified gel. Enzyme (ADH) activities after modification were investigated and compared with unmodified ones by kinetic studies of the conversion reaction of HCHO to CH_3OH.

Experimental

Synthesis of mPEG-modified ADH. 3.5 mg ADH and 10.5 mg activated mPEG were dissolved in 5 mL of 0.1 M phosphate buffer (pH7.0) and the solution was kept gently stirring for 2 h under room temperature. The degree of modification was 90% determined by using trinitrobenzene sulphonic acid (TNBS) to react with the unPEGylated amino groups and measuring the amount of the product that has a characteristic adsorption at 420nm detected by an UV-visible spectrophotometer (U-2800, Hitachi).

Preparation of gel and immobilization of ADH. The improved sol-gel immobilization processes are illustrated in **Figure 1**. It involves two ways: (1) immobilization of enzyme in modified gels and (2) immobilization of chemical modified enzymes in typical gels. For (1), mix tetraethylorthosilicate (TEOS), the precursor, with HCl, the catalyst, and PEG600 (MW=600), the gel-modifier, together first, then regulate the pH of the solution to 7.0 by adding NaOH solution to form the modified sol, and finally add a certain amount of enzyme–containing (3.5 mg/ml) 0.01 M phosphate buffer solution (pH7.0) to the sol. A transparent enzyme-containing gel was formed shortly. For (2), mix TEOS with HCl first, then regulate the pH of the solution to 7.0 by adding NaOH solution to form a typical sol, and add a certain amount of mPEG-modified enzyme–containing phosphate buffer solution to the sol. A transparent modified enzyme-containing gel was formed shortly. The gels prepared by the above two ways were aged at 4℃ for 7 days. The aged enzyme-containing gel was put into a dialysis membrane bag, dipped into 0.1 M phosphate buffer solution (pH7.0), and kept at 4℃ with frequent change of the buffer until there is no alcohol was detected by Gas Chromatographer (HP6890, Agilent). The pore size of the gel and its chemical structure were measured by BET (CHEMBET-3000, QUZNTA CHROME) and IR (Nicolet-560, MAGNA-IR) respectively.

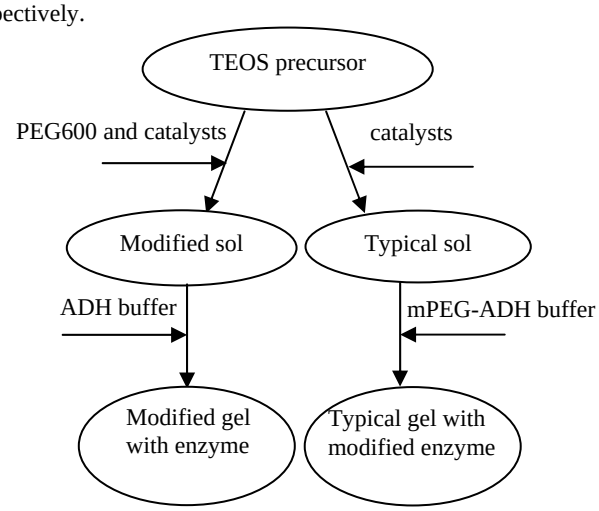

Figure 1. Sol-gel immobilization processes.

Enzymatic reactions. Enzyme activities of ADH were evaluated based on the reaction rates and kinetic Michaelis constants (K_m) of the reduction of HCHO to CH_3OH. Since, during the reaction, the cofactor (NADH), which has a characteristic adsorption at 340 nm, will be converted to NAD^+ that has no adsorption at 340 nm, the reaction progress can be recorded by the detection of the amount of NADH. A UV-visible spectrophotometer (U-2800, Hitachi) was employed to determine the reduction of the concentration of NADH and the reaction rates were calculated accordingly. At 25℃ and pH7.0, by varying the concentration of NADH from 50 to 250 μM and HCHO form 3 to 30 mM, kinetic parameters were obtained based on the ordered mechanism proposed by Dalziel.[3]

Results and Discussion

Structure characterization of gels. The pore size distribution of typical gel and PEG-modified gel are given in **Figure 2**. The average pore size of PEG-modified gel (4.67nm) is larger than that of the typical gel (3.88nm). This is due to the linking function of the PEG between sol particles, resulting in a branched structure with larger mesopores. The infrared spectra of the PEG-modified gels (**Figure 3**) show no new bonds formed, indicating that the linkage between PEG and silica sol particles was by molecular forces or hydrogen bonds.

Stability of free ADH and mPEG-modified ADH in alcohol. The sol-gel process using TEOS as the precursor will produce ethanol

that is harmful for enzyme. The alcohol toleration of both native and mPEG-modified ADH were studied by measuring their reacting activities of free enzymes. After being immersed in 1% ethanol solution for 2 minutes, the mPEG-modified ADH maintained 50% of its original activity, while the native ADH retained 36% of its original one. This denotes that such chemical modification of ADH by mPEG is a valid and significant means of stabilizing ADH in alcohol solutions. This may be due to the less flexibility of the enzyme with a long-chain PEG molecule linked to its surface, leading to steric hindrance of protein unfolding. And also, the hydrophilicity of PEG may provide a more hydrophilic microenvironment that is more preferable for enzyme to stay and function.

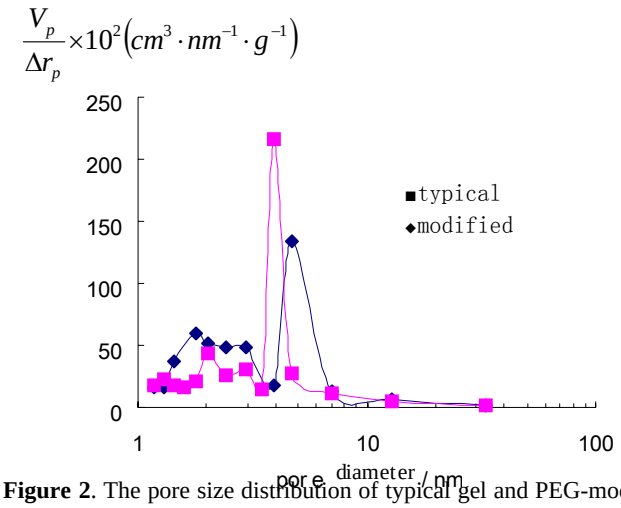

Figure 2. The pore size distribution of typical gel and PEG-modified gel.

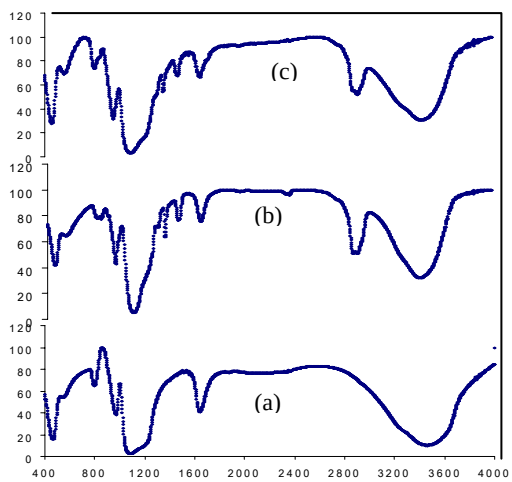

Figure 3. The infrared spectra of (a) typical gel; (b) PEG-modified gel and (c) mPEG-containing gel.

Storage stability of immobilized ADH. As shown in **Figure 4**, the activity of the native ADH encapsulated in typical silica gel was reduced by 17% after 92 days of storage. In contrast, the enzyme activities of ADH in PEG-modified gel and mPEG-modified ADH in typical gel almost showed no decrease after storage for the same period. This may be due to the same reasons mentioned above.

Kinetic parameters. Experimental results showed that all the enzymatic reactions followed Michaelis-Menten kinetics and the kinetic parameters were calculated by Dalziel's double-substrate

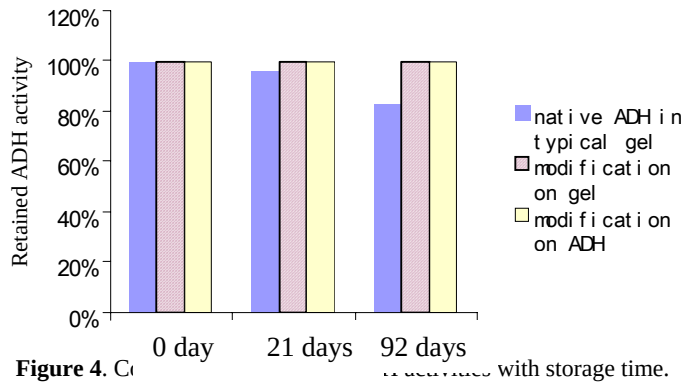

Figure 4. C activities with storage time.

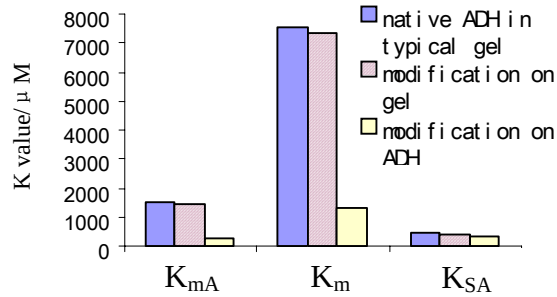

Figure 5. The kinetic Michaelis constants of reactions catalyzed by ADH.

model. Kinetic constants were shown and compared in **Figure 5**. K_{mA} is the Michaelis constant of NADH, while K_{mB} the Michaelis constant of HCHO and K_{SA} the dissociation constant of ADH-NADH pairs. The lower the K_m is, the higher activity the immobilized ADH is. Compared with the unmodified ADH in unmodified gel, both of the two improvement methods work. The mPEG-modified ADH encapsulated in typical gel showed the highest activity among the three cases, indicating that the modification on ADH (improvement method (2)) seems to have a greater effect than the modification on gel (improvement method (1)).

The catalytic activity of ADH immobilized in PEG-modified gel is higher than that in typical gel. This may mainly be attributed to the easier diffusion resulted from the enlarged pore size. These enlarged pores are considered to be more "comfortable" for enzymes to stay and also easier for substrate to diffuse through the pore channel and access to the enzymes. In addition, the improved gel properties such as hydrophilicity and mechanical strength may also provide higher biocompatibility for enzymes.

Acknowledgment

This work was supported by the National Natural Science Foundation of China (No.20176039).

References

1. Obert, R., Dave, B. C., *J. Am. Chem. Soc.*, **1999**, *121*, 12192-3.
2. Wu, H., Jiang, Z. Y., Xu, S. W., Huang, S. F., *Chinese Chemical Letters*, **2003**. *14*(4): p. 423-5.
3. Dalziel, K., *The Journal of Biological Chemical*, **1963**, *238*(8), 2850-3.

USE OF IMIDAZOLIUM TRANSITION METAL HALIDES IN THE SYNTHESIS OF CYCLIC CARBONATES FROM THE COUPLING REACTION OF EPOXIDE AND CO_2

Hoon Sik Kim, O-Sung Kwon, Hyunjoo Lee and Jelliarko Palgunadi

Reaction Media Research Center
Korea Institute of Science and Technology
39-1, Hawolgokdong, Seongbukgu,
Seoul, 136-791, Korea

Introduction

The synthesis of cyclic carbonates by the coupling reactions of epoxides with carbon dioxide has attracted much attention with regard to the utilization of CO_2, which is a responsible for global warming.[1] The importance of cyclic carbonates is increased due to their versatile utilization in many application areas. For instance, they can be used as aprotic polar solvents, electrolytes in secondary and fuel-cell batteries, and valuable raw materials in a wide range of chemical reactions.[2, 3] Accordingly, much efforts have been made on the catalyst development for the synthesis of cyclic carbonates *via* coupling reactions has been reported.[4] While the advances have been significant, there still remain many subjects to be improved in terms of catalytic activity, stability, and recovery of catalyst.

Recently, there have been a considerable number of articles regarding the use of ionic liquids as environmentally benign media in separation, extractions, electrochemistry, and immobilization of homogeneous catalysts.[5] Imidazolium-based ionic liquids have also been introduced as effective catalysts for the synthesis of propylene carbonate from the coupling reaction of propylene oxide and CO_2, but their catalytic activities were not high enough for the industrial purpose.[6]

With a hope to develop highly active catalysts for the coupling reactions, we have imidazolium metal halide complexes and tested their activities for the production of cyclic carbonates from the coupling reactions of epoxides and CO_2. Herein, we report the synthesis and reactivity of a series of ionic liquid-derived imidazolium metal halide complexes consisting of 1-alkyl-3-methylimidazolium cations and metal halide anion.

Experimental

Synthesis of (1,3-dimethylimidazolium)$_2$ZnBr$_2$Cl$_2$. A solution of (1,3-dimethylimidazolium)Cl[7] (2.10 g, 15.83 mmol) in methylene chloride (25 mL) was mixed with a solution of $ZnBr_2$ (1.78 g, 7.90 mmol) in tetrahydrofurane (25 mL) and heated to reflux for 3 h. After cooling to room temperature, the white precipitate was collected by filtration. Yield: 93.9 %; elemental analysis cald.(%) for $C_{10}H_{18}Br_2Cl_2N_4Zn$: C 24.49, H 3.70, Br 32.59, Cl 14.46, N 11.43, Zn 13.33; found: C 24.23, H 3.75, Br 31.83, Cl 14.18, N 11.18, Zn 13.43;

All other imidazolium metal halides were similarly prepared.

Coupling reactions of epoxide and CO_2. The coupling reactions were conducted in a 200 mL stainless-steel bomb reactor equipped with a magnetic stir bar and an electrical heater. The reactor was charged with an appropriate catalyst and an epoxide and pressurized with CO_2. The bomb was then heated to a specified reaction temperature with the addition of CO_2 from a reservoir tank to maintain a constant pressure. After the reaction, the bomb was cooled down to room temperature, and the product mixture was analyzed by Hewlett Packard 6890 gas chromatography equipped with a flame ionized detector and a DB-wax column, and Hewlett Packard 6890-5973 MSD GC-mass spectrometry.

Results and Discussion

As shown in equation (1), a series of imidazolium metal halides, (1-R-3-methylimidazolium)$_b$MX$_a$Y$_b$ (M = Zn, Fe, Mn, In; R = CH_3, C_2H_5, *n*-C_4H_9, $CH_2C_6H_5$; X, Y = Cl, Br; a, b = 2, 3) were prepared by reacting MX$_a$ (X = Cl, Br) with (1-R-3-methylimidazolium)Y (R = CH_3, C_2H_5, *n*-C_4H_9, $CH_2C_6H_5$; Y = Cl, Br) at an ambient temperature or at reflux depending on the nature of halide groups.

R = CH_3, C_2H_5, *n*-C_4H_9, $CH_2C_6H_5$; X, Y = Cl, Br; a, b = 2, 3
M = Zn, Fe, Mn, In

Interestingly, (1-R-3-methylimidazolium)$_b$MX$_a$Y$_b$ was also obtained when MX$_a$ and (1-R-3-methylimidazolium)X were reacted. For example, (1-butyl-3-methylimidazolium)$_2$ZnBr$_2$Cl$_2$, can be obtained either from the reaction of $ZnCl_2$ and (1-butyl-3-methylimidazolium)Br or from the reaction of $ZnBr_2$ and (1-butyl-3-methylimidazolium)Cl.

The catalytic activities of various imidazolium metal halides were evaluated for the coupling reactions of CO_2 and ethylene oxide (EO) or propylene oxide (PO) at 100 ℃ for 1 h.

As shown in Table 1, imidazolium halides and metal halides were hardly able to catalyze the coupling reactions when they were used alone. However, the combination of metal halide with imidazolium halide exhibited much higher activity for the coupling reactions (entry 1-3). Among (1-R-3-methylimidazolium)$_b$MX$_a$Y$_b$ tested, imidazolium zinc tetrahalide exhibited the highest activities. Such enhanced activities are most likely to be attributed to the in situ formation of new active complexes, bis(1-butyl-3-methylimidazolium) zinc tetrahalides from 1-butyl-3-methylimidazolium halide and $ZnBr_2$. This is supported by the fact that (1-butyl-3-methylimidazolium)$_2$ZnBr$_2$Cl$_2$ and (1-butyl-3-methylimidazolium)$_2$ZnBr$_4$ show similar activities to the corresponding catalytic systems of 1-butyl-3-methylimidazolium chloride-$ZnBr_2$ and 1-butyl-3-methylimidazolium bromide-$ZnBr_2$ (entry 9-10). By-products such as polyalkylene oxides and halogenated compounds were not detected by GC and GPC analysis.

The catalytic activities of imidazolium metal halides were greatly influenced by the nature of halide ions bonded to metal atom. The order of reactivity was found to be in the following order: $[ZnBr_4]^{2-}$ > $[ZnBr_2Cl_2]^{2-}$ >> $[ZnCl_4]^{2-}$, suggesting the importance of the nucleophilicity of halide ions. The nucleophilicity of halide ions is likely to be enhanced by the presence of imidazolium cations.

The dissociation of a halide ion and the following attack of the dissociated halide ion on the carbon atom of the coordinated ethylene oxide would take place more easily for more nucleophilic bromide ion.[8] Interestingly, the effect of the alkyl groups on the imidazolium cations is relatively small and can be negligible.

Table 1. Catalytic activities of imidazolium metal halides for the coupling reactions of CO_2 and epoxides[a]

Entry	Catalyst	TOF(h^{-1})[b]	
		EO	PO
1	(1-butyl-3-methylimidazolium)Br	78	37
2[c]	MX_a	n.r.[d]	n.r.[d]
3	(1-butyl-3-methylimidazolium)$_2$ $ZnBr_2Cl_2$	2112	1295
4	(1,3-dimethylimidazolium)$_2ZnBr_2Cl_2$	2697	1001
5	(1-ethyl-3-methylimidazolium)$_2ZnBr_2Cl_2$	2137	1335
6	(1-ethyl-3-methylimidazolium)$_2ZnBr_4$	3588	1617
7	(1-ethyl-3-methylimidazolium)$_2ZnCl_4$	2538	1352
8	(1-ethyl-3-methylimidazolium)$_2MnBr_2Cl_2$	210	79
9	(1-benzyl-3-methylimidazolium)$_2MnBr_4$	2527	1201
10[e]	(1-butyl-3-methylimidazolium)$_3FeBr_3Cl_3$	697	410
11[e]	(1-ethyl-3-methylimidazolium)$_2FeBr_4$	923	439
12[e]	(1-benzyl-3-methylimidazolium)$_3InBr_3Cl_3$	790	359

[a] Reactions were carried out at 100 ℃ and 3.5 MPa of CO_2 for 1 h. Molar ratios of epoxide to imidazolium metal halide complex were set at EO/catalyst = 5,000 and PO/catalyst = 2,000. [b] TOF(h^{-1}): moles of alkylene carbonate/moles of catalyst/hour. [c] MX_a = $ZnBr_2$, $FeBr_3$, $InBr_3$. [d] No reaction. [e] Molar ratios of EO/catalyst = 1,000, PO/catalyst = 500.

The coupling reactions of various epoxides with CO_2 were also conducted in the presence of a imidazolium metal halide, (1-ethyl-3-methylimidazolium)$_2ZnBr_2Cl_2$. As shown in Table 2, corresponding carbonates were produced in high yields and selectivities except for tert-butyl glycidyl ether and glycidyl isopropyl ether. The lower reactivity of tert-butyl glycidyl ether and glycidyl isopropyl ether is likely due to the crowdness around epoxide, which might prevent the attack of CO_2 on the coordinated epoxide.[9] In fact, the yields of cyclic carbonates decreased with increasing bulkiness of the substituent on the epoxide group (entry 1, 2 and 4).

Table 2. Results of catalytic formations of alkylene carbonates from various epoxides by (1-ethyl-3-methylimidazolium)$_2$-$ZnBr_2Cl_2$[a]

Entry	Substrate	yield(%)	Selectivity(%)	TOF(h^{-1})
1	1,2-epoxybutane	98	100	490
2	Tert-butyl glycidyl ether	11	97	55
3	Epichlorohydrin	77	100	385
4	Glycidyl isopropyl ether	23	98	115
5	Styrene oxide	77	99	385
6	Glycidyl methacrylate	98	100	490

[a] Reactions were carried out at 100°C and 500 psig of CO_2 for 1 h. Molar ratio of epoxide to zinc was set at 500. [b] TOF(h^{-1}): moles of cyclic carbonate/moles of catalyst/hour.

Previous reports by Kisch on the synthesis of cyclic carbonates from CO_2 and epoxide suggested the parallel requirement of both Lewis acid-activation of epoxide and Lewis base-activation of CO_2.[9] In the case of imidazolium metal halide-catalyzed reaction, metal center is expected to act as a Lewis acid for the coordination of an epoxide and halide ion is expected to act as a Lewis base to ring-open the coordinated epoxide. The plausible mechanism for the coupling reaction catalyzed by an imidazolium metal halide [MX_2Y_2] is depicted in scheme 1.

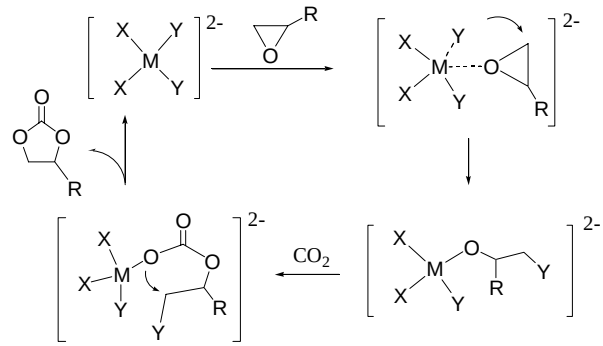

Scheme 1. Proposed reaction mechanism for the coupling reaction of ethylene oxide with CO_2 catalyzed by (1-R-3-ethylimidazolium)$_2$- MX_2Y_2.

Conclusions

A series of ionic liquid-based imidazolium metal halide, (1-R-3-methylimidazolium)$_b$$MX_aY_b$ (M = Zn, Fe, Mn, In; R = CH_3, C_2H_5, *n*-C_4H_9, $CH_2C_6H_5$; X, Y = Cl, Br; a, b = 2, 3), prepared from the reaction of MX_a with (1-R-3-methylimidazolium)Y were effective for the coupling reaction of epoxides and CO_2. The catalytic activity of (1-R-3-methylimidazolium)$_b$$MX_aY_b$ was found to increase with increasing nucleophilicity of halide ion. But, the substitution on the imidazolium cation showed a negligible effect on the catalytic activity.

Acknowledgement

This work was financially supported by the Ministry of Environment of Korea and Honam Petrochemical Co.

References

(1) Darensberg, D. J.; Holtcamp, M. W. *Coord. Chem. Rev.* **1996,** *153*, 155.
(2) Shaikh, S. *Chem. Rev.* **1996**, *96*, 951.
(3) Inaba, M.; Siroma, Z.; Funabiki, A.; Asano, M. *Langmuir* **1996,** *12*, 1535.
(4) (a) Kim, H. S.; Kim, J. J.; Kwon, H. N.; Chung, M. J.; Lee, B. G. Jang, H. G. J. Catal. **2002**, *205*, 226. (b) Paddock, R.; Nguyen, S. *J. Am. Chem. Soc*. **2001**, *123*, 11498. (c) Kim, H. S.; Kim, J. J.; Lee, B. G.; Jung, O. S.; Jang, H. G. Jang, Kang, S. O. *Angew. Chem. Int. Ed.*, **2002**, *39*, 4096. (d) Yamaguchi, K.; Ebitani, K.; Yoshida, T,; Yoshida, H.; Kaneda, K. *J. Am. Chem. Soc.* **1999**, *121*, 4526.
(5) Rogers, R. D.; Seddon, K. R. "Ionic liquid: Industrial Applications to Green Chemistry", ACS symposium series 818, American Chemical Society, Washington DC, **2002**.
(6) Peng, J.; Deng, Y. *New J. Chem.* **2001,** *25*, 639.
(7) Hasan, M.; Kozhevnikov, I. V.; Siddiqui, M. R. H.; Steiner, A.; Winterton, N. *Inorg. Chem.* **1999**, *38*, 5637.
(8) Calo, V.; Nacci, A.; Monopoli, A.; Fanizzi A. *Org. Lett*. **2002**, *4*, 2561.
(9) Kim, M. R.; Jeon, S. R.; Park, D. W.; Lee, J. K. *J. Ind. Eng. Chem*. **1998**, *4*, 122.
(10) (a) Dümler, W.; Kisch, H. *Chem. Ber*. **1990**, *123*, 277. (b) Kisch, H.; Millini, R.; Wang, I. J. *Chem. Ber*. **1986**, *119*, 1090. (c) Ratzenhofer, M.; Kisch, H. *Angew. Chem. Int. Ed. Engl.*, **1980**, *19*, 317.

The Co-activation of CH_4 and CO_2 To Syngas and Ethylene Simultaneously

Changwei Hu, Haili Zhang , Jingjing Wu

Sichuan Key Laboratory of Green Chemistry and Technology,
College of Chemistry, Sichuan University, Chengdu 610064, China

Introduction

Recently, the activation and co-activation of CH_4 and CO_2 have received much attention for environmental and industrial reasons[1-3]. Previous studies focused either on the production of syngas or ethylene. Syngas could be produced either from the partial oxidation or CO_2 reforming of CH_4 over several kinds of catalyst, and ethylene could also be fabricated from the partial oxidation of CH_4 by both O_2 and CO_2. However, in CO_2 reforming of CH_4, the deactivation of the catalyst by coke formation reserves a great challenge in the development of a practical catalyst, and in the partial oxidation of CH_4 to produce ethylene, the deep oxidation forming carbon oxides is inevitable. In order to activate the two green house gases simultaneously and make effective use of both of them, a new process, that is, activating the two gases simultaneously to produce ethylene and syngas, is proposed in present work. The overall reaction could be written as: $5CH_4+CO_2+2O_2 \rightarrow 2CO+2H_2+2C_2H_4+4H_2O$. This path has the following advantages: (1) The reforming of methane with CO_2 is an endothermic reaction, and in contrast, the partial oxidation of methane by O_2 is exothermic. While the proposed process combines the partial oxidation and CO_2 reforming of methane together, resulting in a compensation of heat required and even achieving a thermo-neutral reaction by manipulating the CH_4:CO_2:O_2 ratio[4]. (2) The products (the mixture of CO, H_2 and C_2H_4 with proper ratio) formed from the reaction mentioned above could be used to the synthesis of propanal, and the atom utilization of the later reaction is 100% and the commercial value of natural gas and carbon dioxide could then be elevated. (3) The presence of O_2 in the combination process decreases coke formation [5], though it is a serious and general problem in CO_2 reforming of methane.

Experiment

Catalysts preparation

(1)Grind catalysts. TiO_2 and CeO_2 are ground to 20-40 mesh and impregnated with aqueous solution of the corresponding metal nitrate for 24h. The pastes were dried in vacuum and calcined in air flow for 3h at 500℃ before use.

(2) Monolithic catalysts. Various supports mentioned above were ground to >80 mesh, and treated in a similar way as the preparation of conventional grind catalysts before coating. Cordierite support was cut into small column (length 25mm, diameter 12mm) and impregnated by the paste of the above sample by a special process to coat the catalytic components on the cordierite, and then the sample is dried and calcined at 500℃. A thin surface layer was formed on cordierite

The catalytic reaction

The reaction was carried out in a tubular fixed-bed quartz reactor (15mm o.d., 12.5mm i.d.) under atmospheric pressure. The mole ratio of CH_4、CO_2 and O_2 was controlled to be 1:1:1 with a GHSV of 10^4h^{-1}. The analysis of the effluents mixture was performed by a 1790 gas chromatograph with a plot-C2000 capillary column on line, and a microcomputer was used to quantify the composition.

Results and discussion

It is observed that CO、H_2 and C_2H_4 formed simultaneously on the catalysts investigated in present work. The catalytic activity and C_2H_4 selectivity on the catalysts over the temperature range of 650℃-800℃ are shown in Figure 1 and Figure 2. It is seen that both CH_4 conversion and C_2H_4 selectivity are improved with increasing reaction temperature. On the catalyst Ca-Ni/TiO_2(Ca, 21wt%; Ni, 0.15wt%), CH_4 conversion increases monotonically with increasing temperature over the temperature range tested, while C_2H_4 selectivity increases initially and reaches its maximum value at 770℃. Nevertheless, on the catalyst Ca-Ni*/TiO_2 (Ca,14wt%; Ni, 0.1wt%), the C_2H_4 selectivity increases monotonically with increasing temperature while CH_4 conversion shows its maximum value at 750℃. Higher surface area TiO_2 is also used to prepare Ca-Ni/TiO_2

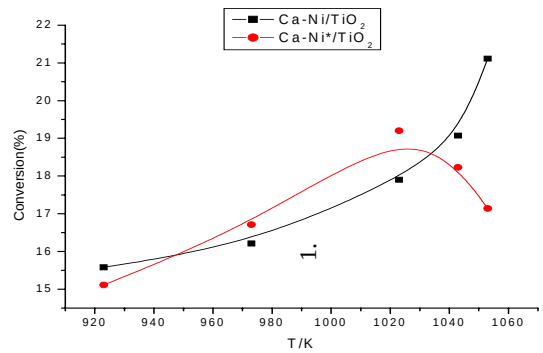

Figure 1 The variation of CH_4 conversion with increasing

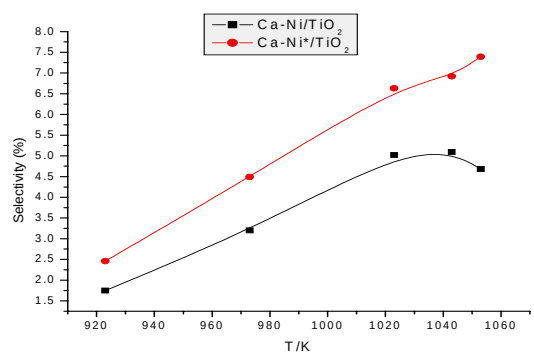

Figure 2 The variation of C_2H_4 selectivity with increasing temperature

catalyst, and it is found that CH_4 conversion and C_2H_4 selectivity are obviously improved and C_2H_4 yield could reach 3.7%. $NaWO_4$ is considered to be an effective promoter in the partial oxidation of CH_4 to ethylene[6], it is used to modified Ca-Ni/TiO_2* system in present work, the resulting catalyst exhibit higher C_2H_4 selectivity, but C_2H_6 is also detected in the efluent. Monolithic cordierite show better mechanical intensity and thermal stability than conventional grind supports, and monolithic catalysts were widely used in the purification of vehicle's exhaust gas and methane combustion, but there are few reports in partial oxidation of methane.[7] In present work, monolithic supported catalysts containing Ni/CeO_2 and Ca/TiO_2 is prepared and used to co-activate methane and CO_2. It is interesting

that the grind forms of Ni/CeO_2 and Ca/TiO_2 show no activity to the target reaction, but they become active when prepared into monolithic catalysts, CO、H_2 and C_2H_4 are obtained at the same time indicating a process intensification effect. Monolithic supported Ca-Ni/TiO_2 catalyst shows activity at about 750℃, and at 770℃, C_2H_4 selectivity reaches 4.3%, and the mole ratio of CO,H_2 and C_2H_4 is 88.5:7.15:4.3.

Conclusions

The simultaneous production of ethylene and syngas from the co-activation of CH_4 and CO_2 is realized over conventional grind Ca-Ni/TiO_2 catalyst. The composition of the catalyst affects the activity and selectivity. The optimal temperature for higher ethylene selectivity over the catalyst Ca-Ni/TiO_2(Ca, 21wt%; Ni, 0.15wt%) is about 770 ℃ .High surface area TiO_2 and $NaWO_4$ promoter is beneficial for the formation of ethylene. Monolithic supported Ni/CeO_2 and Ca/TiO_2 catalysts are also effective in the co-activation of methane and CO_2 simultaneously to ethylene and syngas. Process intensification may be important for the co-activation of methane and carbon dioxide.

Acknowledgement

The authors are grateful for the financial support by the NNSFC (No.20243006), The Special Research Foundation of Doctoral Education of China (No. 2000061028) and the TRAPOYT (2002)

References

(1) Wang Y.,, Yoshimoto, Takahashi, Ohtsuka Y., *J. Catal.* **1999**, *128*, 160
(2) Cheng Z. X., Zhao X. G., Li J. L., Zhu Q.M., *Appl. Catal.* **2001**, *205*, 31
(3) Kus S., Otremba M., Torz A.,Wski M. T. *Appl. Catal. A* **2002**, *230*, 263
(4) Vernon P. D. F., Green M. L. H., Cheetham A. K., Ashcroft A. T., *Catal. Today* **1992**, *13*, 417
(5) Choudhary V.R., Rajput A.M., Prabhakar B., *Catal. Lett.* **1995,** *32*, 391
(6) Jia S. F., Xiao T. C., Li S. B., Xu C. Z., Hou R. L., Coleman K. S., Green M.L.H., *Appl.Catal.A* **2002**, *225*, 271
(7) Tang X. L., Zhang X., Chen Y. Q., Gong M. C., Zhou S. R., Zheng L., Li X. W., *Tian Ran Qi Hua Gong (Chinese)* **2000**, *25*, 4

The Potential of the CO_2 reforming of CH_4 as a method of CO_2 mitigation. A thermodynamic study.

Damien Treacy, Julian R.H. Ross

Centre for Environmental Research,
University of Limerick,
Ireland.

1. Introduction.

Carbon dioxide (CO_2) has been identified as the most significant greenhouse gas arising from anthropogenic activities. Presently, atmospheric levels of CO_2 are thought to be about 25% higher than in pre-industrial times [1]. It is of great importance to reduce anthropogenic CO_2 emissions in order to counteract global warming. In many countries (7 in the EU) a tax related to CO_2 emissions has been introduced in order to encourage better plant efficiency and/or create increased investment in CO_2 mitigation. One method of accomplishing a reduction in CO_2 emissions is fuel switching. As an example, if naphtha is used as a fuel, the following combustion reaction takes place:

$C_{10}H_8 + 12O_2 \rightarrow 10CO_2 + 4H_2O \quad \Delta H^0_{298K} = -5134KJ$ (1)

and 0.085g of CO_2 is released per KJ of energy produced. If the naphtha is replaced with a low-carbon containing fuel such as natural gas the energy:CO_2 ratio becomes more favourable with 0.055g of CO_2 produced per KJ of energy released.

$CH_4 + 2O_2 \rightarrow CO_2 + 2H_2O \quad \Delta H^0_{298K} = -800KJ$ (2)

In the long term one must consider more innovative options for anthropogenic CO_2 reduction. One such method, which is presently being extensively investigated, is the sequestration of CO_2 produced by concentrated sources (such as industry and power stations) and the subsequent disposal of the trapped CO_2 in reservoirs such as the deep sea or in aquifers [3,4]. Ocean disposal is seen as the method with the greatest long-term application possibilities. However there are a number of relevant concerns about this method of CO_2 disposal: how much of the sequestered CO_2 will be returned to the atmosphere and when will it be returned? According to Adams *et al.* [5] the atmosphere and the ocean eventually equilibrate on a timescale of about 1000 years regardless of where the CO_2 is originally discharged. Wong *et al.* [4] estimated that the disposal of CO_2 in to the intermediate waters of the North Pacific would buy only 20-50 years of CO_2 reduction. Another option which may aid in the reduction of CO_2 emissions is the fixation of CO_2 as a chemical. The advantage of CO_2 utilisation (fixation) over CO_2 disposal is that the production of chemicals with an economic value is possible. Aresta *et al.* [6,7] have done extensive research in this area. They have shown that the production of materials such as carbamic esters, urea and methylamines can be produced from CO_2 feedstocks.

Another reaction which consumes CO_2 is the dry reforming of natural gas (CH_4).

$CO_2 + CH_4 \rightarrow 2CO + 2H_2$ (3)

This paper assesses whether dry reforming can be viably used as a method of CO_2 mitigation. We have calculated all-over energy balances for a number of all over process scenarios involving the production of synthesis gas followed by the production of some other product (methanol, sulphur-free diesel and carbon).

2. Methods of Analysis.

Much of the work carried out on dry reforming of CH_4 has been justified by the argument that the reaction offers a route for the conversion of large amounts of CO_2. The product of reaction (3), synthesis gas, is an equimolar mixture of CO and H_2. Synthesis gas can be used to produce higher value products, most notably sulphur free diesel (4), via Fischer-Tropsch synthesis, and methanol (5).

$nCO + (2n + 1)H_2 \rightarrow C_nH_{(2n+2)} + nH_2O$ (4)

$CO + 2H_2 \rightarrow CH_3OH$ (5)

Both of these reactions ((4) and (5)) require H_2 to be added to the reactant synthesis gas feed in order to establish the correct reactant ratio. This hydrogen would usually be supplied by the steam reforming of CH_4 (6).

$CH_4 + H_2O \rightarrow 3H_2 + CO$ (6)

CO_2 and CH_4 are both relatively stable compounds with low potential energies. As a result the dry reforming reaction is highly endothermic and so energy has to be provided in order to drive it in the forward direction. Similarly, the steam reforming of CH_4 is also an endothermic reaction. The most likely energy source to drive these reactions will be the combustion of natural gas (2) and this process, in itself, produces CO_2.

In these calculations we assume CO_2 and steam reforming operate in parallel to form the necessary ratio of synthesis gas to produce; (i) methanol, (ii) sulphur free diesel, represented simply as C_6H_{12} , and (iii) carbon.

In the case of carbon production the process could occur directly via reaction (8);

$CH_4 + CO_2 \rightarrow 2C + 2H_2O$ (7)

or more likely by the production of synthesis gas (3) followed by the reduction of CO (9).

$2CO + 2H_2 \rightarrow 2C + 2H_2O$ (8)

The carbon all-over process does not require additional steam reforming, as the synthesis gas ratio required for reaction (8) is 1.

In these calculations we assumed an all-over energy efficiency of 80%, i.e. 80% of the energy released from the exothermic final reaction step (e.g methanol synthesis) can be recycled to drive the endothermic reforming steps. The remainder of the energy required can be attained from the combustion of natural gas (also at an 80% energy efficiency). For simplicity, we have calculated the enthalpies for the processes involved at a single temperature of 773K. This temperature represents a compromise between the low and high temperature steps (the final reaction and the reforming steps respectively) likely to be involved in the all-over process. For example, methanol is produced by the Synetix (formerly ICI) process in the temperature range 473-573K [7], while reforming reactions are usually carried out in the temperature range 973-1223K [8].

(i) Methanol Synthesis.

In this study methanol is assumed to be produced in two steps. The first step involves the formation of synthesis gas via the combined steam and CO_2 reforming of CH_4 (reactions (3) and (6)). Following the reforming step, methanol is synthesised by reacting the resultant synthesis gas (CO and H_2). This all-over process can be summarised by the following reaction equation;

$CH_4 + CO_2 + 2H_2O + 177KJ \rightarrow 4CH_3OH$ [i.e. $\Delta H^0_{773K} = 177KJ$] (9)

When the heat efficiency of the system is assumed to be 80%, the heat required to drive the reaction increases to 221KJ. This means for 1 mole of CO_2 to be consumed by reaction (9), a heat input of 221KJ is required from an external source. This usually is obtained by combusting natural gas;

$CH_4 + 2O_2 \rightarrow CO_2 + 2H_2O + 800KJ$ [i.e. $\Delta H^0_{773K} = 800KJ$] (2)

This implies that 0.34 moles of CO_2 will be released so as to provide the required energy to drive the all-over methanol synthesis reaction (9).

Therefore the all-over amount of CO_2 consumed in methanol synthesis process is 0.66 moles per mole of CO_2 consumed by the initial reforming of CH_4.

(ii) Sulphur Free Diesel (Fischer-Tropsch Synthesis).
Again this reaction occurs in two steps; the first being the reforming of CH_4 to produce synthesis gas while in the second step the resultant synthesis gas is reacted to produce higher hydrocarbons (C_6H_{12}).
This all over energy process can be represented by reaction (10);
$3CH_4 + CO_2 + H_2O + 23KJ \rightarrow 0.667C_6H_{12} + 3H_2O$ [i.e. ΔH^0_{773K} = 23KJ] (10)
At an energy efficiency of 80%, the amount of energy required to drive reaction (10) is 28.8KJ. This energy is supplied by combusting CH_4 at the expense of 0.05 moles of CO_2 per mole of CO_2 consumed in the Fischer-Tropsch process. Therefore 0.95 moles of CO_2 are mitigated in this process per mole of CO_2 consumed in the initial reforming step.
(iii) Carbon production
This all-over reaction scheme differs from the previous two, as steam reforming is not necessary to provide additional H_2.
$CH_4 + CO_2 \rightarrow 2C + 2H_2O + 12.5KJ$ [i.e. ΔH^0_{773K} = -12KJ] (8)
$\Delta H^0 < 0$ at the reaction temperature examined (indeed $\Delta H^0 < 0$ for all temperatures) and as a result there is no need for additional CH_4 combustion. For every mole of CO_2 consumed in reaction (11) one mole of CO_2 is mitigated.

3. Discussion.
Although there were a number of gross approximations made in calculating the all-over energy results presented in this paper, the results are very informative and may inevitably lead to one gaining a greater understanding of the environmental benefits, if any, of CO_2 reforming.
3.1 Methanol Synthesis.
CO_2 reforming when used in parallel with steam reforming can produce synthesis gas with a CO/H_2 ratio suitable for methanol synthesis or in Fischer-Tropsch synthesis. The all-over methanol synthesis process enables, theoretically, 0.66 moles of CO_2 to be mitigated per mole of CO_2 consumed in the initial reforming stage. A 66% reduction of CO_2 per mole of CO_2 reacted seems a favourable result in terms of CO_2 mitigation. Methanol is a very useful commodity, with a worldwide annual production of approximately 30 million tonnes [7,9]. Industrially methanol is synthesised in a process where synthesis gas is produced solely by the steam reforming of CH_4 [7]. If all the methanol production in the world were to be shifted to a process which combined CO_2 and steam reforming, 10 million tonnes of CO_2 could be consumed in this process. This would correspond to the mitigation of 6.6 million tonnes of CO_2 annually. However this amount of CO_2 is rather insignificant in comparison to global CO_2 emissions; excluding deforestation and land use change CO_2 emissions amounted to 23.9 giga tonnes in 1996 [10]. Therefore an equivalent reduction in global CO_2 emissions of 0.0027% is possible by producing methanol via the CO_2 reforming of natural gas. Unless vast new markets are created for methanol, this method does not constitute a viable potential method of CO_2 mitigation.
3.2 Fischer-Tropsch Synthesis.
Fischer-Tropsch synthesis date back to the nineteen twenties when Fischer and Tropsch first published results concerning the reaction of H_2 and CO over Co, Ni and Fe catalysts to produce paraffins, olefins, waxes and oxygenates. The present and, most likely long term, application of the Fischer-Tropsch (FT) process concerns the conversion of natural gas to liquid transportation fuels (green diesel). The advantage of green diesel fuel over more conventional diesel is that green diesel has a higher cetane rating. Green diesel also contains virtually no sulphur compounds and is low in aromatics, thus greatly reducing soot and particulate emissions. The FT process is highly exothermic: the heat released per mole of CO is approximately 1000 KJ (if one assumes the composition of the end product is primarily C_6H_{12}). From an engineering aspect this highly exothermic reaction causes a number of problems in the design of an effective FT reactor [11]. However, if this heat can be rapidly transported from the reactor to heat exchangers it can be used to provide energy the endothermic CH_4 reforming reactions (3 and 6). The calculations carried out in this study show that the all-over reforming and FT process is slightly endothermic (ΔH = 23 KJ). A small quantity of CH_4 combustion is therefore required to drive the all-over process. This occurs at the expense of 0.05 moles of CO_2 per mole of CO_2 consumed in the reforming-FT all-over process. Therefore, for every mole of CO_2 which is consumed in these all-over process, 0.95 moles of CO_2 can be mitigated. This method however only offers an effective method of short-term CO_2 mitigation (or fixation), as the green diesel will eventually by burnt in an engine consequently releasing the "fixed" CO_2 back into the atmosphere.
3.3 Carbon Production.
The all-over process of CO_2 reforming followed by carbon production is an energy efficient process at 773K. The production of carbon enables 1 mole of CO_2 to be mitigated per mole of CO_2 reacted initially in the reforming reaction. The carbon formed, in principle, can be used for a number of purposes; for example as an adsorbent or as a catalyst support. The carbon could also be used, in theory, in the production of synthetic diamonds. Ni/Fe alloys, which catalyse the diamond synthesis reaction, are also active for reaction (9) (i.e. carbon production from syngas) [12,13]. However, if the aim is solely to remove CO_2 from a flue gas and the cost of CH_4 required is not a serious factor, the carbon formed can be disposed of easily.
If we consider this all-over process as a suitable potential method of CO_2 mitigation it becomes interesting to consider types of catalyst which can be used to carry out the CO_2 reforming and C production reaction steps.
3.4 CO_2 reforming.
The CO_2 reforming of CH_4 has been extensively studied in the literature. The most active catalysts contain either the active phase Ni, Co, noble metals or Mo_2C. A review of these catalysts is carried out elsewhere [8]. One of the main problems with CO_2 reforming is the risk of catalyst deactivation due to coke deposition. This will also be discussed [8].
Acknowledgement. This study was funded by the EU RUCADI project (BRRT-CT98-5098).

References.
[1] H.H. Lamb, (eds.) 1972 Climate Change, Past Present and Future, Fundamentals and Climate Now, London Metheum, vol. 1, London 1974.
[2] P. Reimer, Energy Convers. Mgt., 37 (1996) 665
[3] C.S. Wong and R.J. Matear, Waste Mgt., 17 (1997) 329
[4] E.E. Adams, D.S. Golomb, H.J. Herzog, Energy Convers. Mgt., 36 (1995) 447
[5] M. Aresta (eds.) Carbon Dioxide Recovery and Utilisation, Kluwer Academic Publishers, London (2003).
[6] M. Aresta and I. Tommasi, Energy Convers Mgt., 38 (1997) S373
[7] P.J.A. Tijm, F.J. Waller, D.M. Brown, Appl. Catal. A: Gen., 221 (2001) 275
[8] D. Treacy, J.R.H. Ross, *full paper in preparation.*
[9] A. Baiker, Appl. Organometal. Chem., 14 (2000) 751
[10] D. Gielen, Energy Convers Mgt., 44 (2003) 1027
[11] H. Schulz, Appl. Catal. A: Gen., 186 (1999) 3
[12] Y.V. Babich, B.N. Feigelson, D. Fisher, A.P. Yelliseyev, V.A. Nadolinny, J.M. Baker, Diamond Rel. Mat., 99 (2000) 893
[13] C. Park, N.M. Rodriguez, R.T.K. Baker, J. Catal., 169 (1997) 212.

TRI-REFORMING OF METHANE: A NOVEL CONCEPT FOR SYNTHESIS OF INDUSTRIALLY USEFUL SYNTHESIS GAS WITH DESIRED H_2/CO RATIOS USING CO_2 IN FLUE GAS OF POWER PLANTS WITHOUT CO_2 SEPARATION

Chunshan Song and Wei Pan

Clean Fuels and Catalysis Program, The Energy Institute, and
Department of Energy & Geo-Environmental Engineering,
Pennsylvania State University, 209 Academic Projects Building,
University Park, PA 16802

Introduction

CO_2 conversion and utilization are an important element in chemical research on sustainable development, because CO_2 also represents an important source of carbon for fuels and chemical feedstock in the future [1-3]. The prevailing thinking for CO_2 conversion and utilization begins with the use of pure CO_2, which can be obtained by separation. In general, CO_2 can be separated, recovered and purified from concentrated CO_2 sources by two or more steps based on either absorption or adsorption or membrane separation. Even the recovery of CO_2 from concentrated sources requires substantial energy input [4,5]. According to US DOE, current CO_2 separation processes alone require significant amount of energy which reduces a power plant's net electricity output by as much as 20% [6].

This paper discusses a new process concept that has been recently proposed [7-9] for effective conversion of CO_2 in the flue gases from electric power plants without CO_2 pre-separation, which can be used for the production of synthesis gas (CO + H_2) with desired H_2/CO ratios for synthesizing clean fuels and chemicals. The tri-reforming concept represents a new way of thinking both for conversion and utilization of CO_2 in flue gas without CO_2 separation, and for production of industrially useful synthesis gas with desired H_2/CO ratios using flue gas and natural gas. Experimental results with Ni catalysts will be reported.

Why Using Flue Gas?

Flue gases from fossil fuel-based electricity-generating units are the major concentrated CO_2 sources in the US. If CO_2 is to be separated, as much as 100 megawatts of a typical 500-megawatt coal-fired power plant would be necessary for today's CO_2 capture processes based on the alkanolamines [4-6]. Therefore, it would be highly desirable if the flue gas mixtures can be used for CO_2 conversion but without pre-separation of CO_2. CO_2 conversion and utilization should be an integral part of CO_2 management, although the amount of CO_2 that can be used for making industrial chemicals is small compared to the quantity of flue gas.

Based on our research, there appears to be a unique advantage of directly using flue gases, rather than using pre-separated and purified CO_2 from flue gases, for the proposed tri-reforming process. Typical flue gases from natural gas-fired power plants may contain 8-10% CO_2, 18-20% H_2O, 2-3% O_2, and 67-72% N_2; typical flue gases from coal-fired boilers may contain 12-14 vol% CO_2, 8-10 vol% H_2O, 3-5 vol % O_2 and 72-77% N_2. The typical furnace outlet temperature of flue gases is usually around 1200°C which will decreases gradually along the pathway of heat transfer, while the temperature of the flue gases going to stack is around 150°C. Pollution control technologies can remove the SOx, NOx and particulate matter effectively, but CO_2 and H_2O as well as O_2 remain largely unchanged.

Concept of Tri-reforming

Tri-reforming is a synergetic combination of endothermic CO_2 reforming (eq. 1) and steam reforming (eq. 2) and exothermic partial oxidation of methane (eq. 3, eq. 4). CO_2, H_2O and O_2 in the waste flue gas from fossil-fuel-based power plants will be utilized as co-reactants for tri-reforming of natural gas for the production of synthesis gas.

Tri-reforming of Natural Gas:

$CH_4 + CO_2 = 2\ CO + 2\ H_2$	[Endo: $\Delta H° = 247.3$ kJ/mol]	(1)
$CH_4 + H_2O = CO + 3\ H_2$	[Endo: $\Delta H° = 206.3$ kJ/mol]	(2)
$CH_4 + 1/2\ O_2 = CO + 2\ H_2$	[Exo: $\Delta H° = -35.6$ kJ/mol]	(3)
$CH_4 + 2\ O_2 = CO_2 + 2\ H_2O$	[Exo: $\Delta H° = -880$ kJ/mol]	(4)

Reactions for Coke Formation and Destruction:

$CH_4 = C + 2\ H_2$	[Endo: $\Delta H° = 74.9$ kJ/mol]	(5)
$2\ CO = C + CO_2$	[Exo: $\Delta H° = -172.2$ kJ/mol]	(6)
$C + CO_2 = 2\ CO$	[Endo: $\Delta H° = 172.2$ kJ/mol]	(7)
$C + H_2O = CO + H_2$	[Endo: $\Delta H° = 131.4$ kJ/mol]	(8)
$C + O_2 = CO_2$	[Exo: $\Delta H° = -393.7$ kJ/mol]	(9)

Fig. 1 illustrates the tri-reforming concept as a new approach to CO_2 conversion using flue gases for syngas production. The tri-reforming is a synergetic combination of three catalytic reforming reaction processes. Coupling CO_2 reforming and steam reforming can give syngas with desired H_2/CO ratios for methanol (MeOH) and Fischer-Tropsch (F-T) synthesis. Synthesis gas (syngas) can be made using natural gas, coal, naphtha, and other carbon-based feedstocks by various processes. Steam reforming of methane, partial oxidation of methane, CO_2 reforming of methane, and autothermal reforming of methane are the representative reaction processes for syngas production from natural gas.

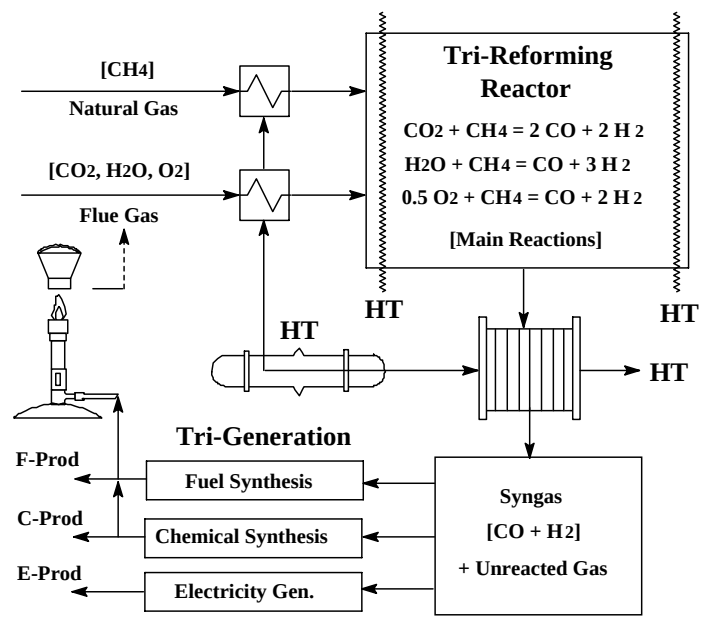

Fig. 1. Process concept for tri-reforming of natural gas using flue gas from fossil fuel-based power plants. HT represents heat transfer or heat exchange including reactor heat up and waste heat utilization .

The combination of dry reforming with steam reforming can accomplish two important missions: to produce syngas with desired H_2/CO ratios and to mitigate the carbon formation problem that is significant for dry reforming. Integrating steam reforming and partial

oxidation with CO_2 reforming could dramatically reduce or eliminate carbon formation on reforming catalyst thus increase catalyst life and process efficiency. Therefore, the proposed tri-reforming can solve two important problems that are encountered in individual processing. The incorporation of O_2 in the reaction generates heat in situ that can be used to increase energy efficiency and O_2 also reduces or eliminates the carbon formation on the reforming catalyst. The tri-reforming can thus be achieved with natural gas and flue gases using the 'waste heat' in the power plant and the heat generated in situ from oxidation with the O_2 that is already present in flue gas.

Thermodynamics of Tri-reforming Reactions

Table 1 shows the equilibrium conversions and the product H_2/CO molar ratios calculated using HSC program [10,11] for tri-reforming under atmospheric pressure. It is possible to perform tri-reforming with over 95% CH_4 conversion and over 80% CO_2 conversion at 800-850 °C when the ratio of CO_2 and H_2O is close to 1.0, O_2/CH_4= 0.1, and the ratio of $(CO_2+H_2O+O_2)/CH_4$ = 1.05. This is close to the cases with compositions of flue gases.

Table 1. Equilibrium CO_2 and CH_4 conversions and product H_2/CO molar ratios for tri-reforming of CH_4 with CH_4:CO_2:H_2O:O_2 =1:0.475:0.475:0.1 at 850C under 1 atm.

Reaction	Equilibrium		
Temperature °C	CH_4 Conv. (%)	CO_2 conv. (%)	H_2/CO Mol Ratio
850	98.54	84.50	1.71
800	96.00	81.10	1.72
750	90.70	73.33	1.77
700	86.00	55.60	2.14

Is Tri-reforming Feasible?

We have not found any previous publications or reports on reforming using flue gases for CO_2 conversion related to the concept proposed [7-9]. Our computational analysis shows there are benefits of incorporating steam (H_2O) and oxygen (O_2) simultaneously in CO_2 reforming of CH_4 [10,11]. Prior work established that CO_2 reforming encounters carbon formation problem, even with noble metal catalysts, particularly under elevated pressure [11-13]. Some recent laboratory studies with pure gases have shown that the addition of oxygen to CO_2 reforming [14-17] or the addition of oxygen to steam reforming of CH_4 [18] can have some beneficial effects in terms of improved energy efficiency or synergetic effects in processing and in mitigation of coking. Inui and coworkers have studied energy-efficient H_2 production by simultaneous catalytic combustion and catalytic CO_2-H_2O reforming of methane using mixture of pure gases including CH_4, CO_2, H_2O and O_2 [19]. Choudhary et al. reported their experimental study on simultaneous steam and CO_2 reforming of methane in the presence of O_2 at atmospheric pressure over Ni/CaO [20,21] or Ni/MgO-SA [22]; they have shown that it is possible to convert methane into syngas with high conversion and high selectivity for both CO and H_2. Ross and coworkers have shown that a Pt/ZrO_2 catalyst is active for steam and CO_2 reforming combined with partial oxidation of methane [23]. Therefore, tri-reforming seems feasible, and we also conducted laboratory studies [7-10].

Catalytic Tri-reforming Reactions

We also conducted catalytic tri-reforming experiments in a fixed-bed reactor using various catalysts prepared at Penn State University (by wet impregnation onto MgO, ZrO_2, CeO_2-ZrO_2, and Mg-CeO_2-ZrO_2 supports) [10]. Figs. 2, 3 and 4 show the CH_4 conversion, CO_2 conversion, and H_2/CO ratio in the products, respectively, for tri-reforming over Ni/MgO, Ni/ZrO_2, Ni/CeO_2, Ni/CeZrO and Ni/MgO/CeZrO catalysts prepared in our laboratory as well as commercial Ni/Al_2O_3 (ICI Synetix 23-4) catalyst. The feed for tri-reforming had the composition of CH_4:CO_2:H_2O:O_2 (mol ratio) = 1:0.48:0.54:0.1. Almost equal amounts of CO_2 and H_2O in the feed were intentionally selected for the convenience of comparing CO_2 conversions in the presence of an equal amount of H_2O in tri-reforming. The tri-reforming reactions were conducted at 700ºC – 850ºC and 1 atm at the space velocity of ca. 32,000 ml/(h.g cat.). Under all these reaction conditions, CH_4 and CO_2 conversions are very dependent on the type of catalysts used, but O_2 conversion is always 100%. Ni/MgO and Ni/MgO/CeZrO show the highest CO_2 conversion in general (Fig. 3). Ni/MgO/CeZrO, Ni/ZrO_2, and Ni/Al_2O_3 (ICI catalyst) give almost the same CH_4 conversions at 800ºC – 850ºC, while Ni/CeO_2 and Ni/CeZrO have relatively lower CH_4 conversions (Fig. 2).. With the reaction temperature decreasing, CH_4 conversion over Ni/MgO declines much faster than that over other catalysts. At 700ºC, the CH_4 conversion over Ni/MgO is the lowest among all the tested catalysts. We speculate that the deactivation of Ni/MgO at lower temperatures cause the fast decline of CH_4 conversion over Ni/MgO and the deactivation is caused by the re-oxidation of Ni. This speculation is justified by the facts that NiO in the NiO/.MgO catalyst is not reducible at temperature below 750ºC and no carbon formation is observed on the used Ni/MgO catalyst. In addition, metal sintering may not be the reason for deactivation because all the catalytic performance tests were first carried out at 850ºC. Then the reaction temperatures were gradually decreased to 700ºC.

Among all the catalysts tested, Ni/CeO_2 has the second lowest CH_4 conversion at reaction temperatures above 750ºC. The low CH_4 conversion over Ni/CeO_2 is probably related to the larger Ni particles over Ni-CeO_2 or the occurring of strong metal-support interaction (SMSI) due to the partial reduction of CeO_2 at high temperatures. Surprisingly, Ni/CeZrO has the lowest CH_4 conversion. Although Ni/MgO, Ni/MgO/CeZrO, Ni/Al_2O_3 (ICI catalyst), and Ni/ZrO_2 have similar CH_4 conversions, their CO_2 conversions are quite different. Ni/MgO shows the highest CO_2 conversion at temperatures above 750ºC, followed by Ni/MgO/CeZrO. Ni/CeO_2 and Ni/CeZrO again show the lowest CO_2 conversion.

The H_2/CO ratio in the products depends mainly on the CO_2 and H_2O conversions in tri-reforming. If more H_2O is converted than CO_2, then the H_2/CO ratio in the product would be higher. Similarly, if less H_2O is converted than CO_2, the H_2/CO ratio would be lower. Therefore, the H_2/CO ratio is a good indicator for comparing the ability to convert CO_2 in the presence of H_2O over different catalysts. Ni/MgO gives the lowest H_2/CO ratio, followed by Ni/MgO/CeZrO (shown in Fig. 4). The H_2/CO ratios over Ni/CeO_2, Ni/ZrO_2, and Ni/Al_2O_3 (ICI catalyst) are similar and slightly higher than Ni/MgO/CeZrO. Ni/CeZrO gives the highest H_2/CO ratio. These results strongly suggest that Ni/MgO enhance the CO_2 conversion most in the presence of H_2O and O_2. Among all the tested catalysts, their ability to enhance the conversion of CO_2 follows the order of Ni/MgO > Ni/MgO/CeZrO > Ni/CeO_2 ≈ Ni/ZrO_2 ≈ Ni/Al_2O_3 (ICI) > Ni/CeZrO.

The different ability to convert CO_2 over different catalysts in tri-reforming is related to the properties of the catalysts. The enhancement of CO_2 conversion over Ni/MgO might be related to its enhanced CO_2 adsorption ability as evidenced by the CO_2-TPD results (not shown here). However, catalysts supported on CeZrO (e.g., Ni/MgO/CeZrO and Ni/CeZrO) do not show more enhancement of CO_2 conversion than Ni/MgO even though these catalysts demonstrate more and stronger CO_2 adsorption than

Ni/MgO as indicated by the large CO_2 desorption peaks at 710-717ºC. To further elucidate the enhancement of CO_2 conversion over Ni/MgO in tri-reforming, a kinetic study was carried out, the result of which will be reported in the future.

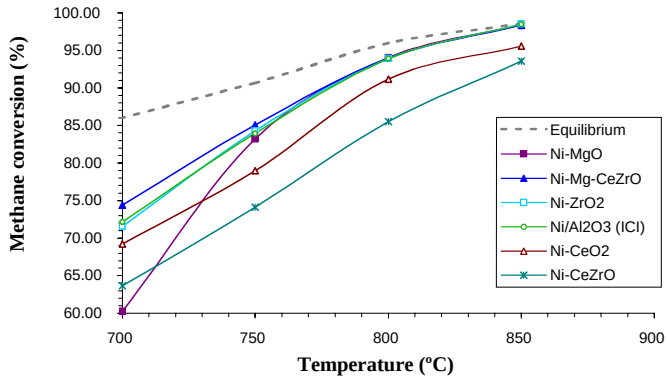

Fig. 2. *CH_4 conversions in the tri-reforming reaction over 100 mg supported Ni catalysts at 1 atm and feed composition of CH_4 : CO_2 : H_2O : O_2 = 1 : 0.48 : 0.54 : 0.1 (CH_4 flow rate = 25 ml/min)*

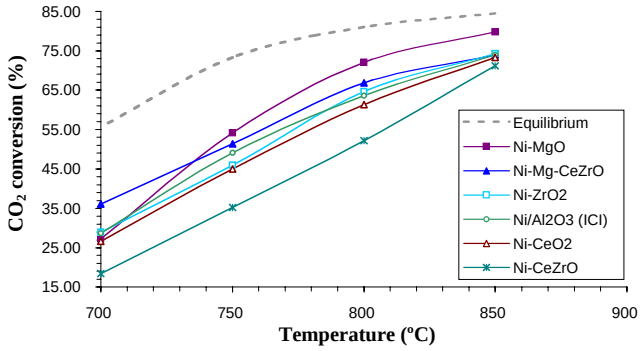

Fig. 3. CO_2 conversions in the tri-reforming reaction over 100 mg supported Ni catalysts at 1 atm and feed composition of CH_4 : CO_2 : H_2O : O_2 = 1 : 0.48 : 0.54 : 0.1 (CH_4 flow rate = 25 ml/min)

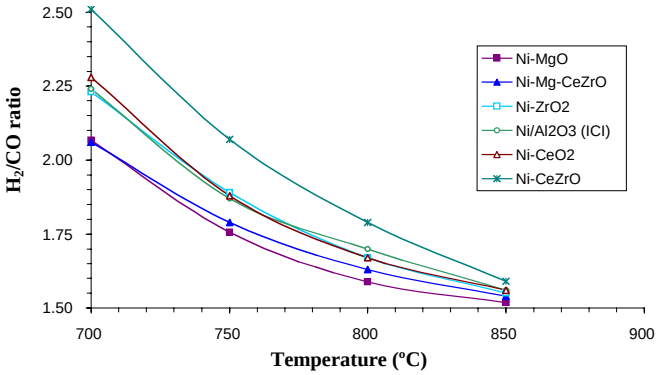

Fig. 4. H_2/CO ratios in the tri-reforming reaction over 100 mg supported Ni catalysts at 1 atm and feed composition of CH_4 : CO_2 : H_2O : O_2 = 1 : 0.48 : 0.54 : 0.1 (CH_4 flow rate = 25 ml/min)

Elimination of Carbon Formation by Tri-reforming Compared to CO_2 Reforming

We conducted temperature-programmed oxidation of the used catalysts from the above tri-reforming experiments and found that except for Ni/ZrO2 catalyst, all the other catalysts (corresponding to the experiments shown in Figs. 2 and 3) showed no sign of carbon formation after the tri-reforming experiments. We have also tested a commercially available Haldor-Topsoe R67 Ni-based catalyst for tri-reforming in a fixed-bed flow reactor using gas mixtures that simulate the cases with flue gases from coal-fired power plants (CO_2:H_2O:CH_4:O_2 = 1:1:1:0.1, mol ratio) and from natural gas-fired power plants (CO_2:H_2O:CH_4:O_2 = 1:2:1:0.1, mol ratio) [28]. For CO_2 reforming of CH_4, carbon formation is an important problem [12,13,24-27]. Temperature-programmed oxidation (TPO) results show that the used Haldor-Topsoe R67 catalyst after 300 min time-on-stream for CO_2 reforming at 850 °C and 1 atm contained 21.8 wt% carbon [28]. On the other hand, the same catalyst employed in tri-reforming showed no sign of carbon formation after 300 min TOS, as the used catalyst appears to be greenish power (versus the black sample from CO_2 reforming). Fig. 5 shows the photographs of the used catalysts after CO_2 reforming and tri-reforming. Therefore, our results show that tri-reforming can be performed with stable operation, and no carbon formation and no appreciable deactivation of catalyst were observed under the tri-reforming conditions.

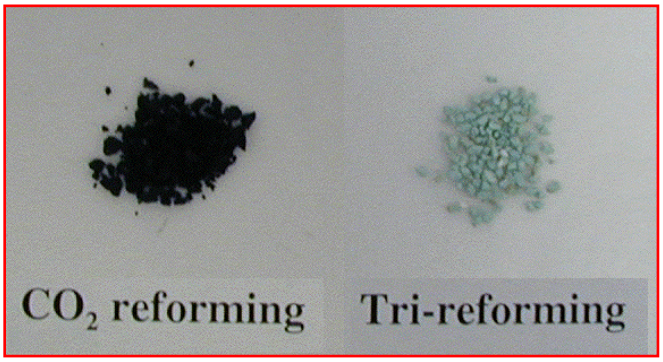

Fig. 5. Appearance of Haldor-Topsoe R67 Ni-based catalyst after 300 min TOS of CO_2-reforming (CO_2:CH_4 = 1:1, used catalyst particles are black in color) and tri-reforming (CO_2:H_2O:O_2:CH_4 = 1:1:0.1:1, used catalyst particles are green in color) at 850 °C.

Does Tri-reforming Consume More Energy Than Steam or CO_2 Reforming ?

A comparative energy analysis by calculation indicated that tri-reforming is more desired for producing syngas with H_2/CO ratios of 1.5-2.0 compared to CO_2 reforming and steam reforming of methane, in terms of less amount of energy required and less net amount of CO_2 emitted in the whole process for producing synthesis gas with H_2/CO ratio of 2.0 [8]. The tri-reforming process could be applied, in principle, to the natural gas-based power plants and coal-based power plants.

Conclusions

Catalytic tri-reforming of methane can be achieved successfully with high CH_4 conversion (>97%) and high CO_2 conversion (>80%) for producing syngas with desired H_2/CO ratios of 1.5-2.0 over supported nickel catalysts at 800-850 °C under atmospheric pressure

without the problem of carbon formation on the catalyst.

The CO_2 and CH_4 conversion as well as H_2/CO ratios of the products from tri-reforming also depend on the type and nature of catalysts.

An important observation is that CO_2 conversion can be maximized by tailoring catalyst composition and preparation method. In other words, certain catalysts with proper feature can give much higher CO_2 conversion than other catalysts under the same reaction conditions with the same reactants feed.

Among all the catalysts tested for tri-reforming, their ability to enhance the conversion of CO_2 follows the order of Ni/MgO > Ni/MgO/CeZrO > Ni/CeO_2 ≈ Ni/ZrO_2 ≈ Ni/Al_2O_3 (ICI) > Ni/CeZrO. The different ability to convert CO_2 over different catalysts in tri-reforming is related to the properties of the catalysts.

Results of catalytic performance tests over Ni/MgO/CeZrO catalysts at 850ºC and 1 atm at different feed compositions confirm the predictions based on the thermodynamic analysis for equilibrium conversions in tri-reforming of methane.

Further studies on improving catalysts are necessary for understanding the factors affecting CO_2 conversion and CH_4 in the presence of steam and oxygen during tri-reforming.

Acknowledgments

We are grateful to US DOE (UCR Innovative Concepts Program) for supporting this work, to Prof. H.H. Schobert and Prof. A.W. Scaroni of PSU for their encouragement of CS's efforts on CO_2 conversion, to Mr. B. Miller and Dr. S. Pisupati of PSU for helpful discussions on flue gas, and to Haldor-Topsoe and ICI for the catalysts. CS thanks Dr. J. Armor of Air Products and Chemicals for helpful discussions on CO_2 reforming.

References

1). Halmann, M. M.; Steinberg, M. Greenhouse Gas Carbon Dioxide Mitigation: Science and Technology. Lewis Publishers, Boca Raton, FL, 1999, 568 pp.

2). Song, C., A. M. Gaffney, and K. Fujimoto. CO_2 Conversion and Utilization. American Chemical Society, Washington DC, ACS Symposium Series, Vol. 809, 2002, 420 pp.

3). Maroto-Valer, M. M., C. Song, and Y. Soong. Environmental Challenges and Greenhouse Gas Control for Fossil Fuel Utilization in the 21st Century. Kluwer Academic/Plenum Publishers, New York, 2002, 447 pp.

4) DOE/OS-FE. Carbon Sequestration. State of the Science. Office of Science and Office of Fossil Energy, U.S. DOE, 1999.

5) Weimer, T., Schaber, K., Specht, M. and Bandi, A. Comparison of CO_2-Sources for Fuel Synthesis. Am. Chem. Soc. Div. Fuel Chem. Prepr., 1996, 41 (4), 1337-1340.

6) DOE/FE. Capturing Carbon Dioxide. Office of Fossil Energy, U.S. DOE, 1999.

7) Song, C. Chemical Innovation (formerly Chemtech, ACS), 2001, 31, 21-26.

8) Song, C., W. Pan and S. T. Srimat. In "Environmental Challenges and Greenhouse Gas Control for Fossil Fuel Utilization in the 21st Century". Edited by M. M. Maroto-Valer, C. Song, and Y. Soong. Kluwer Academic/Plenum Publishers, New York, 2002, Chapter 18, pp. 247-267.

9) Song, C. CO_2 Conversion and Utilization. Am. Chem. Soc. Symp. Ser., 2002, 809, 2-30.

10) Pan, W. Tri-reforming and Combined Reforming of Methane for producing Syngas with Desired H_2/CO Ratios. PhD Thesis, Pennsylvania State University, 2002.

11) Pan W. and C. Song. Am. Chem. Soc. Symp. Ser., 2002, 809, 316-329.

12) Song, C., S. T. Srimat, S. Murata, W. Pan, L. Sun, A. W. Scaroni and J. N. Armor. Am. Chem. Soc. Symp. Ser., 2002, 809, 258-274.

13) Srimat S. T. and C. Song. Am. Chem. Soc. Symp. Ser., 2002, 809, 289-302.

14) O'Connor A.M. and Ross J.R.H. The Effect of O_2 Addition on the Carbon Dioxide Reforming of Methane over Pt/ZrO_2 Catalysts. Catal. Today, 1998, 46 (2-3), 203-210.

15) Ruckenstein E. and Hu Y. H. Combination of CO_2 reforming and partial oxidation of methane over NiO/MgO solid solution catalysts. Ind. Eng. Chem. Res., 1998, 37 (5), 1744-1747.

16) Vernon, P.D.F., Green, M.L.H., Cheetham, A.K., Ashcroft, A.T.. Partial Oxidation of Methane to Synthesis Gas, and Carbon-Dioxide as an Oxidizing-Agent for Methane Conversion. Catal. Today, , 1992, 13 (2-3), 417-426.

17) Choudhary V.R., Rajput A.M., and Prabhakar B. Energy-Efficient Methane-to-Syngas Conversion with Low H_2/CO Ratio by Simultaneous Catalytic Reactions of Methane with Carbon-Dioxide and Oxygen. Catal. Lett., 1995, 32 (3-4), 391-396.

18) Choudhary, V.R.; Mamman, A. S. Simultaneous Oxidative Conversion and CO_2 or Steam Reforming of Methane to Syngas over CoO-NiO-MgO Catalyst. J. Chem. Technol. Biotechnol., 1998, 73 (4), 345-350.

19) Inui T., Saigo K., Fujii Y., and Fujioka K. Catalytic Combustion of Natural Gas as the Role of On-site Heat Supply in Rapid Catalytic CO_2-H_2O Reforming of Methane. Catal. Today,, 1995, 26 (3-4), 295-302.

20) Choudhary V.R., Rajput A.M., and Prabhakar B. NiO/CaO-Catalyzed Formation of Syngas by Coupled Exothermic Oxidation Conversion and Endothermic CO_2 and Steam Reforming of Methane, Angew. Chem. Int. Ed. Engl., 1994, 33 (20), 2104-2106.

21) Choudhary, V. R., and Rajput A.M. Simulataneous Carbon Dioxide and Steam Reforming of Methane to Syngas over NiO-CaO Catalyst. Ind. Eng. Chem. Res., 1996, 35, 3934-3939.

22) Choudhary, V.R.; Uphade, B.S., Mamman, A. S. Simultaneous Steam and CO_2 or Reforming of Methane to Syngas over NiO/MgO/SA-5205 in Presence and Absence of Oxygen. Appl. Catal. A: Gen., 1998, 168, 33-46.

23) Hegarty M.E.S., O'Connor A.M. and Ross J.R.H. Syngas Production from Natural Gas using ZrO_2-Supported metals. Catal. Today, 1998, 42 (3), 225-232.

24) Xu BQ, Wei JM, Wang HY, Sun KQ, Zhu QM. Nano-MgO: Novel Preparation and Application as Support of Ni Catalyst for CO_2 Reforming of Methane. Catal Today, 2001, 68 (1-3): 217-225.

25) Wei JM, Xu BQ, Li JL, Cheng ZX, Wang YQ, Zhu QM. CO_2 Reforming of CH4 over Ni Supported on Nano-ZrO2(I) - Comparison with Conventional Oxide Supported Nickel. Chem. J. Chinese Univ., 2002, 23 (1), 92-97.

26) Wei JM, Xu BQ, Sun KQ, Li JL, Zhu QM. CO2 reforming of CH4 over Ni supported on Nano-ZrO_2(II) Effect of catalyst composition and reaction conditions on catalytic reactivity. Chem. J. Chinese Univ., 2002, 23 (11), 2106-2111.

27) Wei JM, Xu BQ, Li JL, Chen ZX, Zhu QM. Nano-g-Al_2O_3 supported Ni catalysts for CO_2 reforming of CH_4 to syngas. Am. Chem. Soc. Div. Fuel Chem. Prepr., 2001, 46 (1), 97-98.

28) Song, C., Srinivas, S.T., Pan, W. and Sun, L. Technical Program, 17th North American Catalysis Society Meeting, Toronto, Canada, June 3-8, 2001.

Partial Oxidation and Combined Reforming of Methane on Ce-promoted Catalysts

Wei Wang, Susan M. Stagg-Williams, Fabio B. Noronha, Lisiane V. Mattos*, Fabio B. Passos*

Chemical and Petroleum Engineering Department,
University of Kansas, Lawrence KS, 66045
*Laboratório de Catálise , Instituto Nacional de Technologia, Brasil

Introduction

Significant attention has been given to the partial oxidation and reforming of various hydrocarbon sources for the production of synthesis gas. This work has stemmed from the concern about the world dependence on petroleum oil. Many hydrocarbon sources are currently being investigated including bio-based feedstocks, such as ethanol, sunflower oil, and biomass derived oils. However, the most common feedstock is still methane due to its abundance and inexpensive nature.

Many of the natural gas reservoirs are located in remote regions making the recovery and transportation cost prohibitive. The conversion of natural gas into transportation fuels such as gasoline and diesel helps top overcome these costs. The so-called gas-to-liquids technology (GTL) is based on the conversion of natural gas to a synthesis gas prior to the liquid production through the Fischer-Tropsch Synthesis (1). The syngas generation is the most capital and energy intensive part of the production plant (2). Therefore, the economic viability of GTL technology depends on optimizing the process for syngas production. Autothermal reforming (ATR) fulfills the requirements to a syngas with H_2/CO ratio of 2, the ratio necessary for GTL plants. ATR combines non catalytic partial oxidation with steam reforming in one reactor. The ATR technology requires the addition of CO_2 or CO_2-rich gas, in order to adjust the syngas composition to the desired H_2/CO ratio (3).

Catalyst stability in the presence of O_2, CO_2, and H_2O can be a significant issue. It is well established that mixed oxide supports result in improved catalytic performance for the dry reforming reaction due to the ability of the support to participate in the reaction (4). Similar studies for the partial oxidation reaction have shown that the addition of Ce to ZrO_2 results in a catalyst which exhibits minimal deactivation compared to Pt/Al_2O_3 and Pt/ZrO_2 catalysts (5). The mechanism of reaction was shown to proceed through combustion of methane followed by combined steam and CO_2 reforming.

Several studies have been performed on the dry reforming reaction in the presence of oxygen (6,7). The results showed that the conversion of methane increased as the amount of oxygen in the feed increased, but the selectivity towards H_2 decreased. The decrease in H_2 selectivity was more pronounced at lower temperatures where the formation of CO_2 and H_2O were favored. Minimal deactivation was observed on the Pt/ZrO_2 catalyst at low space velocities and with a significant amount of diluent in the feed (6).

This paper focuses on the partial oxidation and combined partial oxidation and reforming reactions over Pt supported on ZrO_2 and $CeZrO_2$. Specifically, we have investigated the effect of the metal loading and effect of the addition of oxygen and water on the activity, stability, and syngas ratio produced. A general reaction mechanism is discussed.

Experimental

ZrO_2 and cerium (18 wt%)-doped ZrO_2 were all obtained from Magnesium Elektron, Inc. Prior to the addition of the metal the supports were calcined at 800°C in stagnant air for 4 hours. Pt was added to the supports using incipient wetness impregnation of an aqueous solution of H_2PtCL_6•$6H_2O$. The metal loading was 0.5 wt% and 1.5 wt%. All of the catalysts were dried overnight at 110°C, and then reduced *in-situ* in H_2 (30 cm^3/min) at 500°C for 1.5 h, prior to reaction.

Partial oxidation experiments were carried out in a quartz flow reactor at 800°C using a CH_4:O_2 ratio of 2:1 and a total flow rate of 100 cc/min. The catalysts were diluted with a 3:1 ratio of SiC to catalyst to help reduce any heat effects. 20 milligrams of catalyst was used for the reaction on the 1.5 wt% catalysts while 60 mg was used for the runs with the 0.5 wt% catalyst, in order to maintain the same metal content in the reactor. For the experiments in the presence of oxygen, the composition of the feedstock was such that the C:O ratio was 1:1. The reactions were performed at 800°C with a total flow rate of 100 cc/min.

Results and Discussion

The surface area of the Ce promoted ZrO_2 support was 48 m^2/g while that of the ZrO^2 was 29 m^2/g. Transmission Electron Microscopy (TEM) was used to determine the dispersion of the 0.5 wt% catalysts. The catalysts were reduced at 500°C and then heated to 800°C in He. The dispersion of the 0.5 wt% Pt/ZrO_2 catalyst was approximately 21% while the dispersion of the 0.5 wt% Pt/$CeZrO_2$ catalyst was near 30%. The dispersion of the 1.5 wt% catalysts was measured using dehydrogenation of cyclohexane after reduction at 500°C. The dispersion after reduction at 500°C before heating to 800°C was measured to be 29% for the 1.5 wt% Pt/ZrO_2 catalyst and 34% for the 1.5 wt% Pt/$CeZrO_2$. TEM of a 1.5 wt% Pt/ZrO_2 catalyst after heating to 800°C showed that the dispersion was closer to 15%. These results are in agreement with previous studies which have shown that the sintering of the Pt/ZrO_2 catalyst during the heating from 500°C to 800°C is much greater than the sintering on the Pt/$CeZrO_2$ catalyst. Based on the dispersion results, it appears as if the metal particle sizes for the 0.5 wt% and the 1.5 wt% catalysts are similar after heating to 800°C.

Table 1. Methane Conversion During the Partial Oxidation Reaction at 800°C and a 2:1 CH_4:O_2 Feed Ratio

	% Methane Conversion		
Catalyst	After 1 hour	After 12 hours	After 24 hours
0.5 wt % Pt/ZrO_2	49	26	13
0.5 wt % Pt/$CeZrO_2$	39	40	37
1.5 wt % Pt/ZrO_2	51	34	13
1.5 wt % Pt/$CeZrO_2$	49	46	37

Table 1 shows the methane conversion during the partial oxidation reaction at 800°C and a 2:1 ratio of CH_4:O_2. The 0.5 wt% Pt/$CeZrO_2$ catalyst had an initial activity that was approximately 10% less than the 1.5 wt% Pt/$CeZrO_2$ and both of the unpromoted ZrO_2 catalysts. However, this material was the most stable of the 4 catalysts studied. Both of the ZrO_2 catalysts exhibited significant deactivation during the reaction which has been ascribed to carbon deposition. The loading of the metal was found not to have any effect on the long term activity of the catalyst which is most likely due to the similarity in the metal particle size after heating to 800°C and reaction for 24 hours.

Figure 1 shows the CO and CO_2 selectivity for the same 24 hour experiment for the $CeZrO_2$ and ZrO_2 catalysts containing 0.5 wt% Pt. Similar profiles were obtained for the 1.5 wt% samples. The CO selectivity for the ZrO_2 catalyst decreased significantly during the 24

hour experiment while the CO_2 selectivity increased. After approximately 10 hours of reaction the CO_2 selectivity became greater than the CO selectivity. In contrast, the CO and CO_2 selectivities of the $CeZrO_2$ catalyst were very stable with CO always being greater than CO_2. Similarly, the H_2:CO ratio remained at 2.6 during the 24 hour reaction for the Ce containing catalysts, while it was initially 2.6 for the ZrO_2 samples, but decreased to 0.8 by the end of the reaction.

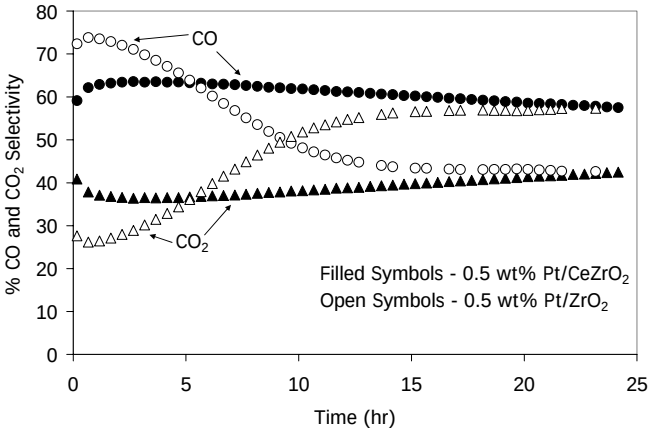

Figure 1. CO and CO_2 selectivity for the 0.5 wt% $Pt/CeZrO_2$ and the 0.5 wt% Pt/ZrO_2 during the partial oxidation reaction at 800°C and a 2:1 CH_4:O_2 feed ratio.

Previous studies (5) on a $Pt/Ce_{0.75}Zr_{0.25}O_2$ catalyst have suggested that the reaction mechanism proceeds via the combustion of methane followed by the combined steam and dry reforming. The observed initial H_2:CO ratio greater than 2 is evidence for the occurrence of the steam reforming reaction and the two step mechanism. The decrease in the CO selectivity and the H_2:CO ratio with the simultaneous increase in CO_2 selectivity is attributed to carbon formation inhibiting the second step of the reaction mechanism. The stability of the Ce-promoted materials is ascribed to the ability of the support to minimize carbon deposition on the Pt particle due to increased oxygen release capability.

The catalysts were exposed to reactions with both CO_2 and O_2 at 800°C with a CH_4:CO_2:O_2 feed ratio of 4:2:1. Reactions were performed such that the C:O ratio remained at 1:1. Figure 2 shows the conversion for the 0.5 wt% catalysts for 10 hours of reaction. The conversion of methane and the deactivation observed on the 0.5 wt% Pt/ZrO_2 is almost identical to that observed for the partial oxidation reaction. The H_2:CO product ratio was initially 1.18 but decreased to 0.95 during the experiment. A significant amount of water was collected using a condenser placed after the reactor. The formation of water could be due to the occurrence of the reverse water gas shift reaction, which also explains the H_2:CO ratio being less than 1. The water could also be formed by the combustion reaction. The partial oxidation studies demonstrated that combustion does occur in the presence of O_2 and that the ZrO_2 catalysts are prone to carbon deposition which can decrease the ability to do combined CO_2 and steam reforming. In order to determine the relative importance of each reaction, combustion and reverse water gas shift, in the overall process a complete mechanistic study is currently being performed.

The 0.5 wt% $Pt/CeZrO_2$ catalyst was very stable in the presence of oxygen and the H_2:CO ratio produced was constant throughout the experiment at 1.25. Higher oxygen contents resulted in an increase in the product ratio and the formation of water.

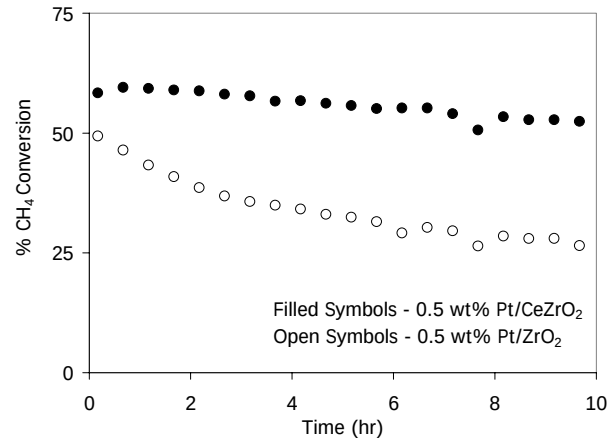

Figure 2. CH_4 conversion for the 0.5 wt% $Pt/CeZrO_2$ and the 0.5 wt% Pt/ZrO_2 during the combined dry reforming and partial oxidation reaction at 800°C and a CH_4:CO_2:O_2 feed ratio at 4:2:1.

Additional reaction studies on the 0.5 wt% and 1.5 wt% $Pt/CeZrO_2$ catalysts have shown that the catalysts are very stable in the presence of water. Switching the feed composition while the reactor was online resulted in the same conversion and product ratio as would be obtained by the individual reactions. Thus, the product ratio can be accurately predicted prior to switching the feed and a variety of syngas ratios can be generated without altering the catalyst performance.

Conclusions

The studies reported here have shown that increasing the Pt metal loading did not have any effect on the long term activity of the catalyst. The initial activity of the 1.5 wt% $Pt/CeZrO_2$ was higher than the 0.5 wt% $Pt/CeZrO_2$ catalyst. However, the deactivation on the 1.5 wt% catalyst was more pronounced resulting in the same activity after 24 hours. The similar long term activity is most likely due to the similar particle size after heating to 800°C. Significant deactivation is observed in the presence of O_2 and water on the Pt/ZrO_2 catalysts which is ascribed to the formation of carbon deposits that hinder the reforming reaction. In the presence of oxygen, the reaction mechanism is believed to proceed through combustion followed by combined dry and steam reforming as opposed to through direct partial oxidation. The Ce-promoted catalysts are very stable in the presence of oxygen and water and are promising for the ATR reaction. Detailed mechanistic studies in the presence of oxygen and water are currently underway.

Acknowledgements. The authors gratefully acknowledge funding from the KU Energy Research Center.

References

(1) M. Prettre, C. Eichner, and M. Perrin, Transactions of the Faraday Society, **1946**, 43, 335.
(2) D. Dissanayake, M. P. Rosynek, and J. H. Lunsford, Journal of Physical Chemistry, 1993, 97, 3644.
(3) V.R. Choudhary, A.M. Rajput, B. Probhaker, Journal of Catalysis, **1993**, 139, 326.
(4) Stagg-Williams S, M; Noronha, F. B; and Resasco, D. E., *J. Catal.*, **2000**, *194(2)*, 240.
(5) L.V. Mattos, E.R. de Oliveira, P.D. Resende, F.B. Noronha, F.B. Passos, Catalysis Today, **2002**, 77(3), 245.
(6) A. M. O'Connor, and J. R. H. Ross, Catalysis Today, **1998**, 46, 203.
(7) Venkatesh Phadnavis, Bakul Pant, and Susan M. Stagg-Williams, *Fuel Chem. Div. Preprints*, **2002**, Vol. 41(1).

CO_2 REFORMING OF METHANE ON $LaA'Ru_{0.8}Ni_{0.2}O_3$ (A'= Sm, Nd, Ca) PEROVSKITES AS CATALYSTS PRECURSORS IN PRESENCE AND ABSENCE OF O_2

E. Pietri[1], M. E. Rivas[1], M. R. Goldwasser[1], M. J. Pérez-Zurita[1], M. L. Cubeiro[1], L Leclercq[2] and G. Leclercq[2]*

1. Centro de Catálisis, Petróleo y Petroquímica, Escuela de Química, Fac. Ciencias, UCV, Apartado 47102, Los Chaguaramos, Caracas, Venezuela; 2. Université des Sciences ET Technologies de Lille, Laboratoire de Catalyse Hétérogene et Homogène, 59655 Villeneuve D'Ascq, Cedex, Francia

Introduction

Over the past years, the CO_2 reforming of methane yielding synthesis gas has been the subject of numerous studies. The objective is to find a suitable material that allows the reaction to proceed at low temperature with a minimum of carbon production. Among these material, the perovskites like oxides ABO_3, in which A-site cation is a rare earth and/or alkaline earth and B-site cation is a transition metal has drawn a lot of attention. The reason for this is because by a careful reduction of the perovskites, the B-site cations will remain distributed in the structure, producing a well dispersed and stable metal particle inhibiting coke formation. Although many previous investigations of the CO_2 reforming of methane were performed over transition metals supported on alumina, silica and magnesia, the use of perovskite has been less studied. The performance of these solids for the CO_2 reforming of CH_4 in the presence (combine) and absence (dry) of O_2 was investigated. The use of oxygen as co-reactant could allow the reaction to proceed at lower temperatures due to its exothermic character.

Experimental

Four Ru-Ni based perovskite type oxides were synthesized by the citrate sol gel method based on the Pechini type reaction route. La in the A-site position was partially replaced by Sm, Nd and Ca to produce $LaRu_{0.8}Ni_{0.2}O_3$, $La_{0.8}Sm_{0.2}Ru_{0.8}Ni_{0.2}O_3$, $La_{0.8}Nd_{0.2}Ru_{0.8}Ni_{0.2}O_3$, and $La_{0.8}Ca_{0.2}Ru_{0.8}Ni_{0.2}O_3$. The procedure has been published elsewhere [1]. The homogeneity and structure of the obtained powders have been investigated before and after reduction and after reaction by ICP, IR, BET surface areas, XRD, TPR and XPS analysis. Catalytic tests were performed in a continuous flow system an integral reactor at atmospheric pressure.

Results and Discussion

The XRD patterns of the as synthesized solids at room temperature revealed that the perovskite structure was the main phase detected for all solids. All perovskites could be indexed with an orthorhombic or cubic symmetry of the ABO_3 type. The ICP analysis showed a close agreement between experimental and theoretical values corroborating the advantage of the sol-gel method. The TPR shows that the perovskite reduction proceeds in two steps. The XRD in situ reduction results seems to indicate, that the first peak of reduction at ~ 400 °C could be attributed to weakly bound Ru-Ni cations and to residues of the precursors. The second peak could be attributed to a simultaneously Ru and Ni reduction to produces Ru^0 and Ni^0 probably with an alloy formation. For all solids, the observed phases after reduction at 700ºC were: Ru metal (alone or allied with Ni), La_2O_3 and CaO, Sm_2O_3 and Nd_2O_3 depending on the composition of the starting perovskite. However, changes in the reducibility pattern were introduced due to the difference in ionic radii of the substituting cations. XRD analysis was also used to determine the metal particles size of the reducible species. It is interesting to point out that the metallic particle sizes were in the order of 10-34 nm as determined by the Scherrer equation [2]. Peaks correspond mainly to Ru (44,37°, 2θ) slightly shifted, due to the presence of Ni.

The experimental results of the methane reforming show high methane conversions both in presence and absence of O_2 (Table 1). However, higher ratios H_2/CO were obtained for the combined reaction. For this reaction, CO_2 conversion was also lower (30%) than that of methane due to the fact that the CO_2 is being generated as a product of the methane combustion in the presence of O_2 [3].

On Sm and Nd containing solids, a great improvement on the H_2/CO ratios was observed for the combine reaction compared to the dry reaction, while the substitution of La by Ca increases the activity and selectivity, as shown in table 1. On this solid, for the dry reaction, the CO_2 conversion is higher than that of CH_4 due to the reverse water gas shift reaction.

The simultaneous oxidative and CO_2 reforming reaction of methane notably diminished coke formation, increasing the syngas production. The addition of oxygen to the CH_4 + CO_2 system decreases the reaction temperature and energy consumption, indicating that the partial oxidation (exothermic) reaction promotes the dry (endothermic) reaction, in agreement with Tomishige et al. result for Ni/Al_2O_3 and Pt/Al_2O_3 catalysts [4].

Acknowledgement. The authors thank Venezuelan FONACIT for its financial support through Agenda Petroleum Project Nº 97-003739.

References

(1) Pietri, E.; Barrios, A.; Gonzalez, O.; Goldwasser, M.R.; Pérez-Zurita, M.J.; Cubeiro, M.L.; Goldwasser, J.; Leclercq, L.; Leclercq, G. *Stud. Surf. Sci. Catal.*,**2001**, *136*, 381.
(2) Bradford, M.C.J. and Vannice, M.A. *Appl. Catal. A: Gen.* **1996**, *142*,73.
(3) Ruckenstein, E. and Wang, H.Y. *Catal. Lett.* **2001**, *73*, 2.
(4) Tomishige, K.; Kanazawa, S.; Suzuki, K.; Asadullah, M.; Sato, M.; Ikushima, K. and Kunimori, K. *Appl. Catal. A:Gen.* **2002**, *233*, 35.

Table 1. CO_2 Reforming of Methane in the Presence and Absence of O_2

SOLIDS	DRY			COMBINE		
	XCH_4	XCO_2	H_2/CO	XCH_4	XCO_2	H_2/CO
$LaRu_{0.8}Ni_{0.2}O_3$	79.0	81.0	0.94	87.0	47.0	1.18
$La_{0.8}Sm_{0.2}Ru_{0.8}Ni_{0.2}O_3$	84.4	67.4	0.75	89.7	39.7	1.04
$La_{0.8}Nd_{0.2}Ru_{0.8}Ni_{0.2}O_3$	83.5	63.8	0.66	81.3	32.3	1.02
$La_{0.8}Ca_{0.2}Ru_{0.8}Ni_{0.2}O_3$	67.9	85.3	0.86	85.0	50.0	1.18

tr =24 h, WHSV =24L/ h.g, CH_4/CO_2 =1, CH_4/O_2=2, W = 200 mg, Tred =700ºC/ 8h, Treac. = 700ºC

DRY REFORMING OF METHANE ON NANO-ZIRCONIA SUPPORTED NICKEL CATALYST

Yajun Zhao, Xinmei Liu and Zifeng Yan

State Key Laboratoty of Heavy Oil Processing, Key Laboratory of Catalysis, CNPC, University of Petroleum, Dongying 257061, China

Introduction

Catalytic reforming of carbon dioxide with methane to synthesis gas has been proposed as one of the most promising technologies for the utilization of these two greenhouse gases. Moreover, this route produces synthesis gas with a suitable CO/H_2 ratio for the production of hydrocarbons and oxygenated derivatives. Supported noble metals catalysts have characteristic of high activity, selectivity and resistance to coke formation. Nevertheless, consideration of high cost and limited availability of noble metals makes the development of a nickel-based catalyst more feasible for industrial practice, but it is rapidly deactivated by carbon deposition.

Nanosized catalysts possess more edges, corners, defects, small-sized particles, large surface area and high metal dispersion, as a result exhibit the good catalytic performance. In this work, we synthesized nano-zirconia and used it as the support of Ni-based catalyst for dry reforming of methane.

Experimental

Preparation of Nano-zirconia Support and Catalysts. The nano-zirconia was synthesized by solid state reaction method. Zirconyl chloride, sodium hydroxide, CTMABr were milled respectively and mixed together. The reaction product was then transferred to the autoclave to age. Finally, the sample was washed and dried.

The nano-zirconia supported nickel catalyst, denoted as NZ, was prepared by incipient wet impregnation method using nickel nitrate as the precursor. For comparison, the catalyst of the same component was prepared by conventional co-precipitation method, denoted as CZ.

Catalytic evaluation. The catalysts behavior was carried out in the continuous flow quartz-fixed-bed reactor under atmospheric pressure. The catalyst was reduced in situ at 673K during 5h with H_2, then the reaction was preformed at 973K with CH_4:CO_2 ratio (mol) of 1:1 and space velocity of 5000cm^3/g·h.

Results and Discussion

Characterization of the Support. Figure 1 exhibits the XRD pattern of nano-zirconia. Evidently, the four peaks appearing at high degrees show that the synthesized zirconia is of tetragonal structure, and the particle size calculated by Sherrer equation is about 3.5 nm.

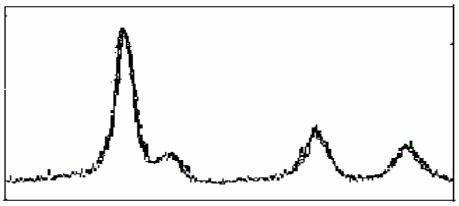

Figure 1. The XRD pattern of nano-zirconia

Figure 2 shows that nano-zirconia possesses mesopore of about 3.6 nm and large specific surface area of about 381.8 m^2/g. Moreover, it is seen that the isotherm exhibits a shape of type Ⅳ with a hysteresis of type H3. It is thought that the mesopore formed by aggregates of plate-like nanasized particles is slit-like.

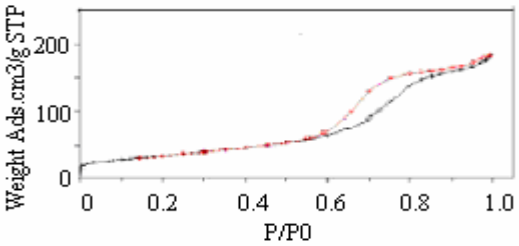

Figure 2. N_2 adsorption / desorption isotherm of nano-zirconia

Two weight loss stages are observed in the TG profile of nano-zirconia as shown in Figure 3. The first one, before 373K, corresponds to desorption of water physically adsorbed in the sample. The second one, after 473K, corresponds to loss of hydroxyl groups bonded on the surface of zirconia. No further weight loss is observed after 773K.

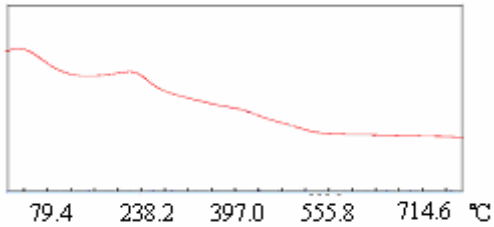

Figure 3. TG profile of nana-zirconia

Characterization of the Catalysts

Figure 4 shows that the pattern of NZ catalyst is the characteristic peaks of nano-zirconia and has no that of NiO, which indicates the dispersion of NiO on the support of nano-zirconia is uniform. However, NZ catalyst is amorphous. At the same time, the surface area, above 125.4 m^2/g, of NZ catalyst is about 2 times higher than that of CZ catalyst.

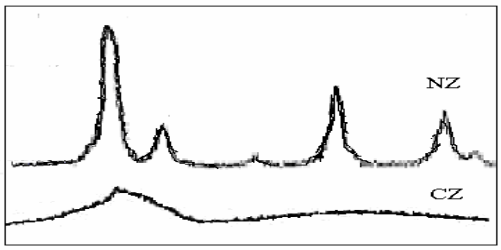

Figure 4. XRD patterns of the catalysts prepared with different method

Figure 5 shows that the weigh loss of NP is slow, has no obvious exothermic spectra, and the reduction temperature is relatively low, which indicate that NiO dispersion is uniform and the interaction of NiO and support is relatively weak. However, the weigh loss of CP is fast, has no obvious exothermic spectra, and the reduction temperature is relatively high, which indicate that the interaction between NiO and ZrO2 is strong and NiO is not easily reduced, this is in accordance with the amorphous phase shown in XRD pattern.

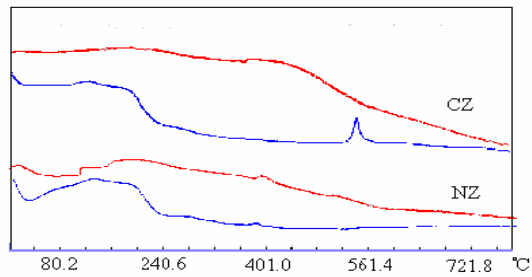

Figure 5. TG profiles of the catalysts prepared with different method in the atmosphere of H_2

Figure 6 shows that the particles of NZ catalyst are small and uniform, have no conglomeration, so the catalyst is considered as the compound of nanosized nickel oxide and zirconia. However, CN catalyst has obvious aggregates.

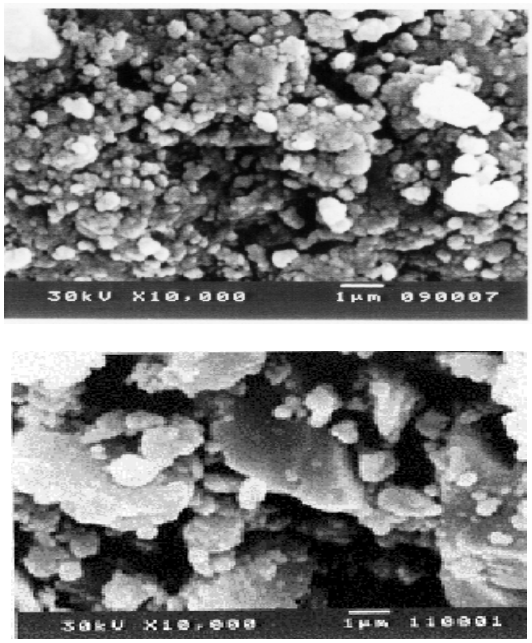

Figure 6. SEM images of the catalysts prepared with different method

Catalytic activity and stability

Figure 7 shows that the conversion of CH_4 on NZ catalyst is much high than that of CZ catalyst. NZ catalyst exhibits high stability, the conversion of CH_4 is 77.8% at the beginning and decreases by about 8% after reacting 170h., however, the conversion of CH4 is 59.22 on average over CZ catalyst. This indicates that the nano-sized catalyst with small-sized particles, large specific surface area and high metal dispersion possesses good catalytic property.

Conclusion

The results of catalytic activity and stability on dry reforming of methane reveals the important role of nano-zirconia to the catalyst. It makes the catalyst possess the characteristic of nana-particles such as more edges, corners, defects and abundant exposed atoms and so on. So nano-zirconia is the proming support of reforming catalysts.

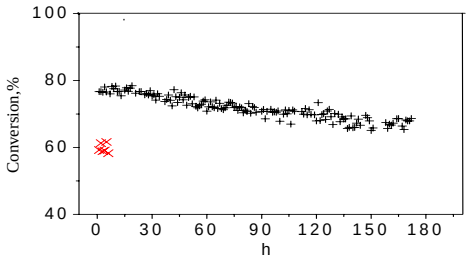

Figure 7. The variation of CH4 conversion on the catalysts prepared with different method as a function of time

References

(1) Yan, Z.F.; Ding, R.G.,; Song, L.H. and Qian, L. *Energy & Fuels* **1998**,*12*, 1114.
(2) Ding, R.G. and Yan, Z.F. *Catal. Today* **2001**, *68*,135.
(3) Ding, R.G.; Yan, Z.F.; Song, L.H. and Liu, X.M. *J. Natural Gas Chem.*, **2001**, *10*, 273.
(4) Mattos, L.V.; Roino, E.; and Noronha, F.B. *Fuel Processing Technol.* **2003**, *83*,147.
(5) Mariana, M.V.M. Souza; Donato, A.G.Aranda and Martin, Schmal. *J. Catal.*, **2001**, *204*,498.

Reforming of Methane and Coalbed Methane over Nanocomposite Ni/ZrO_2

*Qin-Hui Zhang, Yan Li, Bo-Qing Xu**

Innovative Catalysis Program, Department of Chemistry, Tsinghua University, Beijing 100084, China (Email: bqxu@tsinghua.edu.cn)

Introduction

One of the most attractive chemical approaches for the utilization of CO_2 and methane resources, e.g. coalbed gases, could be the catalytic CO_2 reforming of methane (CRM) to produce syngas (a mixture of H_2 and CO). CO_2 molecules in this CRM reaction function as a clean oxidant for the methane molecules. We have discovered recently that nanocomposite Ni/ZrO_2 catalysts, which consists of comparably sized Ni-metal (10-15 nm) and zirconia (7-25 nm) nanocrystals, are highly active and extremely stable for the CRM reaction at 700-800°C with a stoichiometric CO_2/CH_4 = 1.0 mixture [1,2]. However, in some other resources, the molecular CO_2/CH_4 ratio can be below the stoichiometry of the CRM reaction. A simple and convenient technological solution for the utilization of such resources is to add water (steam) as a compensation since catalytic steam reforming of methane (SRM) produces the same kind of products. In the present work, we demonstrate first that the nanocomposite Ni/ZrO_2-AN catalyst [1,2] also exhibits superior catalytic performance than the conventional oxide-supported Ni catalysts (Ni/ZrO_2-CP and Ni/Al_2O_3) for the SRM reaction. Our further study on combined steam and CO_2 reforming of methane (CSCRM) over the nanocomposite Ni/ZrO_2-AN catalyst will show that the extremely stable nanocomposite catalyst could make the CCSRM viable for producing syngas with flexible H_2/CO ratios.

Experimental

Preparation and catalytic testing of Ni/ZrO_2 catalyst Conventional 12.9 wt% Ni/ZrO_2-CP (the BET surface area: 18 m^2/g, reducibility of Ni: 98.5% and Ni-dispersion: 5.8) and nanocomposite 12.1 wt% Ni/ZrO_2-AN (the BET surface area: 38 m^2/g, reducibility of Ni: 95.2% and Ni-dispersion: 9.4) catalysts were prepared according to our previous methods [1-4]. Z107 (13.0 wt% Ni/Al_2O_3-C) sample is a commercial catalyst for the industrial SRM reaction. The catalytic reaction was conducted at 800°C, measured by a thermal couple in a quartz-well inserted into the catalyst bed, in a vertical fixed-bed U-shape quartz reactor (i.d.10mm) under atmospheric pressure as described previously [1-4]. A specially designed chamber was placed ahead of the reactor inlet and used to make the stoichiometric mixture of CH_4 and steam (H_2O/CH_4=1.0). This chamber was heated to 300°C to ensure no condensation of the water reactant. For the combined steam and CO_2 reforming reaction, CO_2 is also mixed with other reactants in the chamber. Unless otherwise specified, the space velocity by the methane reactant was $GHSV_{CH4} = 1.2\times10^4$ ml/(h·g_{cat}). Before the reaction, the catalyst was reduced in situ with H_2 (40ml/min) at 700°C for 3 h. Products from the reactor were analyzed on line by a gas chromatograph (SQ206) equipped with TCD and a carbon molecular sieve (80~100 mesh) column.

Results and Discussion

Figure 1 shows the TEM micrograms of the reduced Ni/ZrO_2-AN and Ni/ZrO_2-CP samples. It is remarkable that the structure of nanocoposite Ni/ZrO_2-AN catalyst is distinctive compared with the conventional Ni/ZrO_2-CP catalyst.

The catalytic data of SRM reaction at conditions of P=0.1MPa, T=800°C, $GHSV_{CH4}$ = 12,000 ml/(h·g_{cat}), H_2O/CH_4=1.0 are given in **Figure 2** by plotting CH_4 conversion against the reaction time on-stream over the different catalysts.

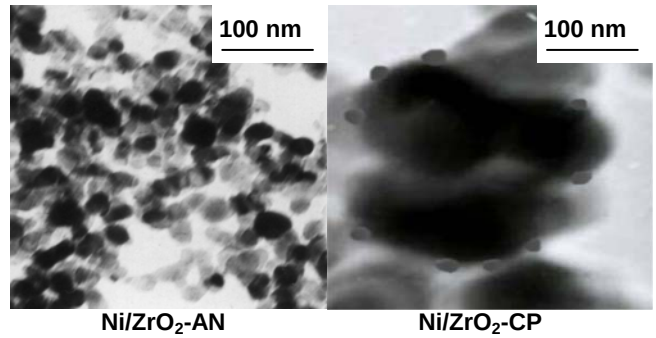

Fig. 1. TEM micrograms of the reduced Ni/ZrO_2 catalysts

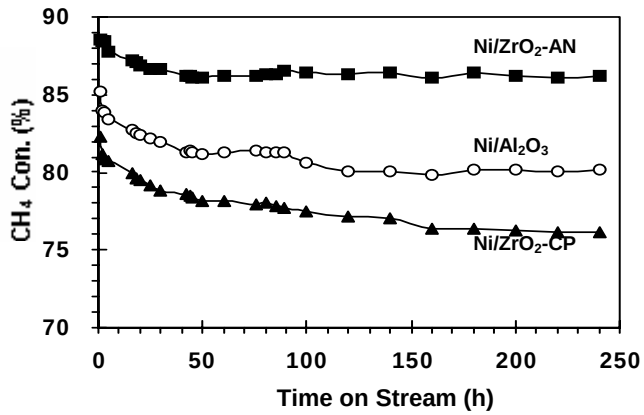

Fig. 2. Catalytic activity and stability during SRM process (P=0.1MPa, T=800°C $GHSV_{CH4}$=12,000 ml/(h·g_{cat}), H_2O/CH_4=1.0

Although all the three catalysts showed high and stable catalytic activities in the SRM process for 240 hrs reaction time on stream with CH_4 conversions of 87-88%, 81-84% and 76-83% respectively which are close to the thermodynamic equilibrium values (90%) at 800°C, the nanocomposite Ni/ZrO_2-AN catalyst is apparently more active as well as more stable than the commercial Z107 and the conversional Ni/ZrO_2-CP catalyst at this space velocity.

To further demonstrate the catalyst stability at methane conversion far below its thermodynamic equilibrium value, all the catalysts were tested with stepwise increasing the space velocity of methane from $GHSV_{CH4}$ = 12, 000 to 96, 000 ml/(h·g_{cat}) and the results are showed in **Figure 3**. The data for the first 150 hrs reaction time on stream, which were the same as those at reaction TOS=150~200 hrs, were not shown in **Figure 3**.

It is evident that the nanocomposite Ni/ZrO_2-AN catalyst showed extremely stable catalysis for the SRM reaction since the observed catalytic methane conversions were stable every time after changing the reaction GHSVs from $GHSV_{CH4}$ = 12, 000 to 96, 000 ml/(h·g_{cat}), and surprisingly, the conversion at every specific GHSV was kept constant after switching between several different GHSVs during 400 hrs reaction time on stream; In contrast, the conventional Ni/ZrO_2-CP and commercial Z107 catalyst began deactivating at high space velocity of $GHSV_{CH4}$ = 48, 000 ml/(h·g_{cat}) and this deactivation is severely irreversible and by the end of 400 hrs they almost had no activity.

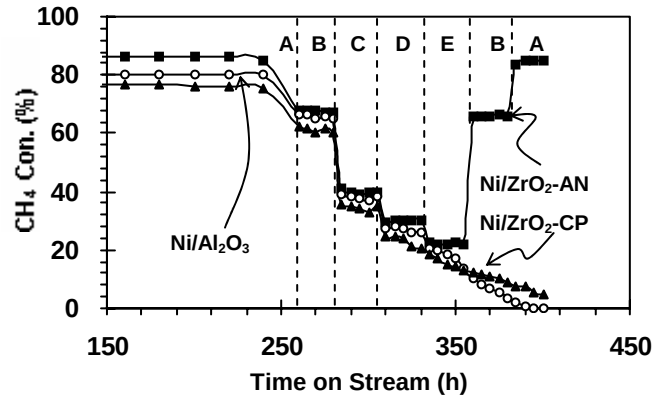

Fig. 3. Catalytic stability test at different methane space velocities of $GHSV_{CH4}$ = 12,000(A), 24,000(B), 36,000(C), 48,000(D), and 96,000(E) ml/(h·g_{cat}) (P=0.1MPa, T=800°C, H_2O/CH_4=1.0)

It should be mentioned that we operated SRM reaction with rather lower H_2O/CH_4 molar ratio=1.0 and high space velocity as compared with most SRM process conducted under an H_2O/CH_4 molar ratio between 2.0-5.0 [6] to avoid the deactivation caused by sever carbon deposition under an H_2O/CH_4 molar ratio below 2.0 at atmospheric pressure [7]. However, with high H_2O/CH_4 molar ratios (>2.0), the following drawbacks exist: (a) the equilibrium of water-gas shift reaction ($H_2O + CO = H_2 + CO_2$) will become favorable, as a result, the H_2/CO_2 mole ratio in product will be high, which is not preferable for the downstream process such as methanol and Fischer-Tropsch synthesis; (b) an enormous amount of energy will be consumed in the production of steam thus the energy efficiency and process economy will decrease. Therefore, the development of nanocomposite Ni/ZrO_2-AN catalyst with high activity and stability under low H_2O/CH_4 molar ratio is promising for commercial utilization in the future SRM process.

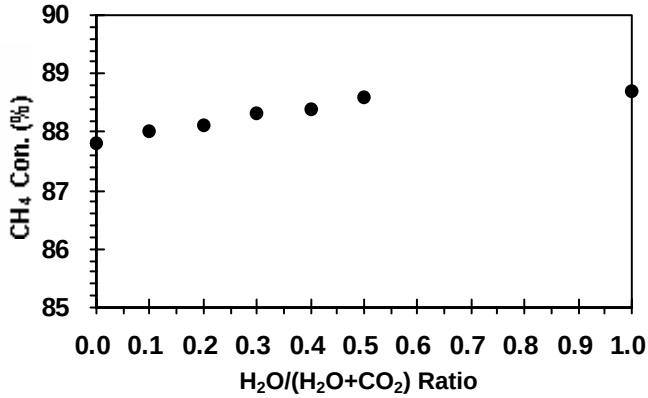

Fig. 4. Effect of the feed $H_2O/(H_2O+CO_2)$ ratio on methane conversion (P=0.1MPa, T=800°C, $GHSV_{CH4}$=12,000 ml/(h·g_{cat}), (H_2O+CO_2/CH_4=1.0)

We further applied the nanocomposite Ni/ZrO_2-AN catalyst in the CSCRM reaction since its remarkable catalytic activity and stability both in CRM [1-4] and SRM reactions. **Figure 4** shows the effect of the feed $H_2O/(H_2O+CO_2)$ ratio on methane conversion. With different H_2O/CO_2 ratios, the CH_4 conversion was stable and maintained between 87.8%-88.8%. **Figure 5** shows the effect of the feed $H_2O/(H_2O+CO_2)$ ratio on the H_2/CO ratios of the products. It is clear that, with the increase of steam content in the feed, the H_2/CO ratios of the products increased from 1.0~3.0. Thus on the nanocomposite Ni/ZrO_2-AN catalyst, we could achieve syngas with flexible H_2/CO ratios of 1.0~3.0 by CSCRM reaction for different downstream synthesis, and could eliminate carbon formation which is a serious problem in the methane CO_2 reforming process [7].

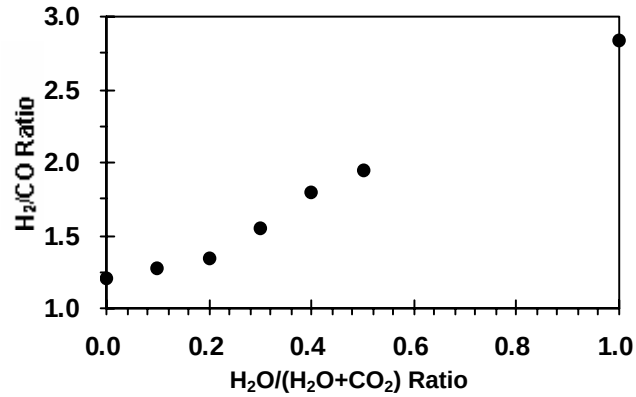

Fig. 5. Effect of the feed $H_2O/(H_2O+CO_2)$ ratio on H_2/CO ratio (P=0.1MPa, T=800°C, $GHSV_{CH4}$=12,000 ml/(h·g_{cat}) $(H_2O+CO_2)/CH_4$=1.0)

Conclusions

This work proves that the nanocomposite Ni/ZrO_2-AN catalyst is highly active and extremely stable for both the steam reforming and the combined steam and CO_2 reforming of methane. In comparison with commercial Ni/Al_2O_3 catalyst, the nanocomposite Ni/ZrO_2-AN catalyst allows the use of a much higher space velocity of the reaction feed and a stoichiometric H_2O/CH_4 and $H_2O/(H_2O+CO_2)$ ratios, which could meet requirements for the commercial utilization of different methane and CO_2 resources.

References

[1] Xu, B. -Q., Wei, J. -M. *et al*., *J. Phys. Chem. B:* **2003**, 107, 5203
[2] Xu, B. -Q., Wei, J. -M. *et al*., *Top. Catal*. **2003**, 22, 77
[3] Y. Li, Q. Ye, Wei, J. -M., Xu, B. -Q., *Chin. J. Catal*., in the press
[4] Wei, J. -M., Xu, B. -Q. *et al*., *Chem. J. Chin. Univ.* **2002**, 23, 2106; *Catal. Today*, **2001**, 68, 217
[5] G. Ertl, H. Knoezinger and J. Weitkamp, Eds., *Handbook of heterogeneous catalysis, Part B: Catalytic process*, (Wiley-VCH, **1997**), Vols. 4 and 5, 1819
[6] J. P. Van Hook, *Catal. Rev. – Sci. Eng.*, **1980**, 21, 1

Efficient Bimetallic Catalysts for the Hydrogen Production from Diesel fuel

Praveen K Cheekatamarla and Alan M. Lane

Department of Chemical Engineering, The University of Alabama, Tuscaloosa, AL-35487

Introduction

Autothermal reforming involves the reaction of oxygen, steam, and fuel to produce H_2 and CO_2. In essence, this process can be viewed as a combination of POX and SR and has recently attracted considerable attention due to its higher energy efficiency than the above processes and also low investment process using a simple system design [1]. The ATR is a stand-alone process in which the entire hydrocarbon conversion is carried out in one reactor aided by partial oxidation. The ATR process is generally defined by an idealized equation written as:

$C_nH_mO_p + x(O_2+3.76N_2) + (2n -2x-p)H_2O = nCO_2 + (2n-2x-p+m/2)H_2 + 3.76xN_2$

where, x is the oxygen-to-fuel molar ratio. When x = 0 equation reduces to the endothermic steam reforming; when x = n-p/2 equation is the combustion reaction.

ATR has several advantages over SR and POX: (1) less complicated reactor design and lower reactor weights, because less thermal integration (i.e. heat exchange between incoming reactants and the hot products) is required; (2) a wider choice of materials of construction; and (3) lower fuel consumption during startup because, for a given reactor mass, the energy required to heat a reformer is directly proportional to its operating temperature.

In the past, various fuels have been investigated for H_2 generation by reforming technologies for fuel cell systems. Suitable fuels involved gaseous HCs such as methane, propane etc. [2] and liquid HCs such as alcohols [3], gasoline [4, #2 diesel [5] etc.

For heavy fuels such as JP-8 or kerosene, autothermal reforming conditions were achieved by using a reformer including a POX zone and a separate SR zone. The operating conditions were maintained such that oxygen (air) was preheated to 450°C, and the temperature of POX chamber and SR chamber maintained at 1375°C and 925°C respectively [6]. It is also reported that in the autothermal reforming of the diesel feed, the thermodynamic equilibrium can be achieved at a Water/C of 1.25 and an oxygen/C ratio of 1 at an operating temperature of 700°C [7].

Although considerable work was done on heavy hydrocarbons, there haven't been any studies related to synthetic diesel fuel and the performance of adiabatic reactors for autothermally reforming the fuel.

The design of ATR catalysts can be challenging, particularly for gasoline/diesel reforming due to the complex and ill-defined nature of the fuel. ATR catalysts have to be active for both steam reforming and partial oxidation, be robust at high temperature and resistant to sulfur and coke formation, especially in the catalytic zone that runs oxygen limited.

Full conversion of all hydrocarbon components is desired; low levels of non-methane hydrocarbons, such as aromatics and olefins can undergo transformations, particularly hydrogenation on the downstream WGS catalyst, thus consuming hydrogen and decreasing the overall efficiency of the fuel processor.

Catalyst formulations for ATR fuel processors depend on the fuel choice and operating temperature. For methanol, Cu-based formulations can be used. For higher hydrocarbons the catalyst typically comprises of metals such as Pt, Rh, Ru and Ni deposited or incorporated into carefully engineered oxide supports such as ceria-containing oxides.

The objective of this investigation was to synthesize and test stable and efficient autothermal reforming catalysts for hydrogen production in auxiliary power units.

Experimental

All the experiments were performed in a 3/8" adiabatic fixed-bed tubular (quartz) reactor. Liquid feed consisting of water and diesel was vaporized and mixed along with air in a pre-heater containing silicon carbide bed to enhance mixing and heat transfer. Calibrated HPLC pumps and unit mass flow controllers were used to control the flow rates. The gaseous mixture from the pre-heater was maintained at a temperature of 400°C. The reactor with the catalyst bed was well insulated to achieve adiabatic reaction conditions. Thermocouples were placed along the catalytic bed to read the temperature profile inside the reactor as the reactions occur over the catalytic surface and the corresponding product composition was measured by sampling at different positions. The hot product gas leaving the reactor was cooled down in a heat exchanger/condenser system to separate water and liquid hydrocarbons from the product gas. The pressure was always less than 2 psig. The dry product gas from the condenser was analyzed using a SRI gas chromatograph to monitor H_2, CO, CO_2, CH_4 and O_2 concentrations.

In each test, 2 g of fresh non-diluted catalyst sample (pellets with an average size of 2 mm) was supported on a layer of quartz wool. The catalysts tested for the ATR activity were prepared by impregnation and co-impregnation techniques.

The experiments reported in this document were performed under the following conditions: Steam/C ratio = 1-3, oxygen/C ratio = 0.5-2, pre-heater and reactor inlet temperature = 400°C, Space Velocity = 17000 hr^{-1}.

Results and Discussion

The role of defect chemistry and the surface oxygen vacancies in determining the catalytic behavior of metal supported mixed oxide systems is well known. The focus was on the autothermal reforming activity of some catalysts, as well as, the effect and role of both the metal and the dopant on the catalytic properties. The experimental work involved developing, testing and characterizing: (a) single metal catalysts supported on reducible or non-reducible support; (b) bimetallic catalysts dispersed on various supports. Reactor studies involved the reforming of synthetic diesel fuel. Catalysts were prepared by impregnation, incipient wetness method and coprecipitation. Metal loadings generally range from 1-2% in the case of noble metals and 5-10% for non-noble metals.

Alumina supported catalysts

The main objective of the present work was to determine whether the autothermal reforming activity of Pt can be improved when a second noble metal (Pd) is added to the alumina substrate. This carrier was selected because of its non-reducible nature, as a part of fundamental study to better understand the performance of autothermal reforming catalysts: metals and metal oxides.

Three model samples were prepared to study the ATR activity of synthetic diesel fuel: Pt, Pd and Pt-Pd catalysts supported on alumina. Two different bimetallic samples were prepared by changing the order of impregnation: Pt (I)-Pd (II); Pd (I)-Pt (II).

The autothermal reforming activity response of alumina supported Pt and/or Pd catalysts is shown in Fig. 1. Before carrying out the activity tests, all the samples were reduced at 350°C in a 5%H_2/N_2 mixture. Samples loaded with Pt or Pd yielded about 50%

hydrogen compared to 45% from bare alumina. The most interesting results are obtained from the mixed metal bimetallic catalysts, the Pt-Pd samples. Each bimetallic sample shows high activity yielding ~60% hydrogen compared to 50% from their monometallic counterparts. The order of impregnation does not seem to have any impact on the performance of these catalysts as noted in the figure. The ATR activity on the Pt, Pd and Pt-Pd catalysts confirms a positive effect of Pt and Pd in the bimetallic sample, because the level of activity of this system was higher than on either of the monometallic components.

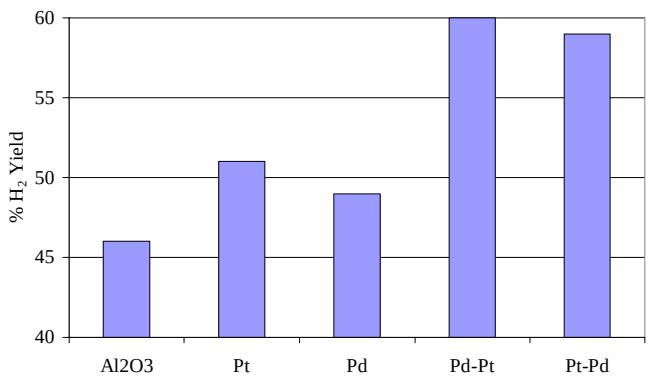

Figure 1. Performance of alumina supported Pd and/or Pt catalysts

This higher intrinsic activity of these catalysts is probably due to the Pt-Pd interaction in the system. Temperature programmed reduction studies and XPS analysis confirmed the expected phenomenon.

TPR profiles of monometallic (Pd and Pt) and the bimetallic (Pt followed by Pd) samples are shown in Fig. 2. TPR pattern of alumina carrier is not shown because of its non-reducible nature.

The TPR profile (Fig. 2) of the Pd sample shows a negative peak at 75°C followed by a positive peak at 110°C. The former can be assigned to desorption of hydrogen from the decomposition of a bulk palladium hydride formed through H-diffusion in to the Pd-crystallites [214], while the latter is attributed to the Pd oxide species. In contrast, the TPR profile of the Pt sample shows a broad reduction profile extending from 50°C to 450°C. All platinum is reduced to Pt metal below 450°C. Two reduction peaks one at about 100°C and the other at 250°C were observed for Pt/Al_2O_3. The broadening suggests the presence of several Pt species. These reduction peaks are slightly lower than the reported reduction temperature [8] probably due to differences in Pt loading, alumina type, calcination temperature and ramp rates during the TPR.

The TPR profile of the bimetallic Pt-Pd catalyst is not simply the sum of the monometallic Pt and Pd samples. The bimetallic reduction profile exhibits peaks typical of PtO reduction (100°C) and PdO (110°C) in addition to the Pd hydride decomposition peak at 75°C, although both are much more intense than in the monometallic samples. Since the metal content is about the same in these catalysts, the increase in H_2 consumption associated with the metal oxide species seems to depend on the presence of second metal. In addition, the broader second peak centered at 400°C, detected in the Pt-Pd sample indicates the reduction of Pd species together with the co-impregnated Pt, probably due to some kind of interaction between the metals. Similar interactions in Pt-Pd systems were reported in TPR studies performed by Noronha et al. [9]. These interactions between the metals leading to the formation of an active phase seem to be a probable reason behind the activity enhancement.

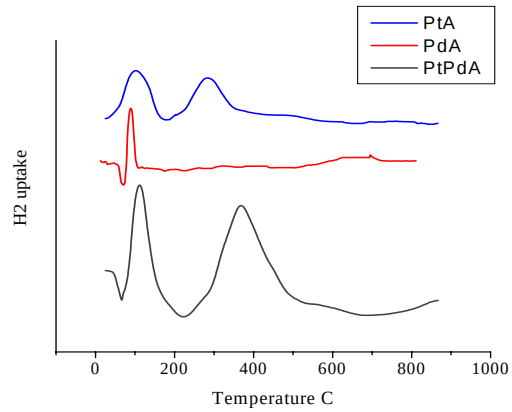

Figure 2: TPR Profiles of alumina supported catalysts

The XPS analysis performed over these samples verify the above conclusions. The high resolution XPS spectra of the Pt 4d and the Pd 3d binding energy regions obtained from the Pt/Al_2O_3, Pd/ Al_2O_3 and Pt/Pd/ Al_2O_3 samples are shown in Fig. 4-48a. Note a slight shift in the Pd 3d5/2 peak (~0.5 eV to higher binding energy) of the Pt-Pd/Al_2O_3 catalyst with respect to that of the Pd/ Al_2O_3 catalyst. The shift in the Pd 3d5/2 peak may be due to the formation of stabilized Pd species due to a strong metal-metal interaction between Pd and Pt in the bimetallic sample.

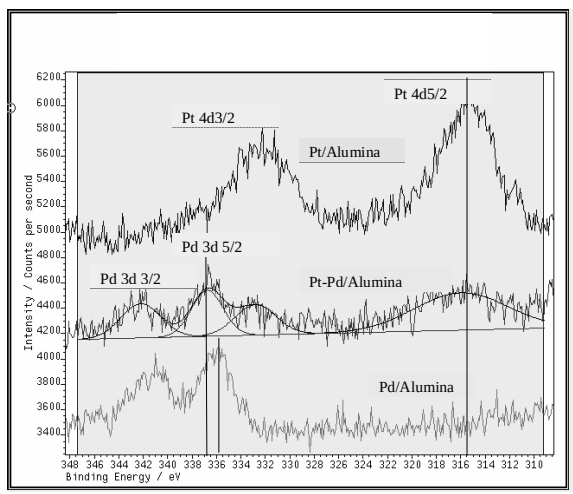

Figure 3: XPS analysis of alumina supported catalysts

Ceria Supported Catalysts.

Two different metals viz. Pt, Ni were chosen for their ATR activity. The ceria supported catalysts include monometallic components and their combinations with Pt (Pt-Ni). Two different bimetallic samples were also prepared by changing the order of impregnation on ceria substrate. It can be noted from Fig. 4 that these metals improved the ATR activity of ceria support. Similar to the

results observed over the alumina supported catalysts discussed in the above section, the selectivity to produce hydrogen from diesel fuel was highest for the bimetallic samples compared to their monometallic counterparts. The impregnation order clearly had an effect on the activity in case of the Pt-Ni bimetallic catalysts as observed in Fig. 4. Also these catalysts exhibited stable performance showing almost complete resistance to sulfur poisoning. A long-term experiment was carried out over these catalysts (Pt, and Pt-Ni). It is clear from Fig. 5 that the bimetallic sample shows stable catalytic activity even in presence of heavy sulfur content due to the JP8 fuel in the ATR tests conducted. The reason for this higher intrinsic activity and stability is underway.

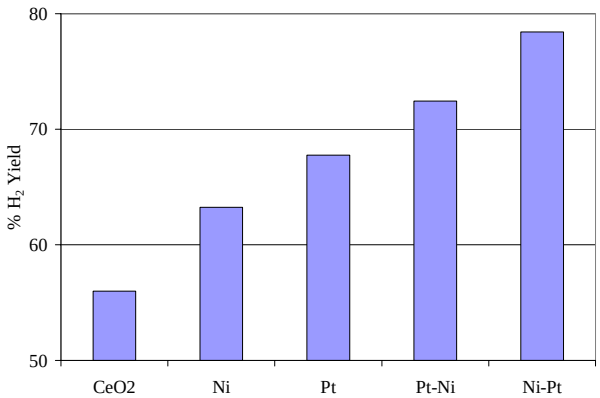

Figure 4: ATR activity of Ceria supported Pt and/or Ni catalysts

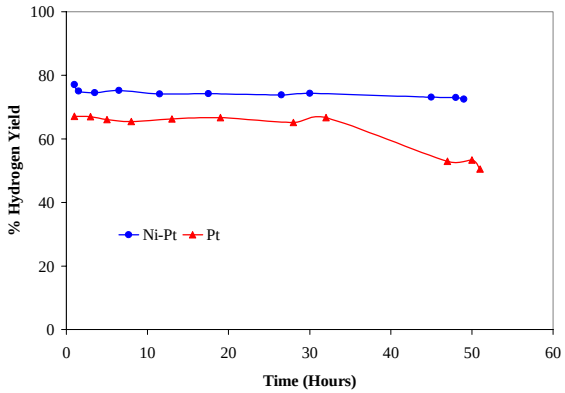

Figure 5: ATR activity (Sulfur resistance) Pt-Ni catalyst

Conclusions

Autothermal reforming of synthetic diesel fuel was investigated for potential applications in auxiliary power units. Experimental results suggest that the presence of a second metal improves the performance of the ATR activity of Pt based catalysts supported on ceria and alumina. Higher intrinsic activity of these samples is possibly due to the interaction between these metals as suggested by TPR and XPS results.

References

(1) Wieland S.; Baumann F.; Startz K.A.; "Proceedings of the fuel cell seminar on new catalysts for autothermal reforming of gasoline and water-gas shift reaction" *Portland, Oregon*, **2000**.

(2) Ayabe S.; Omoto H.;T. Utaka, R.; Eguchi K.; *Applied Catalysis A: General* **2002**, *6352*, 1

(3) Ahmed S.; Krumplet M.; Kumar R.; Lee S.H.D.; *Presented at the Fuel Cell Seminar, Palm Springs, California*, **1998.**

(4) Dong J Moon, Sreekumar K.; Sang Deuk Lee and Hoon Sik Kim, *Applied Catalysis A: General* **2001,** *215*, 1

(5) Pereira C.; Bae J-M.; Ahmed S.; and Krumplet M.; Presented at the US Dept. of Energy, 2000 Hydrogen Program technical review, San Ramon, CA**, May 2000**.

(6) "Apparatus for converting hydrocarbon fuel in to hydrogen gas and carbon dioxide",*US Patent 6254839*.

(7) Thomas Rampe Angelika Heinzel and Bernhard Vogel, *Journal of Power sources* **2000**, *86*, 536.

(8) Lietz, G.; Lieske, H.; Spindler, H.; Hanke,W.; and Wolter, J.; *J. Catal*. **1983**, *81*, 17

(9) Noronha, F. B.; Schmal, M.; Primet, M.; and Fr ety R.; *Appl. Catal*., **1991**, *78*, 125

PARAMETRIC STUDY OF AUTOTHERMAL REFORMING OF LPG

Wuyin Wang, Scott Q. Turn, Vheissu Keffer, Aurelien Douette

Hawaii Natural Energy Institute,
University of Hawaii,
1680 East-West Road, POST 109,
Honolulu, HI 96822
Email: Wuyin@hawaii.edu;
Tel: 808-956-5397; Fax: 808-956-2344

Introduction

Generating electricity by fuel cell technologies is under extensive research recently with a potential for commercialization in the near future. Sources of hydrogen for fuel cell are diverse and fuel processing is a key part to ensure reliable performance and competitive economy of fuel cell applications. Conventional hydrocarbon fuels are cheap and widely available. In Hawaii, the majority of electricity is generated from fossil fuels. There are ample supplies of Liquid Petroleum Gas (LPG) and its price is competitive to that of gasoline. Being safe and non-toxic, LPG is a promising source of hydrogen for off-grid applications in Hawaii.

Hydrocarbon fuels can be converted into high quality hydrogen for PEM fuel cells through reforming, water-gas shift reaction, and CO cleanup. Steam reforming, catalytic partial oxidation and autothermal reforming are the main processes employed to convert hydrocarbons to hydrogen rich gas. Compared with natural gas, LPG, mainly propane, contains C-C bonds that will be broken at higher temperature.

Coking is a main cause of catalyst failure in hydrocarbon reforming. Carbonaceous deposits on catalyst surfaces block active sites, leading to catalyst deactivation. Coke formation from thermal cracking can accompany catalytic reforming above approximate 650°C [1]. Therefore for LPG reforming at high temperature, coking must be carefully controlled.

Ethyl mercaptan is commonly added to LPG as an odorant. Ethyl mercaptan will mainly be converted to hydrogen sulfide in autothermal reforming. For steam reforming catalysts, sulfur will readily bind with nickel causing severe deactivation. The effects of sulfur on catalyst activity are weaker at high temperature and correlate with sulfur concentration in the feedstock [2].

This paper reports preliminary results from a parametric study of autothermal reforming of LPG. Reforming temperature, steam to carbon ratio (S/C), and oxygen to carbon ratio (O/C) were studied. Performance indicators, the extent of LPG conversion and catalyst coking, and sulfur poisoning, are reported.

Experimental

Experiments were performed in a 1.93 cm I.D. tubular reactor. The reactor was heated by electrical furnace with a heating length of 30.5 cm. Two G90 steam reforming catalysts, G-91 EW and C11-NK, from Süd-Chemie were tested. The LPG supply contained 90-100% propane/propylene, 0-2% ethane, 0-10% butane and 40 ppm ethyl mercaptan.

A stream of 2 slpm air was fed into a water vaporizer to produce a steady flow with steam. When temperatures in the reactor reached desired set point values, LPG was introduced and the gas mixture was switched from a bypass mode to the catalyst reactor. Air and LPG flow rates were maintained using mass flow controllers. About 20 to 40 g catalyst were located in the constant temperature zone in the reactor. Temperatures in the reactor were measured at three locations, 7.5 cm in front of the catalyst bed (T1), directly in front of the catalyst bed (T2) and immediately after the catalyst bed (T3). The dry effluent gas was analyzed using a Shimadzu GC 14A equipped with a Carbonex packed column and a thermal conductivity detector. The gas components H_2, N_2, CO, CH_4, CO_2, C_2H_4, C_2H_6, C_3H_6 and C_3H_8, were quantified.

Catalyst temperature, S/C, O/C and catalyst mass (i.e. space velocity) were studied at 2-3 levels. Both steam reforming and autothermal reforming were investigated. Steam-to-carbon ratio was 0.6 or 1.5. Oxygen-to-carbon ratio was 0.76 or 1.0. The amount of catalysts was 20 or 40 g. Temperature of the reformer was set at 680, 770, 850°C. Real temperatures in the reactor were shown by T1, T2 and T3. Temperature at the end of the catalyst bed, T3 was used to represent the catalytic reactor temperature.

Results and Discussion

Catalyst. Two catalysts tested are designed for different feed stocks, G91 EW for natural gas/LPG and C11-NK for naphtha. Both catalysts showed similar activity in LPG conversion, however, G91 EW was more active in converting methane and ethylene (Table 1) under the conditions tested. Since the amount of catalyst was in excess, the influence of catalyst type on hydrocarbon conversion was weak in the test range.

Table 1. Gas Compositions after Reforming by Two Catalysts. S/C=1.5, O/C=1.0, T3=800°C, GHSV=9000 1/h.

%	H_2	N_2	CO	CH_4	CO_2	C_2H_4	C_3H_8
C11 NK	33	46	11	1.4	9.3	0.38	0
G91 EW	35	45	11	0.24	8.7	0.06	0

Temperature. Temperature of the catalyst bed was the most important factor for LPG conversion. Complete conversions of C_3H_8 and C_3H_6 was achieved at catalyst bed temperature of 840°C (average of T2 and T3), at S/C=1.5 and O/C=1.0 (Table 2).

Table 2. Effect of Temperature on Propane Conversion. S/C=1.5, C11-NK 42 g, O/C=1.0.

T bed, °C	704	725	840
C_3H_8 conversion, %	98.5	98.7	100

O/C ratio. In autothermal reforming, the role of oxygen is to provide heat required to drive steam reforming reactions and to break fuel into smaller compounds. At high O/C ratio, the chemical energy of fuel may be converted to sensible heat rather than the desired H_2 product. At low O/C ratio, coke may form due to thermal cracking of hydrocarbons. In the present work, O/C ratio of 1.0 was chosen since experience indicated that coke formation was generally lower at this condition. This ratio was equal to about 30% of oxygen needed for complete combustion of propane. In gasification research, this O/C ratio was usually found to be optimal. Further experiments are planned to quantify the effects of O/C ratio on system performance.

S/C ratio. In autothermal hydrocarbon reforming, partial oxidation reactions occur faster than steam reforming reactions. Since partial oxidation is very exothermic while steam reforming is extremely endothermic, the occurrence of these two sets of reactions can be deduced from the temperature profile in the reactor (Figure 1). The "No LPG" curve indicates that flow through the reactor does not reach the furnace control set point temperature of 770ºC until close the location of x/L=0.5. Compared with this, low S/C ratios of 0.6 and 1.0 resulted in high temperature before the catalyst bed indicating that heat released from oxidation (O/C=1.0) dominated the heat demand of the steam reforming reactions. At S/C ratio of 1.5,

enhanced steam reforming reactions result in lower temperatures at the entrance of the reactor (x/L=0.25). All three S/C ratios have roughly equal temperatures (~850ºC) in excess of the furnace temperature set point at x/L=0.5 indicating the heat release by the oxidation is dominant at this location. Differences in total flow rate through the reactor are not accounted for in this discussion.

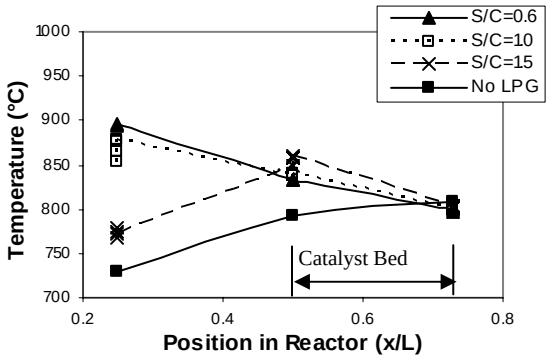

Figure 1. Influence of S/C on temperatures in the reactor. L: total heated reactor length, x: distance from inlet in the reactor. T3=800°C, O/C=1.0, G91 EW: 22 g.

Steam reforming was slow and was kinetically controlled (Figure 2). Though propane and propylene were completely converted, methane levels in the effluent were higher than values predicted by equilibrium calculations. Concentration of ethylene, a precursor of coking, was low. Both methane and ethylene decreased with increasing S/C ratio.

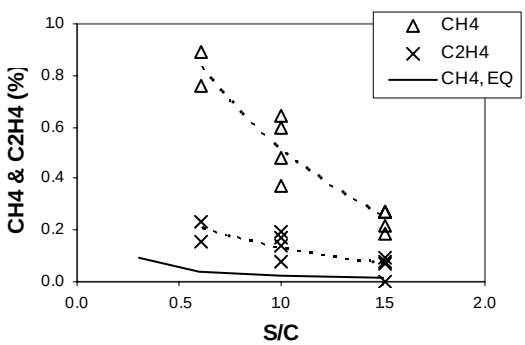

Figure 2. Effect of S/C ratio on methane and ethylene. Equilibrium value for methane is given for comparison. T3=800°C, O/C=1.0, G91 EW:22 g, GHSV=9000 1/h.

S/C ratio affected conversions of C_3H_8 and C_3H_6 to some extent. Trace amount of C_3H_8 was detected at 800°C (T3) when S/C and O/C were lowered to 1.1 and 0.76, respectively.

The choice of a proper S/C ratio should also take into account energy balance of the reformer system. Equilibrium calculations indicate that with preheating of inlet gas by exhaust gas, autothermal reforming could be operated without external heat supply at S/C=1.5 and O/C=1.0.

Deactivation of the catalyst. Autothermal reforming of LPG was tested for more than 40 hours under conditions of S/C=1.5, O/C=1.0, GHSV=9000 1/h, and a reactor set point temperature of 770°C. The gas compositions are plotted in Figure 3. Under these conditions, gas composition was generally stable. No propane or propylene was detected. Hydrogen declined slightly with increasing time on stream. Methane increased considerably, which was a sign of catalyst deactivation. Ethylene increased as well, and ethane started to appear after 35 hours on stream.

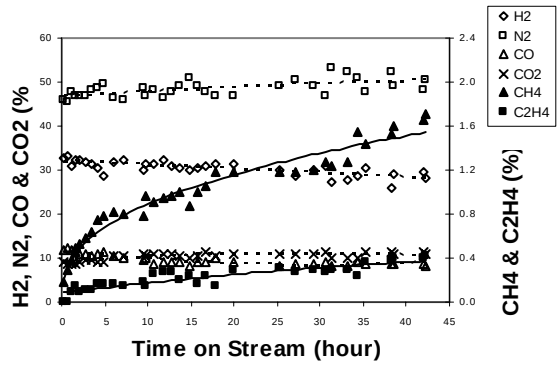

Figure 3. Autothermal reforming of LPG. T3=800°C, S/C=1.5, O/C=1.0, G91 EW: 23 g, GHSV=9000 1/h, ethyl mercaptan in LPG: 40 ppm.

Upon visual inspection at the conclusion of the test, the first piece of the catalyst in the catalytic bed was discolored, indicating partial oxidation was dominant at that point. No clear carbon deposition on the used catalyst was evident. With 40 ppm sulfur in LPG, sulfur poisoning was the likely cause of deactivation due to the formation of nickel sulfide on the active sites of the catalyst surface. More detailed analysis of sulfur on the catalyst surface is expected to be obtained soon.

Conclusions

Effects of different parameters on autothermal reforming of LPG were studied for hydrogen production. Two nickel-based G90 steam reforming catalysts were used. Experiments were carried out in a fixed-bed reactor to study the effects of catalyst type, reforming temperature, S/C ratio, and O/C ratio. Temperature was found to be most important. Complete conversion of LPG was achieved above 800°C (T3). Higher S/C ratio (S/C=1.5) resulted in the reduced levels of methane and ethylene. Controlling O/C and S/C, heat for steam reforming could be provided by partial oxidation in situ and C3 hydrocarbons could be partially oxidized to smaller molecules with less thermal cracking. Finally, autothermal reforming of LPG was tested by more than 40 hours on stream at S/C=1.5, O/C=1.0, 800°C and GHSV=9000 1/h. The propane conversion remained complete, but a slight drop of methane conversion was observed. No clear carbon deposit was found. The deactivation was probably due to poisoning by 40 ppm sulfur from LPG feed.

References

(1) Rostrup-Nielsen, J.R., *Catalysis Today*, **1997**. *37*, 225-232.
(2) Rostrup-Nielsen, J.R., *Catalytic Steam Reforming*, in *Catalysis: Science and Technology*, J.R. Anderson and M. Boudart, Editors. 1984, Springer-Verlag: Berlin. pp. 1-117.

COMPARISON OF AUTOTHERMAL REFORMING FOR HYDROCARBON FUELS

Bijan F. Hagh

ES Logic, LLC
4231 E. Regency Avenue
Orange, CA. 92867

Introduction

The development of fuel cells is promised to enable the distributed generation of electricity in the near future. However, the infrastructure for production and distribution of hydrogen, the fuel of choice for fuel cells, is currently lacking. Efficient production of hydrogen from fuels that have existing infrastructure (e.g., natural gas or gasoline) would remove a major roadblock for acceptance of fuel cells for distributed power generation.

There are a number of fuel processing technologies for hydrogen generation from hydrocarbon fuels, but in actuality these technologies are points along a spectrum that spans combustion and partial oxidation (POX) through steam reforming (SR) (1). Autothermal reforming (ATR) combines partial oxidation (POX) and SR, in a single process. POX reaction is exothermic or produces heat, while SR reaction is endothermic and heat must be generated external to the reformer process. Other exothermic reactions that may simultaneously occur in ATR include water gas shift (WGS) and methanation reactions. Typically, ATR reactions are considered to be thermally self-sustaining, and therefore, do not produce or consume external thermal energy. Catalysts are commonly used to enhance the reaction rate of the reforming processes at lower temperatures.

Independent parameters that affect the performance of an ATR reactor are inlet feed temperature, steam-to-carbon ratio (S/C), oxygen-to-carbon ratio (O_2/C), and pressure. S/C and O_2/C are defined as the ratio of H_2O and O_2 feed to the reaction relative to carbon in the fuel on a molar basis respectively. Dependent parameters include reformate outlet temperature, conversion and reactor heat loss.

In this study, a general framework for comparison of fuel reforming data, in the full range of steam reforming to combustion, is developed based on stoichiometric analysis of autothermal reforming. This framework is then applied to determine the reforming reaction space for various hydrocarbons fuels. H_2 yield from fuel processing is determined based on energy and material balance coupled with chemical equilibrium requirements. The assumptions inherent in the ATR energy and material balance are as follows:

- Complete consumption of O_2 without formation of carbon soot, which is a reasonable assumption at a S/C level of 2 or above (2).
- The carbon in the fuel is reformed to CH_4, CO or CO_2 only. For reforming of methane, CO and CO_2 constitute the only carbon containing reforming products (3).
- SR, WGS and methanation (for non-methane fuels) reactions are assumed to be at equilibrium at ATR outlet temperature. This is again a reasonable assumption based on previous studies (4).
- Adiabatic reaction

Generalized Reforming Reaction Space

ATR reaction stoichiometrics for a generalized fuel, $C_xH_YO_Z$, can be represented as:

$$C_xH_YO_Z + a\,O_2 + b\,H_2O = c\,CH_4 + d\,CO + e\,CO_2 + f\,H_2$$

Where,

Table 1 - Fuel Properties

Fuel - $C_XH_YO_Z$	X	Y	Z	Max Yield = (y/2)+2x-z	$\Delta°H_f$ (kJ/mole) @ 25°C	LHV (kJ/mole)
Hydrogen	0	2	0	1	0	229.16
Methanol	1	4	1	3	-178.96	663.40
Ethanol	2	6	1	6	-203.59	1,251.96
Methane	1	4	0	4	-56.89	785.47
Propane	3	8	0	10	-66.86	2,001.89
Isooctane	8	16	0	24	-174.33	4,731.24
Dodecane	12	26	0	37	-195.10	7,392.41
Hexadecane	16	34	0	49	-248.52	9,791.77

The reference point for all enthalpies is 0 degrees absolute.

$a = O_{2,\,Feed} / C_xH_YO_{Z,Reformed}$
$b = H_2O_{Reacted} / C_xH_YO_{Z,Reformed}$
$c = CH_{4,Reformate} / C_xH_YO_{Z,Reformed}$
$d = CO_{Reformate} / C_xH_YO_{Z,Reformed}$
$e = CO_{2,Reformate} / C_xH_YO_{Z,Reformed}$
$f = H_{2,Reformate} / C_xH_YO_{Z,Reformed}$

The above assumes that all O_2 is consumed in the ATR without formation of carbon soot. Based on atomic balance for O, C and H, it can be shown that:

$b = d+2e-z-2a$
$c = x-d-e$
$f = y/2+b-2c$

Combining all three Equations and rearranging:

$$f = (y/2+2x-z) - 2a - (d+4c) \quad (1)$$

The above equation indicates that maximum theoretical hydrogen yield occurs when all the carbon in the fuel is reformed to CO_2 (i.e., no CH_4 or CO produced), which is consistent with previous literature [5]. For maximum hydrogen yield, Equation (1) reduces to:

$$f_{max} = (y/2+2x-z) - 2a \quad (2)$$

Table 1 summarizes the values of (y/2+2x-z), standard heat of formation and LHV for a number of fuels and Figure 1 shows the linear relationship between LHV and (y/2+2x-z). Defining Stoichiometric Ratio (SR) as the ratio of oxygen reacted to stoichiometric oxygen required for combustion, the maximum hydrogen yield for any fuel can be represented by the following Equation:

$$f_{max}/(y/2+2x-z) = 1 - SR \quad (3)$$

where, $SR = 2a/(y/2+2x-z)$

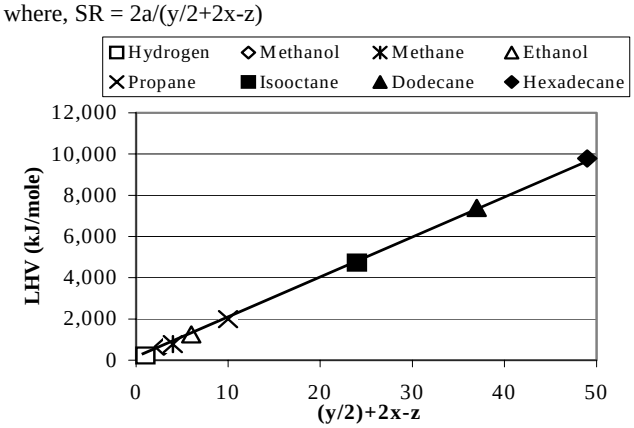

Figure 1. Maximum hydrogen yield for steam reforming of various fuels

Methane Reforming Reaction Space

ATR reaction stoichiometrics for methane fuel can be represented as:

$CH_4 + a\ O_2 + b\ H_2O = c\ CO + d\ CO_2 + e\ H_2$

Where,

$a = O_{2,\ Feed}/(CO+CO_2)_{Reformate} = (O_2/CH_4\ Feed)/X$

$b = H_2O_{Reacted}/(CO+CO_2)_{Reformate}$

$c = CO_{Reformate}/(CO+CO_2)_{Reformate} = (CO/CH_4\ Feed)/X$

$d = CO_{2,Reformate}/(CO+CO_2)_{Reformate} = (CO_2/CH_4\ Feed)/X$

$e = H_{2,Reformate}/(CO+CO_2)_{Reformate} = (H_2/CH_4\ Feed)/X$

$X = CH_4\ Conversion = (CO+CO_2)_{Reformate}/(CO+CO_2+CH_4)_{Reformate}$

The above assumes that all O_2 is consumed in the ATR without formation of carbon soot. Based on atomic balance for O, C and H, it can be shown that:

$b = e-2 = (H_2/CH_4\ Feed)/X - 2$

$c = 2-2a-b$

$d = 2a+b-1$

If $c=0$ or $CO/CO_2=0$,

$e = 4-2a$

$b = 2-2a$ or $a = 1-0.5b$

$d = 1$

The above means that a plotted versus e versus a will be straight lines. The upper solid line in Figure 2 represent the case of $CO/CO_2=0$.

If $d=0$ or $CO/CO_2=\infty$,

$e = 3-2a$

$b = 1-2a$ or $a = 0.5-0.5b$

$c = 1$

The lower solid line in Figure 2 represents the case of $CO/CO_2=\infty$. In general, it can be shown that for a given CO/CO_2 in the reformate:

$e = A-2a$

Where, $A = [3\ (CO/CO_2)+4]/[(CO/CO_2)\ +1]$

and, $3 \le A \le 4$

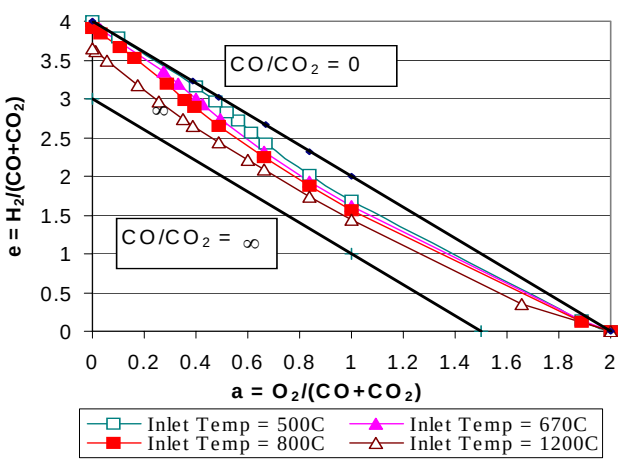

Figure 2. Refrming reaction space for methane at S/C = 6, and P = 97 psig (770 kPa)

ATR Fuel Comparison

Figures 3, 4 and 5 show the reaction space and the effect of inlet temperature on H_2 yield for autothermal reforming of a number of fuels at S/C=3. In these plots of SR versus Hydrogen Ratio (HR), the equilateral triangle bounded by HR = 0, SR = 0 and Equation (3) constitutes the ATR reaction space in the full range of combustion to steam reforming for any fuel. HR is defined as the ratio of the moles of H_2 produced per moles of fuel reformed to (y/2+2x-z). HR is a normalized hydrogen yield, where HR = 1 represents the maximum hydrogen yield for reforming of a given fuel. It is important to mention that the ATR reaction space is independent of conversion, S/C, pressure, temperature, heat loss, assumption of equilibrium, or choice of fuel. Figures 3-5 show that higher inlet temperature generally yields more hydrogen with the maximum hydrogen yield shifting to a lower SR at a given S/C. Table 2 summarizes the maximum H_2 yields and provides the reactor inlet and outlet temperatures for the reforming data shown in Figures 3 to 5. These figures show that HR (i.e. normalized hydrogen yield) increases and experiences a maximum with respect to SR for all fuels. The beneficial effects of increasing inlet feed temperature and fuel LHV on the maximum HR are shown in Figures 6 and 7.

Table 2 - Maximum Normalized H_2 Yield for Various Fuels

Fuel	SR	S/C	Pressure psig (kPa)	T in (°C)	T out (°C)	Maximum HR
Methane	0.254	3	5 (136)	500	649	0.639
	0.199	3	5 (136)	670	649	0.675
	0.181	3	5 (136)	800	649	0.698
Propane	0.244	3	5 (136)	500	649	0.638
	0.179	3	5 (136)	670	649	0.680
	0.131	3	5 (136)	800	649	0.707
Isooctane	0.226	3	5 (136)	500	649	0.646
	0.162	3	5 (136)	670	649	0.687
	0.115	3	5 (136)	800	649	0.713
Dodecane	0.217	3	5 (136)	500	649	0.653
	0.165	3	5 (136)	670	677	0.694
	0.112	3	5 (136)	800	677	0.729
Hexadecane	0.207	3	5 (136)	500	649	0.659
	0.142	3	5 (136)	670	649	0.699
	0.116	3	5 (136)	800	663	0.729

Conclusions

The stoichiometric analysis of the autothermal reaction for a generalized fuel is used to determine the reforming reaction space for methane, propane, isooctane, dodecane, and hexadecane, in the full range of steam reforming to combustion. A methodology is shown for normalizing hydrogen yield data to facilitate direct comparison. The hydrogen yield appears to increase with S/C and inlet temperatures for all fuels. The simulation data and conclusions of this paper are applicable to any ATR regardless of size and are independent of feed flowrates.

References

[1] Hagh, B.F. *International Journal of Hydrogen Energy*, **2003**, 28, 1369-1377.

[2] Douvartzides, S.L.; Coutelieris, F.A.; Demin, A.K.; Tsiakaras, P.E. *AIChE Journal*, **2003**, 49, 248-257.

[3] Ming, Q.; Healey, T.; Allen L., Irving, P. *Catalysis Today*, **2002**, 51-64.

[4] Brown, L.F. *International Journal of Hydrogen Energy*, **2001**, 26, 381-397.

[5] Ahmed, S.; Krumpelt, M. *International Journal of Hydrogen Energy*, **2001**, 26, 291-301.

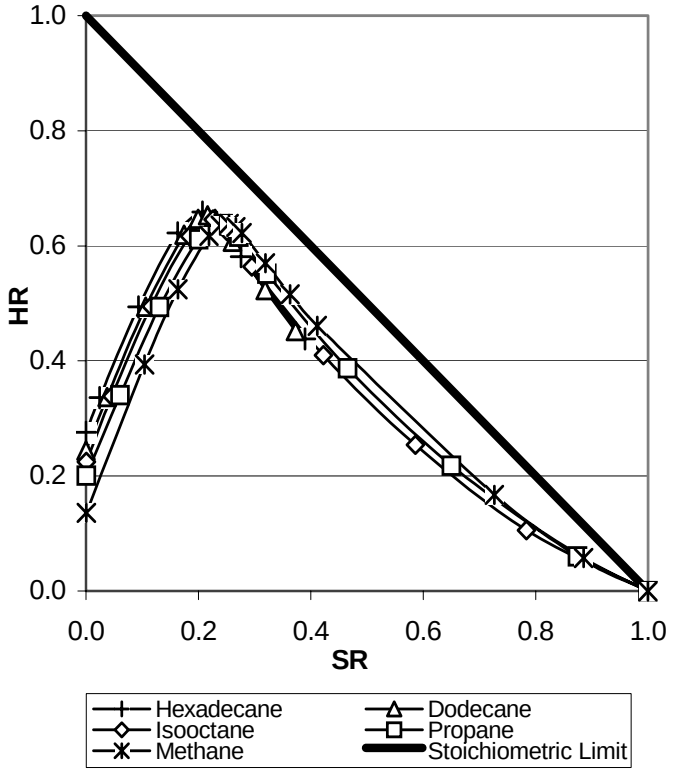

Figure 3. Inlet temperature = 500°C, S/C = 3, P = 5 psig (136 kPa)

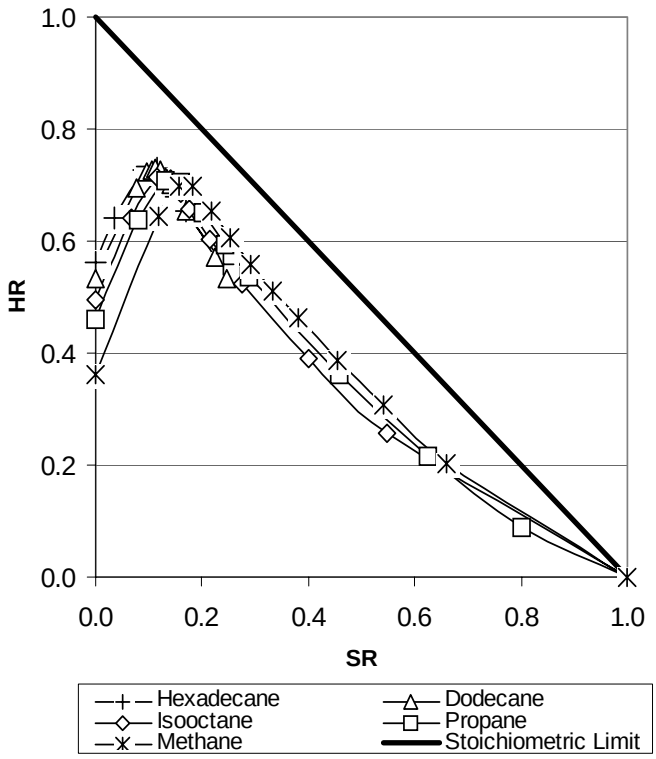

Figure 5. Inlet temperature = 800°C, S/C = 3, P = 5 psig (136 kPa)

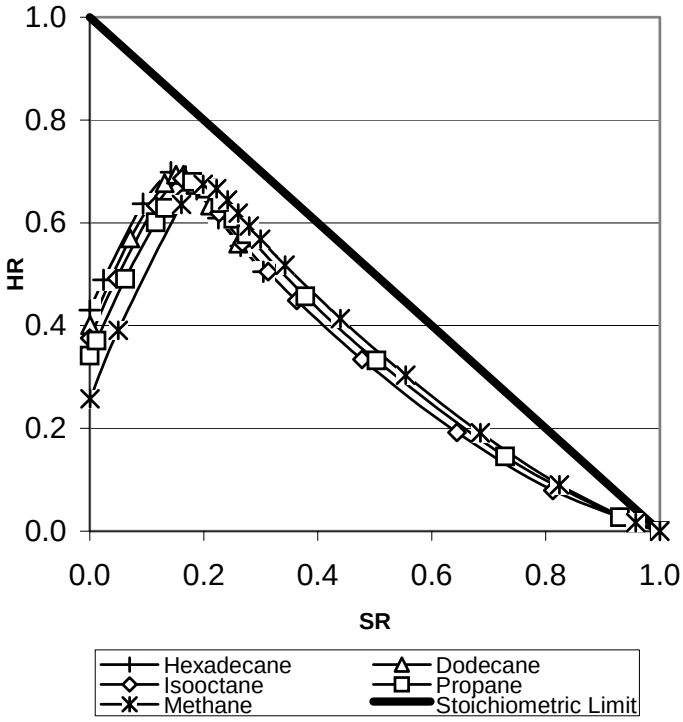

Figure 4. Inlet temperature = 670°C, S/C = 3, P = 5 psig (136 kPa)

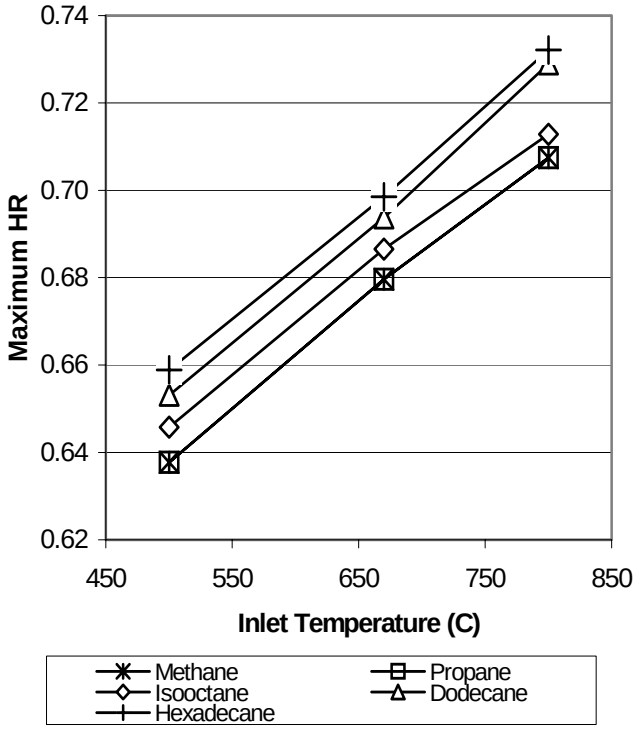

Figure 6. Maximum hydrogen yield at S/C = 3, P = 5 psig (136 kPa)

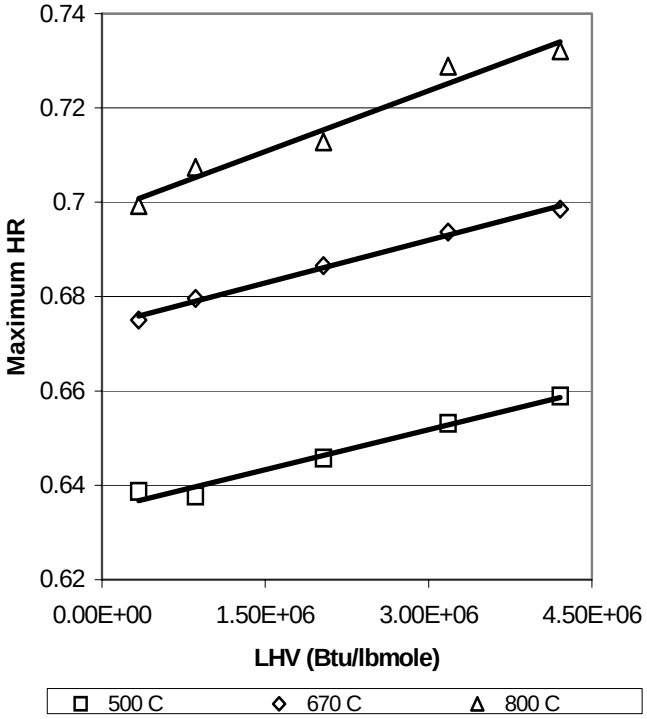

Figure 7. S/C = 3, P = 5 psig (136 kPa)

CATALYTIC REACTOR PERFORMANCE OF A BOROHYDRIDE HYDROGEN GENERATOR

Ying Wu, Qinglin Zhang, Kevin McNamara, Gregory Smith, Joseph Podsiadlik, Ibrahim Qureshi*

Millennium Cell Inc.
1 Industrial Way West, Eatontown, NJ 07724

Introduction

Hydrogen storage is one of the most important issues and potentially the biggest technical barrier to the implementation of a hydrogen economy. Both physical and chemical storage methods are under investigation in order to solve this challenging technical problem. Among all the options, hydrogen storage systems based on chemical hydrides[1,2] have demonstrated gravimetric and volumetric hydrogen storage densities that meet the near term targets and approach the long-term targets of the FreedomCar Initiative. Particularly, sodium borohydride ($NaBH_4$) based systems[3] have shown impressive system performance characteristics.

Sodium Borohydride reacts with water to generate high purity humidified hydrogen gas (H_2) (Eq. 1) suitable for use in proton exchange membrane (PEM) fuel cells. This hydrolysis reaction takes place spontaneously in an un-stabilized solution, and the reaction rate increases dramatically with temperature. Addition of a base such as NaOH or KOH to aqueous solutions of $NaBH_4$ can stabilize the solution against hydrolysis, but the reaction can be initiated again with a suitable catalyst. It is this catalyzed hydrolysis that forms the basis of the Hydrogen on Demand™ (HOD™) technology.

$$NaBH_4 + 4\ H_2O = NaB(OH)_4 + 4\ H_2\uparrow \qquad (1)$$

An effective catalyst is critical to quantitatively and controllably extracting the hydrogen stored in mixtures of borohydride and water. One of the first reports on the catalyzed hydrolysis by Brown[4] examined a number of metals and established relative rates for hydrogen generation using these catalysts. According to Brown, noble metals such as ruthenium (Ru) and rhodium (Rh) are excellent catalysts for this reaction. More recently, less costly metal-boron alloys such as nickel boride and cobalt boride are also reported to be effective catalysts.[5,6]

The desired catalyst has to offer superior reactivity to ensure fast hydrogen generation. High conversion of $NaBH_4$ to H_2 is critical. It is desirable that the catalyst is capable of operating with high concentration $NaBH_4$ fuel over a wide range of fuel throughput (or space velocity). The catalyst also needs to provide fast start-up and be sufficiently durable. Optimization of reactor throughput will result in reduction of catalyst chamber volume and weight, thereby reducing the balance of plant (BOP) in the hydrogen storage system and increase overall gravimetric and volumetric storage efficiencies.

Many factors influence the activity and reactor performance of a catalyst, such as catalyst preparation procedures, catalyst support materials, chemical and morphological transformations of the catalyst surface during reaction, as well as reactor design, operating conditions, and heat and mass transfer issues. To understand the catalyst system, each of these factors should be isolated and studied in detail to the extent possible. In this paper, we report preliminary reactor performance results on a few critical parameters, which include %$NaBH_4$ conversion, liquid feed space velocity, and catalyst durability, of the HOD™ catalysts in a packed bed reactor operating under various hydrogen flow conditions. Results from these studies provide information and direction for further improvements in the catalyst technology.

Experimental

Catalyst Preparation and Fuel Composition The active metal catalyst was supported on a suitable metallic substrate according to methods taught in U.S. Patent 6,534,033 B1[7]. Two catalysts, BMR05 and BMR06, which contain different loadings of active catalyst were selected for detailed evaluation. The fuel solution used in the experiments typically contains 20 wt% $NaBH_4$.

Measurements of Hydrogen Generation Catalyst activity is measured by the apparent hydrogen evolution rates. In many previous reports, hydrogen generation rates were measured from batch type reactors, where a specific amount of catalyst is placed in stagnant or stirring borohydride solution and the resultant hydrogen generation rates measured. In such a configuration, the product sodium metaborate ($NaB(OH)_4$) is mixed with reactant $NaBH_4$ in the same solution, and it is often difficult to achieve close to quantitative conversion of $NaBH_4$ without providing external heating to the solution.

In the results reported below, all hydrogen generation rates were measured using a flow reactor. In a typical experiment, a cylindrical reactor of certain volume is packed with a constant amount of catalyst for testing. One end of the reactor is connected to a fuel line via a metering pump. The rate of liquid flow into the reactor is monitored by the weight change of the fuel reservoir. The other end of the reactor is connected to a liquid-gas separator where hydrogen gas and the liquid by-product, $NaB(OH)_4$ solution, are separated. In the flow reactor, metaborate does not back mix with the $NaBH_4$ reactant solution. The separated hydrogen stream then passes through a condenser and a drying column to remove water and ensure accurate measurement of hydrogen flow rate. Conversion of borohydride to hydrogen, or reaction yield, is calculated by dividing the measured hydrogen flow rate by the theoretical hydrogen flow rate calculated based on the fuel feed rate.

Catalyst Durability Data were collected from semi-continuous operation. The reactor was operated at a constant liquid feed space velocity for 6-8 hours a day. At the end of the day, reactor was shut down and catalyst bed rinsed with water. The next day, same procedures were repeated, and on-stream hours accumulated.

Results and Discussion

Conversion Efficiency and Throughput Sodium borohydride conversion efficiency was measured over a range of fuel flow rates. One of the advantages of borohydride hydrolysis is that the reaction

can go to 100% completion with no side reactions. The challenge in a flow reactor is to maximize the fuel throughput rate while preserving 100% conversion of the reactant. The higher the throughput, the smaller the reactor volume required for a given hydrogen output level. Figure 1 shows typical experimental conversion results. It can be easily seen from the graph that for space velocity up to ~1.25 min^{-1} (or 75 hr^{-1}), conversion of borohydride to hydrogen remains above 95%.

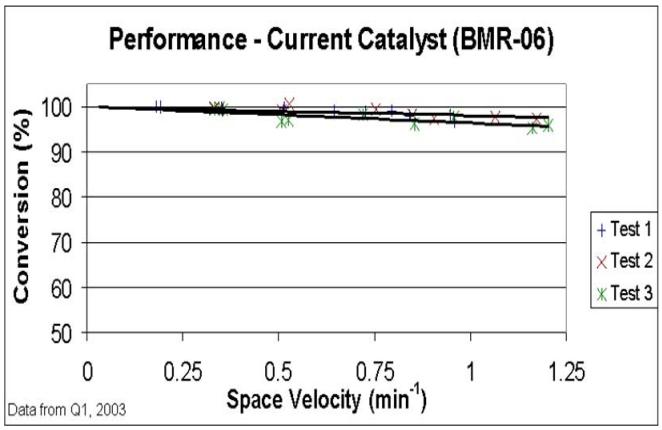

Figure 1. Conversion of $NaBH_4$ at various liquid feed space velocity.

Durability Durability of the catalyst was measured to ensure that there is no drastic deactivation of catalyst. Figure 2 depicts a durability study of catalyst BMR05. Constant performance level was demonstrated for more than 400 hours of run time. Hydrogen generation rate remained relatively constant, about 8.1 SL/min, at a constant liquid fuel feed rate of 18 g/min, corresponding to ~95% $NaBH_4$ conversion throughout the experiment. The three thermocouples evenly spaced along the reactor length recorded steady temperatures between 140-150°C. In a separate durability test

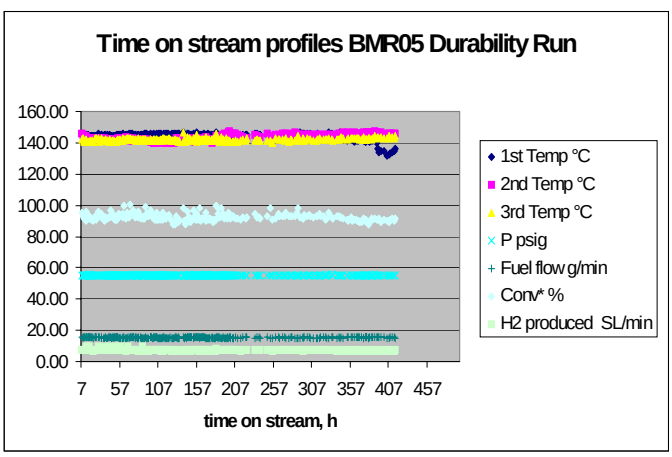

Figure 2. Time on Stream Profile of BMR05. Sodium borohydride conversion, hydrogen flow rate, fuel flow rate, system pressure, and reactor temperatures are plotted as a function of time on stream.

of catalyst BMR06 (based on a slightly modified recipe), more than 700 hours of run time has been accumulated and no significant drop in performance level has been observed. In both experiments, the liquid feed space velocity was maintained at 0.25 min^{-1} (or 15 hr^{-1}), and the system pressure was regulated at 55 psig.

Additional data also indicate that durability of the catalyst varies with different catalyst supports. In some cases, only a few days of high conversion operation was sustained before the catalyst became ineffective. Furthermore, catalyst durability often decreased with increasing liquid feed space velocity. More extended durability studies will be carried out as catalyst preparation procedures and materials properties are optimized. We expect to be able to demonstrate catalyst durability on the order of several thousand hours.

Conclusions

Higher sodium borohydride conversion can be achieved over a wide range of fuel feed space velocity in a packed bed flow reactor system. The reaction is self-sustaining, without need for external heating to achieve higher % conversion. Initial durability studies indicated that the current generation of catalyst can be operated for more than 700 hours on stream without significant loss in activity. Further improvements can be made on durability by optimizing catalyst preparation procedures and reactor engineering.

Overall optimization of the catalyst will depend on our increased understanding of the catalyst composition, structure, as well as reactor operation conditions.

References

(1) Bogdanovic, B.; Schwickardi, M. *J. Alloys Compounds* **1997**, 1-9.

(2) Schlapbach, L.; Zuttel, A. *Nature* **2001**, 353-358.

(3) Mohring, R. M.; Eason, I. A.; Fennimore, K. A. *SAE Technical Paper # 2002-01-0098* **2002**.

(4) Brown, M. C. *Journal of American Chemical Society* **1962**, *84*, 1493-1495.

(5) Holbrook, K. A.; Twist, P. J. *J. Chem. Soc. (A)* **1971**, *1971*, 890-894.

(6) Dong, H.; Yang, H.; Ai, X.; Cha, C. *International Journal of Hydrogen Energy* **2003**, 1095-1100.

(7) Amendola, S.; Binder, M.; Sharp-Goldman, S.; Kelly, M.; Petillo, P.; Millennium Cell Inc.: USA, 2003.

CHEMICAL HYDROGEN STORAGE IN NANO-STRUCTURED MATERIALS. CONTROL OF HYDROGEN RELEASE AND REACTIVITY FROM AMMONIA BORANE COMPLEXES.

Tom Autrey, Anna Gutowska, Liyu Li, John Linehan, Maciej Gutowski

Pacific Northwest National Laboratory, Richland, WA 99352, USA

Introduction

The DOE has recently issued a Grand Challenge in Hydrogen Storage to compliment existing programs on Hydrogen Production and Fuel Cell development.[1] In response to this challenge we have initiated a program that uses a combination of experimental and computational approaches to investigate the potential of NH_xBH_x (x=1-4) as chemical hydrogen storage materials for on-board hydrogen storage. Our initial computational results suggest that the step-wise process is not greatly exothermic.[2] If true, these materials may provide great hope for a reversible hydrogen storage material with high volumetric and gravimetric density for on-board storage.[3] The optimum thermal decomposition reaction $NH_4BH_4 \rightarrow BN + 4H_2$, occurs by a four-step process and provides a theoretical yield of 24 wt% hydrogen far exceeding DOE's most ambitious goals. Even if two of the four steps prove feasible H_2 capacities of greater than 12 weight % would be realized. In this present work we have focused our experimental efforts on ammonia-borane [NH_3BH_3]. In the solid state ammonia-borane (AB) undergoes a rapid dehydropolymerization reaction upon melting at 115 ˚C to yield polyammonia-borane [$(NH_2BH_2)_n$], an inorganic analog of polyethylene, + H_2.[4] In a subsequent step the $(NH_2BH_2)_n$ decomposes to [$(NHBH)_2$], an inorganic analog of polyacetylene, + H_2 at 170 ˚C.[5] An undesirable side reaction, formation of the cyclic borazine $(NHBH)_3$, an inorganic analog of benzene, has also been observed to form from the bulk material at the higher temperatures. Borazine is an undesirable side product due to its high vapor pressure. Given the stringent requirements of hydrogen purity for fuel cell applications it will be important to minimize side reactions. One of the major goals of this work was to use the nanometer diameter pores of mesoporous templates to control the selectivity of the hydrogen release pathways from ammonia-borane and polyammonia-borane.

Experimental

Ammonia borane was purchased from Aldrich (90% tech) and purified by recrystallization from diethyl ether followed by a wash with ethanol to remove polymeric and borate impurities to yield >99% pure NH_3BH_3 by ^{11}B NMR. Analyses were performed using a Netzsch STA 409 TGA/DSC and a Pfeiffer QMS300 MS or a Setaram C80 Calorimeter. In the Netzsch equipment a heated fused silica capillary (200 ˚C) was used to transfer the off gas from the TGA to the MS. The MS uses a standard electron impact ionization detector. The MS scanning rate was 12 seconds for a range of 1 to 100 amu. A thermal ramp of 5 ˚C/min from room temperature to 250 ˚C using an argon flow of 100 cc/min was used in our analysis.

Results and Discussion

Preparation of mesoporous templated ammonia-borane. Mesoporous silica templates have extremely high surface area and a highly ordered pore structure by virtue of surfactant templated synthetic process.[6] The material used in this work, SBA-15, prepared according to literature procedures for another project, was characterized and found to have average particle 100-200 μm, surface area 1000 m^2/g, pore diameter 3 nm. A sample of 50 mg of the SBA-15 was exposed to a 300 μL methanolic solution containing 50 mg of AB. Given the porous nature of the material we expected capillary action to fill the internal channels of the mesoporous template. The 'wet' SBA-15 was dried under vacuum to produce a sample with an internal coating of ammonia-borane (ca. 1:1 wt% AB to SBA-15). Comparison of SEM images of the material before and after coating with AB showed very similar features as shown in Figure 1. We expected to visually observe clumping of the solid AB on the template if we were not successful in our attempt to coat the internal channels. An EDM scan of the 1:1 mixture of AB:SBA-15 sample also produced very little signal from N and B and we again would have expected a greater signal if the AB was not efficiently deposited within the core structures of the SBA-15. Given these negative observations we assumed that we had a sample of SBA-15 mesoporous template with internal pores coated with monomeric ammonia-borane.

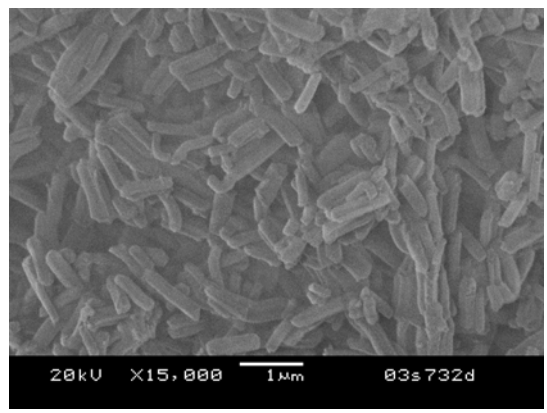

Figure 1. SEM image of 1:1 Mixture of AB:SBA-15. We could observe no difference in the image before or after AB was added. The EDM scan showed no evidence for either Boron or Nitrogen. These observations lead us to assume that the AB was deposited as a thin layer within the mesoporous template.

Calorimetric and mass spectroscopy studies of ammonia-borane , thermolysis in mesoporous silica templates. In order to test our hypothesis that the yield of borazine [*c*-$(NHBH)_3$], an inorganic analog of benzene, would be reduced when the AB was heated as a 1:1 weight mixture, we undertook differential scanning calorimetry (DSC) experiments to compare the neat bulk material to our 1:1 AB:SBA-15 sample prepared as described above. It is likely that hydrogen formation occurs by an intermolecular dimerization pathway as shown in equation 1,[7] however a two-step mechanism can not be completely ruled out, eqs 2 and 3.

(1) $2\ NH_3BH_3 \rightarrow NH_3BH_2\text{-}NH_2BH_3 + H_2$

(2) $NH_3BH_3 \rightarrow NH_2{=}BH_2 + 2H_2$

(3) $2NH_2{=}BH_2 \rightarrow NH_3BH_2\text{-}NH_2BH_3$

If reaction 1 is the mechanistic pathway then it follows that the dimer would form oligomers through subsequent bimolecular dehydopolymerization pathways. Each step that forms a new B-N bond also forms hydrogen, eqs 4 and 5.

(4) $NH_3BH_3 + NH_3BH_2\text{-}NH_2BH_3$
$\rightarrow NH_3BH_2\text{-}NH_2BH_2\text{-}NH_2BH_3 + H_2$
(5) $NH_3BH_3 + NH_3BH_2NH_2BH_2\text{-}NH_2BH_3$
$\rightarrow NH_3BH_2\text{-}NH_2BH_2\text{-}NH_2BH_2\text{-}NH_2BH_3 + H_2$

As the temperature approaches 170 ˚C additional hydrogen is released, eqs, 6 and 7. However, a competing side reaction is cyclization to form borazine, eq 8.[8]

(6) $(NH_3BH_2NH_2BH_2\text{-}NH_2BH_3)_n$
$\rightarrow (NH_3BH_2NH_2BH{=}NHBH_3)_n + H_2$
(7) $(NH_3BH_2NH_2BH{=}NHBH_3)_n$
$\rightarrow (NH_3BH{=}NHBH{=}NHBH_3)_n + H_2$
(8) $(NH_3BH{=}NHBH{=}NHBH_3)_n \rightarrow$ borazine + H_2

Under optimum conditions we want to minimize cyclization, reaction (8) and optimize further dehydrogentation, i.e., reactions (6 and 7). We expected that if the AB was coated on the inside of the mesoporous silica template that the template would minimize borazine formation by controlling linear polymer growth and minimizing cyclization. To test this hypothesis DSC experiments were preformed with both the neat AB and the 1:1 mixture of AB:SBA-15. Two results are notable. First, as hoped, borazine formation appears to have been substantially reduced when AB is heated as the 1:1 composite with SBA-15. It is below the detection limits of our mass detector. Even when the flow rate of argon is reduced to 40 cc/minute we did not detect borazine, though hydrogen release was still observed at ca. 170 ˚C, temperature corresponding to borazine formation in the neat AB. Second, a surprising result, the observation that hydrogen is released in the initial step, eq 1, at a significantly lower temperature when the AB is heated as the 1:1 composite with SBA-15! This result is illustrated in Figures 2. This novel finding is especially attractive given that a

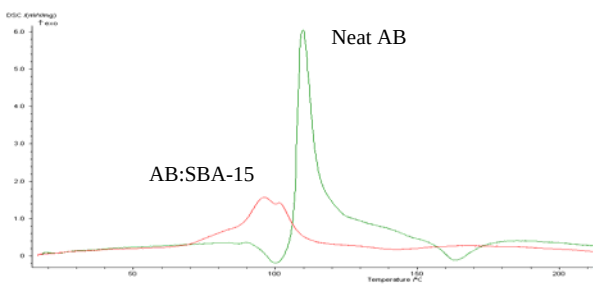

Figure 2. Comparison of DSC scan (temperature vs power) of neat AB (green line) and 1:1 AB:SBA-15 mixture (red line). Ramp rate 5 ˚C/min from room temperature to 250 ˚C. The peak of the exotherm is 110 ˚C for neat AB and 96 ˚C for the mixture.

fundamental requirement for on-board storage is the release of H_2 at temperatures below 100 ˚C. In the 1:1 AB:SBA-15 sample hydrogen is released at 96 ˚C compared to the 110 ˚C for the neat AB sample.

Conclusions

In this paper we present the results of our efforts using the mesoporous silicate template (SBA-15) to control the chemistry of dehydropolymerization of ammonia-borane (AB) to yield gaseous hydrogen. Thermolysis of AB in the SBA-15 template shows two profound effects different than observed in the bulk thermal reaction: (i) hydrogen is released from AB at significantly lower temperatures (well below 100 ˚C) and (ii) contrary to observations that borazine is formed in bulk AB thermolysis, no borazine is detected in AB thermolysis in the mesoporous template.

Acknowledgement. This research was performed in part using the Interfacial and Nano Science facility in the William R. Wiley Environmental Molecular Sciences Laboratory, a national scientific user facility sponsored by the U.S. Department of Energy's Office of Biological and Environmental Research and located at the Pacific Northwest National Laboratory. Pacific Northwest is operated for the Department of Energy by Battelle. The authors wish to acknowledge support from the Laboratory Directed Research and Development Program at the PNNL and the Nano Science and Technology Initiative and Dr. Yongsoon Shin for providing us with the SBA-15 and Jim Coleman for the SEM images. TA wishes to thank T Baker (LANL), L Sneddon (U Penn) and M Heinekey (U Washington) for very informative discussions on AB chemistry.

References

(1) Hydrogen, Fuel Cells & Infrastructure Technologies Program, 2003 Merit Review and Peer Evaluation Meeting, May 19-22, Berkeley, CA.
(2) See Fuel Prints this issue Symposium on Molecular Modeling and Reaction Chemistry. M. Gutowski and T. Autrey, *Prepr. Pap. –Am. Chem. Soc., Div. Fuel Chem.* **2004**, 49(2) xxxx.
(3) It has recently been shown that conversion of ammonia-borane to polyaminoborane is exothermic by less than 7 kcal/mol. G. Wolf, J. Baumann, F. Baitalow, F.P. Hoffman, *Thermochim. Acta* **2000**, *343*, 19.
(4) V. Sit, R.A. Geanangel, W.W. Wendlandt *Thermochim. Acta* **1987**, *113*, 379.
(5) F. Baitalow, J. Bauman, G. Wolf, K. Jaenicke-Röβler, G. Leitner *Thermochim. Acta* **2002**, *391*, 159.
(6) Zhao, D., Feng, J., Huo, Q., Melosh, N., Fredrickson, G. H., Chmelka, B. F., Stucky, G. D. *Science* **1998**, *279*, 548.
(7) C. A. Jaska; K Temple; A. J. Lough; I. Manners. *J. Am. Chem. Soc*. **2003**, *125*, 9424.
(8) T. Wideman, L.G. Sneddon *Inorg. Chem.* **1995**, *34*, 1002.

THEORETICAL PERSPECTIVE ON IMPROVING KINETICS IN Mg HYDROGEN STORAGE

Jian-jie Liang, Nazy Khosrovani

Accelrys Inc.
9685 Scranton Rd
San Diego, Ca 92121

Introduction

Magnesium, forming ionic, transparent MgH_2 containing 7.6 mass% hydrogen, is among those that are most-promising in hydrogen-storage materials for mobile applications [1]. However, the formation from bulk Mg and gaseous hydrogen is not only extremely slow, but requires elevated temperatures (300 °C at 1 bar pressure) as well, with the reverse process requiring similar conditions [2]. Numerous factors can contribute to the kinetics of the forward and reverse reactions in the hydrogen storage processes [3]. Among them, molecular hydrogen dissociation and hydrogen diffusion are two factors of primary concern. It's already known that hydrogen diffuses only extremely slowly in crystalline Mg, with a diffusion constant in the order of 10^{-16} cm^2/s [4]. This translates to that the mean time ($d^2/6D$, where D is the diffusion constant) for hydrogen to diffuse through a 1 μm Mg particle will be in the order of 10^3 S. One may hope that reducing the particle sizes to nanometers will speed up the kinetics, only to see no significant improvement [5]. It therefore appears that molecular hydrogen dissociation on Mg surfaces is a rate-limiting process.

It had been demonstrated recently [6] that Density Functional Theories (DFT) approach can be used to successfully explore tailoring the energetics of Mg hydrogen sorption/desorption processes, fundamentals that are responsible for properties such as diffusion rate and nucleation. The same principles should apply in exploring aspects in the hydrogen dissociation process, as shown in the literature [7, 8]. In the present work, DFT method was used to look at hydrogen dissociation on both unmodified- and transition metal modified-Mg 100 surface. Energy barrier, surface sorption energy, and surface diffusion barrier are the main focuses of the work.

Method

$Dmol^3$ [9], a Density Functional Theory (DFT) method available in the software package, Materials Studio, was used in the calculations. The setup parameters were similar to those used previously in the thermochemical studies of similar materials [6].

Experimental structure of Mg [10] was used as starting model to obtain the DFT relaxed structure that was identical to what was found in previous study [6]. The 100 surface (Fig. 1A) was constructed based on the DFT optimized bulk structure. Surface suppercell of 4 x 2 was built such that the calculated hydrogen dissociation barrier (see later sections) becomes invariant as a function of cell size, with respect to a set of k-point density. To model the surface environment, a vacuum space of 20 Å was added on top of the surface such that 3D periodic conditions can be used in the summation of the energy terms in the DFT calculations. A total of 4 Mg layers (corresponding to 4-unit cell depth perpendicular to the 100 surface) were used in the calculations. Mg atoms in the surface layer and the layer immediately beneath were allowed to relax prior to introducing hydrogen into the systems. In most cases, one of the surface Mg atoms would be replaced by a transition mental atom (e.g., Fe as in Fig. 1D), and the surface structure reoptimized.

For unmodified Mg 100 surface, two hydrogen dissociation geometries were considered (Fig. 1B&C), corresponding to the hydrogen molecule approaching the surface towards the center of gravity ("atop") of a single Mg atom and towards the "bridge" between two Mg atoms, respectively, and dissociate into the nearby hollows surrounded by 3 Mg atoms. For transition metal-doped surfaces, only the atop configuration was considered, as the bridge configurations were not stable in these circumstances and evolved into atop configuration eventually. A single hydrogen molecule was placed in the middle of the vacuum space (~ 10 Å above the surface) for the initial configuration of the dissociation process.

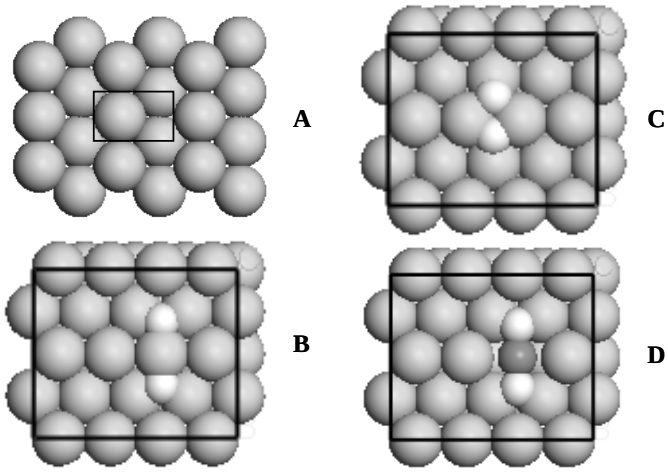

Figure 1. Mg 100 surface used in the calculations. A. the surface layer (1-unit cell depth). The rectangle outlines the original surface unit cell; B. actual simulation cell (4 x 2 x 4) with the adsorbed hydrogens through the "atop" configuration; C. same as B, but with the adsorbed hydrogens through the "bridge" configuration; D. same as B, but with a transition metal (here Fe) atom replacing Mg. Large grey ball: Mg; small, light grey ball: H; small, dark grey ball: Fe.

Transition state search engine available in the Dmol3 package was used for all transition state calculations. Full LST/QST [11] search were performed on each and every sample system, and usually followed by a transition state optimization calculation.

When transition state search failed to produce a transition state (usually associated with transition metal-doped surfaces), the approach of potential energy surface (PES) was used to confirm the nature of unactivated dissociations of hydrogen on such surfaces.

Results and Discussions

The calculated energy barriers, along with the energetic and structural parameters of the corresponding transition states (if exist) are given in Table 1. Note here the enthalpy of reaction (ΔH_f) refers to the difference directly between the total energy of the state when the hydrogen molecule is in the middle of the vacuum space (~ 10 Å above the surface) and that when hydrogen is dissociated into the hollows (state obtained through geometry optimization).

Dissociations on unmodified Mg 100 surface. Hydrogen Dissociations are activated in either atop or bridge configuration (Table 1), with dissociation barriers of ~ 92 kJ/mol. This is in qualitative agreement with earlier theoretical and experimental studies [8, 12] on a different surface (Mg 0001). It's important to note that the enthalpies of reaction are very small (slightly exothermic in atop configuration and slightly endothermic in the bridge configuration) compared to the energy barrier (Fig. 2). In other words, the activation

barrier is the factor that controls the rate of both forward (sorption) and reverse (desorption) processes, and the barrier height dictates the temperature and pressure conditions of both the sorption and desorption processes.

Table 1. Thermodynamic and structural data of H_2 dissociation/absorption on Mg 100 surface

Surface dopent	Ea (kJ/mol)	ΔH_f (kJ/mol)	Ed (kJ/mol)	d_{H-H} (Å)
Unmodified				
atop	91.92	-1.92	minimal	1.28
bridge	92.42	14.52	minimal	1.12
V	51.80	-111.13		1.14
Pd	60.79	-3.56	20.46	1.39
Cu	64.64	-15.86	22.47	1.29
Ni	17.28	-63.85	45.23	1.20
Fe		-100.75	52.05	
Co		-90.04	59.08	
Ti		-105.56	56.44	

Ea: activation energy
ΔH_f: enthalpy of reaction (surface sorption)
Ed: surface diffusion barrier, corresponding to hydrogen diffusion from a hollow with the transition metal being one of the 3 coordinating atoms to a nearby hollow
d_{H-H}: H – H distance at transition state

Dissociation on transition metal-doped surfaces. Most experimental and theoretical studies on the interaction of hydrogen with metal surfaces today involve elemental d-transition metal surfaces; some concern transition alloy surfaces [3]. However, due to the intrinsically low weight percentage of absorbed hydrogen in pure transition metals, and the problem of alloy degradation after repeated cycling of hydrogen sorption and desorption, it becomes increasingly urgent for new thinking in materials design, probably based on the known potential hydrogen storage materials.

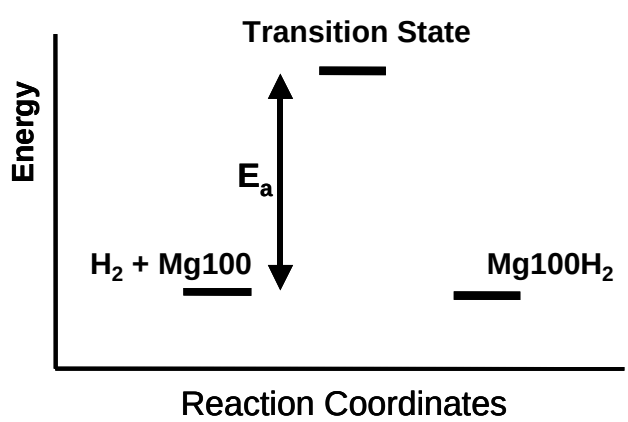

Figure 2. Activated dissociation (with energy barrier, Ea) of hydrogen on Mg 100 surface through the "atop" configuration. Note there is only a minimal difference in system energy (1.92 kJ/mol) between the starting materials (H_2 + Mg 100) and the final product (Mg 100 H_2).

Surface doping on Mg nanoparticles may offer a solution to the dilemma – transition metals doped on the particle surface may accelerate the dissociation of the hydrogen molecules, and particle size in nano-scales will make a very slow diffusion of hydrogen in, e.g., Mg particles to complete in an acceptable time scale.

It can be seen from Table 1 that activation barriers can indeed be lowered substantially, some even become unactivated (when doped with Fe, Co, or Ti). It is interesting to recognize that hydrogen dissociation over a transition metal (when doped on to the Mg 100 surface) may behave differently as appose to that on the corresponding bulk transition metal surface. For example, dissociation over Pd metal surface had been shown both experimentally and theoretically to be unactivated [13, 14, 15]. However, when doped on to the Mg 100 surface, the dissociation on the Pd atom will be activated, with a barrier of ~ 61 kJ/mol (Table 1).

Among the 7 (Table 1) commonly considered transition metals in hydrogen storage applications, 3 (Fe, Co, Ti) show unactivated dissociation when hydrogen molecule approaches the transition metal doped on to the Mg 100 surface. However, notice the associated exothermic enthalpies of reaction between 90 and 106 kJ/mol, which are in the same order of magnitude as that of the energy barrier of hydrogen dissociation over unmodified Mg 100 surface (Fig. 3). That means, while unactivated in the forward (sorption) process, it'll take similar pressure and temperature conditions for the reverse (desorption) process as for pure Mg. It is also important to notice the relatively high diffusion barrier (note there is essentially no surface diffusion barrier on unmodified Mg 100 surface), signifying potentially added difficulty diffusing into the Mg lattice beneath.

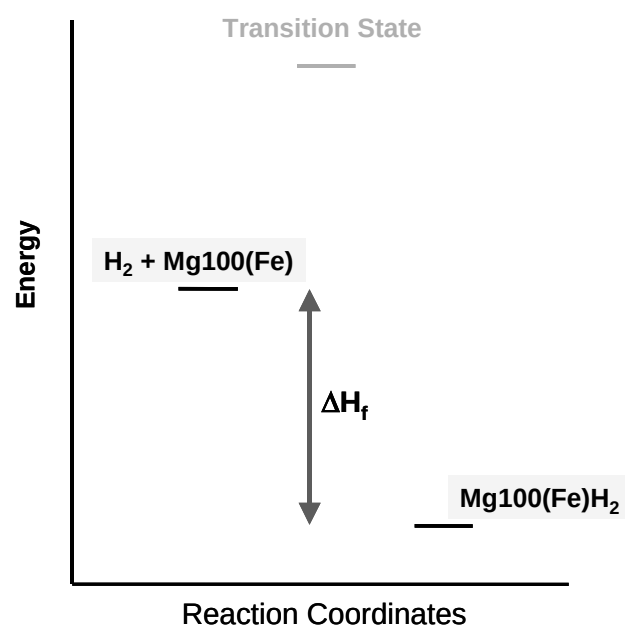

Figure 3. Unactivated dissociation of hydrogen on Fe-doped Mg 100 surface through the "atop" configuration (centered on the Fe atom. Refer to Fig. 1D). The energy barrier (the water-marked "Transition State") of the activated dissociation on unmodified Mg 100 surface was shown as a reference. ΔH_f: enthalpy of formation of the reaction.

Among the 4 doping transition metals (V, Pd, Cu, Ni) that are associated with activated dissociation, although giving a low activation barrier of ~ 17 kJ/mol, Ni is associated with a rather high enthalpy of reaction of ~ 64 kJ/mol. The combined energy needed for the reverse (desorption) process is 81 (17 + 64) kJ/mol, which approaches the barrier associated with unmodified Mg 100 surface. That probably explains why, while the hydrogen sorption process of the Mg2Ni alloy is relatively rapid, the desorption process was found to remain sluggish [1]; Vanadium presented a rather undesirable combination of relatively high activation barrier and the enthalpy of reaction, and was not considered further; Pd and Cu offer a reduction of ~ 30 kJ/mol in activation energy, and relatively low enthalpies of reaction, together with low surface diffusion barriers. In particular, Pd is associated with a minimal enthalpy of reaction (~ 3 kJ/mol), making reduced pressure and temperature conditions possible for both sorption and desorption processes.

Conclusions

Hydrogen dissociations on unmodified Mg 100 surface were found to be activated, with barriers around 92 kJ/mol. When doped with transition metals, the dissociation barrier can be lowered, in some cases to the extent of being unactivated. Pd doping was found to be the most promising, based on the considerations of the activation barrier, energy requirement for reverse (desorption) process, and surface diffusion barrier.

Acknowledgement: We thank Niri Govind, Accelrys Inc., for providing preprint on the publication on the LST/QST method. We also thank the HP Company for the computing resources.

References

1. L. Schlapbach and A. Zuttel, Nature **414**, 353 (2001)
2. L. Schlapbach (e.d.) Hydrogen in Intermetallic Compounds I. Electronic, Thermodynamic, and Crystallographyic Properties (Topics in Applied Physics Vol 63) (Springer, 1988)
3. L. Schlapbach (e.d.) Hydrogen in Intermetallic Compounds II. Surface and Dynamic Properties, Applications (Topics in Applied Physics Vol 67) (Springer, 1992)
4. P. Spatz, H. A. Aebischer, A. Krozer, and L. Schlapbach, Z. Phys. Checm. 181 (1993) p. 393
5. S. Orimo and H. Fujii, Appl. Phys. **A** 72 (2001) p. 167
6. J. Liang, Appl. Phys. **A** (2003) in press
7. J. Harris: Appl. Phys. **A** 47 (1988) p. 63
8. D. M. Bird, L. J. Clarke, M. C. Payne, I. Stich, Chem. Phys. Lett. 212 (1993) 518
9. B. Delley, J. Chem. Phys. **92**, 508 (1990)
10. R.W.G. Wyckoff, in *Crystal Structures*, volume 1 (Interscience, John Wiley & Sons, 1963).
11. N. Govind, M. Petersen, G. Fitzgerald, D. King-Smith, J. Andzelm, Computational Materials Science (2003), in press
12. R. B. Murphy, J. M. Mundnar, K. D. Tsuei, E. W. Plummer: Bull. Am. Phys. Soc. **33**, 655 (1988)
13. K. D. Rendulic, G. Anger and A. Winkler, Surf. Sci. 208 (1989) 404
14. A. Gross, S. Wilke, and M. Scheffler, Phy. Rev. Lett. 75 (1995) 2718
15. A. Eichler, J. Hafner, A. Grob, and M. Scheffler, Phys. Rev. B 59 (1999) 13297

Modeling Fireside Slag Formation and Deposition in Tangentially-Coal-Fired Boilers

Edmundo Vásquez
Alliant Energy Corporate Services
744 Heartland Trail
Madison, WI 53717-1934

Zhanhua Ma
RMT Incorporated
744 Heartland Trail
Madison, WI 53717-1934

Steven A. Benson, Donald P.McCollor, Robert Jensen, Li Yan, A.S.M. Rokanuzzaman, and Lingbu Kong
Energy & Environmental Research Center
University of North Dakota
P.O. Box 9018
Grand Forks, ND 58202-9018

Introduction

Fireside ash deposition is a major problem that impacts the efficiency and operability of coal-fired utility boiler. The ash deposition problem is dependent on fuel composition, boiler design, and operating conditions. In general many of the chemical and physical processes involved in ash formation and deposition are understood and this understanding has assisted many utilities in minimizing ash deposition problems in utility boilers. Many of these processes have been formulated into computer codes. For example, computer codes exist to predict the particle-size and composition distribution (PSCD) of the ash produced upon combustion (1) and simplified transport deposition and growth programs for specific locations in the boiler (2). However, no integration of these programs with boiler models to predict the effects of deposit growth on heat transfer has occurred.

The advances made over the past several years in predicting ash behavior have been made possible as a result of more detailed and better analysis of coal and ash materials. These advanced techniques, such as computer-controlled scanning electron microscopy (CCSEM), are able to quantitatively determine the chemical and physical characteristics of the inorganic components in coal and ash (fly ash and deposits) on a microscopic scale (3). Many of the mechanisms of ash formation, ash deposition, and ash collection in combustion systems are more clearly understood as a result of these new data. This understanding has led to the development of better methods of prediction that include advanced indices and phenomenological models.

Advanced indices programs provide coal ranking with respect to a coals potential to cause deposition in various sections of the boiler such as the waterwalls and high-temperature and low- temperature convective pass. The index is based on advanced methods of analysis, detailed understanding of key processes that influence fouling, and full-scale performance data (4).

Phenomenological or mechanistic models have been developed and are being used to predict the effects of ash-forming constituents as a function of coal composition, combustion conditions, systems geometry, and operating conditions. ATRAN is a model that has been developed to predict the PSCD of ash produced in utility boilers. The results achieved with this model have been verified with full-scale experience for both pulverized coal (pc) and cyclone-fired boilers with a favorable outcome. ATRAN is a vital part of other methods used to predict the effects of ash species, since the PSCD is needed to predict ash deposition (5).

Recently work has been conducted to integrate the predictive methods and incorporate them into a computational fluid dynamics code. The results presented here will illustrate the ability of the model to predict upper wall slagging in a tangentially fired boiler utilizing. Black Thunder, a Powder River Basin coal.

Computational Fluid Dynamics

SmartBurn® uses numerical simulations of processes to compare design and operational alternatives and to identify the underlying limitations of boiler performance. Once these limitations are identified, a cause and effect relationship can be established and a more complete understanding of the combustion process is obtained. The tool of choice for performing such an investigation for pulverized coal combustion in an enclosed fluid atmosphere is computational fluid dynamics (CFD). This type of numerical simulation resolves the Navier-Stokes equations and incorporates several numerical schemes for fluid flow, heat transfer, turbulence, and chemistry within the given geometry and for a set of operating conditions and, most importantly, solves the coupled solution of these equations.

Coal particles are simulated with the Discrete Phase Model (DPM) in a two way coupled solution utilizing stochastic tracking for turbulence interaction in a Lagrangian reference frame. The DPM model is defined to simulate the moisture evaporation, de-volatilization, and char burnout of the coal particles. Seven chemical species are solved for the gas phase in which the Magnussen-Hjertajer turbulence-chemistry interaction model is employed. Radiation is modeled using the Discrete Ordinate (DO) model, which provides for particle radiation interaction.

A CFD model was built for Columbia Unit 1 (6,7) a tangentially fired 1975-vintage 512 MW boiler. Columbia Unit 1 was one of the first-generation T-fired units designed to burn PRB coal and therefore has a small firebox with a high heat release. The output of the CFD model provides the basic information used in the ash behavior model.

Results and Discussion

A diagram of the boiler modeled is illustrated in Figure 1 (7). The portion of the boiler that will be used to illustrate the ability of the model to predict performance is the upper wall section above the burner level. The ash impaction rates are shown in Figure 2.

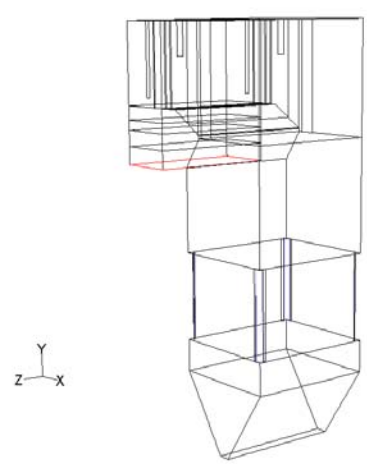

Figure 1. Schematic diagram of tangentially-fired boiler.

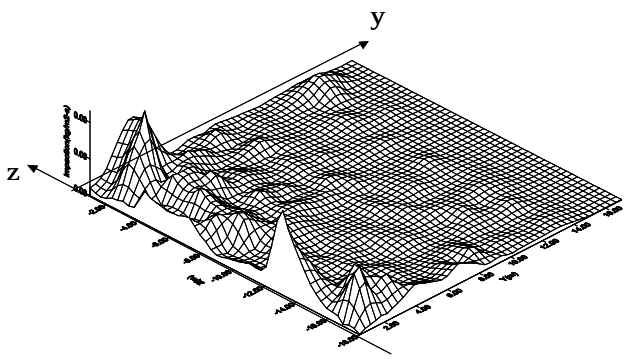

Figure 2. Ash Particle Impaction Rate Distribution on Furnace Upper-Front Wall

Currently work is being conducted to validate the model. Figure 3 shows the heat flux measurements made at several locations on the upper wall panel that is being modeled. Figure 4 shows the results from the model.

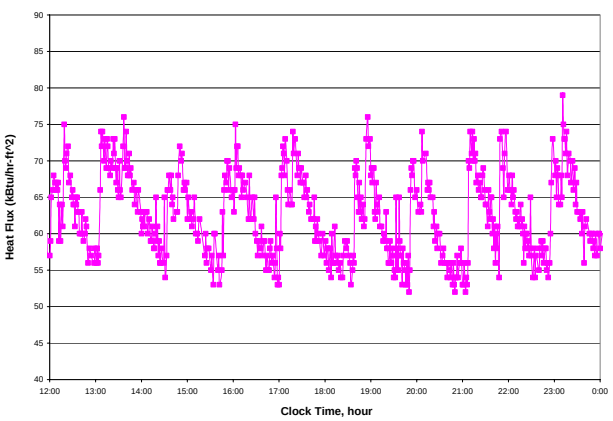

Figure 3. Measured Heat flux at the full scale utility on the wall panel is illustrated in Figure 2.

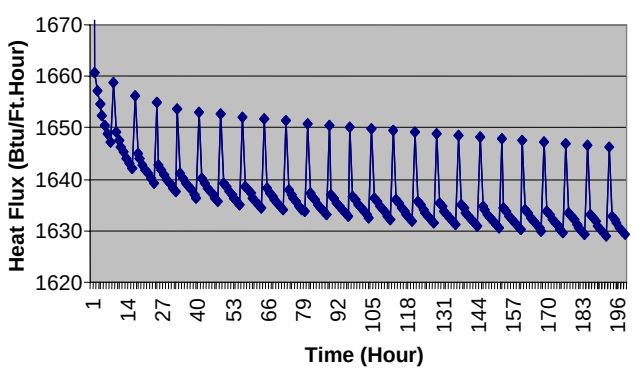

Figure 4. Predicted heat flux based on fuel quality, boiler design, and operating conditions.

Currently the modeling efforts show promise in being a very valuable tool to predict plant performance.

Conclusions

The resulting integration of CFD simulations with predictive methods for ash behavior in tangentially coal-fired boilers, provide a quantitative and qualitative description of the fireside slag formation and deposition processes within the furnace. As a result, the method permits the determination of the deposit thickness; chemical composition; physical properties and heat transfer properties. The utilization of this procedure to different types of boilers, fuel types and operating conditions is in progress.

References

1. Benson, S.A.; Steadman, E.N.; Zygarlicke, C.J.; Erickson, T.A. Ash Formation, Deposition, Corrosion, and Erosion in Conventional Boilers. In Applications of Advanced Technology to Ash-Related Problems in Boilers; Baxter, L.; DeSollar, R., Eds.; Plenum Press: New York, 1996; pp 1-15.
2. Benson, S.A.; Sondreal, E.A. Impact of Low-Rank Coal Properties on Advanced Power Systems. In Ash Chemistry: Phase Relationships in Ashes, Special Issue of Fuel Process. Technol. 1998, 56 (1-2), 129-142.
3. Steadman, E.N.; Zygarlicke, C.J.; Benson, S.A.; Jones, M.L. A Micro analytical Approach to the Characterization of Coal, Ash, and Deposits. In Seminar on Fireside Fouling Problems; ASME Research Comm. on Corrosion & Deposits from Combustion Gases: Washington, DC, 1990.
4. Zygarlicke, C.J. Predicting Ash Behavior in Conventional and Advanced Power Systems: Putting Models to Work. In Impact of Mineral Impurities in Solid Fuel Combustion; Gupta, R. .Ed.; Kluwer Academic/Plenum Publishers: New York, 1999; pp 709-722.
5. Yan, L., Jensen, R.R., Laumb, J.D. and Benson, S.A. Predicting Ash Particle Size and Composition Distribution From Coal Biomass Cofiring, Proceedings of Engineering Foundation Conference, Production in the 21st Century: Impacts of Fuel Quality and Operations, October 28 November 2, 2001, Snowbird, Utah.
6. Vásquez, E; Sears, R., Combustion Control Techniques achieve 0.15 lbs/MMBtu NO_x levels without SCR, Power Engineering, Vol 107, No 1, 39-42, January 2003.
7. Vásquez, E.; Mara, F.; Maas, D.J.; Ma Z.; McQuistan, K.; Gadalla, H.; Iman, F. Application of SmartBurn^{SM} Technology for NO_x Control in Tangentially Fired Coal Boilers, PowerGen International, December 9-11, 2003, Las Vegas, Nevada USA

EVOLUTION OF FLAME-BORNE MINERAL MATTER IN A 350 MW_e PULVERISED COAL-FIRED BOILER

Glenn P. Devir[a]
Co-operative Research Centre for Coal in Sustainable Development
School of Chemical Engineering
University of Queensland
Sir Fred Schonell Drive
St Lucia QLD 4072 AUSTRALIA

John H. Pohl
Alexandria Research Institute
Department of Mechanical Engineering
Virginia Tech
Suite 400, 206 N. Washington St
Alexandria VA 22314

Introduction

The mineral matter present in burning pulverised coal particles will experience rapid, high temperature transformations in the gas path of a utility boiler. These inorganic combustion residues may remain inert, melt, spheroidise, coalesce, vesiculate, fragment, freeze, crystallise, vapourise, and/or condense during transport from the bulk gas phase, across the cooler boundary layer, to heat transfer surfaces. The evolution of such flame-borne mineral matter will be dependent upon the size, composition and time-temperature history of each mineral inclusion in the parent coal particle.

The local gas environment is likely to be reducing for flame-transformed mineral matter on or beneath the surface of receding char particles. Conversely, mineral particles which have been liberated from the coal substance during milling will experience oxidising conditions in the gas path of a boiler, as will flame-transformed mineral matter which is released from the char during char burnout.

The evolution of flame-borne mineral matter during pulverised coal combustion is being studied as part of an investigation into the mechanisms of slagging in a 350 MW_e opposed-fired boiler. The observed transformation phenomena of mineral matter in the gas phase are described in terms of classical sintering theory. Possible explanations for the observed absence of various transformation phenomena are also proposed. It is hoped that the interpretation accompanying the images presented in this paper will contribute to a qualitative understanding of particulate transformations in pulverised coal-fired boilers. This paper concludes by identifying future research directions to hopefully resolve the uncertainties of such transformations.

Methodology

The mineralogy of the sub-bituminous coals fired in this minemouth power station typically consist of 60-70% kaolinite ($4SiO_2.2Al_2O_3.4H_2O$), 10-20% siderite ($FeCO_3$) and 5-15% quartz (SiO_2), with minor quantities (<2%) of other minerals present. The mineral matter transformations occurring in the hottest region of the furnace are assessed by using a water-cooled probe to quench and withdraw particulates through a port eight metres above the top row of burners. Particles are examined under the scanning electron microscope (SEM) to ascertain probable physical and chemical transformation mechanisms.

[a] Present address (and to where all correspondence should be addressed): Process Engineer, HRL Technology, 1 Acirl St, Riverview QLD 4303, AUSTRALIA, gdevir@acirl.com.au

Results and Discussion

The most predominant type of particle sampled was glassy sub-micron non-porous aluminosilicates. However, considerable evidence was found to support the notion that kaolinite-derived particles coalesced to various degrees with other kaolinite-derived particles.

An approximate solution for the rate of surface tension driven coalescence of two spheres with single point contact was first proposed by Frenkel[1]. The rate of neck growth, relative to the instantaneous radius a of one of the growing spheres, was shown to be proportional to $(\gamma/\eta)^{-}$, and inversely proportional to $(a\gamma)^{-}$, where γ and η are the surface tension and viscosity of the coalescing species. However, this approach, and many subsequent attempts to model coalescence, both empirically and theoretically, have been based on non-porous particles of like composition.

The time required for pore closure in a viscous body due to capillary forces was shown by Frenkel[1] to be proportional to $a_o\eta$ and inversely proportional to γ, where a_o is the initial pore radius. A kaolinite-derived particle in the furnace of a boiler may possess[2] a pore-free viscosity of 10 Pa.s and a surface tension of 0.4 Nm^{-1}. For a 5 μm initial pore radius, the time required for pore closure would therefore be anticipated to be less than one millisecond. However, it is evident from Figures 1 to 3 that pore closure is not complete in the residence time of the furnace, which is likely to be somewhere in the order of one second.

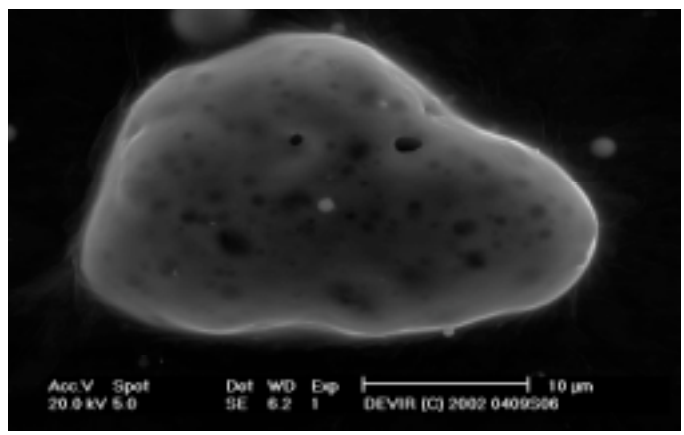

Figure 1. Partial coalescence of several large kaolinite-derived particles. Secondary electron image.

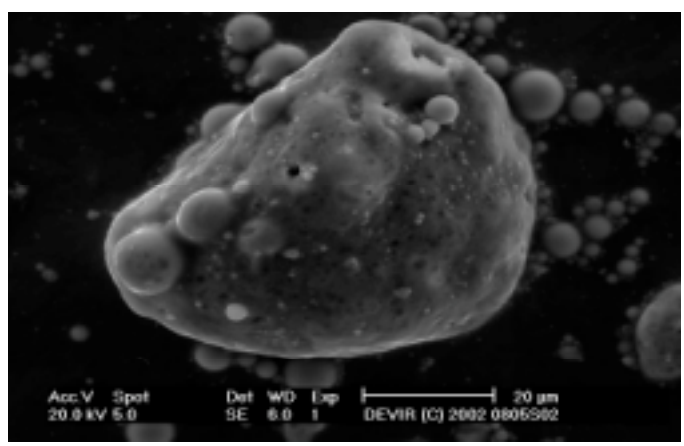

Figure 2. Partial coalescence of many various-sized kaolinite-derived particles. Secondary electron image.

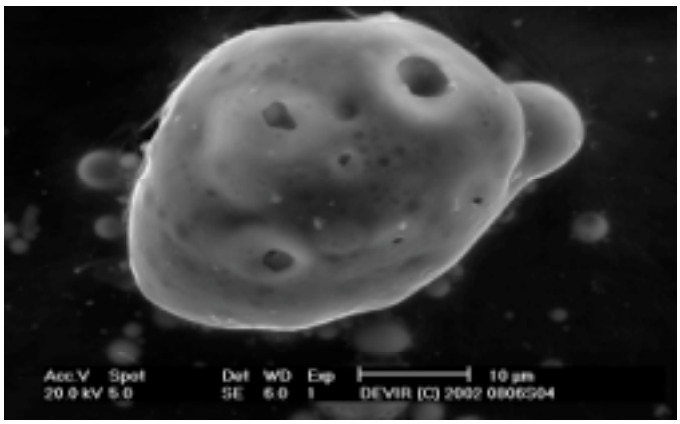

Figure 3. Large rounded kaolinite-derived particle with large pores. Secondary electron image.

The interfaces of real coalescing fluids possess complex rheological properties, and may exhibit viscous, viscoelastic or even elastic behaviour, with both spatial and temporal variations[3]. It is apparent from these images that the kinetics of pore closure in flame-borne kaolinite-derived particles are somewhat slower than that predicted by viscous sintering theory. The retardation of pore closure may explain the incomplete coalescence of large kaolinite-derived particles in the furnace, as evidenced in Figures 1 to 3.

The presence of pores may either increase or decrease the effective viscosity, depending upon the pore morphology. Spherical pores are thought to decrease the effective viscosity, due to the much lower viscosity of the gas phase. Non-spherical pores, however, may increase the effective viscosity of the particle due to their higher resistance to shearing stress, and hence viscous flow.

Many large irregularly-shaped, slightly rounded particles were observed, with varying degrees of surface porosity. Qualitative analysis of various points on each particle was performed using energy dispersive x-ray analysis (EDXRA). It was found that spot compositions ranged from almost pure silica (SiO_2) to the composition of metakaolinite ($4SiO_2.2Al_2O_3$), with regions of low surface porosity corresponding to high silica point concentrations. It was concluded that kaolinite-derived particles had wet the inert surface of large quartz particles, forming a molten porous layer. Figure 4 shows one of these particles.

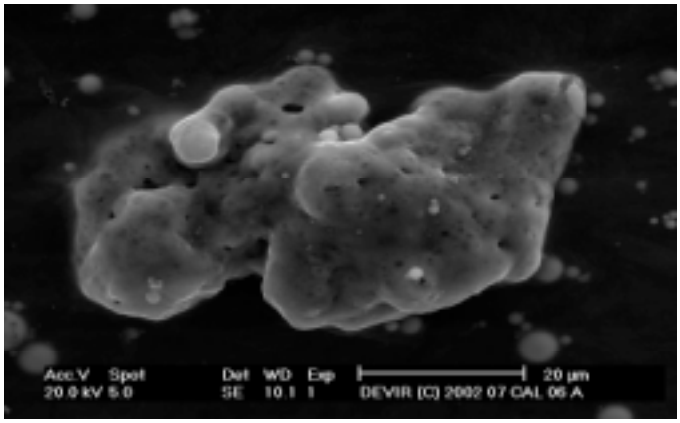

Figure 4. Wetting of inert quartz particle by mobile porous aluminosilicate layer. Secondary electron image.

There was no conclusive evidence to ascertain the primary transformation mechanism of siderite-derived ('FeO_n') particles in the boiler furnace. Iron oxide particles were predominantly less than 1 µm in diameter, suggesting that fragmentation may have been a dominant mechanism. Raask[4] documented the fragmentation of siderite-derived particles into sub-micron particulates, and attributed this phenomenon to the rapid evolution of carbon dioxide from a low viscosity liquid. Iron oxide particles between 5 and 10 µm were rarely observed, suggesting that coalescence of siderite-derived particles was not likely.

There was no evidence found to support the idea that kaolinite-derived particles coalesced with siderite-derived particles to form low melting temperature aluminosilicate particles. Sintering literature suggests that a broad range of responses are possible in mixed powder systems, depending upon the physical and chemical properties of each component[5]. Sintering and coalescence will occur readily where there is intersolubility between the mixed powders, thereby allowing chemical potential gradients to dominate the surface energy driving force for viscous flow. However, resistance to coalescence will occur when at least one of the species possesses a low solubility in the other, or indeed if one or more species is very porous.

SEM images of cross-sectioned boiler deposits suggest that siderite-derived particles are very soluble in aluminosilicate regions, but not vice versa[6]. This observation may provide a qualitative explanation as to why coalescence is observed in some coal mineralogical systems and not others.

Conclusions

This paper examined the evolution of flame-borne mineral matter during the combustion of sub-bituminous coals in a 350 MW_e pulverised coal-fired boiler. The observed transformation phenomena were documented and described in terms of viscous sintering theory. It was concluded that the thermodynamic data currently available in the literature to help describe the high temperature mineral matter transformations occurring in coal combustion is inadequate. This data is largely restricted to compositions and temperatures of interest to metallurgists and ceramists, and therefore is of limited use to combustion engineers. It is recommended that a database of thermodynamic properties (e.g., viscosity of solid-liquid and liquid-gas mixtures, solubility, diffusivity, activity coefficients, etc.) be generated for slag compositions and temperatures of interest to combustion engineers. The high temperature transformations of mineral matter occurring in the gas phase of the boiler may then be better understood.

Acknowledgements The authors gratefully acknowledge the interest and co-operation shown by Dr Chris Spero and Mr Adrian Hughes of CS Energy. We also wish to acknowledge the financial assistance provided by the Co-operative Research Centre for Coal in Sustainable Development, which is funded in part by the CRC Programme of the Commonwealth Government of Australia.

References

(1) Frenkel, J. *J. Phys.*, **1945**, *9* (5), 385.
(2) Verein Deustcher Eisenhüttenleute, *Slag Atlas*, 2nd Edition, Verlag Stahleisen GmbH, Dusseldorf, Germany, 1995
(3) Hiram, Y and Nir, A. *J. Coll. Int. Sc.* **1983**, *95 (2)*, 462.
(4) Raask, E. *Mineral Impurities in Coal Combustion – Behaviour, Problems and Remedial Measures*, Hemisphere Publishing Corporation, Washington, D.C., USA, 1985
(5) German, R. M. *Sintering Theory and Practice*, John Wiley & Sons, Inc., New York, NY, USA, 1996
(6) Devir, G.P. *Ph. D. Thesis in Progress*, University of Queensland, St Lucia, QLD, Australia, 2004

PREDICTION OF PHASE EQUILIBRIA AND VISCOSITY IN COMPLEX COAL ASH SLAG SYSTEMS

*E.Jak, *D.Saulov, **A.Kondratiev, and **P.C.Hayes

*Centre for Coal in Sustainable Development (CCSD),
** Pyrometallurgy Research Centre, School of Engineering,
The University of Queensland, Brisbane, QLD, 4072, Australia
http://pyrosearch.minmet.uq.edu.au; E.Jak@minmet.uq.edu.au

Abstract

Significant improvements in predictive capabilities in relation to the melting behaviour of the mineral matter in coal have been achieved through the use of i) thermodynamic modelling of phase equilibria, and ii) viscosity modelling studies.

The thermodynamic modelling has been carried out using the computer system FactSage, which is used for the calculation of multi-phase slag / solid / gas / matte / alloy / salt equilibria in multi-component systems of industrial interest. A modified quasi-chemical solution model is used for the liquid slag phase. New model optimisations have been carried out, which have significantly improved the accuracy of the thermodynamic models for coal combustion processes. The database for the Al-Ca-Fe-O-Si system has recently been extended to characterise effects of Mg, K and Na. Viscosity modelling, using a modified Urbain formalism, is carried out in conjunction with FactSage calculations to predict the viscosities of fully liquid as well as heterogeneous, partly crystallised slags.

The solution of a range of problems in coal utilisation technologies, including ash slag flow in slagging gasifiers, deposit formation, slagging, fouling, fusibility tests, fluxing, blending etc related to the melting behaviour of the mineral matter in the coal can be obtained with the assistance of the new models.

Introduction

Many coal companies and electrical power utilities are faced with difficult technical issues associated with the melting and flow behaviour of coal mineral matter. A range of problems in coal utilisation technologies, including ash slag flow in slagging gasifiers, deposit formation, slagging, fouling, fusibility tests, fluxing, blending etc, are related to the melting behaviour of the mineral matter in the coal. The wide ranges of coal mineralogies, ash compositions and process conditions experienced in the various parts of each reactor and in different coal utilisation technologies highlight the need for powerful tools to predict the behaviour of the mineral matter. Fundamental knowledge of the melting and flow behaviour of coal mineral matter/flux mixtures can greatly assist in the design and operation of these power generation technologies.

The prediction of phase equilibria and viscosities of the coal ash following combustion is a longstanding problem for users of various coal-based power generation technologies. The empirical "ash fusion tests", such as the cone deformation tests, thermo-mechanical tests (e.g. TMA) and empirical slagging indices are widely used to estimate and compare the relative behaviours of coal ashes. Recent scientific approaches to the prediction of these properties are, however, starting to produce results that will have a significant impact on the industry. Improvements in chemical thermodynamic and viscosity models of oxide systems, the development of computational methods, computer software and hardware now make it possible to predict the phase equilibrium and flow behaviour in complex multi-component coal ash slag systems. The purpose of this paper is to demonstrate how the latest advances in chemical thermodynamic and viscosity modelling can be used to characterise the melting and flow behaviour of mineral matter present in coal combustion systems.

Development of modelling tools

FactSage Database. One of the predictive tools used successfully in coal ash applications is the computer package FactSage[1]. FactSage is used worldwide in various industries to predict chemical equilibria, the proportions of liquid and solid phases as a function of temperature, composition and atmospheric conditions. One of the strengths of FactSage is its ability to describe the melting behaviour of the oxide systems, commonly referred to as slags. Accurate and reliable prediction, however, requires the development of a thermodynamic database with model parameters for all possible liquid and solid phases.

A new thermodynamic database of the system Al-Ca-Fe-O-Si has been completed by researchers at the Pyrometallurgy Research Centre (PYROSEARCH), The University of Queensland, in collaboration with the Centre for Research in Computational Thermochemistry, Polytechnique de Montreal, Canada[2]. This database has recently been extended to characterise effects of Mg, K and Na on liquidus temperatures[3-4]. The new thermodynamic database incorporates the latest experimental data and more advanced thermodynamic models of the oxide phases. The new database is the result of the systematic thermodynamic optimisation of the multi-component systems, and it provides improved accuracy and reliability in the description of phase equilibria in the coal ash system.

Viscosity Model. A new slag viscosity model for the system Al_2O_3-CaO-'FeO'-SiO_2 used in conjunction with FactSage has recently been completed by the present authors[5-7]. The model enables the viscosities of homogeneous (completely molten) liquid slag systems as well as heterogeneous (partially crystallised) slag systems, to be predicted as a function of the bulk slag composition and operating temperature over the complete range of conditions at metallic iron saturation. FactSage is used to calculate the proportions of solids and the composition of the remaining liquid in the partly crystallised slag systems. The original Urbain formalism[8-11] has been modified to make viscosity predictions possible over the whole composition and temperature ranges. This was achieved by taking into account the different contributions of various oxides (in this particular case, CaO and FeO) on the viscosity of the slag[6]. The model parameters for the individual oxides have been derived from critically reviewed experimental data. The Roscoe equation[12], with parameters obtained by fitting model predictions into experimental points by Hurst[13-15], is used to characterise the "slurry" effect in partly crystallised slag. Examples of the application of the new viscosity model have been reported in the literature[5-7].

Table 1. Comparison of Different Viscosity Models Using the Mills' Parameter

System	Modified Urbain model[5-7]	Watt-Fereday model[17]	T-shift model[18]	Kalmanovich-Frank model[19]
SiO_2	19.1	99.9	N/A	99.9
Al_2O_3-SiO_2	30.1	66.9	N/A	41.5
CaO-SiO_2	10.9	84.3	40.3	24.3
'FeO'-SiO_2	8.1	213.8	378.1	717.6
Al_2O_3-CaO-SiO_2	31.2	49.5	49.2	24.6
CaO-'FeO'-SiO_2	9.9	115.4	339.8	594.4
Al_2O_3-CaO-'FeO'-SiO_2	29.2	96.0	94.0	169.6

The agreement between experimental data and model predictions was evaluated using the parameter proposed by Mills et al.[16]: $\Delta = \frac{1}{N}\sum^{N}\left|\frac{(\eta_n)_{calc} - (\eta_n)_{ex}}{(\eta_n)_{ex}}\right|$, where N is a number of points and n is a particular slag system, the subscripts *calc* and *ex* refer to the calculated and experimental viscosities at a given composition and process condition. Table 1 shows the comparison of the viscosity models[5-7,17-19] for a number of chemical systems.

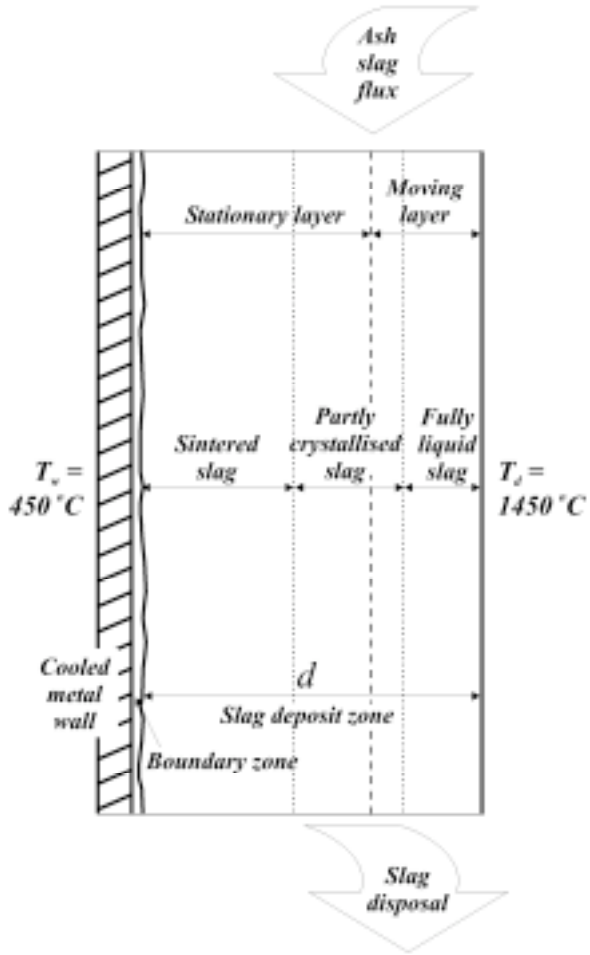

Figure 1. Schematic of the flowing slag deposit.

Applications of the models to entrained flow coal gasification systems

A number of examples of the application of the FactSage computer package and viscosity models to coal ash related problems by the authors can be found in recent scientific literature[2,3,5,20-25]. Increasing attention is being given to the development of entrained flow coal (slagging) gasifiers since they offer potential advantages in terms of improved energy efficiencies and environmental outcomes. A key factor in the operation of these technologies is the flow properties of the slags; these properties are principally dependent on

- liquid composition,
- proportion of liquid,
- proportion of solids,
- oxygen partial pressure, and
- temperature.

These in turn can be controlled or varied in the process by adjustments to

- coal blending,
- flux addition and
- gasifier temperature and operating oxygen partial pressure.

Depending on the gasifier type, the limiting requirements for slag viscosity and temperature can vary from 5 to 25 Pa.s and from 1100°C to 1500°C, respectively[26-28]. These requirements are usually determined empirically by the tappability of the slag in a gasifier. Exact specifications should be identified by individual power generation utilities. Provided the slag can flow from the reactor, and can also fulfil any requirements, such as the incorporation of other minor elements, then it is possible to operate at sub-liquidus conditions.

Using the new thermodynamic and viscosity models described above it is now possible to predict the stability of the liquid slag and solid crystalline phases as well as the viscosity of the liquid slag for the complex coal ash slag systems. This is illustrated in the present paper with analysis of the use of two coals A and B (see Table 2) in a slagging gasifier.

Table 2. Compositions of the Coal Ash Slags (wt pct)

#	Al_2O_3	CaO	'FeO'	SiO_2
Ash A	25.44	27.53	12.50	34.53
Ash B	30.51	25.87	6.26	37.36

One of the common problems in coal gasification is the formation of slag deposit on the walls of a slagging gasifier; these deposits affect the overall heat balance, temperature of the out-gases and tappability of slag (i.e. ability of slag to flow freely from a gasifier)[26,29-30]. The following example shows the application of the thermodynamic and viscosity models developed in the Pyrosearch Centre to the problem of deposit formation in the slagging zone of a gasifier.

A typical section of flowing slag deposit on a reactor wall in the slagging zone[29] is shown in Figure 1. The temperature of the slag at the water-cooled wall of a gasifier T_w is taken ~450°C, while temperature of the slag surface T_d is ~1450°C. The temperature gradient across the slag deposit leads to the formation of different sub-layers across the deposit: 1) a stationary layer of sintered slag (glass and crystalline phases) and partly crystallised slag with high proportion of solids, and 2) a moving layer, which also contains partly liquid slag but with lower percentage of solids, and fully liquid slag. Assuming the linear temperature profile across the slag layer, the proportion of solids across the layer was calculated by FactSage[1] with the new thermodynamic database[4]. The slurry viscosity was predicted by the model developed in PyroSearch Centre[5-7]. Using the Navier-Stokes equation for steady-state, laminar flow of a slag layer of constant thickness under gravity force the slag velocity across the layer was predicted. Thickness of the deposit layer was then calculated from mass balance and geometry of a gasifier. The examples of these calculations for two different coal ash slags (marked Ash A and Ash B) are shown in Figure 2.

Figure 3 shows the thickness of the deposit layer for coal ash slags A and B as a function of the temperature of slag surface determined by the temperature of the reaction zone. It can be seen that ash A has wider operational range of temperatures than ash B.

The conditions of the operations always fluctuate. The analysis of the effects of different factors on crystallisation and viscous flow behaviour therefore is important. Figures 4 through 6 give detailed analysis of the effects of temperature, atmospheric conditions(reducing / oxidising) and composition changes on proportions of liquid and solid phases and on viscosities of the slags corresponding to coals A and B.

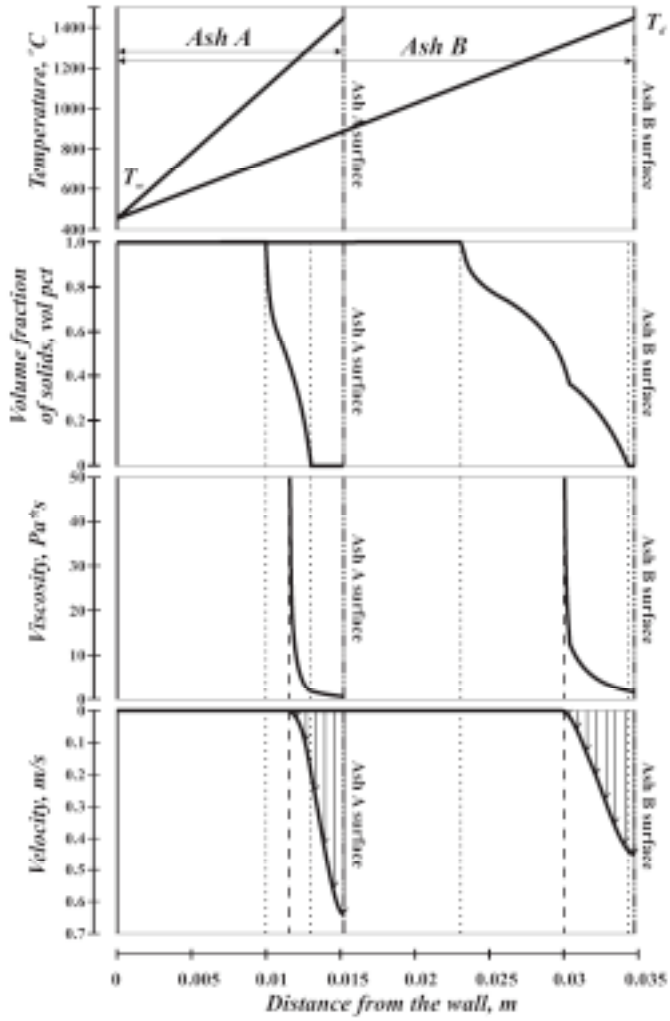

Figure 2. Temperature, proportions of solids, viscosity and slag flow velocity profiles predicted with new models for coals A and B.

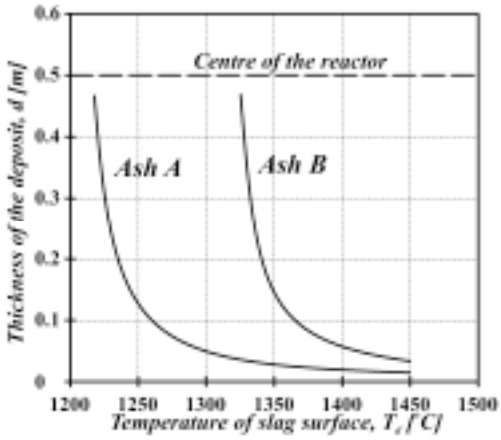

Figure 3. Thickness of the deposit as a function of temperature of the slag surface for coals A and B.

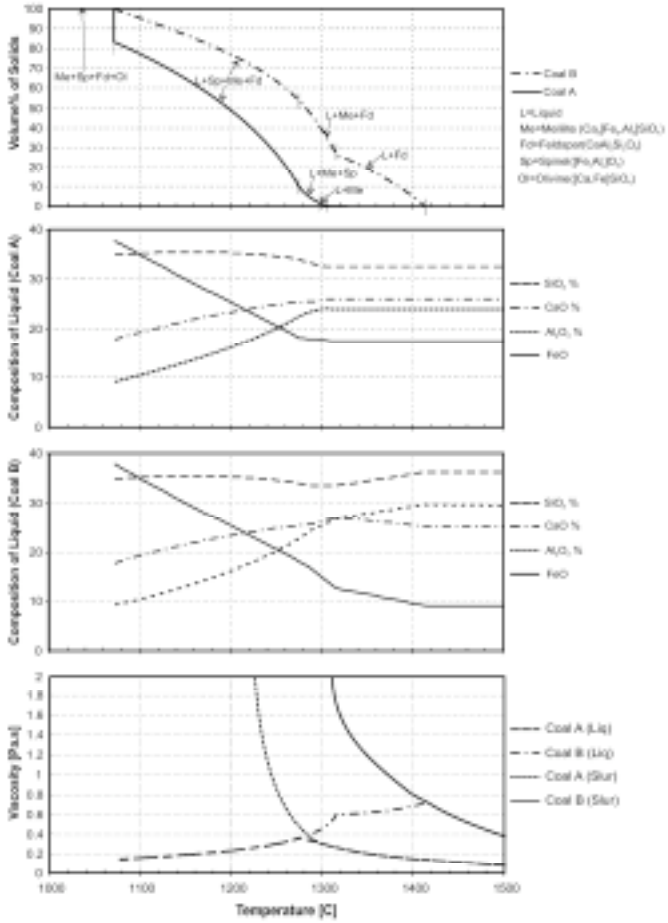

Figure 4. Crystallisation characteristics and viscosities of the coals A and B at metallic iron saturation as a function of temperature.

Conclusions

Using new chemical thermodynamic and viscosity models it is now possible to predict the behaviour of complex slag systems relevant to coal utilisation technologies. Properties such as phase equilibria, liquidus temperatures and viscosities of single and multiphase slags can be systematically analysed as functions of a given compositional variable through the selection of appropriate sections in compositional space. This has been illustrated with examples for the system FeO-Fe_2O_3-CaO-SiO_2-Al_2O_3 for a range of compositions and temperatures relevant to entrained coal gasification technologies. Effects of MgO, Na_2O and K_2O on phase equilibria can also be now predicted.

Acknowledgement. The authors would like to acknowledge the support of the Centre for Coal in Sustainable Development for the financial support of the development of the FactSage database; staff of the Centre for Research in Computational Thermochemistry, Montreal in particular Dr S. Degterov and Prof. A.D. Pelton for their contributions to the development of the thermodynamic database; the Australian Research Council for financial support for the viscosity model development, Dr A. Klimenko for his contribution to the deposit flow modelling.

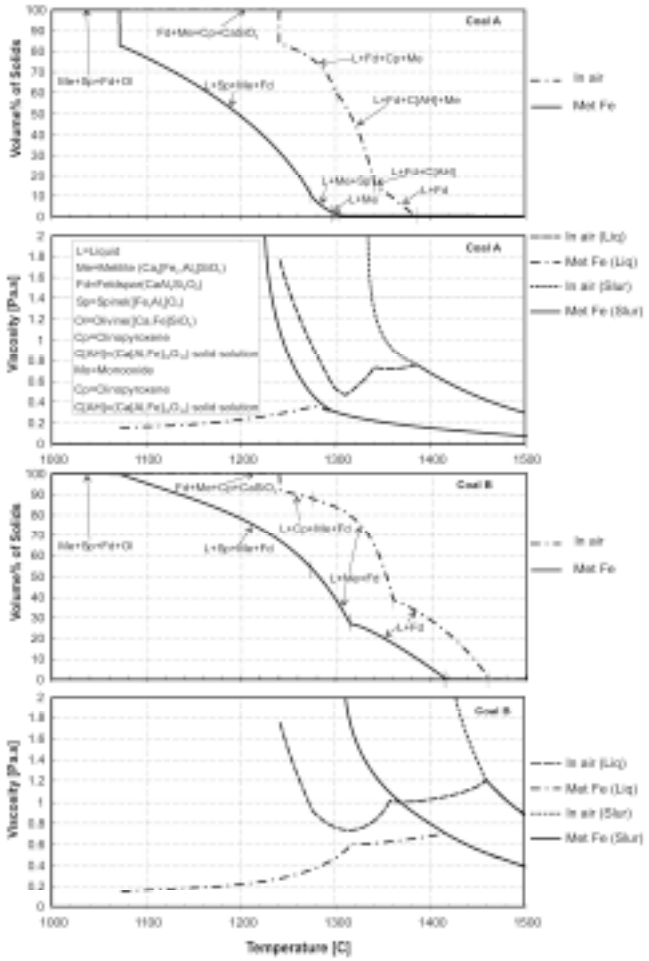

Figure 5. Effect of atmosphere conditions on crystallisation characteristics and viscosities of the coals A and B (at metallic iron saturation compared to air) as a function of temperature.

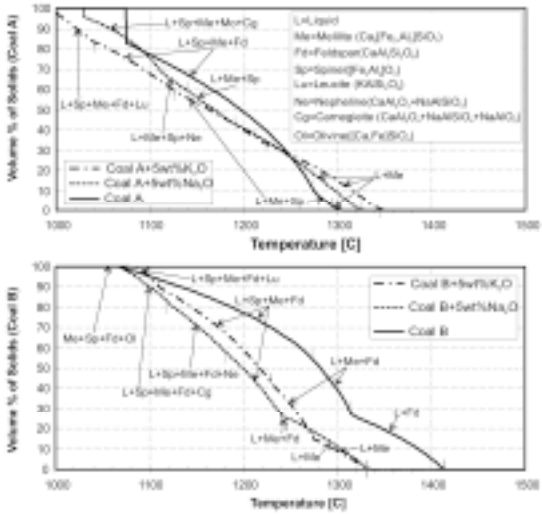

Figure 6. Effect of Na2O and K2O on crystallisation behaviour of the coals A and B at metallic iron saturation as a function of temperature.

References

(1) Bale C.W., Chartrand P., Degterov S.A., Eriksson G., Hack K., Mahfoud R. Ben, Melançon J., Pelton A.D., and Petersen S.: *Calphad*, **2002**, 26 (2), 189-228.

(2) Jak E. and Hayes P.C.: *Applications of the new FACT database for the prediction of melting behaviour of coal mineral matter*, 9th Australian Coal Sci. Conf. "Solutions for Industry", Brisbane, Nov. 2000, ed. J.H.Pohl, publ. Australian Institute of Energy, Toukley, NSW, Australia, http://www.aie.org.au , ISBN # 1864993960.

(3) Jak E. and Hayes P.C.: *Thermodynamic Modelling of the Coal Ash Systems in Black Coal Utilisation (a new FactSage database of the SiO_2-Al_2O_3-CaO-FeO-Fe_2O_3 system and the effects of MgO, K_2O and Na_2O on liquidus)*, 18th Annual Intl. Pittsburgh Coal Conf., Newcastle, NSW, Australia, 4-7 Dec. 2001, ISBN 1-890977-18-7, publ. Pittsburgh Coal Conference, Univ. of Pittsburgh, Pittsburgh, PA, USA.

(4) Jak E., D.Saulov and Hayes P.C.: *New thermodynamic database for prediction of high temperature phase equilibria for the SiO_2-Al_2O_3-CaO-FeO-Fe_2O_3 system with addition of MgO, K_2O and Na_2O with FactSage computer package*, Report, 2003, Centre for Coal in Sustainable Development, Brisbane, Australia.

(5) Kondratiev A. and Jak E.: *Fuel*, **2001**, 80(14), 1989-2000.

(6) Kondratiev A. and Jak E.: *Metall. Trans. B*, **2001**, 32B, 1027 - 1032.

(7) Kondratiev A. and Jak E.: *Metall. Trans. B*, **2001**, 32B, 1015 - 1025.

(8) Urbain G., Cambier F., Deletter M. and Anseau M.R.: *Trans. J. Br. Ceram. Soc.*, **1981**, 80, 139-141.

(9) Urbain G.: *Steel Res.*, **1987**, 58, 111-116.

(10) Mills K.C. *Viscosities of molten slags*, Chapter 9, Slag Atlas, 2nd edition, Berlin, Springer-Verlag, 1995, pp. 349-402.

(11) Urbain G. and Boiret M.: *Ironmaking & Steelmaking*, **1990**, 17, 255-260.

(12) Roscoe R.: *Br. J. Appl. Phys.*, **1952**, 3, 267-269.

(13) Hurst H.J. *Personal communication*, 1999, CSIRO DET, North Ryde, Sydney, Australia.

(14) Hurst H.J., Novak F. and Patterson J.H.: *Fuel*, **1999**, 78, 439-444.

(15) Hurst H.J., Novak F. and Patterson J.H.: *Fuel*, **1999**, 78, 1831-1840.

(16) Mills K.C., Chapman L., Fox A.B., Sridhar S.: *6th Int. Conf. Slags Fluxes Molt. Salts*, 2000, KTH, Stockholm, CD-ROM, paper #433.

(17) Watt J. D. and Fereday F.: *J. Inst. Fuel*, **1969**, 42, 99-103.

(18) Browning G.J., Bryant G.W., Hurst H.J., Lucas J.A., and Wall T.F.: *Energy & Fuels*, **2003**, 17, 731-737.

(19) Kalmanovich D.P. and Frank M.: *Proc. Eng. Foundation Conf., Miner. Matter Ash Deposition*, **1988**, pp. 89-101

.(20) Jak E., Degterov S., Hayes P.C. and Pelton A.D.: *Fuel*, **1997**, 77,77-84.

(21) Jak E., Degterov S., Pelton A., Happ J. and Hayes P.: In *Impact of Miner. Impurities in Solid Fuel Combust.*, ed. Gupta R.P., Wall T.F., Baxter L., Kluwer Academic/Plenum Publ., NY, USA, 1999, pp. 723-734.

(22) Jak E., Degterov S., Zhao B., Pelton A. and Hayes P.: *Metall. Trans. B*, **2000**, 31B, 621-630.

(23) Vladimirov I., Christie S. and Jak E.: *Computer modelling of physical-chemical properties of complex coal ash slag systems in multi-dimensional compositional space*, 18th Annual Intl. Pittsburgh Coal Conf., Newcastle, NSW, Australia, 4-7 Dec. 2001, ISBN 1-890977-18-7, publ. Pittsburgh Coal Conference, Univ. of Pittsburgh, Pittsburgh, PA, USA.

(24) Jak E. (2002): *Fuel*, **2002**, 81 (13), 1655-1668.

(25) Jak E., Kondratiev A., Christie S. and Hayes P.C.: *Metall. Trans. B*, **2003**, 34B, 595-603.

(26) Hoy H.R., Roberts A.G., and Wilkins D.M.: *Inst. Gas Engrs. J.*, **1965**, 5, 444-469.

(27) Patterson J.H., and Hurst H.J.: *Slag characteristics of Australian bituminous coals for utilization in slagging gasifiers*, Proceedings of the Workshop "Impact of Coal Quality on Thermal Coal Utilisation", 1996, CRC Black Coal Utilisation, Brisbane, Australia.

(28) Harris D.J. and Patterson J.H.: *Aust. Inst. Energy News J.*, **1995**, 13, 22-32.

(29) Reid W.T. and Cohen P.: *Trans. ASME*, **1944**, 66, 685-690.

(30) Reid W.T. and Cohen P.: *Trans. ASME*, **1944**, 66, 83-97.

SLAG FOAMING IN ENTRAINED FLOW GASIFIERS

Chulbum Cho and Myongsook S. Oh

Department of Chemical Engineering
Hongik University
72-1 Sangsudong Mapogu, Seoul, Korea

Introduction

In the entrained flow type of gasifiers, the slag viscosity is an important parameter which determines gasification conditions.[1] The slag viscosity has been measured experimentally under a reducing condition, and also estimated by various empirical models.[2-4] Most viscosity measurements were conducted under isothermal conditions or very low cooling rates such as 2 or 3°C/min. These data were used to determine the gasification temperature in the slurry-feed gasifiers to ensure continuous flow and, therefore, continuous removal of slag. In the dry-feed gasifiers which operate at temperatures well above 1500°C, the viscosity is used as a guide for minimizing the refractory wear. The isothermal measurements, however, do not render any information on slag behavior under rapid cooling conditions at the slag tap.

As the cooling rate increases, the viscosity at a given temperature decreases,[5] and the slag remains fluid to quite low temperatures. The low viscosity helps the slag flow out of the slag tap, so it was not a concern until one particular coal, Denisovsky coal, was tested. Denisovsky coal was a Russian sub-bituminous coal and was one of the nine coals tested under the project, "Development of fundamental Technologies for the IGCC systems," funded by Korean Ministry of commerce, Industry and Energy.[5] All nine coals were tested in two pilot scale entrained flow gasifiers: a 3-ton/day dry-feed gasifier at the Institute of Advanced Engineering (IAE), Suwon, Korea, and an 1-ton/day slurry-feed gasifier at Korean Institute of Energy Research (KIER), Taejeon, Korea. While the Denisovsky coal slag didn't cause any operational problem at the high temperature of the dry-feed gasifier, slag foaming filled up most volume of the slurry-feed gasifier vessel, resulting a major repair of the unit.

The cause of foaming was investigated in the laboratory. The slag viscosity was measured at two cooling rates, 2 and 10°C/min, and the cooled slag was examined using (a) Scanning Electron Microscope (SEM).

Experimental

Slag sample: The slag produced from the IAE dry-feed gasifier was used. The composition of the slag is shown in Table 1. The Denisovsky slag contains high concentrations of SiO_2 and Al_2O_3, and low concentration of CaO. The numbers in Table 1 were normalized to give 100, excluding refractory components such as Cr_2O_3 and ZrO. The concentration of refractory components varied widely from sample to sample. The average concentration of refractory components was 3-4%, but some contains over 10% of Cr_2O_3.

Table 1. Normalized Composition of Denisovsky Coal Slag

Al_2O_3	SiO_2	Fe_2O_3	CaO	MnO	TiO_2	MgO	K_2O	Na_2O	P_2O_5
30.5	49.3	9.13	5.63	0.19	0.99	1.70	1.68	0.53	0.44

Viscometer: Brookfield HB-DVIII viscometer with Searle type coaxial cylindrical cell was used in viscosity measurements.[6] The cell(stationary crucible and the rotor) was made of high density alumina and was placed in a high temperature furnace with the maximum attainable temperature of 1600°C. In order to simulate a reducing atmosphere, 80/20 (volume %) mix of CO_2/CO was injected from the bottom of the furnace at 1000cm^3/min. Approximately 70g of slag samples were broken into the sizes less than 2mm and slowly fed to the crucible at 1550°C. When all the slag was fed and the rotor was assembled, the temperature of the furnace was lowered at the rate of 2 or 10°C/min. The viscosity was measured every 30s at the shear rate of 10 rpm, until the torque on the rotor reached the 90% of the viscometer limit. Then, the rotor was removed from the molten slag and the whole assembly was allowed to cool down naturally. The cooled slag was cut as needed and examined using a SEM (Hitachi model).

Results and Discussion

Figure 1 shows the viscosity of Denisovsky coal slag as a function of temperature at two cooling rates. The viscosity was typical of a glassy slag at both cooling rates, and, as expected, shows lower values at 10°C/min. Under 2°C/min cooling rate, the maximum viscosity measured was about 5000 poise at 1380°C, while at 10°C/min, was 4000 poise at 1350°C. Measurements at a higher cooling rate were not possible due to the large mass of the cell and slag employed, and also due to excessive swelling, as discussed below. Once the hot slag boils over the crucible, it damages the furnace seriously.

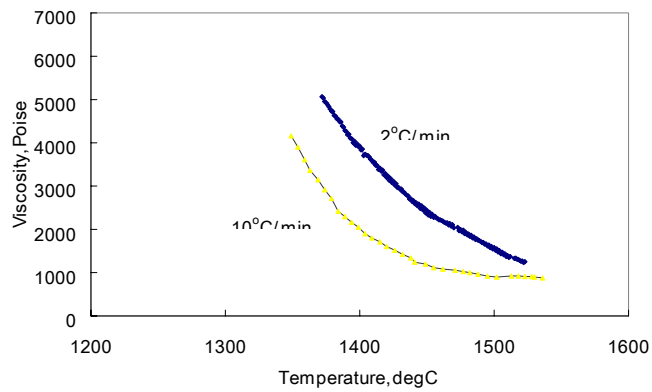

Figure 1. Viscosity of Denisovsky coal slag as a function of temperature at two cooling rates.

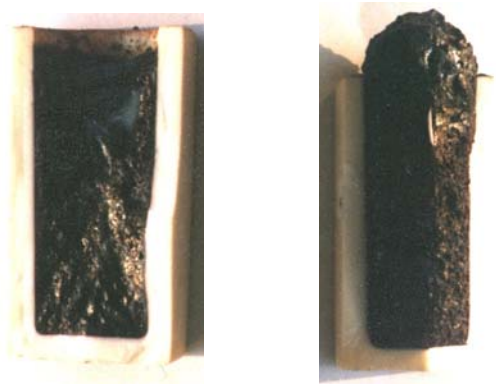

(a) After 2℃/min Cooling (b) After 10℃/min Cooling

Figure 2. Photographs of Denisovsky coal slag after viscosity measurements.

Figure 2 shows the shape of Denisovsky coal slag after viscosity measurements. At 2°C/min cooling, the slag remained inside the crucible, but filled the space which had been occupied by the rotor. The slag contained large number of small spherical pores though out the sample. At 10°C/min, the slag shows excess swelling. The slag not only filled out the rotor space, but also expanded above the crucible. The portion extruded above the crucible had rusty color coating and relatively high strength. The hardness decreased towards the bottom of crucible, becoming very brittle to the point that it could be crushed by hand. Many big spherical pores were observed at the bottom of crucible. Excess swelling or foaming of the slag after viscosity measurements was not observed in any other coal slags tested.

The SEM micrographs of the extruded top portion of the slag cooled at 10°C/min are shown in Figure 3. The overall area (Figure 3(a)) shows glassy background with needle-shape crystalline phases. The analysis by SEM/EDX identified these crystals as Al-Cr-oxide, a phase found in the refractory of the IAE gasifier. SEM/EDX composition analysis of a pore (Figures 3.b and 3.c) revealed that the pore had higher concentration of Fe than the glassy matrix, and the Fe concentration decreased towards the edge of the pore.

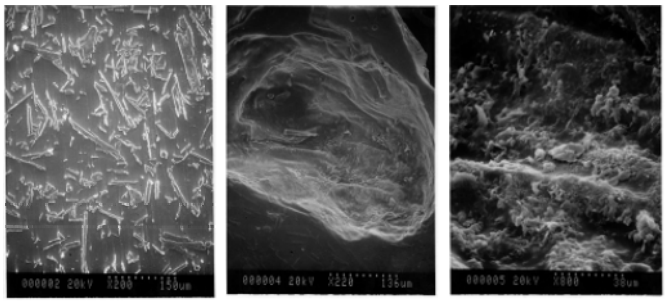

(a) Glassy Matrix (b) Pore (c) Inside of Pore

Figure 3. SEM micrographs from the top of Denisovsky coal slag cooled at 10°C/min.

The SEM micrographs of the bottom part of the slag are shown in Figure 4. The large spherical pores at the bottom have smooth, clear boundary which indicates their origin as gas bubbles in molten state. Figure 4(b) is the center area of Figure 4(a), magnified by 10 times, and shows the glassy matrix with Al-Cr-oxides and spherical droplets with white boundary. The SEM/EDX revealed that the droplets were made of metallic Fe. Metallic Fe droplets were also found in the large pores shown in Figure 4(c) and (d). Therefore, one can conclude that the pores were from O_2 gas bubbles which were released from Fe-oxides as they were reduced to Fe in a reducing gas atmosphere.

The SEM micrographs of the slag cooled at 2°C/min were similar to those in Figure 3. The top was also coated with the hard rusty red layer. The slag contained a high concentration of refractory components. Although the pores were smaller in size and number than those in 10°C/min slag, they also contained metallic iron inside.

The compositions of the top, middle, and bottom portion of 10°C/min slag cooled at 10°C/min, and one sample from 2°C/min slag were determined by XRF analysis. The compositions of 4 samples were very close to those shown in Table 1, confirming that there was no difference in composition between the hard top portion and porous bottom of the 10°C/min cooled slag, and also between the slags from two cooling rates.

The difference in pore size was resulted from the different actual cooling rates. When the cell assembly was allowed to cool down naturally after viscosity measurements, the cooling rate of the extruded portion of the slag is expected to be much faster than that of the bottom. The fast quenching and subsequent solidification of the slag inhibited the reduction of iron oxides and growth of bubbles, while, at the bottom, slow cooling allowed bubbles to expand to larger sizes.

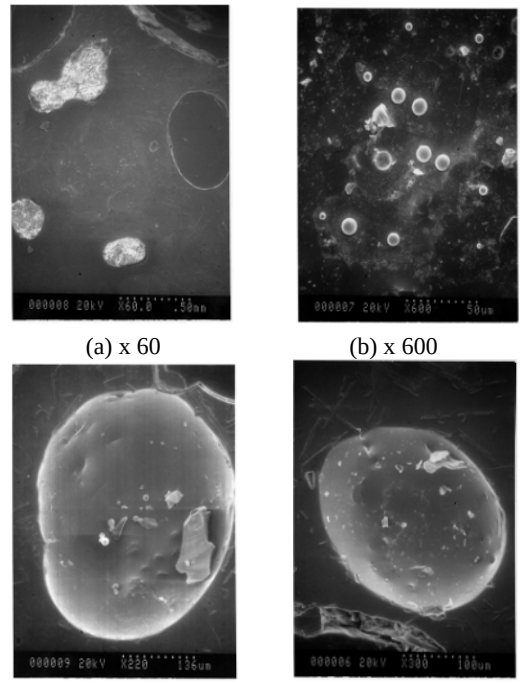

(a) x 60 (b) x 600

(c) Pore at × 220 (d) Pore at ×300

Figure 4. SEM micrographs from the top of Denisovsky coal slag cooled at 10°C/min.

The difference in the extent of swelling of the slag samples from two cooling rates can be explained by the viscosity. When the reduction of iron oxides started, the oxygen bubbles grew more readily in the slag matrix with the lower viscosity.

Conclusions

Reduction of iron oxides to metallic Fe can cause excessive slag foaming by O_2 gas when it occurs in a relatively low viscous glassy slag. Even in the slag with high isothermal viscosity, the low viscous condition can occur under a rapid cooling condition, such as at the slag tap of the gasifier. The slag foaming by iron oxides reduction can cause a serious damage to gasifiers which operate at temperatures around 1300°C. The swelling tests under rapid cooling in a reducing atmosphere must be performed for glassy slags prior to gasification.

Acknowledgement. This work was supported by Korean Ministry of Commerce, Industry and Energy under Contract 1996 N-CO02-P5.

References

(1) Corey, R. C., US Bureau Mines Bull. No. 618, 1964.
(2) Oh, M. S., and 4 others, *Fuel Processing Technol*., **1995**, *44*, 191.
(3) Watt, J. D., and Fereday, F., J. Inst. *Fuel*, **1969**, *42*, 99.
(4) Urbain, G., and 3 *Trans. J. Br. Ceram. Soc.*, **1981**, *80*, 139.
(5) Report to Korean Ministry of Commerce, Industry and Energy, 1996-N-CO02-P-5, **2000** and 2000-N-CO02-P-01, **2003.**
(6) Cho, D. H., Moon, I. S., Whang, S. Y., and Oh, M. S., *Korean J. Ind. Eng. Chem.* **2001**, *7*(1), 30.

Behavior of Minerals During Anthracite Graphitization

Margaret L. Laumb and Steven A. Benson
Microbeam Technologies Incorporated
4300 Dartmouth Drive
Grand Forks, ND 58203

Peter Pappano and Harold H. Schobert
The Energy Institute
Pennsylvania State University
University Park, PA 16803

Introduction

Anthracite coal was heated to three different temperatures to induce graphitization. The goal of the work was to determine how heating affected the mineral content and texture of the coal. This paper will focus on the various mineral transformations underwent during the heating process. The mineral transformations were measured using scanning electron microscopy and x-ray microanalysis.

Heating of the anthracite samples was conducted at Pennsylvania State University (1). Anthracite and heat-treated samples were analyzed by Microbeam Technologies Incorporated (MTI) to determine size, composition, and abundance of mineral and transformed mineral grains using computer-controlled scanning electron microscopy (CCSEM). In addition, morphological analysis was conducted to provide images and chemical compositions of selected features in the anthracite samples (2). The quantities of minerals and transformation products were determined at 2000°C, 2500°C, and 2600°C.

Experimental

LCNN anthracite was heated to three different temperatures: 2000°C, 2500°C, and 2600°C to induce graphitization. The samples were heat-treated in a Centorr Vacuum Industry Series 45 furnace, accurate to ±10°C. Graphite crucibles containing 12 grams of sample under graphite lids were placed in the hot zone of the furnace. The environment of the hot zone was purged by pulling a vacuum, and then backfilling with ultra-high purity argon three times. Following this purge, the samples were heated to 2000, 2500, and 2600° C with a heating rate of 10°C/min and held at the maximum temperature for one hour (in vacuum). The heat-treated samples were prepared and analyzed to determine size, composition, and abundance of mineral grains using CCSEM.

Samples of the raw and heat-treated anthracite were prepared for scanning electron microscopy analysis by mixing two grams of sample material with three grams of melted carnauba wax. This mixture was poured into a small rubber mold and, after solidifying, was backed with epoxy. The epoxy is used to increase the strength of the resulting plug. Plugs were allowed to harden overnight, and polished to expose cross-sections of the particles. Polished plugs were cleaned and coated with carbon to improve conductivity in the electron microscope.

Prepared samples were analyzed to determine size, composition, and abundance of mineral grains using fully automated computer-controlled scanning electron microscopy. The CCSEM technique characterizes up to three thousand individual particles in a single sample. Elemental compositions are used to categorize individual mineral types.

MTI also performed scanning electron microscope (SEM) morphology analysis to obtain representative photographs of the samples and determine variations in inorganic content between the organic matrix and mineral matter. Backscattered electron imaging, which best shows compositional differences, was used to examine the minerals present in the samples.

Results and Discussion

Table 1 shows the results of the CCSEM analyses for a raw anthracite and three heated samples. Mineral content for the raw coal was 6.8 wt%, and ranged from 1.1 wt% (at low temperature) to 0.6 wt% (at high temperature). This indicates significant loss of mineral phases from the coal due to decomposition and vaporization during heating. Figure 1 shows backscattered electron images of polished cross-sections of raw anthracite and heat-treated samples. The images show some changes in the shape of the minerals upon heating. Figure 1c shows void spaces where minerals may have been associated. These minerals likely volatilized during heating.

Mineral assemblages vary considerable between the raw and heated coals. Clays and aluminosilicates are abundant in the raw coal but absent from heated coals. This trend occurs for kaolinite, illite, and aluminosilicate. Calcium aluminosilicate, gypsum containing aluminosilicate (mixture of calcium, sulfur, and aluminosilicates), and unknown or amorphous material are most abundant in the sample heated to 2000°C. Pyrite, a sulfide mineral, is absent from the heated coal samples. Calcite-derived (or calcium oxide) and calcium-rich phase are important minerals in the heated coals, with the highest concentrations in the sample heated to 2500°C. Rutile (TiO_2), which is nearly absent in the raw coal sample and scarce in the 2000°C sample, is a dominant phase in the sample heated to 2500°C. Rutile and calcium oxide are stable at high temperatures and are not prone to volatilize during heating. Quartz and alumina are both present in the raw coal and the coal heated to 2000°C, but alumina is not present in the higher temperature samples, and quartz is not present in the 2600°C sample. Iron oxide increases in abundance as the temperature of treatment increases.

Conclusions

Significant mineral transformations were found when comparing the mineral types and abundance in the raw and heated coals. Clay minerals including kaolinite, illite, and aluminosilicate were abundant in the raw coal but absent from heated coals. These materials interacted with other components to produce calcium aluminosilicate, gypsum-containing aluminosilicate, and unclassified materials. The unclassified materials are typically glassy amorphous phases. Pyrite, a sulfide mineral, was absent from the heated coal samples. As a result of the decomposition of pyrite, iron oxide increases in abundance as the temperature of treatment increases. Calcite-derived (or calcium oxide) and calcium-rich phases are important minerals in the heated coals with the highest concentrations in the sample heated to 2500°C. Rutile and calcium oxide are stable at high temperatures and are not prone to volatilize during heating.

References

1. Pappano, P.J. "A mechanism of Pennsylvania anthracite graphitization involving carbide formation and decomposition." Ph.D. Dissertation. The Pennsylvania State University, University Park, PA. **2003**.
2. Laumb, M.L., Benson, S.A, and Laumb, J.D., Ash Behavior in Utility Boilers: A Decade of Fuel and Deposit Analysis, Proceedings of Engineering Foundation Conference, Production in the 21st Century: Impacts of Fuel Quality and Operations, October 28 - November 2, **2001**, Snowbird, Utah.

Acknowledgement
The authors gratefully acknowledge the support by The Consortium for Premium Carbon Products from Coal at the Pennsylvania State University.

Table 1. CCSEM analysis results for untreated LCNN anthracite and three heated LCNN anthracites. Results are expressed as weight percents normalized to 100% on a mineral basis.

Mineral/ phase	Raw	2000°C	2500°C	2600°C
Quartz	1.2	8	2.5	0.4
Iron oxide	0.5	1.1	1.5	2.8
Periclase	0	1.5	0	0
Rutile	0.8	9	42.7	38.5
Alumina	1.1	3.2	0	0
Calcite/calcite derived	1.6	8.2	12.3	9.2
Dolomite	1.4	0.1	0.4	0.1
Ankerite	0	0	0	0
Kaolinite	60.4	0.2	0.2	0
Montmorillonite	2	0.2	0	0.2
Illite	7.5	0	0.3	0
Fe Al-silicate	1.5	0	0	0
Ca Al-silicate	0.3	16.2	0.1	0.7
Na Al-silicate	0.5	0	0	0
Aluminosilicate	5.3	0.3	0	0
Mixed Al-silica	0.9	0.1	0.8	0
Fe silicate	0	0	0	0
Ca silicate	0	0.9	0.2	0
Ca aluminate	0	0.1	0	0
Pyrite	4.9	0	0	0
Pyrrhotite	0	0	0	0
Oxidized pyrrhotite	0.1	0.2	0	0
Gypsum	0.1	0.9	1.7	0.4
Barite	0	0	0	0
Apatite	0.5	0	0.6	0
Ca Al-P	0.1	0	0	0
KCL	0	0	0	0
Gypsum-Barite	0	0.8	0.1	0.2
Gypsum-Al-silic.	0.1	9.3	0.8	0
Si-rich	0.3	2.3	0.5	0.3
Ca-rich	0.8	6.1	8.5	5
Ca-Si-rich	0	0	0	0
Unknown/amorphous	8.1	31.6	26.9	42

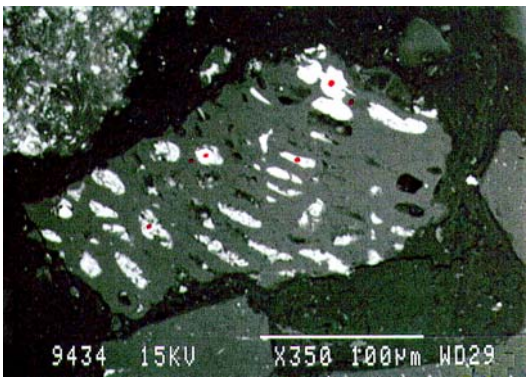

a. Raw anthracite

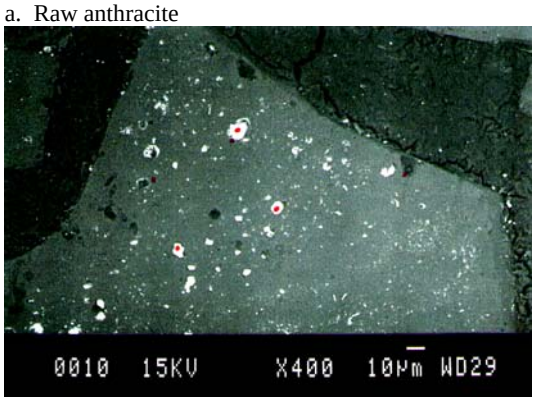

b. Heated to 2000°C

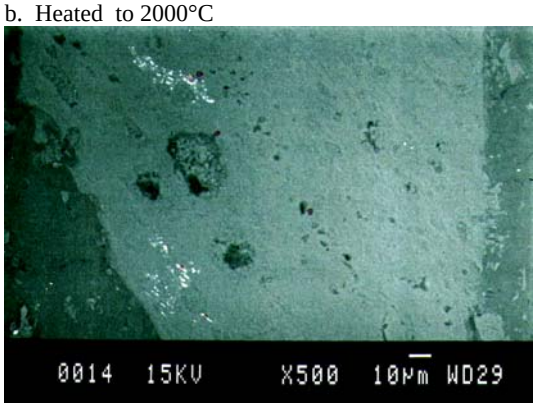

c. Heated to 2500°C

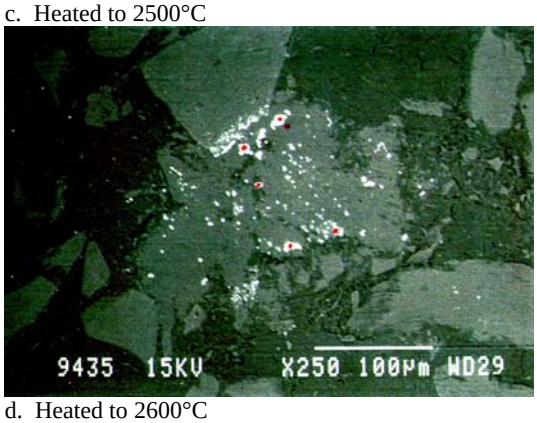

d. Heated to 2600°C

Figure 1. Backscattered electron images of polished cross-sections of raw coal and heat-treated samples.

Sulfur Retention in North Dakota Lignite Coal Ash

Bruce C. Folkedahl and Christopher J. Zygarlicke

Energy &Environmental Research Center
University of North Dakota
15 N. 23rd St.
Grand Forks, ND 58203

Introduction

Emissions from power plants such as particulate and sulfur are regulated by state health agencies and the U.S. Environmental Protection Agency (EPA). Much of the sulfur in the flue gas of coal-fired power plants is in the form of SO_2, with 1%–3% in the form of SO_3. SO_2 can be effectively controlled using commercial flue gas desulfurization (FGD) systems such as wet scrubbers. Sizing of these FGD systems affects the capital cost as well as the operational cost of the units. When the FGD system is sized, a coal analysis provides the amount of sulfur present in the coal, all of which is assumed to be SO_2 at the entrance to the FGD unit. The FGD system is then sized according to this concentration of sulfur. However, during combustion and depositional processes in the combustion system, some of the sulfur is retained in the ash because of reaction with basic oxides in the coal inorganics. The alkali and alkaline-earth elements are primarily responsible for this capture phenomena, with calcium and sodium being the most important. By accounting for the sulfur capture before the FGD, a more accurate determination of the FGD size and efficiency can be made. This report presents data from combustion tests performed at the University of North Dakota (UND) Energy & Environmental Research Center (EERC) on lignite coal, with an emphasis on evaluating the sulfur retention capability of the ash derived from the combustion. Statistical analysis and modeling of the sulfur retention and evaluation of a previous sulfur retention model developed at the EERC by Gronhovd et al. (1) is also presented.

Experimental

Coal Characterization The coal used in this test was obtained from core drilling of a mine area. Samples from the core drilling were contained in plastic bags and ranged from 0.13 to 29.5 lb per sample. Samples were put into three categories according to their sulfur levels. The categories were devised with low-sulfur samples having 0%–0.67% sulfur, medium-sulfur with a sulfur range of 0.68%–1.15% sulfur, and high sulfur having a sulfur content in the coal of greater than 1.16%, all on an as-received, weight percent basis of coal. The individual sample bags were placed into barrels of the three categories. The combined samples were then air-dried and thoroughly mixed. Samples of the three coal divisions were then analyzed using computer-controlled scanning electron microscopy (CCSEM), chemical fractionation, and x-ray fluorescence (XRF) of the ash for bulk oxide content. Table 1 shows the results of the average ultimate analysis for the three sample sulfur levels on an as-received basis. The bulk oxide composition of the ash generated from the coal sample composites as determined by XRF is shown in Table 2.

Combustion Tests The coal composite blends were tested in the conversion and environmental process simulator (CEPS), an intermediate-scale downfired combustor that fires 0.5–2.0 kg (1–5 lb)/hr of fuel, simulates conditions of a full-scale utility boiler, and can generate realistic combustion test results for a variety of fuels and combustion conditions. Control of gas temperatures and composition throughout the CEPS is possible, independent of the heat capacity of the fuel, because of its external electric heating. Flue gas temperatures can reach a maximum of 1500°C (2732°F) in the radiant section and can be maintained at 500°–1200°C (932°–2200°F) in the convective pass section and 120°–250°C (248°–482°F) in the baghouse. There is ample access for sampling, observation, and optical diagnostics through access ports located throughout the CEPS. A personal computer displays and records temperature, gas flow, feed rate, and flue gas (O_2, CO_2, CO, SO_2, and NO_x) composition, which is sampled from ports in the radiant section and after the collection device. Figure 1 is a schematic of the CEPS.

The CEPS furnace test conditions were standard operating conditions to simulate pulverized coal (PC)-fired combustion of coal. Coal was fed at a rate of 5 lb per hour, and the first six heated sections were maintained at temperatures of 1000°, 1500°, 1500° 1400°, 1250°, and 1100°C starting at the top of the combustion zone. Air was introduced into the system at the rate of 30 standard liters per minute (SLPM) as primary air and 137 SLPM as secondary air. The ash generated in the system was collected at the baghouse as well as at the horizontal section just after the combustion chamber. This ash was analyzed for sulfur content and the amount of sulfur exiting the system obtained by difference when compared to the total sulfur contained in the coal. These data were used to evaluate the sulfur retention model developed at the EERC in a previous study.

Table 1. Ultimate Analysis for the Three Composite Samples (as-received basis)

	Low Sulfur	Medium Sulfur	High Sulfur
Hydrogen	6.49	7.12	6.66
Carbon	30.46	33.41	34.25
Nitrogen	0.50	0.56	0.54
Sulfur	0.51	0.95	1.61
Oxygen	47.25	48.24	42.47
Ash	14.78	9.74	14.49
Btu	5830.00	6008.50	5961.50

Table 2. XRF Bulk Oxide Composition of Ash of Coal Sample Composites (weight percent, mineral basis)

	Low Sulfur	Medium Sulfur	High Sulfur
Silica	39.13	23.16	24.18
Aluminum	13.14	8.95	7.66
Iron	1.94	5.65	14.87
Titanium	0.93	0.55	0.43
Phosphorus	0.29	0.19	0.11
Calcium	17.36	18.39	13.14
Magnesium	6.44	6.82	4.77
Sodium	5.31	6.61	4.53
Potassium	0.52	0.40	0.40
Sulfur	14.36	28.92	29.44
Barium	0.58	0.36	0.46

Results and Discussion

Regression Analysis Statistical analyses of nine different samples of recently obtained lignite and 40 other lignite samples from a previous study by Gronhovd et al. (1) have been used to determine the efficacy of a model developed at the EERC in a previous study to predict sulfur emissions. Because calcium seemed either to be heavily affected by other factors or else insignificant, it was not included as a factor in the new model. Instead, silicon and aluminum contents were

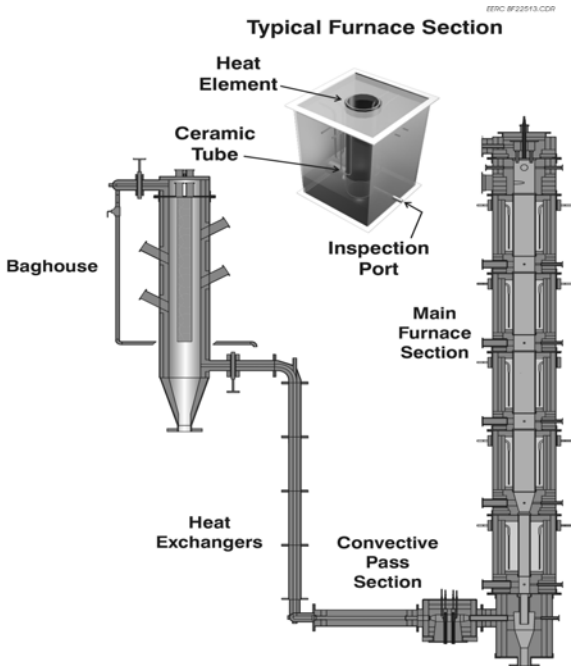

Figure 1. Schematic of the EERC CEPS.

included, which had seemed important to sulfur emissions in the previous tests. Aluminum was later disregarded as neither its effect nor its interactions proved important (the previous tests seemed to find a correlation between Al_2O_3 and sulfur emissions, but this may have been due to a correlation between aluminum and some other element). The final model developed in this study was as follows:

$$173.5!16.77(Na_2O)!2.207(SiO_2)!78.62(S)+0.2608(Na_2O)(SiO_2) +7.898(Na_2O)(S)+1.961(SiO_2)(S)$$

where the Na_2O and SiO_2 are given in weight percent oxide from the bulk ash XRF analysis and the sulfur is from the weighted average ultimate analysis from the three composite samples. The sulfur was computed on a moisture-free basis by weighting the measured sulfur level for each sample that went into the composite by the amount of sample in grams. These values are listed in Table 3 along with the measured sulfur in the collected combustion ash. The model r^2 term was 0.65, and its standard deviation was 10.1. This r^2 was slightly lower than the model developed previously at the EERC by Gronhovd. Statistically, the new model developed using the Grohovd data and the new lignite data has slightly better accuracy than did Grohovd's previous model. The results of the newly developed model are shown in Figure 2 and Table 4.

Table 3. Sulfur Levels in the Coal and the Collected Combustion Ash

	wt% in Coal (coal basis)	wt% in Combustion Ash (ash basis)
High Sulfur	3.29	2.1
Medium Sulfur	1.57	4.5
Low Sulfur	0.95	4.3

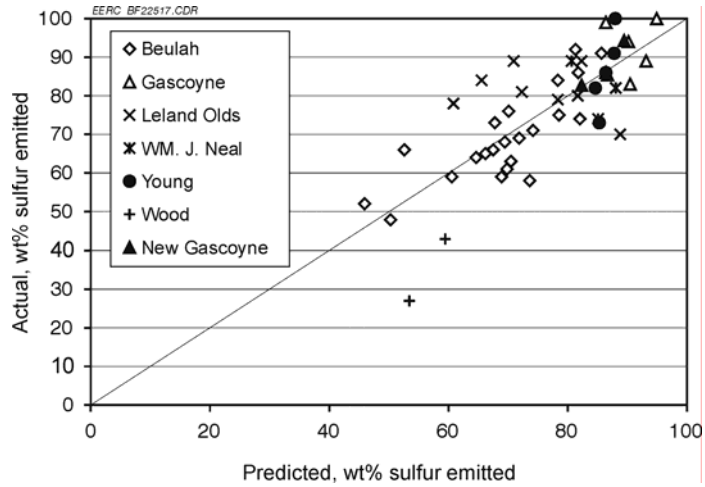

Figure 2. Predicted vs. actual percent sulfur emissions based on our current model.

Table 4. Predicted Versus Actual Sulfur Emitted from the Combustion Tests (percent of sulfur in coal)

	Predicted	Actual
High Sulfur	79	93
Medium Sulfur	70	83
Low Sulfur	87	87

Conclusions. The coal samples used in this study were divided into three composite samples. The coal came from core drilling of the lignite mine area. Core samples ranged in size from 0.13 to 29.5 lb per sample. The three composite samples were compiled according to sulfur levels of low, mid, and high, having values of 0%–0.67%, 0.68%–1.15%, and 1.16% and above, respectively. CCSEM analysis showed increasing amounts of pyrite and pyrrhotite and decreasing quartz and clays as the sulfur level increased. Chemical fractionation data indicate minor differences in the amount of material organically bound and carbonate materials in the three composite samples. The combustion tests of the three composite samples showed sulfur retention in the ash of roughly 7%–17% of the total sulfur in the coal. A new model developed from the data set produced in this study, as well as the data set from Gronhovd's previous study, indicates a slight increase in predictive capability over Gronhovd's previous model.

The regression model indicates that the original model developed by Gronhovd at the EERC in previous studies remains an adequate representation of the sulfur emissions expected from low-rank coals (1). While the newly developed model is statistically superior, the difference is minimal. Another point of the study is that the results from combustion studies performed in the EERC CEPS match the full-scale data from the previous study very well, validating the use of this pilot-scale equipment for modeling reactions in full-scale systems.

References

1. Some Studies on Stack Emissions from Lignite-Fired Powerplants: Technology and Use of Lignites Proceedings: Bureau of Mines, University of North Dakota Symposium 67, North Dakota, May 9–10, **1973**.

SCR CATALYST BLINDING DUE TO SODIUM AND CALCIUM SULFATE FORMATION

Charlene R. Crocker, Steven A. Benson, Jason D. Laumb

Energy & Environmental Research Center
University of North Dakota
15 North 23rd Street
Grand Forks, ND 58203

Introduction

Ash-related impacts on selective catalytic reduction (SCR) catalyst performance depend upon the composition of the coal, the type of firing systems, flue gas temperature, and catalyst design (1–5). The problems currently being experienced on SCR catalysts include the following:

- Formation of sulfate- and phosphate-based blinding materials on the surface of catalysts.
- Carrying of deposit fragments, or popcorn ash, from other parts of the boiler and depositing on top of the SCR catalysts.
- Catalyst poisoning from arsenic.

Licata and others (1) conducted tests on a South African and German Ruhr coal and found that the German Ruhr coal significantly increased the pressure drop across the catalyst because of the accumulation of ash. They found that the German coal produced a highly adhesive ash consisting of alkali (K and Na) sulfates. In addition, they reported that the alkali elements are in a water-soluble form and highly mobile and will migrate throughout the catalyst material, reducing active sites. The water-soluble form is typical of organically associated alkali elements in coals. The German Ruhr Valley coal has about 9.5% ash and 0.9% S on an as-received basis, and the ash consists mainly of Si (38.9%), Al (23.2%), Fe (11.6%), and Ca (9.7%), with lower levels of K (1.85%) and Na (0.85%) (2). Cichanosicz and Muzio (3) summarized the experience in Japan and Germany and indicated that the alkali elements (K and Na) reduced the acidity of the catalyst sites for total alkali content (K+Na+Ca+Mg) of 8%–15% of the ash in European power plants. They also found that alkaline-earth elements such as calcium react with SO_3 on the catalyst, resulting in plugging of pores and a decrease in the ability of NH_3 to bond to catalyst sites. The levels of calcium in the coals that caused blinding ranged from 3% to 5% of the ash. FactSage™ calculations indicate that the concentration of potassium and sodium in the gas stream increases more than proportionally with the addition of secondary fuels such as refuse-derived fuel, poultry litter and meat and bone meal (6). Cofiring 25% e/e poultry litter, in particular, increased the gaseous alkali concentrations dramatically.

The mechanisms for this type of low-temperature deposition have been examined and modeled in detail at the Energy & Environmental Research Center (EERC) in work termed Project Sodium and Project Calcium in the early 1990s; however, the focus of those projects was specific to primary superheater and economizer regions of boilers and not SCR systems (4, 7). Deposit buildup of this type can effectively blind or mask the catalyst, diminishing its reactivity for converting NO_2 to N_2 and water and potentially creating increased ammonia slip (1). In examining deactivation mechanisms related to alkali and alkaline earth metals, Senior et al. reported that vanadium tended not to form sulfates on the SCR catalyst in the presence of SO_2(g) but that the catalyst substrate (anatase) and modifiers (molybdenum) do (8).

Arsenic and phosphates, which are not uncommon in low-rank coals, may also play a role in catalyst degeneration. Arsenic is a known catalyst poison (9) in applications such as catalytic oxidation for pollution control. Phosphates can occur in low-temperature ash deposits to create blinding effects. Beck and others (10) found high concentrations of phosphorus compounds as constituents of the bio-residue (sewage sludge) in cofiring with coal to have a significant effect on the rate of catalyst deactivation. Phosphates also occur with arsenic and can cause catalyst poisoning (7). The blinding process involving pyrosulfates has more liquid-phase materials as compared to the calcium sulfate formation processes reported by Siemens (11) who described sulfate materials blocking catalyst pores with 50% catalyst deactivation after 5000 hours for a Powder River Basin (PRB) coal.

The purpose of this research was to obtain fundamental information on the formation of phases and components that comprise SCR blinding deposits. Calcium aluminum phosphate minerals have been observed in North Dakota lignites and PRB coals. Information on how these phosphate-rich phases develop and form will be invaluable for predicting SCR deposition and formulating ash deposit mitigation measures.

Experimental

Several coals were selected for testing based on coal type, geographical origin, and phosphorus-mineral-bearing content to obtain a variety of samples types. All test coals were analyzed for proximate, ultimate, heating value, and bulk inorganic composition using standard American Society for Testing and Materials procedures. Among the coals selected for the test matrix were a 48/52 blend of low-sulfur U.S. bituminous and PRB coals (LSUS–PRB) and a 100% PRB coal. Ash from the coals was produced under simulated combustion conditions in the conversion and environmental process simulator (CEPS), a down-fired combustion system that burns 2–4 lb/hr of fuel (Figure 1). The ash was collected and size fractioned using 3-stage cyclone to partition the ash. The 1–3-µm particles were characterized using scanning electron microscopy (SEM) to determine the distribution of elements as a function of particle size and vapor phase.

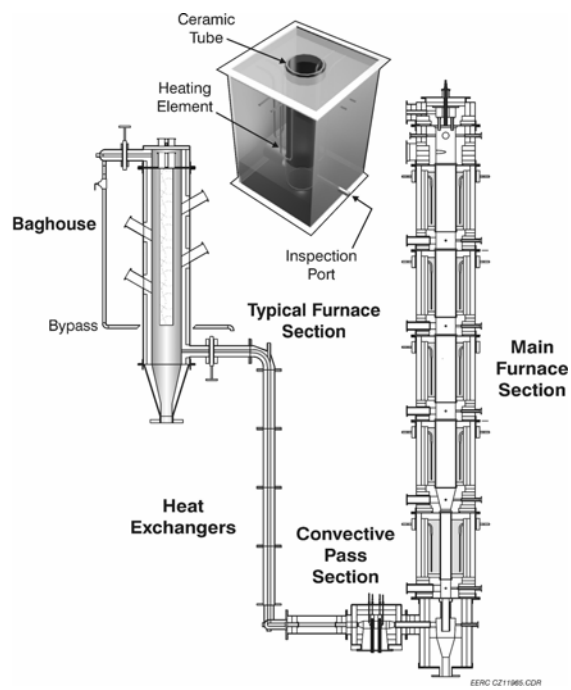

Figure 1. Schematic of the CEPS with furnace section detail.

The impacts of temperature and the presence of the catalyst on the ability of ash to form sulfates were examined. Isothermal tests to develop reaction rate as a function of temperature and gas composition were conducted using thermogravimetric analysis (TGA) with a DuPont model 951 module interfaced to a TA 2100 thermoanalyzer and data processor. The instrument has a 100-mg capacity and a maximum heat-up rate of 100°C/minute. TGA testing was conducted on the 1–3-µm-size fraction of ash produced from the LSUS–PRB and 100% PRB coals and exposing them to vapor-phase sulfur dioxide with and without catalyst at several temperatures. Testing was conducted to determine the weight gain with flue gas containing ammonia. Gas composition for the TGA tests was 74% N_2, 8% H_2O, 14% CO_2, 4% O_2, 100–300 ppm NH_3, 0.04% SO_2, 1–1000 ppm P.

Scanning Electron Microscopy. The SEM method utilizes electron probe microanalysis techniques to chemically analyze individual ash particles. Particles collected in the 3-stage cyclone of the CEPS and exposed in the TGA analyzer were finely dispersed on carbon tape and analyzed for major and minor elements using the ZAF method, which corrects x-ray intensities for differences in the atomic number (Z), absorption (A), and fluorescent (F) effects of the calibration standards relative to the sample. The chemical composition obtained in this manner is semiquantitative at best because of the short x-ray counting time employed (10 s), the use of flat mineral standards for calibration, and the fact that no matrix corrections for particle diameter, shape, or density were applied.

Results and Discussion

Table 1 contains the proximate and ultimate analysis of the selected test materials. The 100% PRB coal had twice the moisture (24.1 vs. 12.9 wt%) of the LSUS–PRB blend. It also contained about 14 wt% more oxygen and 7.5 wt% fixed carbon. Hydrogen and nitrogen content were similar between the coals. The percent ash of the LSUS–PRB blend was about 3.5 wt% higher than the 100% PRB. The sulfur content was also higher (8.3 vs. 5.6 wt% of the ash). Table 2 shows the ratio of mineral constituents in the as-received coals. The 100% PRB coal ash has a higher proportion of Ca than Al and Si. The ashed coal also contained S, Mg, Fe, and small amounts of Ti, Na, and K. The P content was less than 1%. The greatest change resulting from the blending of the PRB with LSUS was the aluminosilicate nature of the ashed blend. The Ca content was one third that of the 100% PRB, and the Mg was half the PRB content. The rest of the elements were present in similar proportion to the 100% PRB coal ash

Table 1. Proximate and Ultimate Analysis of Coal, as received

	100% PRB	LSUS–PRB
Air Dry Loss, %	17.58	9.86
Moisture, %	24.1	12.9
Volatile Matter, %	35.6	35.72
Fixed Carbon, %[1]	36.03	43.59
Ash, %	4.27	7.8
H, %	6.19	5.44
C, %	52.06	62.48
N, %	1.26	1.61
S, %	0.24	0.65
S, % of mineral constituents	5.6	8.3
O, %[1]	35.99	22.03
Calculated Calorific Value	8904	10,830

[1] By difference.

Table 2. SEM Analysis of the Mineral Content of the Coals

Oxide content, SO_3 free	100% PRB	LSUS–PRB
Al_2O_3	32.0	48.3
CaO	20.3	29.7
Fe_2O_3	7.1	5.3
K_2O	1.7	1.8
MgO	1.1	0.4
Na_2O	28.5	9.5
P_2O_5	7.6	2.9
SiO_2	1.1	0.8
TiO_2	0.5	1.3
Al_2O_3	32.0	48.3

The aim of the TGA testing was to determine the potential of the formation of sulfates to cause particle-to-particle bonding that leads to the formation of deposits in the temperature range where SCR catalysts are used. The TGA testing is focused on determining the reactivity of the 1–3-µm ash produced from the LSUS–PRB and 100% PRB coals to sulfur dioxide and gas-phase phosphorus species as a function of temperature. Testing was conducted to determine the weight gain with flue gas containing ammonia. The impact temperature on the weight gain due to the formation of sulfates for the LUSU–PRB blend is shown in Figure 2. The rates of sulfation were found to increase with increased temperature. The increase in the weight gains was magnified when ammonia and phosphorus were added. Ground catalyst was mixed with the 100% PRB ash in the TGA. Increases in weight gain were observed when catalyst was added as compared to baseline cases for 100% PRB, as shown in Figure 3. The presence of catalyst enhances the formation of sulfates.

The ash exposed in the TGA was examined using the SEM. Figure 4 shows the LSUS–PRB blend. The analysis included points at the margins of the spheres to identify coating elements and points in the center of the large spheres to excite as much of the underlying particle as possible. A comparison of the coating and ash particle composition (Table 3) shows higher Ca and S content in the coating material, supporting evidence of sulfate—as $CaSO_4$—formation on the ash particles under SCR reactor conditions.

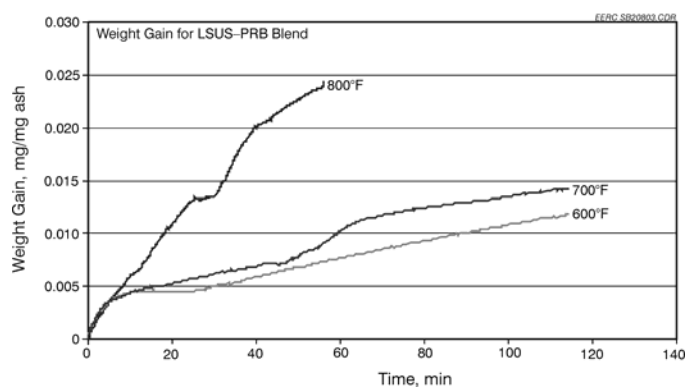

Figure 2. Weight changes for LSUS–PRB coal ash exposed to simulated flue gases and ammonia at three temperatures.

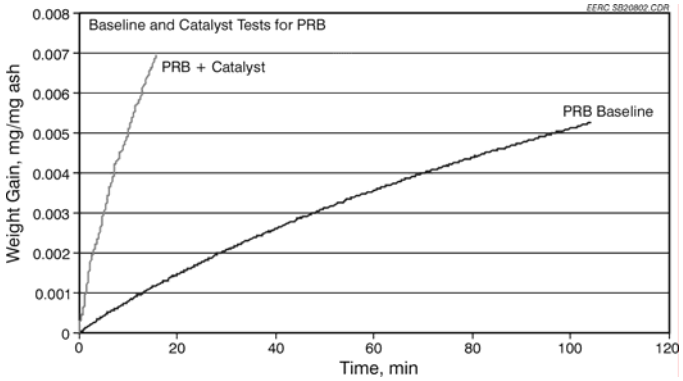

Figure 3. Weight changes for 100% PRB coal ash exposed to simulated flue gases and ammonia as with and without SCR catalyst present at 800°F.

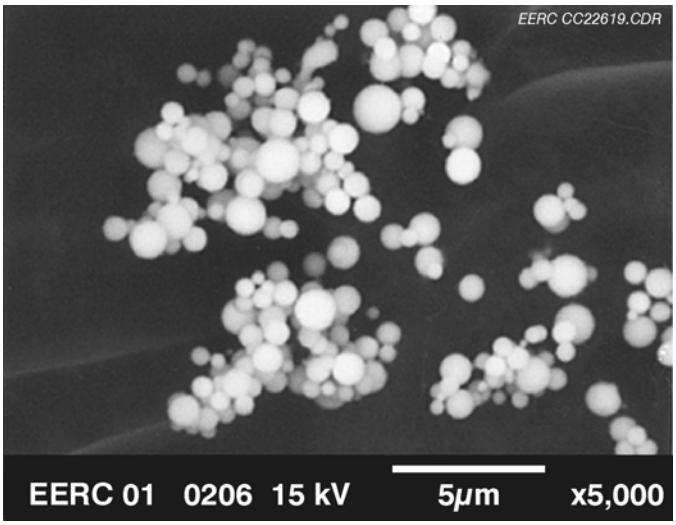

Figure 4. SEM micrograph of LSUS–PRB-blend coal ash exposed to simulated flue gases and ammonia at 800°F (no catalyst present).

Table 3. SEM Analysis of the LSUS–PRB Ash Exposed to Simulated Flue Gas, Ammonia, and Phosphorus in the TGA

Elemental Content	Coating, wt%	Particle and Coating, wt%
Al	15.9	12.6
Ba	0.0	1.0
Ca	20.0	10.6
Cl	0.1	0.0
Cr	0.0	0.0
Fe	4.9	5.6
K	1.7	1.0
Mg	2.1	3.1
Na	0.4	0.5
P	2.0	4.0
S	1.0	0.0
Si	14.5	21.8
Ti	0.9	3.0
O	36.4	36.5

Conclusions

The following observations were noted from the bench-scale phase of this research:

- PRB and lignite coals have the potential to blind SCR catalysts.
- A high blinding potential exists for LSUS–PRB blends.
- The addition of ammonia, phosphorus, and catalyst enhances the formation of phosphates and sulfates.
- Morphology analysis of fly ash exposed to SO_2, ammonia, and P in the TGA shows that sulfates and phosphates accumulated on the surface of the ash.

Acknowledgment. This investigation was supported by Alliant Energy, AmerenUE, Dynegy Midwest Generation, Kinectrics Inc., Ontario Power Generation, Otter Tail Power Company, EPRI, the Industrial Commission of North Dakota, Hitachi, Haldor-Topsoe, and Cormetech through the EERC Jointly Sponsored Research Program, which is supported by the U.S. Department of Energy National Energy Technology Laboratory under Cooperative Agreement No. DE-FC26-98FT40321.

References

(1) Licata, A.; Hartenstein, H.U.; Gutberlet, H. Utility Experience with SCR in Germany. 16th Annual International Pittsburgh Coal Conference, Pittsburgh, PA. Oct 11–15, 1999.

(2) Cichanovicz, J.E.; Broske, D.R. An Assessment of European Experience with Selective Catalytic Reduction in Germany and Denmark. EPRI–DOE–EPA Combined Utility Air Pollution Control Symposium: The MEGA Symposium, Atlanta, Georgia, Aug 16–20, 1999.

(3) Cichanovicz, J.E.; Muzio, L.J. Twenty-Five Years of SCR Evolution: Implications for U.S. Applications and Operation. EPRI–DOE–EPA Combined Utility Air Pollution Control Symposium: The MEGA Symposium, AWMA, Chicago, IL, Aug 20–23, 2001.

(4) Benson, S.A.; Fegley, M.M.; Hurley, J.P.; Jones, M.L.; Kalmanovitch, D.P.; Miller, B.G.; Miller, S.F.; Steadman, E.N.; Schobert, H.H.; Weber, B.J.; Weinmann, J.R.; Zobeck, B.J. *Project Sodium: A Detailed Evaluation of sodium Effects in Low Rank Coal Combustion Systems;* Final Technical Report; EERC publication, July 1988.

(5) Franklin, H.N. The Effect of Fuel Properties and Characteristics on Selective Catalytic Reduction Systems. In *Proceedings of the 1996 Joint Power Generation Conference*; Volume 1, ASME 1996, EC-Vol. 4/Fact-Vol. 21, pg. 421–428.

(6) Vredenbregt, L.H.J.; Meijer, R. The Effect of Cofiring Large Amounts of Secondary Fuels on SCR Deactivation. In the National Energy Technology Laborabory Web site. http://www.netl.doe.gov/ (accessed 12/10/03). In *Proceedings of the 2003 Conference on Selective Catalytic Reduction and Non-Catalytic Reduction for NO_x Control*, Pittsburgh, PA, October 29–30, 2003.

(7) Hurley, J.P.; Erickson, T.A.; Benson, S.A.; Brobjorg, J.N.; Steadman, E.N.; Mehta, A.K.; Schmidt, C.E. Ash Deposition at Low Temperatures in Boilers Firing Western U.S. Coals. International Joint Power Generation Conference; Elsevier Science, 1991; pp 1–8.

(8) Senior, C.;Linjewile, T.; Bockelie, M.; Baxter, L.; Bartholomew, C.; Hecker, W.; K. Whitty, K.; Eddings, E.. SCR Deactivation Mechanisms Related to Alkali & Alkaline Earth Elements. In the National Energy Technology Laborabory Web site. http://www.netl.doe.gov/ (accessed 12/10/03). In *Proceedings of the 2003 Conference on Selective Catalytic Reduction and Non-Catalytic Reduction for NO_x Control*, Pittsburgh, PA, October 29–30, 2003.

(9) Bullock, D.W.; Hartenstein, H. Full-Scale Catalyst Regeneration Experience of a Coal-Fired U.S. Merchant Plant. In the National Energy Technology Laboratory Web site. http://www.netl.doe.gov/ (accessed 12/10/03). In *Proceedings of the 2003 Conference on Selective Catalytic Reduction and Non-Catalytic Reduction for NO_x Control*, Pittsburgh, PA, October 29–30, 2003.

(10) Beck, J.; Unterberger, S.; Hein, K.R.G. Deactivation Mechanisms of SCR Catalysts During the Co-Combustion of Bio-Residues. In the National Energy Technology Laborabory Web site. http://www.netl.doe.gov/ (accessed 12/10/03). In *Proceedings of the 2003 Conference on Selective Catalytic Reduction and Non-Catalytic Reduction for NO_x Control*, Pittsburgh, PA, October 29–30, 2003.

(11) Rigby, K.; Johnson, R.; Neufort, R.; Gunther, P.; Hurns, E.; Katt, A.; Sigling, R. SCR Catalyst Design Issues and Operating Experience: Coals with High Arsenic Concentrations and Coals from the Powder River Basin. Presented at the International Joint Power Generation Conference, IJPGC2000-15067, July 23–26, 2000.

PLAMSAS FOR GREENHOUSE GAS UTILIZATION

Huy Le, L. L. Lobban and R. G. Mallinson

School of Chemical Engineering and Materials Science
University of Oklahoma
100E. Boyd Street, Room T335
Norman, OK 73019
mallinson@ou.edu

Introduction

Natural gas is considered the energy source of the future, because it is environmentally friendly with clean and low carbon emissions. However, it is not an easy-to-transport fuel. Unfortunately, many of the large proven reserves are located far away from the major markets, and it is not economical to transport the gas to the markets.

Methane, the major component of natural gas, is currently used primarily for its heating value. However, methane has a tremendous potential to be used as a building block to form other more valuable fuels and chemical feedstock. In indirect methane conversion processes, methane is first converted to synthesis gas, a mixture of CO and hydrogen, either via partial oxidation or steam reforming of methane. From synthesis gas, chemicals can be produced via many routes, or hydrogen can be extracted and used as a clean fuel used to power fuel cells. These indirect methane conversion processes are energy-intensive and less feasible at small capacity due to the high operating cost of the syngas generation unit.

Different advanced gas conversion technologies are desired to utilize and monetize the natural gas resources, whether it is stranded gas or not. From methane, different chemicals such as oxygenates, unsaturated C_2 hydrocarbons, and heavier hydrocarbons could be directly produced via different routes. The gas conversion technology using the non-equilibrium plasma generated by the AC corona discharge is such a technology, which can be used to convert methane to hydrogen and C_2 hydrocarbons under atmospheric pressure and room temperature.

The applications of indirect gas conversion technologies can be dated back before the 1950s. These technologies were based on the Fischer-Tropsch reaction (FT), discovered in the 1920s by the German scientists Franz Fischer and Hans Tropsch. They heated coal to produce synthesis gas, which when passed over a metal catalyst produced liquid hydrocarbons. Since synthesis gas can also be produced from natural gas, several processes have been designed and built to make liquid hydrocarbons from natural gas (GTL process). SASOL, the South Africa's state-owned oil company, is the most experienced in GTL processes. They have built GTL plants since the 1950s. Exxon-Mobil also has a 10 thousand barrel per day plant in Bintulu, Malaysia, in which synthesis gas was produced using pure oxygen. Other major energy companies such as Cocono-Phillips are developing similar GTL processes, which would be built on large scale.

Non-equilibrium Plasmas

Non-equilibrium plasma technology has been used to convert methane to various products. It can be non-catalytic or catalytic.[3-25] Methane is converted to other products, such as C_2s and synthesis gas, under the temperature and pressure conditions that traditional chemistry cannot.

The non-equilibrium plasma is a type of plasma, in which the electron has much higher energy or temperature than the neutral gas species.[2, 3] In the non-equilibrium plasma, total number density of the charged particles is much less than the total number density of the neutral particles. When a potential difference is imposed across a gaseous mixture, the electric field acts upon the charged particles such as the electron but not the neutral species. The interaction transfers energy from the field to those charged particles in terms of kinetic energy. The electron, due to its light weight, is accelerated to higher velocity in the time between collisions. The electron has higher kinetic energy than the energy of gas molecules in random motion, if the applied field is high enough. Then, the non-equilibrium plasma is generated.

There are five common types of non-equilibrium discharges: glow discharge, silent (dielectric barrier) discharge, radio frequency discharge, microwave discharge, and corona discharge. The corona discharge is not homogenous, while the silent discharge is considered homogeneous and both can occur at atmospheric pressure conditions. This is the plasma type used in most recent work when a high voltage AC or pulsed waveform on the order of several KVs is applied across two metal electrodes. In the case of the silent discharge, a dielectric barrier such as glass electrically isolates one or both electrodes. The average electron energy in these discharges is in the range of 1-10 eV and both cause only a small degree of ionization.[2]

The only commonly known industrial application using plasmas to produce chemicals is ozone production using the silent (DBD) discharge. However, plasmas have been used in large screen plasma televisions. The electron in the traditional CRT TV, emitted by an electron gun and accelerated via a strong electric field, is replaced by the electron initiated inside the plasma. The plasma TV can be as thin as 4 inches and as large as 72 inches.

Equilibrium Plasmas

The non-equilibrium plasma is different from the thermal plasma, or equilibrium plasma, in which all particles have approximately the same high temperature or kinetic energy. Thermal plasmas will not be discussed here as they may be generally regarded in many respects as conventional high temperature homogenous processes, with some exceptions. Also, these plasmas typically have prohibitively large energy input that is unsuitable to cost effective methane and CO_2 utilization. An intermediate category might be considered for plasmas that are nearly thermal, but of more moderate temperature. An example would be what might be called an igniting plasma in which the primary purpose of the plasma is to provide a rapid preheating of the gas where once the plasma has initiated the reactions they become thermally self sustaining.

Partial Oxidation of Methane

Many efforts have been concentrated on the partial oxidation of methane using the AC plasmas. Liu[4] introduced helium into the methane-oxygen feed as a diluting species. The frequency was in the range of 10 Hz to 60 Hz. With methane to oxygen ratio varying from 2 to 10, it was reported that as the oxygen mole fraction increased, the methane conversion and the carbon monoxide selectivity increased, however, the ethane selectivity decreased. The ethylene selectivity did not change much. Theoretically, it is expected that hydrogen and acetylene be present in the product. However, these two species were not reported in this work.

The partial oxidation of methane using helium as a diluting species was also conducted in a higher frequency range from 150 Hz to 300 Hz.[8] It was reported that increasing the oxygen mole fraction up to 20% increased the methane conversion and decreased the C_2 selectivities. Hydrogen and acetylene were not reported, as in Liu's case. This could be due to the limitation of the GC analysis. Even though the C_2 yield was said to reach a maximum at 0.6 atm helium

partial pressure, the major C_2 product was ethane, which is not a very useful product. The CO_x selectivity did not change noticeably. This implies that helium does not help the partial oxidation of methane.

The partial oxidation of methane using the AC plasma was also studied by Caldwell.[9] The operating frequency was between 100 Hz and 800 Hz, covering the higher frequency range that previous works left. Increasing the oxygen mole fractions from 5% to 33% was reported to increase the methane conversion and energy efficiency. The CO_2 selectivity varied from 1% to 6%, suggesting that over-oxidation of methane was not excessive. The methane throughput compared to Liu and Hill's could be eight times higher, while the obtained methane conversions were in similar range, confirming that it was more energy efficient not to use any diluting species such as helium in the feed. The hydrogen selectivity was as high as 55%. All C_2 hydrocarbons and CO_x were reported in the products as expected. At 33% oxygen mole fraction in the feed, the carbon monoxide selectivity reached 55%. The lowest energy consumption was 6 eV per methane molecule converted. In addition to pure oxygen, air was used as the oxygen source. The energy consumption when using air was higher than the energy consumption when using pure oxygen. The lowest energy consumption reported in the air-methane system was ~15 eV/molecule of methane converted, higher than that in the methane-oxygen system, suggesting that nitrogen dilutes the feed and decreases the reaction rates. This result is consistent with the results from the methane-oxygen-helium system.

In Liu's work, it was reported that under a constant applied voltage, the methane conversion reached a maximum at 30 Hz. The maximum C_2 yield, obtained at 60% conversion of methane, was around 20%. It was explained that as the frequency was reduced to 30 Hz, the discharge changed from the corona discharge to the spark discharge. According to Eliason,[2] this change occurs when the applied voltage has exceeded a threshold. This implies that as the frequency was reduced the actual applied voltage to the electrodes increased. Therefore, at 10 Hz and 20 Hz frequencies, the discharge should also be the spark discharge. The authors did not give an explanation why the methane conversion at 10 Hz (~ 5%) was much lower than that at 30 Hz (~ 58%). The change in the input power with varying the frequency was not reported. Thus, there was no reported conclusion if the frequency influenced the energy efficiency of the system.

Hill[8] also studied the effect of frequency with the same approach as Liu. It was reported that the methane conversion decreased when the frequency was increased from 150 Hz to 300 Hz, and the applied voltage was kept constant. The input power decreased from 15 W to 10 W, and the methane conversion decreased from 32% to 17%. Therefore, the energy efficiency did not change much within this frequency range.

Similarly, Caldwell[9] studied the effect of the frequency with a different approach. Instead of keeping the applied voltage constant, the input power was kept constant. It was reported that the methane conversions were similar at the frequencies between 100 Hz to 800 Hz. The experimental data, such as flow rate, power, and oxygen ratio, were not reported.

Supat[7] and Caldwell[9] reported that increasing the input power by changing the frequency or increasing the applied voltage resulted in increasing the methane conversion. However, as the input power reached a certain threshold, excessive coke formation started. It could be because the heating of the bulk gas led to thermal dehydrogenation of methane to form coke.[9] A higher input power would allow more energy to form more CH and CH_2, which are less stable than CH_3. Therefore, there were more CO, unsaturated C_2s as well as coke produced, when the input power increased.

Hill[8] reported that at a constant feed flow rate and applied voltage, increasing the gas gap between the two electrodes increased the methane conversion. It could be explained that increasing the gas gap increased the residence time, therefore, increased the methane conversion.

The Steam Reforming and the Combined Steam Reforming with Partial Oxidation of Methane

The conventional steam reforming normally involves high temperature and catalysts. However, plasma technology allows it to be carried out at much lower temperatures. Hammer[10] used the silent discharge in a Dielectric Barrier Discharge (DBD) reactor to study the steam reforming of methane. The steam mole fraction was varied from 50% to 75% at temperatures in the range of 200°C to 600°C. The products included CO_x, C_2s, C_3s, and butane. Based on the author's data, the energy consumption per methane molecule converted was in the range of 50 eV to 100 eV, an order of magnitude higher than the energy consumption in the partial oxidation of methane. High energy consumption has been the main disadvantage of the DBD system.

Supat[7] studied the combined steam reforming and partial oxidation at the steam mole fractions less than 50%. The methane to oxygen ratio (MTOR) was in the range of 2:1 to 5:1. The CO selectivity was as high as 62%. The estimated H_2 selectivity (not reported by the author) was 80%, about 20% higher than that in the partial oxidation of methane. The lowest energy consumption per molecule of methane converted was 9 eV, much higher than that in the partial oxidation of methane.

Also using the combined steam reforming and partial oxidation with air as the oxygen source, Bromberg[11] reported a high efficiency plasmatron producing hydrogen from natural gas using the catalytic DC plasma. The feed conversions were as high as 100%. Most of the methane was converted to carbon monoxide. There was only a small amount of ethylene reported. Even though the input power was high (270 W), the high feed conversions as well as high methane throughput led to a low energy consumption: ~ 0.24 eV/molecule of methane converted. This is the lowest energy consumption ever reported and may reflect more of an ignition phenomena than an initiation phenomena. Since the partial oxidation and steam reforming of methane is thermodynamically favored at high temperatures, the use of catalysts at high operating temperatures helps increase the feed conversions. The plasma source could be considered as an ignition stage providing heat to preheat the gas and the catalysts. As a result, the plasmas could be replaced by a conventional heater without impacting the results.

Dry reforming of methane has been studied using the AC Dielectric Barrier Discharge[22], the AC arc discharge[24], and the pulsed discharge.[21] The CO selectivity above 82% was obtained in the AC DBD[22] and the AC arc discharge.[24] The ethylene selectivity was not reported[22] or was very low (2.3%).[24] On the other hand, the ethylene selectivity, as high as 64%, was obtained in the pulse discharge.[21] The lowest energy consumption per molecule of carbon (including CH_4 and CO_2) converted was 15 eV.[24] This seemed to be more efficient than the steam reforming of methane. However, the energy consumption was still much higher than that that in the partial oxidation of methane.

Conclusions and Prospects

Methane as a greenhouse gas is misleading in the context of GHG utilization in that methane that is consumed is produced for its utilization (or might be recovered for that purpose in relatively small quantities). Thus it seems that the primary impact of plasma

based processes on GHG utilization when converting methane would be to reduce CO_2 emitted as a result of its consumption, e.g. to be more energy efficient than conventional processes. As a crude comparison, methane has an energy content of about 8 eV/molecule and conventional steam reforming is about 70 percent efficient, using direct fired combustion for the input heat, thus approximately 5.6 eV/molecule is retained in the products (hydrogen and CO). For a plasma, the allowable energy "cost" is then about 2.4 eV/molecule. However if this is supplied by electricity, generated with an efficiency of about 35 % (single cycle fossil energy), then the maximum electrical energy that can be supplied competitively is about 0.8 eV/molecule of methane converted. No plasma system has yet achieved this. The silent discharge systems appear to be sufficiently inefficient that this will be difficult to conceive, however some corona discharge results are certainly within an order of magnitude and perhaps substantially closer to this. So there seems to be some promise that improvements may make this achievable and may also apply to steam combined with CO_2 reforming to some extent. This could be particularly valuable where CO_2 is a significant contaminant of the natural gas resource. (Note that CO_2 reforming as a net sink for CO_2, say recovered from power production, is not a net sink for CO_2!).

In the case of partial oxidation, no net energy input is required for convention conversion due to its exothermicity, and therefore even for an ignition type plasma system, the net greenhouse gas "consumption" for a plasma will always be less. Fortunately, oxygen is the most efficient initiator for methane conversion in low temperature plasmas and energy consumption can be quite low under the best conditions, approximately 1eV/molecule. So even here, other factors, such as the ability to operate on a much smaller scale, with less need and cost, for heat recovery, may allow application of low temperature corona type plasma methane conversion even with some loss in net energy efficiency (and therefore greenhouse gas consumption) compared to conventional processes.

References

1. Strategic Plan for DOE Hydrogen Program, US Department of Energy, Jan **1998**
2. Eliasson, B.; Kogelschatz, U.; "Nonequilibrium Volume Plasma Chemical Processing". *IEEE Trans. Plasma Sci*. **1991**, 19 (6), 1063-1077
3. Chang, J.-S.; Lawless, P. A.; Yamamoto, T.; "Corona Discharge Process". *IEEE Trans. on Plasma Sci.* **1991**, 19 (6), 1152-1166
4. Liu, C.; Marafee, A.; Hill, B.; Xu, G.; Mallinson, R.; Lobban, L.; "Oxidative Coupling of Methane with ac and dc Corona Discharges." *Ind. Eng. Chem. Res*. **1996**, 35, 3295- 3301
5. Larkin, D.W.; Caldwell, T.A.; Lobban, L.L.; Mallinson, R.G.; "Oxygen Pathways and Carbon Dioxide Utilization in Methane Partial Oxidation in Ambient Temperature Electric Discharges." *Energy and Fuels* **1998**, 12, 740-762
6. Fan, W. Y.; Knewstubb, P. F.; Kaening, M.; Mechold, L.; Roepcke, J.; Davies, P. B.; "A Diode Laser and Modeling Study of Mixed (CH4-H2-O2) AC Plasmas." *Journal of Physical Chemistry A* **1999**, 103(20), 4118-4128
7. Supat K, Chavadej S., Lobban, L. L, Mallinson, R. G.; "Combined Steam Reforming and Partial Oxidation of Methane to Synthesis Gas Under Electrical Discharge." *Ind. Eng. Chem. Res.* **2003**, 42 (8), 1654-1661
8. Hill, J. B.; "The Oxidative Coupling of Methane Using an AC Electric Gas Discharge." A Thesis for Master of Science, University of Oklahoma, **1997**
9. Caldwell, T.A.; Le, H.; Lobban, L. L.; and Mallinson, R. G.; "Partial Oxidation of Methane to Form Synthesis Gas in a tubular AC Plasma Reactor." *Studies in Surface Science and Catalysis* **2001**, 136, 265-270
10. Hammer,T.; Kappes; T.; Schience, W.; **"**Plasma Catalytic Hybrid Reforming of Methane." *Preprints of Symposia - American Chemical Society, Division of Fuel Chemistry*, **2002**, 47(1), 278-279.
11. Bromberg, L.; Cohn, R. D.; Rabinovich, A.; Heywood, J.; "Emissions Reductions Using Hydrogen from Plasmatron Fuel Converters." *Diesel Engine Emission Reduction Workshop*, San Diego, CA August **2000**
12. Mallinson, R.G.; Braun, R.L., Westbrook; C.K., Burnham, A.K., "Detailed Chemical Kinetics Study of the Role of Pressure in Butane Pyrolysis." *Ind. Eng. Chem. Res.*, **1992**, 31 (1), 37-
13. Larkin, D.W.; Lobban, L.L.; Mallinson, R.G.; "Production of Organic Oxygenates in the Partial Oxidation of Methane in a Silent Electric Discharge Reactor." *Ind. Eng. Chem. Res*. **2001**, 40, 1594-1601
14. Larkin, D.W.; Zhou, L.; Lobban, L.L.; Mallinson, R.G.; "Product Selectivity Control and Organic Oxygenate Pathways from Partial Oxidation of Methane in a Silent Electric Discharge Reactor." *Ind. Eng. Chem. Res*. **2001**, 40, 5496-5506
15. Liu, C.; Marafee, A.; Mallinson, R. G.; Lobban, L. L.; "Methane Conversion to Higher Hydrocarbons in a Corona Discharge over Metal Oxide Catalysts with OH Groups." *Appl. Catal. A*., **1997,** 164 (1-2) 21-33
16. Liu, C.; Mallinson, R.G.; Lobban, L.L.; "Nonoxidative Methane Conversion to Acetylene over Zeolite in a Low Temperature Plasma." *J. Catal.* **1998**, 179, 326-334
17. Marchionna, M.; Lami, M.; Anna, M.; Raspolli G.; "Synthesizing Methanol at Lower Temperature*." Chemtech* **1997**, 15, 27-31
18. Thanyachotpaiboon, K.; Chavadej, S.; Caldwell, T. A.; Lobban, L.L.; Mallinson, R. G.; "Conversion of Methane to Higher Hydrocarbons in AC Nonequilibrium Plasmas." *AIChE J.* **1998**, 44 (10), 2252-2257
19. Savinov, S. Y.; Lee, H.; Song, H. K. Na, B.-H. "Decomposition of Methane and Carbon Dioxide in a Radio-frequency Discharge." *Ind. Eng. Chem. Res*. 1999, 38 (7), 2540-2547
20. Yao, S. L.; Takemoto, T.; Ouyang, F.; Nakayama, A.; Suzuki, E.; "Selective Oxidation of Methane Using a Non-Thermal Pulsed Plasma." *Energy and Fuels* **2000**, 14 (2), 459-463
21. Yao, S.; Nakayama, A., Suzuki, E.; "Methane Conversion Using a High-Frequency Pulsed Plasma: Important Factors." *AIChE Journal* **2001**, 47 (2), 413-425
22. Zhou, L. M.; Xue, B.; Kogelschatz, U.; Eliasson, B.; "Nonequilibrium Plasma Reforming of Greenhouse Gases to Synthesis gas." *Energy & Fuels* **1998a**, 12 (6), 1191-1199
23. Zhou, L. M.; Xue, B.; Kogelschatz, U.; Eliasson, B.; "Partial Oxidation of Methane to Methanol with Oxygen of Air in a Nonequilibrium Discharge Plasma." *Plasma Chemistry and Plasma Processing* **1998b**, 18(3), 375-393
24. Huang, Aimin; Xia, Guanguang; Wang, Jinyun; Suib, Steven L.; Hayashi, Yuji; Matsumoto, Hiroshige. "CO2 Reforming of CH4 by Atmospheric Pressure ac Discharge Plasmas**."** *Journal of Catalysis*, **2000**, 189(2), 349-359
25. Sorensen, S. L.; Karawajczyk, A.; Stromholm, C.; Kirm, M.; "Dissociative Photoexcitation of CH_4 and CD_4." *Chem. Phys. Lett*., **1995**, 232, 554

RF Plasma Modification of Supported Pt Catalysts for CO_2-CH_4 Reforming

Jason Zhan[1], Praveen Boopalachandran[1], Ben W.-L. Jang[1], Jai Choi[2], Richard B. Timmons[2]

[1]Department of Chemistry, Texas A&M University-Commerce, Commerce, TX 75429-3011
[2]Department of Chemistry & Biochemistry, U. of Texas-Arlington, Arlington, TX 76019

Introduction

Numerous studies dealing with CO_2/CH_4 reforming have been recently published. Edwards and Maitra (1), in a detailed review, have suggested that further catalyst development is the major hurdle before this reforming can be widely commercialized. Literature shows that the supported Group VIII elements in their reduced forms, especially Ni, Co, Ru, Rh, Pd, Ir and Pt, are active for CO_2/CH_4 reforming. Among these metals, Ni, Pt, Ru and Rh are the most studied elements.

Many different support materials, such as SiO_2, Al_2O_3, ZrO_2, TiO_2 and mixed oxides, have been studied for CO_2/CH_4 reforming. Results suggest that supports have a strong effect on the activity and the stability of CO_2 reforming catalysts. For example, replacing γ-Al_2O_3 by single crystal MgO as support material for Ni results in low coking and high catalytic activity (2). The support materials apparently influence the growth of carbon by controlling the type of metallic clusters that are sites for carbon formation (1). The acid/base properties of the support material are also important to the activity and stability of the catalysts. Tang et al. report that the increase in base strength of catalysts decreased the coke deposition rate on both SiO_2 and Al_2O_3 supported Ni catalysts (3). Ferreira-Aparicio et al have suggested that surface hydroxyl groups are involved with the reaction mechanism (4).

Strong support-metal interactions can result in changes in catalytic activity, selectivity, and stability. For example, Ni/Al_2O_3 forms $NiAl_2O_4$ (which is inactive for CO_2 reforming with CH_4) at high temperatures. Modifiers such as La_2O_3 and CeO_2 promote the activity of alumina supported Ni catalysts for CO_2 reforming. It is reported, by Bitter et al., that the available perimeter around Pt-ZrO_2 interfaces is critical for the reforming activity in that CO_2 reduction occurs close to the metal-support boundary (5). Verykios also proposed that active carbon containing species on Rh/Al_2O_3 are in the reaction pathway of CO formation during CO_2/CH_4 reforming (6). These results confirm the importance of metal-support interactions.

Recently, non-thermal plasma based techniques for catalyst preparation have attracted significant attention (7,8). Materials with unusual and highly advantageous catalytic properties, including high metal dispersion and enhanced metal-support interaction resulting in better catalyst stability, have been achieved via the plasma route. These advances have been documented in symposia and detailed in recent reviews (9-11). For example, Zhang et al. reported plasma activation of a Ni/α-Al_2O_3 catalyst for methane conversion to synthesis gas using a radio-frequency (RF) argon plasma for the decomposition of $Ni(NO_3)_2$. The resulting catalyst exhibited improved activity and catalytic lifetime compared to material obtained using conventional high temperature methods (12). More recently, a Ni-Fe/Al_2O_3 catalyst, prepared first by glow discharge plasma treatment followed by calcination, was studied for partial oxidation of methane by Wang et al. (13). The resultant catalyst exhibited overall improved performance compared to a catalyst of identical composition prepared via calcination. In addition, the plasma treated Ni-Fe/Al_2O_3 catalyst also exhibited better resistance to carbon deposition (13).

The present study examines further the utility of plasma processing in developing improved catalysts for eventual use in CO_2/CH_4 reforming operations. Specifically, we report plasma modification effects on metal-support interactions of 1%Pt/Al_2O_3 catalysts. By substituting plasma treatment for the conventional high temperature calcination step, both higher metal dispersions and improved sintering resistance are observed with the resultant catalysts. Additionally, the distribution of CO_2 adsorption sites on the catalyst is observed to be strongly regulated by various plasma treatments.

Experimental

Catalyst Synthesis. Alumina pellets, 1/8 in., (from Alfa Aesar) with 1.14 ml/g pore volume and a 255 m^2/g surface area were crushed and screened to 20-40 mesh. The 20-40 mesh alumina particles were dried at 200°C for one hour then cooled in a dissicator to room temperature. The resultant alumina particles were then impregnated with H_2PtCl_6 solution based on the incipient wetness technique to provide 1% Pt loading. The materials were dried at 120°C for 2 hours and are designated as 1%Pt/Al_2O_3(A).
Powder aluminum hydroxide (from Aldrich) was used as the alumina precursor to prepare impregnated Pt catalysts for acid/base studies. Aluminum hydroxide and the Pt precursor were mixed in water and heated until dry. The dried sample was then calcined at 500°C in air for 3 hours and it is designated as 1%Pt/Al_2O_3(H).

Plasma Treatment. Plasma treatments were carried out in a custom-designed 360° rotating RF plasma system. The system consists of three major components: power supply, reaction chamber, and a gas delivery and pumping system. The power supply includes an ENI A-300 amplifier, Tetronix pulse generation (Model 2101), and a Wavetech function generation (Model 166). A custom designed matching network was employed to minimize the reflected power. Power wattage is measured by the combination of a Bird watt meter (Model 4412), and a Leader oscilloscope (Model LS1020). This system is operable from milli-torr to a few torrs, with a base pressure of 10 mtorr. For O_2 plasma, 150W peak power and a 10ms/10ms plasma on/off cycle was used. For H_2 plasma, 200W and 10ms/10ms on/off cycle was employed. Typically, one gram of catalyst was loaded into the plasma chamber for treatment. The times for plasma treatment ranged from 1 to 3 hours. Both O_2 and H_2 gases were UHP grade.

H_2-Chemisorption. H_2-Chemisorption tests were performed with the automatic catalyst characterization system, AMI-200 (Altamira Instruments). Approximately 70mg samples were heated in H_2, with a 5°/min ramping rate, to 450°C or 600°C before cool down in argon to 35°C. Hydrogen-chemisorption was carried out by pulsing H_2 over clean metal surfaces until saturation. The consumption of H_2 due to chemisorption is measured by TCD for metal dispersion determination.

CO_2/NH_3-TPD. Catalyst samples (~70 mg) were heated in UHP helium at 20°C/min to 500°C before cooling down to 50°C for adsorption with 10% CO_2/NH_3 in helium for an hour. CO_2/NH_3-TPD is recorded with TCD using a ramp rate of 10°C/min from 50°C to 500°C in helium.

Results and Discussion

Pt Dispersion. Pt metal dispersions of 1%Pt/Al_2O_3(A), determined by H_2-chemisorption after reduction at different temperatures, are summarized in Table 1. After hydrogen reduction at 450°C, both O_2 and H_2 plasma treated samples show higher dispersions than the plasma untreated control sample. The O_2 plasma is more effective than the H_2 plasma in promoting the dispersion with 39.5% (O_2) vs 34.1% (H_2) compared to 31.1% for the untreated sample. After 600°C reduction for 5 hours, both O_2 and H_2 plasma treated samples show much higher dispersions than the untreated sample. The Pt dispersions are 34.1%, 34.7% and 24.4% for O_2 plasma, H_2 plasma and untreated samples, respectively. These results suggest that the sintering resistance of these catalysts is improved by the plasma treatments. The relative improved resistance is even more prominent after extended reductions at 600°C. After reduction at 600°C for 12 hours, H_2 plasma treated sample shows superior sintering resistance over O_2 plasma treated and untreated samples. As shown in Table 1, no apparent decrease in Pt dispersion is detected for the H_2 plasma treated sample while metal dispersion on the O_2 plasma treated sample decreased by 22% while the untreated one decreased by 34.7%. These results demonstrate that both O_2 and H_2 plasmas are effective in promoting increased metal dispersion, with the H_2 treated materials also exhibiting improved sintering resistance.

NH_3-TPD. The NH_3-TPD results of calcined, H_2 plasma treated and O_2 plasma treated 1%Pt/Al_2O_3(H) are shown in Figure 1. Both H_2 and O_2 plasmas modify the acidic sites for NH_3 adsorption. The O_2 plasma shows a stronger effect on 1%Pt/ Al_2O_3(H) increasing strongly the surface density of weak, medium and strong sites for NH_3 adsorption. In contrast, the H_2 plasma treatment apparently results in a more selective increase in the concentration of the weakly acidic sites, relative to smaller increases in the medium and strong NH_3 adsorption sites.

CO_2-TPD. CO_2-TPD results of calcined, H_2 plasma treated and O_2 plasma treated 1%Pt/Al_2O_3(H) are listed in Figure 2. As shown in Figure 2, H_2 plasma has little effect on the population and the distribution of CO_2 adsorption sites. O_2 plasma, on the other hand, is highly effective in the generation of strong and medium CO_2 adsorption sites on 1%Pt/Al_2O_3(H). Oxygen plasmas are well known for etching ability and are used extensively for that purpose. It is likely that O_2 plasma creates vacancies which serve as new sites for CO_2 adsorption. H_2 plasma, on the other hand, is known for passivation effects (14) and is less efficient for site generation. However, after site generation by O_2 plasma, a subsequent H_2 plasma treatment alters the properties of generated sites, as shown in Figure 3. Figure 3 lists the CO_2-TPD results of samples with the 3-h O_2 plasma treatment followed by H_2 plasma treatments of 1 to 6 hours. As shown in Figure 3, one hour of H_2 plasma treatment largely reduces the strong sites generated by the 3-h O_2 plasma treatment and simultaneously increases the sites with less strength (mainly weak sites) for CO_2 adsorption. As the H_2 plasma time increases from 1 hour to 3 hours, the strong site population further decreases and, simultaneously, both weak and medium sites decrease. Further increase of the H_2 plasma treatment time to 6 hours results in further decease of the weak sites, with relatively no changes of medium sites. These results indicate that H_2 plasma is effective in reducing the strength of CO_2 adsorption sites while O_2 plasma generates CO_2 adsorption sites with medium to high strengths. Thus, it appears the combination of O_2 and H_2 plasma treatments, especially an initial O_2 plasma followed a subsequent H_2 plasma, can manipulate the population and distribution of CO_2 adsorption sites. It is anticipated that regulation of the nature and surface density of active sites should affect the activity and stability of catalysts employed in CO_2/CH_4 reforming. Present studies involve a continuation of this work and they include examination of the effect of similar plasma treatments on CH_4 adsorption site densities. The RF plasma treatment approach described offers a viable route to evaluation of the role of active surface site densities on the CO_2/CH_4 reforming process, and thus a potentially important route to synthesis of improved catalysts for this purpose.

Conclusions

Both O_2 and H_2 plasmas are effective in promoting increased metal dispersion. Additionally, H_2 plasma treatments results in catalysts having improved resistance to sintering. The CO_2-TPD study indicates that the combination of O_2 and H_2 plasma treatments, especially the O_2 plasma first followed by H_2 plasma, can manipulate the population and distribution of CO_2 adsorption sites. Further studies of these effects are currently in progress in our labs.

Acknowledgement. Authors wish to acknowledge the financial support of an Organized Research Grant and an equipment grant from the College of Arts and Sciences at TAMU-Commerce.

Table 1. Metal dispersion results of 1%Pt/Al_2O_3(A).

Catalyst	Reduction at 450°C for 2 hr	Reduction at 600°C for 5 hr	Reduction at 600°C for 12 hr
Uncalcined	31.1	24.5	20.3(-34.7%)
H_2 plasma, 1 hr	34.1	34.7	35.1(~0)
O_2 plasma, 1hr	39.5	34.1	30.8 (-22.0%)

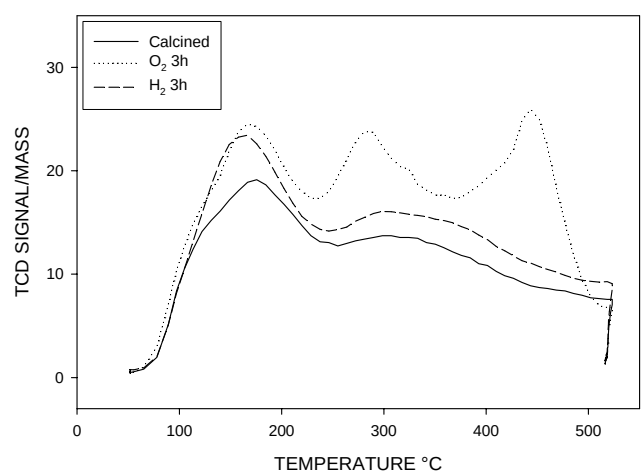

Figure 1. NH_3-TPD of calcined, O_2 treated and H_2 plasma treated 1%Pt/Al_2O_3(H).

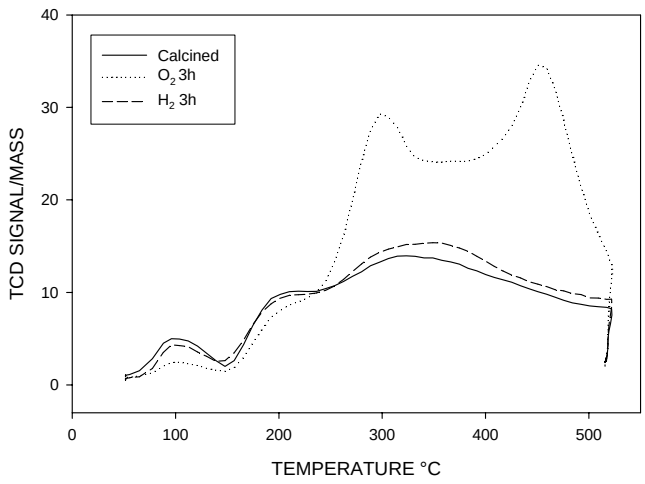

Figure 2. CO_2-TPD of calcined, O_2 treated and H_2 plasma treated 1%Pt/Al_2O_3(H).

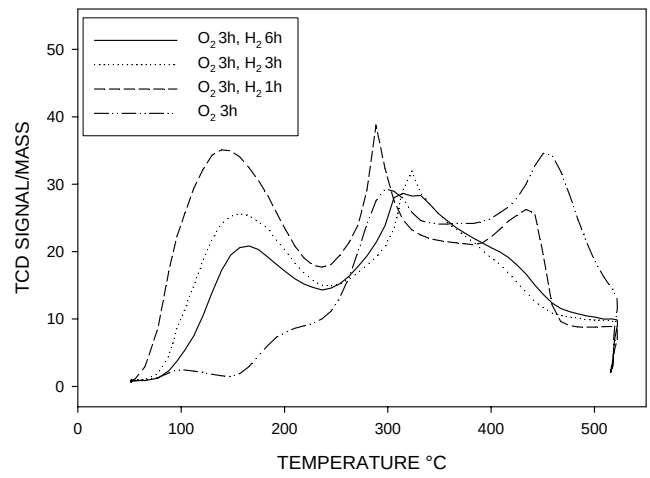

Figure 3. CO_2-TPD of calcined 1%Pt/Al_2O_3(H) with combinations of O_2 plasma and H_2 plasma treatments.

References

[1] Edwards, J.H.; Maitra, A.M. *Fuel Processing Technology* **1995**, *42*, 269.

[2] Gadalla, A.M.; Sommer, M.E. *Chemical Engineering Science* **1989**, *44(12),* 2825.

[3] Tang, S.-B.; Qiu, F.-L.; Lu., S.-J. *Catal. Today* **1995**, 24, 253.

[4] Ferreira-Aparicio, P.; Rodriguez-Ramos, I.; Anderson; Guerrero-Ruiz, A. *Appl. Catal. A*, **2000**, *202*, 183.

[5] Bitter, J.H.; Seshan, K.; Lercher, J.A. *J. Catal.* **1998**, *176*, 93.

[6] Verykios, X.E. *Appl. Catal. A*, **2003**, *255*, 101.

[7] "Catalysis and Plasma Technology" symposium organized by B.W.-L. Jang, J.G. Reynolds, M. Boutonnet and J.J. Spivey, the 220th ACS National Meeting at Washington DC in August, **2000**.

[8] "Plasma Technology and Catalysis" symposium organized by B.W.-L. Jang, C.-J. Liu and T. Hammer, the 225th ACS National Meeting at New Orleans, LA in March, **2003**.

[9] Liu, C.-J.; Vissokov, G.P.; Jang, B.W.-L. *Catal. Today*, **2002**, *72*, 173.

[10] Kizling, M.B.; Jaras, S.G. *Appl. Catal.,* A. **1996**, *147*, 1.

[11] Vissokov, G.P. *J. Material Sci.,* **1998**, *33*, 3711.

[12] Zhang, Y.; Chu, W.; Cao, W.; Luo, C.; Wen, X.; and Zhou, K. *Plasma Chem. Plasma Processing*, **2000**, *20*, 137.

[13] Wang, Jian-guo; Liu, Chang-jun; Zhang, Yue-ping; Yu, Kai-lu; Zhu, Xin-li; He, Fei *Catal. Today*, in press.

[14] Luo, B.; Ren, F.; Lee, K.P.; Pearton, S.J.; Wu, C.-S.; Kopf, R.F.; Johnson, D.; Sasserah, J. N. *Solid-State Electronics* **2001,** *45(9),* 1613.

MINIMUM ENERGY REQUIREMENT FOR METHANE STEAM REFORMING IN PLASMA-CATALYST REACTOR

Tomohiro Nozaki, Nahoko Muto, Shigeru Kado, Ken Okazaki

2-12-1 O-okayama, Meguro, Tokyo Japan 152-8552
TN: tnozaki@mech.titech.ac.jp

1. Introduction

This paper descries advanced steam reforming of methane in plasma-catalyst hybrid reactor. Synergistic effect between non-thermal plasma (DBD) and Ni-catalyst was observed at lower reaction temperature (400°C-600°C). Methane conversion exceeded far beyond equilibrium conversion, while product selectivity tended to follow equilibrium composition at given conditions: energy cost and energy efficiency were improved by 134 MJ/kg_H_2 and 69%. According to numerical simulation of streamer propagation in pure methane, production of large number of vibrationally excited methane seems to contribute significant increase in methane conversion since vibrational species promoted dissociative chemisorption on nickel surface at lower temperature. Based on those experimental and numerical evidences, minimum energy required in plasma-catalyst hybrid reactor for methane steam reforming was estimated. The energy consumption might be reduced by one-quarter of experimental result, which also means that hybrid reactor might be able to regenerate low temperature thermal energy during low temperature plasma catalysis of methane (400°C-600°C).

2. Methane steam reforming by plasma-catalyst hybrid reactor

Experimental. Authors developed Barrier-discharge Enhanced Catalytic-bed (BEC) reactor for methane steam reforming (1-5). The wire-to-tube (I.D. 6 mm) reactor packed with 3wt%Ni/SiO_2 catalyst pellets (1.2 mm and 0.9 mm) was situated in a constant temperature bath (120°C). High voltage sine wave (76 kHz) was applied between wire and external electrodes. Methane and water-vapor mixture was fed into the reactor at various mixture ratio and flow rate. Three different conditions were investigated: (1) 3wt%Ni/SiO_2, (2) plasma and 3wt%Ni/SiO_2, and (3) plasma with SiO_2. Detailed description of reactor and experimental conditions are presented elsewhere (1).

Synergistic effect between plasma and catalyst. Figure 1 (a) compares methane conversion characteristics for three different reaction systems, and (b), (c) show product selectivity. Barrier discharge is able to decompose methane at lower temperature, and 25% conversion was achieved at 200°C. However, methane conversion falls far short of equilibrium at higher temperature since methane activation by electron impact is basically independent of gas temperature (within 25°C -700°C). On the other hand, nickel catalyst does not show catalytic activity below 400°C, and methane conversion was half of the equilibrium at 600°C. If the temperature reached 700°C, methane conversion abruptly increased and attained equilibrium. We didn't observe major changes in methane conversion and product selectivity with respect to pellet diameter.

When barrier discharge and catalyst was combined, methane conversion exceeded equilibrium over the tested temperature range. The strong synergistic effect of barrier discharge and nickel catalyst was observed between 400°C and 600°C: methane conversion exceeded combined result of barrier discharge and nickel catalyst. On the other hand, catalytic reaction predominated over barrier discharge above 700°C, and synergistic effect was not observed below 200°C. Methane conversion curve for Ni/SiO_2 shifted 200°C towards lower temperature region in the presence of barrier discharge: the apparent activation temperature for nickel catalyst seemed to be lowered due to the existence of barrier discharge.

Figure 1 (b) and (c) show product selectivity obtained by BEC reactor. When the temperature was 200°C, reaction characteristics were very similar to those obtained by DBD reactor: 50% of carbonaceous products were C_2 (mainly ethane) and C_3 (propane) hydrocarbons. Product selectivity approaches equilibrium curve (dotted line) with increasing reaction temperature, and perfectly follows equilibrium curve over 600°C. It is interesting to note that methane conversion largely exceeded equilibrium value, but product selectivity follow equilibrium. This means that electron impact process plays an important role during gas phase methane activation: not only ground state methane molecule, but also excited molecule can be decomposed on nickel catalyst, leading to apparent low temperature activation of methane.

3. Radical formation by electron impact

Model. We performed numerical simulation on streamer development in pure methane for better understanding of elementary

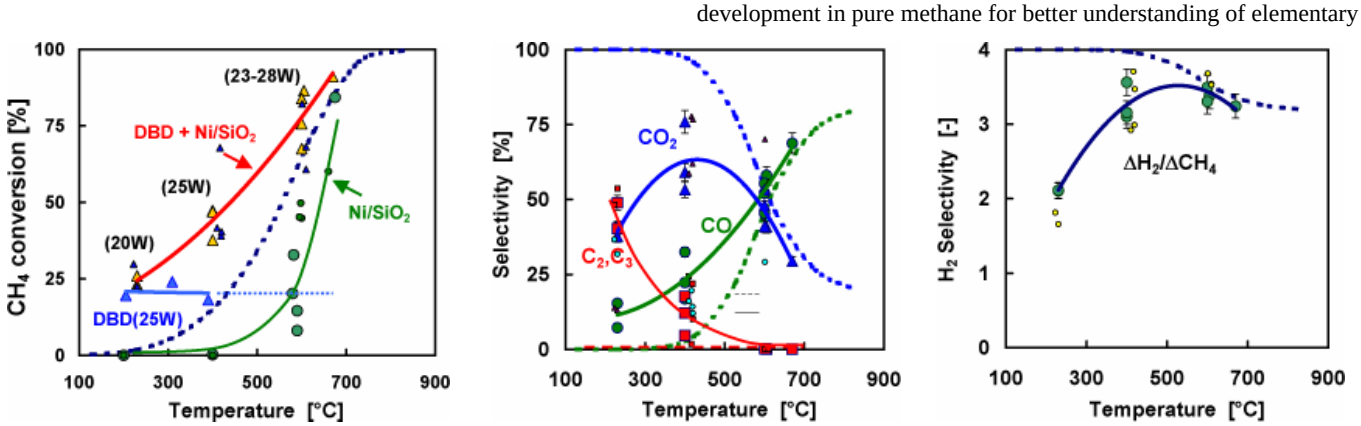

(a) Methane conversion (b) CO, CO_2, C_2 selectivity (c) H_2 selectivity

Fig. 1 Methane conversion and product selectivity at different temperatures, showing synergistic effect of plasma and Ni catalyst on methane decomposition. (--- Equilibrium). Smaller symbols represent results obtained with 0.9 mm Ni/SiO_2 pellet.

electronic and chemical processes. We assumed that streamer was one-dimensional cylinder with 100 μm radius and 2 mm long. We simulated Anode Directed Streamer (ADS) ignited from tiny plasma spot located in front of the cathode. Basic equations were continuity equations for electron, ions, and neutral species, and Poisson's equation. 38 elementary reactions including 8 inelastic collisions were simultaneously solved. During streamer development, electric energy input and radical formation efficiency was analyzed in detail. After the termination of streamer development (~5 ns), ionic and free radical chemistry that would last for 10 ms was performed with the reaction scheme proposed by Tachibana et al (6). 16 neutral species, 4 positive ions, and 2 vibrationally excited species were considered in our model. Temperature and pressure were 300 K and 760 Torr, respectively.

Energy branching to radicals. Table 1 shows energy branching and relative radical density during streamer propagation. Excitation threshold for vibrational excitation is of the order of 0.1-0.3 eV; however, 40% of input electrical energy was consumed since rate constants are 10 times larger than that for other reactions. Vibrational population was 150 times larger than electron number density. Density of CH_3 was the highest among other methane fragments due to hydrogen abstraction reaction:

$$CH_4 + H \rightarrow CH_3 + H_2 \qquad \text{(R1)}$$

(R1) is obviously independent of electronic processes. In fact, energy branching to CH_3 is the same order as other inelastic collisions. From this point, decomposition of vibrationally excited methane poses significant importance in order to improve energy cost.

4. Minimum energy consumption in BEC reactor

In general, production of vibrational species leads to significant energy loss in many plasma processes since reactivity of vibrational species is generally low. However vibrational methane seems to increase reactivity significantly in hybrid system since it increases dissociative chemisorption on Ni surface at lower temperature. We calculated energy consumption which is necessary to decompose 1 mol of methane by electron impact, and estimated minimum energy required in methane steam reforming. Main assumptions are as follows:

1. Assume stoicheometric mixture of methane and water vapor, i.e. $CH_4 : H_2O = 1 : 2$.
2. One-third of energy spent by single streamer is utilized for methane activation.
3. Ignore reactions related to H_2O and ion lose.
4. All vibrational species react on Ni catalyst to produce hydrogen.
5. Inelastic collision by electron is independent of temperature.

When external field strength is 200 Td, a single streamer spends 0.150 μJ electrical energy during propagation, and vibrationally excited methane in streamer, on space average, is populated by 1000ppm. Assume those vibrational methane is able to fully decompose if Ni catalyst is present, then 0.85×10^{-13} mol of methane is supposed to decompose to produce hydrogen, which corresponds to 0.757 μJ of heating value. That is,

$N_{methane} = 2.55 \times 10^{-9}$ mol $\times$ 0.001 $\times$ (1/3) = 8.5×10^{-13} mol
Heating value for $N_{methane}$: 890 kJ/mol $\times$ 8.5×10^{-13} [mol] = 0.757 μJ
Heating value for $N_{hydrogen}$ (= $4N_{methane}$): 0.757 $\times$ (1144/890) = 0.973 μJ
Energy absorbed by steam reforming: 0.973-0.757 = 0.216 μJ

About 70% of endothermic reaction enthalpy (0.15 μJ/0.216 μJ =0.7) must be supplied through electronic process, while 30% is from low temperature thermal energy source. This relation is schematically expressed in Fig. 2. Although current plasma-catalyst hybrid reactor spends 744 kJ of electrical energy per 1 mol of methane, it might be minimized by 176 kJ if ion current and any other loses could be neglected.

5. Concluding remarks

The result does not necessarily mean that plasma fuels processing must be combined with catalyst. The point is that plasma processing, in principle, accompanies considerable energy loses during inelastic electron impact process. Even though 50% of electrical energy is utilized by radical production, minimum energy requirement incredibly amounts to 6000 kJ per 1 mol of methane without help of vibrational methane since population of those radical is very small (3×10^{-14} mol in a single streamer). Authors strongly recommend plasma hybrid system which promotes decomposition of vibrational species or chain reactions in a given condition.

References

(1) T Nozaki, Catalysis Today, in print (2003).
(2) T Nozaki et al, Part 2, Catalysis Today, in print (2003).
(3) H H Kim et al., IEEE Trans. Ind. Appl., **35**(6) (1999) 1306-1310.
(4) A Ogata et al., IEEE Trans. Ind. Appl., **37**(4), (2001) 959-964.
(5) H Kabashima et al., IEEE Trans. Ind. Appl., **39**(2) (2003) 340-345.
(6) K Tachibana et al., J Phys D: Appl Phys **17** (1984) 1727-1742.

Table 1. Electric processes and energy branching (200 Td, 300 K-760 Torr, $N_e \approx 10^{14}$ cc^{-1}, 1 μs)

$CH_4 + e \rightarrow$	ε_i [eV]	Density	Energy branch %
$CH_4(\nu 24) + e$	0.162	$150N_e$	11.9
$CH_4(\nu 13) + e$	0.361		24.5
$CH_3 + H + e$	9.0	$10N_e$	17.0
$CH_2 + H_2 + e$	10.0		13.2
$CH + H_2 + H + e$	11.0	N_e	10.8
$C + 2H_2 + e$	12.0		9.3
$CH_4^+ + e + e$	12.6	N_e	9.4
$CH_3^+ + H + e + e$	14.3		4.0

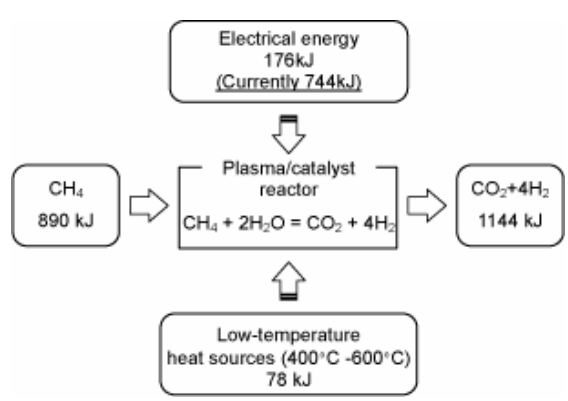

Figure 2. Schematic representation of energy balance

CONVERSION OF NATURAL GAS TO HYDROGEN AND CARBON BLACK BY PLASMA AND APPLICATION OF PLASMA BLACK

Wonihl Cho, Seung-Ho Lee, Woo-Sung Ju and Youngsoon Baek

LNG Technology Research Center, Korea Gas Corporation R&D Division, Incheon, Korea

Introduction

Natural gas is an environment-friendly resource as a clean fuel and a feed-stock for production of synthesis gas and power plant and it has provided the most abundant energy resource in the recent decade. In the future, it will play an important role as raw material for chemical supplies.

Most of natural gas conversion processing is to produce the synthesis gas in accordance with reforming of methane and then it synthesizes liquid fuels as methanol, DME (dimethyl ether) and other higher hydrocarbons (1).

Recently the direct conversion of methane, which is main component of natural gas, using various plasma technologies has widely been studied in order to obtain synthesis gas or hydrogen-rich gas without CO_2 emission (2,3). In general, there are many processes for production of hydrogen-rich gas with CO_2; steam reforming, partial oxidation, auto another reforming and carbon dioxide reforming of methane or natural gas. However, these processes cause the reduced efficiency due to the high cost of energy and device.

Therefore, the attention is being concentrated on the direct process, which makes decomposition of methane into the production hydrogen-rich gas. In this study, we will illustrate our recent research on the development of a microwave plasma-catalytic reaction process to produce hydrogen and carbon black from natural gas (4). In our plasma system of high power discharge, hydrogen and carbon black is produced by the decomposition of methane, which nearly resembles thermal cracking.

It may be assumed that decomposition of methane produces hydrogen and carbon black by the following single reaction:

$$CH_4 \quad + 75.3kJ/mol \rightarrow \quad C \quad + \quad 2H_2$$

Methane is a preferred raw material for the production of hydrogen from a hydrocarbon because of its high H to C ratio (H/C = 4), availability and low cost. Furthermore, the C produced can be sold as a co-product into the carbon black market (ink, paints, tires, batteries, etc). Several processes of carbon black production are currently used to produce furnace black, lampblack, channel black, thermal black, and acetylene black, which represent 95% of world production and consume primarily petroleum byproducts (5). In the present study, a plasma black was used as a for lithium ion battery. The carbon black is not only acts as an electron pathway by formation of a conducting network of active material but also improves electrical conductivity of interfacial electrode surface.

According to Fulcheri and Schwob (6), the total enthalpy of methane decomposition at 1600℃ is 181.8 kJ/mol, and the energy related to carbon mass varies approximately between 3 and 5 kWh per kg of carbon produced. This paper discussed the decomposition of methane by microwave plasma and possible application to CO_2-free hydrogen production.

Experimental

Figure 1 schematically shows the experimental apparatus for the microwave plasma system. In order to investigate the plasma catalytic reaction, the reactor was designed to be able to insert the catalyst pellet.

Plasma System Reactor In our experiments, microwave plasma (2.45GHz, iplas Co.) was used to produce hydrogen and carbon black from methane. The maximum microwave power is 6 kW. Plasma reactor consists of quartz tube of 6" O.D. that is connected to a microwave waveguide and resonator. It is mainly composed of (Figure 1):

-6kW magnetron power source and plasma generator (resonance)
-cold plasma reactive zone where methane is introduced
-separation bag filter of hydrogen and carbon
-water and air cooling and gas supply systems

Prior to characterization and plasma-catalytic reactivity measurements, the samples were annealed at 473K in the presence of N_2 and hydrogen gas could be used during reaction as plasma gas.

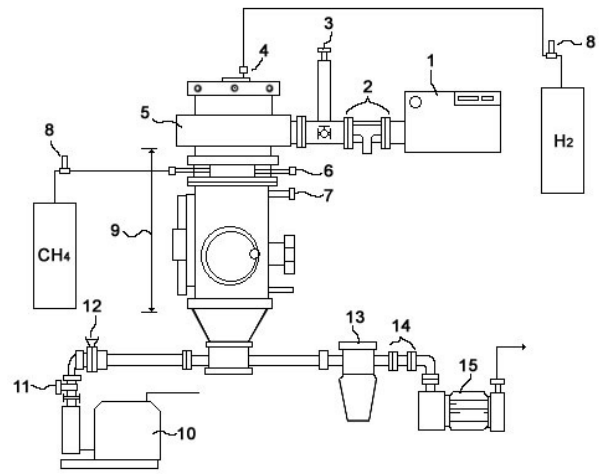

Figure 1. Experimental set for microwave plasma and catalytic reaction process; Magnetron (1), Waveguide (2), E-H tuner (3), microwave quartz tube (4), Plasma Generator (5), Jet inlet nozzle (6), Cooling line inlet, (7) MFC, (8) Microwave plasma reactor, (9) Vacuum pump, (10) Control valve for pressure (11, 12), Cyclone (13), filter (14), Mechanical diaphragm pump (15)

Thermal conductivity analyzer (Teledyne, 2000A-EU) analyzed the reaction product (hydrogen, methane and C2+ chemicals). Scanning electron microscopy (SEM) was used to observe the nano size of carbon black. SEM observation was conducted using a transmission electron microscopy operation at 15kV.

Plasma Black Characteristics The plasma black was treated at 800℃(PB800), 1300℃(PB1300) and 2100℃(PB2100) at 10^{-3} torr pressure in order to improve its conductivity. To determine the property of plasma black, surface area and porosity analysis, temperature programmed desorption (TPD), volume resistivity measurement experiments were performed.

Results and Discussion

Conversion of methane and yields of hydrogen and carbon black as a function of applied power are exhibited in Figure 2. The conversion of methane obtains up to 96% of a plasma and catalytic reaction at 3kW of applied power. Furthermore, the yield of hydrogen is from 83% to 95% at above condition. The yield with respect to carbon black and hydrogen increases with increasing applied power. When an input of 1 mole of methane was introduced, 0.6 mole of carbon and 1.62 mole of hydrogen were produced. Also, we carried out the microwave heating catalysis in order to improve

the performance of methane conversion. The microwave heating of the catalysts might have an important advantage over conventional thermal heating. The catalyst may play a role of abstracting more hydrogen from methane as improving the reactions of radicals. between catalyst surface and reactant gas. Our observation reveals that hydrogen and carbon black are produced at the rate of almost 2:1.

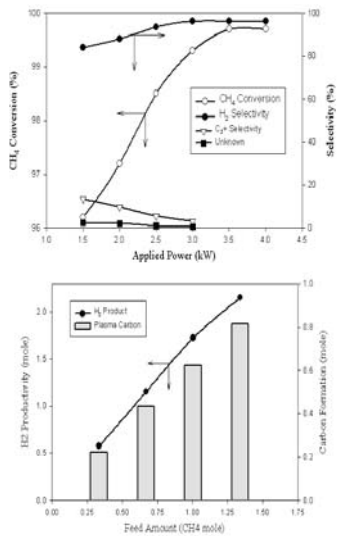

(a) (b)

Figure 2. Conversion of methane and yields of hydrogen and carbon black as a function of applied power (a) and the productivity of hydrogen and carbon as a function of feed amount (b).

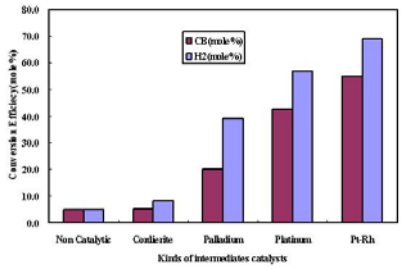

Figure 3. Comparison of various catalysts in the plasma-catalytic reaction; 200ml/min of flow rate, 30 torr of system pressure and applied plasma power is 3.0 kW.

Figure 3 illustrates the comparison of various catalysts in the plasma-catalytic reaction of methane decomposition. Among the novel metals, Pt-Rh catalyst is good for methane decomposition and production H2/carbon black. Conversion methane to hydrogen is 72% and to carbon black is 54%.

In order to determine the effects of heat treatment on surface area, surface heterogeneity, electrical resistivity and morphology of carbon black, we carried out electrochemical behavior of the carbon black as a conductor of lithium secondary battery electrode. The BET surface area of various carbon black as well as carbon black produced by plasma (plasma black) and average particle size were described as shown in Table 1. In order to compare the size, we determined the acetylene black and the plasma black by TEM as shown Figure 4.

The result of measurement of BET (213.23 m^2/g) showed that the carbon black by manufactured under a microwave plasma catalytic reaction system is very similar to classical furnace black.

Table 1. BET surface area of various carbon black

Carbon black	Surface area (BET : m2/g)	Surface area (Langmuir : m2/g)	Average particle size (nm)
Thermal black	50-120	75.7-171	40-200
Furnace black	100-ab. 200	150-300	ca. 20-30
Plasma black	213.23	293.05	20-30

Heat-treatment carbon black of produced plasma reaction has highest conductivity and highest purity. Four different samples including raw plasma black were added to $LiCoO_2$ to investigate effects of properties of plasma black as conductors on electrochemical characteristics as shown Figure 5. Plasma black conductors with low amount of surface functional groups and high electrical conductivity enhanced initial discharge capacity.

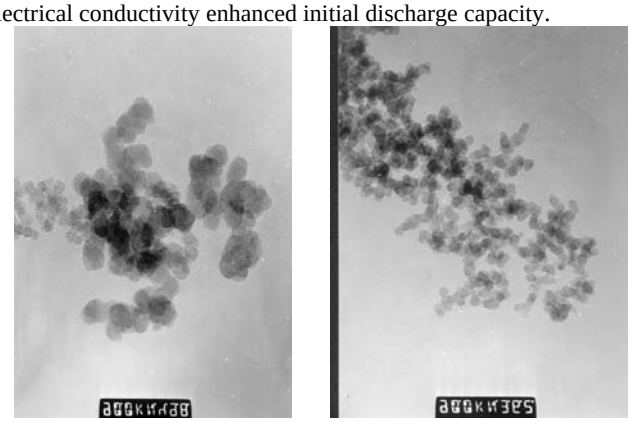

(a) (b)

Figure 4. High-resolution TEM photographs(x 900,000)of acetylene black(a) and plasma black(b)

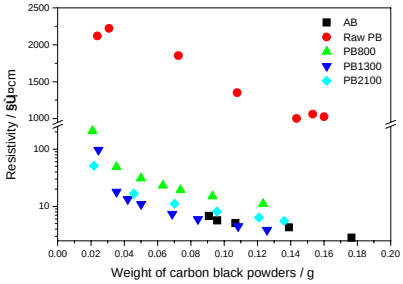

Figure 5. Volume resistivity of packed bed carbon black powders, AB(acetylene black), PB(plasma balck) and heat treated samples at 800℃, 1300℃, 2100℃.

Conclusions

An environment-friendly process for hydrogen and carbon black from natural gas was developed by microwave plasma and catalytic reaction. The high frequency discharge is an effective method to decompose methane to hydrogen and carbon black in the present catalyst. The catalytic reaction enhances the decomposition of methane to hydrogen and carbon black due to abstract more hydrogen electron from methane as activating the reaction of radicals. The plasma process appears to have better than conventional hydrogen production processes. And the performance of plasma black has almost the same electronic resistivity with that of acetylene black.

Acknowledgement Supports from MOCIE (Ministry of Commerce, Industry and Energy) and Korea Gas Corporation are very much appreciated.

References

(1) Lee, S-. H.; Cho, W; Ju, W-. S. Ju; Cho, B-. H.; Lee, Y-.C. and Baek, Y-. S. *Catalysis Today*, **2003**, in press.
(2) Liu, C.; Mallinson, R. and Lobban, L. *J. Catal*., **1998**, *179*, 326.
(3) Cho, W; Baek, Y; Moon, S.-K and Kim, Y. C. *Catalysis Today*, **2002**, *74*, 207.
(4) Cho, W; Baek, Y; Kim, Y. C. and Anpo, M. *Res. Chem. Intermed*., **2002**, *28*, 343.
(5) Gaudernack, B and Lynum, S., *Int. J. Hydrogen Energy*, **1998**, *23*, 1087.
(6) Fulchri, L. and Schwob, Y., *Int. J. Hydrogen Energy*, **1995**, *20*, 197.

Liquid phase fuel reforming at room temperature using non-thermal plasma

Yoshihiko MATSUI, Souichirou KAWAKAMI*, Kazutoshi NISHINAKAMURA*, Kazunori TAKASHIMA*, Shinji KATSURA* and Akira MIZUNO***

*Department of Ecological Engineering, Toyohashi Univ. of Tech., 1-1Tempaku-cho, Hibarigaoka, Toyohashi, Aichi, 441-8580, Japan.
**Okazaki National Research Institutes, Institute for Molecular Science, 38 Nishigo-Naka, Myodaiji, Okazaki, Aichi 444-8585, Japan.

Introduction

Hydrocarbon fuel reforming is a very important technology for a variety of applications. For example in cracking process, it is necessary to get various useful hydrocarbon gases and oils. Hydrogen manufacturing from hydrocarbon fuels is also important and could be used for many applications. These applications introduced the fuel cells used in stationary electric power production and in vehicular propulsion, such as refueling stations for hydrogen-powered vehicles. Hydrogen manufacturing is also needed for many industrial applications. Many catalytic methods were investigated for fuel reforming to get the gas phase hydrocarbons and H_2. However, almost catalysts are composed by valuable metals and materials. Then, catalytic methods require high temperature, around 300°C to 800°C to get the activation for reforming.

Recently, a novel technology of plasma and catalytic processes were studied by many researchers for hydrocarbon reforming[1-3]. In this study, a new type of plasma reactor was investigated for fuel reforming at room temperature. Positive square pulsed high voltage generates strong plasma in the oils. We expected that liquid oil change to gas and solid.

Experimental setup and procedure

Plasma reactor and a power source. Liquid phase plasma reactor consists of a plastic column vessel, metal plate as both, high voltage and ground electrodes and metal chips. Aluminum or copper plates and chips were investigated as the electrodes. Reactor was filled with 100ml of iso-octane or diesel oil. A magnetic stirrer and a stirring bar to stirr the oil and metal chips were placed into the reactor. Spark plasma, including light and heat, was generated by the high voltage in many points of contact between the metal electrodes and chips. It was a spark discharge including light and shock wave.

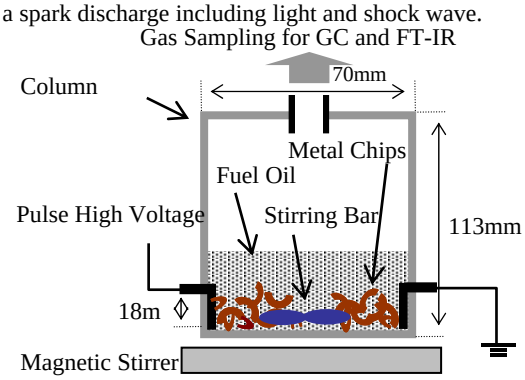

Figure1 Liquid phase plasma reaction

The plasma reactor was driven by positive pulsed square high voltage generated by a rotary spark gap (RSG) switch. The rise time of the pulsed voltage was about 40nsec, and the repetition frequency of the pulse was set at 240Hz. The high voltage applied was about 10kV peak to peak. During the rising time, spark discharges are produced and few amperes of current are flow to reform the hydrocarbon fuels.

Characterization Methods. Much gas and black powder were generated from the oil during plasma operation. H_2, N_2, O_2, CO, CO_2 and many low molecular hydrocarbons were detected and analyzed by GC-FID(Shimazu 14B) equipped with a metanizer(GL Science MT-21), GC-TCD(Shimazu 8A) and FT-IR(Bio-rad FTS3000). The black power was inspected using E-SEM and analyzed by XRD after evaporation of liquid oils.

For the E-SEM and XRD analysis, samples were prepared as follows: carbon powder deposited on the bottom of the reactor was taken, with a pipette, filtered with a quartz fiber filter (Whatman QM-A) and dried during 6h in an oven at 200°C.

Results and Discussion

The reforming process of iso-octane and diesel oil was investigated using plasma reactor at room temperature, in this study.

The generated gas compounds from iso-octane from 5 to 20 minutes are shown in Fig1 (A). Generation of gases was in the following order to H_2> CH_4 >> C_2H_4 >> CO, C_2H_6, C_3, C_4. More than 60% of H_2 gas was generated during high voltage application. Focusing the H_2 and CH_4, 86% of selectivity (H_2+CH_4) was obtained from the gas generate in this case. Fig.1 (B) shows the time elapse change of the gas compounds. The H_2 and CH_4 concentrations gradually decreased with the increment of CO_2 and CO concentrations in this case. Proportionally, the C_2H_6, C_3, and C_4 hydrocarbons gradually increased with time. On the other hand, black powder was rapidly obtained in the liquid phase when starting at high voltages, and this powder also increased with the time. After the plasma application, the temperature of the liquid iso-octane was increased at around 55°C to 65°C

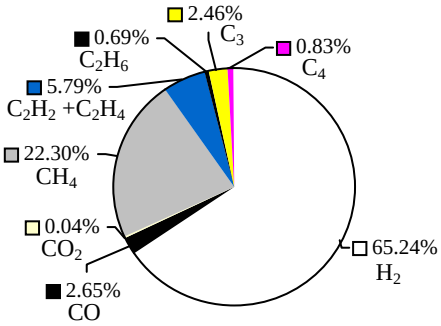

(A) Generation of gas compounds from iso-Octane (5-20min)

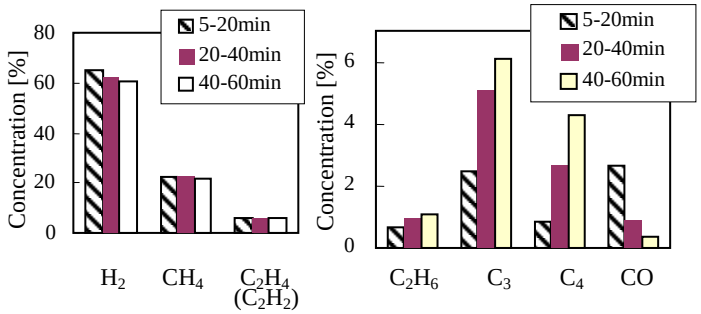

(B) Time elapse change of gas compounds from iso-octane

Figure2 Gas compounds generation and time elapse change from liquid phase iso-octane using liquid phase plasma reactor

After the experiments, the surface of both electrodes and the aluminum chips had many black points. These aluminum chips did not have such points before the experiment. Moreover almost all chips decreased their size losing their edges. E-SEM (E-SEM-2700) photograph show aluminum particles around sub-micro meter to several ten micro-meter in diameter. Aluminum and carbon were detected by X-ray micro analyzer (HORIBA EDX). On the other hand, a large aluminum peak was obtained from XRD (RINT 2500) measurements. These results indicated that iso-octane was reformed to gas and solid by high voltage application through electrodes and contact points of aluminum chips. At the same time, aluminum electrodes and chips were melted by the heat generated by the shock wave with spark discharge.

Gas generation rate using plasma reactor with aluminum chips is shown in Fig.3. The total gas flow rate included H_2, CH_4 and other hydrocarbons obtained were 17ml/min and 80ml/min for an applied power of 10W and 32W respectively. In this case, H_2 gas was flowed at 11ml/min and 52ml/min with an energy efficiency of 8.6g/kWh. Gas generated rates were proportional to the input energy in this case.

On the other hand, electrolysis has about 20g/kWh of energy efficiency to get H_2 from water[1][4]. Almost catalytic methods could get very large amount of H_2 compared with the electrolytic method and this method. However, catalysts need a very high temperature of more than 400°C to get high concentration of H_2 gas. Liquid plasma method and electrolysis also could be driven at room temperature. Moreover, plasma method has the possibility of fuel cracking control, producing the various carbon compounds and other many reactions. Focusing only in H_2 generation for industrial application, it requires large amount of H_2 generation efficiency. We must explore the catalytic reactions by combination of plasma and catalysts.

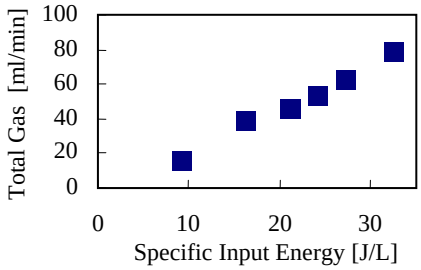

Figure3 Gas generation rate using plasma reactor with aluminum chips

Reforming of diesel oil was also investigated in this study. Fig.4 shows the gas compounds generation and the time-elapse change using the liquid phase plasma reactor. Comparing Fig.4 with Fig.2, it is clearly different the amount of N_2 and O_2 formed during the first 20 minutes as it is shown in Fig.4 (a). On the other hand, N_2 and O_2 disappeared during the next 20min as it is shown in Fig.4 (b). It can be suggested that N_2 and O_2 gas were already present into the diesel oil, and they were rapidly derived to the gas phase when plasma was applied. The amount of gases generated were in the following order: H_2> C_2H_4 >> CH_4 >> CO, C_2H_6, C_3, C_4 in the case of (b). Ethylene selectivity is very high compared with the iso-octane case.

Fig.5 shows the XRD pattern of black powder from diesel oil using three types of metal chips and electrodes. Type I using aluminum electrodes and chips, type II using copper, and type III using a mixture of aluminum (2g) and copper (9g) chips.

When using aluminum chips, aluminum peaks and Al_4C_3 peaks were obtained. Only when using copper chips, its corresponding peaks appeared. When using aluminum and copper chips mixed type their corresponding peaks appeared. However, many small peaks also appeared for the copper-aluminum mixed type, which seems to be sulfur and copper compounds (CuS_2 or Cu_8S_5). These results suggested that plasma might transform some compounds into solid crystals in the diesel oil, indicating this, a way for the removal of compounds by plasma treatment at low temperature.

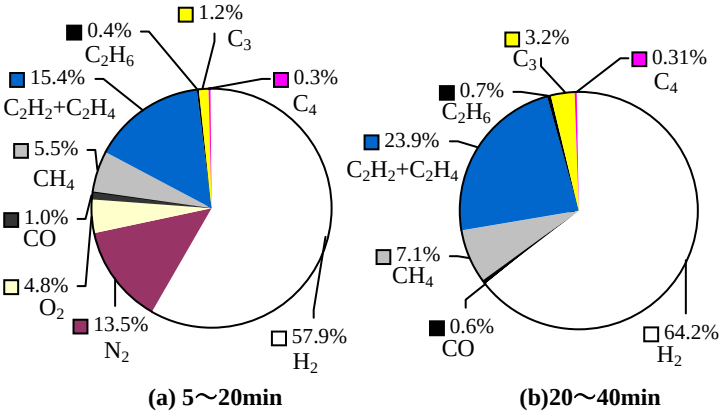

Figure4 Gas compounds generation and time elapse change from diesel oil using liquid phase plasma reactor

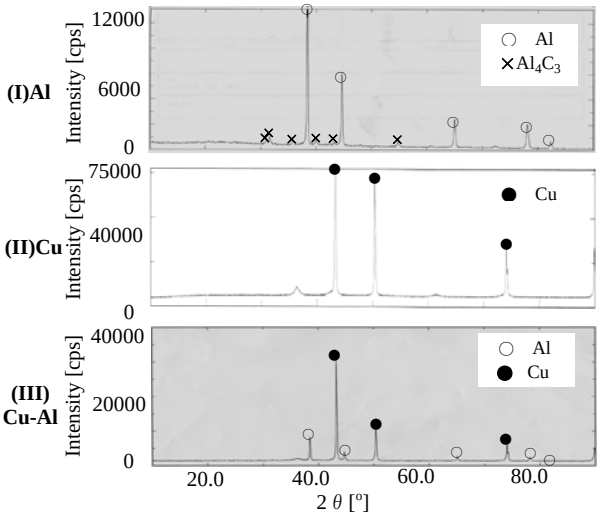

Figure5 XRD patterns of black carbon powder using aluminum, copper and aluminum-capper mixed metallic fragments

Acknowledgment

The authors wish to thank Prof. Graciela Prieto from the National University of Tucuman, Argentine, and Mr. Sigeo Nomura of DENSO Co. for valuable discussions. This work was partially supported by Japan Society for the Promotion of Science Research Fellowship for Young Scientists (8345) from the ministry of Education, Culture, Sports, Science and Technology.

References

(1) H. Kabashima, H. Einaga and S.Futamura, IEEE, Trans. Ind. Appli. Vol.39, No.2, pp. 340-345, MARCH/APRIL, **2003**

(2) M. Okumoto, A. Mizuno et al IEEE, Trans. Ind. Appli., Vol.37, No.6, pp.1618-1624, NOV/DEC, **2001**

(3) M. G. Sobacchi, A. V. Saveliev, A. A. Fridman, L. A. Kennedy, S. Ahmed, and T. Krause, Hydrogen Energy 27, pp.635-642, **2002**

(4) H. Wendt and V. Plzak, Kerntechnik 56, No.1 pp.22-28, **1991**

SURFACE ANALYSIS OF MO/HZSM5 CATALYST PREPARED BY MICROWAVE HEATING FOR NON-OXIDATIVE AROMATIZATION OF METHANE

*Suitao Qi, **Bolun Yang** and Le Lang*

Department of Chemical Engineering,
Xi'an Jiaotong University, Xi'an 710049, China

Introduction

The direct conversion of methane into hydrogen and other high-value-added products such as aromatics has recently attracted considerable attention. It makes the natural gas resource become one attractive feed which produce the aromatic hydrocarbon products following petroleum, and open up the new route to the utilization of natural gas resources.

There has been a general agreement that methane aromatization catalyzed by Mo/HZSM-5 has been recognized as a promising route for producing aromatics in an oxygen-free atmosphere [1-2]. Several factors such as the acid site density, the zeolite channel structure, and the oxidation state and location of the molybdenum species have been recognized to affect the performance of methane conversion into aromatics[3-4]. Despite prolific research activity worldwide, progress in this field has been hampered by serious catalyst deactivation, which is responsible for the decrease in conversion into useful products. As the performance of the catalyst often depends on surface status, and the surface status of catalyst is related with the preparation method, it is therefore necessary to seek better preparation method and analyze surface species for improving the catalyst performance.

Nowadays, the impregnation method is the major method for its easier operation and economical cost. The novel method i.e. microwave heating is recently applied in the oxidative coupling of methane. Seen from the results of reaction, the performance of catalysts prepared by microwave heating is better than that of catalysts prepared by impregnation, and this method is also very simple. Here a series of catalysts are prepared by microwave heating, the oxidation state and location of the Mo species were analyzed by XRD, and the surface distribution of catalysts and form of carbon deposit of catalysts after reaction were investigated by TEM.

Experimental

Catalysts preparation The zeolite [HZSM-5, (Si/Al=25), from Nankai chemical reagent factory of China] and the required amount of ammonium heptamolybdate [$(NH_4)_6Mo_7O_{24}.4H_2O$, from Jinduicheng molybdenum chemical division of china] were mechanically mixed, subsequently, the mixtures were calcined under proper power in the microwave oven for some time, and then the solid samples were pressed, crushed, and sieved to separate catalyst grain in the size range 20-35 mesh for subsequent use in aromatization reactions. In addition, the same Mo loading catalyst is prepared by impregnation so that there is the contrast between two methods on the characterization of catalyst.

Reaction testing Catalysts reaction testing has carried out at atmospheric pressure by a fixed-bed continuous flow system with a quartz reactor of 8-mm-i.d., in which 0.5 g of catalyst was loaded. It was connected to a gas feeding unit and analytical equipment. The reaction temperature 973K was controlled by a sheathed thermocouple embedded in a 35-mm-high catalyst layer. CH_4 was fed to the reactor at mass-flow controlled rates sweeping the methane hourly space velocity range of 3600mL (STP) $\cdot h^{-1} \cdot g^{-1}$. The gaseous reaction products were analyzed by means of a HP gas chromatograph equipped with a flame ionization detector (FID) connected to a PLOT-Q capillary column (30 m long and 50μm i.d.) supplied by J&W Scientific Cop.

Catalysts characterization The surface species analysis of catalysts was carried out with the RIGAKUD/MAX-2400 diffract meter by Rigaku Corporation of Japan using Cu Kα radiation at 36kV and 80mA. The spectrums were recorded over a 2θ range of 5º--60º at a scanning rate of 5º min^{-1}. The surface states of catalysts before and after reaction were carried out using JEM-200CX Transmission Electron Microscope supplied by Electric Corporation of Japan. The samples were dispersed in ethanol reagent, and then one of them was selected and suspended on the copper web for analysis under different multiple of enlargement.

Results and discussion

XRD analysis Figure 1 showed the XRD spectrum of 6% Mo based catalysts prepared by different methods, in which spectrum 1 is the XRD spectrum of catalyst prepared microwave heating, spectrum 2 is catalyst prepared by impregnation, and spectrum 3 is the used catalysts prepared by microwave heating. Seen from figure 1, all of spectrums have a majority of same peaks with the XRD spectrum of HZSM5 from corresponding literature[5], but the loading of Mo species makes the characteristic diffraction peaks lower. It reveals that the Mo species on the HZSM5 are dispersive relatively. There are three characteristic diffraction peaks of MoO_3 species when 2θ is about 30º in all spectrums; the MoO_3 species signal in spectrum1 is higher than that in spectrum 2. It's implied that most of MoO_3 species spread the outer surface of the catalyst prepared by microwave method. The main reason of this phenomenon is the difference of calcination mode of catalysts. The microwave heating have the characters of high speed and from inside to outside compared with conventional heating, as the result of it, the shift of Mo species from outer surface to inner channel of zeloite stopped and the blockage of zeolite channel could be avoided. It leaded to the higher selectivity to benzene of catalysts. Compared with specturm1, 2 and 3, all of characteristic diffraction peaks sharply decreased in spectrum 3, the new characteristic diffraction peak was found when 2θ is about 39º. That's because the carbon accumulated at a higher rate on the surface of catalyst, blocked active sites and thus caused gradual deactivation. The new characteristic diffraction peaks occurred was thought as Mo_2C species according to literature [6]. It is consist with the statement that Mo occurred as molybdenum carbide (say Mo_2C) under reaction conditions. The Mo_2C is real active species during reaction.

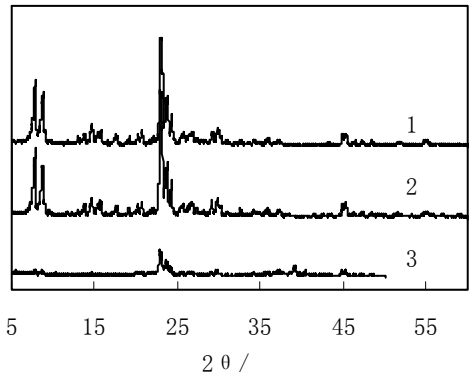

Figure 1. XRD spectrum of a series of 6% Mo/HZSM5 catalysts

TEM analysis Methane aromatization is an endothermic equilibrium-controlled reaction, and the high temperature is required to yield meaningful conversions into aromatics during the reaction. However, such severe conditions are favorable for carbon deposition.

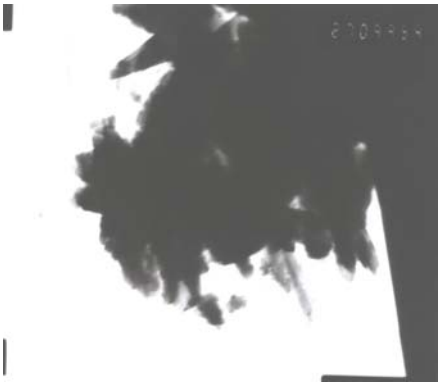

2a. 27×1000 before reaction

2b. 180×1000 before reaction

They occurred as the form of carbon nanotube during the reaction. Figure 2 showed the TEM pictures of 6%Mo/HZSM-5 catalyst before and after reaction. Figure 2a and 2b showed the surface state before reaction under different multiple. Seen from figure 2a, the massive material in the right is the HZSM-5 zeolite, and the Mo species are in the middle. The active Mo species was closely attached to carrier. Figure 2b was obtained under 180×1000 multiple. It showed the surface distribution of catalyst clearly. The size of Mo species is 20~30 nm, which is much larger than that of ZSM-5 zeolite channel (0.54nm×0.56nm), so the most of Mo species should be spread the outer surface of carrier, the active species were highly dispersed on zeolite. It is consistent with the results of XRD analysis. No fibriform material can be seen on surface of catalyst in figure2a and 2b.

Figure 2c and 2d are the TEM pictures of catalyst under different multiple. They represent the surface carbon deposit of catalysts after reaction. Seen from figure2c, the fibriform materials are winding on the surface of catalyst, which indicates that the coke occurred. In the figure 2c, the fibriform materials are the carbon deposit and the massive material is carrier. Figure 2d was pictured under 100×1000 multiple. A brunch of tubular material can be seen clearly. They are the carbon nanotubes due to carbon accumulation. One end of each carbon nanotube was attached to catalyst, the other end extended to outside. They are slim and have same size range of 10-20 nm. The similar phenomenon was reported in Ni catalysts[7]. As the Brønsted acid site is the major position of accumulating carbon deposits at high temperature, in addition to the existence of Mo species on the surface of zeolite, the carbon nanotube generate under interaction of Mo species and the Brønsted acid site, then stretch out towards outside.

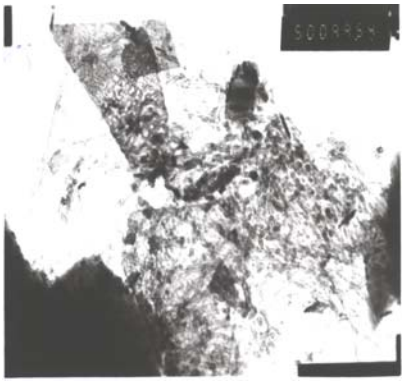

2c. 50×1000 after reaction

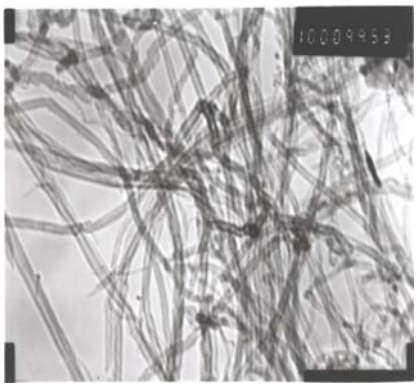

2d. 100×1000 after reaction

Figure 2. TEM picture of 6% Mo/HZSM5 catalysts before and after reaction

Conclusion

The analysis of XRD showed that the Mo species highly dispersed on outer surface of carrier for catalyst prepared by microwave heating method. Mo_2C is the real active species during the reaction, and its characteristic diffraction peaks can be found on surface of catalyst after reaction. Analysis of TEM further proved the high dispersion of Mo species. The size of Mo species is 20-30nm. The form of carbon deposit in methane aromatization is the hollowed carbon nanotube. The size of them is 10-20 nm. They grew up with the carbon accumulation.

References

1. L. Wang, L. Tao, M. Xie, X. Guo, Catal. Lett. **1993**, 21, 35-41.
2. Y. Xu, L. Lin, Appl. Catal. A, **1999**, 188, 53-67.
3. Suitao Qi, Bolun Yang, Modern Chemical Industry. **2002**, 22, 13-17.
4. V. T. T. Ha, L. V. Tiep, P. Meriaudeau, C. Naccache, J. Mol. Catal. A, **2002**, 181, 283-290.
5. Y. Shu, D. Ma, L. Xu, X. Bao, Y. Xu, Chinese J. Catal., **2002**, 23, 24-28.
6. F. Solymosi, A. Szoke, J. Cserenyi, Catal. Lett., **1996**, 39, 157-162.
7. P. Chen, P. Wang, G. Lin, B. Zhang, Q. Cai, Chem. J. Chinese University, **1995**, 16, 1783-178

Carbon Dioxide Reforming of Methane over a Novel Ni/Al_2O_3 Catalysts

*Minhua Zhang, Dang-guo Cheng, Yue-ping Zhang**

Key Laboratory of Green Chemical Technology of Ministry of Education, School of Chemical Engineering, Tianjin University, Tianjin 300072, China

Introduction

A lot of attentions have been recently paid to the CO_2 reforming of methane to syngas. A major reason for it is that this reaction can provide us a syngas with a 1/1 ratio of H_2 and CO, which is typically suitable for the synthesis of valuable oxygenated chemicals.[1] Among the catalysts developed, Al_2O_3 supported Ni catalysts were extensively investigated due to their relatively high activity and low cost. The major problem for the further practical application of these nickel catalysts is the deactivation of the catalyst, suffered from carbon deposition on the catalyst during reactions. Many investigators are working on the improvement in this nickel catalyst by using the addition of promoters,[2-5] using novel reactor configurations,[6,7] and using different supports.[3] In this work, we attempt to use a glow discharge plasma treatment following by thermal calcinations to achieve a better catalyst with higher activity at lower temperatures and better stability.

Experimental

The preparation or the plasma treatment of catalyst has been described elsewhere.[8,9] The principal procedure of the catalyst preparation includes: 1) impregnation conventionally; 2) drying; 3) glow discharge plasma treatment; and 4) calcination thermally. During the plasma treatment, we use argon glow discharge plasma to treat the catalyst. The loading amount of nickel on the alumina support is 9 wt.%. The reaction of CO_2 reforming of methane was carried out at atmospheric pressure in a 6 mm i.d quartz-tube fixed-bed reactor. A thermocouple placed in the center of the catalyst bed was used to measure the reaction temperature. The reaction temperature was maintained at 873 K, 923 K and 973 K, respectively. The reaction time is 48 h for all the temperatures. Argon was used as the dilution gas during the reaction. The ratio of the feeding gases is 1:1:2 of methane/carbon dioxide/argon. The total flow rate is 40 ml/min with a space velocity of 48000 ml/h·gcat. The reactants and products were analyzed with an online gas chromatography (Agilent 4890D) with a Porapak Q column. An ice-cold trap was set between the reactor exit and the GC sampling valve to remove the water formed during the reaction. CO_2, CH_4 conversions and H_2, CO selectivities were calculated according to the following formulas:

$$X(CH_4)\% = (FCH_{4,IN} - FCH_{4,OUT})/FCH_{4,IN} \times 100\%$$

$$X(CO_2)\% = (FCO_{2,IN} - FCO_{2,OUT})/FCO_{2,IN} \times 100\%$$

$$S(H_2)\% = FH_{2,OUT}/[2\times(FCH_{4,IN} - FCH_{4,OUT})]\times 100\%$$

$$S(CO)\% = FCO,_{OUT}/[(FCH_{4,IN} - FCH_{4,OUT}) + (FCO_{2,IN} - FCO_{2,OUT})]\times 100\%$$

$$F_i = Ci*F_{total}$$

where X, S and F are conversion, selectivity and gas flow rate, respectively. F_{total} is the total feed rate or the gas effluent flow rate. C_i is the molar fraction of component i in the feed gas or in the gaseous effluent that is detected by GC.

The morphology of the used catalysts was observed by TEM with a JEOL JEM –100CXII transmission electron microscope.

Results and Discussion

The stability test was investigated at 873K, 923K and 973K, respectively. Figure 1 and Figure 2 present the conversions of methane and carbon dioxide at different reaction temperatures. Evidently, the catalyst prepared with glow discharge plasma treatment following by calcination thermally is very stable, especially, at the reaction temperature of 923 K. At lower temperatures, the stability of the catalyst is also very well but the catalytic activity is lower. At higher temperature, however, the catalytic activity reduces slightly with the reaction time. Compared to the reported results with Ni/Al_2O_3 catalysts, [2,5] the catalyst reported in this work shows a better low temperature activity.

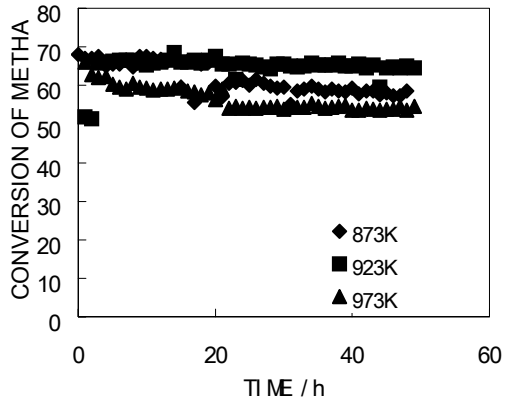

Figure 1. Catalytic activity and stability of Ni/Al_2O_3 catalyst represented by methane conversion (reaction conditions: CH_4:CO_2:Ar=1:1:2, space velocity=48000 ml/h·gcat.)

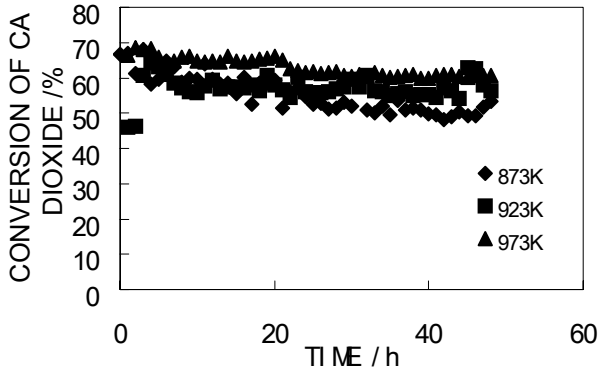

Figure 2. Catalytic activity and stability of Ni/Al_2O_3 catalyst represented by carbon dioxide conversion (reaction conditions: CH_4:CO_2:Ar=1:1:2,space velocity=48000 ml/h·gcat.)

Figure 3 and Figure 4 show the selectivities of hydrogen and carbon monoxide at reaction temperature of 873 K, 923 K and 973 K. With temperature varying from 873 K to 973 K, the selectivities of products increased significantly. Parvery *et al.*[5] have reported a promoted mixed $LaNi_xAl_{1-x}O_3$ perovskite catalysts prepared by a sol-gel related method for dry reforming of methane. Compared to their results, both of the two works achieved good activities of catalysts. However, the catalyst prepared with glow discharge plasma in this work showed a better stability. This means that the glow discharge treatment followed by calcinations thermally leads to a plasma-

enhanced catalytic stability. The TEM provides us evidence with this enhanced stability. It is well known that the carbon deposition is the main reason for the deactivation of the conventional catalysts with the dry reforming of methane. However, the glow discharge treated catalysts exhibit an excellent anti-carbon deposit performance, as shown in Figure 5. Figure 5 shows a TEM image of the used plasma-treated catalyst, taken from the stability test at 923 K. Evidently, some well defined facets of Ni can be observed. This suggests that the carbon deposition is not serious under this reaction condition over the plasma-treated catalyst. Further investigation is being conducted for a better understanding of the plasma-enhanced catalytic stability.

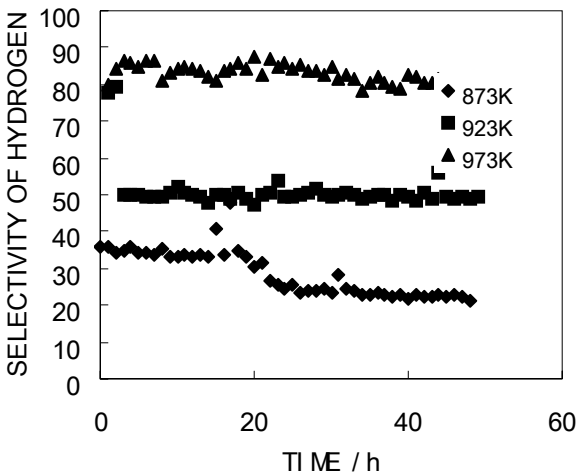

Figure 3. Catalytic activity and stability of Ni/Al_2O_3 catalyst represented by hydrogen selectivity (reaction conditions: CH_4:CO_2:Ar=1:1:2, space velocity=48000 ml/h·gcat.)

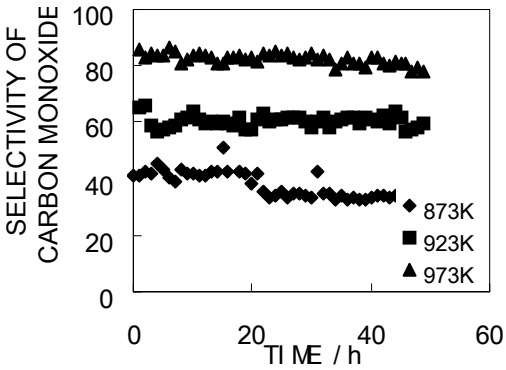

Figure 4. Catalytic activity and stability of Ni/Al_2O_3 catalyst represented by carbon monoxide selectivity (reaction conditions: CH_4:CO_2:Ar=1:1:2, space velocity=48000 ml/h·gcat.).

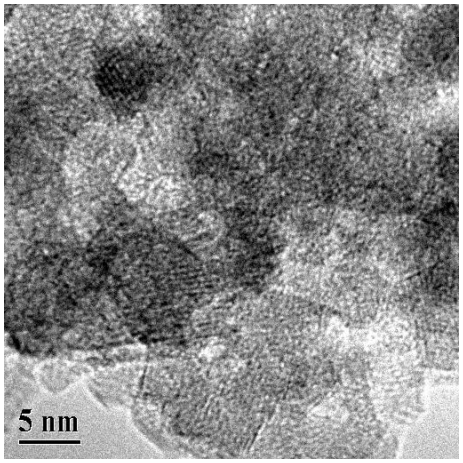

Figure 5. TEM image of used catalyst taken after the stability test (reaction conditions: reaction temperature=923 K, CH_4:CO_2:Ar=1:1:2, space velocity=48000 ml/h·gcat.)

Conclusion

The present investigation confirms that the plasma catalyst preparation described in this work can lead to a production of catalyst with a better low temperature activity and an enhanced catalytic stability for CO_2 reforming of methane. Such prepared catalyst exhibits some well-defined Ni facets after the stability test. This means that the glow discharge plasma treatment would improve the metal-support interaction significantly and induce a better anti-carbon deposit performance.

Acknowledgement

The support from the Major Research Foundation of Ministry of Education of China (under the contract of Major 0212) is very appreciated. Part of equipment and instrument used in this work was donated by ABB Switzerland Ltd., which is also very appreciated.

References

[1] Lunsford, J.H., *Catal. Today*, **2000**, *63*, 165.
[2] Lemonidou, A.; Vasalos, I.A., *Appl. Catal. A*, **2002**, *228*, 227.
[3] Chang,J.-S.;Park, S.E; Yoo,Y.W.;Park J.-N., *J. Catal*., **2000**,*195*, 1.
[4] Frusteri, F.; Arena, F., *Catal. Commun*., **2001**,*2*, 49.
[5].Parvary, M.; Jazayeri, S.H., *Catal. Commun.*, **2001**,*2*,357.
[6] Wang, L.; Murata, K.; Inaba, M., *ACS Symp. Series*, **2003**, *852*, 57.
[7] Supat, K.; Chavadej, S.; Lobban, L.L.; Mallinson, R.G., *ACS Symp. Series*, **2003**, *852*, 83.
[8] Liu, C.-J.; Vissokov, G.P.; Jang, B., *Catal. Today*, **2002**, 72, 173.
[9] Wang, J.-G.; Liu, C.-J.; Zhang, Y.P.; Zhu, X.L.; Eliasson, B., *Chem. Lett.*, **2002**, 1068.

ENERGY SAVING POTENTIAL FOR NATURAL GAS HYDRATE TRANSPORTATION

Takamichi Daimaru, Minoru Fujii[1], Akihiro Yamasaki[2], Yukio Yanagisawa

Graduate School of Frontier Sciences, The University of Tokyo
7-3-1 Hongo, Bunkyo-ku, Tokyo 1138656 Japan
[1] National Institute for Environmental Studies
16-2 Onogawa, Tsukuba 3058506 Japan
[2] National Institute of Advance Industrial Science and Technology
16-1 Onogawa, Tsukuba 3058569 Japan

Introduction

Gas hydrates are inclusion compounds in which cage-like structures formed by hydrogen-bonded water molecules can hold a variety of guest molecules such as methane, CO_2. Applications of gas hydrates have drawn attentions in the field of energy and environment. Gudmundson et al.[1] proposed a new concept of transportation of natural gas in the form of gas hydrates. Major components of natural gases, methane and ethane, could form gas hydrates. The guest molecules are densely included in the hydrates; the volume per one mole is 1/170 of that of gas at the atmospheric pressure. This is favorable for the storage and transportation of gases in the form of hydrates. In addition, gas hydrates are stable under the conditions of higher temperatures than liquefaction temperature of the natural gas components. This would lead an advantage of the transportation process in the form of gas hydrates over the conventional liquefied natural gas (LNG) transportation, because milder conditions during the transportation are required for the gas hydrates, which will reduce the cost of heat insulation to prevent the dissociation or evaporation.

The reduction of the energy consumption is of primary importance for the implementation of the NGH transport process. Several studies have been conducted on the evaluation of energy consumption by NGH transportation, and the results demonstrated that NGH transportation is advantageous both from energy consumption and cost. For more reduction of the energy consumption for the transport, several options can be considered. One option is a utilization of additives on the hydrate formation to moderate the hydrate equilibrium conditions, which could result in the reduction in the energy consumption for the hydrate formation as well as that during the transportation in a carrier ship of NGH. In this study, the effect of the additives on the energy consumption of NGH transport scenario was examined quantitatively, and energy-saving potential was estimated.

Natural Gas Hydrate Transportation Process

Overview. Natural gas produced from a gas well will be pressurized and cooled to a hydrate formation condition, and converted to natural gas hydrate (NGH) in a stirred tank type reactor. Then, the NGH will be loaded in a hydrate carrier ship, and transported to a consumption site located 6000 km distance from the gas well. In the consumption site, the NGH will be dissociated by heating with seawater flow, and natural gas will be recovered for use.

Assumptions and procedure for energy consumption estimation. The following assumptions were made for the estimation of the energy consumption for the NGH transport scenario.

1. Natural gas production rate

Production rate of natural gas from a natural gas field is assumed at 1.13×10^7 m^3/day, which corresponds to a typical natural gas well. Since the heat generation by the combustion of methane is 890 kJ/mol, the total energy potential in the natural gas produced is 4.49×10^{12} J/day. The condition of the produced natural gas is at the atmospheric pressure (0.1 MPa), and at the temperature of 288.15 K. The composition of the natural gas is assumed as pure methane, and no separation or purification process is necessary before hydrate formation.

2. Pre-treatment of natural gas for hydrate production

The feed gas is pressurized by a compressor from 0.1 MPa to a set pressure for the hydrate formation by an adiabatic compression process of ideal gas with the compression efficiency at 0.8. The cooling of the compressed gas is carried out by 2 step; 1st step: cooling to 323.15 K by using seawater flow at 298.15 K; 2nd step: brine refrigeration with the coefficient of performance, COP = 4.

3. Hydrate formation process

Hydrate production is conducted in a stirring vessel type reactor at a given condition of hydrate formation. The pressure and temperature of the hydrate formation conditions are set as operational variables for the energy consumption estimations. The base temperature is assumed at 275.15 K, and the base pressure is assumed at 6.0 MPa.

The feed water is supplied by a pump, and cooled from 298.15 K to the hydrate formation temperature by a brine refrigeration system with COP = 4. The hydration number of the methane hydrate is assumed at 5.75 corresponding fully occupied cages in type I hydrate. Hydrate formation rate is taken from experimental data conducted in a laboratory-scale experimental set-up (volume = 1.2×10^{-3} m^3, reaction rate = 3.72×10^{-4} mol/s at 25 rps stirring rate). The power consumption for the stirring process in the model reactor is given by the Nagata's equation, and results on laboratory-scale experiments can be scaled-up under the assumption that the energy consumption for stirring per unit volume of the feed mixture is constant in the scaled-up reactor. The energy consumption for the removal of the heat of formation is considered for the pumping energy of the brine, and cooling for recovery of the brine temperature.

4. Refrigeration of methane hydrate

After removal of the remained water from the natural gas hydrates, the hydrate will be refrigerated to a lower temperature in which the hydrate is stable under the atmospheric pressure. The remained water at the surface of methane hydrate is assumed at 12.0 wt. %. The energy for refrigeration is calculated for a refrigeration process with COP = 4, and specific heat and latent heat of ice are taken from the literatures.

5. Transportation of natural gas hydrate by a NGH carrier ship

The hydrate is transported in an adiabatic tank in the transportation ship. The energy consumption for the transportation is 2.8×10^{-3} kg-Fuel/t/mile (http://nippon.zaidan.info), which corresponds to 87.5 J/kg/m. The transportation distance is assumed at 6000 km.

6. Dissociation of natural gas hydrate -recovery of natural gas

The dissociation of the hydrate is carried out by heating the hydrate by a seawater flow of which the temperature is 298.15 K.

Energy Consumption Results

Energy consumption for the base case was shown in Table 1. Since the combustion energy in the natural gas is 5.195×10^3 MW, about 14 % of total energy will be consumed in the NGH transportation scenario. More than half of the energy consumption

could be attributed to the transportation process in a NGH carrier ship, and next major energy consumption sector is pretreatment of the natural gas for hydrate formation including pressurization and cooling. In the following sections, the influences of the operational parameters on the energy consumption were investigated.

Table 1. Breakdown of Energy Consumption for The Transport Scenario of NGH (base case)

Energy consumption sector	Energy consumption [MW]	Percentage [%]
Pretreatment	190.56	25.31
Hydrate formation	130.77	17.34
Refrigeration	14.18	1.88
Transportation	410.35	54.49
Dissociation	7.16	0.95
Total	753.0	100.00

1. *Effect of the hydrate formation rate*

Hydrate formation rate is a function of a variety of factors such as agitation rate, temperature, and pressure. Some additives such as surfactants can dramatically increase the hydrate formation rate. Figure 1 shows the influence of the hydrate formation rate on the energy consumption of the hydrate formation process.

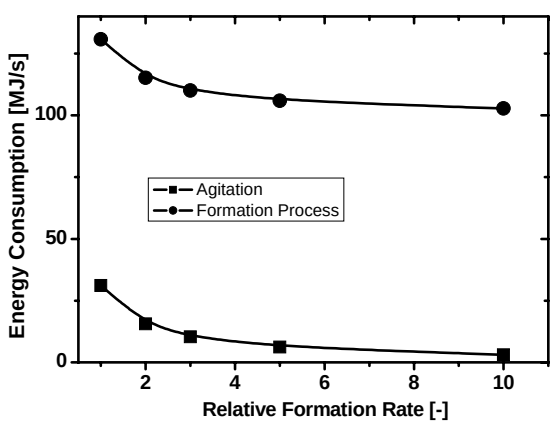

Figure 1 Effect of the hydrate formation rate on the energy consumption in the hydrate formation process

Energy consumption of the agitation for the hydrate formation gradually decreased with an increase in the hydrate formation rate. For the case with 10 times larger hydrate formation rate, the energy consumption for the agitation could be reduced at about 1/10 resulting in about 3.7 % of the total energy consumption.

2. *Effect of the temperature for the hydrate transport*

NGH is transported in a carrier ship at the temperature under which the hydrate is stable under the atmospheric condition. This temperature could be changed by using hydrate formation helper compounds. Also, some additives used for the promotion of the hydrate formation rates could be used as stabilizer of the hydrate during the transportation. Considering the above effect, effect of the hydrate transport temperature on the energy consumption is calculated and the results are shown in Figure 2. In the present cases, the energy consumption for the refrigeration is shown. Although energy consumption for the refrigeration decreased linearly with the increase in the transport temperature, but the effect of the reduction on the total energy consumption is less than 1 % at the highest temperature studied, i.e., 273.15 K.

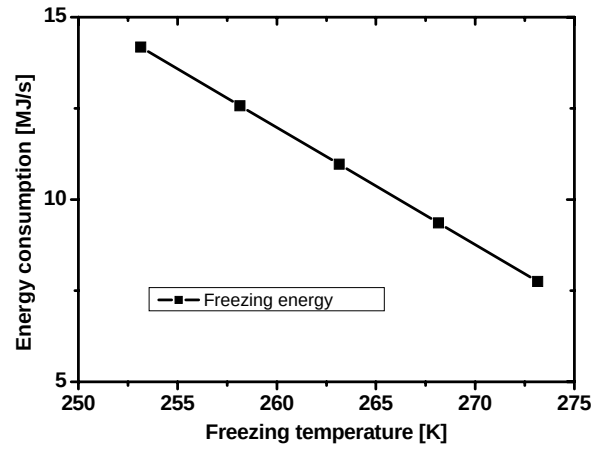

Figure 2 Effect of the hydrate transport temperature on the energy consumption for the refrigeration

3. *Effect of the hydrate formation conditions*

Hydrate formation conditions could affect the pre-treatment process of natural gas stream before the hydrate formation process. Figure 3 shows the effect of the hydrate formation pressure on the energy consumption for the pre-treatment (pressurization and cooling) process. The energy for the pre-treatment process increased with an increase in the hydrate formation pressure, and the energy saving potential for the case of 3.0 MPa is about 7.7 % compared with the base case at 6.0 MPa.

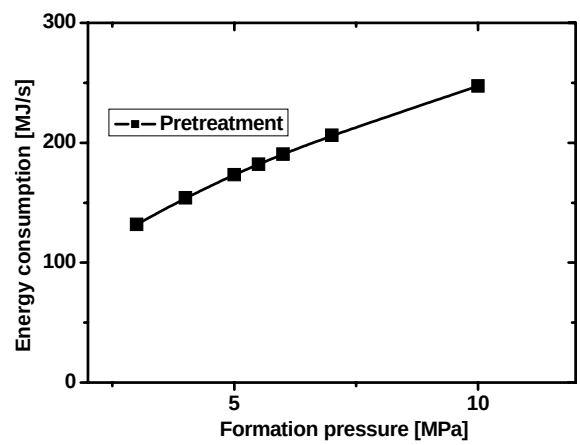

Figure 3 Effect of the hydrate formation pressure on the energy consumption for the pre-treatment process of natural gas stream before hydrate formation

References

[1] Gudmundson, J. S. et al., *Proc. 2nd International Conference on Natural Gas Hydrates* (**1996**).

Remarkable Enhancement in the Low-temperature Activity of Catalysts Prepared via Novel Plasma Reduction-Calcination Method for Methane Conversion

Yue-ping Zhang[1,2], Pei-sheng Ma[2], Kai-lu Yu[2], Xin-li Zhu[2], Dang-guo Cheng[2], Jian-guo Wang[2], Yu-heng Ben[2], Jijun Zou[2], You Han[2] and Chang-jun Liu[2]*

[1] Department of Chemistry, [2] Key Laboratory of Green Chemical Technology and School of Chemical Engineering, Tianjin University, Tianjin 300072, China

Introduction

Methane valorization is very important to the present world. Due to the stability of methane molecule, methane conversion normally requires a high temperature operation, which induces an intense energy input and poor selectivity. We previously reported a novel plasma catalyst preparation, with which the catalyst is first treated by a glow discharge and then the plasma treated catalyst is calcined thermally [1-8]. During the plasma treatment, the metal ions loaded will be normally reduced. A plasma reduction is thereby occurred. And, during calcination thermally after plasma treatment (no plasma employed in this step), the metal particles will be oxidized again. We nominated this preparation as Plasma Reduction and Calcination method (PR&C). This PR&C preparation can lead to a better catalyst preparation with a high dispersion of metal active species, a significantly enhanced acidity, an improved low-temperature activity and a remarkable promotion of catalyst stability.

The Plasma Reduction and Calcination Method

The catalyst preparation using PR&C method has been reported elsewhere [1-8]. The procedure for this method includes: the conventional incipient wetness impregnation, drying (sometimes no drying needed), plasma treatment and calcination thermally. For the plasma treatment, several plasma phenomena, e.g., glow discharge, dielectric-barrier discharge and microwave discharge, can be employed. The different discharge plasma treatment would induce a very different catalytic performance. In this work, we focus on the discussion of PR&C method with glow discharge plasma treatment. Glow discharge is a kind of plasma that is created by inserting two electrodes in a cell filled with gas at low pressure (e.g.,1 Torr). During the glow discharge plasma treatment, the catalyst was hold in a quartz container and placed in a glow discharge tube. A high-voltage (DC or AC) generator is used to generate the glow discharge plasma. The catalyst powder or particles are usually placed in the "positive column" of glow discharge where it was characterized with highly energetic electrons at low gas temperature [2]. Argon, helium, nitrogen, hydrogen, carbon dioxide and others can be applied as the plasma-forming gas for PR&C preparation. In the following discussions, we focus the use of argon as the plasma-forming gas. After the plasma treatment, the catalyst is then calcined thermally. The calcination temperature exhibits a significant effect on the dispersion and other catalytic performances that will be discussed in the future.

As mentioned above, during plasma treatment, the catalyst is normally reduced. Figure 1 exhibits XRD patterns of plasma treated catalyst samples. Evidently, some metal species present after the plasma treatment. A plasma reduction is thereby addressed. XPS analysis of the plasma treated catalysts gives us further evidences of the plasma reduction [2,8]. The reduced metal species would play an important role in the plasma-enhanced dispersion. During the oxidation of the reduced metal species in calcinations thermally, the new-formed metal oxide will induce an intense electric field. The metal species with the same electric properties will therefore exclude each other, which induces a highly dispersion [8].

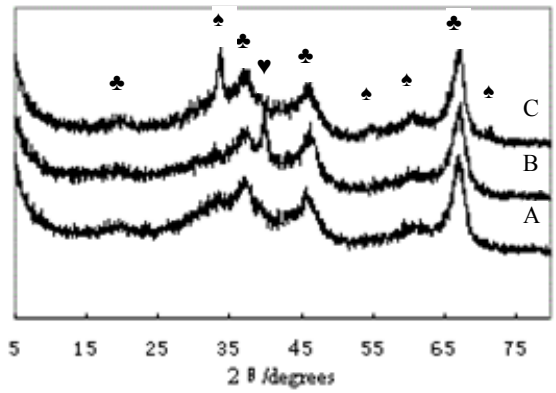

Figure 1. The XRD patterns of Pd/Al_2O_3 catalysts by different preparations
A: Pd/Al_2O_3 (conventional catalyst); B: Pd/Al_2O_3 (catalyst after plasma treatment); C: Pd/Al_2O_3 (PR&C prepared) [8]

Plasma Enhanced Acidity

The catalysts prepared with PR&C method normally show a plasma-enhanced acidity [2-4]. We used IR–pyridine adsorption to analyze the effect of plasma treatment on the Brönsted and Lewis acidities for further understanding the plasma enhanced catalytic performance. The PR&C preparation normally leads to enhanced Brönsted and Lewis acidities of the supported catalyst. For example, the amount of Brönsted acid sites of the plasma prepared Pd/HZSM-5 catalyst is 1.13 times larger than that of the catalyst prepared thermally, while the amount of Lewis acid sites is 1.21 times higher. Table 1 presents the results obtained over Pt/NaZSM-5 catalyst [4].

Table 1. Acid site amount of Pt/NaZSM-5 catalysts based on the IR-pyridine adsorption [4]

	0.1wt%Pt/Na ZSM-5 (conventinal)	0.1wt%Pt/Na ZSM-5 (PR&C prepared)	The increased amount of acidic sites
Lewis acid (mmol/g)	1.944	2.147	10%
Brönsted acid (mmol/g)	0.0332	0.0369	11%

Plasma Enhanced Dispersion

Remarkable plasma enhanced dispersion has been achieved from the PR&C preparation. Tables 2 and 3 present some comparisons of the dispersion between Pd/HZSM-5 and Pt/NaZSM-5 catalysts prepared by PR&C and by the conventional way [3,4]. The results were obtained from hydrogen chemisorption. The calculations from XRD give us further supporting evidence, as shown inTable 4 [2].

Table. 2. Results of H_2-chemisorption measurement of

catalysts	Metal dispersion/%	Active particle diameter/nm
Pd/HZSM-5 (conventional)	4.57	24.5
Pd/HZSM-5 (PR&C prepared)	5.92	18.9

2wt%Pd/HZSM-5 [12]

Table 3. The results of H_2-chemisorption for dispersion of 0.1wt%Pt/NaZSM-5 [4]

	0.1wt%Pt/NaZSM-5 (conventional)	0.1wt%Pt/NaZSM-5 (PR&C prepared)
Pt dispersion	4.2	63.3
Surface area of Pt (m^2/g sample)	0.02	0.28
Surface area of Pt (m^2/g metal)	18.5	281.8
Diameter of Pt particle (nm)	27.0	1.8

Table 4. Particle size of PdO obtained by Scherrer formula for 2wt%Pd/HZSM-5 [2]

	Full width at half maximum / rad	Particle size / nm
Pd/HZSM-5 (conventional)	0.00691	21.0
Pd/HZSM-5 (PR&C prepared)	0.00904	16.0

The Ni-supported catalysts prepared via PR&C method exhibit an unusual dispersion characteristic. From hydrogen chemisorption, XRD characterization and TEM analysis, no metal particles can be identified [5,6]. One possibility is that the metal species is ultra-highly dispersed over the support. Another possibility is that the Ni species changes to amorphous species after the plasma treatment. Further investigation is being conducted to study this unusual dispersion performance.

Plasma Enhanced Low-temperature Activity

All the catalysts prepared by PR&C method and tested by far show a better low-temperature activity, esp., those for methane conversion. We reported a comparison between methane combustion over Pd/HZSM-5 catalysts prepared via PR&C and the conventional catalyst [2,3]. Obviously, the plasma prepared catalyst presents a better low-temperature activity and an enhanced stability over the catalyst prepared conventionally. The methane conversion over the plasma treated catalyst is close to 100% at 450 °C, but it is only 50% at the same temperature over the conventional catalyst. The alumina supported Pd catalysts exhibit a similar plasma-enhanced low-temperature activity. The light-off temperature of the plasma prepared catalyst is 370 °C, 50 °C lower than that obtained from the conventional catalyst [7,8].

Ni-Fe/Al_2O_3 catalyst for partial oxidation of methane prepared via PR&C exhibits a better low-temperature activity too over the catalyst prepared thermally [5]. The conversion of methane and the selectivity of CO and H_2 over the plasma prepared catalyst are 97.44%, 100% and 100% at 875 °C, while, at the same temperature, they are 90.09%, 97.28% and 97.09%, respectively, over the catalyst prepared without plasma treatment. At the same methane conversion, the reaction temperature with the plasma prepared Ni-Fe/Al_2O_3 is at least 80 °C lower.

The PR&C prepared Pt/NaZSM-5 catalyst for NO reduction by CH_4 exhibits a highly dispersion of metal active species and a remarkable improvement in the low-temperature activity, compared to the catalyst prepared conventionally [4]. The conventional 0.1wt%Pt /NaZSM-5 catalyst shows no activity at temperatures below 673 K, while at 673 K, the NO conversion to nitrogen reaches 61.3% over the plasma prepared 0.1wt%Pt /NaZSM-5 catalyst. The initiated temperature for the plasma prepared 0.1wt%Pt/NaZSM-5 catalyst can be as low as 548 K.

Plasma Enhanced Stability

During our investigation on methane combustion, we have confirmed a remarkable enhanced stability of catalysts from the PR&C preparation. The investigations for partial oxidation of methane to syngas [5] and carbon dioxide reforming of methane [6] over Ni supported catalysts give us further evidences for the plasma-enhanced stability. The Ni supported catalyst is active for both reactions but this catalyst suffers from a deactivation, principally due to the carbon deposit. The catalysts prepared via PR&C presents a very different carbon species, compared to the conventional catalyst. A plasma-enhanced stability has also been observed over the Pt/NaZSM-5 catalyst for NO reduction by methane [4]. It is well known that the catalyst for NO reduction is structure-sensitive. The PR&C preparation would make an improvement too with the structure-sensitive catalyst.

From the present understanding, the plasma-enhanced acidity plays a very important role in the plasma-enhanced dispersion and stability, which makes the catalyst prepared via PR&C method exhibit better low-temperature activity and better thermal stability.

Conclusions

The principal procedure of the catalyst preparation using PR&C method can be summarized: 1) impregnation conventionally; 2) drying or no drying; 3) plasma treatment; and 4) calcination thermally. The PR&C preparation will normally induce a significantly plasma-enhanced acidity and dispersion, which further leads to a low-temperature catalytic activity. A remarkable improved in the stability of catalysts has also obtained with the PR&C catalyst preparation. This improved stability is achieved principally thanks to the plasma-enhanced acidity and the improvement in the interaction between metal species and the support. Further improvement in the PR&C preparation is leading to a development of a novel and practical catalyst preparation technology.

Acknowledgement. This work was supported partly by the National Natural Science Foundation (under the contract #20225618), by the Sino-PEC (under the contract #X501031), by Natural Science Foundation of Tianjin City (under the contract #023606311), by Major Foundation of Ministry of Education of China (under the contract #Major 0212) and by ABB Switzerland Ltd.

References

(1) Wang, J.G.; Liu, C.-J.; Zhang, Y.P.; Zhu, X.L.; Zou, J.J.; Yu, K.L.; Eliasson, B. *Chem. Lett.* **2002**, 1068.

(2) Liu, C.-J.; Yu, K.L.; Zhu, X.L.; Zhang, Y.P.; He, F.; Eliasson, B. Characterization of Plasma Treated Pd/HZSM-5 Catalyst for Methane Combustion, *Appl. Catal. B.* (in press).

(3) Liu, C.-J.; Yu, K.L.; Zhang, Y.P.; Zhu, X.L.; He F.; Eliasson, B. *Catal. Commu.*, **2003**, *4*, 303.

(4) Zhang, Y.P.; Ma, P.S.; Zhu, X.L.; Liu, C.-J.; Shen, Y.T. A Novel Plasma-treated Pt/NaZSM-5 Catalyst for NO reduction by methane, *Catal. Commu*. (in press).

(5) Wang, J.G.; Liu, C.-J.; Zhang, Y.P.;Yu, K.L.; Zhu, X.L.; He, F. Partial Oxidation of Methane to Syngas over Glow Discharge Plasma Treated Ni-Fe/Al_2O_3 Catalyst, *Catal. Today* (in press).

(6) Liu, C.-J.; Cheng, D.G. In: *Proc. of the 7th International Conference on Carbon Dioxide Utilization*; Lee, K.W.; Park, S.E., Eds.; Seoul, Korea, Oct. 2003, p.103.

(7) Han, S.; Yu, K.L.; He, F.; Liu, C.-J. *J. of Chem. Ind. and Eng. (China)*, **2003**, *54*, 702.

(8) Yu, K.L.; Liu, C.-J.; Zhang, Y.P.; He, F.; Zhu, X.L.; Eliasson, B. The Preparation and Characterization of Highly Dispersed PdO over Alumina for Low-temperature Combustion of Methane, *Plasma Chem. Plasma Processing* (accepted)

PLASMACHEMICAL SYNTHESIS AND REGENERATION (ACTIVATION) OF NANOSTRUCTURED CATALYSTS FOR METHANE STEAM CONVERSION

Gheorghy P. Vissokov

Institute of Electronics, Bulgarian Academy of Sciences,72, Tsarigradsko Chaussee Bulvd.,1784 Sofia, Bulgaria

There are 2D models of axially symmetric plasma-chemical reactors (PCR) for motion, heating, melting and evaporation (thermal destruction) of micron-sized particles (Ni, NiO, Al, Al_2O_3, CaO, Mg and MgO) developed. By means of these models, profiles of plasma (gas) density; temperature and rate in the plasma generator (plasmatron) in a PCR with "cold" (T_w = 500 K) and "warm" (T_w = 1500 K) walls are established, as well as the particle diameter changes along the length of the PCR; trajectory of the particles in the PCR, etc. A system of equations that describes the gas motion; equations for particle temperatures depending on the gas temperature; and equations for particle motion are used to model the hydrodynamic and heat-exchange processes in an axially symmetric PCR.

A universal programme is used and the equilibrium parameters of the multicomponent heterogeneous Ni-Al-O-Ca-Mg system are defined at for different initial ingredient compositions at a pressure of 0.1 MPa within the temperature range 1000 - 3700 K, as dependencies of the respective compound concentration in gas or condensed phase at an equilibrium system composition on the temperature are built. We set out to develop a three-dimensional model for the motion, heating, melting and vaporization (thermal destruction) of micron-size particles (Ni, NiO, Al, Al_2O_3, CaO, Mg and MgO) in an axisymmetric plasmachemical reactor (PCR), to determine the equilibrium parameters of the multicomponent heterogeneous Ni-Al-O-Ca-Mg system for the plasma-temperature range, and to carry out experimental studies concerning the plasma-chemical synthesis (PCS) of a catalyst for CH_4 steam conversion.

Considering the results of the model and thermodynamic calculations, we designed and built equipment for PCS and/or regeneration of spent catalyst for CH_4 steam conversion. Under the conditions of an electric-arc low-temperature plasma (LTP), we studied the Ni-O-Al system and performed a comprehensive physicochemical analysis of the ultradispersed product obtained.

It's the first time world-wide when the conditions of plasma-chemical synthesis and/or regeneration of CH_4 steam conversion catalysts under the conditions of electric-arc LTP are investigated, as depending on the plasma-chemical process (PCP) parameters and the plasma-chemical reactor (PCR) type (with CW- "cold walls" T_W = 500 K or WW - "warm walls" T_W = 1500 K), samples with a specific surface of to 120 m^2/g are obtained.

Plasma-chemically synthesised and/or regenerated samples have a homogenous chemical composition similar to that Girdller (USA) the conventional industrial catalyst. It is empirically established that the optimal temperature range in PCR for synthesis of maximum dispersity samples is 2000 - 3000 K. Results from investigation on plasma-chemically synthesised and/or regenerated CH_4 steam conversion catalysts dynamics and kinetics show that under LTP conditions premises for catalyst compositions formation are established. They are reduced 3 to 4 times faster than their industrial analogues.

The heightened catalytic activity of the plasma-chemically synthesised and/or regenerated natural gas reforming catalysts is determined by a whole complex of specific sample properties as follows: defective/faulty crystal structure of catalytically active phases with a lowered crystal lattice parameter; even distribution of the promoting ultra-dispersed components; high porosity, specific surface and dispersity; and appropriate chemical composition of the samples.

High specific surface of the samples, homogenous composition, high rate of active chemical surface forming by reduction, faulty crystal lattice of catalytically active phases and mostly high catalytic activity make them a potential competitor of their industrial analogues upon their probable production in catalyst shops.

NANOCRYSTALLINE GOLD CERIA-BASED WATER –GAS SHIFT CATALYSTS FOR FUEL CELL APPILICATIONS

Ivan C. Lee and Deryn Chu

AMSRD-ARL-SE-DC
US Army Research Laboratory
2800 Powder Mill Road
Adelphi, MD 20904

Abstract

New gold/ceria-based water-gas shift (WGS) catalysts have been developed to clean up carbon monoxide in hydrogen-rich gas for fuel cell applications. The new water-gas shift catalyst, $Au/MgO/Ce_{0.8}Sm_{0.15}Gd_{0.05}O_{1.9}$, is non-pyrophoric and has high WGS activities at low temperature (below 300 ^oC) with $H_2/CO=1$ in the feed. This nanocystalline(<10nm) $Au/MgO/Ce_{0.8}Sm_{0.15}Gd_{0.05}O_{1.9}$ catalyst was synthesized by carbonate co-precipitation of doped ceria followed by gold deposition with urea. The durability of Sm- and Gd-doped ceria as low-temperature water-gas shift (WGS) catalysts was tested with argon gas saturated with water at elevated catalyst temperatures. The SEM and BET surface area analysis indicated that there were no significant changes at 350°C for 10 hours. We have evaluated the WGS activities of various ceria-based catalysts containing Au, Sm, Gd, Zr and Mg at CO/H2= 1. Our results indicate that the presence of Au and MgO in $Au/MgO/Ce_{0.8}Sm_{0.15}Gd_{0.05}O_{1.9}$ plays significant roles in the WGS reaction. No methane is produced in our studies.

Introduction

An integrated system of a fuel reformer and a fuel cell can provide portable and mobile power for battery chargers and scout vehicle silent watch. Diesel fuel reformers produce hydrogen for fuel cells[1,2]. Unfortunately, the diesel fuel reformers also produce appreciable amount of CO. For instance, catalytic partial oxidation gives ~ 48 % CO (N_2-free and dry basis)[1], while steam reforming produces 16% CO (dry basis)[2]. Since the tolerable level of carbon monoxide in PEM fuel cells is about 10 ppm, one or several intermediate carbon monoxide cleanup steps (such as water-gas shift reactor) are necessary.

The primary objective is to develop a novel low temperature water-gas shift catalyst to clean up carbon monoxide in the hydrogen-rich reformate. The water-gas shift (WGS) reaction ($CO + H_2O \rightleftharpoons CO_2 + H_2$) currently attracts lots of attention because the deactivation of commercial $Cu/ZnO/Al_2O_3$ water-gas shift catalysts is a major technical barrier for fuel processors. Gold/ceria-based catalysts can potentially replace the copper-based catalysts for water-gas shift reaction[3-7]. However, there have been some controversies on the reducibility of ceria[8] and the deactivation of gold/ceria materials[9].

This paper summarizes our recent research efforts to develop metal/doped-ceria as low-temperature WGS catalysts. Our approach for water gas shift catalyst development is to prepare nanocrystalline ceria-based catalysts, and then measure the catalyst activity with realistic reformate compositions (H_2/CO ratio =1). Oxides of Mg, Zr, as well as lanthanides, such as Ce, Sm and Gd, have been chosen as support materials in this study.

Experimental

Material Synthesis. The synthesis of gold catalyst was a two-step process. First, nanocrystalline supports made of ceria doped with samarium and gadolinium were prepared by carbonate co-precipitation. Next, gold nanocrystallites were deposited onto doped ceria support materials by deposition-precipitation with urea.

Doped ceria support materials were produced via co-precipitation using ammonium carbonate and solutions of 0.15 M $Ce(NO_3)_3$, $Sm(NO_3)_3$ and $Gd(NO_3)_3$. Typically, 80 cm^3 of $Ce(NO_3)_3$, 15 cm^3 of $Sm(NO_3)_3$ and 5 cm^3 of $Gd(NO_3)_3$ were added into 100 cm^3 of 1.5 M ammonium carbonate solution. The mixture was stirred continuously and was controlled at 65°C by a circulated water bath. The resultant suspension was homogenized and then filtered under vacuum. The precipitate was washed with de-ionized water and then with ethanol. The precipitate was allowed to dry overnight. Finally, it was crushed and was calcined in a tube furnace under flowing O_2 (150 cc/min) at 600°C. The ramping and cooling rates of the furnace were controlled at 5°C/min. The calcination temperature of 600°C was chosen based on our thermogravimetric analysis (TGA) with a Perkin Elmer TGA7 analyzer.

Characterization. X-ray diffraction (XRD) measurements were performed using a Philips PW 1840 diffractometer operated at 40 kV/20 mA. Line broadening analysis of <220> and <111> planes determined the crystallite sizes of doped ceria and gold, respectively.

Multi-point BET surface areas of the water-gas shift materials were determined with a Micromeritics ASAP 2010 Automatic Physisorption Analyzer. The samples were degassed at 250°C, and the sample tubes were backfilled with nitrogen. Then 11 equilibrium data points of nitrogen adsorption were taken at relative pressures between 0.05 and 0.3.

The material morphology and elemental composition analysis were performed with a Hitachi S4500 field-emission scanning electron microscope (SEM) equipped with an energy dispersive X-ray spectrometer (EDX). The sample morphology was further examined with a JEOL 2010 transmission electron microscope (TEM) operated at 200 kV. High resolution images show lattice fringes and allow the examination of particle size and crystalline structure. The sample powder was suspended in ethanol using a ultrasonic bath and was deposited on a 400-mesh Cu grid.

Durability and Activity Tests. The durability of the gold catalyst was tested by flowing humidified argon at an elevated temperature. 75.0 sccm of argon was saturated with H_2O with a gas bubbler at 76.2^{o}C. This corresponds to about 50 sccm of water vapor. This humidified argon stream was fed into a quartz tube with 0.2 g of supported gold catalyst in a tube furnace at 350°C for 3 or 10 hours. Then the catalysts were analyzed with SEM, TEM and BET surface area measurements.

We measured the reaction rates for WGS at atmospheric pressure with powder catalysts loaded at the center of a ¼"tubular quartz reactor. All catalysts were non-pyrophoric, and they were used as prepared without activation. We injected the water into the flowing gas stream by a HPLC liquid pump and vaporized in the heated gas line before entering the reactor. The water in the reactor exit stream was collected by an ice-water condenser. The product gas stream was then analyzed on line simultaneously by two columns of an Agilent 3000 micro-gas chromatograph. A molecular sieve column (using argon as carrier gas) separates the carbon monoxide, hydrogen and methane; the Plot U column (using helium as carrier gas) separates the carbon dioxide. Then the reaction rate was calculated by the carbon dioxide product, and the rate was normalized by the weight of catalyst.

Results and Discussion

Tables 1 and 2 illustrate some characterization results of the water-gas shift materials developed in this work. Our results indicate that we can produce ceria particles of less than 10 nm by carbonate (co)precipitation (Table 1). For comparison, we also synthesized ceria by thermal deposition of solid cerium nitrate hexahydrate [$Ce(NO_3)_3*6H_2O$]. We used TGA to determine the optimum calcination temperatures of all ceria materials from their precursors. The optimum calcinations temperatures were chosen based on our TGA profiles and the subsequent XRD diffraction patterns so that ceria was produced in a fluorite crystal structure.

Table 1. Characterization of Pure Ceria, $\phi = 6/(S\rho)$; Density of Pure Ceria, $\rho = 7.184$ g/cm^3

Method	Surface Area (S), m^2/g	Spherical Diameter (ϕ), nm
Thermal Decomposition	57	14.8
Carbonate (Co)Precipitation	129	6.47
Flame Synthesis	154 [10]	5.44

The XRD and BET analysis (Table 2) show that thermal decomposition (Sample II) produces ceria with larger crystallites and a smaller surface area than carbonate precipitation (Sample I). Table 2 also indicates that doping ceria with 20% of other lanthanides, such as Sm and Gd (Samples III-V), would increase the crystallite size and would decrease the surface area. The reaction temperatures of Samples IV and V are different during co-precipitation. Higher reaction temperature in Sample V increased the surface area of the doped ceria. Supported gold catalysts (Sample VI) were prepared using Sample V as the support materials.

Table 2. Characterization of Water-Gas Shift Materials.

	Materials	Crystallite Size (XRD), nm	Multipoint BET Surface Area, m^2/g
I	Ceria (Carbonate Precipitation)	4.93 <220>	129.0
II	Ceria (Thermal Decomposition)	11.8 <220>	56.6
III	$Ce_{0.8}Sm_{0.2}O_{1.9}$	5.85 <220>	85.0
IV	$Ce_{0.8}Sm_{0.15}Gd_{0.05}O_{1.9}$	9.76 <220>	79.5
V	$Ce_{0.8}Sm_{0.15}Gd_{0.05}O_{1.9}$	8.99 <220>	94.3
VI	Au/ $Ce_{0.8}Sm_{0.15}Gd_{0.05}O_{1.9}$	6.74 (Au, <111>)	103.8

Table 3. Elemental Analysis of Doped Ceria Prepared by Carbonate Co-Precipitation.

	Atomic %		
Spot #	Ce	Sm	Gd
1	78.4	16.0	5.7
2	78.2	15.8	6.1
3	80.4	14.9	4.7
Average	79.0	15.6	5.5

Elemental analysis of the doped ceria by EDX (Table 3) shows that elemental compositions of Ce, Sm and Gd in the doped ceria matches the nominal compositions of the Ce^{3+}, Sm^{3+} and Gd^{3+} in the nitrate mixture. In other words, the atomic % of Sm and Gd in ceria can be achieved by mixing the nitrate solutions in a desired volumetric ratio. This is consistent with a recent paper in which a single lanthanide element is doped in the ceria[11]. Since the XRD pattern of the doped ceria prepared in this work matched the literature pattern of a fluorite structure[7], the composition of doped ceria was assigned to be $Ce_{0.8}Sm_{0.15}Gd_{0.05}O_{1.9}$. Our inductively coupled plasma mass spectroscopy (ICP-MS) results confirmed the materials composition of our doped ceria. And the atomic absorption spectroscopy (AAS) analysis quantified the gold content in the Au/$Ce_{0.8}Sm_{0.15}Gd_{0.05}O_{1.9}$ to be 7.1 wt %. If all the gold in solution are deposited onto the ceria, the gold content of our catalyst would be 7.6 wt %.

Some of the major limitations of commercial $Cu/ZnO/Al_2O_3$ water-gas shift catalysts include the thermal aging (or sintering) and the stability with water[12,13]. A recent study has suggested some deactivation mechanism of Au/CeO_2 catalysts[9]. Here, we investigated the effects of both thermal aging and water vapor on the Au/$Ce_{0.8}Sm_{0.15}Gd_{0.05}O_{1.9}$. These effects were examined simultaneously by flowing Ar gas (saturated with water) over the Au/$Ce_{0.8}Sm_{0.15}Gd_{0.05}O_{1.9}$ that was controlled at 350°C. Table 4 summarizes the durability test results of Au/$Ce_{0.8}Sm_{0.15}Gd_{0.05}O_{1.9}$ (Sample VII). Sample VII was prepared using Sample IV as the support material. The BET analysis showed that flowing humidified Ar over the Au/$Ce_{0.8}Sm_{0.15}Gd_{0.05}O_{1.9}$ at 350°C had insignificant effects on the BET surface area (Table 4). The change in surface area was less than 5% for 10 hours. Figure 1 illustrates a SEM image of the Sample IX. Other images of Samples IV, VII, VIII and IX with different magnifications (500x, 5000x and 50000x) are not shown here. The SEM images illustrates that there is no significant morphology difference among the samples. Particle size analysis with transmission electron microscopy (TEM) is shown in Figure 2. The TEM image suggests that the Au/$Ce_{0.8}Sm_{0.15}Gd_{0.05}O_{1.9}$ remains nanoscale after 10 hours.

Table 4. Durability of Au/ $Ce_{0.8}Sm_{0.15}Gd_{0.05}O_{1.9}$ under Humidified Argon Treatment at 350°C.

	Materials	Duration for Humidified Ar Treatment (hrs.)	Multipoint BET Surface Area, m^2/g
IV	$Ce_{0.8}Sm_{0.15}Gd_{0.05}O_{1.9}$	0	79.5
VII	Au/$Ce_{0.8}Sm_{0.15}Gd_{0.05}O_{1.9}$	0	75.1
VIII		3	78.7
IX		10	77.8

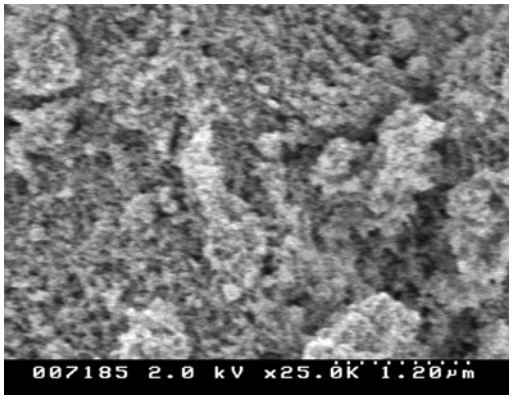

Figure 1. SEM micrograph of Au/ $Ce_{0.8}Sm_{0.15}Gd_{0.05}O_{1.9}$ treated with humidified Ar for 10 hrs at 350 ^oC (Sample IX).

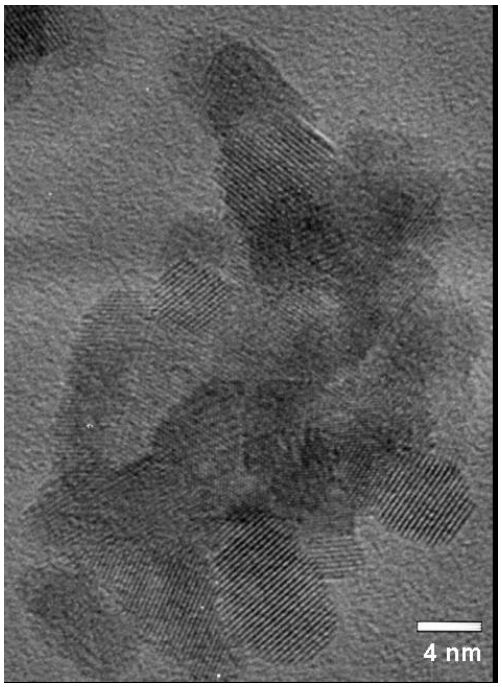

Figure 2. TEM micrograph of Au/ $Ce_{0.8}Sm_{0.15}Gd_{0.05}O_{1.9}$ treated with humidified Ar for 10 hrs at 350 ^oC (Sample IX).

The WGS reaction rates of ceria-based samples are compared in Figure 3. We kept the conversion < 10% and the pressure drop < 10 psig in all cases. Therefore, the catalyst bed temperature can be assumed to be constant, and mass transfer-free operating conditions are established for each temperature. We observe no methane in all our experiments. The BET surface area analysis results are shown in Table 5.

The activities of two Au/CeO2 catalysts are shown in Figure 3. The difference is the preparation of ceria, while the conditions of gold deposition are the same. Sample XI has a larger surface area and higher activity than Sample XII (Figure 3 and Table 5).

Although surface area and crystallite size are generally believed to be two of the major factors for catalytic activities, dopants in Ce crystal structure also play critical roles in the WGS activity. This work shows that nanocystalline (< 10 nm, XRD) Au/$Ce_{0.8}Sm_{0.15}Gd_{0.05}O_{1.9}$ with high surface area (>100 m^2/g) can be synthesized by carbonate co-precipitation followed by deposition with urea. As indicated in Tables 1 and 2, the surface area and the crystallite size are process-dependent. On the other hand, Au/$Ce_{0.8}Sm_{0.15}Gd_{0.05}O_{1.9}$ has a higher surface area than Au/$Ce_{0.75}Zr_{0.25}O_2$ (Table 4), but the latter is a better WGS catalyst below 400 ^oC (Figure3). To elucidate other important parameters, we have investigated the WGS activities of Mg-, Sm-, Gd- and Zr-doped ceria (Figure 3).

We demonstrated earlier that the additions of Sm and Gd into Ce crystal structure thermally stabilize the material, but these dopants apparently hinder the oxygen mobility (below 400°C). In contrast, Zr seems to improve both thermal resistance of the ceria and oxygen storage/release capacity. This is consistent with some general understanding of Ce-Zr materials[14,15]. On the other hand, Au/MgO has been shown to be a very active catalyst for CO oxidation[16], but there is no published result on its WGS activity. Here our results indicate that doping Mg into $Ce_{0.8}Sm_{0.15}Gd_{0.05}O_{1.9}$ structure greatly improves the WGS activity of Au/ $Ce_{0.8}Sm_{0.15}Gd_{0.05}O_{1.9}$. This implies that MgO improves the oxygen transport and the CO oxidation step in the WGS reaction. The TEM image of our Au/MgO/$Ce_{0.8}Sm_{0.15}Gd_{0.05}O_{1.9}$ is shown in Figure 4. The activity of this catalyst is shown in Figure 3.

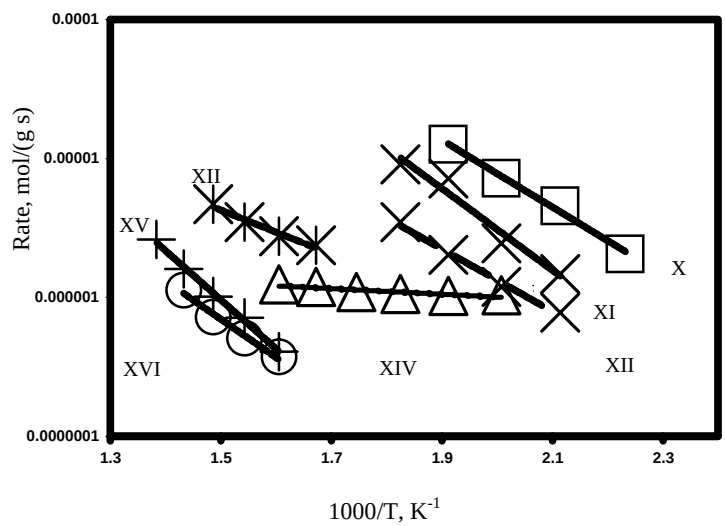

Figure 3. An Arrhenius plot for the water-gas shift rates on ceria-based catalysts (Samples X to XVI, Table 5). (Inlet gas contains 5%CO and 5%H_2, and H_2O(g)/CO=5.)

The significance of this work is that we have developed a non-pyrophoric low temperature WGS catalyst for fuel processor. Our catalysts have two important characteristics. First, all the catalysts shown in Figure 4 are not sensitive to air (i.e. non-pyrophoric) while typical Cu/ZnO/Al_2O_3 catalysts are air sensitive. In contrast to industrial plants, this feature is particularly important for objective force applications because these applications involve frequent on-off cycles during which air enters the system. Using non-pyrophoric materials often means a safer system. Another important characteristic is that our catalysts show high activities at H_2/CO ratio = 1. Previously, most of the water-gas shift catalyst research projects

focus on gas feed at very low or in absence of hydrogen. Only recently the literature[3,8] shows some interests in the water-gas shift catalyst that works at a reasonable hydrogen level (relative to CO). Note that hydrogen is the main fuel for fuel cell applications, particular polymer electrolyte membrane (PEM) fuel cells. Fuel processors break down the hydrocarbon fuel into reformate which contains smaller molecules including H_2, CO and others. Here we have tailored our catalysts at H_2/CO =1 which is realistic for catalytic partial oxidation of diesel fuel[1].

Table 5. Characterization of Ceria-Based WGS Catalysts Shown in Figure 3.

Sample	Materials	Preparation Method of Ceria or Doped Ceria	Multipoint BET Surface Area, m^2/g
X	$Au/MgO/Ce_{0.8}Sm_{0.15}Gd_{0.05}O_{1.9}$	Carbonate Coprecipitation	73.4
XI	Au/CeO_2	Carbonate Coprecipitation	94.9
XII	Au/CeO_2	Thermal Decomposition	70.1
XIII	$Au/Ce_{0.75}Zr_{0.25}O_2$	Sol gel	57.9
XIV	CeO_2	Carbonate (Co)Precipitation	129.0
XV	$Au/Ce_{0.8}Sm_{0.15}Gd_{0.05}O_{1.9}$	Carbonate Coprecipitation	103.8
XVI	$MgO/Ce_{0.8}Sm_{0.15}Gd_{0.05}O_{1.9}$	Carbonate Coprecipitation	73.8

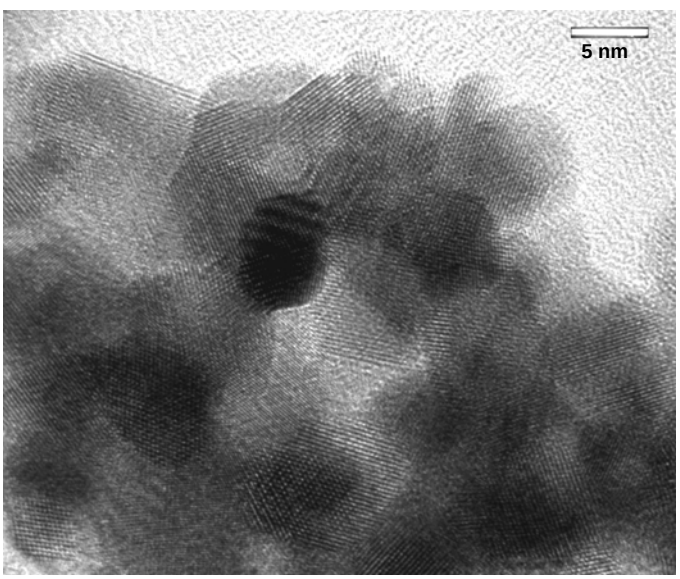

Figure 4. The TEM image of $Au/MgO/Ce_{0.8}Sm_{0.15}Gd_{0.05}O_{1.9}$.

Conclusions

We have developed a new water-gas shift catalyst, $Au/MgO/Ce_{0.8}Sm_{0.15}Gd_{0.05}O_{1.9}$, which is non-pyrophoric and has high WGS activities at low temperature (below 300 ^oC). This nanocystalline(<10nm) $Au/MgO/Ce_{0.8}Sm_{0.15}Gd_{0.05}O_{1.9}$catalyst was synthesized by carbonate co-precipitation of doped ceria followed by gold deposition with urea. The durability of Sm- and Gd-doped ceria as low-temperature water-gas shift (WGS) catalysts was tested with argon gas saturated with water at elevated catalyst temperatures. The SEM and BET surface area analysis indicated that there were no significant changes at 350°C for 10 hours. We have evaluated the WGS activities of various ceria-based catalysts containing Au, Sm, Gd, Zr and Mg. Our results indicate that the presence of Au and MgO in $Au/MgO/Ce_{0.8}Sm_{0.15}Gd_{0.05}O_{1.9}$ plays significant roles in the WGS reaction.

Acknowledgement. This work was supported by FY03 Army Research Laboratory Director's Research Initiative (DRI) Award. Dr. Mattew Ervin and Dr. Wendy Sarney have provided help in electron microscopy.

References

(1) Krummenacher, J. J., West, K. N. and Schmidt, L. D., *J. Catalysis* **2003**, *215*, 332.
(2) Cable, T. L., Brakas, A. B., Ruhl, R. C. and Milliken, C. E., US Patent 6,238,816 (**2001**).
(3) Fu Q, Saltsburg, H. and Flytzani-Stephanopoulos, M., *Science* **2003**, *301*, 935.
(4) Cameron, D., Holliday, R. and Thompson, D., *J. Power Sources* **2003**, *118*, 298.
(5) Sakurai, H., Ueda, A., Kobayashi, T. and Haruta, M., *Chem. Commun.* **1997**, *3* , 271.
(6) Andreeva, D., Idakiev, V., Tabakova, T., Ilieva, L., Falaras, P., Bourlinos, A. and Travlos, A., *Catalysis Today* **2002**, *72*, 51.
(7) Fu, Q., Weber, A. and Flytzani-Stephanopoulos, M., *Catalysis Letters* **2001**, *77*, 87.
(8) Zalc, J. M., Sokolovskii, V. and Loffler, D. G., *J. Catalysis* **2002**, *206*, 169.
(9) Kim, C. H., Bej, S. K. and Thompson, L. T., AIChE 2002 Annual Conference.
(10) Pati, R. K., Lee, I. C., Chu, D. and Ehrman, S. H., *Preprint Paper-American Chemical Society, Division of Fuel Chemistry* **2003**, *48*, 812.
(11) Li, J., Ikegami, T., Mori, T. and Wada, T., *Chem. Mater.* **2001**, *13*, 2913.
(12) Twigg, M. V. and Spencer, M. S., *Applied Catalysis A: General* **2001**, *212*, 161.
(13) Lindstrom, B. AND Pettersson L. J., *Catalysis Letters* **2001**, *74*, 27.
(14) Duprez, D. and Descorme, C. In *Catalysis by Ceria and Related Materials*; Trovarelli, A. , Ed.; Imperial College Press: London, 2002; pp. 243-280.
(15) Trovarelli, A., Boaro, M., Rocchini, E., de Leitenburg, C. and Dolcetti, G., *J. Alloys and Compounds* **2001**, *323*, 584.
(16) Guzman, J. and Gates, B. C., *J. Phys. Chem. B* **2002**, *106*, 7659.

CATALYTIC NANOCOMPOSITE MEMBRANES FOR CO ABATEMENT IN FUEL CELL APPLICATIONS

K. A. Carrado[1], R. Kizilel[2], G. Sandi[1], S. Seifert[3] C. L. Marshall[4], M. J. Castagnola[4]

[1]Chemistry, [3]Experimental Facilities and [4]Chemical Engineering Divisions, Argonne National Laboratory, 9700 S. Cass Ave., Argonne, IL, [2]Chemical & Environmental Engineering Dept., Illinois Institue of Technology, 10W 33rd Street, Chicago, IL

Abstract

Catalytic nanocomposite membranes have been prepared by ion exchanging Pt^{2+} for Li^{+} in a synthetic hectorite clay and dispersing this inorganic component within a polymeric matrix. Transparent, self-supporting membranes from the polymer-clay nanocomposite are then made. The reduction of Pt^{2+} to Pt(0) nanoclusters is accomplished by thermal reduction under H_2 at temperatures higher than 120°C. Loadings are in the 1-2 wt% Pt range. The size of the Pt(0) nanoparticles is determined by in situ small angle x-ray scattering (SAXS) techniques at about 5 nm. The membranes are stable to 200°C. These membranes have been tested for H_2 and CO diffusion at room temperature. Without any other reactive gases present (such as O_2), a selectivity enhancement from 1:1 to 3:1 H_2:CO is observed through the membrane.

Introduction

A major hurdle in current fuel cell technology is to provide a high purity gas feed. Fuel cells that operate at relatively low temperatures (<130°C) are adversely affected by even low levels of carbon monoxide (CO). Production of H_2 from the reforming of natural gas (or possibly other carbon reserves) and the water gas shift reaction yields CO as a byproduct at levels that poison fuel cell anodes. Therefore, additional technology is required to decrease the CO to ppm levels.

Current methods for removing residual CO include pressure-swing adsorption, preferential oxidation, and catalytic methanation, all of which add cost and complexity to the fuel processing system[1]. A call for basic research to supply alternative solutions to this problem was recently made, including more active catalysts for the low-temperature water-gas shift reaction, better gas stream separation processes and membranes, and CO-tolerant catalysts at the fuel cell anode[1].

We are currently testing the separation and oxidation of CO from a H_2-rich gas by taking advantage of decreased permeation of CO over H_2 through a polymer-clay nanocomposite membrane and simultaneous catalytic CO oxidation via Pt(0) nanoclusters that are supported by the membrane. It is envisioned that such a membrane would be placed just before the fuel cell.

Experimental

Synthesis of Catalytic Membranes. The preparation of synthetic lithium hectorite (SLH) clay has been reported in detail[2]. Loading of Pt(II) is accomplished by adding 0.5 gm SLH to a 2.5 mM aqueous $Pt(NH_3)_4Cl_2$ solution and stirring for 24 hr. This yields a material that has 65% of the cation exchange capacity loaded with Pt(II), or 4.65 wt% Pt. The desired amount of poly(ethylene oxide) (PEO) is then added and the mixture is stirred for another 24 hr, with a final loading of 2.4 wt% Pt on a 1:1 nanocomposite. Films were prepared by puddle-casting the slurries onto Teflon-coated glass plates and air-drying. Further drying is carried out at 120°C under an inert atmosphere for 24 hr. The ion-exchanged membrane is then reduced in a flow of H_2 at 200°C for 3 hr.

In Situ Small Angle X-Ray Scattering (SAXS). *In situ* SAXS was carried out at the Sector 12 of the Advanced Photon Source at Argonne National Laboratory. Monochromatic x-rays (18 keV) were scattered and collected on a 15 x 15 cm^2 CCD camera. The scattering intensity is corrected for adsorption and instrument background. The differential scattering cross section is expressed as a function of scattering vector *q*. The value of *q* is proportional to the inverse of the length scale ($Å^{-1}$). The instrument was operated with a sample to operator detector distances of 228 cm and 390 mm to obtain data at $0.01 < q < 0.3$ $Å^{-1}$ and at $0.08 < q < 2.3$ $Å^{-1}$, respectively. For these studies, a specially designed sample holder was used to heat the sample and collect SAXS data at the same time. Films of about 1.25 cm in diameter and 40 □m in thickness were placed in the sample holder and held using Kapton tape. The furnace temperature program was set to ramp from room temperature to 200°C at 5°C/min, and the gas flow of H_2 and He was started at room temperature.

Reactor Design. A new s.s. tubular reactor that consists of a catalytic membrane in the middle of the reactor standing perpendicular to flow was designed. Special temperature-resistant O-rings were used to eliminate the possible leaks during the experiments. The experimental setup consists of a reactor, a feed and exhaust lines, flow meters, flow controllers, temperature controller, and safety and check valves (see Figure 1). Gases are fed into the reactor tube and the temperature can ramp to 250ºC. A thermocouple is placed in the reactor bed. The reactor is housed in a clamshell furnace controlled by an Omega oven controller (TIC-500) equipped with a temperature limit switch set for 30ºC higher than the reaction temperature. From the reactor tube, the feed gas flows into saltwater/ice bath where the products and remaining reactants are condensed and collected for analysis. The collector can be isolated from the reactor and removed to collect the sample. The reactor is designed to handle a variety of conditions under continuous flow conditions at ambient pressure. The feed from the top of the reactor consists of He, CO, and H_2. The oxygen source will be air added in countercurrent flow with respect to CO and H_2.

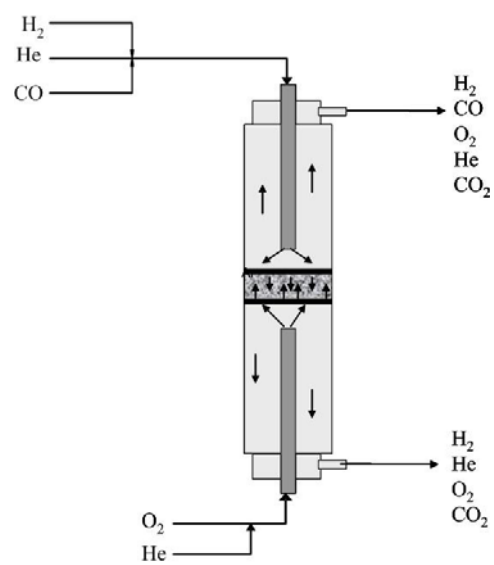

Figure 1. Reactor design for testing of catalytic membranes.

Results and Discussion

In Situ Pt Reduction. The Pt^{2+} reduction process was monitored under either H_2 (reducing) or He (inert) flow at different temperatures with simultaneous collection of SAXS data. When the

membranes were heated under a He flow (see Figure 2), the SAXS data could be fit using one structural layer throughout the entire temperature range in the so called general unified fit (GUF). This fitting procedure is explained in detail by Beaucage et al.[3]:

$$I(q) \approx G\exp\left(\frac{-q^2R_g^2}{3}\right) + B\left[\frac{\left(erf\left(qR_g/\sqrt{6}\right)\right)^3}{q}\right]^P$$

where G is the Guinier prefactor, B is the prefactor specific to the type of power-law scattering, q is the momentum transfer, Rg is radius of gyration and P is a constant. The derived Rg values are provided in Table 1.

This is a general equation developed to describe scattering functions that contain multiple length-scales (Guinier regimes) separated by power-law scattering regimes. Under He, scattering from the membrane itself should dominate. In contrast to the results with He, the addition of H_2 at relatively high temperatures produces significant changes in the SAXS results (see Figure 3). Under these conditions, the data fit better to two structural levels, with an additional length-scale added as seen in Table 1. This is presumbed to arise from the reduction of Pt^{2+} to Pt(0) nanoclusters. Harrison et al.[4] have claimed that the reduction of Pt^{2+} occurs at 140°C. Our SAXS measurements indicate that Pt(0) nanoparticles with a diameter of 4.8 nm form at 120°C. Diameters of the particles are calculated by multiplying the radius of gyration, which is derived from fitting results, by a constant of 2.6 (Rg = R/1.29 for spherical particles). The results also show that further heating to 200°C does not form significantly larger agglomerates.

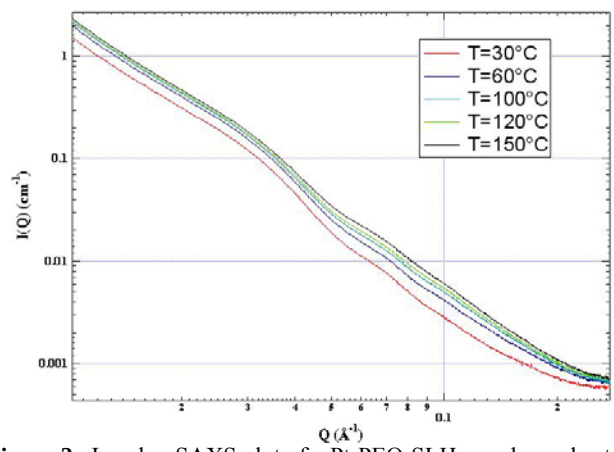

Figure 2. Log-log SAXS plot of a Pt-PEO-SLH membrane heated to various temperatures under He (non-reducing) flow.

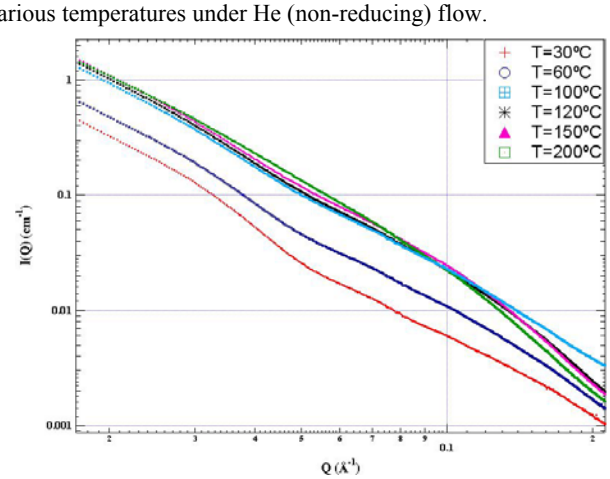

Figure 3. Log-log SAXS plot of a Pt-PEO-SLH membrane heated to various temperatures under H_2 flow.

Table 1. Microstructural Beaucage GUF SAXS Analysis of Pt-PEO-SLH Catalytic Membranes under Various Atmospheres

	Rg (Å)		
Temp. (°C)	He	H_2	
	Layer 1	Layer 1	Layer 2
30	81.3	80.0	-
60	79.2	81.9	-
100	79.7	84.2	-
120	81.7	88.1	18.6
150	82.0	90.5	19.0
200	89.8	104.7	19.8

Membrane Testing for H_2 and CO Performance. H_2-rich gas is fed from one end of the reactor. Permeation through the membrane alone acts to reduce the CO concentration. A selectivity enhancement from 1:1 H_2:CO to 3:1 H_2:CO has been observed upon feeding through a reduced Pt-PEO-SLH membrane at room temperature. Future experiments will feed a dilute CO stream with a countercurrent flow of O_2 at elevated temperature to convert the CO to CO_2 catalytically. The rates of CO oxidation depend on a variety of factors such as the thickness of the catalyst layer, its catalytic activity, and reaction conditions. Experimentation is directed toward formulating, evaluating, and establishing catalytic solids that promote the oxidation of CO with O_2.

Conclusions

A Pt-PEO-SLH catalyst is reduced successfully by thermal reduction under a H_2 flow at temperatures higher than 120°C. SAXS results (not shown) confirm that the reduction process does not degrade the polymer structure, although the polymer relaxes from crystalline to amorphous at >60°C. At low temperatures, CO poisons Pt(0). This is unfortunate because at higher temperature, Pt(0) is active for the catalytic oxidation of CO to CO_2. This is a higher temperature reaction than the operating temperature of low-temperature (<130°C) fuel cells, however, so this reaction cannot be exploited in current cells. It is envisioned that by using a membrane separator outside of the fuel cell, the possibility of catalytic oxidation of CO becomes a possibility. Low-temperature fuel cells are unstable above 135°C because of the Nafion. The PEO-membranes described here can go to 200°C. In the future, more thermally stable polymers will be tested. Pure clay could be used (laponite makes excellent films, for example), but the speculation is that the polymer helps to solvate the metal clusters and keep them from aggregating[5].

Acknowledgement. S. Landers fabricated the reactor flow cell. This work was performed under the auspices of the U.S. Department of Energy, Office of Basic Energy Sciences, Division of Chemical Sciences, Geosciences, and Biosciences under contract number W-31-109-ENG-38.

References

1. "Basic Research Needs for the Hydrogen Economy", report from the DOE-BES Workshop on Hydrogen Production, Storage, and Use, held May 13–15, 2003; available on www.sc.doe.gov/bes.
2. Carrado K. A., *Appl. Clay Sci.*, **2000**, *17*, 1.
3. Beaucage G., Schaefer D. W. *J. Non-Cryst. Solids*, **1994**, *172-174*, 797.
4. Harrison J. B., Berkheiser V., Erdos G. W., *J. Catal.*, **1988**, *112*, 126.
5. P. Balbuena, personal communication.

DEFECT-FREE ZEOLITE THIN FILM MEMBRANES FOR H_2 SEPARATION

Margaret E. Welk and Tina M. Nenoff*

Chemical and Biological Technologies, Sandia National Laboratories, P.O. Box 5800, MS 0734, Albuquerque, NM 87185-0734, USA E-mail: mewelk@sandia.gov.

Introduction

Much effort has recently been devoted to the synthesis of inorganic zeolite membranes because of their potential applications in the domains of gas separation, pervaporation, reverse osmosis or in the development of chemical sensors and catalytic membranes.[1,2,3,4,5] Specifically, development of new technologies for H_2 separation and purification has a high priority for the future of H_2 as a fuel source. H_2 is commonly produced by the reformation of hydrocarbons and must be purified. Zeolite membranes in particular combine pore size and shape selectivity with the inherent mechanical, thermal, and chemical stability necessary for long term separations.

The effective pore size distribution of the zeolite membrane, and hence its separation performance, is intrinsically governed by the choice of the zeolitic phase.[6,7,8,9] This applies when molecular size exclusion sieving is dominant and no other diffusion pathways bypass the network of well defined zeolitic channels; otherwise viscous flow through grain boundaries prevails. Zeolite membranes are typically synthesized on porous substrates by two different methods,[10]: one step hydrothermal reaction on a pristine substrate from an aluminosilicate gel or by seed-promoted hydrothermal crystallization of the zeolitic layer. In both cases, the synthesis is affected by many complex interrelated factors such as the overall composition, concentration and viscosity of the gel, its pH, the source of silica and its degree of polymerization, the temperature and duration of the reaction. The optimization of these parameters is crucial to obtaining reliably "defect free" membranes. We report here on the synthesis of ZSM-5 and silicalite membranes[11] on porous alumina disk supports, their characterization and their permeation performance for pure He, SF_6, H_2, CO_2, O_2, CH_4, N_2, and CO gases. We also show the reproducibility of the permeation values and the durability of a number of these films.

Experimental

Gases: Reagent grade pure gases were purchased from Trigas. H_2, CO_2, O_2, CH_4, N_2, CO were used to test the permeation of the membranes for reforming gases. SF_6 was used to detect defects, He was used to purge and clean the unit.

Permeation Measurements: The membrane permeations were measured at room temperature using pure gases and a constant trans-membrane pressure of 16 PSI controlled by a backpressure regulator. The membrane was sealed in a Swagelok fitting using Viton O-rings. The gas flow through the membrane was measured using an acoustic displacement flowmeter (ADM 2000 from J&W) and a digital bubble flowmeter (HP-9301). Between permeation measurements with different pure gases (SF_6, H_2, CO_2, O_2, CH_4, N_2, CO), the whole system is purged, flushed with Helium and evacuated several times. The ideal gas selectivity was calculated as the ratio of the permeances in the steady regime.

Characterization Techniques: The zeolite membranes and seeds were characterized by X-ray diffraction (Siemens D500 diffractometer, Cu Kα radiation, Bragg-Brentano geometry) and by Scanning Electron Microscopy (JEOL–6300V equipped with a Link Gem Oxford 6699 EDAX attachment).

Membrane Synthesis: In this work, the growth of both the ZSM-5 and silicalite (Al-free ZSM-5) membrane on the porous support is achieved by hydrothermal synthesis on supports seeded by rubbing.

The α-alumina substrates supplied by Inocermic Gmbh have a 1.8 micron average pore size, a diameter of 13 mm and a thickness of 1mm. The alumina substrates were first cleaned ultrasonically in acetone, rinsed in DI water and calcined at 1000°C overnight to remove any contaminants. All membranes in this work were obtained using seeded substrates to promote the nucleation and growth of the zeolite layer.

Tetra Propyl Ammonium (TPA) templated silicalite seeds were prepared under mild hydrothermal conditions in order to limit the size of the crystallites.[12] A rubbing method of seeding was used. The seeded alumina substrates were then heated in air to 500°C for 6 hours, and then cooled to room temperature using a ramp rate of 4°C /min to remove the TPA template and attach the seeds to the substrate. They were then stored in a desiccator for later use.

The difference in zeolite type resulted from the type of gel used for the hydrothermal synthesis. For ZSM-5, water, sodium hydroxide and alumina sulfate were mixed together and stirred until all reactants dissolved. Ludox-30 (Aldrich) was added to the mixture, which was then aged hours at room temperature for 24 hours. For Silicalite, the silicon source for the membrane synthesis is colloidal silica Ludox SM-30 (Aldrich); the organic template used is Tetra Propyl Ammonium (TPA) from TPAOH and TPABr (both from Alfa Aesar), and NaOH is the alkalinity source. Each gel was aged while being stirred at room temperature for 24 hours.

The seeded substrates were held vertically in the Teflon lined Parr reactor using Teflon holders to prevent sedimentation on top of the membrane. The homogenous gel was then poured in the reactor until the membrane was fully immersed. The hydrothermal syntheses were carried out in Parr reactors with a 23ml Teflon liner at temperature ranging from 160°C to 180°C and reaction time from 12 hours to 48 hours.

After synthesis, the membrane was washed with DI water and dried in air at 50°C for few hours. A permeation test on the as synthesized membrane allows the rapid assessment of its quality before the time-consuming calcination step. At that stage, a good quality membrane should be gas-tight, or impermeable, for SF_6. The SF_6 kinetic diameter of 5.5 Å is slightly larger than the pores of the ZSM-5 zeolite (minimum diameter 5.1 Å) thus SF_6 diffusion indicates the presence of membrane defects.[13] Any existing defects (partial coverage of the substrate and micro-cracks) can be repaired by a second hydrothermal synthesis step, using a shorter reaction time and more diluted starting gel. These modifications to the original synthesis parameters help to avoid the growth of columnar zeolite crystals (or agglomerates of crystals) on top of the first layer, as they would not contribute to the plugging of the existing cracks or voids in the film. The silicalite membranes presented here were gas-tight prior to calcination and did not require a second hydrothermal treatment.

Once the adequacy of the membrane was established, the organic template was removed from the membrane pores by calcination in air. The calcined membranes are whitish in color, indicating that no carbon deposit is present on the surface.

Results and Discussion

Examination of the membranes by SEM showed dense coverage of zeolite crystals on the alumina support. The thickness of the crystalline layer is on average 10 microns and was found to be fairly uniform throughout the individual membranes. Selectivity values are listed in Tables 1 and 2.

ZSM-5: For H_2 purification, ZSM-5 membranes were synthesized on flat α-alumina disks. They were tested for selectivities toward the pure gases. Much as expected, the permeation preferences were dictated by size selectivity; He > H_2 > CO_2 > O_2 > N_2 > CO > CH_4. In particular, these membranes have separations of $H_2/N_2 \geq 61$, $H_2/CO_2 \geq 80$, $H_2/CH_4 = 7$, $CH_4/CO_2 \geq 11$. Although these membranes required additional secondary growth procedures to produce a "defect-free" membrane, the flux through the films was extremely high, on the order of 10^{-6} mole/(m^2Pa sec).

Investigation of the performance and longevity at room temperature of the ZSM-5 membranes showed a moderate decrease over time. After more than 60 hours of continuous measurement under H_2, the flow rate was about 85% of its peak flow value. Calcination to 500°C restores the ZSM-5 membrane to its original flow value. Most likely, water vapor that was not removed from the permeation unit during the He gas purge and evacuation step is responsible for this decrease in flow. Longevity tests continue with other pure gases as well as industrially important mixed gases.

Silicalite: An interesting feature of these membranes is that the permeance with CO_2 is higher than that of any other gas tested, including He or H_2, even though the kinetic diameter of CO_2 is significantly larger than that of He or H_2. This property is observed reproducibly for every silicalite membrane synthesized and tested in our lab. As the CO_2 to air permeance ratios we observed are between 2 and 3, and CO permeances up to 6×10^{-7} [mole/m^2 s Pa] our membranes could at room temperature separate CO_2 from air. The higher permeance of CO_2 than other gases is likely due to surface diffusion of the CO_2 (coexisting with Knudsen diffusion), which has apparently a good affinity for this zeolite surface.

We tested a broad series of light gases (He, SF_6, H_2, CO_2, O_2, CH_4, N_2, and CO), targeting those associated with methane reforming for H_2 production. Results show that methane exhibits a behavior similar to that of CO_2, diffusing faster than both He and H_2, although the enhancement is less pronounced. CO does not seem to interact strongly with the membrane, with permeance values very similar to those of O_2 or N_2.

Investigation of the performance durability and longevity of the silicalite membranes showed that the permeance for CO_2 decreases slowly with time. After more than 60 hours of continuous measurement under CO_2, one of the membranes (22B) showed only about a third of the initial flow value. The non-interacting gases such as He do not show a marked reduction in permeance over time. Importantly, the membrane could be partially "regenerated" by heating it with a temperature profile similar to that employed for the initial calcinations. The gas flow increased to about half the starting values. This gradual decrease of permeance with time observed with pure gas will likely occur over a longer time scale when gas mixtures are used.

Conclusions

"Defect-free" ZSM-5 and Silicalite membranes have been grown reproducibly through experimentation with the synthetic parameters. The membranes are of uniform thickness and good quality as shown by the consistency and quality of the permeation data and the low SF_6 permeance. Although ZSM-5 and Silicalite are structurally identical (ZSM-5 has substituted aluminum into a portion of the silicon framework sites), they show remarkably different permeation properties. The permeation characteristics of silicalite membranes show an interesting preference for pure CO_2 gas, which flows through the silicalite membranes faster than He gas or H_2 gas, despite the larger kinetic diameter of CO_2. Modifications of the permeation unit to allow the use of gas mixtures at different temperatures are in progress and will allow the determination of the best regime for these membranes.

Acknowledgement. Sandia is a multiprogram laboratory operated by Sandia Corporation, a Lockheed Martin Company, for the United Stated Department of Energy's National Nuclear Security Administration under contract DE-AC04-94-AL85000. We thank the DOE/Hydrogen, Fuel Cells, and Infrastructure Technologies Program for continued funding.

Table 1. ZSM-5 and Silicalite Single Gas Selectivities. Trans-membrane pressure: 16 PSI.

SNL TPA/Si (Silicalite 2-sided) ≈ 10^{-6} – 10^{-7} mole/(m^2 Pa sec)

$H_2/N_2 = 1.4$	
$H_2/CH_4 = 0.625$	$CO_2/N_2 = 4.2$
$He/N_2 = 1.1$	$CO_2/O_2 = 4.9$
$CH_4/N_2 = 2.28$	$CO_2/H_2 = 3.0$
$H_2/CO_2 \geq 0.34$	$CO_2/CO = 4.2$
$H_2/O_2 = 1.7$	$CO_2/CH_4 = 1.8$
$CH_4/CO_2 = 0.54$	
$H_2/CO = 1.43$	

SNL Na/Al/Si (ZSM-5 2-sided) Knudsen Selectivity Lit. (values for Al/Si) ≈ 10^{-6}mole/(m^2 Pa sec) ≈ 10^{-7}-10^{-10} mole/(m^2Pa•s)

$H_2/N_2 \geq 61$	$H_2/N_2 = 3.73$	$H_2/N_2 = 3.91$
$H_2/CH_4 = 7$	$N_2/CO_2 = 1.00$	$N_2/CO_2 = 0.625$
$He/N_2 \geq 7$	$He/N_2 = 2.64$	$H_2/N_2 = 100$; 150°C
$CH_4/N_2 \geq 1.4$	$CH_4/N_2 = 1.32$	10^{-10} perm.
$H_2/CO_2 \geq 80$		
$H_2/O_2 \geq 11$		
$CH_4/CO_2 \geq 11$		

Table 2. Silicalite Single Gas Permeance (10^{-7} mole/ m^2 s Pa). Trans-membrane pressure: 16 PSI.

Gas / (Kinetic ∅ (Å)) Membrane	He (2.6)	SF_6 (5.5)	H_2 (2.8)	CO_2 (3.3)	O_2 (3.5)	CH_4 (3.8)	N_2 (3.6)	CO (3.7)
18A	1.8	<0.05	2.4	2.9	1.4	-	-	1.6
21A	1.2	<0.04	1.6	3.0	1.3	1.7	1.1	-
22A	1.5	<0.02	2.0	5.9	1.2	3.2	1.4	1.4
22B	1.5	<0.03	2.9	4.9	-	-	-	-
22B regenerated	1.1	-	1.4	2.9	-	-	-	-
28A	0.8	<0.03	1.9	5.1	1.3	2.6	1.6	1.6

References

(1) Armor, J. N. *J. Membr. Sci.* **1998**, *147,* 217.
(2) Caro, J.; Noack, M.; Kolsch, P.; Schafer, R. *Microp. Mesop. Mat.* **2000**, *38,* 3.
(3) Chiang, A. S. T.; Chao, K-J. *J. Phys. Chem. Solids* **2001**, *62*, 1899.
(4) Noack, M.; Kolsch, P.; Schafer, R.; Toussaint, P.; Caro, *J. Chem. Eng. Technol.* **2002**, *25*, 221.
(5) Thoma, S. G.; Trudell, D. E.; Bonhomme, F.; Nenoff, T. M. *Microp. Mesop. Mat.* **2001**, *50*, 33.
(6) Vroon, Z. A. E. P.; Keizer, K.; Gilde, M. J.; Verweij, H. Burggraaf, A. J. *J. Membr. Sci.* **1996**, *113,* 293.
(7) Geus, E. R.; den Exter, M. J.; van Bekkum, H. *J. Chem. Soc. Faraday Trans.* **1992**, *88*, 3101.
(8) Bakker, W. J. W.; Kapteijn, F.; Poppe, J.; Moulijn, J. A. *J. Membr. Sci*. **1996**, *117*, 57.
(9) Bai, C.; Jia, M-D.; Falconer, J. L.; Noble, R. D. *J. Membr. Sci.* **1995**, *105,* 79.
(10) Lin X.; Kita, H.; Okamoto K-I. *Ind. Eng. Chem. Res.* **2001**, *40,* 4069.
(11) Bonhomme, François; Welk, Margaret E.; Nenoff, Tina M. *Microp. Mesop. Mat.* **2003**, *66,* 181.
(12) Persson, A. E.; Shoeman, B. J.; Sterte, J.; Otterstedt, J. E. *Zeolites* **1994**, *14*, 557.
(13) Breck, D.W. *Zeolite Molecular Sieves*, John Wiley and Sons, New York 1997.

NANOSTRUCTURED ELECTRODES FOR HYDROGEN FUEL CELLS

*Mahesh Waje, Cheng Wang, Jason M. Tang, , Yushan Yan**

Department of Chemical and Environmental Engineering, College of Engineering – Center for Environmental Research and Technology, Center of Nanoscale Science and Engineering, University of California, Riverside, CA 92521

* Corresponding author, email: Yushan.Yan@ucr.edu

Introduction

As a potential candidate for an environmentally benign and a highly efficient electric power generation technology, hydrogen fuel cells, a type of proton exchange membrane fuel cells (PEMFC) are now attracting enormous interest for various applications such as low/zero-emission vehicles, distributed home power generators, and power sources for small portable electronics.[1-4] One of the challenges in the commercialization of PEMFCs is the high cost of noble metals used as catalyst (e.g., Pt). Decreasing the amount of Pt used in a PEMFC via the increase of the utilization efficiency of Pt has been one of the major concerns during the past decade.[5] To effectively utilize the Pt catalyst, the Pt must have simultaneous access to the gas, the electron-conducting medium, and the proton-conducting medium. In the catalyst layer of a Pt-based conventional fuel cell prepared by the ink-process, the simultaneous access of the Pt particle by the electron-conducting medium and the proton-conducting medium is achieved via a skillful blending of Pt-supporting carbon particles and Nafion. The carbon particles conduct electrons and the Nafion conduct protons. However, even with the more advanced conventional electrodes, there is still a significant portion of Pt that is isolated from the external circuit and/or the PEM, resulting in a low Pt utilization. For example, Pt utilization in current commercially offered prototype fuel cells remains very low (20-30%) although higher utilization has been achieved in laboratory devices. Efforts directed at improving the utilization efficiency of the Pt catalyst have focused on finding the optimum material configurations while minimizing the Pt loading and satisfying the requirements of proton access, gas access, and electronic continuity. In the conventional ink-process, a common problem has been that the necessary addition of Nafion for proton transport tends to isolate carbon particles in the catalyst layer, leading to poor electron transport.

Due to their unique structural, mechanical, and electrical properties, carbon nanotubes have been recently proposed to replace traditional carbon powders in PEMFCs and have been demonstrated by making membrane electrode assemblies (MEA) using a carbon nanotube powder through a conventional ink process.[6-8] However, their results did not show many advantages over carbon black (Vulcan XC-72) since the Pt utilization within the PEMFC catalyst layer remained unaddressed. Growing carbon nanotube arrays directly on the carbon paper and then subsequently electrodepositing the Pt selectively on the carbon nanotubes promises to improve the Pt utilization, thus securing the electronic route from Pt to the supporting electrode in a PEMFC. The use of carbon nanotubes and the resulting guaranteed electronic pathway eliminate the previously mentioned problem with conventional PEMFC strategies where the Nafion would isolate the carbon particles from the electrode support. Eliminating the isolation of the carbon particles from the electrode support would thereby improve the utilization rate of Pt.

Generally, there are two categories of carbon nanotubes: single-walled nanotubes (SWNTs) and multi-walled nanotubes (MWNTs). A SWNT is a single graphene sheet rolled into a cylinder. A MWNT is comprised of several coaxially arranged graphene sheets rolled into a cylinder. According to theoretical predictions, SWNTs can be either metallic or semiconducting depending on the tube diameter and helicity.[9] The semiconducting band gap is proportional to the reciprocal diameter, 1/d, and the band gap becomes comparable to thermal energies at room temperature when a nanotube diameter is around 3 nm.[10] Whereas for the MWNTs, scanning tunneling spectroscopy (STS) measurements indicate that the conduction is mainly due to the outer shell,[11] which are usually larger than 3nm. Therefore, MWNTs should have a relatively high electrical conductivity at room temperature. In this paper, we will focus on MWNTs as a support for the Pt catalyst in PEMFCs because current synthetic methods for MWNTs are simpler than those for SWNTs.

Earlier attempts to deposit MWNTs on carbon paper were conducted by S. Désilets and his group,[12,13] who dipped carbon paper in a solution containing silica and Group VIII metal salts and used this silica gel on carbon paper to catalyze the growth of the MWNTs on the carbon paper by an ohmic heating process. Although MWNTs are firmly attached on the carbon paper, electrical contact between the MWNTs and the carbon paper could be hindered by the existence of silica. Our group is currently working on fuel cells that use MWNTs as a Pt catalyst support by directly growing MWNTs on carbon paper through a chemical vapor deposition (CVD) process using electrodeposited Co as the catalyst for MWNT growth and subsequently depositing Pt catalyst selectively on these MWNTs. This non-ink process ensures that all of the electrodeposited Pt catalyst particles are electronically accessible to the external circuit of a PEMFC.

Experimental

MWNT synthesis on carbon paper. The Co catalyst for MWNT growth is electrodeposited on one side of the carbon paper by a three-electrode dc method in a 5 wt. % $CoSO_4$ and 2 wt. % H_3BO_3 solution at 20ºC.[14] The deposition potential is 1.0 V vs SCE (saturated calomel electrode). The loading of Co is varied from 0.26 to 20 mg/cm^2 by controlling the total charge deposited assuming 100 % yield of the electrodeposition.

The MWNTs were grown with a chemical vapor deposition (CVD) procedure described elsewhere[16] with slight modifications. Carbon paper with Co electrodeposited on one side of the paper was placed in a furnace at ambient pressure and heated to 550ºC in 3 hrs under a 150 sccm N_2 flow and 7.5 sccm H_2 flow. These conditions were maintained for 30 minutes. The temperature was then raised to 700ºC over a 30 minute time interval. Upon reaching 700ºC, acetylene was introduced at 7.5 sccm for 1hr to facilitate MWNT growth. Finally, the acetylene and H_2 flow was cut off and the furnace cooled to room temperature in 150 sccm N_2 flow.

Pt deposition and MEA preparation. Following the CVD growth of the MWNTs, Pt was electrodeposited on the MWNTs by a three-electrode dc method in 5 mM H_2PtCl_6 and 0.5 M H_2SO_4 aqueous solution.[17] The deposition potential used was 0 V vs. SCE (saturated calomel electrode, Aldrich) and the loading of Pt was controlled by the total charge applied.

An MEA was prepared using two such MWNT-carbon paper composite electrodes by first immersing the two electrodes into 5% commercial Nafion solution for 30 mins and subsequent hot pressing these two electrodes with a Nafion 115 membrane in between the two electrodes.

Characterization. The carbon paper samples with electrodeposited Co, the subsequent MWNT/carbon paper samples and the Pt electrodeposited electrode samples were characterized by SEM (Philips XL30-FEG). MWNTs were further characterized by TEM (Philips CM300). Brunauer-Emmett-Teller method (Micromeritics ASAP 2010) was used to determine the surface area of MWNTs and carbon paper. The MWNT-carbon paper composites were tested by cyclic voltammetry in 5mM potassium ferricyanide (III) solution to determine the active surface area.

The performance of MEA prepared was tested using a fuel cell test station (ElectroChem. Inc., USA).

Results and Discussion

Figure 1 shows the SEM images of the carbon paper with and without electrodeposited Co. The carbon paper is made of fibers having a diameter between 5 and 10 µm (inset in Figure 1A) and the surface of the carbon fiber is clean before deposition. The hydrophobic property of carbon paper enables the selective deposition of Co on the side of the carbon paper facing the electrolyte solution, which also makes it possible for selective growth of MWNTs on one side of carbon paper. This is also necessary for fuel cell applications because further selective deposition of Pt catalyst becomes feasible. After applying 2 coulombs charge on 2.55 cm^2 circular carbon paper for depositing cobalt, which equals 0.26 mg/cm^2 of Co loading, nanocrystalline Co could be found on the surface of carbon fibers (Figure 1A). The particle size is in the range of 20 to 50 nm. With the increase of Co loading, the particle size increases. We observed dendrimeric nanocrystalline Co (Figure 1B) when the loading was 4 mg/cm^2. Further increases in loading, for example to 20 mg/cm^2 as shown in the inset of Figure 1B, made it possible to cover and connect the carbon fibers on the whole surface of carbon paper by a porous Co structure.

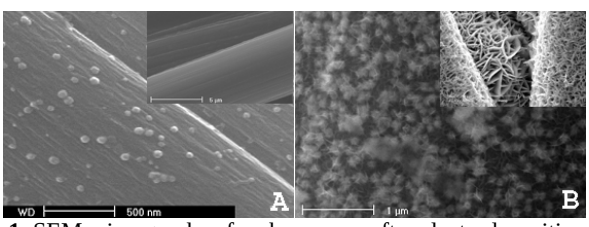

Figure 1: SEM micrographs of carbon paper after electrodeposition of Co: A) with 0.26 mg/cm^2 Co (inset is bare carbon paper) and B) with 4 mg/cm^2 Co (inset is 20 mg/cm^2 Co).

An important aspect of the MWNTs is the high surface area for subsequent Pt deposition. Considering the fact that small catalyst particles are beneficial for the growth of MWNTs with small diameters (therefore high surface area), a loading of 0.26 mg/cm^2 Co on carbon paper was employed in all of the subsequent experiments.

For the MWNT growth, CVD was employed due to its suitable growth temperature and ease to scale-up.[15] Figure 2 presents the SEM and TEM pictures of the resulting MWNTs after CVD growth using a 0.26 mg/cm^2 Co loading. As shown in Figure 2A, a thin layer of MWNTs covers the carbon paper. The as-prepared MWNTs are wavy with lengths in the micrometer range and diameters in the range of 20 to 40 nm (Figure 2B). Some bright particles on MWNTs can also be observed from Figure 2B, which were identified as Co under electron diffraction x-ray spectroscopy (EDX). The TEM image in Figure 2C shows two MWNTs with outer shell diameters of 30 and 40 nm along with some metal particles present in the inner cavity of the MWNTs. The inner diameters of the MWNTs are about 10 nm.

To obtain a high yield of MWNTs on carbon paper to serve as the Pt catalyst support for fuel cell applications, a higher loading of Co on the carbon paper through repetitions of both Co electrodeposition and subsequent CVD carbon nanotube growth was attempted. However, a higher loading of Co on the substrate caused an increase of Co particle size, and the diameter distribution of MWNTs becomes broader, such as 20-130 nm. Also, repetitions of electrodeposition and CVD carbon nanotube growth resulted in amorphous carbon generation.

Figure 2D shows the SEM image of the Pt electrodeposited on the MWNTs. The average diameter of these particles is about 25 nm. The successful deposition of Pt indicates a good electrical contact between the MWNTs and the substrate.

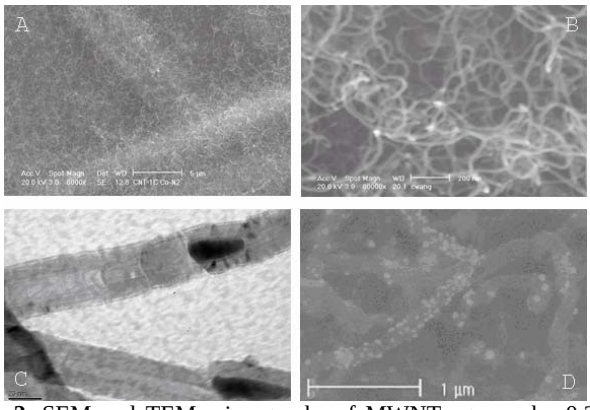

Figure 2: SEM and TEM micrographs of MWNTs grown by 0.26 mg/cm^2 Co loading on carbon paper; A) SEM with low magnification showing high coverage of MWNTs on carbon paper; B) SEM with higher magnification showing the diameter of the MWNTs and presence of Co catalyst particles; C) TEM of MWNTs, D) SEM of Pt particles electrodeposited on MWNTs.

The surface area of the MWNT-carbon paper composite electrode is determined to be in the range between 80-140 m^2/g from nitrogen adsorption by the Brunauer-Emmett-Teller method, while that of carbon paper alone is less than 2 m^2/g. This is consistent with

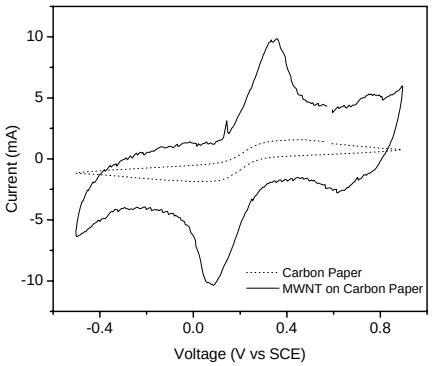

Figure 3: Cyclic Voltammetry in a $K_3Fe(CN)_6$ solution (5 mM $K_3Fe(CN)_6$ + 0.5 M K_2SO_4) of: 1) 3.46 cm^2 of carbon paper alone; 2) MWNTs grown by 0.26 mg/cm^2 Co loading covering the same 3.46 cm^2 carbon paper. Scan rate: 50 mV/s.

what we have obtained from cyclic voltammetry (CV) measurements in potassium ferricyanide (III) solution (Figure 3) where the redox current is much higher for the MWNT-carbon paper composite, further indicating that MWNTs are electrically connected to the carbon paper substrate

Figure 4 shows the performance of the MEA prepared with thee MWNT-carbon paper composite electrodes. Although the performance of the CNT based fuel cell is still lower than that of the conventional PEMFC with comparable Pt loading, the feasibility of our design involving electrodeposition of catalyst for MWNT growth directly on the carbon paper and subsequent electrodeposition of Pt on the MWNTs is demonstrated. It is expected that once the yield and diameter of the MWNTs and the Pt particle sizes are optimized, the carbon nanotube based fuel cell will show superior performance. Work on the optimization of the MWNT loading and nanotube dimensions, as well as on the decrease of Pt particle size, is under way in order to ultimately achieve a high performance PEMFC.

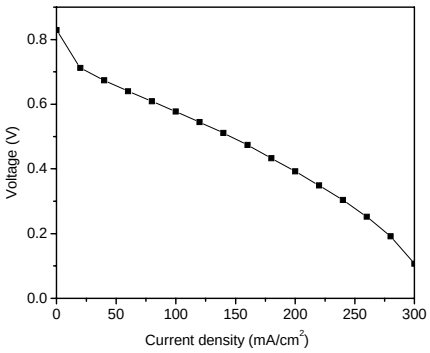

Figure 4: Polarization curve of a MEA prepared by electrodeposition of Pt on MWNTs grown by 0.26 mg/cm^2 Co loading. Pt loading on both electrodes: 0.2 mg/cm^2. Membrane: Nafion 115. Operating conditions: cell temperature, 70°C; humidifier temperature, 80°C; pressure, 2 atm.

Acknowledgement: This work is supported by Pacific Fuel Cell Corporation, UC-Discovery Grant, and California Energy Commission.

References:

(1) Toda, T.; Igarashi, H.; Uchida, H.; Watanabe, M. *J. Electrochem. Soc.* **1999,** *146*, 3750.
(2) Springer, T. E.; Zawodzinski, T. A.; Gottesfeld, S. *J. Electrochem. Soc.* **1991,** *138*, 2334.
(3) Cleghorn, S.J.C.; Ren, X.; Springer, T.E.; Wilson, M.S.; Zawodzinski, T.A.; Gottesfeld S. *Int. J. Hydrogen Energ.* **1997,** *22*, 1137.
(4) Service, R. *Science* **2002,** *296*, 1222.
(5) Srinivasan, S.; Velev, O. A.; Parthasarathy, A.; Manko, D. J.; Appleby, A. J. *J. Power Sources* **1991,** *36*, 299.
(6) Li, W.Z.; Liang, C.H.; Qiu, J.S.; Zhou, W.J.; Han, H.M.; Wei, Z.B.; Sun, G.Q.; Xin, Q. *Carbon* **2002,** *40*, 787.
(7) Li, W. Z.; Liang, C.H.; Zhou, W.J.; Qiu, J.S.; Zhou, Z.H.; Sun, G.Q.; Xin, Q. *J. Phys. Chem. B* **2003,** *107*, 6292.
(8) Liu, Z.L.; Lin, X.H.; Lee, J.Y.; Zhang, W.D.; Han, M.; Gan, L.M. *Langmuir* **2002,** *18*, 4054.
(9) Saito, R.; Fujita, M.; Dresselhaus, G.; Dresselhaus, M.S. *Appl. Phys. Lett.* **1992,** *60*, 2204.
(10) Dresselhaus, M.S.; Hishi, R.A.; Dresselhaus, G.; Inomta, D.; Nakao, K.; Saito, R. *Mol. Cryst. Liq. Cryst. Sci. Tech., Sect. C: Mol. Mater.* **1994,** *4*, 27.
(11) Kasumov, A.Y.; Bouchiat, H.; Reulet, B.; Stephan, O.; Khodos, II.; Gorbatov, Y.B.; Colliex, C. *Eurphys. Lett.* **1998,** *43*, 89.
(12) Smiljanic, O.; Dellero, T.; Serventi, A.; Lebrun, G.; Stansfield, B.L.; Dodelet, J.P.; Trudeau, M.; Désilets, S. *Chem. Phys. Lett.*, **2001,** *342*, 503
(13) Sun, X.; Stansfield, B.L.; Dodelet, J.P.; Désilets, S. *Chem. Phys. Lett.* **2002,** *363*, 415.
(14) Iwasaki, T; Motoi, T.; Den, Y. *Appl. Phys. Lett.*, **1999,** *75*, 2044.
(15) Li, W.Z.; Wang, D.Z.; Yang, S.X.; Wen, J.G.; Ren, Z.F. *Chem. Phys. Lett.* **2001,** *335*, 141.
(16) Yuan, Z. H.; Huang, H.; Dang, H. Y.; Cao, J. E.; Hu, B. H.; Fan, S. S. *Appl. Phys. Lett.* **2001,** *78*, 3127.
(17) Thompson, S.D.; Jordan, L.R.; Shukla, A.K.; Forsyth, M. *J. Electroanal. Chem.* **2001**, *515*, 61.

.

A RELIABLE METHOD FOR THE DETERMINATION OF HYDROGEN STORAGE CAPACITY AT HIGH PRESSURE AND ITS APPLICATION TO CARBON MATERIALS

James M. Blackman, John W. Patrick, Colin E. Snape

Nottingham Fuel & Energy Centre,
School of Chemical, Environmental and Mining Engineering (SChEME), University of Nottingham, University Park, Nottingham NG7 2RD, United Kingdom,
enxjmb@nottingham.ac.uk

Introduction

In recent years, activated carbons, carbon nanofibers and carbon nanotubes have all attracted considerable attention as potential hydrogen storage materials.[1-3] However, determining the hydrogen storage capacity of these materials at high pressure (>10 MPa) has been found to be problematic due to difficulties with reliability and obtaining a satisfactory degree of accuracy.

Primarily, there are two methods that are applied to directly study hydrogen storage capacity of solid materials at high pressures, gravimetric and volumetric. The gravimetric method determines the hydrogen storage capacity of a material by measuring the change of weight of a sample during an adsorption-desorption cycle. The experiments are carried out with *ca* 10 mg of sample in custom built thermo-gravimetric apparatus, which have a high pressure balance chamber.[4] However, this technique is sensitive to all gases sorbed as in principle, it is only based on weighing and this problem is magnified by the very small sample size used for each experiment so is best suited to materials that have high hydrogen storage capacities.

The volumetric method determines the hydrogen storage capacity of a material by measuring the pressure drop resulting from adsorption after exposing the sample to hydrogen at constant volume. This method has the advantage that the conditions are similar to that of a storage tank. Most of the work reported using this method has been carried out using direct pressure measurement in customer built rigs based on the Sieverts type apparatus which is used to determine the hydrogen storage capacity of metal hydrides.[5] However, at high pressures, the Sieverts type apparatus is very sensitive to temperature instability, leaks and additional pressure effects caused by expanding the hydrogen from the reservoir to the sample cell. Recently a second volumetric method has been introduced using a differential pressure method in an attempt to minimise many of these problems.[6]

The difficult nature of the determination of hydrogen storage capacity of a material has contributed to the inconsistencies that have arisen in this field. The reported values for hydrogen storage capacity for carbon materials range from <0.1 wt% for activated carbons, graphite, nanofibers and nanotubes to ~65 wt% for carbon nanofibers.[7,8]

Recognising the difficulties encountered in measuring the adsorption of hydrogen at high pressure, a volumetric differential pressure method has been developed to improve the accuracy of the determination of the hydrogen storage capacity of carbon materials at pressures of *ca*. 10 MPa to a limit of detection of 0.1 wt%. This method has been applied to a series of carbon nanofibers and activated carbons and their adsorption characteristics have been compared.

Experimental

Materials The carbon nanofibers were prepared by carbon vapor deposition from a series of copper-nickel catalysts using ethylene-hydrogen (1:4) as the reactive gas.

The catalyst precursors were prepared by co-precipitation from stoichiometric aqueous solutions of nickel nitrate hexahydrate and iron nitrate nonahydrate using sodium hydroxide solution as the base. Sodium hydroxide was selected over weaker bases used previously to give better definition on precipitation. The resulting suspension was then filtered and the precipitate dried at 107 °C for 24 hours. The product was then calcined at 400 °C for 4 hours to afford the mixed metal oxide catalyst precursor. The catalyst precursor was then finely ground and 50 mg placed in a horizontal quartz reactor tube and reduced for 16 hours under a hydrogen gas flow (100 ml/min) at 450 °C. The reactor then was heated to 600 °C under inert atmosphere. The ethylene-hydrogen (60:240 ml/min) reaction gas was passed over the catalyst for 3 hours. The resulting nanofibers were cooled to room temperature under an inert atmosphere. The carbon nanofibers received no further treatment before adsorption analysis.

The activated carbons used are commercially available and were used with no further treatment.

Adsorption Analysis The nitrogen BET surface area measurements were carried out on an ASAP 2010 and the hydrogen adsorption measurements were made on a custom built volumetric differential pressure apparatus (Figure 1).

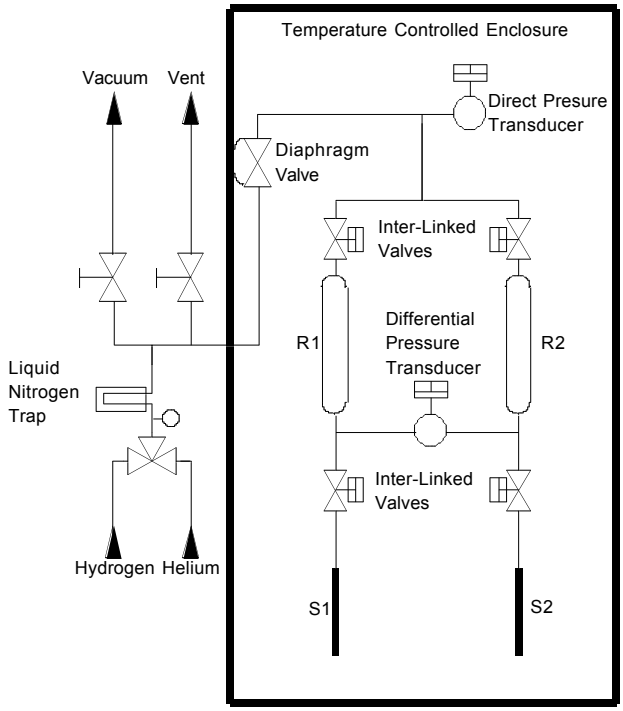

R1 and R2 are reservoir 1 and 2 respectively
S1 and S2 are sample cell 1 and 2 respectively

Figure 1. Schematic of the volumetric differential pressure hydrogen adsorption apparatus

The limb R1+S1 is symmetrical to the limb R2+S2 and the differential pressure transducer has a ±5 bar operational range so that both S1 and S2 can be used as the sample cell. The following protocol is used to operate the apparatus. Using S1 as the sample cell and S2 as the blank, the sample (1-2.5 g) is loaded into S1 and sealed to the apparatus by a high pressure o-ring fitting. The free space in S1+R1 is then determined by helium free space analysis using the differential pressure cell relative to vacuum. The whole apparatus is then evacuated to 0.2 Pa and S1 heated to

150 °C for 2 hours. The heating to S1 is then switched off and the enclosure is then allowed to equilibrate at the operating temperature of 30 °C. The lower inter-linked valves (air-actuated high pressure bellows valves) are then closed. Helium is then admitted to the desired pre-expansion pressure. The top interlinked valves are then closed isolating the limbs and the apparatus isolated by closing the diaphragm valves. The experiment then commences by opening the lower inter-linked valves. After 7 hours the experiment is stopped. The experimental procedures are then repeated using hydrogen.

Results and Discussion

Apparatus The volumetric differential pressure hydrogen adsorption setup has several advantages over the more traditional Sieverts apparatus. Differential pressure transducers have much higher accuracy than direct pressure transducers and by applying the equation of state equation the hydrogen adsorption capacity can be calculated solely using the differential pressure measurement.

$$A = \frac{\Delta PVM_H}{50RTm_C} \quad (1)$$

A=Hydrogen adsorbed (wt%)
M_H=Relative atomic mass of hydrogen
m_c=Mass of sample

The differential pressure system also helps to minimise the errors resulting from minor temperature fluctuations (*ca* ±0.1 °C) of the equipment as R1+S1 and R2+S2 are affected by the same conditions. To prove this, the apparatus was pressurised to 100 bar and both the differential pressure gauge and direct pressure gauge were monitored (Figure 2). The direct pressure reading fluctuated systematically and correlated with the minor temperature changes but the differential pressure reading remained level throughout.

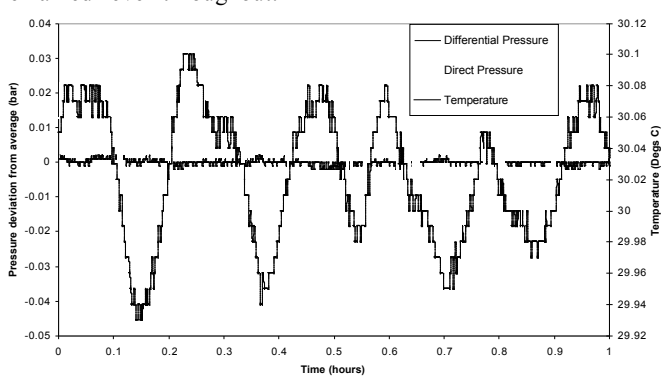

Figure 2. The effect of minor changes in temperature on differential pressure and direct pressure recorded on the volumetric differential pressure hydrogen adsorption apparatus at 10 MPa

The helium run prior to the hydrogen adsorption run acts as a leak detection test. After three hours, all disturbances caused by the expansion of the R1 and R2 into S1 and S2 respectively have returned to equilibrium, so any change in pressure can only be the result of a leak. The helium run is also used as a baseline correction for the hydrogen adsorption run. The initial expansion causes gas at over 11 Mpa to be expanded through a tiny port to a vessel initially at vacuum. This is believed to have a cooling effect on the gas in both limbs, which is dominant in the blank limb as the blank sample cell has more void space to be filled. The result is the pressure is slightly reduced on the blank limb side relative to the sample limb, which is corrected quickly as the apparatus returns the gas to equilibrium pressure. Therefore, the baseline correction is required to give the differential pressure reading an adsorption free reference point; reducing error caused temperature expansion effects and other non-adsorption related phenomena. Without the correction an exaggerated hydrogen adsorption measurement can be observed with and inaccurate profile recorded (Figure 3). This result exaggeration becomes more pronounced with poorer hydrogen adsorbents as the cooling effect becomes increasingly dominant over the adsorption. The true adsorption profile is also lost if a correction is not carried out.

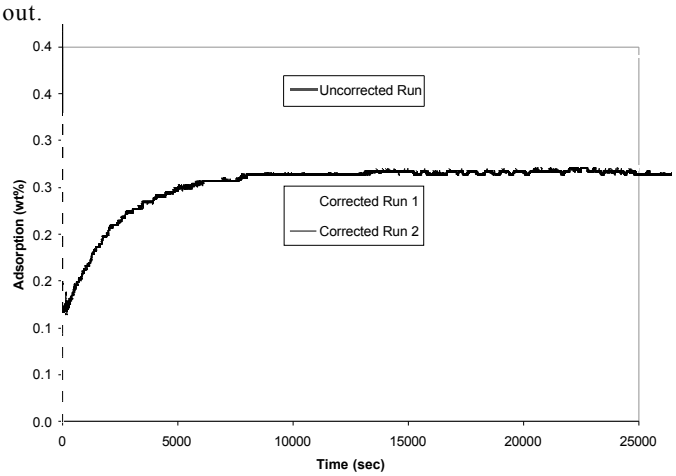

Figure 3. Hydrogen adsorption profile at 10 MPa of carbon nanofibers grown from Cu-Fe-Ni (5:85:10) showing measurement reliability and the error observed if the run is not baseline corrected

The apparatus is guarded from slow leaking through the valves by using low leak rate valves and a pressure buffer between the top inter-linked valves and the diaphragm valve, which is maintained at 5 bar above the operating pressure. The use of 1-2.5 g of sample for a run also enhances the sensitivity of the apparatus, as this is larger than most previous measurements made, which tend to use below 1 g, this ensures that the measurement taken is representative of the sample. The repeatability of the measurements made on volumetric differential pressure hydrogen adsorption apparatus has been found to be excellent. This can clearly be seen for the corrected run 1 & 2 for carbon nanofibers grown from Cu-Fe-Ni (5:85:10).

Adsorption on Carbons As stated a series of activated carbons and carbon nanofibers were analysed for BET nitrogen surface area. The carbon nanofibers were also analysed by XRD and confirm their graphitic nature.

Carbon Nanofibers	Activated Carbons
Fe-Ni (1:9)	Fisher FDC
Fe-Ni (2:8)	Fisher Charcoal FGA
Fe-Ni (3:7)	Norit FGD
Fe-Ni (4:6)	Speakman
Fe-Ni (5:5)	1526-r-98
Fe-Ni (6:4)	1523-r-98
Fe-Ni (7:3)	
Cu-Fe-Ni (5:85:10)	

Table 1. Carbons used for adsorption experiments

The activated carbons analysed were observed to adsorbed 90+ % of their hydrogen adsorption capacity instantly. This is consistent with physisorption being the dominant mechanism of adsorption.

The carbon nanofibers prepared from bi-metallic catalysts were found to have a much lower adsorption capacity than the activated carbons. The carbon nanofibers were observed to adsorb 50-70 % instantly which is assumed to result from physisorption on the surface of the nanofibers. The remainder of the adsorption occurs on a timescale of *ca* 60 minutes, which is thought to result from the hydrogen penetrating between the graphite layers of the carbon nanofibers.

Most of the carbons studied followed the basic trend of their nitrogen BET surface area showing a broadly linear relationship with their final hydrogen adsorption capacity (Figure 4). However, carbon nanofibers grown from a Cu-Fe-Ni (5:85:10) were observed to adsorb more hydrogen than would be expected relative to the recorded nitrogen BET surface area measurement (circled in Figure 4). This may be the result of hydrogen penetration of the graphitic layers which is inaccessible to nitrogen.

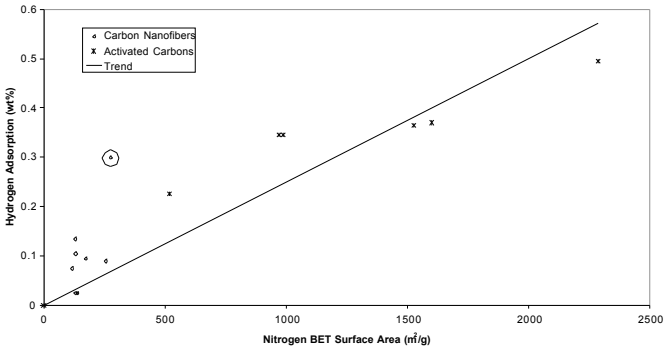

Figure 4. Graph outlining the relation ship between final hydrogen adsorption capacity at 10 MPa of the carbon and the corresponding nitrogen BET surface area values

Conclusions

The volumetric differential pressure hydrogen adsorption apparatus developed has been shown to be reliable and accurate method for determining the hydrogen adsorption capacity of a material to 0.1 wt%. The carbons studied displayed a broadly linear correlation between their hydrogen adsorption capacity and nitrogen BET surface area. However, certain carbon nanofibers did deviate from this trend to be favorable towards hydrogen. If carbon nanofibers do have the potential to adsorb large amounts of hydrogen it would appear that their structure is critical.

Acknowledgement The work was supported by Air Products and Chemicals, Inc. and the EPSRC research council. We gratefully acknowledge the technical advice from Dr. G. Pez (Air Products and Chemicals, Inc.), Mr. F. Anderton and Mr. M. Fletcher and the XRD analysis carried out by Mr. D. A. Clift.

References

(1) Cheng, H. M.; Yang, Q. H.; Liu, C. *Carbon* **2001**, *39*, 1447-1454.
(2) Zuttel, A.; Sudan, P.; Mauron, P.; Kiyobayashi, T.; Emmenegger, C.; Schlapbach, L. *Int. J. Hydrog. Energy* **2002**, *27*, 203-212.
(3) Darkrim, F. L.; Malbrunot, P.; Tartaglia, G. P. *Int. J. Hydrog. Energy* **2002**, *27*, 193-202.
(4) Strobel, R.; Jorissen, L.; Schliermann, T.; Trapp, V.; Schutz, W.; Bohmhammel, K.; Wolf, G.; Garche, J. *J. Power Sources* **1999**, *84*, 221-224.
(5) Fan, Y. Y.; Liao, B.; Liu, M.; Wei, Y. L.; Lu, M. Q.; Cheng, H. M. *Carbon* **1999**, *37*, 1649-1652.
(6) Browning, D. J.; Gerrard, M. L.; Lakeman, J. B.; Mellor, I. M.; Mortimer, R. J.; Turpin, M. C. *Nano Lett.* **2002**, *2*, 201-205.
(7) Tibbetts, G. G.; Meisner, G. P.; Olk, C. H. *Carbon* **2001**, *39*, 2291-2301.
(8) Chambers, A.; Park, C.; Baker, R. T. K.; Rodriguez, N. M. *J. Phys. Chem. B* **1998**, *102*, 4253-4256.

Dynamic Measurement of Hydrogen Storage/Release Properties Using Tapered Element Oscillating Microbalance for Mg Doped with Nano-sized Pd Catalyst

Xiaochun Xu, Jian Zheng and Chunshan Song*

Clean Fuels and Catalysis Program, The Energy Institute, and Department of Energy & Geo-Environmental Engineering, The Pennsylvania State University, 209 Academic Projects Building, University Park, PA 16802, USA

* Contact E-mail: csong@psu.edu; Fax: 814-865-3248

Introduction

Hydrogen storage is one of the key enabling technologies for the advancement of hydrogen power systems, such as fuel cells, in transportation, stationary, and portable applications. For practical application, a reliable measurement of hydrogen absorption/release data is important for the proper design of hydrogen storage devices.

Three different techniques, i.e., volumetric method,[1] gravimetric method[2] and thermal desorption spectroscopy (TDS)[3], have been applied for studying the hydrogen storage/release in solids. The volumetric method measures the pressure drop owing to hydrogen absorption after applying a hydrogen pressure to the specimen contained in a constant volume. Similarly the pressure increase or gas blow off due to desorption can be measured. For volumetric measurement, one has an accumulation of the error. Furthermore, any leakage or temperature instability of the apparatus may give rise to large experimental errors. The gravimetric method measures the weight changes of the specimen due to absorption or desorption of hydrogen. However, data obtained by the gravimetric method are influenced by effects associated with flow patterns, bypassing, and aerodynamic factors such as buoyancy. Gas flow rate smaller than 100 ml/min is required for a reliable measurement.[4] Furthermore, this technique is not sensitive to the nature of gasses absorbed or desorbed since it is only based on weighing. At high temperature or high pressure, the mass resolution of the gravimetric apparatus is significantly reduced. In addition, the response time is 10 to 30 sec, which is not suitable for short duration and kinetics study. Thermal desorption spectroscopy (TDS) measures only the hydrogen desorption in high vacuum utilizing mass spectrometry.

In our laboratory, we are using a technique called tapered element oscillating microbalance (TEOM), where the solid sample is examined as a packed bed, through which the gas passes through. This technique circumvents most of the above problems associated with volumetric method, gravimetric method or TDS.

The main feature of the TEOM technique is an oscillating element that is based on inertial forces, instead of weight, to measure the amount adsorbed. Therefore, errors associated with leakage, flow patterns, bypassing, and aerodynamic factors can be eliminated. Mass resolution of TEOM is also not reduced at higher temperature and high pressure. Consequently, TEOM allows accurate and reproducible measurements. In addition, the fast response time up to 0.1 second makes the short-residence-time measurement and kinetic study possible and reliable. However, there is little literature report on the measurement of hydrogen absorption/release in metal hydride by TEOM.

In this paper, hydrogen storage/release properties of magnesium and palladium-doped magnesium were investigated by using the TEOM technique. The hydrogen storage/release data measured by TEOM were compared with those of measured by the volumetric method.

Experimental

An integrated flow system designed on the basis of a Rupprecht & Patashnick TEOM 1500 pulse mass analyzer (100-mg sample volume) was used for measurement of hydrogen storage and release properties. The active element of the TEOM consists of a tube constructed of a material having a special taper. A feedback system maintains the oscillation of the tapered tube. The natural frequency will change in relation to the mass in the tapered tube. The mass uptake is then determined by the change of the oscillating frequency. The mass uptake is then determined by the change of the oscillating frequency through equation 1.[5]

$$\Delta M = K_0\left(\frac{1}{f_1^2} - \frac{1}{f_0^2}\right) \qquad (1)$$

where ΔM is the weight change, K_0 is spring constant, f_0 is oscillation.

A simplified diagram of the oscillating element is shown in Figure 1. Gases are fed to the unit using Brooks mass flow controllers. The total pressure in the oscillating element is controlled by a backpressure controller. Quartz wool was used at the top and the bottom of the sample bed to keep the hydrogen storage materials firmly packed, which is essential for the stable measurement. Both the feed gas and purge gas was hydrogen and both the feed gas and purge gas flow rate was 100 ml/min. About 30 mg sample was used in the measurements. A detailed description of the TEOM apparatus is available in the literature.[5,6]

Samples used in this paper are magnesium (Aldrich, 99.8%, 325 mesh) and palladium nanoparticle-doped magnesium. The nanoparticle palladium-doped magnesium was prepared by an in-situ catalyst deposition method.[7] The hydrogen absorption was carried out at 573 K and 400 psi. The hydrogen release was measured at 613 K and ambient pressure.

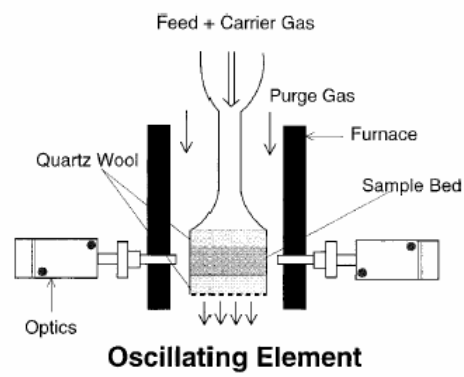

Figure 1. Simplified diagram of the oscillating tapered element with a sample bed.

Results and Discussions

1. Hydrogen absorption measurement

The hydrogen absorption performance of Pd-doped magnesium were measured by TEOM and compared with that measured by volumetric method in our previous study.[7] Figure 2 compares the hydrogen absorption properties of Pd-doped magnesium measured by TEOM and volumetric method at 573 K under 400 Psi. The hydrogen storage capacity measured by TEOM is almost the same as that measured by volumetric method, which indicates the accuracy of the two measurement methods. However, the hydrogen absorption rate measured by TEOM is faster than that measured by the volumetric method. When the hydrogen absorption is measured by volumetric method, the Pd-doped magnesium is sealed in a vessel with high pressure hydrogen gas. Therefore, the hydrogen storage is carried out

in static status and hydrogen concentration gradient exists in the adsorption bed, which results in the slow mass transfer in the absorption bed and slow hydrogen absorption rate. On the other hand, when the hydrogen absorption is measured by TEOM, a high flow rate forces hydrogen gas flow through the adsorption bed, which improves the mass transfer in the adsorption bed and accelerates the hydrogen absorption rate. Another important feature is that the response time for TEOM is very fast, as short as 0.1 second, whereas the response time for the volumetric method is very long. TEOM makes the fast measurement and kinetic study possible and reliable. Chen et al[6] also reported that TEOM provided more accurate data on the catalyst deactivation kinetics than the conventional microbalance.

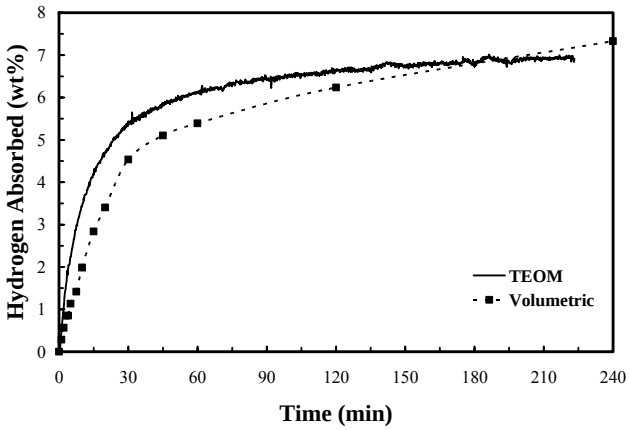

Figure 2. Comparison of hydrogen absorption properties of Pd-doped magnesium measured by TEOM and volumetric method at 573 K and under 400 Psi.

2. Hydrogen release measurement

The hydrogen release properties of Pd-doped magnesium were also measured by TEOM and compared with that measured by volumetric method in the previous study.[7] Figure 3 compares the hydrogen release properties of Pd-doped magnesium measured by TEOM and volumetric method at 613 K and atmosphere pressure. Similarly, the hydrogen release rate measured by TEOM is also faster than that measured by the volumetric method. Due to the elimination of hydrogen concentration gradient in the adsorption bed and the fast response time of TEOM, TEOM provides a more accurate and detailed information on the hydrogen absorption and release kinetic than the volumetric method or other gravimetric methods, which is important for the design of next generation high performance hydrogen storage materials and for the proper design of hydrogen storage devices in practical application.

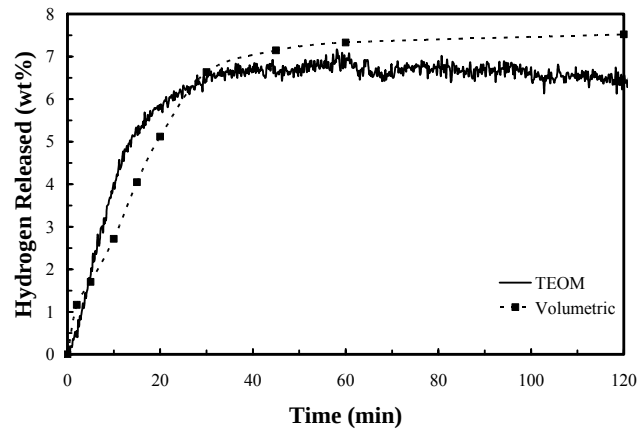

Figure 3. Comparison of hydrogen release properties of Pd-doped magnesium measured by TEOM and volumetric method at 613 K and under ambient pressure.

3. Effect of nano-sized Pd catalysts on hydrogen release

The effect of nanoparticle palladium catalysts on the hydrogen release properties of magnesium hydride was measured by TEOM at 613 K and under ambient pressure and the results are shown in Figure 4. Apparently, the rate of hydrogen release for palladium-doped magnesium hydride is much faster than that for the un-doped magnesium hydride, which is in consistent with that of measured by volumetric method.[7] While the Pd-doped magnesium readily releases hydrogen, the un-doped magnesium needs 5 minutes of incubation time before it releases hydrogen. At 10 minutes, the magnesium hydride and Pd-doped magnesium hydride releases 0.76 wt% and 4.03 wt% hydrogen, respectively. After 40 minutes of hydrogen release, Pd-doped magnesium hydride almost releases all the absorbed hydrogen and the un-doped magnesium hydride only releases about 50% of the absorbed hydrogen.

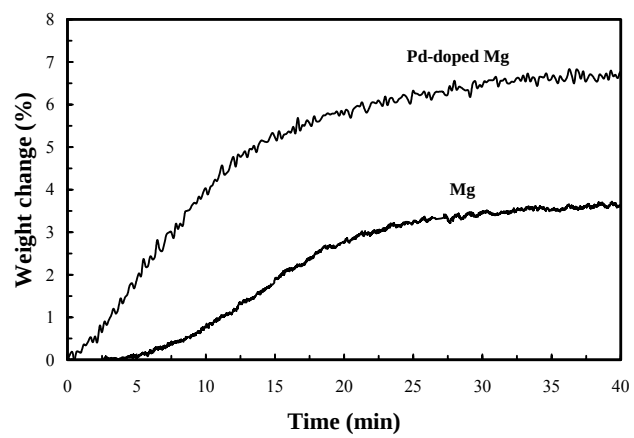

Figure 4. Effect of nanoparticle palladium catalysts on the hydrogen release properties of magnesium measured by TEOM at 613 K and under ambient pressure.

Conclusions

TEOM provides a dynamic, and more accurate information on the hydrogen absorption and release kinetics than the volumetric method or other gravimetric methods, which is important for the design of next-generation high-performance hydrogen storage materials and for the proper design of hydrogen storage devices in practical application.

Acknowledgement. Financial support from the Hydrogen Energy Center at the Pennsylvania State University in the form of a Seed Grant is highly appreciated.

References

(1) Bogdanoviæ, B.; Sandrock, G. *MRS Bulletin* **2002**, 712.
(2) Ströbela, R.; Jörissena, L.; Schliermannb, T.; Trappc, V.; Schützd, W.; Bohmhammele, K.; Wolfe, G.; Garchea, J. *Journal of Power Sources* **1999**, *84*, 221.
(3) Dillon, A. C.; Jones, K. M.; Bekkedahl, T. A.; Klang, C. H.; Bethune, D. S.; Heben, M. J. *Nature* **1997**, *386*, 377.
(4) Patashnick, R., TEOM measurement, Personal Communication.
(5) Zhu, W.; Graaf, J. M. v. d.; Broeke, L. J. P. v. d.; Kapteijn, F.; Moulijn, J. A. *Industrial Engineering Chemical Research* **1998**, *37*, 1934.
(6) Chen, D.; Gronvold, A.; Rebo, H. P.; Moljord, K.; Holmen, A. *Applied Catalysis A: General* **1996**, *137*, L1.
(7) Xu, X. C.; Song, C. S. *Preprints of Symposia - American Chemical Society, Division of Fuel Chemistry* **2003**, *48*, 941.

Mercury Regulatory Policy and Electric Utilities

Michael T. Rossler

Edison Electric Institute
701 Pennsylvania Avenue, NW
Washington, DC 20004-2696

Introduction

On December 15, 2003, Environmental Protection Agency (EPA) Administrator Leavitt signed the "Utility Mercury Reductions" proposal—the first-ever proposed rule to regulate mercury emissions from new and existing coal-based power plants and nickel emissions from new and existing oil-based power plants. The Utility Mercury Reductions proposal contains two alternative control plans—a market-based cap-and-trade approach and a Maximum Achievable Control Technology (MACT) standard. This paper will give a brief history, synopsis, and critique of this regulatory proposal, and how it compares to other proposed policies aimed at controlling mercury emissions from the electric utility industry.

Regulation of Power Plant Mercury Emissions

The Clean Air Act Amendments (CAAA) of 1990 authorize EPA to regulate mercury emissions and other air toxics from electric utilities, if necessary, to protect against specific threats to public health caused by these emissions. On December 14, 2000, EPA issued a "regulatory determination" under the Clean Air Act (CAA) that regulation of mercury is "appropriate and necessary" for coal- and oil-based power plants, and that certain other hazardous air pollutants (HAPs) pose a "potential concern for carcinogenic effects…[and] public health."[1] EPA listed coal-based power plants for regulation under §112(c) of the Clean Air Act—the list of source categories for which EPA must develop emissions standards based on the Maximum Achievable Control Technology (MACT). Under the MACT program, emissions restrictions based on the levels achieved in practice by the best performing 12 percent of plants must be applied to all existing plants.

The EPA regulatory determination noted, "there are uncertainties regarding the extent of the risks due to electric utility mercury emissions."[2] Previously, in its Mercury Research Strategy, in which EPA describes its strategic approach for its mercury research program through 2005, the agency stated that "[t]he amount of mercury deposited in the United States that can be directly attributed to domestic combustion sources remains uncertain."[3] Notwithstanding these conclusions, EPA began to craft a proposed standard for mercury that would require MACT. Under the terms of a consent decree, EPA proceeded on a track to issue a proposed rule by December 2003, a final rule by December 2004, and to require compliance by December 2007.

The December 2000 regulatory determination limited the EPA Administrator's policy options, specifically with respect to implementing a flexible and cost-effective program. Electric utilities are explicitly treated differently under the CAA than other major sources of HAPs. Under §112(n)(1)(A) of the CAA, EPA is not required to regulate electric utility plants using the MACT program. As EPA stated, "if EPA determines that regulation of mercury emissions from electric utilities is necessary and appropriate, EPA would have the full set of regulatory tools available under §112 to address those emissions, including §112(f), as well as any alternative control strategies the Agency has identified in its Report to Congress."[4]

Mercury Emissions From Power Plants

Trace amounts of mercury are naturally present in coal. As a trace metal that is emitted during coal combustion, mercury is transformed into three major chemical species: elemental, ionic (or oxidized), and particulate. The chemical species of mercury formed during the combustion process and post-combustion conditions vary significantly from one plant to another. Of the total mercury formed, the amount of elemental mercury varies from 10-90 percent. Elemental mercury usually travels great distances from its source, and can remain in the atmosphere for months to years. Ionic mercury is water soluble, and as such, falls or washes out of the air. Deposition of ionic mercury is typically in the local vicinity (50–100 km) of its source.

In order to assess mercury emissions from coal-based power plants, in 1998 EPA issued an Information Collection Request (ICR)[5] that required owner/operators to report for calendar year 1999 the quantity of fuel consumed and the mercury content of that fuel. In addition, 84 plants were selected to measure flue gas mercury emissions and its chemical form. Based on analysis of the ICR data, EPA concluded that U.S. electric utilities release about 48 tons of mercury every year, which is roughly one-third of the total anthropogenic emissions of mercury in the United States, less than 10 percent of total North American emissions, and about one percent of total global mercury emissions.

Mercury Controls

A power plant which burns fossil fuels for the generation of electricity is typically equipped with a high-efficiency baghouse—fabric filter (FF)—or electrostatic precipitator (ESP) for particulate removal; staged-combustion burner configurations for low-nitrogen oxides (NO_x) emissions; and post-combustion flue gas treatment devices for NO_x and sulfur dioxide (SO_2) control—selective catalytic reduction (SCR) and selective noncatalytic reduction (SNCR) technologies for NO_x control, and high-efficiency flue gas desulfurization (FGD) scrubbers for SO_2 control. Not all power plants utilize all these control devices. For example, about 65 percent of plants use only an ESP, 10 percent use only a FF, and 25 percent use a combination of an ESP and wet FGD to control particulates; about 25 percent of plants use scrubbers and the rest either use low-sulfur coal or fuel-switch to control SO_2.[6]

Mercury control options are highly dependent on the existing power plant's design, operating characteristics, and fuel used—in the case of coal, the type of coal used is also important. Thus, potential mercury emissions are unique to each unit. For some plants, mercury emission reductions of 70–90 percent may be impossible to achieve. In addition, there is still considerable uncertainty in the measurement of mercury emissions, since mercury CEMs will most likely not be commercially available, accurate, or reliable within the next few years.

The characteristics of the coal-based plant that most affect emissions of mercury and the type of control technology used are the mercury content and other chemical aspects of the coal (particularly the chloride content); the boiler operating conditions; the design and operation of any particulate collection devices; the design and operation of any flue gas treatment systems; and the use of advanced NO_x removal technology, such as SCR and SNCR.

In addition to removing specific pollutants, such as fine particulates, SO_2, and NO_x, currently installed air pollution controls may also remove mercury. Measurements at a variety of U.S. power plants performed under EPA's mercury ICR indicate that existing emission control devices for particulates (fly ash) and SO_2 capture, on average, approximately 40 percent of the mercury present in the flue gas from burning coal, as well as a large amount of non-mercury HAPs. Mercury removal rates, however, varied from 0 to more than 90 percent among the power plants that were tested.[7]

EPA, DOE, and others are in agreement that the implementation of further controls for reducing SO_2 and NO_x as required in the proposed Interstate Air Quality Rule (IAQR), will result in significant additional reductions in mercury emissions. Focusing on these "co-benefits" of reduced mercury emissions also would allow adequate time for the development and commercialization of mercury control technologies that are currently in progress.

MACT Alternative Control Plan

One alternative control plan in the Utility Mercury Reductions proposal to set national emission standards for hazardous air pollutants (NESHAP) pursuant to §112 of the CAA. The proposed §112 MACT rule would require coal- and oil-based power plants to meet HAP emissions standards reflecting the application of the MACT determined pursuant to the procedures set forth in CAA §112(d).

In October 2002, the final report of the Utility MACT Working Group was submitted to the Clean Air Act Advisory Committee. This report included recommendations of the "Industry Stakeholder Group," which comprised owners and operators of electric utility steam generating units from both the public and private sectors, fuel suppliers, labor unions, and others. The Group summarized major issues and posed options to be considered by EPA in developing a MACT rule.

Among the major issues raised, a couple remain with respect to the MACT alternative control plan: first, the presumptive three-year compliance period contained in §112(d) is too short. Based on real-world considerations, and particularly for those facilities that would be required to make major capital expenditures (e.g., installing a scrubber), it will take many years to bring all coal-fired electric utility steam generating units into compliance with a MACT standard. Second, the extremely restrictive emission limits for new sources do not appear to be justified based on the rationale for the emission limits for existing units.

Although the MACT alternative allows for some flexibility for power plants to achieve those reductions—subcategorization by coal type, accounting for variability in emissions and plant operations in the MACT floors, a 12-month rolling average to measure compliance, allowing facility-wide averaging, the format of the standard for existing units—analyses by the U.S. Energy Information Administration (EIA)[8] and others indicate that a command-and-control reduction program would be significantly more expensive than a cap-and-trade system that would achieve the same levels of mercury emission reductions.

Cap-and-Trade Alternative Control Plan

Emissions trading is a system of establishing a cap on emissions and allowing sources the flexibility to choose the emissions reduction plan that works best for their situation, including increasing efficiency, using lower-emitting fuels, installing pollution control equipment, and trading. Trading allows a source that can over-control its emissions to sell extra reductions to another source for which controls would be very expensive or technologically difficult (e.g., small units). Without trading, small units may have to shut down, even though their total emissions are low. Emissions trading gained prominence with the implementation of the Title IV (Acid Rain Control) trading program for SO_2 in the 1990 CAAA.

The other alternative control plan in the Utility Mercury Reductions proposal is a market-based cap-and-trade approach. The proposal would amend CAA §111 rules and would establish a mechanism by which mercury emissions from new and existing coal-based power plants would be capped at specified, nation-wide levels. EPA states that the primary goal of this approach is to reduce power plant mercury emissions 70 percent from current levels by 2018, and sets a 15 ton cap on these emissions in 2018. A near-term cap is also set in 2010 at a level that reflects mercury "co-benefits"—defined as the maximum reduction in mercury emissions that could be achieved through the installation of FGD and SCR units that will be necessary to meet the 2010 caps for SO_2 and NO_x in the proposed IAQR.

Some critics view emissions trading as "buying the right to pollute," expressing concern about local "hot spots" where emissions could increase as a result of emissions trading. Many groups accept this logic for mercury and oppose mercury trading due to perceived "localized effects on public health." Based on many years of real-world experience, studies of the SO_2 allowance trading program conducted by EPA,[9] the Environmental Law Institute,[10] and Resources for the Future[11] demonstrate that trading did not significantly change where emission reductions actually occurred. The clear success of the acid rain SO_2 trading program provides evidence to allay fears about localized effects.

There are two major reasons which suggest that localized effects will not occur with a mercury emissions trading program. One, the trading of allowances is most likely to involve large coal-based power plants controlling their emissions more than required and selling allowances to smaller plants. This viable assumption is based on the basic economics of capital investment in the utility industry. Under a trading system where emission-removal effectiveness is unrelated to plant size, it makes more economic sense for the utility to allocate pollution-prevention capital to its larger facilities than to smaller plants (since more allowances will be earned). Thus, any economies of scale of pollution control investment will favor investment at the larger plants. Two, the species of mercury that are deposited locally—oxidized and particulate mercury—are controlled by the same equipment that controls fine particles, SO_2 and NO_x. As noted earlier, these species of mercury are more likely to be deposited locally than gaseous elemental mercury, which is transported long distances from the source. As utilities install controls to comply with the new fine particle and ozone control regulations of the IAQR, a "co-benefit" in mercury control will accrue as particulate controls, scrubbers, and SCR units are installed on an increasing percentage of coal-based power plants. Therefore, the economics of a trading system are likely to favor controls of mercury that are likely to be deposited locally, thereby reducing any local hot spots.

Legislative Multi-Emissions Approach.

Many in government, industry, and academia believe that the current regulatory approach—with its uncoordinated and inconsistent air quality regulations—is duplicative, costly, and complex, and presents significant challenges and uncertainties. Coal-based electric generators are currently subject to more than 20 major environmental regulations aimed at reducing power plant air emissions. For these reasons, many policymakers and regulators have concluded that there is a better way to achieve air quality goals, while protecting the environment and public health. A "multi-emissions" strategy, if properly designed, could streamline the current regulatory process, provide greater certainty to electric companies, accomplish the nation's air quality goals at a fraction of the cost, and maintain a reliable supply of electricity.

The National Energy Policy report released in May 2001[12] noted that uncertainty about future environmental controls is of particular concern for companies that operate existing coal-based power plants, and that future coal electricity generation will need to meet new challenges to reduce mercury emissions. To address these concerns, the report recommended that EPA work with Congress to propose legislation that would establish a flexible, market-based program to reduce and cap emissions of SO_2, NO_x, and mercury from electric

power generators. The report concluded that such a program would provide significant public health benefits even as electricity supplies are increased.

As a result of the report's recommendations, numerous proposals have surfaced to reduce utility mercury emissions. These range from applying "co-benefits," to 90 percent-plus removal. In February 2003, the "Clear Skies Act of 2003" was introduced, which requires sulfur dioxide (SO_2), nitrogen oxides (NO_x), and mercury emissions from power plants to be reduced by about 70 percent over the next decade using a market-based cap-and-trade approach.

A legislative strategy for improving air quality—with clear, congressionally-mandated emissions cuts—would provide far greater certainty and produce air quality improvements almost immediately. The Utility Mercury Reductions proposal's cap-and-trade alternative approximates the requirements of the Clear Skies Act, but ultimately leaves the design of the program up to individual states. This could be potentially confusing to implement and prove more costly to electricity customers than a national cap-and-trade program, which would reduce emissions just as fast. The MACT alternative would be far more expensive—yet no more effective—than a cap-and-trade approach. EPA Administrator Mike Leavitt, in announcing the Utility Mercury Reductions proposal, said it best himself: "Enacting Clear Skies is by far the best route to better air quality in the most cost-effective manner."

Conclusion

Federal efforts to limit electric utility mercury emissions continues to proceed on two tracks. In the Utility Mercury Reductions proposal, EPA has recognized that scientifically justified and verifiable mercury reductions can be achieved while at the same time providing the electric utility industry some flexibility to achieve those reductions. Further, EPA acknowledges that this flexibility can be achieved by subcategorization based on coal type, and by taking into account plant operational variability over time in setting the emission limits. However, allowing for market-based mechanisms such as trading will help achieve overall reductions and further increase the cost-effectiveness of any program.

The scientific data underlying these policy options to reduce utility mercury emissions is still evolving. EPA recognized this in its explanation of the agency's proposal to revise the regulatory finding that it made on December 20, 2000. The electric utility industry continues to test the effectiveness of various pollution control systems in reducing mercury emissions, and is funding additional health effects, fate-and-transport, and other related research. Accordingly, electric utilities are committed to working with DOE and EPA to address concerns with respect to the efficacy of emerging, mercury-specific control technologies, which are relatively new and untested on a commercial scale.

The electric power industry is subject to a broad array of federal, state, and local statutes and regulations, and is one of the nation's most regulated industries. Electric companies have exceeded many statutory and regulatory emission reduction targets, despite a growing national demand for electricity and increased electricity production. The electric utility industry understands the importance of continuing to work with EPA as the regulatory process proceeds to the next step of promulgating a final rule.

As federal efforts continue, the industry will work to ensure that critical data on the effectiveness of various pollution control systems, as well as health effects and other important related research, are available to assist EPA in developing a mercury emissions reduction program that is protective of public health, scientifically sound, flexible, and cost-effective.

References

1 Regulatory Finding on the Emissions of Hazardous Air Pollutants from Electric Utility Steam-Generating Units. *Fed. Regist.* **2000**, *65*, 79825-79831 (December 20, 2000).

2 Ibid.

3 *Mercury Research Strategy*; EPA/600/R-00/073; U.S. Environmental Protection Agency: Washington, DC; September, 2000.

4 Regulatory Finding on the Emissions of Hazardous Air Pollutants from Electric Utility Steam-Generating Units. *Fed. Regist.* **2000**, *65*, 79825-79831 (December 20, 2000).

5 Agency Information Collection Activities: Proposed Collection; Comment Request; Electric Utility Steam Generating Unit Mercury Emissions Collection Effort. *Fed. Regist.* **1998**, *63*, 17406-17409 (April 9, 1998).

6 Brown, T.D.; Smith, D.N.; Hargis, R.A.; O'Dowd, W.J. Mercury Measurement and Its Control: What We Know, Have Learned, and Need to Further Investigate; *J. Air & Waste Manage. Assoc.* **1999**, *49*, 1-97.

7 An Assessment of Mercury Emissions from U.S. Coal-Fired Power Plants—Final Report; Electric Power Research Institute: Washington, DC; September 2000.

8 *Analysis of Strategies for Reducing Multiple Emissions from Electric Power Plants: Sulfur Dioxide, Nitrogen Oxides, Carbon Dioxide, and Mercury, and a Renewable Portfolio Standard*; U.S. Energy Information Administration: Washington, DC; July 2001; available online at *http://www.eia.doe.gov/env/env_pub.html*.

9 Acid Deposition Standard Feasibility Study; U.S. Environmental Protection Agency: Washington, DC; available online at http://www.epa.gov/airmarkets/articles/depfeas/index.html.

10 Swift, B. Allowance Trading and Potential Hot Spots—Good News from the Acid Rain Program; *Environment Reporter*, Vol. 31, May 12, 2000.

11 Burtraw, D.; Mansur, E. Environmental Effects of SO2 Trading and Banking; *Environ. Sci. Tech.*, **1999**, *33*.

12 Report to the National Energy Policy Development Group; available online at *http://www.whitehouse.gov/energy*.

ASSESSING THE IMPACTS OF LOCAL DEPOSITION OF MERCURY ASSOCIATED WITH COAL-FIRED POWER PLANTS

T. Sullivan[1], B. Bowerman[1], J. Adams[1], C. Ogeka[1], F. Lipfert[2], S. Renninger[3]

[1]Environmental and Waste Technology Division
Brookhaven National Laboratory
Upton, NY 11973
[2] Private consultant
[3] Department of Energy, National Energy Technology Laboratory

Introduction

Mercury emissions from coal fired plants will be limited by regulations enforced by the Environmental Protection Agency. However, there is still debate over whether the limits should be on a plant specific basis or a nationwide basis. The nationwide basis allows a Cap and Trade program similar to that for other air pollutants. Therefore, a major issue is the magnitude and extent of local deposition.

Computer modeling suggests that increased local deposition will occur on a local (2 to 10 Km) to regional scale (20 to 50 Km) with the increase being a small percentage of background deposition on the regional scale.[1,2] The amount of deposition depends upon many factors including emission rate, chemical form of mercury emitted (with reactive gaseous mercury depositing more readily than elemental mercury), other emission characteristics (stack height, exhaust temperature, etc), and meteorological conditions. Modeling suggests that wet deposition will lead to the highest depostion rates and that these will occur locally. Dry deposition is also predicted to deposit approximately the same amount of mass as wet deposition, but over a much greater area.[2] Therefore, dry deposition rates will contribute a fraction of total deposition on the regional scale.

The models have a number of assumptions pertaining to deposition paramaters and there is uncertainty in the predicted deposition rates. A key assumption in the models is that the mixture of reactive gaseous mercury (RGM) to elemental mercury Hg(0) is constant in the exhaust plume. Recent work suggests that RGM converts to Hg(0) quickly. Deposition measurements around coal-fired power plants would help reduce the uncertainties in the models,.

A few studies have been performed to examine the deposition of mercury around point sources. Measurement of soil mercury downwind from chlor-alkali plants has shown increased deposition within a few Km.[3] Studies of soils, sediments, and wet deposition around coal plants typically find some evidence of enhanced deposition; however, the statistical significance of the results is generally weak. A review of these studies is found in Lipfert.[4]

This study combines combines modeling of mercury deposition patterns with soil mercury measurements. The model used emissions data, meteorological conditions, and plant data to define sample locations likely to exhibit deposition in excess of background, that can be attributed to the power plant. Data were collected at the specified locations in November, 2003.

Deposition Modeling

In this attempt to validate the modeled enhanced deposition of Hg around coal-fired power plants, a field study was conducted around a large coal-fired power plant in the Midwest. The plant typically emits several hundred pounds of mercury per year. Meteorological data for a five year period were reviewed to determine wind patterns under dry and wet conditions. Under dry condtions, the prevailing winds ran along an axis from the nortwest towards the southeast. Winds occurred regulary in each direction along the axis. Under wet conditions, winds were generally from the north and east. This leads to predictions of wet deposition near the plant and to the southwest. Deposition modeling based on the meteorological data predicted highest deposition rates within 10 Km of the plant in a southwesterly direction, Figure 1. Dry depostion rates were lower than wet depostion rates and were not predicted to be a major contributor to deposition in the region. This analysis was used to select appropriate sample locations in the vicinity of the plant.

Experimental

Soil Samples. Soil samples were collected at 54 selected sites around the coal-fired power station as shown in Figure 1. At each site, five samples were collected. Three surface samples from the top five centimeters of soil separated by approximately 3 m, one deep sample at a depth of 5 – 10 cm, and one sample of the vegetation. The general layout of sample locations suggested by the modeling was modified to account for site-specific conditions (e.g., inaccessibility of sample locations, site activities, and changes in soil type which would alter background levels of mercury). The sampling area south and west of the plant covered an approximately square region of 64 km^2. The land surrounding the power plant was either part of an active strip mine or agricultural. Although many sampling sites were within the strip mine permit area, most of the land had been reclaimed. Strip mine personnel identified sites that had been fully reclaimed, or were at least known not to have been disturbed for at least a year. Agricultural area sampling sites were chosen because they appeared undisturbed for at least one year (i.e. had not been plowed). Many of the agricultural sites were at the crest of roadside ditches, adjacent to a plowed or mowed area.

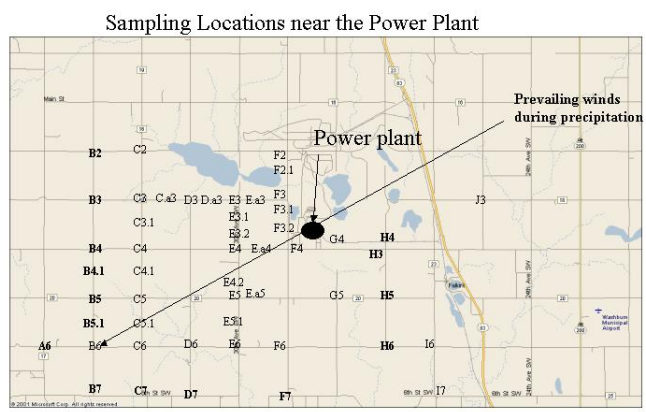

Figure 1. Soil Sample locations around the power plant.

Samples of approximate 100 grams weight were collected in water-tight wide-mouth 250 mL plastic screw-top cups. Samples were collected using stainless steel trowels, which were rinsed with tap water and wiped dry between each use. Blind field duplicates were collected every 10th sample. Latitude and longitude for each sample location were identified using a GPS locator system (Garmen Etrex) with a resolution of 6 meters.

Mercury Analysis Methods. The soil samples were shipped back to Brookhaven National Laboratory for analysis using a Direct Mercury Analyzer (DMA-80, Milestone, Inc, Monroe, CT). In the DMA-80, controlled heating in an oxygenated decomposition furnace liberates mercury from the solid samples. Flowing oxygen to the catalytic section of the furnace carries the decomposition products, where oxidation is completed and halogens and nitrogen/sulfur oxides are trapped. The remaining decomposition products are then carried to a gold amalgamator that selectively traps mercury. After the system is flushed, the amalgamator is rapidly heated, releasing mercury vapor, which is then carried through absorbance cells positioned in the light path of a single wavelength (253.7 nm) atomic absorption spectrophotometer. The typical working range for this method is 0.05-600 ng of mercury. Since soil samples are at most about 0.5 grams, the DMA-80 easily measures levels below 1 ppb (ng/g).

DMA-80 analyses were conducted on soil samples as is. Moisture content was determined separately for all samples, and mercury concentrations were adjusted to a dry weight basis.

Quality assurance was evaluated through taking blind duplicates of 10% of the samples, measurement of empty sample boats in the DMA-80, and use of two NIST mercury soil standards (SRM 2709 and SRM 2710) at every 10th measurement. Soil samples will be counted in triplicate to examine for heterogeneity of the samples.

Results and Discussion

Sample analysis is underway and all of the soil locations have been analyzed for mercury, on as received (wet) basis at least once. At each sample location, the three surface soil samples were averaged to give a composite. Typically, the three adjacent surface samples from any site had agreement in the mercury levels to within 10%. At the fifty-four locations the average value was 21.5 ng/g (wet weight basis), with a standard deviation of 5.7. The minimum value was 8.9 ng/g and the maximum value was 43 ng/g.

Comparison between the predicted deposition versus measured mercury concentrations in the soil was accomplished by placing the deposition map over the sampling map coded to measured concentration. Areas of increased deposition are anticipated to have increased soil mercury concentrations. Figure 2 is the graphical representation of the analysis. Predicted regions of enhanced deposition are covered by the dark filled contour. Sample locations with symbols representing measured mercury levels represent the measured data.

Examining Figure 2 shows that the modeled and measured data match reasonably well. The overall shape of the region of excess deposition matches, however, the measured data suggest that the main finger of the plume is slightly south of the area predicted by modeling. There is scatter in the data, as expected with an environmental data set. Statistical analyses will be performed to determine the degree of confidence in these results. The results presented are preliminary and will be refined after completion of the analysis of all soil and vegetative samples.

Although there is evidence of excess deposition near the plant, mass balance calculations comparing emissions with increased soil levels of mercury indicate that less than 5% of emissions are deposited over the sampling domain.

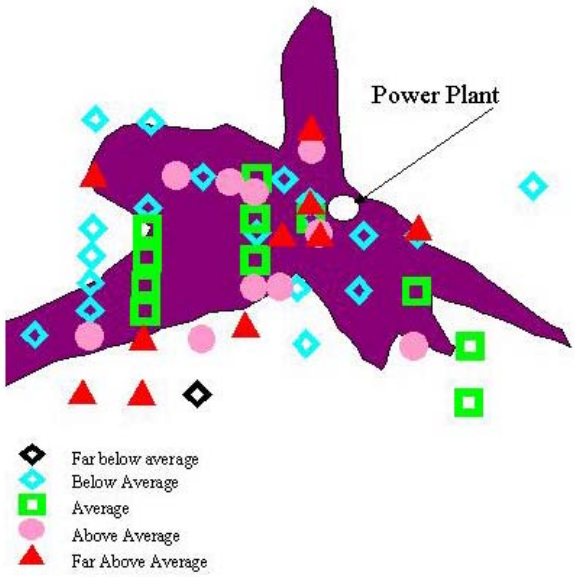

Figure 2. Comparison of modeled deposition pattern (solid contour) with measured data.

Acknowledgment

The National Energy Technology Laboratory, Office of Fossil Energy, U.S. Department of Energy supported this work.

References

1. U.S. EPA. " Mercury Study Report to Congress, Vol. III:" EPA-452/R-97-005, December **1997**.
2. Sullivan, T.M., Lipfert, F.D., Morris, S.M., BNL-7554-2003, May **2003**
3. Biester, H., Muller, G., Scholer, H.F., Sci of the Tot.Env., **2002,** 284, 177-189,.
4. Lipfert, F., Sullivan, T., Renninger, S., (this proceedings), ACS Symposium, **2004**.

ASSESSING THE MERCURY HEALTH RISKS ASSOCIATED WITH COAL-FIRED POWER PLANTS: ISSUES IN ATMOSPHERIC PROCESSES

F. Lipfert[1], T. Sullivan[2], S. Renninger[3]

1. Consultant, Northport, NY
2. Brookhaven National Laboratory, Upton, NY
3. U.S. Department of Energy, Pittsburgh, PA

Introduction

The rationale for regulating air emissions of mercury from U.S. coal-fired power plants largely depends on mathematical dispersion modeling, including the atmospheric chemistry processes that affect the partitioning of Hg emissions into elemental (Hg_0) and the reactive (RGM) forms that may deposit more rapidly near sources. This paper considers and evaluates the empirical support for this paradigm. We consider the extant experimental data at three spatial scales: local (< 30 km), regional (< ~300 km), and national (multi-state data). An additional issue involves the finding of excess Hg levels in urban areas.

Local Evidence

Our search of the literature found seven studies dating back 30 years in which various manifestations of local Hg deposition were related to coal-fired power plants (Table 1). These experiments involved concentrations of Hg in soil, lake sediments, precipitation and fish. To place these results in a common framework, we estimated the relationships between background concentrations and those obtained near the plant and the fractions of emitted Hg that had been deposited and retained during the period of facility operation. Where possible, we accounted for these relationships as a function of the receptor's distance from the plant.

Soil Composition. The earliest attempts at assessing Hg impacts from coal-fired power plants were based on the Hg content of surficial soil samples[1-3]. This technique is highly dependent upon definition of the background soil content, which was not always reliable. The reported incremental Hg concentrations ranged from 29%[1] to 42%[2] above background, corresponding to retention of 3-5% of cumulative emissions. The Four Corners study[3] did not measure background but concluded that "mercury was not accumulating in the soil", based mainly on comparisons of local soil Hg concentrations with those reported in the literature for other locations. However, reanalysis of the published data on individual soil samples shows a significant overall (log-log) slope of -0.11 ($p < 0.005$) as a function of downwind distance. Moreover, scatter plots showed wide variation by wind direction, a more rapid decrease in soil Hg near the plant, and the suggestion of a secondary peak at about 10-15 km downwind. A possible rationale might thus be a close-in peak due to rainout and a more distant peak due to plume touchdown and dry deposition. We assumed various values of background Hg in order to estimate the fraction of emissions deposited and retained in the soil; the wide range of these estimates shows the sensitivity to this parameter. It appears that around 10% of the plant's Hg emissions may have been deposited and retained in the soil, which would correspond to excess deposition rates of about 60%. Such estimates are also sensitive to the maximum downwind distance considered, which was 20-30 km in these various examples.

Sediments. Three studies[2,5,6] include data on the Hg content of sediment cores obtained from nearby water bodies. This technique has the advantage of potential relevance to impacts on fish but has the disadvantages of uncertain time periods and the difficulty of considering decay rates in terms of downwind distance. At the Kincaid plant[2], the excess Hg in sediments was reported to be about 30%. In Texas[6], there was about 18% more Hg in sediments from a lake near the plant than from two lakes about 30 km away. The decreases in Hg with depth within the core were also substantially larger in the sediment cores from the nearby lake.

Precipitation. Two studies[5,7] considered variations in the Hg content of precipitation as a marker for local impact. In Slovenia[5], it was not clear that valid annual averages had been obtained and no comparisons were made with local background. In Indiana[7], the authors reported no significant difference between the precipitation Hg data collected near the power plant and that collected at 3 other sites in the state. However, precipitation chemistry is frequently sensitive to the rate and thus amount of precipitation, and when this factor is taken into account in a multiple regression analysis, the site near the plant appears to have an excess Hg level of about 12% (Figure 1). With normalized deposition (deposition/precipitation) as the dependent variable, the increment is just significant ($p < 0.03$).

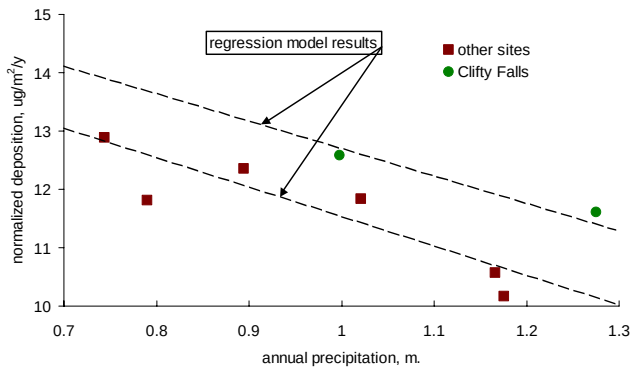

Figure 1. Comparison of wet deposition at Clifty Falls Mercury Deposition Network (MDN) monitoring site.

Fish Hg Content. Two studies[2,4] reported the Hg content found in various species of fish collected in or near the impacts zones of power plants. At Kincaid[2], the fish caught near the plant had substantially less Hg than those from more distant locations, but it was not clear whether this comparison included adjustments for fish size. For each of the 23 farm ponds in the Dickerson study[4], fish lengths and detailed water chemistry data were also reported, which turned out to be important. To examine these factors, we estimated wet deposition of Hg to each pond based on the modeled isopleth plots in the paper. In multiple regression analysis, the log of fish Hg content was significantly ($p < 0.01$) associated with the log of wet Hg deposition (coefficient = 0.5), pond water conductivity (coefficient = -0.5), and fish length for sunfish and bass pooled (n=37). Fish length was essentially a surrogate for fish species. Water conductivity, hardness, and alkalinity were highly inter-correlated; pH was not a significant predictor of fish Hg. Water quality was not associated with estimated Hg wet deposition. Figure 2 is scatter plot of these data, based on fish Hg adjusted to a common level of pond water conductivity. Note that only one sample clearly exceeds the EPA guideline for fish Hg content (0.3 ppm), notwithstanding the effects of the power plant; 3 samples exceeded this level in the unadjusted data.

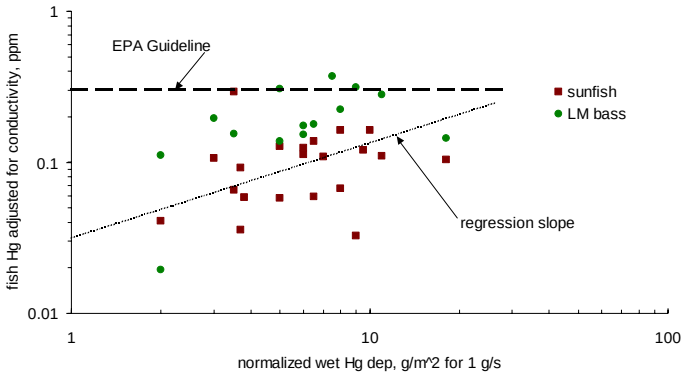

Figure 2. Comparison of measured fish Hg (ppm) as a function of predicted wet deposition.

Regional Data

As an example of regional relationships, we used data on Hg emissions from power plants[8] and on 1998-2002 wet Hg deposition obtained from the Mercury Deposition Network (MDN)[9], both for Pennsylvania. The 8 MDN stations operated for various portions of this period; each annual wet deposition estimate was thus treated as a separate observation (n=22). The straight-line distance between each MDN site and each of the 36 plants, whose Hg emissions ranged from 637 kg to 45 g, totaling 3622 kg, was computed from latitude-longitude data, and each emission rate was weighted by the inverse square of this distance and summed. For the 8 MDN sites, these sums ranged from 0.09 kg/km^2 to 1.7 kg/km^2.

Multiple regression analysis was then used to deduce source-receptor relationships, considering the year, site elevation, and site latitude as possible confounders. No account was taken of other point sources of Hg (such as urban areas or out-of-state sources) or of prevailing wind directions for precipitation events. MDN site latitude was included as a possible confounder because the national map of Hg wet deposition seems to show consistent increases from north to south in the eastern states.

The coefficients for site elevation and year were far from significant and were dropped from further consideration. Latitude and (emissions/distance^2) were moderately (negatively) correlated, which posed a co-linearity problem. However the best fit to these 22 observations was obtained in a log-log regression based on the emission parameter alone, which had a log-log coefficient of 0.11 ($p<0.010$). This result implies that 11% of the wet Hg deposition in Pennsylvania is associated with coal-fired power plants in the state, under the modeling assumptions stated above. It also implies that wet deposition of Hg may decrease more slowly with downwind deposition than originally assumed. However, when various assumed levels of background wet deposition are subtracted from the measured MDN values, the regression coefficients are increased, at the expense of poorer model fits.

As an example, this empirical model would predict the following annual deposition (μg/m^2)-distance relationship for an isolated point source of 636 kg Hg per year: 1 km., 19.5; 3 km, 15.3; 10 km, 11.7, 30 km, 9.2; 100 km, 7.1. Taking the last figure as "background", the annual wet deposition would be about 1.1% of emissions and the total Hg deposition, about 2.2%.

Additional information on Hg deposition at the regional scale is provided by the results of Lopez-Alonzo et al.[10], who analyzed the Hg content of calf kidneys in relation to distances between the farms and major point sources of Hg in Northwest Spain. (e.g. 1200 kg/y from coal-fired power plants and similar amounts from other industries). Downwind distances ranged up to 140-200 km; the duration of this deposition was not mentioned. Based on approximations from the scatter-plots[10], it appears that deposition decreased with downwind distance to the 0.4 power for the power plants and 0.7 power for the industrial area. Neither of these slopes is significantly different from the expected square-root relationship.

The National Scale

We used state-level data on Hg deposition (MDN) and fish Hg concentrations[11] to deduce larger scale source-receptor relationships. The deposition data were averaged over time (1997-2002) and the fish Hg data were considered by species (9 different species). A simple regression model was used in which ln(fish Hg) was regressed against ln(deposition) and dummy variables for fish species. This model assumes that all species react to deposition in the same way and provides fish Hg concentration increments relative to a referent species, in this case large-mouth bass. This approach provided 105 combinations of states and fish species (only 31 states were represented). Channel catfish, bluegills, common carp, white suckers, and yellow perch all had significantly lower Hg concentrations than bass, walleye, or northern pike (as expected). However, the effect of Hg deposition, as averaged over entire states, was significantly negative in this model ($p < 0.025$). Latitude was not an important confounder when both eastern and western states were considered. When large-mouth bass were considered alone (n=20), the relationship with deposition was positive but far from significance (log-log coefficient = 0.21).

A further consideration at the national scale is provided by the recent global modeling study of Seigneur et al.[12], who estimated that 25-32% of the total Hg deposition to the contiguous US came from North American anthropogenic sources. These sources total 200.1 metric tons/y, of which electric utilities comprise 52.7 tons, or 26.3%. Assuming proportionality, the utility share of deposition would then be about 6.6-8.4%, which is in line with the various estimates above that are based on actual measurements. Comparison of these figures suggests a minor role for Hg deposition at distances > ~100 km.

Discussion

The above findings lead to the overall conclusion that atmospheric deposition of Hg is affected by emissions from coal-fired power plants. However, because of the numerous assumptions required and the use of simplistic models, it is not possible to accurately describe these relationships on this basis. Complex atmospheric chemistry and dispersion models are required to predict precise concentration and deposition contributions, and aquatic process models are required to predict effects on fish.

These caveats notwithstanding, it is still useful to summarize the consistencies and inconsistencies in our findings. In terms of excesses over background, we see local soil concentration Hg increments of 30%-60%, sediment increments of 18-30%, and wet deposition increments of 11-12%. If we accept the finding[7] that fish Hg is proportional to the square root of wet deposition (after controlling for water chemistry), then the contribution of coal-fired power plants to fish Hg would be about 5-6%. It is possible that the absence of local impacts on fish at Kincaid was due to water chemistry. Local differences in water chemistry may also help explain the absence of a relationship between state-level fish concentrations and wet deposition levels.

Effects on public health should be less than a few percent as more than 90% of the population currently meets the EPA exposure guideline and few individuals consume large quantities of fresh-water fish where coal is burned.

Finally, it should be noted that none of these simple analyses have accounted for possible impacts from urban areas, as implied by recent findings of excess urban deposition.[13,14] A mass-balance study of Hg deposition to Lake Michigan[15] showed a slow rate of decrease in deposition (in terms of distance from Chicago), as did the data on power plants discussed above.

Given the resources required to control mercury from power plants, a comprehensive campaign to measure their mercury impacts in detail and to monitor any ensuing changes would be prudent.

Acknowledgment

This work was supported by the National Energy Technology Laboratory of the U.S. Department of Energy.

References

1. Klein, D.H., Russell, P., *Environ Sci Tech*, **1973**, *7*, 357-8.
2. Anderson, W.L., Smith, K.E., *Environ Sci Tech*, **1977**,*11*, 75-80.
3. Crockett, A., Kinnison, R.H., *Environ Sci Tech*, **1979**, *13*, 712-5.
4. Pinkney, A.E., Logan, D.T., Wilson, H.T., *Arch Environ Contam Toxicol*, **1997**, *33*, 222-9.
5. Kotnik, J., Horvat, M., Mandic, V., Logar, M., *Science Total Environ*, **2000**, *259*, 85-95.
6. Menounou, N., Presley, B.J., *Arch Environ Contam Toxicol*, **2003**, *45*, 11-29.
7. Risch, M., in Proc. Great Lakes Regional Workshop, Measuring Atmospheric Mercury: Goals, Methods, and Results. March 26, **2003**. Available at http://www.deq.state.mi.us/documents/deq-aqd-toxics-HgWorkshop.doc
8. State Mercury Emissions Estimates from Power plants, June **2001**, http://www.epa.gov/ttn/atw/combust/utiltox/utoxpg.html#DA1
9. Mercury Deposition Network, http://nadp.sws.uiuc.edu/mdn/
10. Lopez Alonzo, M., Benedito, J.L., Miranda, M., Fernandez, J.L., Castillo, C., Hernandez, J., Shore, R.F., *Environ Pollut*, **2003**, *125*, 173-81.
11. Environmental Protection Agency, "The National Survey of Mercury concentrations in Fish: Data Base Summary 1990 - 1995," EPA 823-R-99-014, **1999**.
12. Seigneur, C., Vijayaraghavan, K., Lohman, K., Karamchandani, P, Scott, C., *Environ Sci Tech*, in press.
13. Landis, M.S., Vette, A.F. Keeler, G.J., *Environ Sci Tech*, **2002**, *36*, 4508-17.
14. Nadim, F., Perkins, C., Liu, S., Carley, R.J., Hoag, G.E., *Chemosphere*, **2001**, *45*, 1033-43.
15. Landis, M.S., Keeler, G.J., *Environ Sci Tech*, **2002**, *36*, 4518-24.

Table 1 Local Hg deposition from coal-fired power plants

		emissions	deposition data, ppb in soils, ug/m^2/yr in precip				percent	
reference	plant data	kg/y	type	# samples	mean	background	deposited	remarks
Klein & Russell	Campbell, MI (?)	~290	soil	90	10.2	7.9	2.7	irregular impact area
(1973)	650 MW							
	122 m stack							
Anderson & Smith	Kincaid (IL)	531	soil	90	22	15.5	4.6	limited to 1 sector of the impact area
(1977)	1200 MW		sediment	36	49	37		~1% of emissions deposited in lake
	2 152 m stacks		fish	120	70-82	110-560		fish near plant unaffected
Crockett & Kinnison	Four Corners (NM)	595	soil	70	14.5	*0	20.6	*assumed background values
(1979)	2150 MW					*3	16.3	
	2 76, 2 91 m stacks					*6	12.0	
						*9	7.8	
Pinkney et al.	Dickerson (MD)	~240	fish	69 sunfish				fish Hg in 23 small farm ponds
(1997)	543 MW			42 LM bass				increased with (Hg dep)^0.5
Kotnik et al.	Sostanj, Slovenia	314	precip		7.4-13.7 ug/m2		5	based on 20 km radius and dry dep = wet
(2000)	775 MW		lake sediments		53-166			higher values in surface layers
	100, 150, 230 m stacks							
Menounou & Presley	Gibbons Cr (TX)	~430	lake	13	94	80	30	based on 25 km radius and median
(2003)	460 MW		sediments	(cores)	(data from top layers)			excess deposit of 0.094 ug/cm2
Risch (2003)	Clifty Cr (IN)	184	precip	4 sites,	12.3	11		ug/m2/y at 110 cm precip
	1300 MW			2 yrs				(monitor 3 km from plant)
								Other plants in Ohio and Kentucky
								not considered

EVALUATION OF COAL COMBUSTION BY-PRODUCT MERCURY RERELEASE POTENTIAL

Loreal V. Heebink and David J. Hassett

University of North Dakota
Energy & Environmental Research Center
15 North 23rd Street
Grand Forks, ND 58203

Introduction

Mercury, known to be present in coal combustion by-products (CCBs) including primarily fly ash and flue gas desulfurization (FGD) materials, presents a potential environmental problem depending on the stability of the mercury under a variety of reuse of disposal conditions. The U.S. Environmental Protection Agency (EPA) announced on December 14, 2000, that it would regulate Hg emissions from coal- and oil-fired electric utility steam-generating power plants. EPA plans to issue final regulation by December 2004 and is expected to require compliance by December 2007.[1] As technologies are developed to reduce the air emissions of Hg, the amount of Hg in CCBs will likely increase. Recent studies have indicated that from 0% to 70% of the Hg originally in the coal can be associated with the fly ash.[2,3]

The Energy & Environmental Research Center (EERC) has investigated the potential for the rerelease of Hg from CCBs under a variety of conditions in an effort to address various ash management scenarios. Four conditions that have been examined are leaching, long-term ambient-temperature vapor release, microbiologically mediated vapor release, and high-temperature thermal release.[4,5] Leaching of CCBs has been ongoing at the EERC for over 25 years and vapor and thermal release methods have been investigated for the last several years.

Leaching is the most likely mechanism of transport of constituents from disposed or utilized CCBs contacted by water. Leaching is typically performed on CCBs to characterize them for management purposes. Recently, EPA proposed a leaching method for evaluating CCBs based on its interest in CCBs that may be affected by Hg emission controls. These recommendations do not adequately address some typical long-term behaviors of reactive alkaline CCBs under hydration conditions.

Thermal release, particularly of Hg, is important for long-term utilization, storage, and disposal of CCBs. Although the concentration of Hg in CCBs is relatively low, the large volumes of CCBs produced annually cause concern about potential Hg release. Ambient, near-ambient, and elevated-temperature studies of Hg release have resulted in the development of apparatuses to determine Hg release from CCBs. Vapor transport experiments evaluate Hg release from a bed of CCBs at ambient and near-ambient temperatures with constant airflow through the bed. The design of these and future experiments is critical to produce laboratory results that can be compared to field experiments at CCB management sites.

The wide distribution and variety of microorganisms in the environment indicate that microbiological Hg release needs to be investigated. A wide variety of specific microbe interactions can affect key elements associated with CCBs, including oxidation–reduction and alkylation–dealkylation reactions. In order for microbes to be metabolically active, a few constraints must be satisfied. In some CCB management options, these criteria are unlikely to be met, but for options where they can be met, laboratory experiments will simulate appropriate scenarios.

Experimental

Work is ongoing at the EERC to examine the rerelease of Hg from CCBs under four conditions including leaching, long-term ambient-temperature vapor release, microbiologically mediated vapor release, and high-temperature thermal release up to 700°C. CCBs with atypically high levels of total Hg content were selected as having a significant potential for releasing measurable amounts of Hg vapor for use in the long-term ambient-temperature and microbiologically mediated vapor-release experiments.

Leaching. Leaching of CCBs using various batch laboratory methods has been ongoing at the EERC for over 27 years. It became apparent early in EERC work that the methods being advocated and used were generating scientifically invalid and often misleading data. The EERC identified the inappropriate use of acetic acid in leaching solutions for CCBs understanding that CCBs would be unlikely to contact acetic acid under typical management conditions. Agreement by numerous research groups and government agencies that the use of acetic acid-based leaching solution is not appropriate for CCBs has led to many questions regarding what leaching methods are appropriate. Work at the EERC identified formation of secondary hydrated phases in alkaline CCBs, and it was determined that formation of these hydrated phases had a demonstrated influence on concentrations of certain trace elements in leachate. As a result of these observation, the EERC developed the SGLP (synthetic groundwater leaching procedure), including long-term leaching (LTL), to address discrepancies with existing methods.[6]

The SGLP batch-leaching procedure is a relatively simple test that follows many of the conditions of the toxicity characteristic leaching procedure (TCLP), EPA Method 1311.[7] The test utilizes a 20:1 liquid-to-solid ratio, end-over-end agitation at approximately 30 rpm, and usually employs a leaching solution consisting of water from the site, water that has been prepared in the lab similar to water likely to contact the ash, or distilled deionized water. For the long-term component of this procedure, multiple bottles are set up and analyzed at different time intervals. A typical SGLP and LTL test might consist of 18-hour, 30-day, and 60-day equilibration times. Although 60 days is often not long enough to have achieved complete equilibrium, it is generally long enough to determine the concentration evolution of individual parameters. The most important factor when performing LTL is to have at least three equilibration times to determine a true trend.

The majority of the leachate data on file was generated using leaching procedures with a 20:1 liquid-to-solid ratio with a few 4:1 liquid-to-solid ratio leachings. The 20:1 liquid-to-solid ratio leaching procedures included SGLP, LTL with 30- and 60-day equilibration times, TCLP, synthetic acid leaching (SAL), and synthetic precipitation leaching procedure (SPLP).[8] Distilled deionized water leachings were completed with 18-hour, 2-week, and 4-week equilibration times using a 4:1 liquid-to-solid ratio.

A wide variety of CCBs have been leached at the EERC. Sample types have included atmospheric fluidized-bed combustion (AFBC) char fly ash, AFBC spent bed material, boiler slag, bottom ash, circulating FBC fly ash and bottom ash, coal fines, FBC bottom ash, FBC fly ash, FGD material, and FGD–fly ash mixtures, fly ash, fly ash with Hg sorbent material, and particulate test combustor (PTC) fly ash.

Long-Term Ambient-Temperature Vapor Release. Long-term vapor release of Hg has been investigated utilizing six CCB samples obtained from members of the Coal Ash Resources Research Consortium^{K} (CARRC^{K}). The ashes selected included two eastern bituminous fly ashes, two South African fly ashes, one Powder River Basin (PRB)–pet coke fly ash, and one PRB FGD material.

A 150-gram aliquot of ash was placed and compacted into 250-mL tall wide-mouth bottles with a bonded Teflon liner cap. The cap was drilled with two holes to accommodate a Teflon outlet bulkhead fitting and a silicone tube for gas inlet (see Figure 1). Two samples of each CCB were set up for duplicate analyses. Breathing-quality air from a cylinder was passed through several sets of gold-coated quartz traps for Hg removal and admitted to each of the bottles through a gas distribution manifold that routed the gas through 0.23-mm gas chromatography (GC) capillary tubing to each of the individual bottles. The pressure drop across the GC capillary tubing allowed for the regulation of air flow through each bottle by simply adjusting the length of tubing to each bottle. The length of tubing was a nominal 65 cm using GC tubing with an ID of 0.25 mm. This length of tubing, when pressurized to between 1 and 2 psig through a gas distribution manifold, provided a convenient means of regulating gas flow to approximately 2 cm^3/min. Because of the variability of particle sizes between different ash samples, the sample with the initial highest gas flow was left with a 65-cm length of GC tubing and other samples had their tubing lengths shortened until all samples had approximately the same flow rate. The air exiting the GC tubing was given a final scrubbing to remove Hg vapor using gold-coated quartz just prior to entering the bottle containing the CCB. After entering the bottle, the air passed through the ash and exited to a central Hg collection tube containing two separate gold-coated quartz traps. The gold-coated quartz nearest the exit bulkhead fitting was analyzed at regular intervals to determine the mass of Hg vapor released from the CCBs while the top trap, in the same tube, was present to prevent Hg contamination from atmospheric Hg. This setup is clearly illustrated in Figure 1.

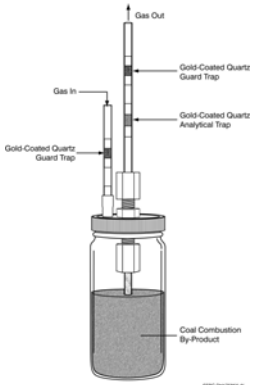

Figure 1. Long-term Hg-vapor release collection apparatus.

The gold-coated quartz collection tubes were desorbed for analysis by heating to approximately 500°C, and the mass of Hg released was determined using atomic fluorescence. The tubes were desorbed several times with varying periods of collection over the length of the experiments. Following the collection of Hg from the CCBs in Test 2, blank values were determined for each separate bottle by emptying the bottles of ash and flowing gas through the empty bottles for two 90-day periods. The gold-coated quartz tubes were analyzed for Hg as described above.

Microbiologically Mediated Vapor Release. Four CCBs have been examined for the microbiologically mediated vapor release of Hg. The tested CCBs have included a neutralized subbituminous FGD material, a hydrated subbituminous fly ash, and two eastern bituminous fly ashes.

The apparatus used for this testing has been improved numerous times over the course of the research; therefore, only the latest setup will be described here. A 250-mL Erlenmeyer flask fitted with an impinger inlet/outlet tube with the inlet center shortened to 6 cm below the standard taper. Gas inlet flow was regulated in the same manner as in the long-term Hg vapor release experiments described above; however, all GC capillary tubing was approximately 60 cm in length. The Hg vapor-collection system differed from the long-term ambient-temperature setup, consisting of two traps. The nearest trap contained Supelco Carbotrap, which collected organomercury compounds. This was followed by a gold-coated quartz trap, which collected Hg^0.

The flasks were placed on a 16-flask wrist-action shaker. The experimental matrix consisted of eight flasks under aerobic conditions (using breathing-quality air) and eight flasks under anaerobic conditions (using argon). In each set of eight flasks, two contained only buffer, three contained the CCB with buffer, and three contained the CCB with buffer and glucose. An 80-gram aliquot of CCB was placed in the flasks and 100 mL of a phosphate buffer (with or without glucose) was added to create a neutral pH. The ash-containing flasks also had 100 µL of mixed bacterial culture added. The source of bacteria was a mixed bacterial inoculum from a brackish wetland. This apparatus is shown in Figure 2.

Figure 2. Microbiologically mediated Hg vapor-phase collection apparatus.

The experiments were conducted for 30 days. The total mercury collected on the carbon traps was determined. The gold-coated quartz collection tubes were desorbed for analysis by heating to approximately 500°C, and the mass of Hg released was determined using atomic fluorescence. For bacterial counts at the completion of the 30-day period, a 1-mL aliquot of solution was taken from each flask. The aqueous supernate was serially diluted in 0.1% sodium pyrophosphate buffer (pH 7.0) and then used to inoculate a series of tubes containing 1% peptone, tryptone, yeast extract, and glucose broth. The tubes were incubated at 30°C, and growth, as turbidity, was monitored over a 3-week period.

High-Temperature Thermal Release. A schematic for the controlled thermal desorption of Hg and Hg compounds was assembled and is shown schematically in Figure 3. The apparatus was constructed using an atomic absorption (AA) spectrophotometer for Hg detection and included a small tube furnace and temperature controller for thermal desorption. A Hewlett Packard 3395 integrator was used for data collection. Detection of thermally desorbed Hg and Hg compounds was done in an electrically heated quartz cell operated at 800°C. The use of a heated cell allowed detection of Hg compounds by thermally decomposing compounds to form Hg^0, which can be detected by AA. Gas flow was 20 cm^3/min of nitrogen. The temperature controller was ramped from ambient temperature to

700°C at a rate of 25°C per minute. A more complete description along with a description of the experimental protocol can be found elsewhere.[9]

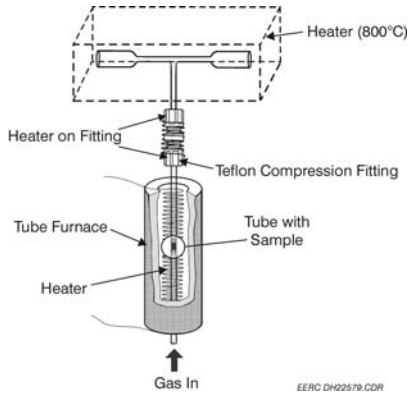

Figure 3. Hg thermal desorption apparatus.

Results and Discussion

An overview of some of the results obtained from the various Hg release techniques is included below.

Leaching. Over the last nearly 28 years, researchers at the EERC have leached a large number of varying CCBs, initially using the more common standard tests.

Data from the past ten years contain 256 Hg leachate values. Only 32 of those values (12%) had detectible Hg values, ranging from 0.01 to 0.39 µg/L. The average is 0.064 µg/L, and the median is 0.02 µg/L. Hg values above the detection limit were obtained in all procedures used except SAL, SPLP, and the 4:1 liquid-to-solid ratio 4-week distilled deionized water. Detectible Hg leachate values resulted from AFBC char fly ash, AFBC spent bed material, boiler slag, bottom ash, fly ash, fly ash with Hg sorbent material, and PTC fly ash.

A total of 38 Hg leaching data points of fly ash resulting from the use of full-scale Hg control technologies are in the current data set. Eleven of the data points are at or above the detection limit of 0.01 µg/L used on those samples.

Long-Term Ambient-Temperature Vapor Release. To date, two complete sets of long-term release experiments have been completed on six CCBs. Tests 1 and 2 were conducted for 263 and 264 days, respectively. The averaged duplicate results from Test 2 are shown in Table 1. It is apparent that all but one of the ash samples appear to be sorbing Hg. The total Hg contents of the ashes had a range of 0.112–0.736 µg/g.

Table 1. Comparison of Emission Rates Between the Empty Bottles and the Bottles Containing Ash in Test 2, pg/day

Sample	Bottles with Ash	Bottles without Ash	Difference
99-188	2.237	2.161	0.076
99-189	0.077	1.127	!1.050
99-692	0.081	2.454	!2.373
99-693	0.077	4.328	!4.251
99-722	0.696	7.165	!6.469
99-724	0.411	4.436	!4.025

Microbiologically Mediated Vapor Release. Two CCB samples with various electron acceptors added were analyzed in the first microbiologically mediated Hg vapor-release experiment. Results from this test were very confusing with the sterile sample releasing the most Hg. It was decided that the CCB would suffice as a source of the various electron acceptors.

Testing of three CCBs has been completed using the matrix described in the experimental section, including one of the fly ash samples from the first experiment. Results have been confusing; however, general trends have emerged. The Hg released from the CCB slurry was generally higher in the samples fed with glucose versus starved samples and in aerobic versus anaerobic conditions. The bacterial count has also generally followed that trend. The Hg^0 vapor captured on the gold-coated quartz traps has been higher than seen in the long-term ambient-temperature vapor-release experiments. The flasks containing buffer only have been treated as blanks.[5,10]

High-Temperature Thermal Release. A large variety of CCBs have been analyzed for the thermal release of Hg. Most of the thermal curves generated were straightforward, containing only one or two major desorption peaks.

Thermal desorption curves were rather difficult to interpret since there is no way, at present, using this apparatus to determine exactly what is happening during the thermal treatment. There are several possible scenarios:

- Hg and Hg compounds, as sorbed, are being released unchanged during the thermal desorption procedure.
- Hg compounds are being desorbed by a mechanism of thermal decomposition whereby sorbed compounds such as HgO are thermally decomposed to Hg and oxygen during the thermal desorption.
- Hg or Hg compounds are chemically reacting with the CCB components then thermally desorbed according to the first or second scenario as described above.

Conclusions

Currently, many CCBs contain relatively little Hg; however, in the future, as Hg emissions are controlled, Hg-containing sorbent in CCBs will likely cause Hg concentrations to increase. The issue of Hg emissions from disposed or utilized CCBs requires additional study.

A variety of CCBs have been leached using a variety of batch-leaching procedures. In the overall data set over the past 10 years, 12% of the leachate values were above the detection limit and 29% of the leachings from full-scale Hg control technology CCBs yielded detectible Hg values. That number of samples is low; therefore, the effect of Hg control technologies on the leachability of Hg from CCBs is yet to be seen.

Long-term ambient-temperature release experiments have indicated that five of six CCBs analyzed acted as Hg sinks, although these samples were previously reported as having released small amounts of Hg vapor.[11]

The most likely species of Hg to be released in the absence of biological activity is elemental Hg because of its significant vapor pressure although other species are likely in CCBs at room temperature. All have extremely low vapor pressures and are unlikely to be released in significant amounts at ambient temperatures.

Acknowledgements. Funding for this project was provided by U.S. Environmental Protection Agency (EPA) through the Center for Air Toxic Metals[K] (CATM®) and by the U.S. Department of Energy (DOE) through CARRC. Although the research described in this article has been funded wholly or in part by EPA through grant/Cooperative Agreement No. R8267649-01 to the University of

North Dakota and the EERC, it has not been subjected to the Agency's required peer and policy review and therefore does not necessarily reflect the views of the Agency, and no official endorsement should be inferred. This article was prepared with support of the DOE, under Cooperative Agreement No. DE-FC26-98FT40321. However, any opinions, findings, conclusions, or recommendations expressed herein are those of the authors and do not necessarily reflect the views of the DOE. Information on the CATM® and CARRC programs can be accessed through the EERC Web site at www.undeerc.org.

References

(1) U.S. Environmental Protection Agency. http://www.epa.gov/mercury/actions.htm (accessed Nov 26, 2002).
(2) Laudal, D. L.; Heidt, M. K. *Evaluation of Flue Gas Mercury Speciation Methods*; EPRI Report No. TR-108988; Dec. 1997.
(3) Carey, T. R.; Hargrove, O. W., Jr.; Richardson, C. F.; Chang, R.; Meserole, F. B. Factors Affecting Mercury Control in Utility Flue Gas Using Sorbent Injection. Presented at the Air & Waste Management Association 90th Annual Meeting & Exhibition, Toronto, ON, Canada, June 1997; Paper No. 97-WA72A.05.
(4) CATM Staff. *2000 Annual Report of the Center for Air Toxic Metals*; Energy & Environmental Research Center: Grand Forks, ND, Jan 2001.
(5) CATM Staff. *2001 Annual Report of the Center for Air Toxic Metals*; Energy & Environmental Research Center: Grand Forks, ND, Feb 2002.
(6) Hassett, D. J. Synthetic Groundwater Leaching Procedure, Encyclopedia of Environmental Analysis and Remediation, pp 4797–4803, John Wyley & Sons, Inc., 1998.
(7) U.S. Environmental Protection Agency. Toxicity Characteristic Leaching Procedure. Method 1311, Test Methods for Evaluating Solid Waste: Physical/Chemical Methods (SW-846), 1992, 35 pp.
(8) U.S. Environmental Protection Agency. Method 1312: Synthetic Precipitation Leaching Procedure (SPLP), Test Methods for Evaluating Solid Waste: Physical/Chemical Methods (SW846), Vol. 1C, 3rd Ed. 1990.
(9) Pavlish, J. H. *Mercury Stability in the Environment.* Final Topical Report (April 15, 1998 – June 30, 1999) for U.S. Department of Energy Cooperative Agreement No. DE-FC26-98FT40320; EERC Publication 99-EERC-09-03; Energy & Environmental Research Center: Grand Forks, ND, Sept 1999.
(10) CATM Staff. *2002 Annual Report of the Center for Air Toxic Metals*; Energy & Environmental Research Center: Grand Forks, ND, 2003.
(11) Hassett, D. J.; Heebink, L. V.; Pflughoeft-Hassett, D. F. Potential for Mercury Release from Coal Combustion By-Products. In *Proceedings of the Air Quality III: Mercury, Trace Elements, and Particulate Matter Conference*; Arlington, VA, Sept 10–12, 2002; Energy & Environmental Research Center: Grand Forks, ND, 2002.

Implications of Mercury Interactions With Band-Gap Semiconductor Oxides
Proceedings of the 227th ACS National Meeting, March 28-April 1, 2004

Evan J. Granite, William P. King, and Henry W. Pennline

United States Department of Energy National Energy Technology Laboratory
P.O. Box 10940; MS 84-311
Pittsburgh, PA 15236-0940
tel (412) 386-4607; fax (412) 386-6004,
e-mail: evan.granite@netl.doe.gov

Abstract

Titanium dioxide is a well known photo-oxidation catalyst. It will oxidize mercury in the presence of ultraviolet light from the sun and oxygen and/or moisture to form mercuric oxide. Several companies manufacture self-cleaning windows. These windows have a transparent coating of titanium dioxide. The titanium dioxide is capable of destroying organic contaminants in air in the presence of ultraviolet light from the sun, thereby keeping the windows clean. The commercially available self-cleaning windows were used to sequester mercury from oxygen-nitrogen mixtures.

Samples of the self-cleaning glass were placed into specially designed photo-reactors in order to study the removal of elemental mercury from oxygen-nitrogen mixtures closely resembling air. The possibility of removing mercury from ambient air with a self-cleaning glass apparatus is examined. The intensity of 365-nm ultraviolet light was similar to the natural intensity from sunlight in the Pittsburgh region. Passive removal of mercury from the air may be less costly than point source clean-up at combustion facilities.

There are several common band-gap semiconductor oxide photocatalysts. Sunlight (both the ultraviolet and visible light components) and band-gap semiconductor particles can impact the global cycle of mercury in the environment. The potential environmental consequences of mercury interactions with band-gap semiconductor oxides are discussed. Heterogeneous photooxidation might impact the global transport of elemental mercury emanating from flue gases.

Introduction

Mercury is typically present in air at extraordinarily low concentrations of around 1 part per trillion by volume [1-15]. Mercury can exist in air in the elemental, oxidized, and particulate-bound forms. Between 97-99% of the mercury in air is believed to be in the elemental form [1-15]. Oxidized forms of mercury in the atmosphere are believed to include mercuric chloride and mercuric oxide [1-15]. The element and many of its compounds are powerful neurotoxins [16].

Mercury is a semi-noble metal, with a standard electrode potential for oxidation similar to palladium. This relative inertness allows elemental mercury emissions, once in the atmosphere, to transport across the globe. Elemental mercury is slowly oxidized in the atmosphere by ozone and hydroxyl radicals [8]. The low concentrations of elemental mercury, ozone, and hydroxyl radicals contribute to the long residence time of elemental mercury in the air. Elemental mercury in the atmosphere has an estimated lifetime of approximately one year [8]. Elemental mercury is insoluble in water, whereas oxidized forms of mercury are typically much more soluble. Oxidized mercury is scrubbed from the atmosphere by precipitation and deposits in bodies of water. In oceans, lakes, rivers, streams, ponds, bogs, and marshes, oxidized mercury can be methylated by bacteria, plankton, and algae, thereby entering the food chain. Mercury can accumulate at the top of the food chain in large predator fish such as tuna, sword fish, and sharks. Consumption of certain species of fish has been of concern for pregnant women and young children. Numerous fish advisories have been recently posted in the United States [17].

Point source removal of mercury from coal-burning power plants is a difficult endeavor [16,18-23]. Mercury is present in flue gas at low concentrations of around 1 part per billion by volume [16]. The composition of a typical flue gas is given in Table 1. The use of activated carbon sorbent has been the most extensively examined method for removal of mercury from flue gas. There are many deficiencies in the use of activated carbon for mercury capture from power plant flue gas [16,18,19,21,23]. Carbon is a general adsorbent; it will adsorb many of the components of flue gas to some extent, with some in competition with mercury. Carbon sorbents work best at low temperatures. The final state of mercury on the spent carbon sorbent is a concern for the ultimate disposal or use of fly ash. Injection of activated carbon into the duct work of a power plant upstream of an electrostatic precipitator results in poor contact between the sorbent and flue gas. As a result of the poor contacting methods typically employed, a high carbon to mercury mass ratio of 3,000:1 to 50,000:1 is used to achieve a high level of mercury removal [16,18]. Activated carbons can be expensive, with a price of around $500 - 3,000/ton [16,18]. Alternatives to activated carbon injection for point source removal of mercury have been developed both in-house at the National Energy Technology Laboratory and through contracted research funded by the United States Department of Energy [24-35].

The U.S. EPA has announced pending regulation of mercury emissions from U.S. power plants [36,37]. However, these regulations may not reduce the number of fish consumption advisories in the United States. U.S. coal-burning power plants are estimated to have stack emissions of 48 tons of mercury per year [32]. This is approximately 1% of the annual emissions of mercury around the globe from both anthropogenic and natural sources [32]. The growing unregulated emissions of mercury from Asian economies, as well as the global transport of elemental mercury emissions, suggest that other actions may be needed to slow or halt the accumulation of mercury in the food chain.

Passive removal of mercury from air may represent a better solution to the problem [38]. It is proposed that self-cleaning glass, a new and inexpensive product [39-41], could be an important component in the passive collection of mercury from the environment [38].

Self-cleaning glass is coated with titanium dioxide, a well-known photo-oxidation catalyst [39-41]. It can capture mercury from the air as mercuric oxide. The use of self-cleaning glass is envisioned in automobiles and buildings [38]. Mercuric oxide is slightly soluble in water. It can wash down the window with the rain. A thin, unobtrusive, and porous sorbent cartridge, such as activated carbon, can be placed at the bottom of the window in order to capture the mercury [38]. The capacity of the sorbent cartridge is such that it will last the lifetime of the cars and buildings. Proper disposal of the cartridge will prevent mercury from entering the food chain. Automobiles and buildings using these modified windows could constitute millions of passive mobile and stationary collectors of mercury from the air [38]. The concept is similar to that described by Hoke [42] for the use of metal catalyst stripes on automobile radiators for the destruction of air pollutants. Wang [43] described an attempt to alleviate air pollution in Asia by use of titania-coated building materials.Additionally, there are several common band-gap semiconductor oxides, including titanium dioxide, zinc oxide, tin oxide, and iron oxide, which can behave as photocatalysts for the oxidation of mercury [44]. These minerals are common constituents of the earth's crust and are present in the fine particulate matter present in air. These particles are released into the air by volcanoes, forest fires, dust storms, incineration of wastes, and combustion of fossil fuels. It is suggested that the interactions between mercury, long-wave ultraviolet radiation, and band-gap semiconductor oxides play an important role in the global cycling of mercury in the environment.

Experimental

The assembly used for studying the heterogeneous photocatalytic oxidation of mercury is a modified version of an apparatus described earlier [29]. It consists of an elemental mercury permeation tube within an air blending system, and various quartz or pyrex photoreactors with an ultraviolet lamp. Quartz or pyrex are used for the photoreactors because they are transparent to 365-nm light. An 8-in.-long, 6-W ultraviolet lamp from Spectroline (Spectronics BLE-6365S) is used as the source of the 365-nm light. The quartz tubes, pyrex reactors, and titania-coated glass plates are initially cleaned by rinsing first with trace-metals-grade 37% hydrochloric acid, then with distilled water, and last with reagent grade acetone. The permeation tube, located in a heated bath, is held at 212° F in a nitrogen stream at all times and releases 151 ng of elemental Hg/min.

A quartz photoreactor was employed for examination of the removal of mercury from oxygen-nitrogen-carbon dioxide-water vapor mixtures by a high surface area titanium dioxide powder. The fresh titanium dioxide powder contains 0.2 ppm of mercury, and has a BET surface area of 200 m^2/gram. The photoreactor is a 1/4-inch-outer diameter tube described in an earlier paper. A 6 Watt ultraviolet lamp was used as the source of 365-nm radiation in all of the experiments. The intensity of the incident long-wave ultraviolet light upon the powder was 1.0 mW/cm^2. The gas compositions examined were oxygen-nitrogen-carbon dioxide mixtures similar to air. These compositions are:

A: 14% O_2, 270 ppb Hg, 240 ppm CO_2, 86% N_2
B: 21% O_2, 270 ppb Hg, 360 ppm CO_2, 79% N_2
C: 21% O_2, 270 ppb Hg, 360 ppm CO_2, 0-2% H_2O, 77-79% N_2

The gas flow-rate used was 60 ml/min. All experiments were conducted at ambient temperature and pressure.

Samples of the self-cleaning glass were obtained from a PPG-approved supplier. A small pyrex and large pyrex photoreactor were constructed for the glass samples. The small reactor was a 4-cm inner diameter by 25-cm pyrex vacuum trap from Southeastern Laboratory Apparatus. The trap was positioned horizontally over the ultraviolet lamp parallel to its major axis. Smaller irregular-shaped, cut plates were inserted into the reactor with the titania-coated surface face down. Gas was introduced through the center tube and vented from the trap inlet. To reduce bypassing, gas flow in later experiments was directed across the titania-coated glass by use of low density polyethylene bags wadded to produce a baffle and wedged behind the glass sample. Measured light intensities were between 1.2 and 1.8 mW/cm^2.

The large photoreactor was a 4000-ml pyrex kettle. Rectangular-shaped samples (15-cm by 10-cm) of the self-cleaning glass were inserted into the large reactor. The gas stream was introduced by a 0.3-cm outer diameter teflon tube located near the center of the glass samples. Light intensity at the plate surface was approximately 0.4 mW/cm^2.

Cold vapor atomic absorption spectrophotometry (CVAAS) was used to determine the mass of mercury contained on both the used titania powder (yellow in color) and titania-coated glass plates. Acidic solutions were employed to dissolve the mercury; the resulting solutions were analyzed by CVAAS. X-ray photoelectron spectroscopy (XPS) and scanning electron microscopy with energy-dispersive X-ray methods (SEM-EDX) were utilized to confirm the formation of mercuric oxide on the titania surfaces.

Results

A high surface area titania powder was examined in the 1/4-inch photoreactor. The powder was exposed to Gas A for 350 minutes. A large percentage (44.2%) of the mercury was captured as yellow mercuric oxide (Table 4). Little mercury was captured in the absence of long-wave ultraviolet light. These results encouraged further tests with the self-cleaning glass plates.Table 5 shows the mercury levels present in the titania-coated glass blanks. The freshly cleaned glass plates have a very low concentration of mercury (below 0.0001 μg/cm^2). Capture of mercury is not observed upon exposure of the titania-coated glass to Gas A in the absence of long-wave ultraviolet radiation.

The mercury removal by titania-coated glass exposed to Gas A and irradiated by 365-nm light is shown in Table 6. A variable level of mercury was captured by the glass. XPS analysis determined that mercury is present on the surface of the used plates as mercuric oxide. The removal varies with the exposure time and superficial glass surface area. The removals appear to be surface area

limited. The radiation intensity is comparable to mid-day summer incident sunlight in Pittsburgh.

Mercury capture by the glass plates exposed to Gases B and C and irradiated by 365-nm light is presented in Table 7. The presence of water vapor in Gas C appears to significantly enhance the capture of mercury.

There is scatter in the mercury removals obtained by irradiation of Gas C using the 25 cm^2 coated glass plate, as shown by the 33% standard deviation. Several factors impact the uncertainties in the mercury removals. The intensity of light diminishes with the square of the distance from the source. The uncertainty in the distance between the lamp and the photoreactor was ± 1/16 in., introducing an uncertainty in the intensity of 15%. Additionally, an uncertainty in the mercury capture is introduced by the CVAAS analysis. The uncertainty associated with the recovery and CVAAS measurement of mercury is at least ± 10%. The mercury output from the permeation tube has an uncertainty level of at least ± 6%. Therefore, the scatter in the mercury removals is not surprising. Nevertheless, analyses with XPS and SEM-EDX showed that mercury in the oxygen-nitrogen mixtures is oxidized by the titania powder and coated glass, forming mercuric oxide.

Discussion

The screening results shown in Tables 6 and 7 suggest that titania-coated glass plates can sequester mercury from the air. It is noted that the concentration of elemental mercury (270 ppb) used in the experiments is five orders of magnitude greater than the concentration of elemental mercury typically found in ambient air (1 ppt). The extraordinarily small concentration of elemental mercury in air will result in fewer collisions between mercury atoms and the titania surface. This may result in less efficient capture of mercury by titania-coated glass in ambient air.

The addition of water vapor to the oxygen-nitrogen mixtures resulted in a greater level of mercury capture. This result was expected, as both gas phase oxygen and water vapor can serve as oxidants with a titania photocatalyst [44].

In addition, there are other oxidizable compounds present in air, such as methane, hydrogen, carbon monoxide, and sulfur dioxide, shown in Table 2 [45]. It is expected that a titania surface will catalyze the oxidation of these species, possibly in competition with the oxidation of elemental mercury. This may reduce the capture of elemental mercury from air by titania-coated glass plates.

Heterogeneous photocatalytic oxidation can affect the fate of mercury in the atmosphere. Mercuric oxide, associated with fine particulates, has been detected recently in the tropopause [3,4]. Ambient concentrations of elemental mercury in the polar regions has been found to vary with seasonal changes in sunlight [5].

Table 3 lists several common band-gap semiconductors. The bang-gap energies and corresponding maximum excitation wavelengths are tabulated [46]. The maximum excitation wavelengths are typically in the ultraviolet or visible light regions. Photons containing the band-gap energy can induce the formation of reactive radicals such as hydroxyl, as well as other reactive oxygen species, on the semiconductor surface [44]. Kaluza found that elemental mercury can be photooxidized by titania, zinc oxide, tin oxide, and cerium oxide [44]. Kaluza also speculated that hydroxyl radicals (OH) and a chemisorbed charged oxygen species (O_2^-) are responsible for the photooxidation of mercury on titania [44]. Alpha alumina, and silica were found to be inactive photocatalysts for the oxidation of elemental mercury [44].

Various dopants have been previously examined to improve the efficiency of titania photocatalysts for the oxidation of hydrocarbon pollutants. Other band-gap semiconductor oxides have been studied for the oxidation of pollutants. These strategies could be employed in order to improve the capture of elemental mercury by coated glass, as well as to enhance the self-cleaning properties of the windows.

It is currently thought that elemental mercury is removed from the atmosphere by gas phase oxidation by ozone and hydroxyl radicals, viz [8]:

$$Hg_{(gas)} + OH_{(gas)} \rightarrow HgO_{(gas)} + H_{(gas)} \quad (2)$$

Reaction (1) is the gas phase oxidation of elemental mercury by ozone to form mercuric oxide. Reaction (2) is the gas phase oxidation of elemental mercury by hydroxyl radical to form mercuric oxide and a hydrogen radical. The gas-phase concentrations of elemental mercury, ozone, and hydroxyl, as well as the rate constants for reactions (1) and (2) are consistent with the long half life of elemental mercury in the atmosphere [8].

In the polar regions, halogen and halogen oxide radicals originating from sea spray are hypothesized to oxidize mercury, viz [10]:

$$Br/Cl_{(gas)} + O_{3(gas)} \rightarrow ClO/BrO_{(gas)} + O_{2(gas)} \quad (3)$$
$$BrO/ClO_{(gas)} + Hg_{(gas)} \rightarrow HgO_{(gas)} + Br/Cl_{(gas)} \quad (4)$$
$$Hg_{(gas)} + 2\ Br/Cl_{(gas)} \rightarrow HgBr_2/HgCl_{2(gas)} \quad (5)$$

Reaction (3) is the photochemical depletion of ozone by halogens. Reaction (4) is the gas phase oxidation of elemental mercury by halogen oxides to form mercuric oxide and halogen radicals. Reaction (5) is the oxidation of elemental mercury by halogen radicals to form gas phase mercuric chloride and mercuric bromide. This mechanism has been proposed by Lindberg in order to account for the depletion of ambient elemental mercury observed during springtime polar sunrise [10].

The heterogeneous photooxidation of elemental mercury by band-gap semiconductors is another potential route for the deposition of mercury. The overall reactions can be crudely represented by equations (6) and (7):

$$Hg_{(gas)} + \text{band-gap particle} + \text{light} + O_{2(gas)} \rightarrow HgO_{(ad)} + \text{radicals}_{(surf)} \quad (6)$$

$$Hg_{(gas)} + \text{band-gap particle} + \text{light} + H_2O_{(gas)} \rightarrow HgO_{(ad)} + \text{radicals}_{(surf)} \quad (7)$$

The surface radicals or charged oxygen entities can recombine to form oxygen or water, or react with other

oxidizable adsorbed species. Band-gap semiconductors which potentially could participate in reactions (6) and (7) include titanium oxide, zinc oxide, tin oxide, iron oxide, cerium oxide, and carbon. Xie found titanium and zinc present in Arctic aerosols [9]. The ubiquitous nature of these common fine band-gap semiconductor particulates suggests that they may play a role in the oxidation of elemental mercury in the atmosphere. Schroeder had earlier found mercuric oxide associated with fine particulates in the upper atmosphere of the Arctic [5].

The possibility that carbon fine particles can act as heterogeneous photocatalysts for the oxidation of elemental mercury requires further examination. The band-gap energy of carbon (Table 3) suggests that short wave ultraviolet radiation is required for it to behave as a photocatalyst for the oxidation of mercury. This could occur in the upper atmosphere, where short wave ultraviolet light is more prevalent than in the lower atmosphere.

Conclusions

Photo-oxidation of mercury with self-cleaning glass is a method for sequestration from ambient air. A preliminary estimate suggests that a substantial quantity of mercury could be removed from the atmosphere by wide-scale utilization of the self-cleaning glass-sorbent cartridge apparatus. Passive removal of mercury from air has several advantages over costly point source removal techniques and is a unique approach to the problem of mercury in the food chain. Capture of elemental mercury from oxygen-nitrogen mixtures has been demonstrated. The intensity of the incident long-wave ultraviolet radiation is comparable to sunlight. Passive removal of mercury should be reliable as no moving parts or external power supplies are necessary. The presence of moisture resulted in higher levels of mercury capture, possibly due to the formation of hydroxyl radicals on the glass surface. Future research should focus on mercury capture from more dilute mercury mixtures (at part per trillion by volume levels) representative of air. The effect of other oxidizable species present in air (such as methane, hydrogen, carbon monoxide, and sulfur dioxide) upon the removal of mercury needs to be determined. Other band-gap semiconductor oxide coatings should be studied for the capture of elemental mercury, as well as to enhance the self-cleaning properties of the windows.

Sunlight is a major factor in the transport and transformations of mercury in the environment. The interactions of mercury with band-gap semiconductor oxides may be a significant factor in the global mercury cycle. The ubiquitous nature of long-wave ultraviolet radiation and band-gap semiconductor oxide fine particles suggests that they drive the atmospheric transformations of mercury between the elemental, oxidized, and particulate-bound forms. Photo-oxidation by band-gap semiconductor oxide fine particles could be a factor in the seasonal fluctuations of elemental mercury in the atmosphere. Photocatalytic oxidation of elemental mercury by carbon particulates, if confirmed, would have major implications for the global cycle of mercury.

Acknowledgments

Robert Thompson of Parsons Power Services, Inc. determined the mercury content of the titanium dioxide powders and glasses. NETL scientist John Baltrus deduced the form of mercury on the titanium dioxide powders and glasses. The authors thank NETL colleague Rich Hargis for helpful suggestions. Phil Granite provided stimulating discussions and ideas.

Disclaimer

Reference to any specific commercial product or service is to facilitate understanding and does not imply endorsement by the United States Department of Energy.

References

(1) *Mercury Study Report to Congress*; EPA 452/R-97-003; U.S. Environmental Protection Agency, Office of Air Quality Planning and Standards: Washington, DC, Dec. 1997.

(2) Sommar, J.; Gardfeldt, K.; Stromberg, D.; Feng, X. A kinetic study of the gas-phase reaction between the hydroxyl radical and atomic mercury. *Atmospheric Environment* **2001**, *35*, 3049.

(3) Murphy, D.M. The Composition of Aerosol Particles at 5-19 km Altitude. Presented at the Annual Meeting of American Geophysical Union, San Francisco, CA, Dec. 6-10, 1998.

(4) Murphy, D.M.; Thomson, D.S.; Mahoney, M.J. In Situ Measurements of Organics, Meteoritic Material, Mercury, and Other Elements in Aerosols at 5-19 Kilometers. *Science* **1998**, *282*, 1664.

(5) Schroeder, B. Springtime Transformation of Atmospheric Mercury Vapor in the Arctic. Presented at the Annual Meeting of American Geophysical Union, San Francisco, CA Dec. 6-10, 1998.

(6) Anlauf, K.G. Arctic Ozone Measurements. Presented at the Annual Meeting of American Geophysical Union, San Francisco, CA, Dec. 6-10, 1998.

(7) *National Air Quality And Emissions Trend Report 1997*; EPA 454/R-98-016; United States Environmental Protection Agency, Office of Air Quality: Research Triangle Park, NC, 1998.

(8) Lin, C-J; Pehkonen, S.O. The Chemistry of Atmospheric Mercury: A Review. *Atmospheric Environment* **1999**, *33*, 2067.

(9) Xie, Y-L; Hpke, P.K.; Paatero, P.; Barrie, L.A.; Li, S-M Identification of source nature and seasonal variations of Arctic aerosol by multilinear engine. *Atmospheric Environment* **1999**, *33*, 2549.

(10) Lindberg, S.E.; Brooks, S.; Lin, C-J; Scott, K.J.; Landis, M.S.; Stevens, R.K.; Goodsite, M.; Richter, A. Dynamic Oxidation of Gaseous Mercury in the Arctic Troposphere at Polar Sunrise. *Environ. Sci. Technol.* **2002**, 36, 1245.

(11) Ebinghaus, R.; Koch, H.H.; Temme, C.; Einax, J.W.; Lowe, A.G.; Richter, A.; Burrows, J.P.; Schroeder, W.H. Antarctic Springtime Depletion of Atmospheric Mercury. *Environ. Sci. Technol.* **2002**, 36, 1238.

(12) Lalonde, J.D.;Poulain, A.J.; Amyot, M. The Role of Mercury Redox Reactions in Snow on Snow-to-Air Mercury Transfer. *Environ. Sci. Technol.* **2002**, 36, 174.

(13) Temme, C.; Einax, J.W.; Ebinghaus, R.; Schroeder, W.H. Measurements of Atmospheric Mercury Species at a Coastal Site in the Antarctic and over the South Atlantic Ocean during Polar Summer. *Environ. Sci. Technol.* **2003**, 37, 22.
(14) Landis, M.S.; Stevens, R.K. Comment on "Measurement of Atmospheric Mercury Species at a Coastal Site in the Antarctic and over the South Atlantic Ocean during Polar Summer". *Environ. Sci. Technol*. **2003**, 37(14), 3239.
(15) Temme, C.; Ebinghaus, R.; Einax, J.W.; Schroeder, W.H. Response to Comment on "Measurement of Atmospheric Mercury Species at a Coastal Site in the Antarctic and over the South Atlantic Ocean during Polar Summer". *Environ. Sci. Technol*. **2003**, 37(14), 3241.
(16) Granite, E.J.; Pennline, H.W.; Hargis, R.A. Sorbents For Mercury Removal From Flue Gas. *Topical Report DOE/FETC/TR-98-01*, National Energy Technology Laboratory: Pittsburgh, PA, Jan. 1998.
(17) Gorman, J. Does Mercury Matter? Experts Debate the Big Fish Question. *NY Times*, July 29, 2003.
(18) Granite, E.J.; Pennline, H.W.; Hargis, R.A. Novel Sorbents for Mercury Removal from Flue Gas. *Ind. Eng. Chem. Res.* **2000**, *39*(4), 1020.
(19) Granite, E.J.; Pennline, H.W.; Hargis, R.A. Novel Sorbents for Mercury Removal From Flue Gas. *Proceedings of 16th Annual Int. Pittsburgh Coal Conference*, Paper 19-2, Pittsburgh, PA, Oct. 1999.
(20) Livengood, C.D.; Huang, H.S.; Wu, J.M. Experimental Evaluation of Sorbents for the Capture of Mercury in Flue Gases. *Proceedings of 87th Annual Meeting of Air Waste Manage. Assoc.*, Cincinnati, Ohio, June 1994.
(21) Granite, E.J.; Pennline, H.W.; Hargis, R.A.; Haddad, G.J. An Investigation Of Sorbents For Mercury Removal From Flue Gas. *Proceedings of 15th Annual Int. Pittsburgh Coal Conference*, Paper 18-4, Pittsburgh, PA, Sept. 1998.
(22) Brown, T.D.; Smith, D.N.; Hargis, R.A.; O'Dowd, W.J. Mercury Measurement and Its Control: What We Know, Have Learned, and Need to Further Investigate. *J. Air Waste Manage. Assoc.* **1999**, *6*, 1.
(23) Granite, E.J.; Pennline, H.W. Comparison of Sorbents For Mercury Removal From Flue Gas. *AIChE Fall National Meeting* Paper 263f, Reno, NV, November 2001.
(24) Livengood, C.D.; Mendelsohn, M.H. Investigation of Modified Speciation for Enhanced Control of Mercury. *Proceedings of Advanced Coal-Based and Environmental Systems 97 Conference* Pittsburgh, PA, July 1997.
(25) Granite, E.J.; Pennline, H.W.; Hoffman, J.S. Effects of Photochemical Formation of Mercuric Oxide. *Ind. Eng. Chem. Res.* **1999**, *38*(12), 5034.
(26) Granite, E.J.; Pennline, H.W.; Stanko, D.C. Photochemical Removal of Mercury From Flue Gas. *Proceedings of 17th Annual Int. Pittsburgh Coal Conference*, Paper 25-5, Pittsburgh, PA, Sept. 2000.
(27) Granite, E.J.; Pennline, H.W. Photochemical Removal of Mercury From Flue Gas. *Proceedings of the 11th International Conference on Coal Science*, San Francisco, CA, Sept. 2001.
(28) Granite, E.J.; Pennline, H.W. Photochemical Removal of Mercury From Flue Gas. *Proceedings of 223rd ACS National Meeting - Div. Env. Chem.*, Paper 92, Orlando, Fl., April 2002.
(29) Granite, E.J.; Pennline, H.W. Photochemical Removal of Mercury From Flue Gas. *Ind. Eng. Chem. Res.* **2002**, 41(22), 5470.
(30) Granite, E.J.; Pennline, H.W. Method For Removal of Mercury From Various Gas Streams. *U.S. Patent 6,576,092*, Issued June 10, 2003.
(31) Pennline, H.W.; Granite, E.J.; Freeman, M.C.; Hargis, R.A.; O'Dowd, W.J. Thief Process for the Removal of Mercury from Flue Gas. *U.S. Patent 6,521,021* Issued Feb. 18, 2003.
(32) Feeley, T.J.; Murphy, J.T.; Hoffmann, J.W.; Granite, E.J.; Renninger, S.A. A Review of DOE/NETL's Mercury Control Technology R&D Program for Coal-Fired Power Plants. EM Magazine, Oct. 2003.
(33) Biswas, P.; Wu, C.Y. Control of Toxic Metal Emissions From Combustors Using Sorbents: A Review. *J. Air Waste Manage. Assoc.* **1998**, *48*, 113.
(34) Biswas, P.; Wu, C.Y.; Lee, T.-G.; Tyree, G.; Arrar, E. Capture of Mercury in Combustion Systems by In Situ Generated Titania Particles with UV Irradiation. *Environ. Eng. Sci.* **1998**, *15*(2), 137.
(35) Shi, L.; Khairul Alam, M.; Bayless, D.J. Mercury Removal Using Titania-coated Membrane Collectors in Electrostatic Precipitators. *Proc. of 19th Int. Pitts. Coal Conf.*, Univ. Pittsburgh, Pittsburgh, PA **2002**.
(36) U.S. EPA information on pending regulation of mercury available on the web at http://www.epa.gov
(37) "President Bush Announces Clear Skies & Global Climate Change Initiatives" **2002**, Feb. 14, http://www.epa.gov/epahome/headline2_021402.htm
(38) Granite, E.J.; Pennline, H.W.; King, W.P. Passive Removal of Mercury From the Atmosphere, *NETL Report of Invention*, April 2002.
(39) Spice, B. Magic Panes. *Pittsburgh Post Gazette*, A8, July 15, 2002.
(40) SunClean Windows web site: www.ppgsunclean.com
(41) Activ Windows web site: www.activglass.com
(42) Hoke, J.B.; Heck, R.M.; Allen, F.M. Method and device for cleaning the atmosphere. *U.S. Patent 6,569,393* Issued April 29, 2003.
(43) Wang, L. Paving Out Pollution. *Sci. Amer.*, Feb. 2002.
(44) Kaluza, U.; Boehm, H.P. Titanium Dioxide Catalyzed Photooxidation of Mercury. *J. of Catalysis*, **1971**, 22, 347.
(45) Himmelblau, D.M. Basic Principles and Calculations in Chemical Engineering, 4th edition, Prentice-Hall, Englewood Cliffs, NJ, 1982.
(46) Weast, R.C. editor CRC Handbook of Chemistry and Physics, 63rd edition, CRC Press, Boca Raton, Fl. **1983**.

Table 1. Typical Untreated Flue Gas Composition From a Pulverized Coal Combustor Burning a Low-Sulfur Bituminous Coal [16, 29]

Species	Concentration (by volume)
H_2O	5-7%
O_2	3-4%
CO_2	15-16%
total Hg	1 ppb
CO	20 ppm
hydrocarbons	10 ppm
HCl	100 ppm
SO_2	800 ppm
SO_3	10 ppm
NO_x	500 ppm
N_2	balance

Table 2. Typical Composition of Air (Dry-Basis) Near Sea Level [8, 45]

Component	Concentration (by volume)
N_2	78.1 %
O_2	20.9 %
Noble Gases	0.9 %
Total Hg	1 ppt
CO_2	360 ppm
CH_4	2 ppm
H_2	0.5 ppm
CO	trace
SO_2	trace
NO_2	trace
others	balance

Table 3. Band-Gap Semiconductors Present in Air [46]

Semiconductor	Band-Gap E_{gap} (eV)	Maximum Excitation Wavelength $\lambda_{max} = hc/E_{gap}$ (nm)	
TiO_2	3.0	414	(long wave ultraviolet)
ZnO	3.2	388	(long wave ultraviolet)
Fe_2O_3	2.0	620	(visible light)
SnO_2	3.6	345	(long wave ultraviolet)
CeO_2	3.2	388	(long wave ultraviolet)
Carbon	5.2	239	(short wave ultraviolet)

Table 4. Mercury Capture By Titania Powder

Gas	Exposure (min)	Mercury Capture (%)
A	350	44.2
A (No UV)	350	1.2

Table 5. Mercury Levels in Titania-Coated Glass Blanks

Glass Area cm^2	Exposure (min)	Loading µg Hg/cm^2
155	0	less than 0.0001
16	0	less than 0.0001
155 (Gas A)	300 (no UV)	less than 0.0001

Table 6. Mercury Capture By Titania-Coated Glass Plates: Small Reactor, Gas A

Glass Area cm^2	Exposure (min)	Loading µg Hg/cm^2	% Mercury Capture
16	350	0.2	5.9
155	360	0.03	8.9
33	745	0.37	10.1
16	990	0.16	1.8
139	990	0.48	42.4
5	1050	0.23	0.7
33	1369	0.22	3.2
4	2490	0.47	0.5

Table 7. Mercury Capture By Titania-Coated Glass Plates: Gases B&C

Glass Area cm^2		Exposure (min)	Loading µg Hg/cm^2	% Mercury Capture
25	Gas B	990	0.03	0.5
25	Gas C	995	0.51	8.5
25	Gas C	3900	5.0	21.2
25	Gas C	4065	7.0	28.7
25	Gas C	3900	3.4	14.4

EVALUATIONS OF A NOVEL SAMPLE CONDITIONING SYSTEM FOR THE CONTINUOUS REAL-TIME MONITORING OF MERCURY IN FLUE GAS FROM COAL-FIRED UTILITY BOILERS

Kevin Fisher, Scott McLaren, Trevor Ley, Rick Slye

Apogee Scientific, Inc.
2895 W. Oxford Ave, Suite 1 Englewood, CO 80110

Introduction

Mercury (Hg) from combustion sources is recognized as a major concern to the nations air quality. In December 2000, EPA announced that it would regulate mercury emissions from coal-fired boilers under Title III of the Clean Air Act Amendments of 1990. A key aspect of achieving and assuring compliance is the ability to accurately measure mercury at a regular interval. The optimal solution is a continuous emissions monitor for mercury that could be operated and maintained in a similar manner as already done with SO_2 and NO_x CEMs at utilities. Although a few mercury analyzers show promise for measuring elemental mercury, a reliable sampling system that will allow these analyzers to measure total (particulate plus vapor) and speciated mercury continuously in the flue gas of coal-fired utility boilers has not been demonstrated and recent development efforts are still in the early stages.

Real-time continuous monitoring of mercury in flue gas is essential for several reasons. Control of Hg emissions from coal-fired utility boilers is currently being considered, and if implemented will likely cost billions of dollars each year (i). Most of the Hg control strategies being proposed for coal-fired utility boiler flue gas include some type of sorbent injection. Prior to installing a control system, more accurate measurements of Hg emissions would allow EPA and the utility to make more informed decisions concerning their needs and control options. Real-time continuous monitoring of Hg would provide options for advanced process control feed-back as well as for monitoring the performance of the control system, thus minimizing sorbent usage and lowering the cost of controls. Other applications of this technology include Hg emission monitoring from other sources, such as municipal waste incinerators, commercial/industrial boilers, medical waste incinerators, and crematories.

In a effort to advance the art of mercury measurements, Apogee was awarded a Phase I and II Small Business Innovative Research Grant (SBIR) from EPA and additional funds from the Electric Power Research Institute (EPRI) to develop a prototype Sample Conditioning System (SCS) that, in conjunction with currently available analyzers (e.g., cold vapor atomic absorption spectrometers (CVAAS), cold vapor atomic fluorescence spectrometers (CVAAFS)), will enable real-time monitoring of total vapor-phase mercury (TVM), elemental mercury (EM), and oxidized mercury (OM) as well as total mercury (TM), consisting of particulate mercury (PM) and TVM.

The overall goal of this program is to define a new state-of-the-art mercury measurement system by developing a novel "front-end" conditioning system for the continuous real-time monitoring of mercury in flue gas from coal-fired utilities. The SCS will provide a method to use an analyzer such as CVAAS or CVAFS to measure TVM, EM, and TM.

Great River Energy (GRE), PSEG Fossil, LLC, WE Energies and Xcel Energy offered their support and one of their facilities as test sites. Field evaluations of the SCS were conducted at the three test locations to demonstrate the mercury SCS at plants firing low-chlorine North Dakota lignite, a high-chlorine low-sulfur eastern bituminous coal, and a Powered River Basin (PRB) coal. The complete system was evaluated at the low-chlorine coal site (Site 1) using procedures described in the EPA PS-12. Testing included calibration zero and drift checks over a seven-day period, calibration error evaluations, and relative accuracy test using the Draft Ontario Hydro method as the reference method. Long-term evaluations at the high-chlorine coal site (Site 2) and the PRB site (Site 3) have been concluded. A month-long evaluation of the system is currently underway at a PRB site (Site 4). Data from this evaluation will be presented at the conference.

Experimental

Sample Conditioning System

There are around a dozen commercially available Hg CEMs and all have their pros and cons. The real challenging part of any system is the sample conditioning portion or also called the front-end. Challenges include: fly ash interactions with the Hg in the flue gas, adsorption and absorption, obtaining a TM concentration, which includes particulate phase, and obtaining a particulate free gas stream with minimal maintenance.

The SCS, as shown in Figure 1, will provide a method to use an analyzer such as a CVAAS, Zeeman, or CVAFS to measure TVM, EM and TM. The vapor-phase portion of the system is a dual pass design, where TVM passes through one line and the elemental fraction through the second line. Particulate is removed from a common sampling probe and the flow is split to the two lines. All components in the two lines are identical except that soluble OM is removed from the sample gas stream upstream of other components in the first line. In both lines, the gas stream then passes through a catalyst to convert mercury to the elemental form. The gas is then conditioned to remove possible interfering gases and stabilize the EM prior to transport to an analyzer for measurement. In the system, sample conditioning takes place at the stack and only EM is being conveyed from the stack to the analyzer. Thus, problems related to reactivity and surface losses are minimized. For TM, a slipstream of flue gas is isokinetically extracted and heated to thermally desorb mercury from the fly ash. The effluent is then filtered and passed through a second TVM SCS line for measurement.

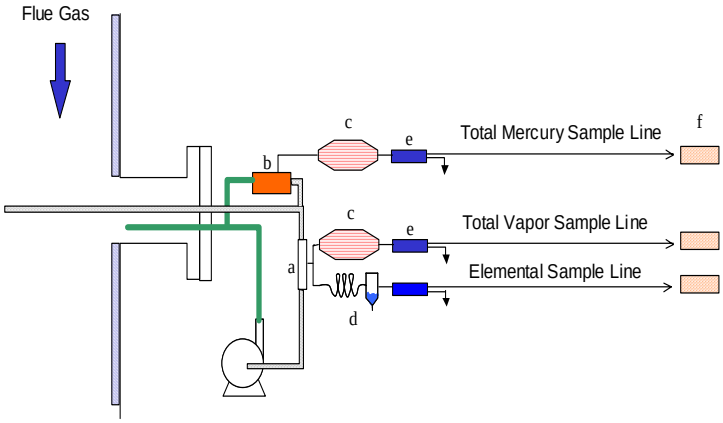

Figure 1. SCS arrangement for simultaneous measurement of TM, TVM, and EM.

Evaluation Methods

During field evaluations at the low-chlorine coal site, the performance specification test procedure identified in EPA's Draft

Performance Specification (PS-12) (see Table 1) was followed.

Apogee utilized two techniques to calibrate the mercury analyzer during SCS operation. The primary technique was the batch injection method. For this technique, a precise volume of mercury vapor is drawn off a flask containing liquid elemental mercury using a glass/Teflon™ syringe. A temperature and pressure measurement was taken before each sample drawn. When continuous concentrations of mercury are required, Apogee uses an elemental mercury permeation tube. If tests are conducted at a field site where the environmental conditions vary significantly, the mercury emitted from the permeation tube is referenced to the spike calibration technique. When a continuous concentration of OM was required for calibration, gas from the EM permeation tube was passed through a catalyst that converted 100% of the EM to OM. This technique simplifies calibration because the concentration of total mercury measured by the analyzer should remain unchanged regardless of the presence of the EM to OM conversion catalyst.

During the zero drift evaluation, no mercury was injected into the analyzer. A sample collection time of zero was set prior to evaluation. After the zero drift evaluation, a calculated amount of mercury vapor (approximately 50% of the duct concentration) was injected. Both the known concentration and the analyzer concentration were recorded. Other analyzer parameters were recorded as well to further evaluate analyzer performance. A second calibration concentration (approximately 100% of the duct concentration) was injected into the purge dry-gas line of the analyzer.

To confirm the measurements obtained with the SCS while on-site, a standard impinger based method was initially used. A reduction solution of stannous chloride in hydrochloric acid was used to convert OM to EM. The solution is mixed as prescribed in the draft Ontario Hydro Method for Manual Mercury Measurements. To measure speciated mercury, an impinger of potassium chloride (KCl) solution mixed as prescribed by the draft Ontario Hydro Method was used to capture oxidized mercury. Impinger solutions are continuously refreshed to assure continuous exposure of the gas to active chemicals.

Results and Discussion

Site 1 (Low-Chlorine Coal)

Apogee has completed field evaluations at one coal-fired utility that burns North Dakota Lignite coal, a low chlorine coal that produces a flue gas with primarily elemental mercury. The unit has two cold-side ESPs operating in parallel followed by a single scrubber. The test location was downstream of the ESP and upstream of the scrubber for a dry, low chlorine sample. The system was subjected to the EPA draft PS-12 and performed very well. Results from this site have been presented previously at numerous conferences.

Site 2 (High-Chlorine Coal)

Apogee has completed field evaluations at a coal-fired utility that burns a bituminous fuel; a high chlorine coal that produces a flue gas with primarily oxidized forms of mercury. The unit has two cold-side ESPs operating in parallel. The test location was downstream of the ESPs. The oxidized removal module performed very well at the site, however the total vapor mercury (TVM) module initially encountered some difficulties with the flue gas chemistry. The TVM module's initial performance was characterized by an initially stable mercury concentration that would begin to decay over time until finally no mercury was being transported to the analyzer at all. After investigation it was determined that vapor-phase selenium was being reduced to hydrogen selenide, which was reacting with the elemental mercury at the exit of the module. A gas stream additive was found which eliminated the problem. Evaluations were performed to verify the performance of the system with the selenium mitigation. The results were very good, despite the fact that the mitigation method had not been optimized. The TVM module was operated with an overboard calibration system to verify its performance. Data will be presented at the conference showing the performance of the TVM and also a discussion of the selenium-mitigation modification.

Site 3 (PRB)

A long-term evaluation of the TVM module has been concluded at a PRB utility at a test location downstream of a wet-venturi scrubber. This evaluation compares the performance of the TVM module with the standard wet chemical method. The performance of the system was very good and results agreed with those seen in the wet-chemical system very well. Data will be presented at the conference concerning this evaluation.

Site 4 (PRB)

A month-long evaluation of the TVM module is currently underway at an additional PRB fuel site. The test location is downstream of a cold-side ESP. No data is currently available; data from this evaluation will be presented at the conference.

Conclusions

It is possible to measure mercury in the flue gas from coal-fired boilers using mercury analyzers and current "wet chemistry" technologies, however theses techniques require significant care and attention by highly skilled personnel to achieve reasonable results. As of yet, this is not currently an option for meeting the emissions measurement needs beyond research applications. Several groups, including Apogee, are developing techniques to advance the way mercury measurements are taken. These techniques will require more field evaluations to assure that they are reliable in the majority of flue gas streams and able to be utilized over long periods.

Acknowledgements

Apogee would like to acknowledge the funding of EPA through an SBIR grant (Contract 68-D-01-060) and Project Manager James Gallup, EPRI's generous support and Project Manager Chuck Dene, and the support of Great River Energy, PSEG Fossil, and Xcel Energy.

References

1 Brown, Thomas, William O'Dowd, Robert Reuther and Dennis Smith. "Control of Mercury Emissions from Coal-Fired Power Plants: A Preliminary Cost Assessment." Presented at the DOE Conference on Air Quality: Mercury, Trace Elements, and Particulate Matter, December 1-4, 1998, McLean VA.

2 Sjostrom, Sharon, Trevor Ley, and Richard Slye, "Continuous Real-Time Monitoring of Mercury in Flue Gas from Coal-Fired Boilers: Field Experience." Presented at the Nineteenth Annual International Pittsburgh Coal Conference, September 23-27,2002.

3 Sjostrom, Sharon, Trevor Ley, "Development of a Sample Conditioning System for Reliable, Continuous Mercury Measurements in Coal-Fired Flue Gas." Presented at the Air Quality III Conference, September 11-12, 2002.

Characters of Activated Carbon for Hg Removal of Flue Gas with H_2S and Iron Oxide for Hg Removal of Coal Derived Fuel gas with H_2S

Shengji Wu , Tsuyosi Morimoto*, Md.Azhar Uddin**, Naoki Togaki*, Shinsuke Nagamine*, and Eiji Sasaoka**

* Department of Environmental Chemistry and Materials, Okayama University
3-1-1 Tsushima-naka Okayama Japan, 700-8530

** Chemical Engineering, School of Engineering, The University of Newcastle
University Drive, Callaghan NSW2308 Australia y

Introduction

The major anthropogenic sources of mercury emission are coal combustion and municipal waste incineration. However, it is very difficult to remove the mercury compounds, particularly elemental mercury vapor, which is not effectively captured in typical air – pollution control devices. It has been reported that activated carbon, particularly activated carbon impregnated with sulfur, chlorine, and iodine, are effective for Hg removal.[1-4] However, the major drawbacks of activated carbons are high cost, poor capacity, narrow temperature range and slow regeneration and adsorption rates.

We have presented a novel Hg removal method using H_2S and adsorbents.[5,6] This method based on the reaction of H_2S and Hg over adsorbents. Although the reaction mechanism is not well understood yet, but it has been suggested in our previous report that Hg reacts with H_2S and forms HgS.[5] The sublimation point of HgS(cubic) is 446°C. If the reaction (adsorption) between Hg and H_2S over suitable adsorbent (catalyst) occurs at a temperature well below the sublimation point of HgS, then elemental mercury can be removed from the flue gas effectively. In this study, we tried to clarify the removal characters of an activated carbon and an iron oxide for the removal of Hg vapor: The activated carbon was useful for the Hg removal from a combustion flue gas; the iron oxide was useful for the Hg removal from a coal derived fuel gas.

Experimental

Sorbents. Activated Carbon (AC) was purchased from Wako Pure Chemical Co. LTD. The raw material of this activated carbon was coconut shell. The granular active carbon was washed with de-ionized water and calcined for 3h at 300° in the N_2 flow. The granular AC particles were sieved into an average diameter of 1.0mm. BET surface area measured using liquid nitrogen was ca. 1100m^2/g.

An iron oxide sample was prepared by a precipitation method using a reagent grade $Fe(NO_3)_3.9H_2O$ and NH_3aq at room temperature. The precipitant was washed with de-ionized water and dried for 25h at 110°C under atmosphere. The dried sample contained FeO(OH). BET surface of the sample was ca.200m^2/g.

Apparatus and Procedure. The evaluation of the reactivity of the samples was carried out using a flow-type packed bed reactor under atmospheric pressure. About 0.5 cm^3 or 0.25 cm^3 of the sample particles (diameter: 1.0m.) was set in quartz tube reactor. The reaction temperatures range examined was from 80 to100^{o}C. The reaction for Hg removal of flue gas was carried out with a mixture of Hg (4.8ppb), H_2S (0 or 40ppm), SO_2(0 or 250ppm), CO_2 (13%), H_2O(8%), O_2(5%), and N_2 (balance gas) at 500cm^{3}STP/min (SV:6.0X10^4 h^{-1}). The reaction for Hg removal of coal derived fuel gas commenced when a mixture of Hg(4.8ppb), H_2S(400ppm), CO(30%), H_2(20%), H_2O(8%), and N_2 (balance gas) was fed into the reactor at 500 cm^{3}STP/min (SV:12X10^4 h^{-1}). The measurement of the inlet and outlet concentration of mercury were carried out using a cold vapor mercury analyzer.

Results and Discussion

Character of AC for removal of the flue gas with H_2S.

Effect of the temperature on the Hg removal in the both presence of H_2S and SO_2. As shown in **Figure 1**, there was a suitable temperature: the

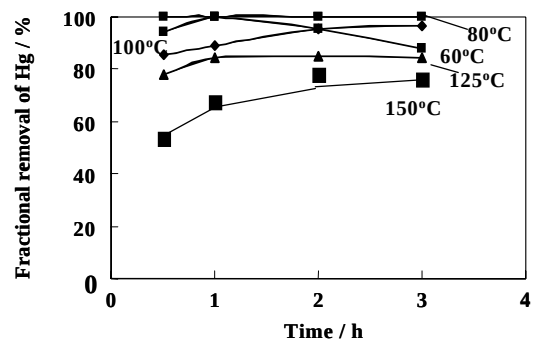

Figure 1. Effect of temperature on the Hg removal.

temperature range was 80 ^{o}C. The reason of this dependency of the temperature on reactivity may be explained by the removal mechanism if the mechanism is clarified.

Effect of the presence of SO_2 and H_2S on the Hg removal

The AC removed a negligible amount of Hg at 150°C in the presence of SO_2 or H_2S. However, in the both presence of SO_2 and H_2S, the AC could remove the considerable amount of the Hg as shown in **Figure 1**. This result may suggest that Claus reaction occurred over the AC and the produced sulfur reacted with the Hg vapor.

$$SO_2 + 2H_2S = S_{ad} + 2H_2O \quad (1)$$

$$S_{ad} + Hg = HgS \quad (2)$$

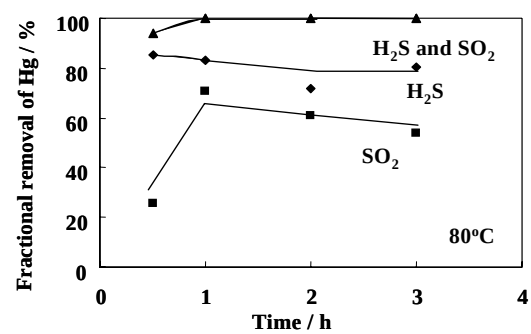

Figure 2 Effect of the presence of SO_2, H_2S and SO_2-H_2S.

As shown in **Figure 2**, the AC could remove a considerable amount of the Hg vapor in the only presence of SO_2 or H_2O at low temperature (80°C),. In the both presence of SO_2 and H_2S, the AC could almost perfectly remove the Hg vapor as shown in Figure1. This result suggests that the mechanism of the Hg removal with AC is different at the low- and the high-temperature. Furthermore, the difference of the mechanism in the temperature range may be a cause of the existence of the suitable temperature for the Hg removal.

Effect of the presence of H_2O on the Hg removal

The presence of H_2O at 100 and 80°C accelerated the Hg removal

with the AC in the both presence of H_2S and SO_2. However, the presence of H_2O at 150°C depressed the Hg removal with the AC as shown in **Figure 3**. This result also suggests that the mechanism of the Hg removal is different at the low and high temperature.

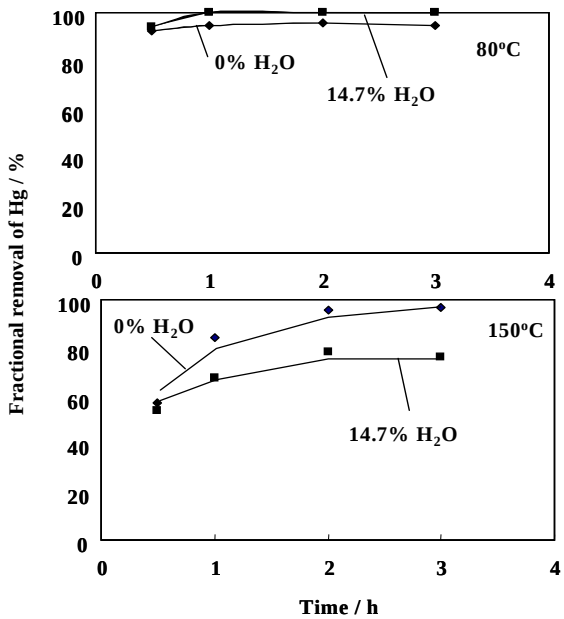

Figure 3. Effect of the presence of H_2O.

Character of the Iron oxide for Hg removal of the coal derived fuel gas with H_2S.

Effect of the temperature on the Hg removal

As shown in **Figure 4**, the activity of the iron oxide for the Hg removal increased with the decrease of the reaction temperature. After use of the iron oxide under the low temperature60 and 80°C, the sample was not changed when it was exposed to the air. However, at the high temperature 150°C, the temperature of the used sample

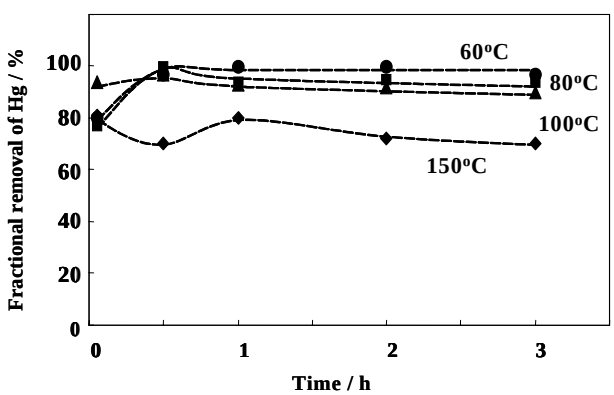

Figure 4. Effect of temperature on the Hg removal.

was increase when the used sample was exposed to the air. Furthermore, the sulfur smelled up from the sample at that time. After cooling in nitrogen atmosphere, another used sample was measured with XRD. We confirmed the formation of magnetite in the sample. From these results, it was suggested that the formed sulfur over the sample vaporized by heating when the sample magnetite exothermally changed to hematite with air. Form these experimental results and consideration, it was supposed that sulfur formed from H_2S over the iron oxide contributed to the Hg removal and also the surface oxygen or part of the lattice oxygen of the sample iron oxide contribute to produce of sulfur from H_2S.

Effect of the presence of CO and H_2Oon the Hg removal

As shown in **Figure 5**, the presence of CO at 150°C accelerated the Hg removal but the acceleration of the presence of it at 80oC was not observed. The effect of the presence of H_2 at 80°C also did not observed

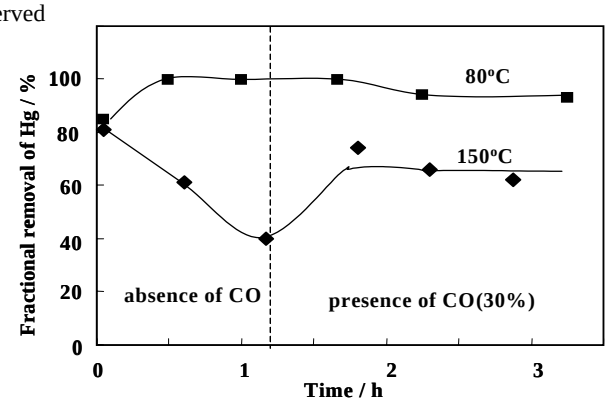

Figure 5. Effect of the presence of CO on the Hg removal

The presence of H_2O depressed the Hg removal in the temperature hole range from 60 to 150oC.

Conclusion

The characters of the Hg removal for the flue gas with the AC and the Hg removal for the fuel gas with the iron oxide could be considerably clarified.

Acknowledgment

This work was supported by the Steel Industrial Foundation for Advacemenet of Environmenral Protection Technology.

References

1) R. K. Sinha and P. L.Walker,"Removal Mercury by Sulfurized Carbon". *Carbon*,**1972**,10, 754.
2) Y. Otani, C. Kanaoka,C.Usul, S. Matuui, and H.Emi. "Adsorption of Mercury Vapor on Particles". *Environ. Sci. Technol*, **1986**,20,735.
3) S, V. Krishnan, B.K.Bullett, and W.Jozewicz. "Sorption of Elemental Mercury by Activated Carbon". . *Environ. Sci. Technol*, **1994**,28,1506.
4) H. C. Hsi, M. J. Rostam-Abadi, M. Chen, S.Chang, "Effects of sulfur impregnation temperature on the properties and mercury adsorption capacities of activated carbon fibers Aces". *Environ. Sci. Technol*, **2001**,35,1506
5) W. Nakajima, N. Tougaki, S.Wu, S.Nagamine, and E.Sasaoka. "Removal of Gas Phase Mercury by Solid Sorbent". Trace Element Workshop **2002**,18-19,July Yokohama, pp257.
6) Naoki Togaki, Md.Azhar Uddin,Wataru Nakasima, Shengji Wu, Shinsuke Nagamine, and Eiji Sasaoka. "Activity of Adsorbents for Removal of Mercury Vapor with H_2S" 20th Pittsburgh Coal Conference, 36-4, 2003, 15-19,September, Pittsburgh, PA USA.

Inorganic Components in Coal and Their Behavior at Elevated Temperatures

Steven A. Benson

Energy & Environmental Research Center, University of North Dakota, 15 North 23rd Street, Grand Forks, ND 58203, Fax: 701-777-5181, sbenson@undeerc.org

The unexpected behavior of inorganic components in coal at elevated temperatures has humbled many researchers and technology developers. Many coal utilization technologies are developed with out an adequate assessment of the impacts of the inorganic components present in coal. The abundance and forms of inorganic components vary between coal types, coal seams and within the seams. Subbituminous and lignitic type coals contain organically associated and minerals. Bituminous and anthracite coals contain mainly minerals. During heating the inorganic components are transformed to gases, liquids, and solids. The characteristics of the inorganic gases, liquids, and solids reflect the association and abundance of the inorganic components in the coal and system conditions such as temperature and gas composition. Analysis of fly ash produced during combustion is highly complex and variable both in size and composition. Fly ash typically has a bimodal size distribution. The submicron size particles form as a result of condensation of flame-volatilized species upon gas cooling. The larger sized particles are derived from the non-volatile inorganic components. The physical and chemical properties of the ash intermediate species can cause significant challenges to the efficient and reliable operation of coal utilization technologies. The challenges include wear of system components, maintaining slag flow in wet bottom system, formation of deposits on heat transfer surfaces, formation of agglomerates in fluidized bed system, blinding and plugging of selective catalytic reduction systems for NOx, and controlling the emission of toxic inorganic components. Many of the adverse impacts of inorganic components are being minimized through the use of more sophisticated methods of coal analysis and prediction. In addition, control technologies are being demonstrated to control the emission of volatile inorganic components such as mercury.

A full manuscript will be published in Fuel.

Self assembly during the pyrolysis of coking coals and its exploitation for the synthesis of new carbon materials and nanomaterials

Robert Hurt

Division of Engineering, Brown University, Box D, Providence, RI 02912, Fax: 401-863-9120, robert_hurt@brown.edu

The formation of ordered carbon during the thermal treatment of some bituminous coals occurs by a unique natural process of discotic fluid self assembly and covalent capture. The report by Brooks and Taylor in 1965 of this ordered fluid intermediate, carbonaceous mesophase, represents the original discovery of the discotic nematic liquid crystalline phase. This talk will describe the origin, properties and behavior of carbonaceous mesophase and its relation to other discotic materials. The discotic assembly process occurring naturally in coal can also be systematically directed by templates and nanoconfined spaces to make unique supramolecular disk assemblies that can be converted to carbons by thermal treatment. The talk will discuss the synthesis of new carbon nanofibers and nanotubes as well as ordered and patterned thin films, whose graphene layer arrangements and properties can be molecularly engineered by this principle.

A full manuscript will be published in Fuel.

Pyrolysis mechanisms of coal model compounds

Phillip F. Britt and A. C. Buchanan III,

Chemical Sciences Division, Oak Ridge National Laboratory, Building 4500N, MS-6197, P.O. Box 2008, Oak Ridge, TN 37831-6197, Fax: 865-576-7956, brittpf@ornl.gov

In the thermochemical conversion of coal, product formation is controlled by the relative rates of bond breaking, hydrogen donation, cross-linking, rearrangements, and mass transport. As a consequence of the structural complexity and heterogeneity of coal, it has been difficult to determine the reaction pathways at the molecular level. Thus, the pyrolysis of compounds that model key structural features found in coal has been studied to gain insight into the reaction pathways in coal, provide fundamental data for the development of kinetic models to describe the processing of coal at the molecular level, and provide fundamental knowledge to guide the design of more efficient strategies for the conversion of coal to higher value products. Over the past decade, our research group has focused on the impact of restricted mass transport on free radical reactions, reaction pathways of oxygen functional groups in low rank coal and lignin, and the role of carboxylic acids in cross-linking reactions in low-rank coal. Highlights from these mechanistic studies will be presented and its relevance to the thermal processing of coal discussed.

A full manuscript will be published in Fuel.

Harold Schobert and the JP-900 Jet Fuel Program

Michael M. Coleman

Pennsylvania State University, University Park, PA 16802,
mmc4@psu.edu

It is truly a pleasure to have been asked to contribute to this Storch Award symposium honoring Professor Harold Schobert. Some 12 years ago, I was approached by Harold who asked me if I was interested in joining a multi-disciplined research group that he was forming. He explained that the research group was going to attempt to make a new generation of thermally stable coal-based jet fuels that could withstand temperatures of 900°F (JP-900) and that my expertise as a polymer physical chemist could be useful in understanding the carbonaceous reactions that occur upon thermal degradation. My immediate reaction was, "he's crazy"! 900°F, that's almost 500°C! Surely there is no organic fuel that can withstand such temperatures. However, I agreed to join the group (I was a little short of research funds at the time!), and in this seminar I will describe how, with a little luck and perseverance, a JP-900 fuel was successfully developed.

A full manuscript will be published in Fuel.

Extreme coalification: From lignite to anthracite in one career

Harold H Schobert

The Energy Institute, Pennsylvania State University, C211 Coal Utilization Lab, Unversity Park, PA 16802, Fax: (814)863-8897, schobert@ems.psu.edu

A retrospective and idiosyncratic review of coal chemistry. The specific emphasis focuses on (1) internal hydrogen transfer during coal reactions (without an external hydrogen source or hydrogen donors); (2) the role of net hydrogen as a correlative parameter for coal reactions; and (3) the advantages for coal conversion process development for producing high-value carbon products along with coal chemicals or liquid fuels. Examples will be drawn from the liquefaction chemistry of low-rank coals; co-coking of high-volatile bituminous coals for simultaneous production of coal-based jet fuel and needle coke; using medium-volatile bituminous coals as a source of hydrogen; and explorations of the chemistry of anthracite, including graphitization reactions.

A full manuscript will be published in Fuel.

THE PRESIDENT'S HYDROGEN FUEL INITIATIVE

Steve Chalk, Pat Davis, Pete Devlin, JoAnn Milliken, and John Petrovic

Office of Hydrogen, Fuel Cells and Infrastructure Technologies, U.S. Department of Energy, 1000 Independence Avenue SW, Washington, DC 20585

In his 2003 State of the Union address, President Bush launched the Hydrogen Fuel Initiative, "so that America can lead the world in developing clean hydrogen-powered automobiles". The elements of this Initiative involve research, development and demonstration activities on hydrogen production and delivery, hydrogen storage, fuel cells, technology validation, safety, codes/standards, and education. The DOE-OHFCIT goals and objectives for each of these aspects will be described. Research and development needs and opportunities in chemistry and materials science related to hydrogen production, storage, and fuel cells will be highlighted. The Hydrogen Fuel Initiative will provide the RD&D necessary or a decision in 2015 by U.S. industry to commercialize fuel-cell-powered vehicles.

ENERGY-RELATED RESEARCH IN THE DOE OFFICE OF BASIC ENERGY SCIENCES

Patricia M. Dehmer

Office of Basic Energy Sciences, U. S. Department of Energy, SC-10/Germantown Building, 1000 Independence Avenue, SW, Washington, DC 20585-1290

The $1 billion Basic Energy Sciences (BES) program in the Department of Energy's Office of Science sponsors fundamental research in materials sciences and engineering, chemistry, geosciences, and biosciences that impacts energy resources, production, conversion, efficiency, and the mitigation of the adverse impacts of energy production and use. BES supports a large extramural research program, with approximately 40% of the program's research activities sited at academic institutions. BES also plans, constructs, and operates major scientific user facilities, including synchrotron radiation light sources, neutron scattering facilities, electron-beam microcharacterization centers, nanoscale science research centers, and facilities for materials synthesis and processing.

Dr. Patricia Dehmer, Director of BES, will give an overview of emerging research opportunities including summaries of three recent workshops that will shape the future course of the program – *Basic Research Needs for a Secure Energy Future*, *Basic Research Needs for the Hydrogen Economy*, and *A 20-year Basic Energy Sciences Facilities Roadmap*. Specifically, she will highlight BES' priorities related to the Administration's Hydrogen Fuel Initiative and the BES-sponsored hydrogen workshop report.

BASIC RESEARCH NEEDS FOR THE HYDROGEN ECONOMY

Mildred S. Dresselhaus

Massachusetts Institute of Technology, 77 Massachusetts Avenue, Cambridge, MA 02139

A summary is presented of a recent BES/DOE sponsored report that addresses the basic research needs in the areas of hydrogen production, storage, and use in fuel cells that would be necessary to bridge the large gap between present scientific knowledge/technical capabilities and what would be required for the practical realization of a hydrogen economy. In this report, research opportunities that might be effective in bridging this gap are identified in the areas of advanced materials (especially nanostructured materials), catalysis, modeling and simulations, bio-inspired approaches, and interdisciplinary efforts.

BASIC RESEARCH NEEDS IN HYDROGEN PRODUCTION FOR A HYDROGEN ENERGY ECONOMY

Thomas E. Mallouk[1] *and Laurens Mets*[2]

[1]Department of Chemistry, 152 Davey Laboratory, The Pennsylvania State University, University Park, PA 16802

[2]Department of Molecular Genetics and Cell Biology, University of Chicago, 1103 E. 57th St, Chicago, IL 60637

We report the findings on hydrogen production from a recent Department of Energy sponsored workshop on hydrogen production, storage, and use. The development of large scale, cost-effective, and sustainable hydrogen production methods poses many technical challenges. We consider basic research needs in the context of the scale of the problem, current methods of hydrogen production, and the timeline for implementation of hydrogen as an energy currency for transportation and other uses.

HYDROGEN STORAGE ISSUES IN A NEW HYDROGEN ECONOMY

Puru Jena

Physics Department, Virginia Commonwealth University,
Richmond, Virginia 23284-2000

The limited supply of fossil fuels, its adverse effect on the environment, and growing worldwide demand for energy has necessitated the search for new and clean sources of energy. The possibility of using hydrogen to meet this growing energy need has rekindled interest in the study of safe, efficient, and economical storage of hydrogen. Unfortunately, the current methods for storing hydrogen as a compressed gas or liquid do not meet the industry requirements. An alternate method for hydrogen storage involves metal hydrides. The conventional intermetallic hydrides store hydrogen at interstitial sites and are reversible at around room temperature. However, the relative weight of stored hydrogen in these materials is rather low (1 – 3 wt %) and do not meet the requirement of the transportation industry (~10 wt %). A novel approach for hydrogen storage is to combine the favorable kinetics and thermodynamics of conventional metal hydrides with that of the large hydrogen storing capacity of organic molecules such as CH_4. Although alanates, with the chemical composition $[M^{n+} (AlH_4)^{n-}$, M= Li, Na, K, Mg], belong to this class, the desorption temperature of hydrogen in these materials is rather high. It was recently discovered that doping of Ti-based catalyst in $NaAlH_4$ can significantly lower the hydrogen desorption temperature, but why and how Ti accomplishes this task remains a mystery. Using first principles calculations, we will provide a molecular level understanding of the role of Ti in lowering the hydrogen desorption temperature in $NaAlH_4$ and $LiBH_4$. It is hoped that the understanding gained here can be useful in designing better catalysts as well as hosts for hydrogen storage.

FUEL CELLS: THE FINAL STEP IN A HYDROGEN ECONOMY

Francis J. DiSalvo

Department of Chemistry and Chemical Biology, Cornell University, 102 Baker Laboratories, Ithaca, NY 14853

Fuel Cells transform the chemical energy carried by a fuel into electrical energy. Hydrogen fuel cells are especially well suited for this task because they operate with high efficiency, they do not produce pollution, and they provide electrical power that can be tailored to a wide variety of applications – from large stationary power plants to transportation vehicles to consumer devices like cell phones and personal computers – all assuming that the challenges of hydrogen production and storage can be met.

The basic fuel cell types span a remarkable range of operating temperatures, construction materials, and performance specifications. Although fuel cells offer many advantages for a diverse set of applications, so far they have been introduced only on a limited scale and at high cost. There are serious and difficult obstacles to widespread implementation of fuel cell technology. Most of the challenges arise from the need for inexpensive, more durable materials that also have better operating characteristics, especially in the case of the electrocatalysts, membranes (ionic conductors) and reformer catalysts.

Reformers offer the potential for operating fuel cells by using a range of primary fuels based on gaseous or liquid hydrocarbons. Some current and proposed fuel cell power systems that are capable of using fuels other than hydrogen, either directly or through reformers, may serve as transitional technologies along the path to a full hydrogen economy. These hydrocarbon-based fuel cells may be important in increasing the efficiency of fuel use and in decreasing emissions or noise, a highly valued aspect in some military, commercial and consumer applications in the shorter term. However, some of the fundamental problems in fuel cell technology are independent of the fuel source, as we will discuss in this presentation.

In this presentation, we discuss primarily the challenges and problems associated with low-temperature fuel cells (operating from 40 to 150 or 200 ^{o}C) and, to a lesser extent, with high-temperature (650 to 1000 ^{o}C) fuel cells. Low temperature fuel cells, in particular, are the focus of current automotive fuel cell R&D activities that, when implemented, would be a major component of a hydrogen economy.

The development of efficient, durable and low cost fuel cells is a grand challenge that will take substantial and sustained efforts in chemical and materials research. These challenges can only be met by new materials with improved, or even revolutionary, properties and performance. A basic, exploratory research program of significant size and scope is needed to produce these enabling discoveries.

This presentation will outline many of the challenges and opportunities that need to be addressed with basic research in materials synthesis, analytical studies of the processes and kinetics of reaction as well as materials degradation, theoretical modeling, etc. It is hoped that by outlining the challenges, the scientific community can be energized to be engaged in the process of discovery and invention to produce the breakthroughs necessary to enable this vision of an energy future that promises less pollution and less reliance on energy imports.

Review of Novel Methods for Carbon Dioxide Separation from Flue and Fuel Gases

Evan J. Granite

United States Department of Energy, National Energy Technology Laboratory, Pittsburgh, PA 15236-0940

Introduction

The President recently announced the U.S. Global Climate Change Initiative (GCCI) to reduce greenhouse gas (GHG) intensity by 18% by 2012.[1] The GCCI proposal would slow the growth in U.S. emissions of carbon dioxide. Alkaline sorbents and scrubbing solutions are often employed to separate carbon dioxide from various gas matrices. Cryogenic separation of carbon dioxide is also commonly used. A comprehensive review of carbon dioxide capture methods is given by White.[2-4] Novel methods could have the potential to reduce the cost of carbon dioxide sequestration. These methods include electrochemical, membrane, enzymatic, photosynthesis, and catalytic routes for CO_2 separation or conversion.[2-5]

This paper reviews some of the more novel methods for carbon dioxide separation from flue and fuel gas streams. These methods include electrochemical pumps, photosynthesis, membranes, and biomimetic-enzyme approaches to CO_2 separation. Electrochemical pumps discussed include carbonate and proton conductors. The various bioreactors employed for photosynthesis are surveyed. Selective membranes for hydrogen separation are discussed as a method for carbon dioxide concentration in fuel gas streams. The selective membranes include mixed ionic-electronic (solid electrolyte-metal) films as well as palladium-based materials. Biomimetic methods utilizing the enzyme carbonic anhydrase are reviewed. The fundamental mechanisms behind these techniques will be explained, and recent advances in these methods are emphasized. Future research directions are suggested and an extensive list of references is provided.

Electrochemical Pumps for Separation of CO_2 from Flue Gas

Carbonate Ion Pumps

The molten carbonate and aqueous alkaline fuel cells have been studied for use in separating carbon dioxide from both air and flue gases.[6-13] Operation of the molten carbonate fuel cell in a closed circuit mode (with application of an external emf) will result in the transport of carbonate ions across the membrane.[6-13] The molten carbonate electrochemical separator requires oxidizing conditions for the formation of carbonate from carbon dioxide, and is less applicable for direct separation of CO_2 from fuel gases. This pioneering work was first performed by Winnick .[6-8] Winnick proposed the use of molten carbonate fuel cell membranes for separation of carbon dioxide from air for space flight (Sky Lab).[6-8] Winnick first examined molten carbonate membranes for separation of CO_2 from power plant flue gas.[6-8] More recently the Osaka Research Institute in Japan , British Petroleum in the UK, and Ansaldo Fuel Cells in Italy have also experimented with molten carbonate electrochemical systems for CO_2 capture from flue gas.[9-13]

There are several advantages of molten carbonate electrochemical cells for CO_2 separation. A large knowledge base exists for the use and application of molten carbonate from its use in fuel cells. Molten carbonate is nearly 100% selective for the transport of carbonate anions at elevated temperatures. It exhibits high conductivity of around 1 S/cm at 1100EF, or equivalently a diffusivity of 10^{-5} cm^2/sec for the carbonate anion.[6-8] The parasitic power requirements for the separation of carbon dioxide from power plant flue gases are low and estimated to be less than 5%.[8] The cost for CO_2 capture from flue gas was estimated at $20/ton in 1990 by Winnick .[8]

Unfortunately there are major disadvantages in the application of molten carbonate electrochemical cells for separation of carbon dioxide from power plant flue gas. Molten carbonate is a corrosive paste. The high temperatures, along with the extremely corrosive nature of the molten carbonate, make fabrication and handling extremely difficult. The small applied voltages allowable in order to avoid decomposition of the molten carbonate result in low currents. The current represents the flux of carbonate anions across the membrane. This necessitates the use of huge stacks to obtain a significant flux of carbonate ions across the device.[8-13] Sulfur dioxide present in flue gas poisons the cell, resulting in sulfate formation.[8-13] There are also severe problems with electrolyte segregation and electrode degradation in the severe high temperature flue gas environment.[8-13]

A solid electrolyte membrane for the separation of carbon dioxide from flue gas could solve many of the problems associated with molten carbonate.[14-16] Solid electrolytes are solid ionic conductors, and are used in sensors, catalyst studies, and fuel cells.[17] Millions are used in automobiles as the oxide air-fuel ratio sensors. Most solid electrolytes are ceramics. Solid electrolytes often operate at lower temperatures than molten carbonate cells. A solid electrolyte would be easier to handle, have far reduced corrosion problems, and would possess a longer operating life than its molten carbonate counterpart. The development of a highly conductive carbonate ion solid electrolyte is an area of active research.[14-16] The possibility of using alkali carbonate or alkaline earth carbonate solid electrolytes for the separation of carbon dioxide from flue gas is discussed by Granite.[14-16] Granite and Pennline propose doping alkaline earth carbonates in order to increase the ionic conductivity by orders of magnitude.[14-16] Recent evidence suggests that it will be difficult to obtain mobile carbonate anions within a solid electrolyte matrix.

Electrochemical Pumps for Concentrating CO_2 from Fuel Gas

Proton Pumps

Hydrogen gas can be produced by IGCC plants, steam gasification reactions, the pyrolysis of coal, the electrolysis of water, and biochemically. Each of these processes generate hydrogen with associated impurities, such as carbon monoxide, carbon dioxide, methane, nitrogen, water, and oxygen. Oxygen must be removed from hydrogen streams in order to avoid explosion hazards.

Previous hydrogen purification processes involved the step-wise removal of the impurities through absorption processes such as MEA (ethanolamine) washing to remove the carbon dioxide, TEG (glycol) dehydration of the gas, as well as the catalytic (Pt) removal of trace oxygen. A far simpler and potentially more cost-effective means of hydrogen separation and carbon dioxide concentration can be accomplished in one step by an electrochemical pump.[17-22] These electrochemical pumps are efficient, silent, and non-polluting. The electrochemical pumps can be based upon the readily available β@ alumina, nafion, and barium cerium oxide solid electrolytes.[17-22] An analysis of the electrochemical hydrogen pump, similar to the analysis of the carbon dioxide pump above, follows

The application of an external EMF (voltage) to a proton-conducting solid electrolyte through a closed circuit will cause hydrogen to be selectively transported (pumped) to/or from a metal electrode. The rate of hydrogen transport is given by the current

(flux of protons) across the membrane as:

$$\text{flux of } H_2 = I/2F \qquad (1)$$

where F is Faraday=s constant, 96,487 coulombs/mole.

There are several factors which limit the transport of hydrogen (current) across the membrane, and these are the conductivity of the electrolyte, thermodynamic stability of the electrolyte, and the electrode kinetics.

For an ohmic membrane (V = IR), current is inversely proportional to the resistance or proportional to the conductivity. The doped barium cerium oxide, $BaCe_{0.9}Y_{0.1}O_{2.95}$, has a conductivity of 10^{-1} $ohm^{-1}cm^{-1}$ at 1832EF.[18-20] The conductivity of β@ alumina is 10^{-6} $ohm^{-1}cm^{-1}$ at 212EF. [17,21-22] Nafion (polymer electrolyte) is typically employed at temperatures of around 212EF. The higher conductivity of the doped barium cerium oxide allows a higher flux of protons to be pumped to a metal electrode.

The maximum value for the applied external voltage is determined by the decomposition potential of the solid electrolyte. This is found from the thermodynamic stability, the free energy of formation, ΔG_f, of the material, namely:

$$\Delta G_f = -nFE \qquad (2)$$

where E is the maximum applied voltage.

More stable electrolytes can be subjected to higher applied voltages. Typically a one to two volt potential can be applied to a ceramic membrane. Therefore, the rate of transport of protons across the membrane is limited by both the conductivity (resistance) and stability of the electrolyte.

Electrode kinetics also plays a key role in the rate of separation of hydrogen. Consider the example of a closed β@ alumina electrochemical cell having palladium electrodes. Hydrogen must be first adsorbed from the impure gas stream on to the palladium electrode. Hydrogen then dissociates to hydrogen atoms. Charge transfer occurs, with protons forming. The protons migrate across the electrolyte under the influence of the externally applied field (voltage). Finally, the protons reverse the earlier steps, and form hydrogen gas at the opposite palladium electrode. At the interface between the gas, metal electrode, and solid electrolyte (the three-phase boundary), the overall reaction can be written as:

$$H_{2(gas)} \equiv 2\,H^+ + 2\,e^- \qquad (3)$$

Therefore an electrode must efficiently adsorb and dissociate hydrogen so as to not limit the rate of hydrogen transport across the electrolyte. The electrode must be porous to allow gas to diffuse in and out, yet continuous, to avoid short-circuits. Electrodes can be formed by thermal decomposition of organometallic precursor compounds on the electrolyte surface or with metal pastes.

The overall resistance of the pump is the sum of the resistances due to the electrode, electrolyte, and the electrode and electrolyte contact. Overall resistance can be minimized by: 1. use of a thin electrolyte and electrodes, 2. having intimate contact between electrode and electrolyte, and 3. selecting an electrolyte with high conductivity.

The power consumed by the membrane separator is given by:

$$\text{Power} = VI = I^2R$$

For the lab-scale separator, with an applied voltage of around one volt, and a resulting current in the milliamp range, the power requirements will be on the order of milliwatts. Granite and Jorne applied external voltages to β@ alumina and barium cerium oxide membranes to obtain the selective transport of deuterium from D_2-N_2 mixtures. [17, 21-22] Balachandran recently applied an external voltage to a yttria-doped barium cerium oxide membrane to obtain the selective transport of protons.[18-20] The mechanism of proton conduction by $SrCe_{0.95}Y_{0.05}O_{3-\delta}$ is discussed by Balachandran.[20]

Conclusions

The novel CO_2 capture technologies have advantages and disadvantages when installed in a power-generation system. Initial evaluations by Herzog [23] indicate that certain technologies for CO_2 control from flue gas from conventional PC-fired power plants create a substantial thermal efficiency power loss. A study by Kosugi[24] investigated the various technologies by using a graphical evaluation and review technique. The target CO_2 capture technologies were compared for different levels of development. Although some of the technologies presently have larger penalties than others, future research and development will improve the projected energy efficiencies.

Electrochemical membranes have the potential to economically separate carbon dioxide from flue gas. Material science issues such as reducing corrosion (molten carbonate pumps) and increasing conductivity (solid electrolyte pumps) need to be addressed. More research on electrochemical methods for the separation of carbon dioxide from flue and fuel gases is recommended.

Acknowledgement.

The author thanks NETL colleagues Henry Pennline, Curt White, Brian Strazisar, Jim Hoffman, and Rich Hargis for helpful suggestions.

References

1) S. Global Climate Change Initiative information available on the web at http://www.epa.gov A President Bush Announces Clear Skies & Global Climate Change Initiatives@ **2002**, Feb. 14, http://www.epa.gov/epahome/headline2_021402.htm .
2) White, C.M.; Strazisar, B.R.; Granite, E.J.; Hoffman, J.S.; Pennline, H.W. Separation and Capture of CO_2 from Large Stationary Sources and Sequestration in Geological Formations-Coalbeds and Deep Saline Aquifers, *J. A&WMA* **2003**, 53, 645-715.
3) White, C.M.; Strazisar, B.R.; Granite, E.J.; Hoffman, J.S.; Pennline, H.W. Separation and Capture of CO_2 from Large Stationary Sources and Sequestration in Geological Formations-A Summary of the 2003 Critical review, *EM* **2003**, June, 29-34.
4) Chow, J.C.; Watson, J.G.; Herzog, A.; Benson, S.M.; Hidy, G.M.; Gunter, W.D.; Penkala, S.J.; White, C.M. Critical Review Discussion - Separation and Capture of CO_2 from Large Stationary Sources and Sequestration in Geological Formations, *J. A&WMA* **2003**, 53, 1172-1182.
5) Granite, E.J. A Review of Novel Methods for Carbon Dioxide Separation From Flue and Fuel Gases, *20th Int. Pitt. Coal Conf.*, **2003**, paper 29-1, Pittsburgh, PA.
6) Winnick, J.; Toghiani, H.; Quattrone, P. Carbon Dioxide Concentration for Manned Spacecraft Using a Molten Carbonate Electrochemical Cell; *AIChE J.* **1982**, 28(1), 103-111.

7) Weaver, J.L.; Winnick, J. The Molten Carbonate Carbon Dioxide Concentrator: Cathode Performance at High CO_2 Utilization; *J. Electrochem. Soc.* **1983**, 130(1), 20-28.
8) Winnick, J. Electrochemical Membrane Gas Separation; *Chem. Eng. Prog.***1990**, 41-46.
9) Itou, K.; Tani, H.; Ono, Y.; Kasai, H.; Ota, K-I High efficiency CO_2 separation and concentration system by using Molten Carbonate; Proceedings of GHGT-6, paper F3-5, Kyoto, Japan **2002**.
10) Amorelli, A.; Wilkinson, M.B.; Bedont, P.; Capobianco, P.; Marcenaro, B.; Parodi, F.; Torazza, A. An Experimental Investigation Into The Use Of Molten Carbonate Fuel Cells To Capture CO_2 From Gas Turbine Exhaust Gases; Proceedings of GHGT-6, paper F3-4, Kyoto, Japan **2002**.
11) Sugiura, K.; Takei, K.; Tanimoto, K.; Miyazaki, Y. The Carbon Dioxide Concentrator By Using MCFC; poster to be presented at Eighth Grove Fuel Cell Symposium, **2003**, London, UK.
12) Sugiura, K.; Yanagida, M.; Tanimoto, K.; Kojima, T. The Removal Characteristics of Carbon Dioxide in Molten Carbonate for the Thermal Power Plant; Proceedings of GHGT-5, **2000**, Australia.
13) Sugiura, K.; Takei, K.; Tanimoto, K.; Miyazaki, Y. The carbon dioxide concentrator by using MCFC, *J. of Power Sources*, **2003**, 118, 218-227.
14) Pennline, H.; Hoffmann, J.; Gray, M.; Siriwandane, R.; Granite, E. Recent Advances in Carbon Dioxide Capture and Separation Techniques at the National Energy Technology Laboratory; *AIChE National Meeting*, **2001**, Reno, NV.
15) Granite, E.; Kazonich, G.; Pennline, H. Electrochemical Devices For Separating and Detecting Carbon Dioxide; *DOE Carbon Sequestration Program Review Meeting*; **2002**, Pittsburgh, PA.
16) Granite, E.; Kazonich, G.; Pennline, H. Electrochemical Devices For Separating and Detecting Carbon Dioxide; *19th Int. Pitt. Coal Conf.*, paper 45-3, **2002**, Pittsburgh, PA.
17) Granite, E.J. Solid Electrolyte Aided Studies of Oxide Catalyzed Oxidation of Hydrocarbons, **1994**, PhD Thesis, Chemical Engineering, University of Rochester, Rochester New York.
18) Balachandran, U.; Ma, B.; Maiya, P.S.; Mieville, R.L.; Dusek, J.T.; Picciolo, J.; Guan, J.; Dorris, S.E.; Liu, M. Development of mixed-conducting oxides for gas separation; *Solid State Ionics* **1998**, 108, 363-370.
19) Guan, J.; Dorris, S.E.; Balachandran, U.; Liu, M. Transport properties of $SrCe_{0.95}Y_{0.05}O_{3-\delta}$ and its application for hydrogen separation; *Solid State Ionics* **1998**, 110, 303-310.
20) Song, S-J; Wachsman, E.D.; Dorris, S.E.; Balachandran, U. Defect chemistry modeling of high-temperature proton-conducting cerates; *Solid State Ionics* **2002**, 149, 1-10.
21) Granite, E.J. Electrochemical Pumps for the Separation of Hydrogen; NETL Project Proposal, **1999**, US Department of Energy, Pittsburgh, PA.
22) Granite, E.J.; Jorne, J. A Novel Method for Studying Electrochemically Induced ACold Fusion@ Using a Deuteron-Conducting Solid Electrolyte; *J. Electroanal. Chem.* **1991**, 317, 285-290
23) Herzog, H.; Drake, E.; Tester, J.; Rosenthal, R. A Research Needs Assessment for the Capture, Utilization, and Disposal of Carbon Dioxide from Fossil Fuel-Fired Power Plants; **1993**, Final report DOE Contract No. DEFG-02-92ER30194; MIT Energy Laboratory: Cambridge, MA
24) Kosugi, T.; Hayashi, A.; Matsumoto, T.; Akimoto, K.; Tokimatsu, K.; Yoshida, H.; Tomoda, T.; Kaya, Y. Evaluation of CO_2 Capture Technologies Development by Use of Graphical Evaluation and Review Technique. Presented at GHGT-6, Kyoto, **2002**; Paper B4-3.

SILICALITE – 1 ZEOLITE MEMBRANES FOR CO_2 SEPARATION

Margaret E. Welk, François Bonhomme, Tina M. Nenoff*

Chemical and Biological Technologies, Sandia National Laboratories, P.O. Box 5800, MS 0734, Albuquerque, NM 87185-0734, USA

*Presenting Author. Tel.: +1-505-284-9630; fax: +1-505-844-1480. E-mail: mewelk@sandia.gov.

Introduction

Much effort has recently been devoted to the synthesis of inorganic zeolite membranes because of their potential applications in the domains of gas separation, pervaporation, reverse osmosis or in the development of chemical sensors and catalytic membranes.[1,2,3,4,5] Specifically, development of new technologies for H_2 separation and purification has a high priority for the future of H_2 as a fuel source. H_2 is commonly produced by the reformation of hydrocarbons and must be purified, while CO_2 is created as a by-product; CO_2 must subsequently be sequestered. Zeolite membranes in particular combine pore size and shape selectivity with the inherent mechanical, thermal, and chemical stability necessary for long term separations.

The effective pore size distribution of the zeolite membrane, and hence its separation performance, is intrinsically governed by the choice of the zeolitic phase.[6,7,8,9] This applies when molecular size exclusion sieving is dominant and no other diffusion pathways bypass the network of well defined zeolitic channels; otherwise viscous flow through grain boundaries prevails. Zeolite membranes are typically synthesized on porous substrates by two different methods: [10] one step hydrothermal reaction on a pristine substrate from an aluminosilicate gel or by seed-promoted hydrothermal crystallization of the zeolitic layer. In both cases, the synthesis is affected by many complex interrelated factors such as the overall composition, concentration and viscosity of the gel, its pH, the source of silica and its degree of polymerization, the temperature and duration of the reaction. The optimization of these parameters is crucial to obtaining reliably "defect free" membranes. We report here on the synthesis of silicalite membranes on porous alumina disk supports, their characterization and their permeation performance for pure He, SF_6, H_2, CO_2, O_2, CH_4, N_2, and CO gases. We also show the reproducibility of the permeation values and the durability of a number of these films.

Experimental

Gases. Reagent grade pure gases were purchased from Trigas. H_2, CO_2, O_2, CH_4, N_2, CO were used to test the permeation characteristics of the membranes for reforming gases. SF_6 was used to detect defects, He was used to purge and clean the unit.

Permeation Measurements. The membrane permeations were measured at room temperature using pure gases and a constant trans-membrane pressure of 16 PSI controlled by a backpressure regulator. The membrane was sealed in a Swagelok fitting using Viton O-rings. The gas flow through the membrane was measured using an acoustic displacement flowmeter (ADM 2000 from J&W) and a digital bubble flowmeter (HP-9301). Between permeation measurements with different pure gases (SF_6, H_2, CO_2, O_2, CH_4, N_2, CO), the whole system is purged, flushed with Helium and evacuated several times. The ideal gas selectivity was calculated as the ratio of the permeances in the steady regime.

Characterization Techniques. The zeolite membranes and seeds were characterized by X-ray diffraction (Siemens D500 diffractometer, Cu Kα radiation, Bragg-Brentano geometry) and by Scanning Electron Microscopy (JEOL–6300V equipped with a Link Gem Oxford 6699 EDAX attachment).

Membrane Synthesis. In this work, the growth of the silicalite (Al-free ZSM-5) membrane on the porous support is achieved by secondary hydrothermal synthesis on supports seeded by rubbing.

The α-alumina substrates supplied by Inocermic Gmbh have a 1.8 micron average pore size, a diameter of 13 mm and a thickness of 1mm. The alumina substrates were first cleaned ultrasonically in acetone, rinsed in DI water and calcined at 1000°C overnight to remove any contaminants. All membranes in this work were obtained using seeded substrates to promote the nucleation and growth of the zeolite layer.

Tetra Propyl Ammonium (TPA) templated silicalite seeds were prepared under mild hydrothermal conditions in order to limit the size of the crystallites.[11] A rubbing method of seeding was used. The seeded alumina substrates were then heated in air to 500°C for 6 hours, and then cooled to room temperature using a ramp rate of 4°C /min to remove the TPA template and attach the seeds to the substrate. They were then stored in a desiccator for later use.

A hydrothermal gel is used in a secondary growth step to produce a defect free membrane. The silicon source for the membrane synthesis is colloidal silica Ludox SM-30 (Aldrich); the organic template used is Tetra Propyl Ammonium (TPA) from TPAOH and TPABr (both from Alfa Aesar), and NaOH is the alkalinity source. Each gel was aged while being stirred at room temperature for 24 hours.

The seeded substrates were held vertically in the Teflon lined Parr reactor using Teflon holders to prevent sedimentation on top of the membrane. The homogenous gel was then poured in the reactor until the membrane was fully immersed. The hydrothermal syntheses were carried out in Parr reactors with a 23ml Teflon liner at temperature ranging from 160°C to 180°C and reaction time from 12 hours to 48 hours.

After synthesis, the membrane was washed with DI water and dried in air at 50°C for a few hours. A permeation test on the as-synthesized membrane allows the rapid assessment of its quality before the time consuming calcination step. At that stage, a good quality membrane should be gas-tight, or impermeable, for SF_6. The SF_6 kinetic diameter of 5.5 Å is slightly larger than the pores of the zeolite (minimum diameter 5.1 Å) thus SF_6 diffusion indicates the presence of membrane defects.[12] Any existing defects (partial coverage of the substrate and micro-cracks) can be repaired by a second hydrothermal synthesis step, using a shorter reaction time and more diluted starting gel. These modifications to the original synthesis parameters help to avoid the growth of columnar zeolite crystals (or agglomerates of crystals) on top of the first layer, as they would not contribute to the plugging of the existing cracks or voids in the film. The membranes presented here were gas-tight prior to calcination and did not require a second hydrothermal treatment.

Once the adequacy of the membrane was established, the organic template was removed from the membrane pores by calcination in air. The calcined membranes are whitish in color, indicating that no carbon deposit is present on the surface.

Results and Discussion

Examination of the membranes by SEM showed dense coverage of zeolite crystals on the alumina support. The thickness of the crystalline layer is on average 10 microns and was found to be fairly uniform throughout the membrane.

An interesting feature of these membranes is that the permeance

of CO_2 is higher than that of any other gas tested, including He or H_2, even though the kinetic diameter of CO_2 is significantly larger than that of He or H_2. This property is observed reproducibly for every membrane synthesized and tested in our lab. See Table 1. As the CO_2 to air permeance ratios we observed are between 2 and 3, and the CO_2 permeances are up to $6x10^{-7}$ [mole/m^2 s Pa] our membranes could at room temperature separate CO_2 from air. The higher permeance of CO_2 than other gases is likely due to surface diffusion of the CO_2 (coexisting with Knudsen diffusion), which has apparently a good affinity for this zeolite surface.

We tested a broad series of light gases (He, SF_6, H_2, CO_2, O_2, CH_4, N_2, and CO), targeting those associated with methane reforming for H_2 production. Results show that methane exhibits a behavior similar to that of CO_2, diffusing faster than both He and H_2, although the enhancement is less pronounced. CO does not seem to interact strongly with the membrane, with permeance values very similar to those of O_2 or N_2.

Investigation of the performance durability and longevity of the silicalite membranes showed that the permeance for CO_2 decreases slowly with time. After more than 60 hours of continuous measurement under CO_2, one of the membranes (22B) showed only about a third of the initial flow value. The non-interacting gases such as He do not show a marked reduction in permeance over time. Importantly, the membrane could be partially "regenerated" by heating it with a temperature profile similar to that employed for the initial calcinations. The gas flow increased to about half the starting values. This gradual decrease of permeance with time observed with pure gas will likely occur over a longer time scale if gas mixtures are used. This "fouling" of the membrane should be of chief concern in any envisioned application since remediation by heating or pressure swings with inert gas will have to be used for performance recovery. Work continues with binary mixtures of gases and industrially relevant gas mixtures.

Table 1. Single Gas Permeance (10^{-7} mole/ m^2 s Pa). Trans-membrane pressure: 16 PSI.

Gas (Kinetic ∅ (Å)) Membrane	He (2.6)	SF_6 (5.5)	H_2 (2.8)	CO_2 (3.3)	O_2 (3.5)	CH_4 (3.8)	N_2 (3.6)	CO (3.7)
18A	1.8	< 0.05	2.4	2.9	1.4	-	-	1.6
21A	1.2	< 0.04	1.6	3.0	1.3	1.7	1.1	-
22A	1.5	< 0.02	2.0	5.9	1.2	3.2	1.4	1.4
22B	1.5	< 0.03	2.9	4.9	-	-	-	-
22B regenerated	1.1	-	1.4	2.9	-	-	-	-
28A	0.8	< 0.03	1.9	5.1	1.3	2.6	1.6	1.6

Conclusions

"Defect-free" Silicalite membranes have been grown reproducibly through experimentation with the synthetic parameters. The membranes are of uniform thickness and good quality as shown by the consistency and quality of the permeation data and the low SF_6 permeance. The permeation characteristics of silicalite membranes also show an interesting preference for pure CO_2 gas, which flows through the membranes faster than He gas or H_2 gas, despite the larger kinetic diameter of CO_2. CO_2 to air separation factor of 3 with permeance in the $5x10^{-7}$ [mole/m^2 s Pa] were observed. Modifications of the permeation unit to allow the use of gas mixtures at different temperatures are in progress and will allow the determination of the best regime for these membranes. The longevity and reproducibility of these membranes for gas separations make them valuable for CO_2 removal and sequestration in important methane reforming processes used for the production of H_2.

Acknowledgements. Sandia is a multiprogram laboratory operated by Sandia Corporation, a Lockheed Martin Company, for the United Stated Department of Energy's National Nuclear Security Administration under contract DE-AC04-94-AL85000. We thank the DOE/Hydrogen, Fuel Cells, and Infrastructure Technologies Program for continued funding. We thank John Heald for his powder x-ray diffraction help.

References

1 Armor, J. N. *J. Membr. Sci.*, **1998,** *147*, 217.
2 Caro, J.; Noack, M.; Kolsch, P.; Schafer, R. *Microp. Mesop. Mat.* **2000**, *38*, 3.
3 Chiang, A. S. T.; Chao, K-J. *J. Phys. Chem. Solids*, **2001,** *62*, 1899.
4 Noack, M.; Kolsch, P.; Schafer, R.; Toussaint, P.; Caro, J. *Chem. Eng. Technol.*, **2002,** *25*, 221.
5 Thoma, S. G.; Trudell, D. E.; Bonhomme, F.; Nenoff, T. M. Microp. Mesop. Mat. **2001**, *50*, 33.
6 Vroon, Z. A. E. P.; Keizer, K.; Gilde, M. J.; Verweij, H. Burggraaf, A. J. *J. Membr. Sci.* **1996**, *113*, 293.
7 Geus, E. R.; den Exter, M. J.; van Bekkum, H. *J. Chem. Soc. Faraday Trans.* **1992**, *88*, 3101.
8 Bakker, W. J. W.; Kapteijn, F.; Poppe, J.; Moulijn, J. A. *J. Membr. Sci.*, **1996**, *117*, 57.
9 Bai, C.; Jia, M-D.; Falconer, J. L.; Noble, R. D. *J. Membr. Sci.*, **1995**, *105*, 79.
10 Lin X.; Kita, H.; Okamoto K-I. *Ind. Eng. Chem. Res.*, **2001**, *40*, 4069.
11 Persson, A. E.; Shoeman, B. J.; Sterte, J.; Otterstedt, J. E. *Zeolites*, **1994**, *14*, 557.
12 Breck, D.W. Zeolite Molecular Sieves, (John Wiley and Sons, New York 1997).

Regenerable Aqua Ammonia Process for CO_2 Sequestration

James T. Yeh[1], Kevin P. Resnik[2], and Henry W. Pennline[1]

(1) National Energy Technology Laboratory, U.S. Dept. of Energy, NETL P.O. Box 10940, Pittsburgh, PA 15236-0940, Fax: 412-386-6004 james.yeh@netl.doe.gov, (2) National Energy Technology Laboratory, Parsons Project Services, Inc

Introduction

The monoethanolamine (MEA) process is currently the most widely-used industrial process for CO_2 purification for various commercial applications. If the source of CO_2 comes from fossil fuel combustion, the cost of CO_2 capture is acceptable by current users because of the high value of the final product. However, the MEA process is considered to be too expensive for greenhouse gas reduction purposes because of the excessively high quantity of CO_2 that must be captured from coal-burning power plants. Additionally, the regeneration step of the MEA process is energy intensive, and the CO_2 product has little commercial value due to the anticipated overproduction.

It is envisioned that the MEA process could be replaced with an aqua ammonia process to capture all three major acid gases (SO_2, NO_x, and CO_2, plus HCl and HF), that may exist in the flue gas. Since SO_2 and NO_x emissions must comply to certain limitations, a single process to capture all acidic gases is expected to reduce the total cost and complexity of emission control systems. Currently CO_2 is not regulated in the United States, although a limit on CO_2 emissions in the future could become a reality. Unlike the MEA process, the aqua ammonia process is not expected to have degradation problems due to SO_2 and oxygen. In addition, the ammonia solution has a higher CO_2 loading capacity than MEA. A rich ammonia solution requires much less thermal energy to regenerate than a rich MEA solution.

Very few research reports in the usage of ammonia for CO_2 capture are available. China has combined an aqueous NH_3 solution and CO_2 gas to produce ammonium bicarbonate (ABC) fertilizer for about 40 years. Currently (2003), 43% of the fertilizer used in China is ABC [1]. Bai and Yeh [2] reported on the study of CO_2 absorption by aqueous ammonia and the resultant CO_2 loading capacity. Yeh and Bai [3] compared CO_2 loading capacity of aqueous ammonia and MEA solutions.

The following reactions show the reaction byproducts between CO_2 and aqueous ammonia:

$$2\,NH_3 + CO_2 \leftrightarrow NH_2COONH_4 \quad (1)$$
$$NH_2COONH_4 + CO_2 + 2H_2O \leftrightarrow 2NH_4HCO_3 \quad (2)$$
$$NH_2COONH_4 + H_2O \leftrightarrow NH_4HCO_3 + NH_3 \quad (3)$$

$$NH_3 + H_2O + CO_2 \leftrightarrow NH_4HCO_3 \quad (4)$$

$$2NH_3 + H_2O + CO_2 \leftrightarrow (NH_4)_2CO_3 \quad (5)$$
$$(NH_4)_2CO_3 + CO_2 + H_2O \leftrightarrow 2NH_4HCO_3 \quad (6)$$

In this study, experiments were conducted to determine the CO_2 loading of aqueous ammonia solutions that were subjected to three absorption and regeneration cycles. A reasonable loading was determined and used in the preparation of a process flow diagram for the process as a basis of comparison to the current MEA process. Studies of the regeneration of prepared solutions of ABC and ammonium carbonate (AC) were also conducted.

Experimental

Absorption. The absorption tests take place in a semi-batch bubble reactor equipped with a mixer operating at 1600 rpm. A simulated flue gas consisting of 15%vol CO_2 and 85%vol N_2 is bubbled through ⅜" tubing at a flow rate of 7300 sccm. The absorber is a 3-liter glass container filled with 1500-ml aqueous ammonia solution. The temperature of the solution is controlled by pumping water from a recirculating heater through an immersed ¼" tubing coil. Typically, absorption tests were conducted at 27°C. The reactor pressure is maintained at 1 psig to supply motive energy to the gas analysis system. A reflux condenser dries the gas to a dewpoint of approximately -12°C. The gas is bubbled through the reactor until the CO_2 concentration is 95% of the inlet, or the flow stops due to plugging of the gas inlet tubing as a result of precipitation of the ABC. Data from an infrared CO_2 gas analyzer is analyzed to determine the amount absorbed as a function of time.

Regeneration. Regeneration tests utilize much of the same equipment, with the following exceptions. The ¼" heating coil is replaced with a ⅜" coil to increase the heat transfer. The mixer is replaced with a magnetic stirrer. A 2000 ml reactor is used to minimize the headspace and gas residence time. Although the regeneration is performed in a batch mode, the gas inlet is rerouted to the reactor's vent line and metered nitrogen acts as a sweep gas to the analyzer. The temperature of the solution to be regenerated is ramped from ambient to at least 82°C, with stops at 49°C, 54°C, 60°C, and 71°C.

Test Matrix. In the first series of tests, regeneration experiments with mixtures of ABC and AC were conducted to determine the amount of CO_2 evolved from the solution as a function of temperature.

In the second series of tests, aqueous ammonia solutions containing 7%, 10.5%, and 14% ammonia are prepared by diluting a 28% NH_3 solution. An absorption test is conducted. The saturated (rich) liquid is then regenerated at 82°C. The lean solution is used in an absorption test. The absorption / regeneration cycle is repeated for a total of three times (approaching a steady-state condition), and the totalized amount of CO_2 absorbed or regenerated is calculated.

Results and Discussion

Figure 1 shows the amount of CO_2 liberated by thermal regeneration from standard solutions of ABC and AC as a function of temperature. The dependent variable in **Figure 1** represents the total percentage of the original carbon in the solution that was evolved up to that temperature. It is evident that as the proportion of bicarbonate in the solution increases, the CO_2 is more easily regenerated. It is demonstrated that as much as 60% of the carbon in the solution can be regenerated, which in a continuous process would free the ammonia for the absorption cycle.

Table 1 shows the effect of cycling various initial compositions of ammonia on the absorption and regeneration capacity for each step of the three-step cycling process.

Table 1. CO_2 Absorbed (g/g solution) per Cycle at Varying NH_3 Concentrations

Initial NH_3 (%)	7.0	10.5	14.0
1st Absorption	0.111	0.141	0.157
2nd Absorption	0.044	0.054	0.067
3rd Absorption	0.039	0.053	0.068

For each of the three initial NH_3 concentrations, the data show that after the first cycle, the amount of CO_2 absorbed is converging to a constant value. It is important to note that the NH_3 concentration listed is the initial NH_3 concentration for the solution. As expected, there is an evaporation of NH_3 into the vent gas from the reactor, primarily during the first absorption cycle, partially explaining the reduction in the capacity of the solution to absorb CO_2 in subsequent cycles. For example, based on mass balance calculations, 36% of the NH_3 was lost during the first absorption cycle with an initial NH_3 concentration of 14%. After the three absorption/regeneration cycles, the residual solution contained approximately 8% ammonia. It is believed that incomplete regeneration of the solution is responsible for the remainder of the absorption capacity loss.

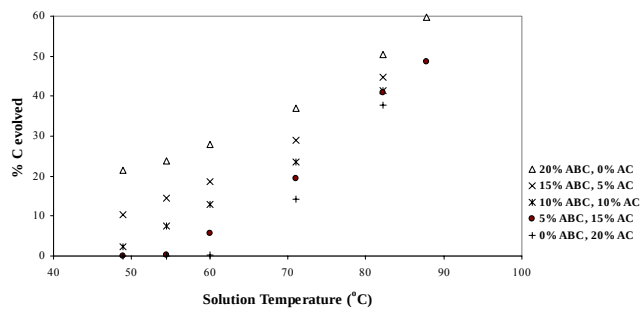

Figure 1. Regeneration Test Summary

The heat required for regeneration is a combination of sensible heat, heat of reaction, and latent heat of vaporization. **Table 2** shows the relative contribution from these energy requirements for both MEA and aqueous ammonia solutions. Three potential reactions could be responsible for liberation of CO_2 during the thermal regeneration:

$2NH_4HCO_3(aq) \leftrightarrow (NH_4)_2CO_3(aq)+CO_2+H_2O$ H_r= 6.4 kcal/mol (7)
$NH_4HCO_3(aq) \leftrightarrow NH_3(aq) + H_2O + CO_2(g)$ H_r= 24.1 kcal/mol (8)
$(NH_4)_2CO_3(aq) \leftrightarrow 2NH_3(aq)+H_2O+CO_2(g)$ H_r= 15.3 kcal/mol (9)

Due to current uncertainty of the dominant regeneration reaction, the three potential reactions are compared in **Table 2**.

Based on the CO_2 loading data derived from the cycling tests and the calculated energy requirements, a basic process flow diagram for an aqueous ammonia process was developed. The proposed process flow diagram is shown in **Figure 2**, and a comparable MEA process flow diagram is shown in **Figure 3**.

Table 2. Regeneration Energy Required of an 8% Aqua Ammonia Process Compared to Current 20% MEA Technology

	ΔH_{rx} (kcal/mol)	Sensible Heat* (kcal/mol)	Heat of Vaporization (kcal/mol)	Total (kcal/mol)	Reduction from MEA process (%)
MEA	20.0	79.4	18.9	118.3	0
NH_3 (eq. 7)	6.4	36,0	0	42.4	64
NH_3 (eq. 8)	24.1	36.0	0	60.1	49
NH_3 (eq. 9)	15.3	36.0	0	51.3	57

* Sensible heat = mass of solution(g/mol CO_2) * C_p (assume .001 kcal/g-°C) * ΔT_{rx} (°C)

Absorption can take place between 16°C and 38°C in the aqua ammonia process. The CO_2-rich stream is pumped through a heat exchanger to the regenerator, where the solution is heated to 82°C and CO_2 gas is released from the heated solution. The pure CO_2 can be collected for later sequestration. The CO_2-lean solution from the regenerator is recycled back to the absorber for reuse. During the regeneration, not all of the CO_2 in the solution will be released. A similar procedure is used in the MEA process.

The advantages of the aqua ammonia process include: a lower liquid flow rate, lowering capital equipment and pumping costs; no stripping steam is required for the regeneration; a higher CO_2 capture capacity per gram of solution; and a lower heat of reaction. The last three advantages result in a potential regeneration energy savings of up to 64% compared to the current MEA process.

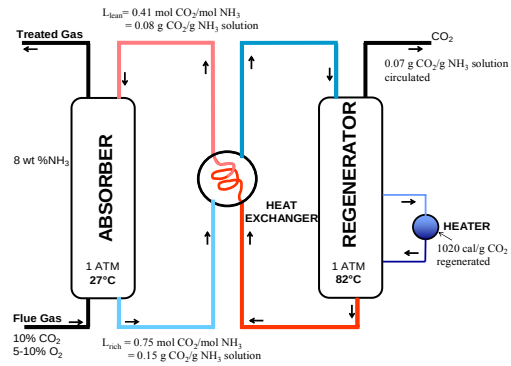

Figure 2. Process Flow Diagram for Aqua NH_3 CO_2 Capture Process

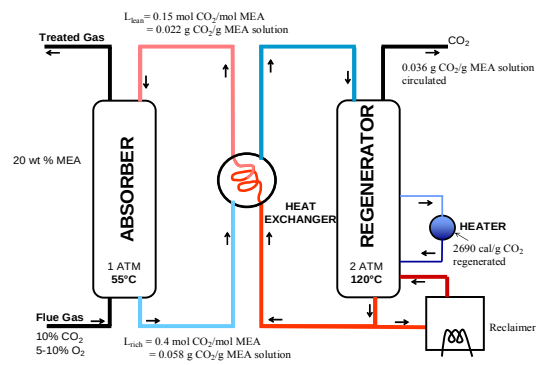

Figure 3. Process Flow Diagram for Typical MEA CO_2 Capture Process

Conclusions

Carbon dioxide transfer capacities of aqueous ammonia solutions and monoethanolamine (MEA) solutions were compared. The CO_2 carrying capacity in grams of CO_2 per gram of NH_3 solution circulated is 0.07 as compared with 0.036 grams of CO_2 per gram of MEA solution, thus the energy requirement for liquid mass circulation of an ammonia solution is approximately 50% that of an MEA solution for equal weight of CO_2 carried. In another comparison, the thermal energy required to regenerate CO_2 from the rich solution is substantially less as compared to the MEA process.

References

[1] Zhang, Zemin , et al – *New Type of Nitrogen Fertilizer-Long Lasting Ammonium bicarbonate,* Chemical Industry Publishing, Beijing, China, January, 2000. IBSN 7-5025-2619-6.

[2] Bai, H. and A.C. Yeh, Removal of CO_2 Greenhouse Gas by Ammonia Scrubbing. I.E.C.Res., Vol. 36, No.6, 1997.

[3] Yeh, A.C. and H. Bai, Comparison of Ammonia and Monoethanolamine Solvents to Reduce CO_2 Greenhouse Gas Emissions. The Science of Total Environment, pp 121-133, 1999.

ABSORPTION CHARACTERISTIC OF CONTINUOUS CO_2 ABSORPTION PROCESS

Sung-Youl Park, Byoung-Moo Min, Jong-Sup Lee, Sung-Chan Nam, Keun-Hee Han and Ju-Soo Hyun

Combustion Gas Clean-up Technology Center
Korea Institute of Energy Research
71-2, Jang-Dong, Yuseong-Gu, Daejeon, Korea

Introduction

Carbon dioxide is widely recognized as a major component of greenhouse gas contributing to global warming and produced in large quantity from various industrial sources, including fossil fuel firing electric power generation, steel production, chemical and petrochemical manufacturing, cement production, etc. Due to the increased CO_2 mediated global warming problems, strong and adverse affects on the development of a large number of industries in the near future are expected. As a means of mitigating the global warming, removal of CO_2 from industrial flue gas is considered important. The means of CO_2 removal include absorption by chemical solvents, physical absorption, cryogenic separation, membrane separation and etc. Among these methods, CO_2 absorption by alkanol amine(MEA) aqueous solution has been considered as the most efficient way and various research activities were conducted by this method and most commercial processes for the bulk removal of CO_2 from gaseous streams involve the use of amines[1,2,3]. Traditionally, only random packings are used as the gas-liquid contacting media inside the absorption and regeneration towers. It has been suggested that using high efficiency column packings in these towers could substantially improve the efficiency of the gas treating process which reduce its capital cost. Hydrodynamics and mass transfer characteristics, including flooding capacities, gas and liquid mass transfer coefficients, interfacial area and liquid hold up are essential for evaluating the effectiveness of the tower packings and also important for the reliable design and operation of the CO_2 absorption processes[4].

Experimental

CO_2 Absorption Process. The configuration of apparatus used in this experiment has typical arrangement of CO_2 absorption process as shown in **Figure 1**.

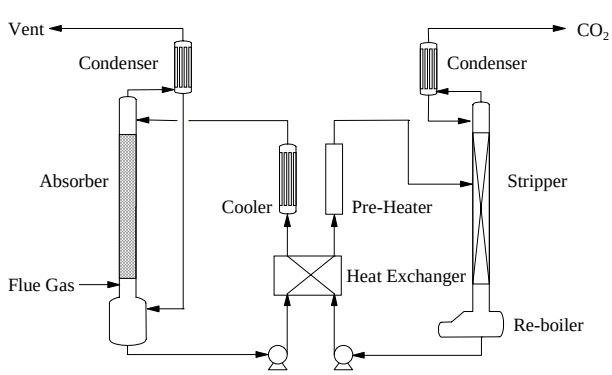

Figure 1. Simplified diagram of CO_2 absorption process.

The facility consists of diesel oil boiler, flue gas reservoir, flue gas supply pump, packed column absorber, sieve tray stripper, re-boiler for absorbent regeneration by evaporation, preheater for heating of CO_2 rich absorbent before stripping, heat exchanger for CO_2 rich and regenerated absorbent and condensers for vent gas of absorber and stripper.

Flue Gas and Absorbent. Flue gas used in this experiment is generated from the combustion of kerosene. After cooling, the generated flue gas is transferred to flue gas storage reservoir and then supplied to CO_2 absorber under flow rate control by dry gas flow meter. Boiler operation is appropriately manipulated to prevent soot generation and keep CO_2 concentration of flue gas about 12vol%.

Absorbent used in this experiment is prepared by the mixing of MEA with distillated water. 99.0wt% MEA(Nippon Sakubai) is diluted to 30wt% of aqueous MEA solution. Before absorbent loading, absorber and stripper is cleaned by distillated water and nitrogen.

Packing Material. As a packing material, raschig ring, intalox saddle and Pro-Pak is randomly packed in absorber. Physical properties of the packing material are shown in **Table 1**.

Table 1. Physical Properties of Packing Material

Packing material		Raschig ring	Intallox saddle	Pro-Pak
Size	(inch)	1/4	3/8	1/4
Packing density	(kg/m^3)	960	801	336
Specific surface area	(m^2/m^3)	710	801	1220
Void fraction	(%)	62	67	96

Measurement and Analysis Methods. Flue gas flow rate is measured by dry gas flow meter and absorbent flow rate is measured by liquid flow meter. Analysis of flue gas components is performed for absorber inlet and stripper outlet. CO_2, O_2 and N_2 of flue gas are analyzed by on-line gas chromatograph(HP6890) equipped with TCD and packed column(Carboxen 1000).

Results and Discussion

The design of absorption column and similar equipment is necessarily based on information concerning the diffusion from one to the other of two phases being contacted[5]. Operating hold-up is an important factor in gas-liquid mass transfer. Operating hold-up is defined as the difference between total hold-up and static hold-up. Static hold-up is the liquid volume per unit volume of the bed which does not drain from the packing when the liquid supply to the column is stopped[6]. Operating hold-up and flue gas pressure drop of absorber using different types of packing material was measured and shown in **Figure 2.**

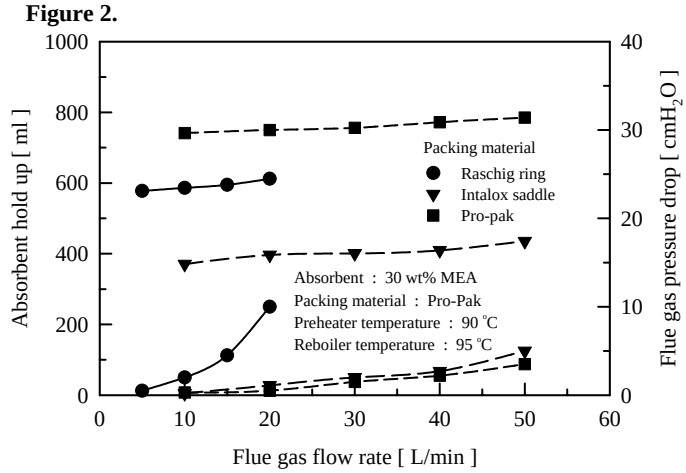

Figure 2. Operating hold-up and flue gas pressure drop of packing materials under different flue gas flow rate.

The absorption of CO_2 in absorbent is directly related to the contact time of flue gas and absorbent. Longer contact time means larger operating hold-up and closely related to specific surface area of packing material. Flow rates of flue gas and absorbent also important factor for CO_2 absorption under specific packing material. In view of gas-liquid contact time, flue gas flow rate should be inversely proportional to absorbent flow rate to keep constant gas-liquid contact time. Therefore, both flow rates should be adjusted to prevent absorbent flooding. Flooding happens when the gas flow rate is so high that absorbent can not flow down and it is related to void fraction of packing material. The experiment results presented in **Figure 1** showed that Pro-Pak has highest operating hold-up and lowest flue gas pressure drop. When compared with other packing materials used in this experiment, it can be expected that Pro-Pak would show highest CO_2 absorption.

As already mentioned, flue gas flow rate is also one of important factors for gas-liquid contact and CO_2 absorption. CO_2 removal efficiencies under different flue gas flow rate and packing materials were shown in **Figure 3**. Absorbent flow rate is 1.0L/min and flue gas flow rate was controlled to prevent flooding.

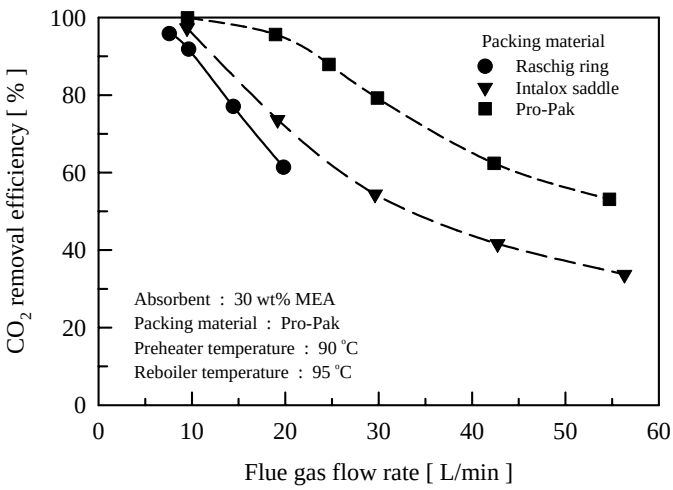

Figure 3. CO_2 removal efficiencies under different flue gas flow rates and packing material.

As expected, CO_2 removal efficiencies using Pro-Pak presented in **Figure 3** showed highest value entire range of flue gas flow rates. It means that CO_2 absorption is proportional to specific surface area of packing material and gas-liquid contact time. Higher flue gas flow rate under constant absorbent flow rate means shorter gas-liquid contact time and lower CO_2 absorption. It is also consistent with already mentioned expectation.

CO_2 absorption has close relation to gas-liquid contact time and the effect of packing material and flue gas flow rate on CO2 absorption were shown in **Figure 2** and **3**. Another factor affecting gas-liquid contact time is absorbent flow rate. As already mentioned, flooding happens when flue gas flow rate is too high absorbent to flow down and the operation of absorption process is failed.

The effects of absorbent flow rate on CO_2 removal efficiencies were observed under different flue gas flow rate and presented in **Figure 4**. L/G ratio is defined as the ratio of absorbent mole flow rate to flue gas mole flow rate. High L/G ratio means low flue gas flow rate under constant absorbent flow rate and much CO_2 absorption. As shown in **Figure 4**, 18-38 kg-mole absorbent/kg-mole flue gas of L/G ratio was required to achieve over 90% CO_2 removal efficiency under this experimental condition. The design of CO_2 absorption process is based on gas-liquid contact time and optimum low rates of flue gas and absorbent to achieve specific CO_2 removal efficiency are could be used for this purpose.

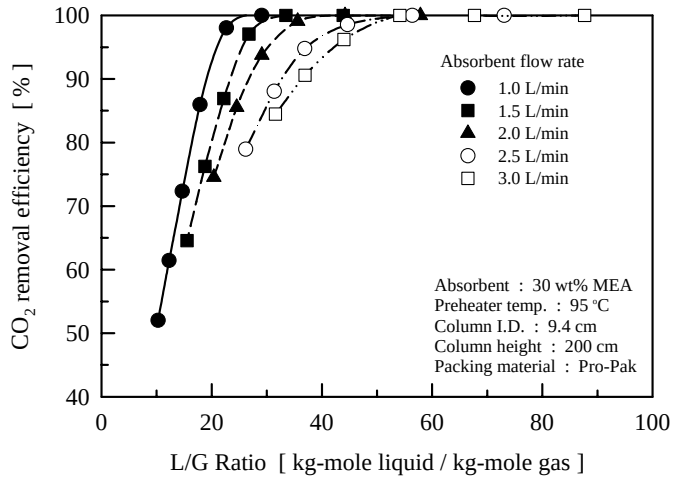

Figure 4. CO_2 removal efficiencies under different L/G ratio.

Conclusions

In this study, Pro-Pak showed highest CO_2 removal efficiency. It means that specific surface area affecting operating hold-up and void fraction affecting flue gas pressure drop are important physical properties for the selection of packing material. The design basis of CO_2 absorption process is gas-liquid contact time needed to achieve specific CO_2 removal efficiency. For the determination of desired gas-liquid contact time, CO_2 removal efficiencies were calculated under different flow rates of flue gas and absorbent. 18-38 kg-mole absorbent/kg-mole flue gas of L/G ratio was needed to achieve over 90% of CO_2 removal efficiency under experimental condition.

In addition to data showed in this study, experiments under various packing material, column type, absorbent type and operating conditions were performed and dynamic properties such as flue gas mean residence time, superficial velocity and overall mass transfer coefficient were calculated but did not show in this study.

The experimental results can be used as basic data for scale up of CO_2 absorption process and experimental apparatus can be used for durability test of absorbent.

Acknowledgment

This work was supported by Ministry of Commerce, Industry and Energy, Korean government.

References

1. Sheng H. Lin, Ching T. Shyu, Waste Management, **1999,** 19, 255-262.
2. T. Mimura, T. Suda, I. Iwaki, A. Honda, H. Kmazawa, Chem. Eng. Comm. **1998**, 170, 245-260.
3. Sartori G., Savage D. W., Ind. Eng. Chem. Fundam., **1983**, 22, 239-249
4. Paiton T., Ener. Conser. Manage., **1996**, 37, 935-940.
5. M.E. Edwards, Chemical Engineer's Hand Book, 6th edn., McGraw Hill, NewYork, 1984.
6. K. R. Rao, Can. J. Chem. Eng., **1993**, 71, 685.

ASPEN SIMULATION OF CO_2 ABSORPTION SYSTEM WITH VARIOUS AMINE SOLUTION

Seok Kim, Hyung-Taek Kim

Dept. of Energy Studies, Ajou University
Wonchon-dong San-5, Paldal-gu
Suwon, Korea 442-749

Introduction

The desire to alleviate the problem of global warming has resulted in the environmental concern over a reduction of greenhouse gas emissions from industrial sources. CO_2 is the major contributor to the global warming phenomena due to its abundance comparing to other greenhouse gases, as a result, it is considered to be a primary target for reduction. The gas absorption process with a chemical reaction using amine is recognized as the most cost effective and has the best proven operability record. The main purpose of this study is to minimize the amount of energy required in the desorption (commonly called regeneration) process through the simulation of various process concept of solvent absorption and to suggest the optimum operating condition to the actual CO_2 absorption experimental setup. Bench-scale, continuous CO_2 absorption reactor (capacity =5 Nm3/hr) located in the Korea Institute of Energy Research is modeled and simulated with ASPEN Plus for this purpose.

In the present research, CO_2 absorption process is simulated with commercial ASPEN Plus code and various combination of the operating parameters, such as flow rates of flue gas and amine solution, concentration of amine solution, temperature of absorption and regeneration tower, etc. Every set of operating condition of CO_2 absorption process is compared in terms of energy usage.

Methods

Carbon Dioxide Absorbents

Absorbents utilized in the CO_2 absorption technology can be classified according to their reactivity/solubility with CO_2. Widely-used absorbents in the industrial application are family of alkanolamines. Alkanolamines are usually utilized as aqueous solution in the CO_2 absorption process. Alkanolamines are divided into three classes: primary, secondary and tertiary amines according to their functional group. The classification is based on the substitute of the hydrogen on the nitrogen atom. Primary amines, which are most reactive among amine compounds, represent monoethanolamine (MEA) and diglycoamine (DEA).Initially, monoethanolamine (MEA) is used in the simulation investigation of CO_2 absorption.

The reactions of MEA and CO_2 are mainly occurred by electrochemical reaction in the aqueous solution. Typical reaction mechanism are as in the following equations.

$$2RNH_2 + CO_2 + H_2O \leftrightarrow (RNH_3)_2CO_3$$

$$(RNH_3)_2CO_3 + CO_2 + H_2O \leftrightarrow 2RNH_3HCO_3$$

$$2RNH_2 + CO_2 \leftrightarrow RNHCOONH_3R$$

Description of Absorption Process

Flue gases containing CO_2 are introduced into a direct cooler where they are cooled by a circulating stream of water. The gas is then compressed with a blower to overcome the pressure drop inside the absorber. The flue gases are flowed through the absorber in the countercurrent direction to the flow direction of absorbent solution. Inside absorber tower, the absorbent solution reacts chemically with the carbon dioxide in the flue gases. The CO_2-lean gases then enter the wash section of the absorber, where and entrained absorbent are removed and returned to the absorber. The washed gases are vented to the atmosphere. For the simulation, the CO_2 concentration in the washed gas is set to less than 1%.

The CO_2-rich solution leaves the absorber and is pumped to the lean/rich cross heat exchanger. In the cross heat exchanger, the CO_2-rich solution is heated and the CO_2-lean solution is cooled. The CO_2-rich solution is entered into regeneration tower where the absorbent amine solution is regenerated. To regenerate the solvent, the CO_2-rich solution is heated in a reboiler using low-pressure steam. Due to the heating, water and absorbent are vaporized. The water vapor and absorbent vapor leave the reboiler and enter the regenerator. The vapors move up in the condenser section of regenerator while liberating the CO_2 and heating the down-coming solution. Some vapor and CO_2 enter the wash section of the regenerator where absorbent vapor is removed. Water vapor and CO_2 enter the reflux condenser where the water vapor is condensed and the CO_2 is cooled. The condensed water is returned to the regenerator.

The CO_2-lean solution leaves the reboiler and enters the cross heat exchanger where it is cooled. The solution is then pumped and cooled further before it re-enters the absorber. The entire schematic diagram of CO_2 absorption process is illustrated in **Figure 1**.

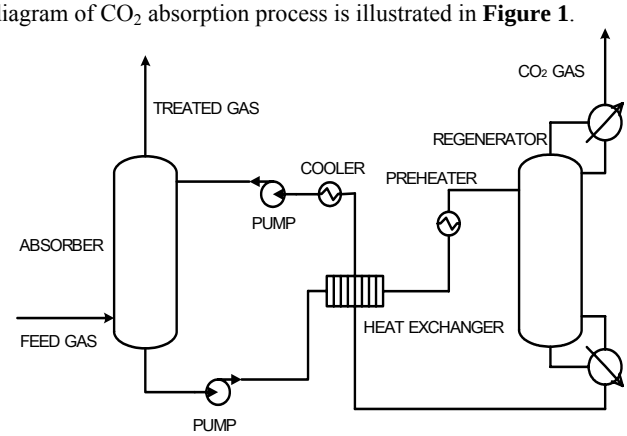

Figure 1. ASPEN Plus Block Diagram of CO_2 Absorption Process

Results and Discussion

Carbon dioxide absorption phenomena with amines is simulated with ELECNRTL method in the ASPEN PLUS. The ELECNRTL Property Method is the most versatile electrolyte property method. It can handle aqueous and mixed solvent systems.

During the simulation, The concentration of MEA solution is varied for sensitivity analysis. Concentration of MEA solution is fixed at 30 w% for the initial simulation study. Flue gas flow rate was set as 35 l/min and the composition of flue gas is CO_2=13.89%, N_2=82.56% and O_2=3.55%.Within this simulation set-up, the absorber pressure is varied from 1 to 10 atm. The results are illustrated in **Figure 2**. The increase of absorber pressure resulted in the better absorption rate up to the absorber pressure 3 atm. The absorption rate was almost saturated at about 3 atm or more.

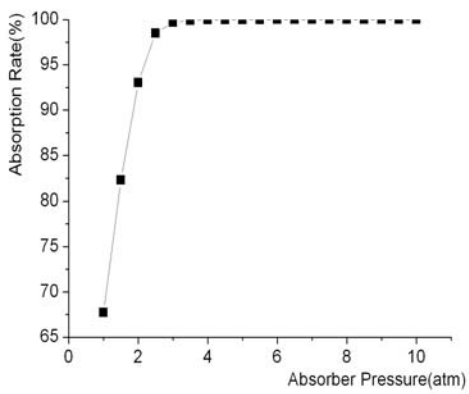

Figure 2 The effect of Absorber Pressure Variation

The effects of flue gas flow rate and MEA solution flow rate on CO_2 absorption rate are plotted all together in **Figure 3** when the concentration of MEA solution set as 30 %. As the flow rate of flue gas increased or flow rate of MEA solution decreased, the absorption rate has the decreasing tendency. The optimum condition represents when the flow rates of feed gas of 9 kg/h and MEA solution of 65 kg/h with over 97% CO_2 absorption.

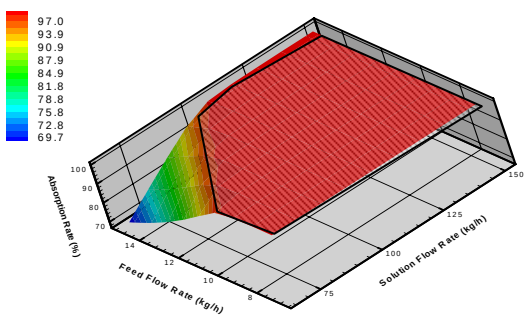

Figure 3 The effect of flue gas flow rate and MEA solution flow rate on CO_2 adsorption rate

Conclusion

The simulation using ASPEN Plus is progressed for an evaluation of optimum operating condition of the laboratory-scale continuous absorption apparatus treating 5 Nm^3/hr which is located in the Korea Institute of Energy Research.

Results of the simulation showed:

1) The increase of an absorber pressure and MEA solution flow rate causes the increase of CO_2 absorption rate and absorption rate reaches 97% at 3 atm.

2) The optimum condition represents when the flow rates of feed gas of 9 kg/h and MEA solution of 65 kg/h with over 97% CO_2 absorption.

References

(1) Chris, H. ; Carbon Dioxide Removal from Coal-Fired Power Plants, Kuwer Academic Publishers, pp. 17~49, Netherlands (1994)

(2) Klaus S. , Hans J. F., Thermal Separation Processes, VHC Publishers, pp. 239-280, 1994

(3) Guido S., David W. S., Sterically Hindered Amines for CO_2 Removal from Gases, Ind. Eng. Chem. Fundam., 22, pp. 239, 1983

(4) ASPEN PLUS manual, Physical Property Model, 2002

PLAINS CO_2 REDUCTION (PCOR) PARTNERSHIP

Thomas A. Erickson, John A. Harju, Edward N. Steadman

Energy & Environmental Research Center
15 North 23rd Street
Grand Forks, ND 58203

The Energy & Environmental Research Center (EERC) is leading one of seven regional partnerships developed by the U.S. Department of Energy (DOE) to assess regional carbon sequestration opportunities. The Plains CO_2 Reduction (PCOR) Partnership (which is a designated DOE Regional Carbon Sequestration Partnership [RCSP]) is focused on addressing future sequestration options from a holistic viewpoint, including source characterization, infrastructure needs, deployment, issues, public outreach, sink characterization, environmental impacts, long-term issues, and monitoring. The PCOR Partnership region includes North Dakota, South Dakota, Minnesota, Montana, and Wyoming, as well as the Canadian provinces of Saskatchewan and Manitoba (see Figure 1). The partnership is focused on a wide range of geological and terrestrial sequestration opportunities for both current CO_2 sources and future industrial and utility point sources.

Figure 1. PCOR Partnership region.

As shown in Table 1, the PCOR Partnership features a diverse, multipartner team under EERC leadership that brings together the key government, private sector, technical, and outreach groups needed to undertake the activities in the four performance tasks. The PCOR Partnership team is well suited to assess the regional baseline and infrastructure and to involve stakeholders in developing action plans for future demonstration projects.

The PCOR Partnership team includes 1) industry sponsors that provide cost share and serve as advisors; 2) research partners that are funded under the PCOR Partnership venture; and 3) collaborators that, in most cases, provide in-kind support. The industry sponsors have significant and active operations in all five states of the region. The knowledge base, expertise, and hands-on experience of the PCOR Partnership research team encompass the entire region.

Table 1. PCOR Partnership Team

Industry Sponsors	Research Partners
Basin Electric Power Cooperative	Dakota Gasification Company
Center for Energy & Economic Development (CEED)	EERC
Great River Energy	Fischer Oil and Gas, Inc.
Montana–Dakota Utilities Co.	Interstate Oil and Gas Compact Commission
North Dakota Industrial Commission (NDIC)	Nexant, Inc.
Otter Tail Power Company	North Dakota State University
U.S. Department of Energy	Prairie Public Television
	Western Governors' Association
Collaborators	
Amerada Hess Corporation	Natural Resources Trust
Bechtel Corporation	NDIC Oil and Gas Division
Chicago Climate Exchange	North Dakota Department of Health
Eagle Operating, Inc.	North Dakota Geological Survey
Environment Canada	North Dakota Petroleum Council
Minnesota Pollution Control Agency	Petroleum Technology Transfer Council
Montana Department of Environmental Quality	Tesoro Refinery
Montana Public Service Commission	

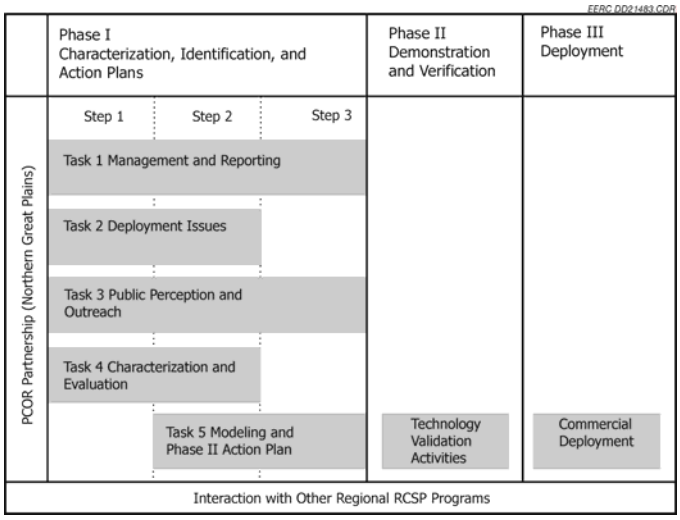

Figure 2. PCOR Partnership project in the context of DOE's 3-phase RCSP program.

The Phase I goals of the PCOR Partnership are being accomplished through a 3-step approach (see Figure 2). Step 1 is characterizing technical issues and the public's understanding and attitudes concerning CO_2 sequestration, including development of a database on sources, sinks, separation and transportation options, regulatory permitting requirements, and environmental benefits and risks. Step 2 will identify regional opportunities for sequestration and inform the public about options and risk. Step 3 will develop a detailed action plan for implementing Phase II demonstration projects in the PCOR Partnership region. The PCOR partners will contribute over the life of the project through working groups designated to focus on key topical areas.

A conceptual model has been developed to characterize the sequestration opportunities in the PCOR region and determine the best projects for demonstration and verification in Phase II demonstration projects. As shown in Figure 3, detailed characterization data will be provided to stakeholders, and sequestration opportunities will be evaluated on the basis of technical and economic feasibility. The potential sequestration projects will then be ranked on the basis of overall deployment feasibility. It is anticipated that several sequestration opportunities will be selected for Phase II demonstration projects.

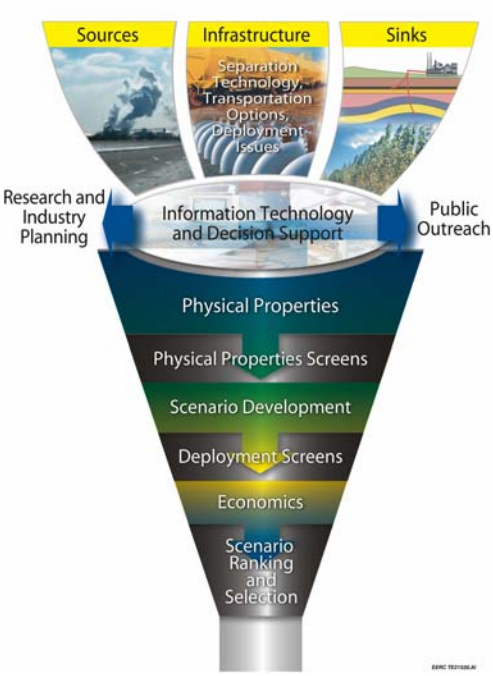

Figure 3. PCOR Partnership model.

AMINOPROPYL-FUNCTIONALISED SILICAS AS HIGH CAPACITY CO_2 ADSORBENTS

Gregory P Knowles, Jeremy V Graham, Seamus W Delaney and Alan L Chaffee

School of Chemistry, Monash University, Victoria, Australia

Introduction

One approach to reduce greenhouse gas emissions from fossil fuel combustion and so maintain the future viability of coal fired power generation is to capture and then sequester the product CO_2. Thus, there is growing interest in the development of improved CO_2 capture and separation technologies. The development of high capacity, CO_2 selective adsorbents that can be used in pressure swing adsorption (PSA) processes is one way forward.

Adsorbents based on high surface area inorganic supports that incorporate basic organic groups, usually amines, are of particular interest. The interaction between the basic surface and acidic CO_2 molecules may result in the formation of surface ammonium carbamates (Figure 1)[1-3]. Thus, in dry CO_2, adsorption capacities are limited to 1 mole CO_2 for every 2 moles surface bound amine groups. Therefore it is desirable to develop adsorbents with the highest possible concentration of basic nitrogen groups accessible to CO_2.

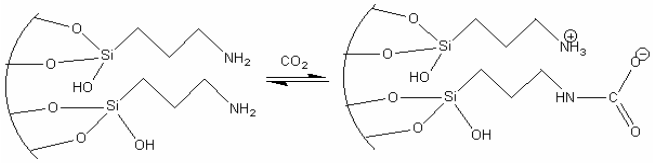

Figure 1. Surface reaction of tethered amine groups with CO_2.

A number of groups have now reported the preparation of 3-aminopropyl-functionalised silicas based on the derivatisation of mesoporous amorphous silica gels[3-7] and/or mesoporous periodic framework structures like SBA-15[2,5], MCM-41[1,8,9] and MCM-48[6]. Such mesoporous substrates are attractive because they possess pores that are (believed to be) large enough to access with derivatising reagents. Post-functionalization, they (are believed to) still retain sufficient porosity to facilitate rapid gas diffusion to and from the surface as required by the PSA process.

The specific CO_2 adsorption capacities reported for any of these materials to date are not outstanding. However, there is insufficient data in the literature to distinguish whether the limitation in CO_2 adsorption capacity is due to sub-optimal coverage of the mesopore surface with amine groups, due to poor accessibility of CO_2 to the surface amine groups, due to geometric constraints limiting the acid-base interaction at the surface and/or other unknown factors.

This report describes an investigation into the effects of mesopore structure (e.g., pore geometry, pore spacing, pore volume, surface area and surface silanol concentration) on the extent of surface functionalization and consequent CO_2 adsorption capacities. A new approach to characterizing the extent of surface modification (per unit of substrate surface area) is described and applied to the prepared materials, providing a better understanding of the modification and adsorption phenomena.

Experimental

Silica substrates. Amorphous silica gel 40 (Sigma Aldrich) was treated at 475 °C to give silica substrates S2 with a surface silanol concentration of 2.0 (i.e., 2 hydroxy groups per nm^2)[10].

Mesoporous periodic structures of the HMS type were prepared via a neutral templating technique using dodecylamine[11]. For HMS substrate H2, the template was removed by calcination at 475°C. By analogy with the work of van der Voort *et al*[10] this material is also estimated to possess 2 silanol groups per nm^2. For HMS substrates H5a, H5b and H5c, the template was removed via EtOH extraction. Following treatment at 150°C under vacuum, it is estimated that these substrates possess approximately 5 silanol groups per nm^2.

Substrates H2 and H5a-c all gave XRD peaks expected for HMS materials and indicated pore center separations of 46, 44, 32 and 38Å, respectively.

Preparation of aminopropyl-functionalised substrates. Approx. 1g of each pre-dried substrate was dispersed in 100 ml dry toluene and treated with variable quantities of aminopropyl-trimethoxysilane (apts), always in molar excess relative to the estimated silanol content of the substrate. Treatment proceeded at room temperature for 2 hours in most cases. The product was collected, washed with several volumes of dry toluene, then dried at 150°C for 24 hours under vacuum to complete the surface modification and also to remove residual solvent and silane.

Characterization of Materials. N_2 adsorption/desorption experiments were conducted at –196°C using a Micromeritics ASAP 2010 instrument. Total pore volumes were calculated from the N_2 volume adsorbed at P/P_0= 0.995. BET surface areas were determined from N_2 volume adsorbed over the partial pressure range 0.08 – 0.12. BJH pore diameters were determined from the N_2 volume desorbed between P/P_0 = 1 and P/P_0 = 0.15. Elemental analyses were determined by CMAS Pty Ltd, Belmont, Vic. for C and N. X-Ray diffraction (XRD) data were recorded using a Scintag X-Ray Diffractometer. For HMS materials, the distance between pore centers (s) was calculated from the distance between d_{100} symmetry planes (d) for the major diffraction peak between 1 and 5 (2θ) as follows: $s=2d*3^{0.5}$.

Carbon Dioxide Adsorption. CO_2 adsorption experiments were conducted on a Setaram Thermogravimetric Analyzer (TGA). Typically, samples were dried at 150 ºC, then cooled to 20ºC under a flow of dry Ar. The gas flow was then switched to a mixture containing 90% CO_2 and 10% Ar. Adsorption capacities were determined from the weight increase observed after 10 minutes.

Extent of Surface Modification (tether-loading). The extent of substrate modification by apts treatment was characterized as the number of tethers per nm^2 of <u>substrate</u> surface area ('tether-loading'). The tether-loading was calculated by assuming a cylindrical pore model based on the BJH pore radius (r_{prod}), the N content (N_{prod}) and the surface area (SA_{prod}) of the product, together with the BJH pore radius (r_{sub}) of the substrate, according to the following equation:

$$\frac{\#tethers}{SA_{sub}} = \frac{N_{prod}(g.g^{-1}) * \frac{6.023*10^{23}(atoms.mol^{-1})}{AtomicWt[N].(g.mol^{-1})}}{SA_{prod}(m^2.g^{-1}) * 10^{18}(nm^2.m^{-2})} * \frac{r_{prod}}{r_{sub}} * \frac{\#tethers}{\#N}$$

Results and Discussion

Table 1 provides basic preparation and characterization details for each of the substrate and product materials used in this study.

The results show that, in each case, treatment with apts led to reduction in pore volume, pore diameter and surface area and also led to an increase in both N and C content. The x-ray diffraction patterns for the HMS product materials were only slightly broadened relative to their corresponding substrates, demonstrating that the ordered framework structure was retained throughout modification.

The molar C/N ratios of the modified materials are consistent with the formation of tethers that (on average) are linked to the surface in either a tridentate fashion, or else in a bidentate fashion where the third methoxy group from apts has been hydrolysed (as illustrated in Figure 1) or crosslinked to an adjacent tether. However, given the density of silanol groups at the surface (2 to 5 per nm^2), tridentate coordination is considered unlikely.

It is noted that the H5c-p96 material has a higher N content (mass basis) than any other aminopropyl-functionalised silica material reported to date. Nevertheless, the H5c-p96 material has a

lower tether-loading than values reported for similar, but lower surface area substrates[4,7]. This suggests that it should be possible to prepare materials with still higher N content.

Table 1. Basic Preparation and Characterization Details for Substrate and Product Materials*

	Vol apts added $ml.g^{-1}$	SA $m^2.g^{-1}$	Pore Vol $ml.g^{-1}$	BJH dia. Å	N mass %	C mass %	CO_2 adsorb mass%
Typical Std Dev	± 0.1	± 10	±0.02	± 0.4	± <0.1	± <0.1	± 0.1
S2		567	0.67	36.8	-	0.0	1.57
S2-p2	1.25	419	0.45	36.3	1.6	4.3	2.74
H2		909	1.06	29.6	-	0.5	2.17
H2-p2	4.0	706	0.66	23.2	2.5	6.9	3.50
H5a		762	1.02	30.0	<0.1	3.2	2.18
H5a-p2	4.0	638	0.60	25.2	2.7	7.0	4.02
H5b		1268	-	24.1	<0.1	0.0	n/a
H5b-p2	3.0	1194	-	20.3	2.3	8.5	3.14
H5c		1198	-	20.6	-		2.66
H5c-p2	4.0	1176	-	20.4	2.1	6.4	3.80
H5c-p24	4.0	1125	-	19.0	3.2	9.4	6.31
H5c-p96	4.0	1113	-	19.5	3.4	9.3	5.70
H5c-p96r	4.0	1195	-	19.3	3.3	9.3	6.14

* p: product; 2/24/96: 2/24/96h treatment @ RT; 96r: 96h treatment @ reflux

Figure 2 illustrates the tether-loading of the various product materials as a function of the quantity of silane added to the reaction mixture per unit substrate surface area. As illustrated by the trend line, the results show that the higher quantities lead to improved tether-loadings (for 2h treatment of HMS substrates).

It can be noted that products from substrates with both low (2.0) and high (5.0) silanol content fall on this trend line, indicating that, within the range of preparative procedures investigated, higher silanol content does not necessarily lead to higher tether loadings.

The product prepared from amorphous silica, S2-p2, gave a substantially higher tether-loading than for the HMS derived products at low silane concentration. It is thought that the morphology of the amorphous silica, i.e., the greater accessibility of the mesopores and the larger average pore diameter, permits better entry and faster diffusion of reagent molecules.

Figure 2 also indicates that longer treatment times (H5c-p24) lead to improved tether-loadings for the HMS substrates, presumably because additional time helps to overcome diffusion limitations within the mesopores. However, extending the treatment beyond 24 hours (H5c-p96) or to higher temperature (H5c-p96r) does not lead to any further increase in tether-loading. Thus, it appears that for these conditions equilibrium loadings have been achieved.

It is interesting that the apparent equilibrium loadings for the HMS substrates are lower than for Silica 40 at the same apts concentration. The reason is unclear, but one possibility is that the sharper internal curvature of the HMS cylinders makes it more likely that initially adsorbed apts-tethers will block access of subsequent apts groups to the surface.

Table 1 also lists the CO_2 adsorption capacity determined for each material on a mass % basis. To our knowledge the capacity reported for H5c-p24 (6.31%) is the highest yet reported for any apts functionalised material[4,5,11,12]. All products exhibited capacities that correspond to a CO_2/N molar ratio of ~0.5, consistent with the postulated carbamate mechanism. Marginally greater CO_2/N ratios observed for products with lower tether-loadings are probably due to the occurrence of some additional CO_2 adsorption at surface silanol sites.

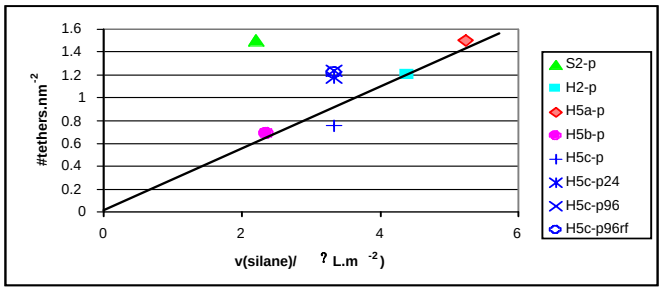

Figure 2. Tether-loading of aminopropyl-functionalised mesoporous

Figure 3 shows the CO_2 adsorption capacity of each material as a function of tether-loading. There is a general increase in capacity at higher loadings. However, the most significant observation is that the higher surface area substrates lead to apts modified products with the best CO_2 adsorption capacities (on a mass basis).

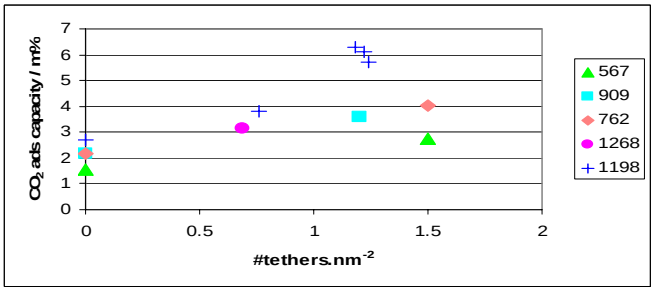

Figure 3. The CO_2 adsorption capacity of materials prepared from the various substrates as denoted by substrates surface area.

Conclusions

The characterization of these organic-inorganic hybrid adsorbents on the basis of substrate surface area has usefully enhanced our understanding of the factors which have, so far, limited the extent of surface functionalization and, consequently, the CO_2 adsorption capacities that can be achieved. In the course of this work, we have prepared hybrid adsorbents (of this type) with the highest N loadings and highest CO_2 adsorption capacities so far reported and expect to be able to improve upon this further.

Acknowledgements. The authors thank Mr Alex Perisa, who assisted the preparation of S2-p2, and also acknowledge the financial support of the Australian Research Council.

References

(1) Delaney, S.W.; Knowles, G.P.; Chaffee, A.L. *Am. Chem. Soc., Div. Fuel Chem.*, **2002**, *47*, 65-66.
(2) Chang, A.C.C; Chuang, S.S.C; McMahan, G.; Soong, Y. *Energy & Fuels*, **2003**, *17*, 468-473.
(3) Leal, O.; Bolivar, C.; Ocalles, C.; Garcia, J.J.; Espidel, Y. *Inorganica Chimica Acta*, **1995**, *240*, 183-189.
(4) Walcarius, A.; Etienne, M.; Bessiere, J. *Chem Mater*, **2002**, *14*, 2757-2766.
(5) McKittrick, M.W.; Jones, C. *Chem. Mater.* **2003,** *15*, 1132-1139.
(6) Huang, H.Y.; Yang, R.T.; Chinn, D.; Munson, C.L. *Ind. Eng. Chem. Res.*, **2003**, *42(12)*, 2427-2433.
(7) Vranken, K.C.; Van Der Voort, P.; Possemiers, K.; Vansant, E.F. *J. Coll. & Interf. Sci.* **1995,** *174*, 86-91.
(8) Yoshitake, H.; Yokoi, T.; Tatsumi, T. *Chem. Mater.*, **2003**, *15*, 4536-8
(9) Lin, X.; Chuah, G.K.; Jaenicke, S. *J. Molec. Catal. A: Chem.* **1999,** *150*, 287-294.
(10) Van der Voort, P.; Gillis-D'Hamers, J.; Vranken, H.C.; Vansant, E.G. *J.Chem.Soc, Faraday Trans* **1991**, *87 (24)*, 3899-3905.
(11) Tanev,P.T.; and Pinnavaia,T.J. *Science* **1995**, *267*, 865-867.

Improved Immobilized Carbon Dioxide Capture Sorbents

M. L. Gray[1], Y. Soong[1], K. J. Champagne[1], H. Pennline[1], J. Baltrus[1],R.W. Stevens, Jr.[2], R. Khatri[2], S. S. C. Chuang[2], and T. Filburn[3]*

[1]US Department of Energy, National Energy Technology Laboratory, P.O. Box 10940, Pittsburgh, PA, 15236. gray@netl.doe.gov
(412) 386-4826, Fax (412) 386-4808.
[2]Chemical Engineering Department, University of Akron, Akron, OH, 44325-3906.
[3]College of Engineering, University of Hartford, CT, 06117

Introduction

The rise of greenhouse gases (i.e. CO2, CO, SO2 and NOx) [1] in our atmosphere is promoted by the combustion of fossil fuels for the generation of electricity. Carbon dioxide is considered to be the one of the major greenhouse gases that is directly influencing the global climate changes that are occurring within the earth's ozone layer. It is estimate that 36% of the United State's anthropogenic CO2 [2] is produced from coal-fired power plant. Consequently, the capture of CO_2 from flue-gas streams is an essential step for the carbon management for sequestrating CO_2 from our environment.

The capture and separation of CO_2 can be achieved by using solvents, cryogenic techniques, membranes, and solid sorbents. The large-scale operation of these technologies is energy intensive when applied to capturing CO_2 in a dilute stream, such as flue gas, which consist of 15 volume % CO_2 for most coal combustion systems. Amine-based [3-4] wet scrubbing systems have been proposed as capture techniques for CO2 removal from flue gas streams, but are energy intensive due to the large amount of water needed in these systems. Excessive water is required because of the mechanism, corrosiveness and air flow problems created by the use of monoethanolamine (MEA), diethanolamine (DEA), or methyldiethanolamine (MDEA) in these aqueous-based, CO_2-capture systems. The proposed reaction sequences [5] in aqueous system using primary, secondary, and tertiary alkanolamines reacting with dissolve CO_2 are shown below.

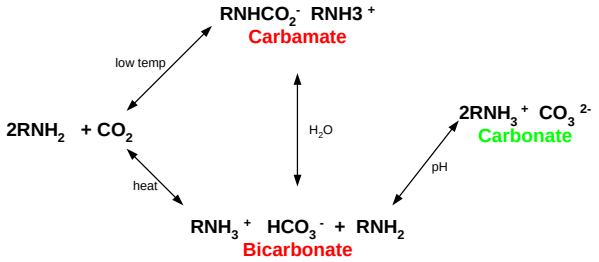

Figure 1. Proposed reaction sequence for the capture of carbon dioxide by liquid amine- based systems.

According to Figure 1, the majority of the CO_2 captured will result in the formation of bicarbonate in these liquid amine capture systems. In aqueous media, there is a requirement of 2 moles of amine/ mole of CO_2 for the formation of stable bicarbonate compounds resulting in the capture of CO_2.

Solid-amine CO_2 sorbents may have similar reactions with gaseous CO_2, water vapor, and the amine site on its surface. As a result, immobilized amine sorbents (IAS) are being used in aircraft, submarine, and spacecraft technologies [6-9]. However, the cost of these sorbents is too expensive for large-scale applications in the utility industry. Thus, SBA-15, a novel amine-based sorbent and a reformulated immobilized amine sorbent (R-IAS), are currently being examined as a cost efficient sorbent for the capture of CO2 from gas streams containing moisture. Consequently, a comparison performance study of the SBA-15, R-IAS and the IAS sorbents will be discussed within this paper.

Experimental

Preparation of the R-IAS. The reformulated immobilized amine sorbent (R-IAS) was prepared by the method described in the literature [8-9]. The exact composition of the secondary amine used in this sorbent will not be discussed due to pending patent applications.

Preparation of SBA-15. SBA-15 was prepared by using TEOS (tetraethylorthosilicate) as a silica precursor, Pluronic P123 ($PEO_{20}PPO_{70}PEO_{20}$, poly(ethylene glycol)-block-poly(propylene glycol)-block-poly(ethylene glycol) as a template, TMB (1,2,3-trimethyl benzene) as an expander, and HCl to control pH. [10-11] The specific steps for preparation of SBA-15 consist of :(1) dissolving 4.0 g of Pluronic P123 in 30 g of water and 120 ml (2.0 M) of HCl solution at room temperature, (2) mixing the resultant solution with 30 g TMB at 35 ^oC for 2 hours, (3) adding 8.5 g TEOS into the resultant homogeneous solution and stirring it at 35 ^oC for 22 hours, (4) aging the solution without stirring at 120 ^oC for 24 hours, and (5) calcining the resultant solid particles from filtering the aging solution in flowing air at –270 ^oC /min to 500 ^oC and holding it 500 ^oC hour for 6 hours. [10-12] The surface area of the SBA-15 was determined by N_2 BET measurement at 77 K.

Preparation and Characterization of the Sorbent. SBA-15 grafted with γ -aminopropyltriethoxysilane (APTS) was prepared by impregnating an APTS/toluene solution into SBA-15. [13] The impregnated sample was heated at 423 K for 20 h in a vacuum oven to obtain APTS-SBA-15. ATPTS-SBA-15 denotes the SBA-15 grafted with APTS. X-ray photoelectron spectra (XPS) of SBA-15 and APTS-SBA-15 were determined by a PHI5600ci instrument with monochromatic Al Kα X-rays.

CO_2 Capture Capacity. The chemical CO_2 capture capacities were determined by the combination of Temperature Programmed Desorption (TPD) and Mass Spectroscopy (MS) analyses. The adsorption of CO_2 was achieved in the presence of moisture at 25 ^oC and the total desorption of CO_2 was achieved over the temperature range of 30 – 60 ^oC. The composition of the experimental gas stream used in these test runs was 10% CO_2/H_2O/He. The detailed operating conditions for this procedure were previously described in the literature. [14-15]

XPS Analysis. The amount of nitrogen (N1s Peak) on the surface of the amine-enriched sorbent was determined by XPS analysis. The XPS analysis were conducted at 1 X 10^{-8} torr with the surface analysis depth range from 30 -50 angstroms. Under these conditions the chemically and the strongly adsorbed amines can be determined for each of the CO_2 capture sorbents. The details of this experimental procedure have been reported in the literature. [16]

Results an Discussion

Preliminary results of these types of sorbents have been reported early in the literature. [17] Initially, the performance of the prepared amine-enriched silicon sorbent (SBA-15) and the reformulated immobilized amine sorbent (R-IAS) were compared to an existing industrial solid amine sorbent (IAS). Each sorbent was placed in a 10% CO_2/H_2O/He stream and TPD and MS analyses were conducted to determine the performance of these CO_2 capture sorbents. The adsorption/desorption of CO_2 for these sorbents were determined over the temperature range of 25 – 60 ^oC. According to the TPD/MS analysis, all of the sorbents were successful in the capture of CO_2 from the moist experimental gas streams. The comparison of the CO_2 capture performances and XPS results for these sorbents are summarized in Table 1.

Table 1: TPD CO_2 Desorption and XPS Data of the Amine- Enriched Sorbents

Sorbents	μmol/g CO_2 captured	XPS % Nitrogen (N1s peak)
SBA-15-fresh	2011.4	7.1
SBA-15-1st Regeneration	1908.5	NA
SBA-15-2nd Regeneration	1748.3	NA
IAS-fresh	1603.9	17.7
IAS- 1st Regeneration	1922.6	NA
IAS-2nd Regeneration	1528.1	NA
R-IAS-fresh	4188.1	21.9
R-IAS-1st Regeneration	2690.2	NA
R-IAS-2nd Regeneration	2169.4	NA

As shown in Table 1, the SBA-15 had a lower % nitrogen value of 7.1 verses the IAS % nitrogen value of 17.7. The SBA-15 sorbent was prepared with a primary amine (propyl amine type) while the exact type of the amine used in the IAS was unknown. Despite the differences in the nitrogen values, the sorbents had similar average CO_2 capture capacities. The SBA-15 and the IAS sorbents were regenerated at 60 ^oC over two additional test runs and the average CO_2 capture capacity values were **1889.4 μmol/g** and **1820.8 μmol/g**, respectively. However, there was a significant improvement in the performance of the R-IAS sorbent over the other sorbents when tested under similar conditions. With the increase in the secondary amine loading in the R-IAS which is indicate by the higher % nitrogen value of 21.9, the average CO_2 capacity was increased to **3015.6 μmol/g**. It is assumed that the higher CO_2 capture capacity of the R-IAS can be attributed to the increase loading of the secondary amine. Furthermore, the use of a secondary amine appears to have superior performance over sorbent prepared with primary amine. Currently, additional research for the preparation of SBA-15 and R-IAS sorbents using different secondary amines are now underway and will be reported on in future publications.

Conclusions

Preliminary results indicate that the R-IAS has a higher average CO_2 capture capacity over the SBA-15 sorbent and IAS which is currently being used environmental CO_2 controlled life sorbent. It was determined the higher amine loading and the uses of secondary amines improved the CO_2 capture capacity of these types on immobilized amine sorbents.

References

(1) Marland G., Pippin A., Energy Systems and Policy, **1990**, 14, 319.

(2) Stringer, J. C. Opportunity for Carbon Control in the Electrical Power Industry, In Carbon Management: Implication for R&D in the Chemical Sciences and Technology, National Research Council, **2001**, p.60.

(3) Blauwhoff, P. M. M., Versteeg, G. F., Van Swaaij, W. P. M. Chem. Eng. Sci. **1984**, 39, p. 207-225.

(4) Tontiwachwuthikul, P., Meisen, A., Lim, C. J., J. Chem. Eng. Data, **1991**, 36, p. 130-133.

(5) Hook, R. J., Ind. Eng. Chem. Res., 36, **1997**, pp. 1779-1790.

(6) Veawab, A., Tontiwachwuthikul, P., Chakma, A., Ind. Eng. Chem. Res., **1999**, 38, p. 3917-3924.

(7) Satyapal, S., Filburn, T., Trela, J., Strange, J., Energy Fuels, **2001**, 15, p. 250-255.

(8) Birbara, P. J., Filburn, T. P., Nalette, T. A., US patent 5, 876, 488, **1999**.

(9) Birbara, P. J., Nalette, T. A., US Patent 5,492,683, **1996**.

(10) Stucky, G. D.; Chmelka, B. F.; Zhao, D.; Melosh, N.; Huo, Q.; Feng, J.; Yang, P.; Pine, D.; Margolese, D.; Lukens, W., Jr.; Fredrickson, G. H.; Schmidt-Winkel, P. PCT Int. Appl. 9937705, **1999.**

(11) Morey, M. S.; O'Brien, S.; Schwarz, S.; Stucky, G. D. *Chemistry of Materials* **2000**, 12, 898-911.

(12) Luan, Z.; Maes, E. M.; Heide, P. A. W. v. d.; Zhao, D.; Czernuszewicz, R. S.; Kevan, L. *Chemistry of Materials* **1999**, 11, 3680-3686.

(13) Vrancken, K. C.; Possemiers, K.; Van Der Voort, P.; Vansant, E. F. *Colloids Surf., A*, **1995**, 98, 235-241.

(14) Chuang, S. S. C.; Brundage, M. A.; Balakos, M. W.,Srinivas,G. *Appl. Spectrosc.*, **1995**, 98, 235-241.

(15) Soong, Y., Gray, M. L., Siriwardane, R. V., Champagne, K. J.,Stevens, Jr., R. W., Toochinda, P., and Chuang, S. S. C. "Novel Amine Enriched Solid Sorbents for Carbon Dioxide Capture," Fuel preprint, **2001**, 46 (1), pp. 285.

(16) Gray, M. L., Champagne, K. J., Soong, Y., Killmeyer, R. P., Baltrus, J., Maroto-Valer, M. M., Andersen, J. M., Ciocco, M.V., and Zandhuis, P.H., ACS Chapter Book, " Environmental Challenges and Greenhouse Gas Control for Fossil Fuel Utilization in the 21st Century", Kluwer Academic / Plenum Publishers, **2002**, p. 403.

(17) M. L. Gray, Y. Soong K. J. Champagne, H. Pennline, J. Baltrus, R. W. Stevens, R. Kharti and S. S. C. Chuang "Capture of Carbon Dioxide by Solid Amine Sorbents" accepted **9/4/2003**, International Journal of Environmental and Pollution, unpublished.

Effect of Type of Polymers Loaded in Mesoporous Carbon Dioxide "Molecular Basket" Adsorbent on Carbon Dioxide Separation from Gas Mixtures

Xiaochun Xu, Bronwyn Graeffe, and Chunshan Song*

Clean Fuels and Catalysis Program, The Energy Institute, and Department of Energy & Geo-Environmental Engineering, The Pennsylvania State University, 209 Academic Projects Building, University Park, PA 16802, USA

* Corresponding author. E-mail: csong@psu.edu; Tel: 814-863-4466; Fax: 814-865-3248

Introduction

Separation of CO_2 from various gaseous streams is becoming increasingly important in the field of energy production and sustainable use of fossil energy.[1] Currently, CO_2 separation is applied in industry during natural gas processing and during hydrogen production processing. On the other hand, significant increase in the global atmospheric CO_2 concentration has caused serious concern for the global climate change and has led to a worldwide effort in research and development on control of CO_2 emission.[2] Moreover, CO_2 also represents an important source of carbon for fuel and chemical feedstock in the future.[3] These have further created a demand for cost-effective CO_2 separation technology.

The known options for carbon dioxide separation include chemical and physical absorption, physical and chemical adsorption, cryogenic separation and membrane separations.[1] The key issue for adsorption separation is to prepare high performance adsorbent. Recently, we developed a new kind of high-capacity, highly selective carbon dioxide adsorbent, which is called carbon dioxide "molecular basket".[4,5] By loading CO_2-philic materials, such as sterically branched polymer polyethylenimine (PEI), into mesoporous molecular sieve MCM-41, carbon dioxide adsorption capacity was significantly increased.[4,5] In this paper, different types of PEI are investigated to further improve the carbon dioxide adsorption separation performance of the novel "molecular basket".

Experimental

The "molecular basket" adsorbents were prepared by modifying the siliceous MCM-41 with PEI through a wet impregnation method.[4,5] Two types PEI, i.e., linear PEI (Aldrich, Mn: ~423) and branch PEI (Aldrich, Mn: ~600) were used. The molecular structures of the linear PEI and the branch PEI are illustrated in Figure 1. From the molecular formula, it can be seen that the branch PEI consists of primary, secondary and tertiary amine groups, while the linear PEI only contains mainly the secondary amine group. The PEI loading for the "molecular basket" adsorbents is 50 wt%. The as-prepared adsorbents are denoted as MCM-PEI-L and MCM-PEI-B, where L represents linear PEI and B represents branch PEI.

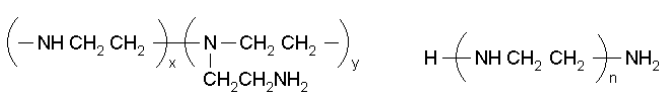

(a) (b)

Figure 1. Illustration of the molecular formulas for branch PEI (a) and linear PEI (b).

The adsorption and desorption performance of the adsorbent was measured by using a PE-TGA 7 analyzer.[4,5] Adsorption capacity in mg of adsorbate/g-adsorbent and desorption capacity in percentage were used to evaluate the adsorbent and were calculated from the weight change of the sample in the adsorption/desorption process. Desorption capacity in percentage was defined as the ratio of the amount of the gas desorbed over the amount of gas adsorbed. The adsorption/desorption temperature of 75 ^oC and the adsorption and desorption time of 150 min were selected because our previous investigation showed that the MCM-41-PEI exhibited the best adsorption/desorption performance at 75 ^oC; and that the adsorption nearly reached equilibrium and the desorption was complete after 150 min.[4,5]

The adsorption separation was carried out in a flow adsorption separation system described in reference 6.[6] Simulated flue gas mixture containing 14.9% CO_2, 4.25% O_2 and 80.85% N_2 was used as the adsorbate. The adsorption time was 120 minutes and the desorption time was 600 minutes. The concentration of the gases in the effluent gas and the gas flow rate were measured every 5 minutes. Adsorption capacity in ml (STP) of CO_2/g-adsorbent and desorption capacity in percentage were used to evaluate the performance of the adsorbents. The adsorption/desorption capacity was calculated from the mass balance before and after the adsorption. The separation factor, $\alpha_{i/j}$, was calculated from equation 1 as the ratio of the amount of gases adsorbed by the adsorbent, $(n_i/n_j)_{adsorbed}$, over the ratio of the amount of gases fed into the adsorbent bed, $(n_i/n_j)_{feed}$:

$$\alpha_{i/j} = \frac{(n_i / n_j)_{adsorbed}}{(n_i / n_j)_{feed}} \qquad (1)$$

Results and Discussions

1. Influence of PEI Type on CO_2 Adsorption/Desorption

Figure 2 shows the single CO_2 adsorption/desorption properties measured by TGA. The CO_2 adsorption capacities are 153.5 mg/g-adsorbent and 117.2 mg/g-adsorbent for MCM-PEI-L and MCM-PEI-B, respectively. The CO_2 adsorption capacity for MCM-PEI-L is 31% higher than that for MCM-PEI-B. The desorption for MCM-PEI-L and MCM-PEI-B are all complete, which indicates that the "molecular adsorbent" may be used in many cyclic operations. Our previous results showed that the MCM-PEI-B was stable in ten cyclic adsorption/desorption operations.[5,6]

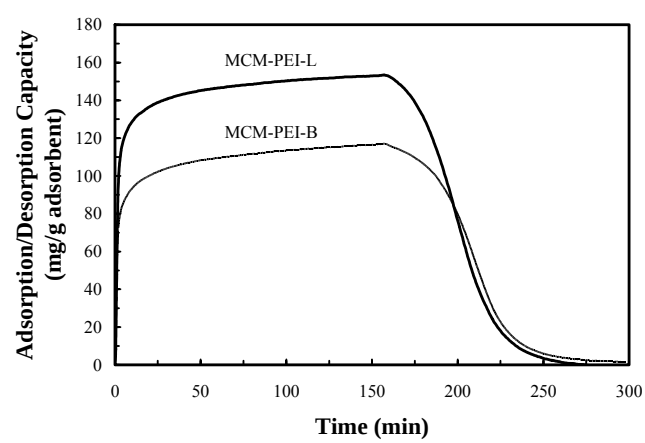

Figure 2. CO_2 adsorption/desorption properties of MCM-PEI-L and MCM-PEI-L measured by TGA.

Types of PEI also greatly affect the CO_2 adsorption/desorption rate of the "molecular basket" adsorbents. From Figure 2, it is clear

that CO_2 desorption rate for MCM-PEI-L is faster than that for MCM-PEI-B. However, the difference in CO_2 adsorption rate for MCM-PEI-L and MCM-PEI-B, especially at the beginning of the adsorption, is not clear from Figure 2. In order to clarify the CO_2 adsorption kinetics, CO_2 adsorption in the first 5 minutes is plotted and shown in Figure 3. Obviously, the rate of CO_2 adsorption for MCM-PEI-L is much faster than that for MCM-PEI-B. Since different types of amines groups have different heats of adsorption, the difference in the CO_2 adsorption/desorption capacity and in the adsorption/desorption rate of the "molecular basket" adsorbents may be explained by the different types of amine groups in the PEI. The fast adsorption and desorption kinetic is important for the adsorption separation.

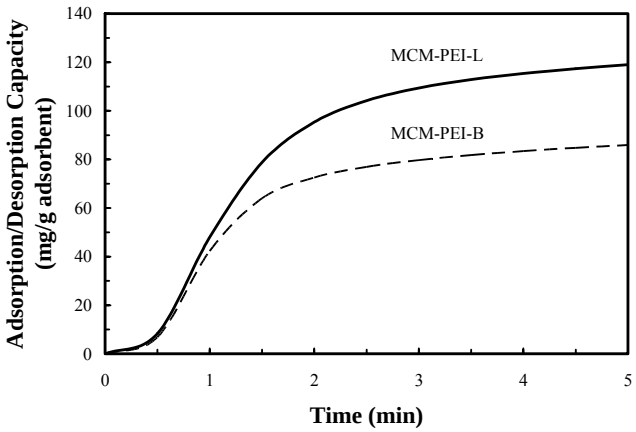

Figure 3. Comparison of the CO_2 adsorption kinetics of MCM-PEI-L and MCM-PEI-B measured by TGA.

2. Effect of PEI Type on CO_2 Separation from Simulated Flue Gas

Figure 4 compares the breakthrough curve of CO_2 in the separation of CO_2 from simulated flue gas, which contains 14.9% CO_2, 4.25% O_2 and 80.85% N_2, for MCM-PEI-L and MCM-PEI-B. At the beginning of the separation, CO_2 is completely adsorbed by the "molecular basket" adsorbents and the CO_2 concentration is below the detection limit of the gas chromatography, i.e. < 100 ppm. After 55 minutes of adsorption, CO_2 began to breakthrough for MCM-PEI-B, while CO_2 is still completely adsorbed for MCM-PEI-L. The breakthrough time for MCM-PEI-L is 90 minutes. The calculated CO_2 breakthrough capacities are 67.1 ml/g-adsorbent and 40.9 ml/g-adsorbent for MCM-PEI-L and MCM-PEI-B, respectively. The CO_2 breakthrough capacity for MCM-PEI-L is 64% higher than that for MCM-PEI-B. Both adsorbents hardly adsorb any N_2 and O_2. The estimated separation factors for CO_2/N_2 and CO_2/O_2 are larger than 1000.

Figure 5 compares the desorption performance of MCM-PEI-L and MCM-PEI-B. For both adsorbents, the adsorbed CO_2 can all be desorbed in 6 hours. However, the rate for CO_2 desorption for the two adsorbent is different. The MCM-PEI-L desorbs CO_2 faster than the MCM-PEI-B, which is in accordance with that observed in the TGA measurements.

Conclusions

Highly effective CO_2 "molecular basket" adsorbent can be prepared by using mesoporous molecular sieve MCM-41 and polyethylene imine with a linear structure. The adsorbent with linear PEI shows not only a higher CO_2 adsorption capacity, but also a faster CO_2 adsorption/desorption rate, than those for the "molecular basket" adsorbent with branched PEI.

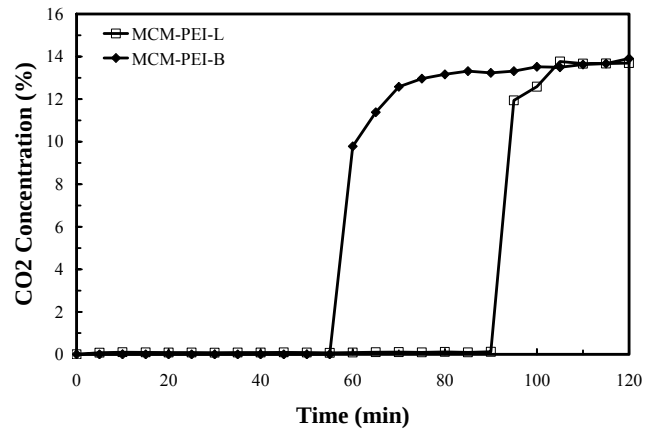

Figure 4. Comparison of CO_2 breakthrough curves in the separation of CO_2 from simulated flue gas for MCM-PEI-L and MCM-PEI-B. Operating condition: Weight of adsorbent: 2.0 g; Feed flow rate: 10 ml/min; Temperature: 75 ^oC.

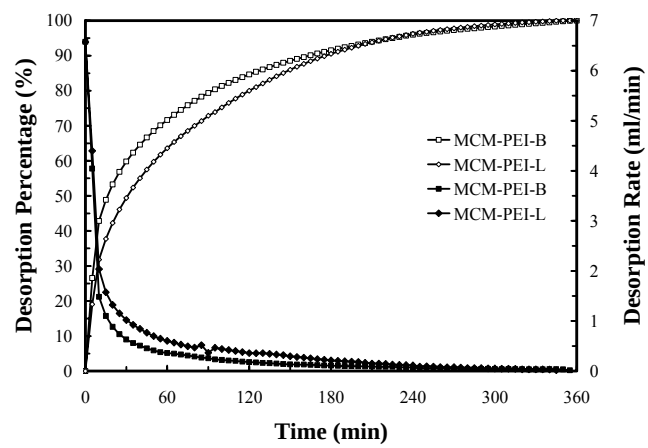

Figure 5. Comparison of CO_2 desorption in the separation of CO_2 from simulated flue gas for MCM-PEI-L and MCM-PEI-B. (◊, □) desorption percentage, (■, ▲) desorption rate.
Operation condition: Weight of adsorbent: 2.0 g; Temperature: 75 ^oC; Sweep gas flow rate: 50 ml/min.

References

(1) Office of Science and Office of Fossil Energy, U.S.D.O.E. Carbon sequeatration. State of the Science. Washingtn, DC, 1999.
(2) Azar, C.; Rodhe, H. *Science* **1997**, *276*, 1818.
(3) Song, C.; Gaffney, A. M.; Fujimoto, K. *CO_2 Conversion and Utilization.*, **2002**; Vol. 809.
(4) Xu, X. C.; Song, C. S.; Andresen, J. M.; Miller, B. G.; Scaroni, A. W. *Microporous and Mesoporous Materials* **2003**, *62*, 29–45.
(5) Xu, X. C.; Song, C. S.; Andresen, J. M.; Miller, B. G.; Scaroni, A. W. *Energy & Fuels* **2002**, *16*, 1463.
(6) Xu, X. C.; Song, C. S.; Andresen, J. M.; Miller, B. G.; Scaroni, A. W. *International Journal of Environmental Technology and Management* **2003**, in press.

ETHYLENEDIAMINE-MODIFIED SBA-15 AS REGENERABLE CO_2 SORBENTS

Feng Zheng, Diana N. Tran, Brad Busche, Glen E. Fryxell, R. Shane Addleman, Thomas S. Zemanian, Christopher L. Aardahl

Pacific Northwest National Laboratory
P.O. Box 999, MSIN: K6-28
Richland, WA 99352

Introduction

The linkage between anthropogenic CO_2 and global climate change has been well established. Significant reduction of CO_2 emission from large point sources such as fossil fuel power plants is necessary to stabilize atmospheric concentration of CO_2[1]. Compared to the commercial liquid alkanolamines currently used in the absorption of CO_2 from power plant flue gas, solid regenerable sorbents can offer the advantages of lower toxicity and corrosiveness and can potentially reduce equipment cost and energy consumption. Such solid regenerable sorbents are also useful for CO_2 removal from enclosed habitable environments such as submarines and spacecrafts due to their small footprints and reusability.

Mesoporous silica that is chemically modified with amine functionalities is an attractive candidate as high performance CO_2 sorbents because of the combination of their high surface areas in mesopores and the chemical specificity of amines. Alkylamine groups can be grafted on to silica by the condensation of appropriate aminoalkoxysilanes. For example, silica gels and mesoporous silica grafted with 3-aminopropyl groups were reported to be able to adsorb CO_2 reversibly [2-5]. Ethylenediamine (EDA)-modified silica gel and mesoporous silica were also reported to adsorb CO_2 but there are few data on their adsorption capacity [7-8]. In this report we present CO_2 adsorption isotherm as well as breakthrough capacity data on an EDA-modified SBA-15 mesoporous silica.

Experimental

EDA-modified mesoporous silica synthesis. The SBA-15 mesoporous silica substrates were synthesized following the established procedures [6]. The BET surface area of the SBA-15 substrate was 700m^2/g. A typical batch of 10 grams of SBA-15 silica was dispersed in 150ml toluene and 3.2ml water and stirred for one hour for surface hydration. 10ml of N-[3-(trimethoxysilyl)propyl] ethylenediamine (approximately one monolayer equivalent, assuming 4 silanes/nm^2) was subsequently added and the reaction mixture was heated to reflux. After 4 hours at reflux, the reflux condenser was removed and replaced with a short-path still-head and the methanol and water azeotrope were distilled off. After the distillation was complete, the reaction mixture was allowed to cool, and product was collected by filtration, washed twice with 100ml isopropyl alcohol, and air dried. The EDA loading was calculated to be 3.0mmol/g based on final product weight.

Characterization Methods. The as-synthesized and the EDA-modified SBA-15 mesoporous silica samples were characterized by nitrogen adsorption measurements for BET surface area using a Quantachrome Autosorb system. FTIR and NMR measurements were also done to verify surface bonding of the EDA functional groups. Thermal gravimetric analysis (TGA) measurements were performed using a Netzsche STD 409 coupled with a mass spectrometer. The thermal stability of the modified SBA-15 in helium and air was studied with a temperature ramp of 10°C /min to 650°C. CO_2 adsorption isotherms were also measured from 0 to 750 torr CO_2 partial pressure using the TGA system. Breakthrough measurements and temperature programmed desorption (TPD) were carried out using a flow system, where the CO_2 concentrations in the feed gas were varied from 1% to 70% by volume with balance N_2 and in some tests also 2% water vapor. During TPD the sorbent sample was heated to 110°C at 10°C/min. The gas phase was analyzed using a mass spectrometer.

Results and Discussion

The TGA data taken in air are shown in Figure 1 with weight loss peak assignments based on simultaneous mass spectrometer data. The TGA data reveal that the CO_2 adsorbed from ambient air by the EDA-modified SBA-15 was released at 110°C. The EDA sorbent was found to be stable up to 220°C in air and over 300°C in helium.

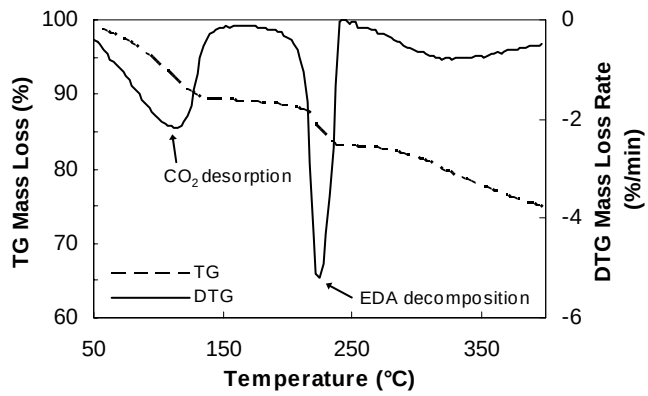

Figure 1. TGA data of the EDA-modified SBA-15 sorbent in air.

The CO_2 breakthrough time and adsorption capacity were measured using the flow system. In Figure 2, the gas phase CO_2 concentration, measured by a mass spectrometer during two consecutive breakthrough/TPD cycles, was shown. After breakthrough, the CO_2 concentration increased quickly to feed gas level, indicating fast adsorption kinetics. The sorbent can be regenerated by thermal swings to 110°C at 10°C/min, as evidenced by the same height of the two desorption peaks. When the EDA-SBA-15 sorbent was subjected to ten cycles of adsorption and desorption, it retained its CO_2 adsorption capacity and was fully regenerable.

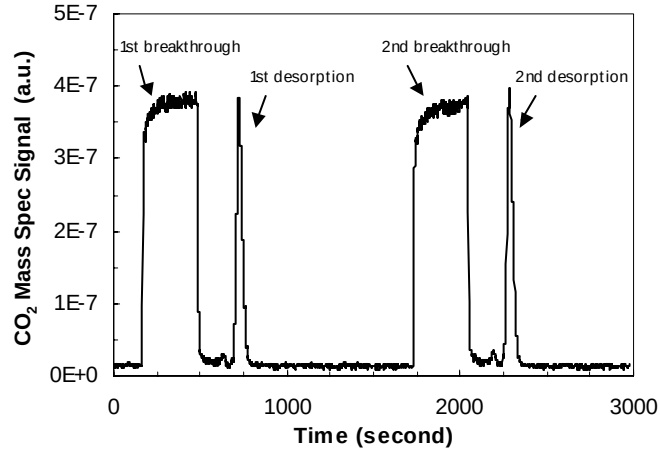

Figure 2. Gas phase CO_2 concentration during cyclic adsorption/desorption tests.

The isothermal adsorption capacity data on the EDA-SBA-15 sorbent are summarized in Figure 3. The EDA-SBA-15 silica adsorbs around 20mg/g of CO_2 at 25°C and 1 atm with 15% CO_2 (by volume) in N_2 in the flow system. At the same partial pressure of pure CO_2, the sorbent uptakes about 25 mg/g of CO_2 at 22°C based on the TGA data. At 1 atm CO_2 partial pressure, the adsorption capacity is 86 mg/g, which is lower than the stoichiometric chemisorption capacity of 132mg/g based on the initial estimate of 3.0mmol/g EDA loading, but compares favorably to the capacity of the aminopropyl-modified silica sorbents previously reported (20 to 90 mg/g at 1 atm CO_2 partial pressure at room temperature). It is believed that the actual available EDA loading on the EDA-SBA-15 sorbent is lower than 3.0mmol/g and can be increased by improvements in synthesis.

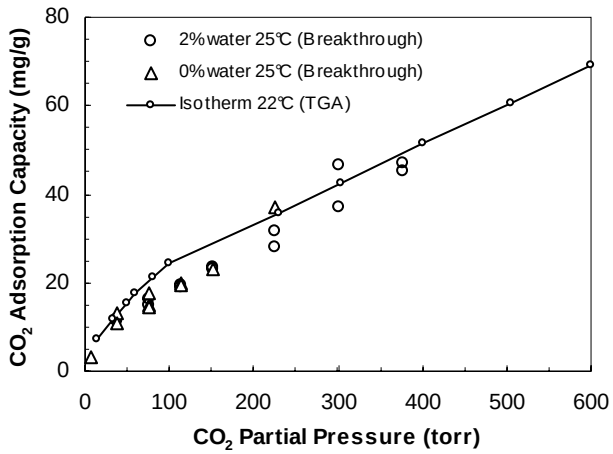

Figure 3. CO_2 adsorption isotherms of the EDA-SBA-15 sorbent.

The adsorption isotherm based on the TGA data agrees with the capacity data from breakthrough tests within experimental error. The presence of 2% water vapor in some of the breakthrough tests did not influence the CO_2 uptake. This behavior, although different from those of previously reported aminopropyl-modified silica, is expected as each EDA group contains two amine groups and can adsorb one CO_2 molecule. Two aminopropyl groups are necessary to bond one CO_2 molecule if no water is present. Carbamate formation on EDA-SBA-15 is of the intramolecular type that does not involve water molecules, and it should proceed faster than on aminopropyl-modified silica sorbents. It is believed that by tailoring the amine groups, CO_2 adsorption capacity and kinetics can be further improved.

Conclusions

We have synthesized an EDA-modified SBA-15 mesoporous silica and characterized its CO_2 adsorption properties. The CO_2 adsorption capacity of the EDA-SBA-15 sorbent is around 20mg/g at 25°C and 1 atm with 15% CO_2 (by volume) in N_2. This is comparable to the adsorption capacity of aminopropyl-modified mesoporous silica. However, while the adsorption of the latter decreases in the absence of water, the CO_2 adsorption capacity of the EDA-modified mesoporous silica is not influenced by humidity. Additionally, the EDA functional group allows CO_2 capture via intramolecular carbamate formation and therefore favorable kinetics. By tailoring the amine groups, it is expected that CO_2 adsorption capacity and kinetics can be further improved.

Acknowledgement. Pacific Northwest National Laboratory is operated by Battelle for the U.S. Department of Energy under Contract DE-AC06-76RLO 1830.

References

(1) White, C. M; Strazisar, B. R.; Granite, E. J.; Hoffman, J. S.; Pennline, H. W. *J. Air Waste Management Association* **2003**, *53*, 645-715.
(2) Burwell, R. L.; Leal, O. *J.Chem.Soc., Chem.Commun*. **1974**, 342.
(3) Leal, O.; Bolivar, C.; Ovalles, C.; Garcia, J. J.; Espidel, Y. Inorganica *Chimica Acta* **1995**, *240(1-2)*, 183-189.
(4) Huang, H. Y.; Yang, R. T.; Chinn, D.; Munson, C. L. *Industrial & Engineering Chemistry Research* **2003**, *42(12)*, 2427-2433.
(5) Chang, A. C. C.; Chuang, S. S. C.; Gray, M.; Soong, Y. *Energy & Fuels* **2003**, *17(2)*, 468-473.
(6) Zhao, D.; Huo, Q.; Feng, J.; Chmelka, B. F.; Stucky; G.D., *J. Am. Chem. Soc.* **1998**, *120*, 6024-6036.
(7) Aresta M.; Dibenedetto, A. *6th International Conference on Greenhouse Gas Control Technologies*; Tokyo, **2002**.
(8) Chaffee, A. L.; Delaney, S. W.; Knowles, G.P. *Abstracts of Papers of the American Chemical Society* 223: 076-FUEL Part 1 April 7, **2002**.

DETAILED CHEMICAL KINETIC MODELING; IS THERE LIFE AFTER GRI-MECH 3.0?

Henry J. Curran

National University of Ireland, Galway, Ireland

Introduction

Throughout the 1990s, the Gas Research Institute (GRI) sponsored a research program that focused on the development of an optimized detailed chemical reaction mechanism capable of the best representation of natural gas flames and ignition[1]. Altogether, there were three releases of the mechanism, GRI-Mech 1.1, 2.11, and GRI-Mech 3.0. This mechanism was optimized for methane and natural gas as fuel in the temperature range 1000—2500 K, in the pressure range 10 Torr to 10 atm, and at equivalence ratios from 0.1 to 5 for premixed systems.

GRI-Mech 3.0 includes all steps thought to be important for describing natural gas ignition and flame propagation (including NO formation and reduction) using rate parameters that reflect current understanding of elementary reaction rate theory. Some aspects of natural gas combustion chemistry are not described by GRI-Mech 3.0. These include soot formation and the chemistry involved in selective non-catalytic reduction of NO. The latter may be important in natural gas reburning at lower temperatures[1].

Even though GRI-Mech does include reactions for species pertinent to natural gas combustion (e.g. ethane, propane, methanol, ethylene and acetylene), GRI recommend that the mechanism should not be used to simulate these pure fuels since the optimization did not include targets relevant to them.

Despite, these drawbacks, the GRI program was very successful, being the first of its kind to make the mechanism readily available over the Internet. Unfortunately, in February 2000 support for this work was discontinued.

The purpose of the current study is to develop a detailed chemical kinetic mechanism in a similar manner to the methodology employed in the GRI study. To date, a mechanism has been developed to reproduce fuel oxidation over a wide range of conditions for hydrogen, carbon monoxide, methane, and associated oxygenated species such as methanol, formaldehyde and acetaldehyde. It is our aim to further extend the study to create a reliable chemical kinetic mechanism to describe the oxidation of fuels up to C_3 hydrocarbon species and larger.

Hydrogen

Since hydrogen is a major component of all hydrocarbon fuels, the hydrogen submechanism is an essential foundation mechanism. To that end we have developed and validated a detailed H_2 mechanism[2] in the temperature range 298 to 2700 K, in the pressure range 0.05 to 20 atm, and at equivalence ratios from 0.2 to 6. To present the full range of data validated is beyond the scope of this paper. Two sets of data are chosen to illustrate the mechanism performance.

Mueller et al[3] studied moderately lean to moderately rich H_2/O_2 mixtures diluted in nitrogen in the temperature range 880—935 K and in the pressure range 0.30—15.7 atm. Figure 1 illustrates experimental (points) versus model-predicted (lines) profiles for hydrogen oxidation at different reactor temperatures. Overall, excellent agreement is observed between the model and experiment.

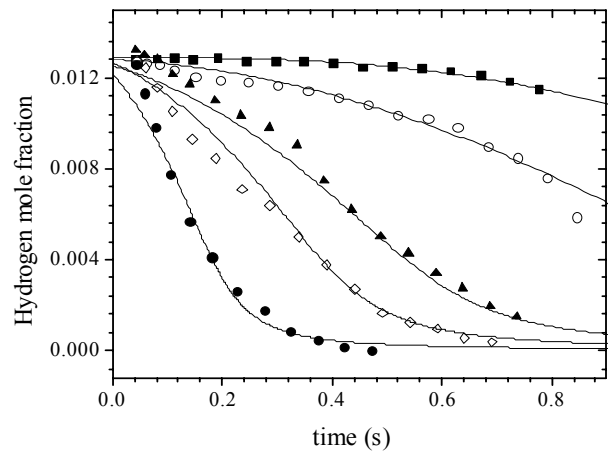

Figure 1. Comparison of experimental flow reactor[3] hydrogen concentration (points) and simulations (lines) versus residence time at 1.3% H_2, 2.2% O_2, P=6.5 atm. ■ 884 K, ○ 889 K, ▲ 906 K, ◊ 914 K, ● 934 K.

Moreover, Tse et al.[4] measured mass burning velocities for $H_2/O_2/He$ mixtures in the equivalence ratio range $0.5 \leq \phi \leq 3.5$, at 1, 5, 10, 15 and 20 atm, at an initial temperature of 298 K. It was reported that flames became increasingly unstable at elevated pressures, and thus true, stretch-free flame speeds became more difficult to measure. For the 10—20 atm data, the oxygen to fuel ratio was reduced to suppress diffusional-thermal instability and delay hydrodynamic instability. Using helium as the diluent also helped minimize instability up to 20 atm by reducing the Lewis number of the flame and retarding the formation of flame cells.

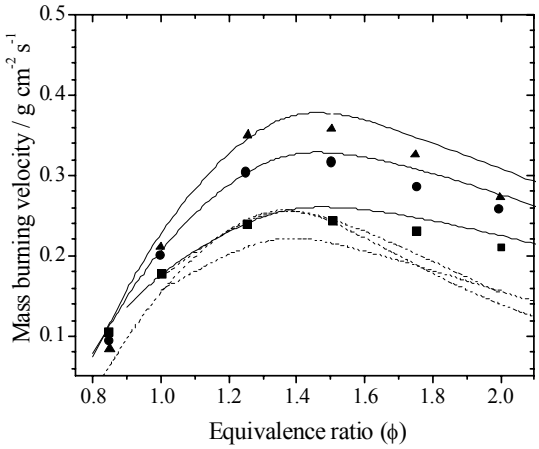

Figure 2. Comparison of experimental[4] (points) versus model predicted (lines) mass burning velocities for $H_2/O_2/He$ flames as a function of equivalence ratio. O2:He = 1:11.5, ■ 10 atm, ○ 15 atm, ▲ 20 atm. Solid lines are current mechanism prediction, dotted lines GRI-Mech 3.0.

[1] Smith, G. P., Golden, D. M., Frenklach, M., Moriarty, N. W., Eiteneer, B., Goldenberg, M., Bowman, T., Hanson, R. K., Song, S., Gardiner, Jr., W. C., Lissianski, V.V., and Qin, Z., http://www.me.berkeley.edu/gri_mech/

[2] O'Conaire, M., Curran, H. J., Simmie, J. M., Pitz, W. J., Westbrook, C. K., submitted to *Intl. J. Chem. Kin*et. Nov. 2003.

[3] Mueller, M. A.; Yetter, R. A.; Dryer, F. L.; *Intl. J. Chem. Kinet.* **31**:113--125 (1999).

[4] Tse, S. D., Zhu, D. L., Law, C.K., *Proc. Combust. Inst.***28**:1793—1800 (2000).

Methane

Methane is the main component of natural gas and being the simplest stable C_1 species, its oxidation mechanism forms the foundation for all other hydrocarbon mechanisms. Several experimental shock tube studies have been simulated over the temperature range $700 \leq T \leq 2400$ K, in the pressure range 0.3—260 atm and in the equivalence ratio range $0.4 \leq \phi \leq 6.0$. Flame speed measurements between 1 and 5 atm in the equivalence ratio range $0.4 \leq \phi \leq 1.8$ have also been simulated. Both of these data sets, particularly those recorded at high pressure, are of particular importance in validating a kinetic mechanism, as internal combustion engines operate at elevated pressures and temperatures and rates of fuel oxidation are critical to efficient system operation.

Petersen et al.[5] conducted an analytical study to supplement extreme shock tube measurements of CH_4/O_2 ignition at elevated pressures (4—26 MPa), high dilution (fuel plus oxidizer ≤ 30%), intermediate temperatures (1040—1500 K), and equivalence ratios as high as 6.

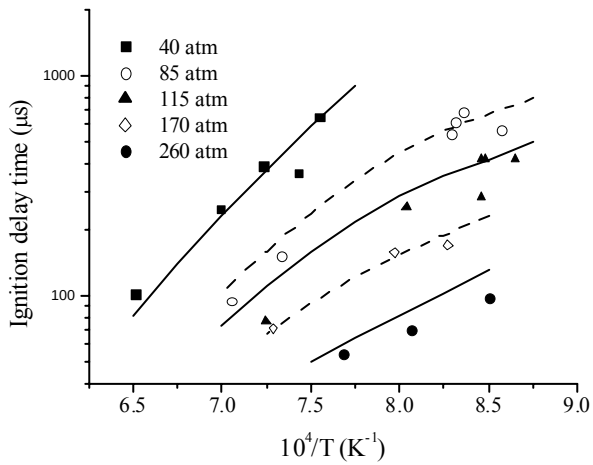

Figure 3. Comparison of experimental[5] (points) versus model predicted (lines) shock tube ignition delay times at 20% CH_4, 13.3% O_2, 66.7% Ar, ϕ = 3.0.

Figure 3 depicts experimental[5] and model predicted ignition delay times as a function of inverse temperature. It is observed that both the experimental data and the mechanism prediction show a decrease in activation energy at temperatures below approximately 1175 K. This is due to intermediate temperature chemistry where the $CH_3O_2 + CH_3 = CH_3O + CH_3O$ reaction is important. The Petersen study highlights the need to include the CH_3O_2 radical species and reactions in a reaction mechanism in order to correctly simulate methane oxidation chemistry under high-pressure, intermediate temperature conditions; conditions which prevail in high pressure natural gas combustors. The CH_3O_2 radical species and reactions are not included in GRI-Mech 3.0.

Methanol

Methanol is a component species in the natural gas submechanism, and has been validated using Princeton flow reactor data[6] in the temperature range 781—1043 K, in the equivalence ratio range $0.051 \leq \phi \leq 2.59$ and at pressures of 1, 2.5, 10, and 15 atm. Figure 4 depicts a comparison of the model-predicted intermediate profiles against the experimental data. Overall, the mechanism is able to reproduce the experimental data quite accurately.

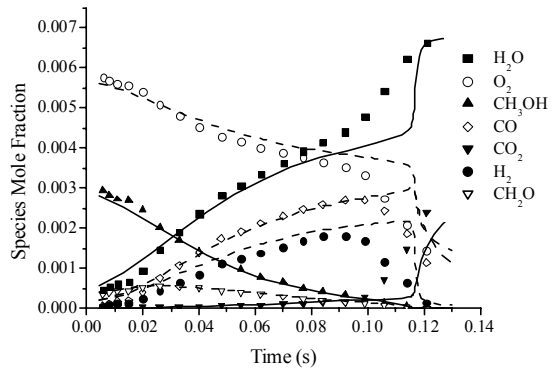

Figure 4. Comparison of experimental[6] (points) versus model predicted (lines) flow reactor species mole fractions for CH_3OH oxidation. 1010 ppm CH_3OH, ϕ = 0.86, P = 1.0 atm, T_i = 1043 K. τ_{offset} = -0.065 s.

In addition, experiments performed by Bowman[7] behind reflected shock waves in the temperature range 1545--2180~K, at reflected shock pressures of 1.5, 3, 3.5 and 4.5 bar and in the equivalence ratio range $0.75 \leq \phi \leq 6.0$, were also used to validate the mechanism. Figure 5 shows the influence of oxygen concentration on ignition delay time. Increasing the oxygen concentration from 1% to 4% results in a marked increase in the reaction rate—a positive shift in ignition delay time occurs as the oxygen content is increased at constant temperature. This trend is also well reproduced by the detailed mechanism.

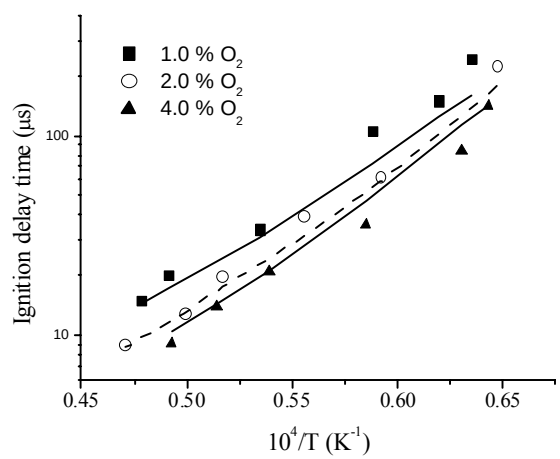

Figure 5. Comparison of experimental[7] (points) versus model predicted (lines) shock tube ignition delay times. 1.0% CH_3OH in Ar, P ≈ 3.0 bar.

[5] Petersen, E.L., Davidson, D.F., Hanson, R.K. *J. Prop. Power* (1999) **15**:82—91.

[6] Held,T.J., Dryer, F. L., *Int. J. Chem. Kinet.* **30**: 805—830 (1998).

[7] Bowman, C. T., *Combust. Flame* **25**: 343—354 (1975).

Efficient lumping technique for the automatic generation of n-heptane and iso-octane oxidation mechanism

S. S. Ahmed, G. Moréac, T. Zeuch and F. Mauss

Division of Combustion Physics, Lund University of Technology, P.O. Box 118

SE-22100 LUND, Sweden

Introduction

The future demands of engine development are to have highly efficient engines with almost no emissions. It is a global trend for the automotive industry to look forward in this area, mainly due to fact that the demands of energy consumption are increasing more and more and almost 90% of this came from the fossil fuels, which are becoming obsolete from their natural resources. New sources of energy and highly fuel-efficient existing conventional engines with low emissions are the demands of future. Low fuel consumption and increased efficiency is desirable both due to considerations of pollutant emissions (CO_2 production is contributing to the greenhouse effect) and economy (cost effectiveness). This all leads to the continuation in developing a better understanding of the combustion process, specially the oxidation process of large hydrocarbon fuels such as n-heptane and iso-octane over a wide range of engine operating conditions. These primary reference fuels (PRF) oxidation mechanisms are quite complex and large in terms of species and reactions such as 1033 species and 8476 reactions for example. An urgent need is there to reduce the size and complexity of the mechanism in order to implement this mechanism in the three dimensional computational fluid dynamics codes which are used to study different engine parameters and combustion processes and yet having the same reliability and results as the detailed ones. This could be done by generating a semi-detailed mechanism first and then its simplification by lumping process and further on by necessity analysis. Some previous works have been done on lumping procedures by Ranzi et al.[1] and Fournet et al.[2]

Mechanism

This work has been done to generate a semi-detailed mechanism for n-heptane and iso-octane oxidation mixture. The construction of the mechanism is systematically in accordance with Curran et al.[3] using the reaction classes and rate constants suggested by the authors as a reference. Intermediate reactions, considered of low importance for the timing of ignition, are simplified substantially by optimizing it. The mechanism contains the pathways involve the fuel species, iso-octane and n-heptane, and also the lower alkene sub-mechanisms of C_7, C_6 and C_5 species (where the C_4 and below is the part of the base mechanism[4]). The detailed mechanism contains 241 species and 1905 reactions. Lumping procedure has been applied on n-heptane mechanism which reduces the mechanism size to 223 species and 1869 reactions including iso-octane sub-mechanism. In the present mechanism all the reaction paths which are known to be pertinent from both high and low temperatures are included in order to cover the full range of temperature and pressure. To reduce the mechanism size in order to make it faster and fewer complexes, its reduction has been done first by lumping technique and further on by necessity analysis. Lumping is the procedure of substituting different species of similar molecular structure into one species called "lumped species". The new lumped species is related not only to the original species concentrations but also on the important parameters. Necessity analysis is the process to calculate the contribution of reaction steps to the production rate of necessary species and hence eliminate the non-important reactions. The mechanism is used in study the effect of elevated pressure and temperature of the n-heptane and iso-octane oxidation mixture in engine for different operating conditions.

The calculations have been performed for the 1st and 2nd ignition delay times using the constant volume flow model and then also Homogenous Charge Compression Ignition (HCCI) engine model in- house ignition code,[5] for both detailed and lumped mechanisms.

Lumping Procedure. The species of similar molecular structure and position of H-abstraction from secondary sites are lumped together. This is because the rate parameters and thermodynamic data vary slightly between different structures of the similar ring size species. At first four species of similar ring size 5, are lumped together to form new lumped species. The rate constants were calculated for each lumped species reactions individually for both forward and backward reactions. The concentration of new lumped species is then balanced by dividing the backward rate constants as shown in equation (1) for each individual reaction with the number of species lumped together which is four in this case. Similar approach has been made to lump the other species of the same ring sizes and molecular structure and further on in other reaction types of the mechanism as well. **Figure 1** is showing the concentration profiles of the lumped species against the four added species. **Figure 2** is showing the product species before and after lumping.

$$\frac{d[5r-HEOOH]}{dt} = \sum\left([2-C_7H_{15}O_2]+2\times[3-C_7H_{15}O_2]\right)k_{1f} + [4-C_7H_{15}O_2]k_{2f} - \left([5r-HEOOH]\,k^*_{1b}/4 + [5r-HEOOH]\,k^*_{2b}/4\right) \quad \rightarrow eq(1)$$

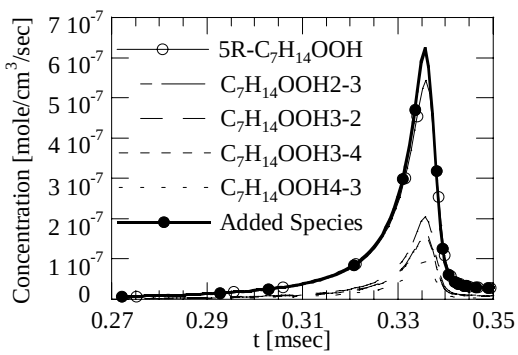

Figure 1 Concentration of new lumped species 5R-C7H14OOH is plotted by shifting the ignition delay time 0.034 sec to have better view against the added concentration of four species at initial pressure set to 40 bar, phi is 1.0 and initial temperature is 800 K.

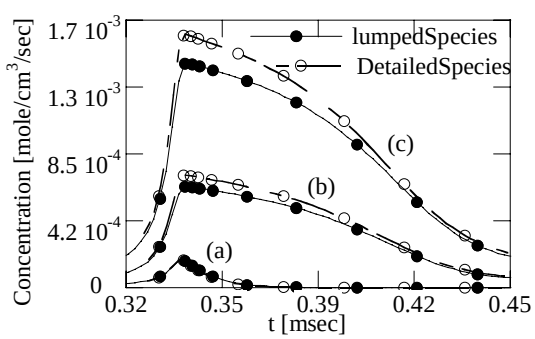

Figure 2 Concentration profile of a product species N-$C_4CH_9COCH_2$ (a), N-C_4H_9CHO (b) and N-C_3H_7CHO (c) before and after lumping at initial temperature of 800 K.

Validation

The lumped reaction model and the semi-detailed n-heptane and iso-octane mixture oxidation mechanism have been first validated against the shock tube experimental data from Fieweger et al.[6]and Ciezki et al.[7] Calculated and experimental ignition delay times have been compared at low and high temperatures. In the negative temperature regime, where the ignition occurs as a two-stage process, we compare in addition the timing of the occurrence of the low temperature oxidation. The mechanism was validated for fuel lean and rich conditions, a range of octane numbers and pressures from 13 bar to 40 bar. The initial temperature range from 700 to 1300 K is set for all the cases. Fuel-air equivalence ratio (ϕ) is equal to 0.5, 1.0 and 2.0, and Research Octane Number (RON) is 0, 20, 40, 60, 80, and 100. In general, there is a good agreement between the semi-detailed mechanism calculations and experimental ignition delay timings and then lump mechanism calculation fits well with the detailed one. Result for RON 0, ϕ=1 and P=40 atm is shown in the **Figure 3** as an example. This verifies the efficiency of the lumping technique.

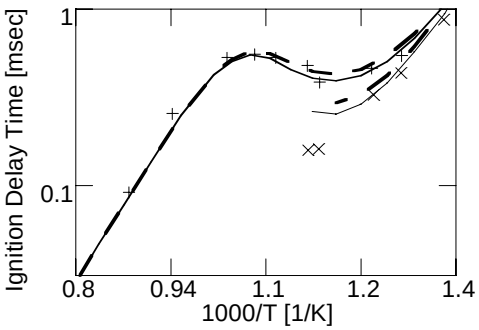

Figure 3 Ignition delay time for n-heptane at P=40 atm and ϕ=1.0. Experimental data (symbols). Calculated data (lines). 1st Ignition (×), 2nd Ignition (+). Detailed mechanism straight line. Lumped mechanism dashed lines.

The mechanism has been further validated against HCCI engine experiments using the same computer program[5], which was used for the constant volume calculations. For these calculations a zero-dimensional engine model was applied. The model compresses the gas to auto-ignition, using temperature and pressure at a certain crank angle position obtained from engine experiments as initial conditions.

The calculated data from the ignition code is validated against the experimental data, which was provided by Christensen et al.[8] The engine experiments were performed in a Volvo TD100 engine modified to run on one cylinder and with a secondary piston in the cylinder head giving the opportunity to vary the compression ratio. Iso-octane and n-heptane were mixed to achieve various octane numbers. The fuel was supplied via port injection. The charge temperature was varied between 30 and 130 °C. The compression ratio was adjusted between 21.4 and 10.8 in order to have an optimal point of ignition in each case. The validation of the detailed mechanism was performed for different cases of RON. Air-fuel equivalence ratio was set to 3.0 for all the cases and the engine speed were 1000 rpm. The initial pressure at inlet valve closing (IVC) for the calculations was consequently set to the measured cylinder pressure minus 0.1 bar, the wall temperature was chosen to be 490 K and EGR (5% residual gas) for all the cases. The semi-detailed mechanism calculation and the measured cylinder pressure for the RON 83 case is shown in **Figure 4**, at initial temperature of 330 K (at IVC), there is a good agreement between the detailed mechanism and the experiments; it can be seen in cylinder pressure trace and then it is a good agreement between detailed and lumped mechanism calculations. Ignition occurs at the same Crack Angle Degree (CAD) as experiment. The maximum pressure from the calculation is a bit high as compared to the experiment due to the assumption of homogeneity of the model[5], but altogether it follows the experimental data quite well especially in the low temperature region.

Conclusions

A semi-detailed reaction mechanism of n-heptane and iso-octane oxidation with special focus on optimizing it to the ignition delay timings of the shock tube experimental data from Fieweger et al.[6] and HCCI engine conditions has been presented. The mechanism was constructed using a reaction type concept as used for the automatic generation of mechanism. The size of the mechanism is limited by making use of lumping. This is very simple and straight forward approach which works very efficiently to generate automatically lumped mechanism, which has the same, performance as the detailed mechanism. The developed mechanism has been validated against the experimental data from shock tube and HCCI engine experiments. The ignition delay is well predicted for the shock tube experiments, at low and high temperatures and at low and high octane numbers. In the negative temperature regime the occurrence of low temperature reactions is well predicted. For the HCCI engine experiments there has been a significantly good agreement between model predictions and experimental data and in all the cases there is a good agreement between the lumped and detailed mechanism calculations. This work provides a detailed kinetic oxidation mechanism for mixture of n-heptane and iso-octane containing a reasonable low number of species and reactions, which provides a good base for further reduction of the mechanism, using sensitivity, reaction flow, lumping and necessity analysis.

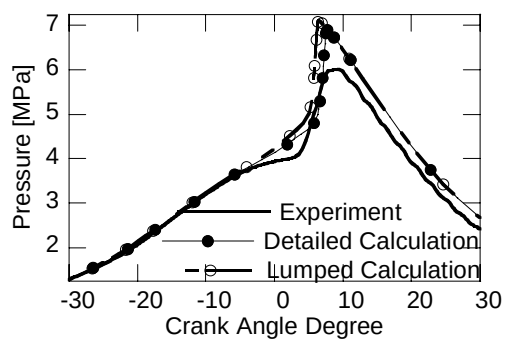

Figure 4 Cylinder pressure for RON83 at initial temperature of 359K

References

(1) Ranzi, E., Faravello, T., Gaffuri, P., and Sogaro, A. *Combustion and Flame*, **1995**, *102*: p. 179-192.

(2) Fournet, R., Warth, V., Glaude, P.A., Côme, G.M., Battin-LeClerc, F., and Scacchi, G. *International Journal of Chemical Kinetics.* **2000,** *32 (1)*: p. 36-51.

(3) Curran, H.J., Gaffuri, P., Pitz, W.J., and Westbrook, C.K. *Combustion and Flame*, **1998**, *114*: p. 149-177.

(4) Zeuch, T., Thesis Dissertation, Universität Göttingen, Germany, **2003.**

(5) Amnéus, P., Thesis Dissertation. Division of Combustion Physics Lund Institute of Technology, Sweden, **2002.**

(6) Fieweger, K., Blumenthal, R. and Adomeit, G. *Combustion and Flame*, **1997**, *109*: p. 599-619.

(7) Ciezki, K. and Adomeit, G. *Combustion and Flame*, **1993**, *93*: p. 421-433.

(8) Christensen, M., Hultqvist, A. and Johansson, B. **1999,** *SAE* 1999-01-3679.

AUTOMATIC OPTIMIZATION OF DETAILED KINETIC MECHANISM FOR HCCI-ENGINE SIMULATION

Bellanca[1], R., Mauss[1], F. and Wang[2], H.

1) Division of Combustion Physics, Lund University, 2) Mechanical Engineering, University of Delaware

Introduction

In recent years detailed kinetic models have been developed and validated for both auto ignition and laminar combustion processes. The range of validity of these models is limited by the range of physical parameters covered by the available experimental data. At high pressure, for example, shock tube data for the validation of ignition delay times are available for the investigated fuels with air-fuel equivalence ratios smaller than 2.0. Homogeneous Charge Compression Ignition (HCCI) engines are known to be operated with fuel-air equivalence ratios greater than 2.0, or with high rates of Exhaust Gas Recirculation (EGR). These conditions are not within the range of validity of the available kinetic models, and a re-optimization of the models is necessary.

Optimization

The optimization of reaction models has been automated in the past. The development of the GRI-Mech has been done using a semi-automated procedure[1], based on sensitivity analysis for the selection of reactions suitable for optimization and response surfaces method for the search of the best reaction coefficients. In this work a similar procedure has been applied to optimize a gasoline fuel reference mechanism consisting of 1905 reactions and 241 species as developed by Zeuch[2] for the base mechanism (C1-C4) and Ahmed, Blurock and Mauss[3] for larger hydrocarbons following the rules specified by Curran and Westbrook for automatic mechanism generation[4]. This model was used to simulate autoignition in a HCCI engine, using a homogeneous reactor model.

The optimization technique is based on the parameterization of model responses in terms of model parameters by simple algebraic expressions. The ignition delay time, deduced from the pressure profile as the crank angle corresponding to the maximum gradient, was used as optimization target (response). The pre-exponential factors in the reaction's rate Arrhenius expression were chosen as optimization parameters. Second order polynomial expressions were used to map the solution. The interpolation polynomial coefficients were obtained by computer experiments arranged in a fractional factorial design.

Simulations. The HCCI-process was modeled as a compressed homogeneous reactor[5]. The EGR was modeled, by running five consecutive engine cycles from Inlet Valve Closing (IVC) at -167 Crank Angle Degree (CAD) to Exhaust Valve Opening (EVO) at 167 CAD. The calculated gas composition at EVO was mixed with the fresh gas composition at IVC. Computations have been carried out on a PC with CPU time requirements of few minutes for each simulation and few hours for a complete optimization process. The entire procedure was performed inside a graphical user interface environment[6]. A sensitivity analysis of the temperature on the Arrhenius coefficients of all reactions included in the kinetic model was performed. The frequency factors of the most sensitive reactions were used as optimization parameters. The selection procedure is visualized in Figure 1. The colors in the graphic indicate the sensitivity level (red, yellow, green, blue, and shades of blue) of the reactions for the cases considered in the calculation.

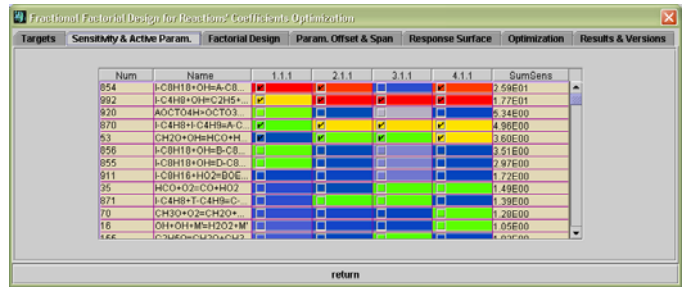

Figure 1 Screen Snapshot of the Optimization Section of the Graphical User Interface. Selection of Active Optimization Parameters for Each Target.

Experiments.

The data, needed for the optimization procedure, particularly the ignition delay times, were obtained from experiments conducted at Lund Institute of Technology on a modified Volvo TD100 engine with variable compression ratio and port injection mixes of iso-octane/n-heptane7. A fuel ratio of 0.333 and inlet pressure of 0.9 bars were used. As showed in

Table **1**, a combination of three different inlet temperatures and fuel mixtures was considered, for a total of nine cases. In Table 2 the engines parameters are reported.

Table 1 Simulations Initial Conditions for: Inlet Temperature, Fuel Mixture and Compression Ratio

N	T[K]	Fuel (I-C8H18/N-C7H16) %	CR
1	330	100 - 0	21.45
2	359	100 - 0	19.94
3	407	100 - 0	17.04
4	330	83 - 17	16.68
5	359	83 - 17	15.70
6	407	83 - 17	14.86
7	330	51 - 49	13.24
8	359	51 - 49	12.17
9	407	51 - 49	10.84

Table 2 Engine Parameters

Displaced Volume	1.602e-3 [m3]
Bore	0.12065 [m]
Stroke	0.14 [m]
Rod	0.26 [m]
Speed	1000 [m/s]
Wall Temperature	490 [K]
Start / End DCA	-167 / 167
EGR_Amont	0.05 [%]
EGR Cycles	5

Results and Discussion

In the framework of this preprint we selected four cases to demonstrate the functionality of the optimization tool (cases 1,2,3 and 6). This gave a reduced system of four targets to be optimized with respect to four reaction rate parameters. The corresponding reactions, their original coefficient and the optimization span, are reported in **Table 3**.

Table 3 Optimized Reactions

N	Name	Original	Optimized	Δ
53	CH2O+OH=HCO+H2O	3.4E9	2.0E9	2
854	I-C8H18+OH=A-C8H17+H2O	1.5E10	1.25E10	2
992	I-C4H8+OH=C2H5+CH3CHO	1.0E14	5.0E13	2
870	I-C4H8+I-C4H9=A-C8H17	8.5E10	9.9E10	2

The pressure profiles for the experimental data compared with those obtained with both the original and optimized model are shown in figure 1-4. For all cases the agreement of the ignition timing with the experiment got improved after the optimization. Shortcomings caused by the simple reactor model, such as to high pressure after ignition, or to short combustion duration can not be improved. The optimization of case 3 is not as good as for the other cases. However, for this case other sensitive reactions (level green in Figure 1) were found. Further optimization runs are prepared that will include these reactions as optimization parameter.

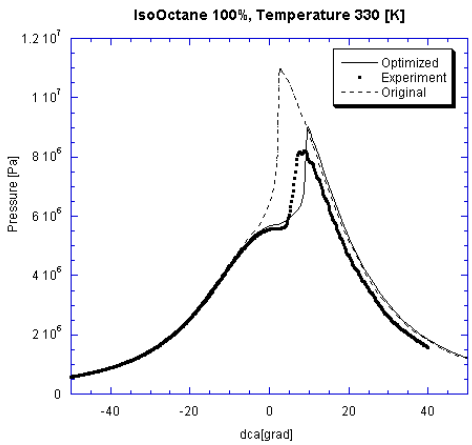

Figure 2 Pressure Profile vs. Crank Angle Degree for case 1.

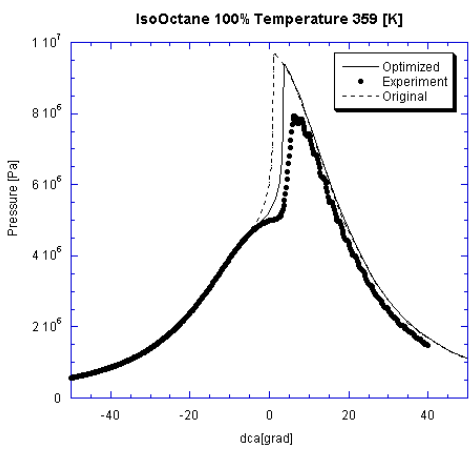

Figure 3 Pressure Profile vs. Crank Angle Degree for case 2.

Conclusion

An automatic optimization procedure, based on the solution mapping method, was used to optimize a detailed reaction mechanism for mixtures of n-heptane and iso-octane fuels at varying octane numbers under fuel lean conditions. This was done for HCCI-engine cases, by using a simple compressed reactor model. The optimization target, the maximum pressure rise, was taken from engine experiments. It was shown, that the agreement of mechanism and experiment can be significantly improved, while the effort needed for the procedure is reasonable. Further calculations will be performed, including more engine cases and additional optimization parameters.

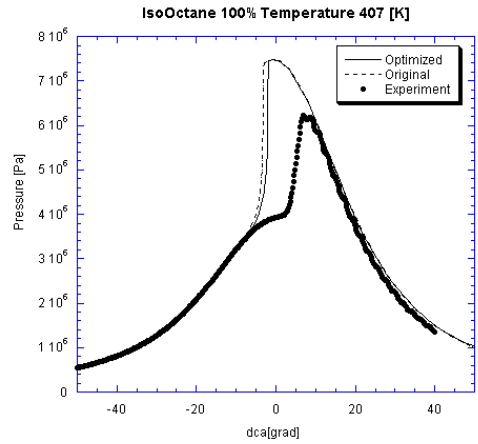

Figure 4 Pressure Profile vs. Crank Angle Degree for case 3.

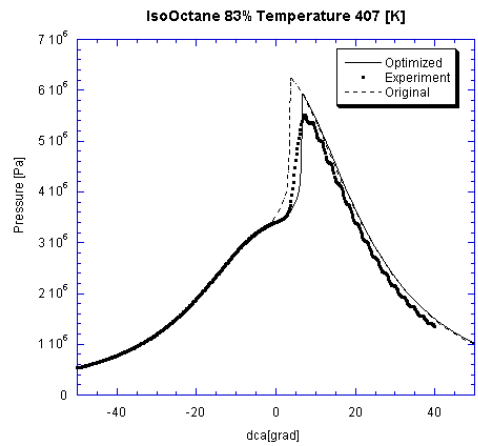

Figure 5 Pressure Profile vs. Crank Angle Degree for case 4.

References

[1] Frenklach, M.; Hai, W.; and Rabinowitz M.J. – Prog. Energy Combustion. Sci., 1992, 18, pp 47-73

[2] T. Zeuch, Thesis Dissertation, Universität Göttingen, Germany, 2003

[3] Ahmed, S.S., Blurock, E., and Mauss, F. - Proceedings of Scandinavian-Nordic and Italian Section of the Combustion Institute. 2003, 3.4, 1-4.

[4] Curran, H.J., Gaffuri, P., Pitz, W.J., and Westbrook, C.K. A comprehensive modelling study of n-heptane oxidation. Combustion and Flame, 1998, 114: p. 149-177

[5] Mauss F.; and Bellanca R. In "Ignition Code for the calculation of instationary combustion processes" Internal Report, Division of Combustion Physics, Lund University.

[6] Bellanca R. In "http:// forbrf.lth.se /chem. /blueBellMouseNew /intro.htm"

[7] Christensen M., Hultqvist A. and Johansson B. - SAE 1999, 01, 3679

THE DEVELOPMENT AND USE OF RATE-CONSTRAINED CHEMICAL EQUILBRIUM WITH HCCI COMBUSTION MODELING

Scott B. Fiveland
Engine Research
Caterpillar, Inc.

Chris Rutland
Engine Research Center, University of Wisconsin-Madison

Caterpillar, Inc.
Technical Center – F
P.O. Box 1875
Peoria, Il 61656-1875

Introduction

Homogeneous Charge Compression Ignition (HCCI) engines are essentially a combination of conventional spark ignited (SI) and compression ignited (CI) engines. As in a conventional SI engine, a homogeneous air-fuel mixture is achieved either in the inlet system or early during the compression stroke (direct injection). As in the diesel combustion process, ignition is achieved by compressing the mixture until it auto-ignites. Thus, the energy release event is dominated by the kinetic timescales. Accurate modeling requires the coupling of a detailed chemical kinetic description to the proper fluid-dynamic resolution (1).

The evolution of chemical reaction can, in principle, be solved accurately if a chemical mechanism for the conversion of fuel to products is available. The solution of practical chemical kinetic systems requires numerical methodologies that resolve the chemical process, down to the highest frequency mode, while maintaining numerical stability. As a result, the numerical solution of chemical kinetics problems is very computationally expensive because the process is occurring on multiple timescales, as some radical species are being formed and depleted rapidly while other species exhibit a slow evolution (such as H_2O or CO_2). The presence of a range of timescales is known as stiffness (13). Stiff kinetic systems require a large number of time-steps, thus making the numerical solution time-consuming. Current computing capability makes it possible to simulate homogeneous chemically reacting systems, but detailed chemical kinetic calculations coupled with computational fluid dynamic (CFD) simulations of chemically reacting flows are still unrealistic as the basis for a parametric simulation tool (1).

The solution of the kinetic system, even when using the most efficient solver, may be too computationally expensive. Therefore, the modeler must sacrifice some details within the kinetic scheme to improve the solution speed. Many techniques have been developed to generate reduced mechanisms such as quasi-steady state analysis (QSSA) (9), intrinsic low dimensional manifolds (ILDM) (10), partial equilibrium assumption (PEA), (8), computational singular perturbation (CSP) (5), sensitivity analysis (17), integral and local reaction flow analysis (17), time-scale analysis (15), and computer augmented reduced mechanism (CARM), (16). The application of these tools sets out to eliminate both species and reactions. The disadvantage of these reduction approaches is that the reduced mechanism is valid only for a very limited range of thermodynamic conditions. If the combustor conditions, such as pressure, temperature, or equivalence ratio (i.e. load range) increase or decrease outside the applicable range, the reduction procedure must be repeated and a new reduced equation set developed.

Several techniques exist to speed the solution of the chemistry while not reducing the chemical kinetic mechanism information, and hence the accuracy of the system. The common ones are rate-constrained chemical equilibrium (RCCE) and *in-situ* adaptive tabulation (ISAT) (7). The RCCE method was first proposed by Keck (4) and extensively developed by Metghalchi and co-workers (3). This work focuses on the extension of the RCCE method to model HCCI ignition events with the introduction of automatic constraint generation.

Rate Constrained Chemical Equilibrium – Overview

The general basis of the RCCE idea is that the chemical composition is constrained from equilibrium, at any time, due to slowly evolving constraints that are imposed in the system. The system evolves in time through a series of quasi-equilibrium states. The physical premise for the idea is that only equations describing the slowly evolving constraints need to be integrated. Much of the discussion in this section follows Hamiroune *et al.* (3). The RCCE approach is based on the following stated assumptions:

1. A complex chemically reacting system can be described by a relatively small number of degrees of freedom.
2. These degrees of freedom are constraints imposed on the system by slowly evolving reactions.
3. Other reactions are fast enough that they can equilibrate the system subject to the constraints imposed by the slow reactions.
4. The system thus progresses to chemical equilibrium through a series of quasi-equilibrium states.

RCCE Mathematical Formulation

The time-dependant constraints are a linear combination of species given by:

$$C_j = \sum_{i=1}^{ns} a_{ij} N_i \,, \tag{1}$$

where C_j is the molar concentration of constraint j and a_{ij} the number of moles of species i in constraint j. Once the differentiated form of equation (1) has been integrated, the constrained equilibrium composition may be determined with the method of element potentials using Lagrange undetermined multipliers as outlined by Keck (4) and Reynolds (13). We refer to this method as RCCE-A. Using this method, once the Lagrange multipliers are determined, the species compositions are found by:

$$N_i = Q_i \exp\left(-\sum_{j=1}^{nc} a_{ij}\gamma_j\right),\ Q_i = \frac{p_0 V}{RT}\exp\left(-\mu_i\right) \tag{2}$$

where γ_j is the undetermined multiplier conjugate to constraint j and μ_i is the Gibbs free energy of species i. Keck (4) points out that the computation of the constrained equilibrium at each time-step may be expensive because of the iterative procedure involved in determining the Lagrange multipliers. He presents an alternative method of solving for the constrained equilibrium composition. We refer to this alternative method as RCCE-B and discuss it below. All RCCE calculations in this work use the RCCE-B method (11).
Rather than directly integrate the constraints and then solve equation (2) for the species, rate equations for the Lagrange multipliers may be

derived with some manipulations. The equations for the rate of change of the Lagrange multipliers are given as follows:

$$\sum_{n=1}^{nc} C_{jn}\dot{\gamma}_n - C_{jT}\frac{\dot{T}}{T} - C_{jV}\frac{\dot{V}}{V} + \sum_{i=1}^{ns} a_{ij}\dot{\omega}_i = 0\,, \quad (3)$$

where $C_{jn} = \sum_{i=1}^{ns} a_{ij}a_{in}N_i$, $C_{jT} = \sum_{i=1}^{ns} a_{ij}\frac{E_i}{RT}N_i$, and

$$C_{jV} = \sum_{i=1}^{ns} a_{ij}N_i\,.$$

In the case where the temperature is not constant, an additional equation for the temperature (or energy) must be solved and this is given as:

$$\sum_{i=1}^{ns}\sum_{n=1}^{nc} E_i a_{in} N_i \dot{\gamma}_n - \sum_{i=1}^{ns} C_{iE} N_i \frac{\dot{T}}{T} - \sum_{i=1}^{ns} E_i N_i \frac{\dot{V}}{V} + \dot{E} = 0\,, \quad (4)$$

where $C_{iE} = \left(c_{v,i}T + \frac{E_i^2}{RT} \right)$ and E is the internal energy of the system. The rate of energy change in the system is described using the energy equation with the appropriate source and sink terms for work and heat transfer (11). Once the values of the Lagrange multipliers are determined by numerically integrating equations (3) and (4), the constrained equilibrium composition may be determined without any iteration. The equations are integrated using an implicit stiff ODE solver based on a backward differencing formulae (BDF) method (2).

Constraints - Overview

The constraints that have been used in works using the RCCE method were based on constraints generated through physical intuition (3,6). The most common constraints are conservation of elements. In this study, the system has four elements – C, H, O, and N and these are four "fixed" constraints, i.e. they do not depend on time. Time-dependant constraints include constraints on:

1. Total number of moles due to slow three body reactions,
2. Moles of ions due to slow radical reactions,
3. Moles of CO_2 due to slow oxidation of CO ,
4. Moles of fuel,
5. Moles of fuel radical,
6. Moles of oxygen, and
7. Moles of formaldehyde radical.

Results & Discussion

In understanding the RCCE method, it is instructive to look at the values of the constraint potentials as the constraints evolve over time. Figure 1 shows the constraint potentials for two "fixed" constraints, elemental nitrogen and elemental hydrogen, and two time-dependant constraints, total moles and free valences. The potentials for the time-dependant constraints reach a value of 0 as the system reaches equilibrium while the potentials for the fixed constraints reach their equilibrium values. This is because, at equilibrium, the system is constrained only by the elemental constraints and thus the potentials for the other constraints must be zero. It may be useful to note that an elemental constraint potential represents the contribution of the element to the chemical potential of a species that contains that element.

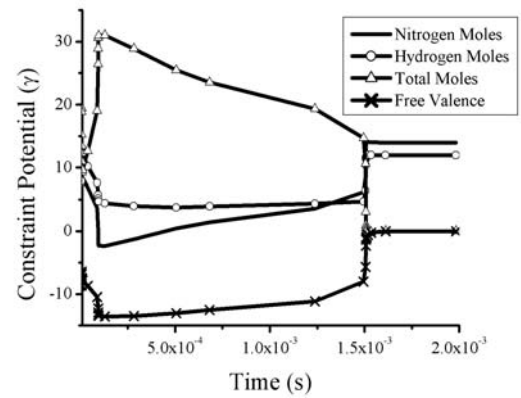

Figure 1. Evolution of Constraint Potentials vs. time

The constraints used in this study were based on constraints used by Gao and Methghalchi (6). In the work by Rao et al.(11), the RCCE method was compared to the detailed kinetic integration for lean and rich conditions through a range of gas temperatures.

Comparison of RCCE with Experiments

The comparison of the RCCE method with HCCI experiments for the 2% mass fraction burned point obtained in the Volvo TD-100 is shown in figure 2 for a methane-air blend. The reader is referred to Rao et. al. for a review of the experimental setup. This fuel study was a subset of a two-component fuel study (11) For this particular case study, the engine was operated under naturally aspirated conditions at an equivalence ratio of 0.3, an intake manifold temperature that ranged from 175C to 162C, and an engine speed of 1000 RPM. The compression ratio in the engine tests was reported at 19.8. It is shown in the figure that the RCCE method does a reasonably good job of predicting the trend with decreasing manifold temperature. For example, at a manifold temperature 171C the model exhibits a 2 CA-deg error when predicting the 2% mass fraction burned point. The RCCE prediction is closer to the experimental observation if the standard deviation (shown as error bars) in the experimental quantities is considered. It is noted that observed error could be a result of inaccuracies within the HCCI thermal description, the GRI kinetics mechanism or the assumed constraint matrix applied to the RCCE method.

Automatic Constraint Generation

The use of this method for larger chain hydrocarbon molecules will depend on the ability to efficiently develop the constraint matrix (3, 18). Yousefian has presented an algorithm for the selection of constraints. The algorithm is based on using equilibrium relations for fast reactions, since the RCCE method implicitly assumes that all fast reactions are in equilibrium. Recently, work by Rao et al. has developed/demonstrated an automatic constraint methodology for use with a hydrogen-air combustion scenario (12). Specifically, their work used a novel partial equilibrium criterion with the constraint generation scheme proposed by Yousefian (18).

In order to validate the RCCE solution, induction times for H_2-O_2-Ar mixtures were computed using the RCCE method against shock tube experiments (12). The experiment was performed at a pressure of 5 atm. with a composition comprising 8 mole percent H2 and two mole percent O2 in Ar. The initial temperature was varied from 964 K to 1075 K. The computations were carried out assuming constant volume and adiabatic combustion. An example of a

comparison between the detailed solution and the RCCE method for a hydrogen-air mixture is shown in figure 3..

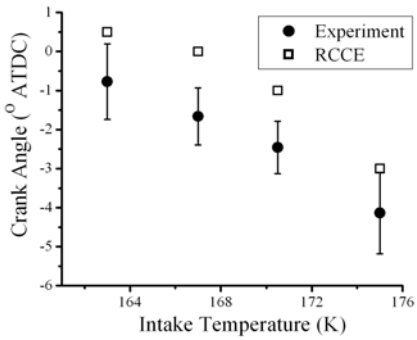

Figure 2: Methane-air simulation vs. experimental 2% mass burned point. 1000rpm, equivalence ratio (0.3), an intake pressure of 1 bar,

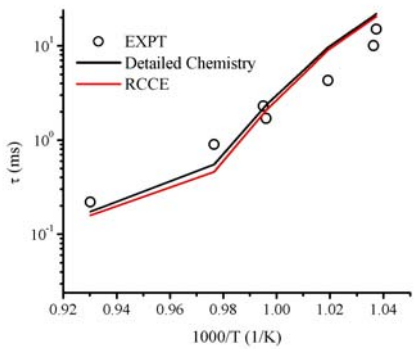

Figure 3: Comparison of computed and measured induction times for H_2-O_2-Ar mixtures

Conclusions

The RCCE method has been successfully applied to describe the time-evolution of hydrogen and methane-air combustion in constant and variable volume environments. Good agreement between RCCE and detailed chemistry calculations is obtained for a variety of initial conditions in various environments. Temperature and species profiles are predicted well by the RCCE method, as are induction times and ignition delay times for methane-air mixtures. CPU time usage is reduced for RCCE calculations as compared to calculations utilizing detailed chemical kinetics. There is potential for further reduction in computational cost by improving the numerical characteristics of the system and improvement in the accuracy of the method through improved selection of constraints. The RCCE method is used to simulate HCCI combustion of methane in a Volvo engine and good agreement against experimental data for burn durations is obtained. More work is needed to developed a robust automatic constraint generation method.

References

(1) Assanis, D.N., Lavoie, G.A., and Fiveland, S.B., Chapter 6, Overview of HCCI Modeling Approaches, *Homogeneous Charge Compression Ignition (HCCI) Engines Key Research and Development Issues,* SAE 2003.

1. (2) Brown, P. N., Hindmarsh, A. C. and L. R. Petzold (1994), *Using Krylov methods in the solution of large-scale differential-algebraic systems*, SIAM Journal of Scientific Computing, **15**: 1467-1488
2. (3) Hamiroune D, Bishnu P., Metghalchi M., and Keck J.C. (1998), "Rate-controlled Constrained-Equilibrium method using constraint potentials", Combustion Theory and Modeling, **2**:81-94
3. (4) Keck J.C. and Gillespie D. (1971), *Combustion and Flame*, **17**:237
4. (5) Lam S.H. and Goussis D. A. (1994), "The CSP Method of Simplifying Kinetics", *International Journal of Chemical Kinetics,* 26:461-486
5. (6) Gao Y. and Methghalchi M. (2002), Personal Communication
6. (7) Maas U.A. and Pope S.B. (1992), "Simplifying Chemical Kinetics: Intrinsic Low-Dimensional Manifolds in Composition Space", *Combustion and Flame*, **88**:239-264.
7. (8) Mott, David (1999), "New Quasi-Steady-State and Partial Equilibrium Methods for Integrating Chemically Reacting Systems", *Ph.D. Thesis*, Department of Aerospace Engineering and Scientific Computing, University of Michigan
8. (9) Peters, N. (1985), *Lecture Notes in Physics* Springer, Berlin, pg. 90–241.
9. (10) Pope S.B. (1997), "Computationally Efficient Implementation of Combustion Chemistry using In Situ Adaptive Tabulation," Combustion Theory and Modeling, **1**:41-63.
10. (11) Rao, S., Rutland C.J., and Fiveland S.B. (2003) "A Computationally Efficient Method for the Solution of Methane-air Chemical Kinetics with Application to HCCI Combustion," Submitted to SAE World Congress, 2003.
11. (12) Rao, S., Rutland, C.J., and Fiveland, S.B., Reduced Chemistry Modeling –A new method for identifying reactions in partial equilibrium, 16th AIAA Computational Fluid Dynamics Conference, Session: High Speed and Chemically Reacting Flows, 2003.
12. (13) Reynolds W.C. (1986), "The Element Potential Method for Chemical Equilibrium Analysis – Implementation in the Interactive Program STANJAN, Version 3", *Department of Mechanical Engineering*, Stanford University
13. (14) Shampine, L.F. (1985), "Measuring Stiffness", *Applied Numerical Mathematics*, 1:107-119.
14. (15) Soyhan, H. S., et al., (2000), "Automatic reduction of detailed chemical reaction mechanisms for autoignition under SI engine conditions," SAE Paper No. 2000-01-1895.
15. (16) Sung, C. J., Law, C. K., and Chen, J.-Y., "Further Validation of an Augmented Reduced Mechanism for Methane Oxidation: Comparison of Global Parameters and Detailed Structure," *Combust. Sci. Tech.,* 156, pp. 201-220 (2000).
16. (17) Warnatz J., Mass U., Dibble R.W. (1999), *Combustion Physical and Chemical Fundamentals, Modeling and Simulation, Experiments, Pollutant Formation*, Springer, pg. 97.
17. (18) Yousefian V. (1998), "A Rate-Controlled Constrained-Equilibrium Thermochemistry Algorithm for Complex Reacting Systems", *Combustion and Flame*, 115:66-80

SURFACE REACTIVITY AS A MANY BODY MULTISCALE PROBLEM

Ashish B. Mhadeshwar, Jeffrey Ludwig, Abhijit Chatterjee, and Dionisios G. Vlachos

Department of Chemical Engineering
and Center for Catalytic Science and Technology
University of Delaware
Newark, DE 19716-3110

In this talk, we will demonstrate that surface reactivity even of the simplest heterogeneous reactions is a many body problem. The disparity in length and time scales encountered in these processes is tremendous. Phenomena at the fluid-surface interface, at quantum and molecular length and time scales, range from Å to several nanometers and render classical continuum equations, often referred to as mean field equations, inapplicable. Examples of such phenomena include intermolecular forces, nucleation, spinodal decomposition, and quantum reaction effects. On the other hand, reactors are often in the meter length scale with a residence time of seconds to minutes. Application of quantum calculations and molecular simulations, such as Monte Carlo or molecular dynamics, to the entire spectrum of scales is currently impractical.

In this talk, we describe hierarchical multiscale simulations for modeling such reaction systems from first principles. The unity bond index, quadratic exponential potential (UBI-QEP) or bond-order conservation (BOC) of Shustorovich and co-workers is employed as an efficient, semi-empirical means of predicting activation energies of large reaction mechanisms of catalytic reactors with input from experiments or density functional theory. Transition state theory is employed to estimate pre-exponentials, which in conjunction with the energetics, provide an initial set of reaction rate constants for each local arrangement (class) of adsorbates. Density functional theory (DFT) is used to refine the input to the semi-empirical technique and/or to assess self-consistency of the important reaction steps identified via sensitivity analysis Refinement of such reaction rate constants is possible using suitable experimental data and efficient optimization tools. These data are then used as input in lattice Monte Carlo simulations. The latter simulations solve directly a master equation as a Markov process and are properly coupled with continuum, reactor scale simulations. Application of this approach to understanding the chemistry in partial oxidation of methane on Pt and ammonia decomposition on Ru will be presented and contrasted to experiments.

While MC simulations can capture nanometer spatial inhomogeneities, they are too intensive for larger scales. Novel coarse-grained Monte Carlo simulations will be presented and demonstrated to be an important step toward meeting the length scales gap.

The Importance of Gas Phase Kinetics Within the Anode Channel of a Solid Oxide Fuel Cell (SOFC)

Chad Sheng and Anthony M. Dean

Chemical Engineering Department
Colorado School of Mines
Golden, CO 80401

Introduction

A complete SOFC model is very complex, requiring descriptions of kinetics in multiple phases and coupling these kinetics to multiple transport processes. [1] Chemical reactions within the SOFC occur in three regions: in the anode channel (gas-phase kinetics), on the surface of the porous anode (heterogeneous catalysis) and at the three-phase boundary layer between the anode and electrolyte (electrochemical catalysis). Thus the homogeneous and heterogeneous kinetics have the potential to substantially change the nature of the species that ultimately undergo electrochemical oxidation. It is essential to account for such kinetic modifications to properly characterize SOFC operation and predict the overall efficiency.

As a first step toward characterizing the complex kinetics, we want to make sure that we properly understand the gas-phase hydrocarbon chemistry. The effect of gas phase reactions of methane in SOFCs has previously been reported. [2] There it was shown that the electrochemical production of H_2O and CO_2 did indeed significantly impact the predictions regarding deposit formation. In this work we extend this approach to butane, which is significantly more reactive than methane and thus more representative of a range of hydrocarbon fuels.

Experimental

The experiments used n-butane as the fuel over a temperature range of 550 – 800ºC, with a nominal five second residence time through a tubular flow reactor operating at an ambient (high-altitude) pressure of ~0.8 atm. The reactor used in these experiments was a 24 cm length x 6 mm ID (12mm OD) quartz tube, which was housed within a 14.5 cm length single-zone clamshell 2.5 cm ID electric tube furnace. The product stream flowed through a water trap, and the de-humidified product stream then flowed to a Hewlett-Packard 5890 Series II+ gas chromatograph. Axial temperature profiles were measured and used in the plug flow model.

Three different fuel mixtures were used: neat n-butane (100% n-butane), a 50:50 n-butane:N_2 mixture and a 50:50 n-butane:H_2O(g) mixture. The neat n-butane case is intended to simulate the situation near the entrance of the anode channel where little CO_2 and H_2O would be present. Likewise the nC_4/H_2O mixture represents a mixture further down the channel where the products of the electrochemical reaction would be coming into the fuel stream. The nC_4/N_2 mixture was used to account for the effect of simple dilution with an inert in contrast to dilution with steam, which could possibly be a reactant.

Reaction Mechanism

The reaction mechanism that was utilized in this study consists of 291 species and 2498 elementary reactions. It is an extension of a previous mechanism[3], which included formation of C_4 hydrocarbon species. The extensions include substantially more molecular weight growth chemistry, especially involving propargyl radical pathways, and explicit inclusion of certain C_6 hydrocarbon species, including n-hexane, cyclohexane, and 2,3-dimethyl butane. The current mechanism is similar to the one recently used by Walters, *et al*.[2] in their analysis of methane kinetics under SOFC conditions.

Comparison to Model Predictions

Butane Conversion The ratio of the predicted final/initial mole fraction of butane is compared to that observed for the neat and nC_4/N_2 mixture cases in Fig. 1.

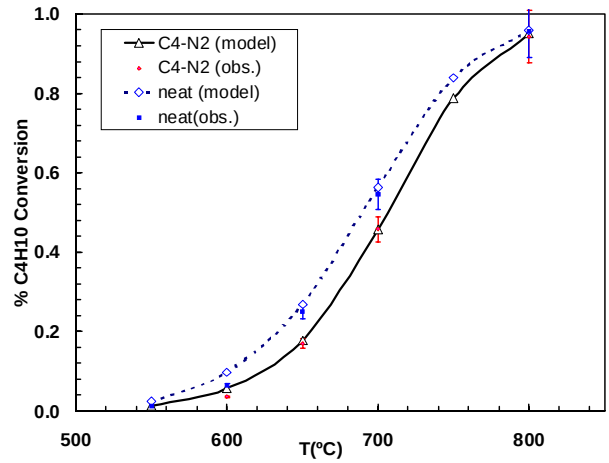

Figure 1. Comparison of predicted butane conversion to that observed for the neat butane case and for the 50% butane/50% nitrogen mixture.

The modeling predictions are in excellent agreement with the observations for both the neat and the nC_4/N_2 fuel mixture cases. The predictions clearly capture the observed temperature dependence for both the neat and nitrogen fuel mixture cases. From both the model predictions and the observed experimental data, it is also clear that the conversion for the neat n-butane case is higher than the nC_4/N_2 case. This difference is simply due to dilution in the nC_4/N_2 mixture. This good agreement, achieved without any modifications to the gas-phase kinetic mechanism, was very encouraging and suggests that the model can account for conversion of light hydrocarbons fuels under SOFC conditions.

Product Selectivity Four major products are observed: methane, ethane, ethylene, and propylene. The predicted selectivities are in reasonable agreement with those observed. For methane, the observed selectivity ranges from ~32% at 600ºC to ~38% at 800ºC, while the model predictions range from 32% to 35%. The propylene selectivity is observed to decrease with increasing temperature, from ~34% at 600ºC to ~13% at 800ºC. The predictions vary from ~32% at 600ºC to ~20% at 800ºC, not dropping off quite so rapidly with temperature as observed. The observed ethylene selectivity increases sharply from ~21% at 600ºC to ~42% at 800ºC. The predictions follow this reasonably well, ranging from ~19% at 600ºC to ~34% at 800ºC. This underprediction of the ethylene yield at 800ºC is reflected in an overprediction of the ethane yield. It was observed to vary from ~12% at 600ºC to ~5% at 800ºC, while the predictions yielded ~16% at 600ºC to ~10% at 800ºC. Thus one problem with the current model is the inability to precisely account for the distribution within the C_2 branch (ethane and ethylene) and with the C_1-C_3 branch (methane and propylene). Note that the predictions for the total C_2 branch are very consistent with the observations and properly account for the increase with temperature. Similarly, the sum of the methane and propylene selectivities show good agreement between predictions

and that observed, including the decrease in overall selectivity with temperature.

Deposit Formation One of the major concerns with the use of hydrocarbon fuels in solid oxide fuel cells is the propensity for deposit formation. In our experiments, qualitative observations of deposit formation were made by examining the quartz reactor after running a specific mixture through the reactor for 4 hours. We observed no apparent deposit formation within the reactor for any of the mixtures at 650ºC or lower temperatures. As the reactor temperature was increased to 700ºC, an obvious deposit film was observed on the inner walls of the quartz reactor with the neat butane mixture. The deposit film was noticeably less dense for the nC_4/N_2 mixture, and barely evident for the nC_4/H_2O mixture. The first inference from these qualitative observations is that dilution does play a role in minimizing deposit formation. This is to be expected, since the lower concentration of reactive species would be expected to decrease the rate of molecular weight growth leading to deposits. The marked difference in the nitrogen and steam mixtures suggests that the steam is either actively participating in inhibition of molecular weight growth or that it is participating in some type of gasification of the deposit. All three mixtures show significant deposit formation at 800ºC.

To compare to the model, we considered all species in the model predictions above C_4 (denoted as C_5^+) as potential deposit precursors. The predicted C_5^+ mole fraction is a very strong function of temperature as illustrated in Fig. 2. It is encouraging to note that the predicted rapid increase in deposit precursors near 700ºC is consistent with the experimental observations.

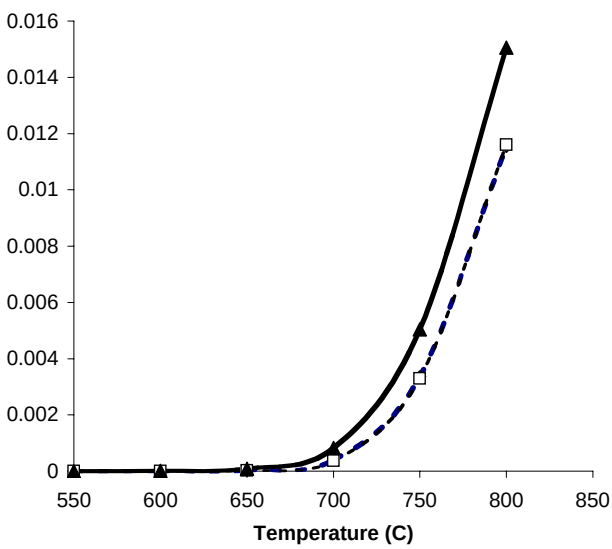

Figure 2. Predicted effect of temperature on the mole fraction of C5+ species.

The predicted C_5^+ values for the steam and nitrogen dilution cases are virtually identical. This is consistent with our observation that any gas-phase reactions of steam are very slow under these conditions, and thus steam is simply acting as a diluent, just like nitrogen. This is in contrast to the experimental observations that steam diminished deposit formation. This effect is probably due to heterogeneous reactions. The ratio of C_5^+ predicted for the neat butane case to that of the diluted mixtures decreases from approximately five at 550ºC to only slightly greater than unity at 800ºC. Thus at the higher temperatures, the predictions suggest that the inhibition of deposit formation by dilution is much less effective.

Kinetics Overview

The results from a sensitivity analysis indicate that, although the system consists of ~2500 reactions, there are only 10 reactions that dominate the formation or consumption of the five major species. These reactions suggest that butane pyrolysis can be described in terms of a simple Rice-Herzfeld mechanism. After initiation by breaking the C-C bonds in butane, the radicals formed abstract from the parent butane to form $n\text{-}C_4H_9$ and $s\text{-}C_4H_9$ radicals. The primary radicals lead to the C_2 products via beta-scission, while beta-scission of the secondary radicals lead to the C_1 and C_3 products. Thus the selectivity to these two product pairs can be traced to the selectivity of forming the two radicals in abstraction from the parent. An interesting complication is that the propylene product has an easily abstractable hydrogen, and the formation of allyl acts to inhibit conversion by modifying the nature of the free radical pool. This same allyl radical was also shown to be responsible for the small amounts of molecular weight growth observed since it can add to ethylene, forming cyclopentene. This pathway is accelerated since it is chemically-activated, and the initially energized linear adduct can directly form the cyclic species prior to collisional stabilization.

Conclusion

The butane pyrolysis experiments demonstrate that substantial gas-phase chemistry does occur under SOFC conditions, and that this must be accounted for when predicting fuel cell efficiency. These data were compared to predictions using a plug-flow model that incorporated the experimentally measured temperature profile along the reactor. Comparisons of the model predictions to the experimental data show that the model, without any modifications, captures the observed strong temperature dependence of n-butane conversion and is also able to capture the changes in product selectivity with temperature for the neat butane and the diluted butane mixtures. The model also properly predicts the observed onset of deposit formation near 700ºC. Both conversion and selectivity are shown to be sensitive to only a very small subset of the reactions in the mechanism. Comparison of the rate coefficients of this subset to literature values, where available, are generally reasonable and suggest that the kinetic model employed is adequate for describing reactions of small hydrocarbons in the anode channels of a SOFC. Thus such models should provide a useful tool to estimate the importance of gas-phase chemistry for various proposed SOFC operating conditions.

Acknowledgement. The authors would like to thank ITN Energy Systems, Inc. for the use of their facilities, where the experimental work was conducted under DARPA Contract Number MDA972-01-C-0068. The authors appreciate Katie O'Gara's contributions to the experiment and data compilation. We also would like to thank Hans-Heinrich Carstensen and Chitral Naik for providing some of the elementary reaction rates used in the current model. Chitral Naik also perfomred some of the modeling calculations.

References

(1) Zhu, H. and R.J. Kee, *A general mathematical model for analyzing the performance of fuel-cell membrane-electrode assemblies.* Journal of Power Sources, 2003. **117**(1-2): p. 61-74.

(2) Walters, K.M., et al., *Homogeneous Kinetics and Equilibrium Predictions of Coking Propensity in the Anode Channels of Direct Oxidation Solid-oxide Fuel Cells Using Dry Natural Gas.* Journal. of Power Sources, 2003. **123**(2): p. 182-189.

(3) Mims, C.A., et al., Radical chemistry in methane oxidative coupling: Tracing of ethylene secondary reactions with computer models and isotopes. J. Phys. Chem., 1994. 98(50): p. 13357-13372.

COMPUTATIONAL STUDIES OF BORON/NITROGEN AND ALUMINUM/NITROGEN COMPOUNDS FOR CHEMICAL HYDROGEN STORAGE

Maciej Gutowsk[1,2] and Tom Autrey[1]

[1] Chemical Sciences Division, Pacific Northwest National Laboratory, Richland, WA 99352, USA,
[2] Department of Chemistry, University of Gdansk, 80-952 Gdansk, Poland

Introduction

The DOE Office of Energy Efficiency and Renewable Energy have recently proposed a Grand Challenge for on-board Hydrogen Storage in response to the Presidents 2003 State of the Union Address.[1] To meet the target of the long-term DOE volumetric (0.09 kg H_2/kg) and energy density (3.0 kWh/kg) targets further development and understanding of hydrogen storage materials will require substantial new research effort.

Much work thus far has focused three systems to store hydrogen for potential on-board applications, metal hydride storage involving the reversible uptake and release of H_2 from $Na^+AlH_4^-$,[2] chemical hydrogen storage involving the irreversible hydrolysis of $Na^+BH_4^-$ → H_2 + borate[3] and storage on carbon materials involving physi- and chemi-sorption of hydrogen on single walled carbon nanotubes.[4] None of these current systems are likely to meet the long-term DOE goals system making a strong argument for the discovery of new storage possibilities. In this paper we discuss our computational approaches to screen for potential new hydrogen storage materials. Our hope is to find a material that is a solid, high weight percent hydrogen, and reversibly releases (or uptakes) hydrogen under moderate conditions. The thermodynamics of the ideal material would be thermoneutral for hydrogen release.

We start with an analysis of the current most studied hydrogen storage material, the complex hydride $NaAlH_4$. Since this material only stores hydrogen on the anionic site only, AlH_4^-, a dramatic improvement in capacity is envisioned if hydrogen is stored on both the cationic and anionic sites. Another improvement is feasible with the substitution of B (FW=10.8) for Al (FW=27). NH_4^+, BH_4^-, and AlH_4^- are known building blocks of ionic solids, which are isoelectronic with Na^+, F^-, and Cl^-, respectively. Ionic solids built of NH_4^+ and XH_4^- (X=B, Al) are expected to be insulating and dense (to meet the density requirements) and both Boron and Nitrogen are light elements (to meet the volumetric requirements). Furthermore, several of the NH_xBH_x series of compounds are reported to be both *water and air stable*[5] as opposed to many of the complex hydrides currently under investigation.

Given these favorable specifics we undertook a computational approach to investigate the potential of amine boranes as potential solid hydrogen storage materials.[6] These materials are quite attractive from both volumetric and gravimetric considerations, for example NH_4BH_4 and NH_3BH_3, store 0.24 kg H_2/kg and 0.19 kg H_2/kg respectively! The storage capacity is well above any currently studied material. The optimum decomposition reaction is NH_4BH_4 → BN + $4H_2$, outlined in a stepwise process below, eqs 1-4. Even if only two of the four steps proved feasible H_2 storage capacities greater than 0.12 kg H_2/kg could be realized.[7]

$$NH_4BH_4 \rightarrow NH_3BH_3 + H_2 \quad (1)$$
$$NH_3BH_3 \rightarrow NH_2BH_2 + H_2 \quad (2)$$
$$NH_2BH_2 \rightarrow NHBH + H_2 \quad (3)$$
$$NHBH \rightarrow NB + H_2 \quad (4)$$

Methods

Computational studies have been performed for (i) isolated NH_4^+, BH_4^-, and AlH_4^- species and (ii) solids NH_4BH_4, NH_3BH_3, NH_4AlH_4, BN, and AlN. For molecular clusters and complexes we have used highly correlated electronic structure methods (coupled cluster level of theory with single, double, and non-perturbative triple excitations, Green's function (propagator) methods, etc.) and augmented correlation-consistent basis sets, as implemented in the NWChem code[8]. For solids, we used density functional theory with gradient-corrected exchange functionals (PW91, as implemented in the VASP code[9]). Periodic boundary conditions were assumed for the solids and static optimizations have been completed. The sodium chloride, cesium chloride, zinc blende, and wurtzite structures of NH_4AH_4 (A=B, Al) were explored. The hexagonal planar, zinc blende, and wurzite structures have been optimized for BN and the wurzite and zinc blende for AlN.

Results and Discussion

Relative stability of solid phase materials. Our computational results allow several thermodynamic comparisons to be drawn between the NH_4BH_4 (**1**) and NH_4AlH_4 (**2**) as potential chemical hydrogen storage materials. The first noticeable characteristic difference is the in thermodynamic stability between the zinc blende and wurzite crystalline structures for the two species (Figure 1). In the case of NH_4BH_4 the zinc blende phase was found the more stable then the wurzite phase by 0.23 eV per BN unit. The density of the zinc blende structure is 0.554 g/cm^3. The opposite was found for the case of NH_4AlH_4 where the wurzite phase was found to be more stable than zinc blende by0.12 eV per AlN unit. The density of the wurzite structure is 0.663 g/cm^3. The most stable phase of BN is hexagonal graphite-like, rather than cubic (zinc blende) or hexagonal (wurtzite). This unique feature will be important for the hydrogen mobility in the reloading/releasing cycles. Knowledge of these phase compositions will be important for the hydrogen mobility in the reloading/releasing cycles.

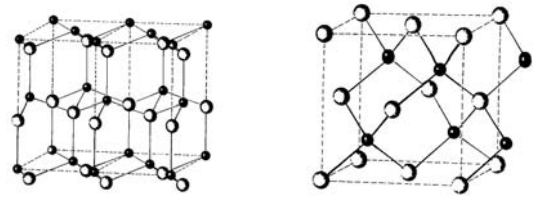

NH_4BH_4 (**1**) (zinc blende) NH_4AlH_4 (**2**) (wurzite)

Figure 1. Thermodynamically stable phase of NH_4BH_4 (ammonium borohydride) is zinc blende. Thermodynamically stable phase of NH_4AlH_4 (ammonium aluminum hydride) is wurzite phase. Hydrogen atoms are not shown in structure for simplicity.

Relative energetics of decomposition pathways. Initial computational results on the solid materials show the reaction energetics are neither extremely exothermic nor too endothermic for loss of hydrogen for NH_4BH_4(solid). These results are promising because it strongly suggests that reversal uptake of hydrogen is feasible under moderate conditions. Furthermore, it is predicted by theory that hydrogen elimination, eq 5, is more favorable, than N-B bond scission, eq 6. Hydrogen elimination is exothermic by less than 0.3 eV/BN unit whereas B-N bond scission is predicted to be

endothermic by 1.1 eV. Similar results are predicted for hydrogen loss from NH_4AlH_4, eq 7, more favorable than N-Al bond scission, eq 8. However, in the case of NH_4AlH_4 hydrogen loss is far more exothermic, 1.07 ev per AlN unit compared to the endothermic Al-N bond scission of 0.7 eV. This is an interesting result that may have implications on regeneration of the hydrogen storage materials. If the reaction is too exothermic it likely require greater effort to regenerate the material. Alternatively, the system may still be reversible if the end product is NH_xAlH_x (x=1-3) rather than AlN.

$$NH_4BH_4(s) \rightarrow BN(s) + 4H_2(g) \quad (5)$$
$$NH_4BH_4(s) \rightarrow NH_3(g) + \tfrac{1}{2} B_2H_6(g) + H_2(g) \quad (6)$$
$$NH_4AlH_4(s) \rightarrow AlN(s) + 4H_2(g) \quad (7)$$
$$NH_4AlH_4(s) \rightarrow NH_3(g) + AlH_3(g) + H_2(g) \quad (8)$$

A more detailed investigation of the step-wise loss of hydrogen from NH_4BH_4 reveals some intriguing features in Scheme 1. The release of hydrogen from NH_4BH_4 proceeds through intermediate steps, forming linear polymers[10] and hydrogen gas with specific thermodynamic characteristics (ΔE in kcal/mol).

Scheme 1.

$$NH_4BH_4(s) \rightarrow NH_3BH_3(s) + H_2(g) \quad \Delta E = -2.3$$
$$NH_3BH_3(s) \rightarrow NH_2BH_2(poly) + H_2(g) \quad \Delta E = 8.8$$
$$NH_2BH_2(poly) \rightarrow NHBH(poly) + H_2(g) \quad \Delta E = -3.2$$
$$NHBH(poly) \rightarrow BN(s) + H_2(g) \quad \Delta E = -9.2$$

Alternatively, cyclic polymer structures, starting with perhydroborazine, **3**, as shown in Scheme 1, could be involved in the decomposition pathways of amine borane. Sneddon and coworkers[11] report that at moderate temperatures borazine, **4**, undergoes a dehydropolymerization to yield hydrogen and a borazine polymer. At higher temperatures the polymer undergoes further dehydrogenation to yield a polyborazylene (BN) polymer. This observations merit further study to investigate the feasibility of reversible hydrogen storage.

Scheme 2.

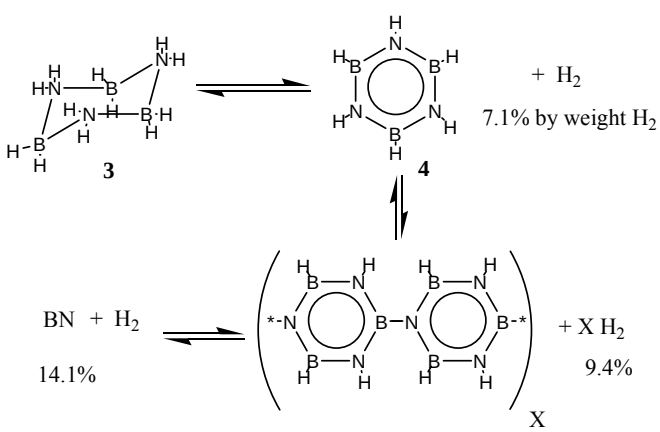

Conclusions

Computational methods offer an attractive approach to screen new potential chemical hydrogen storage materials. Two potential systems were examined in this study, hydrogen releases from NH_xBH_x (amine/ammonium borohydrides) and NH_xAlH_x (amine/ammonium alanates). Both materials could potentially meet the long term DOE requirements for volumetric and energy density requirements. Theoretical calculations predict that hydrogen loss is the thermodynamically favored pathway over B-N or Al-N bond scission. However, the loss of hydrogen from the NH_xBH_x series of compounds is predicted to be less exothermic than hydrogen loss from the NH_xAlH_x series of compounds. This could be an important observation to enhance the economic considerations for recycle.

Acknowledgement. The authors wish to acknowledge support from the Laboratory Directed Research and Development Program at the Pacific Northwest National Laboratory and the Nanoscience Initiative. Some calculations have been performed at the National Energy Research Scientific Computing Center (NERSC).

References

1 Hydrogen, Fuel Cells & Infrastructure Technologies Program, 2003 Merit Review and Peer Evaluation Meeting, May 19-22, **2003**, Berkeley, CA.
2 B. Bogdanovic and M. Schwickardi, *J. Alloys Comp.* **1997**, *253*, 1.
3 Y. Wu; R. M. Mohring, *Fuel Preprints* **2003**, *48*(2) 940.
4 A.C. Dillon; M. J. Heben. Appl. Physics A-Materials Science & Proc. **2001**, *72* (2), 133.
5 H.C. Brown, L. T. Murray, *Inorg. Chem.* **1984**, *23*, 2746.
6 The synthesis of NH4BH4 was first reported by S.G. Shore, R.W. Parry, *J. Am. Chem. Soc.* **1958**, *80*, 8.
7 The Freiberg group has been investigating hydrogen loss from amine borane (NH3BH3). See *Advances in Boron Chemistry*, Ed., W. Siebert, Royal Society of Chemistry **1997**, pp 514-517.
8 NWChem, A Computational Chemistry Package for Parallel Computers, Version 4.0.1, **2001**, R.H. Harrison et al.
9 G. Kresse and J. Hafner, Phys. Rev. B **47**, 558 (1993); G. Kresse and J. Furthmüller, Comp. Mat. Sci. **6**, 15 (1996).
10 It has recently been shown that catalytic loss of hydrogen from amine borane occurs by a bimolecular pathway. C. A. Jaska; K Temple; A. J. Lough; I. Manners. *J. Am. Chem. Soc.* **2003**, *125*, 9424.
11 P. J. Fazen; E. E. Remsen; J. S. Beck; P. J. Carroll; L. G. Sneddon. *Chem. Mater.* **1995**, *7*, 1942.

Tom.Autrey@pnl.gov
Maciej.Gutowski@pnl.gov

EXPERIMENTAL STUDY OF MERCURY HOMOGENEOUS REACTION CHEMISTRY UNDER POST-FLAME CONDITIONS

Richard Sterling, Jianrong Qiu, and Joseph J. Helble

Department of Chemical Engineering, University of Connecticut, 191 Auditorium Road, Unit 3222, Storrs CT 06269-3222

Introduction

In the United States, coal combustion remains the primary anthropogenic source of mercury air pollution (1). Calculations have shown that gas phase oxidized mercury is thermodynamically favored at stack conditions, but recent studies suggest that conversion is kinetically limited (2-5). Efforts to reduce mercury emissions require knowledge of mercury speciation at stack conditions, since the oxidation state directly affects mercury capture efficiencies. Oxidized forms such as $HgCl_2$, for example, are water-soluble and easily captured by wet scrubbers, whereas elemental mercury is insoluble and therefore difficult to remove.

Several recent studies have focused on developing an elementary kinetic mechanism for homogeneous Hg oxidation to predict Hg conversion in coal combustion systems. Sliger et al. (5) proposed a four step mechanism that incorporated a global reaction with Cl_2. Widmer et al. subsequently presented an 8 step mechanism that included chlorinated species such as HOCl (6). Edwards et al. (3) expanded the Cl chemistry, Niksa and coworkers incorporated NOx chemistry and recalculated several rate constants (4), and Qiu and co-workers further refined the rate constants and expanded the Cl chemistry (7). In each of these efforts, Cl atoms were identified as a key component in the oxidation pathway.

While the models have provided considerable insight into possible reaction pathways, detailed experimental studies of mercury oxidation in the presence of important coal combustion product gases such as SO_2 and NO in systems with the relevant radical pool are lacking. For example, Hall et al. (8) examined Hg oxidation by HCl in a heated quartz tube using bottled gas mixtures consisting of 10% O_2 in N_2. Sliger et al. (5) used the product gases from a natural gas flame in a high quench rate system to examine Hg oxidation by HCl. Neither SO_2 nor NO were considered in this study. Similarly, Mamani-Paco and Helble (9) examined Hg oxidation by both HCl and Cl_2 in the post-flame gases produced by a methane flat flame burner. Insights into reaction pathways were gained from these studies, but there is no information provided on the importance of SO_2 and NO. Ghorishi et al. (10) conducted bench scale isothermal experiments to investigate the effects of SO_2 and H_2O and temperature on mercury oxidation in simulated flue gas mixtures, and found that no Hg oxidation by HCl occurred at temperatures below 250°C. At higher temperatures oxidation did occur, but inhibition was reported at 754°C with the addition of SO_2. As part of an investigation that studied the effects of flue gas constituents on speciation methods, Laudal et al. (11) also examined the effects of SO_2 and NO. Results indicated that both SO_2 and NO could inhibit Hg oxidation by Cl_2.

While these studies provide insight into inhibitory effects associated with SO_2 and NO, the relevant studies were either performed without SO_2 and NO, or with bottled gas mixtures that do not reproduce the radical pool associated with a flame environment. This study was undertaken to address these questions.

Experimental

Homogeneous oxidation of mercury was examined in a flame-fired bench-scale system shown schematically in Figure 1. Combustion gases were generated by oxidation of metered methane-oxygen-nitrogen mixtures fed to a Research Technologies Inc. multi-element micro-diffusion flat flame burner. For these experiments, the equivalence ratio was adjusted to vary the temperature profile and the flue gas composition downstream of the flame. All experiments were conducted under either stoichiometric or fuel lean combustion conditions. A rectangular insulated stainless steel mixing chamber (0.21 m tall, 0.16 m in length and 0.17 m wide) was placed on top of the diffusion burner for gas mixing. At the back of the mixing chamber, three 6.35 mm ports were used for the injection of the mercury laden vapor stream, any chlorine containing species, and other contaminant gases (SO_2 and NO in nitrogen). Mercury vapors were generated from a mercury permeation device using nitrogen as the carrier gas. The permeation device was held in a constant temperature heating bath throughout the course of each experiment. The mercury-containing flue gas mixture then exited the mixing chamber through an outlet 0.13 m in diameter.

Gases exiting the mixing chamber flowed into a quartz reactor 80 cm long and 12.7 cm in diameter. The reactor- chamber junction was sealed with castable cement before the start of each experiment. To prevent the accumulation of condensed water as the simulated flue gases were cooled the reactor was mounted at 10 degrees to the horizontal. Heating tapes and insulation were wrapped around the reactor to provide additional heating and to reduce heat losses to the environment. Four ball and socket ports were located along the length of the reactor for sampling the reacting gas mixture.

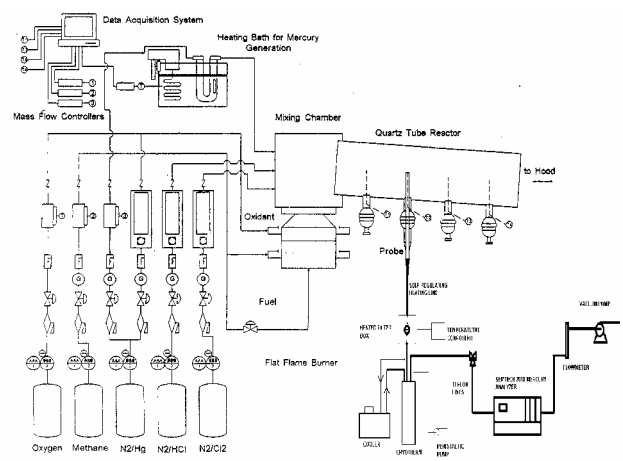

Figure 1: Schematic diagram of the mercury homogeneous oxidation experimental apparatus, modified from (9).

Quartz probes were used to collect flue gas samples from the center of the reactor. To measure the temperature at the sample ports, a thin-wire K-type thermocouple was inserted in a quartz capillary at the center of each probe.

Flue gases were sampled by a quartz probe connected to a self regulating heating line (SRHL). The SRHL core was made of Teflon^{TM} tubing wrapped in a heating cable with a temperature controller used to maintain a tubing surface temperature of 150°C. Gas flows leaving the SRHL entered a glass fiber filter enclosed in a miniature heated filter box used to separate any particles from the gas stream. Reaction gases then entered a series of three glass impingers enclosed in a container through which water at a temperature of less than 5°C was recirculated to keep the surfaces of the impingers cold.

Gases exiting the impingers were fed to a Semtech cold vapor atomic absorption spectroscopy-based continuous Hg analyzer for analysis of Hg concentrations. Differences between oxidized and elemental mercury were determined by cycling the oxidizer (HCl or Cl_2) on and off in 30 or 60 second intervals during the course of an experiment.

The range of conditions considered in this study is presented in Table 1. In all cases, samples were extracted from sampling port 2 at a system temperature of approximately 350°C.

Table.1: Experimental test matrix used for evaluating Hg homogeneous oxidation. All concentrations in ppm.

#	Cl_2	HCl	NO	SO_2
1	250	0	0	0
	500	0	0	0
2	250	0	100/300	0
	500	0	100/300	0
3	250	0	0	100/400
	500	0	0	100/400
4	150	0	0	0
	250	0	0	0
5	0	100/300	0	0
6	0	100/300	100/300	0
7	0	100/300	0	100/400
8	0	300	0	0

Results and Discussion

Experiments were conducted with varying concentrations of NO, SO_2, HCl, Cl_2, and O_2 as described above and in Table 1. Typical results for an experiment involving NO and HCl addition are shown in Figure 2, and for an experiment involving SO_2 and Cl_2 in Figure 3. Error bars in each figure represent the standard deviation about the mean for a series of repeat experiments, with N ranging from 3 to 5. Addition of NO (beyond any thermal NO) is seen to have a slight inhibitory effect on Hg oxidation by HCl at HCl concentrations of 300 ppm. In contrast, SO_2 is seen to have

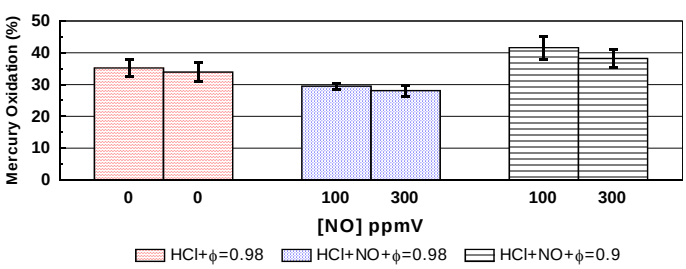

Figure 2 Hg oxidation in the presence of NO and 300 ppm HCl.

a large inhibitory effect on oxidation by Cl_2. Not shown are results from experiments with HCl and SO_2; here, very little effect was observed. In the presence of 100 ppm HCl at a flame equivalence ratio of 1, 6% of the Hg present was oxidized to $HgCl_2$. In the presence of 100 ppm SO_2, oxidation remained unchanged at 6%. Increasing the SO_2 concentration to 400 ppm resulted in a statistically insignificant change in Hg oxidation to 7%.

As implied by the data in Figures 2 and 3, increasing oxygen levels also contribute to an increase in Hg oxidation. Results from a series of experiments at two different flame stoichiometries in the presence of varying levels of HCl are shown in Figure 4. Differences at low HCl concentrations are minimal but become apparent as HCl concentrations increase above 200 ppm.

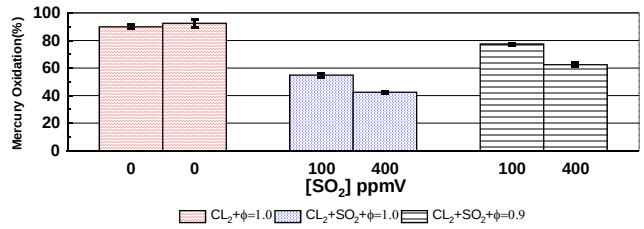

Figure 3 Hg oxidation in the presence of SO_2 and 500 ppm Cl_2.

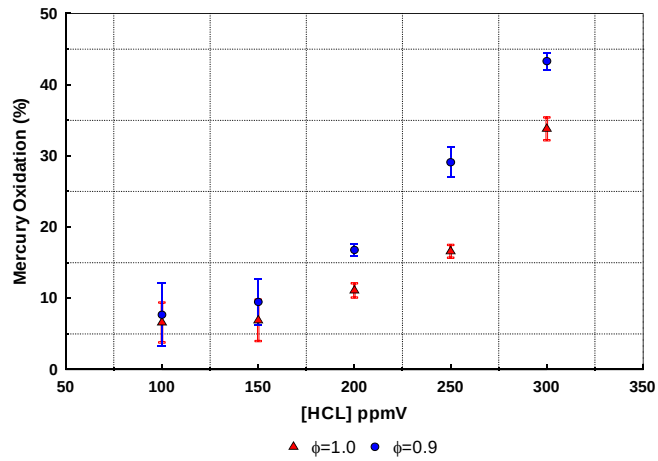

Figure 4 Hg oxidation as a function of equivalence ratio ϕ and [HCl]

Acknowledgement

This project was supported by US EPA STAR grant number R-82817001-1

References

1. US EPA, Mercury Study: Report to Congress, **1997**.
2. Senior, C.L., Sarofim, A.F., Zeng, T., Helble, J.J., Mamani-Paco, R., *Fuel Proc. Tech.* **2000**, 63, 197-213.
3. Edwards, J.R., Srivastava, R.K., and Kilgroe, J.D., *J. Air & Waste Manage. Assoc.* **2001**, 51, 869-877.
4. Niksa, S., Helble, J.J., and Fujiwara, N., *Environ. Sci. Tech.* **2001**, 35, 3701-3706.
5. Sliger, R. N.; Kramlich, J. C.; Marinov, N. M. *Fuel Process. Technol.* **2000**, 65-66, 423-438.
6. Widmer, N.C.; West, J.; Cole, J.A. *Proc. A&WMA Annual Conference*, **2000**, Salt Lake City.
7. Qiu, J., Sterling, R., and Helble, J.J., *International Conference on Coal Science*, **2003**, Cairns Australia, November.
8. Hall, B.; Schager, P.; Lindqvist, O. *Water, Air, and Soil Pollution* **1991**, 56, 3-14.
9. Mamani-Paco, R. M.; Helble, J. J. *Proc. A&WMA Annual Conference*, **2000**, Salt Lake City, AWMA.
10. Ghorishi S. B. and C.W. Lee, EPA report, EPA-600/R-98-014, **1998**.
11. Laudal, D. L.; Brown, T. D.; Nott B.R. *Fuel Process. Technol.* **2000**, 65-66, 157-165.

THE MECHANISTIC MODEL FOR FLUE GAS–MERCURY INTERACTIONS ON ACTIVATED CARBONS: THE OXIDATION SITE

E.S. Olson, B.A. Mibeck, S.A. Benson, J.D. Laumb, C.R. Crocker, G.E. Dunham, R.K. Sharma, S.J. Miller, and J.H. Pavlish

Energy & Environmental Research Center, University of North Dakota, Box 9018, Grand Forks, ND 58202-9018

Introduction

Injection of fine-powdered activated carbon (AC) into the hot flue gas stream has been successful in removing a large portion of the mercury in flue gas from coal combustion, even when the mercury is mainly elemental. To minimize the amount of sorbent used, high heterogeneous reaction rates of the gas-phase elemental mercury on the carbon sorbent surface may be needed to capture the mercury in the short contact time demanded when the sorbent is quickly removed from the gas stream, such as with electrostatic precipitation of ash and carbon particulates. Part of our work has focused elucidating the nature of the interactions between the mercury and the flue gas components on AC surfaces, particularly the ACs derived from Texas (Norit FGD) and from Fort Union lignites (prepared at the Energy & Environmental Research Center [EERC]). This understanding is crucial to developing a model for mercury chemisorption and subsequent design of carbons with faster kinetics and greater capacities.

AC is an effective chemisorbent for mercury in combustion flue gas. Initial studies included a large factorial series of tests using powdered ACs that were conducted in a bench-scale system consisting of a thin fixed-bed reactor in gas streams (100° to 150°C) containing 11 to 15 µg/m^3 of Hg^0 in various simulated flue gas compositions consisting of acidic SO_2, NO_2, and HCl gases plus a base mixture of N_2, O_2, NO, CO_2, and H_2O (1, 2). The results of these experiments showed that NO_2 or HCl–O_2 is required for effective Hg^0 capacity, no breakthrough occurred when SO_2 was omitted, and increasing SO_2 concentration gave shorter breakthrough times. H_2O is also required for breakthrough to occur. Increasing NO_2 concentration gave shorter breakthrough times. The Hg emitted after breakthrough is mostly oxidized and can exceed inlet Hg concentration. Related work showed that Hg emitted after breakthrough in the absence of HCl was $Hg(NO_3)_2$ (3). Thus the chemisorption of Hg is seriously affected by flue gas component concentrations, especially SO_2.

Based on these capacity data, an initial model was presented (4) that described the chemisorption events following adsorption of Hg^0. Oxidation of Hg^0 to form a bound Hg(II) species occurs with the electrons donated to the carbon and eventually to NO_2 or O_2. But following oxidation, the binding site for Hg(II) must be basic in nature, since the Hg(II) is a Lewis acid. At breakthrough, the basic binding sites are completely occupied by acidic species derived from the flue gas, especially those derived from SO_2, and then Hg(II) salts are displaced from the binding sites. As breakthrough occurs, the oxidation reaction decouples from the binding reaction(s), since nearly 100% oxidation occurs even after complete breakthrough, when the binding sites are completely occupied. This fact argues against any explanation for loss of capacity based on pore plugging by species resulting from acid gases, since this would inhibit both reactions. The Hg(II) species that forms or is released after breakthrough is volatilized as $HgCl_2$ or $Hg(NO_3)_2$.

The nature of the mercury–flue gas–sorbent interactions was further elucidated in x-ray photoelectron spectroscopy (XPS) experiments performed with two AC sorbents, Norit FGD and the EERC lignite-derived AC, exposed to various simulated flue gas compositions containing Hg^0 with various levels of SO_2, NO_2, HCl, and H_2O for time periods before and after breakthrough of mercury (5). Because of the interference caused by silicon, XPS data could not be obtained for the mercury species present in the exposed sorbents. These studies verified that sulfur(VI) (sulfate, bisulfate, sulfonate, or sulfuric acid) is the major sulfur species on all the exposed sorbent samples, and the longer the exposure to SO_2, the more sulfate is found in the sample. When NO_2 or H_2O was omitted from the flue gas, less sulfate was accumulated.

Thus adsorbed SO_2 is clearly oxidized on the sorbent surface to sulfur(VI) species in a process facilitated by NO_2 and H_2O, and the sulfur(VI) is the main poison for the basic sites. The XPS data also indicate that two types of chlorine are present: ionic and covalent, and that both chlorine forms disappeared from the sample at breakthrough. That chlorine is present as both chloride ion and covalent (organic) chlorine indicates that the HCl in the flue gas can donate a hydrogen ion to a basic site as well as add both hydrogen and chlorine to a basic site to form the organochlorine product. The accumulation of chlorine in the absence of SO_2 as well as the disappearance of chlorine after continued exposure in SO_2 is explained by competition of HCl with bisulfate or sulfuric acid. As more bisulfate is generated from SO_2 at the carbon surface, it displaces the HCl, owing to the high volatility of HCl.

Refined Model for the Hg(II) Binding Site

A refinement of the binding site model was proposed (6) that offers more detail on the nature of the carbon site and its interaction with flue gases and Hg (Figure 1). This model uses the concept of zigzag carbene structures recently proposed for states at the edges of the carbon graphene layers (7) rather than oxygen functional groups suggested by other authors. In the carbene model, the zigzag carbon atom positioned between aromatic rings is hypothesized to be the Lewis base site. The zigzag Lewis basic carbene reacts with the Hg(II) species as shown in Figure 1 to form an organomercury carbenium ion and also with HCl, H_2SO_4, and SO_2 to form carbenium ions with associated chloride and sulfate, that can combine to form the observed organochlorine and possibly also ester moieties. Sulfinate functionality could also form from SO_2.

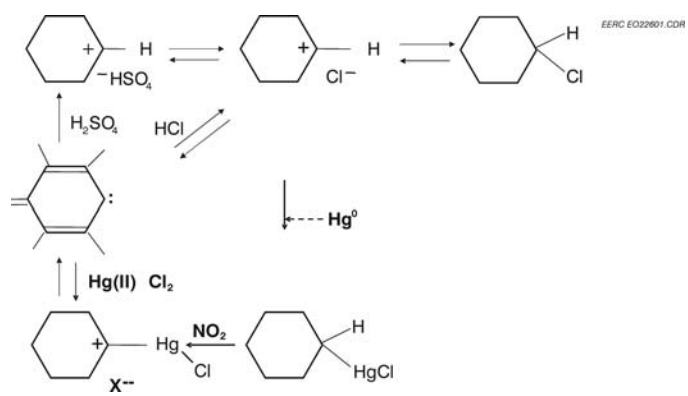

Figure 1. Oxidation mechanism – carbenium ion oxidant.

The Role of HCl

In tests conducted at relatively high HCl concentrations (50 ppm), the capture of mercury at the start was always very high (less than 5% of inlet concentration), but in very low HCl concentrations such as those obtained when low-Cl coals are burned (1 ppm), an initial breakthrough was observed at about 50%–60% of

inlet (8), followed by an increase in capture efficiency to the 5%–10% level. The higher HCl concentration thus eliminated this induction period where poor capture is obtained. It is clear that HCl is not an oxidizing reagent, since it is already in the most reduced state. This is, therefore, a promotional effect of the HCl on the activity of the carbon in catalyzing the oxidation of mercury. A similar promotional effect of adding aqueous HCl to the sorbent was reported recently by Ghorishi et al. (9).

Oxidation Site Models and Tests

The previously described carbene model for the acid gas interactions, while consistent with the breakthrough capacity and spectroscopic data, also secures the foundation for the Hg^0 oxidation reaction(s). A variation of this scheme, as shown in Figure 1, explains the promotional effect of HCl. In this oxidation mechanism, the carbenium ion intermediate, formed when protonic acids add to the carbene exactly as described above is actually the oxidation site for the adsorbed Hg^0. Donation of electrons from the Hg^0 to the carbene forms an organomercury species. A subsequent oxidation step with NO_2 or O_2 will generate the organomercury carbenium ion. Thus HCl or other protonic acids promote the oxidation step by generating the positive carbenium ion oxidation sites, but the reaction site eventually becomes cluttered with sulfuric acid molecules. Thus at breakthrough, there are still carbenium ions for oxidation of Hg^0, but the reaction is driven toward loss of the more volatile species, mercury and HCl.

An alternative mechanism involving the same carbene site is depicted in Figure 2. In this model, a radical carbon chlorine pair is formed either from a radical addition of HCl to a triplet state of the carbene or by homolytic cleavage of the organochlorine intermediate. The chlorine atom could oxidize the Hg^0 to form Hg(I)Cl that could combine with the carbon edge radical to form the organomercury species identical to that formed via carbenium addition. It should be noted, however, that Hg oxidation occurs perfectly well without HCl, once the sorbent is active.

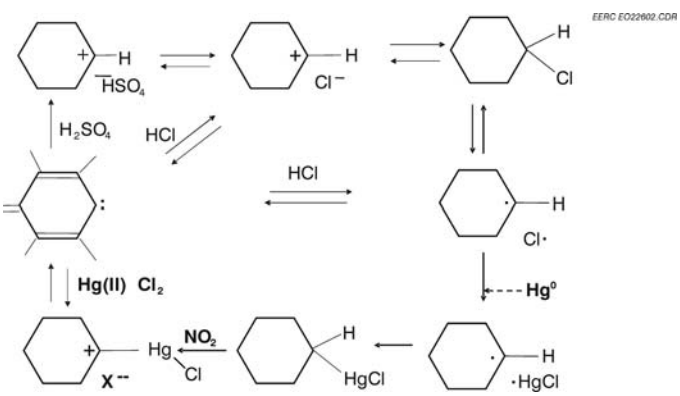

Figure 2. Oxidation mechanism – chlorine atom oxidant.

An experiment was performed to test the hypothesis that chlorine atoms are generated on the carbon surface and are responsible for the accelerated oxidation. An FGD carbon sorbent was pretreated with HCl and then with radical scavengers which should reduce reactivity. The mercury capture results showed that this sorbent oxidized Hg^0 equally as well as a sorbent untreated with radical scavenger.

Conclusions

The refinement of the mechanistic model for Hg^0 oxidation and binding is now proposed that offers more detail on the nature of the carbon site and its interaction with flue gases and Hg. This model uses a zigzag carbene edge structure model to explain how the carbon graphene surface can provide a basic site for which acid gas components compete and how a reactive oxidation site is generated as a result of the acid addition. An alternative mechanism for oxidation involving generation of a chlorine radical was not consistent with the result from addition of a radical scavenger that would have depleted the chlorine atoms.

Acknowledgments. Support is gratefully acknowledged from the EERC Center for Air Toxic Metals[K] funded by the U.S. Environmental Protection Agency through Grant No. R827649-01. It was not subjected to the Agency required peer review process and does not necessarily reflect the views of the Agency, and no official endorsement should be inferred.

References

(1) Miller, S.J.; Dunham, G.E.; Olson, E.S.; Brown, T.D. *Fuel Process. Technol.* **2000**, *65–66*, 343–363.
(2) Olson, E.S.; Miller, S.J.; Sharma, R.K.; Dunham, G.E.; Benson, S.A. *J. Hazard. Mater.* **2000**, *74*, 61–79.
(3) Olson, E.S.; Thompson, J.S.; Pavlish, J.H. *Anal. Bioanal. Chem.* **2002**, *374*, 1045.
(4) Olson, E.S.; Laumb, J.D.; Benson, S.A.; Dunham, G.E.; Sharma, R.K.; Miller, S.J. Pavlish J.H. *Prepr. Pap.—Am. Chem. Soc., Div. Fuel Chem.* **2002**, *47* (24), 481.
(5) Laumb, J.D.; Benson, S.A.; Olson, E.S.; *Fuel Process. Technol.*, in press.
(6) Olson, E.S.; Laumb, J.D.; Benson, S.A.; Dunham, G.E.; Sharma, R.K.; Miller, S.J.; Pavlish, J.P. *Prepr. Pap.—Am. Chem. Soc., Div. Fuel Chem.* **2003**, *48* (1), 30–31.
(7) Radovic, L.R.; Bockrath, B. Fuel Chem. Div. Prepr. **2002**, 47(2), 428.
(8) Pavlish, J.H.; Holmes, M.J.; Benson, S.A.; Crocker, C.R.; Galbreath, K.C. *Proceedings of the Air Quality III: Mercury, Trace Elements, and Particulate Matter Conference*; Arlington, VA, Sept 9–12, **2002**; Paper A4-4.
(9) Ghorishi, S.B.; Keeney, R.M.; Serre, S.D.; Gullet, B.K.; Jozewicz, W.S. Environ. Sci. Technol. **2002**, 36, 4454-4459.

PILOT-SCALE EVALUATION OF ACTIVATED CARBON-BASED MERCURY CONTROL OPTIONS FOR UTILITIES BURNING LIGNITE COAL

Michael J. Holmes, John H. Pavlish, Ye Zhuang,. Steven A. Benson, and Matthew J. Fritze

University of North Dakota Energy & Environmental Research Center, PO Box 9018, Grand Forks, ND 58202-9018

Abstract

Activated carbon sorbents were evaluated for mercury removal potential in bench- and pilot-scale systems at the Energy & Environmental Research Center (EERC). The Ontario Hydro method and continuous mercury monitors were used to measure mercury species concentrations across the control technology devices with and without sorbent injection. Primarily elemental mercury (Hg^0) was measured when lignite coals from the Poplar River Plant and Freedom Mine were combusted. The effects of sorbent injection rate, particle size, and gas temperature on mercury removal were evaluated for four particulate control device options. Increasing injection rates, decreasing gas temperatures, and improving contact between the sorbent and flue gas all generally promoted mercury capture. Relative to eastern bituminous coal combustion flue gases, higher sorbent injection rates were generally required to effectively remove mercury from the lignite coal combustion flue gases. Similar issues of high Hg^0 and slow kinetics apply to other western coals as well. This paper summarizes the effects of chlorine and other additives on the oxidation and removal of mercury from flue gas.

Introduction

In general, lignite coals contain comparable levels of mercury but significantly lower levels of chlorine compared to bituminous coals. Lignite coals are also distinguished by their much higher calcium contents. These compositional differences have important effects on the quantity and form of mercury emitted from a boiler and the effectiveness of different control technologies to remove mercury from flue gas. The high chlorine content (>200 ppm) that is characteristic of many bituminous coals increases the fraction of the more easily removable mercuric compounds (Hg^{2+}), most likely mercuric chloride ($HgCl_2$), in the total mercury emission. Conversely, experimental results and information collection request data indicate that low-chlorine (<200 ppm) coal combustion flue gases contain predominantly Hg^0, which is substantially more difficult to remove than Hg^{2+}.[1] Additionally, the generally high calcium contents of lignite coals may further reduce the oxidizing effect of the already low chlorine content by reactively scavenging chlorine species (Cl, HCl, and Cl_2) from the combustion flue gas.[2]

The most commonly considered strategy for removing mercury from coal combustion flue gas streams is the adsorption of mercury species by a solid sorbent injected upstream of a particulate control device such as a fabric filter (FF) or electrostatic precipitator (ESP). Many potential mercury sorbents have been evaluated.[3] These evaluations have demonstrated that the flue gas composition and the chemical speciation of mercury affect mercury capture and its ultimate environmental fate.

Currently, powdered activated carbon (PAC) injection appears to be the most mature and promising technology available for mercury control. Research and test data suggest that activated carbons can effectively sorb both Hg^0 and Hg^{2+}. However, much of the research to date has been performed in fixed-bed reactors that simulate relatively long residence time (minutes or hours) and intimate gas–solids contact on a FF cake.[4–9] It is equally important to investigate short residence time (seconds) in-flight capture of Hg^0 because most of the coal-burning boilers in the United States and Canada use cold-side ESPs for controlling particulate matter emissions. The projected annual cost for activated carbon adsorption of mercury in a duct injection system is significant. Carbon-to-mercury weight ratios of 3000–18,000 (gram of carbon injected per gram of mercury in flue gas) have been estimated to achieve 90% mercury removal from a coal combustion flue gas containing 10 μg/Nm^3 of mercury.[3] Pilot data from this project suggest that, for lignite-fired plants, the carbon-to-mercury weight ratio required may be toward the upper end of this range. More efficient carbon-based sorbents and contacting systems are required to enable lower carbon-to-mercury weight ratios to be used, thus reducing the operating costs of PAC injection.

Researchers at the Energy & Environmental Research Center (EERC) and elsewhere are striving to attain a more thorough understanding of mercury species reactions on activated carbon surfaces in order to produce more efficient sorbents.[10,11] The removal of mercury from flue gas by activated carbon probably occurs through reactions with surface functional groups. Mercury-reactive surface functional groups may include acidic carboxyl, lactone, hydroxyl, and carbonyl or alkaline pyrone and chromene functionalities.[10–15] The potential role of acidic and alkaline surface functional groups on mercury capture is unknown and needs to be investigated. Functional groups containing inorganic elements such as chlorine or sulfur are also possibilities.[10,11,16–20] Although chlorine- and sulfur-bearing surface functional groups are not well characterized, the beneficial role of chlorine and the often negative impact of SO_2 and SO_3 in capturing mercury species on activated carbons are well established.[15,21]

The EERC recently completed the first phase of a 3-year, two-phase consortium project to develop and demonstrate mercury control technologies for utilities burning lignite coal. Phase I objectives were to develop a better understanding of mercury interactions with flue gas constituents, test a range of sorbent-based technologies targeted at removing mercury dominated by the elemental form (Hg^0) from flue gases, and demonstrate the effectiveness of the most promising technologies at the pilot scale. The Phase II objective is to demonstrate and quantify sorbent technology effectiveness, performance, and cost at a sponsor-owned and/or operated power plant. This paper documents the Phase I results and provides a brief overview of the Phase II plans.

Results and Discussion

Bench-Scale Testing. Fixed-bed tests were completed on a NORIT FGD sorbent and a calcium-based sorbent. Two simulated coal combustion flue gas compositions were used during the tests as presented in Table 1. The simulated lignite flue gas composition is based on flue gas measurements made at a lignite-fired power plant and derived from the relatively low chlorine contents of the Luscar (18.0 ppmw), Beulah–Zap (12.6 ppmw), and Center (14.3 ppmw) coals. The second simulated flue gas composition in Table 1 had been used in previous testing, thus enabling comparisons to be made with other sorbent test results. The baseline flue gas contains much higher SO_2, NO, NO_2, and HCl concentrations but lower H_2O concentrations relative to the lignite flue gas. Test results are presented in Figures 1–3. These figures show the temporal changes in total mercury concentration downstream from the fixed-sorbent beds expressed as a percentage of Hg^0 input (nominally 10 μg/m^3) into the system. Figure 1 shows results for the activated carbons prepared at the baseline conditions, unactivated chars, and a calcium-based sorbent tested in the simulated lignite flue gas (Table 1). Mercury was initially passed through the activated carbons and then effectively captured for about 3 hr. After 3 hr, mercury began to

break through the fixed-sorbent beds at progressively higher levels and was released primarily as Hg^{2+} (>90%).

Table 1. Simulated Coal Combustion Flue Gas Compositions

Compone Component, unit	Lignite	Baseline
O_2, vol%	6	6
CO_2, vol%	12	12
H_2O, vol%	15	8
SO_2, ppmv	580	1600
NO, ppmv	120	400
NO_2, ppmv	6	20
HCl, ppmv	1	50
N_2	Balance	Balance

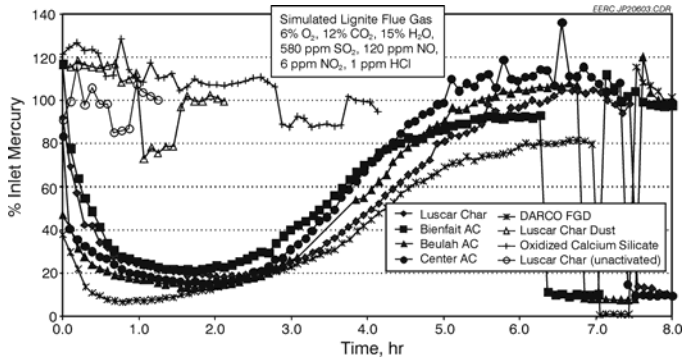

Figure 1. Bench-scale fixed-bed results under simulated lignite flue gas for carbons prepared at baseline conditions.

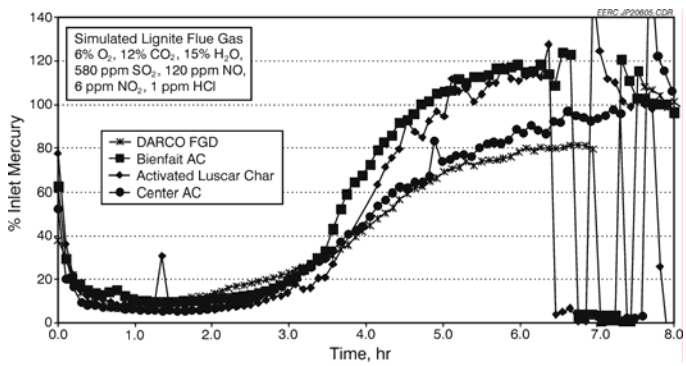

Figure 2. Bench-scale fixed-bed results under simulated lignite flue gas for carbons prepared at an increased temperature.

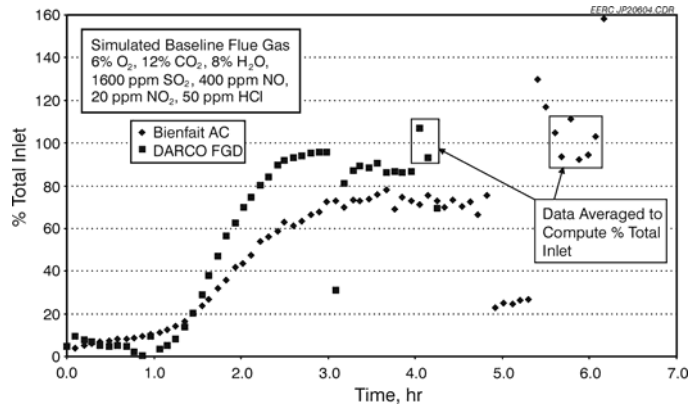

Figure 3. Bench-scale fixed-bed results under simulated baseline flue gas for Luscar coal activated at an increased temperature and NORIT FGD.

The initial breakthrough of mercury during the first 30 to 40 min of testing does not generally occur in flue gases containing higher acid gas concentrations. The unactivated sorbents and calcium-based sorbent were ineffective in capturing mercury; consequently, the tests were discontinued after 2 to 4 hr. Figure 2 compares test results for the carbons activated at an increased temperature and commercial carbon using the simulated lignite flue gas composition. Relative to the carbons activated at baseline conditions (Figure 1), results in Figure 2 indicate improved mercury capture and greater conversions of Hg^0 to Hg^{2+} (>95%). In addition, the initial breakthrough of mercury was not as significant. In order to compare results with a dataset of past test results, the Luscar coal carbon activated at an increased temperature and the NORIT FGD carbon were tested using the baseline flue gas composition in Table 1. Figure 3 test results show better initial mercury capture with no breakthrough. After 1.5 hr, the Luscar coal activated carbon showed less breakthrough compared to the NORIT FGD.

Pilot-Scale Combustor. A 580-MJ/hr (550,000-Btu/hr) pulverized coal-fired unit was used to evaluate mercury sorbent effectiveness in flue gases produced from combustion of lignite coal. The unit, shown schematically in Figure 4, is designed to generate fly ash and flue gas representative of that produced in a full-scale utility boiler. The combustor is oriented vertically to minimize wall deposits. A refractory lining helps to ensure adequate flame temperature for complete combustion. Based on the superficial gas velocity, the mean residence time of a particle in the combustor is approximately 3 seconds. The coal nozzle fires axially upward from the bottom of the combustor, and secondary air is introduced concentrically to the primary air with turbulent mixing. Coal is introduced to the primary air stream via a screw feeder and eductor. An electric air preheater is used for precise control of the combustion air temperature.

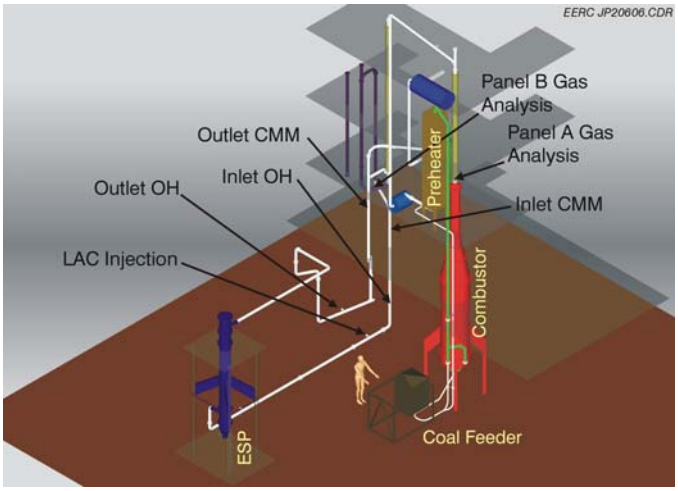

Figure 4. Schematic of the 580-MJ/hr (550,000-Btu/hr) combustion system.

The following particulate control devices were evaluated on the pilot-scale combustor as potential mercury control options: ESP, FF, combined ESPBFF, and *Advanced Hybrid*™ filter technology. Instrumentation enables system temperatures, pressures, flow rates, flue gas constituent concentrations, and particulate control device operating data to be monitored continuously and recorded on a data logger.

Pilot-Scale Tests. The activated (800°C, 1472°F) Luscar char (Bienfait) and DARCO FGD were selected for additional testing in the 580-MJ/hr (550,000-Btu/hr) pulverized coal-fired unit based on sorbent-screening results (reactivity and capacity), physical properties (particle size and surface area), cost, and consensus among project sponsors. The following variables that could potentially affect mercury emission control were tested: lignite coal source (Poplar River or Freedom Mine), control device type (ESP, FF, ESPBFF, or *Advanced Hybrid*™ filter), FF type (Gore-Tex® or Ryton®), sorbent type (steam-activated [800°C, 1472°F] Luscar char or DARCO FGD), particle size (approximate median volume diameters [MVDs] of 20 or 5 µm), sorbent injection rate, and flue gas temperature in the pollution control device. Additional tests were performed to evaluate the effectiveness of chlorine-based additives for enhancing mercury oxidation and removal.

Mercury Speciation. Figure 5 compares the average mercury species distributions, as determined by American Society for Testing and Materials Method D6784-02 (Ontario Hydro [OH]), for the Poplar River and Freedom coal combustion flue gases. The Poplar River coal combustion flue gas contains a higher total mercury concentration; however, the relative proportions of Hg^0, Hg^{2+}, and Hg(p) in both flue gases were very similar at approximately 85%, 15%, and <1%, respectively.

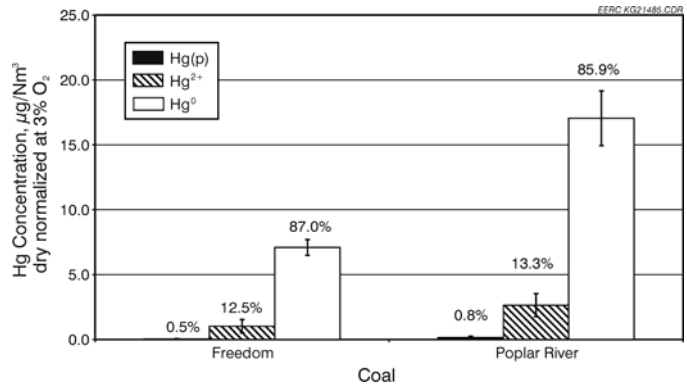

Figure 5. Comparison of average Poplar River and Freedom coal combustion flue gas (149°C, 300°F) mercury speciation results obtained using the OH method.

Effect of Varying Injection Rate on Technology Options. Figures 6 and 7 summarize the impact of varying injection rate for the four particulate technology configurations and the Poplar River and Freedom coals, respectively. For comparison purposes, mercury removal efficiencies for each technology configuration are summarized in Table 2 using the lowest injection rate observed from either coal. In general, the Hg removal efficiencies increased with the carbon injection rate for different particulate control configurations. Clearly, the TOXECON™ configuration (injection downstream of an ESP and upstream of a FF) results in the highest reduction while using the least amount of PAC. However, in batch injection mode, the *Advanced Hybrid*™ filter provides similar performance.

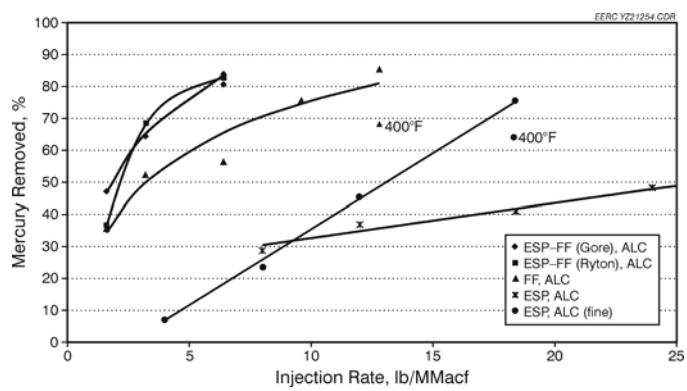

Figure 6. Particulate matter control device efficiencies for removing mercury from 149°C (300°F) Poplar River coal combustion flue gas as a function of activated (800°C, 1472°F) Luscar char injection rate.

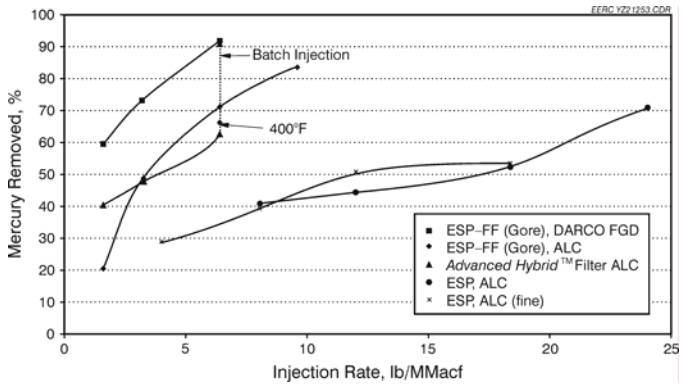

Figure 7. Particulate matter control device efficiencies for removing mercury from 149°C (300°F) Freedom coal combustion flue gas as functions of activated (800°C, 1472°F) Luscar char and DARCO FGD injection rates.

Table 2. Injection Rate (lb/MMmacf)* for Target Removal Rates

Technology Configuration	50%	70%	80%
ESP Only	11.2	17.1	NA
FF Only	3.2	7.8	12.3
ESP–FF	1.9	2.92	4.4
Advanced Hybrid™ Filter	6.0	NA	6.4**

* Lowest observed rate.
** Batch injection at greater than 80% removal.

Effect of Coal. Pilot-scale data showed a higher PAC rate requirement than would be expected based on past results with other coals. Figure 8 compares the mercury removal effectiveness of PAC injection combined with pilot-scale ESP and ESPBFF devices to that obtained by Bustard and others[22] with PAC injection between an ESP–FF (TOXECON™) or ESP installed on full-scale utility boilers. Coal type (i.e., composition) is an important parameter that affects the mercury removal efficiency of a control device. During the pilot-scale lignite tests with TOXECON™ and utility-scale eastern bituminous coal tests, mercury removal efficiency increased with increasing PAC injection rates. Conversely, mercury removal efficiency was never greater than 70%, regardless of the PAC injection rate into the Powder River Basin (PRB) subbituminous coal combustion flue gas. This limitation is probably caused by the low level of chlorine species that can promote mercury–activated carbon adsorption. In addition, the generally abundant lime (CaO) component of PRB subbituminous coal fly ashes reactively scavenges chlorine species (Cl, HCl, and Cl_2) from the flue gas to form $CaCl_2$. Figure 6 indicates that PAC injection combined with the particulate control devices installed on the full-scale boilers generally provided better mercury removal efficiency at a given injection rate relative to PAC injection followed by the pilot-scale ESP. Mercury removal efficiencies for the TOXECON™ configuration shown in Figure 6 are those observed for an eastern bituminous flue gas.

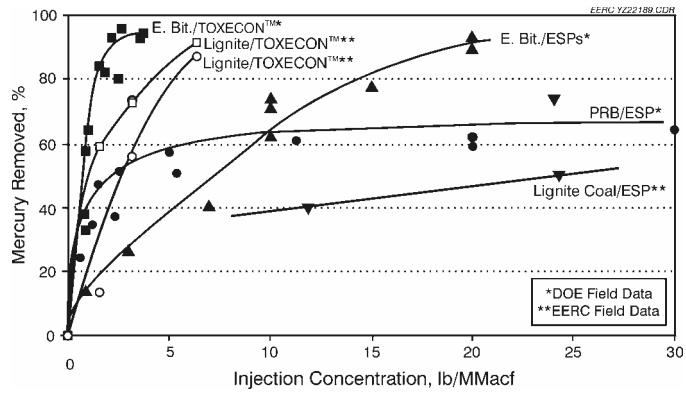

Figure 8. Pilot- and full-scale ESP and TOXECON™ mercury removal efficiencies as a function of PAC injection rate.

Effect of Chlorine. The use of chlorine and carbon-based sorbents for mercury removal has been effective in municipal, hazardous, and hospital waste incineration flue gases. Additionally, chemical kinetic modeling of bench-scale test results indicates that the introduction of HCl or NaCl into the high-temperature furnace region is likely to result in the production of atomic chlorine (Cl) and/or molecular chlorine (Cl_2), which are generally thought to be the dominant Hg^0 reactants in coal combustion flue gases.[23–28] Pilot-scale tests were conducted on two coals to determine if chlorine addition could improve DARCO FGD sorbent reactivity and mercury removal effectiveness from combustion flue gas. Tests were conducted on flue gases from Poplar River and Freedom coals using gaseous HCl and NaCl, respectively. Additional additives were also successfully tested and will be presented in the future.

The first round of testing was conducted on Poplar River coal, using HCl to promote sorbent reactivity. Before tests were conducted with HCl addition, the mercury concentration was measured at the outlet to evaluate the effectiveness of the DARCO FGD sorbent on mercury removal. The mercury concentration dropped from a baseline of approximately 23 µg/Nm^3, prior to sorbent injection, to 5 µg/Nm^3 with increasing sorbent injection rates up to 20 g/hr. At this injection rate, HCl was added at two locations under two separate tests, within the combustion zone and upstream of the ESP and carbon injection location. The flue gas temperature at the first location was approximately 930°C (1700°F) and at the second approximately 149°C (300°F), respectively. The addition of HCl at both locations did not appear to enhance sorbent reactivity and did not significantly improve the mercury removal effectiveness of the tested sorbents. More testing is needed before final conclusions can be drawn.

Additional testing was conducted on Freedom coal combustion flue gas using NaCl for sorbent enhancement. The impacts of NaCl addition with DARCO FGD were evaluated for three different particulate removal technologies: TOXECON™, *Advanced Hybrid*™ filter, and ESP. At baseline conditions, with no sorbent addition, mercury concentrations averaged 10 µg/Nm^3, as illustrated in Figure 9. The addition of sorbent at 20 g/hr resulted in TOXECON™ mercury removal of nearly 72%. The addition of NaCl to the coal feed resulted in an additional 2 µg/Nm^3 and is clearly illustrated in Figure 7. Similar trends were observed with both the *Advanced Hybrid*™ filter and ESP particulate control technologies.

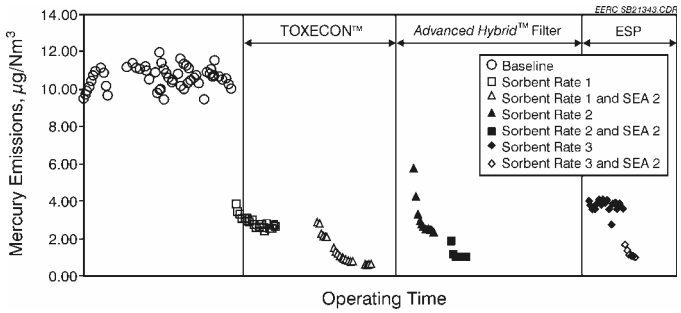

Figure 9. Impact of chlorine addition on mercury removal performance.

The preliminary results from these pilot-scale tests indicate that chlorine additives could be used to enhance mercury removal effectiveness of DARCO FGD, thereby reducing the amount of sorbent needed to achieve removal targets. Further, results suggest that the addition of NaCl to the coal would be more effective in enhancing mercury capture than HCl injection at the furnace outlet; however, differences in the test parameters (i.e., coal type, initial mercury concentration) make direct comparison of HCl and NaCl effectiveness difficult.

Using a chlorine additive has shown the potential to cut carbon rates by more than 50% for a given removal rate by using the additive at a rate below that of the carbon. Current costs for these additives range from $35 to $290/ton, depending on the additive. These values compare to current PAC costs of $1000/ton. Therefore, the $35/ton sorbent enhancement additive (SEA) has the potential to provide greater than 45% reduction in reagent costs (additive + PAC) for Hg control in systems where existing particulate control devices are used. Field testing is needed to better define performance, economics, and balance of plant impacts.

Effects of Temperature, Sorbent Size, Bag Material, and Air-to-Cloth Ratio. The impacts of temperature, sorbent size, filter material type, and air-to-cloth ratio were all presented previously and are summarized here for completeness. Temperature is a very important parameter for effective capture of mercury by PAC. Limited tests were conducted to evaluate temperature effects on sorbent performance in different configurations: ESP only, FF only, and ESP–FF. The flue gas temperature was raised from 149° to 204°C (300° to 400°F). Experimental data in Figures 6 and 7 and data presented previously show that mercury removal efficiencies were dramatically reduced, about 10%–15%, at the elevated flue gas temperature of 204°C (400°F) for all three configurations and for both Poplar River and Freedom coals, as compared to the 149°C (300°F) flue gas temperature.[29] An estimated 14.3% increase of sorbent usage is required to achieve collection efficiencies at a flue gas temperature of 204°C (400°F) similar to those at 149°C (300°F) for both the ESP-only and ESP–FF configurations. However, an estimated 70.7% increase in sorbent usage is needed for the FF configuration when the flue gas temperature was increased from 149° and 204°C (300° and 400°F). One partial explanation for the dramatic increase in carbon usage (70.7%) for the FF only at the flue gas temperature of 204°C (400°F) compared to 149°C (300°F) is the increased pulse rate at higher temperatures (increased A/C ratio) for the FF containing ash and carbon.

Sorbent size is another important parameter for mercury removal in flue gas, especially when mass transfer is an issue. Both the standard and fine MVD (of 20 and 5 µm, respectively) activated Luscar char were injected ahead of the ESP at different rates to examine the corresponding mercury removal efficiencies. The experimental data presented in Figures 3 and 4 show that a reduction in sorbent size did not consistently result in improved mercury capture. At injection rates of >8 lb/Macf, the fine activated Luscar char provides much better ESP mercury removal than that achieved with the more coarse carbon for the Poplar River coal. On the contrary, a reduction in carbon size did not greatly enhance ESP mercury capture in the Freedom coal flue gas. There may be several reasons that caused this inconsistency, such as adhesive agglomeration of the fine sorbent, inconsistency in fineness, poor dispersion of the fine sorbent into the flue gas, etc. More effort is needed before final conclusions can be drawn.

Two different bag materials, Ryton® and Gore-Tex®, were tested in the FF-only case at 149°C (300°F). Based on limited test data as shown in Figure 3, the differences in the FF material, Ryton® versus Gore-Tex®, did not significantly affect mercury capture efficiencies.

The FF was operated at A/C ratios of 6 and 12 with the TOXECON™ configuration to evaluate the impact that increased flows may have on mercury capture. Based on limited tests, the observed differences between 6 and 12 did not appear to be significant with regard to mercury capture. In other words, the increased velocity did not appear to impact mercury removal. Overall, the mercury removal was less when the A/C was 12, mainly due to increased pulsing frequency. This increased frequency translated to poorer utilization of the PAC at a given injection rate. Because the tests were rather short, long-term effects, such as increased blockage, erosion rates, etc., could not be evaluated.

Future Tests. The EERC currently has plans to perform additional tests of additives on bench- and pilot-scale systems, as well as tests at other North Dakota power plants. As part of the second phase of this ongoing project, the applicability of the conclusions from the Phase I bench- and pilot-scale investigations will be evaluated by performing similar PAC injection and flue gas and fly ash measurements at a utility host site equipped with a slipstream FF installed downstream of existing ESPs. Sorbent injection upstream of a pulse-jet-type FF (TOXECON™) is the mercury control technology that will be field-tested at the Poplar River Power Station, which is owned and operated by SaskPower. Activities planned for the field demonstration at the Poplar River Power Station include field-testing a slipstream-scaled version of the TOXECON™ technology, preparing the site and installing the appropriate technology hardware, evaluating sorbent impacts and performance, assessing technology impact on unit operations, assessing ash reuse and disposal impacts, and estimating costs to control mercury. The results from Phase II of the project should provide the lignite industry with a technology option that can be considered by other utilities as they develop their own mercury control strategies. In addition, Phase II data will provide insights into mercury control effectiveness for other coals and particulate control configurations.

Conclusions

The activated (800°C, 1472°F) Luscar char and DARCO FGD were selected for additional testing in a 580-MJ/hr (550,000-Btu/hr) pulverized coal-fired unit, based on sorbent screening results, costs, and consensus among project sponsors. The following variables that could potentially affect mercury emission control were tested: lignite coal source (Poplar River or Freedom Mine), control device type (ESP, FF, ESPBFF, and *Advanced Hybrid*™ filter), FF type (Gore-Tex® or Ryton®), sorbent type (steam-activated [800°C, 1472°F] Luscar char and DARCO FGD) and particle size (approximate MVDs of 20 and 5 µm), sorbent injection rate, SEA use, mercury speciation, and flue gas temperature in the pollution control device. Pilot-scale test results indicated the following:

- The relative proportions of Hg^0, Hg^{2+}, and Hg(p) in the Poplar River and Freedom coal combustion flue gases were very similar at approximately 85%, 15%, and <1%, respectively.
- The relative mercury removal efficiencies of the four control device technologies tested were 1) TOXECON™ and *Advanced Hybrid*™ filter, 2) FF, and 3) ESP, with the performance varying depending on coal and sorbent injection method.
- The pilot-scale results on lignite showed an increase in the required PAC needed for similar removals when compared to full-scale data for eastern bituminous coals.
- Most chlorine additives were effective in enhancing the mercury removal of activated carbon, thereby reducing the amount of sorbent needed to achieve a given level of mercury emission control. However, the use of HCl in the upper furnaces was not found to be effective.

Acknowledgments. This investigation was supported by a consortium of Environment Canada; SaskPower; Basin Electric Power Cooperative; Luscar Ltd.; Minnkota Power Cooperative; North Dakota Industrial Commission (NDIC); Otter Tail Power Company; EPRI; Great River Energy; Minnesota Power, Inc.; and Xcel Energy through the EERC's Jointly Sponsored Research Program, which is supported by the U.S. Department of Energy (DOE) National Energy Technology Laboratory (NETL) under Cooperative Agreement No. DE-FC26-98FT40321. We are grateful to the following colleagues and organizations for their support and advice: Lynn Brickett (DOE NETL), Don Rose (Environment Canada), Dave Smith (SaskPower), Vernon Laning (Basin Electric Power Cooperative), Bob Engler (Luscar Ltd.), Luther Kvernen (Minnkota Power Cooperative), Harvey Ness (NDIC), Terry Graumann (Otter Tail Power Company), Ramsey Chang (EPRI), Mark Strohfus (Great River Energy), Tim Hagley (Minnesota Power, Inc.), and Lee Eberley (Xcel Energy).

References

(1) Pavlish, J.H. EPA Decision Directs Mercury Research. *Center for Air Toxic Metals Newsletter* **2001**, *7* (1), 1 and 4.
(2) Galbreath, K.C.; Zygarlicke, C.J. *Fuel Process. Technol.* **2000**, *65–66*, 289–310.
(3) Pavlish, J.H.; Sondreal, E.A.; Mann, M.D.; Olson, E.S.; Galbreath, K.C.; Laudal, D.L.; Benson, S.A. Special issue of *Fuel Process. Technol.* **2003**, in press.
(4) Carey, T.R.; Hargrove, O.W.; Richardson, C.F. Factors Affecting Mercury Control in Utility Flue Gas Using Sorbent Injection. In *Proceedings of the Air and Waste Management Association 90th Annual Meeting*; Toronto, ON, Canada, June 8–13, 1997; Paper WA72A.05.
(5) Carey, T.R.; Hargrove, O.W.; Richardson, C.F.; Chang, R.; Meserole, F.B. *J. Air Waste Manage. Assoc.* **1998**, *48*, 1166–1174.
(6) Dunham, G.E.; Miller, S.J.; Laudal, D.L. *Investigation of Sorbent Injection for Mercury Control in Coal-Fired Boilers*; Final Report for EPRI and DOE; Energy & Environmental Research Center: Grand Forks, ND, Sept 1998.
(7) Dunham, G.E.; Olson, E.S.; Miller, S.J. Impact of Flue Gas Constituents on Carbon Sorbents. In *Proceedings of the Air Quality II: Mercury, Trace Elements, and Particulate Matter Conference*; McLean, VA, Sept 19–21, 2000; Paper A4-3.
(8) Miller, S.J.; Dunham, G.E.; Olson, E.S. Controlling Mechanisms That Determine Mercury Sorbent Effectiveness. In *Proceedings of the Air & Waste Management Association 92nd Annual Meeting & Exhibition*; St. Louis, MO, June 20–24,1999; Paper 99-898.
(9) Olson, E.S.; Sharma, R.K.; Miller, S.J.; Dunham, G.E. Identification of the Breakthrough Oxidized Mercury Species from Sorbents in Flue Gas. In *Proceedings of the Specialty Conference on Mercury in the Environment*; Minneapolis, MN, Sept 15–17, 1999; pp 121–126.
(10) Benson, S.A.; Olson, E.S.; Crocker, C.R.; Pavlish, J.H.; Holmes, M.J. Mercury Sorbent Testing in Simulated Low-Rank Coal Flue Gases. Presented at the 6th Electric Utilities Environmental Conference, Tucson, AZ, Jan 27–30, 2003.
(11) Crocker, C.R.; Benson, S.A.; Olson, E.S.; Pavlish, J.H.; Holmes, M.J. Surface Compositions of Carbon Sorbents Exposed to Simulated Low-Rank Coal Flue Gases. In *Proceedings of the Air & Waste Management Association 96th Annual Meeting & Exhibition*; San Diego, CA, June 22–26, 2003; Paper 69886.
(12) Coughlin, R.W.; Ezra, F.S. *Environ. Sci. Technol.* **1968**, *2* (4), 291–297.
(13) Tessmer, C.H.; Vidic, R.K.; Uranowski, L. *J. Environ. Sci. Technol.* **1997**, *13* (7), 1872.
(14) Liu, W.; Vidic, R.K.; Brown, T.D. *Environ. Sci. Technol.* **2000**, *34* (1), 154–159.
(15) Ghorishi, S.B.; Keeney, R.M.; Serre, S.D.; Gullett, B.K.; Jozewicz, W.S. *Environ. Sci. Technol.* **2002**, *36*, 4454–4459.
(16) Otanik Y.; Emi, H.; Kanoaka, I.; Nishiro, H. *Environ. Sci. Technol.* **1988**, *22*, 708–711.
(17) Krishnan, S.V.; Gullett, B.K.; Jozewicz, W. *Environ. Sci. Technol.* **1994**, *28*, 1506–1512.
(18) Vidic, R.D.; McLaughlin, J.B. *J. Air Waste Manage. Assoc.* **1996**, *46*, 241–250.
(19) Liu, W.; Vidic, R.D.; Brown, T.D. *Environ. Sci. Technol.* **1998**, *32*, 531–538.
(20) Laumb, J.D.; Benson, S.A.; Olson, E.A. X-ray Photoelectron Spectroscopy Analysis of Mercury Sorbent Surface Chemistry. In *Proceedings of Air Quality III: Mercury, Trace Elements, and Particulate Matter Conference*; Arlington, VA, Sept 9–12, 2002.
(21) Dunham, G.E.; Olson, E.S.; Miller, S.J. Impact of Flue Gas Constituents on Carbon Sorbents. In *Proceedings of the Air Quality II: Mercury, Trace Elements, and Particulate Matter Conference*; McLean, VA, Sept 19–21, 2000; Paper A4-3.
(22) Bustard, J.; Durham, M.; Starns, T.; Lindsey, C.; Martin, C.; Schlager, R.; Baldrey, K. Full-Scale Evaluation of Sorbent Injection for Mercury Control on Coal-Fired Power Plants. In *Proceedings of Air Quality III: Mercury, Trace Elements, and Particulate Matter Conference*; Arlington, VA, Sept 9–12, 2002.
(23) Widmer, N.C.; West, J.; Cole, J.A. Thermochemical Study of Mercury Oxidation in Utility Boiler Flue Gases Presented at the Air & Waste Management Association 93rd Annual Meeting & Exhibition, Salt Lake City, UT, June 18–22, 2000, Paper No. 390.
(24) Mamani-Paco, R.M.; Helble, J.J. Bench-Scale Examination of Mercury Oxidation under Non-Isothermal Conditions. Presented at the Air & Waste Management Association 93rd Annual Meeting & Exhibition, Salt Lake City, UT, June 18–22, 2000.
(25) Sliger, R.N.; Kramlich, J.C.; Marinov, N.M. Towards the Development of a Chemical Kinetic Model for the Homogeneous Oxidation of Mercury by Chlorine Species. *Fuel Process. Technol.* **2000**, *65–66*, 423–438.
(26) Niksa, S.; Helble, J.J.; Fujiwara, N. Kinetic Modeling of Homogeneous Mercury Oxidation: The Importance of NO and H_2O in Predicting Oxidation in Coal-Derived Systems. *Environ. Sci. Technol.* **2001**, *35*, 3701–3706.
(27) Edwards, J.R.; Srivastava, R.K.; Kilgroe, J.D. A Study of Gas-Phase Mercury Speciation Using Detailed Chemical Kinetics. *J. Air Waste Manage. Assoc.* **2001**, *51*, 869–877.
(28) Wang, J.; Cobb, Jr.; J.T.; Elder III, W.W. Study of Mercury Oxidation in the Post-Combustion Zones of Coal-Fired Boilers. Presented at the American Chemical Society Annual Meeting, Chicago, Il, Aug 2001.
(29) Pavlish, J.H.; Holmes, M.H.; Galbreath, K.C.; Zhuang, Y.; Pavlish, B.M. Pilot-Scale Investigation of Mercury Control Technologies for Utilities Burning Lignite Coal. Presented at the Combined Power Plant Air Pollutant Control Mega Symposium, Washington, DC, May 19–22, **2003**.

Novel Nanoporous Sorbents for Removal of Mercury

Shas V. Mattigod, Glen E. Fryxell, Richard Skaggs, and Kent E. Parker

Pacific Northwest National Laboratory, Richland, Washington, 99352, U.S.A

Introduction

There is a significant need for a technology to effectively remove mercury from aqueous effluents of coal-fired power plants such as, blow down water, wet scrubber effluents, and ash pond waters. These effluents typically contain high concentration of dissolved major and dissolved toxic constituents, and exhibit a wide range of pH values (~4 – 12 SU). During the last few years, we have designed and developed a new class of high-performance sorbent material for removing toxic constituents such as mercury from water and waste water. This novel material is created from a combination of a synthetic nanoporous ceramic substrate that had a specifically tailored pore size (~6.5nm) and very high surface areas (~900 m^2/g) with self-assembled monolayers of well-ordered functional groups that have high affinity and specificity for specific types of free or complex cations or anions. Detailed descriptions of the synthesis, fabrication, and adsorptive properties of these novel materials have been published previously[1-3]. We conducted a series of tests to evaluate the effectiveness of a synthetic novel sorbent for removing mercury from coal-fired power plant effluents.

Experimental

The novel substrates were prepared *via* a surfactant templated synthesis. The resulting siliceous structure was calcined to obtain a ceramic substrate with average pore size of 6.5 nm. Mercury is a very soft Lewis acid, and hence, both kinetically and thermodynamically "prefers" to undergo reaction with soft bases, such as thiols. Therefore, we functionalized the pores of the substrate with self-assembled monolayers of alkylthiols (Figure 1). The resulting mercury-specific adsorbent (thiol-SAMMS – thiol Self Assembled Monolayers on Mesoporous Silica) was tested to evaluate its adsorption capacity, specificity, and kinetics. Tests were conducted to: 1) evaluate the adsorption performance over a range of pH and ionic strengths of contacting solution, 2) determine the effects of equimolar concentrations competing cations on Hg-adsorption at two different pH values and, 3) assess the leachability of mercury-loaded SAMMS material using the Toxicity Characteristics Leaching Procedure (TCLP) of U. S. Environmental Protection Agency (USEPA).

A bench-scale treatability test was conducted to evaluate the mercury adsorption performance of thiol-SAMMS from a condensate waste stream. The principal dissolved components in this alkaline waste stream (pH: 8.5) consisted of mainly sodium borate (~30 mM), and sodium fluoride (~9 mM) with minor concentrations of sodium chloride(~3 mM), sodium nitrite (~0.9mM), sodium sulfate (~0.8mM), sodium nitrate (~0.6mM) and sodium iodide (~0.2 mM),. The mercury concentration in solution was measured to be 4.64 mg/L. Trace concentrations (<2 mg/L) of Al, Ba, Ca, Cd, Co, Cr, Cu, Fe, Mo, Ni, PO_4, Pb and Zn were also detected in this waste stream. To test the effectiveness of thiol-SAMMS in adsorbing mercury from this complexing matrix, thiol-SAMMS (Solution to solid ratio 1250 ml/g) was reacted with the waste solution for 8 hours.

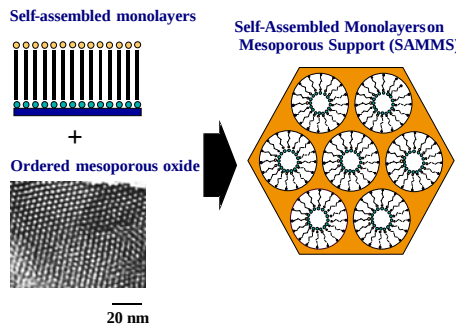

Figure 1. Technological basis of novel nanoporous sorbents

Results and Discussion

Adsorption of mercury by thiol-SAMMS showed a good fit to Langmuir isotherm (Figure 2). From the fitting parameters, the adsorption maximum was calculated to be 625 mg of Hg/g of sorbent, and the Langmuir constant was estimated to be 0.107 l/mg.

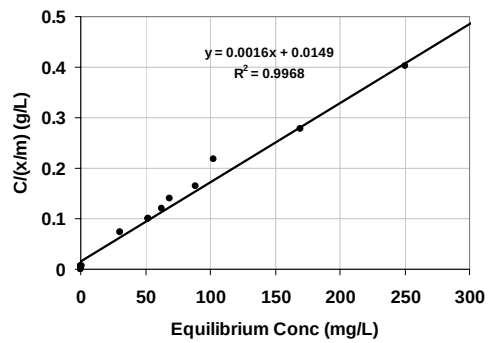

Figure 2. Langmuir Isotherm for Hg Adsorption by thiol-SAMMS

The kinetic data indicated (Figure 3) that adsorption was relatively rapid with ~99% dissolved mercury being adsorbed within the initial five minutes. Results of the TCLP (Toxicity Characteristics Leaching Procedure) tests indicated that Hg-adsorbed by the thiol-SAMMS was highly resistant to leaching (Figure 4).

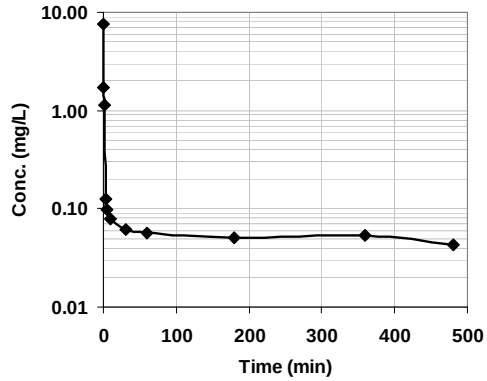

Figure 3. Kinetics of Hg Adsorption by thiol-SAMMS

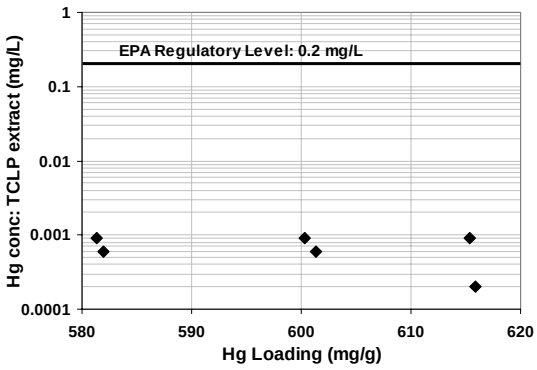

Figure 4. Leach Resistance of Hg-loaded thiol-SAMMS

Variation in pH or ionic strength did not significantly affect the Hg-adsorption affinity of thiol-SAMMS substrate (Table 1). The data showed (Table 2) that the presence of equimolar concentrations of competing cations at both pH values (4 and 7) did not significantly affect the specific adsorption of mercury. These data confirmed that mercury-thiol interaction being a soft acid-base interaction is both kinetically and thermodynamically a preferred reaction thus would not be significantly affected by pH, and the presence of competing cations in solution.

Table 1. Effect of pH and Ionic Strength

pH	K_d (ml/g)	$NaNO_3$(M)	K_d (ml/g)
2	$9.9x10^5$	0.0	$5.5x10^7$
3	$1.4x10^6$	0.1	$3.5x10^7$
4	$1.7x10^7$	0.3	$3.3x10^7$
5	$1.7x10^7$	0.6	$2.4x10^7$
7	$3.9x10^7$	2.0	$5.5x10^7$
8	$4.8x10^7$	3.0	$5.3x10^7$
10	$7.6x10^6$	4.0	$5.6x10^7$

Table 2. Effect of pH and Competing Cations

pH	Cations	K_d (ml/g)
4	Na	$1.5x10^7$
4	Ca, Cu(II), Fe(II), Pb	$1.0x10^7$
4	Ca, Cd, Cu(II), Fe(II), Ni, Pb, Zn	$1.0x10^7$
7	Na	$3.9x10^7$
7	Ca, Cu(II), Fe(II), Pb	$1.1x10^7$
7	Ca, Cd, Cu(II), Fe(II), Ni, Pb, Zn	$4.5x10^7$

The data from the bench scale test of the condensate waste stream indicated that thiol-SAMMS had adsorbed ~98.9% of the mercury initially present in this solution (residual mercury concentration 0.052 mg/L). This solution contained ~0.2 mM of iodide, a strong mercury complexing ligand and the speciation calculations indicated that all the soluble mercury existed in the form of iodide complexes (HgI_2^0: ~52%; HgI_3^-: ~47%, and HgI_4^{2-}: ~1%). These results confirmed previous observation[4] that thiol-SAMMS can effectively remove iodide-complexed mercury from solutions.

Acknowledgement. This study was supported by the Office of Science and Technology of the U. S. Department of Energy**.** Pacific Northwest National Laboratory is operated for the U. S. Department of Energy by Battelle under contract DE-AC06-76RLO 1830.

References

(1) Feng, X.; Fryxell, G. E.; Wang, L. Q.; Kim, A. Y.; Liu, J.; and Kemner, K. M. *Science;***1997**, 276, 923-926.
(2) Fryxell, F. E.; Liu, J.; Hauser, A. A.; Nie, Z.; Ferris, K. F.; Mattigod, S. V.; Gong, M.; and Hallen. R. T. *Chem. Mat.* **1999**, 11, 2148-2154.
(3) Fryxell, G. E; Liu, J.; and S.V. Mattigod. *Mat. Tech. & Adv. Perf. Mat.* **1999**, 14, 188-191.
(4) Mattigod, S.V., Feng, X.; Fryxell, G. E.; Liu, J.; and Gong, M. *Sep. Sci. and Tech.* **1999**, 34, 2329-2345.

COMPARISON OF SORBENTS AND FURNACE ADDITIVES FOR MERCURY CONTROL IN LOW-RANK FUEL COMBUSTION SYSTEMS

Charlene R. Crocker, Steven A. Benson, Michael J. Holmes, Ye Zhuang, John H. Pavlish, Kevin C. Galbreath

Energy & Environmental Research Center
University of North Dakota
15 North 23rd Street
Grand Forks, ND 58203

Introduction

North Dakota lignite-fired power plants have shown a limited ability to control mercury emissions in currently installed electrostatic precipitators (ESPs), dry scrubbers, and wet scrubbers (1). This low level of control can be attributed to the high proportions of Hg^0 present in the flue gas. Speciation of mercury in flue gases analyzed as part of the EPA information collection request (ICR) for Hg data showed that Hg^0 ranged from 56% to 96% and the oxidized Hg ranged from 4% to 44%. The Hg emitted from power plants firing North Dakota lignites ranged from 45% to 91% of the total Hg, with the emitted Hg being greater than 85% elemental. The average emitted from North Dakota power plants was 6.7 lb/TBtu (1, 2).

The composition of a coal has a major impact on the quantity and form of Hg in the flue gas and, as a result, on the ability of air pollution control devices (APCDs) to remove Hg from flue gas. In general, North Dakota lignite coals are unique because of a highly variable ash content, ash that is rich in alkali and alkaline-earth elements, with high oxygen levels, high-moisture levels, and low chlorine content. Experimental results indicate that low-chlorine (<50-ppm) coal combustion flue gases (typical of North Dakota lignite) contain predominantly Hg^0, which is substantially more difficult to remove than Hg^{2+} (3). The generally high calcium contents of lignite coals may reduce the oxidizing effect of the already low chlorine content by reactively scavenging chlorine species (Cl, HCl, and Cl_2) from the combustion flue gas. The level of chlorine in flue gases of recently tested North Dakota and Saskatchewan lignites ranged from 2.6 to 3.4 ppmv, with chlorine contents ranging from 11 to 18 ppmw in the coal on a dry basis, respectively.

The technologies utilized for the control of Hg will ultimately depend upon the EPA-mandated emission limits. The strategies include sorbent injection with and without enhancements upstream of an ESP or fabric filter (FF) and Hg oxidation upstream of a wet or dry flue gas desulfurization system (FGD). The new technologies being investigated include Hg capture using the Energy & Environmental Research Center's (EERC) advanced hybrid particulate collector (AHPC) or the *Advanced Hybrid*™ gold-coated materials, baghouse inserts, and carbon beds (4).

Sorbent injection for removing Hg involves adsorption of Hg species by a solid sorbent injected upstream of a particulate control device such as a FF (baghouse) or ESP. Many potential Hg sorbents have been evaluated (4). These evaluations have demonstrated that the chemical speciation of Hg controls its capture mechanism and ultimate environmental fate. Activated carbon injection is the most mature technology available for Hg control. Activated carbons have the potential to effectively sorb Hg^0 and Hg^{2+} but depend upon the carbon characteristics and flue gas composition (4). The projected annual cost for activated carbon adsorption of Hg in a duct injection system is significant. Carbon-to-mercury weight ratios of 3000:18,000 (lb carbon injected/lb Hg) in flue gas have been estimated to achieve 90% Hg removal from a coal combustion flue gas containing 10 $\mu g/Nm^3$ of Hg (5).

Mercury oxidation technologies being investigated for Fort Union lignites include catalysts, chemical agents, and cofiring materials. The catalysts that have been tested include a selective catalytic reduction (SCR) catalyst for NO_x reduction, noble metal-impregnated catalysts, and oxide-impregnated catalysts. The chemical agents include chlorine-containing salts and cofiring fuels that contain oxidizing agents (6).

Mercury oxidation catalysts have shown high potential to oxidize Hg^0. Results in testing a slipstream at a North Dakota power plant indicated over 80% conversion to oxidized Hg for periods of up to 6 months (6). Tests were also conducted using iron oxides and chromium, with little success of oxidation. Galbreath and others (7) have conducted short-term pilot-scale testing with maghemite (γ-Fe_2O_3) additions and were able to transform about 30% of the Hg^0 in North Dakota lignite combustion flue gases to Hg^{2+} and/or Hg(p) and, with an injection of a small amount of HCl (100 ppmv), nearly all of the Hg^0 to Hg^{2+}. Theoretically, the use of chloride compounds to oxidize Hg^0 to Hg^{2+} makes sense. The evidence includes chemical kinetic modeling of bench-scale test results indicating that the introduction of chloride compounds into the high-temperature furnace region will most likely result in the production of atomic chlorine and/or molecular chlorine, which are generally thought to be the dominant Hg^0 reactants in coal combustion flue gases (4).

The overall purpose of this research is to develop advanced, innovative Hg control technologies to reduce Hg emissions by 50% to 90% in flue gases typically found in North Dakota lignite-fired power plants at costs of one-half to three-fourths of current estimated costs. The specific objectives are focused on determining the feasibility of the following technologies: Hg oxidation for increased Hg capture in dry scrubbers and the use of Hg adsorbents with a baghouse.

Experimental

The pilot-scale evaluations of sorbent injection and sorbent-enhancement agents (SEA) were performed using the EERC's particulate test combustor (PTC) equipped with several particulate control options to evaluate Hg sorbent effectiveness in coal combustion flue gases. Initial tests included a comparison of particulate control technologies with the same sorbents and SEAs. The second phase of the research is focused on evaluating various sorbents and SEAs for Hg control effectiveness in conjunction with the ESP-only configuration.

The PTC is a 550,000-Btu/hr (580-MJ/hr) pc-fired unit designed to generate fly ash and flue gas chemistry representative of that produced in a full-scale utility boiler. Coal is introduced to the primary air stream via a screw feeder and ejector. An electric air preheater is used for precise control of the combustion air temperature. The PTC instrumentation permits system temperatures, pressures, flow rates, flue gas constituent concentrations, and baghouse- or ESP-operating data to be monitored continuously and recorded on a data logger. Two PSA Sir Galahad atomic fluorescence-based continuous mercury monitors (CMMs) were located upstream of the sorbent injection point and at the particulate control device outlet to monitor Hg vapor concentrations continuously throughout the tests. Wet chemistry samples were collected using ASTM Method D6784 (Ontario Hydro Method) to verify CMM measurement and performance of the sorbents with SEA injection.

Freedom coal with a mean Hg content of 0.05 $\mu g/g$ was combusted at the nominal rate of 80 lb/hr. Based on the CMM data, the total Hg vapor concentration (Hg_{gas}) upstream of sorbent injection varied from 7.0 to 9.2 $\mu g/m^3$. The mean flue gas stream Hg level was 7.6 ± 0.5 $\mu g/m^3$ in dry flue gas, 3% O_2. The mean elemental Hg vapor content (Hg^0) was about 6.8 $\mu g/m^3$.

Two forms of Hg removal were evaluated—sorbent injection only and sorbent injection with SEAs. SEAs were added to the coal prior to introduction to the furnace. Sorbents were injected upstream of the ESP using a dual-screw K-Tron feeder. The feeder was calibrated prior to the start of sorbent injection. In addition, the weight of sorbent added during a day was divided by the time of injection to provide a mean feed rate. Average feed rates ranged from 3.75 to 15 lb C/MMacf.

Results and Discussion

The results of the addition of materials with coal at very low levels along with the activated carbon injection (Norit DARCO FGD®) upstream of an ESP–FF (TOXECON™), *Advanced Hybrid*™ filter, and ESP only are illustrated in Figure 1. The first part of the figure shows the baseline data for Hg emissions ranging from 9 to 12 μg/Nm^3, with 80% to 90% of the Hg in the elemental form. The second case is activated carbon injection alone and with the addition of SEA 2, showing a reduction in Hg emissions to 90% removal. The third case is the *Advanced Hybrid*™ filter alone and with the addition of SEA 2, which produced nearly 90% control efficiency. The final ESP-only case also indicated up to 90% control. The control efficiency for the ESP-only case showed significant potential improvement over past results obtained with the ESP only. All three configurations performed significantly better in Hg control with the combination of sorbent injection and SEAs added to the feed coal.

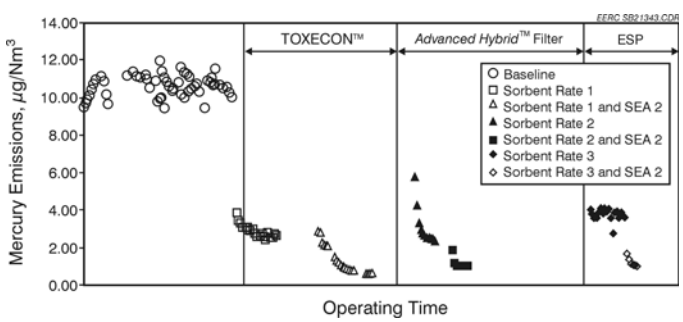

Figure 1. Mercury emissions for activated carbon injection combined with an SEA additive using various particulate control devices.

The second phase of testing included activated carbon sorbent injection and SEA upstream of an ESP for control of Hg emissions from North Dakota lignite. The testing was conducted using the EERC PTC equipped with an ESP only. The results of the first tests are illustrated in Figure 2. Figure 2 shows the inlet total Hg level at 9 μg/m^3 and baseline outlet (initial and final) at 7.2 μg/m^3. Norit DARCO FGD® activated carbon was injected at 3.75 and 15 lb C/MMacf, resulting in 50% to 60% Hg reduction. The addition of SEA with the coal and injection of 3.75 lb C/MMacf resulted in a reduction of over 70% of the Hg emissions.

Conclusions

The comparison tests show that Hg emissions from lignite-fired combustion systems can be reduced significantly using a variety of particulate control devices. Two different ESP–baghouse combinations and the ESP-only configuration were capable of controlling up to 90% of the gaseous Hg emissions when activated carbon sorbent injection was combined with Hg oxidant addition to the coal. This is particularly significant in the case of the ESP-only configuration, as many of the lignite-burning units are currently equipped with this configuration. This technology also has the potential to improve dry FGD baghouse control efficiency. While the

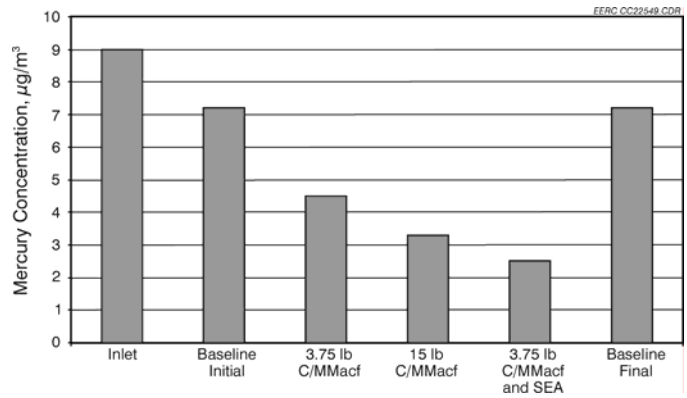

Figure 2. ESP mercury concentrations as a function of sorbent and SEA additive for a North Dakota lignite.

results to date demonstrate effective Hg removal across the ESP, optimization of sorbents and SEA types and the addition ratios is essentially to develop the most cost-effective plan for controlling Hg emissions.

Acknowledgment. This research was prepared with the support of the U.S. Department of Energy (DOE) National Energy Technology Laboratory Cooperative Agreement No. DE-FC26-03NT41897, the Mercury Task Force—the Industrial Commission of North Dakota, Otter Tail Power Company, Basin Electric Power Cooperative, Minnkota Power Cooperative, Inc., Great River Energy, Montana–Dakota Utilities Company, Dakota Westmoreland Corporation, BNI Coal, The North American Coal Corporation—ADA Technologies Inc., Babcock & Wilcox, ALSTOM Power, Haldor Topsoe, Inc., and W.L. Gore &Associates, Inc.

References

(1) Pavlish, J.H.; Holmes, M.J.; Benson, S.A.; Crocker, C.R.; Galbreath, K.C. Mercury Control Technologies for Utilities Burning Lignite Coal. In *Proceedings of Air Quality III, Mercury, Trace Elements, and Particulate Matter Conference*; Arlington, VA, Sept 10–12, 2002; Energy & Environmental Research Center: Grand Forks, ND, **2002**.

(2) Chang, R.; Strohfus, M. *The Evaluation of Chemical Additives for Mercury Emission Control at Great River Energy*; Final Report to the North Dakota Industrial Commission; Jan **2003**.

(3) Felsvang, K.; Gleiser, R. Juip, G.; Nielsen, K.K. Activated Carbon Injection in Spray Dryer/ESP/FF for Mercury and Toxics Control. *Fuel Process. Technol.* **1994**, 39, 417–430.

(4) Pavlish, J.H.; Sondreal, E.A.; Mann, M.D.; Olson, E.S.; Galbreath, K.C.; Laudal, D.L.; Benson, S.A. Status Review of Mercury Control Options for Coal-Fired Power Plants. *Fuel Process. Technol*., **2003**, *82*, (2–3), 89–165.

(5) Pavlish, J.H.; Holmes, M.J.; Benson, S.A.; Crocker, C.R.; Galbreath, K.C. Mercury Control Technologies for Utilities Burning Lignite Coal, In *Proceeding of Air Quality III, Mercury, Trace Elements, and Particulate Matter Conference*; Sept 9–12, **2002**

(6) Sjostrom, S.; Richardson, C.; Chang, R. *Evaluation of Mercury Emissions and Control Options for Great River Energy*; Final Report for North Dakota Industrial Commission, June **2001**.

(7) Zygarlicke, C.J.; Galbreath, K.C.; Toman, D.L. Coal Combustion Mercury Transformations. Presented at the Air Quality II: Mercury Trace Elements, and Particulate Matter Conference, McLean, VA, Sept 19–21, **2000**.

MERCURY CONTROL USING COMBUSTION STAGING

Vitali Lissianski, Peter Maly, Randy Seeker, and Loc Ho

Energy and Environmental Research Corporation (EER)
18 Mason, Irvine, CA 92618

Introduction

In December 2000, the U.S. EPA reported that mercury (Hg) emissions from coal-fired power plants pose significant hazards to public health and must be reduced. The EPA is under court order to propose Hg regulations for coal-fired power plants in 2003 and finalize them in 2004. Present regulatory mechanisms require that such regulations be developed through Maximum Achievable Control Technology (MACT). Several other frameworks for Hg regulations have been proposed recently. The Clear Skies Initiative proposed by President Bush mandates dramatic reductions in power plant SO_2, NO_x, and Hg emissions over the next 15 years. Independent of the EPA's final decision regarding the required level of Hg control, important questions that need immediate answers are (1) what technologies can provide a significant level of Hg removal and (2) can a significant level of Hg removal be achieved for all coal types?

Many utilities are actively seeking effective and inexpensive technologies for controlling multiple pollutants emitted from power plants. Recent experimental data[1,2,3] obtained by EER demonstrated the reduction of Hg emissions through the use of fly ash with high carbon content formed *"in situ"* in the combustion process of coal-based power generating stations. High-carbon fly ash can be formed by low NO_x burners (LNB), overfire air (OFA) injection or in coal reburning. These commercial technologies are currently used to reduce NO_x emissions from coal-fired power plants.

This paper further investigates potential of using high carbon fly ash for Hg control. Objective of this work was to investigate effects of carbon in ash, coal composition, and temperature on the efficiency of Hg removal.

Experimental Facility

Tests on utilization of "in-situ" formed high-carbon fly ash to remove Hg from flue gas were conducted in Boiler Simulator Facility (BSF) described elsewhere[4]. The BSF has a full load firing capacity of 1×10^6 Btu/hr and is designed to provide an accurate sub-scale simulation of the flue gas temperatures and composition found in a full-scale boiler. A schematic of the BSF and setup for Hg sampling are shown in Figure 1. The BSF consists of a burner, vertically down–fired radiant furnace, horizontal convective pass, and ESP. A variable swirl diffusion burner with an axial fuel injector is used to simulate the approximate temperature and gas composition of a commercial burner in a full-scale boiler. Numerous ports located along the axis of the facility allow access for supplementary equipment such as reburning and OFA injectors, and sampling probes.

The cylindrical furnace section is constructed of eight modular refractory lined sections with an inside diameter of 22 inches. The convective pass is also refractory lined, and contains air cooled tube bundles to simulate the superheater and reheater sections of a utility boiler. Heat extraction in the radiant furnace and convective pass can be controlled such that the residence time-temperature profile matches that of a typical full-scale boiler. A suction pyrometer is used to measure furnace temperatures.

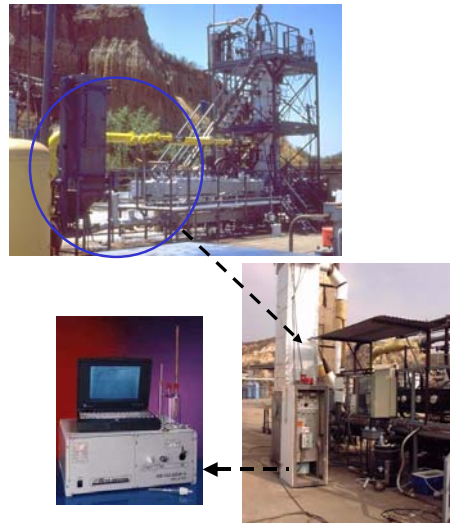

Figure 1. Boiler Simulator Facility.

High-carbon fly ash was formed using air staging. An online Hg analyzer from PS Analytical was used in these tests. The analyzer is capable measuring both total (Hg) and elemental (Hg^0) mercury in flue gas. Mercury concentration in flue gas was measured at ESP inlet and outlet. The ESP for the BSF is a single-field down-fired unit consisting of 12 tubes with axial corona electrodes. The ESP flue gas temperature was controlled by inserting or removing cooling rods situated in the convective pass.

Experimental Results

Objective of pilot-scale testing were to determine effects of combustion staging and ESP temperature on efficiency of Hg removal by fly ash. Tests were conducted with several bituminous coals. Carbon in fly ash (characterized as LOI) was adjusted by staging combustion. Two approaches to stage combustion were used – air staging (overfire air injection or OFA) and fuel staging (reburning). In air staging part of the combustion air is redirected from the main combustion zone into post-combustion zone (overfire zone). Because fuel combustion in air staging occurs in fuel-rich environment, fly ash tends to have higher carbon content than that at typical combustion conditions. Process variables in air staging tests included location of overfire air injection and stoichiometric ratio in the main combustion zone (SR_1). Stoichiometric ratio at the furnace exit (SR_3) in all tests was 1.16 which corresponded to about 3% excess air in flue gas.

In reburning part of the fuel (typically 10-30% of total) is injected above the existing burner zone to produce a slightly fuel-rich environment. Overfire air is injected downstream of the reburning zone to complete fuel combustion. Process variables in reburning tests were amount of the reburning fuel and the flue gas temperature T_{OFA} at which overfire air was injected (T_{OFA} was in the range of 1800-2500 ^oF). The latter was achieved by changing location of the overfire air injection port.

Figure 2 shows dependence of Hg removal efficiency (defined as a difference between Hg introduced with coal and Hg concentration in the gas phase at ESP outlet) as a function of LOI in air staging. Temperature of flue gas in ESP in these tests was 350 ^oF. Figure 2 demonstrates that mercury removal efficiency increases with LOI increase. Efficiency of Hg removal also depends on coal properties, especially for LOI up to 4%. Maximum Hg removal efficiency achieved in air staging tests was ~60%.

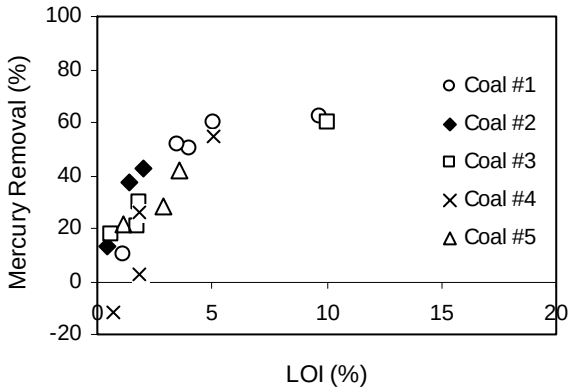

Figure 2. Effect of LOI on Hg removal in air staging.

Figure 3 shows effects of LOI and ESP temperature on Hg removal in reburning for coal#3. Figure 3 demonstrates that efficiency of Hg removal increases with increase in LOI and decrease in ESP temperature. Maximum Hg removal efficiency achieved in reburning tests was about 85%.

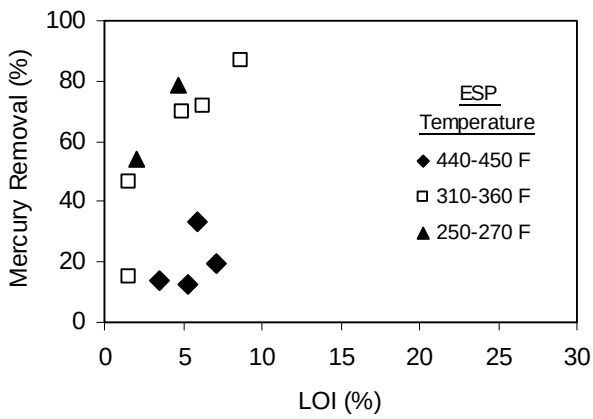

Figure 3. Effect of LOI on Hg removal in air staging for coal #3.

Consol studied[5] effect of ESP temperature on Hg removal on Hg adsorption on fly ash. In these tests high carbon fly ash generated by combustion of bituminous coal was re-injected into the duct of 1.5 MBtu/hr combustor. The flue gas temperature was controlled using both duct humidification and the pilot plant heat exchange. Amount of re-injected fly ash was similar to that generated by combustion of a bituminous coal. Results of the Consol study were combined with present data to determine dependence of Hg adsorption on temperature. Based on these data, transfer function was developed that predicted dependences of the efficiency of Hg adsorption on fly ash on LOI and temperature. Figure 4 shows results of the present and Consol studies (symbols) as well as predictions of the transfer function (lines). Figure 4 shows good agreement between experimental data and modeling predictions.

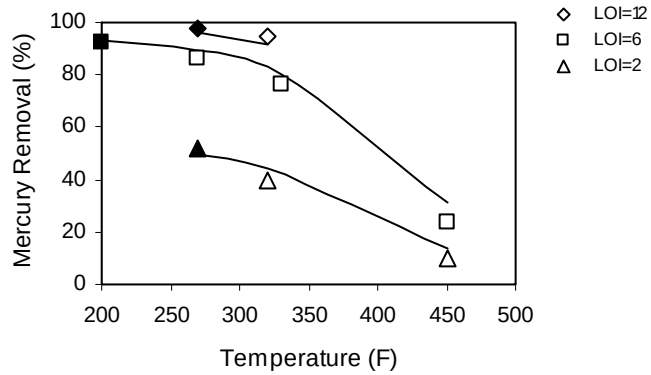

Figure 4. Experimental data (symbols) and modeling predictions (lines) on the effect of temperature on Hg adsorption of fly ash. Solid symbols represent Consol data, open symbols present study.

Figure 5 shows comparison of experimental data for reburning (Figure 3) adjusted to 350 ^{o}F using transfer function with predictions of the transfer function. Figure 5 demonstrates relatively small scatter of experimental data. It also demonstrates that about 80% Hg adsorption on fly ash can be expected at LOI 7-9% and ESP temperature of 350 ^{o}F.

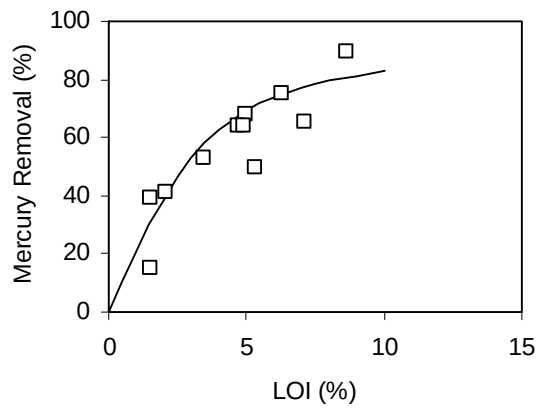

Figure 5. Comparison of experimental data and modeling predictions on the effect of LOI on Hg removal at 350 ^{o}F.

Figure 6 shows predicted by transfer function effect of temperature on Hg adsorption on fly ash. Figure 6 suggests that both temperature and LOI should be considered in selecting optimum conditions for Hg removal: LOI change in the range of 2-8% offers most significant effect on Hg removal. LOI increase to 12% gives only marginal improvement in Hg reduction efficiency. Temperature decrease below acid dew point can result in sulfuric acid condensation and duct corrosion. While acid dew point depends on a number of parameters including coal sulfur content, in most cases it is lower that 290 ^{o}F. Figure 6 suggests that Hg removal efficiency at LOI = 8-12% can be 80-90% at temperatures above 290 ^{o}F.

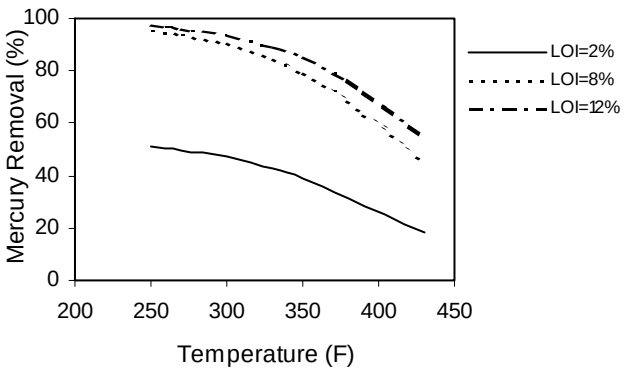

Figure 6. Predicted effect of temperature on Hg removal.

Conclusions

Experimental results confirmed that air staging and reburning could be used to control Hg emissions from coal-fired boilers. Pilot-scale testing demonstrated that this approach can provide 80-90% Hg removal across an ESP for bituminous coals at LOI = 8-12%. Lowering ESP temperatures can further improve Hg removal.

References

(1) Lissianski, V.V., Zamansky, V.M., Maly, P.M., and Seeker, R.W. "Integration of Combustion Modifications with Mercury Control", *Air Quality III Conference*, Washington, DC, September 11, 2002.
(2) Lissianski, V.V., Zamansky, V.M., Maly, P.M., and Seeker, R.W. "Integration of Combustion Modifications with Mercury Control", *Air Quality III Conference*, Washington, DC, September 11, 2002.
(3) Lissianski, V.V., Ho, L., Maly, P., Seeker, W.R., and Zamansky, V.M. "Integration of Combustion Modifications with Mercury Control", *The 2003 EUEC, Tucson, AZ, January 27-30, 2003*
(4) Slaughter, D.M., Chen, S.L., Seeker, W.R., and Pershing, D.W. *Proc. Combust. Inst.*, **1988**, 22, 1155.
(5) Rosenhoover, W.A. Final Technical Report 98-1/1.2B-2, Illinois Coal Combustion Institute, 1999.

ELEGANT ELUSIVE OXIDATION MECHANISM OF MERCURY

Keith Schofield

Materials Research Laboratory, University of California,
Santa Barbara, CA 93106

Introduction

Although the levels of mercury in coal generally are small (0.1-1.0 parts per million by weight (ppmw)), the United States alone currently burns about 900 million tons/year. The problem with combustion or incineration of any material containing traces of mercury is that all the mercury volatizes as atomic elemental mercury and none is retained in any bottom ash. This applies even to crematoria. The behavior stems from its unusual chemistry. Mercury has no condensed phase molecules that are stable above about 600-700 ^{o}C. This is partly why liquid mercury, quicksilver, was discovered in ancient times and is documented by the Phoenicians and Carthaginians. It is easily obtained from its ore cinnabar, HgS, solely by heating in air. Also, the thermal instability of mercuric oxide, HgO, helped Priestley discover oxygen. Even in the gas phase, the only molecule of mercury with significant stability is mercuric dichloride. As a result, what is observed in combustion or other high temperature systems is that the majority of the mercury in the exhaust is atomic. Because of this, and the fact that liquid mercury is very volatile, it is difficult to capture mercury with conventional type ab- or adsorption techniques[1]. Although the formation of the dichloride is thermodynamically favored, there are no direct kinetic channels for its production. Even so, in practice a small and unpredictable fraction of the mercury is exhausted as the dichloride, the two constituting the mass balance of mercury in the system. This partial conversion or oxidation as it is generally referred to, is extremely intriguing and has never been understood. Its important practical significance stems from the fact that whereas atomic mercury is very difficult to capture, the dichloride is readily soluble in water and so can be removed and processed by the already present water scrubbers. Consequently the more mercury present as the dichloride in an exhaust, the less is emitted to the atmosphere.

Extensive gas phase kinetic modeling studies over many years have failed to adequately describe this formation of the dichloride[2] . The dilemma is that its formation has to occur via the monohalide, HgCl. This is chemically weakly bound and will be very short-lived at temperatures much above 400 ^{o}C. Consequently, there are very restrictive constraints imposed on the gas phase chemistry. The temperatures can not be too high or molecular formation is not possible and when they fall low enough the kinetic reaction rates are beginning to freeze because of activation energy barriers. The temperature, time and concentration limitations prove to be very severe in practical combustion systems and the modeling is clearly inadequate in predicting the fractional distribution of mercury between the element and the dichloride. The majority of gas kineticists now acknowledge this fact[3] and conclude that the system is "complex" [4]. In reality, the value of these modeling studies has been two-fold. Firstly, they have established that the gas phase chemistry can only be marginally involved, if at all, in the conversion of atomic mercury to its dichloride. Secondly, they provide a useful reminder to all of us not to hold too firmly to preconceived ideas.

Full-scale combustor observations have never been able to correlate the observed fractional conversion to the dichloride with any operational parameter. Recently, however, it has been increasingly clear that blowing fly ash or particles into the flue gases does enhance the production of the dichloride[5].

A very recent review assesses the current status of all the control options currently being tested by the coal industry[1]. However, the conclusion remains that no method has yet proven to be generally successful or economically attractive.

In previous studies in this laboratory it was found if sodium and sulfur are present in flame gases at very low levels (ppmv) that sodium sulfate forms very efficiently not in the burned gases but on any cooler surface intercepting the flow[6,7]. The reduced dimensionality of the surface, 2-D instead of that of the 3-D gas phase, appears to be very important in facilitating the process as well as changing the chemistry from the gas phase to the condensed phase regime. It was also noted in that work that concepts such as dew point lose all meaning. Because of this experience, and having the experimental system available, it was decided to run test experiments with mercury. These introduced low levels of mercury (ppmv), sulfur and chlorine into flames, the burned gases of which were then intercepted by a cooled probe at various temperatures.

Experimental

Deposition Methods

Cylindrical propane or hydrogen, oxygen, nitrogen flames have been burned on a well-characterised flat flame burner. Mercury was introduced as a fine aqueous aerosol of either its nitrate or acetate solution from an ultrasonic nebulizer such that its flame concentration was in the range of 5-30 ppmv[6-8]. Small quantities of SO_2, HCl or Cl_2 could be added from certified gas mixtures, or alternately via the nebulizer in the form of their appropriate salt solutions. Several cylindrical collection probes were used of either Inconel-600 stainless steel or tightly clad with platinum foil. Air or water internally cooled these and a thermocouple was built into their wall thickness.

Two types of experiments have been accomplished. Those in the hotter burned gases used cooled probes. Such studies are highly quantitative and have resolved the nature of mercury's heterogeneous chemistry and its dependence on the variables in the system. Important additional experiments that relate to cooler downstream flue gas temperatures and industry also were undertaken to simulate the mercury behavior in practical systems. In these cases the probe was located downstream where the burned gas temperature has decayed to about 200 ^{o}C or less. In such experiments an electrically internally heated collection probe was used to maintain a desired probe surface temperature.

Characterization Methods

Four powerful modern analytical systems have helped to fully characterize these observed deposits. These are a Nicolet Fourier Transform Raman Spectrometer, a Bruker High Temperature Powder x-ray Diffractometer, a Thermo Jarrell Ash Inductively Coupled Plasma/Atomic Emission Spectrometer (ICP/AES), and a Mettler Thermogravimetric Analyser. By this means the chemical composition of deposits and their quantitative rates of deposition have been accurately measured. In all, over two hundred experiments now have been studied involving mercury deposition.

Results

From the very first experiment, it was apparent that mercury has a significant propensity for heterogeneous deposition. Provided that the probe temperatures are within a desirable temperature window, deposits are obtained with a formation efficiency that is essentially the same as with alkali metals. The deposits are molecular in nature. Figure 1 illustrates the Raman spectrum of such a deposit. It is immediately apparent that mercuric sulfate deposition is dominant if sulfur is present in the flame. However, the exact nature of the sulfate depends on the amount of sulfur in the flame. A ratio of sulfur

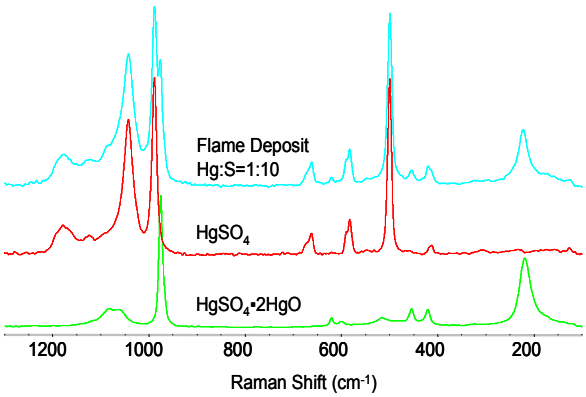

Figure 1. Raman spectrum of a deposit from the burned gases of a propane flame containing traces of mercury (25 ppmv) and sulfur. Compared to spectra of pure samples of mercuric sulfate and its basic sulfate, Schuetteite, $HgSO_4.2HgO$.

to mercury of above 10-fold produces predominantly mercuric sulfate with the basic Schuetteite, $HgSO_4.2HgO$, increasing as the ratio decreases. With no sulfur in the flame a brown deposit results that is pure HgO. These results are validated by auxiliary x-ray analyses of the deposits. As was seen with alkali deposition, the mercury illustrates a preferential ranking that appears to reflect thermodynamic stabilities. On reaching the surface it will make its favored molecule if possible but whether it be sulfate or oxide the rate of deposition remains the same. As indicated in Fig. 2, deposits of sulfate can be obtained in the hot burned gases of a flame over an extended range of temperatures.

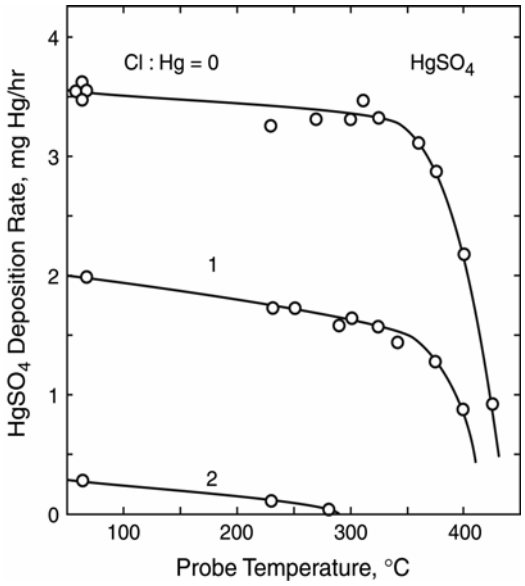

Figure 2. Rates of deposition of $HgSO_4$ as a function of probe temperature and flame chlorine content. Measurements in a fuel lean $C_3H_8/O_2/N_2$; 0.9/5/20 flame 12 ms downstream.

Precise additions of chlorine together with the mercury and sulfur indicate a quantitative reduction of the deposit. Experiments indicate that the chlorine in the flame as HCl vigorously attacks the sulfate deposit converting it to volatile $HgCl_2(g)$ that sublimes back into the gas flows. In normal coal combusters, the levels of impurities generally are S>>Cl>>Hg. As a result, under the right conditions, this heterogeneous conversion will occur naturally. It represents the elusive chemical mechanism missing from models and explains the variability of the amount of $HgCl_2(g)$ observed. Recent analyses

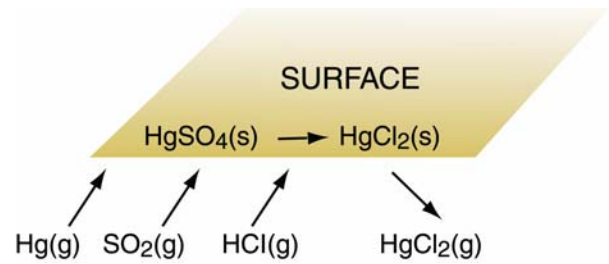

Figure 3. Heterogeneous mechanism whereby gaseous atomic mercury is efficiently converted to gaseous $HgCl_2$.

suggest that the HCl directly ablates $HgCl_2(g)$ from the sulfate and the step through the less stable $HgCl_2(s)$ as indicated does not occur. In this way, the mercury uses the surface as a catalytic means whereby it can satisfy its thermodynamic desire to convert to the stable dihalide.

Flue Gas Measurements and Mercury Control

To confirm the generality of this heterogeneous formation of $HgSO_4$ an internally heated stainless steel probe was positioned downstream in burned gases where mixing had cooled the flows to 200 ^oC or less. Deposits again were obtained however their formation window was narrowed. Temperatures in the range 150-250 ^oC were optimal. Moreover such deposits disappear if chlorine is present in the system. Additionally it is clear that these deposits once formed are stable and are only removed by HCl. They can be converted though to more stable mercury compounds. In other words if a sulfur free system is initially used the deposit is HgO. If a small amount of sulfur is added, this all changes to the basic sulfate and with more sulfur becomes the sulfate. Changes occur up the chain of preferential ranking but once converted the process is irreversible. It is clear that this is a dominant channel and an explanation of the role of fly ash or particle additions. A control method of solely providing adequate surface in the flue gases at the optimal surface temperature and ensuring adequate gas/surface collisions now is recommended[9].

References

(1) Pavlish, J. H.; Sondreal, E. A.; Mann, M. D.; Olson, E. S.; Galbreath, K. C.; Laudal, D. L.; Benson, S. A., *Fuel Process. Technol.* **2003,** 82, 89-165.
(2) Xu, M.; Qiao, Y.; Zheng, C.; Li, L.; Liu, J., *Combust. Flame* **2003**, 132, 208-218.
(3) Fujiwara, N.; Fujita,Y.; Tomura, K.; Moritomi, H.; Tuji, T.; Takasu, S.; Niksa, S., *Fuel* **2002**, 81, 2045-2052.
(4) Laudal, D. L.; Brown, T. D.; Nott, B. R., *Fuel Process. Technol.* **2000**, 65/66, 157-165.
(5) Dunham, G. E.; DeWall, R. A.; Senior, C. L., *Fuel Process. Technol*. **2003**, 82, 197-213.
(6) Steinberg, M.; Schofield, K., *Proc. Combust. Inst.* **1996**, 26, 1835-1843.
(7) Schofield, K., *Combust Flame* **2003**, 133, 147-156.
(8) Steinberg, M.; Schofield, K., *Combust Flame* **2002**, 129, 453-470.
(9) Schofield, K., *U.S. Patent Application No*. 10/429,114, **2003**, May 1.

CARBON DIOXIDE CAPTURE USING AMINE-BASED MOLECULAR ANCHORS ON MULTI WALL CARBON NANOTUBES

Leonard S. Fifield, Glen E. Fryxell, R. Shane Addleman, and Christopher L. Aardahl

Pacific Northwest National Laboratory
P.O. Box 999
Batelle Boulevard
Richland, Washington 99352

Introduction

Carbon dioxide emission from hydrocarbon power plants continues to increase. In fact, atmospheric carbon dioxide levels a century from now are anticipated to exceed twice those of a century ago[1]. Capture and storage/use of carbon dioxide is preferable to directly adding to the carbon dioxide content of the atmosphere.

Solid-state sorbents offer an attractive option for reversible capture of carbon dioxide due to their promise of high operating temperatures and long usage lifetime. Porous materials enabled with carbon dioxide-capturing functionality can provide a high capacity with their large gas-accessible surface areas.

Carbon nanotubes are an appealing option for a high surface area material with large values of thermal conductivity[2]. An option for adding carbon dioxide-capturing capability to carbon nanotubes surfaces without diminishing the desirable thermal properties of the tubes is the use of molecular anchors[3,4]. These bifunctional molecules have an anchor portion that adheres to nanotubes surfaces through hydrophobic and/or pi-stacking interactions and a functional portion to reversibly capture carbon dioxide. Such molecules with pyrene-based anchors have low volatility and high relative thermal stability. Amine-based functional portions of the molecules should enable the temperature-dependent chemical adsorption and desorption of gas-phase carbon dioxide molecules.

Experimental

Molecular Anchor Synthesis. Pyrene methylamine hydrochloride (Aldrich) is coupled with picolinic acid (Aldrich) to form the pyrene methyl picolinimide (PMP) anchor seen in **Figure 1**. Model anchors such as 1-bromoacetyl pyrene and 1-pyrene carboxaldehyde were used as purchased (Aldrich).

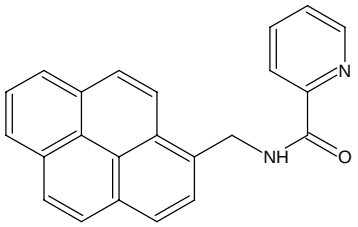

Figure 1. Schematic of bifunctional anchor consisting of pyrene anchor portion and amine carbon dioxide capture portion.

Materials and Deposition. Multi wall carbon nanotubes were used as received (Nanostructured and Amorphous Materials, #1230NMG). Molecular anchors were deposited onto the surfaces of powder-form carbon nanotubes using supercritical fluids. In a typical experiment carbon nanotubes and anchor molecules were mixed and added to a stainless steel vessel, which was placed in a reaction chamber and heated to 150C. The chamber was purged with the reaction gas (propane or carbon dioxide) and sealed. The pressure of the gas in the chamber was then raised to 7500psi using a syringe pump filled with the gas. Mixtures of nanotubes and anchors were held at these conditions for 10 minutes before the reaction fluid/gas was expelled from the system and the vessel was removed from the chamber to cool. Degree of loading of the nanotubes with the anchor molecules was controlled through choice of initial reaction mixture proportions.

Characterization. Presence of anchor molecules on the multi wall carbon nanotubes is confirmed using thermal gravimetric analysis (TGA). Initial attempts at characterizing carbon dioxide uptake of the material have been attempted using a residual gas analyzer (RGA) consisting of a temperature controlled gas flow cell and a mass spectrometer.

Results and Discussion

Carbon nanotubes are seen to be thermally stable when heated in a nitrogen atmosphere to 500C, while pyrene anchors are seen to volatilize and/or decompose resulting in a sample mass loss at around 250C. Degree of anchor loading on the nanotubes can be inferred from the total sample mass loss as seen in **Figure 2**.

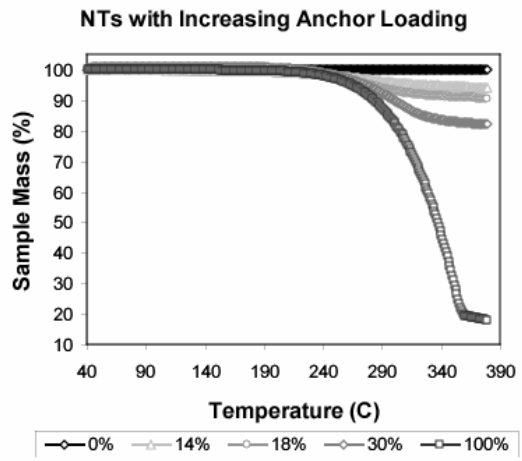

Figure 2. Anchor fraction of sample reaction mixture is seen to track well with TGA mass loss.

Carbon dioxide flowed through a cell containing nanotubes that have been modified with the PMP anchor is seen to adsorb to the material before reaching saturation as see in **Figure 3**.

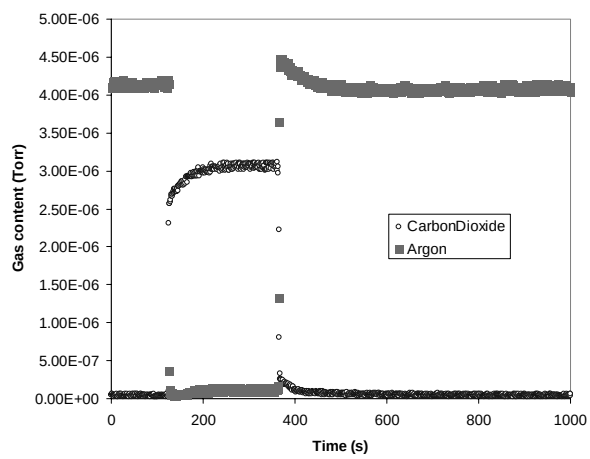

Figure 3. The mass spectrometer in an RGA shows the carbon dioxide breakthrough curve of the PMP anchor loaded onto multi wall nanotubes as flowing argon is switched to a 70% carbon dioxide/nitrogen mix and back.

Conclusions

Carbon nanotubes modified with molecular anchors are pursued as an attractive option for high capacity carbon dioxide sorbent materials. Model compounds based on pyrene anchors have been shown to modify the surface of multi wall carbon nanotubes and can efficiently be deposited using supercritical fluids. A pyrene-based anchor with amine functionality has been synthesized and initial attempts to characterize its effectiveness in capturing carbon dioxide have been made. Determination of the carbon dioxide isotherm of PMP anchors on multi wall carbon nanotubes, as well as the kinetics and magnitude of carbon dioxide uptake on the material, will enable an evaluation of the potential of this material system relative to other carbon dioxide sorbent systems. Alternative amine forms and alternate anchor moieties may be used to optimized performance of the promising molecular anchor on carbon nanotube approach.

Acknowledgement. Grateful acknowledgement is made to Phillip A. Sullivan and Jennifer Craig of the Larry R. Dalton group at the University of Washington Chemistry Department for help in synthesis of the PMP molecular anchor. LF acknowledges fellowship funding from the University of Washington/ Pacific Northwest National Laboratory Joint Institute of Nanoscience and Nanotechnology. The Pacific Northwest National Laboratory is operated by Batelle for the United States Department of Energy.

References

(1) Hoffert, M.I.; Calderia, K.; Benford, G.; Criswell, D.R.; Green, C.; Herzog, H.; Jain, A.K.; Kheshgi, H.S.; Lackner, K.S.; Lewis, J.S.; Lightfoot, H.D.; Manheimer, W.; Mankins, J.C.; Mauel, M.E.; Perkins, L.J.; Schlesinger, M.E.; Volk, T.; Wigley,T.M.L. *Science* **2002**, *298*, 981.

(2) Baughman, R.H., Zakhidov, A.A.; de Heer, W.A. *Science* **2002**, *297*, 787.

(3) Katz, E. *J. Electroanal. Chem.* **1994**, *365*, 157.

(4) Chen, R.J.; Zhang, Y., Wang, D.; Dai, H. *J. Am. Chem. Soc.* **2001**, *123*, 3838.

CO_2 CAPTURE USING ANTHRACITE BASED SORBENTS

Zhong Tang, M. Mercedes Maroto-Valer and Yinzhi Zhang

The Energy Institute and the Department of Energy and Geo-Environmental Engineering, Pennsylvania State University,
209 Academic Projects Bldg., University Park, PA 16802

1. Introduction

Activated carbons are sorbents used in a wide range of household, medical, industrial, military and scientific applications, including gas-phase and liquid-phase processes. The activation process together with the intrinsic nature of the precursors strongly determines the characteristics of the resulting activated carbons. Anthracites have inherent chemical properties, fine structure and relatively low price that make them excellent raw materials for the production of activated carbons [1-5].

New solid-based sorbents are currently being investigated for CO_2 capture. Special attention is being paid to the cost of the sorbent, due to the large amount of sorbent required to control CO_2 emissions. In this work, it is anticipated that high- surface-area powdered anthracites, which have been amine impregnated will satisfy this need and provide a superior low-cost CO_2 sorbent. Accordingly, this paper focuses on the optimization of steam activation of anthracites to produce high surface area activated carbons (AC) and characterize their CO_2 capture capacity.

2. Experimental

2.1 sample characterization and activation. One Pennsylvania anthracite (PSOC-1468) was obtained from the Penn State Coal Bank. Table 1 shows the proximate and ultimate analyses results, as provided by the Penn State Coal Bank. The anthracite was screened and the sample with particle size between 150-250μm was used for producing the activated carbon by steam activation. A fluidized bed was used for the activation experiments. The activation temperature was 850°C, and the steam concentration was 65.8% in the feeding gas stream. The porosity of the samples was characterized by conducting N_2 adsorption isotherms at 77K using a Quantachrome adsorption apparatus, Autosorb-1 Model ASIT. The total pore volume, V_t was calculated from the amount of vapor adsorbed at relative pressure of 0.95, and the total surface area S_t was calculated using the multi-point BET equation in the relative pressure range 0.05-0.35. The micropore (<2nm) size distribution and mesopore (2-50nm) size distribution were calculated by the DFT and BJH methods, respectively.

2.2 CO_2 adsorption/desorption studies. The adsorption and desorption performance of the produced activated anthracites (ACs) was conducted using a PE-TGA 7 thermogravimetric analyzer. The weight change of the adsorbent was followed to determine the adsorption and the desorption performance of the ACs. In a typical adsorption/desorption study, about 20-25mg of the AC was placed in a small platinum pan, heated to 100°C in N_2 atmosphere at a flow rate of 100mL/min, and held at that temperature for 30 minutes. Then the temperature was adjusted to the desired adsorption temperature and 99.8% bone-dry CO_2 adsorbate was introduced at a flow rate of 100mL/min. After adsorption, the gas was switched to 99.995% pure N_2 at a flow rate of 100mL/min to perform the desorption at the same temperature. Adsorption capacity in mg-adsorbate/g-adsorbent and desorption capacity in percentage were used to evaluate the adsorbent, where these values are calculated from the weight change of the sample in the TGA adsorption/desorption process.

3. Results and Discussion

3.1 Effect of activation time on the porosity of the activated anthracites In this study, the activation temperature was selected at 850°C according to previous studies conducted by the authors[5]. The typical isotherms of the resultant activated carbon with different activation time are shown in Figure 1. For comparison, the isotherm of the raw sample is also presented in Figure 1.

Figure 1 shows that the activation dramatically increases the surface area and pore volume of the anthracite. All the isotherms of ACs are Type I according to the BDDT (Brunauer, Deming, Deming, Teller) Classification[6]. This indicates that the ACs made from anthracite have many micropores and only a few mesopores. With increasing activation time, the isotherm shows a more open keen at lower relative pressure of the isotherm, indicating a broader pore size distribution with larger micropores and increasing mesoporosity.

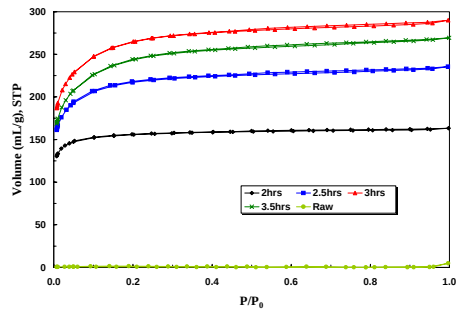

Figure 1. N_2-77K isotherms of the raw anthracite and its steam activated carbons produced at 850°C using different activation times.

Figures 2 and 3 show the micropore and mesopore size distribution of the activated anthracites, respectively. It can be seen that there are no micropores and few mesopores for the raw anthracite. In contrast, after activation, there is a significant amount of mesopores in the ACs (Figures 2 and 3). For the AC after 2 hours activation time, there is a large peak between 0.4-1.0nm. For the ACs produced after 2.5 and 3.0 hours activation time, the peak between 0.4-1.0nm is still there, and there are some additional peaks at 1.6 and 2.0 nm, and also a peak at 2.4 for the AC sample produced after 3 hours steam activation. Furthermore, for the AC sample produced after 3 hours activation time, the largest peak moves to 1.2nm, and the height of the peaks at 1.6, 2.0 and 2.4nm increases. Due to technical limitations of the instrument, it is not possible to get adsorption data at very low relative pressure, and therefore the pore size distribution < 0.4nm cannot be calculated by the DFT method. However, the results indicate that the pore development during activation includes pore opening followed by pore enlargement.

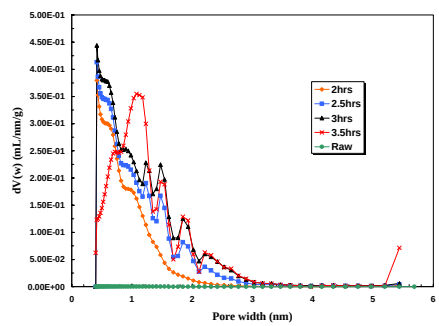

Figure 2. Micropore size distribution of the raw anthracite and its steam activated carbons produced at 850°C using different activation times.

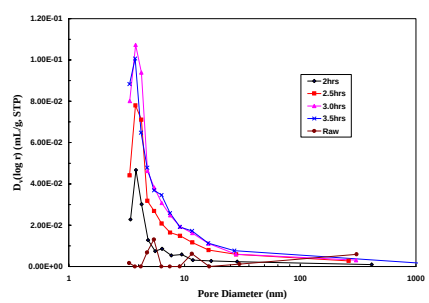

Figure 3. Mesopore size distribution of the raw anthracite and its steam activated carbons produced at 850°C using different activation times.

Figure 3 shows that all the ACs with different activation time have the same mesopore distribution profile. This indicates that the ACs have similar mesopore structure and mesopore size.

The surface areas and pore volumes for the activated carbons produced by steam activation of anthracite are presented in Table 2. It can be seen that the surface and pore volume first increase with increasing activation time and get to a maximum value after 3.0 hours activation (928m^2/g and 0.442mL/g), and then decrease with increasing activation time (855m^2/g and 0.412mL/g for AC with 3.5 hours activation time). However, the ratio of micropore surface area over total surface area and the ratio of micropore volume over total pore volume keep decreasing with increasing activation time. For instance, the ratio of micropore surface area decreases from 98.0% to 95.3%, when increasing the activation time from 2 to 3.5 hours. Similarly, the ratio of micropore volume to total pore volume decreases from 95.6% to 90.3% when increasing the activation time from 2 to 3.5 hours. This indicates that larger pores were produced with increasing activation time.

3.2 CO_2 adsorption/desorption of the activated anthracites Table 3 lists the CO_2 adsorption and desorption results of the ACs at 30 and 75°C. Because the CO_2 adsorption is mainly a physical process, the adsorption capacity decreases with increasing adsorption temperature, and the CO_2 capture capacity of the ACs at 30°C is about half to one-third to that of the ACs at 75°C. It can be seen that at 75°C, the AC with 2.0 hours activation time has the highest CO_2 capture value (26.32mg-CO_2/g-AC), while at 30°C, AC after 3.5 hours activation has the highest CO_2 capture value (60.90mg-CO_2/g-AC). However, it was expected that the AC with the highest surface area would give the highest CO_2 capture value. Table 2 shows that the surface area of AC after 2.0hrs activation is only 540m^2/g, which is the smallest among the four ACs studied here. Furthermore, the surface area of AC after 3.5hours activation is also not the highest among the ACs.

If all the total pore volume was effectively used to adsorb CO_2, it can be calculated that the theoretical maximum amount of the CO_2 adsorbed by the ACs would be 232.7mg/g, 334.2mg/g, 412.4mg/g and 384.2mg/g for the four ACs produced here after 2.0, 2.5, 3.0, and 3.5 hours, respectively. For this calculation it is considered that the liquid density of CO_2 is 0.93g/L, and the adsorbed CO_2 changes to the liquid phase due to capillary condensation[7]. However, Table 3 shows that the adsorbed amount of the CO_2 is much lower than the theoretical values. This indicates that not all the surface area or the pore volume of the AC contribute to the adsorption of the CO_2 and only some pores are used to adsorb CO_2. However, it remains unclear whether the preferred pore size is close to the CO_2 molecular diameter (0.208nm) or whether it should be larger than the CO_2 molecular diameter. Finally, Table 3 shows that for all the samples the desorption is higher than 97%, indicating that these ACs can readily desorb the CO_2 and be reused.

4. Conclusions

An anthracite sample (PSOC-1468) was selected for this study to make activated carbon as adsorbents for CO_2 capture. A lab scale fluidized bed was used for the activation and the activation temperature used was 850°C. The N_2-77K isotherms show that the ACs made from anthracite have highly developed microporosity and a small amount of mesopores. The surface area can get up to 928m^2/g with 3 hours activation time. However, extending the activation time beyond 3 hours decreases the surface area. A TGA instrument was used to characterize the CO_2 capture capacity at 30 and 75°C. The CO_2 capture capacity was 60mg-CO_2/g-sorbent for the AC with 3.5 hours activation time at 30°C adsorption temperature. Contrary to expected, the CO_2 capture results do not show any clear relationship with the surface area. The desorption capacity of the ACs are very high (>97%), indicating that these samples can be reused for CO_2 capture.

Acknowledgements This work is funded by the US Department of Energy (DOE) through a grant of the Consortium for Premium Carbon Products from Coal (CPCPC) at Penn State University.

REFERENCES

(1) Gergova, K.; Eser, S. and Schobert, H.H., Preparation and characterization of activated carbon from anthracite, Energy & Fuels, 1993, 7, 661-668
(2) Mittelmeijer-Hazeleger, M. and Martin-Martinez J., Microporsity development by CO2 activation of an anthracite studied by physical adsorption of gases, mercury porosimetry, and scanning electron microscopy, Carbon, 1992, 30(4), 695-709
(3) Spencer, D. and Wilson J., Porosity studies on activated carbons from anthracite, Fuel, 1976, 55, 291-296
(4) Pis, J.; Parra, J.; Puente, G.; Rubiera, F. and Pajares J., Development of macroporosity in activated carbons by effect of coal preoxidation and burn-off, Fuel, 1998, 77(6), 625-630
(5) Maroto-Valer, M.M and Schobert, H.H., Optimizing the routes for the productionof actvated carbons from anthracites, In: Prospects for Coal science in the 21st Century (Li, B.Q. and Liu, Z.Y. (eds)), pp909, Shanxi Science and Technology Press, Taiyuan, China 1999
(6) Do, Duong D., Adsorption Analysis: Equilibria and Kinetics (Series on Chemical Engineering, Series Editor: Ralph T. Yang), Imperial College Press, London 1998
(7) Cazorla-Amorós, D.; Alcañiz-Monge, J. and Linares-Solano, A., Charaterization of Activated Carbon Fibers by CO_2 Adsorption, *Langmuir*, 1996, 12, 2820-2824

Table 1. Proximate and ultimate analyses of the anthracite sample used (PSOC-1468).

Proximate analysis				Ultimate analysis				
Moisture Wt%	Ash wt%	Volatile wt%	Fixed C wt%	C %	H %	N %	S %	O %
4.51	6.83	3.65	89.52	96.2	1.40	0.84	0.49	1.55

Table 2. Surface areas and pore volumes of the raw anthracite and its steam activated carbons produced at 850°C using different activation times.

Sample number	Activation time, hr	S_t m^2/g	S_{mi} m^2/g	V_t mL/g	V_{mi} mL/g	Average pore diameter, nm
Raw		1				
1	2.0	540	529	0.250	0.239	1.85
2	2.5	762	733	0.360	0.330	1.89
3	3.0	928	891	0.442	0.406	1.91
4	3.5	855	814	0.412	0.372	1.93

Table 3. CO_2 capture results for the produced ACs at 30 and 75°C.

AC sample	30°C		75°C	
	Adsorption mg-CO_2/g-sorbente	Desorption %	Adsorption mg-CO_2/g-sorbente	Desorption %
Raw	38.21	89	16.05	100
2.0hrs	58.52	97	26.32	97
2.5hrs	58.51	97	24.24	98
3.0hrs	53.14	99	21.55	99
3.5hrs	60.90	99	21.68	99

Influence of Moisture on Carbon Dioxide Separation from Simulated Flue Gas by A Novel "Molecular Basket" Adsorbent

Xiaochun Xu, Chunshan Song*, Bruce G. Miller and Alan W. Scaroni

Clean Fuels and Catalysis Program, The Energy Institute, and Department of Energy & Geo-Environmental Engineering, Pennsylvania State University, 209 Academic Projects Building, University Park, PA 16802, USA
* Contact author. E-mail: csong@psu.edu; Fax: 814-865-3248

Introduction

Because of its low energy requirements, cost advantages and ease of applicability over a relatively wide range of temperature and pressure, adsorption separation is receiving increasing attention in the separation of CO_2 from various gas mixtures. Preparation of high-capacity, high-selective CO_2 adsorbents is a key factor to realize the energy-efficient adsorption separation. Recently, a new kind of high-capacity, highly-selective CO_2 adsorbents based on a "molecular basket" concept have been developed in our laboratory.[1-3] The adsorption separation of a simulated flue gas mixture, which contains 14.9% CO_2, 4.25% O_2 and 80.85% N_2, showed that a high CO_2 adsorption capacity of 91 ml (STP)/g-PEI and high CO_2/O_2 and CO_2/N_2 separation selectivity of 180 and >1000, respectively. The CO_2 adsorption capacity and CO_2/O_2, CO_2/N_2 separation selectivity with the CO_2 "molecular basket" are much higher than those of the existing adsorbents, such as zeolites and activated carbons, etc. However, several challenges still need to be overcome toward practical application. One of such challenges is the moisture, which is an important component in the gas mixtures of interest, such as flue gas and the gas from reforming for hydrogen production. On the one hand, moisture may react with the active adsorption species of amine groups in the "molecular basket" adsorbent. Therefore, moisture may compete with CO_2 to react with the active adsorption sites. Clarkson et al suggested that CO_2/CH_4 selectivity was greater for dry coals than for moisture-equilibrated coals.[4] On the other hand, the "basket" material of MCM-41 may not be stable under hydrothermal conditions. The preservation of the MCM-41 structure is critically important for the adsorption separation performance of this novel "molecular basket" adsorbent.[2] In this paper, the adsorption separation of CO_2 from simulated moist flue gas mixture containing CO_2, O_2, N_2 and moisture by using the novel "molecular basket" adsorbent is reported. The effects of moisture on the adsorption separation performance and the stability of the CO_2 "molecular adsorbent" are discussed.

Experimental

"Molecular basket" adsorbent was prepared by loading 50 wt% branched polyethylenimine (PEI, Aldrich, Mn=600) into the mesoporous molecular sieve MCM-41 (MCM-41-PEI-50).[2] The adsorption separation was carried out in a flow adsorption system.[3] Simulated dry flue gas mixture contained 14.9% CO_2, 4.25% O_2 and 80.85% N_2. Simulated moist flue gas mixture was prepared by adding moisture to the simulated dry flue gas mixture. The amount of moisture in the gas mixture was controlled by using a liquid syringe pump.

In a typical adsorption/desorption process, 2.0 g adsorbent was placed in the adsorption column. Before the adsorption separation experiment, the adsorbent was heated up to 100 ^oC in helium flow overnight to remove any CO_2 or moisture adsorbed. The temperature was then decreased to 75 ^oC and the simulated dry or moist flue gas mixture was introduced with a flow rate of 10 ml/min. Generally, the adsorption was carried out for 240 minutes. After the adsorption, helium with a flow rate of 50 ml/min was used to perform the desorption at the same temperature. The time for desorption was 300 minutes. The concentration of the gases in the effluent gas mixture was analyzed by on-line GC. Gas flow rate was measured every five minutes. Adsorption capacity in ml (STP) of adsorbate/g adsorbent and desorption capacity in percentage were used to evaluate the adsorbent. The adsorption/desorption capacity was calculated from the mass balance before and after the adsorption. The separation factor, $\alpha_{i/j}$, was calculated from equation 1 as the ratio of the amount of gases adsorbed by the adsorbent, $(n_i/n_j)_{adsorbed}$, over the ratio of the amount of gases fed into the adsorbent bed, $(n_i/n_j)_{feed}$:

$$\alpha_{i/j} = \frac{(n_i/n_j)_{adsorbed}}{(n_i/n_j)_{feed}} \qquad (1)$$

"Molecular basket" adsorbent before and after adsorption separation was characterized by X-ray diffraction (XRD). The XRD patterns were obtained on a Scintag Pad V using Cu K_α radiation.

Results and Discussions

1. Adsorption separation of CO_2 from simulated moist flue gas

Figure 1 compares the CO_2 breakthrough curve, where the amount of CO_2 is followed as the fraction of the CO_2 concentration in the effluent gas from the adsorption column, C, over that of the CO_2 concentration in the feed, C_0, during the separation of CO_2 from the simulated flue gas mixtures without moisture and with ~ 10% moisture at 75 ^oC and ambient pressure. In the presence of moisture, the "molecular basket" adsorbent can still effectively adsorb CO_2. At the beginning of the separation, CO_2 was completely adsorbed by the adsorbent and the CO_2 concentration was below the detection limit of the gas chromatography, i.e. < 100 ppm. After 60 minutes of adsorption, CO_2 breakthrough was observed in the effluent gas. Compared with the adsorption separation of CO_2 from simulated dry flue gas mixture under the same conditions, the breakthrough time increased when a moist gas mixture was used, which indicates that moisture has a promoting effect on the adsorption of CO_2 by the "molecular basket" adsorbent. Even after 120 minutes adsorption, the "molecular basket" adsorbent still adsorbed ~ 20% of CO_2 from the simulated moist flue gas mixture, whereas only 5% of CO_2 adsorbed from the simulated dry flue gas mixture. CO_2 adsorption capacity increased from 90.4 ml (STP)/g-PEI for simulated dry flue gas mixture to 129.9 ml (STP)/g-PEI for simulated moist flue gas mixture. The increase in the CO_2 adsorption capacity may be explained by the formation of bicarbonate under the moist condition, rather than carbonate under dry condition.

2. Effect of moisture concentrations in the simulated flue gas mixture on the adsorption separation

Figure 2 shows the relationship between the CO_2 adsorption capacity and the moisture concentrations in the simulated flue gas mixture. Since the simulated moist flue gas mixture was prepared by adding moisture to the simulated dry flue gas mixture, CO_2 concentration in the simulated moist flue gas mixture decreased with the increase of moist concentration. However, although the feed CO_2 concentration decreased, CO_2 adsorption capacity increased with the increase of moist concentration in the simulated flue gas mixture. At low moisture concentration, CO_2 adsorption capacity increased rapidly with the increase of the moisture concentration in the feed. The CO_2 adsorption capacity was 90.4 ml (STP)/g-PEI when dry flue gas mixture was used. When 6% moisture was added to dry flue gas mixture, CO_2 adsorption capacity increased to 109 ml (STP)/g-PEI, which was ~20% higher than that when dry flue gas mixture was

used. When the feed moisture concentration further increased to ~ 10%, CO_2 adsorption capacity increased steadily to 127.4 ml (STP)/g-PEI, which was ~20% higher than that of when the moisture concentration was ~6% and ~40% higher than that of when dry flue gas mixture was used. However, when the moisture concentration increased to 16%, the increase in CO_2 adsorption capacity recessed. CO_2 adsorption capacity was only ~5% higher than that of when the moisture concentration was ~10%. It is interesting to note that, when the feed concentration of moisture is lower than that of the CO_2, CO_2 adsorption capacity increases rapidly with the increase of moisture concentration. When the feed concentration of moisture becomes larger than that of the CO_2, CO_2 adsorption capacity can hardly be further increased by the excess water.

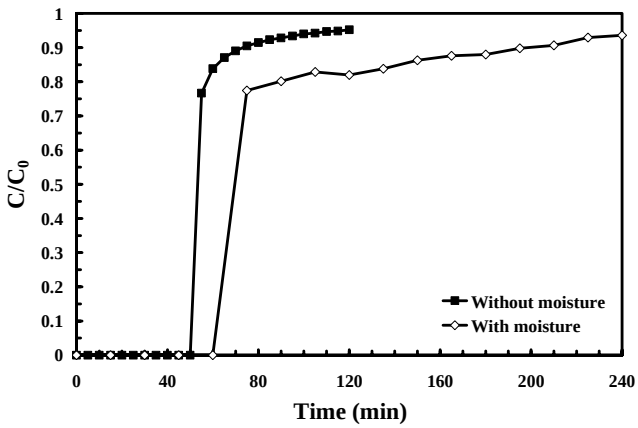

Figure 1. Comparison of CO_2 breakthrough curves with/without moisture in the simulated flue gas. Temperature: 75 ^oC; Feed flow rate: 10 ml/min. Dry feed composition: 14.9% CO_2, 4.25% O_2 and 80.85% N_2; Moist feed composition: 13.55% CO_2, 3.86% O_2, 72.72% N_2 and 9.87% H_2O.

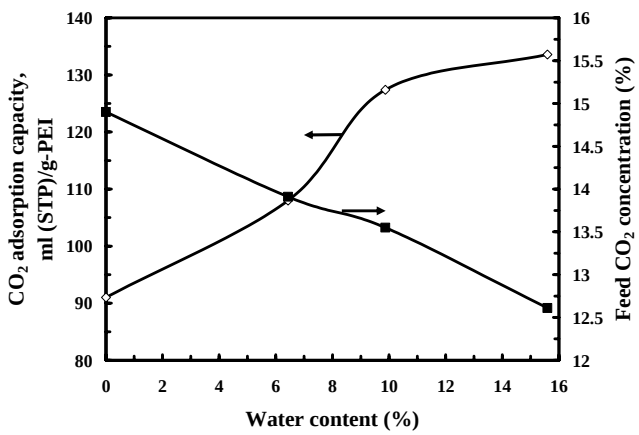

Figure 2. The influence of moisture concentrations in the simulated flue gas mixture on the CO_2 adsorption separation. Operation condition: Weight of adsorbent: 2.0 g; Temperature: 75 ^oC; Feed flow rate: 10 ml/min.

3. Cyclic adsorption/desorption and stability of the adsorbent

For practical application, the adsorbent should not only possess high adsorption capacity and high selectivity, but also show stable performance for hundreds of adsorption/desorption cycles. In our experiment, the cyclical adsorption/desorption was carried out, and the results are shown in Figure 3. During the 10 cycles of separation, CO_2 adsorption capacity hardly changed, which indicated that the desorption was complete and the adsorbent was stable in the cyclic separation process. CO_2 adsorption capacity varied between 138 to 145 ml (STP)/g-PEI. Furthermore, the adsorption selectivity did not change either in the 10 cycles of operation. The stable adsorption and desorption performance suggests that the novel "molecular basket" adsorbent is promising for practical applications.

The structure of MCM-41 and MCM-41-PEI before and after adsorption separation was characterized by XRD (not shown). The structure of MCM-41 alone collapsed only after 1 cycle operation under 10% moisture, while the structure of MCM-41 for MCM-41-PEI preserved even after 10 cycles of operation. This indicated that loading of PEI into the channels of MCM-41 protect the structure of MCM-41. It is well known that the MCM-41 is unstable in the presence of moisture even at medium temperature. Since PEI is more hydrophilic than MCM-41, the adsorption of water by PEI is stronger than that of by MCM-41. When PEI is loaded into the channels of MCM-41, water prefers to be adsorbed by PEI. Therefore, the structure of MCM-41 was protected. The preservation of the MCM-41 structure is critically important for the adsorption separation performance of this novel "molecular basket" adsorbent.[2]

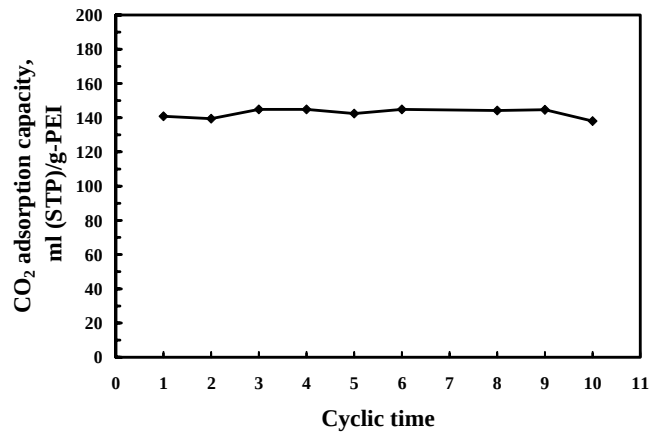

Figure 3. Stability of the "molecular basket" adsorbent in the cyclic CO_2 adsorption/desorption separations. Temperature: 75 ^oC; Feed flow rate: 10 ml/min; Moist flue gas composition: 12.97% CO_2, 3.75% O_2, 70.16% N_2 and 13.12% H_2O

Conclusions

Moisture has a promoting effect on the adsorption separation of CO_2 from simulated flue gas mixture by the novel CO_2 "molecular basket" based on MCM-41-PEI-50. Maximum promoting effect of moisture appears at moisture concentrations approaching that of CO_2 in the flue gas. The cyclic adsorption/desorption separation results show that the novel "molecular basket" adsorbent is stable in the cyclic operations of CO_2 adsorption separation from moist flue gas.

Acknowledgement. Funding for the work was provided by the U.S. Department of Defense (via an interagency agreement with the U.S. Department of Energy) and the commonwealth of Pennsylvania under Cooperative Agreement No. DE-FC22-92PC92162.

References

(1) Xu, X. C.; Song, C. S.; Andresen, J. M.; Miller, B. G.; Scaroni, A. W. *Energy & Fuels* **2002**, *16*, 1463.
(2) Xu, X. C.; Song, C. S.; Andresen, J. M.; Miller, B. G.; Scaroni, A. W. *Microporous and Mesoporous Materials* **2003**, *62*, 29–45.
(3) Xu, X. C.; Song, C. S.; Andresen, J. M.; Miller, B. G.; Scaroni, A. W. *International Journal of Environmental Technology and management* **2003**, in press.
(4) Clarkson, C. R.; Bustin, R. M. *International Journal of Coal Geology* **2000**, *42*, 241.

MOLECULAR MODELING OF HMS HYBRID MATERIALS FOR CO2 ADSORPTION

Alan L. Chaffee

School of Chemistry, Monash University 3800, Victoria, Australia

Introduction

Hexagonal mesoporous silicas (HMS) and related structures (MCM-41, SBA-15, etc) which have long-range periodicity, yet poorly defined short-range order, possess very high surface areas and well hydroxylated surfaces that are amenable to functionalisation.

The grafting, or tethering, of organic groups onto the surface leads to novel inorganic-organic hybrid materials with a variety of potential applications in gas separation, selective adsorption, sensing devices, microelectronics, non-linear optical devices, etc[1].

Surface functionalisation by alkylamino groups is of particular interest, since interactions between the basic surface which is formed and mildly acidic CO_2 molecules may provide a means of selectively adsorbing and separating CO_2 from combustion (flue) gas streams[2].

This molecular modeling study was commenced to aid the synthesis and design of such hybrid materials, by providing insight into the geometric constraints and the molecular mobility limitations that apply: (a) when functionalising reagents are brought into proximity of mesoporous silica surfaces and (b) during adsorbate-adsorbent interactions after surface functionalisation.

Experimental

This molecular dynamics (MD) study made use of the Materials Studio[3] suite of programs, in particular the molecular simulation program *DISCOVER* and the *COMPASS* forcefield[4].

MD runs were carried out using a 1 fs time-step. Equilibration runs (typically 10,000 steps) were carried out prior to production runs of 100,000 steps (total of 100ps). Simulations were carried out at constant volume and temperature (NVT ensemble). Non-bonding Van der Waals and electrostatic interaction energies were calculated using the Ewald summation method[5]. Typically, every 200th configuration was saved for analytical purposes. The simulation temperature was varied according to the purpose of the run.

Results and Discussion

Model preparation. The initial structure for the simulations was generated from a superlattice based on α-quartz using a procedure similar to that described by Kleestorfer *et al*[6]. A hexagonal periodic cell (a=49.10Å, b=49.10Å, c=5.402Å, α=90˚, β=90˚, γ=120˚) was created and used as the progenitor for all HMS models.

A series of HMS models, with varying pore diameter, were prepared by removing successive layers of Si and O atoms from the core of the superlattice. Si atoms with incomplete bonding configurations were fully saturated with hydroxy (OH) groups. The OH saturated models contained ~ 9 OH groups per nm^2 of internal surface. Model construction was, in each case, followed by geometry optimisation (energy minimization), equilibration and, then, a production MD run (100ps at 373K).

The models can be conveniently presented as *pseudo-2D* cross-sections due to the shallow thickness of the periodic cell in the c-direction (~5.4Å). Figure 1 illustrates one frame from an MD simulation of a fully hydrated mesopore that is 30Å in diameter.

Dehydration of fully hydrated mesopores. In Figure 1 adjacent OH pairs are connected by green lines. These mark the distance between the O of one OH group and the H of the adjacent OH group. When these atoms are close enough (<2.5Å) an H-bond is formed.

The circles surround OH group pairs that came closest in proximity during the first MD run at 373K. Their close proximity was deduced by plotting the 'length distribution' (frequency versus separation distance) for both of the two H-bonding atom pairs that are formed by adjacent OH groups. This plot is shown in Figure 2 for one adjacent pair. The plot shows that the adjacent H and O atoms are frequently close enough to form H-bonds and, hence it is assumed, in sufficient proximity for dehydration to occur.

Dehydration at the 6 circled locations by removal of water, leaving Si-O-Si linkages, reduced the surface silanol number from ~9 to ~7 OH/ nm^2.

Iterative replication of the procedure outlined above led to a series of partially dehydrated HMS models with silanol numbers in the range 2.5-7 OH/nm^2. For this purpose the molecular dynamic (MD) simulations were carried out at progressively higher temperatures (438, 498, 623 and 723K) chosen to correlate with the documented relationship between surface silanol concentration and pretreatment temperature for silica gel[7].

Preparing hybrid surfaces. When trimethoxyaminopropyl-silane is introduced into the mesopores, modeling results suggest that it spreads out over the surface, forming plenty of H-bonds (the blue dashed lines in Figure 3). It can be speculated that the formation of this 'surface film' may limit the number of silane molecules that can coordinate to and, hence, react with the surface OH groups. This may be one reason why tether loadings reported[8] for aminoalkylsilanes are not as high as would be expected if all surface silanols were accessible.

Hybrid material models were prepared by attachment of aminopropyl-silyl tethers to the surface, in a bidentate fashion, at silanol sites that provided the greatest (calculated) energy relief. The model illustrated in Figure 4 has 1.6 tethers per nm^2 and possesses a number of structural features (pore diameter, surface area, tether concentration) that are common to materials prepared in our laboratory[8].

It can also be seen that a number of the tethered aminogroups are still hugging the surface, a feature which is indicative of H-bonding interactions between the nitrogen (small blue circles) and the residual silanol groups.

Interactions with CO_2. Figure 4 also illustrates some of the interactions that may occur between the hybrid surface and gas-phase CO_2 when they are brought into proximity of each other. There is a clear tendency for CO_2 to form H-bonds - both with the tethered amine groups and with residual surface OH groups. The figure illustrates a situation where one CO_2 molecule (highlighted in yellow) becomes confined (on the MD timescale) in a structural pocket that might also be thought of as an 'energy-well'. It can be seen (Figure 5) that the mean square displacement versus time for this CO_2 molecule is substantially less than that for the average of all CO_2 molecules.

Conclusions

Visualisation and analysis of simulated molecular behaviour at the gas-solid interface offers fresh perspectives towards understanding the molecular interactions in these systems. This is enabling the development of improved synthetic strategies that will lead to improved CO_2 adsorption capacities.

Acknowledgements. The author acknowledges group colleagues for many stimulating discussions that helped frame and refine the questions addressed by molecular simulation. The financial support of the Australia Research Council is gratefully acknowledged.

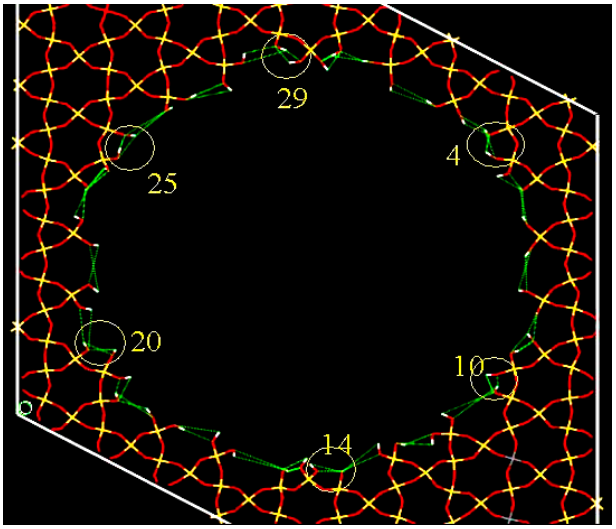

Figure 1. Cross-section of a fully hydroxylated 30Å diameter HMS mesopore.

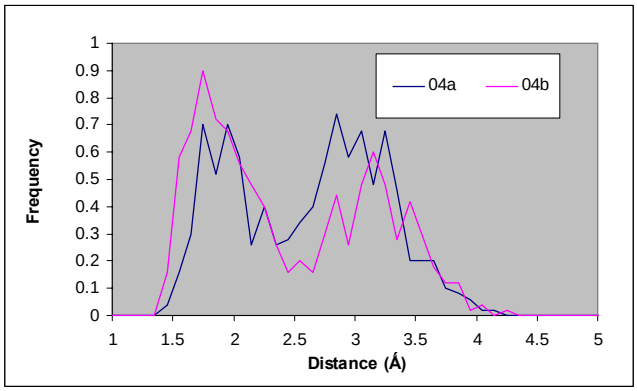

Figure 2. Length distribution for both H-bonds (a and b) that form across the hydroxy pair labeled 4 (refer Figure 1).

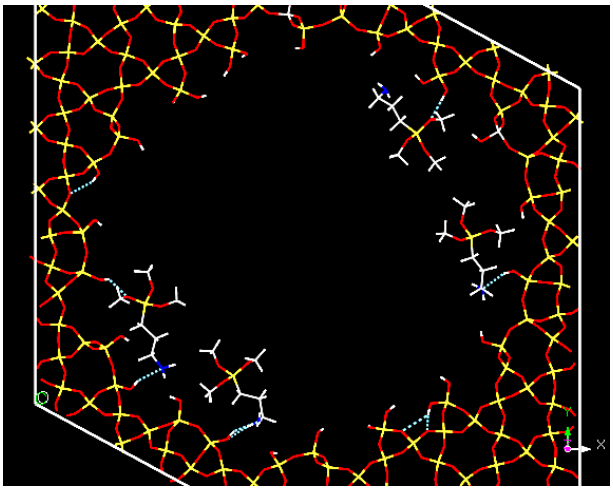

Figure 3. Molecular model illustrating H-bonding (blue-dashed lines) between trimethoxyaminopropylsilanes and a partially dehydrated (5 OH/nm^2) mesopore surface.

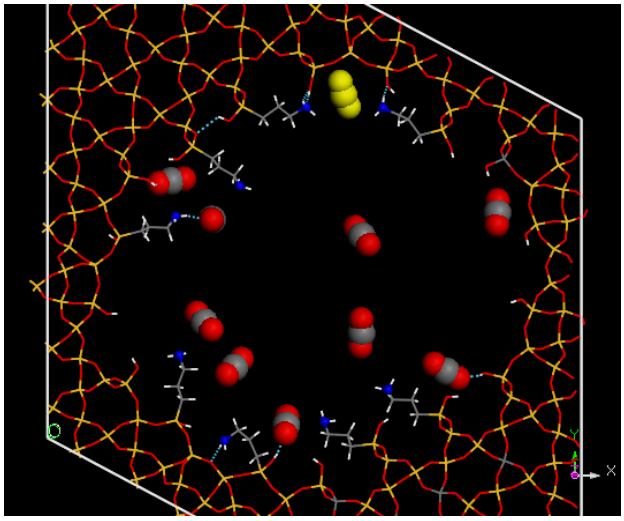

Figure 4. Molecular model illustrating H-bonding interactions between CO_2 molecules and the mesopore surface. The yellow CO_2 molecule appears to be confined by strong H-bonding.

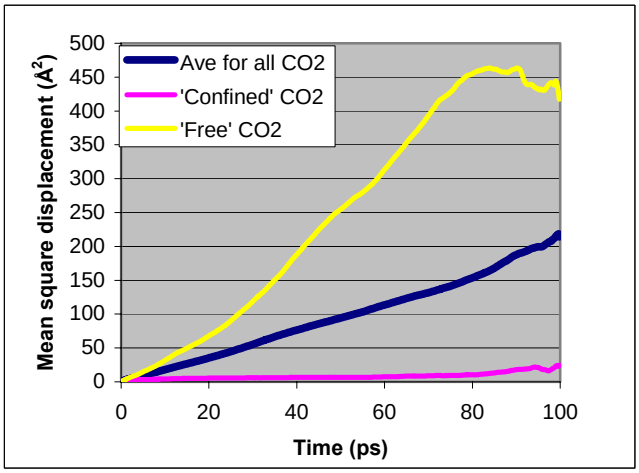

Figure 5. Mean square displacement characterizing (a) the average molecular motion of all CO_2 molecules and (b) the molecular motion of selected individual CO_2 molecules ('confined' and 'free'). Data correspond to the simulation illustrated by Figure 4.

References

(1) Sayari, A., *Studies in Surface Science in Catalysis*, **1996**, *102*, 1-46.
(2) Delaney, SW; Knowles, GP and Chaffee, AL, *Am Chem Soc, Div Fuel Chem, Prepr*, **2002**, *47*, 65-66.
(3) Materials Studio is a product of Accelrys, Inc., San Diego, CA
(4) Sun, H, *J. Phys. Chem..B*, **1998,** *102*, 7338-64.
(5) Tosi, M. P., *Solid State Physics*, **1964**, *16*, 107.
(6) Kleestorfer, K.; Vinek, H.; Jentys, A. *J. Mol. Cat. A: Chemical*, **2001**, *166*, 53-57
(7) van der Voort, P; Gillis-D'Hamers, I.; Vrancken, K.-C., *J Chem Soc Faraday Trans.*, **1991**, *87*, 3899-3905
(8) Knowles, G.P.; Graham, J.V.; Delaney, S.W.; Chaffee, AL, *Am Chem Soc, Div Fuel Chem, Prepr*, **2004**, *49*, this issue.

MICROPOROUS ACTIVATED CARBONS PRODUCED FROM UNBURNED CARBON IN FLY ASH AND THEIR APPLICATION FOR CO_2 CAPTURE

Yinzhi Zhang, M. Mercedes Maroto-Valer and Zhong Tang

The Energy Institute and Department of Energy and Geo-Environmental Engineering, The Pennsylvania State Universtiy, 405 Academic Activities, University Park, PA 16802

Introduction

Fossil fuel electricity generation units rank as the first target to reduce anthropogenic emissions due to their stationary nature. Coal is the most abundant fossil fuel in the U.S., and therefore the reduction of CO_2 emissions from coal-fired units is an imperative to mitigate global climate change, and consequently, to guarantee the key role of coal in the 21st century. The costs of current CO_2 separation and capture technologies are estimated to be about three-fourths of the total cost of ocean or geological sequestration, where the processes involved are very energy intensive and the amine solutions used in the process have very limited lifetimes[1]. Therefore, novel solid sorbents with high CO_2 capacity at flue gas temperatures are being sought.

High carbon content fly ash, which is a byproduct stream from coal-fired combustors or gasifiers, is currently disposed as a waste, and there is a demand to develop technologies to utilize high carbon content fly ash. Following this demand, a one-step activation protocol has been developed by the authors to produce activated carbons from the residual carbon in fly ash, also referred to as unburned carbon[2, 3]. Compared to the conventional two-step process that includes a devolatilization of the raw materials, followed by an activation step, unburned carbon only requires a one-step activation process, since it has already gone through a devolatilization process while in the combustor or gasifier. The produced activated carbons with a fine particle size are not only rich in micropores, but they also present a high content of mesopores, which leads to good mass transfer properties during the adsorption process. Furthermore, a pretreatment process has been previously developed by the authors to modify the properties of unburned carbon in order to produce activated carbons with high surface area and high microporosity[4]. The present paper focuses on the CO_2 adsorption properties of this microporous activated unburned carbon. In addition, a chemical impregnation method to improve the CO_2 capacity of activated unburned carbon is also described.

Experimental

Fly ash samples. Two fly ash samples, FA1 and CC1, were collected and characterized. FA1 was collected from the Penn State University pulverized coal-fired suspension firing research boiler (2 MM Btu/hour) that uses a high volatile bituminous coal from the Middle Kittanning seam. CC1 was collected from a gasifier that uses a sub-bituminous coal as feedstock.

Deashing and oxidation. A conventional acid ($HCl/HNO_3/HF$) digestion step was conducted to remove the ash from the samples and concentrate the unburned carbon. Typically, 50 g of sample was treated with the above acids at 65°C for 4 hours. The deashed samples were labeled as FA1-DEM and CC1-DEM. The FA1-DEM was further treated with 5N HNO_3 at boiling temperature for 1 hour, then washed with distillated water until pH reached 7, and the resultant samples was labeled as FA1-N1.

Characterization of the samples. The loss–on-ignition (LOI) contents of the samples were determined according to the ASTM C311 procedure. The porosity of the samples was characterized by conducting N_2 adsorption isotherms at 77K using a Quantachrome adsorption apparatus, Autosorb-1 Model ASIT. The pore volume was calculated from the volume measured in the nitrogen adsorption isotherm at a relative pressure of 0.95 (V_t). The total specific surface area, S_t, was calculated using the multi-point BET equation in the relative pressure range 0.05-0.35, as described previously[2,5]. From the adsorption isotherm, the micropore (<2nm) volume, V_{mi}, and external surface area, S_{mi}, were calculated using the α_S-method, where non-graphitized non-porous carbon black Cabot BP 280 (S_{BET}=40.2m^2/g) was used as a reference adsorbent[6]. The mesopore (2-50nm) volume (V_{me}) was calculated by subtracting the volume of V_{mi} from the V_t. The pore size distribution was calculated using the BJH method.

One-step activation and chemical impregnation. Both the parent (FA1) and pretreated samples (FA1-DEM and FA1-N1) were activated by steam using a horizontal furnace. The samples were heated under nitrogen flow to 850°C, and then steam was introduced in the reactor, while the reactor was kept under isothermal conditions for 1 hour. The activated carbon samples (AC-FA1, AC-FA1-DEM and AC-FA1-N1) were then impregnated with a PEI (polyetherimine) methanol solution and dried in a vacuum oven at 75°C overnight.

CO_2 adsorption studies. CO_2 adsorption and desorption studies were conducted using a PE-TGA 7 thermogravimetric analyzer at 30°C and 75°C. The weight change of the adsorbent was recorded and used to determine the adsorption capacities of the samples. More experimental information can be found elsewhere[7]. The adsorption capacity was reported in mg-adsorbate/g-adsorbent and was used to evaluate the performance of the samples prepared.

Results and Discussion

Deashing and oxidation. The LOI and pore structure parameters of the studied samples CC1 and FA1 are listed in Table 1. The LOI of the original samples CC1 and FA1 are 38.4% and 58.9%, respectively, which are higher than those reported in previous studies that are typically <15wt%[8]. However, this work focuses on the study of high carbon fly ashes as feedstock for activated carbons, and therefore, fly ash samples with high LOI contents were intentionally selected. The total surface area (S_{mi}+S_{me}) and total pore volume (V_{mi}+V_{me}) of sample CC1 are as high as 284m^2/g and 0.277ml/g, respectively, even prior to any treatment. This is consistent with our previous studies that indicated that some porosity is developed during the combustion or gasification process[2].

Table 1. LOI and pore structure parameters of the studied samples.

Sample	LOI %	Surface area, m^2/g		Pore Volume, ml/g	
		S_{mi}	S_{me}	V_{mi}	V_{me}
CC1	38	48	236	0.021	0.256
CC1-DEM	97	99	632	0.038	0.702
FA1	59	57	18	0.027	0.020
FA1-DEM	97	32	21	0.014	0.026
FA1-N1	99	189	20	0.094	0.024
AC-FA1	43	329	58	0.151	0.062
AC-FA1-DEM	89	704	159	0.318	0.172
AC-FA1-N1	97	1053	86	0.518	0.097

The deashing step used in the present paper can successfully concentrate the unburned carbon, where the resultant unburned carbons, CC1-DEM and FA1-DEM, have LOI values as high as 96.7% and 97.0%, respectively. In the case of CC1, the deashed sample (CCA-DEM) has a total surface area as high as 731m^2/g, compared to only 284m^2/g for the parent sample (CCA). This increase in surface area may partly come from the removal of the inorganic fly ash, which is virtually non-porous. However, the

same deashing step resulted in a decrease of the surface area for sample FA1, from $75m^2/g$ to $53m^2/g$ for FA1 and FA1-DEM, respectively. This surface area decrease was accompanied with a pore size enlargement, where FA1-DEM has more mesopores and less micropores than FA1. Further studies are needed to understand the effect of removing the ash in the porous texture of the samples.

XPS data has shown that the HNO_3 oxidation introduces oxygen functional groups on the surface of unburned carbon[4]. Furthermore, the HNO_3 treatment also resulted in an increase of the surface area of the samples, mainly due to the formation of new micropores, as shown in Table 1. The micropore surface area and pore volume of FA1-N1 are $189m^2/g$ and 0.094ml/g, respectively, compared to $32m^2/g$ and 0.014ml/g before treatment. In contrast, its mesopore surface area and pore volume are very similar before and after HNO_3 treatment ($21m^2/g$ and 0.026 ml/g vs. $20m^2/g$ and 0.024ml/g). Additionally, the HNO_3 oxidation also increased the carbon content of sample to 99 % for FA1-N1 compared to 97% for FA1-DEM.

The pororus texture properties of the samples after activation are also listed in Table 1. Without any pretreatment, the FA1 activated sample (AC-FA1) has a total surface area of 387 m^2/g, compared to 863 m^2/g for the activated sample produced following deashing (AC-FA1-DEM) and 1,139 m^2/g for the HNO_3 treated sample (AC-FA1-N1). In addition to the significant increase in surface area, the HNO_3 treatment can also modify the pore size distribution of the activated sample, resulting in a more microporous sample ($1,053m^2/g$ and 0.518ml/g).

CO_2 adsorption studies. The CO_2 adsorption studies of the CC1 and CC1-DEM samples were conducted at both 30°C and 75°C, and the capacity results are shown in Figure 1. At 30°C, the parent sample CC1 can adsorb around 17.5 mg CO_2/g, while CC1-DEM can adsorb as much as 43.5 mg CO_2/g. This is consistent with the much higher total surface area of the latter, $284m^2/g$ vs. $731m^2/g$ for CC1 and CC1-DEM, respectively (Table 1). As expected from a physical adsorption process, the CO_2 adsorption capacities of both sample decreased to 10.2 mg CO_2/g and 22.0 mg CO_2/g for raw CC1 and CC1-DEM, respectively, when the temperature was rised from 30 to 75°C.

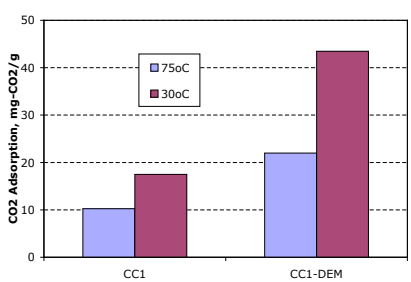

Figure 1. CO_2 adsorption capacities of samples CC1 and CC1-DEM at 30°C and 75°C.

The CO_2 adsorption capacities of samples FA1, FA1-DEM and their activated counterparts at 75°C are shown in Figure 2. Corresponding to its highest surface area and microporosity, AC-FA1-N1 has the largest CO_2 adsorption capacity, 23.2 mg CO_2/g.

The parent samples FA1 and CC1, their deashed and activated counterparts were impregnated with PEI and their CO_2 adsorption capacities at 75°C are shown in Figure 3. After PEI impregnation, all samples have higher CO_2 adsorption capacities, especially the PEI modified CC1-DEM can adsorb as much as 93.6 mgCO_2/g, compared to only 9.7 mgCO_2/g for its non-impregnated counterpart. However, the PEI impregnation was not as effective for all the samples. For example, the CO_2 adsorption capacity of AC-FA1-N1 only doubled after PEI impregnation, 43.8 mgCO_2/g vs. 23.2 mgCO_2/g.

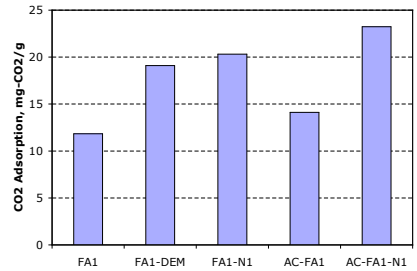

Figure 2. CO_2 adsorption capacities at 75°C for FA1 and its demineralized and activated counterparts.

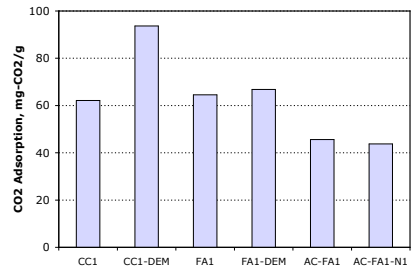

Figure 3. CO_2 adsorption capacities at 75°C for the PEI chemically impregnated samples.

Conclusions

Unburned carbon with carbon content ~97% can be concentrated from fly ash by using conventional acid digestion The deashing process not only can remove the fly ash from unburned carbon, but also changes the porous structure and surface properties of unburned carbon. Activated carbons with high surface area and microporosity, and CO_2 adsorption capacities can be produced from the unburned carbon treated with boiling HNO_3. The impregnation of PEI can improve significantly the CO_2 adsorption of unburned carbon and its activated counterparts, where the PEI impregnated deashed CC1 sample can adsorb as much as 93.6 mg CO_2/g at 75°C.

Acknowledgement This work is supported by the U.S. DOE through the Combustion Byproducts Recycling Consortium (Project number 01-CBRC-E9). The authors would like to thank Dr. Xiaochun Xu for his valuable suggestions and helpful discussions.

References

(1) International Energy Agency, CO_2 reduction – Prospects for coal, 1999
(2) Zhang, Y.; Lu, Z.; Maroto-Valer, M.M.; Andrésen, J.M. and Schobert, H.H., Energy & Fuels, 2003, 17, 369.
(3) Zhang, Y., Maroto-Valer M.M., Lu, Z., Andrésen, J.M. and Schobert, H.H., Proceeding of American Carbon Society, Carbon'01, 2001, CD-Rom Zhang38.1.pdf
(4) Zhang, Y., Tang, Z., Maroto-Valer, M.M. and Andrésen, J.M., Prepr. Pap. - *Am. Chem. Soc., Div. Fuel Chem.*, **2003**, *48(1)*, 65-66.
(5) Zhang, Y.; Wang, M.; He, F. and Zhang, B. *J. Mater. Sci.* ***1997,*** *32*,6009
(6) Kruk, M.; Jaroniec, M.; Gadkaree, K.P., J. Colloid Interface Sci., 1997, 192, 250
(7) Tang, Z., Zhang, Y., Maroto-Valer, M.M., Prepr. Pap. - *Am. Chem. Soc., Div. Fuel Chem.*, **2004**, *49(1),* In this volume.
(8) Hill, R.L.; Sarkar, S.L.; Rathbone, R.F.; Hower, J.C. Cem Concr. Res., 1997, 27(2), 193.

Methodology and Status of the Southeast Regional Carbon Sequestration Partnership

Dr. Patrick R. Esposito
CEO
Augusta Systems, Inc.
3606 Collins Ferry Road, Suite 202
Morgantown, West Virginia 26505

Mr. Kenneth J. Nemeth
Executive Director
Southern States Energy Board
6325 Amherst Court
Norcross, Georgia 30092

Regional Partnership Composition, Technical and Management Capabilities

The United States Department of Energy's (DOE) Office of Fossil Energy projects that the use of fossil energy for power generation will double by 2030. In addition, global emissions of carbon dioxide (CO_2) from human activities are projected to increase 60 percent by 2020. Carbon capture, storage, and sequestration technologies are critical to the Nation's ability to meet the President's Global Climate Change Initiative goal of 18 percent reduction in greenhouse gas intensity by 2012.

The Southeast Regional Carbon Sequestration Partnership (SERCSP) is the Southern States Energy Board's (SSEB) proposed framework to address opportunities for carbon sequestration technology deployment in the South. The Partnership represents nine southeastern states that are SSEB members (Alabama, Arkansas, Florida, Georgia, Louisiana, Mississippi, North Carolina, South Carolina and Tennessee). The Partnership is a diverse group of experts that will collaborate to achieve the project goals and objectives in various roles. SSEB will lead the SERCSP in conducting all activities for Phase I and is responsible for overall project management. Technical Team members will receive funding as well as provide cost sharing related to specific tasks. Besides SSEB, Technical Team members are the Electric Power Research Institute (EPRI); a Mississippi State University team led by the Diagnostic Instrumental Analysis Laboratory (DIAL); Augusta Systems, Inc.; Massachusetts Institute of Technology (MIT); Winrock International; Geological Survey of Alabama (GSA); Advanced Resources International (ARI); Applied Geo Technologies, Inc. (AGT)/Mississippi Band of Choctaw Indians; Tennessee Valley Authority Public Power Institute (TVA-PPI); RMS Research; and, The Phillips Group.

In addition to the Technical Team, the SERCSP Technology Coalition, a joint membership of stakeholders from the public and private sector, will advise, guide and provide input related to advancing carbon sequestration technology deployment in the Southeast. The Technology Coalition is key for identifying viable Phase II pilot projects. Furthermore, these participants are integral to achieving and leveraging the technical information transfer, outreach and public perception activities of the Partnership.

Methodologies to Characterize the Region and Evaluate CO_2 Sequestration Opportunities

Through SSEB, southern governors exercise the unique opportunity to exchange ideas, explore common issues, address pressing problems and seek regional solutions. These states reside in the heart of the southern region of the U.S and share common regulatory frameworks, agriculture and forestry resources, eco-systems, socio-economic conditions and a significant dependence on fossil fuel for electricity.

Thus, these states have a natural link to the future of carbon sequestration. With the potential for a carbon-constrained future, the economic fortunes of these nine states may depend on cost-effective implementation of carbon sequestration strategies. For that reason, the SERCSP is vital to ensuring a viable future for the states, businesses, and citizens of this region.

Project Plan and Approach

Objectives. The SERCSP will seek solutions for capture, transport and storage of CO_2 in the region through the following objectives: promoting the development of a framework and infrastructure necessary for the validation and deployment of carbon sequestration technologies in support of the DOE Carbon Sequestration Program; supporting the President's Global Climate Change Initiative goal of reducing greenhouse gas intensity by 18 percent by 2012; and, evaluating options and potential opportunities for regional CO_2 sequestration.

Scope of Work.The Partnership will develop a framework and infrastructure necessary for the validation and deployment of carbon sequestration technologies. SERCSP will address CO_2 storage and capture, CO_2 transport, regulatory issues, permitting, communication and outreach, public acceptance, monitoring and verification and environmental efficacy of sequestration within the multi-state area encompassing nine Southeast states. The SERCSP will accomplish its objectives by 1) defining similarities in the nine-state region, 2) characterizing the region relative to sources, sinks, transport, sequestration options, and existing and future infrastructure requirements, 3) identifying and addressing issues for technology deployment, 4) developing public involvement and education mechanisms, 5) identifying the most promising capture, sequestration and transport options, and 6) developing action plans for implementation and technology validation. Work will occur during two budget years. The first budget period (October 1, 2003 through June 30, 2004) will encompass three quarters of activity and the second budget period will encompass one calendar year (July 1, 2004 through September 30, 2005). During year 1, the Partnership plans to complete: 100 percent of Task 1.0; 97 percent of Task 2.0; 36 percent of Task 3.0; and to initiate Task 4.0 and Task 5.0. During budget year 2, the Partnership plans to complete 100 percent of all Tasks.

Task 1 Define the Geographic Boundaries. This task highlights the similarities of CO_2 sources and sinks in a region that consumes significant amounts of fossil fuel but has limited production of oil, gas or coal. SSEB has extensive experience in working with industrial partners and its member states to identify permitting considerations relating to energy and environmental technologies.

Task 2 Characterize the Region . The region will be characterized relative to sources, sinks, transport, sequestration options, and existing and future infrastructure requirements. Information gathered during Phase I characterization will be archived in a relational database and geographic information system (GIS).

Task 3 Identify and Address Issues for Technology Deployment. This task undertakes a preliminary assessment of safety, regulatory and permitting requirements, public perception, ecosystem impacts, monitoring and verification requirements and other potential issues associated with wide scale deployment of promising regional opportunities.

Task 4 Develop Public Involvement and Education Mechanisms. The Partnership will develop public involvement and education mechanisms that raise awareness of sequestration opportunities in the Southeast region and provide interested stakeholders with information about supporting technology development efforts.

Task 5.0 Identify the Most Promising Capture, Sequestration and Transport Options. The Partnership will begin its assessment of the most promising options. The Partnership will analyze information gathered in the regional assessment to identify the most promising opportunities for capture, transport and sequestration of CO_2. The initiative will assess and validate the most promising emerging technology developments and identify those minor modifications required to fit the technology to the regional application.

Task 6.0 Prepare Action Plans for Implementation and Technology Validation Activity. The Technical Team will prepare Action plans to implement the framework developed leading to small-scale regional technology validation field tests. In developing the plans, the Partnership will consider cost-effective approaches that provide flexibility for assessing multiple candidate technology options. This task will result in Action Plans for capture, transport and storage options. In addition, the Plans will include assessing terms of public involvement, education and acceptance, regulatory and permitting, and accounting frameworks. Finally, the Partnership will integrate the Action Plans to form a regional strategy.

STUDY OF THE CO_2 ADSORPTION CAPACITIES OF MODIFIED ACTIVATED ANTHRACITES

Zhong Tang, Yinzhi Zhang and M. Mercedes Maroto-Valer

The Energy Institute and Department of Energy and Geo-Environmental Engineering, Pennsylvania State University, 209 Academic Projects Bldg., University Park, PA 16802

1. Introduction

Anthropogenic emissions have increased the CO_2 concentration on the atmosphere with over 30% compared to pre-industrialize levels [1]. Most of these anthropogenic emissions are caused by fossil fuel utilization, where around one-third is due to electricity generation from fossil fuel combustion, mainly from coal-fired units. Furthermore, fossil fuel electricity generation units rank as the first target to reduce anthropogenic emissions due to their stationary nature. However, the costs of current CO_2 separation and capture technologies are estimated to be about 75% of the total cost of ocean or geological sequestration, including the costs for compression to the required pressure for subsequent sequestration [2]. New solid-based sorbents are being investigated, where the amine groups are bonded to a solid surface, resulting in an easier regeneration step [3-5]. The supports used thus far, including commercial molecular sieves and activated carbons, are very expensive and hinder the economical viability of the process. Accordingly, there is a need to find low-cost precursors that can compete with the expensive commercial supports, and develop effective solid sorbents that can be easily regenerated, and therefore, have an overall lower cost over their lifetime performance.

The authors have previously shown that high surface area activated carbon (AC) can be produced from anthracite[6]. However, the CO_2 capture capacity of activated anthracites is lower than that of commercial AC or molecular sieves[7]. Therefore, in this study, several surface treatment methods were used to modify the surface properties of the activated anthracites to improve their CO_2 capture capacity.

2. Experimental

2.1 AC samples. The AC samples used here were produced from anthracite. More details can be found elsewhere[6]. The samples studied are AC1 (activated at 850°C for 3 hours), AC2 (activated at 850°C for 2 hours) and AC3 (activated at 890°C for 3 hours).

2.2 Surface treatment. *(1) NH_3 treatment*: AC1 was used for this treatment. A known amount of AC1 was put into a quartz boat that was placed in the middle of a horizontal tube furnace. NH_3 gas was then introduced, while the furnace was heated up to desired treatment temperature. After the furnace was held at the set temperature for 90 minutes, the NH_3 gas was switched to argon and the furnace was cooled down. The sample was removed from the reactor tube at room temperature. The last three digits of the sample name indicate the treatment temperature.

(2) HNO_3 treatment: 3 g of AC2 was put into 100mL 5N HNO_3 solution. The sample was oxidized in boiling nitric acid for 5 hours, and then filtered and washed with de-ionized water till the pH of the filtrate was around 7. The treated AC was dried at 110°C for overnight, and labeled as AC2-HNO_3.

(3) Amine impregnation: The AC1 and AC3 samples were impregnated with a PEI (polyetherimine) in methanol solution and then dried in a vacuum oven at 75°C overnight. The resultant samples were labeled as PEI-AC3 and PEI-AC4.

2.3 CO_2 adsorption studies. The adsorption performance of the samples was characterized using a PE-TGA 7 thermogravimetric analyzer, as described in a previous study [6]. N_2 adsorption isotherms at 77K were used to characterize the porosity of the samples with a Quantachrome adsorption apparatus, Autosorb-1 Model ASIT. The pore sizes 2nm and 50nm were taken as the limits between micro- and mesopores and meso- and macropores, respectively, following the IUPAC nomenclature[8]. A Kratos Analytical Axis Ultra XPS was used to study the surface chemistry of the modified ACs. XPS quantification was performed by applying the appropriate relative sensitivity factors (RSFs) for the Kratos instrument to the integrated peak areas. The approximate sampling depth under these conditions is 25Å.

3. Results and Discussion

3.1 NH_3 and HNO_3 treatment. The porous texture properties, as determined from the 77K N_2-isotherms, of the parent activated carbons and their counterparts treated with NH_3 and HNO_3 are shown in Table 1. It can be seen that the NH_3 treatment increased the surface area of the activated samples, especially at lower temperatures (650°C), while the HNO_3 treatment decreased the surface area of the activated anthracites. For example, the surface area of the NH_3 treated activated anthracites increased from 928 to 1052 and 952 m^2/g at 650 and 800°C, respectively. Most of the pores of the activated anthracites AC1 and AC2, which were produced from anthracite by steam activation at 850°C using different activation times, are mainly micropores (>92%). The low temperature NH_3 treatment (650°C) can increase the surface area while keeping the sample microporosity (92%). In contrast, the high temperature NH_3 treatment (800°C) increases slightly the surface area of the anthracite, but increases significantly its pore diameter from 1.91 to 1.97 nm. The surface area of the activated anthracite decreased for the HNO_3 treatment, due the formation of mesopores, resulting in an increase of the average pore size from 1.85nm to 2.21nm.

Table 1. Porous texture of the parent activated anthracites and their counterparts treated with NH_3 and HNO_3.

Sample	BET surface area, m^2/g	Pore volume, ml/g	Microporosity ratio, %	Average pore diam., nm
AC1	928	0.442	92	1.91
AC1-NH_3-650	1052	0.523	92	1.91
AC1-NH_3-800	952	0.469	88	1.97
AC2	540	0.250	96	1.85
AC2-HNO_3	195	0.108	86	2.21

3.2 XPS analysis studies. As expected, the NH_3 treatment introduced nitrogen surface groups on the activated carbon, especially at high temperature. The nitrogen content increased from 0.1% in the untreated activated carbon to 1.1% in the NH_3 treated activated carbon, as showed by the XPS data presented in Table 2

Table 2. Summary of the elements detected by XPS (Rel. Atom%)

Sample	C	O	N
AC1	95.7	4.2	0.1
AC1-NH_3-800	94.0	4.9	1.1
AC2-HNO_3	77.6	21.8	1.6

The HNO_3 treatment can introduce oxygen surface functional groups on the activated carbon (Table 2), as found in previous studies[9]. The oxygen content of the treated activated carbon was as high as 21.8%, which is about 4 times higher than the untreated activated carbon, which is 4.2%. The curve fit to the experimental carbon 1s spectra showed that the HNO_3 treatment created a large amount of carboxylic COO^- groups on the surface of the activated carbon. In addition, the HNO_3 acid can also introduce nitrogen groups on the activated carbon, where the nitrogen content increased from 0.1% to 1.6% after HNO_3 treatment.

3.3 CO_2 adsorption studies. The CO_2 adsorption capacities of the activated anthracites and their NH_3 and HNO_3 treated counterparts were determined at 30, 50 and 75°C, as shown in Figures 1 and 2.

It can be seen that there are significant changes in the CO_2 adsorption capacity of the parent and treated anthracites with temperature. At 30°C, the adsorption of the untreated activated anthracites was slightly higher than the treated samples. At higher adsorption temperatures (50°C and 75°C), the adsorption capacities of the treated samples was slightly higher than that of the parent activated anthracite. For instance, at 75°C, the CO_2 adsorption capacity was 21.68, 26.63 and 23.69 mg-CO_2/g-sorbent for AC1, AC1-NH_3-650 and AC1-NH_3-800, respectively. For the HNO_3 treatment, the CO_2 adsorption was 38.85 and 40.47 mg-CO_2/g-sorbent for AC2 and AC2-HNO_3 at 50°C, respectively. This indicates that the treatment process can improve the CO_2 adsorption of the anthracite, particularly at higher temperatures. This is probably due to the introduction of nitrogen groups. Further studies are being conducted to assess the nitrogen functional groups that affect CO_2 adsorption.

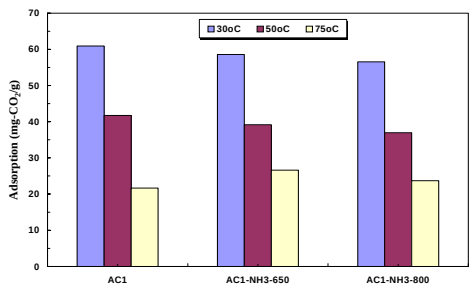

Figure 1. CO_2 adsorption capacities of AC1 and its NH_3 treated samples, AC1-NH_3-650 and AC1-NH_3-800.

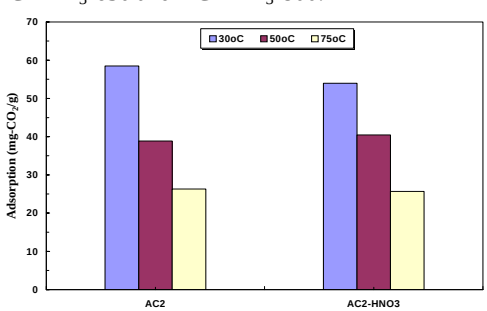

Figure 2. CO_2 adsorption capacities of AC2 and its HNO_3 treated sample, AC2-HNO_3.

Figure 3 shows the CO_2 adsorption capacities of the AC1 and AC3 samples, and their PEI impregnated samples, PEI-AC1 and PEI-AC3. It can be seen that impregnation with PEI increases significantly the CO_2 adsorption capacities, particularly for AC3. For instance, the adsorption capacity increased from 21.55 to 26.3 mg-CO_2/g for AC1 after impregnation. For the AC3 sample, the PEI impregnation increased more significantly the CO_2 adsorption capacity from 16.94 to 37.49 mg-CO_2/g. This increase in the CO_2 adsorbed after amine impregnation is consistent with that founded in molecular sieve materials MCM-41 and in fly ash carbons[5,10]. The higher CO_2 adsorbed amount for AC1 compared to AC3 is probably due to the presence of more micropores (92% vs. 78%). Previous studies conducted on MCM-41 and fly ash carbons have shown that the CO_2 chemical adsorption for PEI impregnated materials is favored by the presence of mesopores that can promote mass transfer within the pores.

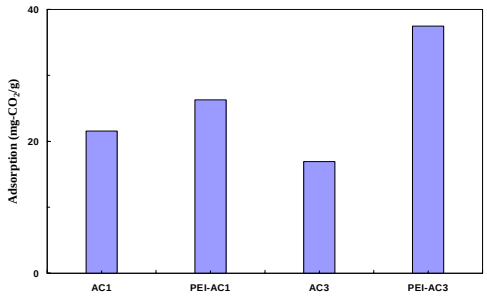

Figure 3. CO_2 adsorption capacities at 75°C of AC1 and AC3 and their PEI impregnated samples, PEI-AC1 and PEI-AC3.

4. Conclusions

NH_3 and HNO_3 treatments can change the pore structure of activated anthracites. NH_3 treatment can introduce nitrogen groups on the surface of activated anthracites. HNO_3 treatment can introduce both oxygen and nitrogen functional groups, where the oxygen groups are mainly carboxylic COO^-. NH_3 and HNO_3 treatments improves the CO_2 capture capacity of the activated anthracites at higher temperatures (50 and 75 °C), due to the introduction of nitrogen and oxygen functional groups. PEI impregnation can increase the CO_2 capture capacity of the activated anthracites. Further studies are being conducted to optimize the treatments described here to improve the CO_2 adsorption capacity of activated anthracites.

Acknowledgements This work was funded by the US Department of Energy (DOE) through a grant of the Consortium for Premium Carbon Products from Coal (CPCPC) at Penn State University. The authors thank Dr. Xiaochun Xu for his valuable suggestions and discussion.

REFERENCES

(1) Keeling, C.D.; Whorf, T. and Trends: A Compendium of Data on Global Change, Oak Ridge, 1998
(2) Herzog, H.J., Proc. Stakeholders' Workshop on Carbon Sequestration, MIT EL 98-002, 1998
(3) Birbara, P.J. and Nalette, T.A., US patent No: 4, 810, 266, 1996
(4) Siriwardane, R.V.; Shen, M.S.; Fisher, E.P. and Poston, J.A., *Energy & Fuels*. 2001, 15, 279
(5) Xu, X.; Song, C.; Andresen J.; Miller, B. and Scaroni, A., Novel polyethyleninine-modified mesoporous molecular sieve of MCM-41 type as high-capacity adsorbent for CO_2 capture, *Energy & Fuels*, 2002, 16, 1463-1469
(6) Tang, Z.; Maroto-Valer, M.M. and Zhang, Y., CO_2 capture with sorbents made from anthracite, Prepr. Pap. - *Am. Chem. Soc., Div. Fuel Chem.*, **2004**, *49(1)*, In this volume.
(7) Siriwardane, R.V.; Shen, M.; Fisher E.P. and Poston J.A., Adsorption of CO_2 on molecular sieves and activated carbon, Energy & Fuel, 2001, 15, 279-284
(8) Sing, K.S.W.; Everett, D.H.; Hual, R.A.W. and et al, Reporting physisorption data for gas/solid systems with special reference to the determination of surface area and porosity, Pure & Appl. Chem., 1985, 57(4), 603-609
(9) Zhang, Y; Tang, Z; Maroto-Valer, M.M. and Andresen, J.M., Development of microporous activated carbons from unburned carbon in fly ash, Prepr. Pap. - *Am. Chem. Soc., Div. Fuel Chem.*, **2003**, *48(1)*, 65-66.
(10) Zhang, Y.; Maroto-Valer, M.M. and Tang, Z., Microporous activated carbons produced from unburned carbon in fly ash and their application for CO_2 capture, Prepr. Pap. - *Am. Chem. Soc., Div. Fuel Chem.*, **2004**, *49(1)*, In this volume.

CO_2 Scrubbing with Novel Lithium Zirconate Sorbents

Daniel J. Fauth, James S. Hoffman,
Randall P. Reasbeck, and Henry W. Pennline

U.S. Department of Energy
National Energy Technology Laboratory (NETL)
P.O. Box 10940
Pittsburgh, PA 15236-0940

Introduction

Electric power generated from the combustion of fossil fuels is accountable for over one-third of the global annual CO_2 emissions. Large stationary sources are, therefore, considered credible targets for carbon sequestration. For this reason, the successful implementation of practical and cost effective CO_2 separation and capture technologies are projected to have a major impact on mitigating environmental problems posed by CO_2 emissions.

Existing commercial operations for removing CO_2 from flue gas make use of chemical absorption with various amine solvents. Inherent deficiencies associated with this process include low CO_2 loadings and significant energy requirements for CO_2 release. Alternative technologies for CO_2 capture are considered necessary.

One promising technology with the potential for significant development employs dry scrubbing with regenerable sorbents.[1-9] These processes are cyclical since the sorbent can successfully remove the gaseous component, be regenerated, and in this step yield a concentrated stream of CO_2, and then reused. Advanced processes based on dry regenerable sorbents may offer attractive benefits over existing solvent-based practices.

Lithium zirconate (Li_2ZrO_3), with its favorable CO_2 sorption characteristics, is considered a promising material for CO_2 removal at high temperature. The chemical reaction for CO_2 capture using Li_2ZrO_3 is illustrated below. The forward reaction pathway depicts absorption of CO_2, whereas regeneration is expressed as the reverse reaction path.

$$Li_2ZrO_3\ (s) + CO_2\ (g) \Leftrightarrow Li_2CO_3\ (s) + ZrO_2\ (s) \qquad [1]$$

Nakagawa and Ohashi[1,2] observed Li_2ZrO_3 powder reacts immediately with CO_2 in the temperature range of 450° to 590°C. Ohashi and Nakagawa[3] also report the addition of potassium carbonate to Li_2ZrO_3 significantly influences its kinetic rate and increases its CO_2 capture capacity. They conclude this acceleration results from the formation of a Li_2CO_3-K_2CO_3 eutectic encapsulating a solid ZrO_2 core. Lin and Ida[5,6] confirm these observations and offer a comprehensive double-shell model describing the mechanism for CO_2 sorption/desorption on pure and potassium-doped Li_2ZrO_3 sorbents.

In this study, we examined the influence of potassium carbonate and other alkaline carbonate eutectic agents for enhancing the direct carbonation of Li_2ZrO_3. Improvement in the CO_2 sorption rate is important for its practical application in design and development of dry, regenerable sorbent materials for CO_2 capture under operating conditions prevailing in Integrated Gasification Combined Cycle (IGCC) processes.

Experimental

High purity Li_2ZrO_3 procured from Aldrich Chemical Co. was used as the primary substrate. Thermogravimetric Analysis (TGA) with a microelectronic recording balance system (Cahn TG-131) was employed to examine the CO_2 sorption properties of pure and molten salt-containing Li_2ZrO_3 powders. A gas cylinder supplied CO_2 of stock gas grade (99.99%) to the TGA apparatus. Sample temperature was measured and controlled with a type K thermocouple located directly below the suspended sample pan. Approximately 100 mg of Li_2ZrO_3 was charged into a platinum sample pan for testing. For molten salt-containing Li_2ZrO_3 samples, 20% by weight of carbonate (or halide) salt was physically admixed with 100 mg Li_2ZrO_3 prior to placing the sample into the TGA instrument. **Table 1** shows the composition and eutectic temperatures of the molten salt-containing Li_2ZrO_3 samples.

Table 1. Composition and eutectic temperatures of molten salt-containing Li_2ZrO_3 sorbent materials

Sample ID	Molten salt composition (mol%)	Eutectic Temp (°C)[a]
B1	K_2CO_3 38% Li_2CO_3 62%	488
B2	K_2CO_3 57.3% Li_2CO_3 42.7%	498
B3	Na_2CO_3 48% Li_2CO_3 52%	500
B4	KF 38% Li_2CO_3 62%	n/a
B5	K_2CO_3 57% $MgCO_3$ 43%	460
T1	K_2CO_3 26.8% Na_2CO_3 30.6% Li_2CO_3 42.5%	393

[a] Physical Properties Data Compilations Relevant to Energy Storage.
1. Molten Salts: Eutectic Data, U.S. Dept. of Commerce, March 1978

Prior to CO_2 sorption, each sample was pre-conditioned and dried in nitrogen by elevating the temperature (at 10°/min) to 500°C and holding for 30 minutes. Upon completion of this step, the surrounding stream of N_2 gas was switched to pure CO_2 while maintaining a flow rate of 140cc/min. CO_2 sorption testing was conducted at 500°C. The change in sample weight with time was recorded during absorption, upon which the experimental conversion of Li_2ZrO_3 to Li_2CO_3 was calculated. Regeneration of the Li_2ZrO_3 samples was performed by switching the feed gas back to N_2 after raising the temperature to 800°C.

X-ray diffraction (XRD) characterization of the modified Li_2ZrO_3 samples after CO_2 sorption at 500°C was conducted using a PANalytical X'pert Pro powder diffractometer with a Cu X-ray source at 45 kV and 40 mA. The XRD patterns were recorded over a 2θ range of 8° to 70°. Phase identification was verified by comparison to the ICDD inorganic compound powder diffraction data base.

Results and Discussion

Figure 1 shows the CO_2 uptake of the Aldrich Li_2ZrO_3 powder at 500°C after the surrounding N_2 gas stream was switched to pure CO_2 (P_{co2} = 1atm). The pure Li_2ZrO_3 sample shows a steady but very slow

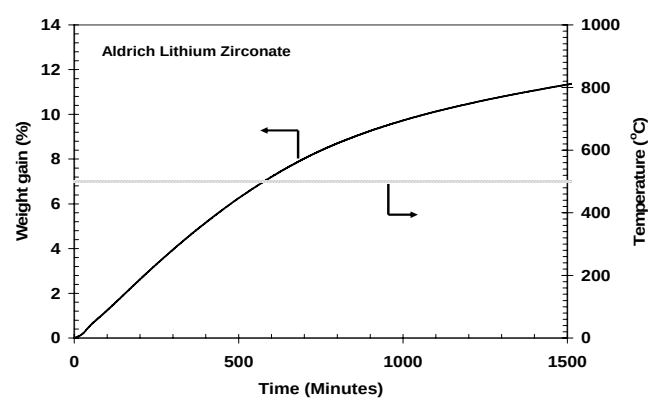

Figure 1. CO_2 sorption profile of Aldrich Li_2ZrO_3 powder at 500°C Initial sample weight: 100 mg Li_2ZrO_3 Gas flow rate: 140cc/min Total pressure: 1 atm

increase in sample weight upon CO_2 exposure. From this figure, pure Li_2ZrO_3 gained nearly 11 wt % CO_2 of its sample weight within 1500 minutes, which corresponds to a reaction yield of 38.3% based on equation 1. (Theoretical maximum uptake of CO_2 for pure Li_2ZrO_3 sample equals 28.7 wt %.) After completion of the first sorption step, the Li_2ZrO_3 sample was successfully regenerated at 800°C in nitrogen. These results were found in good agreement with values reported by Nakagawa and Ohashi,[1-3] Essaki[4] et al. and Lin.[5] XRD analyses identified Li_2ZrO_3, Li_2CO_3 and ZrO_2 as major crystalline phases after CO_2 exposure at 500°C.

The influence of molten salt mixtures of alkaline and alkaline earth carbonates on the rate of CO_2 sorption of the modified Li_2ZrO_3 powders at 500°C is illustrated in **Figure 2**. It should be noted that no attempt was made to optimize the dispersion of the molten salts onto the Li_2ZrO_3 powder. The majority of the binary eutectic containing Li_2ZrO_3 samples absorbed 11 to 13 wt % of CO_2 of the sample weight within 60 minutes. The potassium/lithium carbonate-containing Li_2ZrO_3 samples (designated *B1* and *B2*) have eutectic melting points of 488° and 498°C respectively. These samples show a much faster rate (25 times faster) of CO_2 uptake compared to the pure Li_2ZrO_3. The binary sodium/lithium carbonate doped Li_2ZrO_3 sample (*B3*) and ternary carbonate doped Li_2ZrO_3 sample (T1), consisting of sodium carbonate, potassium carbonate, and lithium carbonate, with a melting point of 393°C, produced comparable rates of CO_2 uptake as the potassium-containing *B1* and *B2* samples.

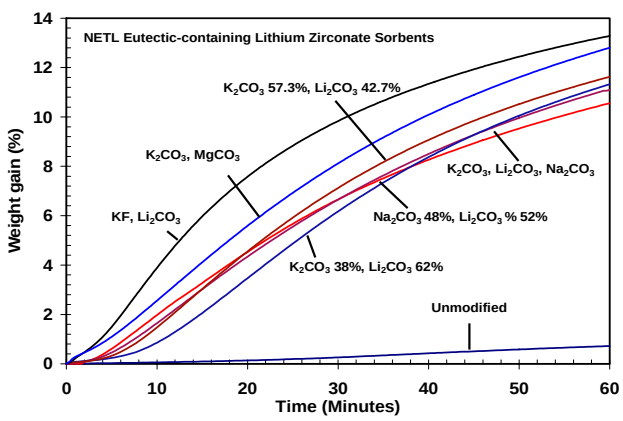

Figure 2 Influence of eutectic additives on rate of CO_2 sorption for NETL promoted Li_2ZrO_3 sorbents. Reaction temperature: 500°C.

The binary K_2CO_3-$MgCO_3$-containing Li_2ZrO_3 sample (*B5*) has a melting point of 460°C, which is nearly 40°C lower than previous binary carbonate Li_2ZrO_3 samples tested. The rate along with its capacity remained high over the entire sixty minutes under a 100% CO_2 flow. Sample *B5* absorbed over 12% of its sample weight, corresponding to 41.7% of its theoretical maximum. **Figure 3** shows a scanning electron micrograph of the spent K_2CO_3-$MgCO_3$-containing Li_2ZrO_3 sample after CO_2 sorption at 500°C. At this magnification, the single particle appears to be dense, non-porous in appearance. The mixed potassium halide/carbonate Li_2ZrO_3 sample (*B4*) gave the fastest rate (40 times faster) of CO_2 uptake compared to the unmodified Li_2ZrO_3 sample. Under IGCC applications, sorbent kinetics is anticipated to improve due to elevated CO_2 pressures. XRD analysis identified Li_2CO_3 and ZrO_2 as major phases upon rapid quenching of carbonated *B4* and *B5* samples in CO_2.

By TEM and EDX analysis, Ohashi and Nakagawa[3] report the existence of a potassium/lithium carbonate eutectic surrounding a solid Li_2ZrO_3 core. In the case of the pure Li_2ZrO_3 sample (without K_2CO_3 additive), formation of an impervious shell of Li_2CO_3 results on the outer surface of the unreactive Li_2ZrO_3 core. This observation suggests diffusion resistance of CO_2 through the solid Li_2CO_3 product layer is the rate-limiting step. In contrast, the potassium/lithium carbonate-containing Li_2ZrO_3 sample reacts with gaseous CO_2 at 500°C to form a molten liquid outer layer and a solid interior ZrO_2 shell. Therefore, the difference in CO_2 sorption rate can be partially contributed to the molten carbonate layer; CO_2 diffuses through the molten carbonate layer at a much faster rate.

Lin and Ida[5] describe a comprehensive double-shell model relating to the mechanism for CO_2 sorption on potassium-doped Li_2ZrO_3. They conclude after the formation of the molten potassium-lithium carbonate layer and ZrO_2 shell, the carbonation reaction will proceed by the diffusion of Li^+ and O^{2-} ions through the ZrO_2 shell along with diffusion of CO_2 through the molten carbonate layer. Strategies for reducing the depth of the solid Li_2CO_3 and ZrO_2 shells formed during reaction should provide additional insight and improvement in sorbent performance.

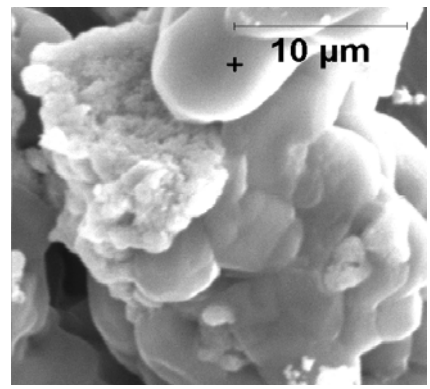

Figure 3. Scanning electron micrograph of K_2CO_3-$MgCO_3$ eutectic containing Li_2ZrO_3 sample (*B5*) after CO_2 sorption at 500°C.

Conclusions

CO_2 sorption performances of alkaline and alkaline earth-containing Li_2ZrO_3 sorbent materials at 500°C show very favorable reaction kinetics for CO_2 capture in comparison to pure lithium zirconate. Future work will focus on the synthesis of molten salt-containing, nanocrystalline Li_2ZrO_3 samples along with CO_2 sorption testing using TGA and a fixed-bed reactor with mixtures of gases simulating fuel gas environments, such as that found in IGGC operations.

References

1. Nakagawa, K.; Ohashi, T. *J. Electrochem. Soc.* **1998**, 45(4), 1344-1346
2. Nakagawa, K.; Ohashi, T. *J. Electrochemistry* **1999**, 67(6), 618-621.
3. Ohashi, T.; Nakagawa, K. *Mat.Res. Soc. Symp. Proc.* **1999**, 47, 249-254.
4. Essaki, K.; Nakagawa, K.; Kato, M. *J. of the Ceramic Society of Japan* **2001**, 109(10), 829-833.
5. Lin, Y.S.; Ida, J. *Environ. Sci. Technol.* **2003**, 37(9), 1999-2004.
6. Ida, J.; Xiong, R.; Lin, Y.S. *Sep. Pur. Technol.* **2003**, article in press.
7. Gupta, H.; Fan, L.S. *Ind. Eng. Chem. Res.* **2002**, 41(16), 4035-4042.
8. Fauth, D.J.; Hoffman, J.S.; Pennline, H.W. *Fuel Chemistry Division Preprints*, **2003**, 48(1), 169-170.
9. Pennline, H.W.; Hoffman, J.S. U.S. Patent No. 6,387,337, **2002**.

Design, Process Simulation, and Construction of an Atmospheric Dual Fluidized Bed Combustion System for *In Situ* CO_2 Capture Using High-temperature Sorbents

Robin W. Hughes, Jinsheng Wang, Edward J. Anthony

Fluidized Bed Combustion & Gasification Group
CETC-O/Natural Resources Canada
1 Haanel Dr., Ottawa
Canada K1A 1M1

Introduction

The need to reduce CO_2 emissions along with pollutants such as SO_2 and NO_X is now generally accepted[1]. At the same time, there is a growing need for increased electrical power generation. If both sets of requirements are to be met without excessive economic disadvantage to the world economy, then new electrical generation methods with low or zero CO_2 emissions must be developed.

The use of the carbonation reaction in a combustion system could potentially meet the needs of a modern, high-volume, CO_2 capture system. The process outlined below operates continuously, producing a flue gas containing less than 3% CO_2 and a marketable CO_2 product stream with a purity exceeding 85%.

The carbonation reaction can remove carbon dioxide from combustion systems at elevated temperatures (~650°C-760°C) and atmospheric pressure *via*:

$$CaO + CO_2 \Leftrightarrow CaCO_3 \qquad (1)$$

The efficiency of systems using dual fluid beds for carbonation and sorbent regeneration have been shown to be comparable to current combustion systems without CO_2 segregation[2,3]. Sulphur dioxide emissions will be on the order of a few parts per million since the calcium required for CO_2 removal will be equivalent to a Ca:S molar ratio on the order of 20-30. Circulating fluidized bed combustors (CFBCs) are intrinsically low producers of NO and are amenable to NH_3 injection if very low emissions of NO are desired[4]. N_2O emissions can be minimized by operating at temperatures around 900ºC or by producing high-temperature windows in the cyclone[5].

The dual fluid bed carbonation process can be applied to stationary emitters of carbon dioxide including coal-fired generating stations and cement kilns. Limestone, the main feedstock, is inexpensive and readily available throughout most of the world allowing this process to have a global impact on greenhouse gases.

Information needed for scale-up to an industrial process using dual fluid bed technology for carbon dioxide capture is not currently available in the literature. To obtain some of the required information, a mini-pilot plant has been constructed. The design and process simulation of this system are presented here.

Experimental

Dual Fluid Bed Design Figure 1 shows a process flow diagram for the twin fluid bed combustion system with CO_2 capture operating at atmospheric pressure. Solid fuel combustion, with air, occurs in the first stage of the carbonating combustor at an optimum temperature for combustion (850ºC-950ºC) while carbonation occurs in the second stage at an optimum temperature for CO_2 capture (650ºC-750ºC for reaction (1)).

The combustion section will operate in the bubbling bed regime with allowance for both primary and secondary combustion air. Heat can be removed from the combustion stage of the Carbonating Combustor to allow high steam cycle efficiency. Sulphur removal is possible using spent sorbent through the reaction:

$$CaO + ½O_2 + SO_2 \Leftrightarrow CaSO_4 \qquad (2)$$

The carbonation section will operate in the bubbling bed regime. Heat removal is possible in the Carbonating stage to control the reaction temperature for reaction (1). A distribution plate separates the combustion stage from the carbonating stage.

The Carbonating Combustor is designed such that it can operate as a single stage circulating fluidized bed combustor with CO_2 removal. This mode of operation is not expected to result in optimum long-term cyclic conversion of the sorbent, however, it may be of interest for commercial retrofit. The sorbent is transported to the regenerator using calciner product gas, composed primarily of CO_2, or by steam. The carbon dioxide or steam is later used as a temperature mediator in the regenerator.

Sorbent regeneration occurs in the second fluid bed; the Oxygen Combustor & Calciner. Heat is supplied in the calciner by burning a low ash fuel such as petroleum coke with oxygen, to supply the heat necessary to drive reaction (1) to the left, releasing carbon dioxide. The Oxygen Combustor/Calciner can be operated as either a bubbling fluidized bed, or a circulating fluidized bed.

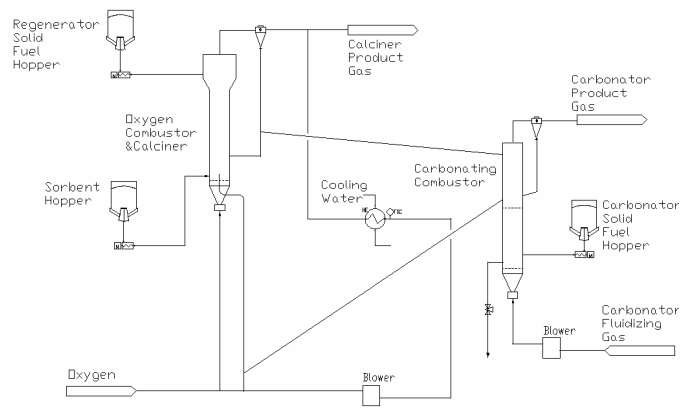

Figure 1. Atmospheric Dual Fluidized Bed Combustion System with CO_2 Capture.

Procedure

Process simulation using ASPEN Plus been used to establish the mass and energy balances of interest for equipment selection and design. A high-level view of the simulation can be seen in Figure 2. Combustion, carbonation, calcination and sulphation are simulated using combinations of the RYIELD, RSTOIC, RCSTR, and REQUIL reactor blocks. Fluidized bed combustion simulation for this system is described by Sotudeh-Gharabaagh *et al.*[6] Sorbent degradation and fluidization requirements are calculated using an Excel calculation block within ASPEN.

Model verification for bubbling fluidized bed combustion and circulating fluidized bed combustion has been verified using an existing 0.1-metre inner diameter CETC-O mini-circulating fluidized bed combustor. Results of mini-pilot plant studies will be used to fine tune process simulations for both atmospheric carbonation as described here, and pressurized carbonation as described by Wang[7].

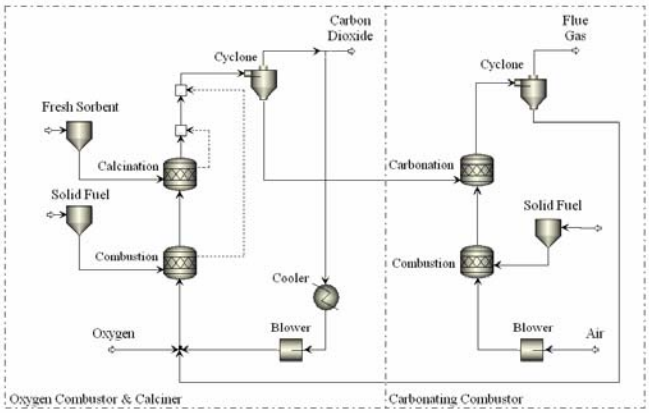

Figure 2. ASPEN Plus Simulation of Fluidized Bed Combustion System with CO_2 Capture.

Results and Discussion

Preliminary investigations using the existing CETC-O mini-fluidized bed combustor indicate that varying operating conditions and limestone sorbents can result in a range of sorbent conversions. In general, the sorbent conversion can be estimated using the model proposed by Abanades[8]:

$$X_N = f_m^N (1 - f_W) + f_W \qquad (3)$$

where X_N is the maximum carbonation conversion obtained after N cycles for a predetermined carbonation time (often reported at 20 minutes). Parameter values of $f_m = 0.77$ and $f_W = 0.17$ for this model have been shown to fit data for unmodified limestone sorbents quite well. This model indicates that conversion is reduced to ~0.17 after 20 carbonation-calcination cycles. Batch studies in the bubbling fluidized bed regime show that the mini-fluidized bed combustor results in conversions similar to those reported for thermogravimetric analysis under most conditions[9]. Limestone type, CO_2 concentration, and operating temperature can affect conversion to a small extent. Sorbent losses through attrition have been found to be low.

Recent pore modification studies[10] at CETC-O indicate that conversion can be greatly increased by a simple treatment step prior to sorbent injection into the carbonator. Conversion as high as 52% after 20 cycles (20-minute carbonation) can be obtained in a thermogravimetric analyzer. Conversions as high as 59% after 20 cycles (20-minute carbonation) are predicted through extrapolation of tests with the number of cycles limited to four. Operating at conditions resulting in these high conversions could result in a combustion process with less than 3% CO_2 in the flue gas, and a separate concentrated CO_2 stream (>85% CO_2). However, the pore modification step increases the friability of the sorbent, which will lead to increased sorbent losses due to attrition. The mini-pilot plant will be used to examine sorbent losses due to elutriation and to study conversion in a continuous process.

Conclusions

A flexible atmospheric dual fluidized bed combustion system using high temperature sorbents for *in situ* CO_2 capture has been designed and constructed. The process simulations developed for the design of the mini-pilot plant will be used for scale-up studies and process verification of commercial scale simulations based on the results of pilot plant operation. The pilot plant is expected to combust coal and petroleum coke in a clean and efficient manner, emitting a flue gas containing less than 3% CO_2, while producing a relatively pure carbon dioxide stream ready for compression. SO_2 emissions are expected to be in the parts per million range.

Acknowledgment. The authors wish to thank Dr. Artruro Macchi of the University of Ottawa for reviewing the design of the dual fluid bed system.

References

(1) Harrison, R.M. (ed.), Understanding our Environment: An Introduction to Environmental Chemistry and Pollution. Royal Society of Chemistry, **1992**.
(2) Shimizu, T., Hirama, T., Hosoda, H., Kitano, K., Inagaki, M., and Tejima, K., A Twin Fluid-bed Reactor for Removal of CO_2 from Combustion Processes. **1999,** Trans IChemE 77, 62.
(3) Abanades, J.C., Alvarez, D., Anthony, E.J., and Lu, D., In-situ Capture of CO_2 in a Fluidized Bed Combustor. Proceedings of the 17th FBC Conference, ASME, Jacksonville, Florida, **2003**.
(4) Grace, J.R., Avidan, A.A., and Knowlton, T.M. (eds.), Circulating Fluidized Beds. Blackie Academic and Professional, **1997**.
(5) Gustavsson, L., Reduction of N_2O in Fluidized Bed Combustion by Afterburning. PhD Thesis, Chalmers University, Sweden, 1995.
(6) Sotudeh-Gharabaagh, R., Legros, R., Chaoiki, J., and Paris, J., Simulation of Circulating Fluidized Bed Reactors using ASPEN Plus. **1998**, Fuel 77(4), 327.
(7) Wang, J., Anthony, E.J., and Abanades, J.C., A Simulation Study for Fluidized Bed Combustion of Petroleum Coke with CO_2 Capture. Proceedings of the 17th FBC Conference, ASME, Jacksonville, Florida, **2003**.
(8) Abanades, J.C. and Alvarez D., **2003**, Energy Fuels 17, 308–315.
(9) Salvador, C., Lu, D., Anthony, E.J., and Abanades, J.C., Enhancement of CaO for CO_2 capture in an FBC environment. **2003**, Chemical Engineering Journal 96, 187.
(10) Hughes, R.W., Lu, D., Anthony, E.J., and Wu, Y., Improved Long-term Capacity of a Limestone Derived Sorbent For In Situ Capture of CO_2 in a Fluidized Bed Combustor. **2004**, Ind. Eng. Chem. Res. *In print.*

CO_2 ADSORPTION WITH ATTRITION OF DRY SORBENTS IN A FLUIDIZED BED

Sang-Sup Lee[1], Jeong-Seok Yoo[2], Gil-Ho Moon[2], Sang-Wook Park[3], Dae-Won Park[3], and Kwang-Joong Oh[1]

(1) Department of Environmental Engineering, Pusan National University, Pusan, 609-735, Korea (2) *Doosan Heavy Industries & Construction Com. Ltd. R&D Center, Changwon, 641-792, Korea* (3) Department of Chemical Engineering, Pusan National University, Pusan, 609-735, Korea

Introduction

A number of techniques have been used for separation of carbon dioxide, one of the main greenhouse gases, from flue gas streams. Of these techniques chemical absorption and fixed bed process are commercially operated. The chemical absorption process can control carbon dioxide with high removal efficiency, but it is a very energy intensive process for carbon dioxide removal and has a problem with corrosion. In addition, fixed bed process is simple to operate, but it also requires much energy for carbon dioxide control, and can not treat high volumes of flue gases. Therefore, new technology is required to decrease the cost for carbon dioxide control and to treat high volumes of flue gases.

A fluidized bed is known as a proper process to control high volumes of flue gases, and dry sorbents can be used to cut down the cost for control, so the use of dry sorbents in a fluidized bed is considered as a proper process to remove carbon dioxide economically[1)]. However, research is required for developments of the fluidized bed process with dry sorbents which have low attrition and high adsorption capacity for carbon dioxide.

Therefore, in this study, activated carbon, activated alumina, molecular sieve 5A, and molecular sieve 13X, which have been used in fixed bed process, are used as dry sorbents to control carbon dioxide in a fluidized bed. In addition, the characteristics of CO_2 adsorption and attrition of the dry sorbents are investigated. The objective of this study is to provide basic data for process development.

Experimental

Apparatus and procedure for attrition experiment. Three-hole air jets used by Gwyn on the basis of a research of Forsythe and Hertwig[2)] were used to investigate attrition of dry sorbent with fluidization.

Air came from a compressor (Hanshin piston), moisture and particles in the air are removed, passing a trap, and mass flow controller (5850E, Brooks Co.) controlled air flow rate. The dry sorbents after the attrition were collected, and the particle sizes of them were measured by sieves of 60, 80, and 140 mesh size.

Apparatus and procedure for adsorption experiment. An experimental fluidized bed reactor has a 6cm diameter and 95cm height, and the air box of the reactor has a 10cm height. The distribution plate was made to 3.11% fractional opening and 3mm thickness, considering pressure drop in the bed. The cyclone was made by standard proportion. This reactor was made from acryl.

Air flow rate was controlled by a flow meter, CO_2 (99.9%) flow rate was controlled by mass flow controller (5850E, Brooks Co.), and then 10% CO_2 inlet concentration was maintained by mixing in a mixing chamber. CO_2 outlet concentration was also measured by CO_2 analyzer (Landfill Gas Analyzer), and the pressure in the reactor was measured by pressure sensors and analyzed by a computer program.

Results and Discussion

The particle sizes of activated carbon were measured after the fluidization for 0, 10, 20, and 30 hours at 10L/min gas flow rate to investigate the attrition characteristics with fluidization time. At each time point, the weight of particles remaining in 60 mesh sieves was 44.10g, 42.05g, and 41.07g, and the weight of carryover particles was 3.69g, 5.32g, and 5.90g, so the attrition of dry sorbents was considered to occur in the beginning of fluidization. Furthermore, carryover particles were considered as the standard to estimate attrition of dry sorbents because their particle sizes were less than 140 mesh size.

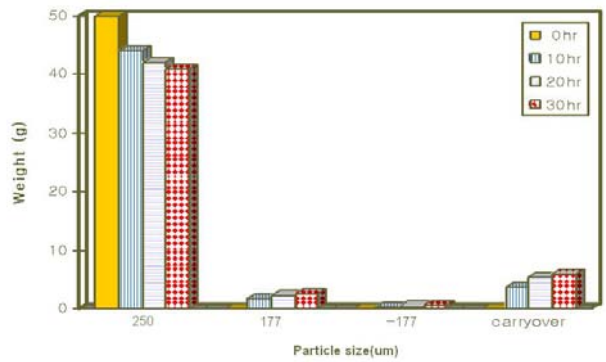

Figure 1. Particle size distribution of activated carbon with time at 10L/min gas flow rate.

Gas velocity is an important operating condition in the fluidized bed process, and it can highly affect the attrition of dry sorbents. Therefore, this study measured the weight remaining in the bed with fluidization time for a gas velocity of 20.59 cm/s, 25.74 cm/s, and 30.89 cm/s to estimate the attrition of dry sorbent with gas velocity. As shown in Fig. 2, attrition mainly occurred in the early stage of fluidization. The attrition rate decreased with time, and the regression equations fit natural log functions. In addition, Fig. 2 showed that the attrition of dry sorbents is highly affected by air velocity in the fluidized bed process.

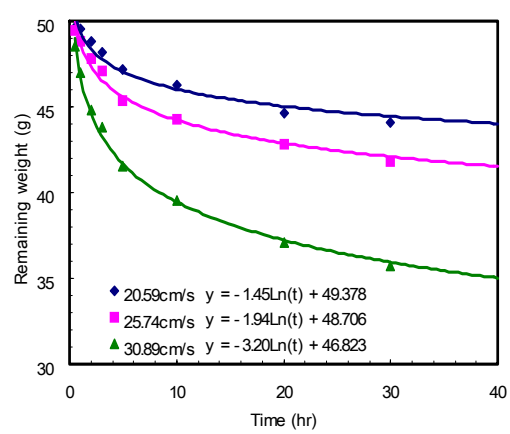

Figure 2. The remaining weight with time for attrition of 40/60mesh activated carbon.

Fig. 3 shows the remaining weight of dry sorbents with time. For every dry sorbent, attrition mainly still occurs in the early stage of fluidization. Moreover, using AI (Attrition Index) on the basis of the weight after 5 hours, the AI of molecular sieve 5A and molecular sieve 13X presented 2.1~4.0-fold higher than the AI of activated carbon and activated alumina. Therefore, the use of them in a fluidized bed can cause high maintenance cost for dry sorbent and problems in the operation of a process.

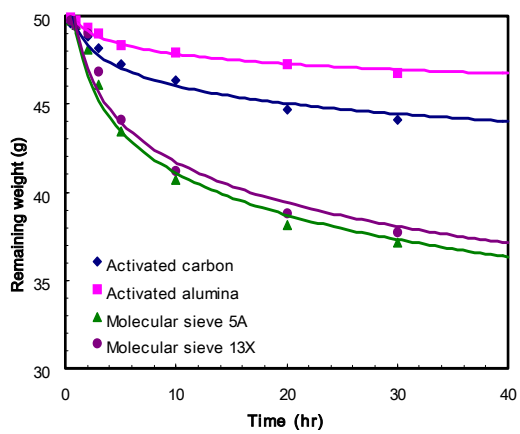

Figure 3. The remaining weight with time for attrition of dry sorbents.

Fig. 4 and Fig. 5 are CO_2 adsorption breakthrough curves and adsorption capacity with dry sorbents. These adsorption experiments were carried out in the operating conditions with an aspect ratio of 2 (L/D) and 12 cm/s gas velocity. The breakthrough points defined as the points in the 5% of inlet concentration were 1.65 minutes for molecular sieve 5A and 1.46 minutes for molecular sieve 13X, and those values were 2.47~3.0-fold higher than activated carbon and activated alumina.

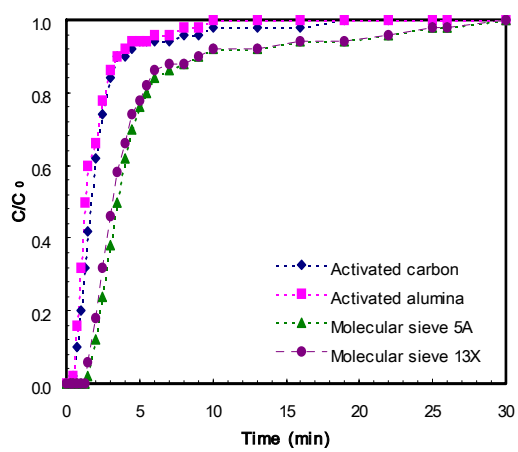

Figure 4. CO_2 adsorption breakthrough curves with dry sorbents in fluidized bed.

Furthermore, as shown in Fig. 5, the adsorption capacities, calculated from the area above the curves in Fig. 4, were 2.35mmol/g for molecular sieve 5A, and 2.23mmol/g for molecular sieve 13X, and those values were 1.5~2.7-fold higher than activated carbon and activated alumina. The relatively high value of the adsorption capacity for activated carbon results from relatively high apparent density.

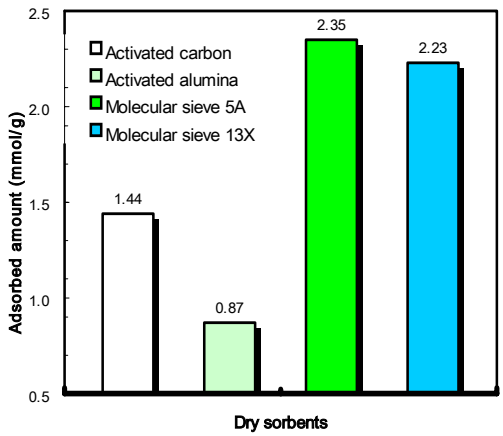

Figure 5. The adsorbed amount of CO_2 with dry sorbents in fluidized bed.

Conclusions

In the fluidized bed process, attrition caused dry sorbent to be carryover. This mainly occurred in the early stage of fluidization and was highly affected by gas velocity. Molecular sieve 5A and molecular sieve 13X presented 2.1~4.0-fold higher attrition than activated carbon and activated alumina, so they possibly cause high maintenance cost for dry sorbent and problems in the operation of fluidized bed process.

On the other hand, the adsorption capacities of molecular sieve 5A and molecular sieve 13X were 2.35mmol/g and 2.23mmol/g, and these values were 1.5~2.7-fold higher than the other sorbents.

Acknowledgement. This research was supported by a grant (DA1-202) from Carbon Dioxide Reduction & Sequestration Research Center, one of the 21st Century Frontier Programs funded by the Ministry of Science and Technology of Korean government.

References

(1) Hoffman, J. S.; Pennline, H. W.; "Study of regenerable sorbents for CO_2 capture," *J. Energy. & Environ. Res.*, **2001**, 1(1), pp. 90～100.

(2) Forsythe, W. L. and Hertwig, W. R., "Attrition characteristics of fluid cracking catalyst," *Ind. Eng. Chem.*,**1949**, 41, pp. 1200～1206.

(3) Cook, J. L.; Khang, S. J.; Lee, S. K.; and Keener, T. C.; "Attrition and changes in particle size distribution of lime sorbents in a circulating fluidized bed absorber," *Powder Technology*, **1996**, 89, pp. 1～8.

(4) Oh, K. J; Lee, S. S; Choi, W. J; Kim, M. C; "CO_2 adsorption characteristics of dry sorbent in fluidized bed.", *Carbon Dioxide Reduction & Sequestration Workshop*, **2003,** pp. 399

Developing and using mechanisms for the oxidation of organic compounds in the atmosphere

M. J. Pilling

School of Chemistry, University of Leeds, Leeds, LS2 9JT, United Kingdom

The master chemical mechanism (MCM) is an explicit chemical mechanism describing the tropospheric oxidation of 125 volatile organic compounds. It is mounted on the Leeds Chemistry website at:

http://www.chem.leeds.ac.uk/Atmospheric/MCM/mcmproj.html

The mechanism has been assembled using a protocol with comparatively few simplifications. The rate data and product yields are based on experiment, theory, estimation and analogy.

Following a brief outline of the website and the protocol, the following issues will be discussed:

- approaches to the determination of mechanism components using direct measurements of reaction rates and chamber experiments;
- uncertainty estimation;
- approaches to reduction and lumping;
- tests of the mechanism using outdoor chamber and field experiments, in clean and polluted environments

AB INITIO STUDY OF THE OXIDATION OF NCN BY O_2

R. S. Zhu, and M. C. Lin

Department of Chemistry
Emory University
Atlanta, GA 30322

I. Introduction

NCN is the major radical formed in the new prompt NO reaction, CH + N_2 → HNCN → NCN + H.[1] The oxidation of NCN radicals to NO is critical to our full understanding of the prompt NO formation mechanism.

In this series of studies, we have investigated the reactions of NCN with O, OH[2] and O_2 by ab initio MO calculations. We report here the result for the latter process NCN + O_2.

II. Computational Methods

The potential energy surface (PES) was calculated at the highest scheme of the G2M method.[3] The Gaussian 03 program[4] was used for the molecular orbital calculations.

The rate constants were computed with microcanonical variational RRKM (Variflex) code.[5]

III. Results and Discussion

A. Potential Energy Surface and Reaction Mechanism

The optimized geometries of the intermediates and transition states are shown in Figure 1. The potential energy diagram obtained at the G2M(CC1)//B3LYP/6-311G(d, p) level is presented in Fig. 2.

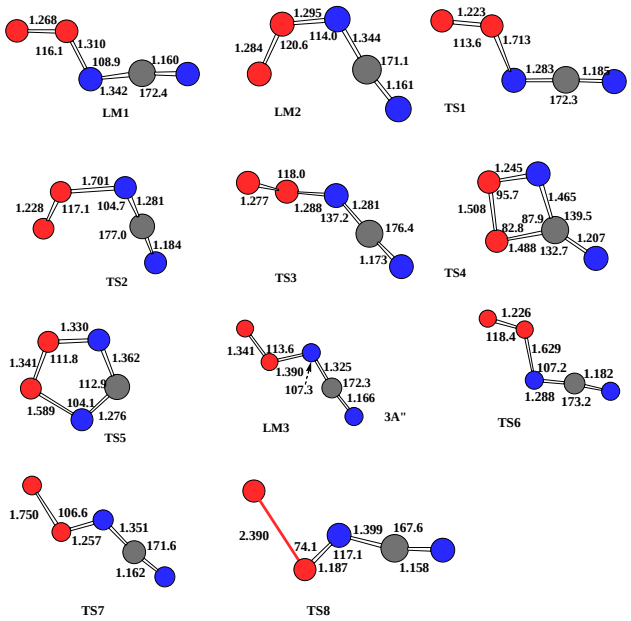

Figure 1. The optimized geometry of intermediates and transition states computed at the B3LYP/6-311G(d, p) level for the NCN + O_2 reaction.

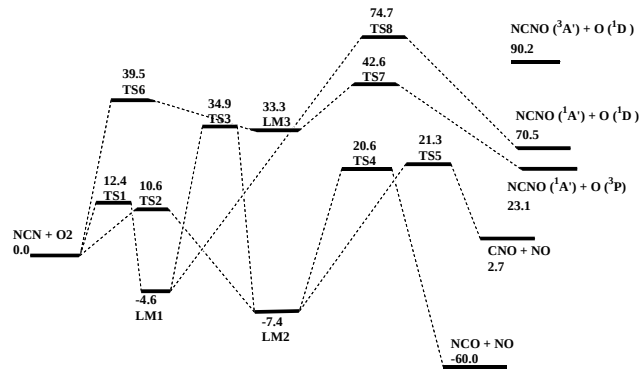

Figure 2. The schematic diagram of the potential energy surface for the NCN-O_2 system computed at the G2M(CC1) level.

The following possible channels are considered for this oxidation reaction:

$$NCN + O_2 \rightarrow NCNOO^{\dagger} \rightarrow NCO + NO \quad (1)$$
$$\rightarrow CNO + NO \quad (2)$$
$$\rightarrow NCNO + {}^{1,3}O \quad (3)$$

The lowest energy isomer is cis-trans-OONCN (LM2), it lies below the reactants by 7.4 kcal/mol at the G2M(CC1) level. It can dissociate to NCO + NO and CNO + NO via four- and five-member ring transition states with barriers of 28.0 and 28.7 kcal/mol. The entrance barrier for this channel is 10.6 kcal/mol. The other isomer, trans-trans-OONCN intermediate (LM1) lies below the reactants by 4.6 kcal/mol with a entrance barrier of 12.4 kcal/mol, which dissociates to NCNO + ^{1}O via a transition state with high barrier, 79.3 kcal/mol. In addition, the stability of the triplet intermediate is also considered, the results show that ^{3}A" trans-trans-OONCN (LM3) lies above the reactants by 33.3 kcal/mol, which means that the triplet path is not favorable for this reaction.

B. Rate constant calculations

The rate constants are calculated in the temperature range of 1000 - 3000 K, the results show that oxidation NCN by O_2 to produce NCO + NO and CNO + NO is rather slow because of the high entrance and exit barriers. The total rate can expressed as:
$k_t = 7.29 \times 10^{-15}\ T^{0.51} \exp(-12365/T)$ cm^3 molecule^{-1} s^{-1}.

IV. Conclusion

The mechanism for the oxidation of NCN by O_2 has been discussed and rate constants for the low-lying channels are calculated. The results show that oxidation NCN by O_2 to produce NCO + NO and CNO + NO is very slow because of the high entrance and exit barriers. This reaction can not compete effectively with the much faster oxidation processes, NCN + O and OH.[2]

Acknowledgement

This work is sponsored by the Office of Naval Research under contract no. N00014 – 02-1-0133, Dr. J. Goldwasser program manager. Acknowledgment is also made to the Cherry L. Emerson Center of Emory University for the use of its resources, which are in part supported by a National Science Foundation grant (CHE-0079627) and an IBM Shared University Research Award.

References

(1) Moskaleva, L. V.; Xia, W. S.; Lin, M. C.. Chem. Phys. Lett. **2000**, *331*(2,3,4), 269.

(2) Zhu, R. S.; Lin, M. C.; to be published.
(3) Mebel, A. M.; Morokuma, K.; Lin, M. C. *J. Chem. Phys.* **1995**, *103*,7414.
(4) M. J. Frisch, M. J. et al., *GAUSSIAN 03, REVISION B.0*1; Gaussian, Inc., Pittsburgh PA, **2003**.
(5) Klippenstein, S. J. ; Wagner, A. F.; Dunbar, R. C. ; Wardlaw, D. M. and Robertson, S. H. VARIFLEX: VERSION **1.00**, **1999**.

The Molecular Origins of NO Selectivity in the Thermal Reduction of NO_x by NH_3

Donghai Sun[†], *William F. Schneider**, *James B. Adams*[†], *Debasis Sengupta*[‡]

[†]Department of Chemical and Materials Engineering, Arizona State University, Tempe, AZ-85287
*Ford Motor Company, Mail Drop 3083/SRL, Dearborn, Michigan 48121-2053
[‡]CFD Research Corporation, 215 Wynn Drive, Huntsville, AL 35805

Introduction

Thermal deNO_x process is an effective way for "lean" NO_x (x= 1, 2) control for stationary sources and attracting serious attention for selective catalytic reduction of NO_x by NH_3 from mobile-sources. The fundamental mechanism underlying the thermal deNO_x chemistry is the selective reduction of NO_x over a large excess of O_2. This mechanism involves generation of the amino (NH_2) radical through chain reactions that involve O atoms and OH radicals,[1, 2] and the NH_2 is reacting directly with NO to ultimately produce N_2. Competition between NO and O_2 for the "activated" NH_2 reductant is thus inherent to the overall chemistry. The reactions of NH_2 with NO and O_2 have been studied extensively both theoretically and experimentally: [3,4,5,6,7,8,9,10,11]

$$NH_2 + NO \rightarrow \text{Products} \qquad (1)$$
$$NH_2 + O_2 \rightarrow \text{Products} \qquad (2)$$

Fortunately, the rate of reaction (1) (10^{-12} cm^3 molecule^{-1} s^{-1} at 2000 K) is observed to be 10 orders of magnitude faster than that of reaction (2) (10^{-21} cm^3 molecule^{-1} s^{-1} at room temperature) although they proceed through topologically similar channels. The primary channels of reaction (1) are: [4,5,7,12]

$$NH_2 + NO \rightarrow N_2 + H_2O \qquad (3)$$
$$\rightarrow HN_2 + OH \qquad (4)$$

The reaction (2) analogs to channels (3) and (4) are:

$$NH_2 + O_2 \rightarrow NO + H_2O \qquad (5)$$
$$\rightarrow HNO + OH \qquad (6)$$

Although reactions (1) and (2) have been studied individually in great detail, little attention has been paid to understanding the origins of the very different kinetics of these superficially similar reactions. In this paper, the potential energy surfaces of these two reactions have been analyzed and the origin of the NO selectivity is attributed to the much greater stability of the initial H_2NNO adduct relative to H_2NOO radical with analysis of their electronic structures.

Computational Method

DFT calculations were performed with the Amsterdam Density Functional (ADF) package with the spin-polarized BLYP approximation. [13,14,15,16] A valence double-ζ plus polarization Slater-type basis was used on all atoms.

Results and Discussion

Figures 1 and 2 summarize the key potential energy surface for reactions (1) and (2) in which analogous steps of both reactions are considered together in parallel for comparison.

The mechanistic origins of the NO selectivity that underpin thermal deNO_x are readily apparent from Figure 1. NH_3 itself is unreactive towards NO and O_2; rather, NH_3 is activated for reaction by removal of an H atom to produces NH_2 radicals. NH_2 radical forms a relatively strongly bound (54 kcal mol^{-1} from BLYP) adduct with NO. Particularly favorable electronic interactions produce strong σ and π bonding in the molecular structure of H_2NNO. In contrast, NH_2 radical forms a relatively weakly bound adduct with O_2 (15 kcal mol^{-1} from BLYP): O_2 has one more electron and less accessible 2π acceptor levels than NO, and H_2NOO radical has neither the strong σ nor π bonds of H_2NNO. As seen in Figures 1 and 2, beyond the adduct formation step the potential energy surfaces for the two reactions are superficially quite similar. The paths to the thermodynamic products involve a sequence of H-transfer, isomerization, and decomposition steps, the most highly activated of which is the initial $H_2NXO \rightarrow HNXOH$ H-transfer (X=N, O). These steps compete with backwards decomposition to reactants, and the balance between forward and backward steps controls the overall reaction rate. For strongly bound H_2NNO, the forward reaction steps are all at lower energy than the entrance channel, and essentially all H_2NNO formed react forward to products in what is in effect a single elementary step. [17] In contrast, weakly bound H_2NOO radical is shifted upwards in energy such that the forward reaction channels involve energy barriers greater than the energy to decompose back to reactants, and only at high temperatures do any of the forward reaction channels occur at an appreciable rate. [18] Remarkably, then, the difference in initial adduct stability alone accounts for the much different rates of the NH_2 + NO and NH_2 + O_2 reactions.

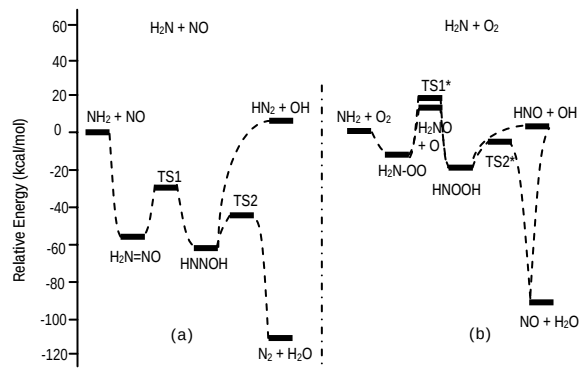

Figure 1. BLYP-calculated potential energy surfaces for reactions (a) NH_2 + NO and (b) NH_2 + O_2. HNXOH (X = N, O) isomerization details hidden for clarity

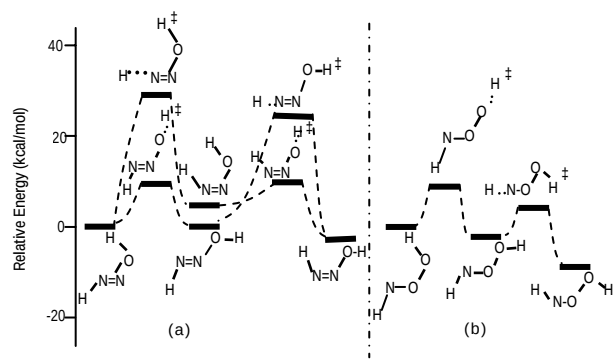

Figure 2. BLYP-calculated potential energy surfaces for isomerization of (a) HNNOH and (b) HNOOH.

It is interesting to consider the generality of this difference in reactivity between NO and O_2. Table 2 compares the R–NO and R–O_2 bond dissociation energies for a number of common alkyl and heteroatomic free radicals R for which data is available. NO is found to readily bind to all the radicals within this sample set: bond strengths range from around 40 to less than 60 kcal mol^{-1}, with the strongest bonds tending to be π donor radicals, such as NH_2 or OH radical. For practical purposes NO does not thermochemically discriminate within this set, and consistent with the behavior typical

Table 1. Comparison of 298 K R–NO and R–O_2 bond strengths (kcal mol^{-1}). All experimental values from ref. [19]

	R–NO	R–O_2	Δ
H	47	49	–2
CH_3	40	33	7
i-C_3H_7	37	37	0
CF_3	43	37[a]	6
HO	49	7[b]	42
CH_3O	42	–4[c]	46
F	57	13	44
Cl	38	6	33
NH_2	48[d]/54[e]	0[e]/15[f]	~40-50

a. Calculated, ref. [20] b. Calculated, ref. [21] c. Calculated, ref. [22] d. Calculated, ref. e. Calculated, ref. f. Calculated, this work.

for free radical combination reactions, the corresponding R + NO high pressure limiting rate constants are large — typically within an order of magnitude of the gas-kinetic limit.[19] O_2 presents an interesting contrast. Within the H and alkyl radical group, the R–O_2 and R–NO bond strengths are comparable and the difference between the two is uniformly small. Consistent with this, the R + O_2 reaction rate constants are comparable to those for R + NO, and thus these R-radicals exhibit little inherent selectivity in reactions with NO over O_2; i.e. neither CH_3 radical nor H radical will selectively combine with or reduce NO in the presence of O_2.

The heteroatom (halogen, O, and N)-centered radicals behave much differently. Here the R–O_2 bond energies are very small—so small that accurate experimental determination is difficult, and the most reliable estimates tend to come from first-principles calculations. While there are uncertainties in some of these R–O_2 bond energies, what is not uncertain is that the bonds are on the order of 40 kcal mol^{-1} weaker the R–NO ones. Because these are association reactions, the relative bond energies dominate the relative reaction rate constants, and the corresponding R + O_2 reactions are similarly much slower than the R + NO ones.[23] (Precise reaction rate comparisons are complicated by the existence of multiple reaction channels, large sensitivities to pressure, temperature, and diluent, and the limited availability of data for the slow R + O_2 reactions.) Thus, these heteroatomic radicals are selective in their reactions with NO over O_2, not because of some inherent preference for NO but rather because of inherent unreactivity towards O_2. While we have only considered in detail the NH_2 radical case here, it is likely that the slow reactions of the other heteroatomic radicals with O_2 have similar explanations in terms of π repulsions and poor σ bonding. Any of these heteroatomic radicals will selectively combine with NO in the presence of O_2; NH_2 radical is particularly useful because reaction with NO ultimately leads to reduction to N_2.

Conclusions

Any useful system for catalytically reducing NO_x in lean exhaust must have as its basis very high selectivity for reactions of reductant with NO_x over O_2, both to counterbalance the great thermodynamic driving force for oxidation reactions and to overcome the large disparities in concentration between small amounts of NO_x and large amounts of background O_2. Within a limited range of conditions, this selectivity is achieved without catalysts in the thermal deNO_x process. NH_2 radicals generated in situ from NH_3 are many orders of magnitude more reactive towards NO than O_2. NH_2 radicals form a strong bond with NO to produce H_2NNO, which provides an entrance into rearrangement channels ultimately yielding the desired products N_2 and H_2O. What is unusual in this system, though, is not the fast rate of the NH_2 + NO reaction—in fact, this reaction proceeds at rates comparable to other radical + NO reactions. Rather, the key feature that underpins thermal deNO_x is the very slow reaction of NH_2 radical with O_2. The H_2NOO adduct is weakly bound, and fragmentation back to reactants competes very effectively with channels ultimately leading to NO and H_2O. This weak binding and slow reaction is characteristic of O_2 reactions with heteroatomic radicals, such as F, OH or NH_2, but not of reactions with H or carbon-centered radicals. Its origins lie in π repulsions and weak σ bonding between O_2 and electron-rich radicals.

These observations provide a different perspective on the selective catalytic reduction of NO_x with NH_3 or hydrocarbons. Effective catalysts clearly must be able to bind and activate reductants and to maintain or enhance selectivity in reductant reactivity between NO and O_2. While mechanistic emphasis tends to be placed on understanding the reactivity of NO_x, the absence of reactivity with O_2 is at least as important to understand.

Acknowledgement

The authors gratefully acknowledge helpful conversations with Ole John Nielsen, Steve Harris, Tim Wallington, Chris Wolverton and Paul Schuck, as well as support from the Department of Energy under grant DE-F603-99ER14985 and from the National Center for Supercomputing Applications for computer resources on their SGI Origin cluster at project RTM (8141).

References

1 Miller, J. A.; Bowman C. T. *Progress in Energy and Combustion Science*, **1989**, *15,* 287.
2 Lyon, R. K. *Diesel Engine Emissions Reduction (DEER) Workshop*, **2001**.
3 Wolf , M.; Yang, D. L.; Durant J. L. *J. Phys. Chem. A* **1997**, 101, 6243.
4 Vandooren , J.; Bian, J.; Tiggelen, P. J. *Combustion & Flame,* **1994,** 98, 402.
5 Diau, E. W.-G; Smith, S. C. *J. Chem. Phys.*, **1997,** 106, 9263.
6 Sumathi , R.; Peyerimhoff, S. D. *J. Chem. Phys.*, **1998**, 108, 5510.
7 Marcy, P. T.; Heard , E. D.; Leone, R. S. *J. Phys. Chem. A,* **2002**, 106, 8249.
8 Park, J.; Lin, M. C. *J. Phys. Chem. A*, **1997**, 101, 5.
9 Miller, J. A.; Glarborg, P. *Int J. Chem. Kinet.*, **1999**, 31, 757.
10 Diau, E. W.; Yu, T.; Wagner, M. A. G.; Lin, M. C. *J. Phys. Chem.*, **1994**, 98, 4034.
11 Yamasaki , K.; Watanabe, A.; Tanaka, A.; Sato, M.; Tokue, I. *J. Phys. Chem.*, **2002**, 106, 6563.
12 Votsmeier, M.; Song, S.; Hanson, R. K.; Bowman, C. T. *J. Phys. Chem. A*, **1999**, 103, 1566.
13 Baerends, E. J.; Ellis, D. E.; Ros, P. *Chem. Phys.*, **1973**, 41, 1.
14 Becke, A. D. *Phys. Rev. A*, **1998**, 38, 3098.
15 Lee, C.; Yang, W.; Parr, R. G. Phys. Rev. B, 1988, 37, 785.
16 Miehlich, B.; Savin, A.; Stoll, H.; Preuss, H. *Chem. Phys. Lett.*, **1989**, 157, 200.
17 Miller, J. A.; Klippenstein, S. J. *J. Phys. Chem. A*, **2000**, 104, 2061.
18 Bozzelli, J. W.; Dean, A. M. *J. Phys. Chem.*, **1989**, 93, 1058.
19 NIST Chemical Kinetics Database, Hhttp://kinetics.nist.govH.
20 Schneider, W. F.; Wallington, T. J. **J. Phys. Chem.**, **1993**, 97, 12783.
21 Denis, P. A.; Kieninger, M. O.; Ventura, N.; Cachau, R. E.; Diercksen, G. H. F. *Chem. Phys. Lett.*, **2002**, 365, 440.
22 Jungkamp, P. W.; Seinfeld, J. H. *Chem. Phys. Lett.*, **1996**, 257, 15.
23 Ruscic, B.; Berkowitz, J. *J. Chem. Phys.*, **1991**, 95, 4378.

Computer Aided Design of Complex Chemical Mechanism for Combustion Applications

F. Mauss

Division of Combustion Physics, Lund University, P.O. Box 118
SE-22100 LUND, Sweden

Introduction

Combustion, in technical applications, occurs under turbulent flow conditions. In modeling combustion devices with numerical tools it is necessary to consider the interaction of chemistry and flow. Chemistry-flow interaction models are demanding in both, computational time and memory. Thus, they limit the number of chemical species that can be explicitly taken into account. Technical fuels are mixtures of aliphatic and aromatic hydrocarbons that introduce chemical mechanism with hundreds of species and thousands of reactions. These numbers make it difficult to compile, analyze or optimize such mechanism; they make it impossible to use these mechanisms together with computational fluid dynamical (CFD) programs. In addition to computational tools for mechanism generation, analysis and optimization, a variety of reduction methods are needed to lump parallel reaction paths, to detect unnecessary reactions and species, and to simplify the model equations for species reacting on time scales that are much shorter than the relevant physical time scales. In this paper an overview over available methods and their interaction is given.

Mechanism development for combustion applications

The compilation of detailed kinetic reaction mechanisms is a difficult and time consuming task. A set of elementary reactions is stated for each fuel. The data for the kinetic rate constants are taken from experiments or, if experiments are not available, from quantum mechanical calculations. Together with the rate constants the uncertainty of the kinetic data has to be stated. If the set of chemical reactions is complete, the mechanism has to be validated against experiments for global parameter such as ignition delay times, flame velocities of freely propagating premixed flames, and extinction limits of counterflow diffusion flames.

The first estimation of the mechanism will, caused by the uncertainties in the elementary reactions, result in a poor agreement between simulation and experiments, and improvements are necessary. The next step in compiling the reaction mechanism is to perform a detailed sensitivity analysis of the global parameter against all chemical rate coefficients. As a result of the analysis one gets a set of reactions that is most important for the currant experiment. Hence the kinetic rate constants of these reactions need to be as accurate as possible. An iterative process of adjusting these rate coefficients and recalculating the experiments for the mechanism validation is utilized until the first set of optimized rate coefficients is reached.

In a second step the mechanism will be refined by controlling local parameter instead of the global ones. These are usually the time- or space resolved profiles for temperature, fuel, oxidizer, and for some intermediate and final products. Again an iteration procedure, as explained above, is employed that finally leads to a more improved reaction mechanism. Further improvement can be reached by controlling more sensitive local parameter like pollutants such as NO_x and soot. For each step, in refining the reaction mechanism special emphasis must be taken to guarantee that the prediction of the targets defined for the prior optimization step is not worsened.

In the past such mechanisms have been constructed manually for hydrocarbon fuels up to butane. These mechanisms contain about 600 reactions and 80 species (see for example reference [1]). But for most of the mechanisms, found in the literature, the more complicated low-temperature kinetics for butane is missing. This is partly caused by, that in most technical application the low temperature oxidation of butane is not sensitive.

For higher hydrocarbon fuels this neglect is not possible, since for some technical relevant processes—for example the occurrence of the engine knock phenomenon in spark ignition engines—low temperature reaction pathways are essential. However the detailed inclusion of low temperature reaction for fuels like *n*-heptane involves more than 500 species and 4000 reactions [2]. It is almost impossible to compile such a mechanism by hand, and early reaction mechanisms were based on simplified models for the low-temperature oxidation of aliphatic fuels. These mechanisms have been validated for global parameter such as ignition delay times and flame velocities, only.

A more detailed description of the low-temperature oxidation is weakly motivated, since the high number of reactions and species involve many practical problems—the demanded effort in computational time and memory, the high number of reactions with unknown rate coefficients. It became visible that an automation of the steps, performed to develop a chemical reaction mechanism is needed to accelerate the progress in the field.

Automation of the mechanism development

The first automation in the process was the development of tools to analyze the chemical processes during combustion processes, i.e. the reaction flow analysis and the sensitivity analysis (see for example the overview article [3]). For the former the reaction fluxes from species to species are calculated in a post process to the combustion calculation, and a map can be drawn that visualizes the flow of atoms. For the latter the frequency factor in the Arrhenius approximation for the reaction velocity is used as a parameter in the system of differential equations. The sensitivity of unknowns on the reaction rate coefficient can be calculated from the sensitivity of the residual of the respective differential equation and the jacobian matrix of the underlying system of equations.

The next automation was the automatic generation of reaction mechanisms. The definition of chemical reactions for certain molecules was replaced by the definition of reactions of certain groups appearing in the molecules [4, 5]. Programs were written that scan through the fuel molecules and the intermediate species to find the specific molecule groups and to apply the corresponding reactions. At the first glance, this approach appears to be simple but the approach is leading to explosions in the number of species and the number of reactions, if no limitation is set. The first generated reaction mechanisms appeared a decade ago, and the number of applications, where a generated reaction mechanism is used is still low.

Finally the optimization of the reaction rate coefficients was automated. In a first step sensitive reactions for the targets—for example, unknowns at certain data points—to be optimized are selected from the matrix of sensitivity coefficients and from the uncertainties in the rate coefficients. Response surfaces for the difference between the experimental values for the targets and the numerically calculated values are produced, and the optimum set of rate coefficients is found by searching the set of rate coefficients with the minimum difference for all targets [6, 7].

Mechanism Reduction

The gap between the number of species allowable for CFD-applications and the number of species introduced by detailed reaction mechanisms shows that the knowledge transfer from fundamental research in combustion kinetics to engineering applications relies on the availability of mechanism reduction

methods. The major reduction methods in use today can be divided into four groups. 1) removement of unnecessary reaction, 2) lumping methods, 3) simplification of the system of differential equation, through time scale analysis, and 4) tabulation methods.

The removal of unnecessary species and reactions is the oldest strategy in reducing chemical mechanism. It is intuitive to demand that an unnecessary species or an unnecessary reaction has a low chemical flux [8] and a low sensitivity on unknowns that the modeler wants to predict with high accuracy [9, 10]. However, the calculated sensitivity coefficients are only of first order accuracy and they may fail to predict, what happens if a species or a reaction is removed from a reaction mechanism. In addition the calculation of sensitivity coefficients is demanding in CPU-time. It is therefore often proposed to detect candidates for removal by reaction flow analysis, only. All strategies demand that the detailed reaction mechanism is first analyzed by a simple reactor model, for the chemistry flow interaction. Further it is demanded that the reduced reaction mechanism is validated against the detailed mechanism. The range of validity of the reduced mechanism is limited by the parameter range for the validation calculations, and by the physical importance of the employed reactor model.

A shortcoming of the necessity analysis is that it is not able to reduce the number of species or reactions in reaction systems, where the chemical flux occurs in many parallel and equally strong paths. This is the situation found for automatic generated reaction mechanisms for low temperature kinetics of aliphatic hydrocarbon fuels. In this situation the chemical lumping can lead to simplified reaction mechanisms [4, 5].

Instead of solving differential equations for the individual species one differential equation for the sum of the lumped species is solved. From this equation, the rate coefficients for the new (or general) species can be calculated. However, it is often necessary to estimate the ratio of concentrations of the lumped species [11]. This is possible if they have similar thermodynamic properties–they have almost equal concentrations.

The quasi steady state assumption (QSSA) is often applied in chemical systems. In combustion system it demands that the chemical processes are much faster than the relevant physical processes. [12] With computational singular perturbation (CSP) the set of equations governing the chemistry is described by a set of base vectors. The resulting eigenvalue problem allows the separation of fast and slow modes. Species found in the fast modes only are in steady state [13–15].

Another way to detect steady state species is to compare the chemical time of species consumption with the physical times of change in species concentration, convection and diffusion [16]. This species lifetime does not take coupled lifetimes into account. It assumes that the Jacobian matrix is diagonal [17].

Species concentrations can be solved from a set of algebraic equations if the QSSA is applied. This decreases the number of species that need to be transported in a CFD application, and thereby the demand on CPU-time and memory. In estimating how much a numerical error in species profile influences the accuracy of a target of a model calculation the sensitivity analysis, as described above can be applied [16]. In this application, sensitivity analysis gains a higher accuracy, since the error in the steady state species profile should be low; the influence of non-linearity in the sensitivity coefficients can be neglected. More steady state species can be detected, by combining the lifetime analysis with sensitivity analysis.

By using CSP fast and slow modes can be separated. A chemical system will move on the fast modes to a lower dimensional manifold, if it is started at any point in the number of species-dimensional chemical hyperspace. The development on the fast modes can be often described as a projection of the starting point on the low-dimensional manifold. A strong reduction in computational time is gained, if the intrinsic low-dimensional manifold (ILDM) is tabulated. This tabulation is done in a pre-process [18].

Conclusion

A variety of algorithms have been developed during the recent years that help the developer to generate, optimize and reduce reaction mechanisms for combustion applications. These developments build on each other and allow a fast knowledge transfer from chemical kinetic development to engineering applications. It got visible that a combination of these tools will allow computer aided design of chemical mechanism for technical applications in the near future.

References

[1] Warnatz, J, Maas, U. And Dibble, R.W., (1996), Combustion, Springer Verlag.

[2] Curran, H.J., Gaffuri, P., Pitz, W.J., and Westbrook, C.K., Combust. Flame, **114**:149–177 (1998).

[3] Tomlin, A.S. and Turnyi, T. and Pilling, M.J. (1997), "Mathematical tools for construction, investigation and reduction of combustion mechanisms", in : M.J. Pilling (Ed.), "Low-Temperature Combustion and Autoignition", Comprehensive Chemical Kinetics, Vol. 35, Elsevier.

[4] Ranzi, E., Faravello, T., Gaffuri, P., and Sogaro, A., Combust. Flame, **102**:179–192 (1995).

[5] Fournet, R., Warth, V., Glaude, P.A., Côme, G.M., Battin-LeClerc, F., and Scacchi, G. Int. J. Chem. Kin., **32**(1):36–51 (2000).

[6] Frenklach, M., Hai, W., and Rabinowitz M.J., Prog. Energy Combustion. Sci., **18**:47–73 (1992).

[7] Wang, H., Proc. Comb. Inst., **28**: (2000)

[8] Wang, H., and Frenklach, M., Combust. Flame **87**:365–370, (1991)

[9] Chen, J.Y., "Development of Reduced Mechanism for Numerical Modelling of Turbulent Combustion", Workshop on "Numerical Aspects of Reduction in Chemical Kinetics", CERMIPS-ENPS Cite Desortes – Campus sur Marne, France, 1997

[10] Soyhan, H.S., Mauss, F., and Sorusbay, C., Combust. Sci. Tech., **174**(11&12):73–91 (2002)

[11] Ahmed, S. S., Moréac, G., Zeuch, T., and Mauss, F., "Efficient lumping technique for the automatic generation of n-Heptane and iso-Octane oxidation mechanism", Prep. Pap.-Am. Chem. Soc., Div. Fuel. Chem. 2004

[12] Peters, N., and Rogg, B. (Eds.), "Reduced Kinetic Mechanism for Applications in Combustion Systems", Lecture Notes in Physics m15, Springer Verlag, 1993

[13] Lam, S.H., and Goussis, D.A., Prodc. Combust. Inst. **22**:931–941

[14] Lam, S.H., and Goussis, D.A., in "Reduced Mechanism and Asymptotic Approximations for Methane-Air Flames" (Smooke, M. Ed.), Lecture Notes in Physics 384, pp. 227–242, Springer Verlag, 1991

[15] Goussis, D.A., J. Comp.Physics, **128**:261–273, (1996)

[16] Lovås, T., Nilsson, D., and Mauss, F., Proc. Comb. Inst. **28**:1809–1815 (2000)

[17] Lovås, T., Amnèus, P., Mauss, F. and Mastorakos, E., Prodc. Comb. Inst. **29**:1387–1393 (2002)

[18] Maas, U. (1998), Efficient Calculation of Intrinsic Low Dimensional Manifolds for Simplification of Chemical Kinetics, Comput. Visual Sci. Vol. 1, pp. 69-81.

New Methods for Predictive Chemical Kinetics

William H. Green, Binita Bhattacharjee, Oluwoleo Oluwole, Jing Song, R. Sumathi, Catherina D. Wijaya, Hsi-Wu Wong, Paul E. Yelvington, & Joanna Yu

MIT Department of Chemical Engineering, Cambridge, MA 02319

Introduction

In most reactive fuel chemistry problems, there are far too many species and reactions for there to be any hope of experimentally determining the thermochemistry of each species and the rate constants of each reaction. Historically, modelers have modeled these systems empirically, constructing a small kinetic model with a few effective parameters which could be regressed from experiment. However, these small kinetic models usually do not capture the real chemistry/physics of the system, and so these models are typically only useful for interpolation, not for extrapolation or predictive design of new systems.

Recently, quantum chemistry has advanced so much that it can provide reliable values of missing rate and thermochemical parameters, at considerably less cost than determining the same values experimentally. However, these calculations are still rather difficult and unreliable, each requiring considerable care and attention. So it is not practical to compute every rate constant and thermochemical parameter that might conceivably be important in a fuel chemistry system.

Even if accurate values of all the rate constants and thermochemical parameters were available, it is still very challenging to construct and solve the appropriate kinetic models. Solving the models is particularly difficult in systems which are spatially inhomogeneous, where the chemistry is significantly coupled to transport.

Many researchers [1] have attempted to move forward in this way:
1) use the computer to construct an approximate kinetic model using approximate rate parameters
2) use this approximate model to identify the most important reactions and species
3) refine the rate parameters for the most important reactions using experiment or quantum chemistry
4) construct smaller kinetic models faithful to the original
5) use the small models in the coupled chemistry-transport simulations.

However, although this concept has been pursued by several research groups in both industry and academia, progress has been rather slow, since each step in the process involves several difficult issues, both from the point of view of chemistry, and from the point of view of computer science/numerics. This preprint reports significant progress we have made on all fronts, based on a radically different software design of the mechanism generation software, a new approach to estimating the reaction rates, and recent advances in numerical algorithms.

Results

A new software paradigm for automated mechanism generation has been developed, which cleanly separates the computer science and chemistry aspects of automated mechanism generation. The key idea is that all of the chemical detail is represented by functional group and reaction template structures and associated parameters. The computer then compares these functional group structures with each molecule in the system, to determine which molecules can react in which ways. The rate and thermochemical parameters are also based on these functional groups. The new approach has the major advantage that chemists can extend and update functional group definitions and reaction rate or thermochemistry estimates without ever touching the source code. This is very important, since our understanding of chemistry is far from complete, and it will be many years before accurate estimates will be available for all the types of reactions important in fuel chemistry. The computer science and numerical aspects of the problem are handled by a robust black box code, while the assumptions made about the chemistry are clearly visible, unambiguous, and easy to document.

Known reaction rates and thermochemistry are stored in an extensible library, and unknown reaction rates and thermochemistry are estimated based on functional group additivity. Classic Benson-type group additivity has been extended to include transition states (to predict rates).[2] This requires the use of larger functional group templates than the simple atom-centered Benson groups. This more flexible group concept is also found to be very useful for estimating the thermochemistry of polycyclic aromatics – using bond-centered groups rather than traditional atom-centered groups doubles the accuracy of the estimation procedure. Several hundred new group values have been determined using quantum chemical methods, some reported elsewhere[3,4,5] and carefully organized into tree structures to avoid ambiguity and to speed computation times. We plan to make these tree structures and the associated parameters publicly accessible over the internet, so that chemists anywhere on the globe can easily improve the estimates.

The new Java software package that implements this new concept, RMG, includes several state-of-the-art features, including on-the-fly computation of k(T,P) using the efficient and accurate algorithm developed by D.M. Matheu et al..[6,7] The software architecture of RMG is considerably different than previous reaction mechanism generation programs, being completely object-oriented, and documented structured using UML.

The large kinetic models generated by RMG can be automatically and optimally reduced to any desired size using the algorithm of Bhattacharjee et al..[8] Valid ranges of the both the large and the reduced models are automatically estimated using a new rigorous method. The reduced models are very useful in reacting flow simulation and in other compute-intensive applications. Several numerical issues arise when using large kinetic models, particularly when coupling them into reacting flow simulations. In particular, it has been found very helpful to take advantage of the inherent sparsity of the Jacobians of large kinetic models [9], and to use operator-splitting methods which converge to the correct solution (rather than popular methods which have $O((\Delta t)^2)$ errors at convergence, since these errors can be very large if the chemistry is stiff).[10] Very recently, new global optimization algorithms have been developed which can guarantee error tolerances over a continuous range of reaction conditions [11], and these allow one to rigorously control the errors introduced by using reduced models rather than the full model.

In some situations, one does not want to simulate a specific known system, but rather to determine an upper bound on what is possible in any process of a particular type. We have run several examples of these upper bound calculations for catalytic oxidations, where the energetics of the surface intermediates are unknown.[12] This problem, the model reduction and range analysis problem, and a variety of safety/operability problems are mathematically related:

they all can be written as types of semi-infinite programs (i.e. optimization problems with an infinite number of constraints). Recent algorithmic advances using interval analysis [11] will allow significant advances in solving all these problems.

Conclusions

The new extensible modular design of mechanism generation software promises to greatly accelerate progress towards predictive chemical kinetics for problems in fuels chemistry. The computer-constructed kinetic models based on a library of small molecule reactions and group-additivity-based estimates of rate and thermochemistry of larger molecules are already quite accurate [7], and the accuracy can be refined by use of sensitivity analysis to identify which rate constants and thermochemical parameters merit further study. The extensible and unambiguous format should encourage community-wide efforts to improve the accuracy of the rate estimates, and to broaden the range of chemistry which can be modeled.

Advances in numerics and computer science are needed to parallel improved understanding of the chemistry. Recent improvements in optimization algorithms and in methods for handling large systems of stiff differential-algebraic equations are keeping pace with our ability to construct large accurate kinetic simulations. Although reacting flow simulations are still very challenging, effective algorithms are becoming available. In most cases the accuracy of the simulations are limited more by our ignorance of the chemistry than by the approximations introduced in order to solve the differential equations.

As the simulations become more complex, a variety of additional software tools are needed to help humans check the accuracy of the models and to correctly interpret the model predictions. Our 20+ year old paradigm of kinetics assumes that a single human can construct, solve, and interpret an entire simulation, doing most of the steps by hand. As the simulations become more detailed, we need to move to a new paradigm that encourages teamwork, and where all of the "well-understood" aspects of the problem are automated, to allow the scientists and engineers to focus on the aspects and issues that are really unresolved.

Acknowledgements

The authors gratefully acknowledge financial support from the National Science Foundation, BP Chemical, and the Department of Energy.

References

[1] Tomlin, A.S; Turanyi, T.; Pilling, M,J.; in *Low Temperature Combustion and Auto-Ignition*, Pilling, M.J. ed., Elsevier (Amsterdam) **1997**, 293-437
[2] Sumathi, R.; Green, W.H. *Theor. Chem. Accts.* **2002**, *108*, 187.
[3] Sumathi,R.; Green, W.H. *J. Phys. Chem. A* **2002**, *106*, 7937.
[4] Sumathi, R.; Green, W.H. *J. Phys. Chem. A* **2002**, *106*, 11141.
[5] Sumathi, R.; Green, W.H. *Phys. Chem. Chem. Phys.* **2003**, *5*, 3402.
[6] Matheu, D.M.; Green, W.H.; Grenda, J.M. *Int. J. Chem. Kinet*. **2003,** *35*, 95.
[7] Matheu, D.M.; Dean, A.M.; Grenda, J.M.; Green, W.H. *J. Phys. Chem. A* **2003**, *107*, 8552.
[8] Bhattacharjee, B.; Barton, P.I.; Green, W.H. *Combust. Flame* **2003. (in press).**
[9] Schwer, D.A.; Tolsma, J.A.; Green, W.H.; Barton, P.I. *Combust Flame* **2002**, *128*, 270.
[10] Schwer, D.A.; Lu, P.; Green, W.H.; Semiao, V. *Combust. Theor. Modelling* **2003**, *7*, 383.
[11] Bhattacharjee, B.; Green, W.H.; Barton, P.I. *Computational Optimization and Applications* **2004** (in press).
[12] Su, Y.S.; Ying, J.Y.; Green, W.H. *J. Catalysis* **2003,** *218*, 321.

PRESSURE-DEPENDENT AUTOMATED MECHANISM GENERATION: SYSTEMATIC MODELS FOR DIFFICULT SYSTEMS

David M. Matheu[a], Anthony M. Dean[b], Jeffrey M. Grenda[c]

[a]National Institute of Standards and Technology
Physical and Chemical Properties Division
100 Bureau Dr. Stop 8380
Gaithersburg, MD 20899-8380

[b]Department of Chemical Engineering
Colorado School of Mines
451 Alderson Hall
Golden, CO 80401

[c]ExxonMobil Research and Engineering Company
1545 Rt. 22 East
Annandale, NJ, 08801

Introduction

Advancement in the design of such important gas-phase processes as hydrocarbon cracking, combustion, and partial oxidation hinges, in part, on the development of correct, detailed chemical kinetic models. But the complexity of the required chemical mechanisms can make them extremely difficult to construct by hand. Modelers turn to software algorithms that build these large mechanisms automatically (e.g. [1], [2]), but the current tools are too limited to treat many difficult systems. We present a new, elementary-step-based mechanism generation algorithm, called "XMG-PDep," which overcomes these limitations with a comprehensive approach to pressure-dependent reactions, and a rational, flux-based criteria for truncating mechanism growth. Applications to the previously intractable methane and high-conversion ethane pyrolysis systems yield predictions which agree well with experimental data, without any parameter adjustment. Important new pathways, not previously considered, but discovered entirely by the new approach, can explain unusual behavior in these systems, and suggest the power of this software tool.

Computational Method: The XMG-PDep Algorithm

XMG-PDep is based upon XMG [3], which developed from NetGen [4]. It employs flux-based termination of the otherwise combinatorial in species and reactions. To do this, the code periodically constructs and integrates the set of differential equations that represent the evolution of the reacting system in time (assuming a well-mixed batch reactor model). It evaluates a characteristic mechanism flux Rchar(t), which is similar to a root-mean-square average of chemical fluxes in the mechanism [5]. XMG-PDep then compares this flux with those to candidate species that have been discovered, but not yet included, in the mechanism. Those species whose fluxes exceed the cutoff flux (equal to a user-specified fraction of Rchar(t)) are included in the mechanism; the rest are not.

XMG-PDep can systematically discover and include arbitrary pressure-dependent reactions, using the algorithm of ref [6]. To allow the most flexibility, XMG-PDep considers any elementary step of the form $A + B \rightarrow C$, $B \rightarrow C$ or $B \rightarrow C + D$ to initiate a partial pressure-dependent network. For each partial network, XMG-PDep uses the QRRK/MSC code CHEMDIS [7] to estimate the k(T,P) values of every net pressure-dependent reaction. It also examines the maximum flux to all non-included portions of the partial pressure-dependent network. If this flux is greater than the cutoff flux, the partial network is "grown" by one isomer, with all its high-pressure-limit elementary steps, and the k(T,P) calculation is repeated. Growth of each partial pressure-dependent network is halted when the flux to non-included portions is less than the cutoff flux. In this way pressure-dependent reactions can be included systematically and rationally. A full description of the integrated algorithm for generating mechanisms is presented in ref. [8].

Finally, XMG-PDep includes a number of other features designed to make it accurate and useful. It employs literature-based libraries of rate constants and thermochemical parameters whenever possible. Its rate rules are subdivided as much as is reasonable to provide the best estimates for high-pressure-limit rates when these are not available from the library. Thermochemical data (when not available from the data library) are taken from a group contribution method [9] and used to ensure thermodynamic reversibility. The code will produce a CHEMKIN mechanism, and a number of analyses of the mechanism (such as the net radical rate of production for each reaction), when finished with generation.

Application to Methane and High-Conversion Ethane Pyrolysis

Methane pyrolysis has been extensively studied for many decades, both for its potential to convert methane to more valuable hydrocarbons, and its importance within larger combustion and pyrolysis mechanisms. But the strange, autocatalytic behavior of methane pyrolysis at extremely low methane conversion has defied mechanistic explanation for at least three decades. The most recent attempt, of Dean in 1990 [10], appeared successful until new thermochemical data for the cyclopentadienyl radical rendered its explanation inadequate.

Applying our tool with the rate rules and thermochemical data described in ref. [8] gives a mechanism which captures the low-conversion autocatalysis, without resort to parameter fitting or adjustment, as shown in Figure 1. The generator suggests that the autocatalytic behavior arises from a number of separate sources, none of which had been considered previously for these conditions. First, cyclopentadienyl radical, produced by the pressure-dependent addition of propargyl radical to acetylene, abstracts a hydrogen from methane to form cyclopentadiene. The cyclopentadiene in turn will dissociate easily to another H atom and cyclopentadienyl radical, causing chain-branching, or a net production of radicals. Second, the reverse disproportionation of methane and allene to form methyl radical and allyl radical plays an important chain-branching role, especially at early times. Finally, as an aggregated group, the set of all reverse disproportionations accounts for about 50% of the chain-branching.

Figure 2 shows a more comprehensive view of the pathways leading to autocatalysis. Many of these pathways are pressure-dependent and could not have been discovered by a tool without this capability. Further validation against other product data, and support for the mechanistic analysis, can be found in ref. [11].

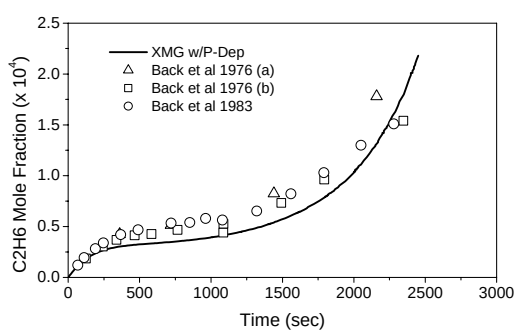

Figure 1. XMG-PDep predicted ethane concentration with time, during static batch pyrolysis of neat methane at 1038 K and 0.58 atm.

The prediction clearly captures the autocatalytic upturn in concentration as reflected in three experimental datasets [12-14].

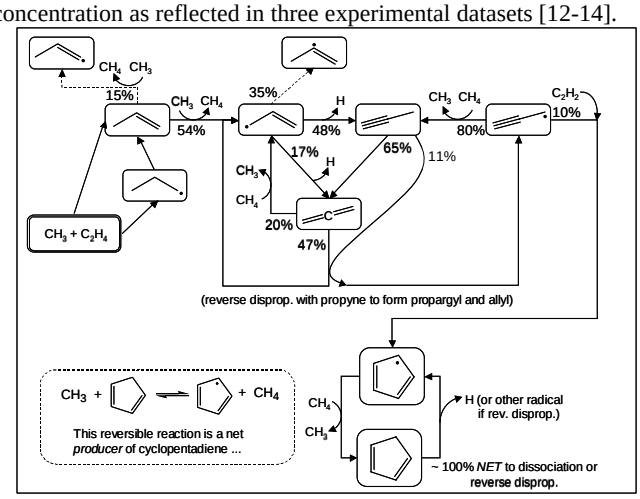

Figure 2. Partial depiction of pathways leading to autocatalysis in low-conversion methane pyrolysis. A number of these pathways are reverse disproportionations; as a whole, the set of all reverse disproportionations provides about 50% of the net radical production. A number of other important pathways (such as the addition of propargyl to acetylene, and the isomerization of allyl radical) are pressure-dependent.

High-Conversion Ethane Pyrolysis. Glasier and Pacey [15] used a laboratory flow reactor to study neat ethane pyrolysis at very high conversion (>98%, 900-1200K, 0.4 atm), in an effort to correlate the concentrations of proposed "soot precursors" with the formation of pyrolytic (deposited) carbon. No existing detailed kinetic mechanism exists for these conditions; the high conversion and large number of pathways make this system extremely difficult to consider by-hand. That fact, coupled with the detailed data available for minor products, makes this experimental work a good but challenging example case for our algorithm. Our generated model's agreement with the data is quite good (as seen in Figures 3 and 4), considering that once again no parameters were adjusted to fit the data, and all steps in the mechanism are "from scratch".

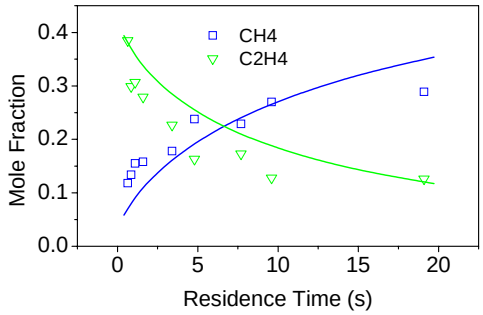

Figure 3. CH_4 and C_2H_4 concentrations with residence time in the Glasier and Pacey flow reactor. Symbols are experimental data points; lines are auto-generated model predictions.

Pathway analysis of the very large mechanism generated for this system suggests that the fates of the minor products, and some major ones, are governed in part by a large and complex set of interconnected reactions. Conventional mechanisms do not capture some of these pathways. Although the Glasier and Pacey system was chosen as a difficult example which would test the limits of strictly elementary-based, gas-phase mechanism generation, the resultant model for these unusual conditions may also prove useful as a base for the understanding of aromatics and soot formation.

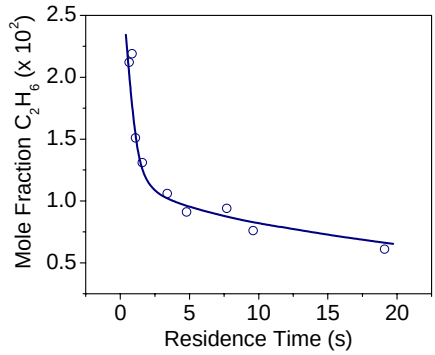

Figure 4. Experimental and predicted ethane concentration with residence time.

Discrepancies in the predictions of H_2 and benzene (not shown here) imply that XMG-PDep is missing whole reaction families for generation, though other explanations (such as globally incorrect rate rules, thermochemistry, or heterogeneous reactions) cannot be ruled out. The lack of good, publicly-available tools for understanding large (>1000 reaction) mechanisms severely hampers the analysis.

Conclusions. The XMG-PDep algorithm for building reaction mechanisms "from scratch", including pressure-dependence, shows promise in helping kineticists understand highly complex systems that could not otherwise be studied easily. The tool suggests new pathways that explain behavior in both of the "demonstration" systems; further work will involve systems of more industrial importance.

References

1. Wauters, S.; Marin, G. B. *Chem. Eng. J.* **2001**, *82*, 267-279.
2. DeWitt, M. J.; Dooling, D. J.; Broadbelt, L. J. *Ind. Eng. Chem. Res.* **2000**, *39*, 2228-2237.
3. Grenda, J. M. ; Androulakis, I. P.; Dean, A. M.; Green, W. H. Jr. *Ind. Eng. Chem. Res.* **2003**, *42*, 1000-1010.
4. Susnow, R. G.; Dean, A. M.; Green, W. H.; Peczak, P.; Broadbelt, L. J. *J. Phys. Chem. A* **1997**, *101*, 3731-40.
5. Song, J.; Stephanopoulos, G.; Green, W. H. *Chem. Eng. Sci.* **2002**, *57*, 4475-4491.
6. Matheu, D. M.; Lada, T. A.; Green, W. H.; Grenda, J. M.; Dean, A. M. *Comp. Phys. Comm.* **2001**, *138*, 237-249.
7. Chang, A. Y.; Bozzelli, J. W.; Dean, A. M. *Z. Phys. Chem.* **2000**, *214*, 1533-1568.
8. Matheu, D. M. *Integrated Pressure-Dependence in Automated Mechanism Generation: A New Tool for Building Gas-Phase Kinetic Models*, Ph.D. Thesis, Massachusetts Institute of Technology, **2002**.
9. Grenda, J. M. and Bozzelli, J. W., "Automated Elementary Reaction Mechanism Generation Incorporating Thermochemistry, Fall-off, and Chemical Activation Reactions of OH with Olefins, A6," *5th Int. Conf. Chem. Kin.*, Gaithersburg, MD, **2001**.
10. Dean, A. M. *J. Phys. Chem.* **1990**, *94*, 1432-39.
11. Matheu, D. M., Dean, A. M., Grenda, J. M., and Green, W. H. Jr. *J. Phys. Chem. A* **2003**, 107, 8552-8567.
12. Chen, C. J.; Back, M. H.; Back, R. A. *Can. J. Chem.* **1976**, *54*, 3175-3184.
13. Chen, C. J.; Back, M. H.; Back, R. A. *Can. J. Chem.* **1975**, *53*, 3580.
14. Chen, C. J.; Back, M. H.; Back, R. A. *Can. J. Chem.* **1977**, *55*, 1624-1628.
15. Glasier, G. F.; Pacey, P. D. *Carbon* **2001**, *39*, 15-23.

SIMULATION OF LIGHT PETROLEUM FRACTIONS

Tareq A. Albahri

Chemical Engineering Dept. - Kuwait University
P.O.Box 5969 - Safat 13060, Kuwait
albahri@kuc01.kuniv.edu.kw

Introduction

Petroleum refiners have not traditionally considered their products on a molecular basis but rather they have modeled and marketed their products as volatility fractions (e.g. gasoline, kerosene, and fuel oil). Current simulation procedures resort to pseudo-component approaches which suffer from many limitations. This work focuses on the development of a molecularly explicit characterization model (MECM) that will allow the simulation of the molecular composition of petroleum fractions using a pre-selected set of pure components. Such molecular-level characterization of petroleum fractions will allow us to simulate the physical separation processes and the chemical reaction processes, as well as allow for catalysts such as zeolites to be designed and optimized for processing complex, multicomponent mixtures such as petroleum.

Technical Development

The concept of the proposed model is that the global properties of a petroleum fraction such as the boiling point, specific gravity, vapor pressure, etc. must be equal to those calculated from the pure components contained in that petroleum fraction. When both bulk and pure component properties are available, the composition of the petroleum fraction may be predicted using optimization algorithms as simplified in Figure 1.

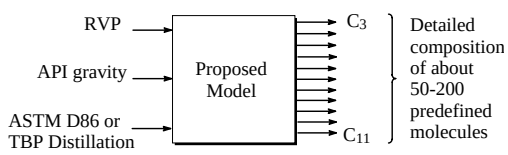

Figure 1. Simplified schematic representation of the proposed model.

Since petroleum fractions contain thousands of molecules the concentration of which is hard or even impossible to measure, it is imperative to simulate such mixtures using a limited set of pure components to avoid prohibitively extensive computation time during kinetic modeling or rigorous phase equilibrium calculations.

The minimum input properties for the model are the true boiling point (TBP), the API gravity, and the Reid vapor pressure (RVP). The internally calculated properties are the molecular weight, the true vapor pressure at 100°F, the specific gravity, the cubic average boiling point (CABP), the mean average boiling point (MeABP), the volumetric average boiling point (VABP), the weight average boiling point (WABP), the molar average boiling point (MABP), the Watson characterization factor (K_w), the refractive index, the carbon to hydrogen ratio (C/H), the kinematic viscosity at 100 and 210°F, the surface tension, the aniline point, the true and pseudo critical temperatures and pressures, the critical compressibility factor, the acentric factor, the freezing point, the heat of vaporization at the normal boiling point, the net heat of combustion at 77°F, the isobaric liquid heat capacity at 60°F, the isobaric vapor heat capacity at 60°F, the liquid thermal conductivity at 77 ºF, and the paraffins, naphthenes, and aromatics content. These properties are calculated for the petroleum fraction using well established methods in the literature or were developed specifically for this project. For example, the molecular weight for the light petroleum fraction is calculated from the boiling point and the specific gravity using the following API recommended equation[1],

$$MW = 42.965\,(T_b^{1.26007}\,S^{4.98308})\,[\exp(2.097.10^{-4}\,T_b - 7.78712\,S + 2.08476.10^{-3}\,T_b\,S)] \qquad (1)$$

Whereas the same is calculated from the pure component composition using the following simple mixing rule,

$$MW=\sum_{i=1}^{n}(MW)_i\,(x)_i \qquad (2)$$

When the pure component properties are not available in databases they can be estimated using group contribution methods available in the literature or others developed specifically for this project.

The difference between the values obtained from equations 1 and 2 for the molecular weight in addition to other equations and mixing rules for the other properties are minimized in the objective function (second line of Equation 3) the purpose of which is to calculate the values of x_i which is the mole fraction of the pure components in the petroleum fraction.

The First line in the objective function represents the sum of errors in the boiling points of the pure components and the corresponding value on the true boiling point (TBP) curve as shown in Figure 2.

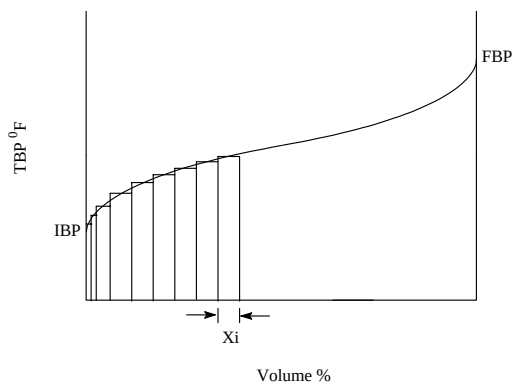

Figure 2. Simulation of a true boiling point (TBP) curve using real components.

The pure component concentrations are determined by minimizing the following objective function,

$$S = \sum_{j=1}^{n}\left((T_{b_j}-T'_{b_j})\times W_o \times 100/T_{b_j}\right)^2 + \sum_{i=1}^{P}\left((Y_i - Y'_i)\times W_i \times 100/Y_i\right)^2 \qquad (3)$$

where i is the index number of the physical property, j is the index number of the molecule, P is the total number of physical properties considered (except boiling point), and n is the total number of molecules. Y_i and Y'_i refer respectively to the actual and predicted property i. T_{bj} and T'_{bi} refer respectively to the boiling point of the pure component *j* and the corresponding value on TBP curve. W_i and W_o are weighting factors and S is the objective function to be minimized.

An optimization algorithm based on the least square method was used to minimize the objective function while calculating the concentration of the pure components. The nonlinear regression algorithm minimizes the sum of the difference between the fuels bulk properties and those estimated from pure components. Using the Microsoft Excel Solver tool and the Generalized Reduced Gradient (GRG2) nonlinear optimization code, convergence was achieved in less than one minute for all cases on a Pentium IV-1.7 GHz PC.

Discussion

The model was tested to simulate the separation process in an industrial naphtha splitter producing light and heavy naphtha from a Hydrocracked naphtha feed according to the validation procedure shown in Figure 3. In one run we used the ASTM D86 distillation data as the input assay for the feed naphtha. In another run we used the detailed hydrocarbon concentrations calculated using the proposed MECM model shown in figures 4 and 5. The MECM model results for the light and heavy naphtha products correlated better with the experimental ASTM D86 distillation data than those using the pseudo-component method incorporated in the HYSYS process simulator.

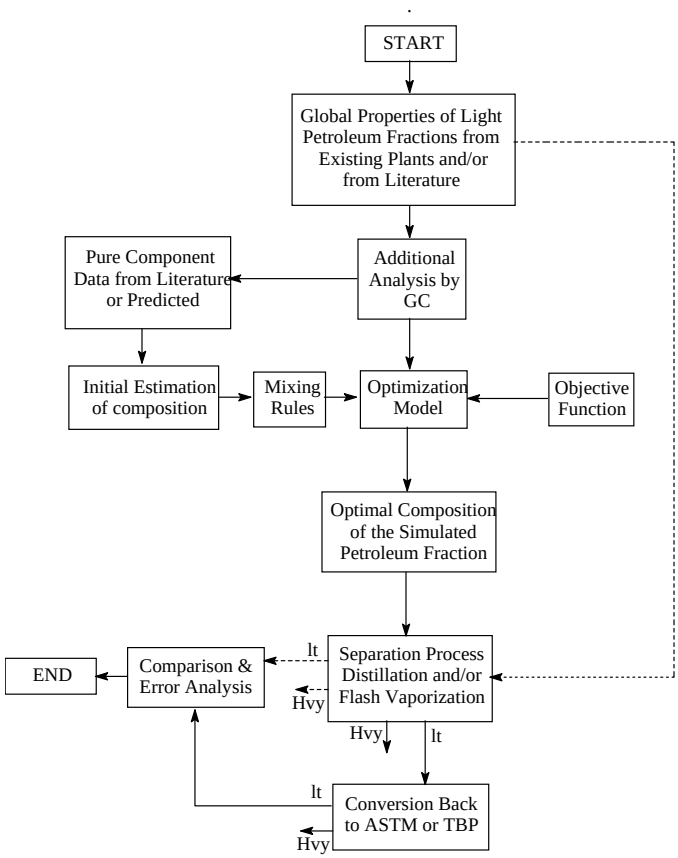

Figure 3. Flow Chart for the methodology used in the proposed model.

The MECM model proves to be a powerful tool for simulating the composition of petroleum fuels. The clear advantage of the method is that the list of pure components used may be tailored to include more or fewer components as needed by the user, to accommodate specific needs, which is an added advantage.

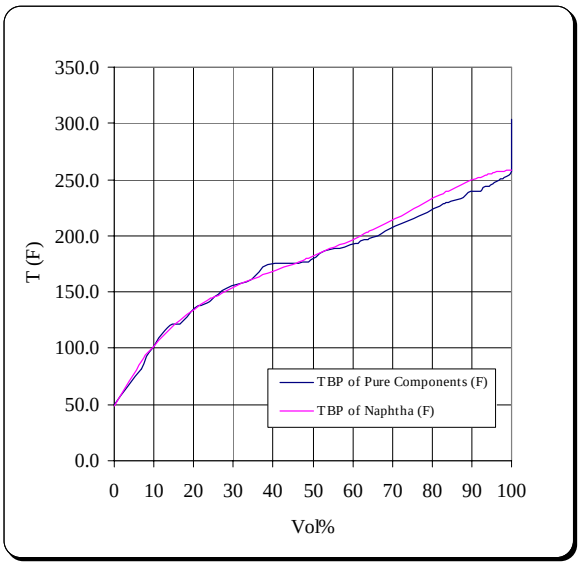

Figure 4. Comparison of Naphtha TBP and Simulated TBP from pure components.

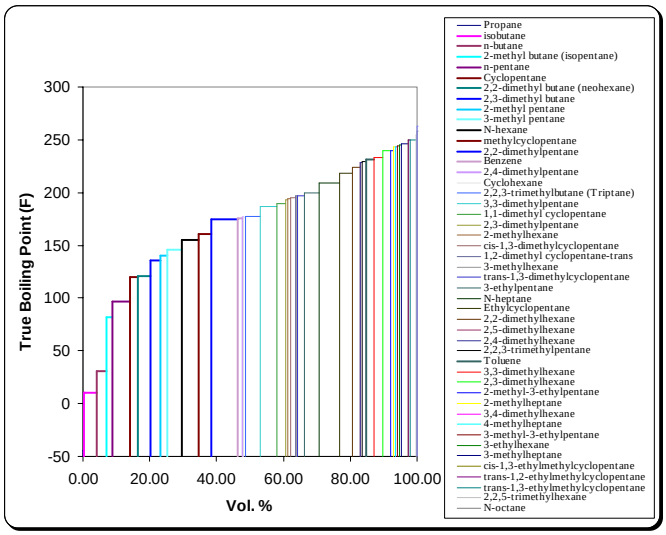

Figure 5. Calculated composition of representative model pure components

This work demonstrates that the complex nature of petroleum fuels may be modeled by a limited set of representative pure components using non-linear-regression optimization models. Considering the difficulty and complexity of accounting for the thousands of compounds in petroleum fuels and the limitations of the pseudo component technique, the proposed method can be an effective alternative.

Acknowledgment

This work was supported by Kuwait University, Research Grant No. EC04/01.

References

[1] Wauquier, J. -P. "Petroleum Refining 1', Editions Technip, Paris, **1995**.

Silica Aerogel Supported Catalysts for Fisher-Tropsch Synthesis

Brian C. Dunn, Paul Cole, Gregory C. Turpin, Zhiru Ma, Ronald J. Pugmire, Richard D. Ernst ,and Edward M. Eyring

Department of Chemistry, University of Utah, Salt Lake City, UT 84112

Naresh Shah and Gerald P. Huffman

College of Engineering, University of Kentucky, Lexington, KY 40506

Introduction

The production of hydrocarbons from Fischer-Tropsch synthesis has been known for nearly a century.[1] The reaction occurs using a heterogeneous catalyst typically composed of iron, cobalt, or ruthenium as the active catalyst supported on an inert oxide such as silica, titania, or alumina. While a vast amount of research has been conducted on modifications of the active catalyst in order to achieve improved reactivity or selectivity, the morphological properties of the oxide support have not received as much attention.

Sol-gel derived silica provides a unique method of creating and controlling texture and porosity of a silica catalyst support. The resulting silica can exist as a relatively dense, microporous xerogel[2] or it can be synthesized as a non-dense, mesoporous aerogel.[3] The three dimensional structure and porosity properties of silica aerogel[4] impart certain advantages over traditional oxide supports. Surface area can be high (>800 m^2/g), average pore size is in the mesoporous regime (2-50 nm), and the pores exist as an interconnected network. These properties lead to enhanced mass transport of reactant molecules to and product molecules away from the active metal surface. In addition, if the size of the metal particle is larger than the pore size of the support, the metal particle is effectively locked into position. This should allow for catalytic reactions to take place at high temperature without the risk of sintering the catalyst.

Experimental

Cobalt Catalyst Preparation. Aerogel supported catalysts were prepared by a modification of a published procedure.[5] A mixture of tetramethoxysilane (Aldrich, 98%) and methanol (Aldrich, spectrophotometric grade) was prepared by combining 15 mL of each reagent. The mixture was stirred until homogeneous. A solution consisting of 7.5 mL of methanol, 6 mL of water (Aldrich, HPLC grade), and 0.75 mL of 2.8% NH_4OH (Mallinckrodt, AR grade) was added to the previously prepared solution and mixed until homogeneous. Cylindrical, polyethylene forms were filled with 10 mL of the sol and gelation occurred in 10 minutes. The gels were aged in their forms for 14 days. The solid gels were removed from their forms and solvent exchanged with ethanol (Aaper, absolute), four times for four hours each, then loaded with $Co(NO_3)_2$ by soaking the gel in an ethanolic solution of $Co(NO_3)_2 \bullet 6H_2O$ of a known concentration. The concentration of $Co(NO_3)_2$ was chosen to yield a catalyst which contained either 2% or 6% by weight Co. The aerogel was formed by removing the ethanol as a supercritical fluid (T_c = 243 ^oC, P_c = 926 psi). The $Co(NO_3)_2$ loaded gels were transferred into a 42 mL autoclave and the remaining volume of the autoclave was filled with the $Co(NO_3)_2$ solution. This prevents leaching of the salt during the drying process. The autoclave was sealed and heated to 250 ^oC at 5 ^oC / min, then to 300 ^oC at 1 ^{o} C/ min. The pressure was allowed to rise to 1800 psi and maintained at this pressure by slowly venting the autoclave. The autoclave was held at 300 ^oC for 1 hour, then slowly vented to atmospheric pressure over a 1 hour period. After cooling to room temperature, the aerogels were removed from the autoclave and calcined in static air at 500 ^oC for 8 hours. The aerogel was crushed, sieved for size, and reduced in flowing hydrogen at 500 ^oC for 4 hours. The resulting aerogel supported catalyst appeared black and showed ferromagnetism indicating successful reduction to metallic cobalt.

Ruthenium Catalyst Preparation. Undoped aerogels were prepared according to the above procedure, then loaded with ruthenium by subliming an open ruthenocene, bis(2,4-dimethylpentadienyl)ruthenium,[6] into the crushed aerogel at reduced pressure.[7] The aerogel gradually took on the color of the open ruthenocene. The open ruthenocene was decomposed to an oxide by heating in flowing oxygen at 300 ^oC. The oxide was reduced to metallic ruthenium by reducing in flowing hydrogen at 500 ^oC. The resulting catalyst contained 10% Ru by weight.

Catalyst Testing. All aerogel supported catalysts were evaluated in a laboratory-scale, packed bed reactor. 240 mg of the catalyst was loaded into a ¼ inch OD, stainless steel tubular reactor and held in place with quartz wool. H_2 and CO were introduced into the 265 ^oC reactor by means of mass-flow controllers. The carbon monoxide was passed through a trap containing PbO_2/Al_2O_3 (Engelhard, E-315) to remove any $Fe(CO)_5$ impurity before entering the reactor. The pressure inside the reactor was maintained at 100 psi with a back-pressure regulator. Hydrocarbon products larger than C_6 were analyzed by means of online GC/MS. Reactants and hydrocarbon products smaller than C_7 were analyzed by an online GC equipped with both TCD and FID detectors. Argon was employed as an internal standard in all measurements.

Results and Discussion

A transmission electron micrograph of the reduced 2% Co catalyst appears in Fig. 1. The aerogel support appears as semi-transparent background and the metallic cobalt appear as well-dispersed particles within the support. The cobalt particle size appears remarkably uniform at approximately 50 nm.

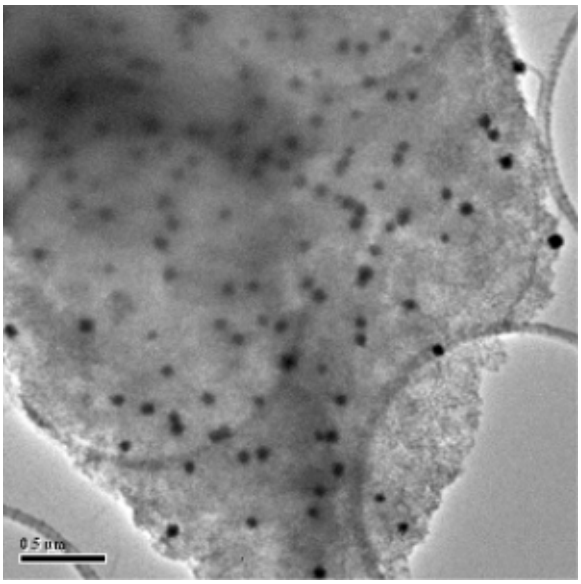

Figure 1. Transmission electron micrograph of the 2% Co catalyst supported on silica aerogel. The particles of metallic cobalt are observed as black dots surrounded by the amorphous aerogel structure.

All the catalysts tested were active towards the Fischer-Tropsch synthesis and product distributions that resulted are shown in Fig. 2. The 10% Ru catalyst was the most active at nearly 50% CO conversion and was selective towards hydrocarbons between C_8 and C_{12}. The cobalt catalysts were less active than the ruthenium catalyst with CO conversions of about 5% for the 2% Co and 22% for the 6% Co catalyst. While these product yields are not exceptionally high compared with traditional catalysts, the amount of actual metal loaded into the reactor is quite small. For the 2% Co catalyst, only 4.8 mg Co is present in the reactor.

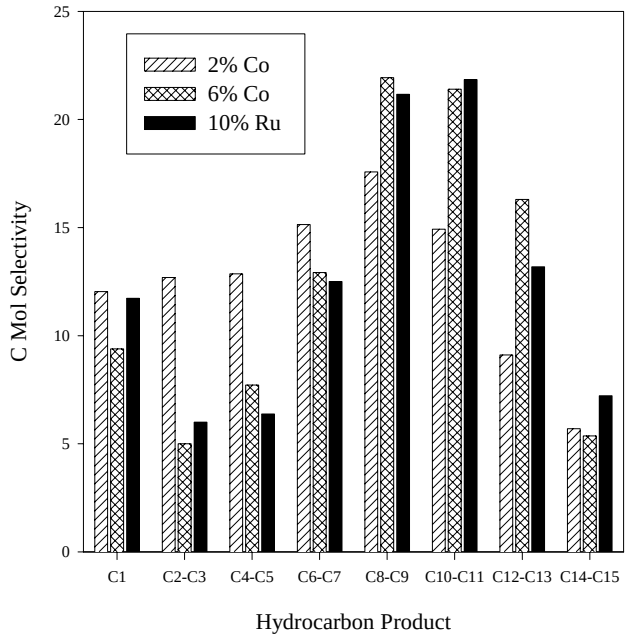

Figure 2. Hydrocarbon product distribution from 3 aerogel supported catalysts. Reaction conditions: 265 ^{o}C, 100 psi, H_2 at 36 sccm, CO at 18 sccm. The hydrocarbons have been grouped in pairs, except for methane, for the sake of clarity.

All three catalysts showed selectivity for hydrocarbons between C_8 and C_{12}. The ruthenium catalyst was particularly selective for this fraction with greater than 50% C mol selectivity for this hydrocarbon range. It has been speculated that increases in mass transport within the catalyst will tend to favor larger hydrocarbon products.[8,9] The nature of the aerogel support leads to high mass transport which in turn leads to higher selectivity towards larger hydrocarbons.

One surprising result was the percentage of olefins produced for the larger hydrocarbons. Fig. 3 shows the fraction of each carbon number which was detected as the 1-olefin. The high production of olefins is probably a direct result of the high mass transport within a catalyst particle. It has been theorized[10] that desorption of the growing hydrocarbon chain from the surface of the catalyst particle yields an olefinic species which then undergoes hydrogenation to yield the saturated hydrocarbon. With high mass transport in the catalyst, the olefinic species can easily diffuse away from the surface of the metal and not undergo hydrogenation. The olefin is then seen in the product stream.

Conclusions

Catalysts containing cobalt or ruthenium supported on silica aerogel have been synthesized and tested for activity towards the Fischer-Tropsch synthesis. After preparation and reduction, TEM indicates that the cobalt exists as discrete particles (diameter ~50 nm) suspended within the silica aerogel matrix. The catalysts are particularly selective towards hydrocarbons in the C_8 to C_{12} range with greater than 50% C mol selectivity for this fraction. The mesoporous nature of the aerogel, as well as the interconnected pore network, lead to high mass transport of H_2 and CO to the metal surface and facilitate diffusion of desorbed products away from the surface. This mass transport effect is suggested by the large fraction of each hydrocarbon which exists as the 1-olefin and the selectivity towards larger hydrocarbons.

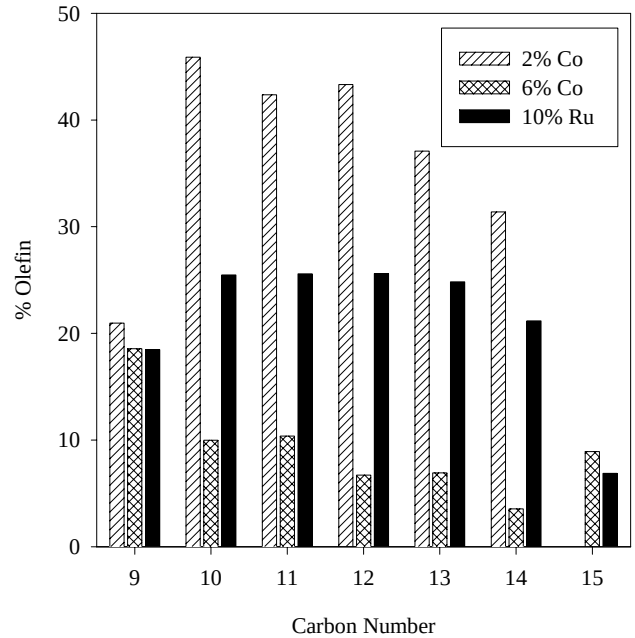

Figure 3. Fraction of each carbon number product which was detected as the olefin. Reaction conditions: 265 ^{o}C, 100 psi, H_2 at 36 sccm, CO at 18 sccm.

Acknowledgement. Financial support by the US Department of Energy, Office of Fossil Energy, under contract number DE-FC26-02NT41954 is gratefully acknowledged.

References

(1) Fischer, F.; Tropsch, H. *Brennst. Chem.* **1923**, *4*, 276-285.
(2) Harreld, J. H.; Ebina, T.; Tsubo, N.; Stucky, G. *J. Non-Cryst. Solids* **2002**, *298*, 241-251.
(3) Ehrburger-Dolle, F.; Dallamano, J.; Elaloui, E.; Pajonk, G. M. *J. Non-Cryst. Solids* **1995**, *186*, 9-17.
(4) Pietron, J. J.; Stroud, R. M.; Rolison, D. R. *Nanoletters* **2002**, *2*, 545-549.
(5) Casula, M. F.; Corrias, A.; Pashina, G. *J. Mater. Chem*. **2002**, *12*, 1505-1510.
(6) Stahl, L.; Ernst, R. D. *Organometallics* **1983**, *2*, 1229-1234.
(7) Merzbacher, C. I.; Barker, J. G.; Swider, K. E.; Ryan, J. V.; Bernstein, R. A.; Rolison, D. R. *J. Non-Cryst. Solids* **1998**, *225*, 234-238.
(8) Ohtsuka, Y.; Arai, T.; Takasaki, S.; Tsubouchi, N. *Energy & Fuels* **2003**, *17*, 804-809.
(9) Iglesia, E. *Appl. Catal. A: General* **1997**, *161*, 59-78.
(10) Davis, B. H. *Fuel Proc. Tech.* **2001**, *71*, 157-166.

Biomarker Fingerprinting: Application and Limitation for Correlation and Source Identification of Oils and Petroleum Products

Zhendi Wang, M. Fingas, C. Yang and B. Hollebone*

Emergencies Science and Technology Division
Environmental Technology Centre, Environment Canada
335 River Road, Ottawa, Ontario, Canada K1A 0H3
Tel: (613) 990-1597, Fax: (613) 991-9485
E-mail: zhendi.wang@ec.gc.ca

INTRODUCTION

Biological markers or biomarkers are complex molecules derived from formerly living organisms. **Figure 1** shows molecular structures of representative cyclic biomarker compounds. Biomarkers are useful because they retain all or most of original carbon skeleton of the original natural product and this structural similarity reveals more information about their origins than other compounds.

Biomarker fingerprinting has historically been used by petroleum geochemists (1) in characterization of oils in terms of the type(s) of precursor organic matter in the source rock, correlation of oils with each other and oils with their source rock, determination of depositional conditions, assessment of thermal maturity of oil during burial, and evaluation of migration and the degree of biodegradation.

The conversion of a vast number of the precursor biochemical compounds from living organisms into biomarkers creates a vast suite of compounds in crude oils that have distinct structures. Further, due to the wide variety of geological conditions and ages under which oil has formed, every crude oil exhibit an essentially unique biomarker "fingerprint". Therefore, chemical analysis of source-characteristic and environmentally-persistent biomarkers generates information of great importance in determining the source of spilled oil, differentiating oils, monitoring the degradation process and weathering state of oils under a wide variety of conditions. In the past decade, use of biomarker fingerprinting techniques to study spilled oils has greatly increased, and biomarker parameters have been playing a prominent role in almost all oil spill work.

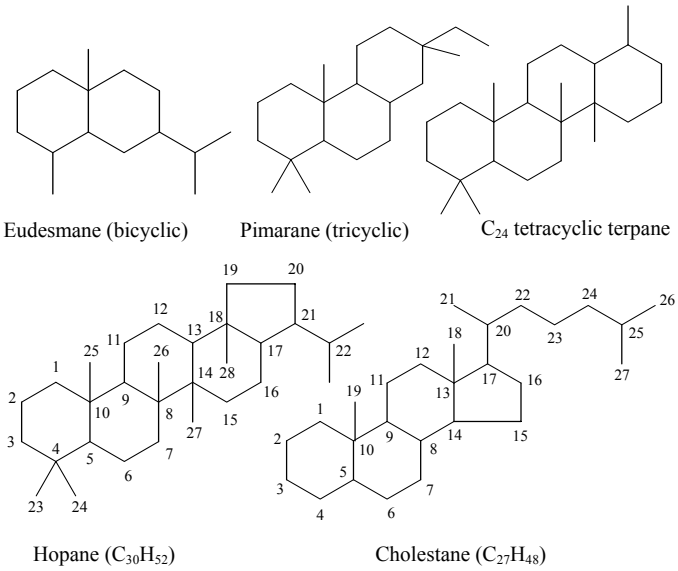

Figure 1 Molecular structures of representative cyclic biomarker compounds.

EXPERIMENTAL

Approximately 0.4 gram of oils or petroleum products were weighed, dissolved in hexane and made up to the final volume of 5.00 mL. A 200 µL of the oil solutions containing ~ 16 mg of oil was spiked with appropriate surrogates (100 µL 200 ppm of o-terphenyl and 100 µL of mixture of deuterated acenaphthene, phenanthrene, benz[a]anthracene, and perylene, 10 ppm each), and then transferred into a 3-g silica gel microcolumns, which was topped with about 1-cm anhydrous granular sodium sulfate and had been pre-conditioned using 20 mL of hexane, for sample cleanup and fractionation.

Hexane (12 mL) and 50% benznene in hexane (v/v, 15 mL) were used to elute the saturated and aromatic hydrocarbons, respectively. For each sample, half of the hexane fraction (labeled F1) was used for analysis of aliphatics, n–alkanes, and biomarker terpane and sterane compounds; half of the 50% benzene fraction (labeled F2) was used for analysis of alkylated homologous PAHs and other EPA priority unsubstituted PAHs; the remaining halves of the hexane fraction and 50% benzene fraction were combined into a fraction (labeled F3) and used for the determination of the total GC-detectable petroleum hydrocarbons (TPH) and the unresolved complex mixture of hydrocarbons (UCM). These three fractions were concentrated under a stream of nitrogen to appropriate volumes (~0.4 mL), spiked with appropriate internal standards (50 µL of 200 ppm 5-α-androstane and 50 µL of 20 ppm C_{30}-ββ-hopane, 50 µL of 10 ppm terphenyl-d_{14}, and 50 µL of 200 ppm 5-α-androstane for F1, F2, and F3 respectively), and then adjusted to an accurate pre-injection volume of 0.50 mL for GC-FID and GC-MS analyses (2, 3).

Analyses for *n*-alkane distribution (n-C_8 through n-C_{41}, pristane and phytane) and TPH were performed on a Hewlett-Packard (HP) 5890 gas chromatograph equipped with a flame-ionization detector (FID) and an HP 7683 autosampler. Analyses of target PAH compounds (including 5 alkylated PAH homologous groups and other EPA priority PAHs) and biomarker terpanes and steranes were performed on an HP 6890 GC equipped with a HP 5973 mass selective detector (MSD). System control and data acquisition were achieved with an HP G1701 BA MSD ChemStation. The individual biomarker compounds were determined using GC-MS in the selected ion monitoring mode (SIM).

RESULTS AND DISCUSSION

Biomarker Distributions

Generally, oil biomarkers of interest to environmental forensic investigation can be categorized into two classes: acyclic or aliphatic biomarkers, and cyclic biomarkers.

The terpanes in petroleum include sesqui- (C_{15}), di- (C_{20}), sester- (C_{25}), and triterpanes (C_{30}). Terpanes are found in nearly all oils. These bacterial terpanes include several homologous series, including bicyclic, tricyclic, tetracyclc, and pentacyclic (e.g., hopanes) compounds. Hopanes with the 17 αβ-configuration in the range of C_{27} to C_{35} are characteristic of petroleum because of their greater thermodynamic stability compared to other epimeric (ββ and βα) series. The steranes are a class of biomarkers containing 21 to 30 carbons that are derived from sterols, and they include regular steranes, rearranged diasteranes, and mono- and tri-aromatic steranes. Among them, the regular C_{27}-C_{28}-C_{29} homologous sterane series are the most common and useful steranes because they are highly specific for correlation.

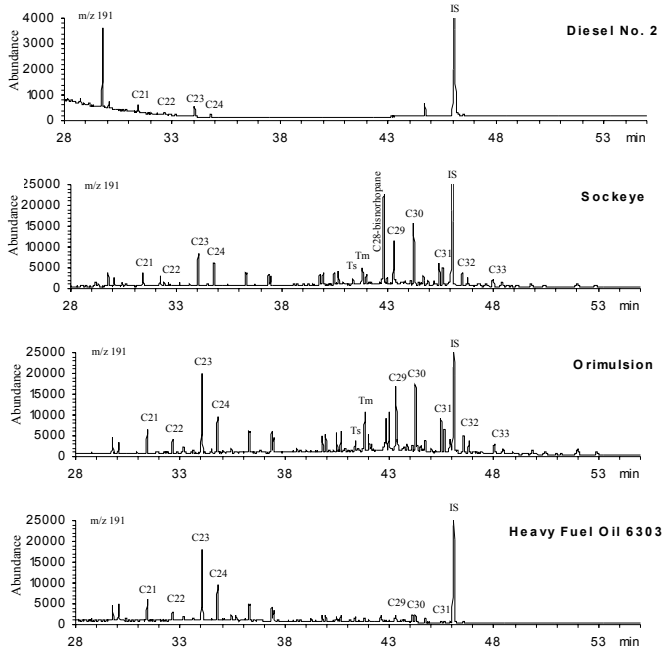

Figure 2 Distribution of biomarker terpane compounds (at m/z 191) for Diesel No. 2, Sockeye oil, Orimulsion, and HFO 6303, illustrating the differences in the relative distribution of terpanes between oils and oil products.

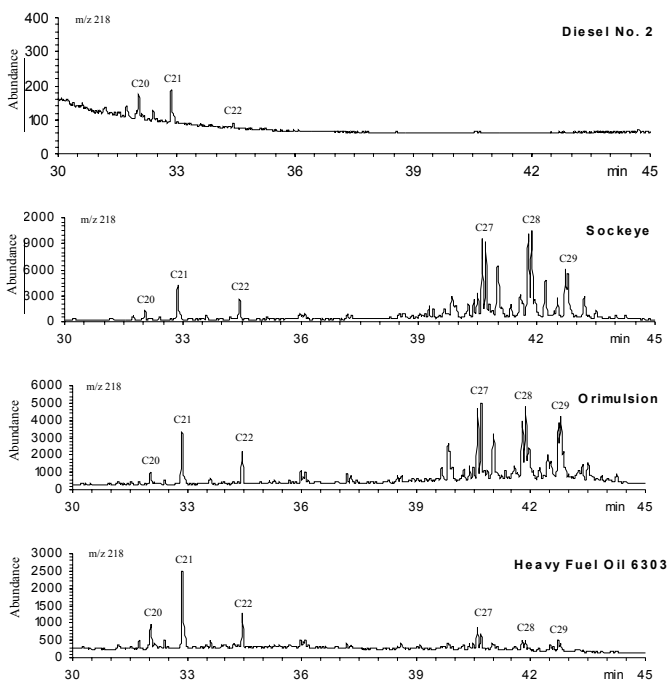

Figure 3 Distribution of biomarker sterane compounds (at m/z 218) for Diesel No. 2, Sockeye oil, Orimulsion, and HFO 6303, illustrating the differences in the relative distribution of steranes between oils and oil products.

Characterization of these biomarker compounds are achieved by using GC-MS at m/z 191 for tricyclic, tetracyclc and pentacyclic terpanes, at m/z 123 for bicyclic sesquiterpanes, at m/z 217 and 218 for steranes, at m/z 217/259 for diasteranes, at m/z 253 for mono-aromatic steranes, and at m/z 231 for tri-aromatic steranes. For many oils, the GC-MS chromatograms of terpanes (m/z 191) are characterized by the terpane distribution in a wide range from C_{20} to C_{30} often with C_{23} and C_{24} tricyclic terpanes and C_{29} αβ- and C_{30} αβ-pentacyclic hopanes being prominent. As for steranes (at m/z 217 and 218), the dominance of C_{27}, C_{28}, and C_{29} 20S/20R homologues, particularly the epimers of αββ-steranes, among the C_{20} to C_{30} steranes is often apparent.

The distribution patterns of biomarkers are, in general, different from oil to oil and from oil to refined products. **Figures 2** and **3** show GC-MS chromatograms at m/z 191 and 218 for Sockeye (California), Orimulsion-400 (Venezuela), HFO 6303, and Diesel No.2 (Ontario). The differences in the relative distribution of terpanes and steranes between Sockeye oil and Orimulsion are very apparent. For Sockeye, C_{28}-bisnorhopane, C_{29} and C_{30} αβ hopane are the most abundant with the concentration of C_{28} being even higher than C_{29} and C_{30} hopane. For Orimulsion, C_{23} terpane is the most abundant and the concentration of C_{29} is lower than C_{30} hopane. For HFO 6303, C_{23} terpane is the most abundant, but nearly no homohopanes of C_{31} to C_{35} were detected. Different from most Bunker C type oils, the concentrations of both terpanes and steranes are quite low in HFO 6303. As for refined products, only trace of C_{20} to C_{24} terpanes and C_{20} to C_{22} steranes were detected in Diesel No. 2. In contrast, most lube oils contain very high quantity of biomarkers. Obviously, refining processes have removed or concentrated high molecular mass biomarkers from the corresponding crude oil feed stocks.

Biomarker distribution in weathered oil

Biomarkers are source-characteristic and highly degradation-resistant. Therefore, for severely weathered oils, they may exhibit completely different GC-FID chromatograms and n-alkane profiles and isoprenoid distribution from their source oil, but their biomarker distribution patterns may be unaltered. Thus the fingerprinting of terpane and sterane biomarkers provides us with a powerful tool for tracking the source of the long-term weathered oil. Characterization of many long-term spilled oils demonstrated that n-alkane and isoprenoid compounds in these severely weathered oil samples can be completely lost, but, the profiles of their GC-MS fingerprints at m/z 191 and 217/218 can be nearly identical. Furthermore, the computed diagnostic ratios of a series of target pairs of biomarker compounds can be also nearly identical, clearly indicating that these samples were from the same source.

Biomarker distribution in petroleum products with similar chromatographic profiles

On some other cases where two oils may exhibit similar or even nearly identical n-alkane and isoprenoid distributions, however, their biomarker distribution may be markedly different. Thus, the successful forensic investigation will require to perform detailed analysis and comparison of not only the concentrations but also the diagnostic ratios of biomarkers among similar product types. **Figure 4** shows the GC-FID chromatograms of three unknown oil samples received form Montreal on March of 2001 for product identification and differentiation. Three samples show nearly identical GC chromatographic profiles and distribution patters. The relative ratios of low abundant hydrocarbons n-C_{17}/n-C_{18}, n-C_{17}/pristane and n-C_{18}/phytane are also very similar. All the GC trace features suggest that the oils are hydraulic fluid type products. The questions which must be answered at this stage are: do these three oil samples really come from the same source or not? The GC-MS analysis for biomarker characterization (**Figure 5**) indicate that samples #1 and

#2 are nearly identical in distribution patterns and profiles of terpanes and steranes, but sample #3 shows markedly different distribution pattern of biomarkers from sample #1 and #2. The concentrations of C_{23} and C_{24}, and the sum of C_{31} through C_{35} homohopanes in sample #3 are significantly lower and higher than the corresponding compounds in samples #1 and #2, respectively. The biomarker analysis results, in combination with other GC analysis results, clearly demonstrated that sample #1 and #2 are identical and from the same source, and the sample #3 is different from sample #1 and #2 and does not come from the same source as samples #1 and #2 do.

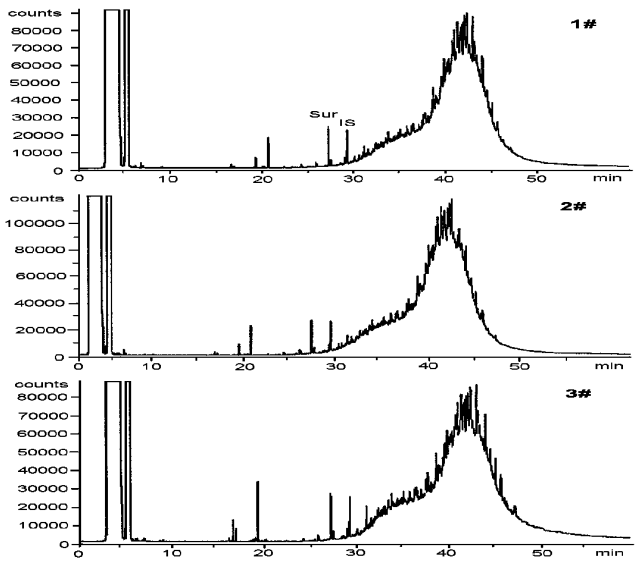

Figure 4 GC-FID chromatograms of Fraction 3 for *n*-alkane and TPH analysis of three unknown oil samples. These three samples show very similar GC chromatographic profiles and distribution patters.

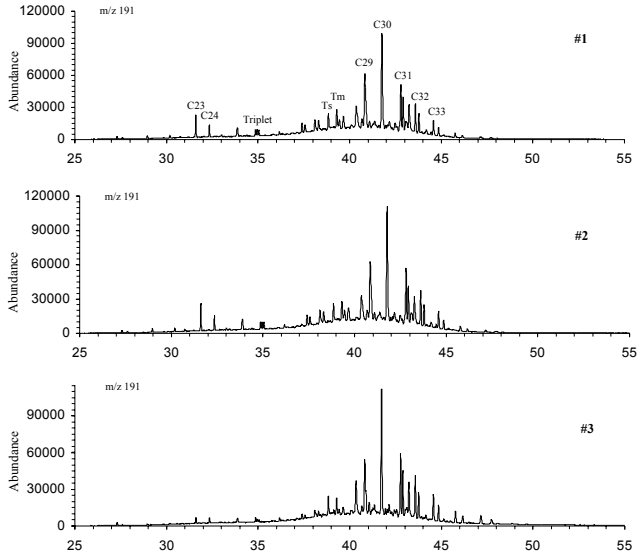

Figure 5 Distribution of biomarker terpane compounds (m/z 191) for the three unknown oil samples. Samples #1 and #2 are nearly identical in distribution patterns and profiles of terpanes, but sample #3 shows markedly different distribution pattern of biomarkers.

Sesquiterpane and Diamondoid Biomarkers in Oils and Lighter Petroleum Products

Refining processes have removed most high-molecular weight biomarkers from the corresponding crude oil feed stocks. Therefore the high boiling point pentacyclic triterpanes and steranes are generally absent in lighter petroleum products jet fuels and most diesels. However, several bicyclic sesquiterpanes including eudesmane and drimane (C_{15}), which boil in diesel range and are ubiquitous in sediments and crude oils, are still present in diesels and certain jet fuels with significant abundances after refining processes. Examination of GC-MS chromatograms of these bicyclic biomarkers at m/z 123, 179, 193, and 207 provide a comparable and highly diagnostic means of comparison for diesel type products (1, 4).

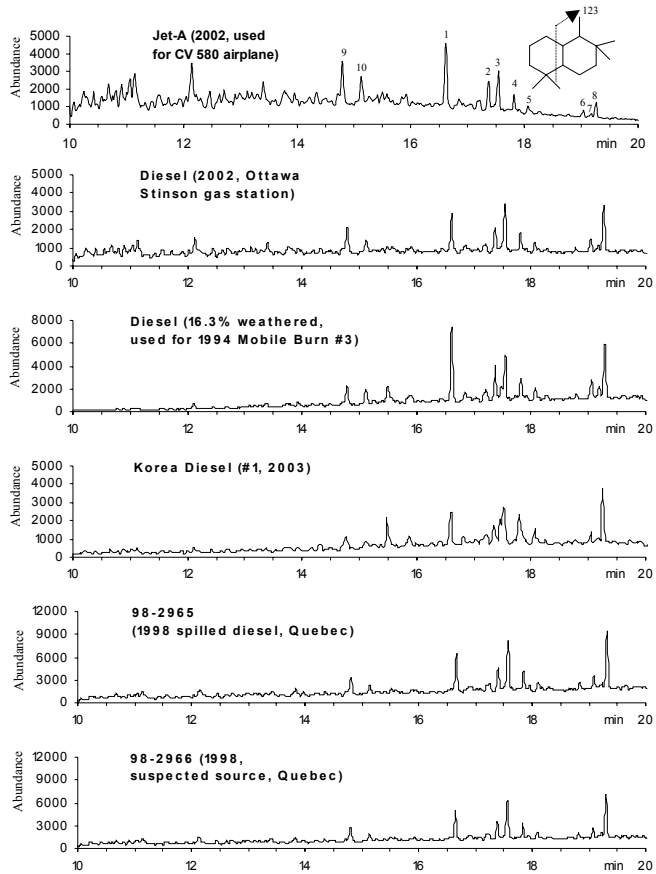

Figure 6 GC-MS chromatograms at m/z 123 for sesquiterpane analysis of Jet A (2002), Diesel No.2 (2002, from Ottawa Stinson Gas Station), Diesel No.2 (for 94 Mobile Burn, 16.3% weathered), a Korea Diesel (#1, 2003, from Korea), 1998-spilled-diesel (from Quebec) and 1998-suspected-source diesel (from Quebec). The different distributions of the sesquiterpanes demonstrates the differences between diesels and between diesel and jet fuel.

Another promising group of low boiling cyclic biomarkers of interest for environmental forensic investigators are "diamondoid" hydrocarbons (the collective term of adamantane (C_{10}), diamantane (C_{14}), and their alkyl homologous series). Diamondoids are rigid, three-dimensionally fused cyclohexane-ring alkanes that have a diamond-like (cage-like) structure. The diamond structure endows these molecules with an unusually high thermal stability and high resistance to biodegradation. Adamantanes and diamantanes are examined at m/z 135, 136, 149, 163, 177, and 191, and at m/z 187,

188, 201, 215 and 229, respectively. The sesquiterpane and diamondoid biomarkers are useful and promising for source correlation and differentiation of refined products, in particular for the weathered refined products, because of their stability and resistance to biodegradation

Figure 6 shows the GC-MS chromatograms at m/z 123 for sesquiterpane analysis of a jet fuel, Diesel No.2 (2002, from an Ottawa Gas Station)), Diesel No.2 (for 94 Mobile Burn, 16.3% weathered), Diesel No.2 (2003, from Korea), 1998-spilled-diesel (from Quebec) and 1998-suspected-source diesel (from Quebec). The different distributions of the sesquiterpanes demonstrates the differences between diesels and between diesel and jet fuel. **Figure 6** also clearly shows the spilled-diesel had nearly identical GC chromatogram with the suspected-source diesel (from Quebec). These similarities, in combined with other GC analysis results (such as hydrocarbon groups, n-alkanes and PAHs), argued strongly that the spilled diesel was from the suspected source.

Unique Biomarker Compounds

Biomarker terpanes and steranes are common constituents of crude oils. However, a few "specific" biomarker compounds including several geologically rare acyclic alkanes are found to exist only in certain oils and, therefore, can be used as unique markers to provide an interpretational advantage in fingerprinting sources of spilled oils and to provide additional diagnostic information on the types of organic matter that give rise to the crude oil. For example, the geologically rare acyclic alkane botryococcane ($C_{34}H_{70}$) was used to identify a new class of Australian non-marine crude oils. The presence of botryococcane indicates that the source rock contains remains of the algae *Botryococcus braunii*.

Other "specific" pentacyclic terpanes include C_{30} 17α (H)-diahopane (it may be related to bacterial hopanoid precursors that have undergone oxidation and rearrangement by clay-mediated acidic catalysis), β-carotane ($C_{40}H_{78}$, highly specific for lacustrine deposition, highly abundant in Green River Shale), gammacerane ($C_{30}H_{52}$, it has been tentatively suggested as a marker for hypersaline episodes of source rock deposition), lupanes and bisnorlupanes (they are believed to indicate terrestrial organic matter input), and bicadinanes (highly specific for resinous input from higher plants).

Diagnostic Ratios of Biomarkers

The diagnostic parameters of biomarkers most used in oil spill fingerprinting include: tricyclic C23/C24, C29 αβ/C30 αβ hopane, oleanane/C30 αβ hopane, homohopane (C31 to C35) distribution, Ts/Tm & Ts/(Ts + Tm), triplet ratio (C24 tertracyclic terpane/C26 tricyclic (S)/C26 tricyclic (R) sterane), regular sterane distribution (C27-C28-C29 ααα and αββ steranes (20S + 20R), C26-C27-C28 triaromatic steranes (TA) and C27-C28-C29 monoaromatic steranes (MA) distribution, and others.

The biomarker fingerprinting results strongly suggest a "*basic rule*" in the environmental forensic investigations: a negative correlation of biomarkers is strong evidence for lake of relationship between samples, and a positive correlation of biomarkers is not necessarily "proof" that samples are related because some oils from different sources can show similar characteristics of biomarkers. In order to reliably and defensively to correlate or differentiate samples, the "multi-parameter approach" must be initiated, that is, analyses of more than one suite of analytes must be performed.

Biodegradation of Biomarkers

It has well recognized that terpane and sterane compounds are very resistant to biodegradation. The studies of biodegradation of nine Alaska oils and oil products and eight Canadian oils by a defined bacterial consortium incubated under freshwater and cold/marine conditions in our lab showed that no changes of biomarkers after incubation, despite extensive saturate and aromatic losses. Also, the ratios of selected paired biomarkers remained constant. Therefore, biomarkers can, in many cases, be and have been used as conserved internal references for estimation of oil weathering percentages.

However, it does not mean cyclic biomarkers can not be biodegraded. Actually, they are still biodegradable in severe weathering conditions. In a recent study on long-term fate and persistence of the spilled Metula oil in a marine marsh environment (5), we found that in highly degraded asphalt pavement samples, even the most refractory biomarker compounds showed various degrees of biodegradation. The degree of biodegradation of biomarkers was not only molecular mass and size dependent, but also stereo-isomer dependent. The biomarkers were generally degraded in the declining order of importance as: diasterane > C_{27} steranes > tricyclic terpanes > pentacyclic terpanes > norhopanes ~ C_{29} αββ-steranes. The degradation of steranes was in the order of $C_{27} > C_{28} > C_{29}$ with the stereochemical degradation sequence 20R ααα steranes > (20R + 20S) αββ steranes > 20S ααα steranes. C29-18α(H), 21β(H)-30 norneohopane and C29 αββ 20R and 20S stigmastanes appeared to be the most biodegradation-resistant terpane and sterane compounds, respectively, among the studied target biomarkers.

REFERENCES

1. Peters, K. E., Moldowan, J. W., *The Biomarker Guide: Interpreting Molecular Fossils in Petroleum and Ancient Sediments*, Prentice Hall, New Jersey, **1993**.
2. Wang, Z. D., Fingas, M., Li, K., *J. Chromatogr. Sci.*, **1994**, 32, 361-366 (Part I) and 367-382 (Part II).
3. Wang, Z. D., Fingas, M., Sergy, G., *Environ. Sci. Technol.*, **1994**, 28, 1733-1746.
4. Stout, S. A., Uhler, A. D., McCarthy, K. J., Emsbo-Mattingly, S., in: *Introduction to Environmental Forensics* (B. L. Murphy and R. D. Morrison, eds.), Academic Press, London, **2002**, Chapter 6.
5. Wang, Z. D., Fingas, M., Owens, E. H., Sigouin, L., Brown, C.E., *J. Chromatogr.*, **2001**, 926, 275-190.

CHARACTERIZATION OF HIGH-MOLECULAR WEIGHT SULFUR CONTAINING AROMATICS IN VACUUM RESIDUES USING FOURIER TRANSFORM ION CYCLOTRON RESONANCE MASS SPECTROMETRY

Hendrik Müller, Wolfgang Schrader, and Jan T. Andersson*

Institute of Inorganic and Analytical Chemistry, University of Münster, Corrensstr. 30, D-48149 Münster, Germany
Fax: +49-251-833 60 13, e-mail: anderss@uni-muenster.de
*Max-Planck Institut für Kohlenforschung, Kaiser-Wilhelm-Platz 1, D-45470 Mülheim an der Ruhr, Germany

Introduction

Millions of tons of vacuum residues are produced annually in oil refineries worldwide. Although being potentially valuable resources for petrochemistry, their further processing is hampered by the fairly large amounts of sulfur present in these heavy fractions. Removal of the largely polycyclic aromatic sulfur heterocycles (PASH) by hydrodesulfurization (HDS) is more inefficient than for lighter petroleum fractions[1]. A better structural knowledge of the recalcitrant PASHs is therefore desirable for the development of new catalysts.

Previous studies proved that even after several chromatographic simplification steps the complexity of the sample is tremendous. Fourier transform ion cyclotron resonance mass spectrometry (FT-ICR-MS) has demonstrated the capability to resolve thousands of compounds in similar samples[2]. Nitrogen and polar compounds were investigated and more than 11,000 unique exact masses were identified. However, a selective measurement of PASHs is not easily feasible with present methods.

To study specifically the sulfur heterocycles in vacuum residues, we are investigating the methylation of the sulfur atoms of the target molecules to methylsulfonium salts[3]. Thus, these compounds are effectively "tagged" in a highly selective reaction prior to injection into the mass spectrometer. The computed mass data show the presence of PASHs with mainly one and two sulfur atoms per molecule in the vacuum residue before and after partial hydrodesulfurization.

Experimental

Vacuum Residue Samples. The residue samples investigated in this study were taken from a Safaniya crude oil before (feed) and after (effluent) partial hydrotreatment with a catalyst. The sample residues were provided by the Institut français du pétrole, Vernaison, France. After removal of asphaltenes by precipitation, the aromatic fraction was isolated by preparative liquid chromatography in order to separate saturate-aromatic-resin compounds according to the SARA method[4]. The aromatic fraction contained 4.66 % sulfur before and 2.91 % after hydrodesulfurization

Ligand exchange chromatography provided a group separation of PASHs from the polycyclic aromatic hydrocarbons (PAH). This separation was achieved using a Pd(II)-bonded stationary phase as described previously[5]. Two fractions were easily separated by using eluents of different polarity and are referred to as the PAH and the PASH fraction.

Methylation of sulfur compounds. PASHs were selectively methylated at the sulfur atom, thus efficiently charging PASHs with a positive charge using a procedure described by Acheson et al[3]. PAH and PASH fractions of 50 mg "feed" and "effluent" and 1 mmol of iodomethane were dissolved in 3 mL of dry 1,2-dichloroethane (DCE). A solution of 1 mmol silver tetrafluoroborate in 2 mL DCE was added and allowed to react for 48 h. The precipitated silver iodide was removed by centrifugation and DCE was distilled off under reduced pressure. The resulting sulfonium salt was dried under vacuum before mass spectrometric analysis. To investigate the influence of alkyl substitution on the efficiency of the methylation, reference compounds were methylated as well. The following compounds were employed: dibenzothiophene, 4-methyldibenzothiophene, 4-ethyldibenzothiophene, 2,4,6,8-tetramethyldibenzothiophene, and 2,7-dimethylbenzothiophene. Except for the commercial dibenzothiophene, they were synthesized in our laboratory[6].

High resolution mass spectrometry. Mass spectra were acquired using an APEX III Fourier transform ion cyclotron resonance mass spectrometer (Bruker Daltonics, Bremen, Germany) equipped with a 7 T magnet and an Agilent electrospray (ESI) ion source. For introduction the samples were dissolved in a 50:50 (v/v) solution of dichloromethane/methanol and injected in the infusion mode using flow rates of 2 µL/min. Typical electrospray conditions were 4.5 kV spray voltage. After ionization the ions were accumulated for 0.5 s in the hexapol before transfer to the cyclotron cell. For a good signal-to-noise ratio at least 64 scans were accumulated. Internal and external calibration was done using the Agilent electrospray calibration solution with the masses 322.04812, 622.02896, 922.00980 covering the mass whole range of the samples.

Calculation of compound classes from accurate mass data. For each mass signal several most probable elemental compositions were calculated using the software "Molecular Weight Calculator" [7], Version 6.25. Mass data and formulas were imported into an Excel spreadsheet. The formulas were evaluated based on them making chemical sense and sorted to provide classes according to the degree of saturation (type) and the number of heteroatoms (class) present[8,9].

Results and Discussion

The methylation reaction presented here together with ESI selectively ionizes PASHs through conversion of the neutral sulfur atom into a sulfonium ion as shown in Figure 1:

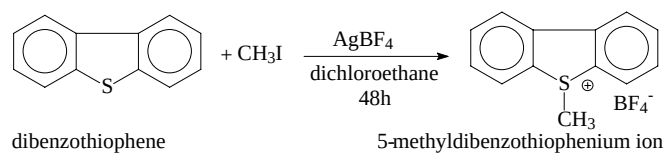

Figure 1. Methylation of PASH with dibenzothiophene as example.

Recalcitrant PASHs most probably are substituted by alkyl groups in the positions adjacent to the sulfur atoms[1] and thus it is likely that they exert a degree of steric hindrance to this reaction. To study this effect, five reference compounds were methylated using the described procedure. After the reaction time was increased from 2h as suggested in the literature to 16 h (necessary for quantitative reaction of 2,4,6,8-tetramethyldibenzothiophene), high yields of thiophenium salts were obtained as judged by matrix assisted laser desorption and ionization time of flight (MALDI-TOF) MS analysis. However, clusters of tetrafluoroborate and two sulfonium aromatic molecules could be observed to some extent.

To reduce the effect of this steric hindrance, which may be even larger in the PASHs in the vacuum residues, the reaction time for the samples was increased to 48 h. An example of the resulting mass spectra is shown in Figure 2. This method allows the selective investigation of complex solutions of sulfur containing heterocyclic compounds. It should be stressed here that without the methylation the atmospheric pressure chemical ionization (APCI) commonly used in LC/MS and MALDI ionization showed poor signal-to-noise ratio and no selectivity towards PASHs.

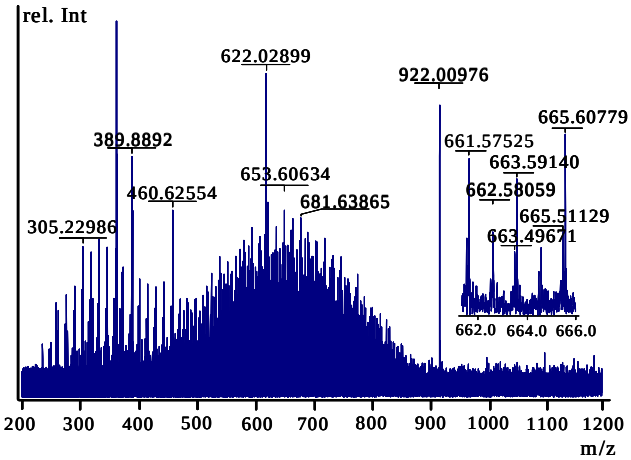

Figure 2. FT-ICR-mass spectrum of the aromatic effluent PASH fraction (only the mass range from m/z 200 to 1200 is shown). The insert shows the region from 662 to 666 m/z in more detail.

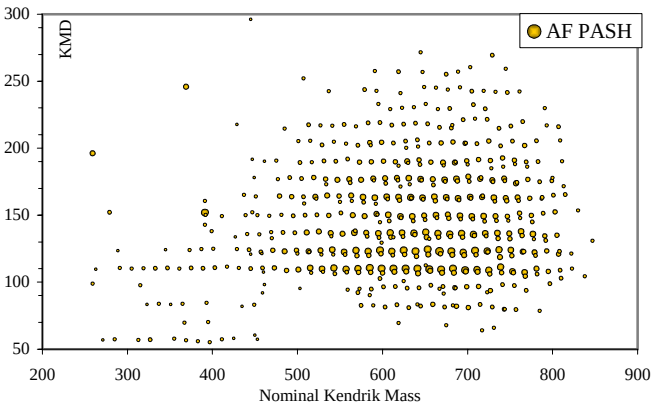

Figure 3. Kendrick mass defect (KMD) is plotted against Kendrick nominal mass. Series of PASH homologues of the aromatic fraction of the feed (AF PASH) appear in horizontal lines.

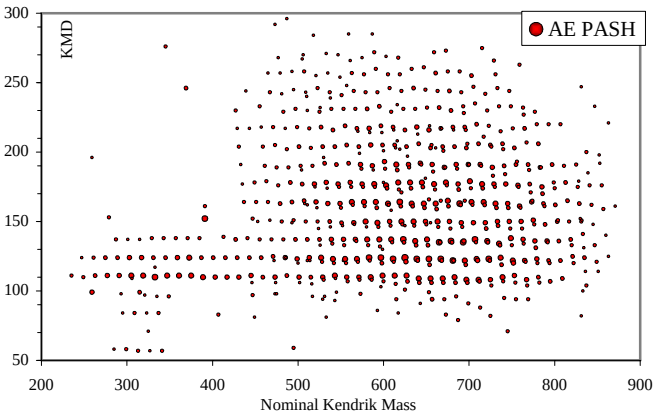

Figure 4. Kendrick mass defect (KMD) is plotted against Kendrick nominal mass. Series of PASH homologues of the aromatic fraction of the effluent (AE PASH) appear in horizontal lines.

Similar mass ranges as those shown in Figure 2 have been observed in previous experiments using different (APCI and MALDI) ionization techniques from nonderivatized samples, therefore the possibility of cluster formation does not seem to be serious. In contrast to these observations, about one third of the signals of samples of this study can only be explained by molecular clusters containing Ag^+ or BF_4^-. This however provides no problem as these clusters can be identified using the high accuracy data from FT-ICR-MS and treated separately.

Series of homologues can be identified visually as horizontal lines by plotting the Kendrick mass defect against Kendrick nominal mass. The Kendrick mass scale converts IUPAC masses by making CH_2 equal to 14.00000 as base of the scale. Kendrick mass defect (KMD) is the difference between nominal (Kendrick mass rounded to nearest integer) and accurate Kendrick mass. As a result members of homologous series feature the same KMD and are spaced at equal distances of 14 mass units. This is shown in Figures 3 and 4 for the PASHs of the aromatic fraction before and after HDS. The size of the dots reflects the intensity in the mass spectra.

The whole process of methylation reaction, ESI ionization, FT-ICR-MS data collection, and final data processing is highly selective towards PASHs. First results show that even in the two PAH fractions (feed and effluent), the large majority of the measured signals result from PASHs containing one (S1), two (S2) sulfur atoms. Compounds with three sulfur atoms (S3) are not as abundant but seem to be present in the sample. In Figure 5 the sum over the intensities of all identified molecules of the S class as well as the sum of intensities of all S2 class, S3 class, and PAH class compounds are given. This shows the tremendous selectivity towards PASHs over the much more abundant PAHs, as most compounds identified in all samples belong to the S and S2 class. Even in the PAH fractions which should consist of PAHs only, given the high selectivity of the Pd(II)-phase, very few masses were tentatively identified as belonging to PAH class compounds, again stressing the high selectivity of the methylation process.

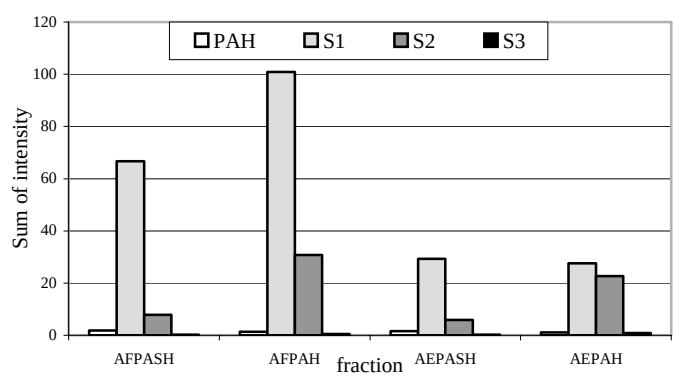

Figure 5. Sum over the intensities of mass signals of all members of one class for the dominant classes ("PAH", "S1", "S2" and "S3") present in sample vacuum residues.

Table 1 gives an overview of the distribution of compounds as a function of hydrogen deficiency in the four sample fractions. For the S1 class in both PAH fractions, more condensed material is present in comparison to both PASH fractions as can be seen from the higher Z number which is a measure for the hydrogen deficiency in the compounds. The same is true for the S2 class, but is not as distinct as for the monosulfur compounds.

	S1 class				**S2** class			
Z "type"	AF PASH	AFPAH	AE PASH	AE PAH	AF PASH	AFPAH	AE PASH	AE PAH
0	7	0	3	0	3	9	9	8
2	3	0	1	0	6	7	9	10
4	10	0	6	0	6	5	10	6
6	11	0	5	0	3	5	7	12
8	44	1	40	0	5	10	7	17
10	39	29	50	5	2	6	3	16
12	28	32	40	4	2	7	4	6
14	21	13	24	2	3	8	2	13
16	37	34	32	11	0	4	4	11
18	29	34	34	10	5	6	4	6
20	20	33	27	13	1	12	5	6
22	18	33	20	18	1	9	5	4
24	10	22	21	10	0	5	0	3
26	4	18	12	17	0	1	0	1
28	4	7	10	19	0	2	1	0
30	5	3	7	10	0	0	0	0
32	0	6	3	8	0	0	0	0
34	0	2	2	8	0	0	0	0
36	0	3	0	2	0	0	0	0
38	0	1	0	0	0	0	0	0

Table 1. Comparison of Compound Classes and Types of AE PASH Fraction and AE PAH Fraction; "Z" is the Value of Hydrogen Deficiency in Chemical Formulas $C_cH_{2c-\underline{Z}}O_oS_s$.

The data shown in Table 1 also demonstrate the effect of the hydrodesulfurization reaction. PASHs that survive the hydrotreatment show a trend towards higher hydrogen deficiency, possibly indicating a more condensed nature of those PASHs that do not react. However, by comparison of KMD plots of AF PASHs and AE PASHs (Fig. 3 and 4) a preferential loss of molecules with lower molecular mass during hydrodesulfurization is not observed.

Acknowledgement. Dr. Stephane Kressman and Dr. François Xavier, Institut français du pétrole, Vernaison, France, are thanked for preparing and supplying the aromatic fractions of the residue samples.

References

(1) Whitehurst, D. D.; Isoda, T.; and Mochinda, I. *Adv. Cata.*, **1998**, *42*, 345.
(2) Hughey, C. A.; Rogers, R. P.; and Marshall, A. G. *Anal. Chem.*, **2002**, *74*, 4145.
(3) Acheson, R. M.; Harrison, D. R. *J. Chem. Soc. C* **1970**, *13*, 1764.
(4) Later, D. W.; Lee, M. L.; Bartle, K. D.; Kong, R. C.; Vassilaros, D. L. *Anal. Chem.*, **1981**, *53*, 1612.
(5) Andersson, J. T.; Schade, T.; Müller, H. Prepr. Pap. - *Am. Chem. Soc., Div. Fuel Chem.* **2002**, *47*(1), 224:115.
(6) http://www.uni-muenster.de/Chemie/AC/anders/Pash/welcome.html
(7) http://www.alchemistmatt.com/
(8) Hughey, C. A.; Hendrickson, C. L.; Rodgers, R. P.; Marshall, A. G. *Anal. Chem.*, **2001**, *73*, 4676.
(9) Hsu, C. S.; Qian, K.; Chen, Y. C. *Anal. Chim. Acta*, **1992**, *264*, 79.

HIGHER ALKYLATED DIBENZOTHIOPHENES IN SOME CRUDE OILS AND HYDRODESULFURIZED FUELS

Jan T. Andersson, and Thomas Schade

Institute of Inorganic and Analytical Chemistry, University of Münster, Corrensstrasse 30, D-48149 Münster, Germany
Fax: +49-251-833 60 13, e-mail: anderss@uni-muenster.de

Introduction

The lowering of the legal limits for sulfur in fuels has led to a massive research effort to find catalysts that can remove sulfur down to the required levels. In the European Union this means that by 2005 gasoline and diesel fuels must meet a limit of 150 ppm with a goal of reducing it further to 10 ppm by 2009. In the USA, the gasoline limit is 120 ppm (2004) and 30 ppm (2006) and 15 ppm by 2007 for diesel[1]. Huge investments in refinery technology have allowed oil companies in Germany to exclusively offer fuels with a sulfur concentration below 10 ppm already by the year 2003. This amount is so low that such fuels are sometimes called "sulfur free fuels", although this is, of course, not correct.

Of the different forms of sulfur in fuel, the sulfur bound in aromatic structures is among the most difficult to remove catalytically. Within the aromatic sulfur species a certain selectivity can also be observed. Of the two most prominently occurring aromatic families of sulfur compounds, benzothiophenes and dibenzothiophenes, the former are generally more easily desulfurized than the latter. A further role is played by alkyl substituents which can exert some steric hindrance to the ability of the substrate to reach the catalyst surface. Thus dibenzothiophenes with alkyl groups in the 4- and/or 6-positions (**Figure 1**) are more difficult to hydrodesulfurize than other isomers and tend to accumulate in the product.

Recently members of a different class of sulfur compounds were shown to possess a high degree of recalcitrance to the catalytic process (**Figure 1**)[2]. They were all found to be 1,1,4a,6-tetramethyl-9-alkyl-1,2,3,4,4a,9b-hexahydrodibenzothiophenes with different alkyl groups in the 9 position.

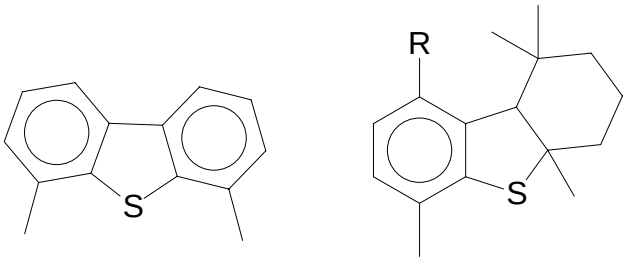

R = H, CH_3, C_2H_5, iso-Pr, iso-Bu

Figure 1: Compounds showing steric hindrance to hydrodesulfurization. 4,6-Dimethyldibenzothiophene (left) and 1,1,4a,6-tetramethyl-9-alkyl-1,2,3,4,4a,9b-hexahydrodibenzothiophene (right)

In such compounds the sulfur is not part of an aromatic ring. Probably due to considerable steric hindrance, this sulfur atom shows a very pronounced resistance toward the hydrodesulfurization process and such compounds therefore accumulate when the sulfur content in fuels is reduced.

We were interested in identifying the sulfur compounds that show this recalcitrance to hydrodesulfurization and have started a program to identify them[3]. Monomethyldibenzothiophenes have long been studied. In this report we therefore concentrate on C_2- to C_4-substituted dibenzothiophenes.

Several C_2-, C_3- and C_4-substituted dibenzothiophenes, with the number denoting the total number of carbon atoms in the alkyl substituents, were synthesized as reference compounds, in most cases from an appropriately alkylated thiophenol and a suitable bromocyclohexanone[4]. In Table I, the compounds thus prepared are listed. The use of reference compounds is necessary for the assignments of unknown peaks in the gas chromatogram and for an estimation of the behavior of compounds with steric hindrance around the sulfur atom on chromatography on the palladium(II) column that was used to separate the sulfur heterocycles from the polycyclic aromatic hydrocarbons.

Table I. Compounds synthesized and studied in this work

<u>C_2-DBT</u>
4-ethyl

<u>C_3-DBT</u>
1,3,7-trimethyl
1,4,6-trimethyl
1,4,7-trimethyl
1,4,8-trimethyl
2,4,6-trimethyl
2,4,7-trimethyl
3,4,6-trimethyl
3,4,7-trimethyl
3,4,8-trimethyl
4-ethyl-6-methyl

<u>C_4-DBT</u>
1,4,6,8-tetramethyl
2,4,6,8-tetramethyl
2,4,6,7-tetramethyl
6-ethyl-2,4-dimethyl

Experimental

The aromatic fraction was isolated from the whole sample by chromatography on silica gel (6-7 g, 10 mm x 100 mm) using cyclohexane (40 mL) to elute the aliphatic compounds and cyclohexane:dichloromethane (3:1, 40 mL) to isolate the polycyclic aromatic compound fraction. After a reduction of the volume to 10 mL on a rotary evaporator, the volume of the solvent was further reduced to ca 500 µL with a slow stream of dry nitrogen. Separation into a PAH and a PASH fraction on a column with the palladium(II) complex of chemically bonded 2-aminocyclopentene-1-dithiocarboxylic acid was performed according to Ref. 5. The fraction eluting with cyclohexane:dichloromethane (7:3) contained the polycyclic aromatic hydrocarbons and the fraction coming with (1.0 % isopropanol in cyclohexane):dichloromethane (7:3) was taken as the aromatic sulfur fraction.

The gas chromatographic analysis was performed on either a DB-5 or a DB-17ms capillary column (30 m x 0.25 mm i.d., the film thickness was 250 µm) with hydrogen (FID) or helium (MSD) as carrier gas. 2-Fluorodibenzothiophene was used as internal standard (IS) for quantification purposes[6]. Mass spectra were recorded using a Finnegan GCQ mass selective detector.

Results and discussion

In Figure 2, the gas chromatogram of the sulfur aromatic fraction of a commercial diesel fuel with a sulfur content of 70 ppm is depicted. Those polycyclic aromatic sulfur heterocycles (PASH) that were identified through direct comparison with the synthesized standards are indicated through their structural formulas or in the legend. Several other components could be assigned to a general substitution pattern through their mass spectra but the exact structure has not yet been elucidated. Work is in progress to extend the identification to these peaks.

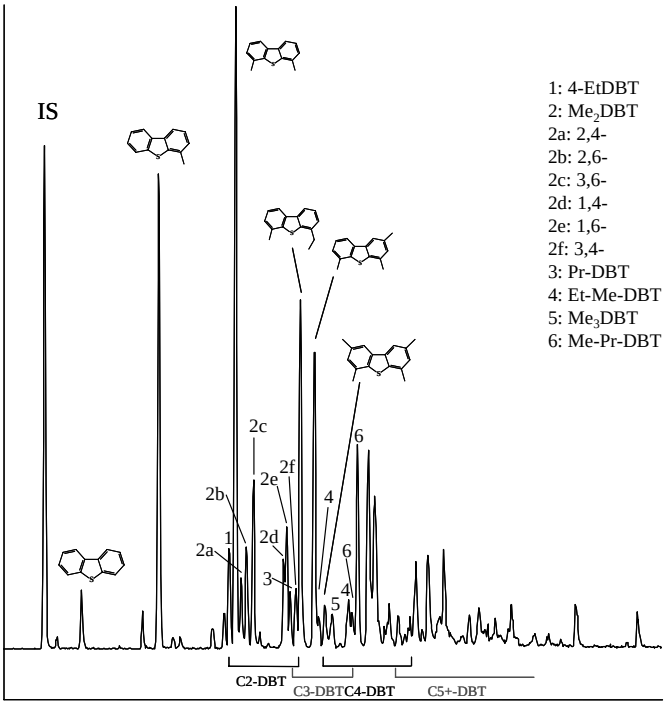

Figure 2. Gas chromatogram with mass selective detection of the polycyclic aromatic sulfur fraction of a commercial diesel fuel containing 70 ppm sulfur. Stationary phase: DB 17ms. IS = 2-fluorodibenzothiophene as internal standard. The following dimethyldibenzothiophenes (Me_2DBT) were identified: *2a*: 2,4-, *2b*: 2,6-, *2c*: 3,6-, *2d*: 1,4-, *2e*: 1,6-, and *2f*: 3,4-dimethyldibenzothiophene

The criteria for these assignments were that the M^+ ion had to correspond to the molecular mass of the congener. This ion is also the base ion (100 %) for polymethyldibenzothiophenes. If an ethyl group is present, the base ion is formed through loss of a methyl group, giving rise to $[M-15]^+$ as the base ion. A propyl group is indicated through the fragment $[M-29]^+$ which corresponds to the formation of the stabilized tropylium ion and is the base peak. This is illustrated in Figure 3 which shows the mass spectrum of peak number 3 in Figure 2. Likewise, the peak we assign to a methylpropyldibenzothiophene shows similar features typical of the two alkyl groups with m/z 211 as the base ion, corresponding to loss of an ethyl group, 226 (76 %) through loss of a CH_2 fragment and an M^+ ion at 240 (23 %).

It is well known that a methyl group in the 4-position of dibenzothiophene exerts enough steric hindrance to the approach of the sulfur atom to the active center on the catalyst surface to lower

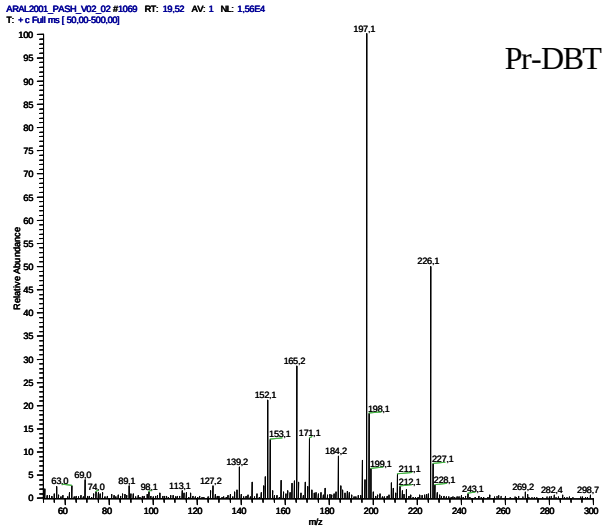

Figure 3. The mass spectrum of peak number 3 in Figure 2, assigned to a propyldibenzothiophene.

the rate of dehydrosulfurization appreciably. The result is that among the mono-methyldibenzothiophenes, only the 4-isomer is found in desulfurized products. In deeply desulfurized fuels, this congener also is removed.

Among the C_2-substituted dibenzothiophenes, 4,6-dimethyldibenzothiophene is always particularly prominent in desulfurized fuels, unlike most crude oils where other isomers are more prominent. 4-Ethyldibenzothiophene, normally a minor peak in the gas chromatogram, also attains some prominence. As can be seen in Figure 2, all the identified dimethyldibenzothiophenes have at least one methyl group in the 4- or 6-position. Gas chromatographic retention index data are available for many lower alkylated dibenzothiophenes[7].

A similar situation is found for the higher alkylated compounds. As shown in Figure 2, we have identified 4-ethyl-6-methyldibenzothiophene as the major C_3 congener, followed by 2,4,6-trimethyldibenzothiophene. Both these compounds exhibit the pattern of 4,6-disubstitution. This knowledge makes it highly probable that the indicated propyldibenzothiophene is substitued in the 4-position.

Sulfur heterocycles have been shown to be useful to identify the source of an oil spill in the environment. The PASH pattern was of particular use to correlate the pattern of the spilled oil with that of suspected sources[8,9] since different oil fields produce crudes with different PASH signatures. However, it is as yet unclear how strongly the provinence of the crude influences the pattern of the desulfurized product. At this time it can only be speculated that much information of this kind is lost through the removal of many sulfur congeners.

As illustrated above, a desulfurized fuel can be distinguished from non-desulfurized fuels not only through the lower sulfur concentration but also the pattern of the congeners. This should also show up in air pollution as the trend toward lower sulfur content in vehicle fuels is gaining ground. This proposal is now under active investigation and the results will be compared with the PASH pattern of commercial desulfurized fuels.

Conclusions

The hydrodesulfurization of crude oil fractions strongly influences the pattern of alkyldibenzothiophenes in fuels such as diesel. Congeners substituted in the 4- and/or 6-positions are enriched in relation to the crude used. In residues from the distillation of crudes, this effect is still more pronounced and alkylated sulfur heterocycles in the less volatile fractions can be considerably more difficult to desulfurize. The change in PASH pattern through desulfurization has consequences for the pattern of PASHs found in the environment.

References

(1) *Environmental Science and Technology*, **2003**, *37*, March 1, 85 A – 86 A.

(2) Charrie-Duhaut, A.; Schaeffer, C.; Adam P.; Manuelli P.; Scherrer, P.; Albrecht P., *Angewandte Chemie-International Edition*, **2003**, *42*, 4646-4649.

(3) Schade, T.; Roberz, B.; and Andersson, J.T., *Polycyclic Aromatic Compounds*, **2002,** *22*, 311-320.

(4) Andersson, J.T.; Schräder, W.; Traulsen, F.; and Werlich, S., *Polycyclic Aromatic Compounds*, **2001**, *18*, 351-360.

(5) Andersson, J.T.; Schade, T.; and Müller, H., *Abstracts of Papers of the American Chemical Society*, **2002**, *224*:115-116, FUEL, Part 1, Aug. 18.

(6) Andersson, J.T.; and Weis, U., *J. Chromatogr. A*, **1994**, *659*, 151-161.

(7) Moessner, S.; and Wise, S.A., *Anal. Chem.* **1999**, *71*, 58-69.

(8) Tibbetts, P.J.C.; and Large, R. in *Petroanalysis '87* (Crump, G.B., Ed.), John Wiley and Sons, New York, **1988**, pp. 45-57.

(9) Stout, S.A.; Uhler, A.D.; and McCarthy, K.J, *Environmental Forensics*, **2001**, *2*, 87-98.

DESULFURIZATION OF FUEL OILS USING AN ADVANCED OXIDATION METHOD

Roberto Flores, Arturo Rodas, and Wendy Chavarria

Gerencia de Materiales y Procesos Químicos
Instituto de Investigaciones Eléctricas
Calle Reforma No. 113
Cuernavaca, Mor., 62490
MÉXICO

Introduction

The sulfur content reduction in fuel oils is traditionally carried out by hydrodesulfurization (HDS), where the C-S bond is broken by hydrogenolysis to produce H_2S and sulfur-free hydrocarbons[1]. However, side reactions occur during the process, such as, hydrogenation and cracking; therefore, high concentration of H_2 and drastic experimental conditions (over 350ºC and 100 bar) are needed in order to eliminate considerable amounts of sulfur.

An interesting alternative for sulfur elimination is the oxidative desulfurization using Fenton-like catalysts and hydrogen peroxide[2-6]. In this case, hydrogen peroxide reacts with the catalyst to generate hydroxyl radicals (·OH), a very strong oxidant agent that reacts with the sulfur compounds to yield sulfoxides and/or sulfones. These compounds are more polar than the no oxidized species, so they can be extracted with a polar organic solvent, like acetonitrile and alcohol, or by passing through an ionic column. This process is achieved at mild reaction conditions (less than 100ºC and atmospheric pressure), but it proceeds very slow.

On the other hand, it has been also found that hydroxyl radical can be produced by ultrasound through cavitations in liquid solutions. It is believed that ultrasonic waves generate and collapse microbubbles very fast, and temperatures around 5000ºC and pressures over 300 bar are reached in the liquid-gas interphase[7-13]. These drastic conditions are able to break molecules to generate free radicals in the following way:

$$H_2O \longrightarrow H\cdot + OH\cdot$$

$$H_2O_2 \longrightarrow 2OH\cdot$$

$$RR' \longrightarrow R\cdot + R'\cdot$$

So, hydroxyl radicals are generated, and the oxidative desulfurization process can be carried out. Additionally, dyhydrogenation and recombination reactions can occur through the free radical mechanism[10-13].

In the present work, the oxidative desulfurization of fuel oils assisted by ultrasound was analyzed. It was studied the effect of hydrogen peroxide concentration, the fuel oil to aqueous solution volumetric ratio, and type of catalyst. The Fenton-like catalysts studied were ferric chloride and cupper sulfate.

Experimental

Fuel Oil Samples. Heavy fuel oil was got from Altamira Refinery (Tamaulipas, Mexico) and used as received. Diesel was purchased in a gas station and used as received.

Reactants. Deionized water was obtained *in situ* by passing distilled water through an ionic bed column. Acetonitrile (HPLC grade), hydrogen peroxide solution (30 wt%), ferric chloride (reactant grade) and copper sulfate (reactant grade) were purchased from J. T. Baker and used as received.

The experiments were made in a Cole Palmer apparatus, model 8890R-MTH, at constant frequency of 47 kHz and using a mechanical stirrer with a variable speed rate.

The experimental procedure consisted on preparing an aqueous solution with or without H_2O_2 and catalyst. This solution was added to the fuel oil and mixed using the mechanical stirrer. Then, the reactive mixture was put in the ultrasonic bath, and the ultrasonic energy was applied during the desired time. After the reaction period, it was allowed the separation between the aqueous phase and the organic phase. Next, the organic phase was washed with acetonitrile and mechanical agitation to extract the oxidized sulfur compounds. Finally, the fuel oil was separated from the acetonitrile solution and its sulfur content was determined.

The sulfur content in fuel oil was determined according to the ASTM-D129 Method.

Results and Discussion

The initial sulfur content in the heavy fuel oil and diesel was 3.85 and 0.04475 wt%, respectively. To determine if the acetonitrile could extract sulfur compounds from the fuel oil, samples of each fuel oil were washed once with acetonitrile. For the heavy fuel oil, the sulfur reduction due to acetonitrile washing was 18.4%; on the other hand, no sulfur reduction was obtained in diesel.

The effect of reaction time was studied for both fuel oils using a 3 wt% hydrogen peroxide aqueous solution without catalyst, and a fuel oil to aqueous solution volumetric ratio of 2. The experimental results are shown in **Figure 1**. The reduction of sulfur was greater in diesel than in heavy fuel oil. This can be explained by the complexity of the sulfur compounds in the heavy fuel oil compared to those in diesel. In the case of heavy fuel oil, the sulfur compounds are more hindered, so the oxidation by the hydroxyl radical is more difficult. On the other hand, it was found that the amount of sulfur eliminated from the heavy fuel oils decreased as the reaction increased from 7.5 to 20 min. This could be due to secondary reactions during the ultrasound treatment. In addition to the oxidation reaction, the ultrasound promotes dehydrogenation, cracking and recombination of heavy molecules, so the large hydrocarbon chains can react to make less available the sulfur compounds, and more difficult to extract during washing with acetonitrile. Also, an increase in the viscosity of the heavy fuel oil was observed after 20 min of ultrasonic treatment, which confirm that some changes in the physicochemical properties have occurred. Therefore, even in the case the sulfur compounds had been oxidized, their extraction with acetonitrile would be more difficult due to mass transfer problems. For diesel no appreciable effect was observed as the reaction time increased, and the small decrease was attributed to experimental error during the experimentation and sulfur content analysis.

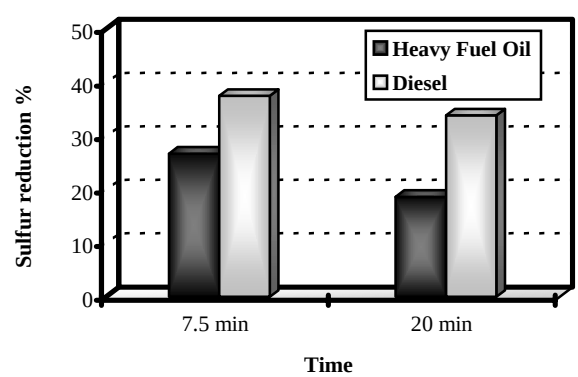

Figure 1. Effect of reaction time in the reduction of sulfur for heavy fuel oil and diesel.

The effect of hydrogen peroxide concentration was studied in both fuel oils. The volumetric fuel oil to aqueous solution was 2 in all experiments, and the reaction time was 7.5 min. The experimental results are shown in **Figure 2**. In absence of H_2O_2 in the reaction mixture, the sulfur was not eliminated from diesel, and the reduction of sulfur from heavy fuel oil was minimal, and even less than when it was just washed with acetonitrile. Again, this could be explained by secondary reactions that impedes the elimination of sulfur polar compounds during the washing stage. As the amount of H_2O_2 increases from 0 to 6 wt%, the reduction of sulfur content increased for the heavy fuel oil. This can be attributed to the generation of more hydroxyl radicals from the H_2O_2, which oxidize more sulfur compounds. Further increase to 10 wt% (not shown in Figure 2) did not enhance the sulfur reduction. On the other hand, the sulfur reduction on diesel enhanced when the H_2O_2 concentration increase to 3 wt%, but further increase in the H_2O_2 concentration to 6 wt% did not improve the sulfur reduction, and even it decreased a little, which was attributed to the experimental error that occurred in both experiments during the reaction and analytical stages.

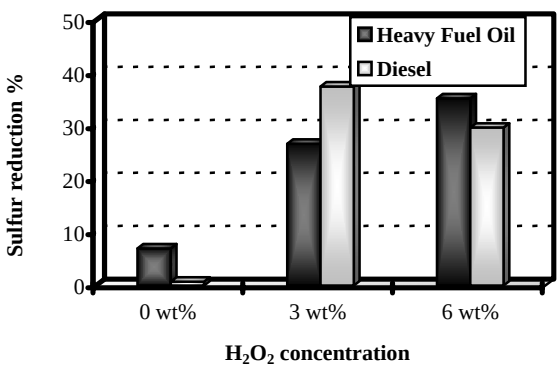

Figure 2. Effect of H_2O_2 concentration in the reduction of sulfur for heavy fuel oil and diesel.

The use of Fenton-like catalysts was studied for the sulfur reduction in heavy fuel oil and diesel at different conditions. The studied catalysts were $FeCl_3$ and $CuSO_4$. In the case of heavy fuel oil, when H_2O_2 was added to the reaction mixture, its concentration in the aqueous phase was 6 wt%. Conversely, for experiments with diesel the concentration of H_2O_2 was 3 wt% when it was included in the reaction mixture. In both cases the reaction time was 7.5 min. The experimental results are shown in **Figure 3**. In the case of heavy fuel oil, it was observed that the absence of H_2O_2 slightly improved the sulfur reduction, and almost the same catalytic activity was observed for both catalysts, around 34%. On the other hand, for diesel no sulfur reduction was observed in the absence of H_2O_2; also, the only active catalyst was $FeCl_3$ getting around 70% of sulfur reduction, and only around 5% of sulfur reduction was obtained when $CuSO_4$ was used.

Finally, the effect of the oil:aqueous solution volumetric molar ratio was studied for heavy fuel oil and diesel at different conditions. In the case of heavy fuel oil, experiments were carried out without catalysts and with a H_2O_2 concentration of 6 wt%; for diesel, the experiments were achieved using $FeCl_3$ and a H_2O_2 concentration of 3 wt%. In both cases, the reaction time was 7.5 min. The experimental results are presented in **Figure 4**. In the case of heavy fuel oil, when the amount aqueous solution increased up to a volumetric molar ratio of 1:1, the sulfur reduction slightly improved from 35 to 39%; however, further addition of aqueous solution decrease the sulfur reduction to 19% when the volumetric molar ratio of oil/aqueous solution was 0.5. On the other hand, for diesel the sulfur reduction always decreased as the amount of aqueous solution augmented in the reaction mixture.

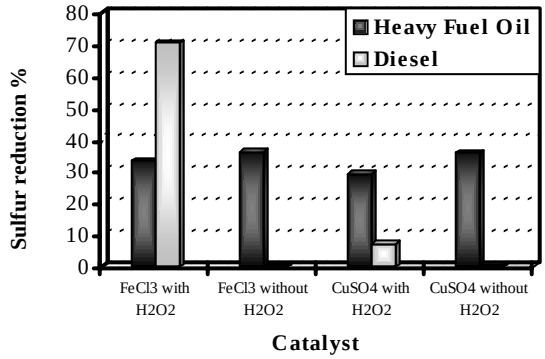

Figure 3. Effect of addition of catalyst in the reduction of sulfur for heavy fuel oil and diesel.

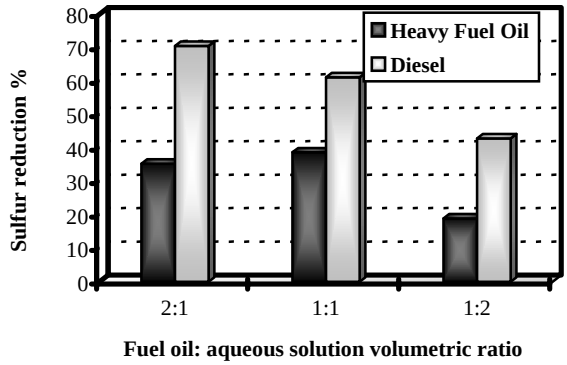

Figure 4. Effect of fuel oil to aqueous solution volumetric ratio in the reduction of sulfur for heavy fuel oil and diesel.

References

1. Speight, J. G., The desulfurization of Heavy Oils and Residua, Marcel Dekker, Inc: New York, 2000.
2. Plantenga, F. L.; Leliveld, R. G., *Appl.Catal. A*, **2003**, 248, 1.
3. Stanciulescu, M.; Ikura, M., U. S. Pat. Appl. Pub., No. 2003/0075483, **2003**.
4. Cabrera, C. A.; Imai, T., U. S. Pat., No. 6,171,478, **2001**.
5. Kocal, J. A., U. S. Pat., No. 6,277,271, **2001**.
6. Funakoshi, I.; Aida, T., U. S. Pat., No. 5,753,102, **1998**.
7. Ince, N. H.; Tezcanli, G. ; Belen, R. K. ; Apikyan, I. G., *Appl. Catal. B*, **2001**, 29, 167.
8. Hua, I.; Hoffmann, M. R., *Environ. Sci. Technol.*, **1997**, 31, 2237.
9. Mei, H. ; Mei, B. W. ; Yen, T. F., *Fuel*, **2003**, 82, 405.
10. Reddy, E. P. ; Davydov, L.; Smirniotis, P., *Appl. Catal. B*, **2003**, 42, 1.
11. Lin, J. R.; Yen, T. F., *Energy Fuels*, **1993**, 7, 111.
12. Dunn, K. ; Yen, T. F., *Fuel Process Technol.*, **2001**, 73, 59.
13. Suslick, K. S.; Gawlenowski, J. J.; Schubert, P. F.; Wang, H. H., *J. Phys. Chem.*, **1983**, 87, 2299.

THE STUDIES OF HYDRODESULFURIZATION OF 4,6-DIMETHYLDIBENZOTHIOPHENE ON SULFIDED Mo/γ-Al_2O_3: THE EFFECTS OF REACTIVE TEMPERATURE AND PRESSURE

Yongqiang Xu, Hongyan Shang, Ruiyu Zhao,Chenguang Liu

Key Laboratory of Catalysis, CNPC
State Key Laboratory of Heavy Oil Processing
College of Chemistry & Chemical Engineering
University of Petroleum (East China),
Dongying, Shandong, 257061, China

Introduction

Deep hydrodesulfurization (HDS) of diesel oil has attracted much attention recently as the more and more strict environmental regulations. Among the sulfur compounds of diesel oil, dibenzothiophenes (DBTs, such as dibenzothiophene (DBT), 4-methyldibenzothiophene (4-MDBT), 4,6-dimethyldibenzothiophene (4,6-DMDBT)) are found the refractory compounds to HDS [1-4]. However, even now scientists have different ideas on the adsorption states of DBTs over the HDS catalysts and carriers [5-7], as a result, they proposed different HDS mechanism of DBTs. On the other hand, the reactive thermodynamics and kinetics of HDS of DBTs are still studied inadequately. Therefore, the studies of HDS of DBTs are the key subjects to the deep HDS of diesel oil.

In this paper, the HDS of 4,6-DMDBT on sulfided Mo/γ-Al_2O_3 catalyst was studied, moreover, the reaction network and mechanisms were advanced on the basis of GC, and GC-MS analyses of the reaction products.

Experimental

Material and Catalyst. DBT was synthesized by a modified procedure of the literature [8]. Its purity is 99.7%, and its melting point is 98.2-98.4°C. 4,6-DMDBT was synthesized according to an improved method of literature [9]. Its purity is 99.6%, and its melting point is 153.5-154.1°C.

Mo/γ-Al_2O_3 catalyst was prepared in the following way. γ-Al_2O_3(20-40 mesh) was impregnated with an aqueous solution of ammonium heptamolybdate, followed by drying at 120ºC for 5h, and calcinations in air at 500ºC for 5h. The Mo/γ-Al_2O_3 catalyst contained 16.7wt%MoO_3.

Reactor and Experimental Procedure. The HDS reaction was carried out in a fixed-bed flow microreactor, consisting of a 17mm i.d. stainless steel tube. 5ml Mo/γ-Al_2O_3 catalyst (20-40 mesh) was packed in the middle section of the tube, and the other sections were filled by quartz sand. The catalyst was presulfided before HDS reaction with 3wt%CS_2 in cyclohexane for 6h at 2.0MPa, 300°C, LHSV, $3h^{-1}$ and H_2/feed ratio (V/V), 200/1. After presulfidation, the reactant (2wt%4,6-DMDBT or 2wt%DBT in toluene) was pumped into the reactor. 6h later, sampling of products was started at intervals of 30 min. the samples were immediately analyzed by gas chromatograph. Reaction pressure and temperature were then changed for studying the effects of them on HDS of 4,6-DMDBT. The reaction pressures used were 2.0, 1.5, 1.0MPa, while the reaction temperatures used were 300ºC, 280ºC, 260ºC.

Analysis

The samples were analyzed by Varian 3800 Chromatograph. The products were identified by GC-MS (Finnigan SSQ710).

Results and Discussion

The Analysis of Products of HDS and The Reaction Network

The products from reactions of 4,6-DMDBT and their yield at 300ºC under 2.0MPa over sulfided Mo/γ-Al_2O_3 were shown in Table 1. The isomerization of 4,6-DMDBT to 3,6-DMDBT and the other C2-DBTs was found on sulfided Mo/γ-Al_2O_3 catalyst as well as HDS. From Table 1 it can propose that the HDS of 4,6-DMDBT may occur through two types of reaction routes: 1) direct desulfurization (DDS), the hydrogenolysis of C-S bond of the 4,6-DMDBT to form 3,3'-dimethylbiphenyl, which can be further hydrogenated into 3-(3'-methyl-cyclohexyl)-toluene; 2) desulfurization through hydrogenation (HYD), which first forms 4,6-dimethyltetrahydrodibenzothiophene(4,6-DMTHDBT) and 4,6-dimethylhexahydrodibenzothiophene(4,6-DMHHDBT), followed by their desulfurization to provide 3-(3'-methyl-cyclohexyl)-toluene. 3,3'-dimethyldicyclohexyl among the products of HDS of 4,6-DMDBT is yielded from the hydrogenation of 3-(3'-methyl-cyclohexyl)-toluene. The reaction network for HDS of 4,6-DMDBT is shown in Scheme 1.

Table 2 shows the products from HDS of DBT and their concentration at 300ºC under 2.0Mpa over sulfided Mo/γ-Al_2O_3. Comparing Table 2 with Table 1, it can be found that under the same reaction conditions, the conversion of 4,6-DMDBT is lower than that of DBT, and the molar ratio of the products of HYD route to DDS route in the products of HDS of 4,6-DMDBT is about 7.42. But to DBT, it is only 1.33, which means that the HDS of 4,6-DMDBT is essentially through the HYD routes, while to DBT, the contributions of both routes is comparable. The methyl groups in 4,6-DMDBT molecule spatially hinds the "end on adsorption" of sulfur atom on the active sites of the catalyst, which depresses the DDS route and leads to the reduction of conversion of 4,6-DMDBT.

On the other hand, although on the Mo/γ-Al_2O_3 catalyst, 4,6-DMDBT is less reactive than DBT, the difference between the two reactants is not as significant as that generally observed on the CoMo/γ-Al_2O_3 catalyst. The reason for that is on the Mo/γ-Al_2O_3 catalyst, the HYD route is important for both compounds. Co can increase remarkably the hydrodesulfurization activity of the sulfided Mo/γ-Al_2O_3 catalyst, especially for the DDS route. This tremendously enhances the rate of DDS route of the HDS of DBT, but for 4,6-DMDBT, the effect is limited for steric hindrance of methyl groups.

The Effect of Reaction Pressure And Reaction Temperature on HDS of 4,6-DMDBT

The concentration of products for HDS of 4,6-DMDBT under different reaction pressures at 300ºC is shown in Fig.1. Fig.1 illustrates that the reaction velocity of HYD routes in HDS of 4,6-DMDBT obviously decreases with the descending of reaction pressure. But the effect on DDS pathway is much smaller than that on HYD. It can also be found that the effect of reaction pressure on the transformation of 4,6-DMDBT is very obvious for the high selectivity of HYD route in the HDS reaction network of 4,6-DMDBT.

The concentration of products of HDS of 4,6-DMDBT at different reaction temperatures under 2.0MPa is shown in Fig.2. From Fig.2 it can be found that the reaction rates of desulfurization products among the HDS products of 4,6-DMDBT all decrease with the descending of reaction temperature, not only that through the DDS route but also that through the HYD route. However, the transformation of 4,6-DMDBT is not remarkably affected since under relatively low reaction temperature 4,6-DMDBT mainly converses into partly hydrogenated products (i.e. 4,6-DMTHDBT and 4,6-DMHHDBT). The electron donor induction of the methyl groups in 4,6-DMDBT can promote the hydrogenation of the adjacent phenyl, leading to the reduction of activation energy of that.

Conclusion

The isomerization of 4,6-DMDBT is found on sulfided Mo/γ-Al_2O_3 catalyst as well as HDS. Its HDS occurs through the DDS route and HYD route. But the contribution of the HYD route on the products exceeds greatly over the DDS route. Under the same experimental conditions, it was found the conversation of 4,6-DMDBT is lower than that of DBT, which indicates that the methyl groups in 4,6-DMDBT cause the spatial restraining for the "end up adsorption" of sulfur atom on the active site of the catalyst, and lead to the low HDS reactivity of 4,6-DMDBT. Effect of reaction pressure on the HYD route is higher than that on the DDS route for HDS of 4,6-DMDBT. Reaction temperature has obvious effect on desulfurization products yielded through both the DDS route and the HYD route. Under relatively low reaction temperature 4,6-DMDBT mainly transforms into partly hydrogenated products (i.e. 4,6-DMTHDBT and 4,6-DMHHDBT). The electron donor induction of the methyl groups in 4,6-DMDBT can promote the hydrogenation of the adjacent phenyl, leading to the reduction of activation energy of the HYD route.

Table1 Concentration of HDS products of 4,6-DMDBT

Product	Concentration, mol%
C2-DBT	0.58
3,6-DMDBT	2.24
4, 6-DMDBT	72.01
4,6-DMTHDBTand its isomers	10.46
4,6-DMHHDBT and its isomers	2.75
3,4'-dimethylbiphenyl	0.06
3,3'-dimethylbiphenyl	2.93
3-(3'-methyl-cyclohexyl)-toluene and its isomers	6.55
3,3'-dimethyldicyclohexyl and its isomer	2.42

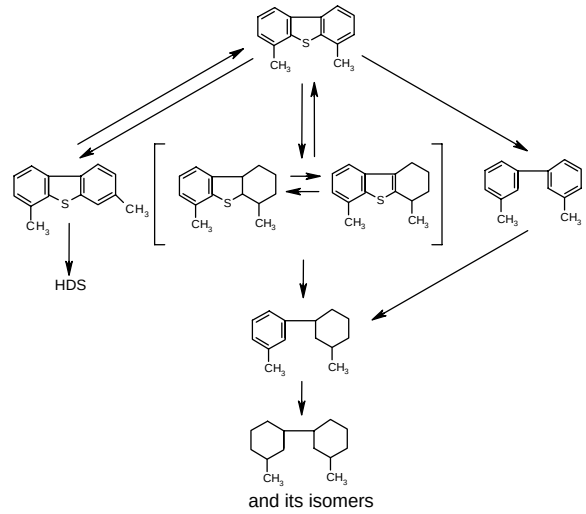

Scheme1 Reaction network for HDS of 4,6-DMDBT on sulfided Mo/γ-Al_2O_3.

Table2. Concentration of HDS products of DBT

Product	Concentration, mol%
DBT	48.37
4H-DBT	5.25
6H-DBT	1.07
biphenyl	22.09
cyclohexylbenzene	21.36
Bicyclohexene and its isomer	1.87

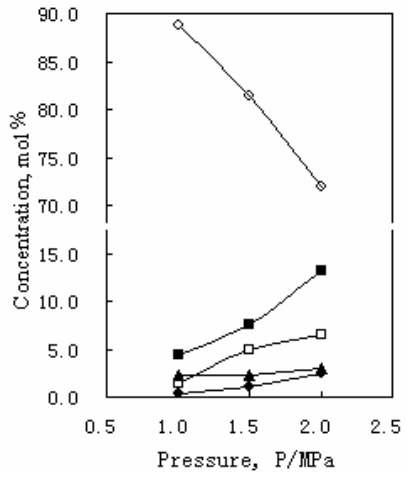

Fig.1 Concentration of hydrodesulfurization products of 4,6-DMDBT under different reaction pressure,
○4, 6-DMDBT, ■ 4,6-DMTHDBT+4,6-DMHHDBT,
□ 3,3'-dimethylcyclohexylbenzene, ▲ 3,3'-dimethylbiphenyl, ● 3,3'-dimethyldicyclohexyl

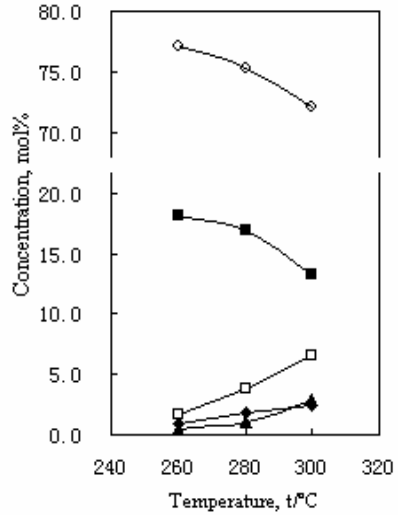

Fig.2 Concentration of HDS products of 4,6-DMDBT under different reaction temperatures,
○4, 6-DMDBT, ■4,6-DMTHDBT+4,6-DMHHDBT,
□ 3,3'-dimethylcyclohexylbenzene, ▲3,3'-dimethylbiphenyl, ●3,3'-dimethyldicyclohexyl

References

(1) Amorelli A., Amos Y. D., Halsig C.P., et al., Estimate Feedstock Processsability [J], *Hydrocarb.Proc*.,1992, *71(6)*: 93-101.
(2) Shih S. S., Mizrahi S., Green L. A., et al., Deep Desulfurization of Distillates [J], *Ind. Eng. Chem. Res.*, 1992, *31*:1232-1235
(3) Kabe T., Ishihara A., Tajima H., Hydrodesulfurization of Sulfur-Containing Polyaromatic Compounds in Light Oil[J], *Ind. Eng. Chem. Res*., 1992, *31*: 1577-1580
(4) Schulz H., Bohringer W., Ousmanov F., et al.,, Refractory sulfur compounds in gas oils[J], *Fuel Processing Technology*, 1999, *61*: 5–41
(5) Macaud M., Milenkovic A., Schulz E.,et al., Hydrodesulfurization of Alkyldibenzothiophenes: Evidence of Highly Unreactive Aromatic Sulfur Compounds[J], *J. Catal.*, 2000,*193*:255-263.
(6) Kabe T., Qian W., Ishihara A., Study of Hydrodesulfurization of Dibenzothiophene on Ni-Mo/Al_2O_3, Mo/Al_2O_3,and Ni/Al_2O_3 Catalysts by the Use of Radioisotope ^{35}S Tracer[J], *J. Catal.*, 1994,*149*: 171-180.
(7) Laudau, M. V., Deep Hydrotreating of Middle Distillates from Crude and Shale Oils[J]. *Catalysis Today*, 1997,*36(4)*:393-429
(8) Gilman, H. & Jcoby, A. L., Dibenzothiophene: Orientation and Derivatives[J]. *J. Org. Chem.*, 1938, *3(2)*:108-119
(9) Kuchm-Caubere, C., Adach-Becker, S., Fort, Y. et. al., Expeditious and Efficient Syntheses of pure 4-Methyl and 4,6-Disubstituted Dibenzothiophene[J]. *Tetrahedron*, 1996,*52(27)*:9087-9092.

DEVELOPING SEQUESTRATION BASELINES FOR THE WEST COAST
WEST COAST REGIONAL CARBON SEQUESTRATION PARTNERSHIP

Larry Myer
University of California Office of the President (UCOP)
1333 Broadway, Suite 240
Oakland, CA 94612
Fax: 510/485-5686; Larry.Myer@ucop.edu

John Kadyszewski
Winrock International

John Clinkenbeard
California Geologic Survey

Richard Rhudy
Electric Power Research Institute

John Ruby
Nexant

Terry Surles
California Energy Commission

Introduction

The West Coast Regional Carbon Sequestration Partnership is one of seven partnerships established by the US Department of Energy (DOE) to evaluate carbon dioxide capture, transport, and sequestration (CT&S) technologies best suited for different regions of the country. The West Coast Region comprises Arizona, California, Nevada, Oregon, Washington, and Alaska. The Partnership will evaluate both terrestrial and geologic sequestration options through five major tasks:

1) Collection of data to characterize major CO_2 point sources, the transportation options, and the terrestrial and geologic sinks in the region;
2) Addressing key issues affecting deployment of CS&T technologies, including permitting, monitoring, and health and environmental risks;
3) Conducting public outreach and education work;
4) Integrating and analyzing data to develop supply curves and cost effective, environmentally acceptable sequestration options;
5) Identifying appropriate terrestrial and geologic demonstration projects in the Region

In order to address the broad range of issues associated with carbon sequestration, the Partnership has assembled a diverse consortium of state natural resource, environmental protection, and other agencies; national labs and universities; private companies working on CO_2 capture, transportation, and storage technologies; nonprofit organizations; commercial users of CO_2 such as the oil and gas industry; policy/governance coordinating organizations; and others.

Characterization of Source and Sinks

Characterization of the CO2 sources and sinks in the region provides the baseline data needed for analyses of best storage options. Overall, the West Coast region represents more than 11% of the nation's CO_2 emissions. As shown in Figure 1, a majority of the region's total CO_2 emissions come from the transportation, industrial, and utility sectors. Terrestrial sinks, both forests, and soils, represent the most tractable sinks for dispersed transportation sources. Geologic storage is an option for the utility and industrial sectors, which have point sources most amenable to capture. Data collected by the IEA Greenhouse Gas Program show that these sectors account for about 56 million metric tons of carbon equivalent (MMTCE) per year in the five states shown in Figure 1. The North Slope of Alaska accounts for an additional amount of about 4MMTCE. The partnership is identifying the major individual point sources in the West Coast region by reviewing available data on power producers, cement manufacturers, oil refiners, and other energy intensive industries. In addition to location and amount of CO_2, collected data includes: plant efficiency performance factors; operations schedule and capacity; description of major components and equipment; energy and other resource consumption; and sources for major plant inputs.

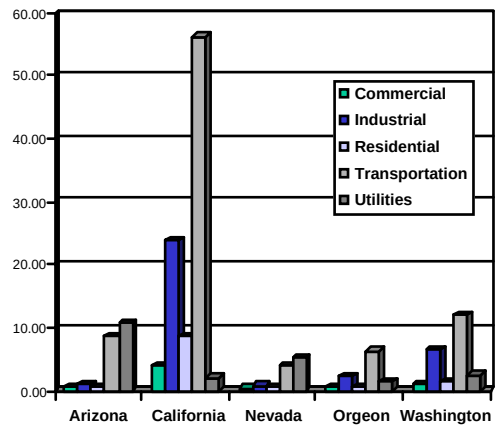

Figure 1. Western Region CO_2 Emissions, 1999 MMTCE

Porous sediments, which represent potential geologic sequestration sites, are found in most of the physiographic provinces within the West Coast partnership region. The Pacific Coast Province is of prime interest, because of its thick sediment sequence and oil and gas fields, which are found primarily in California's Central Valley. The North Slope of Alaska is also of great interest because of its large oil fields. Oil and gas fields in the West Coast Region not only provide large potential capacity, but also provide an opportunity for offsetting costs of sequestration through enhanced oil and gas recovery. Extensive geologic characterization data is also available in oil and gas producing areas. Characterization data including depth, thickness, areal extent, porosity, formation water salinity and total dissolved solids, permeability, pressure, and degree of fracturing is compiled in a Geographic Information System (GIS) layer showing sedimentary basins. This layer is combined with other layers containing data on active faults, urban areas, transportation routes, point source locations, restricted lands, etc, to enable spatial analysis of potential sequestration targets.

The West Coast region has a wealth of forest and agricultural lands where improved management practices could sequester substantial quantities of carbon. For forests, the partnership is

focused on three major types: (1) the Pacific Coast forests of northern California, Oregon, and Washington; (2) the Inland Empire forests of eastern Washington and Oregon and the north and central portions of California's Sierra Nevada range; and (3) the ponderosa pine and pinyon-juniper woodlands of California's southern Sierra Nevada as well as Nevada and Arizona. The region also includes extensive man-made grasslands that could be reforested.

To characterize the terrestrial sink, the partnership is developing a baseline for each state based on data for the 1990s. The carbon data for land use/land cover classes comes primarily from national data sets collected using common definitions and methods. Results are reported by land classes, and displayed in map format. Data types integrated into the partnership's GIS database include: land use, land cover and land suitability, hydrology and water districts, land ownership and tax assessments, soil maps, crop yields by county and income per acre by crop type (STATSGO and USDA), remote sensing (EROS Data Center), National Gap Analysis Program information, national forest inventory and forest heath plots, national resource inventory, and risk of loss (flood zones, fire maps, pest outbreaks, etc).

UTILIZATION OF MACRO-ALGAE FOR ENHANCED CO_2 FIXATION AND ENERGY PRODUCTION

Michele Aresta, Angela Dibenedetto and Grazia Barberio

Department of Chemistry, University of Bari
Campus Universitario – 70126 Bari - Italy

Introduction

The aquatic biomass represents a very interesting source of energy as it has a higher photosynthetic activity with respect to terrestrial plants, an easy adaptability to grow in different conditions, the possibility of growing either in fresh- or marine waters, avoiding the use of land. Either marine micro-algae or sea-weeds could be used as energy source also if the micro-algae have received much attention with respect to the macro-algae.

In this paper we discuss the use of selected Mediterranean macro-algae as source of biofuel. The extraction of oils and biofuel has been carried out using different technologies under mild energetic conditions. Supercritical-carbon dioxide and solvent extraction has been used efficiently to extract the fuel. The SC-CO_2 extraction is quite advantageous. SC-CO_2 is not toxic and, as its critic temperature is quite close to room temperature, it could be also used for the extraction of thermo-labile compounds. A preliminary balance, energetic and economic, will be also presented.

Particular attention has been dedicated to the preparation of samples for extraction in order to ameliorate the efficiency of the process, and to the characterization of the lipidic content.

Results and Discussion

The key step of this work has been the selection of some algae typical of the Adriatic or Jonian sea. In particular, the study has been carried out on two algae, the Chaetomorpha linum (O.F. Müller) Kützing (Cladophorales, Cladophoraceae) and the Pterocladiella capillacea (S.G. Gmelin) Santelices et Hommersand) (Gelidiales, Rhodophyta). Chaetomorpha linum is the dominant species in the bentopleustophytic population of Mar Piccolo in Taranto (Jonian sea), the latter being very much present in the estuary of the Galeso river where it can reach a density of 3 600 g/m^2. P. capillacea, a very good agarophyte, can be found on the rocky substrates in the South Adriatic sea close to Bari and can reach a density of 1 500 g/m^2. Going 150 km further south in the Adriatic sea, it is still present, but in lower amount.

The two species have been selected because of their easy availability and low cost harvesting technology, presence and vegetation all the year long, growth on a large scale in an artificial environment, high percent of compounds that have a potential use as biodiesel.[1]

The effect of several parameters such as biomass production in presence of nitrogen sources, ratio biomass/volume, salinity, temperature and irradiance have been also considered.[1]

In this work, a methodology has been developed for the extraction of biodiesel from algae. Supercritical carbon dioxide has revealed to be particularly suited as extraction solvent. A quali-quanti-tative comparison of the extracts obtained by using this technique with those obtained using the organic solvent extraction has been carried out. The scCO_2 technique revealed to be more efficient and less costly. By using scCO_2 (40-50 °C, 25-30 MPa) in a SITEC apparatus operated in a continuous mode, the extraction of oil from algae has been carried out using either scCO_2 alone or added with methanol (1 mL) as co-solvent.

In order to have an efficient extraction it is necessary to pre-treat the algae. In fact if they are used as collected, no oil is extracted. Among the various techniques, grounding of the dried (at 35 °C) algae in liquid nitrogen is the most effective. The very fine solid obtained, can be extracted under the conditions specified above. Per each sample the amount of extracted oil has been determined per kg of dry matter. The oil content varied from 7 to 20 %. Then the oil has been analysed by CG-MS and its composition determined. Almost all products in the GC were identified so far (96 % of the total) and the mass spectrum of each product was compared with that of an authentic sample used as standard. This has allowed to identify the components of the oil and to calculate the heat content expressed as MJ/kg oil. Such value has been checked through a combustion test. Such studies have shown that the morphological difference of the two algae is associated to a different lipid content, both quantitative and qualitative. In fact, in C. linum methyl myristate, methyl palmitate, methyl linoleate and methyl oleate were found, while P. capillacea was shown to contain besides methyl myristate and methyl palmitate, methyl arachidonate and methyl-all-cis-5,8,11,14,17 eicosanpentaenoate as major components (see Table 1).

Table 1. Principal compound of the oil

Algae	Pressure (bar)	T (°C)	Esters (methyl)	Lipidic content (%)
Chaetomorpha linum	240	50	myristate, palmitate, linoleate, oleate	15
Pterocladiella capillacea	265	50	myristate, palmitate, arachidonate, all-cis-5,8,11,14,17 eicosanpentaenoate	7.5

Studies are still in progress for the complete characterisation of the extract.

A life cycle assessment study has been initiated for the evaluation of the potential of macro-algae for fuel production. Below we discuss the main compounds of the LCA flow-sheet.

Macro-algae need nutrients (N, P, microelements) to which the energy Enu is associated. The cultivation energy is indicated as Ec. A variance analysis has shown that if the energy of nutrients is taken into consideration, the energetic balance may be negative. Therefore, in order to avoid such huge amount of energy input, either effluent water from aquaculture plants should be used, or some selected municipal waters. Algae work as a purifying agent and treated water can be either re-circulated to the fish-pond or immitted into natural basins without paying any penalties. Such use of effluent water, by the way, generates a credit to the process that may be ultimately taken into account. With respect to micro-algae, macro-algae do not need a vigorous stirring. This difference introduces a credit for the macro-algae system when compared to micro-algae. At the end, algae must be harvested, Er. As macro-algae grow either on a solid substrate or free-floating in water, in the former case it is necessary to cut the algae, Eh. The collection is quite easy as it is possible to install a net that when risen allows to collect algae and to let excess water run-off. Also this step is less energy requiring for macro-algae than for micro-algae, that need filtration for their separation. The drying is made by using solar energy or recovered heat, so that the only requested energy is the transfer and mixing, Ee. Once the algae are dried, they need to be pre-treated for the extraction, Epr. Alternatively, algae can be directly used without drying, by using the anaerobic fermentation. As extraction techniques, here the extraction with scCO_2 (Esc) or organic solvents (Eos) have been considered. The utilization of scCO_2 as solvent for the extraction appears quite interesting, as recovered carbon dioxide can be used, making the whole process solvent-free. Comparing the two extraction techniques, it comes out that the energy required for the sc technique is the compression of

CO_2 and heating to 40-50 °C. Therefore the thermal energy input is much lower than using the extraction with solvents. Moreover, by using organic solvents it comes out that the isolation of the oil at the end of the extraction, is much more energy requiring than using scf. In the latter case, it is enough to decompress the gas for isolating the oil. As the scf technique uses a continuous extraction apparatus with recovery of gas, this method appears to be characterized by a lower energy than the organic solvent extraction, and to be more environmentally friendly than the use of solvents. In order to be able to make a correct energetic balance, the extracted oil has been fully (over 96% of the components) characterized for its components. The energetic content has been estimated by using an equation that considers the nature of the components and their heat of combustion, so that the net energy produced by the oil can be calculated (Eq. 1).

$$\underline{\underline{\Delta}}H = 3500 + 650\,\Delta n + (a) \quad \text{kJ mol}^{-1} \qquad (1)$$

This value has been checked using a combustion bomb. The global balance of the process takes into account all the energy inputs and the produced energy. (Eq. 2)

(Eric)+Eb+Ers-Ets-Esa (Escr)-Ed (Ed')-Ec-Enu-Er-Eh-Ee-Epr-Esc(Eso)-Ees=Enet
(2)

Enet indicates the net energy recovered. In Equation 2 the first three terms represent the recovered energy, while others are spent energy. The first term is eventually the energy recovered from the hot flue gases that arrive to the algae pond may be very low. Eb is the energy associated to the solid residue (cellulose). Ets is the energy needed for transportation of the gas from the source, Esa is the energy for separation using monoethanolamine (Escr is the separation energy using the cryogenic technology), Ed is the energy of distribution of gas (Ed' is the energy of distribution in case of non separated flue gas). Ec is the energy of cultivation and other terms have the same meaning as in the text. Such contribution is not included in calculations.

General considerations and process data.

So far, all energetic quantities listed above have been collected. Moreover, data relevant to alternative processes for algae treatment have been gathered, these are reported below for a comparison of technologies. Micro-algae have growing costs much higher than macro-algae. In this study CO_2 is recovered using MEA, we assume that nutrients have not to be added, that the pond is at a maximum distance of 5 km from the source, that treated water from fish ponds is re-circulated to the fish pond. Algae from Jonian or Adriatic sea have been used.

The following balance is possible:
Biofuel energy 22-35 MJ/kg dw
Total energy produced 16-20 MJ/kg dw
Total energy spent for the production and harvesting 11-15 MJ/kg dw
Net energy recovered 5-9MJ/kg dw.
Comparison system
Such data can be compared with some literature data
Gasification of micro-algae: energetic input 10.48 MJ/kg dw; energy produced 17.77 MJ/kg dw; net energy 6.29 MJ/kg dw
Combustion of algae: 3.55 MJ/kg dw

The combustion is the technology that generates less energy, also if it is the most direct. Therefore, it looks like the cultivation of macro-algae for the production of biofuel is a technology that has to be taken into consideration for energy production and carbon recycling. Such data are only the first output and need revision and all steps need optimisation and an up-scaling of the process is necessary. For such study both a longer time and a higher investment are necessary. The treated aspects are very interesting if coupled with aquaculture activities that are very common in Italy.

Acknowledgement. Financial support by CNR, Project CNRC008EBF is gratefully acknowledged.

References

(1) Final Report, Project CNRC008EBF - CNR AGENZIA 2000.

FE/CO_2 FUEL CELLS FOR CO_2 CAPTURE AND SEQUESTRATION PLUS H_2 AND ELECTRICITY PRODUCTION

Greg H. Rau

Institute of Marine Sciences, University of California,
Santa Cruz, CA 95064
and
Energy and Environment Directorate, Lawrence Livermore National Laboratory, Livermore, CA 94550

Introduction

Satisfying an increasing global demand for energy while stabilizing the atmospheric CO_2 concentration may be the greatest societal and technological challenge of the 21rst century.[1] In this context a range of potential CO_2 capture/sequestration technologies have been proposed[2], yet their capacity, economics, practicality, and/or environmental impacts have thus far proven to be impediments to large-scale application. Because of their abundance and important role in the global carbon cycle, carbonates (inorganic compounds containing the -CO_3 moiety) have been studied as possible long-term storage forms for CO_2.[3] The conversion of CO_2 into solid carbonates via reactions such as: $XO + CO_2 \rightarrow XCO_3$ (X=divalent metal) present one such mechanism, but reaction rates with CO_2 are exceedingly slow unless additional energy (heat and/or pressure) is introduced. The conversion of metal oxides to hydroxides and subsequent reaction with CO_2 has also been considered, but the cost of chemically forming such hydroxides (rare in nature) appear to be prohibitive. Thus, despite their desirability as stable CO_2 reservoirs, cost and other factors have proven to be impediments to the formation of solid carbonates as a CO_2 capture/ sequestration strategy.

However, it has been recognized in the geologic CO_2 sequestration field (i.e., subterranean injection of CO_2) that certain geochemical conditions can exist where the formation of $FeCO_3$ would be favored and could provide a stable trap for CO_2 injected underground.[4] Also, the oxidation of iron metal in the presence of CO_2 is well known.[5,6] This proceeds by the reaction:

$$Fe^0 + 2CO_2 + 2H_2O \rightarrow Fe^{2+} + 2HCO_3^- + \uparrow H_2 \qquad (1)$$

which can further lead to the precipitation of a solid carbonate via pH elevation (e.g., removal of excess CO_2):

$$Fe^{2+} + 2HCO_3^- \rightarrow \downarrow FeCO_{3(s)} + \uparrow CO_{2(g)} + H_2O. \qquad (2)$$

The net reaction is then:

$$Fe^0 + CO_2 + H_2O \rightarrow \downarrow FeCO_{3(s)} + \uparrow H_2. \qquad (3)$$

Given the abundance of Fe in nature (globally, 4rth most abundant element) and as a waste metal (US scrap iron production = 10^7 tones/year, ref. 7), it is worth considering purposeful, aboveground iron carbonate formation as a CO_2 sequestration tool. Additionally two valuable by-products can be produced from reaction 1, electricity and hydrogen. Because 2 moles of electrons are transferred per mole of Fe reacted and H_2 formed, electricity could be made to flow between a reactive anode (Fe^0) and a non-reactive cathode (e.g. graphite); the anodic reaction being $Fe^o \rightarrow Fe^{2+} + 2e^-$ and the cathodic reaction being $2CO_2 + 2H_2O + 2e^- \rightarrow H_2 + 2HCO_3^-$. Assuming a conservative Fe reaction rate of 10^{-5} moles m^{-2} s^{-1}, a cell current density of 1.9 A m^{-2} is calculated. The cell potential of 0.44V leads to a power generation of 85kW per mole Fe reacted s^{-1}, or about 421 kWh_e per tonne Fe reacted hr^{-1}. Such energy production is confirmed by voltage and current densities generated in experimental iron corrosion studies (**Figure 1**).

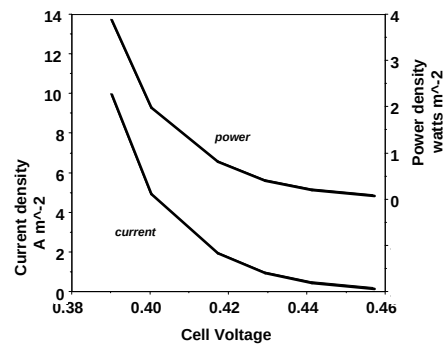

Figure 1. Trends in voltage vs current and power densities in a galvanic cell composed of an unalloyed steel anode in an oxygen-free electrolyte solution saturated with CO_2 at 298˚K (ref. 5).

Fuel Cell Scenarios, Issues, and Concerns

It is envisioned[8] that reaction 1 would occur in vessels or cells in which anodes produced from waste iron and cathodes composed of an appropriate conducting material (e.g., graphite) are submerged in a carbonic acid electrolyte formed by the continuous hydration of waste CO_2 with water. Hydrogen gas and electricity would be produced from such cells while the electrolyte would be continuously or sporadically bled off and the iron carbonates, $Fe(HCO_3)_2$ or $FeCO_3$, concentrated or removed. Possible fuel cell design considerations and operating procedures are further considered below.

The electrodes. Due to cost and the carbon intensity of production, scrap rather than new iron or steel would be preferred as anode material.[8] Waste car bodies might be appropriate given their relatively uniform size, metallurgical composition, and abundance.[9] However, the use of anti-corrosion coatings and non-Fe components in automobiles would require preparation of the scrap bodies via sanding, chemical treatments, or other processes, as well as forming the scrap into useable anodes. The cathodes need only be conductive to electricity and are not consumed in the fuel cell. However, the performance of the cathodes could degrade over time due to ancillary chemical reactions or fouling. The use of graphite is suggested here, but the performance and cost/benefit of using other materials need to be evaluated.

The electrolyte. The electrolyte would be formed by contacting waste CO_2 with water by bubbling the gas stream through the water, by spraying water in the gas stream, or by some other means that is energetically efficient and cost-effective in hydrating CO_2, thus forming a carbonic acid solution. This acid formation could occur within the fuel cell or upstream from it. The higher the CO_2 content in the gas the higher the equilibrium carbonic acid concentration in electrolyte and hence the higher reaction rates. It may be cost-effective to pressurize the gas stream or electrolyte head space in order to increase carbonic acid concentration, reaction rates, and hence the volume density of H_2 and electricity generation and CO_2 mitigation. The purity of the CO_2 waste gas stream could also be an issue, where contaminants such as SO_x, NO_x, heavy metals, etc., common in the gas effluent from coal and oil combustion, could interfere with (or enhance?) reactions 1-3. These contaminants could also affect the quality of the downstream H_2 and liquid and solid wastes from the fuel cell. Use of relatively clean CO_2 waste gas streams from natural gas combustion or gasification could avoid these potential problems. Waste gas from gasification/steam reforming plants and power generators would be especially attractive

because of its high CO_2 content and very low or no O_2, features that would depress electrolyte pH and Eh in equilibrium with such gas, thus maximizing Fe solubilization and minimizing the formation of iron oxides.

With at least 0.3 tonnes of H_2O consumed per tonne Fe reacted, the source, quality, and cost of water are issues for fuel cell operation. Sources of water might include municipal, industrial, or recycled supplies, provided that the contaminants or additives they contain, such as chlorine, do not impede reactions 1-3. On the other hand, the addition of chemicals to the electrolyte such as acids and salts (or use of seawater), known to increase Fe solubility and to reduce anode passivation by $FeCO_3$ deposition[5,6], might enhance fuel cell performance and prove cost effective.

Products, carbon sequestration, and waste streams. The H_2 generated at the cathode could be harvested and stored by employing conventional methods used in the production of H_2 via electrolysis. It is unknown what purity and concentration of H_2 might be achievable, and these issues could affect the end-use and marketability of the hydrogen.

The electricity produced per cell would be low-voltage direct current, requiring multiple cells in series as well as current inversion in order to conform to conventional electrical grid requirements of high voltage AC. An attainable cell power density of about 20 kW m^{-3} is crudely estimated based on that of possibly analogous Fe/air electrochemical cells (40 kW m^{-3}, ref. 10), reduced by 50% considering the likely volume and packing inefficiencies posed by the unconventional anode material proposed. Thus, a battery composed of a minimum of 250 cells in series, each 2 m x 2 m x 2 m (1000 m^2 total battery area) would be needed to generate 40,000 kW at 110 VDC. Inverting this to AC would probably reduce power output by some 20%. Also, varying the load or resistance across the electrodes could modulate the flow of electrons and thus reaction rates within the cells. In the extreme case, close-circuiting the electrodes would forego electricity use, but maximize $Fe(HCO_3)_2$ and H_2 production rates.

The sequestration of carbon could be achieved either through the formation of dissolved $Fe(HCO_3)_2$ (reaction 1), or dissolved or solid $FeCO_3$ (reaction 2). The former compound captures twice the carbon as does the later carbonate, thus doubling the sequestration benefit per tonne Fe reacted. A further sequestration benefit could result by disposing of the dissolved iron bicarbonate in certain areas of the ocean where photosynthesis and hence CO_2 conversion to biomass is Fe-limited. In such regions the tonnes of CO_2 sequestered per tonne Fe^{2+} added has been observed to exceed 20,000:1 (ref. 11), which if realized would dominate the economics of Fe/CO_2 fuel cell operation if a market/societal value of \$10/tonne CO_2 sequestered (or even if DOE's target of \$2.73/tonne, ref. 2) were in place.

Alternatively, spent electrolyte containing dissolved iron bicarbonate/carbonate could be injected/stored underground or the solid iron carbonate precipitated from it. The latter would occur spontaneously as the excess CO_2 in the solution degassed to the atmosphere, thus increasing the pH and saturating the solution with CO_3^{2-}. Once the $FeCO_3$ had been precipitated some care would be needed in storing this solid in order to avoid its slow oxidation via exposure to air and hence CO_2 loss. Conceivably, the carbonate would be precipitated from the electrolyte downstream from the fuel cell with the water recycled for further electrolyte use. The ultimate storage site for solid carbonates in the context of CO_2 sequestration could include abandoned mines or specially dug burial sites[3], or at the bottom of large water bodies containing low or no O_2 which presumably could preserve the iron carbonate indefinitely.

Economics

To calculate the net cost or income from Fe/CO_2 fuel cells, the following costs (per tonne Fe) were assumed[8]: scrap Fe=\$85, anode finishing=\$15, and other capital, operating and maintenance=\$35, for a total investment of \$135. Gross income would include: hydrogen=\$129, electricity=\$21, and carbon mitigation=\$13, with total income=\$163. This assumes the following product market values: \$3,600/tonne H_2, \$0.05/kWe, and \$10/tonne CO_2 avoided. A net income (total gross income – total costs) of \$28/tonne Fe reacted or \$34/tonne CO_2 mitigated is thus calculated. Such a profit estimate is, however, extremely uncertain given that the performance and operating requirements of Fe/CO_2 fuel cells in the preceding context have not been demonstrated. If accurate, a net profit of >\$30/tonne CO_2 mitigated is significantly better than DOE's 2008-2012 sequestration cost targets of \$2.73/tonne CO_2 for non-point-source methods and "...less than a 10% increase in the cost of energy services..." for direct capture and sequestration approaches.[2] This income could therefore provide an important economic incentive for sequestration, while at the same time generating H_2 and electricity free from new atmospheric CO_2 emissions.

Summary and Conclusions

Fe/CO_2 fuel cells pose several advantages over existing carbon mitigation strategies. They could provide a way of producing H_2 and electricity in a manner that consumes rather than generates CO_2, unlike current commercial methods. At the same time they convert waste CO_2 and iron metal into a relatively inert carbon-containing solute or solid that is amenable to verification, long-term storage, and monitoring, important objectives for any CO_2 sequestration strategy.[2] The estimated market value of the H_2 and electricity produced (>\$180/tonne CO_2) raises the possibility that this economic benefit could help drive the implementation of this process. However, such a profit motive for Fe/CO_2 fuel cell utilization critically hinges on accurately determining its capital and operating costs and the market value of the products produced. Is it possible that Fe/CO_2 fuel cells could provide a means of consuming part of industrial society's waste CO_2 and iron while generating "CO_2-free" H_2 and electricity, motivated by economics rather than or in addition to regulatory taxes/incentives?

References

(1) Hoffert, M. I.; Caldeira, K.; Benford, G.; Criswell, D. R.; Green, C.; Herzog, H.; Jain, A. K.; Kheshgi, H. S.; Lackner, K. S.; Lewis, J.S.; Lightfoot, H. D.; Manheimer, W.; Mankins, J. C.; Mauel, M. E.; Perkins, L. J.; Schlesinger, M. E.; Volk, T.; Wigley, T. M. L., *Science* **2002**, 298, 981-987.

(2) DOE. Carbon sequestration project portfolio FY 2002, U.S. DOE/NETL, Wash. D.C. http://www.netl.doe.gov/coalpower/sequestration/pubs/Carbon%20Sequestration%20Project%20Portfolio.pdf

(3) Lackner, K. S., *Ann. Rev. Energy Environ.*, **2002**, 27, 193-232.

(4) Gunter, W. D.; Perkins, E. H.; Hutcheon, I., *Appl. Geochem.*, **2000**, 15, 1085-1095.

(5) Hasenberg, L. In *Dechema Corrosion Handbook: Corrosive Agents and Their Interaction with Materials, Vol. 3*; Behrens, D., Ed.;, VCH: New York, 1988; pp. 159-209.

(6) Kermandi, M. B.; Morshed, A., *Corrosion*, **2003**, 59, 659-83.

(7) U.S. Geological Survey., Mineral commodity summaries – iron and steel scrap, http://minerals.usgs.gov/minerals/pubs/commodity/iron_&_steel_scrap/360303.pdf

(8) Rau, G. H., *Energy Convers. Manag.*, (in press).

(9) Dandapani, B.; Bockris, J.O'M., *J. Hydrogen Energy*, **1986**, 11, 101-105.

(10) Brodd, R. J., In *Handbook of Batteries and Fuel Cells*; Linden, D., Ed.; McGraw-Hill: New York, 1984; pp. 20.17-20.20.

(11) Buesseler, K. O.; Boyd, P. W., *Science*, **2003**, 300, 67-68.

VALUABLE AND STABLE CARBON CO-PRODUCT FROM FOSSIL FUEL EXHAUST SCRUBBING

Danny Day[1], Robert J. Evans[2], James W. Lee[3], and Don Reicosky[4]

[1]Eprida, Inc., 6300 Powers Ferry Road, Suite 307, Atlanta, GA 30339, danny.day@eprida.com
[2]National Renewable Energy Laboratory, 1617 Cole Blvd, Golden, CO, 80401, bob_evans@nrel.gov
[3]Oak Ridge National Laboratory, 4500N, A16, MS-6194, Oak Ridge, TN 37831, leejw@ornl.gov
[4]USDA-Agricultural Research Service, 803 Iowa Avenue, Morris, MN 56267 reicosky@morris.ars.usda.gov

Introduction: A Sustainable Carbon Sink With Hydrogen Production

The increasing anthropogenic CO_2 emissions and possible global warming have challenged the United States and other countries to find new and better ways to meet the world's increasing needs for energy while reducing greenhouse gas emissions. The need for sustainable energy with little greenhouse gas emissions has lead to demonstration work in the production of hydrogen from biomass through steam reforming of pyrolysis gas and pyrolysis liquids. Our research to date has demonstrated the ability to produce hydrogen from biomass under stable conditions.[1] Future large-scale renewable hydrogen production using non-oxidative technologies will generate co-products in the form of a solid sequestered carbon. This char and carbon ("C") material represent a form of sequestered C that decomposes extremely slow[2] and retains the bio-capture CO_2 for centuries. The limitation of the use of this form of carbon is a profit centric use. It was apparent that additional value needed to be added to this material that would justify large-scale handling and usage. In 1990s, C in the form of CO_2, accumulated at rates ranging from 1.9 to 6.0 Pg C/yr and increasing CO_2 levels by 0.9 to 2.8 ppm/yr. [3]. The volume of waste and unused biomass economically available in the United States is over 314 gigatons per year [4]. Sequestering a small percentage as valued added carbon could significantly reduce the atmospheric loading of CO_2 while simultaneously producing hydrogen. Normally hydrogen is referred to as a zero emissions fuel, however from life cycle perspective it can be viewed as a negative emissions fuel. In order to accomplish this economically, the sequestered C must have a very large and beneficial application such as a soil amendment and/or fertilizer.

The concept of utilizing charcoal as a soil amendment is not new. Man-made sites of charcoal rich soils intermingled with pottery shards and human artifacts have been identified covering 50,000 hectares of the Central Amazon rainforest each averaging 20ha and the largest at 350ha. [5] The radiocarbon dating of the sites have shown ages dating back 740–2,460 years BP[6] and 30% of the soil organic matter is made up of pyrolytic black carbon which is 35 times higher than the adjacent poorer quality soils (Oxisols) [7]. Most terra preta sites are identified by their thick black layers of soil (40-80cm) and some have been found in layers up to 2 meters thick[8]. These soils are so rich and fertile that they are dug up and sold as potting soil[9]. The current agricultural methods of the Kayapó (an ancient people with little European contact until the 19th century) has changed little and give evidence to the man-made techniques (slow burning fieldsand biomass) for creation of this fertile and sustainable method of agriculture which can be farmed intensively for up to 11 years . [10] This ability to farm soils without fertilization for many years is an anomaly in the rainforest. Despite the abundance of rainforest growth, their red and yellow soils are notoriously poor: weathered, highly acidic, and low in organic matter and essential nutrients.

Experimental Project Description The approach [11] in our research applies a pyrolysis process that has been developed to produce charcoal like by-product and synthetic gas (containing mainly H_2, and CO_2) from biomass, which could come from both farm and forestry sources. In this novel system [12], a portion of the hydrogen is used to create ammonia where economical, or ammonia is purchased leaving hydrogen for fuel utilization. The ammonia is then combined with the char, H_20 and CO_2, at atmospheric pressure and ambient temperature to form a nitrogen enriched char. The char materials produced in this process contains a significant amount of non-decomposable carbons such as the elementary carbons that can be stored in soil as sequestered C. Furthermore, the carbon in the char is in a partially activated state and is highly absorbent. Recent research has shown that lower temperature charcoal produced at 500°C adsorbed 95% of ammonia versus charcoal produced at 700°C and 1000°C which had higher surface areas but only adsorbed 40%[13]. Masada noted that acidic functional groups such as carboxyl were formed from lignin and cellulose at 400°C -500°C. [14,15]. Charcoals, regardless of biological source, were found to form acidic functional groups at these temperatures which will preferentially adsorb base compounds such as ammonia and that the chemical adsorption plays the primary role over surface area. This research points to the carbonization conditions as a key ingredient in optimizing a charcoal as a nutrient carrier and binding compound for ammonia. Thus when used as a carrier for nitrogen compounds (such as NH_4^+, urea or ammonium bicarbonate) and other plant nutrients, the char binding forms a slow-release fertilizer that is ideal for green plant growth. A combined NH_4HCO_3-char fertilizer is probably the best product that could maximally enhance sequestration of C into soils while providing slow-release nutrients for plant growth.

A flue gas scrubbing process [16,17] utilizing hydrated ammonia was tested in combination with a low temperature char. This approach utilized a chemical process, to directly capture greenhouse gas emissions at the smokestacks by converting CO_2, NO_x, and SO_x emissions into valued added fertilizers (mainly NH_4HCO_3, ~98% and $(NH_4)_2SO_4$ and NH_4NO_3, <2%). These fertilizers can potentially enhance crop growth for sequestration of CO_2 and reduce NO_3^- contamination of groundwater. As discussed above, the low temperature charcoal forms surface acid groups, which adsorbs and binds ammonia to the porous media for nucleation of CO_2. When used as a scrubbing agent with fossil fuel exhaust, a mechanically fluidized cyclone creates a fertilizer-matrix with a commercially acceptable amount of nitrogen and a high percentage of very stable C. In addition, the inorganic carbon component (HCO_3^-) of the NH_4HCO_3 fertilizer is non-digestible to soil bacteria and thus can potentially be stored in certain soil (pH > 7.9) and subsoil terrains as even more sequestered C. This community-based solution operates as a closed loop process, integrating C sequestration, pollutant removal, fertilizer production, increased crop productivity and restoration of topsoil through the return of carbon and trace minerals. The benefits of producing a value added sequestering co-product from coal fired power plants and other fossil energy producing operations, can help bridge the transitions to clean energy systems that are in harmony with the earth's ecosystem. [18] An important benefit of this approach to the power industry is that it does not require compressors or prior separation of the CO_2. The use of biomass in combination with fossil energy production, can allow agriculture, and the agrochemical industry infrastructure to assume a more holistic relationship of mutual support in helping each meet Kyoto greenhouse gas reduction targets.

The char component of the material acts to provide the same benefits as in terra preta sites reducing the leaching of soluble nutrients.[19] This increases plant growth, nutrient uptake and reduces nitrogen runoff. One experimental goal of the project was to identify

process parameters that would produce a carbon material optimized for agricultural use. Since it has been shown that the that charcoal addition from 2000 years ago is still providing significant soil fertility benefits [20] and farmers report up to three times crop yields over immediately adjacent non-terra preta soils. Recent research, conducted by Steiner, on the addition of charcoal to non terra preta soils [21] showed significant crop yield increases.

Charcoal has been found to support microbial communities [22] even greater than activated carbon (which is charcoal processed at higher temperatures with steam). Prior researchers assumed that the porous structure provided safe haven but we propose that it may be the availability of microbial nutrients. The processes of pyrolysis create an intrapore deposition of organic polycondensates[23].The deposition of these materials may increase microbial activity. [24]

Experimental Set-up and Results: SEM Investigation of a Low Temperature Char

The low temperature char particles are hydrophobic in nature and grind easily. The internal gases that escape from the material during the charring help develop charcoals natural porosity. The evolution of this adsorbent material provides a porous internal structure as well. We selected 400 ^{o}C as the target temperature for the char before being discharged from the pyrolysis reactor. The resulting char was cooled for 24 hours then fed through a two-roll crusher and then sieved with a mechanized screen through 30 mesh and 45 mesh screens. The resulting fraction remaining above the smaller screen was chosen as our starting material.

Experimental Set-up & Results: SEM Investigation of an Enriched Carbon, Organic Slow-release Sequestering (ECOSS) Fertilizer

Bench scale demonstrations by Oak Ridge National Laboratory recently demonstrated the removal of flue-gas CO_2 via formation of solid NH_4HCO_3 through ammonia carbonation in the gas phase. [25] The results indicated that it is possible to use NH_3+ H_2O+CO_2 solidifying process in gas phase to remove greenhouse-gas emissions from industrial facilities such as a coal-fired power plant. A study of agriculturally optimized charcoal produced by Eprida were combined with the above process created via the sequestration of a CO2 stream. It was proposed that the char could act as a catalyst (providing more effective nucleation sites) to speed up the formation of solid NH_4HCO_3 particles and enhance the efficiency of the gas phase process. A pilot demonstration was constructed to evaluate production and material characteristics of the NH_4HCO_3-char product. The process also showed promise that it could remove SOx and NOx, enhance sequestration of carbon into soils; providing an ideal "Enriched Carbon, Organic Slow-release Sequestering" ("ECOSS") fertilizer and nutrient carrier for plant growth. The value would be enhanced if the production of NH_4HCO_3 could be developed inside the porous carbon media.

To test the production of a charcoal- NH_4HCO_3 fertilizer, we used a mechanical fluidized cyclone, easily adaptable to any gas stream and injected CO_2, and hydrated ammonia. A 250g charge of 30-45 mesh 400 ^{o}C char was fed in at regular intervals varying from 15-30 minutes. A higher rotor speed increased the fluidization and suspended the particles until they became too heavy from the deposition of NH_4HCO_3 to be supported by fluidized gas flows.

SEM Investigation of the Interior of an ECOSS-15 Char Particle

The material produced was evaluated by scanning electron microscopy. The examinations revealed The very small molecules of $NH_3.H_2O$ (hydrated ammonia) are adsorbed into the char fractures and internal cavities. As CO_2 enters, it converts the $NH_3.H_2O$ into the solid NH_4HCO_3, trapping it inside the microporous material. The SEM's of the original char and the resulting product clearly evidenced the intra-pore development of the fibrous NH_4HCO_3 inside the carbon-charcoal framework. The material accumulated as internal flat-top volcano like structures. This demonstration of the process showed that we can deposit nutrients inside the porous media using a low cost gas phase application. We analyzed the required amounts of hydrogen, reformed from biomass, which would be required as ammonia and calculated that 31.6% of the H_2 would be necessary for ECOSS production leaving (using all charcoal available from the process) leaving 68.4% of the hydrogen for use as a fuel.

The amount of C, directly converted from exhaust CO_2 is equal to 15.2% of the total sequestered carbon as a ammonium bicarbonate and for each 100kg of biomass, we will produce a total of 28.3kg of utilized carbon. In acid soils, this part of the carbon will convert to CO_2 but in alkaline soils, (pH>8) it will mineralize and remain stable. According to USDA reports, 60-70% of worldwide farmland is alkaline, so conservatively allowing for 50% of the bicarbonate to convert to CO_2, this will leave us with approximately 25 kg of stable carbon in our soils for each 100kg of biomass processed. This carbon represents 91.5 kg of CO_2 of which 88% is stored as a very beneficial and stable charcoal. A different way to look at this is to compare the amount of energy produced and the resulting CO_2 impact. With 6.78 kg hydrogen extra produced per 100 kg of biomass, then 25/6.78 = 3.69 kg C/ kg H or 3.66x3.69=13.5 kg CO_2 / kg of hydrogen produced and used for energy. From a power perspective, that is 13.5kg CO_2 / 120,000 KJ of hydrogen consumed as a renewable energy or 112 kg/GJ of utilized and stored CO_2.

Global Potential

The large majority of increases in CO_2 will come from developing countries and a sustainable technology needs to be able to scale to meet the growing population needs. The second point is that The energy from a total systems point of view could create a viable pathway to carbon negative energy as detailed in the IIASA focus on Bioenergy Utilization with CO_2 Capture and Sequestration (BECS) [26]. The effects (i.e. providing 112kg of CO_2 removal for each GJ of energy used) could allow major manufacturers to offset their carbon costs. For a quick test of reasonableness, if we take the atmospheric rise of 6.1GT and divide by 112kg/Gj = 54.5EJ. This number falls amazingly along the 55EJ estimate of the current amount of biomass that is used for energy in the world today. [27] While the potential reaches many times this for the future utilization of biomass, this shows that there is a chance that we can be proactive in our approach. Economic projections of a study based on the ORNL process were compared to this process. Equivalent 20% CO_2 reductions and credits needed to return a 33% ROI was estimated to cost $46 million for a 700MW facility utilizing purchased ammonia. However, if the market for nitrogen were an upper limit, and renewable hydrogen were used for producing the worlds ammonia, and all the world's N fertilizer requirements were met from NH_4HCO_3 scrubbed from power plant exhaust, then the total carbon capture at (1999 N levels) then coal combustion CO_2 could be reduced by ~39.9%. The factors of increased biomass growth with the addition of charcoal as found by Mann[28], Hoshi[29], Glaser[30], Nishio[31], and Ogawa[32] show increase biomass growth from 17% to as 280% with non-optimized char. The direct utilization of an optimized char plus slow release nitrogen/nutrients may allow the increase biomass growth targets worldwide. A portion of this increased biomass growth will be converted to soil organic matter, further increasing C capture (especially if no-till management practices are adopted).

The ability to slow down the release of ammonia in the soil will allow plants to increase their uptake of nitrogen. This will lead to a reduction in NO_2 atmospheric release. For each ton of nitrogen produced, 0.32 tons of C are released, and the 80.95 million tons of nitrogen utilized would represent 26 million tons of C. This is a small a small number in relative terms to the amounts released by combustion of coal (2427 million tons) [33], however if we assume [34] 1.25% of our nitrogen fertilizer escapes into the atmosphere as N_2O,

then 1.923 million tons of N_2O are released, with an CO_2 equivalence of 595.9 million tons or 162.5 million tons of C equivalent.

The economics of hydrogen from biomass has been addressed in the 2001 report by Spath[35]. Our analysis shows that inside plant use of renewable hydrogen would no longer be 2.4-2.8 times the costs from methane, but is approaching 1.6-1.9 times with the increase in natural gas prices. Since market price of nitrogen increases with natural gas prices and this process shows intra plant usage of renewable hydrogen (i.e. no storage or transport expense) becomes significantly more competitive at our current natural gas prices. A review of traditional ammonia processing, shows that due to unfavorable equilibrium conditions inherent in NH_3 conversion, only 20-30% of the hydrogen is converted in a single pass. We determined that the ECOSS process could only utilize 31.6% of the hydrogen as we were limited by the total amount of char produced and the target 10% nitrogen loading. This means that a single pass NH_3 converter could be used and the expense of separating and recycling unconverted hydrogen is eliminated. The 68.4% hydrogen is then available for sale or use by the power company/fertilizer partnership. This last bracket shows that the ECOSS process thus favors the inefficiencies of ammonia production and reduces costs inherent in trying to achieve high conversion rates of hydrogen.

Conclusions

This concept of biomass energy production with agricultural charcoal utilization may open the door to millions of tons of CO_2 being removed from industrial emissions while utilizing captured C to restore valuable soil carbon content. This process simultaneously produces a zero emissions fuel that can be used to operate farm machinery and provide electricity for rural users, agricultural irrigation pumps, and rural industrial parks. The use of value added carbon while producing hydrogen (or energy) from biomass can lead to energy with an associated carbon credit (ie negative carbon energy). With this development non-renewable of carbon dioxide producers can work with agricultural communities to play a significant part in reducing greenhouse gas emissions while building sustainable economic development programs for agricultural areas in the industrialized and economically developing societies.

Acknowledgements: Kim Magrini, Stefan Czernik, Bob Evans and Calvin Fiek and Don Reicosky and James Lee who have been seeking solutions to our CO2 buildup. Thanks to Nigel Smith, Bruno Glaser, Christoph Steiner, Johannes Lehman, Bill Woods, Bill Denevan and Susanna Hecht who has taught us with the history of terra preta and finally Michael Obersteiner for his encouragement.

References

(1) Day, D., Activities web report of a 100 hour production run of hydrogen from biomass in Blakely, GA, USA; **2002** http://www.eprida.com/hydro/

(2) Gavin, D.G., Brubaker, L.B., and Lertzman, K.P. Holocene fire history of a coastal temperate rain forest based on soil charcoal radiocarbon dates. In press for Ecology: **2003**

(3) IPCC, "Climate change 2001: the scientific basis", Intergovernmental Panel on Climate Change, **2001** (see also at http://www.grida.no/climate/ipcc_tar/wg1/index.htm.)

(4) Walsh, Marie et al., Biomass Feedstock Availability in the United States: 1999 State Level Analysis, **1999** http://bioenergy.ornl.gov/resourcedata/index.html

(5) Glaser et.al, The 'Terra Preta' phenomenon: a model for sustainable agriculture in the humid tropics, Naturwissenschaften **2001**, 88: 37–41

(6) Saldarriaga JG, West DC, Holocene fires in the northern Amazon basin. Quat Res **1986**, 26: 358–366

(7) Glaser, et. al., Black Carbon in the Terra Preta Soils of the Brazilian Amazon Region, Proceedings 9th Annual V.M.Goldschmidt Conference, Cambridge, MA **1999**, #7391

(8) Smith NJH, Anthrosols and human carrying capacity in Amazonia. Ann Assoc Am Geogr **1980**, 70: 553–566

(9) Mann, C., The Real Dirt on Rainforest Fertility, Science **2002**; 297:920-923

(10) Hecht, S and D. Posey. "Preliminary Results on Soil Management Techniques of the Kayapó Indians." Advances in Economic Botany **1989**, 7: 174-188.

(11) Y. Yeboah,et al., Hydrogen from Biomass for Urban Transportation, Proceedings of the **2002** US DOE Hydrogen Program Review

(12) Day, Danny; Robert Evans, James Lee U.S. Patent Application, **2002**

(13) Asada, T. et al, Science of Bamboo Charcoal: Study on Carbonizing Temperature of Bamboo Charcoal and Removal Capability of Harmful Gases, Journal of Health Science **2002**, 48(6) 473-479

(14) Matsui, T. et al, Preparation and Analysis of Carbonization Products from Sgi, Cryptomra japonica D. Don) Wood. Nippon Kagakukaishi **2000**; 1:53-61 (Japanese)

(15) Nishimaya, K. et al., Analysis of Chemical Structure of Wood Cjrcoal by X-ray photoelectron spectroscopy **1998**, Journal of Wood Science,44, 56-61

(16) Lee, J. W.; Li, R., A Novel Strategy for CO2 Sequestration and Clean Air Protection, Proceedings of First National Conference on Carbon Sequestration, Washington, DC, May 14,17, **2001**. http://www.netl.doe.gov/publications/proceedings/01/carbon_seq/p12.pdf

(17) Lee, J. W.; Li, R, Method for Reducing CO2, CO, NOx, and SOx Emissions, 1998 Oak Ridge National Laboratory Invention Disclosure, ERID 0631; **2002** U.S. Patent No. US 6,447,437 B1.

(18) Lee, J. W., and R. Li, Integration of Coal-Fired Energy Systems with CO2 Sequestration through NH4HCO3 Production, Energy Conversion Management **2003**; 44: 1535-1546.

(19) Schleppi P., Bucher-Wallin I., Siegwolf R., Saurer M., Muller N. & Bucher J.B., Simulation of increased nitrogen deposition to a montane forest ecosystem: partitioning of the added N; Water Air Soil Pollution **1999**; 116: 129-134

(20) Glaser B., Lehmann J., Zech W. Ameliorating physical and chemical properties of highly weathered soils in the tropics with charcoal – a review. Biology and Fertility of Soils **2002**; 35: 219-230.

(21) Wardle, D. A. et al., The charcoal effect in Boreal forests: mechanisms and ecological consequences**,** Oecologia **1998**; Volume 115 Issue 3: 419-426

(22) Pietikäinen, Janna, Soil microbes in boreal forest humus after fire (thesis **1999**) http://ethesis.helsinki.fi/julkaisut/maa/mekol/vk/pietikainen/soilmicr.html

(23) Runkel, R.O.H and Wilke, K, Chemical composition and properties of wood heated at 140C to 200C in a closed system without free space. Part II Holz als Roh und Werkstoff **1951**; 9: 260-270 (Ger.)

(24) Godsy, E. Michael, Impact of Human Activity on Groundwater Dynamics (Proceedings of a symposium held during the Sixth IAHS Scientific Assembly at Maastricht, The Netherlands, July 2001). IAHS Publication no. 269, **2001**, pp. 303–309.

(25) Li, E. Hagaman, et al., "Removal of carbon dioxide from flue gas by ammonia carbonation in the gas phase," Energy & Fuels **2003**; 17: 69-74.

(26) Oberstiener, et al., Biomass Energy, Carbon Removal and Permanent Sequestration - A 'Real Option' for Managing Climate Risk, Report no. IR-02-042, Laxenburg, Austria: International Institute for Applied Systems Analysis, **2002**.

(27) Hall, D.O., F. Rossillo-Calle, R.H. Williams and J. Woods,: Biomass for energy: Supply prospects. In: Renewable Energy: Sources for Fuel and Electricity [Johansson, T.B., H. Kelly, A.K.N. Reddy, and R.H. Williams (eds.)]. Island Press, Washington, D.C., **1993**:593-652
(28) Mann, C., The Real Dirt on Rainforest Fertility, Science **2002**; 297:920-923
(29) Hoshi, T. (web report of growth studies with charcoal amendments on green tea yields) **2002** http://www.fb.u-tokai.ac.jp/WWW/hoshi/cha
(30) Glaser, et.al, Potential of Pyrolyzed Organic Matter in Soil Amelioration, 12th ISCO Conference, China, **2002**; 3:421
(31) Nishio, M., Microbial Fertilizers in Japan, Bulletin by National Institute of Agro-Environmental Sciences, Japan, **1999**
(32) Ogawa, M., Effect of charcoal on the root nodule and VA mycorrhizal formation of soybean, Proceedings of the Third Inter-national Mycology Congress, Tokyo, Ja-pan, **1983**: 578
(33) World Carbon Dioxide Emissions from the Consumption of Coal, 1992-2001 http://www.eia.doe.gov/emeu/iea/tableh4.html
(34) Mosier, et.al, Closing the Global N2O budget: Nitrous Oxide Emissions through the Agricultural Nitrogen Cycle, Nutrient Cycling and in Agro Ecosystems **1998**, 52: 223-245
(35) Spath, et al, Update of Hydrogen from Biomass -Determination of the Delivered Cost of Hydrogen, National Renewable Energy Laboratory, Milestone Report for the U.S. Department of Energy's Hydrogen Program **2001**, United States

AN INTEGRATED APPROACH TO THE SYNTHESIS OF ORGANIC CARBONATES: DISCOVERY OF NEW CATALYSTS

Michele Aresta, Angela Dibenedetto and Carlo Pastore

Department of Chemistry, University of Bari
Campus Universitario – 70126 Bari - Italy

Introduction

Molecular organic carbonates are versatile compounds used as solvents or reagents in the chemical industry, or as additives to fuels.[1] The latter application and their use as monomers for polymers may expand in the near future, causing a large increase of their demand on the world market. As the current synthetic technology is represented by the use of phosgene (that is banned in several countries) as building block, the development of new synthetic methodologies for organic carbonates is receiving much attention worldwide. The replacement of such toxic raw material with carbon dioxide seems to be very attractive and interesting. In fact, it responds to the "green chemistry" principles by using clean and safe technologies, also implementing the atom-economy strategy. Moreover, the utilization of carbon dioxide represents a way of carbon-recycling, saving natural resources.

In this paper we describe a pool of CO_2-based "convergent synthetic technologies" such as the direct oxidative carboxylation of olefins, the carboxylation of epoxides, the direct carboxylation of alcohols, the alcoholysis of urea coupled with the trans-esterification reaction for the synthesis of organic carbonates, either linear or cyclic. The reactivity of Group 5 (V, Nb, Ta) element compounds, used as catalysts in these reactions, will be discussed and a comparison of their reactivity will be made.

Our goal, besides demonstrating the effectiveness and the benefits of networking such reactions, is the identification of a metal that may provide selective catalysts per each of the routes **a**-**g** in Scheme 1 or better, the development of a many-purpose catalyst that may drive several reactions.

Results and Discussion

Scheme 1 represents the pool of convergent synthetic methodologies for the preparation of either linear **(1)** or cyclic **(2)** carbonates, and the **(1) = (2)** inter-conversion, through the trans-esterification reaction. All synthetic routes respond to the "green chemistry principles" and use safe reagents and operative conditions.

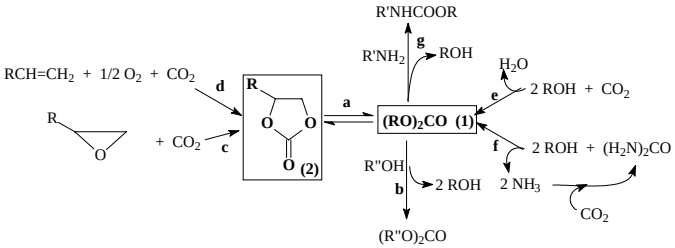

Scheme 1. Convergent methodologies for the synthesis of linear (**1**) and cyclic (**2**) carbonates

Since long, our research group is involved in the use of Nb-compounds as catalysts for the synthesis of organic cyclic carbonates. We have reported[2] that Nb_2O_5 is an active catalyst in the direct oxidative carboxylation of olefins (Eq. 1) and extensively discussed the role of the temperature and solvent on the conversion yield and selectivity.

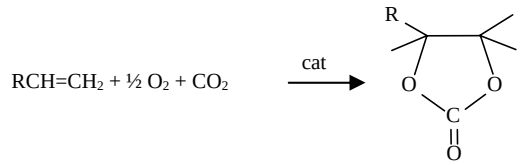

(1)

We have shown that dimethylformamide (DMF) or dimethylacetamide (DMA) are good solvents for such reaction and that heterogeneous catalysts have a longer life-time than homogeneous ones[3] under the same operative conditions. The oxidative carboxy lation of olefins can be split into two reactions, namely the epoxidation of olefins using dioxygen, that is a quite interesting process *per se*, and the carboxylation of the resulting epoxides. The reaction conditions strongly influence the yield and selectivity of the whole process. The nature of the solvent plays a key role in the carboxylation of epoxides, a reaction that is promoted by amides[4] like DMF or DMA that alone are able to carboxylate the epoxides. Conversely, in solvents like aromatics and ethers the reaction does not occur or takes place at a limited extent also in presence of heterogeneous metal systems under the same operative conditions. These findings justify the use of DMF as solvent in the oxidative carboxylation of olefins. The importance of such synthetic approaches (routes **c** and **d** in Scheme 1) results much better if one considers that their coupling to the trans-esterification reaction (route **a** in Scheme 1) may make the oxidative carboxylation of olefins or the carboxylation of epoxides a new approach for the synthesis of both linear and cyclic carbonates.

We have clearly demonstrated the efficacy of Nb(V) and Nb(IV) compounds as catalysts for the conversion of epoxides into the relevant carbonates (Eq. 2) with a selectivity >99%. Also, we have

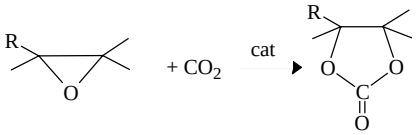

(2)

shown that Nb(V)-oxide is an active catalyst for the carboxylation of pure enantiomers of chiral epoxides with total retention of the configuration.[5] Additionally, Nb(IV) complexes with optically active ligands promote the carboxylation of racemic mixtures of styrene- or propene-oxide with an interesting enantiomeric excess.[5]

Interestingly, we have found that Nb(V) compounds are also active catalysts for the trans-esterification reaction (TER). We have used either $Nb(OR)_5$ compounds or Nb(V)-oxide[6] with interesting conversion yields and 100% selectivity (see below).

Besides such reactions, we have investigated new routes to linear carbonates,[7a] such as the direct carboxylation of alcohols[8] (Eq. 3, or route **e** in Scheme 1) and the reaction of urea with alcohols[9] (Eq. 4 or route **f** in Scheme 1). Also in this case Nb(V) compounds are good catalysts. In particular, $Nb(OR)_5$ (R=Me, Et, allyl) show an interesting activity for the carboxylation of alcohols[8] (Eq. 3), and Nb_2O_5 is active in the alcoholysis of urea[9] (Eq. 4).

$$2\ ROH + CO_2 \longrightarrow (RO)_2CO + H_2O \qquad (3)$$

$$2\ ROH + (H_2N)_2CO \longrightarrow RO)_2CO + 2\ NH_3 \qquad (4)$$

In the carboxylation of alcohols, $Nb(OR)_4(OCOOR)$, generated in the reaction of $Nb(OR)_5$ with CO_2, is the active catalytic species. Although such reaction suffers of thermodynamic limitations, the catalyst can be recovered and used several times as shown in Figure 1, improving the total turnover number.

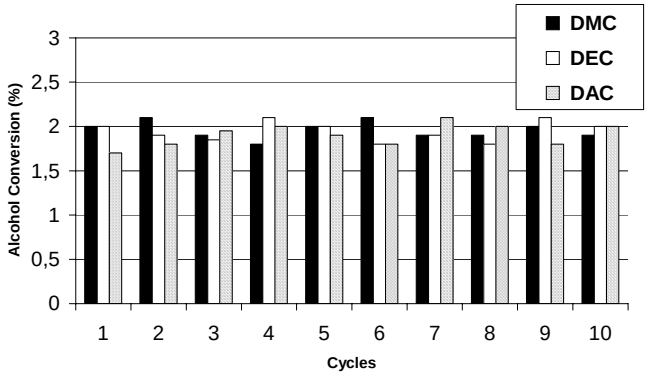

Figure 1. Stability of the $Nb(OR)_5$ catalysts (R= Me, Et, allyl) over ten runs in the carboxylation of the relevant alcohols.

Besides such reaction, $Nb(OR)_5$ has been shown to play a catalytic role also in the trans-esterification reaction (TER) that promotes the inter-conversion of carbonates, as depicted in Scheme 1, route **a**. Conversely, Nb_2O_5 that promotes the carboxylation of epoxides and the oxidative carboxylation of olefins, is also an active catalyst for the alcoholysis of urea and the TER. However, it is possible to utilize a class of catalysts derived from a single element for the synthesis of a wide range of linear and cyclic carbonates by using a sequence of reactions not based on the use of phosgene.

For the trans-esterification reaction, we have also tested several compounds of V and Ta in the oxidation state five, and compared their efficiency to the Nb-systems and to other catalysts (TiO_2) reported in the literature. In such reactions, we have used three classes of compounds, namely pentalkoxo- [$M(OR)_5$, M = Nb or Ta] and oxo-trialkoxo-metal complexes [$MO(OR)_3$, M = Nb, V] (Fig. 2), or metal-oxides [Nb_2O_5, Nb_2O_4, Nb_2O_3, NbO, V_2O_5, V_2O_4, V_2O_3] (Fig. 3).

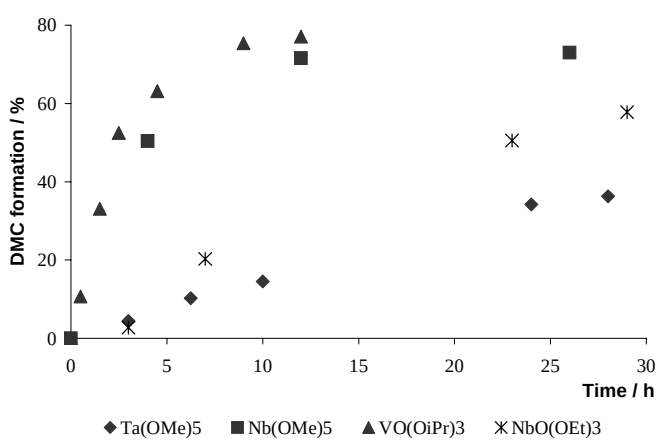

Figure 2. Activity of several Group 5 element alkoxides- or oxo-alkoxides as transesterification (EC→ DMC) catalysts

Ethylene carbonate (EC) was selected as the cyclic carbonate, due to the fact that it can be effectively synthesized from the relevant epoxide and CO_2 using several catalysts, including Nb_2O_5 under heterogeneous conditions, or Nb(IV)- and Nb(V)-complexes as homogeneous catalysts.

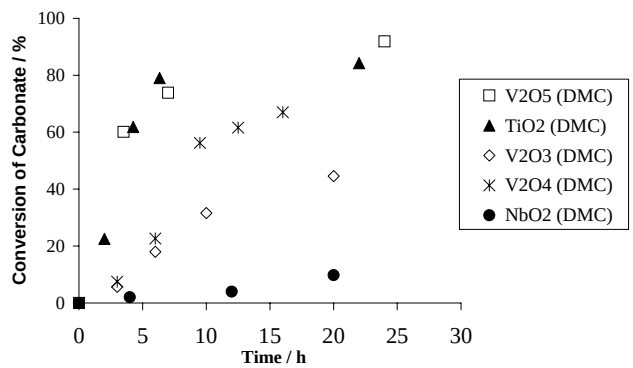

Figure 3: Activity of Group 5 metal oxides as trans-esterification catalysts.

Satisfactory results have been obtained using several of the Group 5 element catalysts in the trans-esterification of ethylene carbonate with MeOH, EtOH or allyl-OH, as shown in Figg. 2 and 3.

In particular, V_2O_5 has shown a higher efficiency, over the long reaction time, than TiO_2 that is used in industrial applications. (Fig. 3)

Conclusions

The network of reactions represented in Scheme 1 has been shown to be fully operative. Using Group 5 element compounds as catalysts it has been possible to develop new synthetic approaches to both linear and cyclic carbonates. The same compounds are good trans-esterification catalysts. Therefore, Group 5 element derivatives represent a class of compounds with a multipurpose application in catalytic processes relevant to CO_2 utilization.

Acknowledgments. We gratefully acknowledge the financial support by MIUR Project 2003039774 and the experimental assistance provided by Ms Olga Burova and Cira Devita.

References

(1) Carbon Dioxide Recovery and Utilization, Aresta, M. Ed., Kluwer Academic Publishers, London **2003**.
(2) Aresta, M.; Dibenedetto, A. *J. Mol. Catal. A: Chemical* **2002**, *182-183*, 399.
(3) Aresta, M.; Dibenedetto, A.; Tommasi, I. *Eur. J. Inorg. Chem.* **2001,** 1801-1806.
(4) Aresta, M.; Dibenedetto, A.; Gianfrate, L.; Pastore C. *J. Mol. Catal. A: Chemical*, **2003**. *204-205*, 245
(5) Aresta, M.; Dibenedetto, A.; Gianfrate, L.; Pastore C. *Appl. Catal.* **2003**. in press.
(6) Aresta, M.; Dibenedetto, A.; Pastore, C. *Studies in Surface Science and Catalysis*, **2003**, in press.
(7) Aresta, M.; Dibenedetto, A.;. Pastore, C. *XXI Congresso Nazionale della Società Chimica Italiana*, Torino, June 22-27, **2003**, IN CO 031; b) Choi, J.C.; Sakakura, T.; Sako, T. *J. Am. Chem. Soc.* **1999**, *121*, 3793; c) Ballivet-Tkatchenko, D.; Douteau, O.; Stutzmann, S. *Organometallics* **2000**, *19*, 4563.
(8) Aresta, M.; Dibenedetto, A.; Pastore, C. *Inorg. Chem.*, **2003**, *42*, 10, 3256.
(9) Aresta, M.; Dibenedetto, A.; Devita, C.; Bourova, O.; Chapukin, O.N. *Studies in Surface Science and Catalysis*, **2003**, in press.

Studies of Direct Carbonylation of Methane on Silica-Supported Transition Metal Catalysts

Lin-Hua Song Zi-Feng Yan, Shi-Kong Shen

Department of Chemical Engineering, University of Petroleum, Dongying 257062, Shandong, P. R. China

Introduction

A considerable effort has been made in the past decade to convert the cheap raw materials ---- methane into more valuable compounds[1,2]. Methane is thermodynamically stable and its activation and transformation pose a great challenge to homogeneous and heterogeneous catalysis. Among various processes the oxidative coupling of methane is of considerable interest because it can produce C_2 compounds in one step. Direct carbonylation of methane to form ethanal and ethanol is a very attractive route for the effective utilization of methane. This reaction is also thermodynamically not allowed in one reaction step, due to the positive change in Gibbs free energy (+18.90 kcal/mol at 500K). This thermodynamic limitation makes it impractical till now. Here we report the new method to achieve the direct carbonylation of methane on silica-supported transition metals.

Experimental

The catalysts were prepared by ion-exchanging the silica support with solutions of transiition metals to yield a nominal 5 wt% metal. The following solution of salts of transition metals were used: $[Fe(NH_3)_6^{3+}$、$Co(NH_3)_6^{3+}$、$Ni(NH_3)_4^{2+}$、$Pd(NH_3)_4^{2+}$ and $Pt(NH_3)_4^{2+}]$.

For each experiment 300mg of the catalyst were placed in the micro-reactor and was reduced in - situ at 723K. Methane decomposition was performed from a flow of 10ml/min of methane. Each of pulses of 0.3ml of CO syn-gas (95% CO + 5% H_2) in a flow of 20ml/min of helium at temperature programmed conditions and at constant temperature conditions was given at each of temperature interval (50K) and at each of time interval (10mins) respectively. Product analysis was performed on line with an ion-trap detector (Finnigan - MAT 700).

Results and Discussion

The direct carbonylation of methane is thermodynamically not allowed in one reaction step, due to the positive change in Gibbs free energy (+18.90 kcal/mol at 500K). A important approach is to split the overall reaction into two reaction steps occurring under different conditions.

$$CH_4 + CO \rightarrow CH_3CHO \quad (1)$$
$$CH_4 \rightarrow CHx + (4\text{-}x)\,H \quad (2)$$
$$CHx + CO + (4\text{-}x)\,H \rightarrow CH_3CHO \quad (3)$$

In such a two-step route the thermodynamic limitation might be overcome. The decomposition of methane (2) is endothermal $\triangle H > O$ $\triangle H^0_s = +96.08$kcal/mol) while the change in entropy is positive $\triangle S > O$ ($\triangle S^0_s = +29.25$cal/mol). The direct carbonylation of CHx (x = 0-3) species to form ethanal and ethanol (3) is exothermic $\triangle H < 0$ (For gas phase reaction under standard conditions, $\triangle H^0_s = -100.26$ kcal/mol) and the change in entropy is negative $\triangle S < 0$ ($\triangle S^0_s = -57.92$ cal/mol). Therefore, the overall reaction could be occurred under certain moderate temperature, where $\triangle G_T < 0$. Practically, the activation of methane[3] and H_2-D_2 exchange reaction[4] of methane on metal surface indicate that the reaction (2) can occur under moderate temperatures. The reaction (3) was extensively studied in the formation of aldehyde and alcohol in the Fischer-Tropsch reaction[5].

Figure 1. CO pulses at different temperature on saturately adsorbed methane on 5wt% Pd/SiO_2 catalyst at 423K

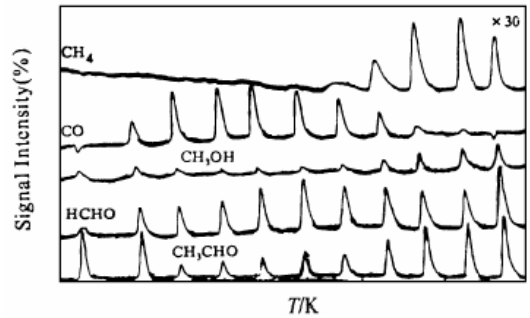

Fig.1 shows that the optimum temperature of carbonylation of CHx(ad) (x < 3) species lies in the range of 523-723K on cobalt. It is interesting that this temperature range is coincident with the range of dissociative adsorption of methane. It means that the two step reactions of the direct carbonylation of methane can be performed at the same temperature. Platinum (Fig.2) exhibits the similar behavior with cobalt, but less activity than cobalt.

Figure 2. TPSR speat ra of methane in H_2 st reem on freah 6w t% Pd/SiO_2 catalyst at different adsorption temperature of methane
a) T = 300K (b) T = 423K (c) T = 523K; (d) T = 673K;

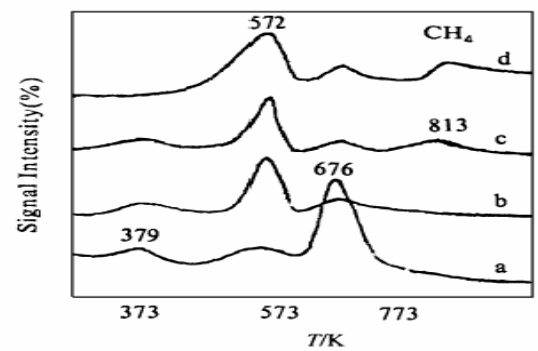

Fig.1 to Fig.3 shows that the catalytic performance and product distribution depends sensitively on the nature of metals and the variance of the reaction conditions, especially the temperature of carbonylation. The result of blank experiment illustrates that no ethanal and ethanol were formed on the silica support under the same reaction conditions. In contrast to cobalt, Fig. 3 illustrates that optimum temperature range of the carbonylation of CHx(ad) species on palladium is enlarged to 823K and that the conversion of the carbonylation is reversely increased along with the increasing of the temperature. TPSR results of adsorbed methane on palladium and Fig.3 show that the hydrogenation to methane and carbonylation of CHx(ad) species formed by the decomposition of methane are the competitive reactions, especially on the H(ad)-enriched metal surface. The interaction of H(ad) with adsorbed surface species results in the formation of hydrogenated products (such as CH_4, CH_3CH_2OH and CH_3OH). Large amounts of H(ad) may be originated from the migration of H(ad) in the subsurface and

bulk phase to surface with the increasing of the temperature. Similar TPPR results of carbonylation of methane on other metals indicated that palladium and nickel catalysts favor the direct carbonylation of methane.

Figure 3. CO pulses at different temperature on saturatelv CH_4 adsorbed 5wt% Pd/SiO_2 catalyst at 573K.

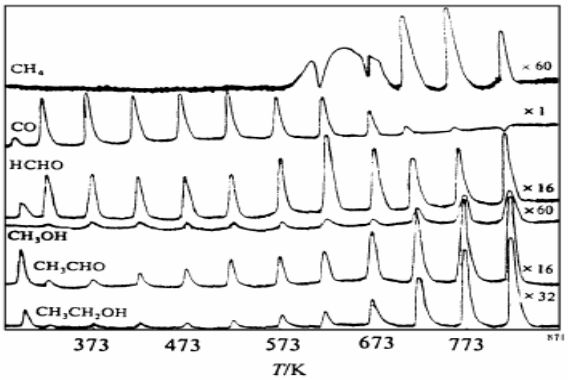

Fig.4 shows that the involvement of H(ad) acts as an important role in the formation of HCHO and ethanol and that adsorbed CO is also the resource of surface carbon species, which can decompose and interact with surface H(ad) to form CHx(ad) species at higher temperature. The comparative experiment of syn-gas on fresh metal catalyst illustrates that surface carbon species formed by the decomposition of carbon monoxide is actually one of the source of surface carbon for carbonylation.

Figure 4. CO Pulses at 423K on Saturately CH_4 adsorbed 5wt% Pd/SiO_2 catalyst

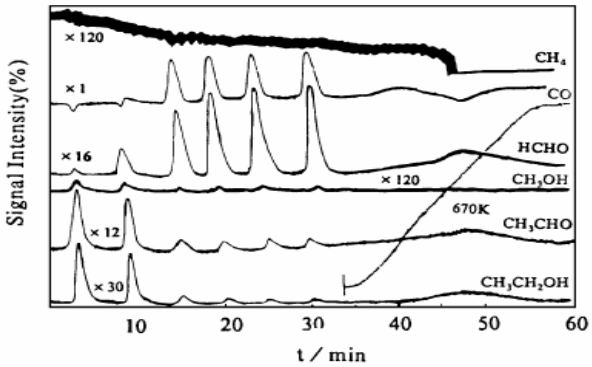

On the methane adsorbed metal surface, the decomposition of CO was very weak and its influence on carbonylation of methane was also very weak. The partial decomposition and hydrogenation of carbon monoxide at higher temperature results in the increasing of the formation of ethanal at 673K with the increasing of the pulse numbers of syn-gas. The comparative experiments indicate that the carbonylation of CHx(ad) species formed by the decomposition of surface probe molecules CH_3I mostly results in the formation of ethanal. It means that the formation of HCHO mainly comes from the direct gas phase reaction of CO and H_2. Optimization of the direct carbonylation of methane might results in the novel process for the effective utilization of methane.

Figure 5. CO pulses at 673K on saturately CH_4 adsorbed 5wt% Pd/SiO_2 catalyst at 673K.

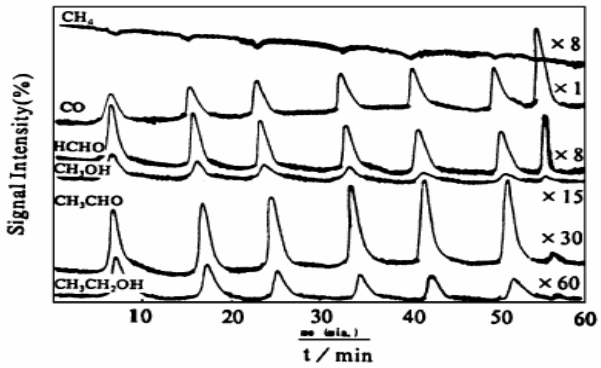

Figure 6. CO pulses at different temperatures on fresh 5 wt % Pt/SiO_2 catalyst

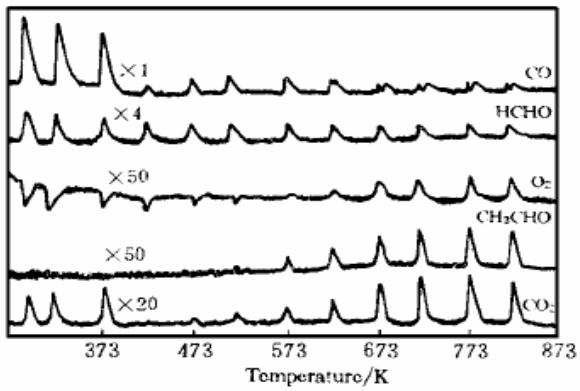

Conclusions

The direct carbonylation of methane on supported transition metal catalysts was extensively investigated by using the temperature programmed pulse reaction (TPPR) and constant temperature pulse reaction (CTPR). An important approach is to split the overall reaction into two reaction steps occurring under moderate conditions. Methane is firstly decomposed by a reduced transition metal catalyst into adsorbed surface carbonaceous species, then carbonylation of surface carbonaceous species was employed at different conditions. In such a two-step route the thermodynamic limitations can be overcome and the homologation of methane may be practically achieved. The catalytic performance and product distribution of direct carbonylation of methane sensitively depend on the nature of transition metals and the variance of the reaction conditions. Carbonaceous species formed by the decomposition of methane on metal surface may be the active intermediate which are responsible for the lengthening of carbon-carbon chain on catalyst surface. Optimization of the direct carbonylation of methane might results in the novel process for the effective utilization of methane.

References

[1] D.M.Bibby, C.D.Chang, R.E.Howe and S.Yurchak, eds., Methane Conversion, Proc. Symp. on the Production of Fuel and Chemicals, Auckland 1987; in: Studies in Surface Science and Catalysis, Vol. 36, eds., B.Delmon and J.T.Yates Jr. (Elsevier, Amsterdam, 1988).

[2] J.S.Lee, and S.T.Omaya, *Catal. Rev. -Sci. Eng*., **1986**, 28, 249.

[3] F.Solymosi, J.Cserenyi, *Catal. Lett.*, **1992**, 16, 399.

[4] A.Frennet, *Catal. Rev. -Sci. Eng*., **1974**, 10, 37.

[5] T.Koerts, R.A.van Santen, *J.Catal.*, **1992**, 134, 13.

The Thermodynamics of Aqueous Potassium Carbonate/Piperazine for CO_2 Capture

J. Tim Cullinane and Gary T. Rochelle

Department of Chemical Engineering
The University of Texas at Austin, Austin, Texas 78712

Introduction

Concern over global warming has sparked the development of technologies for the capture and sequestration of greenhouse gases. Amine-based solvents in absorber/stripper processes have been developed as one option for separating CO_2 from waste gas streams. A new aqueous solvent containing potassium carbonate (K_2CO_3) and piperazine (PZ) shows promise as a commercially viable solvent, possessing favorable equilibrium behavior and a low heat of absorption.

The equilibrium in these solvents can be represented with the reactions shown below. PZ is a cyclic diamine, forming a variety of species. Carbonate and bicarbonate are also present in significant quantities. The pH in useful solutions varies from 8 to 13.

$$PZH^+ + H_2O \leftrightarrow PZ + H_3O^+$$
$$PZ + CO_2(aq) + H_2O \leftrightarrow PZCOO^- + H_3O^+$$
$$H^+PZCOO^- + H_2O \leftrightarrow PZCOO^- + H_3O^+$$
$$PZCOO^- + CO_2 + H_2O \leftrightarrow PZ(COO^-)_2 + H_3O^+$$
$$CO_2(aq) + 2\cdot H_2O \leftrightarrow HCO_3^- + H_3O^+$$
$$HCO_3^- + H_2O \leftrightarrow CO_3^{2-} + H_3O^+$$
$$2\cdot H_2O \leftrightarrow H_3O^+ + OH^-$$
$$CO_2(g) \leftrightarrow CO_2(aq)$$

The evaluation of this solvent for use in a commercial system depends on the ability to effectively model rates of CO_2 absorption, energy requirements, and absorption capacity, requiring a thorough understanding of equilibrium behavior. This work identifies important equilibrium characteristics of the solvent at various concentrations (0.0 to 6.2 m K^+ and 0.0 to 3.6 m PZ) and temperatures (25 to 80°C) and develops a rigorous thermodynamic model applicable over these ranges.

Experimental

Electrolyte NRTL Model. The equilibrium modeling of the solutions was accomplished using the electrolyte NRTL model, originally developed by Chen et al. (1). Previous work has used this model extensively for aqueous electrolyte solutions and acid gas systems (2, 3).

Liquid Speciation. The equilibrium distribution of piperazine and its carbamates was quantified with the use of ^1H spectra from a Varian INOVA 500 NMR. Samples were prepared with 80% H_2O, 20% D_2O, K_2CO_3 or $KHCO_3$, and PZ.

Vapor-Liquid Equilibrium. The equilibrium vapor pressure of CO_2, P_{CO2}*, was determined with a wetted-wall column. A description of the equipment can be found in previous work (4, 5). Nitrogen and CO_2 are fed into the column where it contacts the flowing solvent. The outlet concentration of CO_2 is measured using IR spectroscopy. By adjusting the CO_2 partial pressure in the gas stream, absorption and desorption conditions can be obtained and a flux of CO_2 can be calculated. Interpolating to a flux of zero allows the calculation of P_{CO2}*.

Results and Discussion

An equilibrium model was developed for K^+/PZ mixtures using existing literature data and new experimental investigations. Boiling point elevation, activity of water, and P_{CO2}* data were used to regress parameters relevant to $K_2CO_3/KHCO_3$ solutions (6, 7, 8). P_{CO2}* data for aqueous PZ is available from Bishnoi (4). Speciation in aqueous PZ was previously found by Ermatchkov (9). Additional data for K^+/PZ solutions were investigated in this work.

Parameters for the model are shown in Table 1. In this work, default parameters for water-ion pair and ion pair-water interations are 8.0 and -4.0 respectively. Molecule-molecule interactions are 0.0. The model reference temperature is 353K; therefore, A represents a binary interaction parameter, τ, at 353K and B represents a temperature dependence in the form $B\cdot(1/T - 1/353)$. The regressed parameters show minor variations from default values. Confidence intervals are generally less than 10% for A and 50% for B.

Table 1. Regressed Binary Interaction Parameters in the Electrolyte NRTL Model for K^+/PZ Mixtures

Interaction	A, τ_{353K}	σ_A	B	σ_B
H_2O, (K^+ CO_3^{2-})	9.36	0.21	867	560
(K^+ CO_3^{2-}), H_2O	-4.49	0.04	-331	90
H_2O, (K^+ HCO_3^-)	7.68	0.04	2410	Indet.
(K^+ HCO_3^-), H_2O	-3.40	Indet.	-404	80
H_2O, PZ	12.90	0.25	-3321	Indet.
PZ, H_2O	0.92	0.13	-837	Indet.
(PZH^+ $PZCOO^-$), H_2O	-4.47	0.42	*	N/A
H_2O, (PZH^+ $PZ(COO^-)_2$)	5.46	0.81	*	N/A
(PZH^+ $PZ(COO^-)_2$), H_2O	*	N/A	-625	380
H_2O, (K^+ $PZCOO^-$)	11.21	0.27	-6921	1110
H_2O, (K^+ $PZ(COO^-)_2$)	7.72	0.29	-2098	920
H_2O, (PZH^+ HCO_3^-)	8.93	0.10	*	N/A
H_2O, (PZH^+ CO_3^-)	*	N/A	7987	1270
(PZH^+ CO_3^{2-}), H_2O	-6.40	0.59	*	N/A

* Default parameter used.
Indet. = Indeterminate

Proton NMR was used to speciate various K^+/PZ mixtures. As shown in Figure 1, the addition of 5.0 m K^+ to 2.5 m PZ dramatically changes the distribution of PZ species. Over equivalent partial pressures, the presence of more CO_2 converts free PZ to $PZCOO^-$ and $PZ(COO^-)_2$. Conversely, the carbonate/bicarbonate buffer reduces the protonation of PZ and $PZCOO^-$ resulting in an overall increase in reactive amine species.

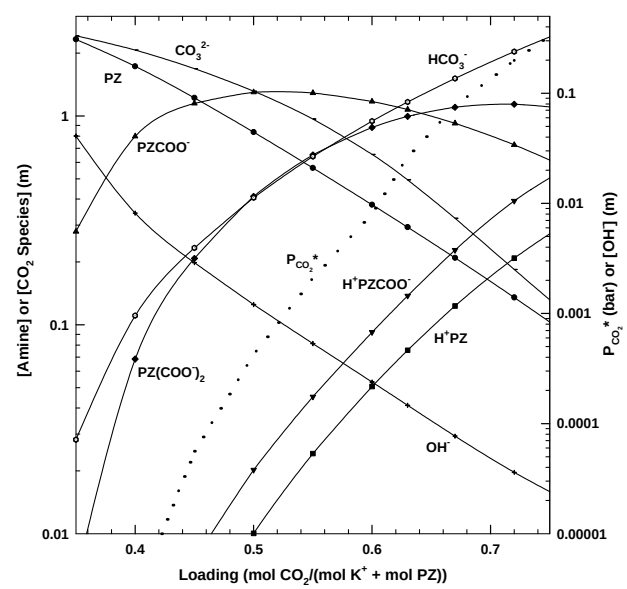

Figure 1. Electrolyte NRTL Prediction of Speciation of 5.0 m K^+/2.5 m PZ at 60°C

The results of VLE experiments for various K^+/PZ solvents at 60°C are shown in Figure 2. The addition of 3.6 m K^+ to 1.8 PZ solutions depresses the P_{CO2}* by as much as a factor of 20. As the solution becomes more concentrated in K^+ and PZ the P_{CO2}* line becomes less steep as evidenced by 5.0 m K^+/2.5 m PZ, showing that the equilibrium behavior approaches that of 7 m MEA solutions. Model predictions are shown to be within 30% of experimental findings.

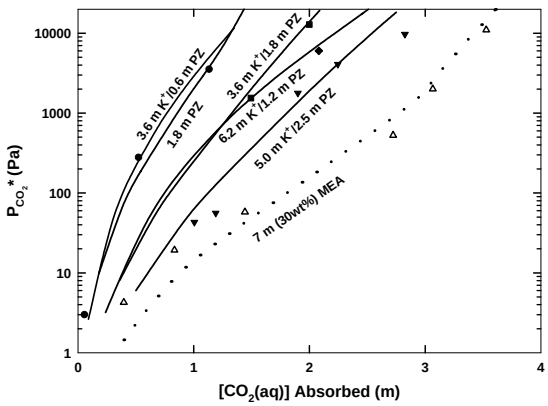

Figure 2. Vapor-Liquid Equilibrium of CO_2 in K^+/PZ at 60°C. Points: Experimental Data. Lines: Model Predictions.

The VLE model was used to predict P_{CO2}* at various temperatures, allowing estimations for the heat of absorption (ΔH_{abs}) of CO_2 at 3000 Pa (Figure 3). The ΔH_{abs} shows a strong dependence on the ratio of PZ to K^+. At low ratios, the value of ΔH_{abs} approaches 8 kcal/mol. With more PZ the heat of absorption increases and approaches a value typical of amine-based solvents (~22 kcal/mol). The 1.8 m PZ solution also has a lower ΔH_{abs}, ~16 kcal/mol, due to protonation of the amine at the high CO_2 partial pressure.

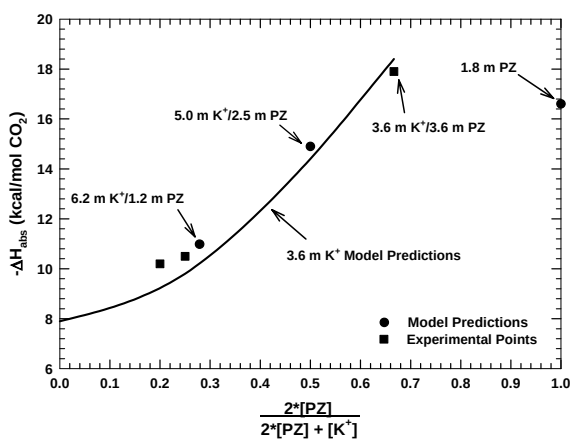

Figure 3. Heat of Absorption of K^+/PZ Mixtures. Model Predictions and Experimental Data at T = 60°C, P_{CO2}* = 3000 Pa

The dependence of ΔH_{abs} on PZ:K^+ reflects a strong dependence on the reaction stoichiometry relevant at given conditions. This behavior is reflected in Figure 4 for 5.0 m K^+/2.5 m PZ. At loading less than 0.4, the reaction of CO_2 with hydroxide has a significant effect. With increasing loading, the absorption of CO_2 is dominated by the formation of H^+PZ and HCO_3^-, reducing the ΔH_{abs}. At even higher loading, the formation of carbamates becomes more prevalent at 60 and 80°C, increasing the ΔH_{abs}. At 40°C, a decline in ΔH_{abs} occurs throughout the range of loading as protonation of the amine becomes more important. Temperature has a marked effect, shifting equilibrium and changing reaction stoichiometry at given loading. It appears that the protonation of PZ becomes more important at higher temperatures as the carbamate stability decreases.

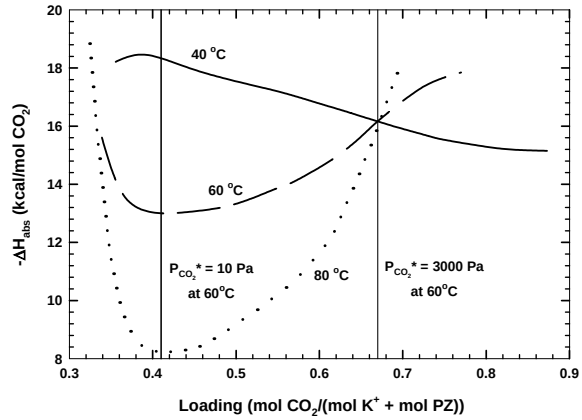

Figure 4. Electrolyte NRTL Model Predictions of the Heat of Absorption of 5.0 m K^+/2.5 m PZ.

Conclusions

The addition of K^+ to aqueous PZ yields significant advantages in both speciation and P_{CO2}* behavior. Large amounts of carbonate/bicarbonate buffer the solution at high pH, reducing loss of the free amine to protonation. Concentrated solutions reduce the vapor pressure of CO_2 over solvents at equivalent loadings. Data has been used to create a robust, thermodynamic model of the solvent applicable over wide ranges of temperature and concentration.

Behavioral differences are reflected positively in the ΔH_{abs} of mixtures. The cost of regenerating the solvent in the stripper could be lowered by 10 to 30% over MEA-based processes with the reduction in ΔH_{abs}, resulting in a more economical process for CO_2 capture.

Acknowledgement. This work was supported by the Texas Advanced Technology Program, contract 003658-0534-2001.

References

(1) Chen, C. -C.; Britt, J. F.; Boston, J. F.; and Evans, L. B. *AIChE J.*, **1982**, *28* (4), 588.
(2) Chen, C. -C.; Evans, L. B. *AIChE J.*, **1986**, *32* (3), 444.
(3) Austgen, D. M. Ph.D. thesis, The University of Texas at Austin, Austin, TX, **1989**.
(4) Bishnoi, S. Ph.D. thesis, The University of Texas at Austin, Austin, TX, **2000**.
(5) Cullinane, J. T. M.S. thesis, The University of Texas at Austin, Austin, TX, **2002**.
(6) Puchkov, L. V. and Kurochkina, V. V. *Zhurnal Prikladnoi Khimii.*, **1970**, *43* (1), 181.
(7) Aseyev, G. G. In *Electrolytes: Equilibria in Solutions and Phase Equilibria. Calculation of Multicomponent Systems and Experimental Data on the Activities of Water, Vapor Pressures, and Osmotic Coefficients.*; Begell House: New York, **1999**; pp. 254-264.
(8) Tosh, J. S.; Field, J. H.; Benson, H. E.; Haynes, W. P. United States Department of the Interior, Bureau of Mines Report of Investigation 5484, **1959**.
(9) Ermatchkov, V.; Kamps, A. P. -S.; Maurer, G. J. *Chem. Thermodynamics.*, **2003**, *35*, 1277.

CO2 EXTRACTION FROM AMBIENT AIR USING ALKALI-METAL HYDROXIDE SOLUTIONS: NICHE MARKETS TO INDUSTRIAL SCALE IMPLEMENTATION

Gregory V. Lowry[1], Joshuah Stolaroff[1], and David Keith[2]

[1]Civil & Environmental Engineering, and
[2]Engineering & Public Policy
Carnegie Mellon University
Pittsburgh, PA 15213

Introduction

Global climate change is one of the most serious environmental problems facing the world. In order to mitigate climate change, deep reductions in carbon dioxide (CO_2) emissions will be required in the coming decades. This necessity is at odds with fossil fuels' overwhelming dominance as an energy source. By capturing and storing CO_2 in sinks other than the atmosphere, atmospheric CO_2 levels can be stabilized or lowered while fossil fuels and their associated infrastructure are phased out more slowly and thus at lower social cost. Given the extent of emissions reductions needed to stabilize atmospheric CO_2 concentrations and the inertia involved in shifting the world's primary energy sources, carbon capture and storage (CCS) will likely constitute a substantial share of emissions reductions in the near- to medium-term.

Nearly all current research on CCS focuses on capturing CO_2 from large, stationary sources, such as power plants, as it is produced. Such plans usually entail capturing CO_2 from flue gas, compressing it, and transporting it via pipeline to a sequestration site. In contrast, the research proposed here focuses on capturing CO_2 directly from ambient air. The capture unit can be located at a favorable sequestration site, avoiding the need for a CO_2-transportation infrastructure. This strategy has the advantage that CO_2 emissions from any sector can be captured: power plants which are difficult to retrofit, point sources in locations where new infrastructure is expensive or impractical to build, and diffuse sources such as automobiles.

Previous research by our group indicated that dilute aqueous alkali-metal solutions derived from CaO- and MgO-rich waste streams (e.g. steel slag and concrete waste) effectively removed CO_2 from ambient air. The economic of CO_2 extraction from air using these wastes can be favorable under certain conditions, but the mass of carbon that can be captured and sequestered is small. The aim of this research is to design and analyze an industrial scale system for capturing CO_2 from ambient air that uses well-understood technologies available today, that is simple and inexpensive, and that is scalable to handle a significant fraction of anthropogenic CO_2 emissions. With these goals, the scheme depicted in Figure 1 has been devised as a basis for analysis. In it, air is forced through a cooling-tower-like structure where an aqueous sodium hydroxide (NaOH) solution is sprayed and collected by gravity. The NaOH droplets absorb CO_2 from the air, yielding $NaHCO_3$(aq). The collected solution is piped to a batch reactor for a sodium-calcium exchange process. The regenerated NaOH is recycled to the contactor and the $CaCO_3$ formed is sent to the Calciner. Upon heating the $CaCO_3$, CO_2 is driven off in a pure stream and pressurized for sequestration. The CaO formed is then recycled to the Na-Ca exchanger.

The Na-Ca exchange process is well-understood and currently used at industrial scales in the pulp and paper industry with almost the precise parameters required for this scheme (Adams, 1989). The calcining (regenerating the CaO) and hydroxylation steps are also well-understood processes used at industrial scales in the pulp and paper industry (*ibid.*) and during cement manufacture. The contactor is the least-specified component of the system and, as such, the subject of this research. A diagram of the proposed contactor is shown in Figure 2. The design is feasible in principle – CO_2 capture at ambient concentration with NaOH solution has been demonstrated

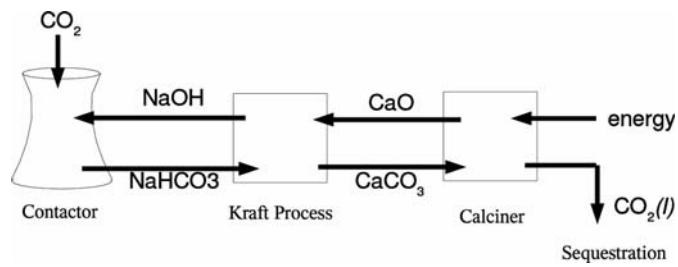

Figure 1: Proposed process for capturing CO_2 from ambient air.

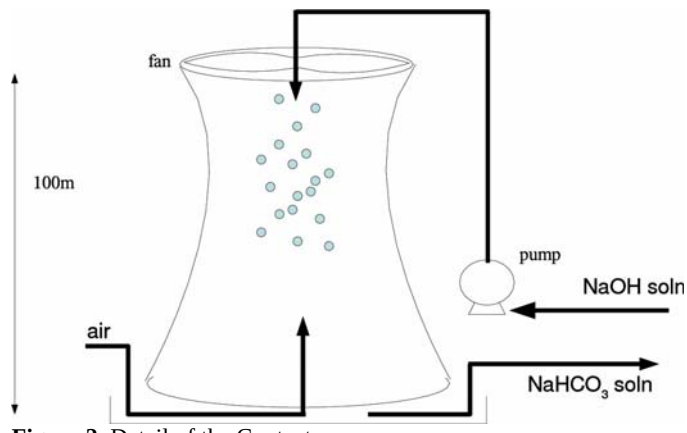

Figure 2: Detail of the Contactor

(Fukunaka, 1992; Spector, 1946; Greenwood, 1953), but the energy and material requirements are not known.

Methods

Numerical model. A numerical model was constructed of a single falling droplet of NaOH solution. The droplet falls by gravity through 100 *m* of air with a uniform velocity of 1 *m/s*. Mass transfer of CO_2 into the drop was modeled with boundary layer theory. Resistance in the liquid layer was considered to be negligible because internal circulation in drops of the size range considered is relatively fast (Pruppacher, 1978). Mass transfer through the air boundary layer was estimated with an empirical relation developed for raindrops (Bird, et al, 1960) and integrated over the fall of the drop.

Experimental. To confirm the theoretical calculations, experimental measurements of CO_2 uptake are performed. Droplets of 1*M* NaOH solution are ejected from an electrostatically-charged nozzle fed by a syringe pump. Droplet diameters between 0.3 and 1.5 *mm* are achieved with voltages of 3-6 *kV*. Droplets fall through a measured distance of atmospheric air and are collected in a buffered (pH~6) solution so that subsequent CO_2 uptake is negligible. The total carbonate in the buffered solution is measured using a model 1100 Total Organic Carbon (TOC) analyzer (OI Analytical). The analyzer acidifies the sample to pH<2 to convert all inorganic carbon to CO_2, purges the sample with N_2, and measures the resulting CO_2 with a nondispersive infrared detector (NDIR). Uptake of CO_2 per drop is calculated based on total CO_2 captured and the total volume

of solution collected. By repeating this experiment for a range of drop sizes an empirical prediction of CO_2 uptake as a function of drop size is generated.

Results

Results of the numerical model are shown in Figure 3. Concentrations of captured CO_2 that approach or exceed 1 *M* are predicted for drops smaller than about 1 *mm*. A more meaningful measure of uptake efficiency may be on a per-energy basis. Energy is required to pump the solution to the top of the tower and to sustain a large enough pressure head to break the solution into mist. The energy required to move air through the contactor was estimated to

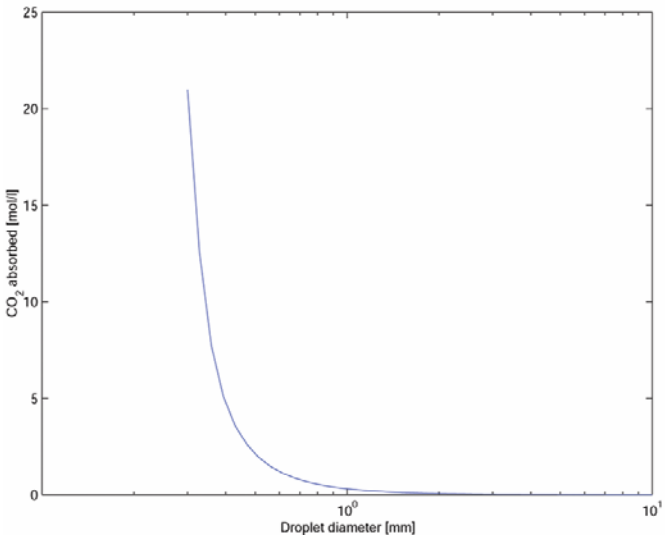

Figure 3: CO_2 absorbed by falling droplets as a function of droplet diameter

be small in comparison. Figure 4 shows the results converted to energy terms. For drop sizes smaller than 1 *mm* or so, the energy requirements are quite modest – less than 1 *kJ/mol* CO_2 for the smallest drops, which compares favorably with, for instance, the heat of combustion of gasoline at 680 *kJ/mol* CO_2. This is also small compared to our preliminary estimates of the energy requirements of the total system (primarily the calciner), which may amount to 220 *kJ/mol* CO_2.

Results of the laboratory experiments are pending.

Discussion

CO_2 capture from ambient air is an understudied but potentially important subset of CCS technology, having several strong advantages over CCS from point sources. The aim of this research is to help develop and analyze such a system that is simple, scalable, and achievable with current technology. The primary goal of this research is to develop a high-quality estimate of the cost of operation of the contacting unit, in dollars per ton of CO_2 captured, that can be used in the cost-accounting of the entire system. The insight and data gained from the prototype experiments, along with data and knowledge from industry contacts, will enable this estimation.

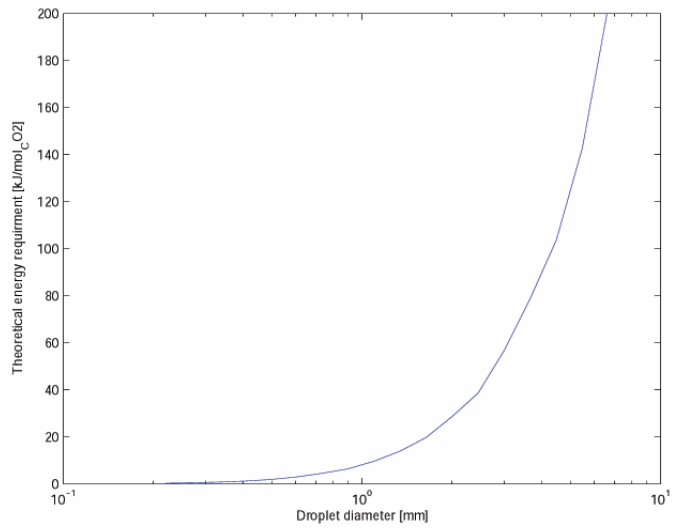

Figure 4: Theoretical energy required for CO_2 capture as a function of droplet diameter

References

Adams, T. N. (1989). Lime Reburning. Pulp and Paper manufacture Vol. 5 Alkaline Pulping. T. M. Grace, B. Leopold and E. W. Malcolm. Atlanta, The Joint Textbook Committee of the Paper Industry. 5: 590-608.

Fukunaka, Yasuhiro (1992). "Absorption of CO_2 Gas into falling droplets of aqueous NaOH solution." Metallurgical Review of MMIJ. 9 (1): 33-50.

Greenwood, K. and M. Pearce (1953). "The Removal of Carbon Dioxide from Atmospheric Air by Scrubbing with Caustic Soda in Packed Towers." Transactions of the Institution of Chemical Engineers 31: 201-207.

Spector, Norman A. and Barnett F. Dodge (1946). "Removal of Carbon Dioxide from Atmospheric Air." Transactions of the American Institute of Chemical Engineers. 42: 827-848.

Bird, R. Byron, Stewart, Warren E., Lightfoot, Edwin N. (1960). ``Transport Phenomena". John Wiley and Sons. New York.

Pruppacher, H. R., Klett, J. O. (1978). ``Microphysics of Clouds and Precipitation". D. Reidel. Boston.

C-LOCK: AN ONLINE SYSTEM TO MAXIMIZE THE VALUE OF AGRICULTURAL CARBON SEQUESTRATION FOR PRODUCERS AND PURCHACERS

Patrick R. Zimmerman[1], Maribeth Price[2], Karen Updegraff[1] and William J. Capehart[1]

(1) Institute of Atmospheric Sciences
(2) Department of Geology,
South Dakota School of Mines and Technology
501 E. St. Joseph St., Rapid City, SD 57701-3995

Introduction

Many industrial and energy firms are interested in lowering their future exposure to financial risk, in the event that greenhouse gas emission caps are implemented. Emissions offsets generated by landowners who retire cropland or move to less intensive tillage, thereby increasing the amount of organic carbon (SOC) stored in soils, have good investment potential. However, soil carbon trades to date have been idiosyncratic events associated with large uncertainties and therefore low prices for the sellers. Institutional deficiences, issues of measurement, monitoring and verification (MMV), and compliance enforcement all conspire to raise offset costs for buyers and lower payments to sellers (1,2).

By standardizing the estimation of SOC sequestered on individual parcels, and subjecting each estimate to rigorous uncertainty analysis and validation, the C-Lock system reduces the risk associated with trades of carbon emission reduction credits (CERCs). Because of reduced dependence on field-level sampling to determine changes in SOC, the system facilitates low-cost performance-based MMV of sequestration projects. This helps to reduce transaction costs and increase the value of soil carbon sequestration for landowners.

An overview of C-Lock and a demonstration application to a South Dakota farm highlights its MMV advantages and potential cost savings compared to sampling-based protocols.

The C-Lock System

C-Lock is comprised of a web interface, a client database, a GIS database and the CENTURY soil carbon model (3), which are linked by a system of Shell and Perl scripts. A Monte Carlo-based repeated simulation procedure is used for uncertainty analysis.

C-Lock will ultimately be licensed to a private entity who will provide administrative and certification services. This entity will need to populate soil, climate and crop history databases and possibly calibrate CENTURY for states other than South Dakota in which the system is applied.

Process Summary. The client creates a private account via a secure web interface. The spatial coordinates of the registered parcel link client data to GIS databases. The client selects management options for defined time blocks between 1900 and 1989 via drop-down menus. For 1990 to the present he is required to specify annual crop and management parameters, including tillage and fertilizer schedules, although default parameter values are available for common crops. The client may specify a future date to which he would like to estimate carbon sequestration. Management parameters specified for 1990-1999 are recycled to create future scenarios.

The location of the client parcel links it to a GIS database of climate (monthly temperature and precipitation) and soil data. Generalized management data for historical time blocks are selected based on the climate zone (MLRA) in which the parcel is located.

The client-specific and general management data, climate and soil parameters are used to create parameter and event-schedule files for CENTURY, which models SOC dynamics over a specified period as a function of substrate, climate, cover type and management. A 3000-year base run is used to establish a stable pre-agricultural SOC pool. Agricultural disturbance begins around 1900. The degree of disturbance is specified through client-selected management options. Sensitivity testing has indicated that specific crops or tillage schedules have less impact on long-term SOC depletion than does the fact that annual tillage occurs.

Based on client input and the GIS-derived soil, climate and management parameters, the CENTURY model produces estimates of soil C that allow the calculation of credits for net C sequestration. However, because of the uncertainty inherent in the estimation of many input parameters and in the modeling process itself, the CENTURY model is run for a given parcel not just once but at least 200 times. Monte Carlo sampling of the most uncertain input parameters, such as soil texture or of parameters describing cultivation impacts, allows the construction of well-defined confidence intervals for credits estimated on a given parcel.

An important advantage of the model-based approach is that it can ensure that the additionality criterion for carbon offset projects is met. While most offset or emissions reduction projects use a simple mean (e.g. 1985-89) emissions rate as the emissions baseline, this approach has shortcomings in a terrestrial C sequestration project. Preliminary tests have indicated that the use of a baseline emissions rate is likely to bias calculated CERCs, since terrestrial emissions are subject to the vagaries of weather. Atypical growing conditions during the baseline period could result in unrealistically high or low estimates of C sequestration..

Therefore, in order to factor out all non-anthropogenic effects on soil C dynamic, the client-defined scenario is modeled in parallel with a business-as-usual (BAU) scenario. Through 1989 the client and BAU scenarios are identical; beginning in 1990 the client scenario is defined by management parameters specified for each year by the client, but the BAU scenario recycles the management option selected by the client for the 1982-1989 time block. Thus, rather than establishing a baseline emissions rate C-Lock establishes a baseline management scenario. The client and BAU scenarios are both subjected to Monte Carlo analysis, using exactly identical "random" weather and parameter files. Consequently any difference in soil C between the two scenarios is due exclusively to management effects.

The client report summarizes trends in soil C resulting from the client-defined CENTURY run, and cumulative CERCs for each decade of the specified contract period. The reported CERCs are based on the 200-iteration Monte Carlo run. Likely ranges of accrued CERCs are defined by the 95 percent confidence intervals for Monte Carlo output, as described below.

Certification of CERCs. C-Lock produces two independent distributions of Monte Carlo output, which are used to define a pool of marketable CERCs associated with a high degree of confidence. These are CERCs that fall between the upper 95th percentile of the BAU output range and the lower 95th percentile of the client output range. These represent the minimum level of CERCs that can be guaranteed at the 95 percent confidence level. A reserve pool of CERCs is based on the upper 95th percentile of the client scenario and the lower 95th percentile of the BAU scenario.

C-Lock verification, measurement and monitoring protocols

The basic C-Lock system incorporates three levels of data verification.

I. Data quality control limits trap or flag unreasonable input values. In addition, routine audits may entail, for example, comparison of producer inputs with remotely-sensed or satellite data regarding land use, or the comparison with FSA records for that field. This type of verification is applied to all registered parcels.

II. A subset of registered parcels will be submitted to a third party auditor, who will re-estimate CERCs.

III. Comparisons of CENTURY outputs with regional data published in the literature. Measured results from long-term study areas subject to systematic sampling, monitoring and analysis provide higher-quality data for model calibration than could be expected from sporadic, site-specific soil sampling.

Quantifying SOC changes. Project guidelines for soil C sequestration typically base MMV protocols on soil sampling to quantify total carbon stocks and stock changes, The focus of C-Lock is on the accurate quantification of incremental changes in SOC, rather than absolute SOC for a site. The C-Lock system uses regional carbon research data to calibrate and validate CENTURY. By taking advantage of comprehensive, systematic regional soil sampling, this approach reduces the need for field level soil samples to define incremental SOC stock changes. Only minimal soil sampling is required to verify the status of the soil carbon reservoir..

Soil sampling is one of the most costly components of sequestration project MMV. A study by Mooney et al (4) estimated aggregate costs per soil sample at $16.37 for Montana farms. At conventionally-recommended sampling rates of 2 samples per ha, each round of soil sampling will cost $33 per contract hectare. To quantify carbon stock changes, this sampling must be repeated regularly, e.g. every 5 years. High sample variability will generally result in significant discounting of potential CERC value. Therefore each reduction in sampling frequency by 1 represents a total cost reduction of over $6,500 for a 400-ha (about 1 section) parcel.

In the last decade, improved atmospheric sampling approaches have estimated regional fluxes of a wide range of trace gas species, using integrated systems of surface observation sites, tall towers and aircraft sampling. The use of such a network to monitor regional carbon balances could serve to provide data for an independent validation of regional soil carbon sequestration.

The C-Lock system requires the producers to periodically update management data used to estimate current and potential C sequestration. Each time the C-Lock client database is updated, CENTURY is re-run for that parcel, and new estimates of certified and reserve CERCs are produced.

If the most recent CERC estimates fail to correspond to the producer's contract commitments, he may be allowed to use his pool of reserve CERCs to temporarily make up the deficiency. At the same time, he would be required to modify his future management scenario to increase the projected rate of C sequestration for contract compliance.

C-Lock and carbon sequestration contracting

The use of project-based (per Mg soil C sequestered) rather than activity-based (per contract hectare) was found to be more economically and socially efficient by Antle et al (5) in the likely event that fields are spatially heterogenous. The main constraint to project-based contracting is the cost of measurement and monitoring, relative to activity-based contracts. The use of a system like C-Lock reduces the need for field sampling, thereby reducing costs and facilitating project-level contracting.

Because of the perceived non-permanence of carbon sequestered in biomass or soil organic matter, the idea of CERC leasing as embodied, for example, in the concepts of "carbon tonne years" and "temporary certified emissions reductions" (6) has gained some popularity. C-Lock is ideally suited to leasing arrangements because of its relatively low MMV overhead and requirement for regular management updates.

Example Application

The C-Lock system was applied to a hypothetical 400-ha farm in eastern South Dakota. We simulated a change from conventional tillage management of a wheat-corn-soybean rotation to no-till management. Assuming a 40-year contract and a price of $10 per Mg C, the guaranteed CERCs generated over the entire parcel would be worth a total of $57,207, or $1430 per contract year.

Apart from costs incurred to shift to no-till, the producer bears the time opportunity cost of initial registration and biannual updates. Based on a 2002 average farm income of $65,757 (7), the time invested in registering and updating parcel information (e.g., 3 hours initially and 1 hour for each update) is worth about $632 to the farmer. Initial and final soil samples, using the assumptions stated above, would cost to $13,096 for the entire parcel.

A contract that relied on soil sampling every 5 years would incur measurement/monitoring costs of $58,932 over the duration of the contract described above. Further, because the samples are less frequent than the producer updates to C-Lock would be, there is less immediate feedback with respect to the impact of management strategies, and hence less opportunity to correct undesirable trends.

Acknowledgement This material is based in part upon work supported by the National Science Foundation/EPSCoR Grant #EPS-0091948 and by the State of South Dakota.

References

(1) Sonneborn, C. Overview of international activities in emissions trading. In*: New Zealand Sustainable Energy Forum 2000* Conference. Dunedin, 7-9 July **2000**, 25p.

(2) Vine, E. and Sathaye, J. *Mitigation and Adaptation Strategies for Global Change*, **1999**, 4,1, 43-60.

(3) Parton, W.; Schurlock, J.; D. Ojima; D. Gilmanov; T. Scholes; R. Schimel; T. Kirchner; J.-C. Menaut; T. Seastedt; E. Garcia Moya; A. Kamnalrut; and Kinyamario, J. *Global Biogeochem. Cycles* **1993**, 7, 785-809.

(4) Mooney, S. and J. Antle and S. Capalbo and K. Paustian. *Contracting for soil carbon credits: design and costs of measurement and monitoring*. **2002**, Department of Agricultural Economics and Economics, Montana State University, Bozeman, MT. Staff Paper 2002-01. 42 pp.

(5) Antle, J. and Mooney, S. *Designing efficient policies for agricultural soil carbon sequestration*, **2001**, Montana State University, Department of Agricultural Economics. http://www.climate.montana.edu/.

(6) Phillips, G. *LULUCF Projects in the CDM: Accounting regimes and proposals for simplified rules and modalities*, Discussion Paper 02-02, **2002,** International Emissions Trading Association Toronto, Canada. 14 pp.

(7) USDA Economic Research Service. *Agricultural Income and Finance Outlook*. Electronic Outlook Report AIS-81, **2003**, Available online: http://jan.mannlib.cornell.edu/reports/erssor/economics/ais-bib/2003/ais-80.pdf.

Enhancement of Soil Carbon Sequestration: A Catalytic Approach

James E. Amonette, Jungbae Kim, and Colleen K. Russell

Pacific Northwest National Laboratory
PO Box 999
Richland, WA 99352

Introduction

One of the approaches to minimizing the possible effects of climate change stemming from the recent and significant increases in atmospheric CO_2 levels involves fixing or storing C as biomass in terrestrial ecosystems. Of the possible terrestrial reservoirs for C storage one of the most proming is organic matter in soil.[1] Currently, this soil organic matter, termed humus, contains about twice as much C as is in the atmosphere.[2]

Historically, many agricultural soils contained as much as 50% more humus before cultivation as they do now. Indeed, before 1970, more C was lost from soils to the atmosphere as a result of land-use changes than was emitted by fossil-fuel combustion.[3] In the present context, this inherited soil-C deficit represents a potential reservoir for C, the refilling of which can help buffer the transition to less C-intensive fuels over the next 30-50 years.

Our research has focused on understanding the fundamental process by which humus is created (i.e., humification) and extending this knowledge to enhance the rate of humification. The rate-limiting step in the humification process appears to be the oxidation of polyphenols to quinones.[4] These quinones then react with peptides and amino acids to form large melanin-like polymers that resist further degradation by microorganisms.

Soil fungi produce enzymes such as polyphenol oxidases and laccases that catalyze the oxidation step.[5,6] Soil minerals, such as iron and manganese oxides, can also perform this function.[7,8,9] We have observed a significant synergetic effect when a polyphenol oxidase (tyrosinase) and a mineral phase (e.g., mesoporous silica, manganese oxide, alkaline fly ash) are both present.[10,11,12] As soil enzyme activity depends on structural conformation, and longevity depends on protection from microbial predation, we are examining the nature of enzyme attachment to soil particles and the impact of physical properties such as pore size on activity and longevity.

In this paper we summarize our results with these co-catalysts and discuss implications regarding reaction mechanisms and management strategies for enhancing soil-C sequestration.

Experimental

Materials. Mushroom polyphenol oxidase (tyrosinase), L-3,4-dihydroxyphenylalanine (L-DOPA), L-serine, L-glycine, monosodium citrate, and vanillic acid were obtained from Sigma Chemical Co. (St. Louis, MO). The tyrosinase had a nominal activity of about 2400 units/mg (oxidation of L-tyrosine to L-DOPA at pH 6.5 and 25°C, 1 unit = ΔA_{280} of 10^{-3} min^{-1} in 3-mL solution). Orcinol, resorcinol, *p*-hydroxybenzoic acid, glycine, silica gel (Davisil, 35-60 mesh, 150Å), and hematite (α-Fe_2O_3), were obtained from Aldrich Chemical Co. (Milwaukee, WI). Sodium hydroxide was obtained from Fisher Scientific (Hampton, NH). Goethite (α-FeOOH) and birnessite (γ-MnO_2) were synthesized in the laboratory. Two alkaline fly ashes were obtained from coal-fired power plants in Texas. One was a Class C ash derived from sub-bituminous coal, and the other was a Class F ash derived from lignitic coal.

Humification Experiments. Several experiments were conducted to determine the impact of fly ash, the Fe and Mn oxides, and pH on a model humification reaction. The basic humification experiment with fly ash was patterned on that of Nelson et al. (1979) and involved the following steps. A 100 mM NaH_2PO_4 solution buffered at pH 6.5 was used to prepare a 2 mM solution of organic monomers (orcinol, resorcinol, p-hydroxybenzoic acid, L-glycine, L-serine, and vanillic acid), and separately, a tyrosinase solution (1 mg tyrosinase ml^{-1}). The pH of the monomer solution was readjusted to 6.5 by addition of NaOH. In sequence, either 1 mg of oxide or 500 mg of fly ash, 1 mL of buffer, 3.5 ml of the buffered monomer solution, and 0.5 ml of the buffered tyrosinase solution were added to a 7.5-ml polystyrene 1-cm pathlength cuvette to yield a final solution volume of 5 mL. Each cuvette was then capped with parafilm and incubated at 22ºC. At selected times after mixing, a representative aliquot of the mixture was taken and centrifuged, and the absorbance spectrum of the supernate collected using a UV-Vis spectrophotometer. The supernate and solid were returned to the 7.5-mL cuvette after this analysis to continue the study. Humification progress was measured as increases in absorbance at a wavelength of 486 nm (A_{486}). As humification progressed, extremely absorbing solutions were obtained, and these required ten-or hundred-fold dilution in order to obtain usable data. The diluted specimens were not returned to the cuvette after analysis. To determine the effect of pH on humification, an experiment was conducted at pHs of 5.0, 6.5, 7.5, and 9.0. No fly ash was added and buffers other than phosphate were used at pH 5.0 (disodium citrate) and pH 9.0 (boric acid).

To determine the activity of the dissolved enzyme, 10 µL from an experimental sample or a freshly prepared stock solution [5 mg tyrosinase in 5 ml of 50-mM phosphate buffer (pH 6.5)] was diluted to 1 mL with a 1 mM L-DOPA/50-mM phosphate solution (pH 6.5) in a 1-cm pathlength cuvette. The absorbance at 478 nm (A_{478}) was monitored for up to ten minutes after dilution using a Shimadzu UV-2501PC (Shimadzu, Japan) UV-Vis spectrometer while the solution was maintained at room temperature (22ºC). The tyrosinase activity for L-DOPA oxidation was calculated from the rate of increase in A_{478} (i.e., ΔA_{478} min^{-1}).

Results and Discussion

Our humification experiments have involved reacting tyrosinase in the presence of three types of "co-catalysts": mesoporous silica particles, metal-oxide minerals, and alkaline fly ashes. With silica particles, the primary effect is to physically protect the enzyme from degradation, thus prolonging its activity and increasing humification. Our experiments (data not shown) suggest that both enzyme and the resulting humic polymers concentrate in the pores of the silica.

With the Fe and Mn oxides, the primary effect is related to the ability of these minerals to act as oxidants. During the first week of reaction, humification enhancement factors (i.e., the amount observed with the co-catalyst present divided by the amount observed when tyrosinase is the only catalyst present), of 1.2±0.1, 1.7±0.3, and 2.9±0.3 were observed for experiments conducted with 0.02 wt% suspensions of α-Fe_2O_3, α-FeOOH, and γ-MnO_2, respectively. Thus, α-Fe_2O_3 had almost no impact on humification, whereas the amount of humification nearly tripled when γ-MnO_2 was present. These results are in the same order as the reduction potentials of the three compounds, as one would expect. However, sorption of tyrosinase to these surfaces, particularly the γ-MnO_2 which has substantial microporosity, may also be involved as a stabilizing mechanism.

With the alkaline fly ashes, the primary effect could be physical, due to the presence of broken silica cenospheres, directly oxidative, due to the presence of metal oxides, or indirectly oxidative, due to the increase in pH. Our experiments, which were conducted using 10 wt% suspensions of the ash (i.e., 500 times more co-catalyst than with the metal oxides), showed humification enhancement factors of 2.4±0.1 and 11±2.3, for the lignitic and sub-bituminous ashes, respectively. Characterization of these ashes showed little difference in their cenosphere or metal oxide contents. However, a large

difference in their titrateable alkalinity (pH 6.5) was observed, with that of the sub-bituminous fly ash (13.4 mmol g^{-1}) being about 4.6 times larger than that of the lignitic fly ash (2.9 mmol g^{-1}), the same factor by which their humification enhancement factors differed. Moreover, for the 0.5-g quantities used in the humification experiments, the alkalinity of both fly ashes was substantially greater than the capacity of the phosphate buffer (ca. 0.5 mmol) resulting in substantial pH increases in these experiments as the fly ashes equilibrated with the humic monomer solution. These results led us to investigate the effect of pH alone on the humification reaction.

Humification experiments at pHs of 5, 6.5, 7.5, and 9 clearly showed a substantial effect of alkaline pH on humification (Fig. 1a). Essentially no humification occurred at pH 5, whereas maximal humification occurred at pH 9. Humification occurred primarily during the first 72-96 hours, and thereafter, little change was observed. Measurement of the enzyme activity during the experiment showed that activity held steady for perhaps 48-60 hours and then dropped rapidly to zero by 96 hours (Fig. 1b). The enzyme activity at pH 9, however, was consistently smaller than that for any other pH, even though the same trend with time was observed. In the absence of tyrosinase, negligible amounts of humification were observed in all but the pH-9 treatments (Fig. 1c), where maximum humification was still only about 5% of that observed when tyrosinase was present.

These results confirm the sequential two-step nature of the humification process, i.e., oxidation of phenolic groups followed by condensation of the resulting quinones with amino acids to form melanins. High pH enhances the process primarily through its effect on the condensation step. Thus, maximum humification rates were obtained at pH 9 even though the enzyme activities were relatively low, whereas no humification was observed at pH 5 when enzyme activities were higher than at pH 9 (Fig. 1a,b). Tyrosinase is needed for the reaction to occur at a useful rate (Fig. 1c), but the level of tyrosinase activity seems less important than high pH in determining the yield of humic polymers. The manner by which condensation is enhanced likely relates to the speciation of the reactants at high pH. Quinones are stabilized, and the pK_a of aliphatic amine groups is near 10. It could be that the anionic form of the amino acids (i.e., a neutral amine group) is critical to the condensation step.

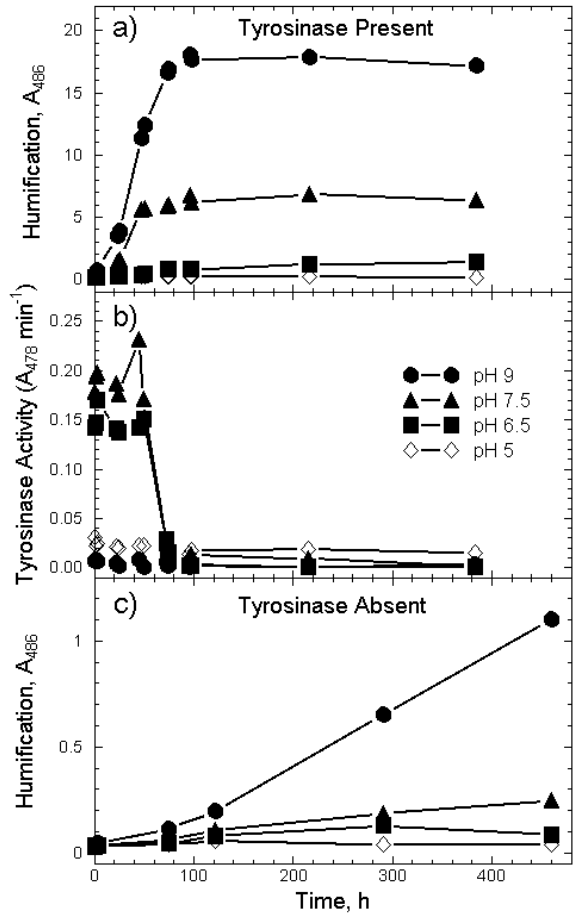

Figure 1. Effect of pH on rates of humification and on tyrosinase activity: a) humification with tyrosinase present; b) tyrosinase activity during the humification experiment; and c) humification in the absence of tyrosinase.

Conclusions

We conclude that co-catalysis of humification occurs by three mechanisms involving physical stabilization of tyrosinase, direct oxidation of the monomers, and promotion of the oxidation and condensation steps by alkaline pH. Although tyrosinase activity is greatest at neutral pHs, the large pH dependence of the condensation step drives the overall reaction to maximum rates under alkaline conditions. Liming of soils to slightly alkaline pH should enhance net carbon sequestration. Alkaline fly ash is a potential liming agent for soils provided that the carbon costs associated with transportation from the source are less than the organic carbon that is humified.

Acknowledgments. Research supported in part by the U. S. Department of Energy's (DOE) National Energy Technology Laboratory, in part by the DOE's Office of Biological and Environmental Research (OBER) through the Carbon Sequestration in Terrestrial Ecosystems (CSiTE) project, and in part by the U. S. Department of Agriculture through the Consortium for Agricultural Soils Mitigation of Greenhouse Gases (CASMGS) project. Research was performed at the W.R. Wiley Environmental Molecular Sciences Laboratory, a national scientific user facility at the Pacific Northwest National Laboratory (PNNL) sponsored by the DOE-OBER. The PNNL is operated for the DOE by Battelle Memorial Institute under contract DE AC06 76RL01830.

References

(1) Metting, F. B. Jr.; Smith, J. L.; Amthor, J. S.; and Isaurralde, R. C. *Climatic Change* **2001**, *51*, 11.
(2) Eswaran, H.; Reich, P. F.; Kimble, J. M.; Beinroth, F. H.; Padmanabhan, E.; and Moncharoen, P. In *Global Climate Change and Pedogenic Carbonates*; Lal, R., Kimble, J. M., Eswaran, H. and Stewart, B. A. Eds.; Lewis Publishers: Boca Raton, FL **2000**. pp. 15-25.
(3) Houghton, R. A.; Hobbie, J. E.; Melillo, J. M.; Moore, B.; Peterson, B. J.; Shaver, G. R., and Woodwell, G. M. *Ecol. Monogr*. **1983,** *53,* 235.
(4) Stevenson, F. J. *Humus chemistry: genesis, composition, reactions. 2nd ed.* Wiley: New York. **1994.**
(5) Martin, J. P.; and Haider, K. *Soil Sci*. **1969**, *107*, 260.
(6) Martin, J. P.; and Haider, K. *Soil Sci*. **1971**, *111*, 54.
(7) Shindo, H.; and Huang, P. M. *Soil Sci. Soc. Am. J*. **1984**, *48*, 927.
(8) Stone, A. T.; and Morgan, J. J. *Environ. Sci. Technol.* **1984**, *18*, 617.
(9) McBride, M. B. *Soil Sci. Soc. Am. J*. **1987**, *51*, 1466.
(10) Amonette, J. E.; Capp, J. A.; Lüttge, A.; Baer, D. R.; and Arvidson, R. S. In *Annual Report 1999, Environmental Dynamics and Simulation*, PNNL-13206/UC-400, **2000**; pp. 3-23 to 3-27.
(11) Amonette, J. E.; Kim, J.; Russell, C. K.; Palumbo, A. V.; and Daniels, W. L. *Proc. 2nd Ann. Conf. Carbon Sequest., Alexandria, VA.* **2003**.
(12) Amonette, J. E.; Kim, J.; Russell, C. K.; Palumbo, A. V.; and Daniels, W. L. *Proc. 2003 Int. Ash Util. Symp. Lexington, KY.* **2003**.

Can We Sequester Large Quantities of Atmospheric Carbon in the Arctic Permafrost?

Professor Alex T. Wilson

Dept. of Geosciences
University of Arizona
Tucson, Arizona 85721

Introduction

A band of Boreal Forest stretches around the Northern Hemisphere land masses. The northern section of this forest becomes stunted trees, which thin out, and muskeg (bog) begins to appear. This area is called the Taiga. Still further north, the trees give way to the Tundra. The Arctic Tundra covers 13 million square kilometers. The surface of the tundra comprises a thin layer of peat, which is thawed and frozen during each annual cycle. By the end of an Arctic winter, everything is completely frozen. During the summer, the surface of the Arctic bog thaws. This thawed layer is called the active layer and its thickness is a constant for a given climate regime. The region under the active layer remains permanently frozen and is called permafrost. It may be hundreds of feet thick.

The plants that grow in this "active layer" have adequate water and a reasonable amount of sunlight, but have a very small supply of nutrients. Since the tundra plants are underlain by permanently frozen ground, the only nutrient supply is via the air. If some way could be found to supply nitrogenous fertilizer to these plants, it would lead to a great increase in the plant production rate. This would raise the level of the surface, which in turn would raise the surface of the permafrost, since the active layer is of constant thickness. The rising of the surface of the permafrost would trap organic matter, removing it from interacting with the atmosphere.

This would lead to the permanent sequestration of atmospheric carbon in the permafrost. This paper suggests how this might be done on a scale that could make a large contribution to the mitigation of the Greenhouse Problem.

Plant Growth Rates in the Tundra

The plant growth or dry matter production rates in the Arctic tundra are incredibly low – of the order of 10 lbs/acre/yr. Compare this to 5,000 lbs./acre /yr on temperate grazing land. The Arctic tundra has adequate water and comparable solar energy, albeit 24 hours a day and only in the summer. The problem is that the nutrient supply is extremely low. The tundra plants are underlain by frozen material and the only nutrient supply is via the air.

The principal source of utilizable nitrogen is probably from the Aurora Borealis--a few pounds of N per acre per year. The most critical nutrient is nitrogen. If nitrogenous fertilizer could be added to these plants, the dry matter production rate would increase, and the surface of the peat would rise. This would cause the permafrost surface to rise, which would lead to the entrapment of large quantities of atmospheric carbon.

The most economical source of nitrogen would be to operate high temperature gas turbines fueled by the abundant quantities of natural gas and methane-water clathrates found in the Arctic. If atmospheric air is heated to high temperatures, for example by lightning, by the Aurora Borealis, by passing through an electric plasma arc, or in a gas turbine, nitrogen is oxidized to nitric oxide and nitrogen dioxide (NOx).

In the natural environment, these rapidly convert to nitrate, and would result in very efficient foliar application (directly to the leaves) of nitrate to the tundra plants. The foliar application of this fertilizer could result in up to a hundredfold increase in the growth rate of tundra plants.

Nitrogen can be oxidized by direct combustion at very high temperatures. Since the reaction is endothermic, the proportion of oxidized nitrogen at equilibrium rises rapidly with the temperature. With the air at atmospheric pressure, the amount oxidized is 1.2 % by volume at 2000 C, and 5.3 % at 3000 C. This was the basis of the industrial fixation of nitrogen. (Birkeland-Eyde process, which used a plasma arc).

Special high-temperature gas turbines could be developed using ceramic parts. By adjusting the temperature of operation of the gas turbines, the amount of fixation and hence the carbon dioxide composition of the Earth's atmosphere could be controlled. The thermodynamic efficiency of a power station is proportional to the difference of the absolute temperature of the turbine and the absolute temperature of the discharge, divided by the absolute temperature of the turbine. Hence, it is desirable for power plants to operate at as high a temperature as possible. In populated areas temperatures are limited by NOx emissions.

In the Arctic tundra the soils, lakes and rivers are all very acidic due to the presence of humic acid. The overall reaction consumes atmospheric nitrogen and produces basic nitrogen compounds, which will lead to the overall reduction of total acidity.

Evidence That Power Stations Can Increase the Growth Rate of Tundra Plants

BP-Alaska has been operating gas turbines at its installation at Prudhoe Bay for the last 30 years. This installation is in the middle of the Central Alaska Caribou Herd range. In 1970, the herd had 3000 animals. At present, the herd has grown to 36,000—a twelve-fold increase. The arctic caribou herds range in distinct areas with little interchange of animals among herds. The Central Arctic Caribou Herd occupies a 15,000 square mile area around Prudhoe Bay, and the herd ranges on 10 million acres in which is situated the BP-Alaska oil field operation at Prudhoe Bay. The adjacent herds have increased slightly but less than a factor of two.

Assume that each caribou consumes 2.5 tons of above-ground dry matter per year. As noted above, in 1970 the herd had 3000 members. This represents a "carrying capacity" of one caribou/3000 ac. This implies a dry matter production rate of 2 lb/ac for this tundra area in its original state. At present, the herd has increased by a factor of 12 – a remarkable feat by normal agricultural standards.

As stated earlier, the increase in the Central Alaska Caribou Herd could be interpreted as a sizable increase in the above-ground dry-matter production rate. There should be a new lens of peat in this area, which could prove direct evidence of sequestered atmospheric carbon.

Clearly, the Prudhoe Bay "experiment" is an important pilot project and should be studied in detail. (Interestingly, BP Alaska has tried to keep its NOx levels as low as possible.) The increase in caribou numbers implies an above-ground dry matter production rate of 24lb/ac/yr. This represents an increase in the total production rate of 110,000 tons/year. To determine the amount of carbon sequestered, we should double this figure, since most plants have as much growth below the ground as above, and multiply by 0.4 (peat contains about 40% carbon).

The implication is that the Prudhoe Bay turbines are sequestering 100,000 tons of atmospheric carbon per year. We might be able to increase this by an order of magnitude. If we burn one ton of carbon (as methane) in a gas turbine situated in tundra muskeg, how many tons of carbon will be sequestered as frozen peat? On the basis of passing the methane through at a 8% fuel/air

ratio, and with the turbine operating at a temperature of 2000 C, we would fix 1.2% of the contained nitrogen, which would be ¼ ton. On the assumption that permafrost peat has a C/N ratio of 800 and that we lose half the nitrogen fixed (through denitrification and other losses), we might expect to remove 100 tons of carbon (as CO2) from the atmosphere. If the turbine could be operated at 3000 C, this number would be 440 tons of carbon sequestered for each ton of methane carbon burned.**Advantages of Sequestering Carbon With High-Temperature Gas Turbines**

This could be a method of controlling, rather than reducing, the CO2 composition of the atmosphere. In addition, it can be done at no net cost to the public; in fact, it can be done at a profit. And this method will enhance and not harm the tundra ecosystem, which comprises 10% of the Earth's land surface.

The Current Importance of the Tundra in Sequestration

Since the end of the last ice age, more than 400 gigatons of carbon has been accumulated as frozen peat in the Arctic permafrost. This represents more than 60 times the amount of carbon put into the atmosphere every year by humankind. If the temperature of the Arctic is allowed to rise (which seems to be happening now) the thickness of the active layer will increase, the surface of the permafrost will melt, and large quantities of carbon will be released to the Earth's atmosphere.

However, even if the temperature of the Arctic rises, we could still prevent the permafrost from melting by making the surface plants grow more rapidly, as is previously described.

The Potential Future of the Tundra

It is interesting to note that the tundra is the only remaining region of our planet with adequate sunlight and water that has not been agriculturally exploited by humankind.

If this proposal was implemented, a possible future scenario might be the following: The tundra would have methane–burning gas turbine power stations at 200 mile intervals on large natural gas pipelines. The turbines would be large and high-temperature, designed to throw their plume high into the atmosphere to get as much coverage as possible. As the productivity rises, other nutrients may be required (e.g. trace elements) and a solution of these could be sprayed into the turbine discharge.

Transmission lines would send electric power to southern population centers. The increased productivity of the tundra would enable reindeer (a domesticated version of caribou) and musk ox ranching, adding to the Arctic economy and providing an additional source of high-quality protein for marketing to the world. Finally, the gas turbine stations would be adjustable to control the carbon dioxide composition of the atmosphere to produce an optimum temperature for the Earth – which might be different than that of the present.

The Current Opportunity

In the Energy Bill before Congress there is a proposal to build a very large natural gas pipeline from Prudhoe Bay to Chicago. This will present a low cost opportunity to set up such a system as proposed above. It offers an opportunity to use large quantities of Alaskan natural gas without any net addition of carbon dioxide to the atmosphere. Further, it would act as a model for using eastern Siberian natural gas in China. There are large deposits of natural gas and vast areas of tundra immediately to the north of China, which could yield large amounts of energy with no addition of carbon to the atmosphere. In fact, it would almost certainly have the net effect of removing carbon from the atmosphere. This may be an alternative to China's use of its coal deposits.

COMMENTS ON THE WEST COAST REGIONAL PARTNERSHIP AND RELATED ACTIVITIES

Terry Surles

Director and CEO, Pacific International Center for High Technology Research (PICHTR), Public Interest Energy Research (PIER) Program Director, California Energy Commission (CEC), 1516 9th Street, Sacramento, CA 95814-5512

The California Energy Commission has recently been given one of the regional CO_2 sequestration partnerships from the US Department of Energy (DOE). The purpose of this talk will be to provide an overview of DOE's efforts in developing a sustained program commencing in 1997. There will also be a discussion on some of the related sequestration efforts by the Energy Commission and its partners which includes Oregon, Alaska, Washington, and Nevada, Electricity Innovation Institute, BP, Shell/AERA, Occidental Petroleum, Lawrence Berkeley and Lawrence Livermore National, Kinder-Morgan, and utility partners. The discussion will focus on the need for a balanced portfolio to address atmospheric carbon dioxide concentration increases within the sequestration area. The discussion will also focus on the need to address key technological and infrastructure barriers, as well as addressing environmental, institutional, regulatory, and public perception issues for terrestrial, geological, and ocean sequestration.

REACTIVITY OF SERPENTINE IN CO_2-BEARING SOLUTIONS: APPLICATION TO CO_2 SEQUESTRATION

J. William Carey, Hans-Joachim Ziock, and George D. Guthrie, Jr.

Earth and Environmental Sciences
Los Alamos National Laboratory
Los Alamos, NM

Introduction

Fossil fuels produce CO_2, which is a significant greenhouse gas that contributes to global warming. Environmentally benign use of fossil fuels requires that CO_2 be captured and sequestered. The reactivity of CO_2 with minerals is important to several sequestration strategies. These include aboveground mineralization in which mined rock is reacted with CO_2 to form permanent carbonates and belowground geologic sequestration in which the amount of *in situ* mineralization is an important factor in repository performance. As part of a general investigation of mineral reactivity in the H_2O-CO_2 system, we have investigated the reactivity of serpentine [$Mg_3Si_2O_5(OH)_4$] with H_2O and CO_2 as a function of pH and the addition of potential catalyzing agents (weak acids). Serpentine is a prime candidate for aboveground mineralization but could also occur as a caprock for the injection of CO_2 belowground.

Experimental

Mineral reactivity studies were conducted in an externally heated, stirred batch reactor (1.8 L Parr autoclave) with a high-pressure CO_2 atmosphere applied using a gas-booster pump. All of the experiments described were conducted at 150 ºC and 2300 psi (15.9 MPa) for periods of 2 to 10 hours. The reactor included a sampling device for extracting fluids during the course of the experiment. Speciation and equilibrium calculations for the fluids were conducted using the Geochemist's Workbench software package with activity coefficients based on the Debey-Hückel equation. The software database was modified to include a more accurate representation of the solubility of CO_2 at elevated pressure.

Results and Discussion

Thermodynamic calculations indicate that in CO_2-rich fluids serpentine should react to produce magnesite ($MgCO_3$) and silica at moderate temperatures and pressures, including those used in our experiments. Many of our experiments were conducted in de-ionized water (DI) or systems containing 1 m NaCl or 1 m NaCl + 0.64 m $NaHCO_3$. None of these simple systems yielded detectable magnesite (0.1-0.2 wt%) over the course of the experiments, and x-ray diffraction analysis of the run products showed that the serpentine was unchanged.

However, experiments with strong acid (HCl) completely destroyed the serpentine and produced solutions rich in Mg^{2+} but from which no carbonate could be directly formed. Back-scattered electron imagery showed that the acid leached the Mg^{2+} from the serpentine, leaving behind a husk of amorphous silica. The leaching effect is highly desirable because it produces an insoluble residue of silica that could be easily separated with the magnesite, if the Mg^{2+} could be precipitated with CO_2.

In an attempt to preserve the aggressive effects of HCl but operate at more moderate pH, the reactivity of serpentine with a series of weak organic and inorganic acids was investigated (Table 1). Some of these acids re also known to be effective chelating agents. None of these experiments with weak acids produced magnesite, although many produced solutions very rich in total Mg. Because of a lack of thermodynamic data, it was not possible to calculate the equilibrium speciation for these solutions. We suspect that many of these solutions contained Mg-ligand complexes that could not be displaced by the carbonic acid generated by the dissolution of CO_2. In other cases, a precipitate formed that was less soluble than magnesite under our experimental conditions.

Table 1. Organic and Inorganic Acids Used to Enhance Serpentine Reactivity

Solution†	Dissolution Extent	Comment
Citric Acid	Large increase	Mg-citrate too strong
EDTA	Large increase	Mg-EDTA too strong
Oxalic acid	Large increase	Mg-oxalate insoluble
Phosphoric acid	Large increase	Mg-phosphate insoluble
Formic acid	Large increase	Solution too acidic
Ascorbic acid	Moderate increase	No carbonate
Maleic acid	Moderate increase	No carbonate
Tartaric acid	Moderate increase	No carbonate
Glycine	Moderate increase	No carbonate
Pthalic acid	Moderate increase	No carbonate
Malonic acid	Moderate increase	No carbonate
Aspartic acid	Moderate increase	No carbonate
Iminodiacetic acid	Small increase	No carbonate
Acetic acid	Small increase	No carbonate
Asparagine	Small increase	No carbonate
Salicylate	Small increase	No carbonate

†NaOH was used in many of the solutions to moderate the pH

Thermodynamic Analysis. Measured solution compositions were used to make equilibrium calculations for experiments in DI, NaCl-$NaHCO_3$, and Na-acetate (Figure 1). These three cases span a range of pH and ionic strength. The DI experiment produced the lowest calculated pH and highest activity of Mg^{2+}, and the NaCl-$NaHCO_3$ experiment produced the highest pH and lowest activity of Mg^{2+}. All of the experiments had solutions that were calculated to be at saturation or supersaturated with magnesite, although none yielded magnesite identifiable by x-ray diffraction.

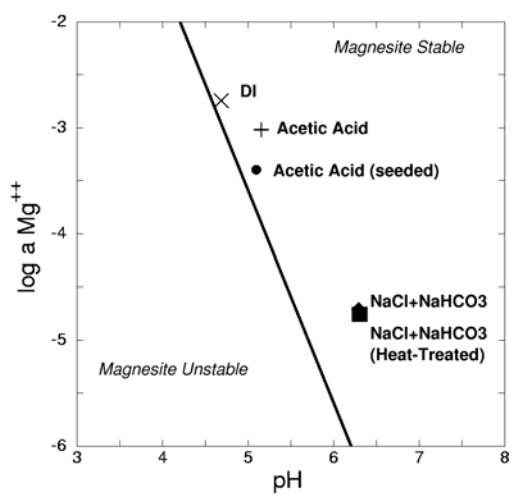

Figure 1. Thermodynamic calculations of solution activities based on measured solution compositions for batch reactor experiments at 150 ºC, 2300 psi total pressure $_{CO2}$ (approximated as with a fugacity of 12.5 Mpa). All of the experiments are saturated or supersaturated with magnesite.

These results suggested a nucleation barrier to the formation of magnesite. However, the Na-acetate experiment was repeated with the addition of 20 wt% magnesite seeds. The x-ray diffraction result

(19.8 wt% magnesite) was indistinguishable from no reaction. In addition, the solution composition was not significantly different than in the unseeded experiment (Figure 1).

The experiment with magnesite seeds indicates that nucleation of magnesite is not rate limiting. This is consistent with experiments on other Mg-oxide phases (see below) that generate magnesite.

Kinetics of Dissolution. The lack of observable precipitation could be explained if the rate of serpentine dissolution was sufficient to reach saturation but insufficient to produce a measurable quantity of magnesite. Carey et al.[1] obtained rates of dissolution for serpentine at far from equilibrium condtions (and in the absence of CO_2), including activation energies, that allow prediction of the evolution of Mg concentration in the batch reactor experiments (Figure 2). These calculations show that as much as 5-10 wt% magnesite could be produced based solely on the dissolution rate of serpentine. These calculations are conservative since the observed concentration of Mg is higher than the predicted concentrations. Consequently, a purely dissolution-limited process does not explain the lack of magnesite.

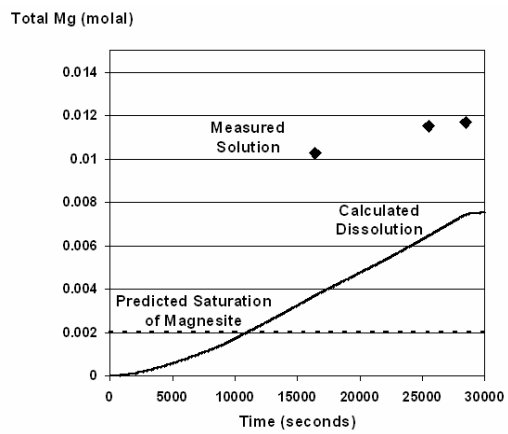

Figure 2. Measured solution compositions for batch reactor experiments at 150 ºC, 2300 psi total pressure CO_2 compared with the Mg concentration at saturation of magnesite and a calculated dissolution path based on the kinetic measurements of Carey et al[1].

Observations of the Reactivity of Other Mg-Oxides. The reactivity of serpentine can be compared with other Mg-bearing silicates and oxides. Periclase (MgO) and brucite [$Mg(OH)_2$] are readily carbonated; forsterite ($MgSiO_4$), with structurally isolated SiO_4 tetrahedra, carbonates to a significant degree; enstatite ($MgSiO_3$), with structural chains of SiO_4 tetrahedra, carbonates slowly; while serpentine, which consists of sheets of SiO_4 tetrahedra, is unreactive. These observations indicate that the greater the degree of silica polymerization, the less reactive is the Mg-silicate.

Methods of Inducing Reactivity in Serpentine. Three energy-intensive methods have been identified that allow carbonation of serpentine. Heat-treatment to 650 ºC dehydroxylates serpentine, disrupting the structure, and permits significant carbonation over a several hour period. Although the heat-treated serpentine can be carbonated, the resulting solution composition is indistinguishable from an experiment using raw serpentine (Figure 1). If the serpentine is heated to 840 ºC and the structure is allowed to recrystallize (to forsterite, enstatite and amorphous residue), then the degree of reactivity is reduced. Intense mechanical grinding, which renders serpentine nearly x-ray amorphous, also permits substantial carbonation[2]. These observations indicate that structural disruption of serpentine enhances reactivity.

A third method for inducing reactivity utilizes a strong acid (e.g., concentrated HCl) to leach the Mg^{2+} from the serpentine, followed by neutralization of the solution with a strong base (e.g., NaOH) to saturate the solution with magnesite. By analogy with thermal and mechanical treatments, it appears that a strong acid can effectively "disrupt" the structure (i.e., render the Mg^{2+} accessible).

None of these methods are likely to be a solution for CO_2 sequestration. They require too much energy or consume too much material. If the cost of sequestration becomes too high, alternative forms of energy become economically favorable.

Conclusions

The exact kinetic factors limiting the reactivity of serpentine remain obscure. Our observations indicate that rate of dissolution of serpentine cannot explain the limited reactivity. We have also shown that nucleation and growth of magnesite occurs in other Mg-oxides and in thermally or mechanically treated serpentine and so limitations due to magnesite cannot explain the lack of carbonation of serpentine.

Our data suggest two possible explanations. We note that Mg-oxides, Mg-silicates with a lower degree of silica polymerization, and thermally and mechanically treated serpentine yield magnesite. On dissolution in water, all of these compounds produce (or are likely to produce) more Mg^{2+} than serpentine does and, upon exposure to CO_2, will be more supersaturated with magnesite than serpentine. In other words, the driving force for the conversion of these materials to magnesite is greater than that for unaltered serpentine. Perhaps, this greater degree of supersaturation overcomes some kinetic barrier, such as the release of Mg^{2+} from the structure or the growth of the Mg-carbonate.

Our second suggestion is that serpentine reacts differently because of the greater degree of silica polymerization (or effectively the lower ratio of Mg to Si). In this model, only the near-surface Mg is accessible for dissolution and precipitation of magnesite. Further growth of magnesite relies on extracting Mg from greater depths in the serpentine crystal where it is effectively shielded by a silica-rich carapace on the serpentine crystal. As a consequence, only a miniscule amount (unmeasurable by x-ray diffraction) of magnesite is produced. Thermal and mechanical treatment of serpentine disrupts the crystal structure thus yielding defects in the silica-enriched carapace. These defects allow for diffusion of Mg^{2+} and the growth of magnesite. The effectiveness of acid may arise from the ability of H^+ ions to penetrate the silica carapace and reasct with the interior Mg-oxy-hydroxy octahedra. This reaction may induce intracrystalline swelling thereby disrupting the carapace. Weak acids promote dissolution (Table 1) but their effectiveness appears to be limited by the reduced concentration of H^+ and the formation of stable Mg-ligand complexes.

Acknowledgement. We thank the National Energy and Technology Laboratory of the Department of Energy for their financial support.

References

(1) Carey, J.W., Rosen, E.P., Bergfeld, D., Chipera, S.J., Counce, D.A., Snow, M.G., Ziock, H.J., Guthrie, G.D., Jr. Experimental Studies of the Serpentine Carbonation Reaction. *Proc. 28th Interna. Tech.l Conf. on Coal Util. & Fuel Sys.* **2003**.

(2) O'Connor W.K., Dahlin, D.C., Nilsen, D.N., Gerdemann, S.J. Rush, G.E., Penner, L.R., Walters, R.P., Turner, P.C. Continuing studies on direct aqueous mineral carbonation for CO_2 sequestration. *Proc. 28th Interna. Tech.l Conf. on Coal Util. & Fuel Sys.* **2003**.

COMPARISON OF PHYSICAL AND CHEMICAL ACTIVATION OF SERPENTINE FOR ENHANCED CO_2 SEQUESTRATION

M. Mercedes Maroto-Valer[1], Matthew E. Kuchta[1], Yinzhi Zhang[1], John M. Andrésen[1], Daniel J. Fauth[2]

[1]The Energy Institute and Department of Energy and Geo-Environmental Engineering, The Pennsylvania State University, University Park, PA 16802, [2]U.S. Department of Energy, National Energy Technology Laboratory, Pittsburgh, PA 15236

Introduction

In response to rising atmospheric concentrations of carbon dioxide (CO_2) and concerns over possible global climate change, focus has been placed on carbon sequestration. Mineral carbonation, the reaction of magnesium-rich minerals with CO_2 to form stable mineral carbonates, is a novel and promising approach to carbon sequestration. Suitable feedstocks include olivine (Mg_2SiO_4) and serpentine ($Mg_3Si_2O_5(OH)_4$) minerals, although serpentine exists in far greater quantities. The reaction of serpentine with CO_2 to form magnesite ($MgCO_3$), silica (SiO_2) and water is shown in Equation 1.

$$Mg_3Si_2O_5(OH)_4 + 3CO_2 \rightarrow 3MgCO_3 + 2SiO_2 + 2H_2O \qquad (1)$$

The mineral carbonation approach offers several inherent advantages: the long term stability of benign mineral carbonates; the vast capacity of natural resources; and the overall process being exothermic, and therefore potentially economically viable. However, the reaction kinetics are a substantial drawback. Previous studies have required extensive communition of the raw minerals (<37 µm), heat treatment (600-650°C), high temperatures (>155°C), high partial pressures (>125 atm), and long reaction times (>6 hours) to overcome the kinetics barriers.

The objective of this research was to investigate the effectiveness of various pretreatment methods aimed to promote and accelerate carbonation reaction rates and efficiencies through surface activation and moisture removal. Previous studies have shown that mineral dissolution rates are surface controlled, and the carbonation reaction stops when the magnesium at the mineral's surface becomes depleted and/or blocked by mass transfer resistance.[1,2] It has also been demonstrated that the inherent water content of serpentine is detrimental to the carbonation process.[1-3] Therefore, it was envisioned that an increase in surface area and decrease in moisture would result in higher reaction rates and efficiencies. This would allow the integration of various synergistic features for the development of a cost-effective sequestration technology, including accelerating the carbonation efficiency without extensive mineral particle communition or heat treatment and lowering the temperature and pressure conditions of the carbonation reactions.

A series of activation experiments were performed on a serpentine mineral to promote its carbonation reactivity. Physical activation was performed with steam, and chemical activations utilized a suite of acids. Several studies were designed to increase the surface area of the mineral and reduce its inherent moisture content, while additional investigations involved the extraction of magnesium from the serpentine to form magnesium-rich solutions and solid magnesium hydroxide ($Mg(OH)_2$). Carbonation studies were then performed with the activated serpentines and solutions.

Experimental

Sample Overview. The serpentine sample was provided by the Department of Energy - Albany Research Center and originally obtained from the Cedar Hills Quarry, which lies along the border between Pennsylvania and Maryland. It was ground to minus 75µm, and a major portion of the iron was removed through a magnetic separation process.

Physical Activation. Physical activation was performed with steam at 650°C in a horizontal tube furnace for 3 hours. Water was supplied by a HPLC pump at 0.5 mL/min and carried by N_2 at 300 mL/min.

Chemical Activation. Chemical activations were performed with a suite of acids: HCl, H_2SO_4, H_3PO_4, and CH_3COOH. Initial activations using HCl, H_2SO_4, and H_3PO_4 were conducted at ambient temperature for 24 hours. Around 200 g of serpentine were reacted with 200 mL of acid in a 2 L beaker and continuously mixed with a magnetic stir bar. Three magnesium extractions were performed at 50°C for 8 hours – two with H_2SO_4 to form $MgSO_4$ solutions and one with CH_3COOH to form a $Mg(CH_3COO)_2$ solution. The extractions were carried out by reacting 50 g of serpentine with 340 mL of distilled water and either 92 g of H_2SO_4 or 57.5 g of CH_3COOH. $Mg(OH)_2$ was precipitated from the leachate of one of the H_2SO_4 extractions by adding NaOH.

Thermogravimetric Analysis (TGA). TGA analyses were performed using a Perkin Elmer TGA 7. The studies were conducted in a non-oxidizing atmosphere of nitrogen (N_2) at atmospheric pressure. Analyses were conducted over a temperature range of 25°C to 900°C, with a constant heating rate of 10°C/minute.

X-ray Diffraction (XRD). XRD analyses were carried out on a Scintag Pad V unit with a vertical theta/2-theta goniometer. The unit utilized a Cu-Kα X-ray source and was operated at a voltage of 35 kV and a current of 30 mA. A quartz zero background holder was used to mount the powder samples during XRD analyses. The samples were analyzed over a 2-theta range of 5.0° to 90.0°, with a step-scan rate of 0.1°/minute. Peaks were identified using the ICDD Powder Diffraction Files.

Inductively Coupled Plasma-Atomic Emission Spectroscopy (ICP-AES). ICP-AES analyses were performed with a Leeman Labs PS3000UV inductively coupled plasma spectrophotometer. Both solutions and solid samples were analyzed, with the solid samples being dissolved by a lithium metaborate fusion technique before analysis. The loss on ignition (LOI) values were calculated by measuring the weight loss of the samples upon heating to 750°C in a muffle furnace for approximately 12 hours, followed by cooling in a dessicator.

Brunauer, Emmett, and Teller Surface Area Analysis (BET). BET surface area analyses were carried out using a Quantachrome Autosorb-1 Model ASIT adsorption apparatus. Adsorption isotherms were obtained under N_2 at a temperature of 77K. The BET surface areas were calculated using the adsorption points at the relative pressures (P/P_o) 0.05 - 0.25.

Scanning Electron Microscopy (SEM). A HITACHI S-3500N was used to conduct the SEM analyses. Experiments were performed using secondary electrons under high vacuum and an accelerating voltage of 20 kV. Images were taken at magnification levels up to 10,000 times, with a working distance of 7-9 mm. The powder samples were mounted on a holder using carbon tape. In addition, the samples were spattered with a thin layer of gold to provide an electrically conductive surface.

Carbonation Experiments. All carbonation experiments were performed at the National Energy Technology Lab (NETL) in Pittsburgh, PA. High temperature and pressure analyses were carried out in a 1 L Hastelloy C-2000 continuous-stirred-tank-reactor (CSTR) unit, while low temperature and pressure carbonation reactions were performed in a 500 mL Hastelloy C-276 CSTR vessel. In a representative high temperature and pressure experiment, 30 g of serpentine and 360 g of buffer solution were charged into the 1 L CSTR, and it was sealed and purged with gaseous CO_2. Liquid CO_2 was injected through a side port until a pressure of 126 atm was

reached. A gas booster pump was used to maintain a relatively constant CO_2 pressure. The unit was heated to 155°C and the carbonation reaction was allowed to proceed for 1 hour. In a representative low temperature and pressure experiment, 180 mL of sample, including buffer, were charged into the 500 mL CSTR, and it was sealed and purged with gaseous CO_2. Liquid CO_2 was injected through a side port until a pressure of 45 atm was reached, and the unit was kept at 20°C. The reaction was allowed to proceed until the CO_2 pressure stabilized. At the end of all carbonation tests, the remaining CO_2 was vented, and the carbonated slurry was flushed from the CSTR and filtered to separate the solids. The solids were washed and dried overnight at 105°C. Carbonation efficiency calculations were based on the concentration of MgO in the starting serpentine solids and the weight gain due to carbonate formation. For the aqueous samples, the conversion was determined by the amount of magnesium that was recovered as magnesium carbonate in the precipitate that formed after carbonation.

Results and Discussion

Characterization of parent and activated serpentine samples XRD results indicated that the primary phase present in the serpentine feed sample was antigorite, $(Mg,Fe^{2++})_3Si_2O_5(OH)_4$. The serpentine was determined to be approximately 39% MgO by weight, with moisture accounting for nearly 14% of the remaining weight. BET surface area analysis reported a surface area of only $8m^2/g$.

After activation, forsterite (Mg_2SiO_4) was the primary phase present in the mineral, along with smaller amounts of antigorite. As expected, physical activation with steam removed much of the moisture from the sample, and the activated serpentine was determined to be 2.6% moisture by weight. An additional 43% of the sample was MgO by weight. The effect on the surface area was minimal (15.8 m^2/g).

The HCl, H_2SO_4, and H_3PO_4 activated serpentines became slightly amorphous after activation, and antigorite was identified as the primary mineral phase present within the samples. The chemical activations did not effectively reduce the moisture content of the minerals, with moisture accounting for approximately 11% of each sample by weight. Surface areas were increased by up to two orders of magnitude, ranging between 80 m^2/g for the HCl activated serpentine and 330 m^2/g for the H_2SO_4 activated serpentine. However, chemical treatments resulted in a net loss of MgO from the serpentine, with the MgO content being reduced to as low as 12% by weight for the H_2SO_4 activated serpentine. Thus, although the chemical treatments of serpentine were effective in raising the surface area of the mineral, they essentially decreased the mineral MgO content, and therefore decreased the amount of CO_2 that could potentially be sequestered by the treated serpentine.

The characterization results from the acid treated solids indicated the possibility of extracting the magnesium into solution as Mg^{2+} ions. In particular, over 70% of the magnesium was removed during treatment with H_2SO_4. Consequently, three additional chemical treatments were performed to produce solutions with high Mg^{2+} ion concentrations.

Two $MgSO_4$ solutions were produced by reacting serpentine with H_2SO_4, and one of the solutions was used to produce solid $Mg(OH)_2$. The $MgSO_4$ solution that was directly carbonated had a magnesium concentration of 13,000 ppm by volume. The precipitated $Mg(OH)_2$ was determined to be approximately 35% MgO by weight. Na_2SO_4, which formed during precipitation with NaOH, and moisture accounted for much of the remaining sample weight. XRD results indicated that the sample consisted primarily of $Mg(OH)_2$ and Na_2SO_4. The magnesium concentration of the $Mg(CH_3COO)_2$ solution was found to be 5,250 ppm by volume. As the ICP-AES results indicate, both H_2SO_4 and CH_3COOH were effective in creating a solution with Mg^{2+} ions being the dominant species, although treatment with H_2SO_4 resulted in a much higher Mg^{2++} dissolution.

Carbonation studies Table 1 contains a summary of the carbonation reaction conditions and conversions for the untreated and activated serpentines and solutions. The chemically activated serpentines (HCl, H_2SO_4, and H_3PO_4) did not sequester any CO_2. In fact, the amount of sample that was recovered at the end of the carbonation experiments was less than that which was originally placed in the reactor. This small weight loss was accredited to the removal of moisture during the experiments. Similarly, the carbonation of the $Mg(CH_3COO)_2$ solution did not result in the formation of a carbonate. The amount of precipitate that formed in the solution was negligible. A sizeable amount of precipitate formed in the carbonated $MgSO_4$ solution. However, XRD analysis of this precipitate identified limited amounts of magnesium carbonate minerals. The primary constituent was determined to be Na_2SO_4. Further investigation into the roles of each chemical species present within the carbonation solutions is necessary to determine why the Mg^{2+} ions in the $MgSO_4$ and $Mg(CH_3COO)_2$ solutions did not react with CO_2 to form carbonates.

On the other hand, the untreated parent serpentine, the physically activated serpentine, and the $Mg(OH)_2$ solution underwent varying degrees of carbonation. The untreated parent sample underwent a 7% conversion at 155°C and 126 atm in 1 hour. Under identical conditions, the steam activated serpentine underwent a 60% conversion, illustrating the benefit of removing moisture from the serpentine. However, high temperature treatment is very energy intensive. CO_2 was also sequestered during the carbonation of the $Mg(OH)_2$ solution. Based on the amount of magnesium recovered in the precipitate after the 3.5 hour reaction, the carbonation efficiency was estimated to be at least 53%.

Carbonation products varied for the reactions and included magnesite ($MgCO_3$) and several hydrated magnesium carbonate minerals. The high temperature and pressure reactions with the untreated parent sample and the physically activated serpentine resulted in the formation of $MgCO_3$. The rhombohedral-shaped $MgCO_3$ crystals that formed during the carbonation of the physically activated serpentine are shown in Figure 1.

Table 1. Summary of Carbonation Experiments with Physically and Chemically Activated Serpentine

Sample	Temperature (˚C)	Pressure (atm)	Time (hr)	Buffer Composition	Conversion
Untreated Parent Serpentine	155	126	1	0.6 M $NaHCO_3$; 1.0 M NaCl	7
Steam Activated Serpentine	155	126	1	0.6 M $NaHCO_3$; 1.0 M NaCl	59
HCl Activated Serpentine	155	126	1	0.6 M $NaHCO_3$; 1.0 M NaCl	---
H_2SO_4 Activated Serpentine	155	126	1	0.6 M $NaHCO_3$; 1.0 M NaCl	---
H_3PO_4 Activated Serpentine	155	126	1	0.6 M $NaHCO_3$; 1.0 M NaCl	---
$Mg(CH_3COO)_2$ Solution	20	45	4	1.34 g NaOH	---
$MgSO_4$ Solution	20	36	6	8.11 g NaOH	---
$Mg(OH)_2$ Solution	20	45	3.5	Reverse Osmosis Water	53

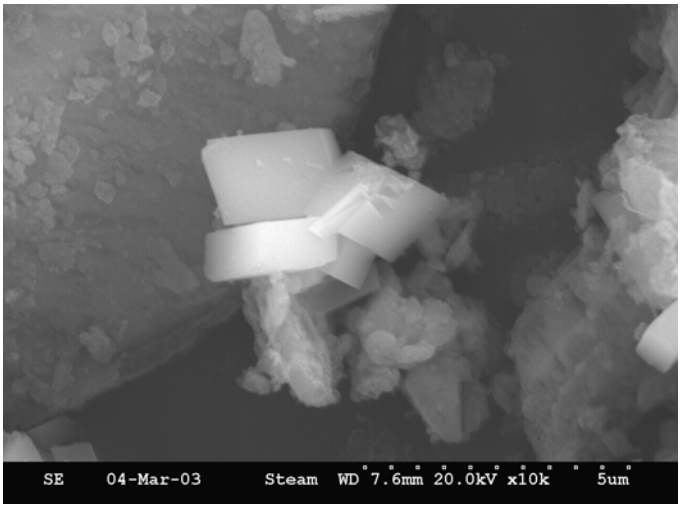

Figure 1. SEM image of magnesite crystals ($MgCO_3$) that formed during the carbonation of the physically activated serpentine (10,000X).

At lower temperatures and pressures, the carbonation of the $Mg(OH)_2$ solution resulted in the formation of various hydrated magnesium carbonates, primarily nesquehonite ($MgCO_3 \cdot 3H_2O$). Figure 2 shows an SEM image of the CO_2 that was sequestered in the carbonated $Mg(OH)_2$ solution and precipitated as nesquehonite.

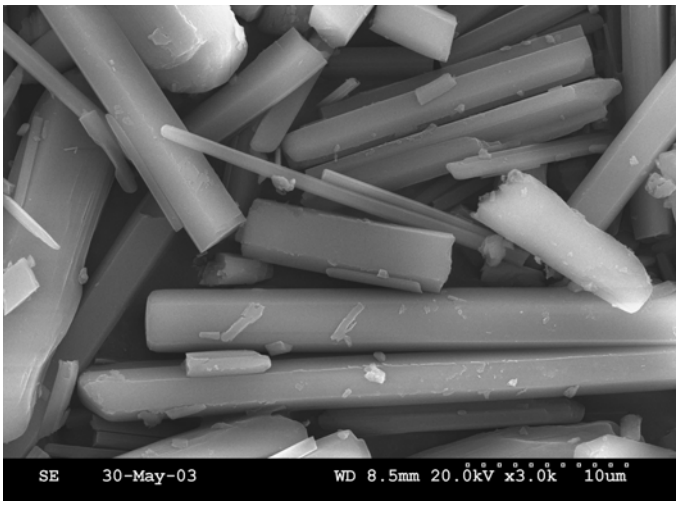

Figure 2. SEM image of nesquehonite crystals ($MgCO_3 \cdot 3H_2O$) that formed in the carbonated $Mg(OH)_2$ solution (3,000X).

The formation of hydrated magnesium carbonates, as opposed to magnesite, is due to the carbonation reaction conditions. During crystallization in aqueous processes, magnesite often associates with 1, 3, or 5 water molecules.[4] This is especially true in reactions conducted at low temperatures and CO_2 pressures, where hydrated forms of magnesite may form more readily than anhydrous magnesite.[5,6]

Conclusions

Mineral carbonation has been studied as a promising approach to carbon sequestration. However, unfavorable reaction conditions have forced previous studies to require energy-intensive operating conditions, including high temperatures and pressures, heat treatment, and extensive particle communition. Thus, the objective of the research presented within this paper was to promote and accelerate carbonation reaction rates and efficiencies through surface activation to the extent that such rigorous reaction conditions were not required. Additional studies were aimed at extracting the magnesium from the minerals for subsequent carbonation under milder reaction conditions.

Experimental results indicate that the surface area of the raw serpentine, which is approximately 8 m^2/g, can be increased through physical and chemical activation methods to over 330 m^2/g. The chemical activations were more effective at increasing the surface area, while the physical activation was more effective at reducing the moisture content of the serpentine. H_2SO_4 was the most effective acid used during the chemical activations, resulting in a mineral surface area greater than 330 m^2/g and the extraction of over two-thirds of the magnesium present within the serpentine.

The most promising results came from the carbonation of the $Mg(OH)_2$ solution. A carbonation efficiency of nearly 53% was observed, comparable to the physically activated serpentine that showed a 60% conversion at 155°C under 126 atm of CO_2 pressure. However, the $Mg(OH)_2$ carbonation reaction was conducted at ambient temperature, 20°C, and low pressure, 45 atm. These reaction conditions are indeed a significant improvement over previous studies that have required temperatures over 155°C and pressures of at least 125 atm. Furthermore, high-temperature heat treatment was avoided and a coarser particle size, 75 µm, was used in this work, compared to <37µm in previous studies. Finally, a provisional patent has been submitted based on this work.

Acknowledgements. The work presented within this paper was funded by the U.S. Department of Energy through their University Coal Research Program, under grant DE-FG2601-NT41286. It was also supported by the Energy Institute and the Department of Energy and Geo-Environmental Engineering at the Pennsylvania State University. The authors would also like to thank W.K. O'Connor from U.S DOE Albany Research Center for providing the serpentine samples and helpful discussions.

References

(1) O'Connor, W.K.; Dahlin, D.C.; Rush, G.E.; Dahlin, C.L.; Collins, W.K. Carbon Dioxide Sequestration by Direct Mineral Carbonation: Process Mineralogy of Feed and Products. *Miner. Metall. Process*. **2002,** *19* (2), 95-101.

(2) O'Connor, W.K.; Dahlin, D.C.; Nilsen, D.N.; Rush, G.E.; Walters, R.P.; Turner, P.C. Carbon Dioxide Sequestration by Direct Mineral Carbonation: Results from Recent Studies and Current Studies. Presented at the 1st National Conference on Carbon Sequestration, Washington, D.C., May 14-17, **2001**.

(3) Lackner, K.S.; Wendt, C.H.; Butt, D.P.; Joyce, E.L.; Sharp, D.H. Carbon Dioxide Disposal in Carbonate Minerals. *Energy* **1995**, *20* (11), 1153-1170.

(4) Park, A.H.A.; Jadhav, R.; Fan, L.S. CO_2 Mineral Sequestration: Chemically Enhanced Aqueous Carbonation of Serpentine. *Can. J. Chem. Eng*. **2003**, *81*, 885-890.

(5) Wendt, C.H.; Butt, D.P.; Lackner, K.S.; Ziock, H.J. Thermodynamic Considerations of Using Chlorides to Accelerate the Carbonate Formation from Magnesium Silicates. Presented at the 4th Int. Conf. on Greenhouse Gas Control Technologies, Interlaken, Switzerland, August 30 - September 2, **1998**.

(6) McKelvy, M.J.; Chizmeshya, A.V.G.; Bearat, H.; Sharma, R.; Carpenter, R.W. Developing a Mechanistic Understanding of Lamellar Hydroxide Mineral Carbonation Reaction Processes to Reduce CO_2 Mineral Sequestration Process Cost. Presented at the 17th Annual Int. Pittsburgh Coal Conf., Pittsburgh, PA, September 11-15, **2000**.

CO_2 MITIGATION VIA ACCELERATED LIMESTONE WEATHERING

Greg H. Rau[a,b], Kevin G. Knauss[b], William H. Langer[c], Ken Caldeira[b]

[a]Institute of Marine Sciences, University of California, Santa Cruz, CA 95064
[b]Energy and Environment Directorate, LLNL, Livermore, CA 94550
[c]US Geological Survey, Denver, CO 80225

Introduction

The climate and environmental impacts of our current, carbon-intensive energy usage demands that effective and practical energy alternatives and CO_2 mitigation strategies be found.[1,2] As part of this effort, various means of capturing and storing CO_2 generated from fossil-fuel-based energy production are being investigated.[3] One of the proposed methods involves a geochemistry-based capture and sequestration process[4,5] that hydrates point-source, waste CO_2 with water to produce a carbonic acid solution. This in turn is reacted and neutralized with limestone, thus converting the original CO_2 gas to calcium bicarbonate in solution, the overall reaction being:

$$CO_{2(g)} + CaCO_{3(s)} + H_2O_{(l)} \Rightarrow Ca^{2+}_{(aq)} + 2HCO_3^-{}_{(aq)}. \quad (1)$$

The dissolved calcium bicarbonate produced is then released and diluted in the ocean where it would add minimally to the large, benign pool of these ions already present in seawater.

Such a process is geochemically equivalent to continental and marine carbonate weathering which can otherwise naturally consume most anthropogenic CO_2, but over many millennia.[6-8] We identify the enhanced form of this process as Accelerated Weathering of Limestone or AWL. Previously, it has been shown that AWL can effectively convert a significant fraction of US CO_2 emissions to long-term storage as bicarbonate in the ocean, while avoiding or possibly reversing environmental impacts associated with either the ongoing passive or the proposed active injection of CO_2 into the ocean.[5,9] Being analogous to the wide-spread use of wet limestone to desulfurize flue gas, AWL reactors could be retrofitted to many existing coastal power plants at a typical cost estimated to be \$20-\$30/tonne CO_2 mitigated.[4,10]

Limestone and Seawater Availability and Cost

Based on reaction 1, it would take 2.3 tonnes of calcium carbonate and 0.3 tonnes of water to react 1 tonne of CO_2 to form 2.8 tonnes of HCO_3^- in solution. It is envisioned that abundant and inexpensive limestone (containing 92-98% $CaCO_3$) would be used. US production of this mineral is presently 10^9 tonnes/yr, with reserves sufficient to satisfy US demand for many decades if not centuries. Channeling the entire yearly US limestone production to AWL could consume roughly 18% of the annual CO_2 generated by electricity production in the US.

However, currently more than 20% of US limestone production and processing results in waste limestone fines (<10 mm) that have little or no market value and are accumulating at limestone mining and processing sites.[11,12] This suggests that a sizeable, free or low-cost source of limestone could be available for AWL whose use could also help alleviate the significant limestone waste problem.

Because of the significant quantities of water required to react the CO_2 and to carry and dilute the resulting bicarbonate (>10^4 tonnes H_2O/tonne CO_2; ref. 4), AWL reactors in close proximity to seawater would be at a distinct advantage. About 12% of CO_2 emissions from US electricity production occurs at plants within 10 km of the US coastline.[10] Fortuitously, the majority of this coastline is also within 400 km of known limestone reserves.[13] This is especially true of the southern and eastern seaboard that also has the highest density of coastal US power plants and coastal electricity-related CO_2 production. For example there is more than 20 GW of fossil-fueled power generation (≈100 billion tonnes CO_2 emitted/yr) by coastal power plants in Florida[10], a state that is almost entirely underlain by carbonate deposits.[14]

In such ideal settings, if both limestone and its transportation costs were negligible, the CO_2 mitigation cost offered by AWL could be \$3 - \$4/tonne CO_2 based on previous cost analyses.[4,10] This would especially pertain if the hundreds of millions of gallons of seawater already pumped and used for cooling by these plants each day were in turn used as a "free" AWL water source. This cost is significantly lower than most other current or proposed abiotic technologies.[3] However, the number of ideal sites and hence the volume of CO_2 that could be treated at this very attractive cost would be small. Considering water, limestone, and transportation cost in more typical coastal settings suggests that 10-20% of US energy CO_2 emissions could be mitigated at \$20-\$30/tonne. This is still very cost-competitive with other methods, especially considering that the cost of conventional amine CO_2 capture (not required for AWL) is generally >\$30/tonne CO_2 (ref. 15).

The preceding assumes an AWL reactor sited at the source of waste CO_2 (i.e. a power plant) and to which limestone and seawater are transported. Alternatively, CO_2 generated at inland locations could be transported to coastal AWL reactors sited at or near limestone quarries. Transport of CO_2 is inexpensive (\$0.06 tonne^{-1} km^{-1}, ref. 16) relative to the cost of transporting the AWL- equivalent (2.5 tonnes) of limestone. However, this would require initial CO_2 separation, capture, and liquefaction, with the associated technology and energy costs that are presently significant, as mentioned above. Still, if inexpensive CO_2 capture/separation is developed, piping CO_2 to coastal AWL reactors could prove cost-competitive with other forms of CO_2 sequestration such as underground storage, especially in regions where the underlying geology is not amenable to CO_2 retention.

Reaction Rates and Densities

The results of experiments in our laboratory yielded limestone dissolution rates ranging from roughly 10^{-7} to 10^{-5} mols m^{-2} s^{-1} with positive sensitivity to flow rate, stir rate, and CO_2 concentration. Dissolution rates in seawater were equal to or higher than those in distilled water under otherwise identical conditions.

Assuming a reaction rate of 10^{-6} mols m^{-2} s^{-1} is achievable in large-scale reactors, a bed of 1mm-diameter limestone particles (typical of waste limestone fines discussed above) yields an surface area/volume of ≥4.4 x10^3 m^2/m^3. Therefore a maximum of 60 m^3 of such limestone particles would be needed to react 1 tonne of CO_2 per day. For a cubic reactor volume (roughly 4m x 4m x 4m), this equates to an areal reaction rate of at least 15 tonnes CO_2 m^{-2} day^{-1}, or about a million times greater than optimum biotic CO_2 uptake and sequestration rates.[16] The experiments suggest that this density of CO_2 conversion to HCO_3^- could be increased by as much as an order of magnitude by increasing stirring and flushing rate, though at added energy and cost penalties.

Effectiveness

Using a box model of ocean chemistry and transport Caldeira and Rau[5] showed that the release of the bicarbonate-charged effluent from carbonate dissolution would more effectively sequester CO_2 over the long term relative to direct CO_2 injection at equivalent ocean depths. This has been subsequently confirmed for releases at several different ocean locations and depths in a 3-D ocean general circulation model (**Figure 1**). Injection of pure CO_2 at great depth in

the ocean effectively stores most of the injected carbon for hundreds of years or more.[5] Therefore, the additional slowing of CO_2 leakage that would be gained by releasing carbonate dissolution effluent at the same depth may not be economically significant. Nevertheless, we note that carbonate dissolution can make a major contribution for less costly shallow-water releases and greatly improves effectiveness of long-term ocean carbon sequestration regardless of the depth at which the effluent is released.

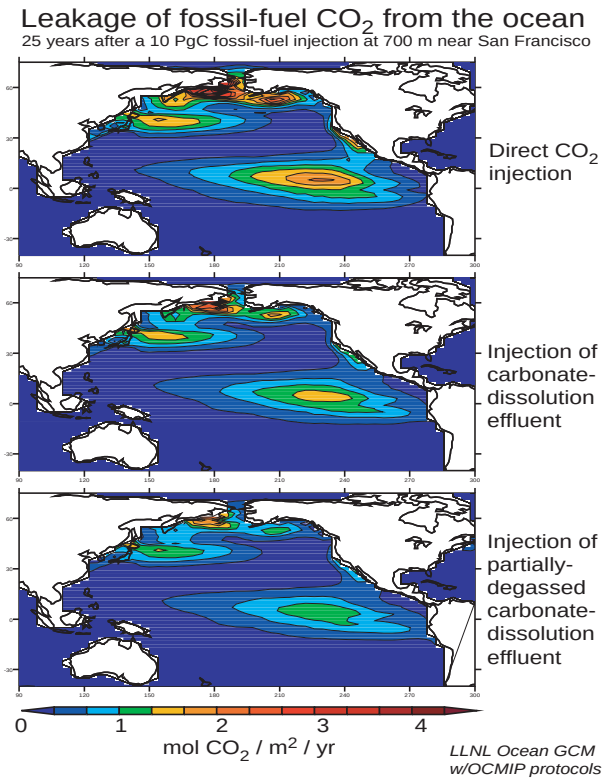

Figure 1. Ocean general circulation model results showing the greater effectiveness (less CO_2 leakage to atmosphere) inherent in the injection of carbonate dissolution effluent as compared to molecular CO_2 at equivalent depths.

Environmental Impacts/Benefits

An increase in ocean acidity (reduction in pH) is a serious environmental issue caused either by the ongoing diffusive uptake of anthropogenic CO_2 from the atmosphere or the proposed purposeful injection of CO_2 into the ocean.[9] Storing waste CO_2 in the form of bicarbonate ions balanced by Ca^{2+} rather by H^+ (i.e., as carbonic acid) substantially lessens the increase in acidity per tone of carbon added to the ocean, while reducing harmful effects to marine biota of direct ocean CO_2 additions.[17,18] In fact, Ca^{2+} and bicarbonate enrichment of seawater has been shown to significantly enhance the calcification and growth rate of marine corals.[19,20]

Nevertheless, negative marine environmental impacts could result via reduction in oxygen concentration in the effluent through partial equilibration with flue-gas streams. As well, impurities released into the effluent solution from the limestone or the flue gas could be biotically impactful. Experimentation is required to quantify such effects. We point out, however, that the ocean naturally receives and accommodates about 2 x10^9 tonnes of dissolved calcium bicarbonate per year produced from continental carbonate weathering as delivered by rivers.[21]

We also note that limestone is already widely used for environmental benefit, flue gas desulfurization and acid mine waste neutralization being prime examples.

Conclusions

In the appropriate settings AWL is an attractive option for CO_2 mitigation because: 1) the required reactants are relatively inexpensive, abundant, and environmentally benign, 2) the technology is relatively simple, low-cost, and amenable to power plant retrofitting, even in developing countries, 3) the storage is effective and long-term, and 4) the waste products are stable and appear to have net positive environmental benefit. All of these features derive from the fact that AWL merely enhances Nature's own CO_2 mitigation mechanism, carbonate weathering. More research is needed, however, to more accurately assess the costs, benefits, and impacts of this means of mitigating CO_2 from point sources.

References

(1) Houghton J. *Global warming: The complete briefing.* Cambridge: Cambridge, **1997**.
(2) Hoffert, M. I.; Caldeira, K.; Benford, G.; Criswell, D. R.; Green, C.; Herzog, H.; Jain, A. K.; Kheshgi, H. S.; Lackner, K. S.; Lewis, J.S.; Lightfoot, H. D.; Manheimer, W.; Mankins, J. C.; Mauel, M. E.; Perkins, L. J.; Schlesinger, M. E.; Volk, T.; Wigley, T. M. L., *Science,* **2002**, 298, 981-987.
(3) D.O.E. *Carbon sequestration project portfolio FY 2002.* NETL and Office of Fossil Energy, U.S. Department of Energy, Wash., D.C., 2003.
(4) Rau, G. H.; Caldeira, K., *Energy Convers. Manag.,* **1999**, 40, 1803–1813.
(5) Caldeira, K.; Rau, G. H., *Geophys. Res. Lett.,* **2000**, 27, 225–228.
(6) Sundquist, E. T., *Quatern. Sci. Rev.,* **1991**, 10, 283-296.
(7) Murray C. N.; Wilson T. R. S., *Energy Convers. Manag.,* **1997**, 38, S287-S294.
(8) Archer, D.; Kheshgi, H.; Maier-Reimer, E., *Geophys. Res. Lett.,* **1997**, 24, 405-408.
(9) Caldeira, K.; Wickett, M. E., *Science* **2003**, 425, 365.
(10) Sarv H.; Downs, W., *CO_2 capture and sequestration using a novel limestone lagoon scrubber – A white paper,* McDermott Technology, Inc, Alliance, OH, **2002**.
(11) Hudson, W. R.; Little, D.; Razmi, A. M.; Anderson, V.; Weissmann, A., *An investigation of the status of by-product fines in the United States.* International Center for Aggregates Res. Report ICAR-101-1, **1997**.
(12) McClellan, G. H.; Eades, J. L.; Fountain, K. B.; Kirk, P.; Rothfuf, C., *Research and techno-economic evaluation: Uses of limestone byproducts.* University of Florida Department of Geological Sciences Final Report for Florida Department of Transportation Contract No. BA589, WPI 0510798, **2002**.
(13) Langer, W. H., *Natural aggregates of the conterminous United States*, U.S. Geological Survey Bulletin 1594, **1988**.
(14) Scott, T. M.; Campbell, K. M.; Rupert, F. R.; Arthur, J. D.; Missimer, T. M.; Lloyd, J.M.; Yon, J. W.; Duncan, J. G., *Geologic map of the State of Florida.* Florida Geol. Survey Map Series 146, Scale 1:750,000, **2001**.
(15) Rao, A. B.; Rubin, E. S., *Environ. Sci. Technol.,* **2002**, 36, 4467-4475.
(16) D.O.E., *Carbon sequestration research and development.* Office of Science and Office of Fossil Energy, U.S. Department of Energy, Wash., D.C., **1999**.
(17) Caulfield, J. A., Auerbach, D. I., Adams, E. E., Herzog, H. J., *Energy Convers. Manag.,* **1997**, 38, S343–S348.
(18) Tamburri, M. N.; Peltzer, E. T.; Friederich G. E.; Aya, I.; Yamane, K.; Brewer, P. G., *Mar. Chemistry,* **2000**, 72, 95-101.
(19) Marubini. F.; Thake, B., *Limnol. Oceanog.,* **1999**, 44, 716-720.
(20) Langdon, C.; Takahashi, T.; Sweeney, C.; Chipman, D.; Goddard, J.; Marubini, F.; Aceves, H.; Barnett, H.; Atkinson, M. J., *Glob. Biogeochem. Cycles,* **2000**, 14, 639-654.
(21) Morse, J. W.; Mackenzie, F. T., *Geochemistry of Sedimentary Carbonates,* Elsevier: Amsterdam,**1990**.

Development of a new carbon dioxide sequestration scenario by the carbonation of waste cement

Atsushi Iizuka[1], *Yasuro Katsuyama*[1], *Minoru Fujii*[2], *Akihiro Yamasaki*[3], *and Yukio Yanagisawa*[1].

(1) School of Frontier Science
The University of Tokyo, Hongo 7-3-1, Tokyo
113-8656, Japan, atsushi.iizuka@yy.t.u-tokyo.ac.jp
(2) National Institute of Environmental Studies, Japan
(3) National Institute of Advanced Industrial
Science and Technology, Japan

Introduction

Sequestrations of CO_2 in the form of carbonates of calcium or magnesium could realize more environmentally benign scenarios because these compounds are extremely stable in the environment. For the implementation of the CO_2 sequestration scenarios in the form of the carbonates, however, a tremendous amount of calcium or magnesium sources is required for the handling of continuous effluent of anthropogenic CO_2. Natural rocks containing calcium or magnesium such as serpentinite [1] or wollastonite [2] have been tested as alkaline earth metal sources for carbonate formation. Although thermodynamic calculations indicate that carbonate formation reactions can proceed spontaneously, the observed reaction rates are extremely slow when these sources were reacted with CO_2 under rather mild conditions. Thus, an appropriate acceleration method is needed for the practical use of the carbonate formation for practical CO_2 sequestration. Several acceleration methods have been examined so far including; increasing of the surface area of rock particles by pulverization [3], use of acceleration medium such as hydrochloric acid [4] or acetic acid [2], and application of high temperature and pressure conditions, where CO_2 is in the supercritical state [1]. Although considerable acceleration of the reaction rates were realized by these methods, they may require more energy consumptions, or treatment of waste acids. In this paper, we proposed a new scenario of CO_2 sequestration by using waste cement as a calcium source for the carbonate formation. Waste cement is a calcium-rich waste product containing calcium in the form of calcium silicate hydrate (such as C_3S; $3CaO \cdot 2SiO_2 \cdot 3H_2O$) and calcium hydroxide ($Ca(OH)_2$). Thus, waste cement is considered as a potential candidate as a calcium source for carbonate formation for CO_2 sequestration in terms of the capacity of CO_2 sequestration.

In this paper, the carbonate formation rates from a sample of waste cement were determined by laboratory-scale experiments. Based on the results, a model process was designed for the treatment of CO_2 emitted from a 100-MW thermal power plant, and evaluated the feasibility of the proposed process in terms of energy consumption and cost.

Outline of the proposed process

Outline of the proposed process is schematically illustrated in **Figure 1**. Waste concrete discharged from dismantled buildings is first pulverized, and classified into aggregates and waste cement particles. The waste cement particles are fed to a high-pressure reactor vessel for extraction of calcium ions with pressurized CO_2 and water. The CO_2 is captured and separated from a point concentrated emission sources such as a thermal power plant. In the extraction vessel, the extraction reactions of calcium ions from waste cement would take place with stirring. Due to the large solubility of $CaCO_3$ under high-pressure conditions of CO_2, extraction reaction

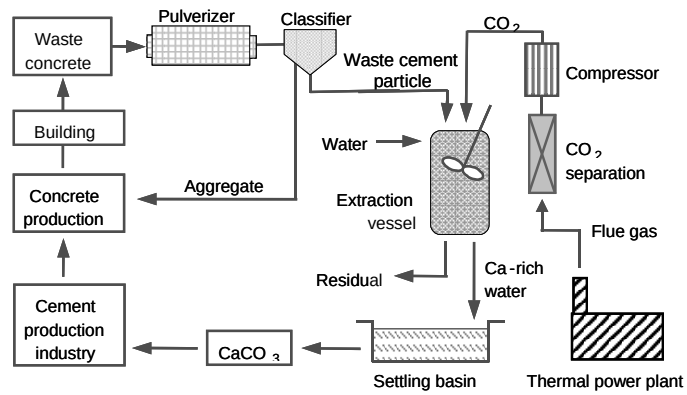

Figure 1 Schematic drawing for the CO_2 sequestration process.

will proceed in the extraction vessel. After a certain period of the extraction, the slurry is filtered and the solution phase is separated. Then, the solution was left under the atmospheric pressure in the settling bath to allow the precipitation of $CaCO_3$. The product $CaCO_3$ can be either used as a raw material of cement production industry or disposed of in appropriate sites. In the former case, the proposed process could be regarded as a recycling process of waste concrete, while the latter case as a sequestration process of CO_2.

Experimental

Waste cement particles. The waste cement sample was kindly supplied by Tateishi construction corp. as a byproduct in a practical recycling plant of waste concrete. The diameter of the waste cement particles distributed in the range of 10 – 200 µm, with a peak at about 25 - 40 µm (area based), or about 80 µm (volume based). The weight fraction of calcium was determined to be 27.3 % of waste cement.

Laboratory equipments and methods. Laboratory equipments are illustrated in **Figure 2**. A given amount of waste cement particles were dispersed in 350 mL water in the batch-type stirring vessel with 500 mL inner volume. The extraction vessel was immersed to the water bath, and heated to an extraction temperature. Gaseous CO_2 was fed to the vessel from CO_2 cylinder. A backpressure-controlling valve installed at the downstream side of the extraction reactor controlled the CO_2 pressure in the vessel. The stirring of the slurry contents in the vessel was conducted by a two-wing puddle type fin of which the stirring rate can be altered in the range of 0 ~ 1000 rpm. During the extraction experiments, the content in the vessel was sampled at a given intervals through a sintered-metal filter with 5 µm meshes. The filtered solution was then depressurized to the atmospheric pressure, and the concentration of calcium ions was determined by an inductively coupled plasma – atomic emission

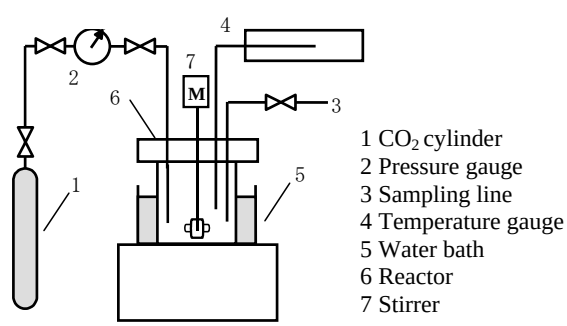

Figure 2 Schematic drawing of the experimental apparatus for calcium extraction from waste cement particles.

spectrometric (ICP-AES, Hitachi, P- 4010) method. The extraction ratio and the rate could be determined from the time course of the concentration change of calcium ions in the sampled solution.

Results and Discussion

Figure 3 shows the one typical example of time course of the calcium concentration in the sampled solution filtered from the reactor for various initial amounts of the waste concrete. For all the runs, the initial amount of water was fixed at 350 g, so that the initial weight ratio of waste cement to water was changed in the range of 0.29 wt% to 2.9 wt%. Other experimental conditions were fixed for all the runs: stirring rate = 900 rpm, temperature = 323 K, p_{CO2} = 3.0 MPa. The calcium concentration increased almost linearly with an increase in the reaction time up to about 10 min for all the cases. After that, the concentration leveled off or slightly decreased. The initial increasing rate of calcium concentration increased with an increase in the initial amount of waste cement. The sampled solution was supersaturated with calcium ions even at the early stage of the extraction reaction except the case with the smallest ratio of the waste cement/water (0.29 wt%). The extraction ratio of calcium after 3 min extraction was about 36 % for the run of the smallest ratio of the waste cement /water (0.29 wt%), and 18 % for the run of the largest ratio (2.9 wt%).

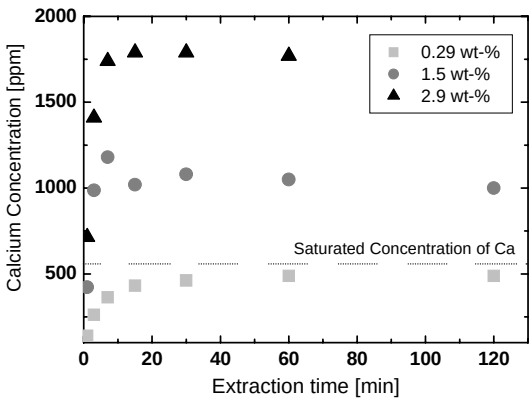

Figure 3 Change of concentration of calcium ion for various initial amounts of waste cement particles. Temperature = 323 K, stirring rate = 900 rpm, and p_{CO2} = 3.0 MPa. Dot line in the figure shows the saturated concentration of calcium ion for the extraction condition.

Process design and evaluation

Based on the experimental results, a CO_2 treatment process was designed and the energy consumption for the operation was estimated focusing the extraction step, and the effect of the extraction conditions such as CO_2 pressure, initial ratio of waste cement to, size of the waste cement particles on the process energy consumption were investigated.

As a model process, treatment of CO_2 emitted from a coal-fired 100 MW thermal power plant with 40 % overall efficiency was considered. The net amount of CO_2 emission from the power plant is 0.0174 t / s, or 5.49×10^5 t / year [5]. Since the weight fraction of active calcium content in the present sample waste cement is about 24.3 %, 2.26×10^6 t / year of the waste cement effluent is necessary to treat the total amount of emitted CO_2 from the power plant assuming 100 % conversion. Generally, cement is mixed with water of about 55 wt% of cement when using as concrete. Thus, 2.26×10^6 t / year of the waste cement is equivalent to 1.46×10^6 t / year of the cement (waste cement consists of water and cement). This number is just about 1.83 % of the total production amount of waste cement in Japan at 2001. An abundant amount of resources of waste cement is available for the treatment of CO_2.

It is assumed that the waste cement is supplied in a form of particles of which the mean diameter is about 5 cm from demolition of buildings, and pulverized to smaller particles to enhance the extraction efficiency. Bond's equation was applied for the estimation of energy required for pulverization. After pulverization, the waste cement particles are mixed with water in stirred tank type reactors, and the CO_2 gas captured from the flue gas of the thermal power plant will be introduced to the reactor to start the extraction reaction. The capture of CO_2 from the gas is conducted by a liquid absorption process with mono ethanol amine. To enhance the extraction efficiency, CO_2 will be pressurized from 0.1 MPa to the reaction pressure (such as 3.0 MPa). The CO_2 will be pressurized before introducing to the extraction reactor by an adiabatic compression with 90 % efficiency. The reactor volume was determined from the CO_2 emission rate and the retention time in the extraction reactor. The retention time is assumed 3.0 min. The reactor is divided into 20 identical reactors. The scheme for scaling-up of the reactor was carried out by adjusting the retention time and the power consumption for stirring per unit volume of the content with those of the extraction vessel used in the experiments. Only power consumption for the stirring was considered for the operation of the extraction reactors because waste heat from the thermal power plant is available for heating up the reactant to the extraction temperature.

After extraction, the solution phase and the remained particles of the waste cement will be separated by a gravitational principle in a settle basin. The solution phase was depressurized to the atmospheric pressure to make calcium carbonate particles deposit. Then the calcium carbonate particles will be disposed of in an appropriate site or recycled to the cement manufacturing industry. Energy requirement for these processes would be negligible compared with those in the extraction process and pre-treatment process before that.

Table 1 shows the energy and cost consumptions for carbon dioxide sequestration in the optimized extraction conditions. Based on the laboratory extraction experiments, the energy consumption for the proposed process to sequester CO_2 emitted from a 100 MW-thermal power plants was estimated to be 1540 kWh / t-C, and the cost was estimated to be about 83 USD / t-C. This value is comparable with the ones with the ocean sequestration scenarios, indicating that the proposed process for CO_2 sequestration is a feasible option.

Table 1 Energy and cost consumptions for carbon dioxide sequestration in the optimized extraction conditions.

	CO_2 Separation	Pressurization	Stirring	Pulverization	$CaCO_3$ selling	Total
Power Consumption [MW]	5.5	13.7	0.32	6.4	-	25.9
Energy Cosumption [kWh / t-C]	326	816	19	382	-	1543
Cost [USD / t-C]	29	73	2	34	-55	83

References

[1] O'Connor et al., Proceedings of the 5th International Conference on Greenhouse Gas Technologies, 322-327, CSIRO, Collingwood, Australia, (2001).
[2] Kakizawa M. et al., *Energy*, **26**, 341-354, (2001).
[3] Kojima, T. et al., *Energy Convers. Mgmt.*, **38**, S461-466, (1997).
[4] Lackner, K. S. et al., *Energy*, **20**, 1153-1170, (1995).
[5] Halmann MM., Steinberg, M. Greenhouse Gas Carbon Dioxide Mitigation" Lewis Publishers Inc., (1998).

OPTIMIZATION AND CONSISTENCY OF A REACTION DATASET

M. Frenklach, R. Feeley, A. Packard

Department of Mechanical Engineering, University of California at Berkeley, Berkeley, CA 94720-1740

and P. Seiler

Department of Mechanical and Industrial Engineering, University of Illinois at Urbana-Champaign, Urbana, IL

Understanding a variety of natural phenomena and industrial processes relies on the knowledge of chemical reaction mechanisms and kinetics. Endeavor in such cases begins with identification of underlying reaction pathways and fundamental mechanisms. When sufficient data accumulate, the interest often shifts to practical applications, motivating the development of mechanistic models.

The "textbook" approach to the development of mechanistic reaction models consists in conjecturing the reaction mechanism, expressing it in a suitable mathematical form, and comparing the predictions of the constructed model to available experimental observations. Typically, such tests result in a mixed outcome, some showing a reasonably close agreement and some not. The apparent inconsistency between the model and experiment obtained in the latter case is argued then to imply either that the model is inadequate or that the experiment (or rather its interpretation) is incorrect.

In some areas, such as heterogeneous catalysis and biochemical systems, the fundamental reaction mechanisms are largely unknown and establishing them form the challenge of the current research. Yet, in other fields, such as atmospheric chemistry and combustion of small hydrocarbons like methane, there are broad consensus over the reaction pathways underlying the mechanisms and the inadequacy of the kinetic models essentially rests in their parameter values. In the following we assume the latter situation.

If the kinetic parameters of such a "known" mechanism were known exactly, then a direct comparison of model prediction with a given experiment, within its uncertainties, would decisively indicate whether that experiment is consistent or inconsistent with the model. In reality, however, the model parameters themselves have uncertainties, and they have to be included in the analysis.

In principle, the parameter identification of chemical kinetic models can be posed as classical statistical inference: given a mathematical model and a set of experimental observations for the model responses, determine the best-fit parameter values, usually those that produce the smallest deviations of the model predictions from the measurements. The validity of the model and the identification of outliers is then determined using analysis of variance. The difficulty of applying standard statistical methods lies in the fact that chemical kinetics models are stated in the form of differential equations that do not possess a closed-form solution. Further complications arise from the highly "ill-structured" character of the objective function, with long and narrow valleys, resulting in ill-conditioned optimization and lack of unique solution.

The optimization problem for general, non-linear dynamic models has been addressed with a series of numerical methods: "direct" gradient search, gradient search based on sensitivities, solution mapping, genetic algorithms, and Monte Carlo techniques. In some cases, it was coupled with statistical inference and estimation of confidence regions. Recent developments also include formulation of the problem in the form of error propagation: given a set of uncertainty ranges of model parameters, estimate the intervals of variations for model predictions.

All of the above methods essentially view the problem as a two-step process: estimation of model parameters from fitting a selected set of experimental data followed by exercise of the obtained model, either as validation against an additional set of experiments or making predictions outside the experimentally accusable conditions.

Recently, we have pursued a different approach, which we call *data collaboration*.[1] In this approach we focus not on parametrization of the parameter uncertainty region, which the above methods engage in and rely upon, but rather on transferring the uncertainties of the "raw" (experimental) data into the model *directly*.[2] Doing so allows harvesting substantially more of the information content of the data, and to obtain more realistic bounds of model predictions. Our approach is anchored in the concept of a *dataset* that unites all the pertinent experimental data and the mechanistic knowledge for a given system, and the numerical analysis is based on combination of Solution Mapping and new developments of the Robust Control Theory. This numerical methodology avoids unnecessary over-constraining of model parameters, which plagues many other techniques due to inherent correlations among parameters, while exploring more closely the true *feasible set* of the parameter space in a computationally efficient manner.

The present work expands further on these ideas. New mathematical developments allow us to address the mutual consistency of experimental observations, within the framework of a dataset.

Acknowledgement. The work was supported by National Science Foundation, Information Technology Research Program, Grant No. CTS-0113985.

References

(1) Frenklach, M.; Packard, A.; Seiler; P.; Feeley, R. *Int. J. Chem. Kinet.* **2004**, in press.

(2) Frenklach, M.; Packard, A.; Seiler; P. In *Proceedings of the American Control Conference*, IEEE Catalog Number 02CH37301C, 2002, pp. 4135-4140.

REACTIVITY EXTRAPOLATION FROM SMALL TO LARGE MOLECULAR SYSTEMS VIA ISODESMIC REACTIONS FOR TRANSITION STATES (RESLIR)

Vadim D. Knyazev

Research Center for Chemical Kinetics, Department of Chemistry
The Catholic University of America, Washington, DC 20064
and
National Institute of Standards and Technology
Physical and Chemical Properties Division, Gaithersburg, MD 20899

Introduction

Numerous applications of chemistry benefit from computational methods of exploring reactivity. Quantum chemistry based techniques of evaluating reaction energy barriers, however, encounter problems when large molecular systems are considered. A number of high-level quantum chemical methods are capable of providing accuracy in evaluating reaction barriers on the order of 1 – 3 kcal mol^{-1}, which is sufficient for many (although not all) practical applications. Unfortunately, these methods are rarely used for the computational treatment of practical systems as they are generally applicable only to relatively small molecules. The computational resources required to use these methods scale as N^7 (where N is the number of atoms in the molecular system considered), making their use impossible in most cases of practical interest. The N^7 scaling also means that, even with the fast pace of progress in the development of computer hardware, one cannot expect a major improvement of these size limitations within the observable future.

Here, a method of evaluating barriers of chemical reactions involving large molecules is presented. The method is based on the extrapolation of reactivity from small molecular systems (for which high-level quantum chemical calculations can be performed) to large ones via low level (and thus low computational cost) calculations. The notation RESLIR (abbreviation of "Reactivity Extrapolation from Small to Large molecular systems via the formalism of Isodesmic Reactions for transition states") is proposed for ease of reference. The RESLIR method is a further development of the technique of isodesmic reactions for transition states (IRTS),[1,2] which has been demonstrated to yield very high accuracy in predicting reactivity in two classes of atom abstraction reactions.

Method Description

Background (IRTS[1,2]) Isodesmic reactions,[3] i.e., (usually) fictitious reactions which conserve the types of chemical bonds and their numbers, are often used in computational thermochemistry (e.g., refs 4-9). Enthalpies of these reactions are usually obtained in quantum chemical calculations and it is expected that computational errors that are specific to a particular bond type will, to a large extent, cancel on both sides of the chemical equation. The IRTS method[1,2] applies the same formalism to transition states. For example, for any two reactions of the same class expressed via chemical equations

$$\text{Reactants}(1) \rightarrow (\text{TS}(1)^{\ddagger}) \rightarrow \text{Products}(1) \quad (1)$$

$$\text{Reactants}(2) \rightarrow (\text{TS}(2)^{\ddagger}) \rightarrow \text{Products}(2) \quad (2)$$

one can write a formal isodesmic reaction

$$\text{Reactants}(1) + \text{TS}(2)^{\ddagger} = \text{Reactants}(2) + \text{TS}(1)^{\ddagger} + \Delta\text{H}(\text{ISO}) \quad (3)$$

provided that the class of reactions is defined by the similarity of the chemical transformations taking place and the structures of the transition states ($\text{TS}(i)^{\ddagger}$ where i in the reaction number).

In the IRTS technique, first, the energy barrier E(Ref) for one of the reactions within the reaction class (a "reference" reaction) is evaluated on the basis of reliable experimental data on the temperature dependence of the reaction rate constant, k(T). Then, for all other reactions within the class, formal isodesmic reaction schemes of the type

$$\text{Reactants}(i) + \text{TS(Ref)}^{\ddagger} = \text{Reactants(Ref)} + \text{TS}(i)^{\ddagger} + \Delta\text{H}(\text{ISO}(i)) \quad (4)$$

are written and their 0 K enthalpies, $\Delta\text{H}(\text{ISO}(i))$, are obtained in quantum chemical calculations. Here, Reactants(Ref) and $\text{TS(Ref)}^{\ddagger}$ are the reactants and the transition state for the "reference" reaction and i is the reaction number. Finally, energy barriers for all cognate reactions are calculated using the values of E(Ref) and $\Delta\text{H}(\text{ISO}(i))$:

$$\text{E}(i) = \text{E(Ref)} + \Delta\text{H}(\text{ISO}(i)) \quad (\text{I})$$

The values of $\Delta\text{H}(\text{ISO}(i))$ are expected to be accurate due to cancellation of errors on both sides of the chemical equation (4); this accuracy is expected to propagate into the values of E(i). Note that for any two reactions within the class (reactions 1 and 2), the 0 K enthalpy of the isodesmic reaction (3) equals the difference in the energy barriers of these reactions. Thus, the primary postulation of the IRTS technique is equivalent to the assumption that, although a particular quantum chemical method may not yield accurate absolute values of energy barriers, differences between the energy barriers of individual reactions can be calculated with a high degree of accuracy for a series of reactions of the same type.

The RESLIR method The RESLIR method is based on the use of the IRTS technique to extrapolate reactivity from small to large molecular systems within the same class of reactions. Unlike the previous applications[1,2] of the IRTS technique, it does not rely on the existence of extensive experimental information on the kinetics of at least one reaction within the class. Instead, high-level predictive calculations are performed for the reference reaction, which is chosen in such a way as to include only small molecules.

The algorithm of the RESLIR method is as follows.

1. A class of reactions is defined by the similarity of the chemical transformations occurring and the structures of the transition states. This class includes reactions involving both small and large molecules.
2. Within this class, a "reference" reaction involving only molecules of small sizes is chosen.
3. Two quantum chemical methods of different levels are selected: a low-level (LL) method and a high-level (HL) method.
4. High-level quantum chemical calculations are performed for the "reference" reaction to evaluate its energy barrier.
5. For other reactions of interest within the same class, including reactions involving large molecules, isodesmic reaction schemes of the type given by equation 4 are designed. 0 K enthalpies of these reactions, $\Delta\text{H}(\text{ISO}(i))$, are computed at the low level of theory.
6. Finally, energy barriers of the reactions of interest are calculated using the relationship of equation I.

The notation RESLIR(HL|LL) is proposed to indicate the HL and the LL methods used within the RESLIR algorithm.

Evaluation of Method Performance

Diels-Alder Reactions The RESLIR method was applied to calculation of energy barriers for a series of eleven Diels-Alder reactions involving molecules of various sizes, ranging from C_6H_{10} to $C_{12}H_{16}O_3$ for reaction products and transition states. The simplest of these reactions, that of cycloaddition of ethylene to butadiene, was

used as the "reference" reaction. A large body of experimental information on the temperature dependences of the rate constants of these reactions in the gas phase exists on the literature (e.g., see ref 10 and references cited therein.). Moreover, it is known that the kinetics of Diels-Alder reactions in non-polar solvents is not influenced by solvent effects; the same values of the rate constants have been obtained for some of these reactions in the gas and in the liquid phases. Thus, it is possible to use both the liquid phase[11] and the gas phase[10] kinetic information to compare theory and experiment.

In this work, the "experimental" values of the reaction energy barriers were derived from the experimental data on the reaction rate constant dependences using transition state theory models based on the molecular structures and frequencies obtained in calculations using the same (low-level) quantum chemical method. The calculated energy barriers were obtained using the RESLIR technique with the QCISD(T)/aug-cc-pvtz(extrapolated)//QCISD/cc-pvdz method as the high-level quantum chemical method. Here the QCISD(T)/aug-cc-pvtz(extrapolated) energies were obtained in a basis set extrapolation scheme via the following formula:

$$\text{QCISD(T)/aug-cc-pvtz(extrapolated)} = \text{QCISD(T)/aug-cc-pvdz} + (\text{MP2/aug-cc-pvtz} - \text{MP2/aug-cc-pvdz}) \qquad \text{(II)}$$

For the low-level quantum chemical methods, the HF/6-311G(d)-level geometry optimization and energy calculation was used and, in addition, two different single-point-energy methods were used with the HF/6-311G(d)-level structures: BH&HLYP/cc-pvtz and MP2/6-311G(d,p).

For all three HL|LL combinations used, the application of the RESLIR algorithm resulted in significant improvement of the agreement between calculation and experiment compared with the results obtained at the LL methods alone. Figure 1 demonstrates the results obtained with LL= HF/6-311G(d). Here, the calculated values of the energy barriers are plotted as a function of those derived from the experimental data. The open symbols represent the barriers obtained at the LL level of quantum chemistry without the use of the RESLIR method. At this level, the barrier values are completely unrealistic. The filled symbols display the barriers obtained with the RESLIR method. As can be seen from the plot, application of the RESLIR method results in dramatic improvement of the agreement.

The average absolute deviations between calculations and experiment are 2.6, 2.5, and 3.1 kcal mol^{-1} for LL = HF/6-311G(d), LL = BH&HLYP/cc-pvtz//HF/6-311G(d), and LL = MP2/6-311G(d,p)//HF/6-311G(d), respectively. The maximum deviations are 7.2, 6.8, and 6.1 kcal mol^{-1}, respectively.

It should be noted that ideal agreement between the calculated barriers and those derived from the experimental rate data is not expected because of the finite accuracy of the determination of the "experimental" barrier values. The latter were derived from transition state theory fits to the experimental k(T) dependences. Since calculated preexponential factors, generally, do not provide perfect agreement with experiment, uncertainties in the preexponential factors propagate into the uncertainties in the derived values of the energy barrier. The "error limits" of the filled data points on the plot indicate the range of the expected uncertainties in the "experimental" energy barriers caused by the imperfect description of the preexponential factors. These "error limits" should be taken as pertaining not to individual data points but rather to the whole group of reactions, approximately indicating the range of uncertainty associated with the determination of the "experimental" reaction barrier values.

Other reactions Evaluation of the performance of the RESLIR method in other reactions, such as addition of radicals to double bonds, are currently underway.

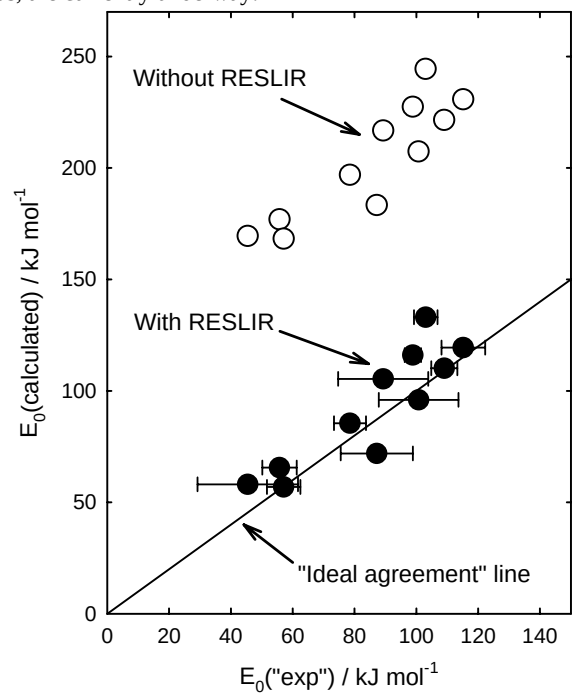

Figure 1. Calculated vs "experimental" values of the reaction energy barriers obtained for a series of Dials-Alder reactions with and without the RESLIR method. Open symbols, barriers obtained at the HF/6-311G(d) level. Filled symbols, barriers calculated using the RESLIR(QCISD(T)/aug-cc-pvtz(ex)//QCISD/cc-pvdz|HF/6-311G(d)) extrapolation method. Error bars for the "experimental" barrier values should be understood as indicating the range of uncertainty resulting from imperfect computational description of the preexponential factors for the group of reactions as a whole, as described in the text.

Acknowledgement. This research was supported, in part, by Division of Chemical Sciences, Office of Basic Energy Sciences, Office of Energy Research, U.S. Department of Energy under Grant No. DE/FG02-94ER14463

References

1. Knyazev, V. D. *J. Phys. Chem. A* **2002**, *106*, 11603.
2. Knyazev, V. D. *J. Phys. Chem. A.* **2003**, *107*, in press.
3. Hehre, W. J.; Ditchfield, R.; Radom. L.; Pople, J. A. *J. Am. Chem. Soc.* **1970**, 4796.
4. Schulman, J. M.; Peck, R. C.; Disch, R. L. *J. Am. Chem. Soc.* **1989**, *111*, 5675.
5. Raghavachari, K.; Stefanov, B. B.; Curtiss, L. A. *Molec. Phys.* **1997**, *91*, 555.
6. Raghavachari, K.; Stefanov, B. B.; Curtiss, L. A. *J. Chem. Phys.* **1997**, *106*, 6764.
7. Petersson, G. A.; Malick, D. K.; Wilson, W. G.; Ochterski, J. W.; Montgomery, J. A. Jr.; Frisch, M. J. *J. Chem. Phys.* **1998**, *109*, 10570.
8. Nicolaides, A.; Radom. L. *Molec. Phys.* **1996**, *88*, 759.
9. Chen, C. C.; Lay, T. H.; Bozzelli, J. W. *J. Phys. Chem. A* **2003**, *107*, 6451.
10. Sauer, J.; Sustmann, R. *Angew. Chem. Int. Ed. Engl.* **1980**, *19*, 779.
11. Craig, D.; Shipman, J. J.; Fowler, R. B. *J. Am. Chem. Soc.* **1961**, *83*, 2885.

Methodology for the modeling of chemical reactions on accurate potential energy surfaces

Michael R. Salazar

Department of Chemistry
Union University
1050 Union University Dr.
Jackson, TN 38343
msalazar@uu.edu

Introduction

The development of methods for the accurate description of how a chemical system changes in time is a very important field, but one that seems to have developed more slowly than methods for describing the stationary state properties of systems. This is very unfortunate since being able to accurately describe, from first principles (*ab initio*), collisional processes and the states of any products formed qualifies as a necessary step for a complete understanding of the chemical sciences.

One of the primary difficulties in being able to calculate the dynamics of a chemical system involves the accurate representation of the potential energy surface (PES) for the system.[1] The PES may be rather simple for some systems or extremely complex for other systems. In general the PES for chemical reactions will be complex and involve multiple electronic states and the couplings between these states. When performing dynamical simulations, one must have the ability to generate the potential and the gradient of the potential for the molecular system of interest at each nuclear configuration encountered during the course of the simulation. There exist an abundance of software packages for the evaluation of these *ab initio* stationary-state electronic energies and gradients. These software packages typically have many levels of theory that may be chosen to calculate these energies and gradients and the level chosen will ultimately depend on the computational cost that one is willing to absorb. Computational scaling factors ranging from linear scaling, $O(N)$, for the lowest level of theory to $O(N^7)$ for higher levels of theory must be spent for *each* energy evaluation, where N is the number of electrons in the system. This so-called method of direct dynamics, i.e., performing an *ab initio* energy and gradient evaluation at each time step has a considerable computational barrier for each simulation being performed. Furthermore, this computational barrier is markedly exacerbated when one must perform 10^3-10^5 simulations in order to obtain meaningful statistics of outcomes.

An alternative methodology for performing molecular dynamics simulations of a chemical system is to absorb the cost of calculating the global PES *a priori* by calculating energy points on a grid and using this grid of data as the basis for an analytic representation of the PES. This approach in no way diminishes the computational scaling factors for each *ab initio* energy evaluation ($O(N)$ to $O(N7)$); instead, once enough of a grid of energies is calculated such that the multidimensional reaction pathway is manifest, then the *ab initio* energy evaluations may cease. Then, already having the *a priori* calculation of the PES, one may perform the dynamical calculations upon this grid of data using analytic representations of the data that have scaling factors that vary according to the number of grid points, K. The following properties of the analytic representations should be expected:[2]

1.) The method ought reproduce the *ab initio* PES data from which it is formulate, i.e., the method should be an interpolant.

2.) The method ought to be completely general and easily portable to the study of very different chemical systems and, thus, very different PESs.

3.) The method ought to be computationally inexpensive. The computational cost ought to reside in the *a priori* calculation of the PES of which the method is independent. If this criteria is satisfied, then this allows for fast dynamical calculations and the possibility of meaningful statistics of outcomes.

4.) The method should not assume any regularity to the grid of *ab initio* data, i.e., features of the PES that are thought to be of extra importance to the reaction should be allowed to have higher densities of *ab initio* data.

5.) The method should require only the *a priori* calculation of the PES and not higher order derivatives. This can be particularly important since it is often the case for higher levels of *ab initio* theory that the programming of higher order derivatives are more slowly developed and their computational costs often exceed that of the evaluation of the energy.

6.) The method should generate an analytic representation of the PES that is smooth and continuous. The conservation of energy and momentum for molecular dynamics simulations will be very sensitive to this requirement.

Methodology

The multiquadric interpolant has been used as an accurate and fast global representation of multidimensional *ab initio* PESs.[2-7] This interpolant may be written as:

$$E(P) = \sum_{i=1}^{K} c_i \sqrt{d_{i,P}^2 + \Delta} \ . \qquad (1.)$$

where $d_{i,P}^2$ is the distance from point i to the point P, (point P being where the energy is being evaluated) and Δ is an *ad hoc* parameter. The interpolant analytically reproduces the underlying grid of energies used in it's formulation. As can be seen from Eq. (1) going to higher dimensionality does not significantly alter the difficulty of employing the interpolant and the interpolant will work for both uniform grids and grids of scattered data. The primary computational cost in the formulation of the interpolant involves solving a K × K system of linear equations. The cost of this evaluation is only required once for a given PES. Once one has solved for the coefficients, c_i, the interpolant may be used to evaluate the energy and higher order derivatives anywhere inside the underlying grid. The computational cost of a single energy or gradient evaluation is $O(K)$ with a very small prefactor. The primary difficulty with the utilization of this interpolant involves the *a priori* solution for the *ad hoc* parameter, Δ. As shown below, the interpolation of the energy is very stable with changes in Δ, but the accuracy of higher order derivatives may be significantly improved with optimization of this parameter. Methods have been developed[2,3] for the *a priori* solution of Δ, but they all involve solving the K × K system of linear equations multiple times.

Results

The multiquadric interpolant has recently been applied to the study of the spin-aligned Bose-Einstein condensate Li_3 system,[2,7] where an accurate and smooth representation of the *ab initio* PES is of critical importance. The global *ab initio* PES consisted of 1122 energy points calculated at the full configuration interaction (FCI) level of theory for the valence electrons and the grid of data was highly non-uniform. This is a very sparse global PES for a system of three degrees of freedom. The accuracy of the multiquadric interpolant was examined by formulating the interpolant using 1072 of the 1122 *ab initio* energies. The remaining 50 data points were used for the purposes of performing numerical tests on the accuracy of the interpolant. Table 1 shows the average, maximum, and minimum errors of the interpolated energies at these randomly

selected 50 points. The input coordinates of the PES had accuracy in the hundred-thousandth place (E-5), while the *ab initio* energies contained accuracy in the millionth place (E-6).

Table 1. Table of the average, maximum, and minimum errors in the interpolated energies at the 50 randomly scattered data points of the Li_3 PES.

Test	Avg. error (a.u.)	Max. error (a.u.)	Min. error (a.u.)
50 points	1.1E-5	1.52E-4	<E-6

As can be seen in Table 1 the interpolant has an average error of 1.1×10^{-5} Hartrees. This average error was found to be insensitive to changes in Δ. The maximum errors were found to reside at data points that were near the edge of the underlying grid of *ab initio* data where there were large gradients due to the close interactions of a Li_2 diatomic.

In addition to examining the accuracy of the energies of the multiquadric interpolant for the Li_3 PES, the accuracy of the interpolated gradients of the energy was also examined. Accuracy and smoothness of these gradients is critical for any molecular dynamics simulations since a classical Hamiltonian is often used for the propagation of the nuclei. Since these gradients were not calculated at the *ab initio* level of theory, the *ab initio* PES was fit to an analytic potential[7] and this analytic potential was used to generate a grid of data at the 1072 points where the *ab initio* energies are known. A new multiquadric interpolant was formulated using these 1072 energy points generated from the analytic potential and the gradients of this newly formulated interpolant were compared against the analytic gradients of the analytic potential. Displayed in Figure 1 is the root mean square error of the interpolated gradients along the symmetry coordinates S_1, S_2, and S_3 as a function of Δ for these 50 data points.

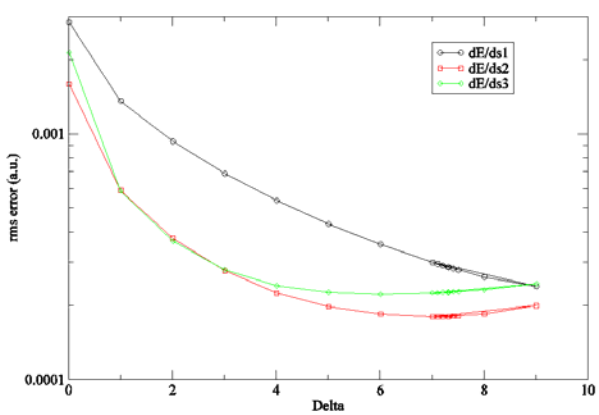

Figure 1. The root mean square error of the interpolated gradients of the energy with respect to the symmetry coordinates S_1, S_2, and S_3 as a function of the ad hoc parameter Δ.

Examining Figure 1 shows that the errors in the gradients are improved by an order of magnitude by the optimization of Δ. Figure 1 also shows that the optimized value of Δ for each of the coordinates resides at very similar values. At the optimized value of Δ, the root mean square error in the gradients at the 50 randomly selected data points ~2.0×10^{-4} Hartree/bohr along each coordinate.

Conclusions and Future

The multiquadric interpolant has been shown to be an accurate and robust method for obtaining an analytic representation of *ab initio* PESs and has further been shown to meet all of the desired properties outlined in the Introduction. The primary difficulty in the employment of the interpolant involves the *a priori* solution of the *ad hoc* parameter Δ for a given PES. Although methods have been developed for this purpose, this remains an area of active research.

Work is now being performed to utilize the multiquadric interpolant for the purposes of being able to model much larger reactive chemical systems. The goal of this work is to accurately model molecular dynamics simulations of large systems employing much higher levels of *ab initio* theory than methods of direct dynamics. As noted earlier, methods of direct dynamics, while having the benefit of using the *ab initio* PES, nevertheless often have the liability of very poor statistical outcomes. As a result, it is tempting to use levels of *ab initio* theory that may be inappropriate for systems that involve multiple electronic surfaces, which results in surface features (barriers, potential wells, etc.) that are highly over- or underestimated. Instead of applying direct dynamics, work is being performed that utilizes the *O(K)* scaling of the multiquadric interpolant to time dependent groups of the total potential for large systems.

Acknowledgement. I would like to thank Walter J. Stevens and James P. Burke for making their Li_3 PES available. I would also like to thank Union University for research support. Acknowledgement is made to the Donors of the American Chemical Society Petroleum Research Fund for partial support of this research. This research was also supported by an award from Research Corporation.

References

(1) Schatz, G. In *Reaction and Molecular Dynamics*; Lecture Notes in Chemistry; Lagana, A. and Riganelli A., Eds.; Springer, Berlin, 2000; pp. 15-32.
(2) Salazar, M. R. *Chem. Phys. Lett*. **2002**, *359*, 460.
(3) Salazar, M. R. and Bell R. *J. Comp. Chem*. **1998**, *19*, 1431.
(4) Salazar, M. R. and Simons J. *J. Chem. Phys*. **1996**, *105*, 10919.
(5) Salazar, M. R. and Simons J. *J. Chem. Phys*. **1999**, *110*, 229.
(6) Bell R. and Simons J. *J. Phys. Chem. A*. **1999**, *103*, 539.
(7) Colavecchia, F.D.; Burke, J.P. Jr; Stevens, W.J.; Salazar, M.R.; Parker, G. A.; Pack, R.T *J. Chem. Phys*. **2003**, *118*, 5484.

THE HIGH TEMPERATURE DECOMPOSITION OF HEXYL RADICALS

Wing Tsang

National Institute of Standards and Technololgy
Gaithersburg, MD 20899

Abstract: This paper is concerned with the breakdown of hexyl radicals to smaller fragments . It is meant as a first step in extending earlier kinetic databases for alkane fuels that have been validated for properties associated with the their combustion to cover soot/PAH formation problems. Sometime ago we experimentally determined the branching ratios for the decomposition of n-hexyl radicals during the pyrolysis of n-hexyl iodide. At that time we did not have the capability for treating the energy transfer effects in the multichannel fragmentation of hexyl radicals We are now able to do so and therefore have applied it to derive from the experimental measurements the high pressure rate constants consistent with bond scission and isomerization processes. From this information we project results over all relevant temperatures and pressures Some of the problems encountered in deriving the rate constants are discussed. Possibilities for reducing the number of new species and reactions for properly describing the overall processes are described.

Introduction: Kinetic databases for the simulation of combustion have usually been validated by reproducing processes such as ignition delay or flame speeds under stoichiometric or lean conditions (1). Validations of this type rarely cover the more general situations involving soot/PAH formation processes. This presentation represents an attempt to build into the database rate constants for the breakdown of hexyl radicals. This is the process that is competitive with hexyl radical oxidation through O_2 attack. The ultimate products are unsaturated compounds and radicals that can now be used as inputs to existing soot/PAH models (2). The inclusion of the pyrolytic reactions will thus generalize the database so that it can cover all combustion situations. Linear alkanes are important components of any hydrocarbon fuel (3). A kinetic database of a linear alkane fuel with n carbon atoms means that it will be necessary to consider all normal alkyl radicals with n-2 carbon atoms. Thus the present work will have an impact all normal alkane fuels with more than 6 carbon atoms.

Scope of work: There are three normal hexyl radicals. The overall decomposition process is complicated by the possibility of isomerization. The reactions involve 4 beta C-C bond cleavage reactions and 4 isomerization processes. Our aim is to derive rate expressions as a function of temperature and pressure for all these processes.

(1) 1-hexyl = ethylene + n-butyl
(2) 2-hexyl = propene + n-propyl
(3) 3-hexyl = 1-butene + ethyl
(4) 3-hexyl = 1-pentene + methyl
(5) 1-hexyl = 2hexyl
(6) 2- hexyl = 1 hexyl
(7) 1-hexyl = 3- hexyl
(8) 3-hexyl = 1-hexyl

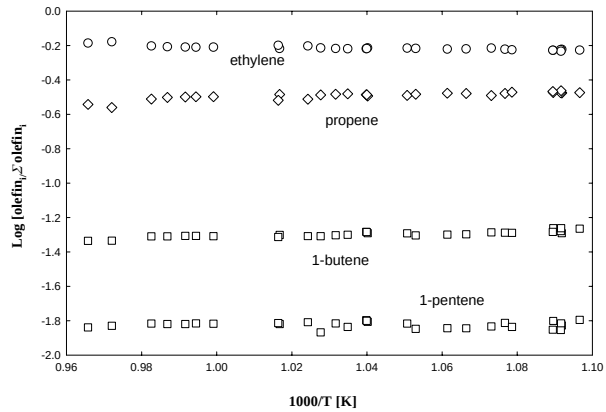

Figure 1: ***Product distribution from the decomposition of n-hexyl radical generated from n-hexyl iodide pyrolysis in single pulse shock tube experiments.***

Past work: Earlier kinetic databases have derived rate constants on the basis of results from similar reactions and thermokinetic assumptions(4). A serious problem is the neglect of energy transfer effects. Thus the effect of pressure is neglected, Several years ago we determined the branching ratio for olefin production from the decomposition of n-hexyl radical generated in single pulse shock tube experiments from the pyrolysis of n-hexyl iodide. Results are summarized in Figure 1 (5) From these data it is possible to assign the hexyl radical precursor for each olefinic product. For example 1-pentene and 1-buetene can only arise from 3-hexyl, 1-propene is derived from 2-hexene and products from 1-hexyl can only arise from the difference between the ethylene and propene yields.

Procedure: Energy transfer effects are of importance for this set of reactions as a consequence of the low reaction thresholds for the processes(6) . An additional complication is that unlike the situation for the single step decomposition reaction usually treated in standard texts it will be necessary to consider explicitly the multichannel nature of the process. Thus all eight reactions must be treated simultaneously, An additional complication is the comparatively large size of the molecule leading to the peak of the distribution function being above the reaction threshold. We have developed a general procedure to treat such situations (7,8). It involves the determination of the time and pressure dependent molecular distribution function from the solution of master equation. Convoluting these results with the RRKM specific rate constants for each channel leads to eight sets of time dependent rate constants. The purpose of this presentation is to demonstrate the procedures necessary to extract rate constants as a function of temperature and pressure and to organize the values in the most efficient manner.

Results: The treatment of the data involves first fitting experimental measurements and determining the high pressure rate expressions and then using the latter to project results over all pressure and temperature ranges. The high pressure rate expressions consistent with this procedure are summarized in Table 1. Even at temperatures as low as 600 K some pressure dependence on the rate constants can be observed. Increasing temperatures or lowering the pressure leads an accentuation of the pressure dependence. The general situation can be seen in Figure 2. This contains a plot

Reactions	Rate Expressions Rate constants at 950
k1: C6H13-1 => C2H4 + nC4H9	$1.5x10^{13}$exp(-13988/T) 6.8
k2: C6H13-2 => C3H6 + nC3H7	$2.7x10^{13}$exp(-14085/T) 7.0
k3: C6H13-3 => 1-C4H8 + C2H5	$2.7x10^{13}$exp(-14070/T) 7.0
k4: C6H13-3 => 1-C5H10 + CH3	$2.7x10^{13}$exp(-15080/T) 6.55
k5: C6H13-2 => C6H13-1	$8.9x10^{11}$exp(-10923/T) 6.96
k6: C6H13-3 => C6H13-1	$4.0x10^{12}$exp(-13788/T) 6.30
k7: C6H13-1 => C6H13-2	$6.7x10^{11}$exp(-9297//T) 7.58
k8: C6H13-1 => C6H13-3	$3.0x10^{12}$exp(-12494/T) 6.77

Table 1*: High pressure rate expressions consistent with the experimental data summarized in Figure 1*

of the temporal history of the four rate constants associated with beta C-C bond fission and the concentration of the three radicals.
Attention is called to the differences from what can be expected for a single channel process. For example the presence of the isomerization channels is responsible for the structure in the rate constants for the decomposition of the 1-hexyl radical. All the other hexyl radicals are formed from isomerization. Therefore their initial rate constants for beta bond scission is higher than the high pressure limiting values. Ultimately of course all the rate constants relax to constant values. It can be seen that these steady state values are only slightly smaller than those at the high pressure limit. However a great deal of interesting chemistry occurs before this is achieved. This can be seen from the plots of the concentrations of the hexyl radicals as a function of time. It is clear that much of the conversion has occurred before steady state distributions have been achieved. This then raises the issue of how to represent the rate constants when they are not constant. We have found it possible, in the cases where rate constants do not vary greatly to reproduce the calculated concentrations in terms of average rate constants

Discussion: When the temperature is increased, without changing the pressure, rate constants will of course increase. However this means that the ultimately all of the molecule will have reacted before the time where reactions can be described in terms of a constant rate constant. Under these conditions it becomes increasingly difficult to fit the data in terms of average rate constants. However rate constants under these conditions are extremely large and they becomes so large that they conversions to the fragments will no longer be disturbed by the oxidation reaction involving radical attack by oxygen molecule. Under such conditions all that is needed is the branching ratios for conversion.

It is of interest to consider the boundary for this process. The reaction of alkyl radicals with oxygen is in the range of $4x10^{12}$ $cm^3mol^{-1}s^{-1}$ (9) .At 1 bar of air this leads to a lifetime of approximately $T/10^{10}$ s^{-1}. It appears that above 1000 K oxidation will no longer be competitive. Under such conditions all that need be considered will then be the branching ratios for the formation of the olefins. It is then possible to ignore the presence of the alkyl radicals and express results in terms

Radical + alkane =olefin(s) + small alkyl radical + Radical-H

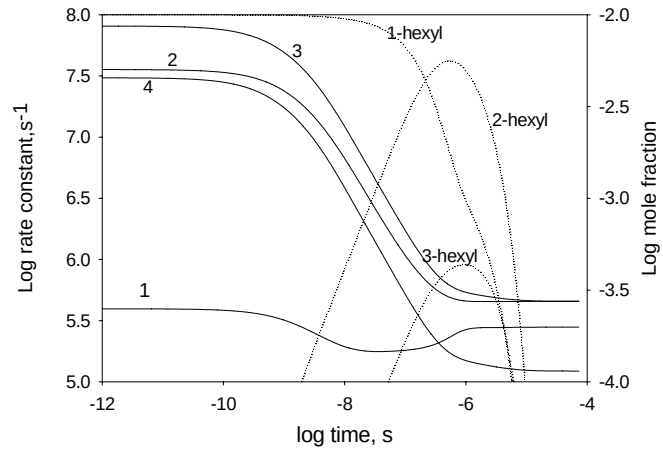

Figure 2: *Rate constants (solid line) and radical concentrations (dotted line) as a function of time at 800 K and 1 bar. The numbers refer to the reactions listed earlier*

Thus under high temperature conditions introducing the pyrolytic reactions necessary to describe the formation of the precursors to PAH/soot does not require the introduction of many more species.

There remains the problem of treating species and reactions in the intermediate temperature region where pyrolytic and oxidation processes are competitive. There are no obvious intuitive ways of carrying this out. More rigorous procedures will probably be necessary. The general situation is made more confusing by the slowness of the isomerization products to achieve the steady state values. We have mentioned the possibility of using an average rate constant to capture most of the features of the temporal behavior of these compounds. It is possible that these problems are accentuated by the treatment of these unimolecular processes in the traditional manner; as a closed system. For these reactions with the thresholds below the peak of the Boltzmann distribution the more appropriate treatment is that of an open system as in chemical activation.

References

(1) Curran, H.J., Gaffuri, P., Pitz, W.J., Westbrook, C.K. (1998) *Combust.Flame, 114.* (1-2):149-177
(2) Richter H, Howard J.B., Prog. Energ. Combust.: 4 565, 2000
(3) Edwards, T., Harrison, W. E. III, and Maurice, L. Q., "Properties and Usage of Air Force Fuel: JP-8", AIAA 2001-0498, 39th AIAA Aerospace Sciences Meeting and Exhibit, Jamuary , 2001 Reno. NV
(4) Benson, S. W. "Thermochemical Kinetics" John Wiley, New York, 1974
(5) Tsang, W., "Pathways for the Decomposition of 1-Hexyl Radicals"; Chemical and Physical Procesess in Combustion", 1996 Fall Technical Meeting, Eastern States Section of the Combustion Institute, Hilton Head, SC., pg 515
(6) Gilbert, R. S. and Smith S. C.,"Theory of Unimolecular and Recombination Reactions", Blackwell Scientific, London, 1990
(7) Tsang, W., "A Pre-processor for the Generation of Chemical Kinetics Data for Simulations" AAIA-2001-0359, 39th AIAA Aerospace Sciences Meeting and Exhibit, Jamuary 8-11, 2001 Reno.
(8) Tsang, W., Bedanov, V. and Zachariah, M. R., J. Phys. Chem., 1996, 100, 401
(9). Baulch, D. L., Cobos, C. J., Cox, R. A., Frank, P., Hayman, G., Just, T., Kerr, J. A., Murrells, T., Pilling, M. J., Troe, J., Walker, R. W. amd Warnatz, J.,J. Phys. Chem. Ref. Data, 24, 1609, 1995

Multi-Channel Chemically Activated Reactions: Comparison of Troe's Weak Collision Model and Exact Solution of Collisional Energy Transfer by Monte Carlo Method

Ameya V. Joshi[1], *Scott, G. Davis*[2], *and Hai Wang*[1]

[1]Department of Mechanical Engineering, University of Delaware, Newark, DE 19716
[2]Exponent, Inc., 21 Strathmore Road, Natick, MA 01760

Knowledge of the collisional energy transfer for a large number of multi-channel unimolecular and chemically activated reactions is often required to successfully model chemically reacting systems. Much progress has been made in our understanding of the collisional energy transfer process[1-5]. Early studies have questioned the "strong collision" hypothesis, which allowed for large energy transfer during collisions. It is known that inefficient collision energy transfer causes the population distribution of molecules above the threshold energy to deviate from the Boltzmann distribution. This results in a pressure fall-off of the thermal rate constant that is different from that predicted using the strong collision approach. For this reason, the strong collision model has in general been abandoned and collisions are effectively treated as "weak collisions".

Kineticists have employed Troe's modified strong collision model[6] to account for weak collisions. In this treatment, a collision efficiency factor β_c is introduced. This factor relates the weak collision rate constant with the strong collision rate constant through $k^{wc} = \beta_c\, k^{sc}$. Although Troe's treatment was intended for use only with single-channel unimolecular reaction, it has been nevertheless used for multi-channel reactions. In recent years, it was recognized that while Troe's collision efficiency factor is simple to calculate, for multi-channel unimolecular reactions the treatment represents a gross simplification of the collision process and the accuracies of the resulting thermal rate constants are highly questionable. Direct solution of master equation[7,8] of collisional energy transfer is a logical approach for multi-channel unimolecular and chemically activated reactions. Nevertheless it is far from trivial to analyze a reaction network of arbitrary complexity and to solve the collision energy transfer coupled with the isomerization of vibrationally excited adducts for such a reaction network.

Here, we approach the solution of master equation of collisional energy transfer and the estimation of thermal rate constants using a Monte Carlo method[9] based on Gillespie's exact stochastic method[10-12]. Our computational capability resolves reaction networks of arbitrary complexity. In this work, we compare the rates computed using the Monte Carlo approach and Troe's modified strong collision method. Rates have been computed for the chemically activated reaction of OH + CO $\rightarrow$ products[13], C_2H_2 + CH_3 $\rightarrow$ products[14] and C_6H_6 + O $\rightarrow$ products. Results show that the rate constants are systematically overpredicted for the stabilization channels by Troe's weak collision model, and as expected, the extent to which the rates are overpredicted increases as the stabilization rates deviate further from their high-pressure limits. On the other hand, the modified strong collision model is sufficiently accurate for rate estimation under many practical conditions.

Acknowledgement. The work was supported by the National Science Foundation (CTS-9874768).

References

(1) Tardy, D. C.; Rabinovitch, B. S. *Chem.Rev.* **1977**, *77*, 369.
(2) Quack, M.; Troe, J. *Gas Kinetics and Energy Transfer*; The Chemical Society: London, **1977**, Vol.2.
(3) Flynn, G.W. *Acc. Chem. Res.* **1981**, *14*, 334.
(4) Krajnovich, D.J.; Parmenter, C.S.; Catlett, D.L.,Jr. *Chem. Rev.* **1987**, *87*, 237.
(5) Oref, I.; Tardy D.C. *Chem. Rev.* **1990**, *90*, 1407.
(6) Troe, J. *J. Chem. Phys.* **1977**, *66*, 4745.
(7) Holbrook, K.A.; Pilling, M.J.; Robertson, S.H. *Unimolecular Reactions*; 2nd Ed.; Wiley: Chichester, **1996**.
(8) Gilbert, R.G.; Smith, S.C. *Theory of Unimolecular Reactions and Recombination Reactions*; Blackwell Scientific: Oxford, **1990**.
(9) Barker, J.R. *Int. J. Chem. Kinet.* **2000**, *33*, 232.
(10) Gillespie, D.T. *J. Comp. Phys.* **1976**, *22*, 403.
(11) Gillespie, D.T. *J. Comp. Phys.* **1978**, *28*, 395.
(12) Gillespie, D.T. *J. Comp. Phys.* **1977**, *81*, 2340.
(13) Larson, C.W.; Stewart, P.H.; Golden, D.M. *Int. J. Chem. Kinet.* **1988**, *20*, 27.
(14) Davis, S.G.; Law, C.K.; Wang H. *J. Phys. Chem. A.* **1999**, 103, 5889.

A study on the initial product channels of cyclohexane pyrolysis behind reflected shock waves

M. Braun-Unkhoff, C. Naumann, P. Frank

German Aerospace Center, Institute of Combustion Technology
Stuttgart, Germany

Introduction

The chemical kinetics of combustion processes of fuels has been the subject of many investigations over the past years. In the last decade, the chemistry of naphthenes – which belong to the main components of practical fuels such as gasoline, diesel, and kerosene – has attracted much attention as their contribution to the formation of aromates can be significant. For example, due to the complexity of kerosene composition – kerosene Jet A1 is a complex mixture of long-chained alkanes as dominant components, of mono- and poly-aromatics and of cycloalkanes or naphthenes (mono- and polycyclic) –, usually a model fuel is designed for simulating its oxidation. In this context, cyclohexane is discussed as a representative for naphthenic species, see e.g. ElBakali et al. /1/. Therefore, a detailed reaction mechanism is needed to describe oxidation of cyclohexane and its way to aromatic species in order to model the formation of aromatics in the oxidation of practical fuels.

Presently, investigations on the thermal decomposition of cyclohexane do not show a consistent picture regarding the initiation steps. From a single-pulse shock tube study (Tsang, 1978 /2/) it was deduced that the main initial process involves isomerisation to 1-hexene, followed by subsequent decomposition of the primary products. The same dominant end products have been also found in VLPP experiments (Brown et al., 1986 /3/). From a flow reactor study at relatively low temperatures, Gulati and Walker (1989) /4/ assumed that benzene was formed in a reaction sequence starting from cyclohexane → cyclohexene → 1,3-cyclohexadiene → benzene. Recently, from high pressure JSR experiments on cyclohexane oxidation (Voisin et al., 1998, /5/) at different mixture conditions, it was concluded that the main initiation step on cyclohexane decomposition occurs via C-C bond fission and results in ethene as the main product. In the same study, a much slower rate coefficient was attributed to the H-elimination reaction step. Furthermore, this scheme was used as part of a big reaction scheme for calculating species profiles measured in a flow reactor study (ElBakali et al., 2000, /1/) for temperatures between 900 K and 1200 K at pressures up to 10 atm over a wide range of equivalence ratio (0.5 to 2). It was found that 1-hexene which is produced via cyclohexane isomerization was formed at 1 atm, but not at 10 atm. A submechanism of 1-butene which was formed in higher concentration at 1atm than at higher pressures was included in the reaction scheme to improve the prediction of 1-hexene. As the main product, ethene was found stemming from a direct C-C fission of cyclohexane. The molecular decomposition channel was found to be mainly responsible for the decay of cyclohexane besides H-atom abstraction via OH– and H-radicals. The model was also able to model laminar burning velocities of atmospheric cyclohexane / air flames at T_0 = 298 K /6/. Therefore, the aim of the present work is to give more insight into the initial decomposition steps during the pyrolysis of cyclohexane, especially to find out whether H atoms, which are most important with respect to ignition, may be formed directly in the thermal decomposition.

Experimental

The experiments were performed behind reflected shock waves under highly diluted conditions applying a very sensitive detection method. Atomic resonance absorption spectroscopy at a wavelength λ = 121.6 nm was applied to monitor time dependent H-atom concentrations. Very small initial concentrations of cyclohexane were used, ranging from 1 to 11 ppm diluted in highly purified argon. Cyclohexane exhibited a relatively strong propensity for wall adsorption. Therefore, in most experiments, its initial concentration was examined by the use of gas chromatography analysis of samples taken from the shock tube immediately before the experiment. The uncertainty was found to be about ± 20% due as an internal standard technique has been applied. Thus it was possible to study the reaction system under very isolated conditions, with only minor influence of subsequent reactions. The experiments cover a temperature range of 1180 to 1900 K at pressures between 1.5 and 2 bar. All experiments of the present study were conducted in a stainless steel shock tube of 7.5 cm internal diameter which was heated to 363 K. Measurements were performed 5 mm away from the end flange. An oxygen spectral filter combined with a L_α-interference-filter (10 nm FWHM) was used. Calculated absorption profiles reported are based on calibration experiments, using the reaction of O-atoms – stemming from the decomposition of N_2O – with H_2 to produce H-atoms.

Results and Discussion

From previous investigations, one might expect that the dominant decomposition reaction occurs via C-C bond fission leading to ethene as the main product:

c-C_6H_{12} → open chain-C_6H_{12} (e.g. 1-hexene) → 3 C_2H_4 (R1a).

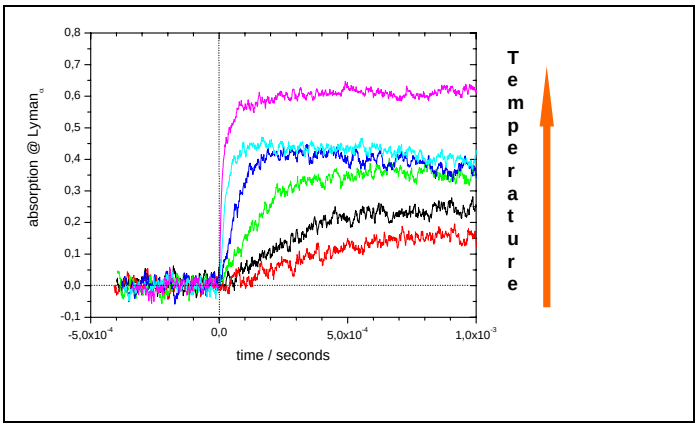

Figure 1: H-atom absorption measured behind reflected shock front. 1.05ppm cyclohexane diluted with argon for T_5 = 1335-1895K & p_5 = 1.77–1.93bar.

Therefore, hydrogen atoms can only be produced by subsequent reaction steps which should reveal a pronounced delay time under the highly diluted conditions of the present investigation. However, time resolved H-absorption profiles measured at the lowest initial cyclohexane concentrations of about 1 ppm (Figure 1) in the temperature range 1335 – 1895 K, clearly show that hydrogen atoms are produced immediately at the onset of the reaction. Therefore it was assumed that H-atoms are produced directly by an additional C-H bond fission according to reaction path R1b, which is followed by a fast H elimination reaction leading (R2) to cyclohexene:

c-C_6H_{12} → c-C_6H_{11} + H (R1b)

c-C_6H_{11} → c-C_6H_{10} + H (R2) .

As a base set for modeling the measured H-atom absorption profiles, the rate coefficient expressions of Voisin et al. (1998) have been used. For the conditions of very low initial concentration used in the present study, a reaction scheme was set up which essentially consisted of the initiation reactions R1a / R1b, R2 and bimolecular reactions like $c\text{-}C_6H_{12}$ / $c\text{-}C_6H_{11} + H \rightarrow c\text{-}C_6H_{11}$ / $c\text{-}C_6H_{10} + H_2$ which are only of minor influence. Figure 2 shows for a typical experimental profile at about 1450 K the influence of the rate values and of the branching ratio of reactions R1a and R1b. With the original values for k_{1a} and k_{1b}, nearly no H-atoms are calculated (full line). Neglecting channel R1a, gives absorption profiles which are still too small (dashed line). Only if the value of k_{1b} is increased considerably by a factor of 7.5, the initial slope of the measured profile is met, but in the later stage, too much H-atoms are predicted (dotted line). With the latter value for k_{1b} and the original value for k_{1a}, the predicted profile is much too low, compared with the observed one (dashed-dotted curve).

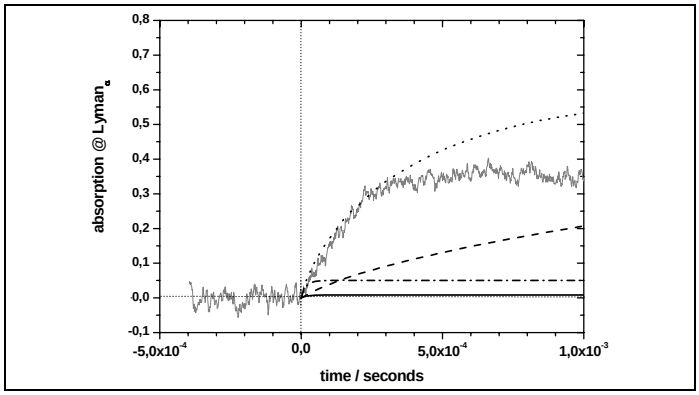

Figure 2. H-atom absorption profile measured behind reflected shock front. 1.05 ppm cyclohexane diluted in argon. T_5 = 1447 K; p_5 = 1.92 bar. Influence of molecular channel. Full line: k1a & k1b from /5/; dashed line: k1a*0, k1b from /5/; dotted line: k1a*0, k1b*7.5; dashed dotted line: k1a from /5/ & k1b*7.5.

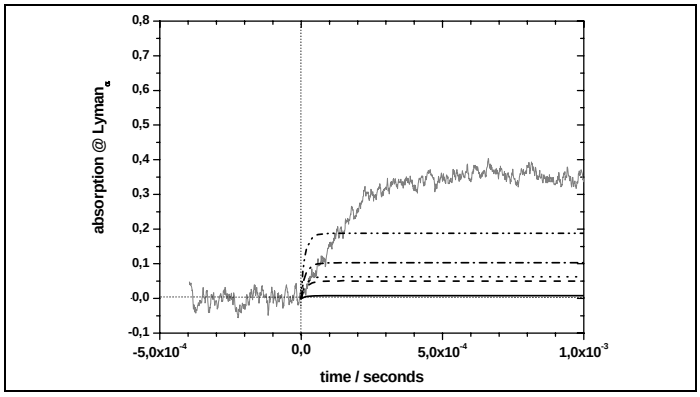

Figure 3. H-atom absorption profile measured behind reflected shock front. Same experimental condition as in Figure 2. Influence of H-atom producing channel. Full line: k1a & k1b from /5/; dashed line: k1a from 5/, but k1b*7.5; dotted line: k1a from /5/, but k1b*10; dashed dotted line: k1a from /5/, but k1b*20; dashed-dotted-dotted-line: k1a from /5/, but k1b*50.

The influence of the H-atom producing channel R1a is depicted in Figure 3. The molecular channel R1a was sticked to the value given by Voisin et al. whereas the rate coefficient of the H-atom producing channel was increased within factors of 7.5 and 50. It can clearly be seen from Figure 3 that the predicted absorption is much too high at the onset of the reaction time interval if R1b proceeds faster and faster. This leads to the conclusion that it is not possible to match the observed H-atom absorption without reducing the rate coefficient of the molecular channel.

Consequently, both values for the rate of the two initial decomposition steps of cyclohexane were modified, with respect to the data given in /5/. As can be seen in Figure 4, the measured absorption profile is reproduced over the entire observation time interval, if the rate coefficient of the molecular channel is reduced considerably by about a factor of 50 and if simultaneously, the H-atom producing channel R1b is increased by a factor of 7.5 (full line).

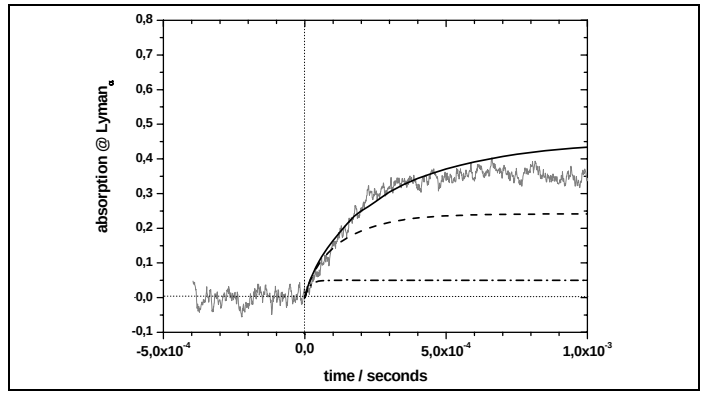

Figure 4. H-atom absorption profile measured behind reflected shock front. Same experimental condition as in Figure 2. Dash dotted line: k1a from /5/, k1b*7.5; dashed line: k1a*0.1, k1b*7.5; full line: k1a*0.02, k1b*7.5

Conclusions

The results of the present study lead to a branching ratio of about 0.5 for k_{1a} / (k_{1a} + k_{1b}). Hence, the molecular channel R1a is much slower than considered up to now, whereas the hydrogen elimination path R1b proceeds much faster, by about a factor of 5 - 10. Further measurements such as non-resonant absorption either of the educt itself and/or some of the product species are needed to determine the rate of the molecular channel R1a. Thus, a much better understanding of the initial reaction steps of the decomposition of cyclohexane would be enabled.

Acknowledgement. The authors are grateful to N. Ackermann for technical assistance. The financial support of the Deutsche Forschungsgemeinschaft DFG, SFB 606 *Instationäre Verbrennung, Transportphänomene, Chemische Reaktionen, Technische Systeme* is gratefully acknowledged.

References

(1) ElBakali, A., Braun-Unkhoff, M., Dagaut, P., Frank, P, Cathonnet, M., Proc. Comb. Inst. 28, 2000, pp. 1631-1638
(2) Tsang, W., 1978, Int.J.Chem.Kinet., **10**, pp. 1119
(3) Brown, T.C., King, K.D,. Nguyen,T.T., J.Phys.Chem. **90**, 1986, pp. 419
(4) Gulati, K.S. and Walker, R.W,. 1989, J.Chem.Soc.Faraday Trans. **2**, 85, pp. 17
(5) Voisin, D., Marchal. A., Reuillon, M., Boettner, J.-C. and Cathonnet, M., 1998, Combust. Sci .and Tech., **138**, pp. 137
(6) Davis, S.G. and Law, C.K., 1998, Combust. Sci. Tech. 140, pp. 427-449

Quantum Monte Carlo study of the thermochemistry of small hydrocarbons*

Alexander C. Kollias[1,2], Dominik Domin[1], Michael Frenklach[3], David Golden[4], and William A. Lester, Jr.[1,2]

[1]Kenneth S. Pitzer Center for Theoretical Chemistry, Department of Chemistry, University of California, Berkeley, CA 94720-1460; [2]Chemical Sciences Division, Lawrence Berkeley National Laboratory Berkeley, CA 94720-1460; [3]Department of Mechanical Engineering, University of California at Berkeley, Berkeley, CA 94720-1740, and Environmental Energy Technologies Division, Lawrence Berkeley National Laboratory Berkeley, CA 94720-1460; [4]Department of Mechanical Engineering, Stanford University, CA 94305

A theoretical study is reported on the thermochemical properties of 20 small hydrocarbons based on the diffusion Monte Carlo (DMC) variant of the quantum Monte Carlo method. The 20 hydrocarbons include both radicals and closed-shell molecular systems containing 1 to 4 carbons centers that appear in combustion reactions. Using DMC trial functions constructed from Hartree-Fock (HF) and multi-configurational self-consistent field (MCSCF) wave functions, we have computed the atomization energies, heats of formation and bond dissociation energies for these systems. The DMC thermochemical results are compared to experimental data as well as complete basis set extrapolations for Moller-Plesset second-order perturbation theory, coupled-cluster singles-doubles (CCSD) with perturbative triples (CCSD(T)), and B3LYP methods to gauge the accuracy of the DMC method.

The amount of non-dynamical correlation energy, or single-reference character in CCSD, was determined by examining the T1 diagnostic test of CCSD calculations.[1] This diagnostic test has been demonstrated to be a better quantifier of multi-reference character than the leading coefficient in a multi-configurational wave function. The results of the T1 diagnostic are correlated with DMC atomization energies in order to provide a measure of the quality of HF trial wave functions. The idea is to gauge the accuracy a priori of a DMC calculation that uses a HF trial function from the T1 diagnostic. In cases where DMC atomization energies from HF trial functions are poor, multi-determinant trial functions will be used to improve the results.

[1]T. J. Lee and P. R. Taylor, *Int. J. Quant. Chem. Symp.* **23**, 199 (1989).

*This work was supported by the Director, Office of Science, Office of Basic Energy Sciences, Chemical Sciences Division of the U.S. Department of Energy under Contract No. DE-AC03-76SF00098. The calculations were carried out at the National Energy Research Supercomputer Center (NERSC).

Thermodynamics of Jahn-Teller molecules

Timothy A. Barckholtz

Corporate Strategic Research
ExxonMobil Research and Engineering
1545 Route 22 East
Annandale, NJ 08801
tim.barckholtz@exxonmobil.com

Introduction

The vast majority of molecules and radicals important in combustion or atmospheric kinetics have relatively simple electronic and vibrational structures. Most stable molecules have singlet ground states with excited states that are close to 100 kcal/mol higher in energy. The vibrational structure of most molecules can be readily described using the simple harmonic oscillator model, possibly with some anharmonic corrections. The thermodynamics of these molecules can be easily handled using standard statistical treatments. While the chemistry of free radicals is quite different from that of molecules, their treatment under statistical thermodynamics is for the most part very similar to that of molecules.[1]

A class of molecules for which the above statements do not hold are those subject to the Jahn-Teller effect. These molecules have by necessity open-shell electronic structures with orbitally degenerate ground states. Two important combustion radicals, the methoxy radical, CH_3O,[2] and the cyclopentadienyl radical, C_5H_5,[3] have ^2E ground states that are subject to a Jahn-Teller distortion. While these two radicals have been investigated for over 50 years, the details of their vibrational structure have only been resolved in the last 5 years.

Quantum mechanics of Jahn-Teller states

The quantum mechanics of Jahn-Teller molecules has been examined in excruciating detail elsewhere.[2] For the purposes of this paper, only a few key points will be summarized.

(1) The quantum mechanis of a Jahn-Teller molecule are most efficiently described via a few small perturbations to the Hamiltonian appropriate for a ^2E state. The molecule is distorted from the higher symmetry geometry, but this distortion is dynamic, not static, for CH_3O and C_5H_5. To analyze the spectroscopic energy levels based on a Hamiltonian appropriate for the distorted geometry would require many more correction terms than the Hamiltonian derived from the higher symmetry geometry.

(2) For most molecules, the Hamiltonian for the vibrational energy levels is separable from the electronic and spin Hamiltonians. This is not the case for ^2E states. Thus, the partition function cannot in general be written as the product of the individual components ($q_{JT} \neq q_{spin}*q_{elec}*q_{vib}$).

In the absence of any Jahn-Teller coupling, q_{elec} is equal to the orbital degeneracy of the state; i.e., 2 for a ^2E state. If the spin-orbit coupling is small, like in C_5H_5, then q_{spin} can be separated out as $q_{spin}=2*S+1$ for all temperatures. The entire spin-vibrational-electronic Hamiltonian must be diagonalized in order to compute q_{JT}. Rotational and translational contributions can still be separated, to make $q_{tot} = q_{JT}*q_{rot}*q_{trans}$.

(3) For non-zero spin-orbit coupling, like in CH_3O, all vibrational energy levels are split into pairs. The splitting energies vary widely, with a general diminishment to zero as the total internal energy is increased. For the purposes of statistical thermodynamics, the spin-orbit splitting of the zero-point level can be used to compute q_s using the normal Boltzman equation.

(4) The vibrational energy levels are not evenly spaced, but instead have very irregular spacings for the first few thousand cm^{-1} of internal energy. However, they maintain intervals that are of the order of vibrational intervals (a few 100 cm^{-1}), rather than spacings of rotational energy levels (a few cm^{-1}). To compute the partition function of the Jahn-Teller vibrations requires a numerical calculation of the energy levels and a numerical calculation of the partition function based on those energy levels.

Conclusions

Several qualitative conclusions regarding the statistical thermodynamics of Jahn-Teller molecules can be made. A quantitative description will be given in the full paper to be published.

(1) The vibrational modes of a Jahn-Teller molecule are not harmonic, but the harmonic approximation may give a reasonably accurate partition function, especially at high temperatures.

(2) Treatment of the electron spin must be included in the thermodynamic calculation. For C_5H_5, the spin-orbit coupling is essentially zero, giving a full contribution of R ln 2 to the entropy at all temperatures. For CH_3O, it is small (60 cm^{-1}), making a difference only at low temperatures. For sulfur-centered radical such as CH_3S, the 250 cm^{-1} spin-orbit splitting makes a larger difference.

(3) The use of the phrase "pseudo-rotation" to describe the motion of a Jahn-Teller molecule is misleading. This phrase implies that the degrees of freedom that account for the Jahn-Teller distortion can be treated by some type of rotational function. In actuality, what is "pseudo-rotating" about the Jahn-Teller moat is not the nuclei, but the electronic wavefunction. Thus, the energy level spacings of the Jahn-Teller distortion are closer to that of a vibration rather than any type of rotation.

(4) The electronic degeneracy must be included in the entropy via an R ln 2 contribution. At low temperatures the contribution is not exactly R ln 2, and but must be computed from the full numerical diagonalization of the Hamiltonian. The commonly used *ab initio* find a singly degenerate state at a distorted geometry, and a singly degenerate excited state that usually is a maximum on the surface. If the excited state is omitted from the partition function, then the computed entropy will be low.

(5) *ab initio* calculations of the minimum can be used as a reasonable approximation to the full Jahn-Teller statistical thermodynamics, provided that the entropy due to the excited states is included. The errors of this approximation are largest at lower temperatures, and diminish significantly at combustion temperatures.

References

(1) Benson, S. W. *Thermochemical Kinetics*; Wiley: New York, NY, 1976.
(2) Barckholtz, T. A.; Miller, T. A. *Int. Rev. Phys. Chem.* **1998**, *17*, 435-524.
(3) Applegate, B. E.; Miller, T. A.; Barckholtz, T. A. *J. Chem. Phys.* **2001**, *114*, 4855-4868; Applegate, B. E.; Bezant, A. J.; Miller, T. A. *J. Chem. Phys.* **2001**, *114*, 4869-4882.
(4) Barckholtz, T. A.; Miller, T. A. *J. Phys. Chem. A* **1999**, *103*, 2321-2336.

ENERGETIC CATALYST-HYDROGEN PLASMA REACTION AS A POTENTIAL NEW ENERGY SOURCE

R. L. Mills, Y. Lu, M. Nansteel, J. He, A. Voigt, B. Dhandapani

BlackLight Power, Inc., 493 Old Trenton Road,Cranbury, NJ 08512

Introduction

Theoretical Predictions. The basic spectral emission of pure helium and hydrogen light sources have been well known for about a century. Recently, however, unique vacuum ultraviolet (VUV) emission lines were found at predicted wavelengths and reported in numerous publications [1-5]. For example, extreme ultraviolet (EUV) spectroscopy was recorded on microwave discharges of helium with 2% hydrogen. Novel emission lines were observed with energies of $q \cdot 13.6\,eV$, $q = 1,2,3,7,9,11$. or $q \cdot 13.6\,eV$, $q = 4,6,8$ less $21.2\,eV$ corresponding to inelastic scattering of these photons by helium atoms due to excitation of $He(1s^2)$ to $He(1s^1 2p^1)$. These strong emissions are not found in any single gas plasma, and cannot be assigned to the known emission of any species of the single gases studied such as H, H^-, H_2, H_2^+, H_3^+, He, He_2^*, and He^+, known species of the mixture such as He_2^+, HeH^+, HeH, HHe_2^+, and HHe_n^+ and He_n, or possible contaminants [1]. However the results can be explained by a novel catalytic reaction of atomic hydrogen [1-5] to lower-energy states given by Rydberg's equation

$$E_n = -\frac{e^2}{n^2 8\pi\varepsilon_o a_H} = -\frac{13.598\,eV}{n^2} \tag{1a}$$

where

$$n = \frac{1}{2}, \frac{1}{3}, \frac{1}{4}, ..., \frac{1}{p}; \quad p \le 137 \text{ is an integer} \tag{1b}$$

replaces the well known parameter

$$n = 1,2,3,... \tag{1c}$$

for hydrogen excited states.

The theory reported previously [1-11] predicts that atomic hydrogen may undergo a catalytic reaction with certain atoms, excimers, and ions which provide a reaction with a net enthalpy of an integer multiple of the potential energy of atomic hydrogen, $E_h = 27.2\,eV$ where E_h is one hartree. Specific species (e.g. He^+, Ar^+, and K) identifiable on the basis of their known electron energy levels are required to be present in plasmas with atomic hydrogen to catalyze the process. In contrast, species such as atoms or ions of Kr or Xe do not fulfill the catalyst criterion—a chemical or physical process with an enthalpy change equal to an integer multiple of E_h that is sufficiently reactive with atomic hydrogen under reaction conditions. The reaction involves a nonradiative energy transfer followed by $q \cdot 13.6\,eV$ emission or $q \cdot 13.6\,eV$ transfer to H to form extraordinarily hot, excited-state H [1, 9-15] and a hydrogen atom that is lower in energy than unreacted atomic hydrogen that corresponds to a fractional principal quantum number given by Eq. (1b). That is, the $n = 1$ state of hydrogen and the $n = \frac{1}{\text{integer}}$ states of hydrogen are nonradiative, but a transition between two nonradiative states, say $n = 1$ to $n = 1/2$, is possible via a nonradiative energy transfer. A catalyst provides a net positive enthalpy of reaction of $m \cdot 27.2\,eV$ (i.e. it resonantly accepts the nonradiative energy transfer from hydrogen atoms and releases the energy to the surroundings to affect electronic transitions to fractional quantum energy levels). As a consequence of the nonradiative energy transfer, the hydrogen atom becomes unstable and emits further energy until it achieves a lower-energy nonradiative state having a principal energy level given by Eqs. (1a) and (1b).

Prior related studies that support the possibility of a novel reaction of atomic hydrogen which produces hydrogen in fractional quantum states that are at lower energies than the traditional "ground" ($n = 1$) state include extreme ultraviolet (EUV) spectroscopy [1-5, 8-11, 14-25], characteristic emission from catalysts and the hydride ion products [10-11, 16-18, 20-21], lower-energy hydrogen emission [1-5], chemically formed plasmas [8-11, 16-21], Balmer α line broadening [1, 2, 9-16, 18, 20-21, 23-24], population inversion of H lines [20-23], elevated electron temperature [12-14, 24], anomalous plasma afterglow duration [19], power generation [2, 4, 14, 24], and analysis of novel chemical compounds [26-28].

$H(1/p)$ may react with a proton, and two $H(1/p)$ may react to form $H_2(1/p)^+$ and $H_2(1/p)$, respectively. The hydrogen molecular ion and molecular charge and current density functions, bond distances, and energies were solved previously [7] from the Laplacian in ellipsoidal coordinates with the constraint of nonradiation. The bond dissociation energy, E_D, of hydrogen molecular ion $H_2(1/p)^+$ was given as

$$E_D = p^2 2.535\,eV + p^3 0.118755\,eV \tag{2}$$

where p is an integer. The bond dissociation energy, E_D, of hydrogen molecule $H_2(1/p)$ E_D was given previously as

$$E_D = p^2 4.151\,eV + p^3 0.326469\,eV \tag{3}$$

The vibrational and rotational energies of fractional-Rydberg-state hydrogen molecular ion $H_2(1/p)^+$ and molecular hydrogen $H_2(1/p)$ are p^2 those of H_2^+ and H_2, respectively. Thus, the vibrational energies, E_{vib}, for the $\upsilon = 0$ to $\upsilon = 1$ transition of hydrogen-type molecular ions $H_2(1/p)^+$ are [7]

$$E_{vib} = p^2 0.271\,eV \tag{4}$$

where p is an integer and the experimental vibrational energy for the $\upsilon = 0$ to $\upsilon = 1$ transition of H_2^+, $E_{H_2^+(\upsilon=0\to\upsilon=1)}$, is given by Karplus and Porter [29] and NIST [30]. Similarly, the vibrational energies, E_{vib}, for the $\upsilon = 0$ to $\upsilon = 1$ transition of hydrogen-type molecules $H_2(1/p)$ are [7]

$$E_{vib} = p^2 0.515902\,eV \tag{5}$$

where p is an integer and the experimental vibrational energy for the $\upsilon = 0$ to $\upsilon = 1$ transition of H_2, $E_{H_2(\upsilon=0\to\upsilon=1)}$, is given by Beutler [31] and Herzberg [32]. The rotational energies, E_{rot}, for the J to $J+1$ transition of hydrogen-type molecules $H_2(1/p)$ are [7]

$$E_{rot} = E_{J+1} - E_J = \frac{\hbar^2}{I}[J+1] = p^2(J+1)0.01509\,eV \tag{6}$$

where p is an integer, I is the moment of inertia, and the experimental rotational energy for the $J = 0$ to $J = 1$ transition of

H_2 is given by Atkins [33]. The p^2 dependence of the rotational energies results from an inverse p dependence of the internuclear distance and the corresponding impact on I. The predicted internuclear distances $2c'$ for $H_2(1/p)$ are

$$2c' = \frac{a_o\sqrt{2}}{p} \tag{7}$$

Experiments to Test the Theoretical Predictions. The reaction Ar^+ to Ar^{2+} has a net enthalpy of reaction of $27.63\,eV$; thus, it may serve as a catalyst to form $H(1/2)$. The product of the catalysis reaction, $H(1/2)$, may further serve as both a catalyst and a reactant to form $H(1/4)$ [2-3]. Also, the second ionization energy of helium is $54.4\,eV$; thus, the ionization reaction of He^+ to He^{2+} has a net enthalpy of reaction of $54.4\,eV$ which is equivalent to $2\cdot 27.2\,eV$. The product of the catalysis reaction, $H(1/3)$, may further serve as both a catalyst and a reactant to form $H(1/4)$ and $H(1/2)$ [2-3].

Since $H_2(1/2)^+$ is a resonant state of $H_2(1/4)^+$, the reaction designated

$$H(1/4)+H^+ \rightarrow H_2(1/4)^+ \tag{8}$$

wherein $H(1/4)$ reacts with a proton to form $H_2(1/4)^+$ is possible with strong emission through vibronic coupling with the resonant state $H_2(1/2)^+$. The energies, E_{D+vib}, of this series due to vibration in the transition state given previously [34] are

$$\begin{aligned} E_{D+vib} &= E_D\left(H_2(1/4)^+\right) - \left(\upsilon^* + \frac{1}{2}\right)2^2 E_{vib\,H_2^+} \\ &= 48.16 - \left(\upsilon^* + \frac{1}{2}\right)1.172\,eV \end{aligned}, \quad \upsilon^* = 0,1,2,3... \tag{9}$$

where $E_D\left(H_2(1/4)^+\right)$ is the bond energy of $H_2(1/4)^+$ given by Eq. (2) and $E_{vib\,H_2^+}$ is the transition-state vibrational energy of H_2^+ given by Eq. (108) of Ref. [7]. In Eq. (9), υ^* refers to vibrational energies of the transition state which must have equal energy separation as a requirement for resonant emission [7, 34]. Thus, anharmonicity is not predicted. The series is predicted to end at 25.74 nm corresponding to the predicted $H_2(1/4)^+$ bond energy of 48.16 eV given by Eq. (2).

The present paper tests theoretical predictions [1-11] that atomic and molecular hydrogen form stable states of lower energy than traditionally thought possible. Substantial spectroscopic and physical differences are anticipated. For example, novel EUV atomic, molecular ion, and molecular spectral emission lines from transitions corresponding to energy levels given by Eqs. (1a) and (1b), Eqs. (2) and (4), and Eqs. (3) and (5-7), respectively, are predicted. The atomic lines have been shown previously [1-4, 24] as well as a series of unique EUV lines assigned to $H_2(1/2)$ [4]. To test additional predictions, EUV spectroscopy was performed to search for emission that was characteristic of and identified $H_2(1/4)^+$ and $H_2(1/4)$. Low pressure plasmas are more highly ionized. Thus, we further investigated the emission of the $H_2(1/4)^+$ vibrational series given by Eq. (9) from microwave discharges of helium-hydrogen and argon-hydrogen mixtures.

The rotational energies provide a very precise measure of I and the internuclear distance using well established theory [29]. Neutral molecular emission was anticipated for high pressure argon-hydrogen plasmas excited by a 15 keV electron beam. Rotational lines for $H_2(1/4)$ were anticipated and sought in the 150-250 nm region. The spectral lines were compared to those predicted by Eqs. (5-6) corresponding to the internuclear distance of 1/4 that of H_2 given by Eq. (7). The predicted energies for the $\upsilon = 1 \rightarrow \upsilon = 0$ vibration-rotational series of $H_2(1/4)$ (Eqs. (5-6)) are

$$\begin{aligned} E_{vib-rot} &= p^2 E_{vib\,H_2(\upsilon=0\rightarrow\upsilon=1)} \pm p^2(J+1)E_{rot\,H_2} \\ &= 4^2 E_{vib\,H_2(\upsilon=0\rightarrow\upsilon=1)} \pm 4^2(J+1)E_{rot\,H_2} \\ &= 8.254432\,eV \pm (J+1)0.24144\,eV \end{aligned}, \quad J = 0,1,2,3... \tag{10}$$

for $p = 4$.

The product $H_2(1/p)$ gas predicted to liquefaction at a higher temperature than H_2 [34]. Helium-hydrogen (90/10%) plasma gases were flowed through a high-vacuum (10^{-6} Torr) capable, liquid nitrogen (LN) cryotrap, and the condensed gas was characterized by ^1H nuclear magnetic resonance (NMR) of the LN-condensable gas dissolved in $CDCl_3$. Other sources of hydrogen such as hydrocarbons were eliminated by mass spectroscopy (MS) and Fourier transform infrared spectroscopy (FTIR). The ^1H NMR resonance of $H_2(1/p)$ is predicted to be upfield from that of H_2 due to the fractional radius in elliptic coordinates [6-7] wherein the electrons are significantly closer to the nuclei. The predicted shift, $\frac{\Delta B_T}{B}$, for $H_2(1/p)$ derived previously [6-7] is given by the sum of that of H_2 and a relativistic term that depends on $p > 1$:

$$\frac{\Delta B_T}{B} = -\mu_0\left(4 - \sqrt{2}\ln\frac{\sqrt{2}+1}{\sqrt{2}-1}\right)\frac{e^2}{36a_0 m_e}(1+\pi\alpha p) \tag{11}$$

$$\frac{\Delta B_T}{B} = -(28.01 + 0.64p)ppm \tag{12}$$

where $p = 0$ for H_2 since there is no relativistic effect and $p = \text{integer} > 1$ for $H_2(1/p)$ where $p = \text{integer} > 1$.

In addition to liquefaction at liquid nitrogen temperature, $H_2(1/p)$ gas was also isolated by decomposition of compounds found to contain the corresponding hydride ions $H^-(1/p)$. The total shift, $\frac{\Delta B_T}{B}$, was calculated previously [6, 18] for the hydride ions $H^-(1/p)$ having a fractional principal quantum number. The shift was given by the sum of that of ordinary hydride ion H^- and a component due to a relativistic effect:

$$\begin{aligned} \frac{\Delta B_T}{B} &= -\mu_0\frac{e^2}{12m_e a_0\left(1+\sqrt{s(s+1)}\right)}(1+\alpha 2\pi p) \\ &= -(29.9 + 1.37p)ppm \end{aligned} \tag{13}$$

where $p = 0$ for H^- since there is no relativistic effect and $p = \text{integer} > 1$ for $H^-(1/p)$ where $p = \text{integer} > 1$. The experimental absolute resonance shift of tetramethylsilane (TMS) is -31.5 ppm relative to the proton's gyromagnetic frequency [35-36]. The results of ^1H MAS NMR spectroscopy were given previously

[18, 26-28] on control and novel hydrides synthesized using atomic potassium as a hydrogen catalyst wherein the triple ionization reaction of K to K^{3+}, has a net enthalpy of reaction of $81.7766\,eV$, which is equivalent to $3\cdot 27.2\,eV$. The KH experimental shift of +1.3 ppm relative to TMS corresponding to absolute resonance shift of -30.2 ppm matched very well the predicted shift of H^- of -30 ppm given by Eq. (13). The ^1H MAS NMR spectrum of novel compound $KH*Cl$ relative to external tetramethylsilane (TMS) showed a large distinct upfield resonance at -4.4 ppm corresponding to an absolute resonance shift of -35.9 ppm that matched the theoretical prediction of p = 4. A novel peak of $KH*I$ at -1.5 ppm relative to TMS corresponding to an absolute resonance shift of -33.0 ppm matched the theoretical prediction of p = 2. The predicted catalyst reactions, position of the upfield-shifted NMR peaks, and spectroscopic data for $H^-(1/2)$ and $H^-(1/4)$ were found to be in agreement [7, 18].

The decomposition reaction of $H^-(1/p)$ is

$$2M^+H^-(1/p)\xrightarrow{\Delta}H_2(1/p)+2M \qquad (14)$$

where M^+ is a metal ion. NMR peaks of $H_2(1/p)$ given by Eqs. (11-12) provide a direct test of whether compounds such as $KH*I$ contain hydride ions in the same fractional quantum state p. Furthermore, the observation of a series of singlet peaks upfield of H_2 with a predicted integer spacing of 0.64 ppm provides a powerful means to confirm the existence of $H_2(1/p)$.

The exothermic helium plasma catalysis of atomic hydrogen was shown previously [12-13] by the observation of an average hydrogen atom temperature of $180\text{-}210\,eV$ for helium-hydrogen mixed plasmas versus $\approx 3\,eV$ for hydrogen alone. Since the electronic transitions are very energetic, power balances of helium-hydrogen plasmas compared to control krypton plasmas were measured using water bath calorimetry to determine whether this reaction has sufficient kinetics to merit its consideration as a practical power source.

Experimental

To investigate the vibrational series of $H_2(1/4)^+$, EUV spectra (20-65 nm) were recorded on light emitted from microwave discharge plasmas of helium, argon, krypton, or xenon or a mixture of 10% hydrogen with each noble gas. Each ultrapure (99.999+%) test gas or mixture was flowed through a half inch diameter quartz tube at 100 mTorr maintained with a total gas flow rate of 10 sccm. The tube was fitted with an Opthos coaxial microwave cavity (Evenson cavity). The microwave generator was an Opthos model MPG-4M generator (Frequency: 2450 MHz). The input power to the plasma was set at 40 W.

The spectrometer was a McPherson 4° grazing incidence EUV spectrometer (Model 248/310G) equipped with a grating having 600 G/mm with a radius of curvature of $\approx 1\,m$ that covered the region $5-65\,nm$. The angle of incidence was 87°. The wavelength resolution was about $0.1\,nm$ (FWHM) with an entrance and exit slit width of $40\,\mu m$. A CEM was used to detect the EUV light. The increment was $0.01\,nm$ and the dwell time was $1\,s$.

Vibration-rotational emission of $H_2(1/4)$ was investigated using an electron gun described previously [37-38] to initiate argon plasmas with 1% hydrogen in the pressure range of 450-1000 Torr. The plasma cell was flushed with oxygen, then pumped down, flushed with argon-hydrogen (99/1%), and filled with argon-hydrogen (99/1%). Krypton replaced argon in the controls, and argon, hydrogen, oxygen, nitrogen, water vapor, nitrogen-oxygen (50/50%), and argon or krypton with oxygen addition up to 100% oxygen served as further controls. The electrons were accelerated with a high voltage of 12.5 keV at a beam current of $10\,\mu A$. The electron gun was sealed with a thin (300 nm thickness) SiN_x foil that served as a 1 mm^2 electron window to the cell at high gas pressure (760 Torr). The beam energy was deposited by hitting the target gases, and the light emitted by beam excitation exited the cell through a MgF_2 window mounted at the entrance of a normal incidence McPherson 0.2 meter monochromator (Model 302) equipped with a 1200 lines/mm holographic grating with a platinum coating. The resolution was $0.5\,nm$ (FWHM) at an entrance and exit slit width of $100\,\mu m$. The increment was $0.1\,nm$ and the dwell time was $1\,s$. The PMT (Model R8486, Hamamatsu) used has a spectral response in the range of 115-320 nm with a peak efficiency at about 225 nm. The emission was essentially flat for $200<\lambda>275\,nm$, but a notch in the response of about 20% existed in the short wavelength range with a minimum at 150 nm. Peak assignments were determined by an external calibration against standard line emissions.

Condensable gas from helium-hydrogen (90/10%) microwave plasmas maintained in the Evenson cavity was collected in a high-vacuum (10^{-6} Torr) capable, LN cryotrap described previously [25]. After each plasma run the cryotrap was pumped down to 10^{-5} Torr to remove any non-condensable gases in the system. The pressure was recorded as a function of time as the cryotrap was warmed to room temperature. Typically, about $45\,\mu moles$ of condensed gas was collected in a 2 hr plasma run. Controls were hydrogen and helium alone.

The mass spectra ($m/e=1$ to $m/e=200$) of ultrahigh purity (99.999+%) hydrogen (Praxair) control samples and samples of the condensable gas from the helium-hydrogen microwave plasmas were recorded with a residual gas analyzer.

Premixed He/H_2 (90/10%) was flowed from a supply bottle through a metering valve and a LN trap just upstream of a 700 mTorr Evenson microwave plasma. A second LN trap downstream of the plasma tube was used to remove any water vapor generated by the plasma. The plasma gas, devoid of impurities due to the LN traps, was flowed through a long capillary tube which was maintained in the temperature range ~12-17 K by a cryo-cooler described previously [34]. Residual gas was pumped from the capillary, condensable gas was collected over a period of several hours, and the system was evacuated to 10^{-5} Torr to remove any non-condensable gases in the system. Controls were hydrogen and helium alone. Two capillary valves were closed to trap any vaporizing gas as the cryo-cooler was stopped, and the tube was warmed to room temperature. Typically about 100 mTorr of gas was collected over a 24 to 48 hour period and then analyzed by mass spectroscopy and compared with the results for a control sample collected in the same way, except that no plasma was present.

Sealed ^1H NMR samples were prepared by collecting the condensed gas from the cryotrap in $CDCl_3$ solvent (99.99% Cambridge isotopes) in an NMR tube (5 mm OD, 23 cm length, Wilmad) maintained at LN-temperature which was then sealed as described previously [25]. Control NMR samples comprised ultrahigh purity hydrogen (Praxair) and the helium-hydrogen (90/10%) mixture with $CDCl_3$ solvent. The NMR spectra were

recorded with a 300 MHz Bruker NMR spectrometer that was deuterium locked. The chemical shifts were referenced to the frequency of tetramethylsilane (TMS) at 0.00 ppm.

$KH*I$ that was prepared under long duration (two weeks) synthesis according to methods given previously [26-28], and about a one gram sample was placed in a thermal decomposition reactor under an argon atmosphere. The reactor comprised a 1/4" OD by 3" long quartz tube that was sealed at one end and connected at the open end with Swagelock™ fittings to a T. One end of the T was connected to the NMR tube containing $CDCl_3$ solvent, and the other end was attached to a turbo pump. The apparatus was evacuated to less than 1 milliTorr with the $CDCl_3$ maintained at LN temperature. The sample was heated to 200 °C under vacuum. A valve to the pump was closed, and the sample was heated in the evacuated quartz chamber containing the sample to above 600 °C until the sample melted. Gas released from the sample was collected in the $CDCl_3$ solvent, the NMR tube was sealed and warmed to room temperature, and the NMR spectrum was recorded. Using identical samples, the NMR-tube end of the collection apparatus was connected directly to the sampling port of a quadrupole mass spectrometer to test for hydrocarbon contamination. FTIR was also performed on the released gas for this purpose.

An NMR sample from $KH*I$ provided by BlackLight Power, Inc. was also prepared and analyzed at the Naval Air Warfare Center Weapons Division, Naval Air Warfare Center, China Lake, CA under the same procedure except that the $CDCl_3$ solvent was maintained at ice temperature during hydrogen gas collection, and the NMR spectrum was recorded with a 400 MHz instrument at China Lake. Control NMR samples of ultrapure hydrogen dissolved in $CDCl_3$ solvent were also prepared, and NMR spectra were obtained under conditions matching those of the $KH*I$ -derived samples.

The excess power was measured by water bath calorimetry on helium-hydrogen (95/5%) plasmas maintained in a microwave discharge cell compared to control plasmas with the same input power as described previously [24]. The water bath was calibrated by a high precision heater and power supply. A high precision linear response thermistor probe (Omega OL-703) recorded the temperature of the 45 L water bath as a function of time for the stirrer alone to establish the baseline. The heat capacity was determined for several input powers, 30, 40, and 50 W ± 0.01 W, and was found to be independent of input power over this power range within ± 0.05%. The temperature rise of the reservoir as a function of time gave a slope in °C/s. This slope was baseline corrected for the negligible stirrer power and loss to ambient. The constant known input power (J/s), was divided by this slope to give the heat capacity in J/°C. Then, in general, the total power output from the cell to the reservoir was determined by multiplying the heat capacity by the rate of temperature rise (°C/s) to give J/s.

Since the cell and water bath system were adiabatic, the general form of the power balance equation with the possibility of excess power is:

$$P_{in} + P_{ex} - P_{out} = 0 \qquad (15)$$

where P_{in} is the microwave input power, P_{ex} is the excess power generated from the hydrogen catalysis reaction, and P_{out} is the thermal power loss from the cell to the water bath. Since the cell was surrounded by water that was contained in an insulated reservoir with negligible thermal losses, the temperature response of the thermistor T as a function of time t was determined to be

$$\dot{T}(t) = \left(1.940\ X\ 10^5\ J/°C\right)^{-1} \times P_{out} \qquad (16)$$

where $1.940\ X\ 10^5\ J/°C$ is the heat capacity for the least square curve fit of the response to power input for the control experiments ($P_{ex} = 0$). The slope was recorded for about 2 hours after the cell had reached a thermal steady state, to achieve an accuracy of ± 1%.

Results and Discussion

EUV spectroscopy of Helium-Hydrogen and Argon-Hydrogen Plasmas. *Detection of Fractional Rydberg State Hydrogen Molecular Ion* $\mathbf{H_2(1/4)^+}$. In the case of the EUV spectra of helium, krypton, xenon, krypton-hydrogen (90/10%), or xenon-hydrogen (90/10%), no peaks were observed below 65 nm, and no spurious peaks or artifacts due to the grating or the spectrometer were observed. No changes in the emission spectra were observed by the addition of hydrogen to noncatalysts krypton or xenon. Only known atom and ion peaks were observed in the EUV spectrum of the helium and argon microwave discharge emission.

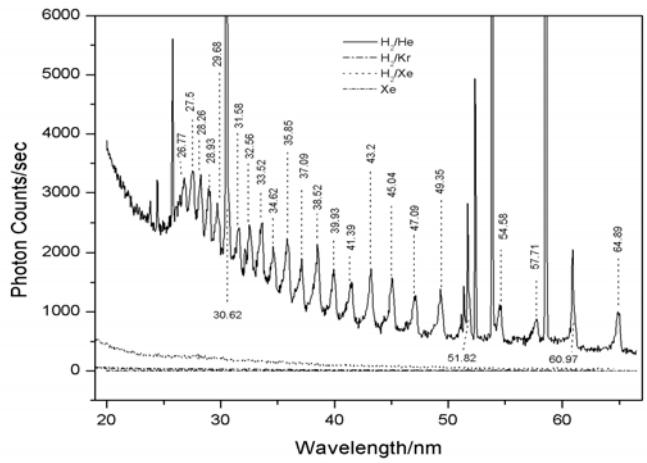

Figure 1. The EUV spectra (20-65 nm) of microwave plasmas of xenon and 10% hydrogen mixed with helium, krypton, and xenon. A vibrational pattern of peaks with an energy spacing of 1.18 eV was observed from the helium-hydrogen plasma having He^+ catalyst. The peaks matched Eq. (9) for $\upsilon* = 0,1,2,3...24$. The series terminated at about 25.7 nm corresponding to the predicted bond energy of $H_2(1/4)^+$ of 48.16 eV given by Eq. (2). No emission was observed from the noncatalyst controls, krypton and xenon alone or with hydrogen. The sharp peaks in the spectrum were assigned to He I and He II.

The EUV spectra (20-65 nm) of the microwave plasmas of xenon and 10% hydrogen mixed with helium, krypton, and xenon are shown in Figure 1. No emission was observed from the noncatalyst controls, krypton and xenon. A characteristic vibrational series was observed for helium-hydrogen (90/10%), but at higher energies than any known molecule by about an order of magnitude. The series was not observed with helium alone as shown in Figure 2. The energies of the peaks observed in Figures 1 and 2 are plotted in Figure 3 as a function of peak number or integer $\upsilon*$. The slope of the linear curve fit in Figure 3 is 1.18 eV, and the intercept is 47.6 eV which matches the predicted series given by Eq. (9) to within the spectrometer resolution of 1%. This energy separation matches the transition-state vibrational energy of the resonant state $H_2(1/2)^+$,

and the series terminates at about 25.7 nm corresponding to the predicted bond energy of $H_2(1/4)^+$ of 48.16 eV given by Eq. (2). Thus, emission in this region was due to the reaction $H(1/4)+H^+ \rightarrow H_2(1/4)^+$ with vibronic coupling with the resonant state $H_2(1/2)^+$ within the transition state. The predicted emission at $E_{D+vib} = E_D\left(H_2(1/4)^+\right) - \left(\upsilon^* + \frac{1}{2}\right)2^2 E_{vib\,H_2^+}$ was observed for $\upsilon^* = 0,1,2,3...24$. All other peaks in the spectra were assigned to He I and He II.

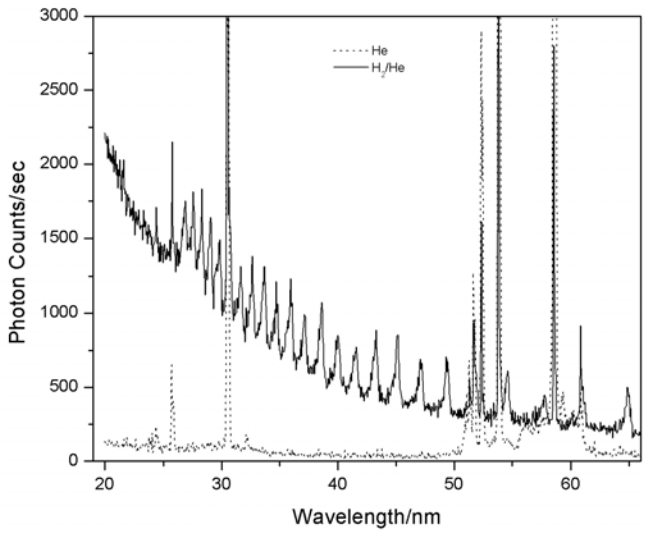

Figure 2. The EUV spectra (20-65 nm) of microwave plasmas of helium-hydrogen (90/10%) (solid) and helium alone (dashed). The vibrational series of peaks assigned to the reaction $H(1/4)+H^+ \rightarrow H_2(1/4)^+$ was observed from the helium-hydrogen plasma having He^+ catalyst and hydrogen, but not from helium alone. The sharp peaks in the spectrum were assigned to He I and He II.

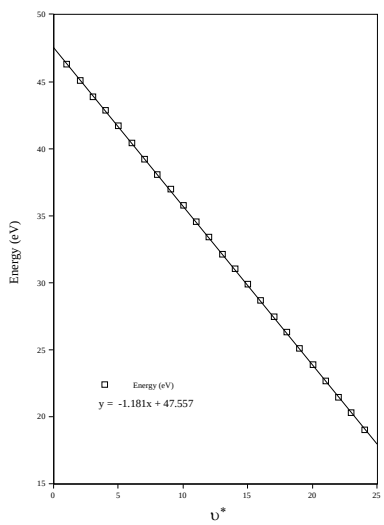

Figure 3. The plot of the energies of the peaks shown in Figures 1 and 2. The slope of the linear curve fit is 1.18 eV, and the intercept is 47.6 eV which matches the predicted emission given by Eq. (9) to within the spectrometer resolution of about 1%.

The EUV spectra (20-65 nm) of microwave plasmas of argon-hydrogen (90/10%) compared with argon alone are shown in Figure 4. The vibrational series of peaks with an energy spacing of 1.18 eV was observed from the argon-hydrogen plasma having Ar^+ catalyst with hydrogen. In contrast, the series was not observed without hydrogen. The peaks matched Eq. (9) for $\upsilon^* = 0,1,2,3...24$.

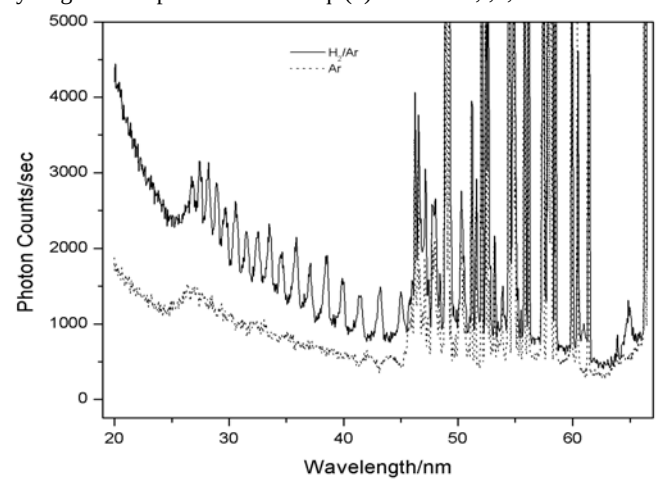

Figure 4. The EUV spectra (20-65 nm) of microwave plasmas of argon-hydrogen (90/10%) (solid) and argon alone (dashed). The vibrational series of peaks assigned to the reaction $H(1/4)+H^+ \rightarrow H_2(1/4)^+$ was observed from the argon-hydrogen plasma having Ar^+ catalyst and hydrogen, but not from argon alone. The sharp peaks in the spectrum were assigned to Ar II.

Detection of Fractional Rydberg State Molecular Hydrogen $\mathbf{H_2(1/4)}$. The observation of emission due to the reaction $H(1/4)+H^+ \rightarrow H_2(1/4)^+$ at low pressure (< 1 Torr) shown in Figures 1 and 2 indicates that $H(1/4)$ formed in the argon-hydrogen plasma. Molecular formation was anticipated under high-pressure conditions (~760 Torr). Thus, EUV spectroscopy of argon-hydrogen plasmas was performed to search for $H_2(1/4)$ from $H(1/4)$ formed by Ar^+ as a catalyst using a 15 keV electron beam to maintain the plasma and to collisionally excite vibration-rotational states of $H_2(1/4)$. The corresponding emission provides a direct measure of the internuclear distance; thus, this method provides the possibility of direct confirmation of $H_2(1/4)$.

The 100-350 nm spectrum of a 450 Torr plasma of argon containing about 1% hydrogen and trace oxygen is shown in Figure 5. Lyman α was observed at 121.6 nm with an adjoining H_2 band, the third continuum of Ar was observed at 200 nm, O I was observed at 130.7 nm, and the $OH(A-X)$ band was observed at 309.7 nm. A series of sharp, evenly-spaced lines was observed in the region 145-185 nm. The only possibilities for peaks of the instrument width are those due to rotation or electronic emission from atoms or ions. The series was not observed when krypton replaced argon. Additional controls of hydrogen, oxygen, nitrogen, water vapor, and nitrogen-oxygen (50/50%) were also negative for the series. No hydrogen lines and no strong O I or O II lines matches any of the lines [30]. In the case that O II is a possibility for some of the lines,

other O II lines of equal oscillator strength were not observed. The O I line at 130.6029 nm having an oscillator strength of over 100 times that of O II lines in this region [30] was weak which made the assignment to O II lines unlikely. No combination of O species exclusively matches the evenly spaced lines in this region. The lines were not observed with argon or krypton with oxygen addition up to 50%, and the lines, when observed with argon, 1% hydrogen, and trace oxygen, did not increase in intensity upon addition of additional oxygen. The series was not observed with argon alone, and only Ar VII and Ar VIII are possible in this region which is not possible at this pressure. Furthermore, no argon species match the observed lines [30].

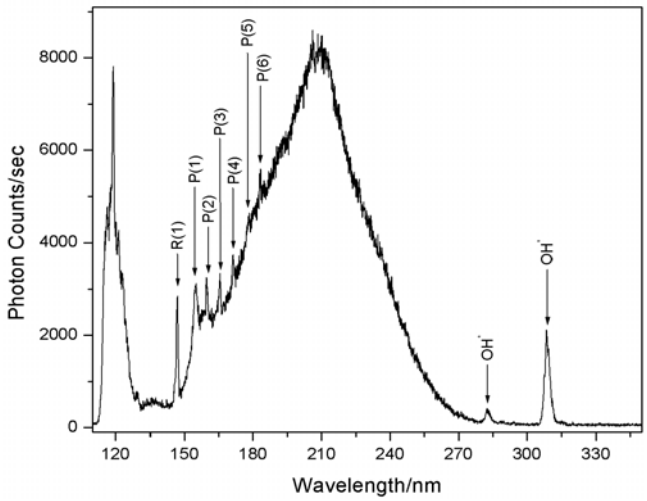

Figure 5. The 100-350 nm spectrum of a 450 Torr plasma of argon containing about 1% hydrogen and trace oxygen using a 15 keV electron gun. Lyman α was observed at 121.6 nm with an adjoining H_2 band, the third continuum of Ar was observed at 200 nm, O I was observed at 130.7 nm, and the $OH(A-X)$ band was observed at 309.7 nm. A series of sharp, evenly-spaced lines was observed in the region 145-185 nm. The series matched the P branch of $H_2(1/4)$ for the vibrational transition $\upsilon = 1 \rightarrow \upsilon = 0$. P(1), P(2), P(3), P(4), P(5), and P(6) were observed at 155.0 nm, 160.2 nm, 165.8 nm, 171.1 nm, 178.0 nm, and 183.2 nm, respectively. The sharp peak at 147.3 nm may be the first member of the R branch, R(0). The R-branch lines appeared to correspond to forbidden transitions. The slope of a linear curve fit is 0.241 eV with an intercept of 8.21 eV which matches Eq. (10) very well for $p = 4$.

The series matched the P branch of $H_2(1/4)$ for the vibrational transition $\upsilon = 1 \rightarrow \upsilon = 0$. P(1), P(2), P(3), P(4), P(5), and P(6) were observed at 155.0 nm, 160.2 nm, 165.8 nm, 171.1 nm, 178.0 nm, and 183.2 nm, respectively. The sharp peak at 147.3 nm may be the first member of the R branch, R(0). The R-branch lines appeared to correspond to forbidden transitions. Selection rules for $H_2(1/p)$ may be $\Delta\upsilon = -1$ and $\Delta J = +1$ in order for a net state change with vibration-rotation coupling. The slope of a linear curve fit was 0.241 eV with an intercept of 8.21 eV which matches Eq. (10) very well for $p = 4$. Using Eqs. (6) and (7) with the measured rotational energy spacing of 0.24 eV establishes an internuclear distance of 1/4 that of the ordinary hydrogen species for $H_2(1/4)$. This technique which is the best measure of the bond distance of any diatomic molecule identifies and unequivocally confirms $H_2(1/4)$.

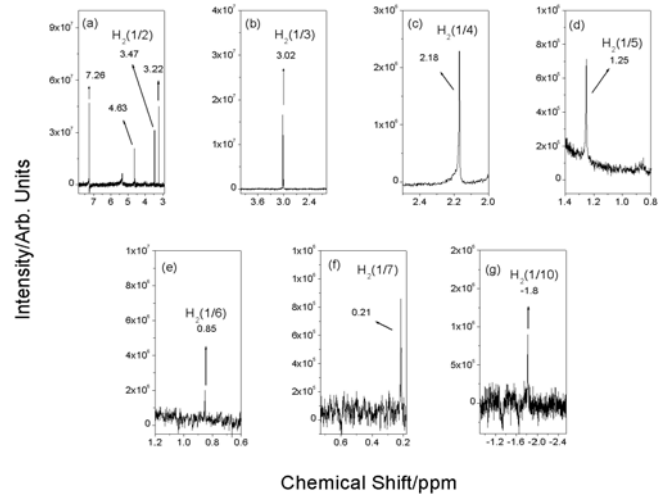

Figure 6 (a)-(g). ^1H NMR spectra on sealed samples of liquid-nitrogen-condensable helium-hydrogen plasma gases dissolved in $CDCl_3$ relative to tetramethylsilane (TMS). The solvent peak was observed at 7.26 ppm, the H_2 peak was observed at 4.63 ppm, and a singlet at 3.22 ppm matched silane. Singlet peaks upfield of H_2 were observed at 3.47, 3.02, 2.18, 1.25, 0.85, 0.21, and -1.8 ppm relative to TMS corresponding to solvent-corrected absolute resonance shifts of -29.16, -29.61, -30.45, -31.38, -31.78, -32.42, and -34.43 ppm, respectively. Using Eq. (12), the data indicates that p = 2, 3, 4, 5, 6, 7, and 10, respectively. The data matched the series $H_2(1/2)$, $H_2(1/3)$, $H_2(1/4)$, $H_2(1/5)$, $H_2(1/6)$, $H_2(1/7)$, and $H_2(1/10)$.

A possible confirmation of the lines identified in this study has been published previously. Ulrich, Wieser, and Murnick [38] compared the third continuum of argon gas with a very pure gas and a spectrum in which the gas was slightly contaminated by oxygen as evidenced by the second order of the 130 nm resonance lines at 160 nm. A series of very narrow lines at the instrument width having an intensity profile that was characteristic of that of a P-branch were observed in the 145-185 nm region. These lines shown in Figure 6 of Ref. [38] matched those in Figure 5. The slope of the linear curve fit was 0.24 eV with an intercept of 8.24 eV which matches Eq. (10) very well for $p = 4$. The series matches the predicted $\upsilon = 1 \rightarrow \upsilon = 0$ vibrational energy of $H_2(1/4)$ of 8.25 eV (Eq. (5)) and its predicted rotational energy spacing of 0.24 eV (Eq. (6)) with $\Delta J = +1;\ J = 1,2,3,4,5,6$ and $\Delta J = -1;\ J = 0$ and where J is the rotational quantum number of the final state. With this assignment all of the peaks in Figure 6 of Ref. [38] could be identified; whereas, the evenly-spaced lines could not be unambiguously assigned by Ulrich et al [38]. The series was not observed in krypton and xenon plasmas. The determination of the presence of the common contaminant, hydrogen, in the argon plasmas is warranted in future studies.

Isolation and Characterization of $H_2(1/p)$. *Cryotrap Pressure.* Helium-hydrogen (90/10%) gas was flowed through the microwave tube and the cryosystem for 2 hours with the trap cooled to LN temperature. No change in pressure over time was observed when the dewar was removed, and the system was warmed to room temperature. The experiment was repeated under the same

conditions but with a plasma maintained with 60 W forward microwave power and 10 W reflected. In contrast to the control case, a liquid-nitrogen-condensable gas was generated in the helium-hydrogen plasma reaction since the pressure due to the reaction product rose from 10^{-5} Torr to 3 Torr as the cryotrap warmed to room temperature.

Mass Spectroscopy. The mass spectrum for the gases collected in the cryotrap from the He/H_2 (90/10%) plasma over the range $m/e=1$ to $m/e=200$ showed that the LN-condensable gas was highly pure hydrogen. The mass spectrum ($m/e=1$ to $m/e=200$) for the gases collected in the cryo-cooler from the He/H_2 (90/10%) plasma only showed peaks in the ($m/e=1$ to $m/e=50$) region. The $m/e=2$ peak was 40-50 times more intense than the $m/e=28$ (nitrogen), $m/e=32$ (oxygen), and $m/e=40$ (argon) peaks that were assigned to very trace residual air contamination. Whereas, without the plasma, the mass $m/e=2$ peak was present in only trace concentration ($\sim 10^{-10}$ Torr) compared with the air contaminant gases that were also present in low abundance ($\sim 10^{-9}$ Torr). Von Engel [39] gives the efficiency of production of various common ions at 70 eV and shows that the cross section for the formation of H_2^+ is 10% of that of air contaminants at the same partial pressure. Thus, hydrogen was ~500 times more abundant in the collected gas than air contaminants which may have originated through back-streaming in the mass spectrometer.

From the phase diagram of helium and hydrogen plotted from data given by Lide [40] and extended to lower pressures and temperatures using the Clausius-Clapeyron equation [41], it is not possible to condense ordinary hydrogen below ~50 Torr at 12-17 K. The condensation of a $m/e=2$ gas in the temperature range of 12-17 K at 700 mTorr that was not removed at 10^{-5} Torr indicates that a novel hydrogen gas formed in the plasma reaction between hydrogen and helium. The results are even more dramatic in the case of the condensation of a $m/e=2$ gas in the temperature range of 77 K using the LN cryotrap.

^1H NMR. The ^1H NMR on $CDCl_3$ showed only a singlet solvent ($CHCl_3$) peak at 7.26 ppm relative to tetramethylsilane (TMS) with small ^{13}C side bands. The ^1H NMR on ultrahigh purity hydrogen dissolved in $CDCl_3$ relative to tetramethylsilane (TMS) showed only singlet peaks at 7.26, 4.63, and 1.57 ppm corresponding to $CHCl_3$, H_2, and H_2O, respectively. The chemical shifts of the $CHCl_3$ and H_2O peaks matched the literature values of 1.56 and 7.26 ppm, respectively [42]. The error in the observed peaks was determined to be ± 0.01 ppm. The ^1H NMR spectroscopic results of the control prepared from the reagent helium-hydrogen mixture was the same as that of the high purity hydrogen control.

H_2 has been characterized by gas phase ^1H NMR. The experimental absolute resonance shift of gas-phase TMS relative to the proton's gyromagnetic frequency is -28.5 ppm [43]. H_2 was observed at 0.48 ppm compared to gas phase TMS set at 0.00 ppm [44]. Thus, the corresponding absolute H_2 gas-phase resonance shift of -28.0 ppm (-28.5 + 0.48) ppm was in excellent agreement with the predicted absolute gas-phase shift of -28.01 ppm given by Eq. (12).

The absolute H_2 gas-phase shift can be used to determine the solvent shift for H_2 dissolved in $CDCl_3$. The correction for the solvent shift can then be applied to other peaks to determine the gas-phase absolute shifts to compare to Eq. (12). The shifts of all of the peaks were relative to liquid-phase TMS which has an experimental absolute resonance shift of -31.5 ppm relative to the proton's gyromagnetic frequency [35-36]. Thus, the experimental shift of H_2 in $CDCl_3$ of 4.63 ppm relative to liquid-phase TMS corresponds to an absolute resonance shift of -26.87 ppm (-31.5 ppm + 4.63 ppm). Using the absolute H_2 gas-phase resonance shift of -28.0 ppm corresponding to 3.5 ppm (-28.0 ppm - 31.5 ppm) relative to liquid TMS, the $CDCl_3$ solvent effect is 1.13 ppm (4.63 ppm - 3.5 ppm) which is comparable to that of hydrocarbons [42].

^1H NMR spectra on sealed samples of condensable helium-hydrogen plasma gases dissolved in $CDCl_3$ relative to tetramethylsilane (TMS) are shown in Figures 6 (a)-(f). The solvent peak was observed at 7.26 ppm, the H_2 peak was observed at 4.63 ppm, and a singlet at 3.22 ppm matched silane. Small ^{29}Si side bands were observed for the latter. The source was determined to be hydrogen-plasma reduction of the quartz tube. The peak was unchanged after three weeks at room temperature. No other silanes, silane decomposition species, or solvent decomposition species were observed even after one month of repeat NMR analysis. Since the plasma gases were first passed through an LN trap before the plasma cell, and the cryotrap was high-vacuum (10^{-6} Torr) capable, no hydrocarbons were anticipated. This was confirmed by mass spectroscopic and FTIR analysis that showed only water vapor in addition to silane as contaminants. Again, the source was determined to be hydrogen-plasma reduction of the quartz tube.

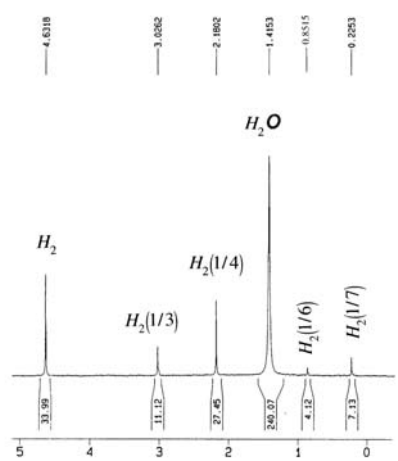

Figure 7. The ^1H NMR spectrum recorded at China Lake on gases from the thermal decomposition of $KH*I$ dissolved in $CDCl_3$ relative to tetramethylsilane (TMS). H_2 and H_2O were observed at 4.63 ppm and 1.42, respectively. Singlet peaks upfield of H_2 were observed at 3.02, 2.18, 0.85, and 0.22 ppm relative to TMS corresponding to solvent-corrected absolute resonance shifts of -29.61, -30.45, -31.78, and -32.41 ppm, respectively. Using Eq. (12), the data indicates that p = 3, 4, 6, and 7, respectively. The data matched the series $H_2(1/3)$, $H_2(1/4)$, $H_2(1/6)$, and $H_2(1/7)$.

As further shown in Figures 6 (a)-(g), singlet peaks upfield of H_2 were observed at 3.47, 3.02, 2.18, 1.25, 0.85, 0.21, and -1.8 ppm relative to TMS corresponding to solvent-corrected absolute resonance shifts of -29.16, -29.61, -30.45, -31.38, -31.78, -32.42, and -34.43 ppm, respectively. Using Eq. (12), the data indicates that p = 2, 3, 4, 5, 6, 7, and 10, respectively. The data matched the series $H_2(1/2)$, $H_2(1/3)$, $H_2(1/4)$, $H_2(1/5)$, $H_2(1/6)$, $H_2(1/7)$, and $H_2(1/10)$. The molecules corresponding to the reaction product atom $H(1/3)$ with products from further transitions as given in Refs. [2-3] are in agreement with the observed molecules.

^1H NMR spectra were recorded at China Lake and at BlackLight Power, Inc. on ultrahigh purity hydrogen and gases from the thermal decomposition of $KH*I$ dissolved in $CDCl_3$ relative to tetramethylsilane (TMS). These samples were determined not to contain hydrocarbons by mass spectroscopy and FTIR analysis. Only the $CDCl_3$, H_2, and H_2O peaks were observed from the controls. As shown in Figure 7, novel singlet peaks upfield of H_2 were observed from a $KH*I$ -derived sample run at China Lake. The peaks at 3.02, 2.18, 0.85, and 0.22 ppm relative to TMS corresponded to solvent-corrected absolute resonance shifts of -29.61, -30.45, -31.78, and -32.41 ppm, respectively. Using Eq. (12), the data indicates that p = 3, 4, 6, and 7, respectively. The data matched the series $H_2(1/3)$, $H_2(1/4)$, $H_2(1/6)$, and $H_2(1/7)$. The observed products were consistent with those anticipated with the catalysis of H by K to form $H(1/4)$ and subsequent transition reactions [2-3, 7, 16, 18].

As shown in Figures 6 and 7, the observation of the series of singlet peaks upfield of H_2 with a predicted integer spacing of 0.64 ppm at 3.47, 3.02, 2.18, 1.25, 0.85, and 0.22 ppm identified as the consecutive series $H_2(1/2)$, $H_2(1/3)$, $H_2(1/4)$, $H_2(1/5)$, $H_2(1/6)$, and $H_2(1/7)$ and $H_2(1/10)$ at -1.8 ppm provides powerful confirmation of the existence of $H_2(1/p)$. Furthermore, the ^1H NMR spectra of gases from the thermal decomposition of $KH*I$ matched those of LN-condensable hydrogen. This provides strong support that compounds such as $KH*I$ contain hydride ions $H^-(1/p)$ in the same fractional quantum state p as the corresponding observed $H_2(1/p)$. Observational agreement with predicted positions of upfield-shifted ^1H MAS NMR peaks (Eq. (13)) of the compounds [7, 18, 26-28], catalyst reactions [16, 18, 20-21], and spectroscopic data [16] supports this conclusion.

The existence of novel alkaline and alkaline earth hydride and halido-hydrides were previously identified by large distinct upfield ^1H NMR resonances compared to the NMR peaks of the corresponding ordinary hydrides [18, 26-28]. Using a number of analytical techniques such as XPS and time-of-flight-secondary-mass-spectroscopy (ToF-SIMS) as well as NMR, the hydrogen content was assigned to $H^-(1/p)$, novel high-binding-energy hydride ions in stable fractional principal quantum states [7, 18, 26-28]. Upfield shifts of the novel hydride compounds matched those predicted for $H^-(1/2)$ and $H^-(1/4)$ (Eq. (13)). Novel spectral emission from $H^-(1/2)$ and $H^-(1/4)$, the predicted products from the potassium catalyst reaction and the supporting results of (1) the formation of a hydrogen plasma with intense extreme ultraviolet (EUV) emission at low temperatures (e.g. $\approx 10^3\ K$) and an extraordinary low field strength of about 1-2 V/cm [8-10, 17-19, 21] or without an electric field or power input other than thermal [19] from atomic hydrogen and certain atomized elements or certain gaseous ions that serve as catalysts, (2) a high positive net enthalpy of reaction [18], (3) characteristic predicted catalyst emission [16, 20-21], (4) ~15 eV Doppler broadening of the Balmer lines [16, 20-21], and (5) inversion of the Lyman lines [20-21] have also been reported previously.

Based on their stability characteristics, advanced hydride technologies are indicated. Hydride ions $H^-(1/p)$ having extraordinary binding energies may stabilize a cation M^{x+} in an extraordinarily high oxidation state as the basis of a high voltage battery. And, a rocketry propellant based on $H^-(1/24)$ to $H_2(1/24)$ may be possible with an energy release so large that it may be transformational. Significant applications also exist for the corresponding molecular species $H_2(1/p)$. The results of this study indicate that excited vibration-rotational levels of $H_2(1/4)$ could be the basis of a UV laser that could significantly advance photolithography.

Power Balance of the Helium-Hydrogen Microwave Plasma. In addition to high energy spectral emission as shown in Sec. IIIA and previously [1-5], other indications of very energetic reactions are observed. For example, population inversion has been observed from plasmas which contain atomic hydrogen with the presence of a catalyst [20-23], and selective H broadening with a microwave plasma having no high DC field present was reported previously [12-14]. Microwave He/H_2 and Ar/H_2 plasmas showed extraordinary broadening corresponding to an average hydrogen atom temperature of $180-210eV$ and $110-130eV$, respectively. Whereas, pure hydrogen and Xe/H_2 microwave plasmas showed no excessive broadening corresponding to an average hydrogen atom temperature of $<2eV$ [12-14]. Only the H lines were Doppler broadened, and this result was shown to be inexplicable by any mechanism based on electric field acceleration of charged species. The observation of excessive Balmer line broadening in microwave driven plasmas as well as other hydrogen-mixed plasmas maintained in glow discharge [9-13] and RF discharge cells [13, 15] as well as unique chemically driven plasmas called resonant-transfer or rt-plasmas [16, 18, 20-21] requires a source of energy other than that provided by the electric field. The formation of fast H only in specific predicted plasmas was explained by a resonant energy transfer between hydrogen atoms and catalysts such as Ar^+ or He^+ of an integer multiple of the potential energy of atomic hydrogen, 27.2 eV [12-14]. Consistent with predictions, noncatalyst plasma mixtures such as Kr/H_2 and Xe/H_2 show no unique features. The observation of the $H_2(1/4)$ rotational lines reported in Sec. IIIAb from Ar/H_2 plasmas but not from Kr/H_2 and Xe/H_2 plasmas also matches predictions.

The excess power of the catalytic reaction was measured by water bath calorimetry. The water bath calorimeter is an absolute standard and indicated $P_{in} = 41{,}9 \pm 1W$ input power at the selected diode settings for all control plasmas. From these results, power input to the helium-hydrogen plasma was confidently known as the diode readings were identically matched for the controls. For example, the $T(t)$ water bath response to stirring and then with selected panel meter readings of the constant forward and reflected

microwave input power to krypton was recorded as shown in Figure 8. Using the corresponding $\dot{T}(t)$ in Eq. (16), the microwave input power was determined to be 41.9 ± 1 W. The $T(t)$ response was significantly increased for helium-hydrogen (95/5%) as shown in Figure 8. From the difference in the $T(t)$ water bath response, the output and excess power of the helium-hydrogen plasma reaction was determined to be 62.1 ± 1 W and 20.2 ± 1 W using Eq. (16) and Eq. (15) with the measured $P_{in} = 41{,}9 \pm 1W$. The sources of error were the error in the calibration curve (±0.05 W) and the measured microwave input power (±1 W). The propagated error of the calibration and power measurements was ± 1 W. Given an excess power of 20.2 W in $3\,cm^3$ and a helium-hydrogen (95/5%) flow rate of 10.0 sccm, the excess power density and energy balance were high, $6.7\,W/cm^3$ and $-5.4\times10^4\,kJ/mole\,H_2$ ($280\,eV/H\ atom$), respectively.

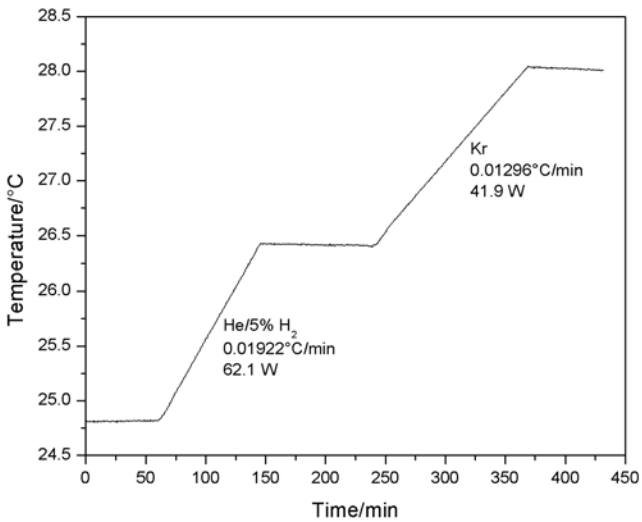

Figure 8. The $T(t)$ water bath response to stirring and then with selected panel meter readings of the constant forward and reflected microwave input power to helium-hydrogen (95/5%) mixture was recorded. Krypton control was run at identical microwave input power readings, and the microwave input power was determined to be 41.9 ± 1 W. From the difference in the $T(t)$ water bath response, the excess power of the helium-hydrogen plasma reaction was determined to be 20.2 ± 1 W.

The results indicate that a new power source based on the catalysis of atomic hydrogen is not only possible, but it may be competitive with gas-turbine combustion. Furthermore, since the identified $H_2(1/p)$ byproduct is stable and lighter-than-air, it can not accumulate in the Earth's atmosphere. The environmental impact of handling fossil fuels and managing the pollution of air, water, and ground caused by the ash generated by fossil fuels or the radioactive waste from a nuclear plant may be eliminated.

Acknowledgments. Special thanks to D. E. Murnick and M. Salvermoser of Rutgers University for providing the 15 keV electron gun. D. C. Harris, Naval Air Warfare Center Weapons Division, Naval Air Warfare Center, China Lake, CA, is acknowledged for suggesting the method of identifying $H_2(1/p)$ by ^1H NMR using $CDCl_3$ solvent. D. C. Harris and L. Merwin are acknowledged for preparing and analyzing a $KH*I$ NMR sample.

References

(1) R. L. Mills, P. Ray, *J. Phys. D: Appl. Phys*., **2003**, *36*, 1535.
(2) R. L. Mills, P. Ray, B. Dhandapani, M. Nansteel, X. Chen, J. He, *J Mol. Struct*., **2002**, *643* (1-3), 43.
(3) R. Mills, P. Ray, *Int. J. Hydrogen Energy*, **2002**, *27*, 301.
(4) R. L. Mills, P. Ray, J. Dong, M. Nansteel, B. Dhandapani, J. He, *Vib. Spectrosc*., **2003**, *31*, 195.
(5) R. Mills, P. Ray, *Int. J. Hydrogen Energy*, **2002**, *27*, 533.
(6) R. Mills, *The Grand Unified Theory of Classical Quantum Mechanics*, September 2001 Edition, BlackLight Power, Inc., Cranbury, New Jersey, Distributed by Amazon.com; January (**2003**) Edition posted at www.blacklightpower.com.
(7) R. L. Mills, "The Nature of the Chemical Bond Revisited and an Alternative Maxwellian Approach," submitted.
(8) R. Mills, J. Dong, Y. Lu, *Int. J. Hydrogen Energy*, **2000**, *25*, 919.
(9) R. Mills, M. Nansteel, P. Ray, *IEEE Transactions on Plasma Science*, **2002**, *30*, 639.
(10) R. Mills, M. Nansteel, P. Ray, *New J. Phys*., **2002**, *4*, 70.1.
(11) R. Mills, M. Nansteel, P. Ray, *J. Plasma Phy.s*, **2003**, *69*, 131.
(12) R. L. Mills, P. Ray, B. Dhandapani, R. M. Mayo, J. He, *J. Appl. Phys.*, **2002**, *92*, 7008.
(13) R. L. Mills, P. Ray, B. Dhandapani, J. He, *IEEE Trans. Plasma Sci*., **2003**, *31*(3), (2003), 338.
(14) R. L. Mills, P. Ray, *New J. Phys*., www.njp.org, **2002**, *4*, 22.1.
(15) J. Phillips, C. Chen, "Evidence of Energetic Reaction Between Helium and Hydrogen Species in RF Generated Plasmas," submitted.
(16) R. L. Mills, P. Ray, *Int. J. Hydrogen Energy*, **2003**, *28*, 825.
(17) R. Mills, Int. J. Hydrogen Energy, **2001**, *26*, 1041.
(18) R. Mills, P. Ray, B. Dhandapani, W. Good, P. Jansson, M. Nansteel, J. He, A. Voigt, "Spectroscopic and NMR Identification of Novel Hydride Ions in Fractional Quantum Energy States Formed by an Exothermic Reaction of Atomic Hydrogen with Certain Catalysts," submitted.
(19) H. Conrads, R. Mills, Th. Wrubel, *Plasma Sources Sci. Technol*., **2003**, *12*, 389.
(20) R. Mills, P. Ray, R. M. Mayo, *IEEE Trans. Plasma Sci.*, **2003**, *31* (2), 236.
(21) R. L. Mills, P. Ray, *J. Phys. D: Appl. Phys.*, **2003**, *36*, 1504.
(22) R. Mills, P. Ray, R. M. Mayo, *Appl. Phys. Lett*., **2003**, *82* (11), 1679.
(23) R. L. Mills, P. C. Ray, R. M. Mayo, M. Nansteel, B. Dhandapani, J. Phillips, "Spectroscopic Study of Unique Line Broadening and Inversion in Low Pressure Microwave Generated Water Plasmas," submitted.
(24) R. L. Mills, X. Chen, P. Ray, J. He, B. Dhandapani, *Thermochim. Acta*, **2003**, *406* (1-2) 35.
(25) R. Mills, B. Dhandapani, M. Nansteel, J. He, P. Ray, "Liquid-Nitrogen-Condensable Molecular Hydrogen Gas Isolated from a Catalytic Plasma Reaction," submitted.
(26) R. Mills, B. Dhandapani, M. Nansteel, J. He, T. Shannon, A. Echezuria, *Int. J. Hydrogen Energy*, **2001**, *26*, 339.
(27) R. Mills, B. Dhandapani, N. Greenig, J. He, *Int. J. Hydrogen Energy*, **2000**, *25*, 1185.
(28) R. Mills, B. Dhandapani, M. Nansteel, J. He, A. Voigt, *Int. J. Hydrogen Energy*, **2001**, *26*, 965.
(29) M. Karplus, R. N. Porter, *Atoms and Molecules an Introduction for Students of Physical Chemistry*, The Benjamin/Cummings

Publishing Company, Menlo Park, California, (**1970**), pp. 447-484.
(30) NIST Atomic Spectra Database, www.physics.nist.gov/cgi-bin/AtData/display.ksh.
(31) H. Beutler, *Z. Phys. Chem*., **1934**, *27B*, 287.
(32) G. Herzberg, L. L. Howe, *Can. J. Phys*., **1959**, *37*, 636.
(33) P. W. Atkins, *Physical Chemistry*, Second Edition, W. H. Freeman, San Francisco, (**1982**), p. 589.
(34) R. L. Mills, Y. Lu, J. He, M. Nansteel, P. Ray, X. Chen, A. Voigt, B. Dhandapani, "Spectral Identification of New States of Hydrogen," submitted.
(35) K. K. Baldridge, J. S. Siegel, *J. Phys. Chem. A*, **1999**, *103*, 4038.
(36) J. Mason, Editor, *Multinuclear NMR*, Plenum Press, New York, (**1987**), Chp. 3.
(37) J. Wieser, D. E. Murnick, A. Ulrich, H. A Higgins, A. Liddle, W. L. Brown, *Rev. Sci. Instrum.*, **1997**, *6* (3), 1360.
(38) A. Ulrich, J. Wieser, D. E. Murnick, Second International Conference on Atomic and Molecular Pulsed Lasers, *Proc. SPIE*, **1998**, *3403*, 300.
(39) A. von Engel, *Ionized Gases*, American Institute of Physics Press, New York, (**1965**), pp. 62-64.
(40) D. R. Lide, *CRC Handbook of Chemistry and Physics*, 76 th Edition, CRC Press, Boca Raton, Florida, (**1995-6**), p. 6-66 and p. 6-140.
(41) I. N. Levine, *Physical Chemistry*, McGraw-Hill Book Company, New York, (**1978**), pp. 174-175.
(42) H. E. Gottlieb, V. Kotlyar, A. Nudelman, *J. Org. Chem*., **1997**, *62*, 7512.
(43) C. Suarez, E. J. Nicholas, M. R. Bowman, J. Phys. Chem. A, **2003**, *107*, 3024.
(44) C. Suarez, "Gas-phase NMR spectroscopy", *The Chem. Educator*, **1998**, 3 (2).

Studies of the Activation and Homologation of Methane on Supported Metal Catalysts

Lin-Hua Song, Zi-Feng Yan, Shi-Kong Shen

Department of Chemical Engineering, University of Petroleum, Dongying 257062, Shandong, P. R. China

Introduction

One of the intriguing problems in heterogeneous catalysis is the activation and direct conversion of methane into liquid fuel and useful chemicals[1]. Methane activation is very difficult because methane is a thermodynamically stable product with a noble gas-like configuration. The very strong tetrahedral C-H bonds (435kJ/mol) offer no functional groups, magnetic moments, or polar distortions to facilitate chemical attack. Of interests are the recent works reported by Belgued[2] and Koerts[3] who achieved the conversion of methane by two-step reaction occurred under the moderate temperatures to form C_2-C_6 alkanes. Here we report the results of activation and homologation of methane to form C_2 to C_6 alkanes at moderate conditions in a two-step route in which methane is first thermally activated. Of special is that the two-step reactions were performed at the same temperature and that the method of transient evaluation of the catalysts was systematically suggested.

Experimental

The catalysts were prepared by ion-exchanging the silica support with solutions of transiition metals to yield a nominal 5 wt% metal. The following solution of salts of transition metals were used: $[Fe(NH_3)_6^{3+}$、$Co(NH_3)_6^{3+}$、$Ni(NH_3)_4^{2+}$、$Pd(NH_3)_4^{2+}$ and $Pt(NH_3)_4^{2+}]$.

For each experiment 300mg of the catalyst were placed in the micro-reactor and was reduced *in-situ* at 723K. Methane decomposition was performed from a flow of 10ml/min of methane. The surface carbon created from methane was characterized by a temperature programmed surface reaction (TPSR) in a flow of 20ml/min of hydrogen. The procedure of the evaluation of homologation of methane is described as follows:

$$\underset{20\text{ml/min}}{\overset{3\text{mins}}{H_2 \longrightarrow}} \; \underset{10\text{ml/min}}{\overset{4\text{mins}}{CH_4 \longrightarrow}} \; \underset{20\text{ml/min}}{\overset{10\text{mins}}{H_2 \longrightarrow}} \; \underset{20\text{ml/min}}{\overset{8\text{mins}}{He \longrightarrow}} \; \underset{20\text{ml/min}}{\overset{5\text{mins}}{H_2 \longrightarrow}} \; \underset{20\text{ml/min}}{\overset{5\text{mins}}{He \longrightarrow}} \; He$$

Product analysis was performed on line with an ion-trap detector (Finnigan-MAT 700).

The presence of surface carbon formed by the decomposition of methane was well manifested by its reaction with hydrogen. After flushing of the reactor with pure helium flow (following methane dissociation at a certain temperature for 5mins and cooling quickly to room temperature) and switching to a hydrogen flow, the desorbed species from the metal surface along with the temperature programmed process were simultaneously testified by the above on-line ion-trap detector.

Results and Discussion

The homologation of methane is thermodynamically not allowed in one reaction step, due to the positive change in Gibbs free energy (+16.8 kcal/mol at 500K). A tentative approach is to split the overall reaction into two reaction steps occurring under different conditions.

$$CH_4 + CH_4 \rightarrow C_2H_6 \qquad (1)$$

$$CH_4 \rightarrow CHx + (4\text{-}x)\,H \qquad (2)$$

$$CHx + CHx + (6\text{-}2x)\,H \rightarrow C_2H_6 \qquad (3)$$

In such a two-step route the thermodynamic limitation might be overcome. The decomposition of methane (2) is endothermal $\triangle H > O$ (For gas phase reaction under standard conditions, $\triangle H^0_s = +96.08$kcal/mol) while the change in entropy is positive $\triangle S > O$ ($\triangle S^0_s = +29.25$cal/mol). The hydrogenation of CHx (x=0-3) species to form higher hydrocarbons (3) is exothermic $\triangle H < 0$ (For gas phase reaction under standard conditions, $\triangle H^0_s = -89.84$ kcal/mol) and the change in entropy is negative $\triangle S < 0$ ($\triangle S^0_s = -15.94$ cal/mol). It means that the changes in Gibbs free energy of the reaction steps (2) and (3) might be both negative under different conditions. Therefore, the overall reaction could be occurred under a certain moderate temperature, hence $\triangle G_T < 0$. Table 1 shows that the two-step reaction method is effective for the homologation of methane and that the conversion of methane depends decisively on the nature of transition metals. It also indicates that the two steps can be performed at the same temperature. Platinum and cobalt exhibit favorable catalytic performance.

Figure 1. Effect of metal loadings on methane homologation at 523K on Co/SiO_2 catalysts

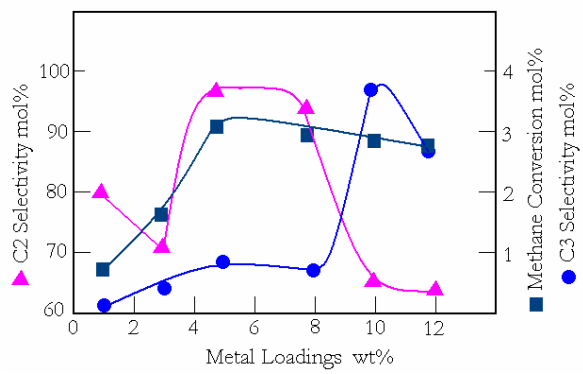

Table 1 Catalytic Performance of Different Transition Metal Catalyst on Methane Homologation at 523K

Catalyst	Metal Load. (wt.%)	CH_4 Conversion (mol%)	Selectivity to (mol%)		
			C_2	C_3	Total
Pt/SiO_2	5.0	9.91	90.13	6.13	96.26
Pd/SiO_2	5.0	0.62	98.06	----	98.06
Co/SiO_2	5.0	2.65	99.06	0.83	99.89
Ni/SiO_2	5.0	0.02	8.03	1.61	9.64
Fe/SiO_2	5.0	0.01	0.55	0.02	0.57

Fig. 1 demonstrates that the optimum transition-metal loading is 5wt%. Fig. 2 illustrates that between the two reactions exists a temperature gap between the optimum adsorption of methane and the subsequently optimum hydrogenation even though the two steps can be performed at the same temperature range. It means that the reactive intermediates of methane homologation are not just only the carbidic species formed by the decomposition of methane firstly suggested by Koerts. The other factors, such as bimetal alloy, metal additives and supports, were also investigated. The results indicate that bimetal and metal additive catalysts show negative effects for methane homologation and that the silica is the most effective support. EDAX data shows that the non-noble metal in bimetal catalysts and the metal additive in additive catalysts largely enriched on the surface of the

catalysts. It means that the transition metals enriched on the catalyst surface act as the unique role of the activation and homologation of methane. Further experiments indicated that the catalytic performance and product distribution sensitively depend on the nature of transition metals and the variance of the conditions of the reactions. This means that the optimization of the homologation of methane on supported transition metals could result in an attractive route for the utilization of methane.

Figure 2 Temperature effect for methane homologation on Pt/SiO_2 catalyst

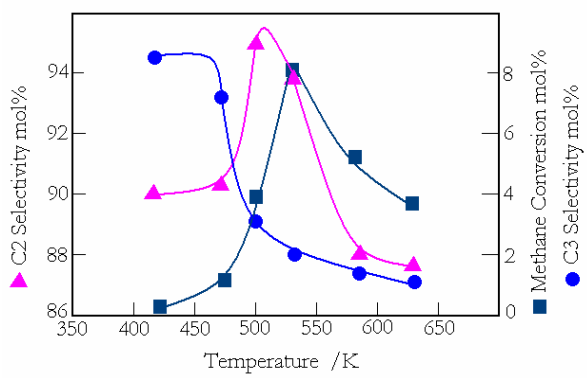

Methane decomposition on transition-metal surface is a thermally activated process. Fig. 3 reveals that methane was initially produced at higher rates on almost all catalysts and higher hydrocarbons was detected only in traces. The result indicate that three kinds of carbonaceous species with different structures and properties are formed by the decomposition of methane on catalyst surface, which are tentatively assigned as follows: Cα (379K), carbidic species; Cβ (572K), carbonaceous CHx (x<3) species and Cγ (813K), graphitic carbon species respectively.

Figure 3 TPSR spectra of adsorbed methane on different metals at 523K.

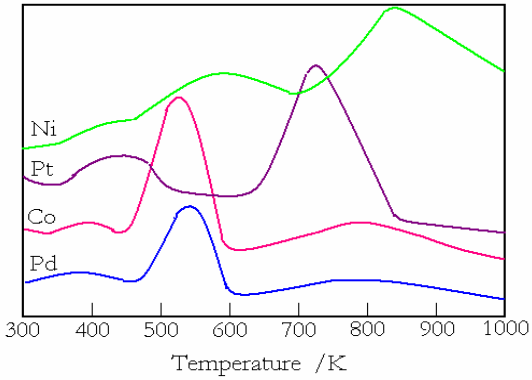

Further experiments showed that the distribution and the features of these different carbonaceous species depend sensitively on the nature of transition metals and the different conditions of methane adsorption. The results of adsorbed methane at different exposure duration at 573K indicate that the adsorbed methane is initially decomposed into high hydrogen-deficient carbidic Cα and carbonaceous Cβ species. The formation of carbidic Cα species was greatly decreased along with the lengthening of methane exposure time. It may be caused by the increasing of the surface carbon coverage. Further experiments even indicated that the formation of Cα is seriously inhibited and the transformation of Cα into Cβ and Cγ species is greatly accelerated with the increasing of carbon coverage and the adsorption temperature of methane. TPSR results of adsorbed methane and results of surface reaction of probe molecules CH_3I showed that the carbidic Cα and carbonaceous Cβ species are the surface intermediates of the homologation of methane and that the presence of reactive Cα species is the origin of the temperature gap between the methane adsorption and subsequent hydrogenation.

Table 2. Catalytic Performance of Transition Metal Catalysts on Various Supports for Methane Homologation at 523K

Catalyst	Support	Metal Loadings (wt%)	CH_4 Conversion (mol%)	Selectivity to (mol%)	
				C_2	C_3
PtS	SiO_2	3.0	1.31	92.91	5.18
PtA	Al_2O_3	3.0	0.66	92.79	3.20
PtT	TiO_2	3.0	----	-----	----
PdS	SiO_2	5.0	0.62	98.06	----
PdA	Al_2O_3	5.0	0.57	97.70	0.73
PdT	TiO_2	5.0	0.52	95.38	1.29
CoS	SiO_2	5.0	2.65	99.06	0.83
CoA	Al_2O_3	5.0	0.01	86.78	6.08
CoT	TiO_2	5.0	0.01	90.00	----
FeS	SiO_2	5.0	0.01	0.55	0.02
FeA	Al_2O_3	5.0	0.01	30.45	----
FeT	TiO_2	5.0	----	-----	----

Each figure should have a number and caption, formatted as follows below the figure:

Conclusions

The homologation of methane on supported transition metal catalysts was extensively investigated by using the transientresponse technique (TRT). The different factors which greatly affect the reaction were also extensively studied. An important approach is to split the overall reaction into two reaction steps occurring under moderate temperatures. In such a two-step route the thermodynamic limitations can be overcome and the homologation of methane may be practically achieved. The optimum conversion of methane on 5wt% Pt/SiO_2 catalyst in the homologation of methane is 9.91% reached at 523K.

The activation of methane on silica-supported transition metals was well investigated by TPSR spectroscopy, which revealed that a large variance of carbon reactivity and their distribution of surface carbons were greatly influenced with the conditions of formation of surface carbon and with the nature of the transition metals. Carbidic Cα and carbonaceous Cβ species formed by the decomposition of methane on metal surface may be the active intermediates which are responsible for the lengthening of carbon-carbon chain on catalyst surface.

References

[1] D. M. Golden, S. W. Benson, *Chem. Rev.*, **1969**, 69,125.
[2] T. Koerts, R. A. van Santen, *J. Catal.*, **1992,** 138,101.
[3] M.Belgued, J. Saint-Just, *Catal. Today*, **1992**, 13, 437.

SURVEY OF ULTRA-TRACE METALS IN GAS TURBINE FUELS

Bruce Rising

New Unit Marketing
Siemens Westinghouse Power Corporation
Orlando, Florida 32826
bruce.rising@siemens.com

Phil Sorurbakhsh

Texas Oil Tech Laboratories
Houston, Texas
psorurbakhsh@txoiltechlabs.com

Jianfan Wu

Gas Turbine Engineering
Siemens Westinghouse Power Corporation
Orlando, Florida 32826
jianfan.wu@siemens.com

Gas turbines are multi-fuel capable power generation systems. Because of their robust design, they can operate on low heating value gases, liquid fuels, natural gases and refinery gases. In a recent industry study, the environmental impact related to gas turbine operation on fuel oil was determined based on the available emissions data for metal emissions from gas turbines. Data collected by EPA reported the noted detectable trace metal emissions during oil operation. However, many of the tests were over fifteen years old, and fuel from the storage tanks at the facility may have been even older. Attempts to determine an accurate environmental assessment were hindered by the quality of the emissions data, and the paucity of fuel sample analytical results for distillate fuels..

Considering the great improvements in the US refining infrastructure, we concluded that any metals in a distillate fuel oil sample would probably be at the ultra-trace level, and would very likely be at the detection limits of the most analytical methods. Further, the concentrations of any hazardous metals (such as lead or mercury) would be extremely low, and the modeled emissions from using such a fuel would yield no measurable health impact. To address this question, we reviewed the existing literature on the subject, and found that no coordinated effort had attempted to identify the concentrations of trace hazardous metals, certainly not using some of the latest measurement methods (in this case ICP-MS).

The next step was to collect samples, and screen them for the presence of eight hazardous metals. Fuel samples (distillate) were collected from around the United States, taken from existing storage facilities, with fuel tanks assigned to a gas turbine power generation unit. Samples were taken to be representative of each Petroleum Administrative Defense Districts (PADD). The survey results revealed no measurable concentrations of Arsenic, Mercury or Lead in any fuel sample taken. No detectable levels of Chromium VI were reported. All samples were screened using Mass-Spec, with detection levels below 1 ppb. These results indicate that the distillate feedstocks available to the power generation industry are essentially free of toxic metals, and pose no health risk to the public when used in a gas turbine. The results also suggest that the petroleum distillate transmission and distribution system does not introduce cross contamination to the fuel supply.

Introduction

Non-combustible materials present in a fuel are typically released into the environment during the combustion process. With low-grade fuels, such as residual fuel oil or coal, metals, including toxic metals can be present in significant concentrations. Such is not the case for distillate fuels. Yet, there has been a widely held perspective that distillate fuels encumbered with potentially toxic metals.

The metals of most concern are those that exhibit a high degree of toxicity, or carcinogenicity, at very low concentrations. Mercury and lead are two key metals where there has been intense interest to reduce or eliminate their release into the environment. Removal of lead from gasoline, and switching to cleaner fuels has had a positive impact in reducing these emissions into the environment. In the twenty years since the removal of lead from gasoline was mandated there has been a steady decrease in lead emissions, and a steady increase in the quality of liquid fuels available for the power generation industry. As the results show here, the quality of distillate fuels is exceptional, and the metal contaminants found in liquid fuel oil are even lower than those mandated in drinking water.

Experimental

Samples from across the US were collected at storage facilities supplying fuel to power generation installations. Thirteen samples were collected and analyzed using ion mass spectrometry to identify the presence of specific metal toxins in the fuels

The toxic metals selected for this study were based on the needs for conducting an environmental health risk analysis related to gas turbine operation. In the risk analysis, emissions from a gas or fuel oil fired gas turbine were determined based on the mass emission rates of each toxic component. Both organic and inorganic emissions were used in the health risk analysis. For liquid fuel (No. 2 fuel oil) operation, the analysis assumed that any metal in the exhaust was due to the presence of metals in the fuel oil. In the initial phase of the study, the dominant metal of concern (based on results of emission tests on gas turbines) was chromium, since emission measurements of chromium yielded the highest emission factors. Yet with chromium, the dominant risk is the Cr-VI oxidation state. However, the existing emissions test data did not attempt to quantify the oxidation state of any metals reportedly detected in the exhaust.

Routine industrial fuel tests, with metal detection levels in the ppm range, report measurable concentrations of arsenic and lead. However, the metals are almost routinely reported at the detection limits of the apparatus, which was not sufficient for our needs. In the risk analysis, the presence of either arsenic or lead at the ppm level would calculate unacceptable risk levels. To address the accuracy of the earlier fuel tests, and to estimate health risks related to emissions from burning liquid fuels, the set of metals selected for a detailed ultra-trace survey was selected. Those metals in selected are shown in the following table.

1. Arsenic	5. Nickel
2. Cadmium	6. Manganese
3. Chromium	7. Selenium
4. Lead	8. Mercury

Metal Analysis from Fuel Samples Selected from Across United States
Samples collected from Gas Turbine Installations around the United States

All concentrations are reported in units of ppb (by weight)

	State or Region	Sample ID	PADD	Arsenic	Cadmium	Total Chromium	Chrome VI	Lead	Manganese	Nickel	Selenium	Mercury
1	California	30352	V	0	0	175	0	3.01	6.9	0	0	0
2	Colorado	30374	IV	0	0	203	0	1.89	6.73	0	0	0
3	Florida	30391	III	0	0	244.6	0	3.48	5.56	0	0	0
4	Wisconsin	30353	III	0	0	226.8	0	2.07	6.03	4.93	0	0
5	Florida	30354	III	0	0	238.2	0	5.29	5.76	12.33	0	0
6	Minnesota	30355	II	0	0	272.1	0	7.2	6.35	184.77	0	0
7	California-South	30405	V	0	0	175.8	0	18.79	10.07	15.05	0	0
8	NC	30423	III	0	0	259.16	0	2.3	6.61	28.95	0	0
9	Arkansas	30424	IV	0	0	202.49	0	46.18	10.95	28.2	0	0
10	Arkansas	30447	IV	0	0	403		61	0	0	0	0
11	Arizona	30494	IV	0	0	306		41	0	0	0	0
12	California-North	30522	V	0	0	165	0	0	0	0	0	0
13	Maine	30425	I	0	0	279.88	0	2.59	7.11	101.78	0	0
	Average			**0**	**0**	**242.4**		**15.0**	**5.5**	**28.9**	**0**	**0**
	SD			**0**	**0**	**65.05**		**20.59**	**3.53**	**54.51**	**0**	**0**
	Max			**0**	**0**	**403**		**61**	**10.95**	**184.77**	**0**	**0**
	Detection Limit, ppb			**0.9**	**0.1**	**0.07**		**0.08**	**0.1**	**0.2**	**5**	**0.2**

Table 1. Summary Of Distillate Oil ICP Results.

Analytical Method. Fuel characterization methods have been used extensively to quantify the presence of various components, including metals, in fuel oil. Historically, most of the test methods have cutoff their analysis at the 1 ppm (1,000 ppb) level, and usually this has been sufficient.

But to accurately determine the impact of burning liquid fuel, and the subsequent release of any metals into the environment, it has been necessary to push for a deeper and more thorough analysis using improved methods methods.

For this study, an Inductively Coupled Plasmas-Mass Spectrometer (Thermo-Elemental X7 ICP/MS) was used. It uses a high temperature plasma between 6000 K and 8000 K, connected to a high sensitivity mass spectrometer. The plasma is formed in an RF chamber, where the sample can be delivered as a solution, vapor, or even solid. The mass spectrometer is a quadrapole mass-spec designed to rapidly measure ions at each mass unit. Detection limits are species dependent, and range from parts-per-trillion (ppt) to parts-per-billion (ppb).

No. 2 Fuel Oil Analysis Results. The results of the survey show that No.2 Fuel Oil to be remarkably clean and of high quality. A detailed summary of the analytical results is shown in Table 1. the most prevalent compound in the fuel samples was chromium, although no Cr-VI was detected. The fuels were essentially free of arsenic, cadmium, selenium, and mercury. The concentration of arsenic permitted in drinking water is higher than the quantities reported in the fuel samples.

Comparison with Other Fuel Samples. As the name implies, residual fuel is the components of the petroleum feedstock that remain after distillation. Because of the nature of the distillation process (atmospheric or vacuum), most of the heavy metals would be expected to be found in the residual fuel oil. This appears to be the general rule that is easily demonstrated.

However, the mere presence of a metal, such as chromium, in the fuel, does not necessarily imply that it is in a toxic form in the turbine exhaust. For chromium, the oxidation state of concern is the +6. A 1998 survey of industrial boilers using heavy oil reported that the metal of critical concern was Nickel. In the case of Nickel, it is the presence of nickel-subsulfide (Ni_2S_3) that is the hazardous component. But it is not the nickel oxide of concern, NiO, but the nickel subsulfide (Ni_2S_3). However, nickel sub-sulfide is in a reduced state, a condition that should be difficult to maintain in intense industrial burner.

With the recent regulatory focus on a wide range of industries, there has been intense focus to determine what compounds represent any real, or potential hazard. A recent survey of residual fuels used in large boilers indicated that nickel was present in ranges from 30-40 ppm, significantly higher than the levels of nickel observed in the current fuel study)[1]. Stack test measurements revealed that there was no evidence of reduced nickel in the particulates, indicating that good combustion (and excess oxygen levels) are effective means of fully oxidizing all the compounds in the fuel. We would expect similar results from the nickel present in the No. 2 fuel oil samples noted in this study.

In a 1999 survey of crude oil samples, McGaw reported data on 18 metals trace metals in a wide range of crude oil samples[2]. A comparison of the average concentrations found in the McGaw reveals are markedly improved compared to the distillate samples from this study.

Table 2. Comparison Of Crude Samples With Distillate Results

Metal	As	Cr	Pb	Ni	Hg	Cd
Concentration in crude oil samples (McGaw 1999 study), ppb	60	270	32	19690	60	10
Concentrations in distillate fuel oil (this study). ppb	0	242	15	28	0	0

In a study on Iowa ground water quality, researchers used similar techniques as those selected here to identify any role between underground storage of fuels and possible aquifer contamination.[3] The Iowa ground water survey examined transportation fuels, which are even more tightly specified than the fuels used in gas turbines. The authors of that study also failed to identify the presence of any mercury in No. 2 diesel fuels taken from selected regional sources. The highest chromium reported in the study was only 31 ppb, although there was no attempt to identify the presence of any specific

oxidation states of the chromium. In essence, this earlier study from a relatively select group of sources further confirms the high quality, and lack of toxic metals, in the US distillate fuels base.

Conclusions

Gas turbine liquid fuel samples were characterized for the presence of eight trace hazardous metals. The study revealed that many of the metals of concerned (including mercury and arsenic) are not present at any level above the detection limits of the ICP-MS used. Chromium is not present in the +6 oxidation state, the oxidation state of most concern. Nickel is present at even lower concentrations, but there is no evidence that nickel could form the toxic sulfide compound during a combustion process that occurs with excess oxygen available. The source of lead is probably due to cross contamination from the small quantities of leaded fuels that are still used today (aviation gasoline is still marketed as a low lead fuel).

References

(1) *"Nickel Speciation of Flyash from Residual Oil-Fired Power Plants"*, Kevin Galbreath, University of North Dakota Energy & Environmental Research Center; presented at Air Quality IV, 22-24 Sep 2003, Arlington, Va.

(2) Magaw, RI, McMillen, SJ, Gala, WR., 1999. Risk evaluation of metals in crude oils: *Proc. 6th Int'l Petrol. Environmental Conf.* Nov. 16-18, Houston, TX, pp. 460-473.

(3) Rich Heathcote, Don Simmons, and Steven Hernholz, *Analysis of Motor-Vehicle Fuels for Metals by Inductively Coupled Plasma-Mass Spectrometry;* Hygenic Laboratory**,** Volume 39, No. 4, pp. 1-4, 2001, The University of Iowa.

STUDY OF REACTION MECHANISMS IN CELLULOSE PYROLYSIS

LIAO Yan-fen 1, WANG Shu-rong 2, Ma Xiao-qian 1

(1 Electric Power College, South China University of Technology., Guangzhou 510640, China)
(2 Clean Energy and Environment Engineering Key Laboratory of Ministry of Education, Zhejiang University，Hangzhou 310027, China)

Introduction

As the concerns for energy supply and the pollution problems caused by burning fossil fuels become more pronounce, a great deal of attention has been paid to using renewable and clean fuels at present, including the use of biomass. Among alternatives of using biomass as an energy source, the thermo-chemical conversion appears to be a promising route, which includes pyrolysis, combustion, and gasification. Pyrolysis is not only the initial process of gasification and combustion, but also an individual technique to form high energy density products in which biomass goes through physical and chemical changes to produce gas, char and bio-oil when it is heated in an inert atmosphere. Researching the reaction mechanisms of biomass pyrolysis would provide a better understanding of the process and be beneficial for the optimization of reaction parameters and reactor design. This study aims at modeling the cellusose pyrolysis and developing simulations to optimize the reaction conditions.

All biomass contain a great ratio of cellulose, and being the major component in biomass, cellulose behaves the whole decomposition regulation of biomass in pyrolysis. So many mechanism researches on biomass pyrolysis are taken with cellulose.

Experiment instruments

In order to study the chemical reaction and mechanism in cellulose pyrolysis, a series of experiments are made on the cellulose material rolled as cylinder in a quarts glass reactor concentric with a silicon carbide pipe (shown in the figure 1), which supplies the heat required in cellulose pyrolysis by radiation through the transparent quarts glass at a maximum electric power of 8KW. In the reactor system, the char is trapped in a char-collection, while the volatile flows with carrier gas into three-stage condensers, which are dipped in a mixture of dry ice with acetone. The condensable volatile condensed into bio-oil when flowing through the condensers, while the incondensable volatile is discharged out and collected into a gasbag for GC analysis. The yields of char, bio-oil and gas in different reacting condition are obtained by controlling the radiant source temperature (RST) and carrier gas flow, and the important components yields in bio-oil also are measured by a quantitative analysis through GC-MS.

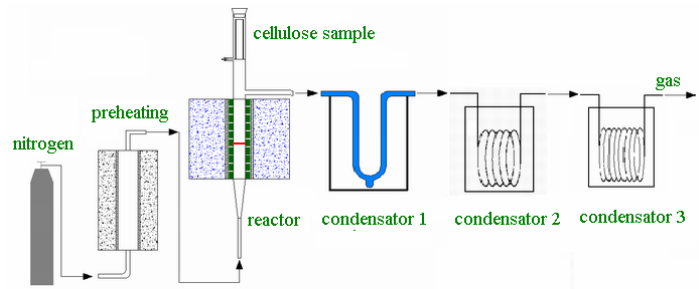

Figure 1. Cellulose fast pyrolysis system

Model Conception

Analyzing the data, a modified kinetic mechanism is brought out basing on the Brodio-Shafizadeh (B-S) mechanism [1], which is described as followed (shown in figure 2): In the initial stage of cellulose pyrolysis, Active cellulose (AC) was formed accompanied by reduction of polymerisation degree of cellulose. If reaction temperature is low, AC will change into charcoal by dehydration.

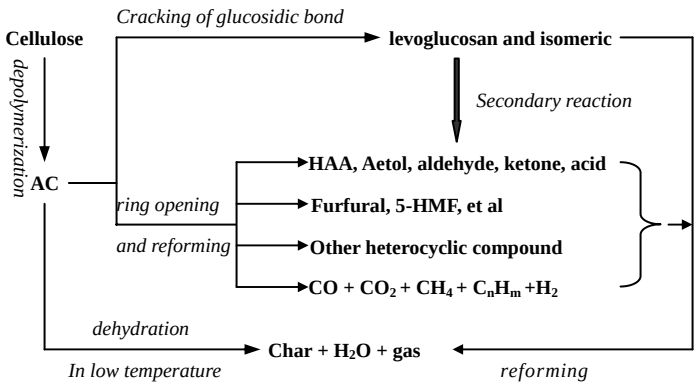

Figure 2. The modified B-S mechanism

As temperature rises higher, AC decomposed by two competitive reactions, cracking of glucosidic bond or opening and reforming of pyranoid ring. Cracking of glucosidic bond will produce levoglucosan (LG) and its isomeric anhydrosugar. At same time, opening of acetal structural ring and cracking of internal C-C bond in pyranoid ring will bring into the formation of hydroxyl-acetaldehyde (HAA), acetol, furfural, CO and other small compounds. Compared with the formation of anhydrosugar, opening and cracking of ring was higher in active energy. At the situation of long gaseous residence, anhydrosugar will undergo secondary decomposition similar with the opening and reforming of pyranoid ring in AC and produce small molecule gas, secondary char and secondary bio-oil which includes almost all the competitive products of AC by reforming of pyranoid ring.

According to the experimental system's feature, when cellulose decomposes, volatile and gas will escape from the solid fabric, then flow into the gas space in reactor and occur the secondary reaction, so the model includes two major parts: the primary react stage in the cellulose fabric structure and the secondary react in gas space. Since other pyrolysis systems also have the solid and gas space, the

conception of this model is also applicable to them. The kinetic model used in gas space for volatiles is the same with the model in solid space. Basing on the modified B-S mechanism, a detail model is made with two stages to simulate the evolving process and path of cellulose, AC, char, gas, LG, HAA, acetol, formaldehyde and furfural which are all the most important compounds in pyrolysis process, and the other volatiles are put together as tar2 (as shown in figure 3).

Figure 3. Kinetic model basing on modified B-S mechanism

In these competitive reacts, the reaction coefficient of each

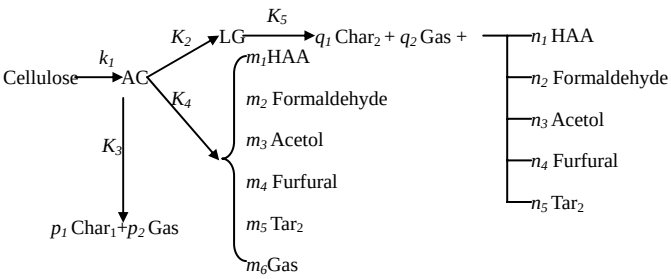

components in K_4 is difficult to be determined, however, they could be obtained by extrapolation of the yield to infinite radiant source temperature. In ideal case, if cellulose was heated at a very high rate to an infinite temperature, and volatile released from cellulose had a very short residence, secondary cracking could be ignored reaction, and the competitive reactions K_4 will take the predominant role in AC consuming process since they have high active energy than the K_2 reaction. Thus, reaction coefficient could be obtained by calculating product's yield at this ideal case, and their ratio is acceptable to the secondary reaction of LG, while the other reaction coefficients such as p_1, p_2 [2]and react kinetic constants (E_i, A_i)[1,3,4,5]，reaction heat ($\triangle H_i$) are selected from literatures [6]. The ratio q_1, q_2 are calculated from the experiments of LG pyrolysis results which don't show in this paper.

Making the feature of this reactor system as the boundary condition of this model, the continuity differential equations and energy conservation differential equations in solid space and gas space are listed respectively. Only cellulose, AC, LG and HAA continuity differential equations in solid space are presented below, other compounds or in gas space are similar with them, so these equations are neglected in the paper.

$$\frac{\partial \rho_{Cellulose}}{\partial t} = -k_1 \cdot \rho_{Cellulose} \tag{1}$$

$$\frac{\partial \rho_{AC}}{\partial t} = k_1 \cdot \rho_{Cellulose} - (k_2 + k_3 + k_4) \cdot \rho_{AC} \tag{2}$$

$$\frac{\partial \rho_{LG}}{\partial t} + \frac{2}{\delta} \cdot (\rho_{LG} \cdot u_f) = k_2 \cdot \rho_{AC} - k_5 \cdot \rho_{LG} \tag{3}$$

$$\frac{\partial \rho_{HAA}}{\partial t} + \frac{2}{\delta} (\rho_{HAA} \cdot u_f) = m_1 \cdot k_4 \cdot \rho_{AC} + n_1 \cdot k_5 \cdot \rho_{LG} \tag{4}$$

All reaction rate constants K_i would be described by Arrhenius Equation, which is expressed by $K_i = A_i \exp(-E_i/RT)$, While u_f in above equations represented gas apparent flow in the void of material, which could be calculated by Darcy Law, R is the gas constant number.

The heat required during cellulose pyrolysis was mainly supplied by thermo-radiation from silicon carbide pipe and by heat convection between carrier gas and material surfaces. In addition, reaction heat in primary reaction and secondary cracking also had influence. As was shown in Equation 5.

$$\frac{\partial}{\partial t}\left(T \sum \rho_i C_i\right) + \frac{1}{\delta}\left(T \sum \rho_i C_i u_i\right) = \frac{2}{\delta} \cdot \left(\alpha_f (T_f - T) + \varepsilon_0 \cdot \sigma (T_{TRS}^4 - T^4)\right) + Q_{react} \tag{5}$$

Where T represented temperature of solid material, while T_f and T_{TRS} the temperature of carrier gas and radiator. C corresponded to specific heat capacity. α_f is the heat convection coefficients between carrier gas with material surfaces. σ is the Stefan-Bolzman constant, and ε_0 referred to black degree of cellulose material. Q_{react} could be described by following Equation 6.

$$Q_{react} = k_0 \Delta H_0 \rho_{Cellulose} + (k_1 \Delta H_1 + k_2 \Delta H_2 + k_3 \Delta H_3) \rho_{AC} + k_4 \Delta H_4 \rho_{LG} \tag{6}$$

According this methods and conception, the paper simulates the pyrolysis behavior of the cylindraceous cellulose about 0.18 mm thickness, including the formation, development or evolution of major compounds in the condition of 700～1300K radiant source temperature, 100~700L/h carrier gas flow

Modeling Results

The simulating results show that the temperature of cellulose material in the reaction process divides into three stages. At the initial stage, all reactions have a low rate and cellulose is heated rapidly by radiation in a pure physical heating method until the temperature reaches about 690K, then the primary decomposing reaction increases its rate, which absorbs almost all the heat transferred by radiation and restrains the increasing of reaction temperature. Even in the high radiant source temperature about 880K, this endothermic effect is still strong and makes cellulose locating in the low temperature about 690~720K during the whole primary reaction stage. At the last stage, the primary pyrolysis is finished and the temperature returns to a high promotion until reach to the equilibrium with surroundings. From the result, we can suppose that in the pyrolysis or gasification techniques, the material's temperature is a variational parameter for the reaction heat effect, so a thermocouple with general response sensitive will induce a measure error.

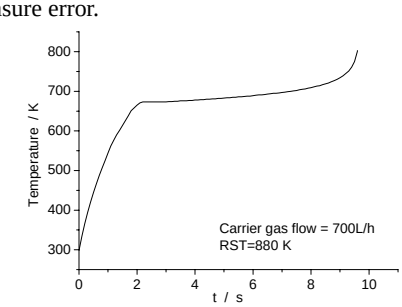

Figure 4. Temperature Vs time

The consumption rate of cellulose is responding with the reacting temperature, and converted completely at the prophase of the second stage. According to the modified B-S mechanism, the transforming of cellulose is only the initial stage; the leading actor deciding the process evolvement and products distribution is this middle component, active cellulose, whose density and temperature determine the evolving rate of the competitive reaction paths by cracking of glucosidic bond or reforming of pyranoid ring.

Figure 5 shows the rules of cellulose and AC converting process, a maximum AC density is just arrived when cellulose is consumed out in middle stage of the process. Comparing figure 5 with figure 4, the beginning point with the third stage of temperature is just when AC consumed away, the coincidence shows it is the endothermic decomposition of AC decides the development of pyrolysis process.

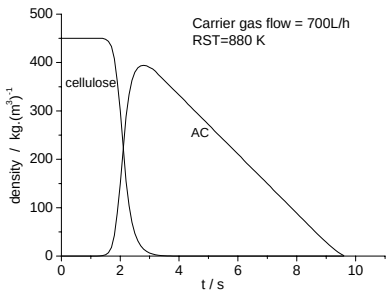

Figure 5. Products' density vs temperature

Char is formed by two ways, one is the dehydration of active cellulose in the low temperature into dehydrated cellulose, which then reformed into primary char and emit gas, the primary char is dependent upon the temperature history of AC and keep the fabric structure of cellulose; the other is coming from the secondary cracking and reforming of LG or other primary volatile. Cellulose, AC, and the primary char form the holing structure in the solid space, in which LG and the other primary volatile occur the secondary reaction when flowing through the holing structure and partially convert into secondary char. So the evolving process of secondary char in solid space is proportional to the density of primary volatile and solid temperature. From calculating, in the condition of radiant resource temperature below 1100K, the temperature of cellulose material is focused between 700~820K, and the secondary react in holing structure is ignorable in the given cellulose thickness (As shown in figure 6).

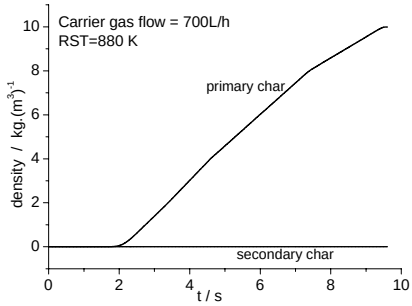

Figure 6. Products' density vs temperature

Being the product of AC by cracking of glucosidic bond in the middle temperature, LG is not only the desiring product in pyrolysis technique but also a precursor of the other volatile, whose formation and evolvement have the same status as AC in the pyrolysis process. The evolvement of LG is dependent upon the integrate effect of reaction rate, conversion degree of AC, local temperature and flow rate of volatile. In the initial stage of pyrolysis, the formation of LG is small and slow for the restrain of low temperature. With the temperature rising, its forming rate and flowing rate from interior to outside increase, which induces a rapid formation and fast flow of LG. Upon the effect of these two process synthetically, LG maintains a stable density for a relatively long time in the middle stage of pyrolysis process. Then AC is going to be consumed out, and a rapid decrease of LG density occurs caused mainly by the fast outward flowing rate.

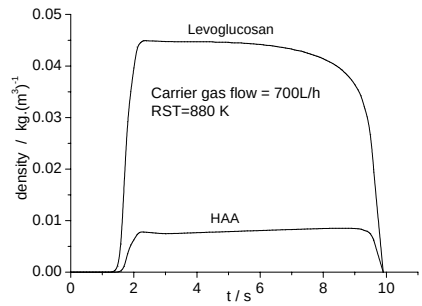

Figure 7. Products' density vs temperature

Similar with LG, the competitive products such as HAA, acetol, formaldehyde and furfural also show a rapid growing and fast flowing process in the middle stage. But they have a slow stepping up in the relatively stable stage, comparing with the stepping down tendency of LG, which just shows the superiority of competitive reaction by the opening and reformation of pyranoid ring in higher temperature. Figure 7 only shows the density distribution of HAA, other compounds are neglected for the same tendency. Since the reaction temperature is restrained in a middle range by endothermic reaction, LG dose not occur abundant secondary cracking in the solid space, so almost all the competitive products are coming from the splitting and reforming of pyranoid ring in AC.

LG and other volatiles escaped from solid space will flow into the gas space taken by carrier gas, and occur the secondary pyrolysis. The gas space is large and some assumption must be made to simple the model, so six controlled volumes are set to simulate the secondary reacting process.

From the results, a similar tendency of gas temperature and volatile density are obtained that they are all transferred from the reactor bottom to the outlet one controlled volume by one controlled volume. And in the carrier gas flow about 700L/h, a very short gas resident time about 0.12 second induces little secondary reaction of LG and almost no difference of volatile density in the six controlled volumes is founded (shown in figure 8), which is just the reason why the pyrolysis technique must keep a very short gas resident time to maximum the yield of bio-oil.

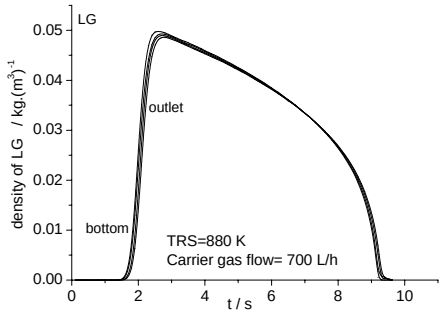

Figure 8. LG density vs time in gas space (short resident time)

Simulation on the condition of middle temperature and large carrier gas flow shows us that neither in the fabric solid space, nor in the gas space, the secondary reaction takes place. So in this conditions, the yield increasing of HAA and acetol with temperature rising is not coming from the secondary cracking of LG, but from the competitive consuming of AC by splitting and reforming of pyranoid ring. This simulating result improves the parallel competitive mechanism in the volatile forming process from another view.

With a small carrier gas flow about 100L/h, a very slow flowing rate make a decreasing of LG density and improving of other volatiles density, this tendency transfers upward one by one and pricks up with temperature rising (shown in figure 9).

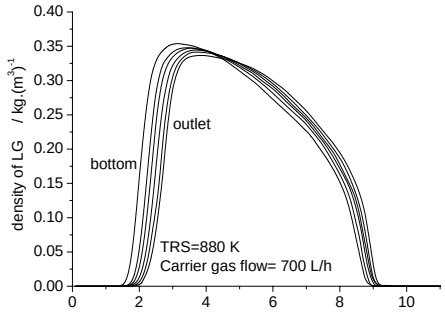

Figure 9. LG density vs time in gas space (long resident time)

Contrary with the decreasing of LG, the distribution of HAA, acetol, formaldehyde in gas space is increasing by degrees with the react time (shown in figure 10), which proves the consumption of LG is supplied to the competitive products by cracking of pyranoid ring. But their increasing tendency is not so intensive as the decreasing of LG since they also occur secondary reaction in the high temperature to form smaller components and gases.

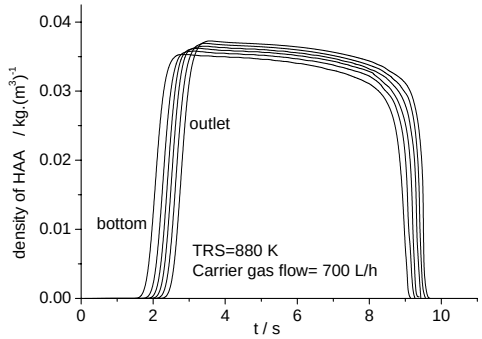

Figure 10. HAA density vs time in gas space(short resident time)

Integrating the density from reactor outlet and flow rate with time will get the yield of compounds. Synthesizing effect of RST and carrier gas flow on pyrolysis process, a good agreement with the experimental results is obtained. Viewing as a whole, in the technique to produce bio-oil, particularly to obtain a high yield of LG, a middle temperature about 700～950K and gas resident time less than 1.0 second is the necessary condition. Temperature has a stronger effect than gas resident time on HAA, acetol, formaldehyde and furfural, and higher temperature is benefit to their formation.

Conclusions

A serious of experiments have been done in a thermal radiant reactor system to study the mechanism of cellulose pyrolysis process, and the forming rules of some important compounds with reaction condition were obtained. Analysis these data, a modified reaction mechanism was brought out from the B-S mechanism model. Combining with the common feature of pyrolysis or gasification equipments with two reaction spaces, a synthesis model with two stages was build to simulate the decomposing and evolving process of AC, LG, HAA, Acetol and furfural in bio-oil.

All reaction and evolvement of compounds are dependent upon the reaction temperature, and the simulating results show that cellulose material is restrained in middle temperature during the major reaction zone for a strong endothermic of primary decomposition. This function is still in effect even in the high RST about 1100K, and so benefits the formation of bio-oil, while decreases the probability of primary volatile cracking into small gas by secondary reactions. So the difference of products density in solid space is evidently due to the competitive ability of different primary reactions, and the secondary reactions have little effect on the products distributions. Increasing the thickness of cellulose, delaying the resident time of primary volatile in fabric structure or enhancing the intensity of heat transfer will improve the temperature of cellulose, and benefit the cracking and opening-ring reactions of pyranoid ring in AC, which decrease the yield of LG.

Almost all the secondary reaction occurs in gas space in this experimental condition, in RTS about 880K and carrier gas flow about 700L/h, the LG escaping from fabric holes seldom happens secondary cracking, but fall the carrier gas flow down to 100L/h, 4.78% LG decomposes in to small compounds and this effect

improves with RST. So an optimum condition for LG yield is obtained about 730K~920K, in addition, the less resident time of volatile staying in reactor, the more yield can be collected since LG is very easy to split into small compounds. Temperature has a stronger effect than gas resident time on HAA, acetol, formaldehyde and furfural, and higher temperature is benefit to their formation.

All these results provide a foundation for the optimization of reaction parameters and reactor design.

Acknowledgement. The authors are indebted to Yu Chunjiang for advices to the model structure and some detailing discussions on the calculations.

References

(1) Bradbury, A. G.W.; Sakai, Y.; Shafizadeh, F. A Kinetic Model for Pyrolysis of Cellulose. *Journal of Applied Polymer Science*., 1979, 23(11), 3271~3280.

(2) Broido, A.; Maxine, A. N. Char Yield on Pyrolysis of Cellulose. *Combustion and Flame*., 1975, 24, 263~268.

(3) Varhegyi, G. P.; Szabo.; Antal, M.J.Jr. Kinetics of the thermal decomposition of cellulose under the experimental conditions of thermal analysis. Theoretical extrapolations to higher heating rates. *Biomass and Bioenergy.*, 1994, 7(1-6),69~74.

(4) Banyasz, J. L.; Li, S.; Lyons-Hart, J.; Shafer, K.H. Cellulose pyrolysis: the kinetics of hydroxyacetaldehyde evolution. *Journal of analytical and applied pyrolysis.*, 2001, 57(2), 223~248.

(5) Shin, E-J.; Nirnlos, M. R.; Evans, R. J. Kinetic analysis of the gas-phase pyrolysis of carbohydrates. *Fuel.*, 2001, 80(12),1697~1709.

(6) Koufopanos, C. A.; Papayannakos, N.; Maschio,G.. Modelling of the pyrolysis of biomass particles. Studies on kinetics, thermal and heat transfer effects. *Can. J. Chem. Engng*., 1991, 69(4), 907~915.

ANALYSIS OF OUTLET FLUE GAS MOISTURE CARRYOVER IN WET LIMESTONE--GYPSUM FLUE GAS DESULPHURIZATION INSTALLATION

Manyin Hu[1], Hezhong Tian[2], Lidong Wang[1], Qiangwei Li[1]

1. Department of Environmental Engineering, North China Electric Power University, Baoding, Hebei Province, 071003, China
2. Department of Environmental Science & Engineering, Tsinghua University, Beijing, 100084, China

1. Introduction

China is one of a few countries throughout the world that its energy production and consumption structure is dominated by coal--a type of fossil fuel with high dust, SO_2 and NO_X pollution. Large amounts of coal combustion directly have caused severe SO_2 and acid rain pollution in China. In 2000, the total SO_2 emissions in China were about 19.95Mt, and 5.54Mt of which came from thermal power plants. Areas with precipitator pH value of lower than 5.6 have occupied more than 30% of Chinese total territory.

In order to comply with the requirements of newly revised Emission Standards for Thermal Power Plants in 2003, newly built coal-fired power plants in China must adopt effective desulphurization installations to reduce SO_2 emissions. By now, among all the desulphurization installations in the world, wet flue gas desulphurization (FGD) is the most widely used process, and wet forced-oxidation limestone-gypsum FGD was especially widely applied in thermal power plants. This process has been selected by utility companies because it is the most economical process among the many process developed and used. It is characterized by high SO_2 removal efficiency, low cost, wide availability of the absorbing reagent, useful gypsum by-product, and does not require a great knowledge in the management of chemical processes.

In a forced-oxidation limestone-gypsum wet FGD installation, limestone slurry is the wet desulphurization absorbent. Limestone reacts with SO_2 which is in flue gas in absorber through spraying, and gypsum($CaSO_4 \cdot H_2O$) is produced. In this way, SO_2 is eliminated. During the process of reaction, the temperature of flue gas entering into absorber is rather high, which will make water in slurry atomize into steam while contacting with limestone slurry. Then the atomized steam is discharged into the air along with disposed flue gas. As a result, the moisture degree is high and there is a certain extent of moisture carryover in purified outlet flue gas, and the magnitude of moisture carryover increases with the unit consuming slurry. In such circumstance, ash will deposit on the impeller in the fan, so much as making the fan vibrate abnormally and run away. At the same time, the entrained water reacts with untreated SO_2 in flue gas and produces sulfurous acid, which erodes metal equipments and accessories such as tail flue duct and fan vane.

In this paper, the common problem of flue gas moisture carryover, which is produced in wet flue gas desulphurization installation, is studied. Based on the mass balance and energy balance in a typical wet FGD scrubber, the calculation formula of moisture carryover is deduced and analyzed in detail. Further, relation between outlet flue gas moisture carryover with the inlet flue gas temperature and inlet slurry temperature.

2. Methodology

In this paper, the mathematical model of flue gas moisture carryover was developed by using mass and energy balance in the wet FGD absorber. The sketch drawing of mass and energy balance of a typical FGD absorber was shown in **Figure 1**.

2.1 Calculation of flue gas moisture carryover

In a wet flue gas desulphurization system, there are two mass balances and one energy balance [1].

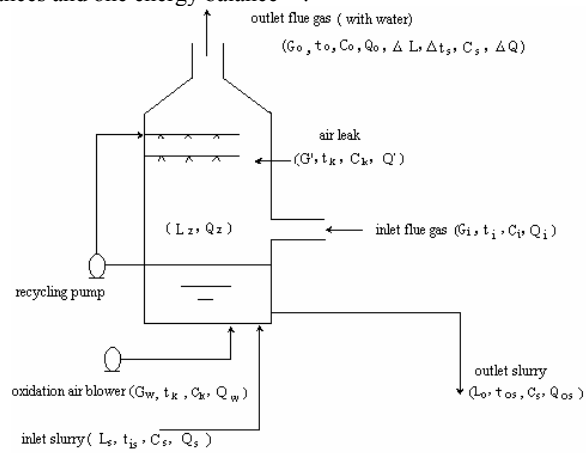

Figure 1 The mass and energy balance in a wet FGD absorber

Balance of gas flow rate. Under the standard conditions, sum of the inlet flue gas rate, air leak rate, and supplying air flow rate equal to the outlet flue gas rate of absorber:

$$G_i + G' + G_w = G_o \quad (1)$$

Balance of water flux. The total ingoing water flux of absorber is equal to the total discharging water flux of absorber:

$$L_s = L_o + \Delta L + L_z \quad (2)$$

Balance of energy. In order to deducing the energy balance in the absorber, some hypotheses as follows were made firstly:

(1) Moisture vaporizing in absorber was considered.

(2) Heat radiating outwards of the system was considered

(3) In the whole system, the specific heat of flue gas, water, and air, is constant.

(4) $C_i = C_o = C_y$, $\Delta t_s = t_0$

Thus, the formula of energy balance can be given as follows:

$$Q_w + Q_i + Q_s + Q' = Q_0 + Q_{os} + \Delta Q + Q_z + Q_d \quad (3)$$

viz. $G_w C_k t_k + G_i C_y t_i + L_s C_s t_{is} + G' C_k t_k$
$= G_o C_y t_o + L_o C_s t_{os} + \Delta L C_s t_o +$
$L_z[C_s(t_o - t_{is}) + 595 \times 4.187] + (G_i + G_o + G_w) C_y \Delta t/2 \quad (4)$

Incorporating equations (1) and (2) into (4), it can be derived:

$$\Delta L = \{G_i C_y (t_i - t_o - \Delta t) + G_w (C_k t_k - C_y t_o - C_y \Delta t) + G'(C_k t_k - C_y t_o - C_y \Delta t/2) + L_s C_s (t_{is} - t_{os}) + L_z[C_s t_{os} - C_s(t_o - t_{is}) - 595 \times 4.187]\}/C_s(t_o - t_{os}) \quad (5)$$

Revising G_i ,G_w and G' into flux of flue gas, supplying air flow rate and air leak rate in actual conditions, respectively:

$$G_i = G_i(273 + t_i)/273 \quad (6)$$

$$G_w = G_w(273 + t_k)/273 \quad (7)$$

$$G' = G'(273 + t_k)/273 \quad (8)$$

introducing equations (6), (7) and (8) into (5), thus:

$$\Delta L = \{G_i C_y (t_i - t_o - \Delta t)(273 + t_i)/273 + G_w (C_k t_k - C_y t_o - C_y \Delta t)(273 + t_k)/273 + G'(C_k t_k - C_y t_o - C_y \Delta t/2)(273 + t_k)/273 + L_s C_s (t_{is} - t_{os}) + L_z[C_s t_{os} - C_s(t_o - t_{is}) - 595 \times 4.187]\}/C_s(t_o - t_{os}) \quad (9)$$

2.2 Calculation of vaporizing quantity in absorber (L_z)

The vaporizing water quantity can be obtained by the formula as follows[2]:

$$L_z = \frac{\left[\Delta t_w - \frac{L_s(t_{os} - t_{is})}{G_i C_p}\right] G_i C_p}{595 + 0.47(t_i - \Delta t_w) - t_{os}} \qquad L_s = \frac{G_i l_w \rho}{1000} \quad (10)$$

Where:

G_i--inlet flue gas rate in absorber (Nm^3/h),

l_w--the unit consuming slurry rate in absorber ($m^3/K \cdot Nm^3$),

ρ--slurry density ($1000kg/m^3$),

Δt_w--fall of flue gas in absorber (℃),

t_{os}--outlet slurry temperature (℃),

t_{is}-- initial slurry temperature (℃),

t_i--inlet flue gas temperature (℃),

C_p--volume specific heat of flue gas, commonly 0.325kcal/km^3·□.

3. Results and Discussion

From equation (9) and (10), it can be seen that all input parameters for calculation of outlet flue gas moisture carryover were measurable. Therefore, flue gas moisture carryover can be calculated if giving all the measurable parameters by field tests.

According to the experiences in the real wet FGD system, some parameters and their range are assumed. Thus, we can obtain the relation curves between flue gas moisture carryover with outlet flue gas temperature and inlet slurry temperature.

3.1 Relation between flue gas moisture carryover with outlet flue gas temperature

As G_i=1.0(Nm3/h), l_w=0.29($m^3/K \cdot Nm^3$), ρ=1000($1000kg/m^3$), G'=0.045(Nm^3/h), G_w=0.05(Nm^3/h), C_y=0.25×4.187=1.047(kJ/kg·□), C_s=4.187(kJ/kg · □), C_k=0.716(kJ/kg · □), C_p=0.325 (kcal/km^3 · □), Δt=4.0(□), t_k=20.0(□), t_{is}=20.0(□), respectively, and selecting t_i=130, 140, 150(□), we can get the trend of flue gas carry-over(ΔL) with outlet flue gas temperature (t_i), as is shown in **Figure 2**.

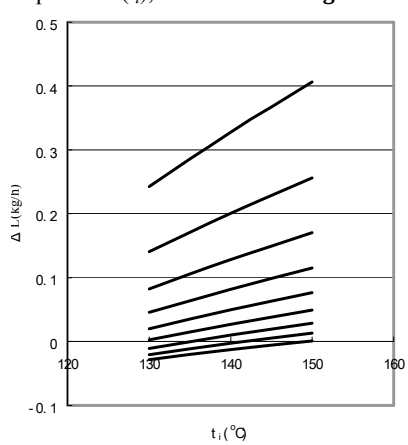

Figure 2 The relation between flue gas moisture carryover with outlet flue gas temperature

Note: Nine curves from the top to down represent the running situations when t_0 at 60□、65□、70□、75□、80□、85□、90□、95□ and 100□, respectively. It can be seen that, flue gas moisture carry-over increase along with the decrease of outlet flue gas temperature.

3.2 Relation between flue gas moisture carryover with inlet slurry temperature

As G_i=1.0(Nm^3/h), l_w=0.29($m^3/K \cdot Nm^3$), ρ=1000($1000kg/m^3$), G'=0.045(Nm^3/h), G_w=0.05(Nm^3/h), C_y=0.25×4.187=1.047(kJ/kg·□), C_s=4.187(kJ/kg · □), C_k=0.716(kJ/kg · □), C_p=0.325 (kcal/km^3 · □), Δt=4.0(□), t_k=20.0(□), t_o=80.0 (□), respectively, and selecting t_i=130, 140, 150(□). Thus, we can get the relation of flue gas moisture carryover (ΔL) with inlet slurry temperature (t_{is}), as is shown in **Figure 3**.

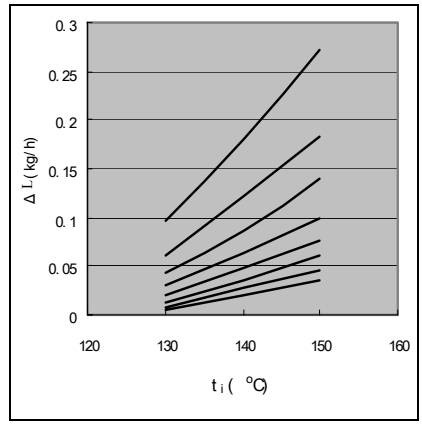

Figure 3 Relation between outlet flue gas moisture carryover with inlet slurry temperature

Note: Eight curves from the top to down represent the running situations when t_{is} is 40.0(□)、35.0(□)、30.0(□)、25.0(□)、20.0(□)、15.0(□)、10.0(□)and 5.0(□), respectively. It can be seen from Fig.3, that flue gas moisture carryover decrease along with the decrease of inlet slurry temperature when other parameters are constant.

Conclusions

According to mass and energy balance in a wet limestone-gypsum desulphurization absorber, the calculation formula of outlet flue gas carryover is deduced and analyzed. It shows that the variety of moisture carryover is consistent with the reality, which proves that the derived calculation formula is credible and feasible. With the formula, flue gas moisture carry-over of all types of wet flue gas desulphurization installations can be estimated.

References

1. Congzhen Fan, Theory of boilers, Chinese electric power press, 1998.
2. Xi'an Thermal Engineering Research Institute. Study and Design Principle of Venturi Precipitator. 1999.

Notation

G_i, G_o, G', G_w-- quantity of inlet, outlet flue gas, air leak and supplying oxygen, respectively (Nm^3/h）

t_i, t_o, t_k-- temperature of inlet, outlet flue gas and air, respectively (℃)

C_i, C_o, C_k--specific heat of inlet, outlet flue gas and air, respectively (kJ/kg. □)

L_s, L_o--flux of inlet and outlet slurry, respectively (kg/h)

t_{is}, t_{os}--temperature of inlet and outlet slurry, respectively (□)

C_s -- specific heat of slurry (kJ/kg.□)

ΔL—moisture carry-over in flue gas (kg/h)

L_z--vaporizing quantity in absorber (kg/h)

Δt_s--temperature of water in flue gas(□)

Δt--temperature difference by external diffusion heat of flue gas(□)

Q_i—quantity of heat of inlet flue gas (kJ)

Q'—quantity of heat of air leak (kJ)

Q_w—quantity of heat of supplying oxygen in oxidation air blower (kJ)

Q_s —quantity of heat of absorbent (limestone slurry) (kJ)

S_o—quantity of heat of outlet flue gas (kJ）

Q_{os}—quantity of heat of outlet slurry (kJ）

ΔQ—quantity of heat of water in flue gas (kJ）

H_z—quantity of heat of vaporizing in absorber (kJ)

Q_d—external diffusion heat in absorber (kJ）

STUDY ON RUNNING SIMULATION FOR ELECTROSTATIC PRECIPITATOR

Manyin Hu[1], Hezhong Tian[2], Xianglin Gao[1], Zhiguang Hu[1]

1. Department of Environmental Engineering, North China Electric Power University, Baoding, Hebei Province, 071003, China
2. Department of Environmental Science & Engineering, Tsinghua University, Beijing, 100084, China

1. Introduction

With the rapid development of electric power industry in China, ESP had become one of the most necessary equipments for safely power generating and environmental protection in power plants. However, owing to various reasons, many ESP in China is in poor operation and maintenance, and approximately 30 percent of them could not attain the designed dust collection efficiency. The principle training simulator for ESP could supply good conditions for technical training on personnel in operation, maintenance and management on ESP. It was mainly composed of hardware system, software system and mathematical models (Tian, 1994).

Description of training simulator for ESP

The principle training simulator for ESP was made up of one host computer, three I/O interfaces and six pieces of simulating dials.

Host computer. It could accomplish mathematical models calculation, signals and induction information collection, then according to the results that had been worked out, it sent out all kinds of instructions to control the whole training simulator.

Interface. STAR-90 intellectual dispersed interfaces were used in the training simulator, which could transform all sorts of operating signals on the high and low voltage simulating dials to digital signals that could be accepted by the host computer, then send them to mathematical models for carrying out simulating calculations. On the other hand, they could also transform the output data which had been produced from the mathematical models that were stored in the host computer to various visual signals, such as indicator lamps, voltage, current meters, etc.

RS-232 series communication was applied between the interfaces and the host computer, 3 pieces of I/O interface boards were all suspended in the simulating control dials. It did not need other hardware in computer, so the connection between them was very clear, it was considerably convenient to debug and operate. In the training simulator, there were totally 3 kinds of interfaces: a digital input (DI), a digital output (DO) and an analogue output (AO). Each of them was connected with the host computer through an interface board. Relevant driven program could be compiled on the host computer, all the datum (input/output) were carried out by the interruption communication style. Through large amounts of tests, it proved that the designation for the I/O interfaces could satisfy real time requisition of the training simulator. Not only was it highly accurate, but also it could save time for the host computer. So, it is an ideal configuration.

Simulating control dials. The principle training simulator for ESP was designed according to a single chamber horizontal wire-plate ESP with three electric fields, which was equipped with the large generating units in coal-burning power plants. Every electric field was made up of 2 simulating control dials: one for high voltage control, the other for low voltage control. So there were totally 3 pieces of high voltage simulating control dials and 3 pieces of low voltage simulating control dials, separately. For convenience of technical training, either of the high voltage simulating control dials or the low voltage simulating control dials was closely similar in functions and hardware configuration with the real control dials that were widely adopted in coal-fired power plants in China. One difference was that a collection efficiency indicator was added to each of the three high voltage simulating control dials, with which the simulating collection efficiency could be indicated. Not only could it display the collection efficiency of local electric field, but also it could give the comprehensive collection efficiency of several electric fields.

Instruction platform. The host computer of the training simulator also acts as the instruction platform, by which the instructor could select various training items, such as system start-up, normal running, system shut-down, parameters alteration, operation supervision and man-made faults installation, et al. Furthermore, during the whole training process, it could send out various instructions that controlled the operation status of the training simulator, for example, parameters printing, freezing/unfreezing, retrieving, and marking, et al.

The simulating mathematical models of ESP

Approximately 100 simulating mathematical models had been constituted, which were suit for the requirements of the principle training simulator for ESP. They primarily included the following mathematical models and some relevant simulating curves:

Models for high voltage energizing system. The mathematical description of the high voltage energizing system, including those of two types of control patterns, which were spark tracing energizing control and intermittent energizing control. There were models of system start-up, system shut-down, normal operation and adjustment and so on.

Models for low voltage control system. There were system start-up, shut-down, normal operation, adjustment of the low voltage control system and so forth, mainly including that of collecting/discharging electrode rapping control, dust removal control and heating control and so on.

Models for common faults in high voltage system. They were models for common faults generating in high voltage energizing system, such as secondary short circuit, secondary open circuit, primary over current, bias-excitation, non-indication on secondary current display, voltage and current rising sharply, high voltage insulation descending, the pointer of secondary current meter vibrating periodically, breakdown voltage descending, operating current being too small, oil-temperature in T/R being too high and so on.

Models for common faults in low voltage system. Include primary faults on positive/negative electrode rapping control system, fly-ash removal control system, heating control system, etc.

Voltage-current curves under various conditions. There were mainly V-I curves of unloading dust-contained flue gas, loading dust-contained flue gas, V-I curve shifting to right, V-I curve rotating to left or right, V-I curve shifting to left and shortening, V-I curve passing through origin, V-I curve when there were slight back corona and serious back corona.

Models for collection efficiency of ESP. It was the qualitatively simulating mathematical models for collection efficiency of ESP. The collection efficiency was under the influence of many factors, including primarily corona power, dust specific resistivity, gas stream distribution pattern, bunch flow and reentrainment, mean diameter of dust particles, gas flow rate, et al. All of these factors were taken into account in the collection efficiency mathematical models.

Parts of simulating models were listed below (Hu Z.G., et. 1993, Tian H.Z., 1994):

(1) Conducting angle of thyristor:

Voltage ascending segment:

$$\phi_i = \pi(1 - e^{-s_1 i})$$

Voltage descending segment:

$$\phi_i = \pi \cdot e^{s_2 \cdot i}$$

Where s_1 and s_2 denoted voltage ascending and descending rate, and i was its half-wave number during one sparking period.

(2) **Primary voltage after smoothed waveform by reactor:**

$$U_1'(t) = \begin{cases} 0 & (i-1)\pi < \omega t \le i\pi - \phi_i \\ \sqrt{2}U_{1i}' \sin(\omega_i t - \beta_i) & i\pi - \phi < \omega t \le i\pi (i = 1,3,5\cdots) \\ -\sqrt{2}U_{1i}' \sin(\omega_i t - \beta_i) & i\pi - \phi_i < \omega t \le i\pi (i = 2,4,6\cdots) \end{cases}$$

Where:

ω was the angle frequency of power supply, (ω=314 radian/s);

ω_i was the angle frequency of ith half-wave, $\omega_i = \frac{\pi}{\phi_i}\omega$;

β_i was the initial phase angle of ith half-wave, $\beta_i = \frac{\pi}{\phi_i}(i\pi - \omega)$;

U_{1i}' was primary voltage virtual value of ith half-wave during the region of $(i\pi - \omega) \sim i\pi$, $U_{1i}' = \sqrt{\frac{\pi}{\phi_i}} U_{1i}$;

(3) Secondary voltage after rectification:

$$U_2(t) = \begin{cases} 0 & (i-1)\pi < \omega t \le i\pi - \phi_i \\ \sqrt{2}U_{2i}' \sin(\omega t - \beta_i) & (i\pi - \phi_i) < \omega t \le i\pi \end{cases}$$

where: U_{2i}' was the secondary sin value of the ith half-wave during the region of $(i\pi - \omega) \sim i\pi$, $U_{21i}' = \sqrt{\frac{\pi}{\phi_i}} U_{2i}$

(4) Secondary current:

$$I_2(t) = \begin{cases} 0 & U_2(t) < U_0 \\ \frac{A\pi\varepsilon_0 k}{cb^2 \ln(4b/\pi a)} U_2(U_2 - U_0) & U_0 \le U_2(t) < U_p \end{cases}$$

Where: U_2--the second voltage between two electrodes, A--the dust collecting area, U_0--the corona voltage, ε_0--was the vacuum dielectric constant, k--was the ionic mobility of the gas, U_p--was the discharging voltage, c--was the half space between the corona lines, b--was the half space between the collecting boards, α--was the minimum curvature radius of the corona line.

(5) **Program control model for positive electrode rapping:**

$$MR(t) = \begin{cases} 0 & nTR < t < nTR + TR_2 \\ 1 & nTR + TR_2 \le t \le (n+1)TR \end{cases}$$

Where $MR(t)$ was the state of the electric motor for rapping. It is equal to 1, implying the motor was in operation. Otherwise, it was in shut-down. $TR=TR_1+TR_2$ denoted the rapping period for positive electrode rapping system, $TR_1$and TR_2 were rapping time and non-rapping time, respectively.

(6) **Auto ash-removal control model:**

$$MX(t) = \begin{cases} 0 & 0 \le t < TX_0 \\ 1 & TX_0 + nTX \le T \le TX_0 + nTX + TX_1 \\ 0 & TX_0 + nTX + TX_1 < t < TX_0 + (n+1)TX \end{cases}$$

Where $MX(t)$ denoted the state of the electric motor for ash removal. If it was 1, implying that the motor was on operation. Otherwise, it was shut-down. $TX=TX_1+TX_2$ was the ash removal period. TX_1 and TX_2 were the time for ash-removal and ash-accumulation separately, whereas, TX_0 denotes the original time which had passed for the first time ash-removal.

(7) V-I simulating curve for shifting to left or right. Owing to sharp changes for dust concentration of flue gas or other reasons, the equivalent resistivity between two electrodes altered greatly (Tian, 1994). It made the V-I curve shifting to left or right (Figure 1).

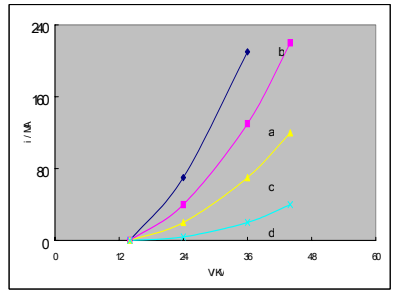

Figure 1 The simulating V-I curve for shifting
a--normal, b--shifting left, c--shifting right, d--shifting right seriously

(8) Simulating curve for back corona. When fly ash resistivity that entraining the electric field exceed about $10^{11}\Omega\cdot$cm, there would happen back corona on the layer adhering on positive electrode (Hu et al. 1995). The simulating curve for back corona was shown in Figure 2.

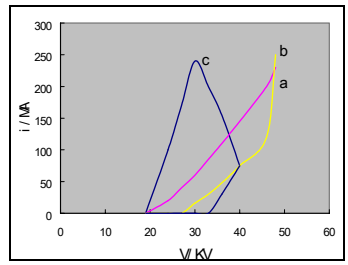

Figure 2 The simulating curve for back corona
a--normal running, b--slight back corona, c--serious back corona

From simulating curves listed above, we would see that they were very closely consistent with those encountered in real ESP.

The Train software for ESP

The training software for ESP was a large comprehensive system with multi-functions. It was established by the way of modularized and structured programming method, developed totally Turbo C. It could be divided into 15 key functional modules, and each was under the administration of the upper management software. Aiming at the main usual faults of electrostatic precipitator, the Fault Diagnosis Expert system was developed. It could judge the faults and provide disposal measures on time.

Conclusions

The configuration of principle training simulator was closely similar to those widely applied ESP in practice, which could accomplish various simulating train functions. By now, Over 1000 workers from coal-fired power plants through China have practiced the relevant operation of ESP on the simulator. It proved that it was an ideal training simulator for technical train of personnel in operation, maintenance and management for ESP. It is very helpful for the safe, efficient and stable operation of ESP in China.

References

1. Hu Z.G., Gao X.L., Hu M.Y., et al. Proc.2nd Int. Con. on Applied Electrostatics, Beijing, 1993: 50-54
2. Hezhong Tian. Study on Simulating Mathematical Models of Electrostatic Precipitator (Thesis), North China Electric Power University, Baoding, China. 1994.
3. Hu M.Y., Gao X.L., Hu Z.G., et al. Electric Power. 1995, 10: 44-47

Experimental multi-phase H_2O-CO_2 brine interactions at elevated temperature and pressure: Implications for CO_2 sequestration in deep-saline aquifers

Robert Rosenbauer and Tamer Koksalan

U.S. Geological Survey, 345 Middlefield Road, Menlo Park, CA 94025

Introduction

The burning of fossil fuel and other anthropogenic activities have caused a continuous and dramatic 30% increase of atmospheric carbon dioxide (CO_2) over the past 150 years[1]. CO_2 sequestration is increasingly being viewed as a tool for managing these anthropogenic CO_2 emissions to the atmosphere. The disposal of this excess CO_2 into deep-saline aquifers is one of several potential storage repositories, but the details of the geochemical reactions between supercritical CO_2 and potential host fluids and formation rocks are largely unknown.

The initial reaction between liquid CO_2 and the aquifer fluid is the dissolution of CO_2 (eqn. 1) and is fundamentally important because it is the aqueous, not the supercritical form of CO_2 that is reactive toward the formation rocks.

$$CO_2 + H_2O \leftrightarrow H_2CO_3 \quad (1)$$

The aqueous solubility of CO_2 is temperature, pressure, and ionic-strength dependent. At 25°C, the solubility of CO_2 in an aquifer fluid with total dissolved solids of ~22% is approximately threefold less than in pure water[2]. The dissociation of carbonic acid into reactive hydrogen ion and bicarbonate (eqn. *2*) potentially initiates a complex series of reactions with aquifer fluids and formation rocks to fix CO_2 in mineral phases.

$$H_2CO_3 \leftrightarrow H^+ + HCO_3^- \quad (2)$$

The dissociation of carbonic acid is also temperature dependent. There is a maximum in the log K of reaction 2 at about 50°C beyond which log K decreases continuously with increasing temperature such that a weak acid becomes increasingly weak at elevated temperature. Reactions involving supercritical CO_2 and carbonic acid with aquifer fluids and formation rocks are many and varied, depending on the matrix of the fluid and the composition of the rock. In general, thermodynamics favor the dissolution of carbonate phases in limestones and dissolution of silicates and precipitation of carbonates in arkosic sandstones.

Reactions in limestone (ionic trapping). Reactions of CO_2 saturated aquifer fluids with limestone are characterized by dissolution of calcite due to the increased acidity produced by the dissociation of carbonic acid (eqn. 3)

$$CaCO_3 + CO_2 + H_2O \rightarrow Ca^{+2} + 2HCO_3^- \quad (3)$$

for a net increase of an additional mole of CO_2 stored as bicarbonate relative to the simple solubility of CO_2. Calcite has a retrograde solubility, becoming less soluble and less efficient at trapping CO_2 at elevated temperature. Similar reactions can be written for the dissolution of dolomite and siderite.

Reactions in arkosic sandstones (mineral trapping). Reactions of CO_2 saturated aquifer fluids with arkosic sandstones are characterized by dissolution of silicates due to the increased acidity produced by the dissociation of carbonic acid and precipitation of carbonates. An example of the mineral trapping of CO_2 is the dissolution of the anorthitic component of palgioclase (eqn. 4)

$$2H^+ + CaAl_2Si_2O_8 + H_2O \rightarrow Ca^{+2} + Al_2Si_2O_5(OH)_4 \quad (4)$$

and the subsequent precipitation of calcite (eqn. 5)

$$Ca^{+2} + HCO_3^- \rightarrow CaCO_3 + H^+ \quad (5)$$

for a net reaction shown in equation 6.

$$CaAl_2Si_2O_8 + H_2CO_3 + H_2O \rightarrow CaCO_3 + Al_2Si_2O_5(OH)_4 \quad (6)$$

The log K of this reaction decreases with increasing temperature, resulting in competing effects of favorable thermodynamics versus kinetic limitations.

We present here the results of CO_2-saturated brine-rock experiments carried out to evaluate the effects of multiphase H_2O-CO_2 fluids on mineral equilibria and the potential for CO_2 sequestration in mineral phases within deep-saline aquifers

Methods

Experimental. Experiments were carried out in a combination of titanium-lined fixed-volume and flexible-gold reactions cells secured to high-temperature-pressure autoclaves and rotating furnaces. Temperature was maintained by a proportional controller (Love™) and measured with a type K thermocouple calibrated to a platinum RTD. Pressure was measured with dead-weight calibrated gauges and transducers. Experiments were carried out at 22° and 120°C and at 300 bars.

Reactants. A natural near-surface brine (PVB) and a synthetic aquifer brine (PVA), both from Paradox Valley, CO, were reacted with limestone from the Leadville Limestone, CO (38% calcite), and arkosic and banded sandstones from Mount Tom, MA and Coconio, AZ, respectively in the presence and absence of liquid CO_2. Both sandstones contained quartz, plagioclase, (oligoclase), K-spar and kaolinite. Brine compositions are given in **table 1**.

Table 1. Composition of Paradox Valley Brines

Species (mg/L)	Surface (PVB)	Aquifer (PVA)
Na	77,000	70,000
K	3,630	2,100
Ca	1,187	10,900
Mg	1,278	1,220
Cl	127,100	132,000
SO_4	5,100	454
TDS	215,000	218,000

Analytical. Periodically, aqueous samples were withdrawn from each experiment and analyzed for total carbon by coulometric titration (UIC Coulometrics™), dissolved cations by inductively coupled plasma (ICP), and dissolved anions by ion chromatograph, except chloride which was determined by coulometric titration (Labconco™). The mineralogy of the solids was determined by x-ray diffraction (XRD) and chemistry by total dissolution and ICP (Xral Cooporation)

Results and Discussion

Limestone PVB Reactions. At 25°C, the reaction of CO_2 saturated PVB is characterized by dissolution of calcite and a pressure dependent enhanced solubility of CO_2 shown in **figure 1**.

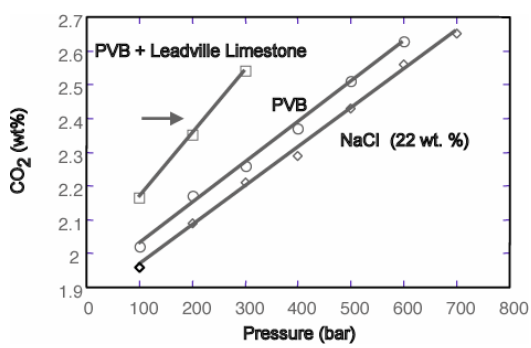

Figure 1. The solubility of CO_2 in PVB in the presence and absence of limestone and in equivalent ionic strength NaCl.

The solubility is enhanced 8.8% at 25°C and 5.7% at 120°C and 300 bars. Also, there is a temperature dependent offset in the solubility of CO_2 between the natural brine and NaCl due to the presence of divalent cations in the brine[2]. At 120°C, the reaction of PVB with limestone is independent of CO_2 concentration except for the dissolution of some calcite early in the experiment containing CO_2. Both experiments are dominated by the precipitation of anhydrite and dolomitization of the limestone shown as a time series plot in **figure 2**. Based on mass balance calculation for Mg, Ca, and SO_4, 25% of the original calcite dissolved or was dolomitized. Net molar volume changes result in a formation porosity increase of 5%.

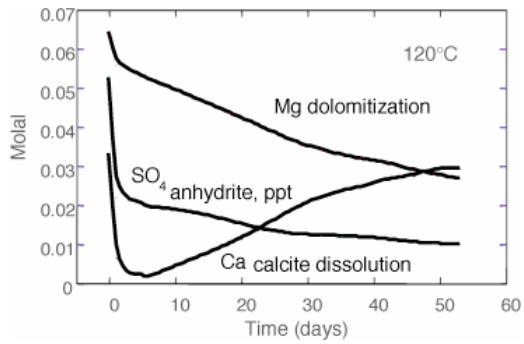

Figure 2. Compositional changes in PVB when reacted with limestone both in the presence and absence of liquid CO_2.

Limestone PVA Reactions. The reaction of limestone with PVA is characterized by calcite dissolution and desiccation of the brine shown in **figure 3**. Dolomite dissolves during heating and it or magnesite precipitate at the experimental conditions of 120°C. These reactions result in a net porosity increase of 2.6%.

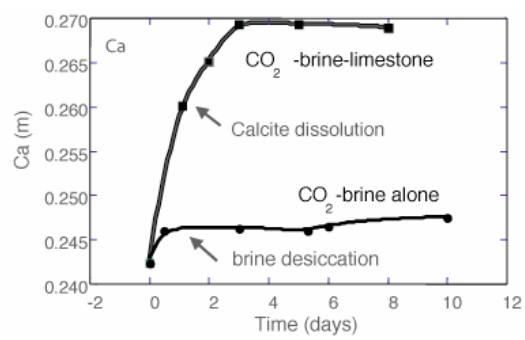

Figure 3. Compositional change in dissolved Ca during reaction of CO_2 saturated brine in the presence and absence of limestone at 120°C.

Sandstone PVA Reactions. Reactions of arkosic and iron-rich banded sandstones with PVA are characterized by large changes in elemental abundances, enhanced CO_2 solubility, and significant desiccation of the brines. Prior to injection of liquid CO_2, changes occurred in dissolved Ca, Mg, K, and Na during equilibration with minerals in the solid phase. After injection of liquid CO_2, total dissolved solids (TDS), including Cl, increased markedly due to transfer of H_2O from the brine to liquid CO_2 as shown in **figure 4**. The solubility of liquid H_2O in liquid CO_2 is temperature and pressure dependent[3] and has implications for solutions already near saturation with mineral phases. Experiments by Kazuba et al[4] have shown a 25% increase in dissolved Cl when CO_2 was injected into a saline brine at 200°C and 200 bars. Highly saline aquifers near saturation with NaCl would precipitate halite under these conditions.

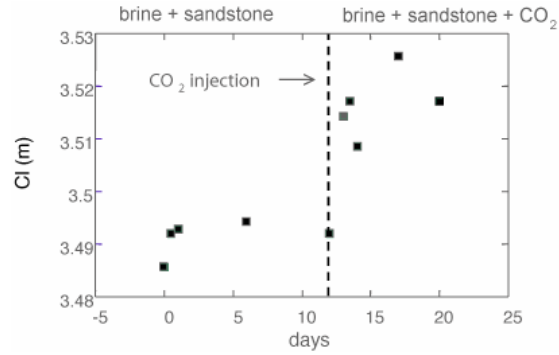

Figure 4. Concentration of dissolved Cl before and after injection of liquid CO_2 when PVA brine is reacted with arkosic sandstone.

Dissolved elemental concentrations did not all increase proportionally with dissolved Cl (7%), and ranged up to 12% for dissolved Mg immediately after injection of CO_2 into the brine, indicative of a variety of fluid-rock interactions. The decrease of dissolved Ca with time when PVA reacts with arkose is shown in **figure 5**, suggesting fixation of CO_2 as calcite. Significant metals were released to solution, in particular from the banded sandstone, leading to the possibility of siderite precipitation.

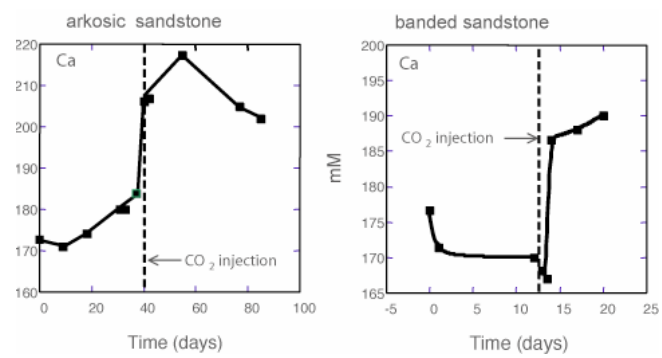

Figure 5. Time series plot of dissolved Ca when PVA is reacted with arkosic and banded sandstones at 120°C and 300 bars.

Conclusions

Experimental results are generally consistent with theoretical thermodynamic calculations. CO_2-saturated brine-limestone reactions are characterized by compositional and mineralogical changes in the aquifer fluid and rock that are dependent on initial brine composition, especially dissolved sulfate, as are the changes in formation porosity. The solubility of CO_2 is enhanced in brines in the presence of both limestone and sandstone relative to brines alone.

Reactions between CO_2 saturated brines and arkosic sandstones are characterized by desiccation of the brine and changes in the chemical composition of the brine suggesting fixation of CO_2 in mineral phases. These reactions are occurring on a measurable but kinetically slow time scale at 120°C.

References

(1) Johnansson, T. B.; Williams, R. H.; Ishitani, H.; Edmonds, J. A. *Energy Policy* **1996**, *24* (10-11), 985-1003

(2) Rosenbauer, R. J.; Koksalan, T. *GSA Annual Meeting*, Denver, CO, October 27-30, **2002**, Paper 135-2

(3) Takenouchi, S. and Kennedy, G. C. *Am. J. Sci.*, **1964**, 262, 1055-74

(4) Kaszuba, J. P.; Janecky, D. R.; Snow, M. G. *Appl. Geochem.* **2003,** 18 (7), 1065-80

PARAMETRIC INVESTIGATION OF CARBON SEQUESTRATION USING BRINE

Matthew L. Druckenmiller and M. Mercedes Maroto-Valer

The Energy Institute and the Department of Energy & Geo-Environmental Engineering, The Pennsylvania State University, 401 Academic Activities Bldg., University Park, PA 16802

Introduction

In the shadow of mass fossil fuel consumption and the looming threat of global climate change, carbon sequestration using brine has emerged as a promising technology in carbon management. Brine is a saline-based solution that is produced as a waste product during the extraction of oil and natural gas. In Pennsylvania annual brine production is estimated at 59 million gallons, while total US production is over 20 billion gallons.[1] The existence of large volumes of brine at the surface provides a potential feedstock for the conversion of CO_2 into geologically stable mineral carbonates, such as calcium carbonate and magnesium carbonate. Under the appropriate conditions, CO_2 dissolves in brine to initiate a series of reactions that ultimately leads to the bonding of carbonate anions to various metal cations inherent in brine to precipitate carbonates.

In addition to ex-situ processing to efficiently drive the reaction, much emphasis has been placed on the injection of CO_2 into subsurface saline formations. US deep saline aquifers are estimated to provide storage for approximately 130 giga-tons carbon equivalent, which is approximately 80 times the US's total carbon emissions in 2001.[2,3] Following the injection of anthropogenic CO_2 below a typical depth of 800 meters, the storage mechanism is initially hydrodynamic as the CO_2 is stored as a dense supercritical fluid. On a separate timescale, and following the dissolution of CO_2 in brine, chemical interactions with the brine may form mineral carbonates.[4]

The rate of the mineral trapping process is slow and serves as the major disadvantage of this technology.[5] It was suggested by Soong et al.[5] that pH has a significant effect on both conversion rates and on the specific species that are precipitated. The conversion to carbonates can thus be promoted by increasing brine pH through the addition of a strong base. Their research qualitatively identifies the effects of various parameters on carbonate precipitation. However, pH evolution throughout the reaction is not documented. The objective of this study is to further investigate the effects of temperature, pressure, and most importantly pH on the formation of mineral carbonates during the reaction of CO_2 with various natural gas well brines. Additionally, the evolution of brine pH following a pH adjustment yet prior to reaction with CO_2 is studied. This analysis will help determine a relationship between brine composition and a brine's ability to maintain an elevated pH over time.

Experimental

Four brine samples were obtained from various natural gas wells: PA-1 and PA-2 from nearby 2800 m wells in Indiana County, Pennsylvania, and OH-1 and OH-2 from a 1158 m well in Guernsey, Ohio and a 1030 m well in Youngstown, Ohio, respectively.

ICP-AES Analysis. The brine samples underwent analysis by inductively coupled plasma – atomic emission spectroscopy (ICP-AES) screening with no acid pretreatment to determine the elemental metal concentrations in the liquid phase. Additionally, ICP-AES screening following acid treatment with HNO_3 was conducted to determine the total metal concentration in solution.

pH Stability Study. The stability of adjustments of brine pH was studied at room temperature and pressure using the four brine samples. Based on the various brine compositions, it was preliminarily determined to raise the pH to a value low enough so that iron hydroxide did not precipitate. Iron hydroxide has a much lower solubility product ($K_{sp} = 4.87 \times 10^{-17}$) than the hydroxyl forms of the other metals. OH-2 had the highest iron composition, and accordingly a pH of approximately 7 would promote precipitation. Using a 0.24 M KOH solution, the pH of each brine sample was adjusted to approximately 6.3. Over a five-day period, the pH was measured using a digital pH meter to obtain a relationship between brine pH and time.

Autoclave CO_2/Brine Reactions. A 250 ml Parr high pressure/high temperature reactor (model series 4576, T316 stainless steel) will be used to conduct reactions between CO_2 and brine. A liquid sampling valve will allow for brine extraction throughout the course of the reaction. Various experiments of 12 hours in duration will be conducted at temperatures and pressures between 20 to 200 °C and 200 to 1200 psi, respectively. Initial brine pH will range from the inherent pH to 11. The CO_2/brine mixture will be constantly stirred to promote interaction and to prevent the settling of precipitates. Samples extracted from the autoclave during reaction will be analyzed using ICP-AES, and the pH will be measured. Additional experiments will be conducted in which no liquid sampling will occur. These studies will yield precipitates that will be characterized using X-ray diffraction (XRD).

Results and Discussion

Brine Characterization. Table 1 presents the ICP-AES analysis results conducted with and without acid pretreatment, and also includes the pH measurements of the natural untreated brine. For the four brine samples studied, the pH values are around 2.3, except for OH-2, which is less acidic with a pH value of 4.2. Both data sets reveal the major compositional differences between the brine samples. Importantly, PA-1 is representative of a relatively calcium-rich brine, while OH-1 represents a magnesium-rich brine. OH-1 also has a significantly lower iron concentration than the other three samples. Finally, the Pennsylvania samples show much higher concentrations of barium and strontium in comparison with the Ohio samples.

Table 1. Metal Concentrations (ppm) as Analyzed by ICP-AES and pH of the Brine Samples

	PA-1	PA-2	OH-1	OH-2
pH	2.3	2.4	4.2	2.3
No Acid Pretreatment				
Ba	1021	696	<5	<5
Ca	33515	21460	19570	19350
Fe	224	121	9	476
K	2520	1490	2225	1180
Mg	1975	1215	3440	2055
Na	60680	41040	69660	48500
Sr	11170	8380	2000	1800
Acid Pretreatment with HNO_3				
Ba	1270	789	5.66	7.3
Ca	42900	23600	22500	21600
Fe	295	223	15.9	635
K	3270	1770	2560	1380
Mg	2650	1440	4070	2380
Na	74400	44900	78900	53900
Sr	13800	8910	2330	2020

In general, the differences between the two data sets reveal that 75 to 95% of the metals are in the liquid phase. An exception exists for iron in PA-2 and OH-1, in which approximately 55% is in the liquid phase. These results clearly show the variability in brine

composition that can be obtained even in the case of nearby wells, such as for PA-1 and PA-2, which are located only 5 miles apart.

pH Stability Measurements. Figure 1 illustrates the results of the pH stability measurements conducted on the four brine samples. OH-1 behaved uniquely in the pH stability study as it was the only brine that remained near the adjusted pH value over the five-day period. The pH of OH-1 remained especially constant over the entire course of the study. In contrast, PA-1, PA-2, and OH-2 experienced a rapid decline in pH during the first 12 hours, after which the decline seemed to level off. This observed difference in stability of brine pH at an adjusted elevated value may be attributed to the major difference in iron composition in the liquid phase between OH-1 and the other samples. OH-1 has a significantly lower iron concentration than the other three brine samples (9 ppm for OH-1 vs. 224, 121 and 476 ppm for PA-1, PA-2 and OH-2, respectively). Further studies are being conducted to understand the relationship between brine composition and observed pH stability.

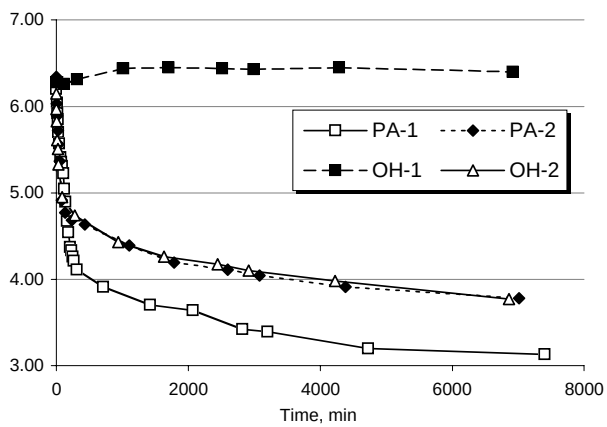

Figure 1. pH measurements of brine samples that underwent a pH adjustment to approximately 6.3 using KOH.

CO_2/Brine Reactions. CO_2 reacts with brine's metal cations to form carbonate precipitates via the following reaction sequence, in which selected likely precipitates are shown:[5,6]

$$CO_2(g) \Leftrightarrow CO_2(aq) \quad (1)$$
$$CO_2(aq) + H_2O \Leftrightarrow H_2CO_3 \quad (2a)$$
$$H_2CO_3 \Leftrightarrow H^+ + HCO_3^- \quad (2b)$$
$$CO_2\,(aq) + OH^- \Leftrightarrow HCO_3^- \quad (3)$$
$$HCO_3^- \Leftrightarrow H^+ + CO_3^{2-} \quad (4)$$
$$Ca^{2+} + CO_3^{2-} \Leftrightarrow Ca\,CO_3\downarrow \quad (5a)$$
$$Mg^{2+} + CO_3^{2-} \Leftrightarrow Mg\,CO_3\downarrow \quad (5b)$$
$$Ca^{2+} + Mg^{2+} + 2CO_3^{2-} \Leftrightarrow CaMg(CO_3)_2\downarrow \quad (5c)$$

The dissolution of CO_2 in water (reaction 1) is dependent on temperature, pressure, and brine salinity. Reactions 2a and 2b represent the formation of carbonic acid, which reduces the pH of the system, and the dissociation of carbonic acid to form bicarbonate, respectively. The bicarbonate ion may then dissociate (reaction 4) to form the carbonate ion, which is necessary to form the carbonate minerals in reactions 5a through 5b. The pH determines which steps dominate the reaction sequence, and accordingly the proportions of the carbonic species.[6] At a low pH (~4), the production of H_2CO_3 dominates, at a mid pH (~6) HCO_3^- production dominates, and at a high pH (~9) CO_3^{2-} dominates.[5] Therefore, at a basic pH the precipitation of carbonate minerals is favored because of the availability of carbonate ions. Oppositely, the dissolution of carbonates increases as the solution becomes increasingly more acidic. The rate limiting step of the overall conversion to carbonates has been identified as the hydration of CO_2 in reaction 2a, which has a forward reaction rate constant of $6.2 \times 10^{-2}\ s^{-1}$ at 25 °C and zero ionic strength.[7]

Conclusions

The abundance of brine both at the surface due to the production of oil and natural gas and in subsurface saline aquifers provides the capacity to sequester a significant amount of anthropogenic CO_2. Subsurface saline aquifers may sequester CO_2 in various forms. However, any ex-situ sequestration process will rely on an efficient conversion to mineral carbonates. An investigation into the parameters, most importantly pH, that affect this conversion rate is warranted. The evolution of brine pH following a pH adjustment and during reaction with CO_2 at various temperatures and pressures is highly variable.

Preliminary results reveal large differences in the metal concentrations of brines from various depths and locations. These compositional differences are related to brine's ability to maintain an elevated pH after treatment with a strong base to address the natural acidity of brine. The CO_2/brine reactor system described herein will allow for the achievement of a relationship between pH and the formation of specific mineral carbonates throughout the duration of an experiment.

Acknowledgements. The authors would like to thank Dr. S. Eser at the Energy Institute at Penn State for the use of the autoclave and Dr. Y. Soong at the National Energy Technology Laboratory of the U.S. Department of Energy for the brine samples. The presenting author would like to acknowledge his research advisor, Dr. M. M. Maroto-Valer, for her continued guidance and encouragement.

References

(1) Jones, A.; Glass C.; Reddy T. K.; Maroto-Valer, M. M.; Andrésen, J. M.; and Schobert, H. H. Prepr. Pap. - *Am. Chem. Soc., Div. Fuel Chem.*, **2001**, *46 (1)*, 321.

(2) DOE. Carbon Sequestration Research and Development; DOE/SC/FE-1; U.S. Department of Energy: Washington D.C., **1999**.

(3) Energy Information Administration, International Energy Annual 2001 Edition. http://www.eia.doe.gov/emeu/iea/carbon.html (accessed March 18, **2003**).

(4) Bachu, S. Sequestration of CO_2 in geological media: Criteria and approach for site selection in response to climate change. *Energy Conversion & Management*, **2000**, *41*, 953-70.

(5) Soong, Y.; Jones, J. R.; Hedges, S. W.; Harrison, D. K.; Knoer, J. P.; Baltrus, J. P.; and Thompson, R. L. Prepr. Pap. - *Am. Chem. Soc., Div. Fuel Chem.*, **2002**, *47 (1)*, 43.

(6) Bond, G. M.; McPherson, B.; Stringer, J.; Wellman, T.; Abel, A.; Medina, M. Prepr. Pap. - *Am. Chem. Soc., Div. Fuel Chem.*, **2002**, *47(1)*, 39.

(7) Bond, G. M.; Stringer, J.; Brandvold, D. K.; Simsek, F. A.; Medina, M.; Egeland, G. Development of integrated system for biomimetic CO_2 sequestration using enzyme carbonic anhydrase. *Energy & Fuels*, **2001**, *15*, 309-16.

Biomimetic Sequestration of CO_2 in Carbonate Form: Role of Produced Waters and Other Brines

Gillian M. Bond,[1] Ning Liu,[1]
Aaron Abel,[2] Brian J. McPherson,[2] and John Stringer[3]

[1]Department of Materials & Metallurgical Engineering
[2]Department of Earth & Environmental Sciences
New Mexico Tech
801 Leroy Place
Socorro, NM 87801

[3]EPRI
3412 Hillview Avenue
Palo Alto, CA 94304

Introduction

The overall purpose of this research from its inception has been to establish the feasibility of essentially permanent sequestration of CO_2 in mineral form, and particularly to examine the possibility of achieving this end by the mimicry of natural processes. A biomimetic approach has been devised, which uses a biological catalyst, carbonic anhydrase. Thus the objective is to develop a system resembling a CO_2 scrubber, in which carbonic anhydrase serves to catalyze the rate of CO_2 hydration for subsequent fixation into stable mineral carbonates. Feasibility of the approach has been demonstrated, and the emphasis is now on development of the approach into a chemical engineering reality. The present focus is on the use of produced waters and other brines as sources of cations for carbonate formation.

Mineralization routes to sequestration

Sequestration of CO_2 in the form of a stable, environmentally friendly solid offers obvious appeal for long-term storage of CO_2 with low risks and minimal monitoring requirements, and would be unlikely to encounter licensing problems. Carbonate minerals, such as calcite, aragonite, dolomite and dolomitic limestone, constitute the earth's largest CO_2 reservoir, estimated to contain an amount of carbon equivalent to 150,000 $\times$ 10^{12} tonnes of CO_2[1]. Thus the geological record demonstrates that large amounts of CO_2 can be stored indefinitely in carbonate form. Two types of geological processes have led to the formation of much of these carbonate minerals, and each of these processes can be viewed as a model for the sequestration of anthropogenic CO_2.

1. Weathering processes result in the generation of carbonates by the silicate-to-carbonate exchange, in which the byproduct is silica. Several other groups are working to develop an analogous process, based on carbonation of serpentinites and peridotites, which could be used on an industrial scale and timeframe. One potential advantage of this approach is that the carbonation reaction is exothermic.
2. Generation of calcium carbonate by various types of marine animals has resulted in the formation of, for example, very extensive oolitic limestone beds. This is the process that we have used as a model in our ongoing work at New Mexico Tech.

Thus we have developed an analogous (biomimetic) process, in which a biological catalyst, the enzyme carbonic anhydrase, is used to accelerate an aqueous processing route to carbonate formation.[2-5] In addition to safe long-term sequestration, the potential advantages of this biomimetic approach include: the possibility of an on-site scrubber that would provide a plant-by-plant solution to CO_2 sequestration; avoiding the need for concentration and transportation of CO_2; and operation at ambient or near-ambient conditions.

Possible cation sources

The counterions for carbonate formation can be supplied from brines. One particularly attractive possibility in the portfolio of possible brines would be produced waters that result from oil and gas production. In areas such as the Permian Basin, a substantial quantity of brine is already being produced, transported, and reinjected by the oil and gas industry. Some of these produced waters are presently used in water flooding for secondary production, but most of the produced waters constitute a waste product requiring disposal. In the Permian Basin, approximately 90% of these waters are reinjected for disposal.

Produced waters from the West Pearl Queen Reservoir (Permian Basin, Southeast NM) and San Juan Basin (Northwest NM) were selected as representative cation sources, corresponding to two very different brine types. Total dissolved solids (TDS) are much lower in brines from the San Juan Basin than in those from the West Pearl Queen Reservoir. Ca^{2+} and Mg^{2+} concentrations in produced waters are, respectively, 0.0871M and 0.1468M for the West Pearl Queen Reservoir, and 0.1743M and 0.0692M for the San Juan Basin.

Experiments with synthetic produced waters

Bench-scale experiments were first performed with synthetic produced waters as follows, prior to larger laboratory-scale experiments. 200µl 0.1mg/ml bovine carbonate anhydrase (BCA) were added to 10.0ml CO_2-saturated deionized (DI) water and mixed well. 10.0ml synthetic produced water and 1.0ml 1M Tris. buffer were added immediately. pH value and precipitation time (time to onset of precipitation) were measured, both in the presence of BCA and in control solutions without BCA. Calcium carbonate precipitated much more quickly in the presence of BCA than from control solution; for example, the precipitation time was 15 sec. (pH=8.54) in the presence of BCA, but 86 sec. (pH=8.53) in the control solution for the synthetic San Juan Basin produced water. For synthetic West Pearl Queen Reservoir produced water, the precipitation times were longer: for example, 254 sec. (pH=8.43) in the presence of BCA and 326 sec. (pH=8.51) in the control solution. This is attributed to the difference in the ratios of Ca^{2+} to Mg^{2+} for the two brines. Magnesium ions are well known to be potent inhibitors of $CaCO_3$ precipitation.

A laboratory-scale reactor has been built and used for subsequent tests on the synthetic brines. In these experiments, the enzyme was immobilized in chitosan-alginate beads. 0.0010g per ml BCA powders were dissolved in 2% (w/v) sodium alginate solution. Chitosan solution was prepared by dissolution of the reagent in 3% (v/v) acetic acid solution (pH=2.5) to give 2% (w/v) of chitosan solution. In order to produce beads, the enzyme-containing alginate solution was dripped with a syringe into a crosslinker solution (comprising 1:1:1 (v/v/v) 0.2M $CaCl_2$:2% (w/v) chitosan solution:DI water) at room temperature.. The pH of the solution was adjusted with 0.1M NaOH or 0.1M HCl to 5. The solution was placed on a magnetic stirrer. Beads were stirred in the solution for 2 hrs, washed with de-ionized water, and refrigerated at 4°C until use.

CO_2-saturated DI-water was pumped with buffer solution into the reaction chamber of the laboratory-scale reactor, where it flowed across enzyme-loaded beads. As the solution left the reaction chamber, synthetic brine was pumped from the brine supply barrel to mix with the H_2CO_3-buffer solution, and then passed through a heating vessel. In the secondary settling pan, $CaCO_3$ precipitated, and the remainder of the solution was re-injected into the H_2CO_3 supply barrel. Inflow rates of the CO_2-saturated DI-water, synthetic brine,

and Tris. buffer were adjusted to give proportions equivalent to those used in the bench-scale tests. The results are listed in table 1.

Table 1. The Results of Laboratory-Scale Experiments with Simulated Produced Water

		Precipitation Time (sec.)	pH Value
West Pearl Queen Reservoir	With BCA	252	8.63
	No BCA	303	8.71
San Juan Basin	With BCA	7	8.58
	No BCA	122	8.65

Injection Capacity Analyses

Another approach to carbon sequestration that utilizes the carbonic anhydrase reactor is the injection of bicarbonate-rich water into subsurface reservoirs. In this process, produced water or other brine pumped from the reservoir to the surface is then enriched with bicarbonate ions by means of the carbonic anhydrase reactor. The resulting solution would then be injected into subsurface reservoirs, for example the West Pearl Queen (depleted oil and gas reservoir) and the Frio Sand (deep saline aquifer, Southeast Texas).

Injection or production capacity is a major consideration when evaluating the disposal of fluids by subsurface injection or optimizing production rate. The term injection (production) capacity can be defined as the maximum injection (production) rate possible for a given reservoir. Reservoir permeability, geometry (thickness), and reservoir conditions (temperature and pressure) influence injection (production) capacity tremendously.

A simple relationship can be applied to a certain set of field-scale parameters to determine the injection (production) capacity of a given reservoir. This can be used to give a reasonable estimation of the amount of CO_2 that could be stored within the reservoir within a given year. L.P. Dake[6] first explored injection (production) capacity in the context of oil and gas reservoir engineering, but we can apply his relationship both to the injection of bicarbonate-rich brine into a reservoir, and to the production of brine as a cation source for surface mineralization. This relationship states that the injection (production) capacity is proportional to the reservoir thickness, reservoir permeability, and the pressure difference between the point of injection (production) and the reservoir.

The main field parameters that enhance injection (production) capacity are permeability and reservoir thickness. The change in pressure applied to the injection (production) of fluids is limited to the maximum overpressure that can be applied to a specific reservoir before reservoir failure. Reservoir engineers have said that this pressure difference must be limited to between 9 and 18 % of the original reservoir pressure to prevent reservoir failure[7]. The West Pearl Queen reservoir permeability has been measured to be approximately 6.91×10^{-13} m^2 and the thickness of the reservoir is approximately 6 meters. These field parameters correspond to an injection (production) capacity of ~0.164 m^3/day. The Frio Sand reservoir permeability of 8.88×10^{-14} m^2 and reservoir thickness of 30 meters correspond to an injection (production) capacity of ~6.80 m^3/day.

The main factor that inhibits injection (production) capacity is the product of permeability and reservoir thickness, as can be noted from the comparison between the capacities of the Frio Sand reservoir and the West Pearl Queen reservoir. The predicted possible cumulative mass injection (production) of brine injected over 365 working days is approximately 65,500 kg (West Pearl Queen reservoir) and 2.7 million kg (Frio Sand reservoir). Throughout certain oil and gas basins there are thousands to hundreds of thousands of wells that inject and produce brine for disposal purposes, and it can be seen that the cumulative capacity for carbon storage within these basins is significant.

It is also important to note that the ability to produce brine as a source of cations is extremely important when evaluating surface mineralization options. Cation (Ca^{2+} and Mg^{2+}) fluxes can be calculated on the basis of chemical analyses of brine compositions and production rate. Cation fluxes for the two field sites (West Pearl Queen and Frio Sand) were calculated given their respective brine compositions. The corresponding estimates were approximately 459 kg of divalent cations per year for the West Pearl Queen site and 5,962 kg of divalent cations per year for the Frio Sand site. These cation fluxes correspond to carbon sequestration potentials via surface mineralization of 502 kg CO_2 stored (West Pearl Queen) and approximately 6,550 kg of CO_2 (Frio Sand).

Conclusions

Demonstrations of the bench-scale and laboratory-scale carbonic anhydrase reactor have been accomplished. Carbonic anhydrase has shown promising results for use as an enzyme to increase the rate of precipitation of carbonate mineral, with produced waters as a cation source. Synthetic produced waters have been used to demonstrate the feasibility of the system. The possibility of overcoming the inhibition of $CaCO_3$ precipitation when the ratio of magnesium ions to calcium ions is higher, by, for example, modest heating of the solution, will be investigated.

Injection (production) capacity analyses performed on several well-scale pilot sites (West Pearl Queen Reservoir and the Frio Sands aquifer) have shown a definitive carbon sink in terms of the possibility of surface mineralization utilizing cations from brines, or the injection of bicarbonate-rich waters at depth.

Acknowledgement

The authors gratefully acknowledge support from EPRI under contract number WO9000-26.

References

1. Wright, J., A. Colling, and Open University Course Team, *Seawater: Its Composition, Properties and Behaviour*, 2nd Edition, Pergamon-Elsevier, Oxford, (**1995**).
2. F.A. Simsek, G.M. Bond and J. Stringer. *World Resource Review* **2001,** 13, 74-90.
3. G.M. Bond, J. Stringer, D.K. Brandvold, F.A. Simsek, M-G. Medina and G. Egeland. *Energy and Fuels* **2001**, 15, 309-316.
4. F.A. Simsek-Ege, G.M. Bond, and J. Stringer. *Environmental Challenges and Greenhouse Gas Control for Fossil Fuel Utilization in the 21st Century*, edited by Maroto-Valer et al., Kluwer Academic Publishers, **2002,** pp. 133-145.
5. G.M. Bond, B.J. McPherson, A. Abel, P. Lichtner, R. Grigg, N. Liu and J. Stringer. *Proceedings of the Second National Conference on Carbon Sequestration*, (May 5-8, 2003, Alexandria, VA) **2003**.
6. Dake, L.P., *Fundamentals of Reservoir Engineering*. Elsevier Scientific Publishing Company, The Netherlands, (**1978**).
7. Hendricks, Chris, *Carbon Dioxide Removal from Coal-Fired Power Plants*. Utrecht, The Netherlands, Kluwer Academic Publishers (**1994**).

Carbon sequestration strategies for the Southwestern United States

Brian McPherson[1]

[1]Petroleum Recovery Research Center
Department of Earth and Environmental Science
New Mexico Institute of Mining and Technology
801 Leroy Place
Socorro, NM 87801

Introduction

Sequestration of carbon emissions in the southwestern U.S. requires strategies tailored for its unique attributes. The region under consideration by the Southwest Regional Partnership for Carbon Sequestration includes five states (Arizona, Colorado, New Mexico, Oklahoma, and Utah) and contiguous areas from three adjacent states (west Texas, south Wyoming, and west Kansas). This region is energy rich (net exporter of electricity, coal, oil and gas), has some of the largest growth rates in the nation, and it contains two major CO_2 pipeline networks that presently tap natural subsurface CO_2 reservoirs for enhanced oil recovery. The ten largest coal-fired power plants in the region produce 50% of the total CO_2 from power-plant fossil fuel combustion, and power plant emissions are close to half the total CO_2 emissions. This paper outlines the first phase of efforts to reduce carbon intensity significantly, including unique scientific and engineering strategies specific for the southwest.

CO_2 Emissions in the Southwest Region

About 70 fossil-fuel power plants are located in the region including Arizona, Colorado, New Mexico, Oklahoma, Utah, and southern Wyoming. Their total emissions in 2001 were approximately 260 million tons. Figure 1 summarizes these emissions by state. Of the 260 million tons of CO_2 emitted from power plants in the region in 2001, about 90% comes from coal combustion. As the largest 28 emitters are all predominantly coal-fired, efforts to make significant reductions in CO_2 emissions must address the large coal-fired power plants. The ten largest power plants emit 50% of the total CO_2 from all power plants in the region (Rick Allis, written communication, 2003). We are investigating those factors contributing to the amount of CO_2 released per MW-hour, which on average is presently at 1.13 tons CO_2 emitted per MW-hour of electricity generated.

Comprehensive, EPA-funded reviews of greenhouse gas (GHG) emissions of the southwestern U.S. considered Utah (1990 and 1993), Oklahoma (1990 and 1999), Colorado (1990) and New Mexico (1990). These reviews illustrate that over 95% of all CO_2 emissions in the region are from fossil fuel combustion. Furthermore, close to half the emissions are from power plants, ranging from 57% in Utah to 44% in Oklahoma in 1990. About 25% of CO_2 emissions are from the transport sector. A comparison of EPA estimates of CO_2 emissions in 1990 and the 1991 to emissions calculated from power plant generation data shows good agreement for Utah and New Mexico, but EPA estimates for Oklahoma and Colorado appear to be more than 20% too high (Rick Allis, written communication, 2003). The EPA estimates also show over 90% of Colorado's CO_2 emissions in 1990 were offset by land use changes (for example, increases in forest carbon storage), whereas this factor was insignificant in other states in the region. We are investigating and quantifying the region's emissions as part of this work.

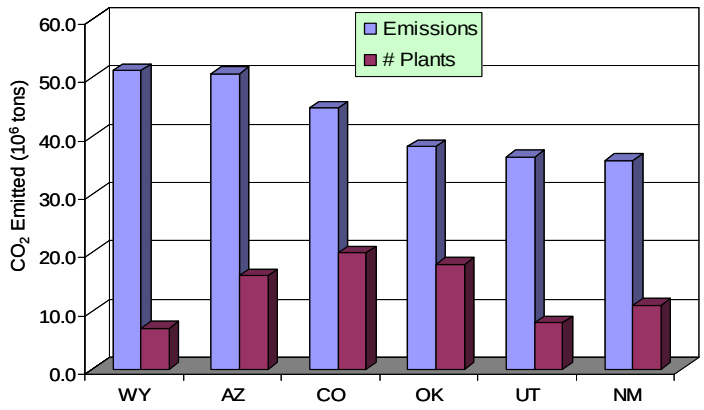

Figure 1. Summary of carbon dioxide emissions in southwestern states.

CO_2 Mitigation Strategies

In the absence of action, current total annual CO_2 emissions in the southwestern U.S. are expected to rise from to 500 million tons CO_2 per year (2001) to close to 750 million tons/year by 2012. The region can offset much of this growth through various sequestration technologies. The region contains the principal CO_2 pipeline infrastructure in the country, much potential exists to offset natural CO_2 production with flue gas CO_2 from the numerous large coal-fired plants, and diverse set of terrestrial, geologic, and mineralization options are available.

Environmental and social consequences are associated with each of these options. Quantifying the consequences is challenging because complex interrelationships link the economy, energy production, population growth, green house gas emissions, and the environment. Establishing and communicating the consequences and tradeoffs between alternative emissions reduction strategies is a possible first step to formulating an effective sequestration program acceptable to the general public. We are also developing and carrying out a unique integrated analysis approach. The analysis is based on a systems-modeling decision framework that provides a means of quantitatively comparing alternative sequestration technologies relative to their associated environmental risks, monitoring and verification requirements, life-cycle costs, and applicable regulatory and permitting constraints. This systems-decision model is being used in: 1) scenario development where policy makers and regulators explore a range of "what if" scenarios, 2) constituency development wherein industry representatives and others can examine the scenario results as a test of environmental viability and practical ability to be implemented, and 3) outreach and education where the model will be taken directly to the public and used as an aid to improve their understanding of CO_2/energy cycle issues and complexity, explain the decision process, and be directly engaged in evaluating possible sequestration options..

Identifying and Ranking Sequestration Options

Terrestrial sequestration and surface mineralization engineering (use of catalysts; see Bond et al., this volume) offer little risk, or at least known risks because these methods are controlled at the surface. Geologic sequestration, however, offers potential risks to ecosystems and the public primarily in the form of CO_2 build-up in the subsurface, unintended mixing of CO_2 in good aquifers via leakage, and possible long-term leakage to the surface from wells or fault systems. Identifying and quantifying these risks for the southwest is being carried out by assigning values of "risk factors" into the integrated assessment model, based on oilfield well data and geologic data gathered to ensure potential risks are considered when

evaluating possible sequestration sites, accounting for various monitoring methods. For the southwest, we are adapting a monitoring and verification approach tailored to site-specific requirements, including: (1) regulatory requirements, (2) location specifics, (3) process specifics, (4) monitoring methods, and (5) information management and verification.

In addition to characterizing potential risks and developing appropriate monitoring and verification approaches, we are also developing field- and regional-scale computer simulation models to evaluate sequestration processes at potential sites for pilot CO_2 sequestration tests. These process simulation models will be used along with the systems-decision model described above to rank possible sequestration sites and technologies.

Acknowledgement

The author gratefully acknowledges support from the U.S. Department of Energy under project DE-PS26-O3NT41983. The author also is extremely grateful to the dozens of individuals in the Southwest Regional Partnership for Carbon Sequestration, many of whom contributed to this paper. In particular, Rick Allis of the Utah Geological Survey provided especially useful analyses of emissions data for the southwest region.

IEA WEYBURN CO_2 MONITORING AND STORAGE PROJECT

Carolyn K. Preston[1]
Michael J. Monea[2]
Waleed Jazrawi[2]

(1) CANMET Energy Technology Centre-Devon, Natural Resources Canada, 1 Oil Patch Drive, Devon, Alberta, Canada T9G 1A8, preston@nrcan.gc.ca
(2) Petroleum Technology Research Centre, 6 Research Drive, Regina, Saskatchewan, Canada S4S 7J7, monea.ptrc@src.sk.ca

Introduction

The IEA Weyburn CO_2 Monitoring and Storage Project is a $28 million (USD) / $40 million (CDN), four year research project that began in August 2000. It builds upon the $1 billion (USD) / $1.3 billion (CDN) commercial CO_2-EOR flood operated by EnCana Corporation of Calgary. The CO_2 commercial flood operation began in late September 2000 following baseline data collection surveys by the IEA Weyburn project. The baseline data set makes this geological monitoring and verification project truly unique compared to its sister projects elsewhere in the world.

The IEA Weyburn project is managed by the Petroleum Technology Research Centre, located in Regina, Saskatchewan. The project has received financial sponsorship from 6 international government organizations and 9 private corporations from the energy and utility sectors. There are 22 research organizations actively engaged in the project from governments, universities and the private sector. Involvement in the project is global in character with participation from Canada, the United States, Europe and Japan.

Project Objective

The overarching objective of the IEA Weyburn project is to predict and verify the ability of an oil reservoir to securely and economically store CO_2. The driving forces are:

- a desire to contribute to the reduction of greenhouse gas emissions
- to improve the understanding of the performance of EOR projects on whose success this method of geologic storage directly depends.

Project Management

Research activities in the project are divided into several objectives, applying leading-edge science and engineering in geophysics, geomechanics, geochemistry, geology, reservoir engineering, risk assessment and economics. The research has been performed in over 55 separate tasks. Efficient and effective project management, coordination and integration have been critical to the success of this project.

EnCana's Commercial EOR Operation

The Weyburn field is located in southeastern Saskatchewan, Canada. 366 million barrels of oil were recovered at the Weyburn Unit under primary recovery and waterflood operation between 1955 and 2000, which was approximately 25% of the original oil in place. The estimated CO_2-enhanced incremental oil recovery over 30 years is 130 million barrels. The CO_2-EOR flood is currently producing over 6000 barrels per day of additional oil.

The source of the CO_2 injected at Weyburn is the Great Plains Synfuels Plant operated by Dakota Gasification Company (DGC) in Beulah, North Dakota. DGC owns and operates a new CO_2 pipeline for EOR operations in southeastern Saskatchewan and northern North Dakota; EnCana is injecting 5000 tonnes per day of CO_2. Currently, EnCana is injecting a further 1200 tonnes per day of CO_2 that is recycled from production wells.

IEA Weyburn Project Results

A regional geoscience model has been developed incorporating a wide variety of information from geological, hydrogeological, and geophysical tools, including core, well-log, seismic, fluid and lineament data obtained throughout the Williston Basin. This geoscience model is being extensively used in reservoir performance assessment and long-term performance assessment modelling activities.

Geochemical modelling has been based upon fluid monitoring surveys from over 40 wells which have been sampled every 4 months over the four year period of the project. The geochemistry model is also an integral part of the long-term performance assessment work. Geochemical modelling has shown that CO_2 is being stored in the reservoir via gaseous, oil, ionic and reservoir rock trapping mechanisms.

There is an important element of human intrusion into the reservoir: over 1000 wells have been drilled at the Weyburn unit, some of which are in active use and some of which have been abandoned. Geomechanics have proven to be critical in understanding the integrity of the wellbores and caprock as well as a key to understanding physical phenomena that may affect the integrity of the natural reservoir "container".

CO_2 movement in the reservoir has been monitored using a variety of geophysical methods including 3D-9C, VSP, crosswell, 4D-3C time-lapse, and microseismic surveys. Deterministic and probabilistic performance assessment methodologies are being investigated to determine the long-term fate assessment of CO_2 in the geosphere and the biosphere.

Expert Review

At the midpoint of the project, the IEA Greenhouse Gas R&D Programme was asked to lead an external expert review of the IEA Weyburn project. The review panel determined that the project has made substantial progress toward meeting its very challenging objectives. Some knowledge gaps were identified which will be addressed in future work undertaken by the project.

Conclusions

The IEA Weyburn project is due to be completed by mid-2004. A second phase of the project is being planned to begin at that time to ensure integrity of the data sets and continued growth of the knowledge base established in phase one. The second phase of the project will focus on determining the most effective monitoring and verification tools for geological storage, developing a better understanding of geological storage and CO_2-EOR using data obtained in phase one of the project, filling knowledge gaps, and developing the beginnings of a geosequestration "toolbox".

Dakota Gasification Company CO_2 Sequestration Verification Project

Doug Huxley / CH2M HILL Inc., Ben Feldman / Natsource LLC, David Peightal / Dakota Gasification Company

CH2M HILL, 9193 South Jamaica Street, Englewood, CO 80112

Introduction

The Dakota Gasification Company (DGC) owns and operates the only commercial synthetic fuel manufacturing facility in North America, the Great Plains Synfuels Plant (GPSP). This facility uses a patented process to convert lignite coal into synthetic natural gas and a number of other byproducts.

One of these byproducts is CO_2. Gas separated from intermediate plant products contains the majority of the CO_2 , and is approximately 95% CO_2, 1% H_2S, and 4% hydrocarbons by volume. This gas was previously fed to plant boilers, to destroy the H_2S and utilize the heating value of the hydrocarbons, then released to the atmosphere.

DGC realized the potential to capture, compress, and transport this byproduct CO_2 for use in oil production, which would allow the sale of an additional product and which would cause a major reduction in GHG emissions. EnCana Corporation expressed an interest in purchasing CO_2 for tertiary oil recovery at its Weyburn production unit in Saskatchewan.

In late 2000, DGC completed the construction of a compression system and a 200-mile pipeline (the "Project") to transport CO_2 to Saskatchewan. EnCana currently purchases approximately 38% of the available CO_2 Product Gas, and injects it into the oil formation. Pipeline capacity is currently available to allow sale of additional CO_2 to other oilfield operators in North Dakota and Saskatchewan.

DGC retained CH2M HILL and Natsource to independently verify the GHG emissions reduction from the Project and to provide advice regarding actions required to allow DGC to take credit for this reduction under applicable regulatory or voluntary GHG programs. This paper presents the results of this effort.

This paper does not address the permanence of the geologic sequestration in the Weyburn oilfield. This topic is the focus of a study coordinated by the International Energy Agency. Draft results of this study are expected in July 2004.

Standards and Analysis

Standards for accounting of project-based GHG reductions are not well established. For corporate GHG accounting, the GHG Protocol developed by the World Resources Institute and the World Business Council for Sustainable Development is the most widely-accepted standard. A "road-test" version of the GHG Protocol Project Quantification Standard was released in September 2003, but was not available for this project. The project was therefore performed by incorporating relevant principles from the Energy Information Administration (EIA) reporting guidance, GHG Protocol corporate reporting guidance, CleanAir Canada Inc.'s (CACI) Pilot Emissions Reduction Trading (PERT) project, and other guidance.

The basic steps performed to verify and evaluate the DGC emissions reduction were as follows:

1. Evaluate project boundaries to capture all relevant primary and secondary impacts to direct and indirect emissions.
2. Evaluate estimated baseline emissions, which are the emissions that would have occurred without the Project.
3. Evaluate quantified changes in all direct and indirect emissions within the project boundary versus the baseline.
4. Verify that the estimate meets relevant reporting principles.
5. Identify potential markets for emission reduction credits, and assess prices for GHG reductions of various vintages.

Results and Discussion

Boundary Definition. The boundaries for this project were defined to include all known impacts to Scope 1 Direct and Scope 2 Indirect emissions, as defined by the GHG Protocol corporate accounting and reporting standard. As such, the boundaries included all operations at the GPSP, the Weyburn unit, and the CO_2 pipeline. The reduction estimate was prepared for reporting by DGC; impacts to Weyburn emission sources were thus defined as indirect impacts.

Scope 1 Direct emissions are defined by the GHG Protocol as emissions from sources owned or controlled by the project developers. The one primary impact to direct emissions was the reduction in CO_2 directly emitted to the atmosphere through the discharge of the CO_2 Product Gas. The GPSP is a highly complex facility with many interconnected process units. Additional fuel, produced internally at the plant, must be fed to the boilers to replace the hydrocarbon content of the CO_2 product gas; the production of this additional fuel and the reduced SO_2 loading on the flue gas desulfurization system (FGD) causes cascading impacts throughout the entire plant. Secondary impacts to direct emissions were therefore quantified for combustion emissions from the supplementary boiler fuel, raw CO_2 content of this fuel, increase in boiler fuel consumption as required to produce additional steam to gasify additional coal to manufacture this fuel, and decrease in CO_2 emissions from the ammonia plant to meet the lower FGD demand. GHG emissions due to maintenance of the CO_2 pipeline were found to be negligible.

Scope 2 Indirect emissions are defined by the GHG Protocol as emissions from purchased energy. Indirect emissions are defined by the "road-test" project standard as emissions that are a consequence of the project developer, but which occur at sources owned or controlled by another company. No primary indirect impacts resulted from the project. Secondary indirect impacts occurred due to electrical consumption of the new CO_2 compressors at the GPSP and Weyburn, and altered electrical consumption at Weyburn due to changes in quantities of managed fluids. Other secondary indirect impacts also resulted from flaring of produced CO_2 and hydrocarbons at Weyburn during initial operation of the CO_2 flood system.

Electrical usage was impacted at a number of other areas in the GPSP. These other secondary indirect impacts include increase in electrical demand of the oxygen plant to allow additional coal gasification to manufacture additional fuel, decrease in electrical consumption of the compressors that deliver unsold CO_2 to the boilers, and changes in electrical consumption at the FGD and the DakSul™ process which converts FGD effluent into fertilizer.

Baseline Definition. Baseline emissions are those GHG emissions that would have occurred in the absence of a project, and are the emissions against which the project reductions are evaluated. The EIA 1605(b) guidance for project reporting[1] defines basic and modified reference cases.

A basic reference case is used where emissions would have continued unchanged from historical levels without the project. Although operations at the GPSP are dynamic, varying based on weather, maintenance events, environmental permits, and other factors, no significant changes in plant equipment or operating procedures were implemented after the Project. A basic reference case was thus used against which to evaluate impacts at the GPSP. The Project was implemented less than one year after the last significant plant modification; as a result, historical data could not be used to directly quantify the baseline and extensive chemical process engineering analysis was instead required. This baseline definition will be reassessed during inventory of future reductions.

Oil production operations naturally change with time. The oil yield from Weyburn would have gradually decreased, and water flood rates would have been increased to compensate for this decline,

without the Project. The Project therefore caused changes to electrical power consumed by pumps, and a modified reference case was used against which to evaluate impacts at Weyburn.

Data Collection and Impact Quantification. The GHG reductions estimate was prepared using data relevant to patent, intellectual capital, and business conditions for both DGC and EnCana. Therefore, the exact reductions estimate is confidential.

The primary and secondary impacts of the Project yield a net reduction of between 0.5 and 1.0 million metric tons of CO_2 equivalent on an annual basis. Greater than 99% of the GHG emission impacts are direct or indirect CO_2, as opposed to other GHG's. The annual net reduction will increase in future years.

Registration of Reductions and Data Management. Because the actual reduction in GHG emissions occurred in the U.S., the Project was registered under a GHG program relevant to U.S. facilities. DGC reported emission impacts via the EIA 1605(b) program.

CH2M HILL developed a data management system for use in estimating future reductions. After identification of secondary impacts as deminimis to the total reduction, a spreadsheet tool was found to be adequate for this purpose. The major advantages of the data management system are that it allows easy identification of the data which must be recorded for estimation of future GHG impacts, allows real-time tracking of impacts, and promotes consistent reporting between years.

Verification of GHG Reductions. To be verifiable, the reduction estimates must meet established estimation protocols and reporting principles. Of the principles noted above, those from the PERT program were most relevant to a project-specific GHG estimate, although PERT is not directly applicable to a U.S. project. The DGC estimate is compared to principles of the PERT project and the subsequently-released GHG Protocol "Road-Test" Project Quantification Standard, below.

The five PERT principles[2] are that the reduction must be real, quantifiable, surplus, verifiable, and unique. The DGC reduction is real because it produces an observable change in emissions, and is not a result in reduction of output of the facilities. It is quantifiable per relevant protocols. It is surplus, in that the GHG reductions were not required by regulation or permit. It is verifiable; the relevant data can be documented and the emission estimated repeated. It is unique, in that no company besides DGC or EnCana can claim the reduction.

The road-test GHG Protocol[3] specifies the principles of relevance, completeness, consistency, transparency, accuracy, and conservatism. Separately, the Protocol discusses additionality, which is similar to the PERT principle of surplus. The estimate is relevant and complete; it includes *all* known primary and secondary impacts. It allows for consistency and transparency; all assumptions are stated, calculations are repeatable, and supporting data is available for review. The estimate is conservative; where engineering analyses were required, calculations were designed to underestimate GHG reductions.

Marketability of Reduction Credits. In conjunction with the verification exercise, an analysis of the potential market value and marketability of the reductions resulting from the Project was undertaken. This analysis focused on several key factors including the cross-border nature of the reductions being achieved by the totality of operations, the withdrawal of the US from the Kyoto Protocol, and the development of market-based state and regional GHG programs in the US. Further, while Canada has ratified the Kyoto protocol, the direct reductions from the Project are not eligible for Kyoto credit because these reductions originate from an emissions source in the US. Because the Project does not generate direct emissions reductions that can be used to satisfy Kyoto requirements, the market assessment focused on the value of future reductions generated by the Project under a variety of regulatory scenarios including US re-entry into the Kyoto system at a future date and the development of alternative federal-level domestic climate policies.

The analysis determined that market value and marketability of current and historic reductions achieved by the Project is quite limited, but that future reductions achieved by the Project might generate significant value under future regulatory/market programs. A key issue in this regard is the extent to which reduction projects undertaken in advance of a regulatory policy would be eligible to generate reduction credits. While the assessment found that the monetary value of the reductions (and ability to monetize the reductions) is highly dependent on future regulatory developments and market participants' expectations with regard to these developments, the development of a rigorous monitoring and verification system for the Project is a prerequisite to the capture of value for the reductions under future programs. As accounting standards are codified, the data streams and analytical methods developed for the monitoring and verification project will form the informational backbone for DGC's future project-based accounting under whatever standards and protocols emerge. Once these standards and protocols are codified, the transparent, replicable monitoring and verification program developed for the Project will enable DGC to determine if its reductions are eligible for credit under future programs. More importantly, the monitoring and verification program will also enable potential market participants to value DGC's reductions based upon their perception of future market and regulatory developments.

Conclusions

To obtain recognition for past or present GHG emission reduction projects under future regulatory or voluntary reporting programs, action is required now to collect data and document results. Required activity data is often unavailable after the fact. Project boundaries and baselines should be established as early as possible, such that pertinent data can be identified and recorded.

The international community has yet to accept a common set of standards for accounting of GHG reductions from specific projects. However, the emerging standards are generally built on accepted standards for corporate GHG emission accounting, with the addition of specific tests needed to test the validity of the project. DGC's emission reduction meets the principles of these emerging standards.

Past and present emission reductions at DGC may ultimately prove to have a discounted monetary value. However DGC is positioned to obtain recognition for its actions under future regulatory programs or voluntary reporting programs. DGC is also well positioned to market credits for future reductions, and has documented project boundaries and baselines in a fashion that should allow verification and certification under likely policy scenarios.

References

1 US Department of Energy, Energy Information Administration, Project-Specific Guidance for each of six sectors: http://www.eia.doe.gov/oiaf/1605/guidelns.html#vol1

2 Clean Air Canada Inc., "Guidance Manual on Emission Reduction Credit Creation Requirements, 2002: http://www.cleanaircanada.org/ercforms.asp

3 WRI/WBCSD, "The Greenhouse Gas Protocol, Project Quantification Standard, Road Test Draft", September 2003: http://www.ghgprotocol.org/reduction/RoadTestIntro.htm

INTEGRATED NEAR-SURFACE MONITORING AND ANALYSIS FOR CO_2 STORAGE VERIFICATION

Jennifer L. Lewicki and Curtis M. Oldenburg

Earth Sciences Division
Lawrence Berkeley National Laboratory
1 Cyclotron Rd.
Berkeley, CA 94720

Introduction

Geologic carbon sequestration is the capture of anthropogenic CO_2 and its storage in deep geologic formations. To verify that this storage is effective and that CO_2 is not migrating to the near surface and seeping out of the ground, resulting in potential health, safety, and environmental risks, monitoring of storage sites will be necessary. Numerical simulations of leakage and seepage have shown that CO_2 concentrations in the shallow subsurface can reach relatively high levels even for modest leakage rates; however, once CO_2 seeps into the atmospheric surface layer, winds are effective at dispersing the CO_2[1,2]. Geologic CO_2 storage reservoirs will be chosen in large part for their low probability of CO_2 leakage away from the target formation within hundred to thousand year time scales. Therefore, CO_2 storage verification will involve searching for *potential* anomalies, likely of small magnitude, over tens of km^2 or more within a system with large spatial and temporal variation of CO_2 fluxes and concentrations arising from natural biological and hydrologic processes.

A range of technologies exists to measure CO_2 concentrations and fluxes in the shallow subsurface and the atmospheric surface layer. These technologies include (1) the infrared gas analyzer (IRGA) for measurement of point CO_2 concentrations, (2) the accumulation chamber (AC) technique[3] to measure point soil CO_2 fluxes, (3) the eddy covariance (EC) method[4] to measure net CO_2 flux over a given area, and (4) light distancing and ranging (LIDAR) to measure CO_2 concentrations over an integrated path. However, these technologies alone cannot solve the fundamental problem of discerning a small CO_2 leakage or seepage signal (LOSS) from the naturally varying background CO_2 fluxes and concentrations. Here, we describe the primary sources of background CO_2 in the near surface and the processes that control the natural variability of concentrations and fluxes of this CO_2. We then propose an integrated measurement, monitoring, and modeling strategy designed to meet the challenge of detecting a small CO_2 LOSS within this variability.

Controls on Background Fluxes and Concentrations. We define "background" CO_2 as CO_2 derived primarily from the atmosphere and biologically mediated oxidation of organic carbon. Background soil CO_2 fluxes and concentrations are dependent on CO_2 production in the soil, movement of CO_2 from sub-soil sources into the soil, and exchange of CO_2 with the atmosphere as controlled by concentration (diffusion) and pressure (advection) gradients. Table 1 shows generalized chemical and isotopic signatures related to different background sources of CO_2. Biologically produced CO_2 in soils (i.e., soil respiration) is derived from root respiration and decay of organic matter. While many factors may influence soil respiration rates, changes in atmospheric and soil temperature and soil moisture have been shown to strongly affect these rates and related concentrations and fluxes. CO_2 that enters soil from sub-soil sources can be derived from groundwater degassing of CO_2 derived from respiration, atmospheric, and carbonate mineral sources. Also, production of CO_2 at sub-soil depths can occur by oxidative decay of relatively young or ancient (e.g., peat, lignite, kerogen) organic matter in the vadose zone. Exchange of soil CO_2 from subsurface sources with the atmosphere can occur by diffusion and/or advection. Diffusive flow depends on the gas production rate and soil temperature, moisture and properties such as porosity, with each of these factors varying in both space and time. Advective flow can be driven by fluctuations in atmospheric pressure, wind, temperature, and rainfall.

Table 1. Chemical and Isotopic Signatures Related to CO_2 Derived from Different Sources

CO_2 source	$\delta^{13}C_{CO2}$ (‰)	$\Delta^{14}C_{CO2}$ (‰)	Near-surface CO_2 conc.	CO_2 conc. profile with depth	O_2 conc. profile with depth
Atmosphere	-7	-70	Low	-	-
Root respiration and decay of young soil organic matter	C_3plants: -24 to –38 C_4plants: -6 to -19	≥ -70	Low to moderate	Increasing through soil zone	Decreasing through soil zone
Decay of ancient organic matter	C_3plants: -24 to –38 C_4/aquatic plants: -6 to –19 Also age dependent	Highly depleted to absent, depending on age	Low	Increasing potentially through vadose zone	Decreasing potentially through vadose zone
Marine carbonate rocks	0 ± 4	Absent	Low	Increasing through vadose zone	No effect
Fossil fuel	Average: -27	Absent	Moderate to high	Increasing through vadose zone	No effect

Carbon-13 and 14 values are expressed relative to PDB and oxalic acid decay corrected to 1950, respectively.

Integrated Monitoring Plan. We assume that a given land area above the storage structure can be delineated as the area at risk from unintended leakage and seepage. This area, called the study area, will normally include the surface injection facilities and may extend for many kilometers away from surface facilities depending on the depth and areal extent of the storage reservoir and nature of subsurface structures and hydrologic systems.

Baseline Monitoring and Modeling. Prior to deep CO_2 injection, background spatial and temporal variability of subsurface and atmospheric CO_2 within the study area should be well understood. Figure 1 shows the general sampling frequencies of the range of background characterization measurements that should be made[5]. Particular attention should be paid to understanding natural variability in areas where CO_2 leakage and seepage would be most likely (e.g., close to the locations of injection and monitoring wells and geologic features such as faults and lithologic contacts). The study area should be characterized with respect to properties (e.g., soil type, soil and soil parent material organic carbon content, vegetation type and density, topography, and surface water hydrology) that could influence and cause important differences in background CO_2 concentrations and fluxes. Ecological modeling (e.g., LSM[6]) and flow and transport modeling (e.g., TOUGH2[1]) should be considered to develop a consistent conceptual model of the sources and sinks of carbon and water within the study area.

To capture both the overall spatial distribution and the small-scale spatial heterogeneity of soil CO_2 fluxes, concentrations, and isotopic compositions, fluxes and concentrations should be measured using the AC method and a portable IRGA, respectively, and soil

gases should be collected for chemical and isotopic determinations within the area along a large grid at widely spaced sampling intervals, and along a smaller grid at closely spaced sampling intervals. These measurements should also be made repeatedly over time at several sites to capture diurnal to seasonal variations. The carbon isotopic compositions of soil and sub-soil organic matter should be determined within the study area and measured repeatedly over time at several representative sites. In addition, pre-existing wells within the study area should be sampled to characterize background sub-soil gas chemistry and isotopic compositions (e.g., CO_2, O_2, $\delta^{13}C$, $\Delta^{14}C$) and their variability with depth.

Soil temperature and moisture and atmospheric temperature, pressure, and wind speed and direction should be monitored contemporaneously with soil CO_2 fluxes. Correlation analysis of CO_2 flux and environmental parameters should be performed. Using regression analysis, empirical relationships between correlated parameters could be established for the overall area, or each sub-region, if appropriate, and used to predict the background CO_2 fluxes expected under a given set of environmental conditions.

If the study area has relatively low slopes and horizontally uniform vegetation type and density as required by the EC method, then an EC station should be deployed during times of meteorologically stable conditions to characterize spatially averaged background CO_2 fluxes. The background temporal variability of these fluxes should be established by making measurements over diurnal to seasonal cycles. Eddy covariance CO_2 fluxes should be compared to average CO_2 fluxes measured by the AC method within the same footprint area to quantify the component of the background EC flux derived from soil and subsoil respiration.

Long-Term Monitoring. A range of measurements should be made within the study area during and after CO_2 injection into the storage reservoir at frequencies that will likely change with time following injection (Figure 1)[6]. The time over which it will be necessary to carry out such monitoring activities following injection is highly uncertain. Monitoring for CO_2 leakage and seepage should focus on rapid, economical, reliable measurements of soil CO_2 concentration and AC surface CO_2 fluxes along grids, supplemented by EC measurements. The objective here is to minimize the number of these measurements and then focus more time- and cost-intensive deep sampling (e.g., of wells, trenches) and isotopic measurements on "high-probability" anomalies. To this end, Bayesian statistical analysis of CO_2 flux and concentration measurements should be used to identify the presence (or absence) of CO_2 anomalies with high confidence. In addition, maps of sampling areas should be contoured for soil CO_2 concentration and flux magnitude and autocorrelation and cross-correlation coefficients of these parameters. Furthermore, measured CO_2 fluxes should be compared to the behavior of background CO_2 fluxes predicted by ecological models under a given set of atmospheric parameters and assessed for deviations from this behavior. Based on these combined analyses, the locations of further more costly and time-intensive sampling can be determined.

Where anomalously high soil CO_2 concentration and flux are located, gases should be sampled from the surface to the water table for chemical and carbon isotopic ($\delta^{13}C$, $\Delta^{14}C$) analyses. An increase in CO_2 concentration with depth would indicate CO_2 production at depth. Measured CO_2 and O_2 concentration-depth profiles should be compared to profiles generated by diffusion models of background CO_2 respiration and O_2 consumption to evaluate a biological respiration source of CO_2 at depth. Carbon-13 values at sub-soil depths should be compared to values for soil CO_2 and organic matter to look for differences indicative of a distinct source. Very low $\Delta^{14}C$ values would be expected at depth with a leaking fossil CO_2 source. The potential contribution of CO_2 derived from oxidation of ancient sedimentary organic matter should also be evaluated. Overall, the observations of CO_2 and O_2 concentration gradients, CO_2 production distribution, surface CO_2 fluxes, and carbon isotopic compositions must be consistent with the CO_2 source.

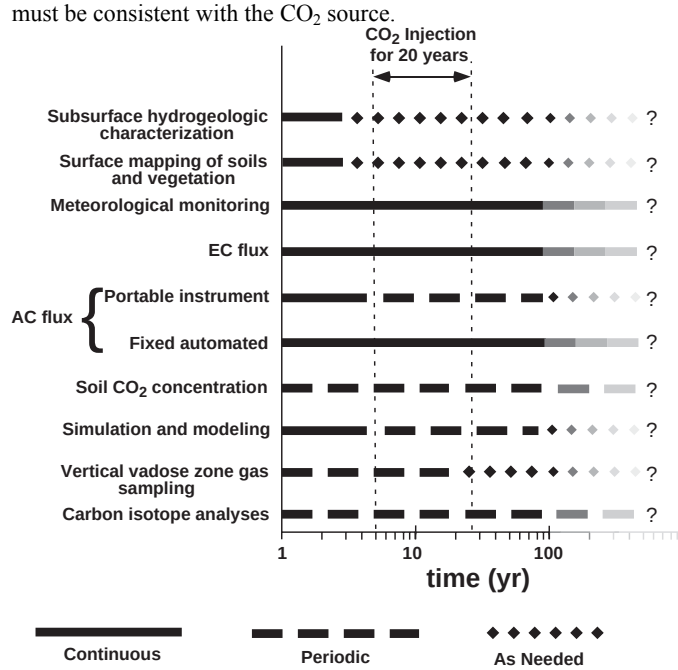

Figure 1. Example activity and schedule chart for CO_2 LOSS detection and monitoring showing generalized frequency of measurements (i.e., continuous, periodic, as needed) over time preceding, during, and following CO_2 injection. Lighter shading indicates increasing uncertainty in need for activities at long times following injection.

Conclusions

A great deal of knowledge and technology exists to detect and monitor CO_2. However, despite these resources, discerning a small CO_2 LOSS from natural variations will be challenging. The strategy that we propose involves comprehensive baseline monitoring and modeling to develop an understanding of and predictive capability for the natural system in the absence of CO_2 LOSS. Once this understanding is achieved and geologic CO_2 storage begins, a program of integrated measurement, monitoring, and modeling that emphasizes time and cost efficiency can be applied during and after the injection period. Measurements in conflict with expectations of the natural system should be thoroughly investigated by detailed vertical profile sampling and chemical and isotopic analyses, the results of which could definitively determine if an anomalous source of fossil CO_2 consistent with the geologic CO_2 storage site is present.

Acknowledgement. This work was supported by the Office of Science, U.S. Department of Energy under Contract No. DE-AC03-76SF00098. We thank Patrick F. Dobson and Sally M. Benson for constructive review of this manuscript.

References

(1) Oldenburg, C. M., Unger, A. J. A. *Vadose Zone J.*, **2003**, *2*, 287-296.
(2) Oldenburg, C. M., Unger, A. J. A. *Vadose Zone J.*, **2003**, submitted.
(3) Norman, J. M., Garcia, R., Verma, S. B. *J. Geophys. Res.*, **1992**, *97*, 18845-18853.
(4) Baldocchi, D. D., Valentini, R., Running, S., Oechel, W., and Dahlman, R. *Glob. Change Biol.*, **1996**, *2*, 159-168.
(5) Oldenburg, C. M., Lewicki, J. L., and Hepple, R. P., Lawrence Berkeley National Laboratory *Report LBNL-54089*, **2003**.
(6) Bonan, G.B., TN-417+STR, NCAR: Boulder, **1996**.

Initial results from a 4 km ocean CO_2 release experiment

Edward T. Peltzer[a], Peter G. Brewer[a], Noriko Nakayama[a], Peter Walz[a], Izuo Aya[b], Ryuji Kojima[b], Kenji Yamane[b], Yasuharu Nakajima[c], Peter Haugan[d], Joakim Hove[d] and Truls Johannessen[d]

a) Monterey Bay Aquarium Research Institute (MBARI)
7700 Sandholdt Road, Moss Landing, CA 95039
b) Osaka Branch, National Maritime Research Inst. (NMRI)
3-5-10 Amanogahara, Katano, Osaka 576-0034, Japan
c)Main Branch, National Maritime Research Inst. (NMRI)
6-38-1 Sinkawa, Mitaka, Tokyo 181-0004, Japan
d) University of Bergen, Allegaten 70, N-5007 Bergen, Norway

Introduction

Direct injection of CO_2 into the ocean is one idea among several carbon dioxide sequestration proposals under consideration to offset the increase of anthropogenic greenhouse gases in the atmosphere. This tactic raises important questions concerning the impacts of pH changes and elevated CO_2 levels for marine ecosystems and the role that ocean sequestration should play in national and international carbon management strategies. While ocean sequestration could reduce the level of atmospheric emissions, it would add to the accumulating burden of fossil fuel CO_2 in the ocean. And while there has been considerable debate regarding rising levels of CO_2 in the atmosphere and whether they constitute a "dangerous anthropogenic interference" with climate, there has been no such debate regarding acceptable oceanic CO_2 levels. In order to address these issues and provide advice to the various world-wide governmental bodies so that policy decisions can be made based upon sound science, new types of *in situ* experimental investigations are required.

For the past 8 years, we have conducted small-scale experiments on the purposeful release of CO_2 into the ocean using MBARI's advanced remotely operated vehicle (ROV) technology. Apparatus and techniques for the transport and release of 0.4 to 45 kg quantities of CO_2 per dive have been developed and we have used this technology to pursue fundamental chemical, physical, and biological studies associated with ocean CO_2 sequestration[1-4]. This technology has also allowed us to conduct several *in situ* experiments mimicking some of the ocean CO_2 sequestration scenarios which have been proposed and to begin the process of understanding the impact of CO_2 on the benthic environment[5-9].

We report here several recent advances in the refinement and development of new technology for experimental releases of CO_2 in the deep sea, and the initial results from an international experiment conducted at 3940m depth in Monterey Bay.

Experimental

56L CO_2 accumulator. For this experiment the 56L CO_2 accumulator[10] was thoroughly re-built. A new carbon fiber reinforced fiberglass barrel was fabricated and the aluminum end-caps and piston were replaced with ones made from titanium to alleviate problems with corrosion. The end-caps and piston were redesigned to eliminate voids on the seawater side, while increasing the depth of the recessed cavity on the CO_2 side to allow for an internal cooling loop. The extended length of the CO_2 end-cap also allowed for a second O-ring seal to solve the leakage problems encountered earlier.

Benthic flume. In order to have more operator control over the plume created during the release experiments, a 'benthic flume' was constructed (Fig. 1). It consisted of a trough for CO_2 150 cm long, 40 cm wide and 25 cm deep; a thruster (driven by a computer controlled brushless DC motor) to generate a variable seawater current along the CO_2 trough; and a wave generator paddle. Both the wave paddle and the thruster were controllable in finite increments by the experimentalist in real-time. A clear panel on the front, and an opaque panel on the back, helped to channel the seawater flow through the flume and aided in viewing of the CO_2 pool under the various stresses. Power and control of the benthic flume was achieved via the ROV by using an underwater mateable connection.

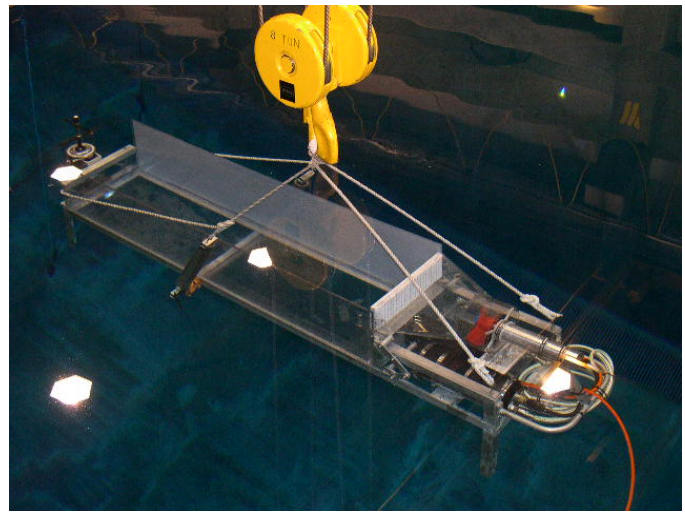

Figure 1. The benthic flume being lowered into the 10m deep test tank at MBARI. The red thruster propeller is visible at the right end of the trough. For the purposes of this test a three axis velocity meter was mounted at the far left-end.

pH probes and calibration. SBE18 pH sensors (Seabird Electronics, Inc., Bellevue, WA 98005) were used. While these sensors have a nominal depth rating of 1200m, we have found that when they are slowly deployed to depth, they can be used as deep as 4000m. The pH electrodes were calibrated using seawater solutions where the pH had been previously adjusted using concentrated HCl or NaOH to ~6 and ~8 as measured by an IQ240 ISFET pH electrode (IQ Scientific Instruments, Inc., San Diego, CA 92127) that was calibrated using commercially available NBS pH standard solutions.

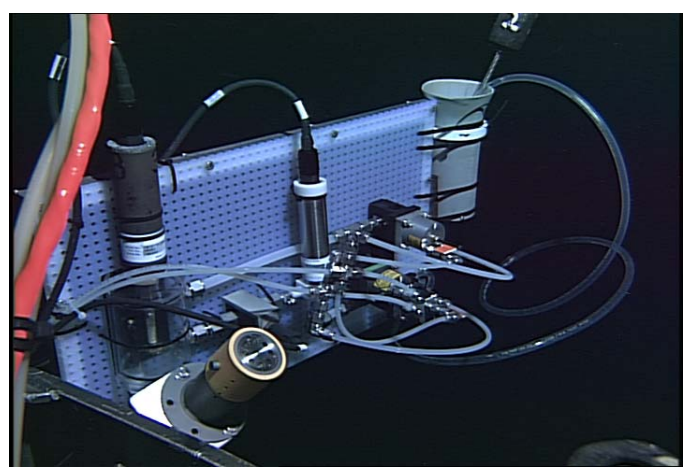

Figure 2. The seawater re-circulation chamber is visible at left with the Seabird SBE18 pH electrode extending from the top. The recirculation pump is the silver cylinder in the middle of the image. Hydraulically activated quarter-turn valves were used to open and close the chamber and to collect ambient seawater samples.

Seawater recirculation chamber. A small volume (~300 mL) chamber (Fig. 2) was equipped with both a pH sensor and a temperature sensor so that samples of CO_2 enriched seawater could be collected and re-circulated. This allowed the kinetics of the CO_2 hydration reaction to be studied. A Seabird submersible pump was used to fill, flush and re-circulate seawater in the chamber. Pumping rates on the order of 0.9-1.2L/min were achieved at depth.

Results and Discussion

Maximization of CO_2 delivery volumes. Delivery of liquid CO_2 in previous experiments was often hampered by less than theoretical yields. Investigation of this phenomenon revealed that the cylinder was often filled with warm water on the seawater side. Heat from this water was conducted through the piston and into the liquid CO_2, thus warming the CO_2 and possibly allowing for gas pockets to form. In order to maximize the amount of liquid CO_2 delivered to the sea-floor, we changed our filling protocol to include pre-filling the seawater side with cold water, and installed an interior copper tube cooling loop on the CO_2 side. Subsequently, all CO_2 deliveries have been within 1-2% of the theoretical delivery volume at depth.

Experimental control of the benthic environment. In previous experiments, we relied upon the ambient current conditions on the sea-floor. Often brisk currents might perturb the experiments, causing noticeable ripples on the liquid CO_2 surface or we might encounter near stagnant conditions, and there was little we could do to modify or control this. With the benthic flume, we can now direct a controlled flow of seawater across the surface of the liquid CO_2. Current speeds of 0.1-1.2 knots are possible and can be adjusted by the ROV pilot in real-time. Additionally, the wave paddle can be controlled in real-time as well to beat from 0.1 to 2 Hz (Fig. 3).

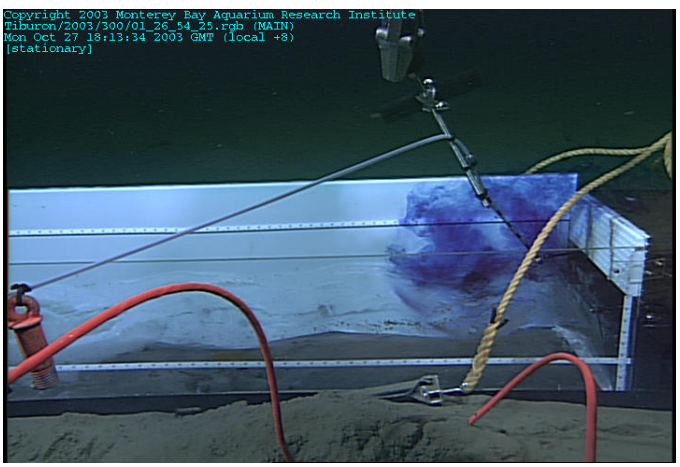

Figure 3. Dye-injection into benthic flume above the liquid CO_2 surface. Sinusoidal waves made by the action of the wave paddle can be clearly seen as the dye cloud drifts above the CO_2-SW interface.

CO_2 hydration kinetics. It is known that the kinetics of the CO_2 hydration reaction are quite slow at atmospheric pressure and room temperature. The half-life of this reaction at 25ºC is about 18 seconds[11]. At lower temperatures, an even longer half-life is predicted (Fig. 4). For example, at temperatures typical of the deep-sea (1.5-2.0ºC), we expect a half-life on the order of 270-300 seconds. However, given that the change in partial molar volumes of the reaction is negative, we predict that the high pressures in the deep-sea will have a positive impact on the reaction rate.

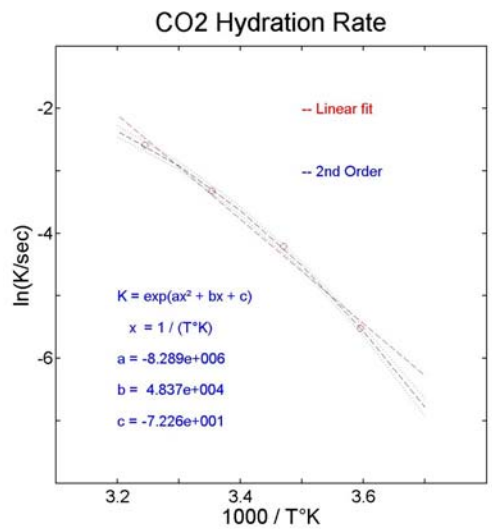

Figure 4. Kinetics of the CO_2 hydration reaction at one atmosphere. Both a linear and a second order fit are shown. The second order equation was used to predict the reaction half-lives at temperatures typical of the deep-sea.

Conclusions

The first ocean CO_2 sequestration experiment at 4 km depth has now been conducted. The benthic flume worked well allowing us to control both the ambient current velocity at the CO_2-seawater interface and to generate regular waves within the liquid CO_2 pool. Both capabilities should aid us in our continued studies of the properties, behavior and impact of liquid CO_2 in the deep-sea.

Acknowledgement. We would like to thank the captain and crew of the R/V Western Flyer, the pilots of the ROV Tiburon; Dale Graves and the MBARI marine operations technicians; without their skill and assistance this work would not have been possible. The authors wish to thank NEDO (Japan), the U.S. DoE and the David and Lucille Packard foundation for support of this research.

References

(1) Brewer, P. G., Orr, F. M., Friederich, G., Kvenvolden, K. A., Orange, D. A. *Energy Fuels*, **1998**, *12*, 183-188.
(2) Brewer, P. G., Friederich, G., Peltzer, E. T., Orr, F. M. *Science*, **1999**, *284*, 943-945.
(3) Brewer, P. G., Peltzer, E. T., Friederich, G., Aya, I., Yamane, K. *Marine Chemistry*, **2000**, *72*, 83-93.
(4) Tamburri, M. N., Peltzer, E. T., Friederich, G., Aya, I., Yamane, K., Brewer, P. G. *Marine Chemistry*, **2000**, *72*, 95-101.
(5) Aya, I., Yamane, K., Shiozaki, K., Brewer, P. G., Peltzer E. T. *Fuel Chemistry Division Preprints*, **2002**, *47(1)*, 27-33.
(6) Aya, I., Kojima, R., Yamane, K., Brewer, P. G., Peltzer, E. T., *Proceedings of GHGT-6*, **2002**, *1*, 739-744.
(7) Brewer, P. G., Peltzer, E. T., Friederich, G., Rehder, G. *Environ. Sci. Tech.*, **2002**, *36*, 5441-5446.
(8) Barry, J. P., Seibel, B. A., Drazen, J. C., Tamburri, M. N., Buck, K. R., Lovera, C., Kuhnz, L., Peltzer, E. T., Osborn, K., Whaling, P. J., Brewer, P. G., *Proc. 2nd Ann. Conf Carbon Seques., Alexandria, VA.*
(9) Aya, I., Kojima, R., Yamane, K., Brewer, P. G. and Peltzer, E. T., *Energy*, (**in press**).
(10) Peltzer, E. T., Brewer, P. G., Dunk, R. M., Erickson, J., Rehder, G., Walz, P., *Fuel Chemistry Division Preprints*, **2002**, *47(1)*, 23-24.
(11) Johnson, K.S. *Limnol. Oceanogr.*, **1982**, *27*, 849-855.

PORE-SCALE STUDIES OF OCEANIC CO_2 SEQUESTRATION

Qinjun Kang, Ioannis N. Tsimpanogiannis, Don Zhang, Peter C. Lichtner

Hydrology, Geochemistry and Geology Group
Los Alamos National Laboratory, MST003, Los Alamos, NM, 87545

The mitigation of CO_2 concentration from the atmosphere while our needs for energy are increasing has attracted significant scientific interest, and various disposal methods (e.g. oceanic, oil reservoirs, saline aquifers, etc.) are under consideration. Direct disposal of liquid CO_2 on the seafloor is one of the approaches for oceanic disposal of CO_2. As its density is higher than that of seawater when the depth is larger than 3000 m, the liquid CO_2 will initially create a pool on the seafloor. In a further step, it will start displacing the seawater in the sediment underneath in a process driven by gravity. At short length scales and/or low infiltration rates (which are expected due to the low permeability of the oceanic sediments), where capillary forces dominate a fingering type displacement is expected, similar to Invasion Percolation (IP) in a destabilizing gradient, since a denser fluid (CO_2) is displacing, downwards, a less dense fluid (water). At large length scales where viscous forces are dominant, a fingering pattern is expected, as well, since we have a less viscous fluid displacing a more viscous fluid.

Additionally, at the CO_2-seawater interface, liquid CO_2 will diffuse into the water and form hydrates with water close to the interface. These processes will modify the porosity and permeability of the seafloor sediment, as well as its composition, affecting thus how deep the liquid CO_2 can penetrate in the sediment. Due to the complex interplay of various phenomena at the micro-level, such processes are difficult to simulate using a continuum hydrogeochemical model.

In this work we have utilized the Lattice Boltzmann (LB) method, a powerful tool in computational fluid dynamics and the Invasion Percolation (IP) in pore networks. These, are two state-of-the-art modeling methods which can be utilized to enhance our understanding of phenomena at the micro-level and enable us to use our findings in refining the macroscopic continuum models.

We have numerically simulated fingering in a two-dimensional channel as well as dissolution and/or precipitation in porous media, two fundamental processes likely to be ubiquitous in oceanic CO_2 disposal. We examined the obtained patterns, as well as the change in porosity/permeability due to hydrate formation and how they depend on various parameters.

Finger penetration in a channel by the LB method

We have studied the effects of viscosity ratio (M), capillary number (u_0), and wettability (θ_1) on finger penetration in a two-dimensional channel using a LB multiphase model. The simulation results show that with an increase of the viscosity ratio or capillary number, both the finger width and the slip distance of the contact lines decrease, while the finger length increases. As shown in Figure 1, with the decrease of the wettability of the displacing fluid, the finger length and its change rate with time increase while the slip distance of the contact lines and its change rate with time decrease, and the minimum capillary number to form a stable finger decreases. Hence, the finger growth is enhanced when the displacing fluid is nonwetting to the wall and otherwise suppressed. An indented part near the beginning of the fingers is clearly observed when a wetting fluid is displacing a nonwetting one. The finger width, however, remains nearly unchanged when the wettability of the fluids changes.

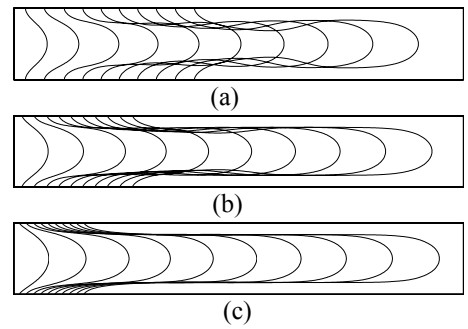

Figure 1: Finger evolution for M=10 at u_0=0.1. (a) θ_1=60°, (b) θ_1=60°, (c) θ_1=119°.

Dissolution and precipitation in porous media by the LB method

We developed a LB model and applied it to simulate fluid flow and dissolution and precipitation in the reactive solid phase in a porous medium. Both convection and diffusion as well as temporal geometrical changes in the pore space are taken into account. The numerical results show that at high Peclet (Pe) and Peclet-Damkohler (PeDa) numbers, a wormhole is formed and permeability increases greatly due to the dissolution process. At low Pe and high PeDa numbers, reactions mainly occur at the inlet boundary, resulting in the face dissolution and the slowest increase of the permeability in the dissolution process. At moderate Pe and PeDa numbers, reactions are generally nonuniform, with more in the upstream and less in the downstream. At very small Pe-Da number, dissolution or precipitation is highly uniform, and these two processes can be approximately reversed by each other. Figure 2 shows the permeability-porosity relationships resulted from these four scenarios.

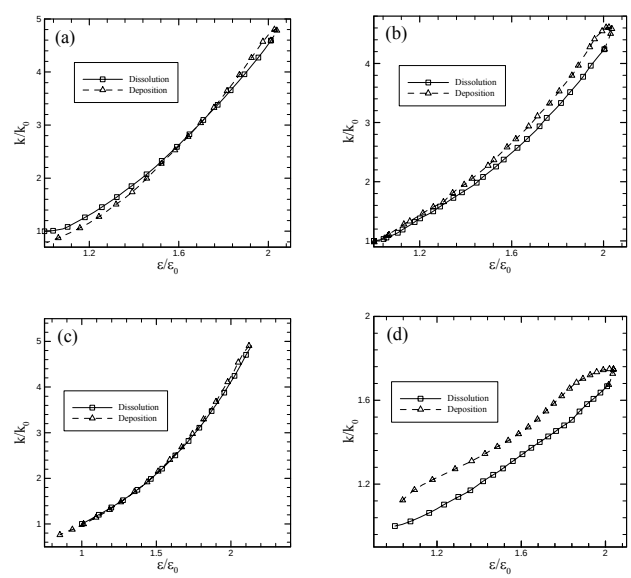

Figure 2: Dependence of permeability on porosity. Both permeability and porosity are normalized by the values of the initial geometry: (a) *Pe*=45, *PeDa*=7.5; (b) *Pe*=0.45, *PeDa*=0.075; (c) *Pe*=0.0045, *PeDa*=0.00075; (d) *Pe*=0.0045, *PeDa*=7.5. Squares denote dissolution and triangles denote deposition.

CO_2 invasion patterns in a pore network

A 2-D pore-network model based on concepts from Invasion Percolation in a gradient was developed to simulate the invasion of liquid CO_2 into the oceanic sediment and the subsequent immiscible displacement of water originally present in the sediment. To capture

the disorder of the oceanic sediment, we assigned random capillary thresholds to the pores during the invasion part of the simulation. This process was also coupled with hydrate formation occurring when the CO_2 entered the Hydrate Stability Zone (HSZ). The reaction process was captured by considering a hydrate forming step, in a pore occupied by CO_2, for every λ invasion steps (smaller λ implies faster kinetics). Figure 3 shows typical invasion patterns obtained for different cases examined, ranging from very fast hydrate formation kinetics (Figure 3a) to essentially no hydrate forming conditions (Figure 3d). Note that at the limit of fast kinetics, as CO_2 enters the HSZ it immediately forms hydrate which results in blocking the pore space, resulting in formation of a thin layer of hydrate which does not allow any further penetration of CO_2 into the HSZ. As a result of the pore blocking, a pool of trapped liquid CO_2 is formed above the HSZ (Figures 3a-b).

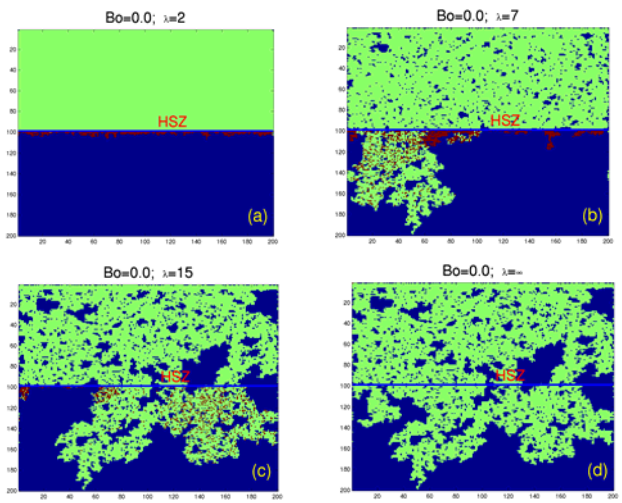

Figure 3: CO_2 invasion patterns in a 200x200 pore-network. Color code: Blue denotes water, green denotes CO_2, and red denotes hydrate.

Drop behavior and energy consumption for CO_2 ocean disposal using a new injection process via a static mixer

Hideo Tajima, Akihiro Yamasaki, and Fumio Kiyono

National Institute of Advanced Industrial Science and Technology
16-1 Onogawa, Tsukuba, Ibaraki 305-8569, Japan

Introduction

Several scenarios of CO_2 disposal into the ocean have been proposed for a long-term sequestration as a counteraction measure for global warming. In the disposal process of liquid CO_2, especially, liquid CO_2 would be released from a pipeline through a nozzle to the ocean at the depth deeper than 500 m.[1] Since the density of liquid CO_2 is smaller than that of seawater at the depth shallower than 3000 m, the released CO_2 drops would ascend to the ocean surface. During the drop ascending process, the CO_2 would be dissolved into the seawater from the drops, and the ascending speed would decrease by the reducing size of the drops. The dissolution process should be completed before reaching the sea surface. Since the ascending and dissolution behavior depends on the size of the released CO_2 drops, the releasing size of the drop should carefully designed and controlled on the injection. On the other hand, the effect of CO_2 hydrate should be considered in the disposal process of liquid CO_2, because the thermodynamic condition of CO_2 hydrate formation would normally be satisfied in the ocean at depths greater than 500 m ($T < 283$ K and $p > 44.5$ bar).[2] The nozzle of the CO_2 pipeline could be blocked by the formation of solid CO_2 hydrate upon injection and sequent the agglomeration of the hydrates, and the blockage should be prevented for a continuous and stable injection process.

Then, we have proposed a novel injection process of liquid CO_2 into the ocean by utilization of a static mixer as a possible solution for the above difficulties.[3] In this research, behavior of released CO_2 drop from the injection process with static mixer was studied, and estimation of energy consumption was conducted for the scale-up of the injection process.

Experimental

The typical experimental pressure and temperature were, respectively, 7.0 MPa and 277 K. The typical flow for liquid CO_2 was 46.6-93.4 ml/min, and liquid CO_2 flow was installed into deionized water flow (0.47-2.98 L/min). The two-phase flow was injected into the Kenics-type static mixer (Noritake Co. Ltd., Japan) by the high-pressure pump at once. In the experiment, before injected into the mixer and after released from the mixer, the two-phase patterns of the mixture could be observed in the observation section made of polycarbonate, and it was recorded by the high-speed video camera (FOR.A Co. Ltd., VFC-1000 and Photron Ltd.).

Results and Discussion

Figures 1-3 shows typical experimental results for the mixture of liquid CO_2 and water. Liquid CO_2 always dispersed in water flow as drops covered with hydrate film. For the mixture flow before injected into the static mixer, the drop size distributions seemed to conform to the logarithmic normal distribution. On the other hand, the drop size distributions and mean drop diameters for the mixture after released from the static mixer are well characterized by the normal distribution and the Sauter mean diameter. The experimental results suggested that the static mixer is effective for producing liquid CO_2 drops with relatively uniform size distribution. Moreover, the pipe-blockage by the hydrate formation could be prevented in the present system due to an effective mixing process in the static mixer. Thus, the utilization of static mixer in the injection process of liquid CO_2 into the ocean would be advantageous over simple nozzle injection methods.

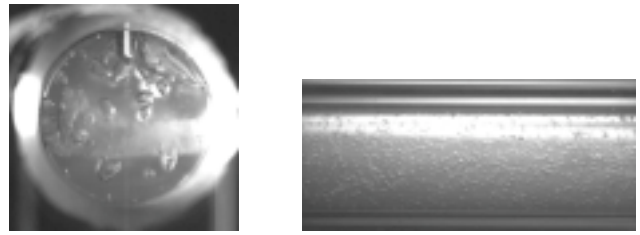

a) before injected into the mixer b)after released from the mixer

Figure 1. Typical results of the mixture of liquid CO_2 and water. Conditions; CO_2 = 93.4 ml/min, Water = 2.03 L/min.

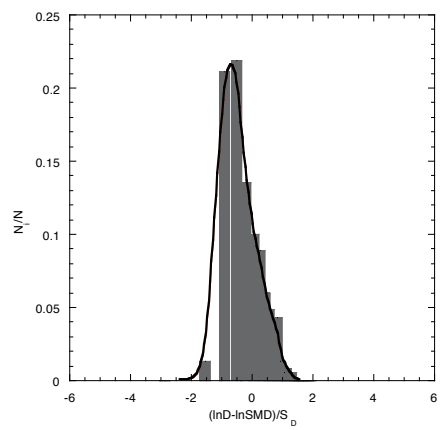

Figure 2. Drop size distribution for Fig.1-a

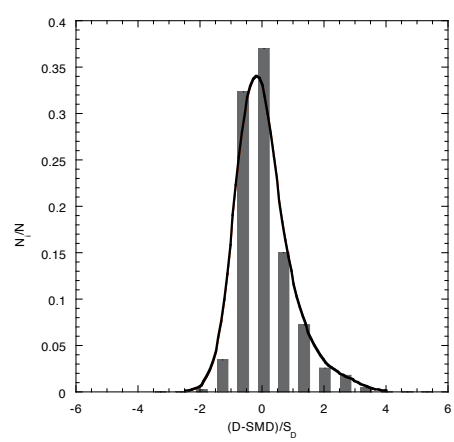

Figure 3. Drop size distribution for Fig.1-b

To examine the feasibility of the present process, a numerical simulation on the fate of the released CO_2 droplets after released from the static mixer was conducted. The fate of the liquid CO_2 in the ocean is one of key information for estimation of the environmental impact caused by the disposed CO_2. The several assumptions were made for the calculations; (1) the released drop is a sphere with uniform initial size, (2) the contribution of the surface hydrate film was ignored because the film thickness is considered much thinner than the drop diameter, (3) the density of liquid CO_2 was constant for simplicity,(4) the drop released would ascend to the sea surface with the terminal velocity determined by the size, density of the drop, (5) the each drop would move independently (no merge or breakup would occur). The dissolution distance of liquid CO_2 drop covered with CO_2 hydrate film, is expressed as a function of dissolution rate[4]. However, this equation is only valid for the drop smaller than 0.4 mm (Stokes region). Then the equation of dissolution distance was extended to the higher Reynolds number region.

Figure 4 shows the ascending behavior of the drop with various initial diameters, assuming the releasing depth of liquid CO_2 500 m. In this condition, the initial diameter should be smaller than 9.1 mm to be dissolved completely before reaching the sea surface. However, liquid CO_2 would be vaporized when the pressure is lower than the saturated vapor pressure, then the ascending rate would be accelerated drastically due to the larger difference in the density between the seawater and gaseous CO_2. To avoid the vaporization, the initial diameter of the drop should be smaller than 4.0 mm to be dissolved completely before reaching the depth of 390 m, where the water pressure equals to the vaporization pressure for 277 K (about 3.9 MPa).

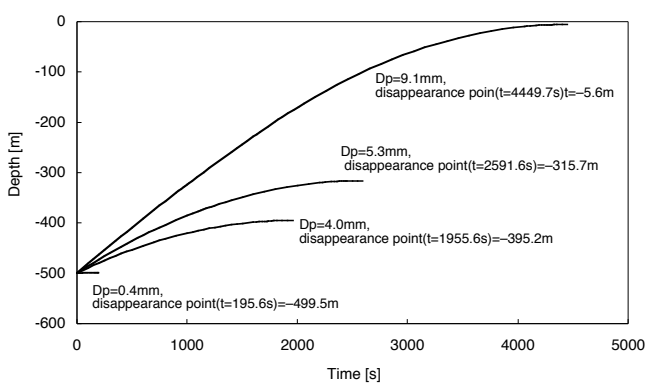

Figure 4. Ascending behavior of the drop with various initial diameters

Energy consumption is also one of important factors to discuss the feasibility of the new injection process. The energy required for the injection process is the pressure drop along the static mixer. The pressure drop is given by the Fanning equation including the individual frictional coefficient of the present static mixer. In the experimental conditions, the maximum energy consumption was estimated to be 0.83 J/g-CO_2. Of course, the energy consumption becomes smaller than this value as a ratio of liquid CO_2 flow rate to water increase.

For the scale-up of the injection process besed on the experimental conditions, we assumed a capture and disposa l process of CO_2 from 100 MW thermal power plant (CO_2 emission rate = 22.9 kg/s, energy generation per unit CO_2 emission = 4365 kJ/kg-CO_2 generation[1]). Because it is known from the experiments that the ratio of the drop mean diameter to the diameter of the mixer is expressed as a function of Weber number, the energy consumption can be estimated by setting up a drop mean diameter. In here, we assumed that the ratio of liquid CO_2 to water flow rate is same to the experimental condition. As summarized in **Table 1**, when the mean diameter of CO_2 drop made to generate in the static mixer was set up in 4.0 mm, the diameter of the mixer was the range of 1.91 from 0.75 m, and the maximum of the energy consumption was 0.406 kJ/kg-CO_2. This is less than 0.01% to the energy generation per unit CO_2 emission. Even if the diameter was set up in 0.1 mm, the rate of the energy consumption was 3.14% of the maximum. Therefore, it can be said that the static mixer is a uniform size CO_2 drop generator of which the energy consumption is very small, and the injection process is very useful for CO_2 ocean disposal.

Table 1. Estimated results of energy consumption for the injection process via the static mixer

SMD [mm]	Partial Ratio of CO2 [kg/kg-total flow]	Mixer Diameter [m]	Mean Flow Velocity [m/s]	We Number [-]	Energy Consumption [kJ/kg-CO2]	Ratio to Power Generation [%]
4.0	0.0136	1.912	0.562	1913	0.406	0.0093
	0.0265	1.462	0.486	1118	0.165	0.0038
	0.0251	1.494	0.492	1168	0.178	0.0041
	0.0480	1.148	0.426	689	0.074	0.0017
	0.0750	0.952	0.385	474	0.041	0.0009
	0.1307	0.747	0.338	292	0.019	0.0004
SMD [mm]	Partial Ratio of CO2 [kg/kg-total flow]	Mixer Diameter [m]	Mean Flow Velocity [m/s]	We Number [-]	Energy Consumption [kJ/kg-CO2]	Ratio of Power Generation [%]
0.1	0.0136	0.422	11.56	93	238.8	3.14
	0.0265	0.322	10.00	54	110.1	1.28
	0.0251	0.330	10.11	57	117.2	1.37
	0.0480	0.253	8.77	34	55.3	0.58
	0.0750	0.210	7.92	23	32.9	0.31
	0.1307	0.165	6.95	14	17.1	0.15

Conclusions

For the new injection process of liquid CO_2 into the ocean using a static mixer, behavior of liquid CO_2 in water and estimation of energy consumption to examine the feasibility were studied. The experimental results suggested that the static mixer is effective for producing liquid CO_2 drops with relatively uniform size distribution. For a simple numerical simulation on the fate of the released CO_2 drops after released from the static mixer, the initial diameter of the drop should be smaller than 4.0 mm to make it dissolve completely when the depth to release liquid CO_2 is supposed 500 m. The distribution of the drop must be taken into consideration to examine in detail. Assuming that the CO_2 injection process was installed in the disposal process of emission CO_2 from 100MW thermal power plant, energy consumption to generate drop with mean diameter 4.0 mm was much smaller than the energy generation per unit CO_2 emission. The static mixer was a very energy consumed device for the generation of uniform size drops. These results indicate that the injection process via a static mixer is a feasible option for the CO_2 disposal process.

References

(1) Halmann M. M.; Steinberg M. In *Greenhouse Gas Carbon Dioxide Mitigation*; Lewis Publishers: Boca Raton, 1999.

(2) Sloan E. D., In *Clathrate Hydrates of Natural Gases*, 2 Ed, Dekker: New York, 1998

(3) Tajima H.; Yamasaki A.; Kiyono F. Prepr. Pap. – *Am. Chem. Soc., Div. Fuel Chem.*, **2003**, 48 (1), 121

(4) Teng H.; Yamasaki A.; Shindo Y. *Int. J. Energy Res.*, **1999**, 23, 295

Thermochemistry and Reaction Paths for Dimethyl Sulfide Radical with O2

Fei Jin and Joseph w Bozzelli

Chemistry, New Jersey Institute of Technology, Newark, NJ 07102

Abstract

The thermo property data on CH_3SCH_2OOH and two radicals $CH_3SCH_2OO\cdot$ and $C\cdot H_2SCH_2OOH$ are important to understand the stability, reaction paths and kinetics of reactions of sulfur hydrocarbons (sulfides) in atmospheric and combustion processes. Thermochemical properties for species and transition states in the methylthiomethyl ($CH_3SC\cdot H_2$) radical + O_2 reaction system are analyzed to evaluate reaction paths and kinetics. Isodesmic working reaction are employed to determine enthalpies of formation ($\Delta H_f^o{}_{298}$) using density functional (B3LYP/6-311G(d,p)) and complete basis set (CBS-QB3) computational methods. Entropy ($S°_{298}$) and heat capacities $C_p(T)$ ($300 \leq T/K \leq 1500$) are determined using geometric parameters and vibration frequencies obtained at B3LYP/6-311G(d,p) level of theory. $\Delta H_f^o{}_{298}$ values estimated at the CBS-QB3 level (unit in kcal/mol): $CH_3SC\cdot H_2$ (32.66±0.50), CH_3SCH_2OOH(–29.14±0.12), $CH_3SCH_2OO\cdot$ (5.17±0.36), $C\cdot H_2SCH_2OOH$ (11.48±1.44). Quantum Rice-Ramsperger-Kassel(QRRK) analysis is used to calculate energy- dependent rate constants, $k(E)$ and master equation analysis is used to account for collisional stabilization of adduct and isomer. The methylthiomethyl radical adds to O_2 to form a methylperoxy racial with a 37.82 kcal/mol well depth. The peroxy radical can undergo dissociation back to reactants, isomerize via hydrogen shift (TS1,E_a=17.06kcal/mol) to form a hydroperoxide methyl radical $C\cdot H_2SCH_2OOH$, decompose via hydrogen transfer (TS2, E_a=37.79kcal/mol) to form $CH_3SC(=O)H$ plus OH radical , or the peroxy radical can also attack the sulfur atom via TS3(E_a=32.92kcal/mol) to form $CH_3S(=O)$ + CH_2O. The $C\cdot H_2SCH_2OOH$ isomer can decompose via TS4 (E_a=24.09kcal/mol) to CH_2O+CH_2S+OH, or through a four-member ring transition state (TS5, E_a =30.77kcal/mol) to form 1,3-Oxathietane + OH.

Introduction

Dimethyl sulfide (DMS) has been recognized as the main natural source of sulfur in the atmosphere[1], which emitted into the atmosphere over the global oceans has a range of effects upon atmospheric composition (mediated through various oxidation products) that may be significant with regard to issues as important as climate regulation. The roles played by DMS oxidation products within these contexts are diverse and complex, and in many instances are not well understood.

At present, the main step of the DMS oxidation in the atmosphere is the reaction with OH radical during daylight and the reactions with NO_3 radical and Cl radical, which will lead to the formation of the $CH_3SC\cdot H_2$ radical.

The $CH_3SCH_2OO\cdot$ peroxy radical is an important intermediate in the atmospheric degradation of dimethyl sulfide. The $CH_3SCH_2OO\cdot$ peroxy radical is produced through the addition of O_2 to the CH_3SCH_2 radical.

$$CH_3SC\cdot H_2 + O_2 \rightarrow CH_3SCH_2OO\cdot$$

It is believed that the reaction of the $CH_3SCH_2OO\cdot$ with the HO_2 radical will lead to the following products:

$$CH_3SCH_2OO\cdot + HO_2 \rightarrow CH_3SCH_2OOH + O_2$$

In this chapter, reaction pathways of the addition of O_2 atoms to $CH_3SC\cdot H_2$ radical are analyzed. CBS-QB3 and density functional methods are utilized estimate thermodynamic properties ($\Delta\Delta H_f^o{}_{298}$, $S°_{298}$ and $C_p(T)$) for reactant $CH_3SC\cdot H_2$, intermediate radicals $CH_3SCH_2OO\cdot$, $C\cdot H_2SCH_2OOH$ and transition states:

TS1: $\overbrace{CH_3SCH_2OO\cdot}$ Intramolecular hydrogen shift to form a hydroperoxy radical.

TS2: $CH_3S\overbrace{CH_2OO\cdot}$ Intramolecular hydrogen shift to form $CH_3S\cdot CHOOH$ radical, and $CH_3S\cdot CHOOH$ rapidly dissociates $CH_3SC(=O)H$ + OH.

TS3: $CH_3\overbrace{SCH_2OO\cdot}$ The peroxy radical can also attack the sulfur atom form $CH_3S(=O)H$ + CH_2O.

TS4: $C\cdot H_2S$-CH_2O-OH β,γ-scission reaction to form a thioformaldehyde plus a formaldehyde and OH.

TS5: $\overbrace{CH_2SCH_2O}$-OH 1,3-Oxathietane + OH.

Isodesmic working reactions are applied to evaluate enthalpies of formation. Contributions to entropy and heat capacities from internal rotation are estimated using direct integration over energy level of the intermolecular rotation potential energy curve, with B3LYP/6-311g(d,p) level calculations for rotation barrier. Activation energies for the transition states are determined and the kinetic analysis is detailed on the base of the thermodynamic properties.

Quantum Rice-Ramsoerger-Kassel (QRRK) analysis is used to calculate the energy dependent rate constant $k(E)$, and master equation analysis is applied to account for collisional stabilization in the $CH_3SCH_2\cdot$ + O_2 adduct and isomers. The thermochemical and kinetic data at relevant pressures and temperatures should be useful to both atmospheric and combustion models

Calculation Methods

Density functional B3LYP/6-311g(d,p) is utilized to calculate structures and vibrational frequencies and potentials for internal rotors. CBS-QB3 methods are utilized to calculate enthalpy in working reaction analysis.

Entropy ($S^o{}_{298}$) and Heat Capacities($C_p(T)$, $300 \leq T/K \leq 1500$)

Entropies and heat capacities (T) were calculated using the rigid – rotor-harmonic – oscillator approximation based on scaled vibrational frequencies and moments of inertia of the optimized BLYP/6-311G(d,p) structures. Contribution to entropy and heat capacity from internal rotation are determined using Pitzer et al,'s treatment based on rotational barrier height and corresponding moments of inertia for the rotors.

High-Pressure Limit *A* Factors(*A*) and Rate Constant (k_∞)

For the reactions where thermochemical properties of transition states are calculated by density functional methods and CBS-QB3 methods. k_∞ values are fit by three parameters, A, n, and E_a over the temperature range from 200k to 2000k, expressed by:

$$k_\infty = A(T)^n \exp(-E_a/RT)$$

Activation energies of reactions are calculated as follows:

$$E_a = [\Delta H_f^o{}_{298,TS} - \Delta H_f^o{}_{298,reactant}]$$

Entropy differences between reactant and transition state are used to determine the pre-exponential factor A, via classical, cannonical TST for a unimolecular reaction, $A = (\kappa_b T/h_p)\exp(\Delta S^{\neq}/R)$ where h_p is the Planck constant and κ_b is Boltzman's constant.

Results and Discussion

Enthalpies of Formation ($\Delta H_f^o{}_{298}$)

The enthalpies of formation ($\Delta H_f^o{}_{298}$) are estimated using total energies and calculated ΔH_{rxn298} for the listed reactions. The total

energies are determined at the CBS-QB3 level; scaled ZPVE's and thermal corrections to 298.15K are listed in Table 1.2.

Thermochemical Kinetic Analysis of the Reaction $CH_3SC{\cdot}H_2 + O_2 \rightarrow (CH_3SCH_2OO{\cdot})^* \rightarrow$ Products

A potential energy diagram for the methylthiomethyl radical with O2 is illustrated in Figure 1.6; energies are calculated at the CBS-QB3 level. Addition of oxygen to the $CH_3SC{\cdot}H_2$ radical forms an energized adduct.

$$CH_3SC{\cdot}H_2 + O_2 \rightarrow CH_3SCH_2OO{\cdot}^* \rightarrow \text{Products}$$

Possible reactions for this activated adduct are described as follows:

Rxn1: $CH_3SCH_2OO{\cdot}^* \rightarrow$ rev rxn - to reactants $CH_3SC{\cdot}H_2 + O_2$

Rxn2: Stabilization ($CH_3SCH_2OO{\cdot}^* \rightarrow CH_3SCH_2OO.$)

Rxn3: Hydrogen atom shift from the methyl group to form a hydroperoxide methyl radical:

$$CH_3SCH_2OO{\cdot}^* \rightarrow C{\cdot}H_2SCH_2OOH \text{ isomer (TS1).}$$

Rxn4: Hydrogen atom transfer from peroxy carbon (TS2)

$$CH_3SCH_2OO{\cdot}^* \rightarrow CH3SC{\cdot}HOOH \rightarrow CH_3SC(=O)H + OH$$

Note CH3SC·HOOH is unstable and immediately dissociates to $CH_3SC(=O)H$ plus OH radical (TS2)

Rxn5: The peroxy radical can also attack the sulfur atom to form a cyclic transition state structure (TS3, a 4-member ring) where the relatively strong S=O bond (near double bond) starts to form; and the weak (SO—OC) peroxide bond in the transition state starts to cleave (ring opening). The initial product from this reaction: a radical intermediate $CH_3S(=O)CH_2O{\cdot}$ will undergo beta scission (carbonyl formation) resulting in $CH_3S(=O) + CH_2O$

The methylthiomethyl radical ($\Delta H_f^o{}_{298}$ =32.66 kcal/mol) adds to O_2 to form $CH_3SCH_2OO{\cdot}$ peroxy radical. The activation energy of TS1 is 17.06 kcal/mol, and TS1 is below the reactants. The $\Delta H_f^o{}_{298}$ for the $CH_3SC{\cdot}HOOH$ radical in Reaction VI are estimated on the base of the result of $C{\cdot}H_2SCH_2OOH$ and their difference of total energy calculated under MP2/6-31G(d,p) level. The activated $CH_3SCH_2OO{\cdot}^*$ adduct crossed TS2, which then undergoes OH elimination to form $CH_3SC(=O)H$, with the barrier 37.79kcal/mol. Reaction V has a barrier of 32.92 kcal/mol.

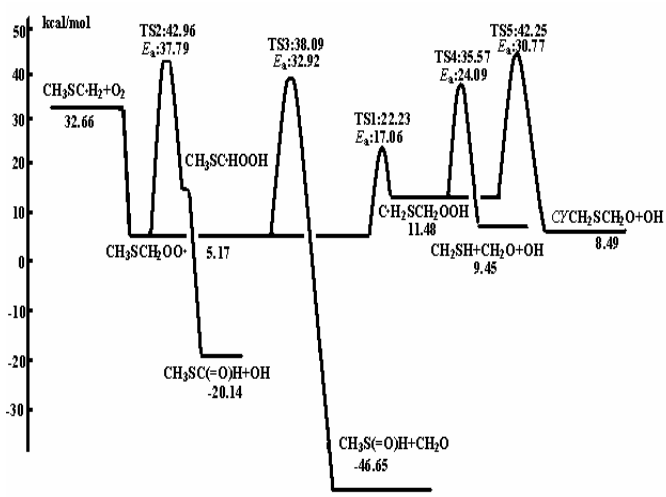

$CH_3SCH_2OO{\cdot} \rightarrow$ Products

The energized $C{\cdot}H_2SCH_2OOH$ can undergo four different reactions, which include reverse reaction back to $CH_3SCH_2OO{\cdot}$ radical, stabilization, CH_2S+CH2O+OH forming through TS4 and reaction through a four-member ring transition state (TS5) to form 1,3-Oxathietane + OH. The activation energy of TS4 and TS5 are respectively 24.09 and 30.77 kcal/mol, based on the CBS-QB3 level of theory.

High-Pressure Limit Rate Constants,
- Input Parameters for QRRK Calculations

	Reaction	$A(s^{-1})$	n	E_a (kcal/mol)
k_1	$CH_3SC{\cdot}H_2 + O_2 \rightarrow CH_3SCH_2OO{\cdot}$	5.82E+12	0.00	0.00
k_{-1}	$CH_3SCH_2OO{\cdot} \rightarrow CH_3SC{\cdot}H_2 + O_2$	4.28E+14	0.00	26.90
k_2	$CH_3SCH_2OO{\cdot} \rightarrow C{\cdot}H_2SCH_2OOH$	1.2231E+07	1.20	17.06
k_{-2}	$C{\cdot}H_2SCH_2OOH \rightarrow CH_3SCH_2OO{\cdot}$	7.5535E+10	-0.26	10.75
k_3	$CH_3SCH_2OO{\cdot} \rightarrow CH_3SC(=O)H + OH$	8.3158E+09	0.92	37.79
k_4	$CH_3SCH_2OO{\cdot} \rightarrow CH_3S(=O)H + CH_2O$	1.7013E+10	0.53	32.92
k_5	$C{\cdot}H_2SCH_2OOH \rightarrow CH_2S$+CH2O+OH	6.4507E+13	-0.47	24.09
k_6	$C{\cdot}H_2SCH_2OOH \rightarrow CYCH_2SCH_2O$+OH	3.7282E+13	-0.70	30.77

Lennard-Jones paramenters : σ =5.54Å,ϵ/k=460 Geometric mean frequency (from CPFIT, :
$CH_3SCH_2OO{\cdot}$ (904.0cm^{-1} ×22.5), $C{\cdot}H_2SCH_2OOH$(736.9 cm^{-1} ×23.0)

k_{-1}, k_{-2} : microscopic reversibility

CH3SCH2. + O2 => Products

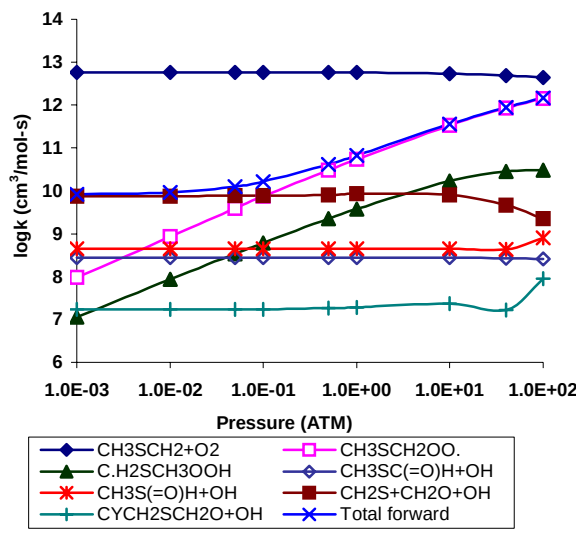

References

(1) Charlson R. J.; Lovelock, J.E.; Andreae. M. O.; Warren, S. G. *Nature* **1987**, *326*, 655.

(2) Hynes A. J.;Wine P. H.;Semmes D. H., J. Phys. Chem., **1986**, *90*, 4148.

(3) Butkovskaya N. I.;LeBras G., *J. Phys. Chem*., **1994**, *98*, 2582.

(4) Resende S. M. ; Almeida W. B. De, *J. Phys. Chem. A*, **1997**, *101*, 9738.

(5) Lovelock J. E., Maggs R. J.;Rasmussen R. A., *Nature*, **1972**, *237*, 452.

(6) Saltzman E. S.; Cooper W. J., in Biogenic Sulfur in the Environment, American Chemical Society, Washington, DC **1989**

(7) *Gaussian 98*, Revision A.9;Gaussian, Inc.: Pittsburgh, PA, **1998**.

(8) Pitzer, K. S.; Gwinn, W. *J. Chem. Phys*. **1942**, *10*, 428

(9) Sheng, C.; Bozzelli, J. W.; Dean, A. M.; Chang, A. Y. *J. Phys.Chem. A* **2002**, *106*, 7276.

Modeling the Reaction of $C_2H_5+O_2$

Chitralkumar V. Naik, Hans-Heinrich Carstensen, and Anthony M. Dean

Chemical Engineering Department
Colorado School of Mines
Golden, CO 80401

Introduction

Modeling of low temperature ethane oxidation requires an accurate description of the reaction of $C_2H_5+O_2$, since its reaction channels either accelerate the oxidation process via chain branching, or inhibit it by forming stable less-reactive products. Before the discovery of the new concerted elimination channel[1], which is the direct formation of $C_2H_4+HO_2$ from ethylperoxy, the isomerization of ethylperoxy ($CH_3CH_2OO\bullet$) to hydroperoxyethyl ($C\bullet H_2CH_2OOH$) was considered the lowest energy channel. According to the Walker and Morley[2] scheme, subsequent reactions of hydroperoxyethyl lead to chain branching, thus promoting ignition. The new lower-lying concerted elimination path is significantly faster than the isomerization, reducing the importance of the isomerization channel and its subsequent chain-branching reactions.

Data are available on different aspects of the $C_2H_5+O_2$ system, for example, on the overall rate constant[3,4] of the reaction and on the production of ethylene[5,6], HO_2[7], and ethylene oxide[6]. Different groups have characterized this reaction theoretically. The latest theoretical studies by Miller et al.[8,9] and Sheng et al.[10], both of which incorporated the concerted elimination channel, can in general explain the observations. However, no reaction mechanism is available that can accurately predict all experimental data.

Our main objective is to develop an accurate mechanism for the $C_2H_5+O_2$ system. We started with a CBS-QB3 potential energy surface (PES) with bond additivity corrections (BAC). Tunneling corrections were included in the calculation of the high-pressure rate constants. These values are used in a chemical activation analysis to calculate pressure-dependent rate coefficients. We tested this mechanism against the wide range of experimental data and found good agreement.

Calculation Methods

The PES was calculated using the CBS-QB3 compound method as implemented in Gaussian 98W[11]. Vibrational frequencies were scaled by 0.99, and vibrational modes resembling internal rotations were replaced by a hindered rotor treatment. Standard statistical mechanics formulas were used to calculate the entropies, heat capacities and thermal contribution to the enthalpy. The electronic energies were converted to heats of formation via the atomization method. We applied bond additivity corrections, similar to the work of Petersson et al.[12] Canonical transition state theory was used to calculate high-pressure rate constants for all reaction channels with pronounced barriers. Contributions from tunneling were incorporated in high-pressure rate constants using Wigner's tunneling correction method[13]. There is no pronounced barrier found for the recombination of C_2H_5 with O_2. In this case, high-pressure rate constants were taken from Miller et al.[9]

The chemically activated reaction of $C_2H_5+O_2$ was then analyzed with the Fortran code CHEMDIS[14]. It uses QRRK theory to calculate energy dependent rate constants k(E). The collisional deactivation is described using the modified strong collision (MSC) approach. Frequency information, to calculate density of states, is provided in form of three representative frequencies with non-integer degeneracies calculated from the heat capacities. The collision parameters required for the MSC model are similar to those used by Sheng et al.[10] In addition to the MSC approach, for a few cases we used solutions of the steady state master equation as described by Sheng et al.[10] The CHEMKIN 3.6.2 package[15] is used for the numerical integration.

Results and Discussion

The major features of the PES calculated at the CBS-QB3 level of theory compare well to those reported by Sheng et al.[10] and Miller et al.[8,9] For example, we find ethylperoxy to be –34.0 kcal/mol relative to the reactants at 0K, compared to –33.9 kcal/mol given by Miller et al. The corresponding value of –34.5 kcal/mol at 298K is reasonably close to –35.3 kcal/mol reported by Sheng et al. All three studies find the barrier of the concerted elimination to be clearly below the reactants: ~2.8 kcal/mol at 0K and ~4.5 kcal/mol at 298K. The differences are somewhat larger for the isomerization reaction. Miller et al. report this barrier to be 3.2 kcal/mol above the reactants at 0K while our calculations yield 1.9 kcal/mol. Our value at 298K is within 0.2 kcal/mol of that reported by Sheng et al. On the other hand, the agreement is not so good when compared to the calculations of the Schaefer group[1].

The high-pressure rate constants calculated in this work are generally higher than those from Sheng et al.[10] The largest difference is found for the isomerization reaction where our value is ~14 times higher at 500K. Many factors may contribute to this deviation. Tunneling accounts for the increase in the rate constant by a factor of 2.7 at this temperature. Another reason may lie in differences in entropy values of the reactants and transition states. The resulting set of pressure-dependent rate coefficients together with additional reactions of peroxy radicals, chlorine and other secondary reactions, will be published elsewhere.

We compared our predictions to the pressure dependence of the overall rate constants of the $C_2H_5+O_2$ reaction observed by Kaiser et al.[3] at 298K. We found our model to underpredict the data in the falloff region by about a factor of two. Moreover, a modified mechanism using rate coefficients for the $C_2H_5+O_2$ system from Klippenstein et al.[16], which were obtained from solutions of the time dependent master equation, showed the same problem. We concluded that the energy transfer process for this system might not be correctly described by generic collision parameters, and that they might underpredict the collision efficiency of He. Thus, we increased the collision cross section by a factor of 2.4 to improve the fit to the falloff curve, and then used this value for all calculations.

Though we cannot present detailed comparisons due to space limitations, we find that our model captures the temperature and pressure dependence of the overall rate constants measured by Slagle et al.[4] Similarly, the predicted pressure dependence of the ethylene yield agrees well with measurements of Kaiser[5].

In recent experiments, Kaiser[6] measured the complex temperature dependence of the ethylene production relative to ethyl chloride. These measurements are compared to the prediction using the current model in Figure 1. We accurately predict the sharp increase in ethylene at 440K that is attributed to the thermal activation of the stabilized $CH_3CH_2OO\bullet$. Also shown are our predictions using the rate coefficients reported by Sheng et al. Their mechanism captures the overall temperature dependence but uniformly underpredicts the ethylene yield.

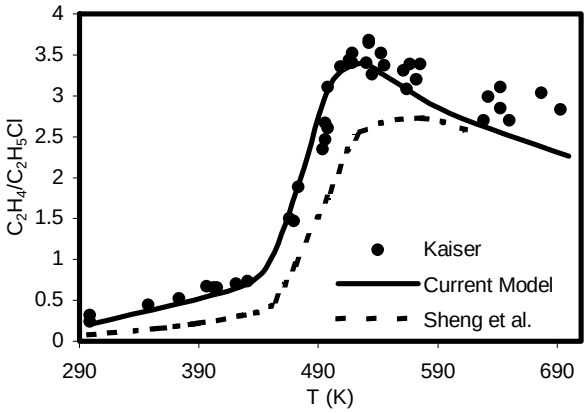

Figure 1. Comparison of the predicted temperature dependence of ethylene production to that reported by Kaiser[6] at a total density of $6.8*10^{18}$ molecules/cm^3. Values shown are the ratio of ethylene to ethyl chloride.

Ethylene oxide (C_2H_4O) is a minor product formed from $C\bullet H_2CH_2OOH$. Kaiser's[6] experimental data provide a test case to validate the relative barriers for isomerization and further reactions of the isomer. Kaiser measured the ethylene oxide production as a function of ethane conversion and of temperature. The comparison of the predicted and measured temperature dependence of the ethylene oxide yield is shown in Figure 2. Initially our model underpredicted ethylene oxide using the originally-calculated barriers. However, by decreasing the isomerization barrier by 1 kcal/mol, the predictions agree well with the measurements. This change did not affect predictions of overall rate constants as well as major products.

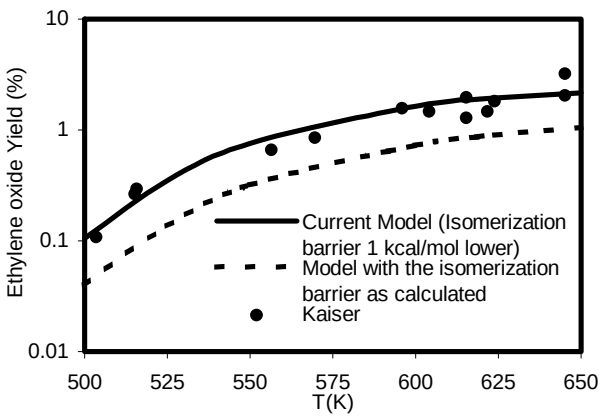

Figure 2. Comparison of the predicted temperature dependence of ethylene oxide yield to that reported by Kaiser[6] at a total density of $6.8*10^{18}$ molecules/cm^3.

Finally, we compared our model to the measurements of HO_2 production by Clifford et al.[7] Since HO_2 reacts quickly with other species, it is important to incorporate secondary reactions in the mechanism. The comparison of the predicted and measured HO_2 concentration profile relative to the initial atomic chlorine concentration at 623K is shown in Figure 3. Note that a fraction of the HO_2 is produced at very early time (due to reaction of the chemically-activated adduct). This is followed by a slower production rate (due to thermally-activated dissociation of ethylperoxy). The entire time profile is predicted accurately. Our prediction of the temperature dependence of the "total" HO_2 yield is also consistent with the measurements of Clifford et al.

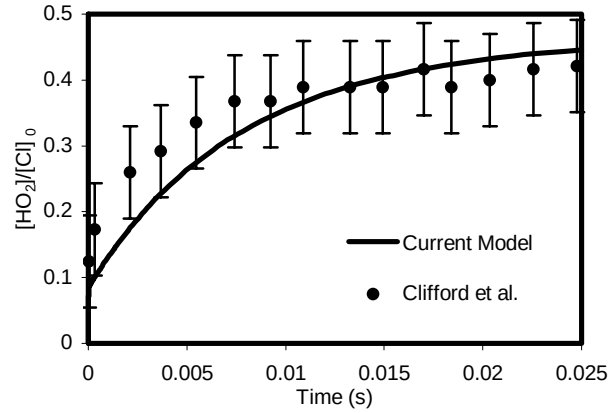

Figure 3. Comparison of the predicted HO_2 time profile relative to the initial chlorine atom concentration to that measured by Clifford et al.[7] at 623K and a total density of $9*10^{17}$ molecules/cm^3.

Conclusions

We have calculated the PES for the $C_2H_5+O_2$ system at CBS-QB3 level with BAC. Tunneling is included in high-pressure rate constants that were used in a QRRK/MSC analysis of the system. The resulting pressure-dependent reaction mechanism accurately predicts a wide range of experimental results including ethylene, HO_2 and ethylene oxide. We feel that this mechanism is suitable to be incorporated in a model of ethane oxidation at low temperatures.

References

(1) Rienstra-Kiracofe, J. C. et al. *J. Phys. Chem. A* 2001, *104*, 9823-9840.
(2) Walker, R. W.; Morley, C. In *Low Temperature Combustion and Autoignition*; Pilling, M. J., Ed.; Elsevier, 1997; Vol. 35, pp 1-124.
(3) Kaiser, E. W. et al. *Chem. Phys. Lett.* 1990, *168*, 309-313.
(4) Slagle, I. R. et al. *J. Phys. Chem.* 1984, *88*, 3648 - 3653.
(5) Kaiser, E. W. *J. Phys. Chem.* 1995, *99*, 707-711.
(6) Kaiser, E. W. *J. Phys. Chem. A* 2002, *106*, 1256-1265.
(7) Clifford, E. P. et al. *J. Phys. Chem. A* 2000, *104*, 11549-11560.
(8) Miller, J. A.; Klippenstein, S. J. *Int. J. Chem. Kinet.* 2001, *33*, 654-668.
(9) Miller, J. A. et al. *Proc. Comb. Symp.* 2000, *28*, 1479-1486.
(10) Sheng, C. Y. et al. *J. Phys. Chem. A* 2002, *106*, 7276 - 7293.
(11) Frisch, M. J. et al.; Revision A.9 ed.; Gaussian, Inc: Pittsburgh, PA, 1998.
(12) Petersson, G. A. et al. *J. Chem. Phys.* 1991, *94*, 6091 - 6101.
(13) Wigner, E. *Zeitschrift fuer physikalische Chemie* 1932, *B 19*, 203.
(14) Chang, A. Y. et al. *Zeitschrift fur Physikalische Chemie* 2000, *214*, 1533-1568.
(15) Kee, R. J. et al.; Release 3.6 ed.; Reaction Design, Inc.: San Diego, CA, 2000.
(16) DeSain, J. D. et al. *J. Phys. Chem. A* 2003, *107*, 4415-4427.

THERMOCHEMICAL AND KINETIC ANALYSIS OF THE ALLYL RADICAL WITH O_2 REACTION SYSTEM

Jongwoo Lee and Joseph W. Bozzelli

Department of Environmental Science and Chemistry,
New Jersey Institute of Technology, Newark, NJ 07102

Introduction

Olefins (Alkenes) are major initial products from pyrolysis, oxidation or photochemical reactions of alkanes and ethers. The double bond in alkenes provides both an unsaturated site for addition reactions and an allylic site for facile abstractions, where the corresponding activation energy is lowered due to electron delocalization on the radical formed. The stability and low reactivity of these alkenyl radicals have been connected to the antiknock effect of fuel additives such as ethyl tert-butyl ether (ETBE).[1] The relatively high octane ratings for olefin blending suggest that olefins play an important role in pre-ignition chemistry related to engine knock. It is valuable to understand the fundamental chemical reaction pathways and kinetics of olefin oxidation in moderate to low temperature combustion chemistry for model development.

Ruiz et al.,[2] Morgan et al.,[3] and Slagle et al.[4,5] have reported the R—O_2 bond energy (17.2, 18.2, 18.4 kcal/mol, respectively) for the allyl (CH_2CHCH_2•, • : radical site) radical. Walker and co-workers[6,7] had studied at a total pressure of 60 Torr between 400 and 520 °C, where the equilibrium in the R + O_2 ⇔ RO_2 addition reaction is shifted to left, the rate constants of the CH_2CHCH_2• + O_2 → products reaction are significantly lower than those observed in the case of alkyl radicals. Baldwin et al.[8] and Lodhi and Walker[6] reported similarly low rate constants for the substituted allyl radicals, $CH_3CH_2CHCHCH_2$• and $CH_3CHCHCH_2$• reactions with O_2. Knyazev and Slagle[5] also studied the kinetics of the reaction $CH_3CHCHCH_2$• + O_2 ⇔ $CH_3CHCHCH_2O_2$• using laser photolysis/photoionization mass spectrometry. Room temperature decay constants of the $CH_3CHCHCH_2$• radical were determined in time-resolved experiments as a function of bath gas density ([He] = (3-24) × 10^{16} molecule cm^{-3}) and the rate constant at 297 K is k = (6.42 ± 0.54) × 10^{-13} cm^3/ (molecule s). At high temperatures (600 – 700K), no reaction of $CH_3CHCHCH_2$• with O_2 could be observed and upper limits to the rate constants were determined (1 × 10^{-16} cm^3/ (molecule s) at 600 K and 2 × 10^{-16} cm^3/ (molecule s) at 700 K).

Chen et al.[9] studied allylic isobutenyl radical with O_2. They reported the forward and reverse rate constants for initiation reaction, $CH_2C(CH_3)_2H$ + O_2 ⇔ $CH_2C(CH_3)_2$• + HO_2 to be 1.86 × 10^9 × $T^{1.301}$ × exp(-40939 cal/RT) cm^3/ (mol s) and 6.39 × 10^8 × $T^{0.944}$ × exp(-123.14 cal/RT) cm^3/ (mol s), respectively. They also proposed an important new reaction path, $CH_2C(CH_2$•$)COOH$ ⇔ $CH_2C(CH_2$•$)CO$• + OH ⇔ $CH_2Y(\underline{CCOC})$ + OH, for methylene oxirane formation.

This study focuses on the reaction mechanism of the allyl radical association with O_2. Thermochemical properties are estimated for reactants, intermediates, products and transition states in the reaction paths using *ab initio* and density functional calculations. The thermochemical parameters are used to calculate high-pressure limit rate constants using canonical Transition State Theory (TST). Rate constants as a function of temperature and pressure are estimated using a multifrequency quantum RRK analysis for k(E) and master equation for falloff. The data at relevant pressures and temperatures should be useful to both atmospheric and combustion models.

Calculation methods

Enthalpies of formation ($\Delta H_f°_{298}$) for reactants, intermediate radicals, transition states and products are calculated using the CBS-Q//B3LYP/6-31G(d,p) composite method and density functionals. The initial structure of each compound or transition state is determined using ROHF or UHF/PM3 in MOPAC,[10] followed by optimization and vibrational frequency calculation at B3LYP/6-31G(d,p) level of theory using GAUSSIAN 98.[11] Transition state geometries are identified by the existence of only one imaginary frequency, structure information and the TST reaction coordinate vibration information. Zero-point vibrational energies (ZPVE) are scaled by 0.9806 as recommended by Scott and Radom.[12] Single point energy calculations are carried out at the B3LYP/6-31G(d,p), /6-311+G(d,p), or /6-311++G(d,p). The CBS-Q method of Petersson and co-workers for computing accurate energies[13,14] is chosen as the determining enthalpies used in our kinetic analysis.

The CBS-Q//B3LYP/6-31G(d,p) calculation sequence is illustrated in Scheme 1 [Corrections for unpaired electron and spin contamination in intermediate overlap (i.e., $0< {}^{\alpha\beta}S_{ij} <1$) between the α- and β-spin orbitals[15] are included].

Scheme 1. CBS-Q//B3LYP/6-31G(d,p) Calculation Sequence

	Level of Theory
Optimized Geometry	B3LYP/6-31G(d,p)
Single Point Calculation	QCISD(T)/6-31+G(d')
	MP4(SDQ)/CBSB4
	MP2/CBSB3 CBSExtrap = (Nmin=10,Pop)

Determination of enthalpy of formation. The method of isodesmic reactions is used to determine the enthalpy of formation ($\Delta H_f°_{298}$) for parent and radical species. It provides higher accuracy for estimates of $\Delta H_f°_{298}$ than heats of atomization does.[16-18]

CH_2=CHCH$_2$OOH + CH_3CH_3 ⇔ CH_2=$CHCH_3$ + C_2H_5OOH (IR1)
CH_2=CHCH$_2$OO• + C_2H_5OH ⇔ CH_2=$CHCH_2OH$ + C_2H_5OO• (IR2)
C•H=CHCH$_2$OOH + C_2H_4 ⇔ CH_2=$CHCH_2OOH$ + C_2H_3• (IR3)
CH_2=C•CH$_2$OOH + CH_2=$CHCH_3$ ⇔ CH_2=$CHCH_2OOH$ + CH_2=C•CH_3 (IR4)
Y$\underline{CCCOO}$ + $(CH_3)_3CH$ ⇔ CY$\underline{CCOOC}$ + $CH_3CH_2CH_3$ (IR5)
Y$\underline{CC•COO}$ + CY$\underline{CCOOC}$ ⇔ Y$\underline{CCCOO}$ + CY$\underline{C•COOC}$ (IR6)
HOCH$_2$Y$\underline{CCO}$ + CH_3CH_3 ⇔ Y$\underline{CCO}$ + $(CH_3)_2C(OH)H$ (IR7)
O•CH$_2$Y$\underline{CCO}$ + CH_3OH ⇔ $HOCH_2Y\underline{CCO}$ + CH_3O• (IR8)

Ab initio calculations for ZPVE and thermal correction energy are performed on all of four compounds in the reaction. The three reference compounds in the working reaction (IR1), excepting the target molecule, CH_2=$CHCH_2OOH$ in (IR1), have experimental or theoretical determined values of $\Delta H_f°_{298}$. The unknown $\Delta H_f°_{298}$ of CH_2=$CHCH_2OOH$ is obtained with the calculated $\Delta H°_{rxn(298)}$ and known $\Delta H_f°_{298}$ of the three reference compounds. The other parent and radical species are calculated in the same manner.

Determination of entropy and heat capacity. The contributions of external rotations, translations, and vibrations to entropies and heat capacities are calculated from scaled vibration frequencies and moments of inertia for the optimized B3LYP/6-31G(d,p) structures. The number of optical isomers and spin degeneracy of unpaired electrons are also incorporated. Contributions from hindered internal rotation for S and $Cp(T)$ are determined using direct integration over energy levels of the intramolecular rotational potential curves. A program, "ROTATOR[19]", is used for calculation

of the energy levels. This technique employs expansion of the hindrance potential in the Fourier series (Eq. I), calculation of the Hamiltonian matrix on the basis of wave functions of the free internal rotor, and subsequent calculation of energy levels by direct diagonalization of the Hamiltonian matrix.[20,21] The torsional potential calculated at discrete torsion angles is represented by a truncated Fourier series:

$$V(\Phi) = a_0 + \Sigma\, a_i \cos(i\Phi) + \Sigma\, b_i \sin(i\Phi) \quad i = 1, 2, 3, \ldots \quad \text{(Eq. I)}$$

Values of the coefficients (a_0, a_i and b_i) are calculated to provide the minimum and maximum of the torsional potentials with allowance of a shift of the theoretical extreme angular positions.[20,21]

High-pressure limit A factor (A) and rate constant (k_∞) determination. For the reactions where thermochemical properties of transition state are calculated by ab initio or density functional methods, k_∞'s are fit by three parameters A, n, and *Ea* over temperature range from 298 to 2000K, $k_\infty = A\,(T)^n \exp(-Ea/RT)$. Entropy differences between reactant and transition state are used to determine the pre-exponential factor, A, via canonical Transition State Theory (TST)

$$A = (k_b T/h_p)\exp(\Delta S^{\ddagger}/R),\ Ea = \Delta H^{\ddagger}$$

(h_p is the Planck constant and k_b is the Boltzmann constant.) Treatment of the internal rotors for *S* and *Cp*(*T*) is important here because these internal rotors are often lost in the cyclic transition state structures.

Kinetic analysis. Thermochemical properties for each species on the potential energy surface for the reaction system are evaluated. Forward or reverse rate constants (high-pressure limit) for each, elementary reaction step are determined from the calculations and use of literature data for enthalpies of stable molecules. Reverse rate constants are calculated from microscopic reversibility.

Multifrequency quantum Rice-Ramsperger-Kassel (QRRK) analysis is used to calculate *k*(E) with a master equation analysis[22] for fall-off in order to obtain rate constants as a function of temperature and pressure. This kinetic analysis is for the chemical activation and the dissociation reaction systems. The master equation analysis[22] uses an exponential-down model for the energy transfer function with $(\Delta E)^\circ_{down}$ = 1000 cal/mol,[23,24] for N_2 as the third body and a 500 cal energy grain is used.

The QRRK/master equation analysis is described by Chang et al.[22,25] Further validated by recent work of Sun et al. ((JP030667l) in press 2003). The QRRK code utilizes a reduced set of three vibration frequencies which accurately reproduce the molecules' heat capacity; the code includes contribution from one external rotation in calculation of the ratio of the density of states to the partition coefficient ρ(E)/Q. Comparisons of ratios of these ρ(E)/Q with direct count ρ(E)/Q's have been shown to result in good agreement.[26] Rate constant results from the quantum RRK-Master equation analysis are shown to accurately reproduce (model) experimental data on several complex systems. They also provide a reasonable method to estimate rate constants for numerical integration codes by which the effects of temperature and pressure can be evaluated in complex reaction systems.

Results and Discussion

Enthalpy of formation ($\Delta H_f°_{298}$). The enthalpies of formation for $CH_2{=}CHCH_2OOH$ are –13.53 and –13.49 kcal/mol by B3LYP/6-31G(d,p) and CBSQ//B3LYP/6-31G(d,p), respectively. The enthalpy of formation for the parent hydroperoxide is important because it allows the evaluation of peroxy radicals.

The bond energies of $CH_2{=}CHCH_2OOH$, $C(OOH)H_2CHO$,[27] C_2H_5OOH,[22] and $CH_3C(=O)OOH$[28] are compared in **Table 1**. The R–OOH bond energy in $CH_2{=}CHCH_2OOH$ is 14 kcal/mol lower than that of C_2H_5OOH, because the radical site is resonantly stabilized. The RO–OH and ROO–H bonds in $CH_2{=}CHCH_2OOH$ are 45.4 and 86.6 kcal/mol, similar to those in C_2H_5OOH, 45.1 and 85.3 kcal/mol, respectively.

Table 1. Comparison of Bond Energies between Allyl Hydroperoxide and three C2 Hydroperoxide

(Units in kcal/mol)	**$CH_2{=}CHCH_2OOH$**	$C(OOH)H_2CHO$	C_2H_5OOH	$CH_3C(=O)OOH$
ROO—H	**86.61**	87.28	85.27	98.33
RO—OH	**45.39**	45.13	45.12	50.95
R—OOH	**57.05**	63.21	71.35	85.22
H--CH=$CHCH_2OOH$	**112.36**	n/a	n/a	n/a
CH_2=C(--H)CH_2OOH	**110.17**	n/a	n/a	n/a
$C(OOH)H_2C(=O)$--H,	n/a	88.65	n/a	n/a
H--CH_2CH_2OOH,	n/a	n/a	103.21	n/a
H--$CH_2C(=O)OOH$	n/a	n/a	n/a	103.95

Entropy ($S^o_{(298)}$) and heat capacity ($Cp(T)$, 300 ≤ T/K ≤ 1500). Entropy and heat capacities are calculated based on vibration frequencies and moments of inertia of the optimized B3LYP/6-31G(d,p) structures. Symmetry, number of optical isomers and electronic spin are incorporated in estimation of $S^o_{(298)}$. Torsion frequencies are omitted in these calculations, instead, contributions from internal rotation for $S^o_{(298)}$ and *Cp*(*T*)'s are determined, using direct integration over energy levels of the intramolecular rotational potential curves[20,21].

Potential energy diagram for $CH_2{=}CHCH_2\bullet + O_2$ reaction system. The energy diagram for the allyl ($CH_2{=}CHCH_2\bullet$) + O_2 reaction is illustrated in two **Figures 1 and 2**. The reactions involving intramolecular hydrogen transfer and direct HO_2 elimination are illustrated in **Figure 1**. Reactions involving peroxy radical addition to each of the π bond carbons, ring formation, and subsequent reactions of the two cyclic peroxide alkyl radicals are illustrated in **Figure 2**. The 14 reaction paths, 6 reaction intermediates, and 14 transition states are illustrated. Enthalpies of formation are from CBSQ// B3LYP/6-31G(d,p) calculations and in units of kcal/mol. Transition state enthalpies are relative to the corresponding stabilized adduct.

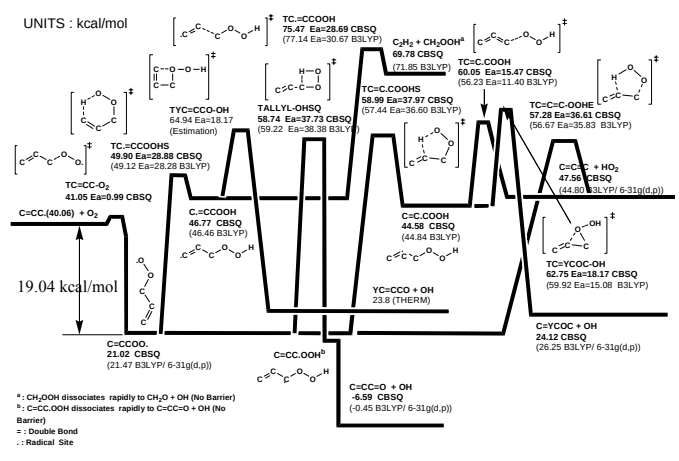

Figure 1. Potential energy I of II for allyl + O_2 (I) Isomerizations via H shifts.

The allyl radical adds to O_2 (*Ea* = 0.99) to form an energized peroxy adduct [$CH_2{=}CHCH_2OO\bullet$]* with a shallow well (ca. 19

kcal/mol); which predominantly dissociates back to reactants under combustion conditions. The reaction channels of the $[CH_2{=}CHCH_2OO\bullet]^*$ adduct include reverse reaction to reactants, stabilization to $CH_2{=}CHCH_2OO\bullet$ radical ($\Delta H_f°_{298}$ = 21.02), decomposition to products, $CH_2{=}C{=}CH_2 + HO_2$ via direct HO_2 elimination with a barrier (*Ea* = 36.61), isomerizations via hydrogen shifts to form $C\bullet H{=}CHCH_2OOH$ or $CH_2{=}C\bullet CH_2OOH$ isomers ($\Delta H_f°_{298}$ = 46.77 or 44.58, respectively) with barriers (*Ea* = 28.88 or 37.97, respectively), or a hydrogen transfer (*Ea* = 37.73) from the ipso carbon to the peroxy radical to form the unstable intermediate $\{CH_2{=}CHC\bullet HOOH\}$, which immediately dissociates to more stable products, 2-propenal plus OH.

The $C\bullet H{=}CHCH_2OOH$ isomer can undergo β scission to products, ($C_2H_2 + \{C\bullet H_2OOH\} \rightarrow C_2H_2 + CH_2O + OH$) (*Ea* = 37.73), a ring closure to form the unstable intermediate {Y<u>CCCO</u>} plus OH, (Y = <u>cyclic</u>) which rapidly dissociates to more stable products, 2-propenal plus OH, or isomerize via a hydrogen shift (*Ea* = 3.13) to form a $CH_2{=}CHCH_2OO\bullet$ isomer.

The $CH_2{=}C\bullet CH_2OOH$ isomer can undergo β scission to products, $CH_2{=}C{=}CH_2 + HO_2$ (*Ea* = 15.47), a ring closure to form methyene oxirane plus OH radical (*Ea* = 18.17), or isomerize via a hydrogen shift (*Ea* = 14.41) to form a $CH_2{=}CHCH_2OO\bullet$ isomer.

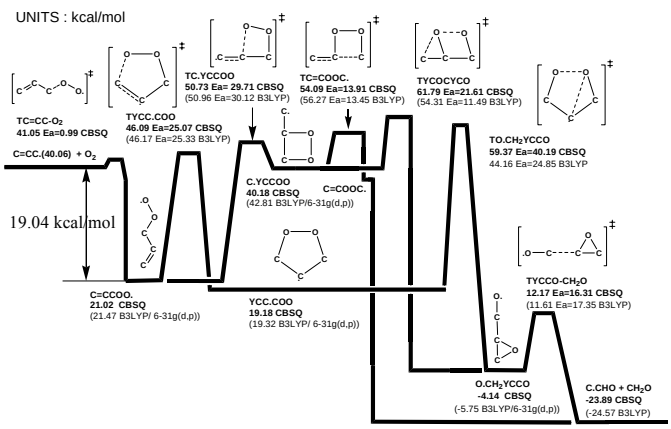

Figure 2. Potential energy II of II for allyl + O_2 (II) Cyclization pathways to form cyclic adducts and further reactions.

Intramolecular peroxy radical addition to sp^2 hybridized carbons - cyclization reaction paths. The $[CH_2{=}CHCH_2OO\bullet]^*$ adduct can also cyclize to four- or five-member cyclic peroxide-alkyl radicals, $C\bullet H_2Y$<u>CCOO</u> and <u>YCC•COO</u> ($\Delta H_f°_{298}$ = 40.18 and 19.18, respectively). $CH_2{=}CHCH_2OO\bullet$ cyclization to four- or five-member cyclic peroxides require barriers, *Ea* = 29.71 and 25.07, respectively), which have slightly higher barriers than reverse reaction (*Ea* = 20.03).

The $C\bullet H_2Y$<u>CCOO</u> adduct can undergo β scission to products, $C\bullet H_2CHO + CH_2O$ (*Ea* = 13.91), form a cyclic epoxide-alkoxy radical, $O\bullet CH_2Y$<u>CCO</u> ($\Delta H_f°_{298}$ = -4.14) via TY<u>COC</u>Y<u>CO</u> (*Ea* = 21.61), or undergo ring open to form $CH_2{=}CHCH_2OO\bullet$ adduct (*Ea* = 10.55). The $O\bullet CH_2Y$<u>CCO</u> intermediate will undergo β scission to products, $C\bullet H_2CHO + CH_2O$ via TY<u>CCO</u>-CH_2O (*Ea* = 16.31).

The 5-member ring Y<u>CC•COO</u> can also form the epoxide-alkoxy radical (above), $O\bullet CH_2Y$<u>CCO</u> via $TO\bullet CH_2Y$<u>CCO</u> (*Ea* = 40.19), undergo ring open to form $CH_2{=}CHCH_2OO\bullet$ adduct (*Ea* = 26.91). This cyclic Y<u>CC•COO</u> adduct further reacts with O_2 to chain branching products: $CH_2O + C(=O)HC(=O)H + OH$.

Comparison of $CH_2{=}CHC\bullet H_2$, $C\bullet H_2CHO$, C_2H_5, and $CH_3C\bullet O$ with O_2. The $CH_2{=}CHC\bullet H_2 + O_2$, $C\bullet H_2CHO + O_2$,[27] $C_2H_5 + O_2$,[22] and $CH_3C\bullet O + O_2$[28] reaction systems have significant differences. The $CH_2{=}CHC\bullet H_2 + O_2$ reaction system of this study has a lower well depth of 19.04 kcal/mol compared to $C\bullet H_2CHO + O_2$, $C_2H_5 + O_2$ and $CH_3C\bullet O + O_2$, which have well depths of 27.5, 35.3 and 35.5 kcal/mol, respectively.

The H shift barriers in the $CH_2{=}CHCH_2OO\bullet$, $C(OO\bullet)H_2CHO$ and $CH_3C(=O)OO\bullet$ peroxy radicals are lower than those of concerted HO_2 elimination, whereas in $C_2H_5OO\bullet$, direct HO_2 elimination has a lower barrier than the H shift.

The well depth and barriers of H shift and HO_2 elimination in the $CH_2{=}CHC\bullet H_2$, $C\bullet H_2CHO$, $C_2H_5\bullet$, and $CH_3C\bullet O$ with O_2 reaction systems are compared in **Table 2**.

Table 2. Comparison of $CH_2{=}CHC.H_2$, $C.H_2CHO$, C_2H_5, and $CH_3C.(=O)$ with O_2

(Units in kcal/mol)		$CH_2{=}CHC.H_2 + O_2$	$C.H_2CHO + O_2$	$C_2H_5 + O_2$	$CH_3C.(=O) + O_2$
Well Depth		**19.04**	27.5	35.3	35.5
Barrier in	1) H Shift[a]	**28.88**	20.25	36.36	26.42
	2) HO_2 Elimination[a]	**36.61**	48.31	30.48	34.58

[a] H shift and HO_2 elimination for the $CH_2{=}CHCH_2OO.$, $C(OO.)H_2CHO$, $C_2H_5OO.$, and $CH_3C(=O)OO.$

Kinetic analysis for allyl + O_2. The QRRK calculations for *k*(E) and master equation analysis for fall-off are performed on this allyl ($CH_2{=}CHCH_2\bullet$) + O_2 reaction system to estimate rate constants and to determine important reaction paths as a function of temperature and pressure. Rate constants at 1 atm pressure versus 1000/T are illustrated in **Figure 3**. Stabilization $CH_2{=}CHCH_2OO\bullet$ is important below 600 K, with reverse dissociation above 600 K. $CH_2{=}CHCH_2OO\bullet$ adduct, cyclic isomers, and H-shift isomers exhibit significant falloff at higher temperatures (above 800 K). Allene + HO_2 products via a HO_2 molecular elimination path, Y<u>CC•COO</u> via cyclization, and H transfer from primary vinyl group to peroxy radical; then β-scission reaction leading to $C_2H_2 + CH_2O + OH$ are major product channels at higher temperatures (above 600 K).

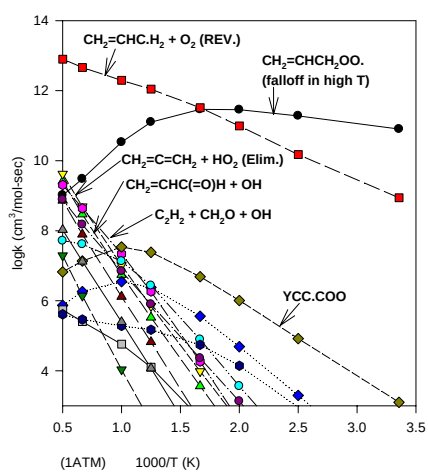

Figure 3. $CH_2{=}CHCH_2 + O_2$ -> products *k* vs. 1000/T at 1 atm.

Conclusions

Thermochemical properties for important species in the allyl radical (CH_2=$CHCH_2$•) + O_2 reaction system are calculated using density functional and *ab initio* methods. Enthalpies of formation ($\Delta H_f°_{298}$) are determined using isodesmic reactions at the CBSQ level. Entropies ($S°_{298}$) and heat capacities ($Cp(T)$) include internal rotor contributions.

The CH_2=CHC•H_2 + O_2 reaction system is found to have a relatively shallow well depth of 19.04 kcal/mol and all product formation pathways from the peroxy radical, involve barriers that are above the energy of the initial reactants. Major reaction paths at 1 atm pressure are stabilization of the peroxy adduct (CH_2=$CHCH_2$OO•) below 600 K, with reverse dissociation above 600 K. Important reaction products are allene + HO_2 products via a HO_2 molecular elimination, Y<u>CC•COO</u> which dissociates or further reacts to chain branching products. C•H=$CHCH_2$OOH from hydrogen transfer, which undergoes β-scission reaction leading to C_2H_2 + CH_2O + OH is important product channel above 600 K.

Acknowledgements. We acknowledge the USEPA Northeast Regional Research Center and the USEPA Airborne Organics Research Center for funding. We would also like to thank to C. Sheng for the SMCPS program.

References

(1) Bach, R. D.; Ayala, P. Y.; Schlegel, H. B. *J. Am. Chem. Soc.* **1996**, *118*, 12758.
(2) Ruiz, R. P.; Bayes, K. D.; Macpherson, M. T.; Pilling, M. J. *J. Phys. Chem.* **1981**, *85*, 1622.
(3) Morgan, C. A.; Pilling, M. J.; Tulloch, J. M.; Ruiz, R. P.; Bayes, K. D. *J. Chem. Soc. Faraday Trans. 2* **1982**, *78*, 1323.
(4) Slagle, I. R.; Ratajczak, E.; Heaven, M. C.; Gutman, D.; Wagner, A. F. *J. Am. Chem. Soc.* **1985**, *107*, 1838.
(5) Knyazev, V. D.; Slagle, I. R. *J. Phys. Chem. A* **1998**, *102*, 8932.
(6) Lodhi, Z. H.; Walker, R.W. *J. Chem. Soc., Faraday Trans.* **1991**, *87*, 681.
(7) Stothard, N. D.; Walker, R. W. *J. Chem. Soc. Faraday Trans.* **1992**, *88*, 2621.
(8) Baldwin, R. R.; Bennett, J. P.; Walker, R. W. *J. Chem. Soc. Faraday Trans. 1* **1980**, *76*, 2396.
(9) Chen, C.; Bozzelli, J. W. *J. Phys. Chem. A* **2000**, *104*, 9715.
(10) Stewart, J .J. P. MOPAC 6.0, J. Frank Seiler Research Lab., US Air Force Academy: Colorado, **1990**.
(11) Frisch, M. J.; Trucks, G. W.; Schlegel, H. B.; Scuseria, G.; Robb,M. A.; Cheesman, J. R.; Zakrzewski, V. G.; Montgomery, J. A., Jr.; Stratmann, R. E.; Burant, J. C.; Dapprich, S.; Millam, J. M.; Danicls, A. D.; Kudin, K. N.; Strain, M. C.; Farkas, O.; Tomasi, J.; Baronc, V.; Cossi, M.; Cammi, R.; Mennucci, B.; Pomelli, C.; Adamo, C.; Clifford, S.; Ochterski, J.; Petersson, G. A.; Ayala, P. Y.; Cui, Q.; Morokuma, K.; Malick, D. K.; Rabuck, A. D.; Raghavachari, K.; Froesman, J. B.; Cioslowski, J.; Ortiz, J. V.; Baboul, A. G.; Stefanov, R. B.; Liu, G.; Liashenko, A.; Piskorz, P.; Komaromi, I.; Gomperts, R.; Matrin, R. L.; Fox, D. J.; Keith, T.; Al-Laham, M. A.; Peng, C. Y.; Nanayakkara, A.; Gonzalez, C.; Challacombe, M.; Gill, P. M. W.; Johnson, B.; Chen, W.; Wong, M. W.; Andres, J. L.; Head-Gordon, M.; Pople, J. A. *Gaussian 98*; Gaussian Inc.: Pittsburgh, PA, **1998**.
(12) Scott, A. P.; Radom, L. *J. Phys. Chem.* **1996**, *100*, 16502.
(13) Nyden, M. R.; Petersson, G. A. *J. Chem. Phys.* **1991**, *75*, 1843.
(14) Petersson, G. A. *J. Chem. Phys.* **1994**, *94*, 6081.
(15) Montgomery Jr., J. A.; Petersson, G. A. *J. Phys. Chem.* **1994**, 101, 5900.
(16) Hehre, W. J.; Radom, L.; Schleyer, P. R.; Pople, J. A. *Ab-Initio Molecular Orbital Theory*, John Wiley & Sons: New York, NY, 1986.
(17) Lay, T. H.; Bozzelli, J. W. *J. Phys. Chem. A* **1997**, *101*, 9505.
(18) Sun, H.; Bozzelli, J. W. *J. Phys. Chem. A* **2001**, *105*, 4504.
(19) Shokhirev, N. V. http://www.chem.arizona.edu/faculty/walk/nikolai/programs.html #programs July, 2002.
(20) Lay, T. H.; Krasnoperov, L. N.; Venanzi, C. A.; Bozzelli, J. W. *J. Phys. Chem.* **1996**, *100*, 8240.
(21) Yamada, T.; Lay, T. H.; Bozzelli, J. W. *J. Phys. Chem. A* **1999**, *103*, 5602.
(22) Sheng, C. Y.; Bozzelli, J. W.; Dean, A. M.; Chang, A. Y. *J. Phys. Chem. A* **2002**, *106*, 7276.
(23) Troe, J. *In Combustion Chemistry*, W.C. Gardiner Jr., Ed.; Springer-Verlag: New York, 1984.
(24) Knyazev, V. D.; Slagle, I. R. *J. Phys. Chem.* **1996**, *100*, 5318.
(25) Chang, A. Y.; Bozzelli, J. W.; Dean, A. M. *Int. J. Res. Phys. Chem. Chem. Phys. (Zeit. Phys. Chem)* **2000**, *214*, 1533.
(26) Bozzelli, J. W.; Chang, A. Y.; Dean, A. M. *Int. J. Chem. Kinet.* **1997**, *29*, 161.
(27) Lee, J.; Bozzelli, J. W. *J. Phys. Chem. A* **2003**, *107*, 3778.
(28) Lee, J.; Chen, C.; Bozzelli, J. W. *J. Phys. Chem. A* **2002**, *106*, 7155.

Computational Study of the Oxygen Initiated Decomposition of 2-Oxepinoxy Radical

John K. Merle and Christopher M. Hadad

Department of Chemistry, The Ohio State University, Columbus, Ohio 43210

Introduction

Benzene is the archetypal aromatic hydrocarbon. Benzene and its derivatives are common fuel constituents in addition to a suitable model from which its oxidative pathways can be used to infer similar oxidation processes for larger polycyclic aromatic compounds. Benzene oxidation has therefore been the subject of numerous studies. Experimental studies using mass spectrometric detection[1,2,3,4,5] at high and intermediate temperatures indicate that the most common products of benzene oxidation are CO_2, CO, C_2H_2 (acetylene), cyclopentadienyl radical, and various unsaturated C_2O_x and C_3O_x species. The commonly accepted mechanism based on intermediate to high temperature experiments for the initiation of benzene oxidation with molecular oxygen is the generation of phenyl radical via reaction (Eqn. 1)[1,4] followed by the addition of molecular oxygen and concomitant lose of oxygen atom (^3P) (Eqn. 2).[1,2,3]

$$C_6H_6 + O_2 \rightarrow C_6H_5 + HO_2 \qquad (1)$$
$$C_6H_5 + O_2 \rightarrow C_6H_5O + O(^3P) \qquad (2)$$

Yu and Lin,[6] however, performed kinetic studies to determine the rate of reaction of phenyl radical with O_2 using cavity-ring down (CRD) spectroscopy and detected phenyl peroxy radical up to 473 K. Norrish and Taylor[7] via identification of ortho and para dihydroxybenzenes, in experiments using a flow system to analyze the reaction of benzene with O_2 in a nitrogen diluent at 685 K, predicted the inclusion of phenyl peroxy radical as a probable intermediate.

Computational studies have also been undertaken in order to determine the most thermodynamically and kinetically viable mechanistic pathways involved in benzene oxidation.[8,9,10] Theoretical studies, based on B3LYP/6-311+G**//B3LYP/6-31G* free energies, by this group, predict that the phenylperoxy radical is the more thermodynamically favored intermediate, verses phenoxy radical at $T \leq \sim 450$ K, while at $T > 450$ K, entropy dominates thereby making phenoxy radical the prominent intermediate. This implies that under low temperature combustion and atmospheric conditions the phenyl peroxy radical is likely to play an important role in the decomposition of phenyl radical.

Carpenter utilized PM3/UHF semiempirical calculations to elucidate possible decomposition pathways for phenylperoxy radical to form cyclopentadienyl radical and CO_2. He considered a pathway in which phenylperoxy radical proceeds through formation of a spirodioxiranyl radical, with an enthalpic barrier of 26.1 kcal/mol, to form thermodynamically stable seven-membered ring radical, 2-oxepinoxy (**1**) shown in Figure 1. Barckholtz et.al. and Fadden et. al. have refined the same energy surface using density functional theory and high-level *ab initio* calculations to study this decomposition process as well as the formation of a dioxetanyl radical intermediate leading to the 2-oxepinoxy radical (**1**).[9,10] Decomposition through the spirodioxiranyl radical was shown to be the most viable reaction path leading to 2-oxepinoxy radical, with a free energy barrier of ~41.6 kcal/mol at 298 K, due to the inclusion of an additional high energy triradical intermediate (Figure 1). Despite the inclusion of the high energy triradical species, this pathway exhibited a lower barrier than that for the formation of phenoxy radical and oxygen atom at ~51.0 kcal/mol. These barriers are rough estimates, however, because of spin contamination in the wavefunctions of the key intermediates. At the B3LYP/6-311+G**//B3LYP/6-31G* level, 2-oxepinoxy radical was calculated to have a ΔG(298 K) energy which is 79.9 kcal/mol lower than separated phenyl radical and $O_2(^3\Sigma_g)$ reactants. Consistent values were obtained with UMP4(SDQ)/6-31G** and UCCSD(T)/6-31G** energy calculations in the same study. Mebel and Lin[11] in a theoretical study of $C_6H_5O_2$ geometrical isomers estimated 2-oxepinoxy radical (**1**) to have a ΔH(0 K) of -91.8 kcal/mol based on PUMP3/6-31G*//UHF/6-31G* energies. The stability of 2-oxepinoxy radical indicates that it should be relatively long-lived upon formation and therefore susceptible to further oxidation by reactive species contained in a typical radical pool.

In this study, we will utilize the B3LYP hybrid density functional theory functional to analyze the potential energy surface for the decomposition of 2-oxepinoxy radical after further peroxy radical formation via addition of O_2 ($^3\Sigma_g$). The energies of minima and activation barriers for decomposition following the initial formation of 1,2-dioxetanyl, 1,3-peroxy, 1,4-peroxy, scission of the O-O peroxy bond, and abstraction of an H-atom by the geminal peroxy moiety. The energies for these surfaces will be evaluated from T = 298-1250 K, the range in which phenylperoxy radical has been shown to be a viable combustion component.

Figure 1. Reaction scheme for the generation of 2-oxepinoxy radical

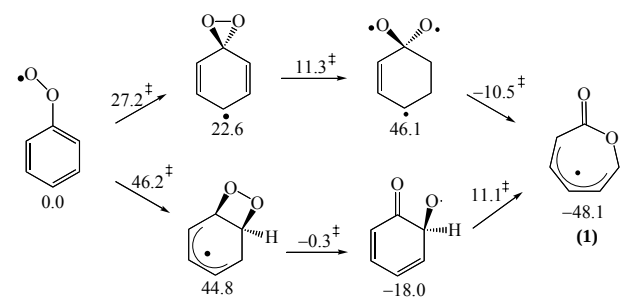

(1). Energies are B3LYP/6-311+G**//B3LYP/6-31G* ΔG(298 K) relative to phenylperoxyl radical.

Oxygen Addition to 2-Oxepinoxy Radical

The addition of O_2 to 2-oxepinoxy radical (**1**) is most likely to occur at three different positions on the 2-oxepinoxy radical ring, forming three distinctive peroxyoxepinone radicals (**1a, 1b,** or **1c, Figure 2**), due to delocalization of the lone electron within the π network of the ring carbons. Addition can occur at the 2, 4 and 6 ring positions, numbered relative to the carbonyl carbon, as position 1, moving counterclockwise. Figure 2 shows the structure of 2-oxepinoxy radical (**1**) and the peroxy radical structures formed after the addition of molecular oxygen. Also shown in Figure 2 are the 298 K free energies (ΔG(298 K)) for each intermediate and transition state relative to reactants at infinite separation. Each free energy of activation barrier is relative to the reactant for that individual step.

2-Addition. Three unique transition state **(TS)** structures for the formation of 2-peroxyoxepinone radical **(1a)** were found. In each transition state, the oxygen molecule approaches perpendicular to the ring plane and differs in the relation of the O-O bond rotation about the forming C-O bond. All three TS wavefunctions have considerable spin contamination, giving $\langle S^2 \rangle$ values of ~ 1.0, rendering the transition state barriers to be suspect. Regardless, the 298 K free energy barrier (ΔG‡(298 K)) for the lowest energy TS structure, with the O-O oxygen bond setting above the C_1-C_2 ring bond, is 17.7 kcal/mol with $\langle S^2 \rangle$ value of 0.96, the least spin contaminated of the

three wavefunctions. The 298 K reaction is endoergic by 10.4 kcal/mol with a reverse ΔG‡(298 K) of only 7.3 kcal/mol.

4-Addition. Two TS structures were found for addition of oxygen to the 6 ring carbon to form 6-peroxy-oxepinone radical **(1b)**. In both transition structures, the oxygen molecule enters from above the ring plane. In the lower energy TS, the O-O bond adds anti to the C-H bond and over the inside of the ring while the higher energy structure has the O-O bond almost eclipsing the C-H bond. Spin contamination for both transition states was also significant, ($\langle S^2 \rangle \sim 1.0$). The ΔG‡(298 K) for the lowest energy transition structure was 17.0 kcal/mol. This barrier is also the lowest for molecular oxygen addition at the three carbon positions. A simple Hückel analysis for the 5-carbon ring π system for **1** indicates that most of the electron density should be localized on the 4 carbon. Examination of the C-C bond lengths on the ring are consistent with Hückel theory, with the two C-C bonds containing the 4 carbon at 1.40 and 1.42 Å, with bond lengths intermediate between typical C–C single and double bond character. The C-C bonds adjacent have lengths of 1.38 and 1.36 Å exhibiting more pure C–C double bond character. Formation of **1b**, however, is endoergic by 13.2 kcal/mol. It is the most unstable addition product likely due to disruption of resonance in the carbon ring π system caused by its formation. Recrossing back to reactants costs a mere 3.8 kcal/mol.

6-Addition. Three transition state structures for the formation of 6-peroxy-oxepinone radical **(1c)** were also found. Each TS structure has the oxygen molecule approaching from above the ring plane and differs only by a rotation of the O-O bond about the forming C-O bond. All three wavefunctions again have considerable spin contamination, $\langle S^2 \rangle$ values of ~ 1.0, making the TS energies suspect. The ΔG‡(298 K) for the lowest energy TS, with the O-O oxygen bond setting above the C-O ring bond, is 17.5 kcal/mol and an $\langle S^2 \rangle$ value of 1.1. The reaction is endoergic by 9.0 kcal/mol making it the most stable of the peroxyoxepinone radical species. Return to reactants has a ΔG‡(298 K) of 8.5 kcal/mol, the largest of the return barriers.

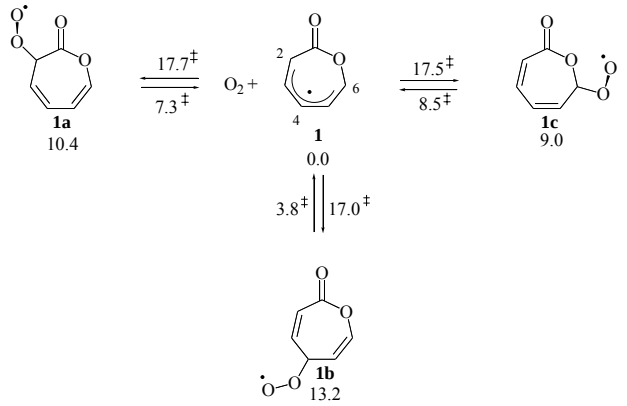

Figure 2. Reaction scheme for the addition of oxygen molecule (^3P) to 2-oxepinoxy radical (1). Energies are B3LYP/6-311+G**//B3LYP/6-31G* ΔG(298 K) relative to O_2 and 2-Oxepinoxy at infinite separation.

Conclusions

Subsequent unimolecular fragmentations emanating from **1a**, **1b**, and **1c** have also been calculated at the same level of theory. Several possible pathways for the decomposition of 2, 4, and 6-peroxyoxepinone radical have been examined at 298, 500, 750, 1000, and 1250 K. Pathways initiated via the formation of a dioxetane, 1,3-peroxy, 1,4 peroxy or hydrogen abstraction via geminal peroxyl radical are competitive with the pathways proposed by Fadden[12] for the unimolecular decomposition of 2-oxepinoxy radical (**1**). The kinetically most favored decomposition pathway at all temperatures involves formation of the 1,4-peroxy intermediate resulting in the formation of furan, CO_2 and formyl radical. Thermodynamically, the most favored pathway forms a 1,2-dioxetanyl intermediate and decomposes to form 1-oxo-pent-2,3-dienyl radical, CO_2 and CO. However, a large entropic penalty is incurred at higher temperatures, thereby making the O_2-addition pathways to the 2-oxepinoxy radical less competitive.

Acknowledgements. We would like to thank the Ohio Supercomputer Center for computing resourses JKM acknowledges support from a GAANN Fellowship.

References

(1) Venkat, C.; Brezinsky, K.; Glassman, I. *Symp. (Int.) Combust., 19th* **1982**, 143-152.
(2) Rotzoll, G. *Int. J. Chem. Kinet.* **1985**, *17*, 637-653.
(3) Frank, P.; Herzler, J.; Just T.; Wahl, C. *Symp. (Int.) Combust., 25th* **1994**, 833-840.
(4) Bermudez, G.; Pfefferle, L. *Combustion and Flame* **1995**, *100*, 41-51.
(5) Chai, Y.; Pfefferle, L. D. *Fuel* **1998**, *77*, 313-320.
(6) Yu, T.; Lin, M. C. *J. Am. Chem. Soc.* **1994**, *116*, 9571-9576.
(7) Norrish, R. G. W.; Taylor, G. W. *Proc. R. Soc.* **1965**, *A234*, 160-177.
(8) Carpenter, B. K. *J. Am. Chem. Soc.* **1993**, *113*, 9806-9807.
(9) Barckholtz, C.; Fadden, M. J.; Hadad, C. M. *J. Phys. Chem. A* **1999**, *103*, 8108-8117.
(10) Fadden, M. J.; Barckholtz, C.; Hadad, C. M. *J. Phys. Chem. A* **2000**, *104*, 3004-3011.
(11) Mebel, A. M.; Lin, M. C. *J. Am. Chem. Soc.* **1994**, *116*, 9577-9584.
(12) Fadden, M. J.; Hadad, C. M. *J. Phys. Chem. A* **2000**, *104*, 8121-8130.

HYDROGEN ATOM CATALYZED ISOMERIZATION OF AROMATIC COMPOUNDS

Mark N. Nimlos[1], Jonathan Filley[2], J. Thomas McKinnon[2]

National Bioenergy Center
National Renewable Energy Laboratory
Golden, Colorado 80401
Department of Chemical Engineering
Colorado School of Mines
Golden, Colorado 80401

Introduction

Isomerization of aromatic compounds plays an important role in the formation of flame-synthesized fullerenes, nanotubes, and in the growth of soot during combustion. During flame synthesis, unfavorable geometries often arise by the proposed zipper mechanism[1,2] in which biaryl molecules zip together losing molecular hydrogen. For instance, the acephenanthrylene molecule, **1**, can zip together to form **3**. At flame temperatures (> 2000 K) the positive entropy of these reactions makes them significant. However, the resulting molecule, **3**, contains adjacent 5-membered rings, which is energetically undesirable. In fullerenes, the 5-membered rings are isolated by 6-membered rings and it is unlikely that a zipper mechanism will lead directly to this type of configuration. An isomerization needs to occur.

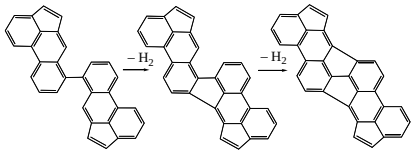

(1)

1 **2** **3**

Fullerene modelers have often invoked the Stone-Wales (SW) rearrangement[2,3] to explain annealing in aromatic compounds. In the simplest example of the SW reaction the 5-membered rings in pyracyclene, **4**, are shifted as shown in eq. 2. This mechanism can be used to isolate 5-membered rings in polycyclic aromatic compounds.

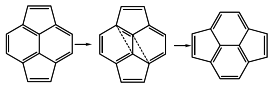

(2)

4

Another interesting annealing reaction is the isomerization of azulene, **5**, to naphthalene, **6**. This reaction may also be important in the zipper mechanism.

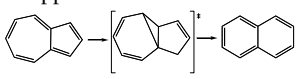

(3)

5 **6**

The calculated barriers for these reactions are fairly high [120 to 130 kcal mol^{-1} for reaction (2) and > 83 kcal mol^{-1} for reaction (3)] which might limit their extent during combustion. We have found that addition of a hydrogen atom to **4** and **5** dramatically reduces the barrier for these reactions and since hydrogen atom is fairly abundant in flames, this catalytic effect may increase the likelihood of these isomerization reactions.

Computational Techniques

The calculations in this study were carried out using the Gaussian 98 suite of programs at the following level: B3LYP/6-31+G(d,p) Local minima and transitions states were found using Berny optimizations. Starting geometries for the transition state optimizations were often located using a potential energy scan, where one internal coordinate was systematically changed while all other coordinates where allowed to relax. The geometry at the calculated maximum of this scan was used as a starting geometry for a TS optimization. Stable structures had only positive vibrational frequencies while transition states had one imaginary frequency. The transition states were confirmed by visual inspection of the imaginary frequency using the Molden visualization package. The transition states were also confirmed using IRC calculations.

Results and Discussion

Stone-Wales

We have considered two mechanisms for the SW reaction in pyracyclene; a two-step mechanism involving cyclopropyl transition states and a cyclobutyl intermediate and one-step mechanism[5] with an sp^3 carbon atom in the transition state. The calculated potential energies for the transition states of these mechanisms are shown in **Figure 1**. Since the product and reactant are the same for this molecule, the two cyclopropyl transition states are necessarily equivalent. As can be seen, the barriers for both of these processes are high (129.8 kcal mol^{-1} for the sp^3 mechanism and 119.3 kcal mol^{-1} for the cyclopropyl mechanism). Furthermore, the level of theory used often underpredicts barrier energies by up to 5 kcal mol^{-1}. These barriers are high enough that other processes, such as C-H bond scissions (*DH* ~ 110 kcal mol^{-1}) will be more likely.

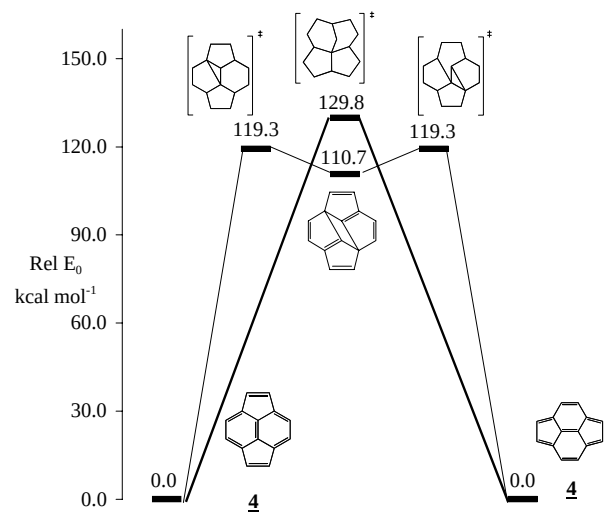

Figure 1. A potential energy plot of the calculated relative energies for the SW reaction in pyracyclene. The energies include the zero point energy.

The addition of a hydrogen atom to the central atom of pyracyclene significantly reduces the reaction barriers for the SW reaction. This is shown in **Figure 2**. As can be seen the relative energy of the cyclopropyl transition state drops from 119.3 kcal mol^{-1} for neat pyracyclene to 66.9 kcal mol^{-1} for H+pyracyclene and the sp^3 transition state dropped from 129.8 kcal mol^{-1} for the neat pyracyclene to 73.3 kcal mol^{-1} for H+pyracyclene. In addition to the lower energy barrier, there is a chemical activation energy that would be available when hydrogen atom adds to pyracyclene. For the molecule shown in **Figure 2** the chemical activation energy is 20.4 kcal mol^{-1}. We have calculated the reaction energetics when a hydrogen atom is added to the external bridge carbon atoms on pyracyclene. The results are shown in Table I. As can be seen,

hydrogen atoms attached to these carbon atoms have a larger chemical activation energy, but have a smaller reduction in the reaction barrier relative to the neat pyracyclene

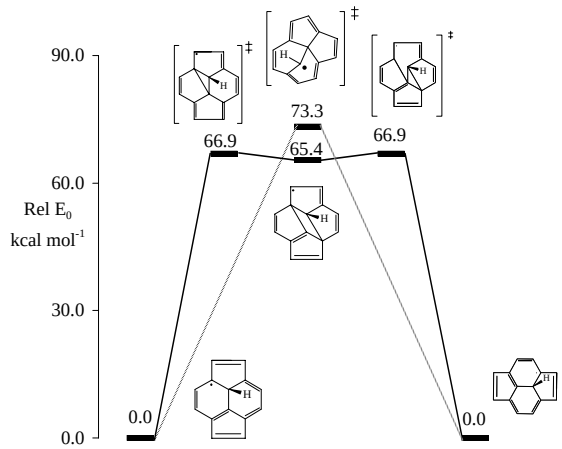

Figure 2. A potential energy plot of the calculated energies for the SW reaction in pyracyclene

Table I Calculated relative energies[a] for SW for pyracyclene and pyracyclene + H atom. (kcal mol^{-1})

React[c]	chem act.[b]	sp^3 mech. TS	TS1	cyclopropyl mech. c-C4	TS2	Prod.
neat		129.8	119.3	110.7	119.3	0.0
H-C13	20.4	73.3	66.9	65.4	66.9	0.0
H-C9	34.5		105.3	97.4	105.3	0.0
H-C1	54.4		128.0	118.8	125.9	14.6

[a]Includes zero point energy [b]The energy of the adduct relative to the energy of H atom + pyracyclene [c]This shows where the H atom is attached on the pyracyclene. See carbon numbering scheme below:

Azulene/Naphtalene Isomerization

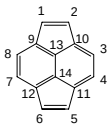

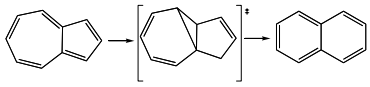

This rearrangement has been the subject of experimental[6-8] and theoretical studies[11]. We find a single transition for the neat molecule with a barrier energy of E_0 = 83.4 kcal mol^{-1}. With the addition of a hydrogen atom to a bridge carbon atom, the energetics changes considerably. **Figure 3** shows a plot of the calculated energies of the intermediates relative to the energy of azulene + H atom. As can be seen, the adduct formed from the addition of H atom to the bridge carbon is –30.9 kcal mol^{-1} lower in energy than the reactants. This chemical activation energy is sufficient to surmount the barriers to naphthalene formation. In this case H atom catalysis makes the isomerization facile.

This mechanism also has an interesting consequence on aromatic formation from the recombination of cyclopentadienyl radical (C_5H_5). It has been proposed that in combustion two cyclopentadienyl radicals can react to form naphthalene by a mechanism which involves two cyclopropyl intermediates. 9,10

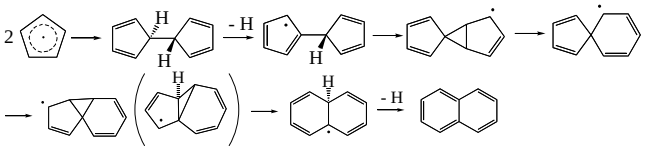

8

The intermediate, **8**, in this mechanism is identical to the cyclopropyl intermediate in the H atom catalyzed transformation of azulene to naphthalene shown in **Figure 3**. Thus, it is possible that the recombination of cyclopentadienyl radicals could lead to the formation of azulene in addition to naphthalene.

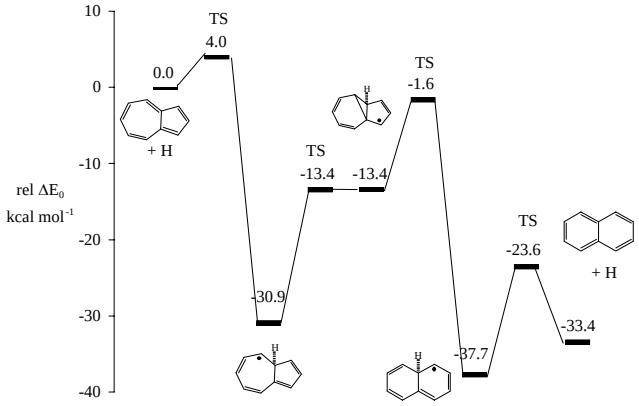

Figure 3. Relative energies of intermediates in the H atom catalyzed isomerization of azulene to naphthalene.

In summary, we have found that rearrangements of 5,6-rings and 5,7-rings in simple compounds that are designed to model more complex rearrangements in fullerenes have barriers that are significantly lowered by the addition of an H-atom to the rearranging framework. The resulting radicals, which are likely to exist in relatively high concentrations due to the high concentrations of H-atoms in flame environments, represent a possible low energy catalytic pathway for the SW and related rearrangements in fullerenes.

Acknowledgment

We would like to acknowledge the National Center for Supercomputer Applications (NCSA Grant # CHE-980028n) for computer time.

References

1. Richter, H.; Howard, J.B. *Prog. Energy Comb. Sci*. **2000**, *26*, 565.
2. Homann, K.H. *Ang. Chem. Int. Ed*. **1998**, *37*, 2435.
3. Stone, A.J.; Wales, D.J. *Chem. Phys. Lett.* **1986**, *128*, 501.
4. Walsh, T.R.; Wales, D.J. *J. Chem. Phys.* **1998**, *109*, 6691.
5. Murry, R.L.; Strout, D.L.; Odom, G.K.; Scuseria, G.E. *Nature* **1993**, *366*, 665**.**
6. Scott, L. T.; Kirms, M. A. *J. Am. Chem. Soc.* **1981**, *103*, 5875-5879.
7. Scott, L. T. *Acc. Chem. Res.* **1982**, *15*, 53-58**.**
8. Alder, R. W.; Whiteside, R. W.; Wittaker, G.; Wilshire, C. *J. Am. Chem. Soc.* **1979**, *101*, 629-632.
9. Melius, C. F.; Colvin, M. E.; Marinov, N. M.; Pitz, W. J.; Senkan, S. M. *26th Symposium on Combustion* 1996, 685-692.
10. Filley J.; McKinnon J.T. *Combust, Flame* **2001**, *124*, 721-723.
11. Alder, R. W.; East, S. P.; Harvey, J. N.; Oakley, M. T. *J. Am. Chem. Soc.* **2003**, *125*, 5375.

COMBINATION AND DISPROPORTIONATION REACTIONS OF ALKYL RADICALS: AN AB INITIO KINETICS STUDY FOR $CH_3 + C_2H_5$

*R. S. Zhu, Z. F. Xu and M. C. Lin**

Department of Chemistry
Emory University
Atlanta, GA 30322

I. Introduction

The kinetically competitive combination and disproportionation of alkyl radicals are important to the global chemistry of hydrocarbon decomposition and combustion processes. The mechanism responsible for these reactions was a subject of much discussions[1-4] after their kinetic data had been measured extensively with the advent of the gas chromatographic technique in the 1950's.

Despite the great advance in ab intio molecular orbital and statistical rate constant calculations in recent years, reliable prediction of the product branching probabilities for the two competitive processes has not been achieved. For example, in a latest paper by Mousavipour and Homayoon[5] published in the course of our preparation for publication of this work, the critical disproportionation process has not been clearly elucidated, the corresponding barrier for this path was predicted to lie between 0.05 and 6.2 kcal/mol by different methods and its rate constant was fitted to experimental data with different energy barriers.

In this work we employed the state-of-the-art computational techniques for both electronic structure and rate constant prediction. Most significantly, the disproportionation reaction, for example, for $CH_3 + C_2H_5$ takes place via a H-bonded CH_3---H--C_2H_4 intermediate, instead of a direct transition state as reported by Mousavipour and Homayoon.[5] This mechanism is expected to be universal for the alkyl-alkyl disproportationation processes as will be demonstrated in the future for the series of the R + R' reactions (where, R = H, CH_3, …; R' = CH_3, C_2H_5,…).

II. Computational Methods

The potential energy surface (PES) was calculated at the G2M (CC2)//B3LYP/6-311+G(3df, 2p) level[6]. Some critical points are also calculated at the CCSD(T)/6-311+G(3df, 2p)//B3LYp/6-311+G(3df, 2p) level. For all the molecular orbital calculations the Gaussian 03[7] and Molpro2002.3[8] programs were used.

The rate constants were computed with microcanonical variational RRKM (Variflex)[9] and ChemRate codes.[10]

III. Results and discuss

A. Potential energy surface (PES) and mechanism

a. Abstraction reactions

$CH_4 + {}^1C_2H_4$ formation. For the direct abstract process, a relatively loose transition state was located at the B3LYP/6-311+G(3df, 2p) level. Because of the importance of the transition state barrier for the prediction of disproportionation rate constant, the barrier height of this transition state was also calculated by other methods. The results show that the barrier is around -1.6 ± 0.5 kcal/mol relative to the reactants. A loose hydrogen-bonding precursor was found to be involved in this process.

Abstraction reactions can also happen on the triplet surfaces to produce $CH_4 + {}^3C_2H_4$, $CH_4 + {}^3CH_3CH$ and ${}^3CH_2 + C_2H_6$ with higher barriers, 15.4, 15.8 and 18.4 kcal/mol, respectively.

b. Association reaction

The interaction of the two unsaturated carbon atoms in CH_3 and C_2H_5 forms association product, C_3H_8. The association energy was predicted to be 89.0 kcal/mol at the G2M (CC2) level.

c. Decomposition of chemically activated C_3H_8

H_2-elimination. The interaction of the two H atoms from the same group of CH_3 or CH_2 and from different groups in $CH_3CH_2CH_3$ will result in H_2 elimination to produce the following different products.

$H_2 + CH_3CCH_3$. The interaction of the two H atoms from the CH_2 group in C_3H_8 eliminates H_2 via a three-member-ring transition state wit a barrier above the reactants by 12.0 kcal/mol and this process has endothermicity by 5.1 kcal/mol.

$H_2 + CH_3CHCH_2$. The are two possibilities to form the products. In the first case, two H atoms, each from the CH_3 and CH_2 groups in $CH_3CH_2CH_3$, form a HHCC four-member-ring transition state with barrier above the reactants by 20.6 kcal/mol. For the second case, H_2 eliminates from one of the CH_3 groups, with simultaneously, one of the H atoms in the CH_2 group migrating to the terminal C to form $H_2 + CH_3CHCH_2$. This process has 14.8 kcal/mol barrier. The exothermicity for the reaction is 61.3 kcal/mol.

H_2 + cyc-C_3H_6. In this channel, the two C-H bonds in CH_3 groups of $CH_3CH_2CH_3$ intermediate are lengthening to form a H-H bond, meanwhile, the two C atoms from the CH_3 groups are connecting to form a C-C bond. Although this is an exothermic process with exothermicity of 52.7 kcal/mol, it has a much higher barrier, 58.9 kcal/mol above the reactants, it will not be kinetically important.

CH_2 elimination. In this channel, one of the H atoms in the CH_3 group of $CH_3CH_2CH_3$ can migrate to the CH_2 group via a three-member-ring transition state to form a loose complex with a barrier of 14.5 kcal/mol above the reactants. The complex lies above the reactants by 11.7 kcal/mol, which further dissociates to produce ${}^1CH_2 + C_2H_6$ with endothermicity of 15.1 kcal/mol.

CH_4-elimination. There are two possible ways to eliminate CH_4 from $CH_3CH_2CH_3$.

$CH_4 + CH_2CH_2$. In this channel, one H atom migrates from one CH_3 groups to the other CH_3 group, simultaneously, one of the C-C bond is breaking via a four-member-ring transition state to form the products with a barrier lying above the reactants by 23.7 kcal/mol. Apparently, this channel is not competitive with the direct abstraction one as discussed in the previous section.

CH_4 + CH_3CH. This path involves one H atom in the CH_2 group transferring to one of the CH_3 group via a three-center transition state to form a loose complex which dissociates to produce products $CH_4 + CH_3CH$. The transition state, complex and products lie above the reactants by 5.7, 2.4 and 2.8 kcal/mol, respectively.

B. Rate constant calculations

The rate constants for those channels with barriers less than 15.0 kcal have been calculated. The results show that the dominant channel in the temperature range of 200 – 3000 K is C_3H_8 formation. The predicated rate constants for association, dissociation processes and the ratio of combination/disproportionation are in reasonable agreement with available values.

IV. Conclusions

Complete potential energy surface (PES) for the reaction of $CH_3 + C_2H_5$ has been calculated at the G2M (CC2)//B3LYP/6-311+G(3df, 2p) level. Rate constant calculations show that formation of C_3H_8 is dominant in the temperature range of 200 ~ 3000 K. Predicted rates reasonably agree with experimental data.

Acknowledgement

This work is sponsored by DOE. Acknowledgment is also made to the Cherry L. Emerson Center of Emory University for the use of its resources, which are in part supported by a National Science Foundation grant (CHE-0079627) and an IBM Shared University Research Award.

References

(1) Konar, R. S. *Int. J. Chem. Kinet.* **1970**, *2 (5)*, 419.
(2) Laidler, K. J. *Int. J. Chem. Kinet.* **1971**, *3*, 377.
(3) Konar, R. S. *Int. J. Chem. Kinet.* **1971**, *3*, 379.
(4) Dannenberg, J. J. and Baer, B., *J. Am. Chem. Soc.* **1987**, *109*, 292.
(5) Mousavipour, S. H.; Homayoon, Z. *J. Phys. Chem. A* **2003**, *107*, 8566.
(6) Mebel, A. M.; Morokuma, K.; Lin, M. C. *J. Chem. Phys.* **1995**, *103*,7414.
(7) M. J. Frisch, M. J. et al., *GAUSSIAN 03, REVISION B.0*1; Gaussian, Inc., Pittsburgh PA, **2003**.
(8) MOLPRO is a package of *ab initio* programs written by H.-J. Werner et al.
(9) Klippenstein, S. J. ; Wagner, A. F.; Dunbar, R. C. ; Wardlaw, D. M. and Robertson, S. H. VARIFLEX: VERSION **1.00**, **1999**.
(10) Mokrushin, V.; Bedanov, V.; Tsang, W.; Zachariah, M. R.; Knyazev, V. D. *ChemRate, Version 1.19*; National Institute of Standards and Technology: Gaithersburg, MD 20899, **2002.**

Ab Initio quantum chemical studies of hydrogen abstraction reactions of hydrocarbons

David W. Ewing and Michael J. Manka

Department of Chemistry, John Carroll University
Cleveland, OH 44118 E-mail: ewing@jcu.edu

Alchemy Software, 1610 Clearglades Drive
Wesley Chapel, FL 33543-5759
E-mail: mjmanka@chemicalsoft.com

Introduction

The accurate prediction of kinetic parameters of hydrogen abstraction reactions of hydrocarbons is of fundamental importance to the kinetic modeling of the commercial processing of natural gas, petroleum, and its derivatives[1], as well as their combustion reactions.[2,3] Results of *ab initio* calculations will be reported here for the reactions $C_2H_6 + H\bullet \rightarrow C_2H_5\bullet + H_2$ and $C_2H_6 + CH_3\bullet \rightarrow C_2H_5\bullet + CH_4$. Reactions of propane will be also discussed in the talk.

Methods

Structures and vibrational frequencies were calculated at the HF/DZP level of theory. Activation energies were obtained at various levels of theory, the highest being MP4/pVTZ//HF/DZP. Morokuma's ONIOM method[4] was also used to find activation energies, using a two layer strategy. The abstracting species, the carbon from which the hydrogen atom was being abstracted, and the other hydrogens attached to that carbon were in the high level layer; all other atoms were in the low level layer. Calculations were done using Gaussian 98[5] running on PC workstations.

Results and Discussion

Previous calculations have shown that accurate activation energies can be obtained for reactions of this type from structures calculated at the HF/DZP level, as long as correlated calculations are done, preferably with a large basis set, for the energetics.[6] Figure 1 gives the calculated HF/DZP structures. Subsequent vibrational frequency calculations yielded only one imaginary frequency for each reaction, the normal modes of which were along the reaction coordinate.

Table 1 gives activation energies at various levels of theory and compares these to experiment. The ONIOM results are seen to give activation energies within 1-2 kcal/mol. For comparison the MP4/pVTZ//HF/DZP activation energy for the reaction of $C_2H_6 + H\bullet$ (without using ONIOM) was found to be 11.2 kcal/mol, less than one kcal/mol closer to the experimental value. This latter calculation took nearly 7 hours on a Pentium II PC and used 900 mbytes of scratch disk, whereas the ONIOM calculation only took 19 minutes and 200 Mbytes.

Table 1. Activation Energies (kcal/mol)

Level of Theory	$C_2H_6 + H\bullet$	$C_2H_6 + CH_3\bullet$
HF/DZP	20.0	29.6
MP2/DZP//HF/DZP	15.1	16.7
MP4/DZP//HF/DZP	13.8	17.2
ONIOM*	11.8	16.4
Experiment[7]	10.8	14-15

*MP4/pVTZ for the high level; HF/DZP for the low level

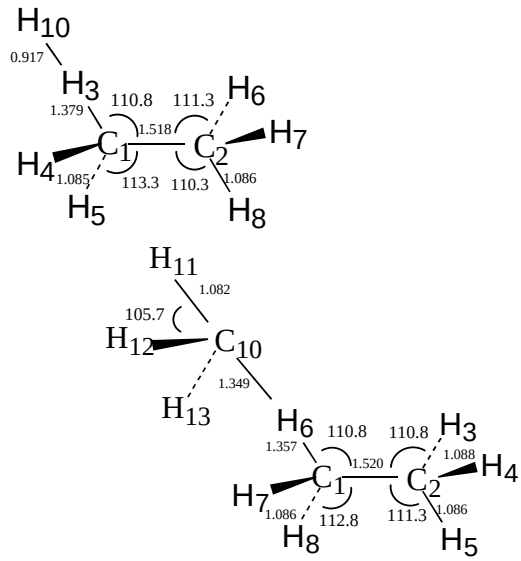

Figure 1. HF/DZP transition state structures for $C_2H_6 + H\bullet \rightarrow C_2H_5\bullet + H_2$ and $C_2H_6 + CH_3\bullet \rightarrow C_2H_5\bullet + CH_4$. Bond lengths are in Å and bond angles are in degrees.

Transition State Theory Calculations

Reaction rate coefficients were calculated using transition state theory (TST) and results from the *ab initio* calculations shown in Table 1. Corrections for barrier tunneling were determined using parabola and the Eckart potential approximations. These calculations were performed using the TS Rate program. The evaluated rate several approximations, including Wigner's, Bell's truncated coefficients for the two hydrogen abstraction reactions are presented in Figures 2 and 3, respectively. The calculated rate coefficient increases with the application of the barrier tunneling corrections. The Wigner approximation, which is applicable for small tunneling corrections near the top of the barrier and does not depend directly on the barrier height, yields the smallest correction and is considered to be inadequate where significant tunneling occurs. Similarly, the truncated parabola, which approximates the barrier as a symmetric parabola, also may only adequately describes the barrier near its top. This correction method is also only applicable for small tunneling corrections. It also appears to grossly over-estimate the tunneling correction where significant tunneling is likely to occur, i.e. at lower temperatures. The Eckart potential function provides a better description of the barrier and the tunneling correction factors are intermediate between the Wigner and Bell approximation corrections.

The calculated results were fitted to the three parameter modified Arrhenius equation to obtain a better fit of the results. The rate coefficient expression has the form

$$\log(k, \mathrm{M^{-1}s^{-1}}) = A - \frac{B}{T} + C\log(T) \qquad (1)$$

where T is the temperature in K. The parameters for the rate expressions for the reactions $C_2H_6 + H\bullet$ and $C_2H_6 + CH_3\bullet$ are given below in Tables 2 and 3, respectively.

These rate coefficient results, except for results obtained using the Bell correction method, were compared to available data from the literature. This comparison is shown in Figures 4 and 5 for the reactions $C_2H_6 + H\bullet$ and $C_2H_6 + CH_3\bullet$, respectively. The calculated results are in better agreement with literature data for the reaction $H\bullet + C_2H_6$ than for $CH_3\bullet + C_2H_6$.

Table 2. Rate Expression Parameters for C_2H_6 + H•

Correction Method	A	B	C
Uncorrected	5.161	2341	1.96
Wigner	5.250	2090	1.90
Bell	-13.920	-556	7.37
Eckart Potential	-7.269	413	5.49

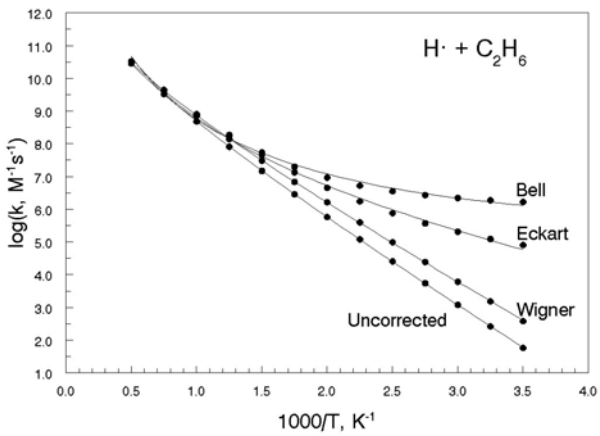

Figure 2. Plot of calculated transition state theory rate coefficients versus temperature for H• + C_2H_6. Corrections for barrier tunneling employing the Wigner, Bell and Eckart approximation methods applied to the uncorrected results.

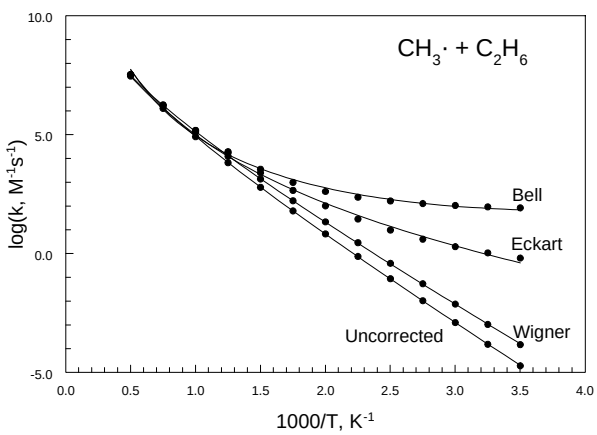

Figure 3. Plot of calculated transition state theory rate coefficients versus temperature for CH_3• + C_2H_6. Corrections for barrier tunneling employing the Wigner, Bell and Eckart approximation methods applied to the uncorrected results.

Table 3. Rate Expression Parameters for C_2H_6 + CH_3•

Correction Method	A	B	C
Uncorrected	-1.173	3178	3.09
Wigner	-0.819	2927	2.96
Bell	-30.205	-1217	11.31
Eckart Potential	-20.703	270	8.66

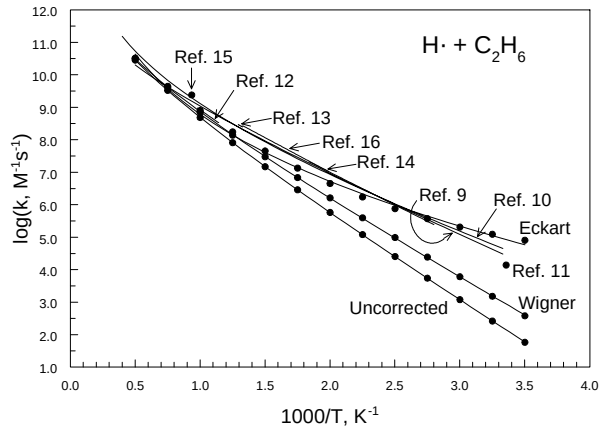

Figure 4. Comparison of calculated transition state theory rate coefficients versus temperature for H• + C_2H_6 and literature data.

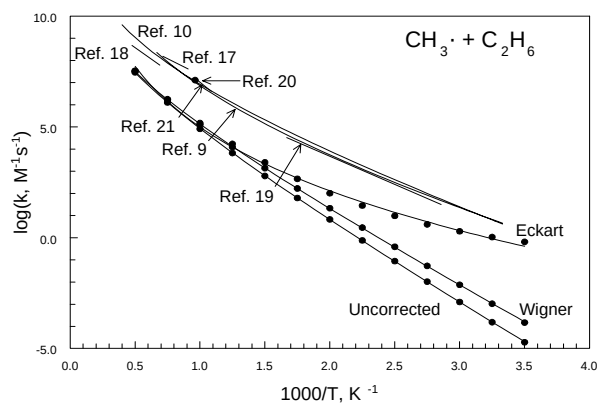

Figure 5. Comparison of calculated transition state theory rate coefficients versus temperature for CH_3• + C_2H_6 and literature data.

References

(1) *Pyrolysis: Theory and Industrial Practice*; Albright, L.F., Crynes, B.L, Corcoran, W.H., Eds.; Academic Press: New York, 1982.

(2) Hucknall,D.J. Chemistry of Hydrocarbon Combustion; Chapman and Hall: London, 1985.

(3) Warnatz, J. In Combustion Chemistry; Gradiner, W.C., Ed.; Springer-Verlag: NewYork, 1984.

(4) Svensson, M.; Humbel, S.; Morokuma, K. *J. Chem. Phys.* **1996**, *105*, 3654.

(5) Gaussian 98 (Rev. A.9), Gaussian, Inc.: Pittsburgh PA, 1998.

(6) Litwinowicz, J.A.; Ewing, D.W.; Jurisevic, S.; Manka M.J. *J. Phys. Chem.* ***1995***, *99*, 9709.

(7) Baulch, D.L.; Cobos, C.J.; Cox, R.A.; Esser, C.; Frank P.; Just, Th.; Kerr, J.A.; Piling, M.J.; Troe, J.; Walker, R.W.; Warnatz, J., *J. Phys. Chem.Ref. Data*, **1992**, *21*, 411.

Methyl Radical and Shift Reactions with Aliphatic and Aromatic Hydrocarbons: Thermochemical Properties, Reaction Paths and Kinetic Parameters

L. Rutz[1] and H. Bockhorn[1] and J. W. Bozzelli[2]

[1]Institute for Chemical Technology, University of Karlsruhe, Karlsruhe, Germany
[2]Department of Chemistry, New Jersey Institute of Technology, Newark, USA

Introduction

The study of soot formation under moderate to low (ca. 1100K), temperatures and pyrolytic conditions, no oxygen, with small hydrocarbons like acetylene, ethylene, methane, propane or propene in flow reactors is of interest for nanotube formation, and for many solid carbon products such as brake pads and carbon black, … etc. A fundamental understanding of soot formation chemistry is important to reducing soot emissions from vehicles and other combustion sources.

Our attempts to model the experimental data in such systems and in our laboratories utilized soot formation models from well established combustion mechanisms. We quickly realized that there are no mechanisms in the literature that serve to model the soot formation experiment data at the lower temperature conditions. Kinetic and sensitivity analysis on the mechanisms shows that the first step - that to break the first carbon - hydrogen or carbon - carbon bond is the limiting in these literature mechanisms.

We have, therefore started a search for alternative ways to generate / initiate radicals to improve the mechanisms. In this symposium we present two new initiation mechanisms and this paper focuses on one of these reactions - that of methyl radical addition to π bonds and substitution in SP^3 Bonds of carbon to form C2 adducts which further initiate the chain and undergo further reaction to molecular weight growth.

Methyl radical, CH_3 is an active species that is well known in combustion research. New results show that it can also play a role in CVD and CVI processes. We have investigated literature and performed computational chemistry calculations on addition and substitution reactions of methyl radical. Two substitution reactions are evaluated: one on aromatic and one on aliphatic systems. One reaction, addition to a p bond of an aromatic or olefin system, occurs via a relatively low energy barrier of only 15 kcal/mole. The second reaction, substitution in an aliphatic at a moderate energy barrier of only 50 kcal/mole, compared to bond cleavage reactions that require energies of about 100 kcal/mole. While both of these reactions are well known in gas phase kinetics, it is not clear that they have been implemented in mechanisms for evaluation of their effects. Soot formation in pyrolysis and combustion conditions occurs at sufficiently high temperatures that the substitution reaction could play a role.

Calculation Methods

Thermodynamic Properties. Geometry optimizations and frequency calculations for reactants, intermediates, and transition states from vinylidene insertion reactions are performed using several Density Functional (DFT) Methods (B3LYP/6-31G(d,p), B3LYP/6-311G(d,p), B3LYP/6-311+G(d,p), B3LYP/6-311++g(3df,2p), B3LYP/SVP and B3LYP/TZV) levels of theory in the Gaussian 98 program suite. The ab initio calculations, MP2/fc-6-311G(d,p), MP2/full-6-311G(d,p) and G3MP2, are also used to improve our calculation level and validate the DFT results. The optimized geometry parameters with B3LYP/6-31G(d,p) level are used to obtain total electronic energies in B3LYP/6-31G(d,p), CBS-lq//B3LYP/6-31G(d,p) single point calculations and the CBSQ//B3LYP/6-31G(d,p) composite method.

Potential Barriers for intramolecular rotation about the carbon-carbon bonds in unsaturated and polycyclic aromatic hydrocarbons are analyzed versus torsional angle using B3LYP/6-31G(d,p). Total energies are corrected by ZPVE, which are scaled by the recommended values by Scott et al.[1] Thermal correction is taken into account using structures and vibrations determined at several of the calculation levels. Transition state geometries are identified by the existence of only one imaginary frequency in the normal mode coordinate analysis, evaluation of the TS geometry, the reaction coordinate vibrational motion and an intrinsic reaction coordinate analyses.

Enthalpies of formation ($\Delta H_f^o{}_{298}$) are estimated using total energies and calculated $\Delta H_{rxn}^o{}_{298}$ with several isodesmic, or group balance working reactions on each species. The calculated $\Delta H_{rxn}^o{}_{298}$ and known $\Delta H_f^o{}_{298}$ of reference species are utilized to estimate $\Delta H_f^o{}_{298}$ of the target molecules in each of the reaction schemes. $\Delta H_f^o{}_{298}$ for the reference species comes from literature thermodynamic properties.

Contributions of vibration, translation, and external rotation to entropies and heat capacities are calculated by statistical mechanics based on the scaled vibrational frequencies and moments of inertia from the DFT optimized structures.

The torsion frequencies are omitted in calculation of $S°_{298}$ and Cp(T)'s, and their contributions are replaced with values from analysis of the internal rotations. Contributions from hindered rotors to $S°_{298}$ and Cp(T)'s are determined by solving the Schrödinger equation with free rotor wave functions and direct integration over energy levels of the intramolecular rotation potential curves which are represented by a truncated Fourier series expansion. The contributions from optical isomers and spin degeneracy of unpaired electrons are incorporated in S values.

Results - Thermochemical Data. The ($\Delta H_f^o{}_{298}$ for reactants, intermediate and products are calculated using total energies and isodesmic reactions with group balance if possible. The ($\Delta H_f^o{}_{298}$ values for transition states are calculated from the ($\Delta H_f^o{}_{298}$ values of reactants plus reaction enthalpy. Thermodynamic parameters ($\Delta H_f^o{}_{298}$, $S°_{298}$ and Cp(300) to Cp (1500) for species in the reaction schemes are listed.

Kinetic Properties. Unimolecular dissociation and isomerization reactions of the chemically activated and stabilized adducts resulting from addition or combination reactions are analyzed by first constructing potential energy diagrams for the reaction system. DFT and ab initio calculations are used to calculate transition state structures and energy for isomerization, beta scission, and dissociation reactions. The enthalpies and entropies are used with conventional transition state theory to obtain high pressure limit rate constants (k_∞) as function of temperature. Nonlinear Arrhenius effects resulting from changes in the thermochemical properties of the respective transition state relative to adduct with temperature are incorporated using a two parameter Arrhenius preexponential factor (A, n) in AT^n. Branching ratios of the energized adduct to stabilization or various product channels are then calculated using multifrequency QRRK analysis for k(E)[2,3] with the steady-state assumption on the energized adduct(s). The QRRK calculation are used to evaluate energy dependent rate constants, k(E), of the energized adduct to the various channels for bimolecular chemical activation reaction systems; they include equilibrium in isomerization reactions. The QRRK / Master equation analysis described by Gilbert[4], Chang et al.[5] and Sheng et al.[6] is shown to yield reasonable results and provides a framework by which the effects of temperature

and pressure can be evaluated in complex reaction systems. The QRRK code utilizes a reduced set of three vibration frequencies which accurately reproduce the adduct heat capacity and include one external rotation in calculation of density of states F(E)/Q. The master equation analysis for falloff uses a 0.3 to 0.5 kcal energy grain to obtain rate constants as a function of temperature and pressure for chemical activation and dissociation reactions. (ΔE)°down of 630 cal/mol is used for master equation analysis as argon is the third body.

Results and Discussion - Reaction Paths, Barriers

One of our objectives is to show a direct reaction path that leads from methyl radicals, CH_3, over aliphatic hydrocarbons to aromatic systems. Therefore we observe some partly well know reactions and there transition states to build up a reaction path for the molecular weight growth[7].

Incipient with a substitution reaction of methyl radical with methane ethane and hydrogen will be formed. This transition state has a barrier of 51.24 kcal/mol and is lower than the bond dissociation in methane with 104 kcal/mol. In the next step CH_3 interacts with ethane to abstract a hydrogen and C_2H_5 and CH_4 is build over an activation barrier of ca. 14 kcal/mol.

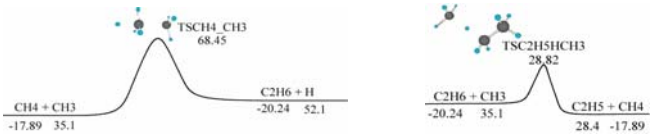

The ethyl radical now can loose second hydrogen and our first unsaturated species is form. This takes 37,77 kcal/mol.

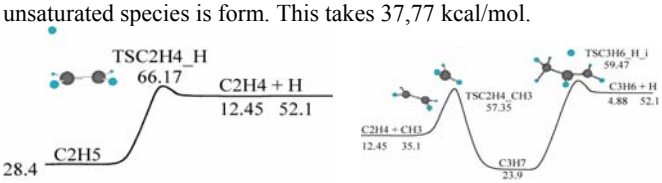

An additional methyl radical reacts now with ethylene and produce n-propyl radical which directly can loose a hydrogen atom and forms propene. The barrier for these are 9.8 respectively 35,57 kcal/mol. Furthermore C_3H_6 can interact with methyl in two different possibilities. One is to generate 1-butene over a H-atom substitution with a barrier of 52,24 kcal/mol. A second route leads over a quite low transition state with 1,59 kcal/mol to the allyl radical while CH_4 is produced.

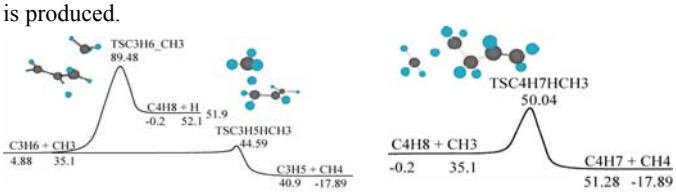

1-butene can follow these recur process and the production of but-3-en-1-yl radical is conceivable. The necessary activation energy will be 15,14 kcal/mol. The abstraction of a hydrogen atom from C_4H_7 take us to next higher homolog unsaturated hydrocarbon, 1,3-Butadiene.

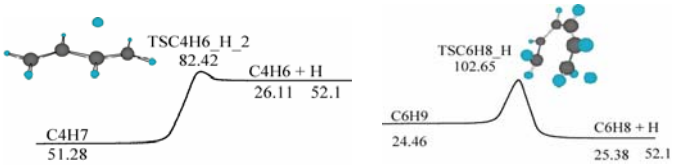

Just as in the previous TST we found a 31,14 kcal/mol barrier. The following transition state shows the internal substitution of a hydrogen in z,z-2,4-Hexadien-1-yl. The barrier is with 78,19 kcal/mol lower than the methane bond energy with 104 kcal/mol.

After the formation of this cyclical hydrocarbon it is an easy exercise to make use of the introduced reaction pattern. 1,3-Cyclhexadiene will be attacked by CH_3 and loose one H atom (8.56 kcal/mol barrier).

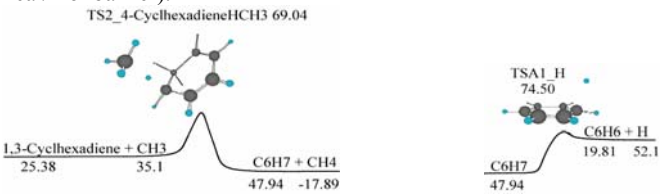

The activation energy to loose the second hydrogen and generate the first aromatic ring is 26.56 kcal/mol. Additional CH_3 form with benzene 2-Methyl-1,4-cyclohexadienyl a subsequently toluene (12.4/43.47 kcal/mol).

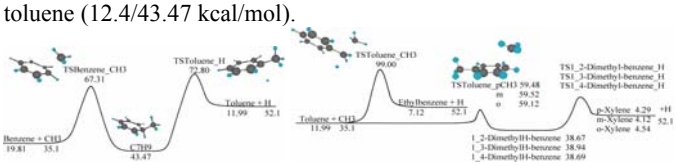

The next methyl radicals can react in the following with the aliphatic or the aromatic part of toluene, which lead to a molecular weight growth on an aliphatic chain or a multi substitution of the ring.

In our study of CH_3 reactions we also analysis shift reactions to explain the formation of big graphite layers and the selective growth on the edge. In a similar pattern we start to look for 1,2-CH_3-shift reactions on small molecules till we end up with a shift reaction on top of an unsaturated ring system.

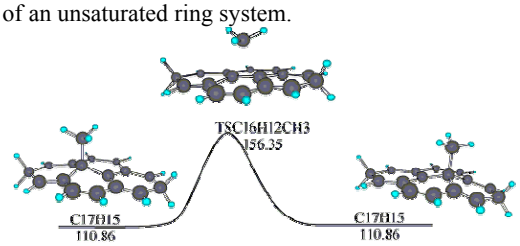

The transition states of this position change are as well investigated as the previous addition of methyl on the surface.

Conclusions

Thermodynamic properties of addition, elimination, substitution and shift reactions in the methyl system were determined by ab initio and density functional calculations. Entropies ($S°_{298}$) and heat capacities (Cp(T)) are also determined, with inclusion of internal rotor contributions. Reaction paths and kinetics are analyzed on methyl reaction system using QRRK for k(E) and master equation for falloff.

Acknowledgement. This work was financially supported by the Deutsche Forschungsgemeinschaft (SFB 551, 'Kohlenstoff aus der Gasphase: Elementarreaktionen, Strukturen, Werkstoffe').

References

[1] Scott, A. P.; Radom, L. *J. Phys. Chem.* **1996**, *100*, 16502
[2] Ritter, E. R.; Bozzelli, J. W. *International Journal of Chemical Kinetics* **1991**, *23*, 767.
[3] Lay, T. H.; Bozzelli, J. W.; Dean, A. M.; Ritter, E. R. *J. Phys. Chem.* **1995**, *99*, 14514.
[4] Gilbert, R. G.; Luther, K.; Troe, J. *Ber. Bunsen. Phys. Chem.* **1983**, *87*, 169.
[5] Chang, A. Y.; Bozzelli, J. W.; Dean, A. M. *Zeitschrift für Physikalische Chemie (München)* **2000**, *214*, 1533.
[6] Sheng, C. Y.; Bozzelli, J. W.; Dean, A. M.; Chang, A. Y. *Journal of Physical Chemistry A* **2002**, *106*, 7276.
[7] Tokmakov, I. V.; Lin M.C., *Int. J. Chem. Kinet*. **2001** 33, 633-653.

Theoretical Study on the Mechanism of $Ni(d^{10}\,{}^1S)+CO_2+3H_2 \rightarrow NiO+CH_4+H_2O$ Reaction

Changwei Hu[1], *Song Qin*[1], *Anmin Tian*[1], *Ning-Bew Wong*[2]

[1]Sichuan Key Laboratory of Green Chemistry and Technology, College of Chemistry, Sichuan University, Chengdu, 610064, China
[2]Department of Biology and Chemistry, City University of Hong Kong, Kowloon, HK

Introduction

Ni-based catalyst is very effective in CO_2 hydrogenation, and its reaction mechanism therefore represents a research topic of great interest[1-3]. Some experimental investigations provide evidences for the formation of adsorbed surface acid species in CO_2 hydrogenation on Ni-based catalysts[4,5]. However, no theoretical study regarding co-interaction of H_2 molecule and CO_2 molecule with Ni atom is available so far to our knowledge. It is shown recently, density functional methods yield reasonable molecular geometries at a relatively low computational cost for transition metal system[6-8]. In present work, the co-interaction of H_2 and CO_2 with Ni is studied by using DTF method in order to find possible reaction intermediates and reaction path in CO_2 hydrogenation on Ni-based catalyst.

Computational Details

Full geometry optimizations and ZPE corrected energies of all intermediates and transition states in the above reaction were performed at B3LYP/6-311+G(2d,2p) level using Gaussian 98 programs. The intrinsic reaction coordination (IRC) method is used to track and verify the minimum energy paths from intermediates to intermediates via transition states.

Results and Discussion

The optimized geometries of various species along the predicted reaction path of the titled reaction and their corresponding ZPE corrected relative energies are shown in **Figure 1**.

Our predicted reaction path can be divided into three stages as the following:

1. $CO_2 + H_2 + Ni(d^{101}S) \rightarrow H_2\text{-}NiCO_2 \rightarrow TS1 \rightarrow HNiCOOH \rightarrow TS3 \rightarrow O\text{-}NiCHOH$
2. $O\text{-}NiCHOH + H_2 \rightarrow H_2\text{-}NiOCHOH \rightarrow TS4 \rightarrow HO\text{-}HNiCHOH \rightarrow TS5 \rightarrow H_2O\text{-}NiCHOH \rightarrow NiCHOH + H_2O$
3. $NiCHOH + H_2 \rightarrow H_2\text{-}NiCHOH \rightarrow TS6 \rightarrow H_2\text{-}NiCHOH' \rightarrow TS7 \rightarrow HNiCH_2OH \rightarrow TS8 \rightarrow HNiCH_2OH' \rightarrow TS9 \rightarrow HONiCH_3 \rightarrow TS10 \rightarrow ONiHCH_3 \rightarrow TS11 \rightarrow ONi\text{-}CH_4 \rightarrow CH_4 + NiO$

In stage 1, reactants H_2 and CO_2 molecules first co-interact with the Ni center with formation the precursor complex H_2-$NiCO_2$ before proceeding to transition state. The calculation shows that, for H_2-$NiCO_2$ species, H_2 is undissotiatively interacted with Ni atom and Ni-CO_2 moiety is very close to the singlet η^2_{co} complex which have been found to be the most stable form in four possible different $Ni(CO_2)$ complex modes[9]. The calculated energies place this species 51.0kJ mol^{-1} lower than that of the free H_2 and η^2_{co} mode of $NiCO_2$ complex, which means that the H_2-$NiCO_2$ complex may be a possible intermediate in CO_2 hydrogenation involving Ni atom. From H_2-$NiCO_2$ complex, the reaction proceeds to form intermediate HNiCOOH in which -COOH fragment is much similar to carboxyl. From intermediate HNiCOOH the reaction continues to form intermediate Ni-HCOOH whose HCOOH moiety were very close to formic acid molecule. The above results indicate that the predicted reaction stage 1 involves the formation of adsorbed formic acid intermediates and leads to the cleavage of C-O bond of CO_2 molecule. This is in accordance with previous experimental investigations which provided evidences that the CO_2 hydrogenation on Ni catalyst involves the formation of adsorbed formic acid.[10]

In stage 2, another H_2 molecule attaches the O-NiCHOH species with formation of the H_2-NiOCHOH complex. For this species, H_2 is undissotiatively interacted with Ni. From this complex, the reaction is predicted to the formation of intermediate HO-HNiCHOH in which H-H bond of H_2 molecule is broken. From intermediate HO-HNiCHOH, the reaction continues to proceed and forms intermediate H_2O-NiCHOH in which the adsorbed water molecule forms. The H_2O-NiCHOH may lose one water molecule and completes this reaction stage with the formation of NiCHOH species.

In stage 3, another H_2 molecule continues to attach the NiCHOH species and forms H_2-NiCHOH complex. In this complex, H_2 molecule is still undissotiatively interacted with Ni atom. From this species, the reaction proceeds via a series of transition states and corresponding intermediates to form the intermediates $HNiCH_2OH$ in which the H-H bond of H_2 molecule is broken and the CH_2OH moiety forms. From this species, the reaction continues to proceed and eventually forms the ONi-CH_4 complex which contains an adsorbed methane molecule. This intermediate may lose the adsorbed methane molecule and completes the whole reaction with formation of NiO and CH_4 products.

The overall exothermicity of this reaction is calculated to be 61.1kJmol^{-1}. B3LYP/6-311+G(2d,2p) level gives the energy between intermediate Ni-HCOOH and transition state TS3 is 246.0kJ mol^{-1} which is the largerest in the whole predicted reaction path, the rate-controlling step therefore may be considered to be from intermediate Ni-HCOOH to intermediate O-NiCHOH via TS3.

Conclusion

A detailed reaction mechanism of CO_2 hydrogenation on Ni atom is carried out at B3LYP/6-311+G(2d,2p) level. The calculation predicts that this reaction involves the formation of some sorts of adsorbed formic acid complex, the exothermicity of overall reaction is calculated to be about 61.1kJ mol^{-1}, and the activation energy is calculated to be about 246.0kJ mol^{-1}. The rate-controlling step is predicted to be the step from intermediate Ni-HCOOH to intermediate O-NiCHOH via TS3.

Acknowledgments. This work is financially supported by the Key Project of National Fundamental Research and Development of China (973) (*No.* G1999022407), NNSF (*No.* 20243006), the Special Research Foundation of Doctoral Education of China (*No.* 2000061028), the Foundation of Science and Technology of Sichuan Province (*No.* 200018-16) and TRAPOYT(2002).

References

1. Nerlov J.; Chorkendorff I., *J. Catal*. **1999**, *181*, 271.
2. Tsuji M.; Kodama T.; Yoshida T.; Kitayama Y.; Tamaura Y., *J. Catal.* **1996**, *164,* 315.
3. Alexander M. M.; Hwang D.-Y., *J. Phys Chem.* **2000**, *104,* 11622.
4. Schild C.; Wokaun A.; Kaepper R. A.; Bauker A., *J. Phys.Chem*. **1991**, *95*, 6341
5. Fujita S.-I.; Nakamura M.; Doi T., *Appl Cata.l A: General.* **1993**, *104*, 87
6. Luis R.-S.; Mariona S.; Vicenc B., *J. Chem. Phys.* **1996**, *22*, 105.
7. Fornier R., *J Chem. Phys*. **1993**, *98*, 8041.
8. Barone V.; Adamo C., *J. Phys. Chem*. **1996**, *100*, 2094
9. Wang J.; Johnson B. G.; Boyd R. J., Eriksson L. A., *J. Phys. Chem*. **1996**, *100*, 63
10. Schild C.; Wokaun A., *J. Phys. Chem.,* **1991** *95*(16) *6341*

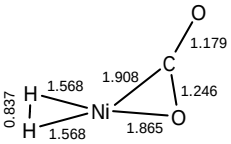

H_2-$NiCO_2$ (-274.7)

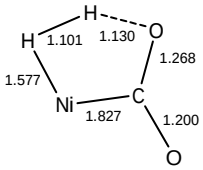

TS1 (-115.8)

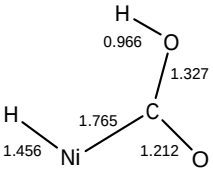

HNiCOOH (-211.0)

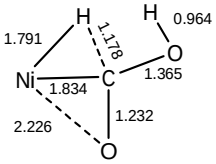

TS2 (-105.8)

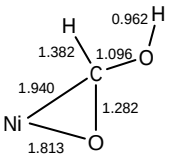

Ni-HCOOH (-162.4)

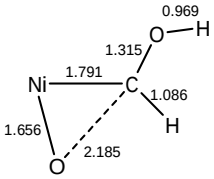

TS3 (83.6)

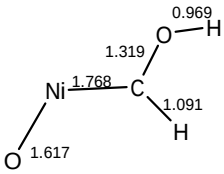

O-NiCHOH (53.9)

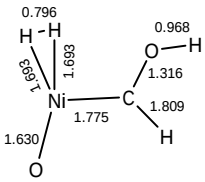

H_2-NiOCHOH (24.0)

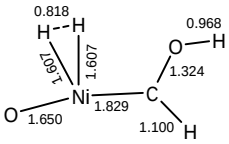

TS4(62.1)

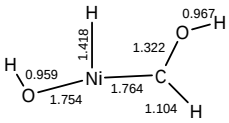

OH-HNiCHOH (-180.5)

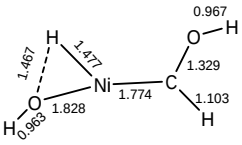

TS5 (-116.5)

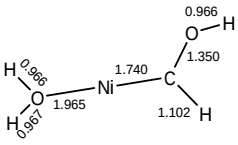

H_2O-NiCHOH (-188.2)

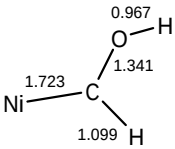

NiCHOH (-104.3)

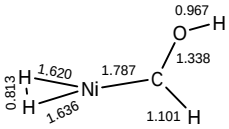

H_2-NiCHOH (-159.5)

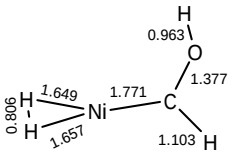

TS6 (-103.7)

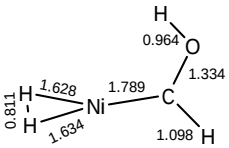

H_2-NiCHOH′
(-174.5)

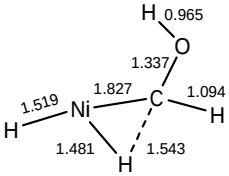

TS7 (-101.8)

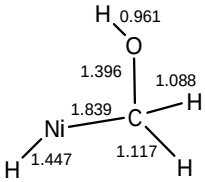

$HNiCH_2OH$ (-207.3)

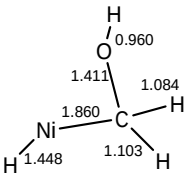

TS8 (-201.7)

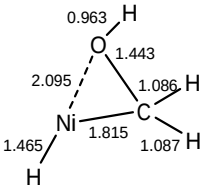

$HNiCH_2OH'$ (-235.0)

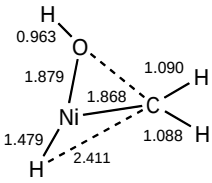

TS9 (-115.7)

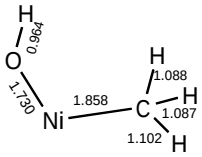

$HONiCH_3$(-318.2)

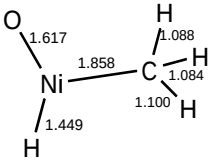

TS10 (-83.5)

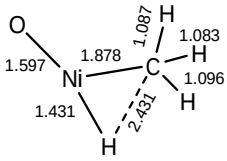

$ONiHCH_3$(-92.3)

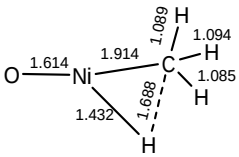

TS11 (-72.4)

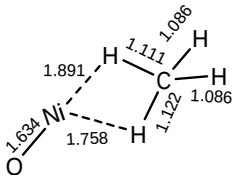

ONi-CH_4 (-121.8)

Products
NiO + CH_4+ H_2O

(-61.0)

Figure 1. Geometries of all species obtained at B3LYP/6-311+G(2d,2p) level along the Ni(d^{10} ^1S)+CO_2+$3H_2$→ NiO+CH_4+H_2O reaction. Bond lengths are in Å, and the ZPE corrected relative energies with respected to reactant [Ni(d^{10} ^1S)+CO_2+$3H_2$] given in kJ mol^{-1} are in parentheses.

The Use of Gasification Pitch and Coal Tar Pitch in Carbon Anodes

Uthaiporn Suriyapraphadilok, Colin Jennis-McGroarty, Adam Zel, and John M. Andresen

The Energy Institute
Pennsylvania State University
407 Academic Activity Building
University Park, PA 16802

Introduction

Carbon anodes are manufactured from calcined petroleum coke, butt fillers and coal tar pitch[1]. Since the demand of the coal tar pitch in the aluminum industry accounts for about 75% of the pitch market and the production of coal tars is rapidly decreasing in the United States as well as throughout the world, the development of alternative binders were considered in this work. Standard binder pitches are obtained from coal tars that are the by-product of bituminous coal coking process used to make coke for blast furnaces in iron production. Coal tars are then distilled to produce distillate products and a residue that is coal tar pitch. Coal tar pitch is mixed with calcined petroleum coke, and recycled anode butts. Petroleum coke is the by-product from the delayed coker in a refinery. Delay coking is a severe thermal cracking process of heavy feedstocks such as vacuum residue. The residue is converted into valuable light products and a by-product petroleum coke. This green coke is then calcined, i.e. heated to about 1250°C, in an inert atmosphere to remove all volatile matters. The mix of binder, filler and some additives are heated to about 50°C above the softening point of the pitch, typically 160°C. This temperature is sufficient to enable the pitch to wet the carbon particles.[3] The mix is then either extruded, vibrated or pressed to form a green anode. The wetting of coke by pitch is very important to the anode property. The pitch has to flow over the coke surface and has to enter into the surface porosity to generate a cohesive paste. Quinoline insolubles or QI play an important role in filling the spaces between petroleum and recycled anode coke particles on which the pitch is supported and prevent the pitch from fully penetrating the pores of the coke particle.[3] It is generally accepted that pitches with up to 15 %wt QI yield better anodes.[4]

The demand of the coal tar pitch in the aluminum industry is accounted for about 3/4 of the pitch market.[5] However, the production of coal tars is rapidly decreasing in the United States as well as throughout the world.[6] Therefore, the development of alternative binders from coal gasification pitches are considered in this work. Gasification pitches are distilled by-product tars produced from the coal gasification process. Since gasification pitches have low QI, it is of interest to mix the gasification pitch with the higher QI coal tar pitch. This would give a flexibility and sustainability to the development of the anode production in the future. The optimum use of pitches and coke is studied in this work to obtain the maximum baked density of the anodes.

Experimental

Materials. There are two types of pitch used in this study: coal tar pitch (CTP) and gasification pitch (GP). Two gasification pitch were used, namely GP 1 and GP 2 with softening points close to a standard coal tar binder pitch.

Petroleum coke and recycled anode butts were crushed and aggregated into three different: (i) Fines: >200 Tyler mesh size; (ii) Intermediate: 60-200 Tyler mesh size; and (iii) Coarse: <60 Tyler mesh size

Optimum Composition. The optimum size distribution of the aggregate (filler) was first determined. Laboratory-scale anodes were made at different size distributions using petroleum coke by keeping the ratio of pitch and coke constant. After the optimum size distribution of the aggregate had been obtained, this distribution was fixed and the amount of binder was varied to optimize the final anode properties.

Mixing and Forming. The aggregate fillers and binders, which weigh about 15 grams in total, were mixed at about 160°C. The CARVER cylindrical mold with an inside diameter of 28.58 mm is preheated to 110-120°C. The hot mix is placed into the mold and rapidly pressed at 9,000 psi for 3 minutes. The final green anode is cylindrical in shape with typically 28.60 mm. in diameter and 13.00-14.00 mm in height.

Baking. The green anodes are baked with a low heating rate to about 1075°C over a period of 5-6 days prior to cooling. The temperature profile is 25°C/hr from 25°C to 575°C and 3.5°C/hr from 575 to 1075°C. The anodes are baked between temperature of 950 and 1075°C for 6 hours and are cooled down in the furnace.

Apparent Density. The apparent densities of both green and baked anodes are calculated using the diameter and height measurement. The amount of pitch loss after baking is calculated by assuming that all the weight loss is resulting from the pyrolysis of pitch. Finally, the volume change of the baked anodes relative to the green ones are calculated.

Results and Discussion

Size Distribution. The optimum size distribution of the aggregate was obtained experimentally. The ratio of fines:intermediates:coarse was 40:35:25. This ratio was held constantly for all anodes studied in this work.

Optimum Pitch Content. **Figure 1** shows the apparent densities of green anodes at various percentages of pitches. The ratio of Butt:Coke is about 3:5 for all compositions. It is shown that all pitches used here represented similar trends where GP 1 gives the best densities and followed by GP 2 and CTP, respectively.

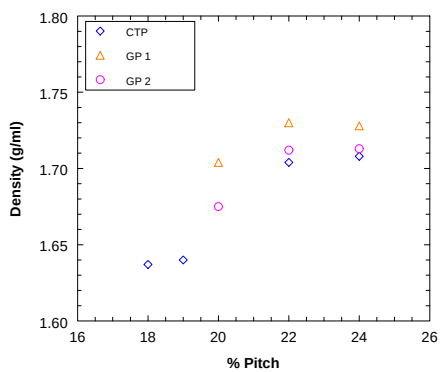

Figure 1. Apparent densities of green anodes at various percentages of pitches. Three different types of pitches are demonstrated: CTP, GP 1 and GP 2

The optimum percentage of pitch for the laboratory setup was found to be 22% somewhat higher than that used by the industry. The pitch concentration of laboratory mixes was a few percentages higher than in a commercial mix due to the finer size particles of the filler for the smaller diameter anodes (< 2 inch) used in this study.[3] The results indicate that the gasification pitch forms a denser green anode than that obtained by a standard coal tar binder pitch. Presumably, the gasification pitch has better wetting ability towards the coke filler particles and is able to penetrate further into the pores of the coke.

Pitch Mixture. Gasification pitch and coal tar pitch were mixed at various percentages while maintaining the total pitch content of 22%. Butt and coke compositions and their size distribution were also held the same as above. Figures 2 and 3 show the apparent densities of the green and baked anodes from the CTP + GP 1 and CTP + GP 2 mixtures, respectively.

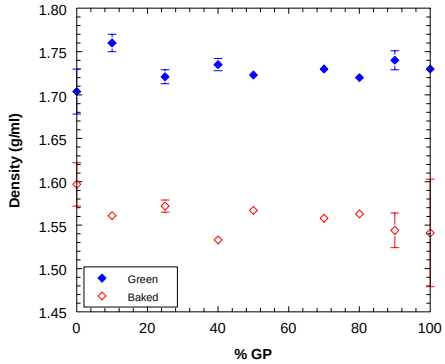

Figure 2. Apparent densities of green and baked anodes: 22% Pitch (CTP and GP 1); 29% Butt; and 49% Coke. The error bars show the standard deviations of each experimental set.

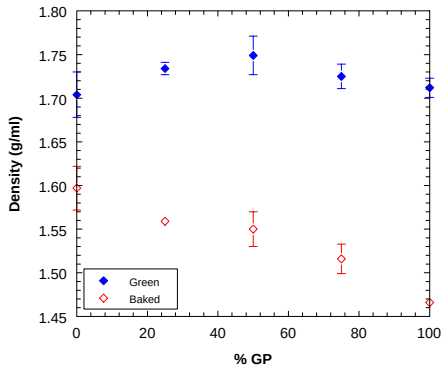

Figure 3. Apparent densities of green and baked anodes: 22% Pitch (CTP and GP 2); 29% Butt; and 49% Coke. The error bars show the standard deviations of each experimental set.

For both mixtures the addition of gasification pitch give an improvement in the apparent densities of the green anodes. For GP1 the green apparent density increases from 1.70 g/cm^3 for SCTP only to about 1.74 g/cm^3 for the GP1 only (Figure 2). Similar results were observed for GP2 (Figure 2). However, this trend does not keep up for the densities after baking. For the GP1 there is a slight reduction in the baked density from 1.60 g/cm^3 for the SCTP to 1.55 g/cm^3 for the GP1 only. For the GP2 there is a significant reduction in the baked density from 1.60 g/cm^3 for the SCTP to 1.46 g/cm^3 for the GP1 only.

The measurements indicate that the main factors for the reduction in baked density is due to increased loss of binder and increased volume during baking as shown in Table 1. The pitch loss was defined as reduction in anode weight over initial pitch content (22%) since the weight loss of the coke material can be neglected. For the baked anodes with increasing GP content the pitch loss increases from 27.9% for SCTP to 46.2% for GP1 only and 53.2% for GP2 only. Also, for most of the GP mixtures a increase in the volume was observed that was not the case for the SCTP (Table 1).

The reason of the high loss of pitch content in the anodes with higher gasification pitch concentration may result from the lack of QI as well as difference in molecular composition. The QI plays a very important role in how pitches perform excellent binder functions, i.e. wetting and penetrating petroleum coke particles during mixing and forming, and bridging between pitch-coke particles during baking.[3] Although the importance of QI is well established, the optimum amount of QI in binder pitch is still not clear.[3] Because pure gasification pitch gives higher apparent green density, it can be hypothesized that this type of pitch wet and penetrate petroleum coke better than SCTP. However, gasification pitches need to be optimized in terms of pitch loss prior to commercial interest. The results indicate that reducing the gasification pitch loss below 40% could make a binder pitch that can compete with SCTP in terms of density.

Table 1. Volume Changes and Amount of Pitch Losses of Baked Anodes: CTP + GP 1 and CTP + GP 2 pitch mixtures.

CTP + GP 1			CTP + GP 2		
% GP	$\frac{\text{Baked Volume}}{\text{Green Volume}} \times 100\%$	% Pitch Loss*	% GP	$\frac{\text{Baked Volume}}{\text{Green Volume}} \times 100\%$	% Pitch Loss*
100	100.65	46.18	100	102.4	53.2
90	102.60	41.33			
80	99.69	41.92			
70	102.21	35.56	75	101.5	48.3
50	102.11	31.65	50	103.5	37.2
40	103.33	33.33			
25	101.82	31.27	25	103.3	31.9
10	105.33	29.53			
0	100.02	27.91	0	100.0	27.9

* reduction in anode weight over initial pitch content

Conclusions

Anodes with pure gasification pitches gave higher apparent green densities than those with pure coal tar pitch. However, baked anodes with gasification pitches lost higher pitch content compared to the anodes with coal tar pitch. This effect was assigned to the effect of reduced QI with increasing gasification pitch content as well to structural differences between the pitches. It seemed that gasification pitch could wet and penetrate petroleum coke very well but it is poor remaining in the anode during baking. This resulted in a high loss of pitch content in baked anodes. The results indicate that reducing the gasification pitch loss below 40% could make a binder pitch that can compete with SCTP in terms of density.

Acknowledgement. The authors would like to thank Kopper Industries and.Sasol CarboTar for the coal tar pitch and gasification pitches, respectively, and Alcoa for the calcined petroleum coke and recycled carbon anode butt material.

References

1. Weng, T. L., and Vera, V. M. *Light Metals* **1984**, 1005-1013.
2. Gary, J. H. Petroleum Refining Technological and Economics; 4th ed.; Marcel Dekker, Inc: New York, 2001.
3. Gray, R. J., and Krupinski, K. C. In Introduction to Carbon Technologies; Marsh, H., Heintz, E. A., and Rodriguez-Reinoso, F., Ed.; Secretariado de Publicaciones, 1997, pp 329-424.
4. Grjotheim, K. a. W., B. J. In Aluminum Smelter Technology; 2nd ed.; Aluminum-Verlag: Dusseldorf, 1988, pp 75-118.
5. CRU International, Carbon Products – Aluminum Raw Materials, London, U.K., May 2002.
6. Rusinko, F., Andresen, J.M. and Adams, A., Ch. 13 in Great Lakes Carbon Corp. 6th Carbon Conf., Sept. 26-28, 2000, Houston, USA.

MEASUREMENTS OF HCFC-142b HYDRATE PROPERTIES RELATING TO THE SEPARATION FROM ITS MIXTURE

Fumio Kiyono, Hideo Tajima, Keiichi Ogasawara and Akihiro Yamasaki

Institute for Environmental Management Technology
National Institute of Advanced Industrial Science and Technology
16-1, Onogawa, Tsukuba, Ibaraki, 305-8569 Japan

Introduction

So far many kinds of fluorocarbone have been used as foaming agents in industry. Until mid of 1990, CFC-11 had been utilized and from mid of 1990, owing to the Global warming problem, HCFC-141b or HCFC-142b has replaced CFC-11. Now, industry begins to use HFC-245fa or HFC-134a, whose ODP is Zero, instead of HCFC. These foaming materials have been provided as heat insulating materials. Thus, wastes of insulating materials include many kinds of fluorocarbon, and in addition, replacement by air progresses in it. To recover a specified kind of fluorocarbon from the wastes, separation of the fluorocarbon from their mixture or that from the air mixture is necessary.

Fluorocarbons are classified according to its van deer Waals diameter in Table 1. Almost all kinds of fluorocarbon can make hydrates if they contact with water under specific temperature and pressure conditions. There are two types of crystal in hydrates. Molecules whose van deer Waals diameter is less than 55 nm make Type I crystals, while that whose van deer Waals diameter is more than 55 nm make Type II crystals.

Table 1. van der Waals Diameter of each Fluorocarbon

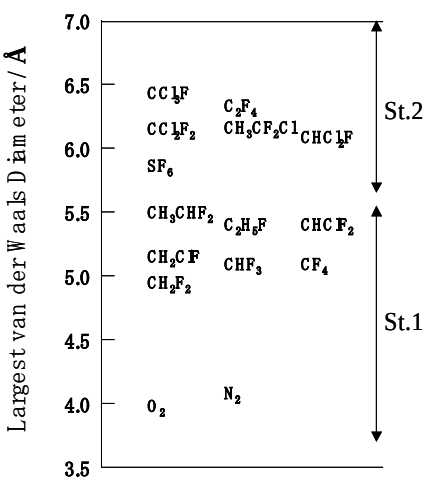

If mixed gases composed of two components whose condition of forming hydrates is different, the molecules which are likely to make hydrates tend to exist in the hydrate phase at high ratio. By repeating formation and dissociation of hydrates we can increase the ratio of the specific component in the hydrates and finally obtained pure substance. In this report HCFC142b is adopted as the representative of fluorocarbones.

Experimental Apparatus and Method

The apparatus used in this experiment is illustrated in Fig.1. The heart of this apparatus was a cylindrical cell made by TAFMAX-V glass whose volume was approximately 300 cm3 and maximum pressure was 1.0 MPa. To reduce the necessary time for reaching an equilibrium state, the cell was equipped with a stirrer (Nitto, S200) driven magnetically from the outside of the cell. It was also equipped with a cooling tube to help the nucleation of hydrates. By cooling the interface between liquid and vapor phases, the hydrates nucleation can be initiated. A gas supply, a vent and a vacuum line were connected to the cell. For evacuation a vacuum pump (Edwards, E2M1.5) was used. The whole cell was immersed in a water-ethanol bath whose temperature was controlled by a constant temperature circulator (EYELA, PCC-7000). The circulator enabled the bath temperature to vary with a maximum rate of 1.0K/min.

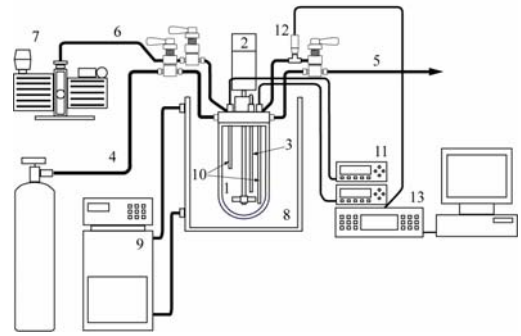

Figure 1. Experimental apparatus for Measurements of HCFC-142b Hydrate Properties

The actual temperature in the cell was measured by platinum resistance probes with thermometers (Hart Sci., 1502A). The probes were calibrated such that deviation from the secondary national standard was within 0.02K. A pressure transducer (Drug, PDCR902, 0.5MPa) and a pressure indicator (Drug, DPI145) were used for equilibrium pressure measurement with claimed accuracy of 0.025% of reading. To minimize the temperature drift of the pressure transducer, room temperature was always kept at 293K.

Tap water was deionized, distilled, purified by an ultrapure water system (Millipore, Milli-Q) and finally provided to experiments. HCFC-142b with stated purity of 99.98 wt% was supplied by Takachiho chemical (Japan).

For the measurement of H-L_w-V equilibrium line, the cell containing about 100cm3 of water was evacuated until the system pressure was almost equal to vapor pressure of water, and then charged with HCFC-142b up to about 0.2MPa. This procedure was repeated three times. After the cell was pressurized by HCFC-142b up to proper pressure with carefully avoiding liquefaction, the cell and inner contents were cooled down to specified temperature. Then hydrate nucleation was induced by injecting liquid nitrogen to the cooling tube. Once phase transformation from false V-L_w two-phase coexistence to H-L_w-V coexistence started, pressure spontaneously approached to the equilibrium pressure. During the phase transformation mixing was continued for six hours. After the mixing was stopped, the cell was placed stationarily for at least eight hours. Then the pressure was adopted as the equilibrium pressure at the specified temperature.

Model

Liquid Phase Model and Vapor Phase Model. To predict the H-Lw-V equilibrium condition a liquid phase and a vapor phase model are necessary in addition to a hydrate phase model. In this research, Soave-Redlich-Kwang equation of state and MHV2 mixing rule were adopted for this purpose. In the MHV2 mixing rule, the van der waals parameter *a* and *b* are obtained by solving the equation

$$q_1\alpha + q_2\alpha^2 = \sum_{i=1}^{c} x_i\left(q_1\alpha_i^0 + q_2\alpha_i^{0^2}\right) + \sum_{i=1}^{c} x_i \log\gamma_i + \sum_{i=1}^{c} x_i \log\frac{b}{b_i^0} \qquad (1)$$

where α is defined by

$$\alpha = \frac{a}{bRT} \qquad (2)$$

x_i represents mole fraction of component i, γ_i is the activity coefficient, q_1 and q_2 denote constants whose values are $q_1 = -0.478$ and $q_2 = -0.0047$ respectively, and the superscript 0 refers to the pure substance.

The activity coefficient γ_i can be calculated by using UNIQUAC model. To apply UNIQUAC model to the activity coefficient calculation we must determine so called UNIQUAC parameters of each molecule. These are the van der Waals volume parameter r_i, the van der Waals area parameter q_i, and the interaction parameter τ_{ij}. The values of r_i and q_i are determined from the geometrical data of each molecule.

Hydrate Phase Model. As for a hydrate phase model, we adopted von dear Waals & Plattuuew model.

$$\mu_w^H = \mu_w^\beta - RT\sum_{i=1}^{2} \nu_i \log\left(1 + C_i f_1^H\right) \qquad (3)$$

In equation (3) the constant C represents the langmuir constant and is given by equation (4).

$$C_{j_k} = \frac{4\pi R_c^3}{k_b T}\int_0^1 \exp\left(-\frac{\tilde{\omega}\left(r^*\right)}{k_b T}\right) r^{*2} dr^* \qquad (4)$$

Here, ϖ is the cell potential and is given by equation (5).

$$\tilde{\omega}\left(r^*\right) = 2z\varepsilon\left\{\frac{\sigma^{*12}}{r^*}\left(\delta^{10} + a_c^*\delta^{11}\right) - \frac{\sigma^{*6}}{r^*}\left(\delta^4 + a_c^*\delta^5\right)\right\} \qquad (5)$$

Here, σ and ε are Kihara potential parameters which express the interaction between molecules. To determine these values regression procedure is necessary. σ indicates the position where the interaction became zero, and ε expresses the depth of the potential well.

Experimental Results and Determination of Molecular Parameters of HCFC-142b

UNIQUAC Parameters of HCFC-142b. Table 2 summarized the values of the UNIQUAC parameters of HCFC-142b and water. These values were obtained by the regression of Carey's V-L data[1]. Figure 2 shows the comparison between calculated and experimental values.

Table 2. UNIFAC Parameters of HCFC142b and Water

r_{142b}	2.678
q_{142b}	2.488
r_{H2O}	0.920
q_{H2O}	1.400
$\tau_{142b-H20}$	1649.606
$\tau_{H20-142b}$	474.884

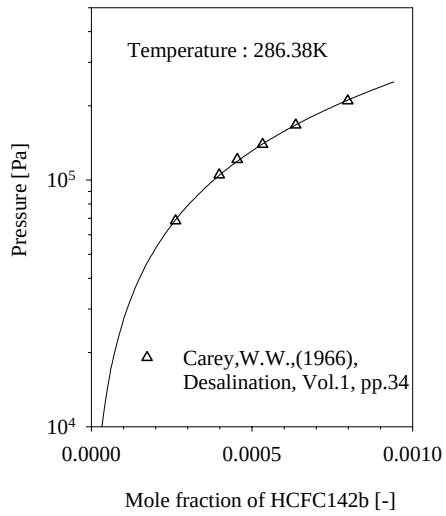

Figure 2. Solubility of HCFC142b in water

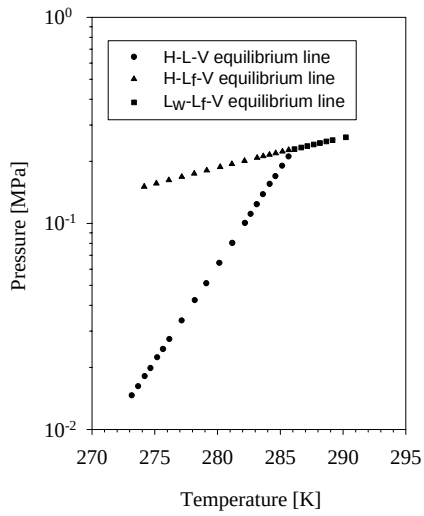

Figure 3. Three phase equilibrium lines of HCFC142b hydrates

Table 3. Kihara Potential Parameters of HCFC-142b

Core radius a	4.6020E-11
Distance parameter σ	4.1969E-10
Depth of potential well ε/k	699.99

Kihara Potential Parameters of HCFC-142b. The whole results of equilibrium measurement are plotted in Figure 3. The values of Kihara potential parameters determined by the regression method were summarized in Table 3.

References

(1) Carey, W.W., Desalination, **1966**, 1,34.

THE INFLUENCE OF IRON ON AMMONIUM ION GENERATION FROM NITRATE ION IN LIQUID PHASE

Youhei Kinoshita, Naoki Okumura*, Kazunori Takashima*, Shinji Katsura* and Akira Mizuno***

*Department of Ecological Engineering,
Toyohashi University of Technology
1-1, Hibarigaoka, Tempaku-cho, Toyohashi, Aichi, 441-8580, Japan
**Institute for Molecular Science,
Okazaki National Research Institute
38, Nishigo-Naka, Myodaiji, Okazaki, Aichi 444-8585, Japan

Introduction

Flue gas cleaning using non-thermal plasma process has been intensively studied and we have tried the NO_X and SO_2 removal process using the wet-type plasma reactor[(1)-(4)]. In this system, NO is oxidized to NO_2 and absorbed as NO_3^- while SO_2 is absorbed as SO_3^{2-} and oxidized in the liquid to SO_4^{2-}. But after the reaction, the pH value of the liquid became acidic and the absorption of NO_X and SO_2 was inhibited. Then, alkalization of the liquid was required. We tried the reduction reaction of NO_3^- to NH_4^+ using discharge above the level of the liquid, then the pH value of the liquid changed to alkaline. It has been reported that NO_3^- in liquid phase can be reduced to NH_4^+ using electrolysis [(5)(6)], and the wet-type plasma process can probably be more efficient [(7)(8)]. The objective of this study is to develop an efficient NH_4^+ generation method from NO_3^- to alkalize the liquid. HNO_3 solution was used and the reduction reaction of NO_3^- to NH_4^+ was tested.

Experimental

NH_4^+ generation from NO_3^- using the discharge plasma was tested using HNO_3 solution. Figure 1 shows the reactor for the discharge above the level of the liquid. A metal plate was placed at the bottom of the reactor as the ground electrode. A steel needle was placed 5 mm above the level of the liquid surface as the high voltage electrode and covered with a silicone tube (I.D.:4mm, O.D.:8mm) up to 2mm from the tip of the needle. Streamer discharge was generated between the tip of the needle and the suface of the liquid. It is well known that NO is effectively oxidized to NO_2 by gas phase plasma chemical reaction, and absorbed by water since NO_2 is soluble. This reactor was used because the discharge above the level of the liquid promotes the gas phase plasma chemical reactions, and the radicals generated in the gas or on the liquid surface are absorbed in the liquid to promote chemical reactions in the liquid. The reactor was driven by 250Hz square wave pulsed high voltage. The discharge power and waveform were measured by a digital power meter (HIOKI 3168) and an oscilloscope (TECTRONIX TDS 644A) respectively. NO_3^- and NH_4^+ concentration before and after the experiment were measured using an ion chromatograph (Metrohm Compact IC-731). Fe^{2+} and Fe^{3+} concentration were measured by colorimetric analysis of 1.10 phenanthroline.

Three types of metal plate, aluminum, platinum and iron were tested as ground electrode to investigate the influence of the metal types. Fifty mL of NO_3^- solution was used as the sample solution. The discharge above the level of the liquid was a streamer discharge. Ar gas was introduced into the gas phase of the reactor at a constant rate of 0.5L/min.

We checked the influence of Fe ion (Fe^{2+} and Fe^{3+}) and initial pH values to generate NH_4^+ from NO_3^-. Fifty mL of NO_3^- and Fe^{2+} sulution was prepared by dissolving Fe powder of less than 150 μm of diameter in HNO_3 solution. This solution is then filtered out through a paper that can let out particles less than 5 μm of diameter. The initial pH value of the liquid was adjusted by HNO_3 and KOH solutions. Pt plate was used as the ground electrode.

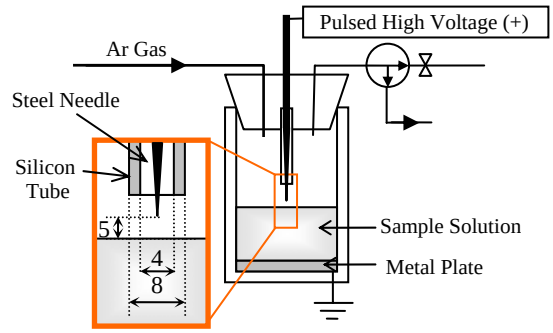

Figure.1 Plasma reactor for discharge above the level of the liquid

Results and Discussion

NO_3^- generation from N_2 and O_2 gas using the discharge above the level of the liquid As the background, NO_3^- generation from N_2 and O_2 gas using the discharge above the level of the liquid was studied. Figure 2 shows the experimental results of the time evolution of NO_3^- and NH_4^+ concentration using the discharge above the level of the liquid. Air at room temperature was used as the gas phase. The platinum plate, which showed low reactivity, was placed as the ground electrode. To remove the dissolved oxigen and nitrogen, 50mL of the pure water was used after 20min of cavitation. The discharge power and the peak voltage were 10W and 10kV respectively. In these conditions, NH_4^+ was not generated and the NO_3^- concentration increased with the time. Because room air was used as the gas phase, NO_3^- might have been generated from N_2 and O_2 gas by the discharge.

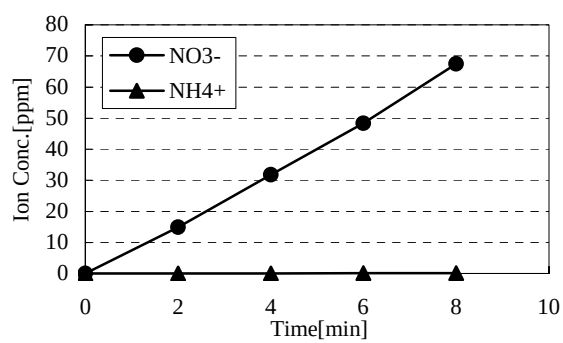

Figure 2. NO_3^- generation using discharge above the level of the liquid (Ground electrode: platinum, Gas phase: Room Air Batch, 10W, 10kV)

Discharge above the level of the liquid using Ar gas flow To eliminate the possibility of NO_3^- generation from N_2 and O_2 gas, Ar gas was fed to the reactor instead of room air. The reactor was filled with Ar gas flowing for few minutes before starting each experiment. Figures 3 and 4 show the NH_4^+ concentration and the pH value for different initial pH values. The discharge power and the peak voltage were 10W and 10kV respectively. NH_4^+ was generated using the discharge with Fe plate as the ground electrode for all the initial pH values (4, 7 and 10). The acidic condition was more effective for the NH_4^+ generation, better than neutral and alkaline conditions. But when aluminum and platinum plate were used, NH_4^+ was not generated for any initial pH values. When NH_4^+ was generated, the

pH value decreased. On the other hand, when the plasma discharge was not applied, NH_4^+ was not generated for none of all the types of electrodes. These results suggested that NH_4^+ was generated from NO_3^- in the case of discharge plasma and Fe plate as the ground electrode with the consequent alkalization of the solution.

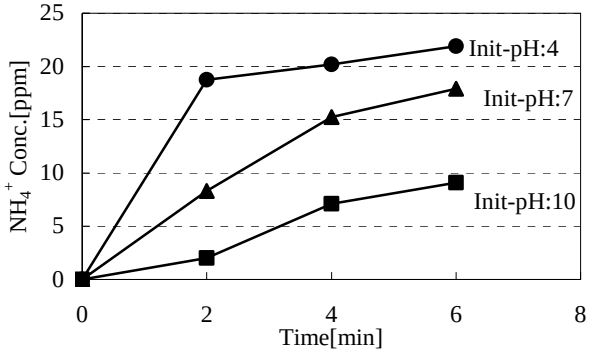

Figure 3. NH_4^+ generation using discharge above the level of the liquid for different initial pH values (GND: Fe plate, Gas: Ar flow 0.5L/min, 10W, 10kV)

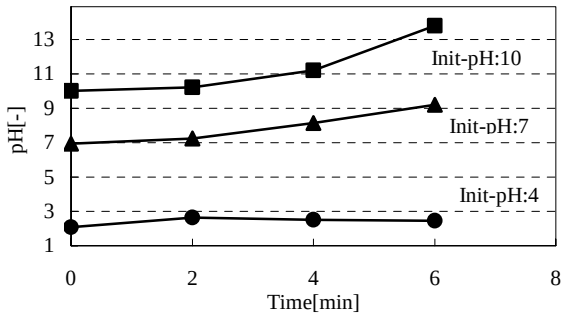

Figure 4. pH values using discharge above the level of the liquid (GND:Fe plate, Gas phase: Ar flow 0.5L/min, 10W, 10kV)

Influence of Fe ion (Fe^{2+} and Fe^{3+}) In the previous experiments, NH_4^+ was only generated when using Fe plate and the discharge above the level of the liquid, then, we checked the influence of Fe ion (Fe^{2+} and Fe^{3+}) to generate NH_4^+ from NO_3^-. Figure 5 shows Fe^{2+} and Fe^{3+} concentration in the acidic solution conditions when NH_4^+ was generated using the discharge above the level of the liquid. The discharge power and the peak voltage were 10W and 10kV respectively. When Fe^{2+} was present in the liquid, NH_4^+ was generated and Fe^{2+} was oxidized to Fe^{3+}. When only Fe^{3+} was present in the liquid, NH_4^+ was not generated and Fe^{3+} concentration did not change. The results showed that the reduction of NO_3^- to NH_4^+ was associated to the oxidation of Fe^{2+} to Fe^{3+}. Fe^{2+} was required to generate NH_4^+ from NO_3^-, and the pH value of the liquid is an important parameter. So the effect of the initial pH value was also tested. The pH value was set in 4, 7 and 10 and controlled by the addition of KOH solution. NH_4^+ was generated for all the pH conditions and Fe^{2+} was oxidized to Fe^{3+}. The pH value always increased after the discharge for all the initial pH values.

Conclusions

From the experimental study of the discharge above the level of the liquid, the following conclusions were obtained:

(1) NH_4^+ can be generated from NO_3^- conversion using the discharge in the presence of Fe in liquid solution. When platinum and aluminum plate were used as ground electrode, NH_4^+ was not generated.

(2) NH_4^+ generation from NO_3^- is related to the oxidation of Fe^{2+} to Fe^{3+}.

(3) The discharge converts NO_3^- to NH_4^+ changing the pH to alkaline levels.

These results suggest that the alkalized reaction by the discharge above the level of the liquid is possible and the wet type plasma reactor is effective for NO_X and SO_2 removal with the minimum consumption of water.

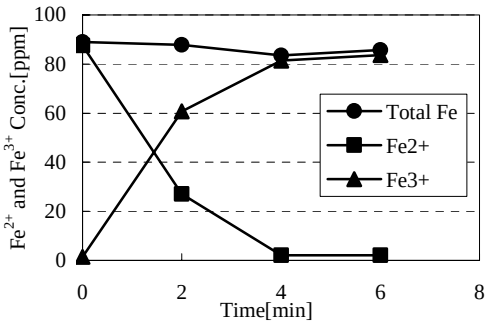

Figure 5. Fe^{2+} and Fe^{3+} concentration using discharge above the level of the liquid (GND: Platinum plate, Gas phase: Ar flow 0.5L/min, 10W, 10kV)

Acknowledgement.

The authors are very grateful for the valuable discussions given by Mr. Matsuda of Electric Power Development Co., LTD. The authors are also very grateful for the support by The 21st Century COE Program "Ecological Engineering for Homeostatic Human Activities", from the Ministry of Education and Culture, Japan.

References

(1) Akira Mizuno, J. S. Clements, and R.H.Davis, “Method for the removal of sulfur dioxide from exhaust gas utilizing pulsed streamer corona for electron energization”, IEEE Trans. Ind. Appl, Vol.22, pp.516-522, May/June 1986.

(2) R.Hackam and H.Akiyama, “Air Pollution Control by Electrical Discharges”, IEEE Trans.on Dielectrics and Electrical Insulation, Vol.7, No.5, pp.654-683, 2000.

(3) Akira Mizuno, Kazuo Shimizu, Tsutomu Matsuoka and Satoshi Furuta, "Reactive Absorption of NOx Using Wet Discharge Plasma Reactor", IEEE Trans. Ind. Appl, Vol.31, pp1463-1468, 1995.

(4) Hyun-Ha Kim, Chunxi Wu, Youhei Kinoshita, Kazunori Takashima, Shinji Katsura and Akira Mizuno, “The Influence of Reaction Condition on SO_2 Oxidation In a Discharge Plasma Reactor”, IEEE Trans. Ind. Appl, vol.37, pp.480-487, March/ April, 2001.

(5) Tsuyoshi Matsumura, Naohiro Goto, Hong-Ying Hu, Koichi Fujie and Toshiaki Tsubone, "Electrolytic Treatment of Nitrate in Wastewater" Journal of Japan Society on Water Environment, No.33, p.260, 1999.

(6) Tsuyoshi Matsumura, Mitsuru Iwasaki, Hong-Ying Hu and Koichi Fujie, ”Removal of Nitrite in Wastewater Using Metal Iron as Reductant”, Journal of Japan Society on Water Environment, No.32, p.84, 1998.

(7) Masato Kurahashi and Akira Mizuno, "Basic study of ammonia synthesis by discharge inside bubbles in solution", Journal of the Institute of Electrostatics Japan, pp.195-198, 1996.

(8) Keita Saito, Youhei Kinoshita, Naoki Okumura, Kazunori Takashima, Shinji Katsura and Akira Mizuno, "Reduction of NO_3^- on Wet Type Plasma Reactor Using Fe Electrode " Journal of the Institute of Electrostatics Japan, pp.117-118, 2002.

FTIR studies of acetylacetonates in supercritical CO_2 using a novel capillary cell: high pressure on a low budget

Matthew C. Henry, Clement R. Yonker

Battelle Pacific Northwest National Laboratory
P.O. Box 999
MS P8-19
Richland WA 99352

Introduction

One of the advantages of using supercritical carbon dioxide as an industrial solvent is the fact that its solvating power may be "tuned" by changing the pressure and temperature. Current spectroscopic techniques are able to explore a wide range of temperatures in SC CO_2, but the pressures that can be explored in conventional high-pressure spectrophotometer cells are typically limited to less than 1 kbar. Yonker and co-workers have reported using fused silica capillary cells in NMR to study pressures up to 5 kbar.[1] In this work, we extend the use of fused silica capillaries to Fourier-transform infrared (FTIR) spectroscopy.

Typical high-pressure IR cells are expensive and difficult to clean. Capillary cells are quite inexpensive (the price of a typical high-pressure cell could buy a sufficient length of capillary to make a thousand capillary cells). The low price allows studies in chemical systems too corrosive for conventional cells. Capillary cleaning is not an issue, since the cells are disposable.

The β-diketone 1,4 pentanedione (AcAc) and its trfiluoro (TFA) and hexafluoro (HFA) analogs shown in Figure 1 are commonly used chelating agents for solubilizing metal ions in supercritical CO_2. Supercritical CO_2 containing fluorinated acetylacetonate has been used for metal ion extraction.[2] The acetylacetonates are interesting because they exist in tautomeric equilibrium between keto and enol forms. The formation of an enolate anion is an intermediate step in the chelation of metal cations.[3] The equilibrium between keto and enol forms is of interest in predicting the chelating ability of acetylacetonates dissolved in SC CO_2.

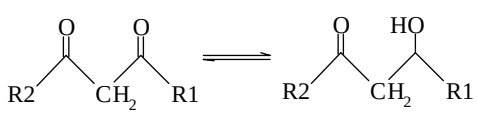

AcAc:R1=R2=CH_3
TFA: R1=CH_3, R2=CF_3
HFA: R1=R2=CF_3

Figure 1. The acetylacetonates used in this study

The enol form of the tautomer is favored by increasing fluorination (HFA>TFA>AcAc) and disfavored by increasing temperature.[1] The role of pressure in shifting the tautomeric equilibrium is uncertain. At low total pressures, the keto form was reported to be favored as pressure was increased.[4] Previous NMR studies show no detectable change in equilibrium with increased pressure.[1]

The pressure dependence of the equilibrium can be related to the change in partial molar volume between the keto and enol forms. The equilibrium constant K_{eq} is given by equation 1

$$K_{eq} = \frac{[enol]}{[keto]} \qquad \text{Eq. 1}$$

The equilibrium constant can be related to the partial molar volume by

$$\frac{\delta \ln K_{eq}}{\delta P} = \frac{-\Delta V}{RT} \qquad \text{Eq. 2}$$

where R is the ideal gas constant, T is the absolute temperature, and P is the pressure.

In this work we will focus on using the capillary cell to obtain information about the pressure equilibrium between the keto and enol forms of AcAc, since it is the prototype of this class of compounds and some literature values are available for lower pressures.

Experimental

Reagents. Acetylacetone was used as received from Aldrich. The carbon dioxide used was SFC grade (Scott Specialty Gases, Plumsteadville, PA).

Instrumentation. The experimental apparatus is shown in Figure 2. All tubing is 1/16-inch stainless steel. All valves and fittings between the CO_2 tank and V 3 are rated to 1.0 kbar, and all fittings after V3 are rated to 4.13 kbar. Valves and fittings were obtained from High Pressure Equipment Inc. (Erie, PA). Pressure was controlled using two syringe pumps. Pump SP1 was an Isco 260D syringe pump (Isco, Inc. Lincoln, NE) while pump SP2 was a High Pressure Equipment 10 cm^3 pressure generator. The pumps were operated in two stages to generate pressures up to 3.1 kbar. The system was pressurized using SP1 until the pressure reached the operation limit of 517 bar. Valve V2 was then closed and the system further pressurized using pump SP2. System pressure was monitored using pressure transducers PX1 and PX2.

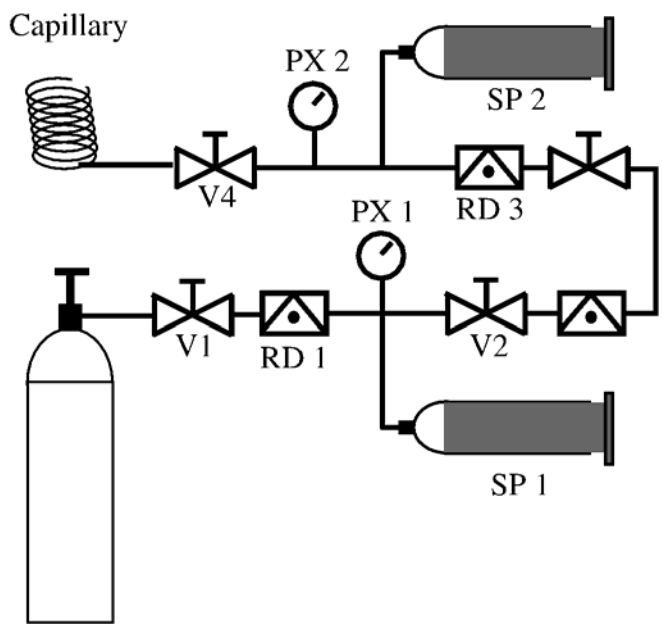

Figure 2. Experimental apparatus. V1-4: Valves, SP1-2 syringe pumps, RD1-3 rupture disks, PX1-2 pressure transducers.

Although the volume of CO_2 contained in the capillary represents a negligible hazard even at 3.1 kbar, the valves and piping contain enough CO_2 to present a safety hazard. All closed spaces within the experimental system are protected by appropriately sized rupture disks to prevent uncontrolled ruptures from occurring. Rupture disks RD1 and RD2 are rated to 586 bar, while RD 3 is rated to 4.0 kbar.

The sample cell used is a 1m length of 355µm OD, 103µ ID polyamide-coated fused silica capillary (Polymicro Technology, Pheonix, AZ). One end of the capillary was flame sealed using a jewelers torch. The exposed fused silica was coated with cyanoacrylate adhesive to protect it from damage. A 0.5-cm window was burned in the polyimide coating approximately 7 cm from the sealed end of the capillary and cleaned using isopropanol. The open end of the capillary was fitted into a Vespel ferrule (Alltech) and glued in place using cyanoacrylate adhesive. All capillary failures during experiments resulted from failures at the ferrule, rather than failure of the capillary itself. Best results were obtained when the adhesive on the ferrule was allowed to harden while the ferrule was compressed in the steel fitting.

The capillary was inserted into an aluminum heating-block and mounted on the microscope stage. The heating block was equipped with two 50W-cartridge heaters and two RTD temperature sensors. Temperature was maintained within 0.75°C by a temperature controller (Watlow; Winona, MN). The temperature can be adjusted between ambient temperature and 270 °C.

FTIR spectra were recorded on a Bruker IFS-66 spectrophotometer using and IRScope-I FTIR microscope equipped with a cryogenically cooled MCT detector. Data processing was carried out using the Bruker OPUS 3.2 software.

All spectra are the average of 1024 scans. The IR scope was equipped with a 34X, 0.4 NA IR lens and a 0.75mm aperture, producing an observed spot size of 50µm. The appropriate spot size was determined by acquiring blank spectra of a capillary containing only CO_2 with successively smaller apertures until a flat baseline was achieved. Too large an aperture produces artifacts due to focussing of the IR beam by the capillary.

Samples were loaded into the capillary using a vacuum fill technique. The open end of the capillary was inserted through a rubber septum into a sample vial containing the acetylacetonate. The open end of the capillary was held below the level of the liquid, while a syringe needle was inserted into the air space above the sample. The needle was withdrawn to create a slight negative pressure within the sample container. This negative pressure was maintained until enough air had been expelled from the capillary to allow the sample to fill a section of the capillary when the vacuum was released.

Results and Discussion

Representative spectra of CO_2, AcAc, and solutions of AcAc in CO_2 are shown in Figure 3. The fused silica capillary has a useable window in the mid-IR between 2000 and 4000 cm^{-1}, with some information available down to 1000 cm^{-1}. The region between 2000 and 4000 cm^{-1} includes the OH and CH stretch bands of the AcAc spectrum, along with the $\nu_1+\nu_3$ and $2\nu_2+\nu_1$ combination bands of the CO_2.

Figures 4A and 4B show the difference spectrum of AcAc in CO_2 (4A) and neat liquid AcAc (4B) at 33°C. Spectra were recorded as the pressure was varied between 0.1 and 3.1 kbar in increments of 35 bar between 0.1 and 0.35 kbar and in increments of 350 bar between 0.35 kbar and 3.1 kbar. As the pressure is increased, there is a decrease in intensity of the CH_2 (AS) band with concomitant increases in the intensity of CH and OH stretches associated with the enol form.

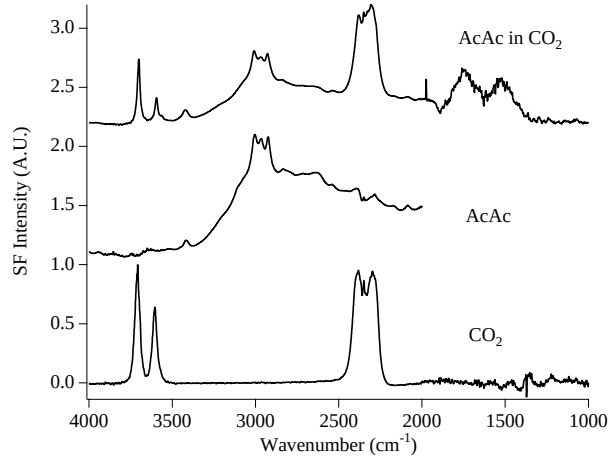

Figure 3. Representative spectra of CO_2, liquid AcAc, and liquid AcAc in CO_2. Spectra have been normalized and offset for clarity.

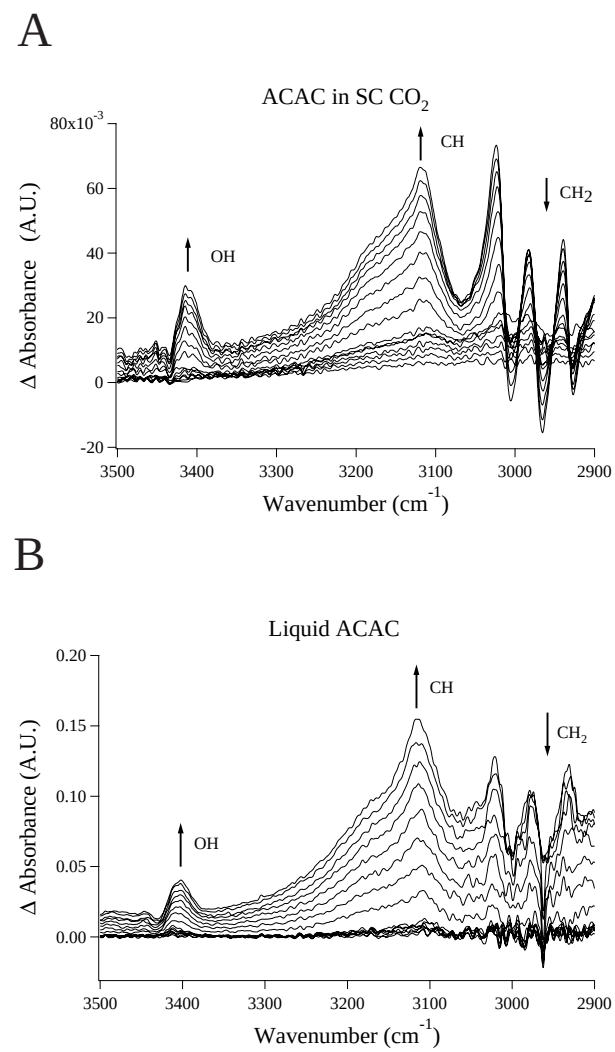

Figure 4. Difference spectra of AcAc in CO_2 (A) and neat liquid AcAc (B) at pressures between 0.1 and 3.1 kbar.

Figures 5A and 5B show the natural log of the ratio of OH to CH_2 peak areas. This ratio is proportional to K_{eq} as shown in Eq. 1. plotted as a function of pressure. The slope of this plot is proportional to the change in partial molar volume between the keto and enol forms of AcAc.

The ΔV value obtained for subcritical CO_2 is -10.88 ± 1.5 cm^3/mol. For supercritical CO_2 at 33°C and 66°C the values are -13.57 ±1.1 cm^3/mol and -15.99 ±1.4 cm^3/mol respectively. For neat liquid AcAc at 66 °C the value was -3.57 ± 0.1. This value is slightly lower than those previously reported for AcAc by Jouanne and Heidberg (-4.7 ± 0.7 for liquid AcAc at 62°C) at lower pressures by NMR.[4] The larger ΔV values obtained in sub- and supercritical CO_2 may indicate that intermolecular hydrogen bonding between molecules in the enol form results the formation of dimer and trimer species. Partial molar-volume values were not obtained for pure AcAc at lower temperatures because the AcAc was observed to freeze in the capillary at high pressure. The pressure-freezing behavior was only observed for the neat liquid samples.

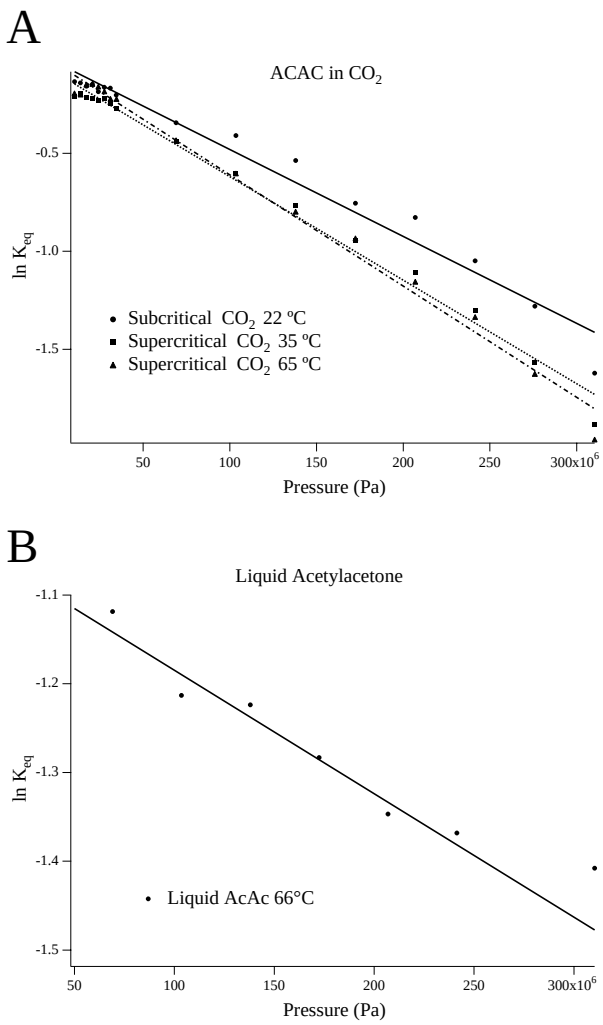

Figure 5. Equilibrium constant K_{eq} plotted as a function of pressure for AcAc in CO_2 (A) and for neat liquid AcAc (B)

Conclusions

We have demonstrated high pressure FTIR spectroscopy in a novel capillary cell. The cell allows acquisition of spectra at pressures of at least 3.1 kbar, significantly higher than the pressures accessible using conventional high-pressure IR cells. This cell has the potential to allow safe, low cost FTIR studies of a variety of industrially relevant processes in SC CO_2.

The capillary cell was used to study the pressure-dependent keto-enol equilibrium of acetylacetone, an important chelating agent for metals in SC CO_2. High pressure was found to increase the content of the enol form in the mixture. This implies that high pressures may be preferred for metal extractions using SC CO_2.

Partial molar volumes were calculated for AcAc as a neat liquid in sub- and supercritical CO_2. The partial molar-volume change between the keto and enol forms was smallest for the neat liquid, larger for subcritical CO_2, and largest for supercritical CO_2. This may suggest that intermolecular hydrogen bonding between enol forms occurs in SC CO_2.

Acknowledgement. Work at the Pacific Northwest National Laboratory (PnP) was supported by the Office of Science, Office of Basic Energy Sciences, Chemical Sciences Division of the US Department of Energy, under Contract DE-AC076RLO 1830

References

(1) Wallen, S. L.; Yonker, C. R.; Phelps, C. L.; Wai, C. M. *J. Chem. Soc., Faraday Trans.* **1997**, *93*, 2391-2394.
(2) Laintz, K. E.; Wai, C. M.; Yonker, C. R.; Smith, R. D. *Anal. Chem.* **1992**, *64*, 2875.
(3) Lin, Y.; Wai, C. M. *Anal. Chem.* **1994**, *64*, 311.
(4) Von Jouanne, J.; Heidberg, J. *J. Mag. Res* **1972**, *7*, 1-4.

$Na_9[PW_5Mo_4O_{34}]$ SOLUTION AS NEW ABSORBENT FOR COMBINED REMOVAL OF SO_2 AND NO_x

Rui Wang

Department of Chemical Engineering, Hainan University, Haikou, 570228, China

Introduction

The removal of SO_2 and NO_x from flue gas has long been a principal task for environmental protection. It is known that many methods have been developed for combined removal of SO_2 and NO_x, but each has unavoidable drawbacks to date. The ammonia reduction method requires high capital invest, moreover, leaking ammonia may cause secondary pollution. Alkaline solution absorption method is ineffective for NO removal. $CaCO_3$ containing yellow phosphorus emulsion is quite effective for simultaneous removal of SO_2 and NO_x, which may achieve conversions as 95% or higher for both, but this is achieved under successive consumption of absorbent.[1] Besides, methods concerning the use of electron beam irradiation or pulse corona, although proved to be effective, are far from practical application at present due to their very high equipment, operation and maintenance cost.[2] Hence, development of new method, effective and economical, without causing secondary pollution, becomes quite attractive.

In view of the reversible redox property and good chemical stability of heteropoly compound (HPC), using aqueous solution of HPC, the author developed a new liquid redox method for combined removal of SO_2 and NO_x.[3] In this paper, $Na_9[PW_5Mo_4O_{34}]$, a Keggin type HPC, was synthesized for such purpose. Characteristics of desulfurization and denitrification are the subject of this paper.

Experimental

Scheme of the experiment flow sheet could be found in literature.[4] Two multiorifice plate glass absorption reactors (hole diameter: 50~70μm) containing equal volume of absorbent solution were used in series to investigate the performance of the absorbent solution. The experimental data gained are the SO_2 and NO_x concentrations in the outlet gas stream. The HPC investigated in this study, namely $Na_9[PW_5Mo_4O_{34}]$, was synthesized and verified by ICP and IR. The feed gas stream with constant concentrations of SO_2 and NO_x, flowing at the rate of 0.5L/min, was prepared by mixing two gas streams of dilute SO_2/NO_x and pure nitrogen after passing through mass flow controllers. The SO_2 concentration was analyzed with a Dioxor II SO_2 detector. NO_x was prepared by addition of $NaNO_2$ solution drop by drop to dilute H_2SO_4 solution at a constant rate, the resultant NO_x was carried by nitrogen gas flowing at a constant rate. The NO_x concentration was analyzed by colorimetry. All other chemicals used were of reagent grade and deionized water was used throughout.

Results and Discussion

The conversions of SO_2 and NO_x increase markedly with the increase in absorbent concentration (Table 1). A favourable absorbent concentration can be recommended to be ca. 6.0×10^{-3} mol/L, corresponding to 97.6% and 90.7% for the conversions of SO_2 and NO_x respectively. The process for the removal of SO_2 tends to decrease when the absorption temperature increases from 30°C to 40°C, suggesting the effect of solubility decrease is predominant. While absorption temperature increases from 40°C to 50°C, the conversion of SO_2 shows a reverse tendency, indicating the predominant effect of the intrinsic chemical reaction between SO_2 and $Na_9[PW_5Mo_4O_{34}]$ (Table 2). As a whole, room temperature should be considered for the effective absorption of both SO_2 and NO_x.

Table 1. The Effect of Absorbent Concentration

$Na_9[PW_5Mo_4O_{34}]$, mol/L	Conversion (%)*	
	SO_2	NO_x
6.0×10^{-3}	97.6	90.7
1.2×10^{-3}	93.3	76.3
6.0×10^{-4}	65.9	44.8
1.2×10^{-4}	54.5	40.2

*$[SO_2]_{in}$=1394.2mg/m^3, $[NO_x]_{in}$=517.5 mg/m^3, T=30 °C, gas flow rate: 0.5L/min, volume of absorbent: 100mL, absorption time: 40min.

Table 2. The Effect of Absorption Temperature

T, °C	Conversion (%)*	
	SO_2	NO_x
30	93.3	76.3
40	87.2	75.4
50	88.9	70.1

*$[SO_2]_{in}$=1394.2mg/m^3, $[NO_x]_{in}$=517.5 mg/m^3; gas flow rate:0.5L/min; absorbent: 1.2×10^{-3}mol/L, 100mL; absorption time: 40min.

As to the effect of feed gas concentration, the emphasis in this study is on the role of SO_2/NO_x ratio. Hence, the feed gas SO_2 concentration was set to remain fixed whereas NO_x concentration varied. From the results listed in **Table 3**, it is apparent that the conversion of SO_2 keeps comparatively stable, regardless of the increase in NO_x concentration in the feed gas. Meanwhile, the conversion of NO_x is enhanced significantly. Accordingly, the favourable SO_2/NO_x ratio in the feed gas could be recommended as 1:1, using mg/m^3 as concentration unit.

Table 3. The Effect of Feed Gas Concentration

Feed gas conc., mol/L		Conversion (%)*	
SO_2	NO_x	SO_2	NO_x
1394.2	209.1	86.7	58.0
1394.2	517.5	85.8	70.5
1394.2	1015.5	86.0	76.8
1394.2	1394.1	86.3	77.6

* T=30 °C; gas flow rate: 0.5L/min; absorbent: 1.2×10^{-3}mol/L, 100mL; absorption time: 40min.

In order to improve the performance of the absorbent system, considering the acid property of SO_2 and NO_x to be treated, several buffering agents were added to $Na_9[PW_5Mo_4O_{34}]$ solution, which forms different absorbent systems comprising $CH_3COOH/NaOH$, NH_4Ac/HAc(Ac stands for CH_3COO^-) and NaAc/HAc in addition, respectively. Results shown in **Figure 1** prove that the desired enhancement effect exists only on the conversion of SO_2. Apparently, the removal of SO_2 was improved to a very agreeable extent, where all absorbent systems give a conversion of 100% or nearly 100%. In contrast, these buffering agents have no positive effect on the conversion of NO_x. On the contrary, the presence of them may cause more or less negative effects on the conversion of NO_x.

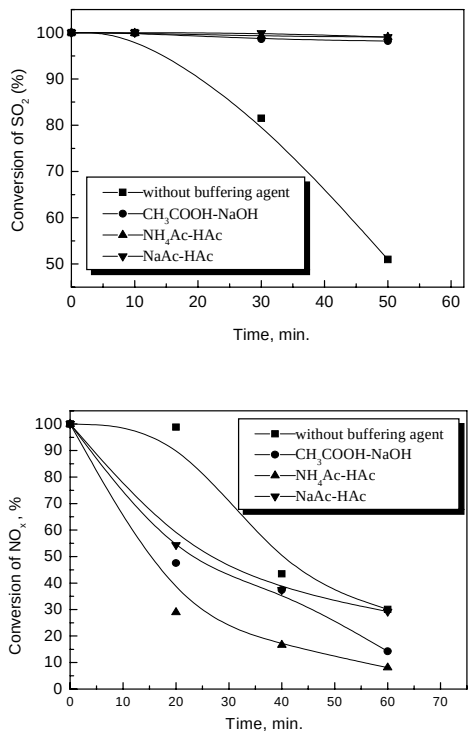

Figure 1. The effects of buffering agents on the performance of the absorbent system

Compared to NO_x, especially NO, SO_2 is quite soluble in water. Such difference can be magnified when the solution alkalinity is increased owing to the addition of buffering agents used herein. This is the reason for the marked difference between the removal of SO_2 and NO_x in the presence of buffering agents. As to the negative effect of buffering agents observed in the case of NO_x removal, it is likely that the redox property change of $Na_9[PW_5Mo_4O_{34}]$ caused by the alkalinity increase in the presence of buffering agents may be the cause. The process for combined conversion of SO_2 and NO_x can be illustrated as shown in **Figure 2**, where HPC_{re} and HPC_{ox} represent the oxidation and reduction form of HPC respectively.

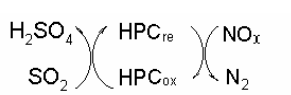

Figure 2. Principle of the process for combined removal of SO_2 and NO_x with HPC

The HPC used in this study is $Na_9[PW_5Mo_4O_{34}]$, which can be reduced from $Na_9[PW_5Mo(VI)_4O_{34}]$ to $Na_9[PW_5Mo(VI)_3Mo(V)O_{34}]$ easily. The latter can be oxidized back to the original. Thus, a sustainable process can be formed, where $Na_9[PW_5Mo_4O_{34}]$ is catalyst in nature. Such process is based on the redox property of HPC. As it is known that HPC possesses a higher redox potential in low alkalinity solution, increasing solution alkalinity is unfavorable to the conversion of both SO_2 and NO_x. Unlike NO_x, the solubility of SO_2 can be improved very considerably as solution alkalinity increases. This overwhelmes the negative effect caused by the decrease in redox potential of HPC. Hence, the results shown in **Figure 1** are the net effects.

Acknowledgement

This work was supported by the National Natural Science Foundation of China (Grant 20206006) and by Foundation for University Key Teachers, the Ministry of Education of China, under contract GG-530-10589-1001.

References

1. Chang, S. G.; Lee, G. C., *Environmental Progress*, **1992**, 11, 66-73.
2. Sun, J.; Bai, X. R.; Ba, Z. Z., *Environmental Science and Technology (Huanjing Kexue yu Jishu)*, **1992**, (2), 31-36
3. Wang, R., *Macro Review*, **2003**, 16, 135-140
4. Wang, R., *J. Fuel Chem. Tech.*, **2001**, 29, 360-366

OZONE OXIDATION OF SOLID DEPOSITS PRODUCED BY THE THERMAL STRESSING OF JET FUEL

R. Venkataraman, O. Altin, A. Piotrowski, S. Eser

Department of Energy and Geo-Environmental Engineering
and
The Energy Institute
The Pennsylvania State University
209 Academic Projects Building, University Park, PA 16802
*Email: sxe2@psu.edu

Introduction

Jet fuel serves as a coolant in military aircraft and it is exposed to higher temperatures before it is burned in the advanced aircraft because of increasing thermal loads. High thermal loads can lead to temperatures as high as 500°C on metal surfaces in the fuel delivery system. Exposure to such high temperatures accelerates the reactions of hydrocarbons and heteroatom species in jet fuel and results in the formation of carbonaceous deposits on metal surfaces. Rapid accumulation of solid deposits on various components of the fuel system, including valves, flow tubes, and nozzles would cause a catastrophic failure of the aircraft engine [1,2].

Temperature Programmed Oxidation (TPO) can be used to characterize the carbon deposits produced by the thermal stressing of jet fuel over various catalytic and non-catalytic substrates. Such characterization is based on the oxidation reactivity of the deposits, which is closely related to their structural morphology[2]. The high temperature and catalytic activity of the substrate may however produce some highly ordered deposits that are artifacts of the TPO analysis. To eliminate the possible complications with analyzing the carbon deposits at high temperatures, deposited substrates can be oxidized with ozone at low temperatures. A rationale for this approach is that ozone (O_3) has a strong oxidation capacity that can be attributed to its ability to form nascent oxygen or free oxygen radicals. This reactive species reacts with different types of carbon samples even at room temperature[3,4]. Thus it can be used for cleaning carbon deposited catalytic and non-catalytic surfaces through oxidation below 200 °C [3].

This study compares the characterization of carbon deposits produced from the thermal stressing of jet fuel by TPO of ozone oxidized samples to characterization by TPO alone.

Experimental

Thermal stressing experiments were carried out at super-critical conditions of 480 °C and 500 psig[1,5] in an isothermal, glass lined flow reactor of OD 1/4". The carbon deposits were collected over 13 cm X 3mm coupons of Ni; Fe/Ni- (55/45); Inconel 600 (composition wt%- Ni:72%, Fe:8%, Cr:15.5%, Mn: 1.0%, Cu:5000ppm, C:1500 ppm, Si:5000 ppm, S:150ppm)[6] stressed with JP-8 (military jet fuel) for 5, 5 and 2 hours respectively; SS321 (composition wt% is Ni:10.5%, Fe:68%, Cr:18%, Mn: 2.0%, C: 0.08%, Si:1%, S:10.03ppm, Ti: 0.6%) stressed with Jet A (commercial aviation) for 24 hours. and SS321 stressed with JP-8 (military jet fuel) for 24 hours respectively. The deposit morphology was studied using Scanning electron Microscopy (SEM) and characterized by TPO in a LECO Multiphase Carbon Analyzer and oxidation with ozone in a reactor connected to a UNIZONE™ LOX Praxair-Trailigaz Ozone generator. The carbon deposited samples were cut into 5cm coupons for the ozone analyses and placed in a quartz boat inside a reactor. During the analysis the sample was exposed to an ozone stream flowing at a rate of 250cc/min at a constant reaction temperature of 150°C. Ozone was produced by converting UHP Molecular oxygen in an ozonator using high voltage at about 19,000V and a conversion efficiency of about 3%. The concentration of the product gases were analyzed using a mass spectrometer and an IR detector. Following ozone oxidation, the samples were again characterized by TPO in the carbon analyzer.

Results and Discussion

As seen in Figure 1, the SEM images and TPO profile of the deposits produced by JP-8 stressed over Ni for 5 hours, suggest that solid deposits of varying oxidation reactivities are produced due to the high catalytic activity of Ni for dehydrogenation[5]. The SEM images show a significant decrease in the amorphous deposits formed over the nickel-sulfide crystals after oxidation using ozone. Comparing the TPO profiles of the sample, shows that the amount of ordered carbon deposits is nearly the same before and after ozone oxidation while most of the reactive deposits have been oxidized.

Figure 2 compares the SEM images and TPO profiles, before and after ozone oxidation of the carbon deposits produced by stressing JP-8 over Fe-Ni (55/45) for 5 hours. The SEM images clearly suggest oxidation, caused by a decrease in the amount of deposits and an increase in void spaces over the metal surface. A comparison of the TPO profiles of this sample before and after ozone oxidation shows that the latter oxidizes almost all the deposits present on the surface except leaving behind a small amount of the highly ordered species oxidizing around 780 °C. This maybe due to the significant Fe content in the substrate that shows high catalytic activity during carbon oxidation.

The thermal stressing of JP-8 over Inconel 600 for 2 hours produces only about 20 μg/cm^2 of carbon deposits, most of which are less ordered in nature as shown in the SEM images of Figure 3. Since considerably less deposits are produced over this sample, the difference in amount of deposits before and after ozone oxidation are not clearly revealed by SEM. As can be seen in the TPO profile of the deposits after ozone oxidation, the intensities of the low temperature and high temperature CO_2 evolution peaks is nearly the same. However the decrease in intensity of the high temperature peak, before and after ozone oxidation is about 1/4 of the decrease in intensity of the low temperature CO_2 evolution peak. The large split in the low temperature CO_2 evolution peaks after ozone oxidation suggests that TPO reflects the different types of deposits on the surface more distinctly with removal of some of the more reactive species.

Comparing the SEM images in Figure 4, we can see that the amorphous deposits produced by thermally stressing Jet A over the SS321 surface for 24 hours have been removed by ozone oxidation revealing the underlying layers of more ordered deposits, metal and metal sulfide crystals. The total carbon amount on the original carbon deposited sample is about 52 μg/cm^2. Ozone oxidation removes about 33 μg/cm^2 of solid deposits over the surface. The TPO profile of this sample also shows that the intensity of the peak at around 350 °C is almost eliminated after ozone oxidation whereas the intensities of the high temperature CO_2 peaks at around 550 °C and 580 °C respectively following ozone oxidation is greater than 50% of the original TPO profile. Since the profile of high temperature CO_2 peaks is nearly unaltered after a significant decrease in the low temperature CO_2 peaks, this suggests that the ordered carbon deposits are produced from thermal stressing and not as an artifact of the TPO analysis.

The CO_2 evolution profile during ozone oxidation, as recorded by a mass spectrometer connected to the output of the reactor suggested the presence of at least two types of carbon deposits over the samples since the rate of reaction initially increased during oxidation of the more reactive species or amorphous carbon deposits, then decreased as most of the less ordered carbon had been removed. At low temperatures the activation energy of the reaction isn't sufficient for the oxidation of the less reactive deposits even by ozone.

Any further increase in the temperature of the reaction caused decomposition of the ozone to molecular oxygen, which was undesirable. The difference in weight between a completely oxidized sample (after TPO) and an ozone oxidized sample confirmed the presence of remaining carbon deposition on the substrate after ozone oxidation.

Exposure to ozone removed about 90% amorphous carbon deposits at 150 ˚C. This temperature during ozone oxidation is very low to cause any structural changes through any thermal or catalytic reactions. The SEM images as shown in Figures 1-5 following ozone oxidation revealed some of the more ordered carbon structures. A very small, low temperature CO_2 peak but a significant high temperature CO_2 evolution peak during temperature programmed oxidation of the ozone-oxidized samples suggests that the less reactive carbonaceous deposits were formed on the substrate during thermal stressing of the jet fuel and not from secondary pyrolysis of the more reactive deposits during TPO as speculated.

The intensity of the high temperature CO_2 peaks in most of the ozone oxidized samples was lower than that of the original carbon deposited sample. This is probably due to the high reactivity of ozone, which along with the amorphous carbon may oxidize some of the more ordered structures. The temperature of CO_2 evolution of the less reactive carbon deposits following ozone oxidation was the same as that of the original TPO profile as shown in Figures 1, 2, 3, 4.

In Figure 5, however, the temperature of peak CO_2 evolution from oxidation of the ordered carbon deposits increased by 120 ˚C after removal of the amorphous carbon deposits by ozone. This may be due to the fact that, in the original sample containing carbonaceous deposits of variant oxidation reactivities, the heat released by the oxidation of the amorphous carbon deposits and associated hydrogen increased the temperature of the sample to about 583 ˚C while the temperature recorded by the furnace was still 462 ˚C, causing an apparent lowering of oxidation temperature of the ordered carbon deposits.

Another possibility for the shift of the high temperature CO_2 peak in Figure 5 could be oxidative coupling of the molecules in the carbonaceous deposits due to the interaction of the decomposed ozone species with the deposits during ozone oxidation. The decomposed ozonide can form hydroxyl, carbonyl and –C-O- surface moieties on the deposit[7].

Conclusions

The presence of a high temperature CO_2 peak after removal of most of the amorphous carbon deposits from the substrate is strong evidence that the highly ordered carbon deposits on the sample surface are created during thermal stressing and not produced as an artifact during the characterization of the samples during TPO.

Although the degree of oxidation by ozone may be inferior to that by a pure O_2 stream it is less energy intensive and the low temperatures can prolong substrate life[8].

Acknowledgement. We are grateful for financial support from the U.S. Air Force Office of Scientific Research.

References

1. Edwards, T. and S. Zabarnick, *Supercritical Fuel Deposition Mechanism.* Ind. Eng. Chem. Res., 1993. 32: p. 3117-3122.
2. Altin, O. and S. Eser, *Characterization of Carbon Deposits from Jet fuel on Inconel 600 and Inconel X Surfaces.* Ind. Eng. Chem. Res., 2000. 39(3): p. 642-645.
3. Sherry, S., M.J. Rossi, and D.M. Golden, *The Heterogeneous reaction of Ozone on Carbonaceous Surfaces.* International Journal of Chemical Kinetics, 1986. 18: p. 1133-1149.
4. Rakitskaya, T.L., et al., *Kinetics of Ozone Decomposition on Activated Carbons.* Kinetics and Calatysis, 1994. 35(1): p. 90-92.
5. Yu, J. and S. Eser, *Thermal Decomposition of C10- C14 Normal Alkanes in Near-Critical and Supercritical regions: Product Distributions and reaction Mechanisms.* Ind. Eng. Chem. Res., 1997. 36(3): p. 574-584.
6. Zhang, F., *Carbon Deposition on Heated Alloy Surfaces From Thermal Decomposition of Jet Fuel, Master's Thesis*, in *Energy & Geo-environmental Engineering*. 2000, Pennsylvania State University: University Park.
7. Yates, J.T.J. and M.D. B, *FTIR study of the oxidation of amorphous carbon by ozone at 300 K - Direct COOH formation.* Carbon, 2001. 39: p. 1167-1173.
8. Hutchings, G.J., et al., *A comparative study of reactivation of zeolite Y using oxygen and ozone/oxygen mixtures.* Applied catalysis, 1987. 34: p. 153-161.

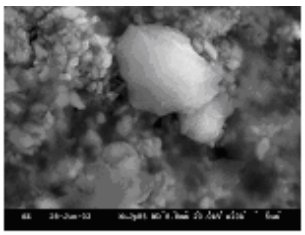

(a) - After thermal stressing

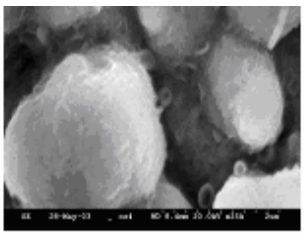

(b) - After Ozone oxidation

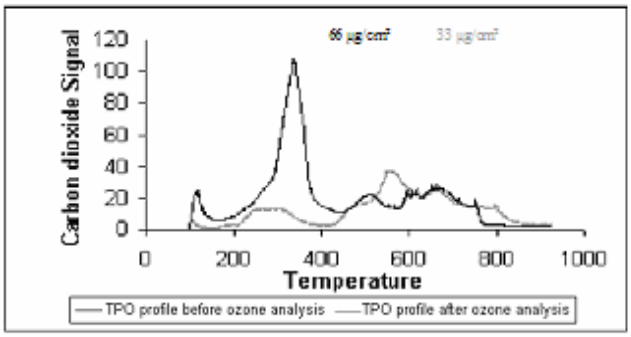

(c)

Figure 1: Comparsion of SEM images and TPO profiles of the carbon deposits produc from JP-8 stressed over Ni for 5 hours before and after ozone oxidation

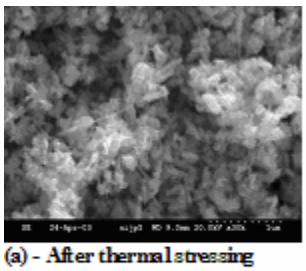

(a) - After thermal stressing

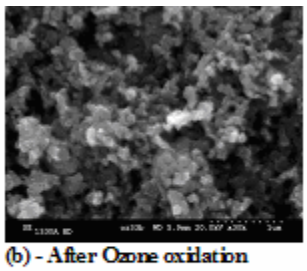

(b) - After Ozone oxidation

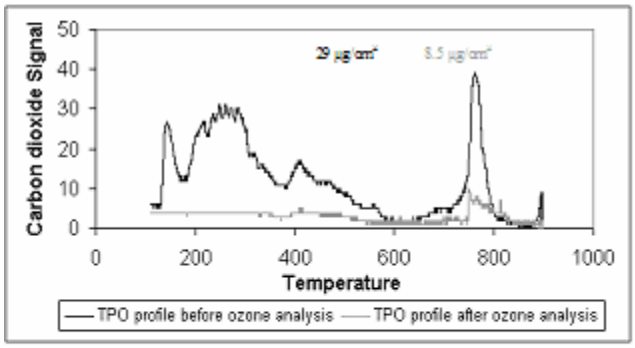

(c)

Figure 2: Comparison of SEM images and TPO profiles of carbon deposits formed from JP-8 stressed over Fe/Ni- 55/45 for 5 hours before and after ozone oxidation

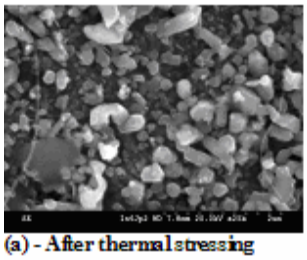

(a) - After thermal stressing

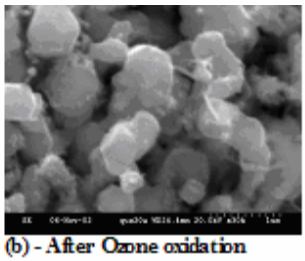

(b) - After Ozone oxidation

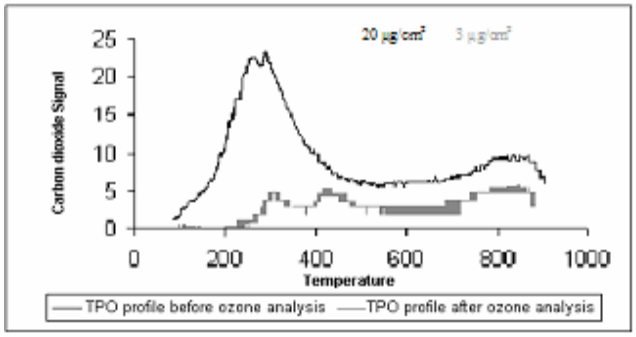

(c)

Figure 3: Comparison of SEM images and TPO profiles of carbon deposits produced from JP-8 stressed over Inconel 600 for 2 hours before and after ozone oxidation

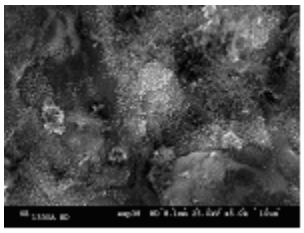

(a) - After thermal stressing

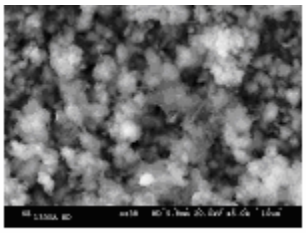

(b) - After Ozone oxidation

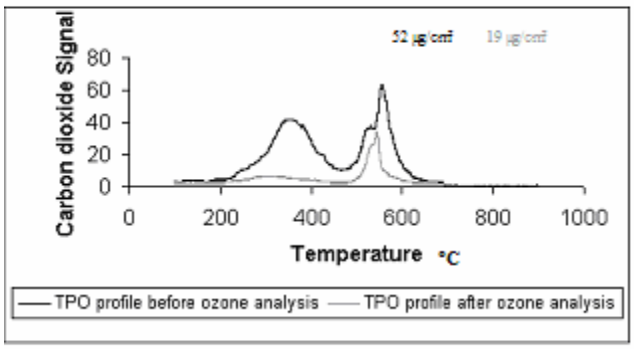

(c)

Figure 4: Comparison of the SEM images and TPO profiles of carbon deposits produced from Jet A stressed over SS321 for 24 hours, before and after ozone oxidation

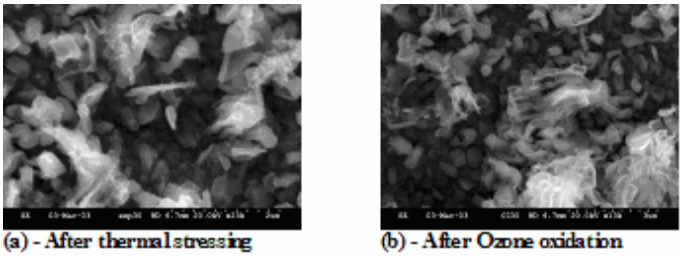

(a) - After thermal stressing (b) - After Ozone oxidation

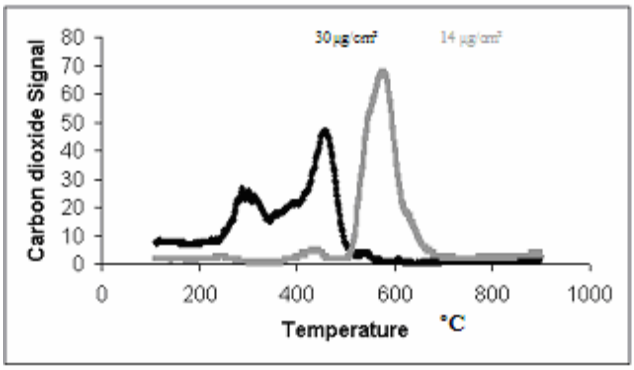

(c)

Figure 5: Comparison of SEM images and TPO profiles of carbon deposits produced from JP-8 stressed over SS321 for 24 hours before and after ozone oxidation